UNIVERSIDAD NACIONAL AUTÓNOMA DE MÉXICO

PROGRAMA DE MAESTRÍA Y DOCTORADO EN INGENIERÍA
INSTITUTO DE ENERGÍAS RENOVABLES
Energía – Fuentes renovables

NUEVOS DIAGRAMAS Y SOFTWARE PARA LA CLASIFICACIÓN DE ROCAS ÍGNEAS ALTERADAS CON APLICACIÓN A CAMPOS GEOTÉRMICOS

TESIS
QUE PARA OPTAR POR EL GRADO DE:

DOCTORA EN INGENIERÍA

PRESENTA:

M.I. MARÍA ABDELALY RIVERA GÓMEZ

TUTOR:

DR. SURENDRA PAL VERMA JAISWAL **IER-UNAM**

COMITÉ TUTORAL:

DR. PANDARINATH KAILASA	*IER-UNAM*
DR. ARMSTRONG ALTRIN SAM JOHN S.	*ICMyL-UNAM*
DRA. LORENA DÍAZ GONZÁLEZ	*CINC -UAEM*
DR. FERNANDO VELASCO TAPIA	*FCT-UANL*

Temixco, Morelos. Agosto 2017

JURADO ASIGNADO:

Presidente:	Dr. Kailasa Pandarinath
Secretario:	Dr. Armstrong Altrin Sam John S.
Vocal:	Dr. Verma Jaiswal Surendra Pal
1 er. Suplente:	Dra. Díaz González Lorena
2 d o. Suplente:	Dr. Velasco Tapia Fernando

Lugar donde se realizó la tesis: **Instituto de energías renovables (IER-UNAM) Temixco, Morelos.**

TUTOR DE TESIS:

Dr. Surendra Pal Verma Jaiswal

FIRMA

AGRADECIMIENTOS

A mi asesor el **Dr. Surendra Pal Verma Jaiswal** por todo el apoyo que me brindo.

A mis sinodales: **Dra. Lorena Díaz González, Dr. Pandarinath Kailasa, Dr. John S. Armstrong Altrin, Dr. Fernando Velasco Tapia**, por todas sus sugerencias en las evaluaciones a lo largo de esta tesis.

A la **Universidad Nacional Autónoma de México (UNAM)** que a través del **Instituto de Energías Renovables (IER)** me permitió realizar el doctorado.

Al **Consejo Nacional de Ciencia y Tecnología (CONACYT)** por el la beca otorgada durante mis estudios de Doctorado.

Al **Programa de Apoyo a los Estudios de Posgrado (PAEP)** por el apoyo económico para la compra de un equipo de cómputo necesario para realizar la tesis.

A la **Lic. Lourdes Araujo Carranza**, por su gran apoyo administrativo.

A **Norma Elia Becerril Salazar y Margarita Zavala**, por su apoyo administrativo.

Al **Lic. Fernando García, Carlos A. Ramírez y Atanacia Vargas** por el gran apoyo en proporcionar en tiempo y forma, el material bibliográfico que se requería, para ampliar y mejorar la base de datos de compilaciones, la cual se utilizó para el desarrollo de esta tesis.

Al **Dr. Maximiliano Valdez González** y a la **Lic. Margarita Pedraza Vargas** de la unidad de Cómputo del instituto, por el apoyo técnico brindado y en la parte de reparación de equipo de cómputo.

Al **Ing. Alfredo Quiroz Ruiz**, de la unidad de cómputo, por el apoyo en la parte de programación y colaboración en los trabajos que se realizaron a lo largo de mi tesis.

A **Juan Manuel Valero** y a **Cristopher** por su gran apoyo, paciencia y amistad que me brindaron en todo este tiempo que realice mi doctorado, gracias por los cuentos y por aceptarme en el taller, fue sin duda una muy buena aventura.

Al **Dr. Antonio del Rio Portilla**, actual director del IER, por su gran apoyo que me brindo y por darme la oportunidad de colaborar con él en un trabajo, es sin duda una gran persona a la cual respeto y agradezco mucho.

Agradezco a mis mejores amigos: **Iris, Cristian, José Campos y Elena**.

A mis compañeros: **Mauricio, Lorena y Alejandra**, por haberme dado la oportunidad de trabajar a su lado.

A mi hermana **Nancy y a su familia** por todo su gran apoyo y cariño.

A la familia de mi esposo, gracias.

DEDICATORIA

Esta tesis se la dedico a cinco personas que han sido una parte muy importante en mi vida, pero especialmente se la dedico a **Dios**, porque él ha sido el que me ha guiado hasta este punto en mi vida, desde que decidí seguirlo y aprender un poco de sus enseñanzas, encontré la paz en mi corazón y mi vida por fin tuvo sentido. “Él es el Alfa y la Omega, el primero y el último, el principio y el fin.”

A mi tutor el **Dr. Surendra Pal Verma**, porque ha sido para mí, un gran maestro durante un poco más de diez años que llevo de conocerlo, le agradezco especialmente porque él forma una parte muy importante en mi vida académica, sin él no hubiese sido posible este logro, gracias por toda su guía y sabiduría, espero que me permita seguir colaborando a su lado muchos años más.

A mi **esposo** y a mi **hermosa hija** por todo su amor, paciencia e inspiración que me brindan día con día para salir adelante en mi vida, los amo con todo mí ser, ustedes son lo más importante en mi vida.

A mi **mami** por todo su amor y apoyo incondicional en toda mi vida, ella me ha dado un buen ejemplo a seguir.

A mi **padre** por sus consejos, cariño y apoyo.

CONTENIDO

LISTA DE FIGURAS

LISTA DE TABLAS

RESUMEN

Esta tesis consta de seis capítulos, una sección de consideraciones finales y cinco anexos o Apéndices que contienen las publicaciones en las cuales participé activamente. Estas publicaciones en revistas internacionales arbitradas e indexadas en el "*Science Citation Index*" fueron obtenidas durante el desarrollo de esta tesis doctoral y se relacionan estrechamente con el presente documento.

El Capítulo 1 describe dos publicaciones referentes a la evaluación y aplicación de diagramas de discriminación tectonomagmática existentes en la literatura (**Apéndices I y II**). Adicionalmente, se menciona otra publicación realizada como coautora, un poco antes del inicio del doctorado.

El Capítulo 2 muestra una descripción detallada de los diagramas propuestos por la Unión Internacional de Ciencias Geológicas (IUGS; *International Union of Geological Sciences*) para la clasificación de rocas ígneas frescas, así como los diagramas que se han propuesto en la literatura para la clasificación de rocas ígneas alteradas. En este capítulo, se menciona una publicación en una revista internacional arbitrada e indexada en el *Science Citation Index*, en la que participé un poco antes del inicio de mis estudios de doctorado**.**

El Capítulo 3 describe el manejo coherente de los datos composicionales, una breve descripción sobre los datos discordantes en un espacio multivariado, así como lo que es el análisis discriminante lineal (LDA; *Linear Discriminant Analysis*)

El Capítulo 4 presenta una breve descripción de los diagramas que se propusieron en esta tesis; como resultado, participé en 3 trabajos publicados en revistas internacionales arbitradas e indexadas en el *Science Citation Index* (**Apéndices III – V**).

El Capítulo 5 describe la metodología computacional así como una breve descripción del uso de los programas orientados a web, los cuales desarrollé durante esta tesis. Este capítulo representa mi mayor contribución al desarrollo de las publicaciones internacionales.

El Capítulo 6 presenta la aplicación de los diagramas a diferentes campos geotérmicos del mundo.

Por lo anterior, se puede constatar que esta tesis, a la hora de su elaboración, cuenta como antecedentes, cinco publicaciones en revistas internacionales (4 publicados y 1 en el proceso de aceptación), mismas que se mencionarán oportunamente. Adicionalmente, al inicio del doctorado, ya contaba con otras tres publicaciones internacionales (la primera en la cual participé en 2011; otra relacionada con mi tesis de licenciatura y la tercera con la maestría – ambas en 2013).

INTRODUCCIÓN

Importancia de este trabajo en la energía geotérmica

Entre los puntos importantes de los estudios de petrogenesis de rocas ígneas se incluye su clasificación litológica y la determinación de su afinidad tectónica. De forma particular, las rocas asociadas a los campos geotérmicos pueden ser alteradas debido a procesos hidrotermales, los cuales pueden complicar la inferencia del origen de la roca, tipo de magma, o del ambiente tectónico predominante.

En el IER-UNAM (**I**nstituto de **E**nergías **R**enovables) se han propuesto nuevos diagramas de discriminación tectonomagmática para magmas ultrabásicos y básicos (Agrawal et al. 2004, 2008; Verma et al. 2006; Verma y Agrawal 2011), intermedios (Verma y Verma 2013), y ácidos (Verma et al. 2012, 2013a). Programas computacionales TecD (Verma y Rivera-Gómez 2013a) y TecDIA (Verma et al. 2015a) han facilitado la tarea de aplicar estos diagramas multidimensionales (p. ej., Pandarinath, 2014; Velasco-Tapia 2014; Verma et al. 2015b; SK Verma 2017).

Sin embargo, es importante conocer el tipo de magma de las rocas alteradas, previo a la alteración, para poder usar de forma correcta, estos diagramas.

El saber el tipo de magma en un campo geotérmico también tiene implicaciones energéticas. Esto se debe a que las propiedades térmicas y temperaturas de emplazamiento de las rocas dependen del tipo magma en el que se formó (ultrabásico, básico, intermedio o ácido). Por ejemplo, los magmas básicos se forman a temperaturas más altas que los magmas ácidos.

El tipo de roca previo a la alteración se utiliza como una de las variables de entrada en el modelado térmico tridimensional, el cual es una herramienta importante para entender la evolución de los campos geotérmicos a escala local y la temperatura presente en los contornos bajo la superficie (p. ej., Verma y Andaverde 2007; Verma y Gómez-Arias 2013).

La Unión Internacional de Ciencias Geológicas (IUGS; *International Union of Geological Sciences*) propuso una serie de recomendaciones para la clasificación y nomenclatura de las rocas ígneas relativamente frescas (Le Bas et al. 1986; Le Bas 2000; Le Maitre et al. 2002), siendo el diagrama TAS (***T**otal **A**lkalis versus **S**ilica diagram*; Le Bas et al. 1986) y la norma CIPW (Verma et al. 2003) los más utilizados en estas recomendaciones.

Mediante el diagrama TAS se puede clasificar las rocas volcánicas en ultrabásicas, básicas, intermedias y acidas, con relación a su contenido de sílice (SiO_2) (Le Bas et al. 1986). Este diagrama y el contenido de sílice están diseñados para las rocas volcánicas frescas más comunes (llamados en la presente tesis colectivamente como de tipo común) y no para rocas ricas en magnesio lo cual es determinado por un conjunto de criterios recomendados por la Unión Internacional de Ciencias Geológicas (Le Bas 2000; Le Maitre et al. 2002), tampoco debería ser utilizado para rocas alteradas o metamórficas. Desafortunadamente, esta advertencia no ha sido rescatada por la comunidad científica debido a varias razones, algunas de las cuales se enlistan a continuación: 1) Muchos científicos no están conscientes del problema; 2) Las alternativas existentes (otros diagramas; ver abajo en esta sección) han sido usadas, en ocasiones pero no siempre; y 3) La comunidad tampoco está consciente o debidamente enterada que estos diagramas alternos no son realmente aptos para reemplazar el TAS.

En Verma et al. (2002), los autores presentaron un programa de cómputo titulado SINCLAS (***S**tandard **I**gneous **N**orm and volcanic rock **CLA**ssification **S**ystem*) para la clasificación de rocas volcánicas frescas, utilizando el esquema IUGS, el cual facilita la aplicación del diagrama TAS, así como proporciona una forma estandarizada para el cálculo de la norma CIPW (Verma et al. 2003).

Verma y Rivera-Gómez (2013b) desarrollaron un nuevo software llamado IgRoCS (***Ig**neous **Ro**ck **C**lassification **S**ystem*), el cual sigue las recomendaciones de la IUGS para la clasificación de las rocas ígneas (plutónicas y volcánicas); este programa representa una versión actualizada y mejorada del programa SINCLAS (Verma et al. 2002).

Debido a que la IUGS no especificó la clasificación para rocas ígneas alteradas, en la actualidad se utilizan los diagramas propuestos hace más de 30 años por Floyd y Winchester (1975, 1978), Winchester y Floyd (1976, 1977) y, más recientemente hace unos 10 años, el de

Hastie et al. (2007). Sin embargo, en el trabajo de Verma et al. (2010b) los autores han demostrado que estos diagramas tienen poca eficiencia , por lo que existe una urgente necesidad de proponer nuevos diagramas de clasificación y nomenclatura para las rocas ígneas alteradas, los cuales sean consistentes con la IUGS y que se aplique correctamente una metodología estadística para el manejo de datos composicionales (Verma et al. 2010a, 2010b).

El objetivo de esta tesis fue realizar mediante el análisis discriminante lineal conjuntos de diagramas de clasificación para rocas ígneas alteradas, los cuales fueran consistentes con la nomenclatura recomendada por la IUGS, así como desarrollar programas computacionales que faciliten el uso de estos diagramas de forma correcta y eficiente.

Durante el desarrollo de la tesis, se logró la publicación de cuatro trabajos y la aceptación de uno en revistas internacionales arbitradas de alto impacto indizadas en el *Science Citation Index*, los cuales se presentan en cinco **Apéndices** (**I–V**). Se menciona la lista de estos trabajos a continuación:

Apéndice I: Rivera-Gómez, M.A., Verma, S.P., 2016. Testing of multidimensional tectonomagmatic discrimination diagrams on fresh and altered rocks. Geologica Carpathica, 67: 195-208.

Apéndice II: Verma, S.P., Pandarinath, K., **Rivera-Gómez, M.A.**, 2016a. Evaluation of the ongoing rifting and subduction processes in the geochemistry of magmas from the western part of the Mexican Volcanic Belt. Journal of South American Earth Sciences, 66: 125-148.

Apéndice III: Verma S.P., **Rivera-Gómez, M.A.**, Díaz-González, L., Quiroz-Ruiz, A., 2016b. Log-ratio transformed major element based multidimensional classification for altered High-Mg igneous rocks. Geochemistry, Geophysics, Geosystems, 17: doi:10.1002/2016GC006652.

Apéndice IV: Verma S.P., **Rivera-Gómez, M.A.**, Díaz-González, L., Pandarinath, K., Amezcua-Valdez, A., Rosales-Rivera, M., Verma, S.K., Quiroz-Ruiz, A., Armstrong-Altrin, J.S., 2017. Multidimensional classification of magma types for altered igneous rocks and application to their tectonomagmatic discrimination and igneous provenance of siliciclastic sediments. Lithos, 278-281: 321-330, doi: 10.1016/j.lithos.2017.02.005.

Apéndice V: Verma, S.P., **Rivera-Gómez, M.A.**, 2017. Transformed major element based multidimensional classification of altered volcanic rocks. Episodes (aceptado).

En esta tesis, se describe brevemente los principales logros obtenidos en estos trabajos aunque mayores detalles se encuentran en los anexos. Además, se incluyen aplicaciones adicionales a campos geotérmicos. Cabe mencionar que adicionalmente se mencionan los antecedentes de otros tres trabajos publicados (Verma et al. 2011; Verma y Rivera-Gómez 2013a; Verma y Rivera-Gómez 2013b), en los cuales participé como coautora, previo al inicio de mis estudios doctorales.

OBJETIVO GENERAL

El presente proyecto doctoral tiene el objetivo de proponer nuevos diagramas de clasificación para rocas ígneas alteradas, desarrollar programas computacionales para la aplicación eficiente de estos diagramas y, finalmente, aplicar los nuevos diagramas a campos geotérmicos.

CAPÍTULO 1

Diagramas de Discriminación Tectonomagmática

Este capítulo está basado en dos trabajos (Rivera-Gómez y Verma 2016 – **Apéndice I** y Verma et al. 2016a – **Apéndice II**) directamente relacionados con la presente tesis, en los cuales participé y mismos que fueron publicados en revistas internacionales arbitradas e indexadas en el SCI (*Science Citation Index*). Además, se cuenta con dos (Verma et al. 2011; Verma y Rivera-Gómez 2013a) que fueron publicados antes del inicio de mi tesis doctoral.

Apéndice I: Rivera-Gómez, M.A., Verma, S.P., 2016. Testing of multidimensional tectonomagmatic discrimination diagrams on fresh and altered rocks. Geologica Carpathica, 67: 195-208.

Apéndice II: Verma S. P., Pandarinath, K., **Rivera-Gómez, M. A.**, 2016a. Evaluation of the ongoing rifting and subduction processes in the geochemistry of magmas from the western part of the Mexican Volcanic Belt. Journal of South American Earth Sciences, 66: 125-148.

1.1 Diagramas de discriminación tectonomagmática

Los diagramas de discriminación tectonomagmática ayudan a inferir el ambiente tectónico en que se originaron las rocas, mediante el análisis de las relaciones de elementos químicos, principalmente aquellos de naturaleza inmóvil ante la alteración o el metamorfismo de bajo grado.

Pearce y Cann (1971, 1973) fueron los pioneros en descubrir que la afinidad tectónica podía ser inferida a partir de la composición geoquímica de las rocas. Desde entonces, muchos diagramas geoquímicos se han propuesto en la literatura para discriminar diferentes ambientes tectónicos, mismos que fueron descritas y evaluadas por Verma (2010).

Específicamente, en el trabajo de Verma (2010), se realizó una evaluación de 28 diagramas de discriminación tectonomagmática para magmas básicos y ultrabásicos, demostrando que los diagramas más eficientes y con mejores tasas de éxito, son los propuestos por Agrawal et al. (2004, 2008) y Verma et al. (2006).

Sin embargo, aplicar estos conjuntos de diagramas requiere de cálculos bastante complejos, por lo que era altamente recomendable contar con una herramienta computacional. Por consecuencia, en el 2010 durante mi tesis de maestría, desarrollé un programa llamado TecD (*Tectonomagmatic Discrimination*), en el cual estos diagramas fueron programados. Posteriormente, TecD fue publicado en el año 2013 un poco antes del inicio de mi tesis de doctorado, en la revista "*Journal of Iberian Geology*" (**Verma y Rivera-Gómez 2013a**). Cabe mencionar que, después de finalizar mi tesis de maestría y justo antes de iniciar doctorado, dediqué tiempo y esfuerzo para adecuar el programa TecD, con el propósito publicarlo en una revista internacional.

En los trabajos de Verma y Verma (2013) y Verma et al. (2012, 2013a), los autores propusieron nuevos diagramas de discriminación tectónica para magmas de tipo intermedio y ácido y, posteriormente, se desarrolló un programa para facilitar el uso de estos diagramas llamado TecDIA (Verma et al. 2015a).

Dado que es necesario conocer *a priori* el tipo de magmas con el fin de escoger el conjunto o los conjuntos de diagramas tectonomagmáticos, se realizaron adecuaciones y mejorías para publicar este trabajo en una revista internacional. Se trata de la evaluación de los diversos programas, tanto comerciales como de acceso libre, incluyendo uno (IgRoCS) escrito por Verma y Rivera-Gómez (2013b); ver el **Capítulo 2**. Cabe mencionar que IgRoCS resultó ser el mejor y sumamente consistente con la IUGS, para inferir el tipo de magmas y de rocas ígneas frescas. Por otra parte, para rocas alteradas, dado que este esquema no es recomendado, se requiere otros procedimientos, mismos que fueron desarrollados en la presente tesis (**Capítulos 4 y 5**).

1.2 Programa de cómputo TecD (*Tectonomagmatic Discrimination"*)

TecD es un programa informático (Verma y Rivera-Gómez 2013a), escrito en *Visual Basic,* el cual contiene cuatro conjuntos de cinco diagramas cada uno, basados en funciones discriminantes (Agrawal et al. 2004, 2008; Verma et al. 2006; Verma y Agrawal 2011), para discriminación de cuatro ambientes tectónicos y para magma de tipo ultrabásico y básico: arco de isla (IAB; llamado así aunque incluye arco continental), rift continental (CRB), isla oceánica (OIB), cordilleras oceánicas (MORB). TecD genera un reporte final, el cual puede ser interpretado por el usuario, de forma sencilla, con el fin de inferir el ambiente tectónico. El diagrama de flujo se muestra en la Figura 1.1.

Verma y Rivera-Gómez (2013a) aplicaron la herramienta computacional a tres ejemplos de diferentes partes del mundo, a fin de ilustrar el uso del programa: (a) *Faroe Islands* edad de ~56 Ma (Océano Atlántico), (b) *Abitibi Greenstone Belt* edad de ~2700 Ma (Canadá) y (c) *Mallina Basin* edad de ~2950 Ma (Australia).

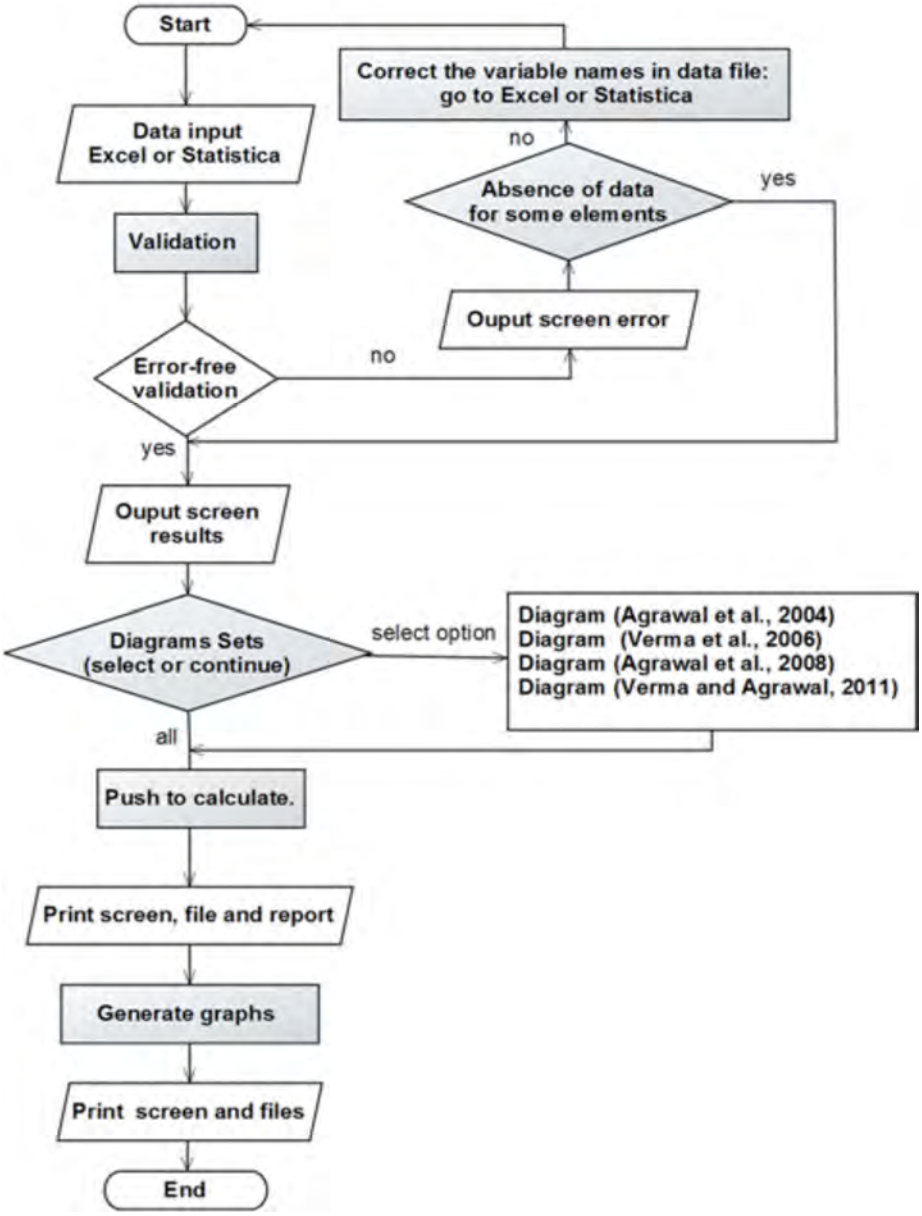

Figura 1.1 Diagrama de flujo TecD, tomada de Verma y Rivera-Gómez (2013a).

1.3 Evaluación de los diagramas de discriminación tectonomagmática

Durante el desarrollo de la presente tesis de doctorado, realicé un trabajo como primer autor, el cual formó parte importante para mi formación y comprensión del funcionamiento de los diagramas de discriminación. El propósito fue evaluar el funcionamiento de un total de 55 diagramas de discriminación multidimensional, para magmas ultrabásicos, básicos, intermedios y ácidos (**Rivera-Gómez y Verma 2016**; **Apéndice I**).

Para este trabajo, realicé una compilación de 2469 de muestras de análisis geoquímicos de rocas ígneas, de las cuales se utilizaron 1034 muestras del Mioceno al Holoceno, para representar las diferentes áreas con ambientes tectónicos conocidos alrededor del mundo y sin controversia entre diferentes autores. Además, las rocas compiladas fueron reportadas por los autores como relativamente frescas. Las muestras restantes fueron usadas para posterior investigación.

En la Figura 1.2 se muestra la localización de las muestras en un mapa. Se dividió la base de datos por países y después se aplicó el programa IgRoCS (Verma y Rivera-Gómez 2013b) para clasificar las muestras por tipo de magma. Posteriormente, se utilizaron los programas TecD (Verma y Rivera-Gómez 2013a) para determinar el ambiente tectónico de las muestras que eran de tipo ultrabásico o básico y TecDIA (Verma et al. 2015a) para tipo intermedio y acido. De esta forma, se compararon los resultados con respecto a los ambientes tectónicos esperados, que los autores reportaban. En total, se evaluaron 18 casos de estudio. Adicionalmente, se usaron 8 casos de aplicación para rocas hidrotermalmente alteradas y meteorizadas. Mayor información se presenta en el **Apéndice I.**

El resultado de esta evaluación fue satisfactorio, ya que, en la mayoría de los casos, la tectónica esperada fue la que se obtuvo con los diagramas, además de que se señaló que la calidad de los datos es un factor determinante para obtener mejores resultados con los diagramas (**Apéndice I)**.

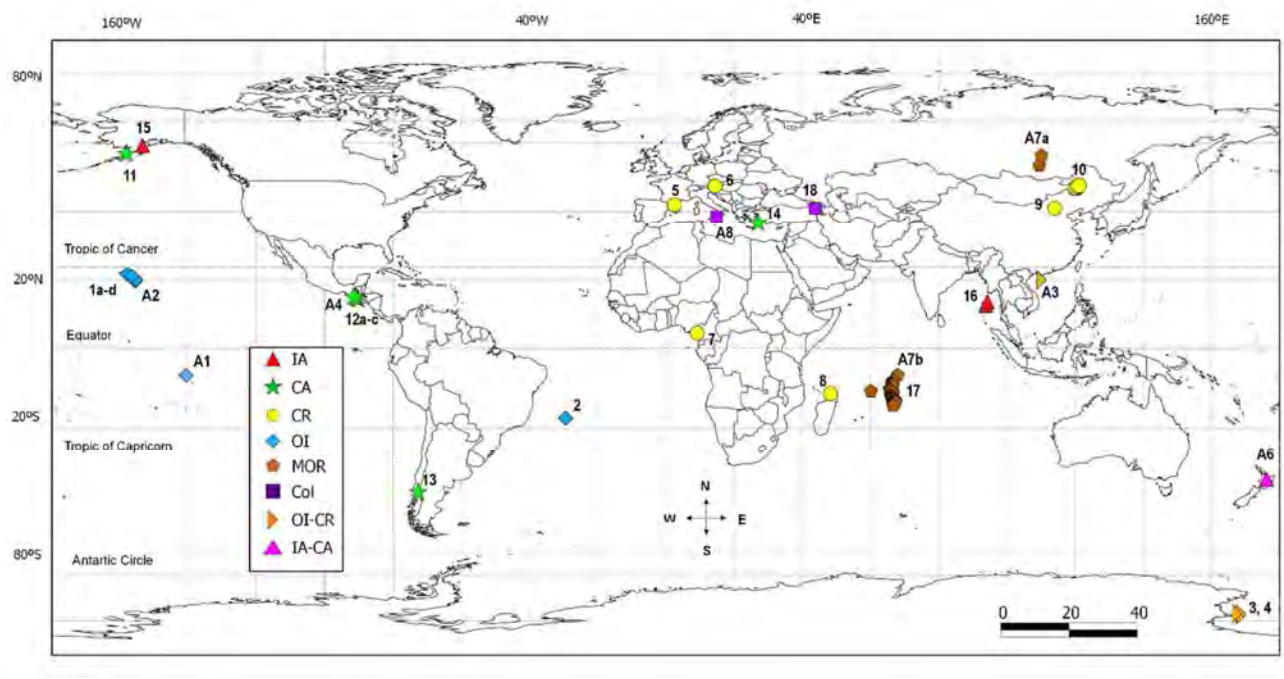

Figura 1.2 Localización de los 18 casos (1-18) y 8 casos de aplicación (A1-A8), tomada de Rivera-Gómez y Verma (2016).

1.4 Aplicación de diagramas al Oeste del Cinturón Volcánico Mexicano (WMVB)

Previo al doctorado, yo había participado ya como coautora en un trabajo (Verma et al. 2011) de la evaluación de diagramas multidimensionales de discriminación tectonomagmática recientemente propuestos (Agrawal et al. 2004, 2008; Verma et al. 2006; Verma y Agrawal 2011) y su aplicación para inferir los ambientes tectónicos de magmas básicos en el Sur de México y América Central.

Durante mi doctorado, también participé en un trabajo con el objetivo de evaluar, mediante la química de las rocas, varios aspectos de los procesos de volcanismo en el oeste del Cinturón Volcánico Mexicano (CVM). Primero, se evaluó el vulcanismo del Mioceno previo al proceso de rift en el bloque de Jalisco asociado al rift de Baja California. Luego, se abordó, además de la subducción actual de las placas de Cocos y Rivera a lo largo del MAT (*Middle American Trench*), el efecto del sistema de tres rifts continentales (**Verma et al. 2016a**; **Apéndice II**).

Para esta aplicación, participé activamente en establecer una compilación de datos geoquímicos de un total de 1512 muestras del Mioceno al Holoceno de la parte oeste del Cinturón Volcánico Mexicano (WMVB). Esta provincia geológica es conocida también como el Cinturón Volcánico Trans-Mexicano (TMVB; *Trans-Mexican Volcanic Belt*).

Las muestras compiladas, para ser analizadas mediante programas de cómputo, se dividieron de acuerdo a su localización geográfica en muestras que se encontraban en zonas de "rifts" y las que se encontraban alejadas de los rift "no-rift".

Varios programas de cómputo fueron utilizados para realizar este trabajo. Primero, para obtener el nombre de la roca y el tipo de magma, se utilizó el programa IgRoCS (Verma y Rivera-Gómez 2013b). El uso de IgRoCS es totalmente justificado ya que las rocas compiladas de acuerdo al reporte de los autores, son relativamente frescas. Posteriormente, se empleó el programa DODESSYS (Verma y Díaz-González 2012) para aplicar pruebas de discordancia y separar los datos discordantes. De igual manera, se aplicó UDASYS (Verma et al. 2013b) para realizar las pruebas de significancia y otros cálculos estadísticos. Finalmente, se utilizaron los programas TecD (Verma y Rivera-Gómez 2013a) y TecDIA (Verma et al. 2015a) para aplicar diagramas de discriminación tectonomagmática a los datos compilados del WMVB.

Las conclusiones fueron que las rocas básicas muestreadas en el área de los rifts representan los porcentajes entre el 48%-71% para el ambiente de rift, mientras que las rocas básicas que se encontraban en el área de "no-rift" sugieren un ambiente de rift o un arco. Sin embargo, las rocas intermedias con una componente de corteza son más consistentes con un arco continental. Las rocas ácidas del área de los rifts con una componente de corteza indican que el ambiente es un rift continental o una transición de arco continental al interior de la placa (*within-plate*), mientras que las del área no-rift, aunque menos numerosos, sugieren un arco. Para mayor información, ver el **Apéndice II**.

CAPÍTULO 2

Diagramas de Clasificación para Rocas Ígneas

En este capítulo, se hace referencia al trabajo publicado en una revista internacional (Verma y Rivera-Gómez 2013b), en el cual participé activamente un poco antes del inicio del doctorado. Este trabajo se relaciona con mi tesis de licenciatura; sin embargo, las mejorías y adecuaciones fueron realizadas posteriormente.

2.1 Diagramas de clasificación para rocas ígneas frescas

La IUGS (Le Bas et al. 1986; Le Maitre et al. 2002) propuso una recomendación para la clasificación y nomenclatura de rocas ígneas relativamente frescas. La clasificación primaria que proponen está basada en el contenido mineral de la roca; sin embargo, cuando es imposible determinar esto por la presencia de vidrio o porque los granos son muy finos, se recomienda realizar la clasificación por medio de la composición química de la roca en el diagrama TAS (Le Bas et al. 1986).

En el trabajo de Verma y Rivera-Gómez (2013b)**,** se presentó el programa IgRoCS, el cual sigue las recomendaciones de la IUGS para la clasificación de las rocas ígneas.

Específicamente, IgRoCS tiene la opción de clasificar las rocas como lo especifica la IUGS mediante la composición mineral de la roca, usando las tablas y diagramas ternarios propuestos, así como también la clasificación mediante la composición química en el diagrama TAS y la norma CIPW.

El diagrama TAS es el diagrama más utilizado para la clasificación de rocas volcánicas. Este diagrama se basa en los datos de la composición química de las sumas del contenido de Na_2O (óxido de sodio) y K_2O (óxido de potasio), los cuales representan los álcalis totales, y el contenido de SiO_2 (óxido de sílice). Generalmente, estos datos son tomados directamente del análisis de la roca en forma de porcentaje en peso (wt%, *percentage by weight)*, mejor dicho de porcentaje en masa/masa (%m/m; Figura. 2.1). Sin embargo, esta práctica es errónea ya que se debe emplear los datos ajustados de los parámetros arriba señalados, después del ajuste del Fe en forma de los dos óxidos (FeO y Fe_2O_3) y suma de 100% en base seca (Le Bas et al. 1986). Afortunadamente, IgRoCS permite el uso correcto del diagrama TAS.

La nomenclatura de este diagrama está diseñada para rocas ígneas volcánicas, también llamadas extrusivas, por lo que para las rocas plutónicas o intrusivas la clasificación y nomenclatura se debe determinar con la composición mineral de la roca en el diagrama QAPF (Streckeisen 1976). Sin embargo, existe un diagrama para clasificar con la química de la roca, propuesto por Middlemost (1994) para rocas plutónicas, el cual es equivalente al diagrama TAS (total álcalis *versus* sílice; Figura 2.2).

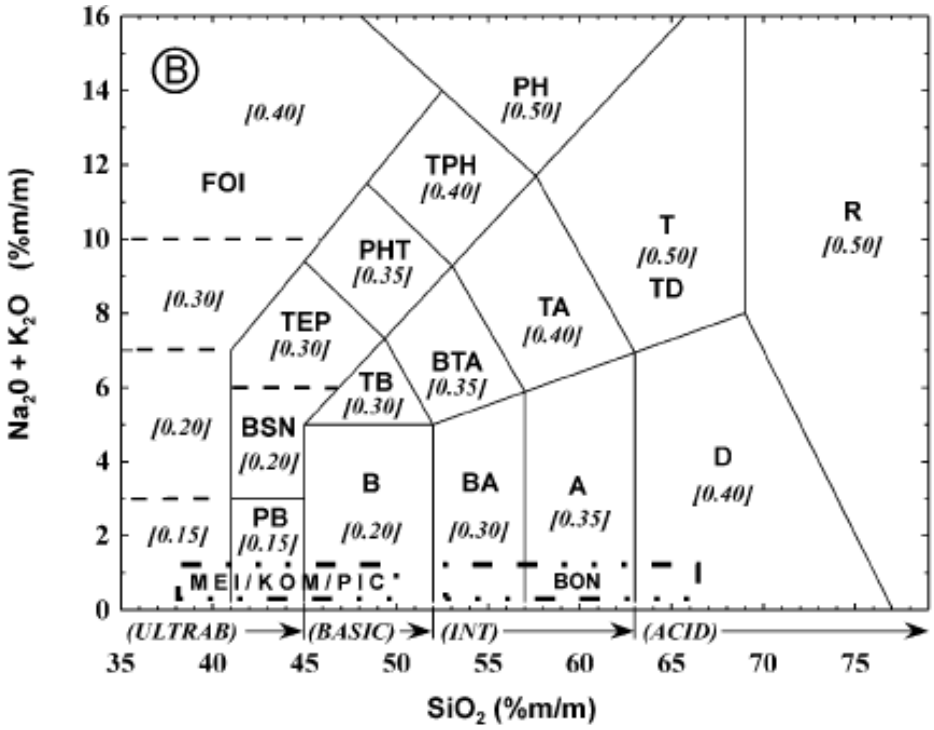

Figura.2.1 Diagrama TAS (*Total Alkalis versus Silica diagram* de Le Bas et al. (1986), tomada de Verma et al. (2002).

2.2 Diagramas propuestos para clasificación rocas ígneas alteradas

La IUGS hasta la fecha no ha propuesto ninguna recomendación o esquema de clasificación para rocas ígneas alteradas. Sin embargo, en la literatura existen algunas alternativas para clasificación de este tipo de rocas, los cuales son ampliamente utilizados, pero el problema principal es que no son consistentes con la nomenclatura propuesta por la IUGS.

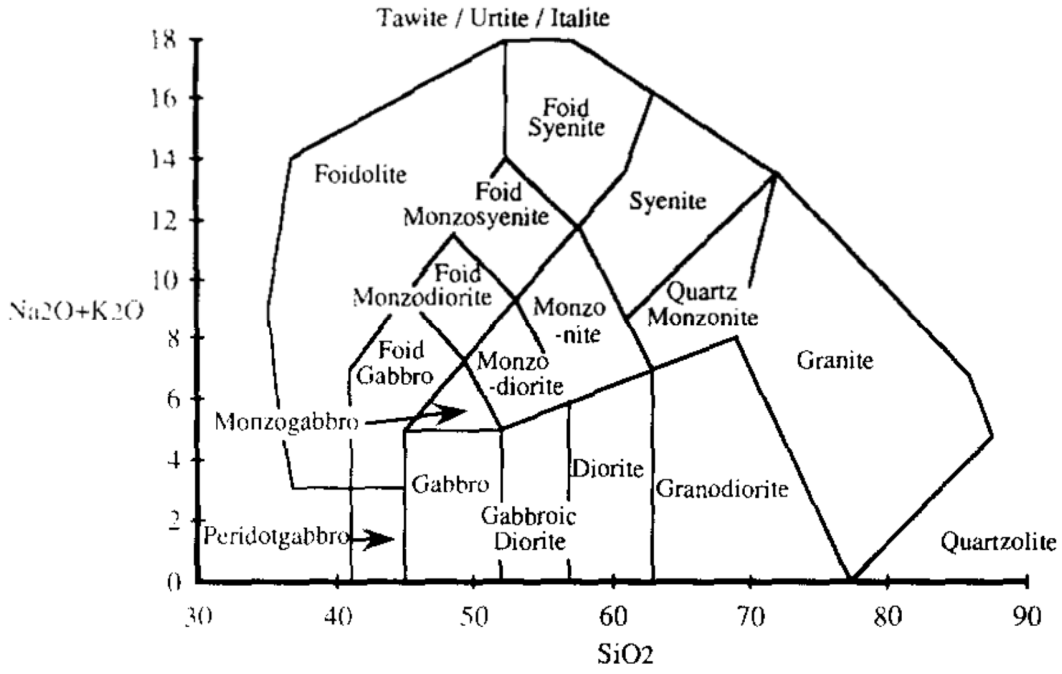

Figura. 2.2 Propuesta de clasificación química y nomenclatura para rocas plutónicas, tomada de Middlemost (1994).

2.2.1 Diagramas de Floyd y Winchester (1975), Winchester y Floyd (1976)

Floyd y Winchester (1975) y Winchester y Floyd (1976) presentaron un conjunto de cinco diagramas, basados en la abundancia de los llamados elementos inmóviles (Ti, P, Zr, Y, Nb) los cuales discriminan entre basaltos alcalinos y toleíticos. Los autores de dichos trabajos indicaron que mediante estos diagramas no se puede hacer una discriminación significativa entre los basaltos continentales y los oceánicos.

Los diagramas que se presentan en este trabajo son los siguientes: (1) TiO_2 – Zr; (2) TiO_2 – Y/Nb; (3) P_2O_5 – Zr; (4) TiO_2 – Zr/P_2O_5; (5) Nb/Y – Zr/P_2O_5. Ver (Figura 2.3):

1. *TiO2-Zr*

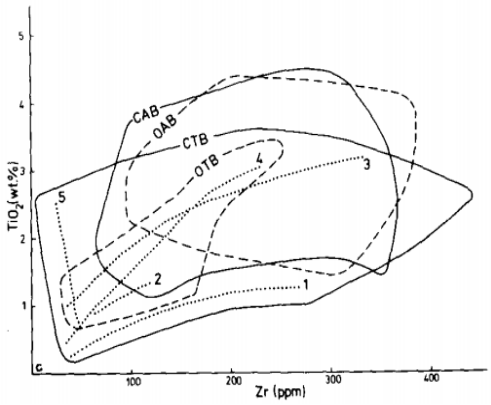

2. *TiO2-Y/Nb*

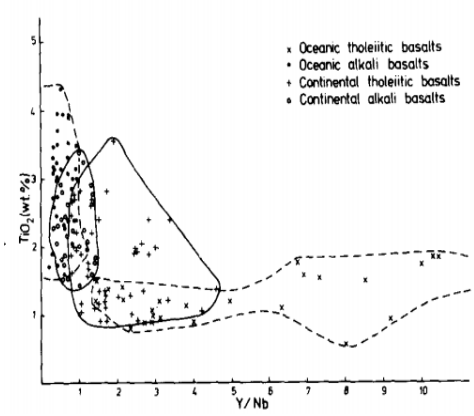

3. *P2O5-Zr*

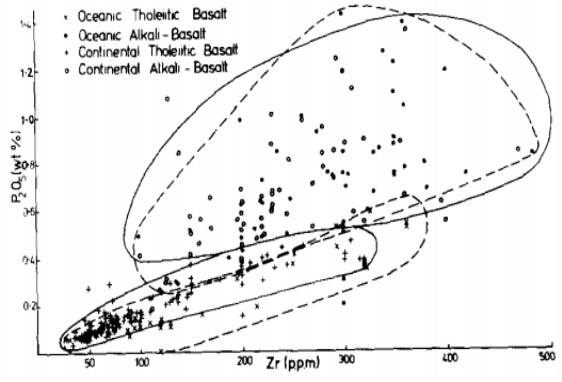

4. *TiO2- Zr/P2O5*

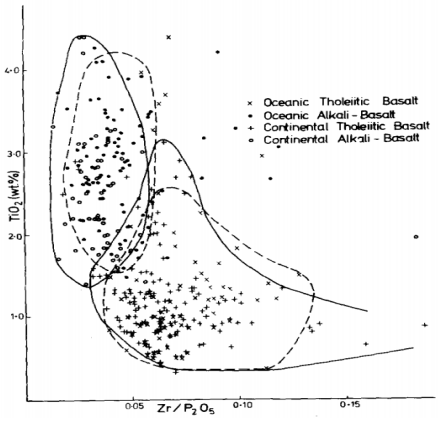

5. *Nb/Y- Zr/ P2O5*

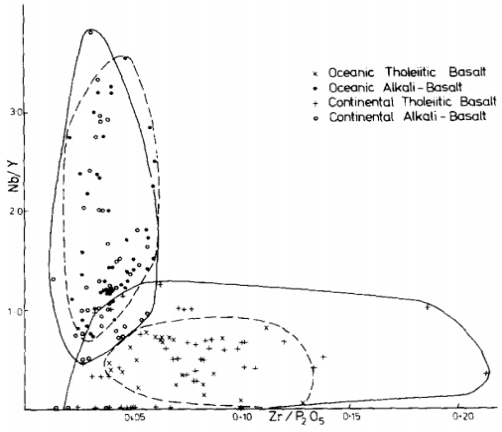

Figura. 2.3 Diagramas propuestos por Floyd y Winchester (1975) y Winchester y Floyd (1976).

2.2.2 Diagramas de Winchester y Floyd (1977) y Floyd y Winchester (1978)

Winchester y Floyd (1977) y Floyd y Winchester (1978) presentaron un conjunto de diagramas basados en un grupo de elementos (Ti, Zr, Y, Nb, Ce, Ga y Sc), los cuales según los autores se considera que permanecen inertes durante el proceso secundario de alteración, incluyendo espilitización, alteración submarina y metaforismo. Esto no es totalmente válido según algunas investigaciones (p. ej., Torres-Alvarado et al. 2007; Pandarinath et al. 2008).

Los autores (Winchester y Floyd 1977; Floyd y Winchester 1978) mencionan que la aportación principal de este trabajo fue la de establecer un medio químico para diferenciar diferentes tipos de rocas y series de magma, los cuales se pueden aplicar a rocas metamórficas o a una extensa gama de rocas alteradas (Figura 2.4). Los diagramas propuestos por estos autores son:

1.- SiO_2 – Zr/TiO_2;

2.- SiO_2 – Nb/Y;

3.- Zr/TiO_2 – Nb/Y;

4.- Zr/TiO_2 – Ce;

5.- Zr/TiO_2 – Ga;

6.- Ga/Sc – Nb/Y.

1. SiO_2-Zr/TiO_2 2. SiO2-Nb/Y

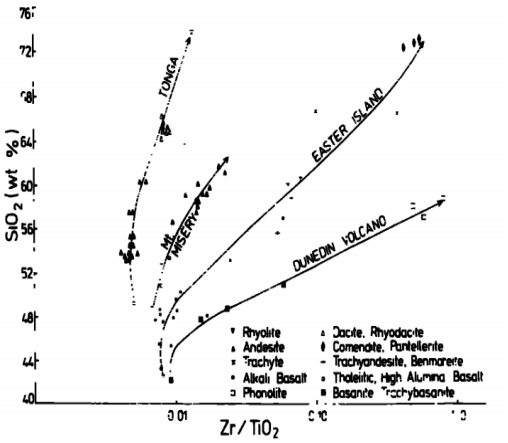

3. Zr/TiO2-Nb/Y

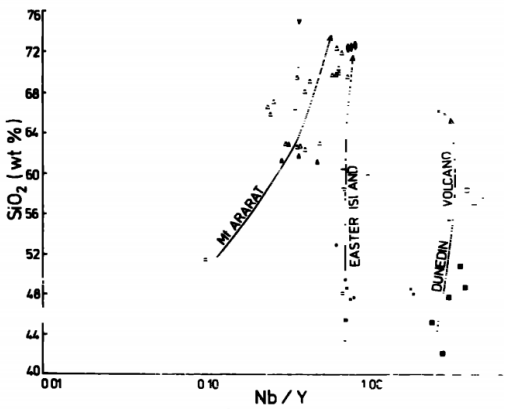

4. Zr/TiO2-Ce

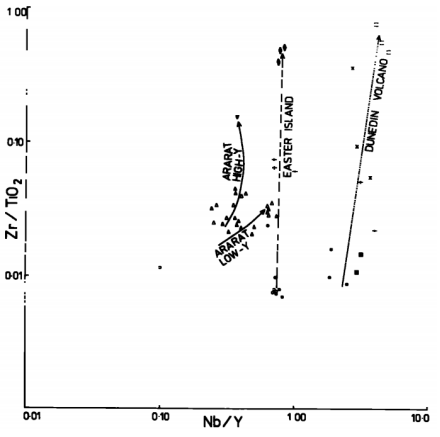

5. Zr/TiO2-Ga

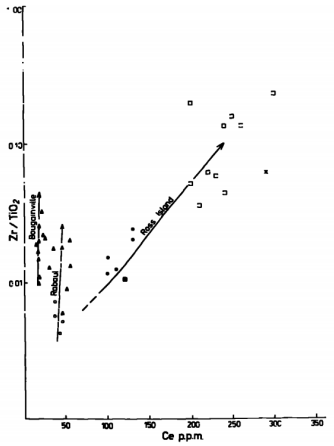

6. Ga/Sc -Nb/Y

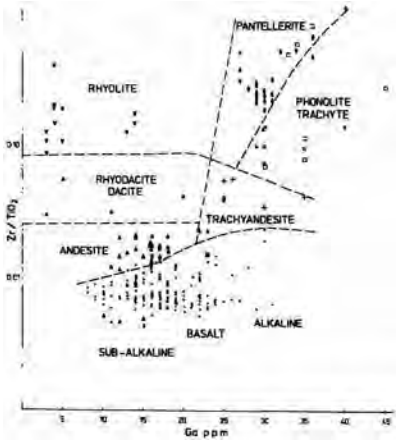

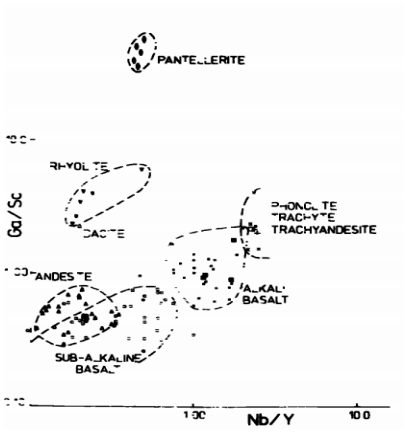

Figura. 2.4 Diagramas propuestos por Winchester y Floyd (1977) y Floyd y Winchester (1978).

2.2.3 Diagrama de Hastie et al. (2007)

Hastie et al. (2007) propusieron un diagrama de clasificación para rocas ígneas alteradas. Ellos reconocieron que existe la necesidad de un método confiable para clasificar rocas, además de que ninguno de los diagramas que se usan frecuentemente, como el de SiO_2-K_2O (Peccerillo y Taylor 1976) y el diagrama TAS recomendado por la IUGS (Le Bas et al. 1986), son apropiados para la clasificación de rocas ígneas alteradas.

Los autores de este trabajo mencionan que, aunque Winchester y Floyd (1977) desarrollaron diagramas con elementos inmóviles, la necesidad sigue existiendo. Por lo tanto, propusieron el uso de dos elementos Co y Th en un nuevo diagrama bivariado.

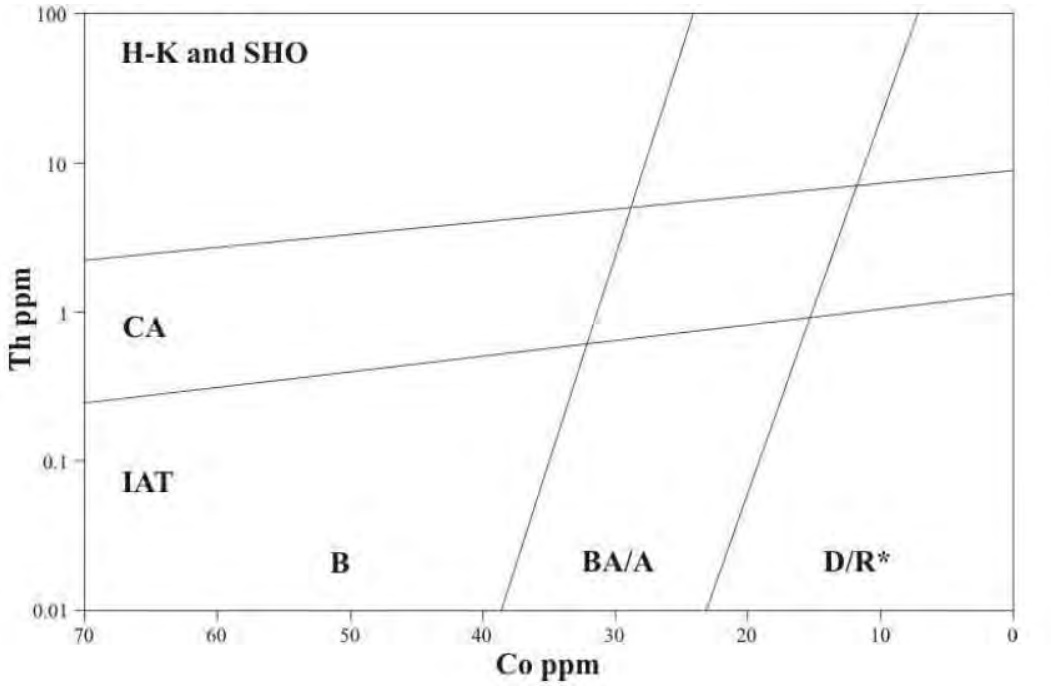

Fig. 2.5 Diagrama Co-Th (Hastie et al. 2007).

Para este diagrama, los autores utilizaron más de 1000 muestras del Terciario-Reciente de arco de isla, obtuvieron el 80% de éxito cuando aplicaron este diagrama a algunos tipos de

roca con alteración hidrotermal. Sin embargo, para la aplicación de este diagrama a rocas alteradas, los autores no señalaron cómo saber de antemano que las rocas efectivamente provienen de un arco, tampoco especificaron qué hacer con las rocas que provienen de otros ambientes tectónicos.

2.2.4 Evaluación estadística de los diagramas clasificación

Verma et al. (2010b) realizaron un análisis de los diagramas existentes en la literatura tales como los diagramas propuestos por Floyd y Winchester (1975, 1978), Winchester y Floyd (1976, 1977) y Hastie et al. (2007).

Estos autores mencionan en este trabajo (Verma et al. 2010b) que no fue posible evaluar los diagramas Zr-P_2O_5; Zr-TiO_2; Y/Nb-TiO_2; Zr/P_2O_5-TiO_2; Zr/P_2O_5-Nb/Y propuestos por Floyd y Winchester (1975) y Winchester y Floyd (1976), debido a que sólo distinguen dos tipos de rocas basálticas toleíticas y alcalinas, y el término toleítico no fue recomendado por la IUGS.

Los diagramas SiO_2-Zr/TiO_2; SiO_2-Nb/Y propuestos por Winchester y Floyd (1977) y Floyd y Winchester (1978), tampoco fueron evaluados porque, entre otras razones, ambos diagramas utilizan la variable "SiO_2", la cual es susceptible a cambios aún bajo procesos de baja alteración.

Tampoco se consideraron los diagramas Zr/TiO_2-Ce; Zr/TiO_2-Ga en la evaluación, debido a que en estos diagramas los diferentes tipos de basaltos y basanitas no se distinguen claramente y, en el caso de los magmas subalcalinos, los elementos Ce y Ga no se incrementan significativamente con la diferenciación.

El diagrama Ga/Sc -Nb/Y propuesto por Winchester y Floyd (1977), no fue evaluado por Verma et al. (2010b) debido a que los datos en los que se basó el diagrama fueron particularmente escasos y las fronteras no fueron propuestas en forma definitiva por los autores de este diagrama.

Finalmente, Verma et al. (2010b) compararon el diagrama Zr/TiO_2-Nb/Y propuesto por Winchester y Floyd (1977), con el diagrama TAS. Lo mismo fue el caso del diagrama propuesto por Hastie et al. (2007).

De acuerdo con Verma et al. (2010a, 2010b), los diagramas de tipo bi-variado no funcionarían bien para rocas volcánicas alteradas. Por esta razón, surgió la gran necesidad de explorar más en este campo y proponer nuevos diagramas de clasificación para las rocas ígneas alteradas mediante métodos estadísticos para identificar datos discordantes, análisis de discriminación lineal, manejo coherente de los datos composicionales y que además sean consistentes con la nomenclatura de la IUGS. La presente tesis y las publicaciones internacionales relacionadas cubren esta deficiencia en la literatura mundial.

CAPÍTULO 3

Análisis de Datos de Composición Química

En este capítulo, se aborda el tema de la complejidad y limitaciones de datos composicionales, siendo un campo de la investigación actual.

1.1 Manejo coherente de datos composicionales

Los datos composicionales nos ayudan a caracterizar de forma cuantitativa una muestra. Debido a la gran cantidad de datos de composición que se utilizan en el área de las Geociencias, se han estudiado los problemas que han surgido al aplicar el análisis estadístico tradicional. Los datos composicionales representan un campo cerrado. Otro problema existente con el uso de datos composicionales es el de la suma constante, el cual fue estudiado por Chayes (1960), advirtiendo que los datos de composición están sujetos a la condición de que la suma de todas las variables del análisis es constante. En palabras sencillas, las variables composicionales no son totalmente independientes, siendo el requisito fundamental para aplicar la estadística convencional.

Verma et al. (2010b) explica este problema mediante una figura (Figura 3.1), en la cual se puede observar que los datos composicionales tienen la limitación de graficarse sólo dentro de un triángulo, por lo que los valores negativos y valores mayores a 100 están prohibidos. De esta forma, los diagramas en los cuales se utilizan datos composicionales en los ejes tienen el problema de que provienen de un campo cerrado, en el cual la suma de sus constituyentes siempre será de 1 para fracciones o 100% para porcentajes (Verma et al. 2010a).

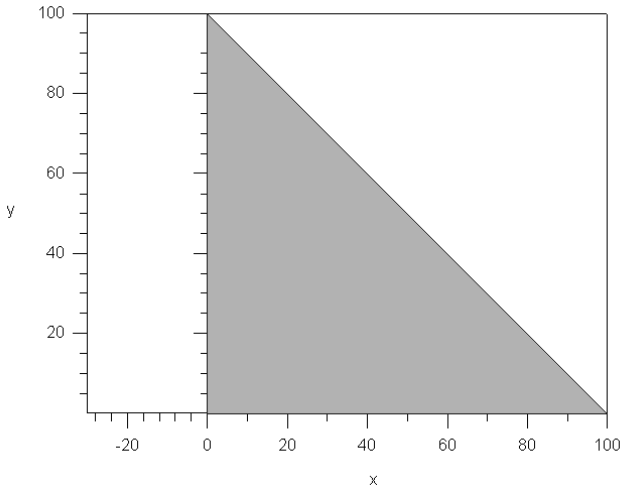

Figura 3.1 Diagrama que muestra el campo cerrado de los datos composicionales, tomada de Verma et al. 2010b).

La solución factible a este problema se encontró hasta los años 80, cuando Aitchison (1982, 1986) formuló una serie de principios a los que debe responder el análisis de datos composicionales. Además, propuso una solución la cual consiste en estudiar el comportamiento de log-cocientes (log-ratios) invariantes por escala, mediante la geometría simplex en un espacio euclidiano, la cual permite representar las composiciones en coordenadas reales.

Desde entonces, los principios formulados por Aitchison para el análisis de los datos composicionales, han sido reformulados por varios autores, tales como Aitchison y Egozcue (2005), Martín-Fernández et al. (2003), Egozcue y Pawlowsky-Glahn (2006). Los principales conceptos asociados a las relaciones logarítmicas, son los siguientes:

- **Invariante bajo cambio de escala**: Las unidades de medición no nos proporcionan información relevante, pero si los logaritmos de las relaciones elementales. La conclusión generada por el análisis de estas relaciones no debería de cambiar al multiplicar las composiciones por una constante.

- **Coherencia sub-composicional:** al extraer y analizar una parte de la composición, el resultado del análisis debe ser compatible con la información de la composición completa.

- **Escala relativa simetrizada:** Egozcue y Pawlowsky-Glahn (2011) explican con un ejemplo este principio:

  "*una concentración de 150mg/l de Na, debe considerarse el triple de otra de 50mg/l, mientras que concentraciones de* $106x10^3$ *y* $106x10^3$+***100mg/l*** *apenas se pueden lograr diferenciar entre sí".*

Entonces, debido a que cada uno de los elementos medidos sobre una muestra tiene una escala relativa, es necesario evitar que las diferencias entre dos concentraciones dependan de su valor. Esto se hace midiendo las diferencias mediante los respectivos logaritmos.

- **Invariancia por permutación: "***las conclusiones de un análisis composicional no deben depender de la ordenación de las partes*" (Egozcue y Pawlowsky-Glahn 2011).

Aitchison (1982, 1986) utilizó estos principios para proponer la llamada transformación relación-log-aditiva (alr, *additive-log-ratio*). En donde el logaritmo natural se aplica a cada una de las componentes, el cociente elimina las unidades que puedan multiplicar a las partes y el logaritmo se hace cargo de la escala relativa.

$$alr(x) = \left[\ln\frac{x_1}{x_D}, \ln\frac{x_2}{x_D}, \cdots, \ln\frac{x_{D-1}}{x_D}\right]$$

donde

$x = [x_1, x_2, \ldots, x_D]$ *Son los elementos del vector de composiciones.*

Ecuación 1

También introdujo la transformación llamada relación-log-centrada (clr, *centred-log-ratio*), la cual consiste en dividir cada parte entre la media geométrica de todas las partes g(x) y calcular el logaritmo como se muestra en las ecuaciones 2 y 3.

$$g(x) = \sqrt[n]{\prod_{i=1}^{n} x_i} = \sqrt[n]{x_1 \cdot x_2 \cdots x_n}$$

Ecuación 2

$$clr(x) = \left[ln\frac{x_1}{g(x)}, ln\frac{x_2}{g(x)}, \ldots., ln\frac{x_D}{g(x)}\right] = \ln\left(\frac{x}{g(x)}\right)$$

Ecuación 3

Egozcue et al. (2003) introdujeron otro tipo de transformación logarítmica, denominada relación-log-isométrica (ilr, *isometric-log-ratio*). Ellos propusieron esta transformación por medio de bases ortonormales y como resultado descompusieron el simplex, como espacio vectorial, en sub-espacios ortogonales y mostraron que esta transformación del simplex a un espacio real multidimensional tiene importantes propiedades. Se observa en la Ecuación 4 (Egozcue et al. 2003).

$$ilr(x) = \sqrt{\frac{i}{i+1}} ln\left[\frac{g(x_1, \cdots, x_i)}{x_{i+1}}\right]$$

$$donde \quad i = 1, 2, \cdots, D-1, \qquad \text{Ecuación 4}$$

Verma (2015) realizó una comparación de los diagramas convencionales ternarios con los nuevos diagramas bivariados basados en relación log y utilizó las tres diferentes propuestas de transformaciones (alr, clr e ilr). Todas las transformaciones proporcionaron exactamente el mismo resultado final cuando se usa la misma base de datos. El autor finalmente llegó a la conclusión que, aunque no hay diferencias significativas entre las tres transformaciones, la ilr es la recomendada como la mejor alternativa de transformación, ser más reciente en comparación con las otras dos, por tratarse de una transformación isométrica y que los datos ilr-transformados se representan en los ejes ortogonales.

Por lo tanto, para este trabajo de tesis se decidió utilizar la transformación ilr para los datos de composición.

1.2 Datos discordantes

Los datos discordantes o también llamados en inglés *"discordant outliers"*, son datos extremos que se encuentran inmersos en un conjunto de datos, con una distribución normal o gaussiana, producto de algún proceso de medición. Por diversas razones, resultan ser "extraños", por lo que son sospechosos de no pertenecer al conjunto de datos en donde se encuentran o simplemente pertenecen a un evento fuera de lo ordinario.

Mediante pruebas estadísticas de discordancia, se pueden detectar los datos discordantes en un conjunto de datos, para poder separarlos y depurar, en gran medida, la información. De esta forma, se puede garantizamos en algún grado, la integridad de nuestra información. Por lo tanto, podemos optimizar los resultados que se obtienen al aplicar técnicas estadísticas multivariadas a los datos (Verma 2016), tomando en cuenta que, para poder aplicar estas técnicas, se debe cumplir el requisito de que el conjunto de datos sean multinormalmente distribuidos.

Para este trabajo de tesis, se aplicó la prueba de discordancia multivariada de Wilks mediante el uso del programa DOMuDaF (***D****iscordant* ***O****utlier from* ***Mu****ltivariate* ***Da****ta through* ***F-****test of* w; Verma et. al. 2016b), para detectar los datos discordantes en un espacio multivariado en el dominio de datos transformados ilr.

3.3 Análisis de Discriminación Lineal (*LDA; Lineal Discriminant Analysis*)

El análisis de discriminación lineal por sus siglas en inglés (LDA, *Linear Discriminant Analysis*), es una técnica estadística multivariada que permite encontrar una combinación lineal de varios elementos, que logre separar dos o más clases de objetos o eventos.

Esta técnica ha sido de gran utilidad durante años en el área de las Geociencias. Sin embargo, la metodología tradicional no había sido del todo satisfactoria por varias razones. Una de ellas fue que la obtención de las líneas de clasificación se realizaba visualmente. No fue hasta que, en el trabajo de Agrawal (1999), al utilizar esta técnica estadística, se podían establecer los límites o las fronteras de las clases de forma objetiva basadas en el uso de probabilidades y no de forma visual. Posteriormente en el trabajo de Agrawal et al. (2004), se presentaron los diagramas de discriminación que distinguieron con éxito diferentes ambientes tectónicos mediante probabilidades para delimitar las fronteras de cada clase. Aún más recientemente (2006-2013), se ha empleado exitosamente la técnica de LDA con el fin de proponer otros diagramas multidimensionales (Verma et al. 2006, 2012, 2013a; Agrawal et al. 2008; Verma y Agrawal 2011; ver también los Capítulos 4 y 5 de esta tesis).

Para el realizar el análisis de discriminación lineal, se utilizó el sub-modulo "*Discriminant Analysis"* en el módulo "*Multivariate Exploratory Techniques"* del software comercial Statistica®.

CAPÍTULO 4

Propuesta de Diagramas de Clasificación para Rocas Ígneas Alteradas

En este capítulo, se describen tres trabajos, en los cuales participé durante el desarrollo de esta tesis de doctorado y se encuentran publicados en revistas internacionales incluidas en el *Science Citation Index*.

Apéndice III: Verma S. P., **Rivera-Gómez, M.A.**, Diaz-Gonzalez L., Quiroz-Ruiz A., 2016b. Log-ratio transformed major element based multidimensional classification for altered High-Mg igneous rocks. Geochemical, Geophysics, Geosystems, 17: doi:10.1002/2016GC006652.

Apéndice IV: Verma S. P., **Rivera-Gómez, M.A.**, Diaz-Gonzalez L., Pandarinath, K., Amezcua-Valdez A., Rosales-Rivera M., Verma, S.K., Quiroz-Ruiz A., Armstrong-Altrin J.S., 2017. Multidimensional Classification of Magma Types for Altered Igneous Rocks and Application to their Tectonomagmatic Discrimination and Igneous Provenance of Siliciclastic Sediments. Lithos, doi: 10.1016/j.lithos.2017.02.005.

Apéndice V: Verma, S.P., **Rivera-Gómez, M.A.**, 2017. Transformed Major Element based Multidimensional Classification of Altered Volcanic Rocks. Episodes (en proceso de aceptación).

4.1 Diagramas de clasificación para rocas con Alto-Magnesio

Se realizó una nueva clasificación en un esquema multidimensional, para rocas alteradas de tipo Alto-Magnesio (*High-Mg*), la cual es consistente con la nomenclatura especificada por la IUGS. Como producto de este trabajo, se obtuvo una publicación, la cual se encuentra en el **Apéndice III**.

Debido a que la IUGS especificó que, antes de realizar la clasificación por el diagrama TAS, se debe evaluar si la roca es de tipo Alto-Magnesio. En este trabajo (**Apéndice III**), se consideró la propuesta hecha por Le Bas (2000) para determinar la nomenclatura de la roca, de acuerdo con la cual se presentan cuatro categorías de rocas de tipo Alto-Magnesio:

1. Si MgO > 8%, SiO_2 > 52% y TiO_2<0.5%, entonces es una boninita (*boninite*).

2. Si MgO >18%, SiO_2 entre 30% y 52% y (Na_2O +K_2O) < 2%. entonces es una komatiita o meimequita, las dos se pueden distinguir por *komatiite* < 1% TiO_2 y *meimechite* > 1% TiO_2.

3. Si MgO > 12%, SiO_2 entre 30 y 52% y (Na_2O +K_2O) < 3%, entonces es una picrita (*picrite*).

4. Si estas condiciones no se cumplen, entonces el siguiente paso es graficar el en diagrama de clasificación TAS con el fin de determinar el tipo de roca ígnea (volcánica o plutónica) común.

Nuestro procedimiento para realizar esta clasificación mediante un esquema multivariable se encuentra basado en una extensa base de datos de elementos mayores (SiO_2, TiO_2, Al_2O_3, $Fe_2O_3^t$, MnO, MgO, CaO, Na_2O, K_2O y P_2O_5).

4.1.1 Base de datos

El primer paso fue realizar una función, la cual pudiera discriminar las rocas de Alto-Magnesio de las de tipo común. Para esto, su utilizó una base de datos de **37,219** muestras de rocas relativamente frescas y del Mioceno-Reciente. Estas muestras fueron procesadas por el programa IgRoCS (Verma y Rivera-Gómez 2013b), para obtener su nomenclatura.

Posteriormente, se realizó la transformación ilr de los elementos mayores de la base de datos y la primera función discriminante utilizando LDA. Los porcentajes de éxito quedaron como se muestra en la Tabla 1.

Tabla 1. *Porcentajes de éxito de la primera función para discriminar Alto-Magnesio (High-Mg) - Común (Common).*

	Porcentaje correcto	**Número de muestras**	
		Alto-Magnesio	*Común*
Alto-Magnesio	84.85%	**863**	154
Común	97.88%	768	**35434**

Tabla 2. *Resumen de datos discordantes que detecto el programa OMUVAF.*

Nombre de la Roca	Total de muestras iniciales	Datos discordantes	Porcentaje de datos discordantes	No. total de muestras sin datos discordantes
Andesite (andesita)	4515	379	8%	4136
Basaltic andesite (andesita basáltica)	4221	337	8%	3884
Basalt, alkali (basalto alcalino)	2212	207	9%	2005
Basalt, subalkali (basalto subalcalino)	8048	704	9%	7344
Basanite, basanite (basanita)	1078	74	7%	1004
Basanite, melanephelinite (basanita, melanefelinita)	468	47	10%	421
Basanite, nephelinite (basanita, nefelinita)	64	5	8%	59
Basaltic trachyandesite, mugearite (traquiandesita basáltica, mugearita)	901	51	6%	850
Basaltic trachyandesite, shoshonite (traquiandesita basáltica, shoshonita)	900	72	8%	828
Dacite (dacita)	3120	370	12%	2750
Foidite, basanite (foidita, basanita)	7	0	0%	7
Foidite, melanephelinite (foidita, melanefelinita)	210	28	13%	182
Foidite, nephelinite (foidita, nefelinita)	108	29	27%	79
Picrobasalt (picrobasalto)	76	4	5%	72
Phonolite (fonolita)	284	17	6%	267
Phonotephrite (fonotefrita)	368	27	7%	341
Ryolite (riolita)	3773	436	12%	3337
Ryolite, peralkaline (riolita peralcalina)	404	16	4%	388
Trachyte (traquita)	1224	109	9%	1115
Trachyte, peralkaline (traquita peralcalina)	198	12	6%	186
Trachyandesite, benmoreite (traquiandesita, benmorita)	526	52	10%	474
Trachyandesite, latite (traquiandesita, latita)	1156	92	8%	1064
Trachybasalt, hawaiite (traquibasalto, hawaiita)	901	72	8%	829
Trachybasalt, potassic (traquibasalto potásico)	724	67	9%	657
Trachydacite (traquidacita)	248	24	10%	224
Tephrite, basanite (tefrita, basanita)	200	11	6%	189
Tephrite, melanephelinite (tefrita, melanefelinita)	98	4	4%	94
Tephrite, nephelinite (tefrita, nefelinita)	30	1	3%	29
Tephriphonolite (tefrifonolita)	140	7	5%	133
Boninite (boninita)	136	10	7%	126
Komatiite (komatita)	82	6	7%	76
Meimechite (meimechita)	195	23	12%	172
Picrite (picrita)	604	58	10%	546
Totales	**37219**	**3351**	**9%**	**33868**

Se utilizó el programa DOMuDaF (***D**iscordant **O**utlier from **Mu**ltivariate **Da**ta through **F-**test of w)* (Verma et. al. 2016b), para detectar **3351** datos discordantes y, de esta forma, lograr a mejorar el resultado del análisis discriminante. La Tabla 2 proporciona los porcentajes de datos discordantes que detectó el programa DOMuDaF (Verma et. al., 2016b) por cada tipo de roca, debido a que el programa IgRoCs proporciona la nomenclatura en idioma inglés, en la Tabla 2 se muestran los nombres de roca en español e inglés.

Para obtener la función de discriminación final, se usó la base de datos depurada; en total, se usaron 33,868 muestras, con 920 de tipo Alto-Magnesio y 32,948 de tipo común.

En la Tabla 3, se comparan los porcentajes de éxito entre el uso de la base de datos original y la libre de valores discordantes. Se observan los porcentajes de éxito que, como se puede observar, se incrementaron de 84.85% a 86.41% para rocas de tipo Alto-Magnesio y del 97.88% a 98.88% para rocas de tipo Común.

Tabla 3. *Porcentajes de éxito de la primera función para discriminar Alto-Magnesio (High-Mg) - Común (Common) después de utilizar el programa OMUVAF.*

	Porcentaje correcto	**Numero de muestras**	
		Alto-Magnesio	*Común*
Alto-Magnesio	**86.41%**	**795**	125
Común	**98.88%**	369	**32579**

La Figura 4.1 presenta en un diagrama TAS las muestras de la base datos tipo común (*Common*) que se utilizaron en el entrenamiento para obtener las funciones discriminantes. En la Figura 4.2, se muestra el mapa de la localización geográfica de estas muestras.

Las muestras de tipo Alto-Magnesio (*High-Mg*), por su naturaleza, son menos abundantes en la tierra. Sin embargo, para la base de entrenamiento se buscó tener la mayor representatividad posible de los cuatro tipos de rocas de Alto-Magnesio, así como también su distribución geográfica en el mundo. En la Figura 4.3, se muestra la distribución de las rocas de Alto-Magnesio, así como la localización de los casos de prueba y los de aplicación, utilizados en el artículo publicado y presentado en el **Apéndice III**.

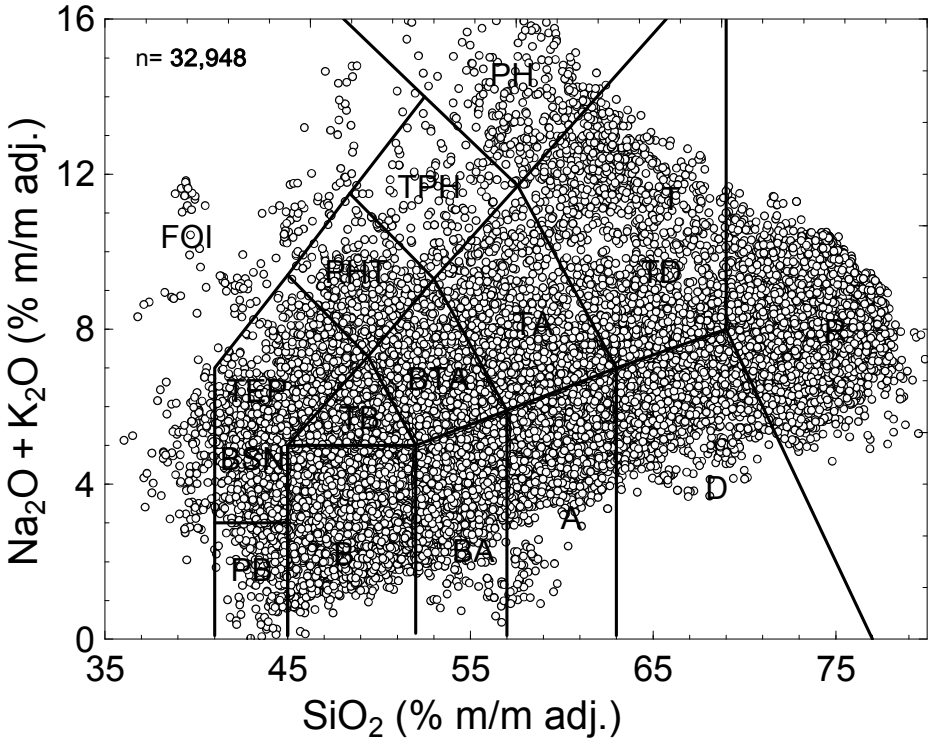

Figura 4.1 Representación de la distribución de las muestras de tipo común en el diagrama TAS (Le Bas et al. 1986).

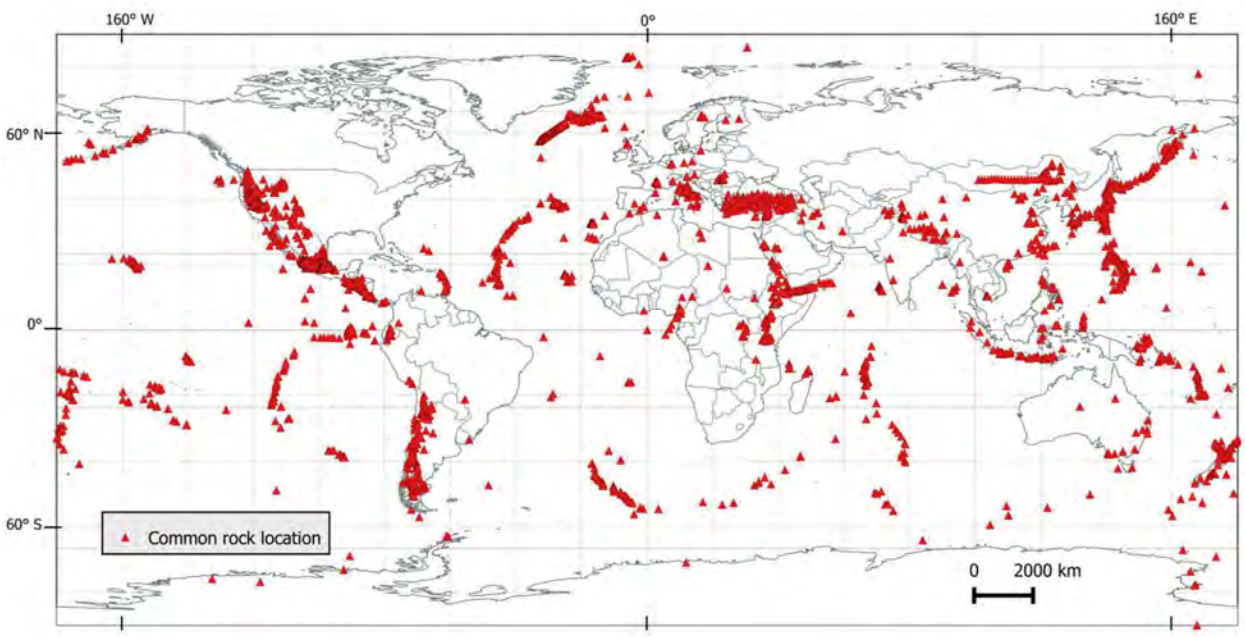

Figura 4.2 Representación de la localización de las muestras de tipo común, tomada de Verma et al. (2016b).

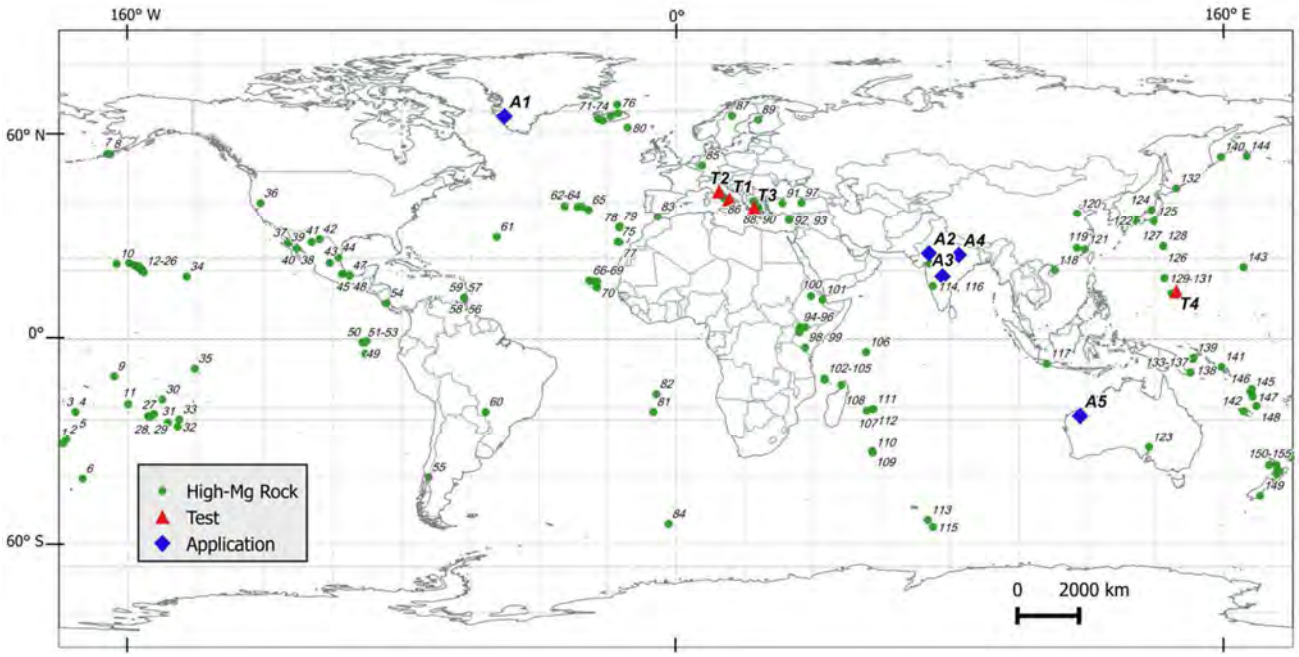

Figura 4.3 Representación de la localización de las muestras de tipo Alto-Magnesio, casos de prueba y casos de aplicación, tomada de Verma et al. (2016b).

4.1.2 Diagrama de discriminación Alto-Magnesio–*Común* (*HighMg–Common*)

La función discriminante para separar rocas de Alto-Magnesio (*High-Mg*) de rocas tipo común (*Common*) se presenta en la Ecuación 5. Más información se encuentra en el **Apéndice III**.

$$\mathrm{DF}_{(\mathrm{HMg-Com})\mathrm{M}} = (7.3517 \times \mathrm{ilr1}_{\mathrm{TiM}}) + (10.3179 \times \mathrm{ilr2}_{\mathrm{AlM}}) + (3.8554 \times \mathrm{ilr3}_{\mathrm{FeM}}) + (4.5485 \times \mathrm{ilr4}_{\mathrm{MnM}}) + (3.5601 \times \mathrm{ilr5}_{\mathrm{MgM}}) + (5.9130 \times \mathrm{ilr6}_{\mathrm{CaM}}) + (5.8599 \times \mathrm{ilr7}_{\mathrm{NaM}}) + (4.7085 \times \mathrm{ilr8}_{\mathrm{KM}}) + (4.6514 \times \mathrm{ilr9}_{\mathrm{PM}}) - 6.2604$$

Ecuación 5

En la Figura 4.4 se muestra la representación gráfica de la clasificación de las muestras de la base de datos de entrenamiento, mediante la función discriminante "DF $_{(Hmg\text{-}Com)M}$" (**ver Ecuación 5**), los porcentajes de éxito que se obtuvieron (**ver Tabla 3**), así como la frontera entre los dos grupos "$(HMg\text{-}Com)_{boundaryM}$" (**Apéndice III**).

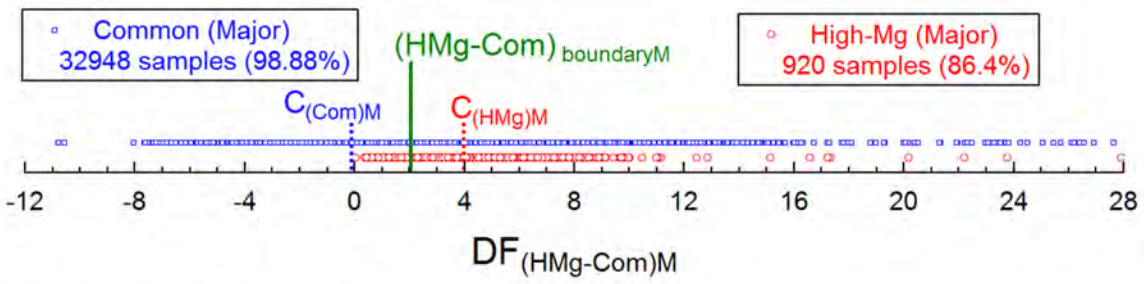

Figura 4.4 Función discriminante DF(HMg-Com)M para *High-Mg* (HMg) y *Common* (Com), tomada de Verma et al. (2016b).

4.1.3 Cinco diagramas para clasificación de rocas tipo Alto-Magnesio

Se utilizó una base de datos de 920 muestras de rocas de tipo Alto-Magnesio, dividida en cuatro clases (Le Bas 2000).

- 76 *komatiite* (komatiita)
- 172 *meimechite* (meimequita)
- 546 *picrite* (picrita)
- 126 *boninite* (boninita)

Mediante análisis discriminante LDA, se calcularon 10 funciones de discriminación en 5 diagramas, para discriminar los cuatro diferentes tipos de rocas de rocas de Alto-Magnesio.

En la Figura 4.5, se puede apreciar los porcentajes de éxito que se obtuvieron en cada uno de los cinco diagramas así como los centroides de las muestras de entrenamiento. Las ecuaciones de las fronteras se encuentran en el **Apéndice III**.

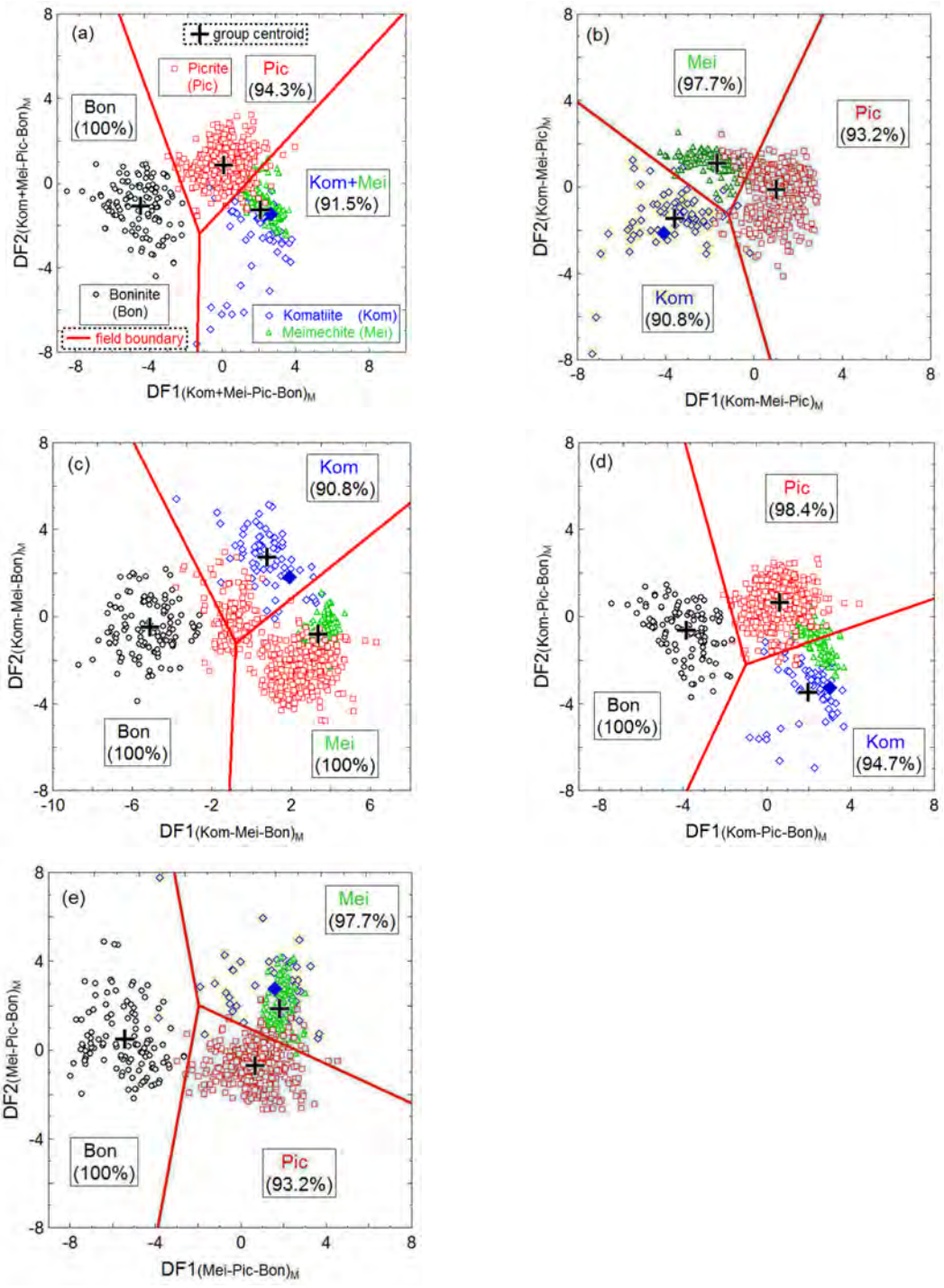

Figura 4.5 Cinco diagramas basados en elementos mayores transformados por ilr, para clasificar 4 tipos de rocas, (komatiita, meimequita, picrita y boninita), tomada de Verma et al. (2016b).

Sin embargo, cabe aclarar que la graficación de las muestras en los diagramas, es sólo para esquematizar al usuario el resultado, debido a que, para llegar a un resultado de la clasificación final, se calcula directamente de la probabilidad de cada una de las muestras en cada diagrama así como las probabilidades obtenidas en los cinco diagramas en conjunto.

Para este trabajo (**Apéndice III**), se realizaron siete casos de prueba de muestras relativamente frescas y que no se encontraran dentro de las base de datos de entrenamiento, para evaluar estos nuevos diagramas de clasificación y sus funciones discriminantes. Información adicional se presenta en el **Apéndice III.** De la misma manera, se evaluaron cinco casos de aplicación.

Este nuevo esquema de clasificación se presentó como una propuesta para la clasificación de rocas alteradas de tipo Alto-Magnesio, demostrando ser más robustos que el esquema propuesto por la IUGS, frente a los cambios de composición causados por alteración.

4.2 Diagramas para clasificar por tipo de magma

Se realizó una nueva clasificación para inferir el tipo de magma en rocas ígneas alteradas, en un esquema multidimensional, utilizando elementos mayores, la cual es consistente con la nomenclatura especificada por la IUGS en términos de cuatro tipos de magma: ultrabásico, básico, intermedio, acido. Como producto de este trabajo, se obtuvo una publicación, la cual se encuentra en el **Apéndice IV**.

4.2.1 Base de datos

Para este trabajo, se utilizó una base de datos de elementos mayores de 33,868 muestras relativamente frescas, del Mioceno al Reciente y distribuidas normalmente.

Las muestras se clasificaron por tipo de magma, mediante el programa IgRoCS (Verma y Rivera-Gómez 2013b), quedando de la siguiente manera:

1,671 ultrabásicas; 12,832 básicas; 11,876 intermedias; y 7,489 ácidas.

4.2.2 Cinco diagramas para clasificación de tipo de magma

Mediante la aplicación de análisis discriminante, se calcularon diez funciones discriminantes en cinco diagramas, para clasificación de cuatro tipos de magma (Tabla 4).

En este trabajo (**Apéndice IV**), realizamos pruebas y aplicaciones a este esquema nuevo de clasificación de tipo de magma, con los siguientes propósitos:

1. Como parte de las pruebas del esquema de clasificación, se utilizaron rocas relativamente frescas, las cuales no fueron incluidas en la base de datos de entrenamiento.

2. Aplicación para datos de inter-laboratorio en materiales de referencia geoquímicos de Japón (Basaltos JB-1 y JB-1a y andesita JA-3).

3. Aplicación a rocas ígneas antiguas para poder decidir el conjunto de diagramas de discriminación tectonomagmática, el cual fuese apropiado al tipo de magma inferido.

4. Aplicación a sedimentos siliciclásticos para el tipo de procedencia ígnea.

Los resultados de las pruebas resultaron coherentes con el esquema convencional de IUGS. Las aplicaciones que se realizaron a materiales de referencia fueron exitosas. De igual manera, se realizaron exitosamente las aplicaciones a las rocas ígneas antiguas para conocer su tipo de magmas y las sedimentarias para inferir su procedencia. Las tablas de resultados se pueden consultar en el trabajo publicado (**Apéndice IV**).

Tabla 4. Diagramas y funciones para discriminación de cuatro tipos de magma.

Diagramas	Funciones discriminantes
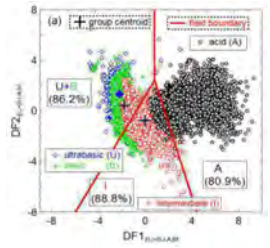	DF1*i*(U+B−I−A)M = (3.1920 × ilr1M) + (3.1505 × ilr2M) + (1.4768 × ilr3M) + (0.2753 × ilr4M) + (0.2201 × ilr5M) + (−0.1721 × ilr6M) + (−0.5571 × ilr7M) + (−0.0887 × ilr8M) + (−0.2205 × ilr9M) − 7.8440 DF2*i*(U+B−I−A)M = (1.4029 × ilr1M) + (5.3998 × ilr2M) + (2.4743 × ilr3M) + (0.1126 × ilr4M)+ (1.0230 × ilr5M) + (0.0599 × ilr6M) + (1.3237 × ilr7M) + (0.5943 × ilr8M) +(0.2240 × ilr9M) − 3.3077
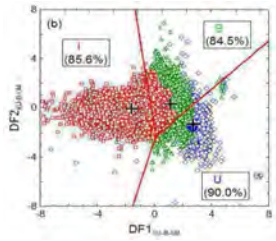	DF1*i*(U−B−I)M = (−4.2259 × ilr1M) + (−1.9064 × ilr2M) + (−1.4579 × ilr3M) + (−1.7889 × ilr4M) + (−0.9671 × ilr5M) + (−0.7498 × ilr6M) + (−0.1510 × ilr7M) + (−0.0047 × ilr8M) + (0.2479 × ilr9M) + 15.5530 DF2*i*(U−B−I)M = (−1.3637 × ilr1M) + (−5.8168 × ilr2M) + (0.5134 × ilr3M) + (2.7915 × ilr4M) + (0.8546 × ilr5M) + (2.8261 × ilr6M) + (2.4547 × ilr7M) + (0.9311 × ilr8M) + (−0.1231 × ilr9M) − 10.3178
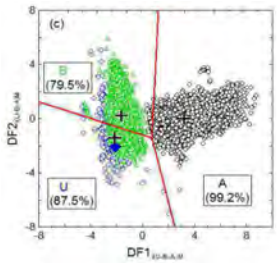	DF1*i*(U−B−A)M = (2.6998 × ilr1M) + (2.5152 × ilr2M) + (1.5243 × ilr3M) + (0.1449 × ilr4M) + (0.0245 × ilr5M) + (0.0233 × ilr6M) + (−0.8195 × ilr7M) + (−0.0785 × ilr8M) + (−0.2399 × ilr9M) − 6.1056 DF2*i*(U−B−A)M = (−1.2574 × ilr1M) + (−6.0060 × ilr2M) + (0.0376 × ilr3M) + (1.4361 × ilr4M) + (0.5251 × ilr5M) + (1.3959 × ilr6M) + (1.3984 × ilr7M) + (0.6415 × ilr8M) + (−0.0229 × ilr9M) − 5.6830
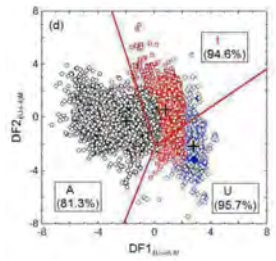	DF1*i*(U−I−A)M = (−2.7734 × ilr1M) + (−2.4119 × ilr2M) + (−1.7030 × ilr3M) + (−0.4884 × ilr4M) + (−0.3979 × ilr5M) + (−0.1366 × ilr6M) + (0.0557 × ilr7M) + (−0.3078 × ilr8M) + (0.2037 × ilr9M) + 9.1719 DF2*i*(U−I−A)M = (−1.7397 × ilr1M) + (−8.4119 × ilr2M) + (−1.5099 × ilr3M) + (0.7283 × ilr4M) + (−0.2239 × ilr5M) + (0.7731 × ilr6M) + (0.1961 × ilr7M) + (0.0299 × ilr8M) + (−0.1904 × ilr9M) − 1.9097
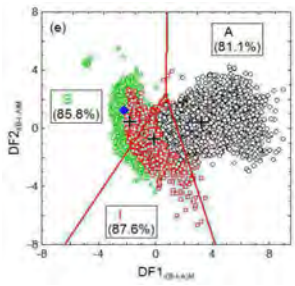	DF1*i*(B−I−A)M = (3.4339 × ilr1M) + (3.5676 × ilr2M) + (1.3212 × ilr3M) + (0.2556 × ilr4M) + (0.1679 × ilr5M) + (−0.2186 × ilr6M) + (−0.6437 × ilr7M) + (−0.0789 × ilr8M) + (−0.2440 × ilr9M) − 8.2314 DF2*i*(B−I−A)M = (1.4078 × ilr1M) + (4.9311 × ilr2M) + (2.5521 × ilr3M) + (0.2645 × ilr4M) + (1.0923 × ilr5M) + (0.3481 × ilr6M) + (1.7256 × ilr7M) + (0.6614 × ilr8M) + (0.1935 × ilr9M) − 4.1001

4.3 Diagramas de Clasificación consistente con TAS en su nomenclatura

Se realizaron nuevos diagramas de discriminación, para clasificación de rocas ígneas alteradas, los cuales son consistentes con la nomenclatura del diagrama TAS. Como resultado de este trabajo, se obtuvo la aceptación de una publicación que se encuentra anexada en el **Apéndice V**.

4.3.1 Base de datos

Se utilizó una base de datos de elementos mayores con 32,948 análisis de muestras de rocas relativamente frescas del Mioceno al Reciente, de rocas de tipo común, excluyendo las rocas de Alto-Magnesio, para dar nomenclatura a 17 tipos de rocas con sus 10 subtipos respectivamente, equivalente al diagrama TAS.

En la Tabla 2 se puede apreciar la cantidad de muestras de cada tipo de roca que utilizamos para el entrenamiento. Estas muestras son las mismas que fueron empleadas para los estudios anteriores (**Apéndices III y IV**).

4.3.2 Diagramas para clasificación para dar nomenclatura a rocas ígneas alteradas

Mediante LDA, se realizaron 48 diagramas y 76 funciones discriminantes (**Apéndice V**). Los resultados de la propuesta multidimensional han sido satisfactorios como se puede constatar en el **Apéndice V**. En consecuencia, ya contamos con una nueva metodología para clasificar las rocas ígneas alteradas. Además, esta clasificación es totalmente consistente con la IUGS. En otras palabras, es capaz de proporcionar todos los nombres de las rocas que proporciona la metodología de la IUGS, pero tiene la ventaja de ser robusta para rocas alteradas.

CAPÍTULO 5

Programación

Debido a la complejidad de las nuevas propuestas multidimensionales para la clasificación de todo tipo de rocas ígneas alteradas, es necesario contar con las herramientas computacionales apropiadas, mismas que se describirán en el presente capítulos.

5.1 Programas de cómputo para uso de los diagramas

Parte del objetivo de esta tesis de doctorado fue la de realizar programas de cómputo, los cuales facilitarán el uso de los diagramas que se propusieron. Por lo tanto, se desarrollaron 3 programas:

1.- HMgClaMSys (***H**igh-**Mg** **Cla**ssification **M**ajor element based **Sys**tem*): Para uso de los diagramas para discriminar rocas de tipo Alto-Magnesio.

2.-MagClaMsys (***Mag**ma **Cla**ssification **M**ajor element based **Sys**tem*): Para uso de los diagramas para discriminar rocas por tipo de magma.

3.-IgRoClaMSys (***Ig**neous **Ro**ck **Cla**ssification **M**ajor element based **Sys**tem*): Para uso de los diagramas de clasificación que proporcionan nomenclatura a las rocas ígneas alteradas.

Estos programas de cómputo fueron escritos en java, usando el *framework* de código abierto ZK para desarrollar aplicaciones web (zkoss.org). El patrón de diseño que se implementó en la mayoría de las veces fue el MVVM que por sus siglas en inglés (Model-View-ViewModel). En la Figura 5.1, se puede apreciar el modo de funcionamiento de este tipo de patrón.

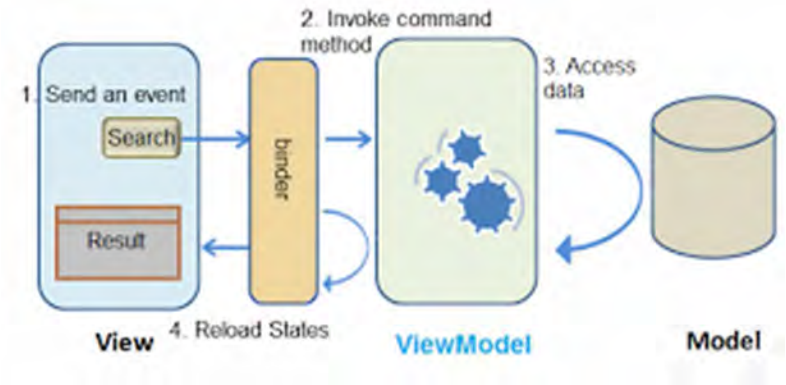

Figura 5.1 Patrón de diseño, MVVM, imagen obtenida de zkoss.org

Este patrón divide una aplicación en tres partes como sigue:

1. El modelo *"Model"*, el cual consta de los datos de la aplicación y las reglas de negocios.

2. La Vista *"View"*, la cual es la interfaz con el usuario.

3. El modelo de la vista *"ViewModel"* es un tipo de abstracción, el cual mantiene su estado y comportamiento.

Existe también un componente llamado "*binder*" que sincroniza los datos entre el modelo de la vista y la vista.

Los diagramas de los programas, se realizaron mediante la biblioteca JFreeChart, la cual permite descargar las figuras en formato JPEG.

5.2 Portal web

Debido a que estos programas de cómputo fueron diseñados como aplicaciones web, realicé, en conjunto con la unidad de cómputo del IER-UNAM, un portal web, para poner a disposición estos programas a la comunidad científica mundial. El portal permitió disponer además otros programas que se han realizado en el grupo de trabajo de Geoenergía del IER-UNAM, en colaboración con otras entidades (UAEM, IPICYT e ICMyL-UNAM), así como otra información y material bibliográfico.

El portal se construyó utilizando Liferay (liferay.com), el cual es un gestor de contenidos que da soporte a múltiples tecnologías. Esto se encuentra albergado en una computadora de escritorio con características de servidor llamado **"Tláloc"** y al cual se puede acceder desde la liga: http://tlaloc.ier.unam.mx

Algunas de las principales razones para seleccionar este gestor de contenido para desarrollar nuestro portal, fue que ofrecía lo siguiente:

- Desarrollo de funcionalidades a través de portlets, los cuales son componentes modulares de las interfaces de usuario gestionadas y visualizadas en un portal web.
- Búsqueda de contenidos
- Gestión de usuarios y permisos
- Personalización de plantillas

Además de que principalmente nos permitió poner a disposición de los usuarios, los programas web desarrollados.

El uso del portal tlaloc está disponible de forma libre. El único requisito para poder acceder a los programas y demás información contenida en él, es crear una cuenta de usuario, lo cual es importante para generar estadísticas sobre el uso del portal.

En la Figura 5.2, se muestra la página principal del portal Tláloc.

Figura 5.2 Página principal del portal http://tlaloc.ier.unam.mx

Para crear una cuenta de usuario en el portal, se accede en la sección "*Create Account*" (Figura 5.3). Posteriormente, se debe llenar un formulario, el cual solicita información básica del usuario como: Nombre completo, dirección de correo electrónico, genero, grado académico, país, información institucional y líneas de investigación en las que trabaja.

Figura 5.3 Sección de portal para crear una cuenta.

Una vez creada una cuenta de usuario se puede acceder al portal y utilizar los programas disponibles en la sección *"Online programs"* y seleccionar el programa que se requiera usar, como se muestra en la Figura 5.4.

Figura 5.4 Barra de menú del portal Tláloc, sección programas en línea *"Online programs"*.

5.3 Programa de cómputo *HMgClaMSys*

Como ya se mencionó, el programa HMgClaMSys es un programa para uso en línea, el cual contiene programadas 11 funciones discriminantes para clasificar rocas ígneas de tipo Alto-Magnesio (Figura 5.5).

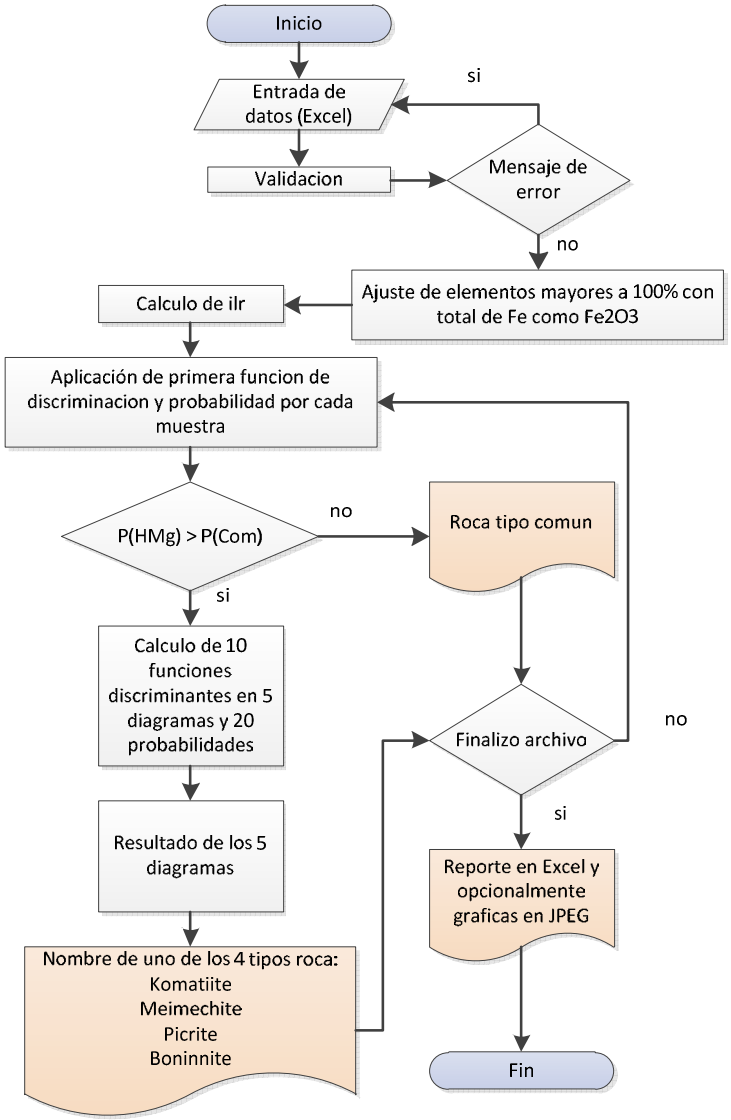

Figura 5.5 Diagrama de flujo del programa HMgClaMSys.

En la Figura 5.5, se muestra el diagrama de flujo del programa HMgClaMSys, en donde se observa que la entrada de datos se realiza mediante un archivo en formato Excel. Este archivo puede ser descargado del portal en la parte izquierda de la pantalla, como se muestra en la Figura 5.6. Posteriormente, el usuario puede introducir sus datos en este archivo o en una copia.

La estructura de las páginas, donde se encuentra cada uno de los programas, es la misma. En la Figura 5.6, se muestra la estructura de la página donde se encuentra el programa HMgClaMsys.

Figura 5.6 Pantalla general de la página del programa HMgClaMSys; 1.-Archivos principales en formato pdf para descarga; 2.- Archivos para descargar; 3.-Programa en línea HMgClaMSys.

Para más información sobre el funcionamiento del programa, se puede descargar el archivo "*ReadMe*" en el sitio de Tláloc.

5.3 Programa de cómputo *MagClaMSys*

El programa MagClaMSys fue diseñado para inferir el tipo de magma de una roca alterada, así como también la procedencia ígnea de un conjunto de muestras de origen sedimentaria siliciclástica, mediante el uso de diez funciones discriminantes (**Apéndice IV**), cinco diagramas y el cálculo de probabilidades. El diagrama de flujo se muestra en la Figura 5.7.

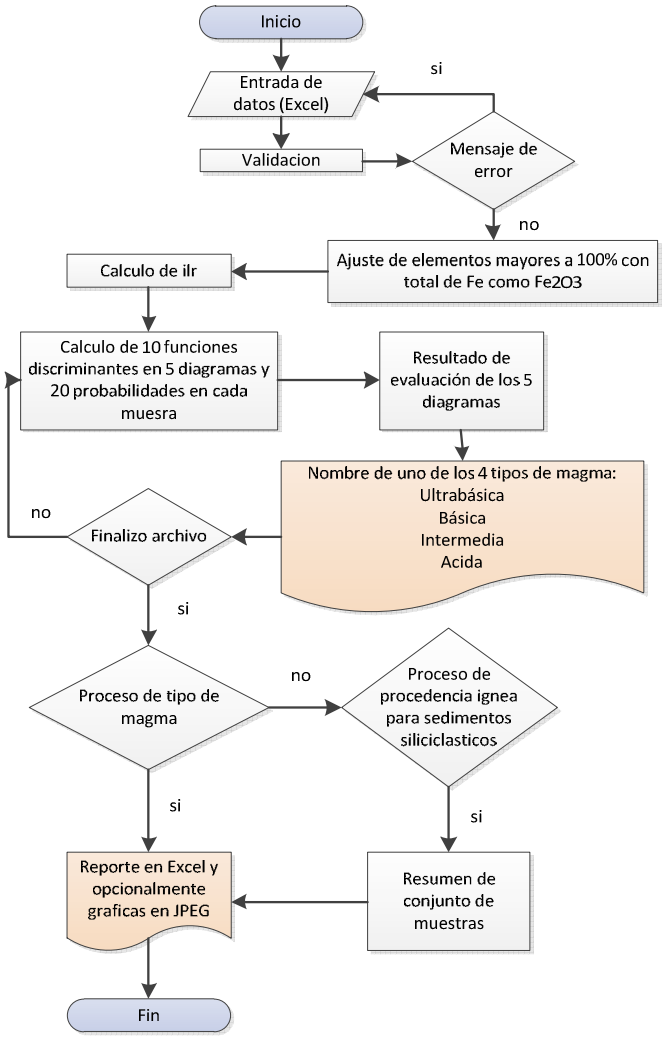

Figura 5.7 Diagrama de flujo de MagClaMSys (Verma et al. 2017).

Se programaron dos módulos, tanto como para HMgClaMSys como para MagClaMSys, para realizar un análisis de sensibilidad de los diagramas de clasificación.

Por otra parte, se determinó la robustez de las nuevas propuestas, tomando en cuenta errores analíticos o de incertidumbres. De igual manera, se evaluó la robustez respecto a cambios de alteración post-emplazamiento.

En los trabajos publicados anexados en los **Apéndices III y IV**, se demostró la robustez de este nuevo esquema de clasificación en comparación con el esquema IUGS convencional.

5.3 Programa de cómputo *IgRoClaMSys*

Finalmente, se realizó el programa IgRoClaMSys para inferir la nomenclatura de una roca ígnea alterada, consistente con el esquema IUGS (**Apéndice IV**). La consistencia se refiere a que el nuevo esquema proporciona todos los nombres de rocas ígneas que le IUGS maneja en su nomenclatura. Las rocas frescas sí reciben, por lo general, los mismos nombres tanto por IgRoClaMSys como por la IUGS (Le Bas et al. 1986). Sin embargo, las rocas alteradas presentan mucho mayor discrepancias en sus nombres por ambos sistemas, indicando claramente que es mejor usar el nuevo sistema para su clasificación que el propuesto por la IUGS.

En la Figura 5.8, se puede observar el diagrama de flujo donde se esquematiza la secuencia de clasificación, para los diferentes nombres de rocas. Cabe señalar que este programa también permite determinar nomenclatura de rocas ígneas intrusivas, utilizando la propuesta hecha en el trabajo de Middlemost (1994). Mayores detalles se encuentran en el **Apéndice IV**.

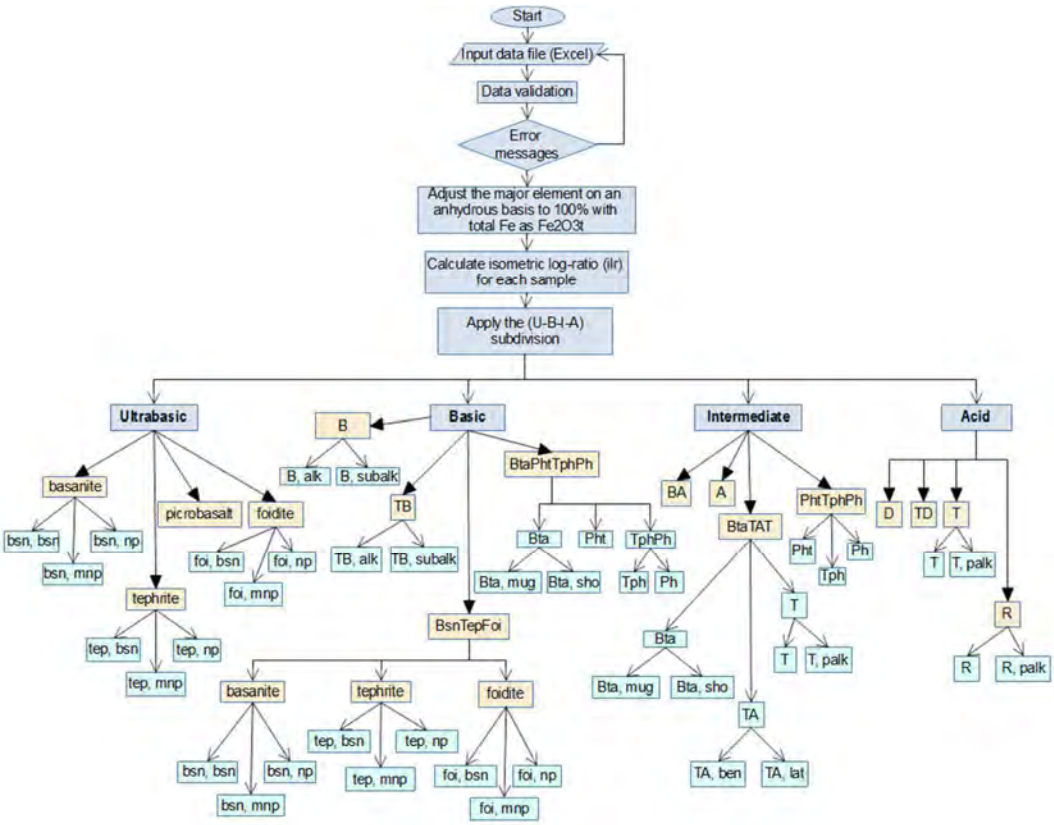

Figura 5.8 Diagrama de flujo de programa de cómputo IgRockClaMSys, tomada de Verma y Rivera-Gómez (2017).

CAPÍTULO 6

Aplicación de los Diagramas a Campos Geotérmicos

En este capítulo, se presenta aplicación del nuevo esquema de clasificación para las rocas ígneas alteradas, provenientes de los campos geotérmicos.

Se aplicaron todos los diagramas de clasificación propuestos en esta tesis a muestras alteradas, publicadas en la literatura, de tres campos geotérmicos (mapa de localización en Figura 6.1):

A1.- Tendaho, Etiopía (Gianelli et al. 1998);

A2.- Tongonan, Filipinas (Scott 2004); y

A3.- Cerro Prieto, México (Herzig 1990).

Se realizó una comparación entre el esquema recomendado por la IUGS y el nuevo esquema de clasificación que se propone en la presente tesis.

Para asignar la nomenclatura y el tipo de magma por el esquema IUGS, se utilizó el programa IgRoCS, mientras que para el uso de los nuevos diagramas de clasificación, se utilizaron los programas descritos en el capítulo anterior.

Se procesaron las muestras de cada una de las aplicaciones, de acuerdo al siguiente orden:

1) HMgClaMSys para determinar si alguna muestra puede pertenecer al grupo de Alto-Magnesio;

2) MagClaMSys para asignar el tipo de magma; y, por último,

3) el programa IgRoClaMSys para determinar el nombre de la roca.

En la primera aplicación, las muestras son del periodo Cuaternario, se encuentra en el rift de Etiopía (Gianelli et al. 1998), el cual es un sistema geotérmico activo. En la Figura 6.1, se indica la localización de esta área.

Se probaron doce muestras, de las cuales siete fueron básicas en el esquema IUGS y resultaron básicas también en el nuevo esquema de clasificación (Tabla 4). Sin embargo, las muestras "TD3-1776" y "TD1-2015" difieren en el nombre de la roca, en el esquema IUGS la nomenclatura fue "*basalt, subalkali*", mientras que en el esquema nuevo de discriminación, el resultado fue de "*basalt, alkali*".

Una muestra se clasificó con magma intermedio y con nomenclatura "*basaltic andesite*", en el esquema IUGS y en el nuevo esquema, esta misma muestra se clasificó con magma básico y nombre de roca "*basalt, subalakali*".

De las cuatro muestras que se clasificaron como ultrabásicas en el esquema IUGS, tres concuerdan en el tipo de magma mientras que una fue clasificada como básica. Solamente una muestra (TD3-643) se clasificó igual en el tipo de magma y nomenclatura en ambos esquemas (Tabla 5). Los nombres de las otras tres muestras (TD2-798, TD3-1001b y TD3-643) fueron diferentes por la IUGS y el nuevo esquema. Estas inconsistencias entre las clasificaciones de IUGS y el nuevo esquema indican claramente que para la nomenclatura de rocas alteradas, se debe usar en nuevo procedimiento propuesto en la presente tesis.

Tabla 5 *Caso de aplicación al campo geotérmico de Tendaho, rift de Etiopía (Gianelli et al.1998)*

No	Nombre de la muestra	Nombre interno asignado	Esquema IUGS		Nuevo esquema de Clasificación discriminante		
			Tipo de magma	TAS	HMgClaMSys	MagClaMSys	IgRoClaMSys
1	TD2-804	GMBC0002	BASIC	Basalt, alkali		BASIC	Basalt, alkali
2	TD2-1200	GMBC0003	BASIC	Basalt, alkali		BASIC	Basalt, alkali
3	TD3-1776	GMBC0008	BASIC	Basalt, subalkali		BASIC	Basalt, alkali
4	TD1-2015	GMBC0012	BASIC	Basalt, subalkali		BASIC	Basalt, alkali
5	TD3-1986	GMBC0007	BASIC	Basalt, subalkali		BASIC	Basalt, subalkali
6	TD1-1594	GMBC0009	BASIC	Basalt, subalkali		BASIC	Basalt, subalkali
7	TD1-2015	GMBC0011	BASIC	Basalt, subalkali		BASIC	Basalt, subalkali
8	TD1-1270	GMBC0010	INTERMEDIATE	Basaltic andesite		BASIC	Basalt, subalkali
9	TD2-798	GMBC0001	ULTRABASIC	PICRITE		BASIC	Basalt, subalkali
10	TD3-1001a	GMBC0005	ULTRABASIC	Picrobasalt		ULTRABASIC	Foidite,melanephelinite
11	TD3-1001b	GMBC0006	ULTRABASIC	Foidite, melanephelinite		ULTRABASIC	Picrobasalt
12	TD3-643	GMBC0004	ULTRABASIC	Picrobasalt		ULTRABASIC	Picrobasalt

El segundo caso de aplicación se realizó sobre el campo geotérmico de Tongonan localizado en Layte, Filipinas. Los datos fueron compilados de Scott (2004). Las muestras son de la época del Plioceno y se encuentran hidrotermalmente alteradas.

De diez muestras que se presentan en el trabajo, la muestra "*Well_410 (-1822)*" fue la única muestra que coincidió en ambos esquemas de clasificación tanto como en tipo de magma como en el nombre de la roca (Tabla 6). En la Tabla 6, se puede apreciar también que, en el esquema de discriminación que hemos propuesto, sólo una de las muestras se clasificó como Boninite, la cual es una roca de tipo Alto-Magnesio; esta roca fue clasificada como "basalt, subalkali" por la IUGS.

Tabla 6 *Caso de aplicación al campo geotérmico de Tongonan, Layte, Filipinas, muestras con alteración hidrotermal, del Plioceno (Scott 2004)*

No	Nombre de la muestra	Nombre interno asignado	Esquema IUGS		Nuevo esquema de Clasificación discriminante		
			Tipo de magma	TAS	HMgClaMSys	MagClaMSys	IgRoClaMSys
1	Well_102 (-960)	SCOT0001	BASIC	Trachybasalt, potassic		BASIC	Basalt, subalkali
2	Well_401 (46)	SCOT0004	BASIC	Basalt, subalkali	BONINITE		
3	Well_503 (-662)	SCOT0009	BASIC	Basalt, subalkali		BASIC	Basaltic trachyandesite, shoshonite
4	Well_202 (-294)	SCOT0002	BASIC	Trachybasalt, potassic		INTERMEDIATE	Basaltic trachyandesite, shoshonite
5	Well_401 (-1245)	SCOT0005	BASIC	Basaltic trachyandesite, mugearite		INTERMEDIATE	Basaltic andesite
6	Well_407 (-1070)	SCOT0007	BASIC	Trachybasalt, hawaiite		INTERMEDIATE	Basaltic andesite
7	Well_407 (-760)	SCOT0006	INTERMEDIATE	Basaltic andesite		BASIC	Basaltic trachyandesite, shoshonite
8	Well_213 (-147)	SCOT0003	INTERMEDIATE	Andesite		INTERMEDIATE	Basaltic andesite
9	Well_410 (-1822)	SCOT0008	INTERMEDIATE	Andesite		INTERMEDIATE	Andesite
10	Well_MN1 (-309)	SCOT0010	INTERMEDIATE	Andesite		INTERMEDIATE	Basaltic andesite

El tercer caso de aplicación es del campo geotérmico de Cerro Prieto, localizado en Baja California, México. Las muestras fueron compiladas del trabajo de Herzig (1990). El autor menciona que las muestras fueron tomadas de la superficie y se encuentran parcialmente alteradas. Este estudio (Herzig 1990) se centró principalmente en evitar que las muestras estén

alteradas, por lo que se espera que los diagramas de discriminación atiendan a pocos cambios en los resultados con respecto al esquema IUGS. En otras palabras, se espera que haya mayor consistencia entre los nombres por la IUGS y el nuevo esquema.

En esta aplicación, fueron presentadas 14 muestras, de las cuales 8 fueron clasificadas como intermedias en el esquema de clasificación IUGS. Cuatro muestras intermedias coincidieron en el tipo de magma y roca por ambos esquemas. Las otras cuatro muestras indicaron como tipo de magma básico. Seis muestras fueron clasificadas con magma tipo ácido y tipo de roca "Dacite" en el esquema IUGS; sólo una no coincidió con el esquema de discriminación ya que el tipo de magma dio fue Intermedio y tipo de roca "Andesite", se puede observar con más detalle en la Tabla 7. Cabe mencionar que aunque el autor original (Herzig 1990) mencionó que se evitó alteración en su muestreo, las diferencias arriba mencionadas pueden deberse a algún tipo de alteración inevitablemente presente aún en la superficie de un campo geotérmico.

Tabla 7 *Caso de aplicación al campo geotérmico de Cerro Prieto, localizado en Baja California, México (Herzig 1990).*

No	Nombre de la muestra	Nombre interno asignado	Esquema IUGS		Nuevo esquema de Clasificación discriminante		
			Tipo de magma	TAS	HMgClaMSys	MagClaMSys	IgRoClaMSys
1	M203-3327	HERZ0001	INTERMEDIATE	Basaltic andesite		BASIC	Trachybasalt, hawaiite
2	M203-3354	HERZ0002	INTERMEDIATE	Basaltic andesite		BASIC	Basalt, subalkali
3	M203-3336	HERZ0003	INTERMEDIATE	Basaltic andesite		BASIC	Basaltic trachyandesite, mugearite
4	M203-3351	HERZ0004	INTERMEDIATE	Basaltic andesite		BASIC	Basaltic trachyandesite, mugearite
5	M205-2754	HERZ0005	INTERMEDIATE	Andesite		INTERMEDIATE	Andesite
6	M205-1795	HERZ0006	INTERMEDIATE	Andesite		INTERMEDIATE	Andesite
7	M205-2382	HERZ0007	INTERMEDIATE	Andesite		INTERMEDIATE	Andesite
8	M205-2360	HERZ0008	INTERMEDIATE	Andesite		INTERMEDIATE	Andesite
9	M203-3927	HERZ0009	ACID	Dacite		INTERMEDIATE	Andesite
10	M203-3921	HERZ0010	ACID	Dacite		ACID	Dacite
11	M203-3969	HERZ0011	ACID	Dacite		ACID	Dacite
12	M203-3930	HERZ0012	ACID	Dacite		ACID	Dacite
13	M203-3942	HERZ0013	ACID	Dacite		ACID	Dacite
14	M203-3957	HERZ0014	ACID	Dacite		ACID	Dacite

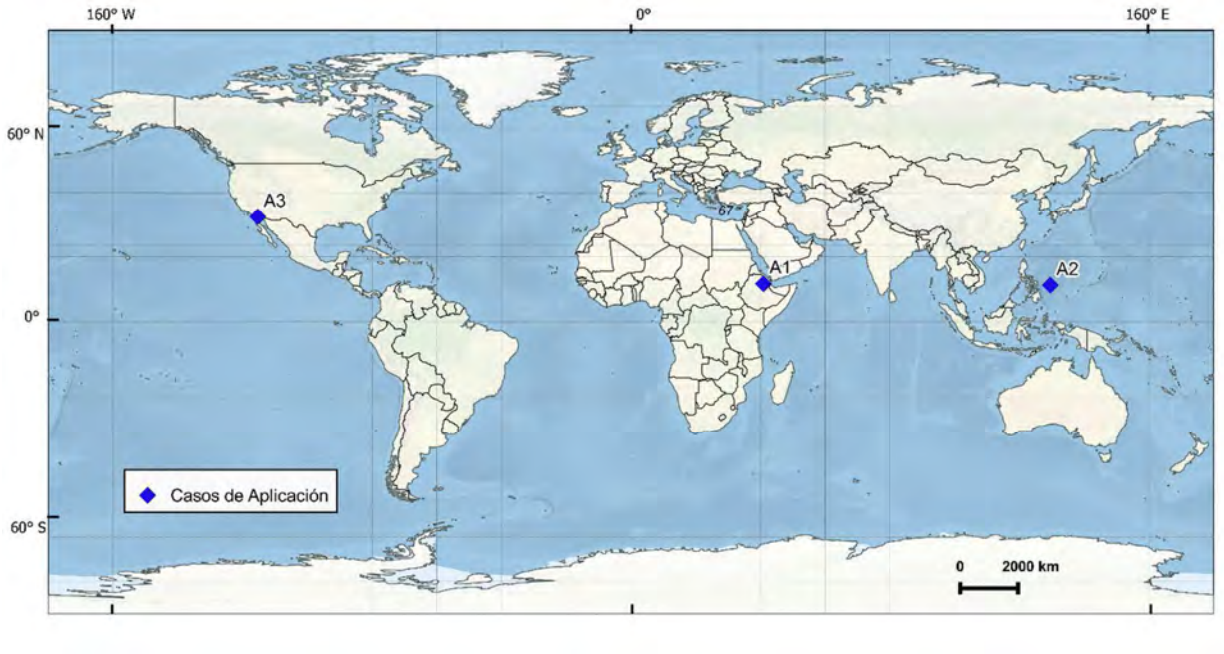

Figura 6.1 Localización de los casos de aplicación a campos geotérmicos.

CONSIDERACIONES FINALES

En esta sección, se presentan conclusiones de la tesis, trabajos que se encuentran en desarrollo.

CONCLUSIONES

En esta tesis se desarrolló una propuesta de clasificación para rocas ígneas alteradas, basada en análisis discriminante lineal usando elementos mayores, la cual demostró ser consistente con la nomenclatura recomendada por la IUGS y una alternativa robusta para la clasificación de rocas ígneas alteradas.

Se desarrollaron tres nuevos programas web: HMgClaMSys, MagClaMSys, IgRoClaMSys, que facilitan y hacen más eficiente el uso de los diagramas de clasificación propuestos en esta tesis.

Se creó un portal web "tlaloc.ier.unam.mx", albergado en un servidor localizado dentro del IER-UNAM, mediante el cual el mundo puede tener acceso a varios programas e información relevante en temas de geoestadística.

Finalmente como producto del trabajo realizado durante esta tesis se obtuvieron cinco publicaciones en revistas arbitradas y con factor de impacto, en las cuales se demostró que los diagramas multidimensionales son herramientas estadísticas que son altamente eficientes para discriminar y clasificar con porcentajes de éxito muy altos.

TRABAJOS EN DESARROLLO

Se desarrolló un manuscrito en conjunto con el Dr. S. P. Verma y la Dra. Diaz-Gonzalez L. en el cual participé:

"A new multidimensional classification scheme of altered igneous rocks from performance comparison of isometric and modified log-ratio transformations of major elements for High-Mg rock varieties and magma and rock types"

En este trabajo se realizaron comparaciones en los resultados sobre el uso de transformacion de elementos, llegando a la conclusión de que el resultado del análisis discriminante lineal es invariante al tipo de transformación lineal que se utilice.

Se desarrolló una nueva herramienta computacional llamas "MICSys" la cual encapsula a tres programas: HMgClaMSys_ilr, MagClaMSys_mlr, IgRoClaMSys_mlr, para procesar las muestras de forma más automatizada en la opción "default process" pasando por los tres programas, para obtener el nombre de la roca (ya sea de alto magnesio o común) y tipo de magma.

El trabajo se encuentra en proceso de enviado a la revista Episodes, la cual es una revista internacional, arbitrada, de alto impacto y esta indizada en el *Science Citation Index.*

Desarrollamos una nueva propuesta de diagramas para clasificación utilizando elementos mayores-traza y estamos desarrollando la herramienta computacional para utilizarlos, en este trabajo resaltamos que al aumentar el número de dimensiones el porcentaje de numero de muestras que son mal clasificadas, disminuye. Se realizará un manuscrito para enviar a una revista internacional, en los próximos meses.

BIBLIOGRAFÍA

Agrawal, S., Guevara, M. y Verma, S.P., 2004. Discriminant analysis applied to establish major-element field boundaries for tectonic varieties of basic rocks. International Geology Review, 46(7): 575-594.

Agrawal, S., Guevara, M. y Verma, S.P., 2008. Tectonic discrimination of basic and ultrabasic rocks through log-transformed ratios of immobile trace elements. International Geology Review, 50(12): 1057-1079.

Aitchison, J., 1982. The statistical analysis of compositional data (with discussion). Journal of the Royal Statistical Society, Series B (Statistical Methodology), 44(2): 137-177.

Aitchison, J., 1986. The statistical analysis of compositional data. Chapman and Hall, London, UK, 416 pp.

Aitchison, J. y Egozcue, J.J., 2005. Compositional data analysis: where are we and where should we be heading? Mathematical Geology, 37(7): 829-850.

Chayes, F., 1960. On correlation between variables of constant sum. Journal of Geophysical Research, 65(12): 4185-4193.

Egozcue, J.J. y Pawlowsky-Glahn, V., 2006. Simplicial geometry for compositional data. In: A. Buccianti, G. Mateu-Figueras and V. Pawlowsky-Glahn (Editors), Compositional data analysis in the Geosciences: from theory to practice. The Geological Society of London Special Publication, London, pp. 145-159.

Egozcue, J.J. y Pawlowsky-Glahn, V., 2011. Análisis composicional de datos en Ciencias Geoambientales. Boletín Geológico y Minero, 122(4): 439-452.

Egozcue, J.J., Pawlowsky-Glahn, V., Mateu-Figueras, G. y Barceló-Vidal, C., 2003. Isometric logratio transformations for compositional data analysis. Mathematical Geology, 35(3): 279-300.

Floyd, P.A. y Winchester, J.A., 1975. Magma type and tectonic setting discrimination using immobile elements. Earth and Planetary Science Letters, 27(2): 211-218.

Floyd, P.A. y Winchester, J.A., 1978. Identification and discrimination of altered and metamorphosed volcanic rocks using immobile elements. Chemical Geology, 21(3-4): 291-306.

Gianelli, G., Mekuria, N., Battaglia, S., Chersicla, A., Garofalo, P., Ruggieri, G., Manganelli, M. y Gerbregziabher, Z., 1998. Water-rock interaction and hydrothermal mineral equilibria in the Tendaho geothermal system. Journal of Volcanology and Geothermal Research, 86: 253-276.

Hastie, A.R., Kerr, A.C., Pearce, J.A. y Mitchell, S.F., 2007. Classification of altered volcanic island arc rocks using immobile trace elements: development of the Th-Co discrimination diagram. Journal of Petrology, 48(12): 2341-2357.

Herzig, C.T., 1990. Geochemistry of igneous rocks from the Cerro Prieto geothermal field, northern Baja California, Mexico. Journal of Volcanology and Geothermal Research, 42: 261-271

Le Bas, M.J., 2000. IUGS reclassification of the high-Mg and picritic volcanic rocks. Journal of Petrology, 41(10): 1467-1470.

Le Bas, M.J., Le Maitre, R.W., Streckeisen, A. y Zanettin, B., 1986. A chemical classification of volcanic rocks based on the total alkali-silica diagram. Journal of Petrology, 27(3): 745-750.

Le Maitre, R.W., Streckeisen, A., Zanettin, B., Le Bas, M.J., Bonin, B., Bateman, P., Bellieni, G., Dudek, A., Schmid, R., Sorensen, H., Woolley, A.R., 2002. Igneous rocks. A classification and glossary of terms: recommendations of the International Union of Geological Sciences Subcommission of the Systematics of Igneous Rocks. Cambridge University Press, Cambridge, 236 pp.

Martín-Fernández, J.A., Barceló-Vidal, C. y Pawlowsky-Glahn, V., 2003. Dealing with zeros and missing values in compositional data sets using nonparametric imputation. Mathematical Geology, 35(3): 253-278.

Middlemost, E.A.K., 1994. Naming materials in the magma/igneous rock system. Earth Science Reviews, 37(3-4): 215-224.

Pandarinath, K., 2014. Tectonomagmatic origin of Precambrian rocks of Mexico and Argentina inferred from multi-dimensional discriminant-function based discrimination diagrams. Journal of South American Earth Sciences, 56: 464-484.

Pandarinath, K., Dulski, P., Torres-Alvarado, I.S. y Verma, S.P., 2008. Element mobility during the hydrothermal alteration of rhyolitic rocks of the Los Azufres geothermal field, Mexico. Geothermics, 37: 53-72.

Pearce, J.A. y Cann, J.R., 1971. Ophiolite origin investigated by discriminant analysis using Ti, Zr and Y. Earth and Planetary Science Letters, 12(2): 339-349.

Pearce, J.A. y Cann, J.R., 1973. Tectonic setting of basic volcanic rocks determined using trace element analyses. Earth and Planetary Science Letters, 19(2): 290-300.

Peccerillo, A. y Taylor, S.R., 1976. Geochemistry of Eocene calc-alkaline volcanic rocks from the Kastamonu area, Northern Turkey. Contributions to Mineralogy and Petrology, 58: 63-81.

Rivera-Gómez, M.A. y Verma, S.P., 2016. Testing of multidimensional tectonomagmatic discrimination diagrams on fresh and hydrothermally altered rocks. Geologica Carpathica, 67(2): 195-208 + supplement i-cxiii (113 pages).

Scott, G.L., 2004. Major active faults determine the location of the Tongonan geothermal field: Evidence provided by rock alteration and stable isotope geochemistry. The Island Arc, 13: 370-386.

Streckeisen, A., 1976. To each plutonic rock its proper name. Earth Science Reviews, 12: 1-33.

Torres-Alvarado, I.S., Pandarinath, K., Verma, S.P. y Dulski, P., 2007. Mineralogical and geochemical effects due to hydrothermal alteration in the Los Azufres geothermal field, Mexico. Revista Mexicana de Ciencias Geológicas, 24(1): 15-24.

Velasco-Tapia, F., 2014. Multivariate analysis, mass balance techniques, and statistical tests as tools in igneous petrology: Application to the Sierra de las Cruces Volcanic Range (Mexican Volcanic Belt). The Scientific World Journal, Article ID 793236, 32 pages.

Verma, S.K., 2017. Precambrian plate tectonic setting of Africa from multidimensional discrimination diagrams. Journal of African Earth Sciences, 125: 137-150.

Verma, S.P., 2010. Statistical evaluation of bivariate, ternary and discriminant function tectonomagmatic discrimination diagrams. Turkish Journal of Earth Sciences, 19(2): 185-238.

Verma, S.P., 2012. Application of multi-dimensional discrimination diagrams and probability calculations to acid rocks from Portugal and Spain. Comunicaciones Geológicas, 99(2): 79-93.

Verma, S.P., 2013. Application of 50 multi-dimensional discrimination diagrams and significance tests to decipher compositional similarities and differences between Hawaiian and Icelandic volcanism. International Geology Review, 55(12): 1553-1572.

Verma, S.P., 2016. Análisis estadístico de datos composicionales. Universidad Nacional Autónoma de México, 746 pp.

Verma, S.P. y Agrawal, S., 2011. New tectonic discrimination diagrams for basic and ultrabasic volcanic rocks through log-transformed ratios of high field strength elements and implications for petrogenetic processes. Revista Mexicana de Ciencias Geológicas, 28(1): 24-44.

Verma, S.P. y Andaverde, J., 2007. Coupling of thermal and chemical simulations in a 3-D integrated magma chamber-reservoir model: a new geothermal energy research frontier. In: H.I. Ueckermann (Editor), Geothermal Energy Research Trends. Nova Science Publishers, Inc., New York, pp. 149-189.

Verma, S.P. y Díaz-González, L., 2012. Application of the discordant outlier detection and separation system in the geosciences. International Geology Review, 54(3): 593-614.

Verma, S.P. y Gómez-Arias, E., 2013. Three-dimensional temperature field simulation of magma chamber in the Los Humeros geothermal field, Puebla, Mexico. Applied Thermal Engineering, 52: 512-515.

Verma, S.P. y Rivera-Gómez, M.A., 2013a. New computer program TecD for tectonomagmatic discrimination from discriminant function diagrams for basic and ultrabasic magmas and its application to ancient rocks. Journal of Iberian Geology, 39(1): 167-179.

Verma, S.P. y Rivera-Gómez, M.A., 2013b. Computer programs for the classification and nomenclature of igneous rocks. Episodes, 36(2): 115-124.

Verma, S.P. y Rivera-Gómez, M.A., 2017. Transformed major element based multidimensional classification of altered volcanic rocks. Episodes, aceptado.

Verma, S.P. y Verma, S.K., 2013. First 15 probability-based multi-dimensional discrimination diagrams for intermediate magmas and their robustness against post-emplacement compositional changes and petrogenetic processes. Turkish Journal of Earth Sciences, 22(6): 931-995.

Verma, S.P., Torres-Alvarado, I.S. y Sotelo-Rodríguez, Z.T., 2002. SINCLAS: standard igneous norm and volcanic rock classification system. Computers & Geosciences, 28: 711-715.

Verma, S.P., Torres-Alvarado, I.S. y Velasco-Tapia, F., 2003. A revised CIPW norm. Schweizerische Mineralogische und Petrographische Mitteilungen, 83(2): 197-216.

Verma, S.P., Guevara, M. y Agrawal, S., 2006. Discriminating four tectonic settings: five new geochemical diagrams for basic and ultrabasic volcanic rocks based on log-ratio transformation of major-element data. Journal of Earth System Science, 115(5): 485-528.

Verma, S.P., Rodríguez-Ríos, R. y González-Ramírez, R., 2010a. Statistical evaluation of classification diagrams for altered igneous rocks. Turkish Journal of Earth Sciences, 19(2): 239-265.

Verma, S.P., Pandarinath, K. y Verma, S.K., 2010b. Statistically correct methodology for compositional data in new discriminant function tectonomagmatic diagrams and application to ophiolite origin. Advances in Geosciences, 27 Solid Earth Science, 11-22.

Verma, S.P., Verma, S.K., Pandarinath, K. y Rivera-Gómez, M.A., 2011. Evaluation of recent tectonomagmatic discrimination diagrams and their application to the origin of basic magmas in Southern Mexico and Central America. Pure and Applied Geophysics, 168(8): 1501-1525.

Verma, S.P., Pandarinath, K., Verma, S.K. y Agrawal, S., 2013a. Fifteen new discriminant-function-based multi-dimensional robust diagrams for acid rocks and their application to Precambrian rocks. Lithos, 168-169: 113-123.

Verma, S.P., Cruz-Huicochea, R. y Díaz-González, L., 2013b. Univariate data analysis system: deciphering mean compositions of island and continental arc magmas, and influence of underlying crust. International Geology Review, 55(15): 1922-1940.

Verma, S.P., Cruz-Huicochea, R., Díaz-González, L. y Verma, S.K., 2015a. A new computer program TecDIA for multidimensional tectonic discrimination of intermediate and acid magmas and its application to the Bohemian Massif, Czech Republic. Journal of Geosciences, 60: 203–218.

Verma, S.P., Verma, S.K. y Oliveira, E.P., 2015b. Application of 55 multi-dimensional tectonomagmatic discrimination diagrams to Precambrian belts. International Geology Review, 57(11-12): 1365-1388.

Verma, S.P., Pandarinath, K. y Rivera-Gómez, M.A., 2016a. Evaluation of the ongoing rifting and subduction processes in the geochemistry of magmas from the western part of the Mexican Volcanic Belt. Journal of South American Earth Sciences, 66: 125-148.

Verma, S.P., Rivera-Gómez, M.A., Díaz-González, L. y Quiroz-Ruiz, A., 2016b. Log-ratio transformed major-element based multidimensional classification for altered High-Mg igneous rocks. Geochemistry, Geophysics, Geosystems, 17, doi:10.1002/2016GC006652.

Verma, S.P., Rivera-Gómez, M.A., Díaz-González, L., Pandarinath, K., Amezcua-Valdez, A., Rosales-Rivera, M., Verma, S.K., Quiroz-Ruiz, A., Armstrong-Altrin, J.S., 2017. Multidimensional classification of magma types for altered igneous rocks and application to their tectonomagmatic discrimination and igneous provenance of siliciclastic sediments. Lithos, 278-281: 321-330.

Winchester, J.A. y Floyd, P.A., 1976. Geochemical magma type discrimination: application to altered and metamorphosed basic igneous rocks. Earth and Planetary Science Letters, 28(3): 459-469.

Winchester, J.A. y Floyd, P.A., 1977. Geochemical discrimination of different magma series and their differentiation products using immobile elements. Chemical Geology, 20: 325-343.

REFERENCIAS ELECTRÓNICAS

zkoss.org: https://www.zkoss.org/zkdemo/getting_started/mvvm

liferay.com: https://web.liferay.com/es/products/liferay-portal/features/portal

Linear Discriminant Analysis: https://en.wikipedia.org/wiki/Linear_discriminant_analysis

Apéndice I

Rivera-Gómez, M.A., Verma, S.P., 2016. Testing of multidimensional tectonomagmatic discrimination diagrams on fresh and altered rocks. Geologica Carpathica, 67: 195-208.

Contiene suplemento de 113 páginas.

GEOLOGICA CARPATHICA, APRIL 2016, 67, 2, 195–208 doi: 10.1515/geoca-2016-0013

Testing of multidimensional tectonomagmatic discrimination diagrams on fresh and altered rocks

M. ABDELALY RIVERA-GÓMEZ[1] and SURENDRA P. VERMA[2]✉

[1]Posgrado en Ingeniería, Instituto de Energías Renovables, Universidad Nacional Autónoma de México, Temixco, Mor., 62580, Mexico; marig@ier.unam.mx
[2]Departamento de Sistemas Energéticos, Instituto de Energías Renovables, Universidad Nacional Autónoma de México, Temixco, Mor. 62580, Mexico; ✉spv@ier.unam.mx

(Manuscript received January 18, 2015; accepted in revised form March 10, 2016)

Abstract: We evaluated 55 multidimensional diagrams proposed during 2004–2013 for the tectonic discrimination of ultrabasic, basic, intermediate, and acid magmas. The Miocene to Recent rock samples for testing the diagrams had not been used for constructing them. Eighteen test studies (2 from ocean island; 2 from ocean island/continental rift; 6 from continental rift; 4 from continental arc; 2 from island arc; 1 from mid-ocean ridge, and 1 from collision) of relatively fresh rocks fully confirmed the satisfactory functioning of these diagrams for all tectonic fields for which they were proposed. Eight additional case studies on hydrothermally altered or moderately to highly weathered rocks were also presented to achieve further understanding of the functioning of these diagrams. For these rocks as well, the diagrams indicated the expected tectonic setting. We also show that for testing or using these diagrams the freely-available geochemistry databases should be used with caution but certainly after ascertaining the correct magma types to select the appropriate diagram sets. The results encourage us to recommend these diagrams for deciphering the tectonic setting of older terranes or areas with complex or transitional tectonic settings.

Key words: tectonic setting, discriminant function diagrams, arc, within-plate, rift, collision.

Introduction

The idea of trying to chemically fingerprint magmas from different tectonic settings is probably best attributed to the pioneer work of Pearce & Cann (1971, 1973). In these papers, the authors identified differences in the geochemical signature of rocks from volcanic arc, ocean floor, and within-plate settings. Since then, numerous bivariate (x-y-type; e.g. Pearce & Gale 1977; Pearce & Norry 1979; Pearce 1982; Shervais 1982), ternary (e.g. Pearce et al. 1977; Wood 1980; Mullen 1983; Meschede 1986; Cabanis & Lecolle 1989), and old multivariate tectonomagmatic discrimination diagrams (Pearce 1976; Butler & Woronow 1986), as well as 20 new multidimensional diagrams (Agrawal et al. 2004, 2008; Verma et al. 2006; Verma & Agrawal 2011) have appeared in the literature for basic and ultrabasic igneous rocks (with $(SiO_2)_{adj}$<52 %; where the subscript $_{adj}$ refers to the adjusted data on an anhydrous 100 % adjusted basis; Le Bas et al. 1986; Verma et al. 2002). The diagrams of the older bivariate or ternary types for the tectonic discrimination of magmas with higher silica (with $(SiO_2)_{adj}$>52 %) are less numerous (Bailey 1981; Pearce et al. 1984; Gorton & Schandl 2000) although, more recently, 35 diagrams have now been proposed (three sets of five diagrams each, i.e., 15 for intermediate magmas by Verma & Verma 2013; and four sets of five diagrams each, i.e., 20 for acid or felsic magmas by Verma et al. 2012, 2013).

From an extensive database of samples from known tectonic settings, Verma (2010) evaluated most of the tectonomagmatic discrimination diagrams for basic and ultrabasic rocks and concluded that only the multidimensional diagrams, particularly the newer ones, worked satisfactorily with high percent success (Agrawal et al. 2004, 2008; Verma et al. 2006). Similarly, Verma et al. (2012) evaluated the highly used Pearce et al. (1984) diagrams for acid or felsic magmas and found them to perform unsatisfactorily, particularly for the collision setting.

Although most of the older bivariate and ternary diagrams have already been extensively evaluated, especially by Verma (2010), this is not the case of the newer multidimensional diagrams, particularly those published after 2010 (Verma & Agrawal 2011; Verma et al. 2012, 2013; Verma & Verma 2013). It is, therefore, worthwhile to evaluate all 55 such diagrams (Agrawal et al. 2004, 2008; Verma et al. 2006, 2012, 2013; Verma & Agrawal 2011; Verma & Verma 2013) using geochemical data from fresh as well as hydrothermally altered or highly weathered rocks from known tectonic settings. The evaluation from fresh rock data will provide an independent test on the functioning of these diagrams. The use of hydrothermally altered or weathered rocks for such an independent evaluation will likely render these diagrams appropriate for older terrains. Recently, Pandarinath (2014a) showed good functioning of these diagrams for hydrothermally altered rocks from seven geothermal wells. We will not present here the application to older terrains such as Precambrian belts; this has been extensively reported recently by Verma & Oliveira (2013, 2015), Pandarinath (2014b), Armstrong (2015), Bora & Kumar (2015), Kaur et al. (2015), Rahman & Mondal (2015), Srivastava et al. (2015), and Verma et al. (2015a,b).

This testing exercise is not trivial for at least four reasons: (1) such an evaluation of the older x-y (where x and y are

simple concentration or element ratio variables) or ternary (generally of three concentration variables) types of diagrams has shown them to perform unsatisfactorily in both igneous and sedimentary rock geochemistry (Armstrong-Altrin & Verma 2005; Verma 2010, 2015a; Verma et al. 2012, 2016; Verma & Armstrong-Altrin 2013, 2016; Armstrong, 2015); (2) the evaluation of the newer multidimensional diagrams can provide statistical information on percent success for the relatively older diagrams (proposed during 2004–2011) and total percent probability values for the newer ones (proposed during 2012–2013); and (3) a routine use of well-known databases, such as GERM, GEOROC-Mainz, and EGDB-USGS, for testing of our diagrams is to be viewed with caution.

Available multidimensional diagrams

These diagrams were proposed from statistical analysis of a large number of Miocene to Recent igneous rock samples from known tectonic settings. Thus, for the tectonic discrimination of basic and ultrabasic rocks from island arc, continental rift, ocean island, and mid-ocean ridge settings, Agrawal et al. (2004, 2008), Verma et al. (2006), and Verma & Agrawal (2011) used geochemical data for 1159, 1645, 2732, and 1877 samples, respectively, and proposed 5 diagrams in each paper. Verma et al. (2012) proposed 5 diagrams for the discrimination of four tectonic settings (island arc, continental arc, combined continental rift and ocean island as within-plate, and collision) from a compilation of 1132 acid rock samples. Similarly, for the proposal of the 15 diagrams each, Verma et al. (2013) and Verma & Verma (2013) employed compositional data for 3056 acid and 3664 intermediate rock samples, respectively, from island arc, continental arc, continental rift, ocean island, and collision tectonic settings.

The diagrams require prior calculations of complex discriminant functions DF1-DF2, whose equations were presented by the respective original authors (Agrawal et al. 2004, 2008; Verma et al. 2006, 2012, 2013; Verma & Agrawal 2011; Verma & Verma 2013). All these equations were also summarized recently by Verma et al. (2015b), which are reproduced here for easy reference as Tables S1-S11 in the Supplementary Material file* (Table S1 for five diagrams of Agrawal et al. 2004; Table S2 for five diagrams of Verma et al. 2006; Table S3 for five diagrams of Agrawal et al. 2008; Table S4 for five diagrams of Verma & Agrawal 2011; Tables S5-S7 for 15 diagrams of Verma & Verma 2013; Table S8 for five diagrams of Verma et al. 2012; and Tables S9-S11 for 15 diagrams of Verma et al. 2013). The computer program SINCLAS (Verma et al. 2002) or IgRoCS (Verma & Rivera-Gómez 2013a) can be used for obtaining the adjusted data referred to in these equations (see the subscript $_{adj}$) and deciding the magma types (basic, ultrabasic, intermediate, and acid; Le Bas et al. 1986).

We also note that these different sets of diagrams are independent of each other although they require complete datasets for all elements in the respective DF1-DF2 functions. For example, the major element based diagrams would require that concentrations of all major elements be available in a given sample; if an element is missing from the data, the set of major-element diagrams cannot be used. Unfortunately, sometimes only major elements are available from a particular area, so the inference can be drawn only from one set of diagrams. Thus, any set of diagrams can be used independently of the other sets.

Database and procedures

The geochemical data were compiled for 1034 samples of Miocene to Holocene relatively fresh as well as hydrothermally altered or weathered igneous rocks from different areas of known, uncontroversial tectonic settings from all over the world (Fig. S1 in the Supplementary Material file; compiled references are in Tables S12 and S13). A synthesis of this compilation for 18 test studies (1 to 18) from fresh rocks is presented in Table S12 and for hydrothermally altered or weathered rocks for 8 application studies (A1 to A8) is provided in Table S13. The cases are arranged according to the expected tectonic setting. The original authors' descriptions of alteration were used to group the samples in application studies as fresh and altered rocks; more details are provided in the relevant sections.

The geochemical data were also examined for the Tonga arc compiled in a freely-available geochemistry database GEOROC-Mainz, which enabled us to show the need for caution in the indiscriminate use of such databases.

We will describe in detail the first Test study under the general heading of "Ocean Island tectonic setting". This (Test study 1) is for the region of the Hawaiian Islands, in which four sub-regions (1a–1d) are separately considered because we wanted to show that these diagrams can be applied and tested with individual datasets. Obviously, if the main objective was to decipher the tectonic setting of a given area or region, all pertinent rock data or evidence should be used. This obviously includes the geological reconstruction of terranes. The approximate coordinates (longitude and latitude) of sample locations are then presented in two columns. The next columns present a subdivision of the compiled samples in terms of basic (B)+ultrabasic (U), intermediate (I), and acid (A) magmas, which allowed the application of appropriate sets of discrimination diagrams (Agrawal et al. 2004, 2008; Verma et al. 2006; Verma & Agrawal 2011 — all these four papers for basic and ultrabasic magmas; Verma & Verma 2013 — for intermediate magmas; and Verma et al. 2012, 2013 — for acid magmas). Thus, for the Mauna Kea area (Test study 1a), complete data were available for 303 basic and 3 ultrabasic rock samples only; no sample proved to be of intermediate or acid magma. Therefore, only diagrams for basic and ultrabasic rocks can be applied and that too for major element based (symbol m1 for Agrawal et al. 2004 and m2 for Verma et al. 2006) and immobile trace element based (symbol t2 for Verma and Agrawal 2011) diagrams; complete data were not available for the other immobile element based diagram set (t1 for Agrawal et al. 2008). Note the table is or tables are also defined where the results of the discrimination diagrams are presented (in this

* Supplementary Material (Tables S1–S54 and Figs. S1–S52) only in an electronical version on www.geologicacarpathica.com

case, Table 1). The next columns show the approximate ages in Ma (or geological epoch or period) and rock types assigned by the original authors (in this case, 0.1–0.4 Ma). The next column synthesizes the tectonic setting indicated by the diagrams (in this case, OIB). The final column lists the references from which the data were compiled (in this case, Rhodes & Vollinger 2004; Rhodes 2012).

For a correct application of the tectonomagmatic discrimination diagrams, the IgRoCS program (Verma & Rivera-Gómez 2013a) was used to obtain the magma types as basic or ultrabasic, intermediate, and acid, following the recommendations of the IUGS (Le Bas et al. 1986; Le Bas & Streckeisen 1991; Le Maitre et al. 2002). It is important to strictly follow the procedure used by the original authors of the diagrams, for example, note the subscript adj in numerous equations listed in Tables S1–S11. These magma names could as well be mafic or ultramafic, intermediate, and felsic, respectively, but because we are using the chemical criterion of adjusted SiO_2 for this distinction and not the contents of Mg, Fe, and Si, we continue to use the nomenclature of the IUGS. Depending on the magma types, appropriate sets of diagrams were used to test if they provided the expected results of the tectonic setting.

To infer the tectonic setting for basic and ultrabasic magmas, we used the software TecD (Verma & Rivera-Gómez 2013b), which allows the application of the diagrams by Agrawal et al. (2004, 2008), Verma et al. (2006), and Verma & Agrawal (2011). The four tectonic settings that can be discriminated from the diagrams contained in this software are as follows: IAB (island arc basic rocks), CRB (continental rift basic rocks), OIB (ocean-island basic rocks), and MORB (mid-ocean ridge basic rocks). TecD automatically counts the samples that plot in a given tectonic setting and provides a synthesis of the counting results of all five diagrams of a given set, both as the number of samples as well as the corresponding percentage values (called percent success for the expected or inferred tectonic setting). Because a given tectonic setting will be missing from one of the five diagrams in any set, the total percentage for any of the four settings will never be 100 %; it will be around 80 % as a maximum value. Further, because of this automatic procedure programmed in TecD, it is not necessary to actually plot the samples in diagrams. Nevertheless, following the suggestion of reviewers we provided the corresponding diagrams for almost all studies, so one can better understand the functioning of TecD.

Another program TecDIA (Verma et al. 2015c) was used for the application of all diagrams for intermediate (Verma & Verma 2013) and acid magmas (Verma et al. 2012, 2013). TecDIA also computes the probabilities of samples for the different tectonic settings and provides a synthesis of these probability values. The tectonic settings that can be discriminated from the diagrams for intermediate and acid magmas

Table 1: Testing of multidimensional diagrams from Quaternary (0.1-0.4 Ma) basic and ultrabasic rocks of Mauna Kea, Hawaii (Rhodes and Vollinger, 2004; Rhodes et al. 2012; Test study 1a).

Figure reference; figure type	Discrimination diagram	Total no. of samples (%)	Predicted tectonic affinity and number of discriminated samples (%)				
			IAB	CRB+OIB	CRB	OIB	MORB
Agrawal *et al.* (2004); adjusted major element concentrations	IAB-CRB-OIB-MORB	306 (100)	0 (0)	---	0 (0)	306 (100)	0 (0)
	IAB-CRB-OIB	306 (100)	0 (0)	---	0 (0)	306 (100)	---
	IAB-CRB-MORB	306 (100)	0 (0)	---	217 (70.9)	---	89 (29.1)
	IAB-OIB-MORB	306 (100)	0 (0)	---	---	306 (100)	0 (0)
	CRB-OIB-MORB	306 (100)	---	---	0 (0)	306 (100)	0 (0)
Test study 1a. Synthesis of all five diagrams of Agrawal et al. (2004)		***1530 (100)***	***0 (0)***	***---***	***217 (14.2)***	***1224 (80.0)***	***89 (5.8)***
Verma *et al.* (2006); log-ratios of major elements	IAB-CRB-OIB-MORB	306 (100)	0 (0)	---	4 (1.3)	300 (98)	2 (0.7)
	IAB-CRB-OIB	306 (100)	0 (0)	---	0 (0)	306 (100)	---
	IAB-CRB-MORB	306 (100)	0 (0)	---	36 (11.8)	---	270 (88.2)
	IAB-OIB-MORB	306 (100)	0 (0)	---	---	306 (100)	0 (0)
	CRB-OIB-MORB	306 (100)	---	---	0 (0)	306 (100)	0 (0)
Test study 1a. Synthesis of all five diagrams of Verma et al. (2006)		***1530 (100)***	***0 (0)***	***---***	***40 (2.6)***	***1218 (79.6)***	***272 (17.8)***
Verma and Agrawal (2011); log-ratios of immobile major and trace elements	IAB-CRB+OIB-MORB	306 (100)	2 (0.7)	303 (99)	---	---	1 (0.3)
	IAB-CRB-OIB	306 (100)	3 (1)	---	1 (0.3)	302 (98.7)	---
	IAB-CRB-MORB	306 (100)	2 (0.7)	---	303 (99)	---	1 (0.3)
	IAB-OIB-MORB	306 (100)	2 (0.7)	---	---	303 (99)	1 (0.3)
	CRB-OIB-MORB	306 (100)	---	---	1 (0.3)	303 (99)	2 (0.7)
Test study 1a. Synthesis of all five diagrams of Verma and Agrawal (2011)		***1530 (100)***	***9 (0.6)***	***303 (---)***	***381 (24.9)***	***1135 (74.2)***	***5(0.3)***

IAB- island (or continental) arc basic rock; CRB- continental rift basic rock; OIB- ocean island basic rock; MORB- mid-ocean ridge basic rock; CRB+OIB- combined continental rift and ocean island, i.e., within-plate (WP) basic rocks; IA, CR,, OI, and MOR will be the corresponding tectonic settings; --- means no samples; the numbers within the parentheses refer to the percent values for the corresponding number of samples; note, for the calculations of percent synthesis values, the samples plotting in the combined CR+OI field (CRB+OIB column) are proportionately distributed between the CR and OI settings.

are as follows: IA (island arc), CA (continental Arc), CR (continental rift) and OI (Ocean Island) together as within-plate, and Col (collision). As for TecD, TecDIA also provides a complete synthesis of the results of all five diagrams in a given set. In fact, TecDIA additionally gives a synthesis of the probability estimates for each tectonic setting in all diagrams as well as the overall percent probability estimates of each diagram set. Therefore, actual plotting of samples in any diagram is really not required. Nevertheless, we also present one example of all diagram types for intermediate and acid magmas (Verma & Verma 2013; Verma et al. 2012, 2013).

Results and discussion

The results of the evaluation are presented in two subsections. The first part corresponds to relatively fresh rocks from known tectonic settings, whereas the second part shows the results for hydrothermally altered and weathered rocks. A lower limit of five samples with complete data for a given diagram set was arbitrarily established for using them for testing or application purposes. Similarly, results are also presented even if the data were available for only one or two sets of diagrams because the evaluation is independently achieved for all diagram sets.

Testing of the diagrams from "fresh" volcanic rocks of ocean island tectonic settings

The first test study of the Hawaiian Islands will be described in greater detail. All other studies will simply be mentioned with the statistical information in order to keep the paper short and avoid excessive repetition.

Test study 1a: Mauna Kea

For the Mauna Kea area, 303 samples of basic and 3 ultrabasic rocks (Table S12; Rhodes and Vollinger 2004; Rhodes 2012) had complete dataset for major-element based diagrams of Agrawal et al. (2004) and Verma et al. (2006) and for only one set of immobile trace element based diagrams (Verma & Agrawal 2011). No samples had complete data for the other set of immobile trace element based diagrams (Agrawal et al. 2008), which could not be used. Similarly, none of the diagrams for intermediate and acid rocks (Verma & Verma 2013; Verma et al. 2012, 2013) could be used for this case because no samples proved to be of these types (missing data shown by — in the "I" and "A" columns in Table S12).

Thus, three sets of diagrams (Agrawal et al. 2004; Verma et al. 2006; Verma & Agrawal 2011) could be tested from the Mauna Kea data; and the results are shown in Table 1. The actual diagrams of Agrawal et al. (2004) for the Mauna Kea samples do not really need to be shown for three reasons: (i) these diagrams are based on only major element concentrations and not on log-ratios; (ii) TecD provides complete summary of all the plots (the first part of Table 1); and (iii) we wanted to conserve journal space by presenting only one set of diagrams based on log-ratios (Fig. 1) in the main part of the paper. Nevertheless, for the sake of completeness and considering that most readers of the journal would like to see the diagrams along with the synthesis in tables, we have added these diagrams (Figs. S2 and S3 for this case study as well as in other figures for other case studies) in the Supplementary file.

In the first set of five diagrams (Fig. S2), all Mauna Kea samples plotted in the OIB fields in four of the five diagrams in which this setting is present. In the diagram (IAB-CRB-MORB) from which OIB is absent, the samples will plot in any other fields; in this case, most of them plotted in the CRB field, followed by the MORB field (Table 1). The synthesis of all diagrams is then presented in Table 1, which shows that the overall percent success for the OIB setting is 80.0 % being the maximum value for such a synthesis provided by TecD. Therefore, these diagrams clearly showed the expected OIB setting for the Mauna Kea samples.

In the other set of diagrams based on log-ratios of major elements (Verma et al. 2006), the Mauna Kea samples are actually plotted in Fig. 1a–e (DF1–DF2 equations from Table S2 were used for the calculations of the x and y coordinates in each diagram) and the results from TecD are also summarized in Table 1. In the first diagram (Fig. 1a), 300 (out of 306) samples plotted in the OIB field, whereas in the other three diagrams (Fig. 1b,d,e) all samples plotted in the OIB field. In the diagram from which the OIB field is missing (Fig. 1c), the samples plotted in the MORB and CRB fields. The overall synthesis of all five diagrams of Verma et al. (2006) also showed a clear result of the OIB tectonic setting with the percent success of 79.6 % (Table 1), very close to the maximum value of 80 %.

Finally, the set of diagrams based on log-ratios of immobile elements (Verma & Agrawal 2011) also showed an OIB setting for the Mauna Kea samples with the percent success of about 74.2 % (Fig. S3; Table 1). In this diagram set, the first diagram has a combined CRB+OIB setting, only three diagrams have an OIB setting, and from one diagram this setting is totally missing. Therefore, the percent success for the OIB can seldom reach the maximum value of 80 %.

Thus, a satisfactory functioning of all three diagram sets for the OIB setting was confirmed from the Mauna Kea data (Test study 1a).

Test study 1b: Mauna Loa

Forty-five (43 basic and 2 ultrabasic) samples from Mauna Loa (Table S12; Rhodes & Vollinger 2004) allowed the testing of three sets of diagrams. Most of the samples plotted in the OIB field in the three sets for major elements (two sets for basic rocks as Figs. S4 and S5 and one set for acid rocks as Fig. S6; percent success amounting to about 75–76 %; Table S14), thus confirming the good functioning of all three sets of diagrams for the OIB setting.

Test study 1c: Maui Island

Only 10 basic rock samples available from the Maui Island (Table S12; Sherrod et al. 2007) allowed the testing of three sets of diagrams. Most of the samples plotted in the OIB field in the three sets (overall percent success of about

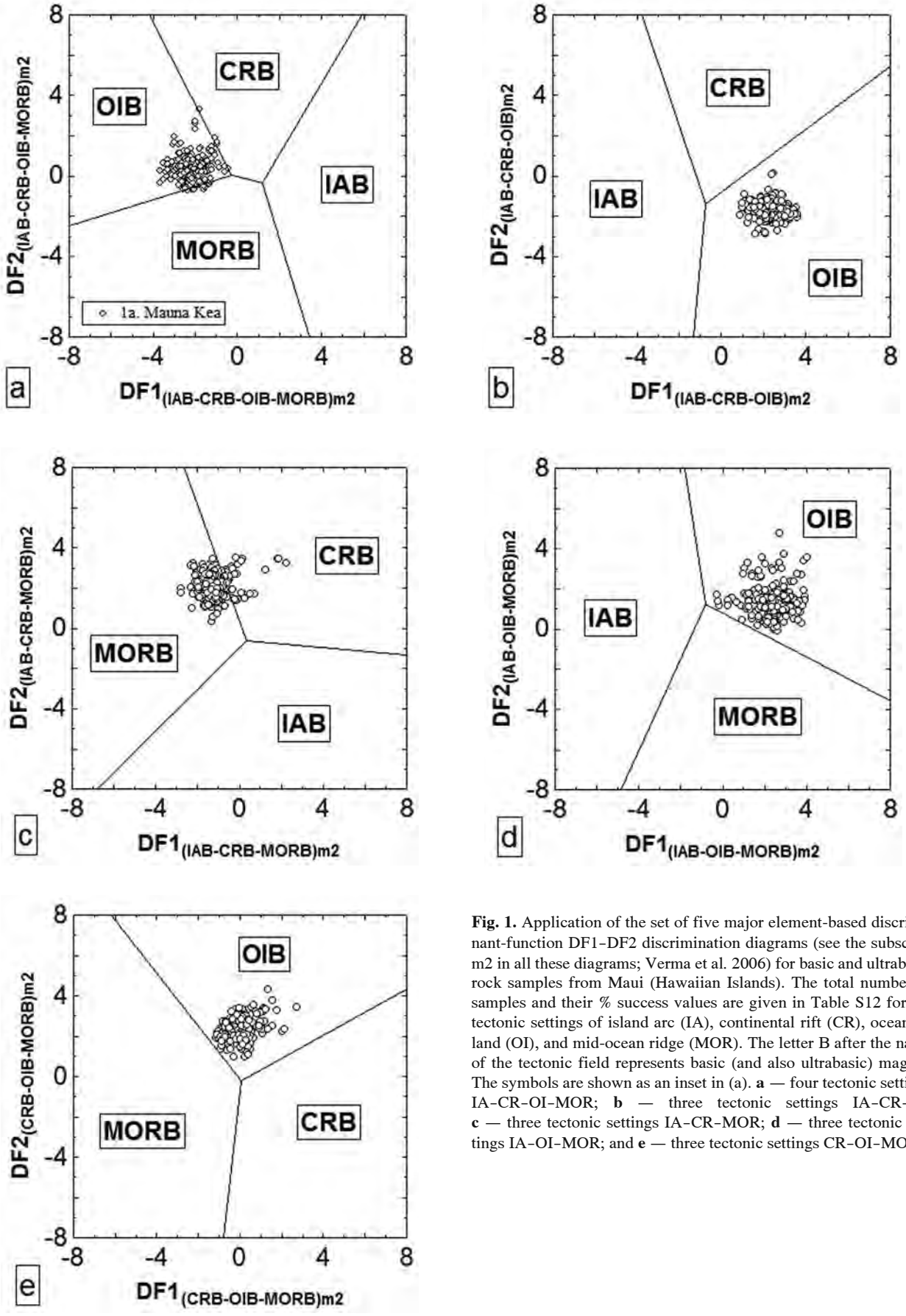

Fig. 1. Application of the set of five major element-based discriminant-function DF1–DF2 discrimination diagrams (see the subscript m2 in all these diagrams; Verma et al. 2006) for basic and ultrabasic rock samples from Maui (Hawaiian Islands). The total number of samples and their % success values are given in Table S12 for the tectonic settings of island arc (IA), continental rift (CR), ocean island (OI), and mid-ocean ridge (MOR). The letter B after the name of the tectonic field represents basic (and also ultrabasic) magma. The symbols are shown as an inset in (a). **a** — four tectonic settings IA–CR–OI–MOR; **b** — three tectonic settings IA–CR–OI; **c** — three tectonic settings IA–CR–MOR; **d** — three tectonic settings IA–OI–MOR; and **e** — three tectonic settings CR–OI–MOR.

62–80 %; Figs. S7–S9; Table S15) and confirmed good functioning of all three sets of diagrams for the OIB setting.

Test study 1d: Oahu Island

Twenty-four samples from the Oahu Island were used (Table S12; Jackson et al. 1999). Nine samples of basic rocks had complete datasets for Agrawal et al. (2004), Verma et al. (2006) and Verma and Agrawal (2011). The set of trace element based diagram (Agrawal et al. 2008) were not used, because the samples with complete data were only four (Table S12) and we had decided to report only the results of at least five samples. The nine basic rock samples indicated the OIB setting in the three sets of diagrams with percent success from 67 % to 78 % (Figs. S10–S12; Table S16).

Complete data for 15 intermediate rock samples were available for two diagram sets (Verma & Verma 2013). For both sets, these samples indicated a within-plate (CR+OI) setting, with about 81 % and 87 % percent probability values (for explanation of probability estimates, see Verma & Verma 2013), respectively, for the complete major and selected immobile element based diagrams (Figs. S13 and S14; Table S17). This inference can be considered consistent with that of the basic rock diagrams, because those for intermediate rocks are incapable of discriminating these two very similar tectonic settings; the distinction between continental rift and ocean island settings can only be made at present from basic and ultrabasic rocks. The testing of the third set is not reported because only three samples with complete data were available (Table S12).

Test study 2: Trindade Island

The compiled rocks from the Trindade Island (Table S12; Marques et al. 1999) included 14 (2 basic and 12 ultrabasic) samples for testing of three sets of diagrams (Agrawal et al. 2004, 2008; Verma et al. 2006) and 24 intermediate rock samples for two sets of diagrams (24 for the major element based and 13 for immobile trace element based diagrams; Verma & Verma 2013).

The testing of the diagrams for basic and ultrabasic rocks was satisfactory because most of the 14 samples plotted in the OIB field, with percent success of 70 %, 70 %, and 62 %, respectively, for Agrawal et al. (2004), Verma et al. (2006), and Agrawal et al. (2008) diagrams (Figs. S15–S17; Table S18). Similarly, the two sets of diagrams for intermediate rocks (major elements and immobile trace elements) were also satisfactorily tested for the within-plate setting, with percent probability values of about 76 % and 80 %, respectively (Figs. S18 and S19; Table S19).

Testing of the diagrams from "fresh" volcanic rocks of ocean island or continental rift tectonic setting

Test study 3: White Island, Ross Sea, Antarctica

Cooper et al. (2007) suggested that rocks from the White Island resulted from rift-related decompression melting rather than the action of a mantle plume earlier suggested by Behrendt et al. (1991, 1992). Therefore, either a CRB or an OIB setting could be the expected tectonic setting. We compiled data for 22 basic rock samples (Table S12), which enabled us to test all four sets of diagrams for basic and ultrabasic magmas. In the major element based diagrams all samples plotted only in the CRB and OIB fields (Figs. S20 and S21; Table S20). The percent success values for Agrawal et al. (2004) diagrams were about 44 % and 56 %, respectively, for the CRB and OIB settings, whereas those for the Verma et al. (2006) diagrams these were about 48 % and 52 %, respectively (Table S20). The trace element based diagrams of Agrawal et al. (2008) indicated a CRB setting with percent success of about 64 %, whereas those of Verma & Agrawal (2011) indicated an OIB setting with the corresponding percent success of about 68 % (Figs. S22 and S23; Table S20). Thus, the diagrams indicate either a CRB or an OIB setting for these rocks. Unfortunately, no clear distinction between these two very similar tectonic settings was achieved from these diagram sets. The geological history and crustal thickness of the White Island might resolve this controversy (Behrendt et al. 1991, 1992; Cooper et al. 2007).

The continental rift and ocean island tectonic settings are very similar, which makes their discrimination a rather difficult task. The four sets of multidimensional discrimination diagrams (Agrawal et al. 2004, 2008; Verma et al. 2006; Verma & Agrawal 2011) available as geochemical discrimination diagrams provided mutually inconsistent results. A combination technique of multidimensional discrimination and petrogenetic processes yet to be proposed and practiced might eventually throw further light on this complex problem because the discrimination diagrams have certain limitations as discussed recently by Verma et al. (2015b) and Verma (2015b, 2015c).

Test study 4: McMurdo area, Antarctica

Drill core basic volcanic glass samples of Miocene age (15.9–18.4 Ma; Table S12; Nyland et al. 2013) were recovered from the McMurdo Sound area, Antarctica. The tectonic setting of the area was not reported by Nyland et al. (2013), but it may well be either a continental rift or an ocean island. The basic rock diagrams might help us to distinguish between them. Fairly complete geochemical data, including alteration information, for 24 glass samples were reported by Nyland et al. (2013). Complete data (Table S12) for 24 samples were thus available for three sets of diagrams (Agrawal et al. 2004; Verma et al. 2006; Verma & Agrawal 2011) and data for 20 (out of 24) samples were complete for the diagrams of Agrawal et al. (2008). The major element based diagram sets indicated an ocean island setting, with about 63 % or 64 % percent success (Figs. S24 and S25; Table S21). The immobile trace element based diagrams of Agrawal et al. (2008) showed percent values of 55 % for the CRB and 45 % for the OIB setting; so they did not provide a clear answer (Fig. S26; Table S21). The other immobile element based diagrams (Verma & Agrawal 2011), however, suggested an OIB setting for these glass samples, with percent success of about 72 % (Fig. S27; Table S21). Therefore, an OIB setting could be inferred for the McMurdo Sound area during the Miocene.

Testing of the diagrams for "fresh" volcanic rocks from continental rift tectonic setting

Test study 5: Garrotxa, Spain

Geochemical data for 16 samples of Quaternary basic and ultrabasic rocks from the NE Volcanic Province of Spain (Garrotxa area) were reported by Cebriá et al. (2000). The use of all four sets of diagrams was possible (Table S12). These diagrams consistently confirmed a continental rift setting for these samples, with percent success values of 60 % to 80 % (Figs. S28–S31; Table S22).

Test study 6: Styrian basin, Austria

Geochemical data for 39 (9 basic and 30 ultrabasic) Quaternary rock samples from this area (Table S12; Ali et al. 2013) clearly indicated a continental rift setting in all four sets of diagrams, with percent success of about 71 % to 80 % (Figs. S32–S35; Table S23).

Test study 7: Cameroon Mountains, Cameroon

Fourteen samples of basic rocks from the year 1999 and 2000 (recent) eruptions (Table S12; Suh et al. 2003) had complete data for three sets of diagrams, all of which were consistent with a continental rift setting, with percent success values of 56 % to 74 % (Figs. S36–S38; Table S24).

Test study 8: Nosy Be Archipelago, Madagascar

Melluso & Morra (2000) reported geochemical data for 27 samples of Miocene mafic alkaline rocks from the Nosy Be Island (Table S12). Three sets of diagrams could be applied, all of which indicated a continental rift setting, with percent success values of about 56 % to 73 % (Figs. S39–S41; Table S25).

Test study 9: Tianheyong, Inner Mongolia, China

Geochemical data for only eight samples of early Miocene were reported by Yang et al. (2009). These samples had complete data for three sets of diagrams (Table S12). The two sets based on major elements (Agrawal et al. 2004; Verma et al. 2006) indicated a continental rift setting, with percent success of about 73 % for both of them (Figs. S42 and S43; Table S26). However, the set based on immobile elements (Agrawal et al. 2008) suggested an ocean island setting for these samples (percent success of 75 %; Fig. S44; Table S26).

Test study 10: Halaha volcanic field, Central Great Xing'an Range, China

Fourteen samples of Quaternary basic rocks (Table S12; Ho et al. 2013) from the Halaha volcanic field, NE China, indicated a continental rift setting (Table S27). Both sets of the major element based diagrams showed higher percent success values of 67 % and 71 % than both sets of immobile element based diagrams (44 % and 49 % only; Figs. S45–S48; Table S27). Nevertheless, the expected CRB tectonic setting was confirmed from all diagram sets.

Testing of the diagrams for "fresh" volcanic rocks from continental arc tectonic settings

Test study 11: Aniakchak ignimbrite, Alaska

Geochemical data for 9 samples from about 3400 years old ignimbrite (Table S12; Dreher et al. 2005) from the Aniakchak caldera, Aleutian Peninsula, were used to test all multidimensional diagrams for acid rocks (Verma et al. 2012, 2013). Both sets based on log-ratios of major elements (Figs. S49 and S50) showed a continental arc setting, with percent probability values of 85 % and 56 % (Table S28). The two sets based on log-ratios of immobile elements also indicated the same tectonic setting with percent probability values of 70 % and 77 % (Figs. S51 and S52; Table S28). This inference seems to be consistent with the continental arc setting for this peninsular part of the Aleutian arc and involvement of crustal material in the genesis of the ignimbritic magma (Dreher et al. 2005).

We will not present more diagrams because the reader should have ascertained from our presentation so far that the diagrams serve the purpose of visualization only and are not really required for the interpretation. TecD and TecDIA provide all necessary information to understand the results of the multidimensional diagrams. Furthermore, for intermediate and acid rocks TecDIA provides probability estimates which cannot be obtained directly from the examination of the respective diagrams.

Test study 12a–12c: Guatemala, Central America

Nine samples of intermediate volcanic rocks from recent eruptions of the Fuego volcanic complex (Test study 12a; Table S12; Chesner & Rose Jr. 1984) allowed the evaluation of the major element based diagram set (Verma & Verma 2013), which indicated the expected continental arc setting for these samples, with the total percent probability value of 65 % (Table S29).

Geochemical data for 40 samples of lava from the Meseta volcano (Test study 12b; Table S12; Chesner & Halsore 1997) also allowed the application of only one set of major element based diagrams (Verma & Verma 2013), which confirmed the expected continental arc setting for these samples, with the total percent probability value of 72 % (Table S30).

The final Test study (12c) from this group was for Quaternary volcanic rocks from the Santiaguito volcanic complex (Table S12; Scott et al. 2013). Eighteen samples of intermediate rocks had complete data for two sets of diagrams, which showed a continental arc setting (total percent probability values of 74 % and 55 %; Table S31). Only five of these samples had complete data for the remaining set of diagrams, which also indicated a continental arc setting for these samples (Table S31). Additionally, 17 samples of acid rocks allowed the application of all four sets of diagrams (Table S32). One set of major element based diagrams indicated an island arc setting for these samples, whereas the other set a continental arc setting. One set of immobile element based diagrams did not provide a consistent answer, indicating, in fact, a transitional continental arc to collision

setting. The final set of diagrams also based on immobile elements, on the other hand, provided a consistent answer of a continental arc setting, with total percent probability of 77 % (Table S32). These inconsistencies seem to be a natural consequence of crustal involvement in the genesis of these magmas as suggested by the original authors (Scott et al. 2013).

Test study 13: Huequi volcano, Chile

Nine intermediate rock samples of historic activity from this volcanic dome complex in the Andean southern volcanic zone (Table S12, Watt et al. 2011) had complete data for two of the three sets of diagrams, which showed the expected continental arc setting with total percent probability values of about 70 % (Table S33).

Test study 14: Nisyros Island, Dodecanese, Greece

Only the major element based diagram set could be tested from Quaternary volcanic rocks of Nisyros Island, Greece (Table S12; Di Paola 1974). Sixteen samples of intermediate rocks indicated a continental arc setting but with a rather low percent probability value of 49 % or a continental arc to collision transitional setting, with the respective probability values of 49 % and 40 %, respectively (Table S34). The acid rocks (11 samples) were also consistent with a continental arc setting and showed much higher percent probability values of 71 % and 75 % (Table S35). These different inferences may be related to different petrogenetic processes for these two magma types.

Testing of the diagrams from "fresh" volcanic rocks of island arc tectonic setting

Test study 15: Augustine Island

One set of diagrams based on major elements in intermediate rocks was tested from the geochemical data for Pleistocene-Holocene volcanic rocks from this small island in the Aleutian arc (Table S12; Johnson et al. 1996). Twenty-one samples consistently plotted in the arc setting, with the island arc predominating over the continental arc (total percent probability of 59 % and 41 %, respectively; Table S36). Thus, the expected tectonic setting of an island arc seems to be confirmed.

Test study 16a: Barren Island, Andaman-Nicobar Islands

Data for 25 samples of Quaternary basic volcanic rocks from the Barren Island were compiled (Test study 16a; Table S12; Chandrasekharam et al. 2009; Streck et al. 2011). In the major element based diagrams these island arc samples showed percent success of about 73 % and 80 % for the Agrawal et al. (2004) and Verma et al. (2006) diagrams, respectively (Table S37). Only 11 samples had complete data for immobile element based diagrams of Agrawal et al. (2008), whereas 24 of them had complete data for Verma & Agrawal (2011) diagrams. Both sets also indicated an arc setting, with high percent success of 80 % (Table S37). Similarly, 21 samples from the Barren Island proved to be from intermediate magma, which, in the major element based diagrams (Verma & Verma 2013) showed an island arc setting with total percent probability of 52 %, followed by about 42 % for the continental arc setting (Table S38). The two sets of immobile element based diagrams confirmed the island arc setting for intermediate rocks, with higher total percent probability of about 74 % (Table S38). Thus, the expected tectonic setting of an island arc seems to be confirmed.

Test study 16b: Narcondam Island, Andaman-Nicobar Islands

For the Narcondam Island, only 10 samples of intermediate and 8 of acid rocks were available (Test study 16b; Table S12; Pal et al. 2007; Streck et al. 2011). Although for intermediate rocks the major element based diagrams indicated an island arc setting, the total percent probability was very low (only about 41 %; Table S39). Eight of these samples with complete data for the two sets of immobile element based diagrams, however, confirmed the island arc setting with total percent probability values of 71 % and 58 % (Table S39). The major element based diagrams for acid rocks also confirmed the island arc setting with total percent probability of about 72 % (Table S40). However, one set of immobile trace element based diagrams indicated a continental arc (total percent probability of about 58 %) rather than an island arc (total percent probability of about 42 %; Table S40). The reasons for this discrepancy will have to be evaluated, but one of them is probably related to the data quality of trace elements (larger analytical errors for trace than for major elements).

Testing of the diagrams for "fresh" volcanic rocks from mid-ocean ridge tectonic settings

Test study 17: Central Indian Ridge

Yi et al. (2014) reported geochemical data for axial positions of the Indian Ridge (Table S12). Thirty-three samples proved to be of basic magma types, whereas 14 turned out to be intermediate rocks. The latter were not used for testing because the mid-ocean ridge setting is missing from the diagrams for intermediate rocks (Verma & Verma 2013). Therefore, the Supplementary file does not have the corresponding report table. Nevertheless, this setting can be included in the future versions of these diagrams. The basic rocks confirmed the mid-ocean ridge tectonic setting in all four sets of diagrams, with high percent success values of 65 % to 76 % (Table S41).

Testing of the diagrams for "fresh" volcanic rocks from collision tectonic settings

Test study 18: Shirak area, NW Armenia

The Pliocene-Pleistocene volcanic rocks of Armenia are considered a key component of the Arabia-Eurasia collision (Neill et al. 2013). Thirteen samples of intermediate rocks had complete data for two sets of diagrams; 9 of these samples could be used for the remaining set of diagrams (Table S12). All diagram sets consistently indicated a collision set-

ting for these samples; the corresponding percent probability values varied from a low 43 % to a considerably high 67 % (Table S42).

Evaluation of the diagrams for "hydrothermally altered" or "weathered" volcanic rocks from different tectonic settings

Test study A1: Eaio Island, Maquesas Islands, French Polynesia

Twenty-five (24 basic and 1 ultrabasic; Caroff et al. 1999; Table S13) hydrothermally altered samples from three drill holes in the Eaio Island were used to evaluate three of the four sets of diagrams, which affirmed an ocean island tectonic setting in all diagram sets (Table S43). In spite of the alteration indicated by high-temperature iddingsite and low-temperature zeolites, gypsum, calcite, and clay minerals (Caroff et al. 1999), most of the compiled samples plotted in the OIB field and showed high percent success values of 75 % to 78 % (Table S43).

Test study A2: Koolau, Haleakala, and Kohala, Hawaiian Islands

Moderately to highly altered rocks (exfoliated shell, corestone, rind, and shell samples) affected by spheroidal weathering from three volcanoes (Koolau, Haleakala, and Kohala) of the Hawaiian Islands, were sampled and analysed by Patino et al. (2003). A sample from a corestone-shell set was divided into three subsuites (corestone, exfoliated shell, andrind) with different degrees of alteration (Patino et al. 2003). The approximate ages of these samples as reported by Patino et al. (2003) were about 2–4 Ma for Koolau (Oahu Island), 0.35–0.4 Ma for Haleakala (Maui Island), and 0.35 Ma for Kohala (Hawaii). For 9 samples of basic and ultrabasic rocks, unfortunately, only major element based diagrams could be tested; complete data for none of the immobile element based diagrams were available. Both sets of major element based diagrams indicated a continental rift setting with 62 % and 71 % percent success; the ocean island setting showed the next setting with 36 % and 25 % (Table S44). Thus, although the expected ocean island setting was not inferred for these moderately to intensely weathered rocks, the inferred continental rift setting is very similar to the expected setting; both of them belong to the within-plate setting.

Test study A3: Hainan Island, China

The geochemistry of basaltic lavas from Hainan Island near the northern edge of the South China Sea (Miocene to Holocene; Table S13) was reported by Wang et al. (2012). The alteration was indicated by high loss on ignition (LOI) values (Wang et al. 2012). We selected 13 slightly to intensely altered basic and 10 intermediate rock samples for this evaluation. The basic rock samples had complete datasets for only the major element based diagrams; for immobile trace element diagrams only four samples had complete data, which were not considered (Table S13). Both major element based diagrams indicated a continental rift setting with percent success of about 69 % and 74 % (Table S45). The 10 intermediate rock samples also had complete data for major elements only; for immobile elements only three samples had complete data. The major element based diagrams showed a within-plate (CR+OI) setting for them, with a high total percent probability of 83 % (Table S46). Thus, in spite of alteration, a consistent result of a continental rift or a within-plate setting was obtained from basic and intermediate rocks, respectively.

Test study A4: Moyuta and Tecuamburro volcanoes, Guatemala

Highly altered rocks (exfoliated shell, corestone, rind, and columnar joint block samples; see also Test study A2 above) affected by spheroidal weathering from two volcanoes (Moyuta and Tecuamburro) of Guatemala, were sampled and analysed by Patino et al. (2003). The ages of the samples from Moyuta were not reported by Patino et al. (2003), although an approximate age of Pliocene–Pleistocene was indicated for the Tecuamburro volcano. As for the earlier Test study), only the major element based diagrams for intermediate rocks could be tested from 7 samples. This diagram set indicated a continental arc setting with about 53 % total percent probability value (Table S47). Thus, the expected tectonic setting was inferred in spite of the intense spheroidal weathering that affected these rock samples.

Test study A5: Sarapiquí Miocene arc, Costa Rica

Gazel et al. (2005) reported geochemical data for rocks from the *Sarapiquí* Miocene (11.4–22.2 Ma) arc (or paleoarc), northern Costa Rica (Table S13). Gazel et al. (2005) stated that pyroclasts in their samples were altered; additionally, H_2O^+ contents in three of the four samples showed relatively high values (1.70–7.00 %). Ten samples of basic rocks (probably of ages 15–22 Ma; Gazel et al. 2005) had complete data for the two major element based diagram sets and one immobile element set and suggested an arc setting for them (Table S48). From the basic rock diagrams, the distinction between an island and a continental arc is at present not possible, because the continental arc setting was not represented in the databases used for proposing these diagrams (Agrawal et al. 2004, 2008; Verma et al. 2006; Verma & Agrawal 2011). However, 14 samples of intermediate rocks (probably of ages 11–15 Ma, somewhat younger than the basic rocks; Gazel et al. 2005) from this paleoarc had complete data for two sets of diagrams, which clearly confirmed an island arc setting, with percent probability values of 67 % for the major element based diagrams and 57 % for one set of immobile element based diagrams (Table S49). It is not clear if this Miocene arc represents an island or a continental arc setting. Nevertheless, because these two tectonic settings are very similar, this inference could be interpreted as a valid result. Finally, only four rock samples proved to be of acid type, which were not used for testing the respective diagrams.

Test study A6: Taupo Volcanic Zone, New Zealand

From the Rotokawa and Ngatamariki geothermal systems, Taupo Volcanic Zone, New Zealand, hydrothermally altered intermediate rocks were sampled from deep drill holes and

analysed for their major and trace elements by Browne et al. (1992). These authors did not report the tectonic setting of their geothermal area with temperatures above 300 °C. Practically no samples escaped the alteration indicated by altered psudomorph (altered hypersthene, titanomagnetite to leucoxene, high LOI up to 6.2 %, and high volatile contents; Browne et al. 1992). The present-day tectonic setting seems to be an active rifting of an arc (Deering et al. 2011). Twenty-eight samples had complete data for the major element based diagrams, which indicated an island arc setting with a relatively low total percent probability value of about 44 %, followed by about 36 % for the continental arc setting (Table S50). The diagram set based on immobile major and trace elements could be tested from only five samples. It also indicated an island arc setting but with higher probability of about 63 % followed by 37 % for the continental arc (Table S50).

Test study A7a: SE Indian and SW Pacific seafloor, Indian and Pacific Oceans

Pyle et al. (1995) reported geochemical data from fresh as well as altered seafloor rocks (dredged and drilled) of different ages (0–4 and 15–23 Ma; Table S13). The presence of micaceous alteration minerals, low CaO/Al_2O_3 reflecting pervasive alteration, unusually high Rb contents, and contamination from seawater alteration were suggested by Pyle et al. (1995) as the symptoms of alteration for most samples. The authors used an intense leaching procedure before sample preparation for geochemical data acquisition. Complete major element data were available for 9 samples, of which 7 samples had complete immobile element data as well. Therefore, all four diagram sets could be tested from these data. The application showed a mid-ocean ridge setting from all diagrams, with a high percent success of about 72–80 % (Table S51).

Test study A7b: central Indian Ridge, Indian Ocean

Geochemical data for mafic and ultramafic rocks were reported for the central part of the Indian Ridge (Yi et al. 2014; Table S13). Most samples are characterized by moderate to intense alteration of primary minerals. In highly altered gabbroic rocks, clinopyroxene is replaced by amphibole and chlorite, plagioclase changed to aggregates of prehnite or cryptocrystalline secondary minerals, and altered veins of Fe-Ti oxide and minor chlorite are present (Yi et al. 2014). In other samples, olivine is altered to aggregates of serpentine, iron oxide, and iron hydroxide; most harzburgites are strongly serpentinized (Yi et al. 2014). Twenty-eight samples with complete major element data indicated a mid-ocean ridge setting with 64 % and 55 % percent success values (Table S52). A lesser number of samples (17 and 20) had complete immobile element data for the respective diagrams. They also indicated a mid-ocean ridge setting for these diagrams with high success rates of about 70 % (Table S52).

Test study A8: Aeolian Island, Italy

Only 17 samples of hydrothermally altered (7 intermediate and 10 acid) rocks could be compiled from Del Moro et al. (2011; Table S13) for this final Test study. The volcanic and subvolcanic rocks underwent alteration processes induced by acid-sulphate hydrothermal systems (Del Moro et al. 2011). According to these authors, some rocks showed argillic to silicic alteration containing abundant hydrous sulphate and hydroxyl-sulphate minerals, whereas other rocks underwent pyrometamorphic processes. Two sets of diagrams for intermediate rocks could be tested; in both sets all samples consistently plotted in the collision field and showed high total percent probability values of about 83 % and 84 % (Table S53). For acid rocks, all four sets of diagrams could be applied. The first set of major element based diagrams showed a collision setting but with a low total percent probability of 42 %, whereas the other set indicated a transitional arc to collision setting (Table S54). However, both sets of immobile element based diagrams were consistent with a collision setting for these samples (total percent probability values of about 82 % and 60 %; Table S54).

Use of freely-available geochemical databases for tectonic discrimination

Agrawal & Verma (2007) were the first to show that freely-available geochemical databases should not be indiscriminately used for tectonic discrimination. Here, we use the example of GEOROC-Mainz to confirm the difficulties in using compiled data without critically examining the original papers from which the data were compiled.

Tongan arc data were downloaded as an excel file on May 27, 2015. This file contains 222 rows of samples compiled from 29 references. However, only 151 samples have complete major element data compiled from 19 references. There may also be discrepancies regarding the information on age or alteration parameters and references listed but we will point out only the discrepancies between the database and the data presented in the corresponding literature references. One problem with the database is that it contains zero (0) concentration values for numerous elements; zero values are not possible because this means that either the element of interest was not measured or it was not determinable by the analytical technique used. Therefore, the zero values should simply be blank cells.

Haase et al. (2002) reported data for 27 samples from the arc setting (Havre, Monowai, Rauol, Vulcanolog, Brothers, and Clark) whereas the GEOROC database has only 5 samples. Similarly, Hergt and Woodhead (2007) reported data for 8 samples from Eua Island whereas the database has only 4 samples from this paper. Furthermore, these two papers (Haase et al. 2002; Hergt and Woodhead 2007) were already compiled and used by the proponents of the multidimensional diagrams; these data therefore should not be used for testing of diagrams. For the data from Pearce et al. (2007), the database shows one sample (s16-95-2) listed as of Tongan arc, but this sample with TiO_2 contents of 3.54 % and Nb of 74.07 ppm is listed in the original paper as an ocean island basalt. Furthermore, in this paper (Pearce et al. 2007), 16 samples listed as Tongan arc are not present in the database. Similar discrepancies are also observed between the database and the original work of Hawkins et al. (1977). The database

reports 5 samples which were not found in Hawkins et al. (1977); these authors did not report any new data rather than average values from earlier papers. Therefore, it is not clear from where these samples were compiled. Fallon et al. (2007) reported data for numerous samples from forearc, ridge, and backarc regions; however, the database contains data for 3 samples from the Melville ridge registered as from the Tongan arc. Thus, it will not be advisable to use the database without prior examination of the original references.

Even if we ignore all the above problems, for five major element-based diagram sets (two for basic and ultrabasic rocks, Tables S1 and S2; one for intermediate rocks, Table S5; and two for acid rocks, Tables S8 and S9), a total of 151 rock samples are available in this database. The database also indicates that in terms of the three main subdivisions for diagram sets, these samples are distributed as follows: 91 samples of basic and ultrabasic rocks (65 basalts, 22 tholeiites, and 4 more basalts listed as basalt/not given); 48 intermediate (9 andesite, 34 basaltic andesite, and 5 boninite); and 7 acid (4 dacite and 3 rhyolite); 5 rock type not given. This subdivision for the use of multidimensional discrimination diagrams would simply not match that obtained from the application of IgRoCS strictly following the IUGS recommendations. When major element data for 151 samples in this database are processed in IgRoCS, the following subdivision was obtained: 84 samples of basic (1 alkali basalt, 1 picrite, 1 potassic trachybasalt, and 81 subalkali basalt) and 2 of ultrabasic rocks (basanite); 52 intermediate (11 andesite, 37 basaltic andesite, and 4 boninite); and 13 acid (9 dacite and 4 rhyolite). Because of these discrepancies, the user will have to process the database in IgRoCS before using the multidimensional diagrams.

Further considerations of the Tongan arc datafile from the GEOROC-Mainz compilation are concerned with the number of samples with valid concentration values for the major-trace or trace element-based diagrams. For basic and ultrabasic rocks, out of 86 samples only 29 and 22 samples are available for the diagram sets of Agrawal et al. (2008; complete data required for La, Sm, Yb, Nb, and Th) and Verma & Agrawal (2011; complete data required for Nb, V, Y, Zr, and TiO_2), respectively.

For the combined major and trace element-based diagram set for intermediate rocks, the required elements with complete data are TiO_2, MgO, P_2O_5, Nb, Ni, V, Y, and Zr (Table S6). Out of 52 samples in the database only 22 samples had complete data for use of this diagram set (in fact, 5 more samples had a 0 value for Nb, which were not counted as valid samples). Similarly, for the trace element-based diagram set for intermediate rocks, 23 samples had complete data for the required elements (La, Ce, Sm, Yb, Nb, Th, Y, and Zr; Table S7). Finally, for the major-trace and trace element-based diagram sets for acid rocks (Tables S10 and S11), complete data were available for only 3 samples and 1 sample, respectively (4 out of 13 samples).

Because of all these difficulties, the multidimensional diagrams were not used for testing these Tongan data. We conclude that the freely-available databases should be used with caution.

Additional explanation on the performance of multidimensional diagrams

We finally mention the possible reasons for obtaining varying percent success values in different diagram sets. Occasionally, the total percent success values are much lower than the highest value of about 80 % for basic and ultrabasic rocks (Agrawal et al. 2004, 2008; Verma et al. 2006; Verma & Agrawal 2011). This highest percent success value could be even somewhat higher for probability-based counting in the diagram sets for intermediate and acid rocks (Verma et al. 2012, 2013; Verma & Verma 2013). When the total percent success values are relatively small (much less than 80 %), we must first resort to the by-chance probability values for a given diagram set. Because the total probabilities are divided into four tectonic settings in the final synthesis of a diagram set, the total by-chance percent probability for a given tectonic setting will be around 25 %. Therefore, this by-chance probability serves the purpose of better interpreting our inferences.

Although the statistical problems associated with the use of crude compositional data (e.g., Pearson 1897; Chayes 1960, 1971; Butler 1979) have been overcome by the log-ratio transformation technique in the new multidimensional diagrams (e.g., Aitchison 1984, 1986, 1999; Egozcue et al. 2003; Thomas & Aitchison 2005; Pawlowsky-Glahn & Egozcue 2006; Buccianti 2013; Verma 2015a), other problems still prevail. Some of them can be summarized as follows: (i) the data quality plays an important role, but the appropriate information is seldom available in the published geochemical literature (only indications are sometimes provided as overall percent errors and not for individual geochemical data); (ii) post-emplacement changes are relatively common in older terrains, which may move the samples from one tectonic setting to another although the multidimensional diagrams are shown to be relatively robust against small concentration changes of a few tens of percent; (iii) age data are seldom available for individual geochemically analysed samples, which renders the sample grouping difficult; (iv) even when age data are available, the corresponding uncertainty may span tens of millions of years, a period relatively large to have caused significant changes in the tectonic setting of a given area; and (v) the different types of magmas in a given region may have originated from different sources (mantle or crustal or both), which is not taken into account in the multidimensional diagrams but will also cause dispersion in such diagrams.

Conclusions

Satisfactory application of the new multidimensional diagrams has been demonstrated for 18 test studies of relatively fresh rocks and 8 application studies of hydrothermally altered or weathered rocks. In most cases studies, the expected tectonic setting was indicated by the respective applicable diagrams. The importance of petrogenetic processes and data quality is highlighted, especially, for cases where the expected tectonic setting was not inferred from the diagrams.

Acknowledgements: This work was partly supported by DGAPA-PAPIIT grant IN104813. M.A. Rivera-Gómez is grateful to Conacyt for her doctoral fellowship. We are grateful to the journal Editor handling our manuscript, three anonymous reviewers, and the managing editor of the journal, for numerous suggestions which helped us improve our presentation.

References

Agrawal S. & Verma S.P. 2007: Comment on "Tectonic classification of basalts with classification trees" by Pieter Vermeesch (2006). *Geochim Cosmochim Acta* 71, 3388-3390.

Agrawal S., Guevara M. & Verma S.P. 2004: Discriminant analysis applied to establish major-element field boundaries for tectonic varieties of basic rocks. *Int. Geol. Rev.* 46, 575–594.

Agrawal S., Guevara M. & Verma S.P. 2008: Tectonic discrimination of basic and ultrabasic rocks through log-transformed ratios of immobile trace elements. *Int. Geol. Rev.* 50, 1057–1079.

Aitchison J. 1984: Statistical analysis of geochemical compositions. *Math. Geol.* 16, 531–564.

Aitchison J. 1986: The statistical analysis of compositional data. *Chapman and Hall*, London, UK, 1–416.

Aitchison J. 1999: Logratios and natural laws in compositional data analysis. *Math. Geol.* 31, 563–580.

Ali S., Ntaflos T. & Upton B.G.J. 2013: Petrogenesis and mantle source characteristics of Quaternary alkaline mafic lavas in the western Carpathian–Pannonian Region, Styria, Austria. *Chem. Geol.* 337-338, 99–113.

Armstrong-Altrin J.S. 2015: Evaluation of two multidimensional discrimination diagrams from beach and deep-sea sediments from the Gulf of Mexico and their application to Precambrian clastic sedimentary rocks. *Int. Geol. Rev.* 57, 1446-1461.

Armstrong-Altrin J.S. & Verma S.P. 2005: Critical evaluation of six tectonic setting discrimination diagrams using geochemical data of Neogene sediments from known tectonic settings. *Sed. Geol.* 177, 115–129.

Bailey J.C. 1981: Geochemical criteria for a refined tectonic discrimination of orogenic andesites. *Chem. Geol.* 32, 139–154.

Behrendt J.C., LeMasurier W.E., Cooper A.K., Tessensohn F., Trehu A. & Damaske D. 1991: Geophysical studies of the West Antarctic Rift System. *Tectonics* 10, 1257–1273.

Behrendt J.C., LeMasurier W.E. & Cooper A.K. 1992: The West Antarctic Rift System — A propagating rift captured by a mantle plume? In: Yoshida Y., Kaminuma K. & Shiraishi K. (Eds.): Recent Progress in Antarctic Earth Science. *Terra Science*, Tokyo, 315–322.

Bora S. & Kumar S. 2015: Geochemistry of biotites and host granitoid plutons from the Proterozoic Mahakoshal Belt, central India tectonic zone: implication for nature and tectonic setting of magmatism. *Int. Geol. Rev.* 57, 1686–1706.

Browne P.R.L., Graham I.J., Parker R.J. & Wood C.P. 1992: Subsurface andesite lavas and plutonic rocks in the Rotokawa and Ngatamariki geothermal systems, Taupo volcanic zone, New Zealand. *J. Volcanol. Geotherm. Res.* 51, 199–215.

Buccianti A. 2013: Is compositional data analysis a way to see beyond the illusion? *Comput. Geosci.* 50, 165–173.

Butler J.C. 1979: Trends in ternary petrologic variation diagrams - fact or fantasy? *Am. Mineral.* 64, 1115–1121.

Butler J.C. & Woronow A. 1986: Discrimination among tectonic settings using trace element abundances of basalts. *J. Geophys. Res.* 91, 10289–10300.

Cabanis B. & Lecolle M. 1989: Le diagramme La/10-Y/15-Nb/8: un outil pour la discrimination des séries volcaniques et la mise en évidence des processus de mélange et/ou de contamination crustale. *Compte Rendu Acad. Sci. Paris* 309, 2023–2029.

Caroff M., Guillou H., Maliaux M., Maury R.C., Guille G. & Cotten J. 1999: Assimilation of ocean crust by hawaiitic and mugearitic magmas: an example from Eiao (Marquesas). *Lithos* 46, 235–258.

Cebriá J.M., López-Ruiz J., Doblas M., Oyarzun R., Hertogen J. & Benito R. 2000: Geochemistry of the Quaternary alkali basalts of Garrotxa (NE volcanic province, Spain): a case of double enrichment of the mantle lithosphere. *J. Volcanol. Geotherm. Res.* 102, 217–235.

Chandrasekharam D., Santo A.P., Capaccioni B., Vaselli O., Alam M.A., Manetti P. & Tassi F. 2009: Volcanological and petrological evolution of Barren Island (Andaman Sea, Indian Ocean). *J. Asian Earth Sci.* 35, 469–487.

Chayes F. 1960: On correlation between variables of constant sum. *J. Geophys. Res.* 65, 4185–4193.

Chayes F. 1971: Ratio correlation. A manual for students of petrology and geochemistry. *The University of Chicago Press*, Chicago and London, 1–99.

Chesner C.A. & Halsor S.P. 1997: Geochemical trends of sequential lava flows from Meseta volcano, Guatemala. *J. Volcanol. Geotherm. Res.* 78, 221–237.

Chesner C.A. & Rose Jr. W.I. 1984: Geochemistry and evolution of the Fuego volcanic complex, Guatemala. *J. Volcanol. Geotherm. Res.* 21, 25–44.

Cooper A.F., Adam L.J., Coulter R.F., Eby G.N. & McIntosh W.C. 2007: Geology, geochronology and geochemistry of a basanitic volcano, White Island, Ross Sea, Antarctica. *J. Volcanol. Geotherm. Res.* 165, 189–216.

Deering C.D., Bachmann O., Dufek J. & Gravley D.M. 2011: Rift-related transition from andesite to rhyolite volcanism in the Taupo Volcanic Zone (New Zealand) controlled by crystal-melt dynamics in mush zones with variable mineral assemblages. *J. Petrol.* 52, 2243–2263.

Del Moro S., Renzulli A. & Tribaudino M. 2011: Pyrometamorphic processes at the magma-hydrothermal system interface of active volcanoes: evidence from buchite ejecta of Stromboli (Aeolian Islands, Italy). *J. Petrol.* 52, 541–564.

Di Paola G.M. 1974: Volcanology and petrology of Nisyros Island (Dodecanese, Greece). *Bull. Volcanol.* 38, 944–987.

Dreher S.T., Eichelberger J.C. & Larsen J.F. 2005: The petrology and geochemistry of the Aniakchak caldera-forming ignimbrite, Aleutian arc, Alaska. *J. Petrol.* 46, 1747–1768.

Egozcue J.J., Pawlowsky-Glahn V., Mateu-Figueras G. & Barceló-Vidal C. 2003: Isometric logratio transformations for compositional data analysis. *Math. Geol.* 35, 279–300.

Fallon T.J., Danyushevsky L.V., Crawford T.J., Maas R., Woodhead J.D., Eggins S.M., Bloomer S.H., Wright D.J., Zlobin S.K. & Stacey A.R. 2007: Multiple mantle plume components involved in the petrogenesis of subduction-related lavas from the northern Lau basin: evidence from the geochemistry of arc and backarc submarine volcanoes. *Geochem. Geophys. Geosys.* 8, doi:10.1029/2007GC001619.

Gazel E., Alvarado G.E., Obando J. & Alfaro A. 2005: Geología y evolución magmática del arco de Sarapiquí, Costa Rica. *Rev. Geol. Am. Cen.* 32, 13–31.

Gorton M.P. & Schandl E.S. 2000: From continents to island arcs: a geochemical index of tectonic setting for arc-related and within-plate felsic to intermediate volcanic rocks. *Can. Mineral.* 38, 1065–1073.

Haase K.M., Worthington T.J., Stoffers P., Garbe-Schönberg D. & Wright I.C. 2002: Mantle dynamics, element recycling, and magma genesis beneath the Kermadec arc-Havre trough. *Geochem. Geophys. Geosys.* 3, 1071, doi:10.1029/

2002GC00035.

Hawkins J.W. Jr. 1977: Petrological and geochemical characteristics of marginal basin basalts island arcs. In: Talwani M. & Pitman W.C.III (Eds.): Deep Sea Trenches and Back-Arc Basins. *American Geophysical Union*, Washington D.C. 355–365.

Hergt J.M. & Woodhead J.D. 2007: A critical evaluation of recent models for Lau-tonga arc-backarc basin magmatic evolution. *Chem. Geol.* 245, 9–44.

Ho K.-S., Ge W.-C., Chen J.-C., You C.-F., Yang H.-J. & Zhang Y.-L. 2013: Late Cenozoic magmatic transitions in the central Great Xing'an Range, Northeast China: Geochemical and isotopic constraints on petrogenesis. *Chem. Geol.* 352, 1–18.

Jackson M.C., Frey F.A., Garcia M.O. & Wilmoth R.A. 1999: Geology and geochemistry of basaltic lava flows and dikes from the Trans-Koolau tunnel, Oahu, Hawaii. *Bull Volcanol.* 60, 381–401.

Johnson K.E., Harmon R.S., Richardson J.M., Moorbath S. & Strong D. 1996: Isotope and trace element geochemistry of Augustine Volcano, Alaska: implications for magmatic evolution. *J. Petrol.* 37, 95–115.

Kaur P., Chaudhri N. & Hofmann A.W. 2015: New evidence for two sharp replacement fronts during albitization of granitoids from northern Aravalli orogen, northwest India. *Int. Geol. Rev.* 57, 1660–1685.

Le Bas M.J., Le Maitre R.W., Streckeisen A. & Zanettin B. 1986: A chemical classification of volcanic rocks based on the total alkali-silica diagram. *J. Petrol.* 27, 745–750.

Le Bas M.J. & Streckeisen A.L. 1991: The IUGS systematics of igneous rocks. *J. Geol. Soc. London* 148, 825–833.

Le Maitre R.W., Streckeisen A., Zanettin B., Le Bas M.J., Bonin B., Bateman P., Bellieni G., Dudek A., Schmid R., Sorensen H. & Woolley A.R. 2002: *I*gneous rocks. A classification and glossary of terms: recommendations of the International Union of Geological Sciences, Subcommission of the Systematics of Igneous Rocks, ed. 2nd. *Cambridge University Press*, Cambridge, 1–236.

Marques L.S., Ulbrich M.N.C., Ruberti E. & Tassinari C.G. 1999: Petrology, geochemistry and Sr-Nd isotopes of the Trindade and Martin Vaz volcanic rocks (southern Atlantic Ocean). *J. Volcanol. Geotherm. Res.* 93, 191–216.

Melluso L. & Morra V. 2000: Petrogenesis of Late Cenozoic mafic alkaline rocks of the Nosy Be archipelago (northern Madagascar): relationships with Comorean magmatism. *J. Volcanol. Geotherm. Res.* 96, 129–142.

Meschede M. 1986: A method of discriminating between different types of mid-ocean ridge basalts and continental tholeiites with the Nb-Zr-Y diagram. *Chem. Geol.* 56, 207–218.

Mullen E.D. 1983: $MnO/TiO_2/P_2O_5$: a minor element discrimination for basaltic rocks of oceanic environments and its implications for petrogenesis. *Earth Planet. Sci. Lett.* 62, 53–62.

Neill I., Meliksetian K., Allen M.B., Navarsardyan G. & Karapetyan S. 2013: Pliocene-Quaternary volcanic rocks of NW Armenia: Magmatism and lithospheric dynamics within an active orogenic plateau. *Lithos* 180-181, 200–215.

Nyland R.E., Panter K.S., Rocchi S., Di Vincenzo G., Del Carlo P., Tiepolo M., Field B. & Gorsevski P. 2013: Volcanic activity and its link to glaciation cycles: Single-grain age and geochemistry of Early to Middle Miocene volcanic glass from ANDRILL AND-2A core, Antarctica. *J. Volcanol. Geotherm. Res.* 250, 106–128.

Pal T., Mitra S.K., Sengupta S., Katari A., Bandopadhyay P.C. & Bhattacharya A.K. 2007: Dacite–andesites of Narcondam volcano in the Andaman Sea — an imprint of magma mixing in the inner arc of the Andaman–Java subduction system. *J. Volcanol. Geotherm. Res.* 168, 93–113.

Pandarinath K. 2014a: Testing of the recently developed tectonomagmatic discrimination diagrams from hydrothermally altered igneous rocks of 7 geothermal fields. *Turk. J. Earth Sci.* 23, 412–426.

Pandarinath K. 2014b: Tectonomagmatic origin of Precambrian rocks of Mexico and Argentina inferred from multi-dimensional discriminant-function based discrimination diagrams. *J. South. Am. Earth. Sci.* 56, 464–484.

Patino L.C., Velbel M.A., Price J.R. & Wade J.A. 2003: Trace element mobility during spheroidal weathering of basalts and andesites in Hawaii and Guatemala. *Chem. Geol.* 202, 343–364.

Pawlowsky-Glahn V. & Egozcue J.J. 2006: Compositional data and their analysis: an introduction. In: A. Buccianti, G. Mateu-Figueras & V. Pawlowsky-Glahn (Eds.), Compositional data analysis in the Geosciences: from theory to practice. *Geol. Soc. London Spec. Publ.*, London, 1–10.

Pearce J.A. 1976: Statistical analysis of major element patterns in basalts. *J. Petrol.* 17, 15–43.

Pearce J.A. 1982: Trace element characteristics of lavas from destructive plate boundaries. In: Thorpe R.S. (Ed.): Andesites. John Wiley & Sons, Chichester, 525–548.

Pearce J.A. & Cann J.R. 1971: Ophiolite origin investigated by discriminant analysis using Ti, Zr and Y. *Earth Planet. Sci. Lett.* 12, 339–349.

Pearce J.A. & Cann J.R. 1973: Tectonic setting of basic volcanic rocks determined using trace element analyses. *Earth Planet. Sci. Lett.* 19, 290–300.

Pearce J.A. & Gale G.H. 1977: Identification of ore-deposition environment from trace-element geochemistry of associated igneous host rocks. *Geol. Soc. London Spec. Publ.* 7, 14–24.

Pearce J.A. & Norry M.J. 1979: Petrogenetic implications of Ti, Zr, Y, and Nb variations in volcanic rocks. *Contrib. Mineral. Petrol.* 69, 33–47.

Pearce T.H., Gorman B.E. & Birkett T.C. 1977: The relationship between major element chemistry and tectonic environment of basic and intermediate volcanic rocks. *Earth Planet. Sci. Lett.* 36, 121–132.

Pearce J.A., Harris N.B.W. & Tindle A.G. 1984: Trace element discrimination diagrams for the tectonic interpretation of granitic rocks. *J. Petrol.* 25, 956–983.

Pearce J.A., Kempton P.D. & Gill J.B. 2007: Hf-Nd evidence for the origin and distribution of mantle domains in the SW Pacific. *Earth Planet. Sci. Lett.* 260, 98–114

Pearson K. 1897: Mathematical contribution to the theory of evolution — on a form of spurious correlation which may arise when indices are used in the measurement of organs. *Proc. Royal Soc. London* 60, 489–502.

Pyle D.G., Christie D.M., Mahoney J.J. & Duncan R.A. 1995: Geochemistry and geochronology of ancient southeast Indian and southwest Pacific seafloor. *J. Geophys. Res.* 100, 22261–22282.

Rahman M.S. & Mondal M.E.A. 2015: Evolution of continental crust of the Aravalli craton, NW India, during the Neoarchaean–Palaeoproterozoic: evidence from geochemistry of granitoids. *Int. Geol. Rev.* 57, 1510–1525.

Rhodes J.M. 2012: Compositional diversity of Mauna Kea shield lavas recovered by the Hawaii Scientific Drilling Project: Inferences on source lithology, magma supply, and the role of multiple volcanoes. *Geochem. Geophys. Geosys.* 13, 2–28.

Rhodes J.M. & Vollinger M.J. 2004: Composition of basaltic lavas sampled by phase-2 of the Hawaii scientific drilling proyect: Geochemical stratigraphy and magma types. *Geochem. Geophys. Geosys.* 5, 1–38.

Scott J.A.J., Pyle D.M., Mather T.A. & Rose W.I. 2013: Geochemistry and evolution of the Santiaguito volcanic dome com-

plex, Guatemala. *J. Volcanol. Geotherm. Res.* 252, 92–107.
Sherrod D.R., Murai T. & Tagami T. 2007: New K–Ar ages for calculating end-of-shield extrusion rates at West Maui volcano, Hawaiian island chain. *Bull. Volcanol.* 69, 627–642.
Shervais J.W. 1982: Ti-V plots and the petrogenesis of modern and ophiolitic lavas. *Earth Planet. Sci. Lett.* 59, 101–118.
Srivastava R.K., Samal A.K. & Gautam G.C. 2015: Geochemical characteristics and petrogenesis of four Palaeoproterozoic mafic dike swarms and associated large igneous provinces from the eastern Dharwar craton, India. *Int. Geol. Rev.* 57, 1462–1484.
Streck M.J., Ramos F., Gillam A., Haldar D. & Duncan R.A. 2011: The intra-oceanic Barren Island and Narcondam arc volcanoes, Andaman Sea: Implications for subduction inputs and crustal overprint of a depleted mantle source. In: Ray J., Sen G. & Ghosh B. (Eds.): Topics in Igneous Petrology. *Springer Science+Business Media*, 241–273.
Suh C.E., Sparks R.S.J., Fitton J.G., Ayonghe S.N., Annen C., Nana R. & Luckman A. 2003: The 1999 and 2000 eruptions of Mount Cameroon: eruption behaviour and petrochemistry of lava. *Bull. Volcanol.* 65, 267–281.
Thomas C.W. & Aitchison J. 2005: Compositional data analysis of geological variability and process: a case study. *Math. Geol.* 37, 753–772.
Verma S.K. & Oliveira E.P. 2013: Application of multi-dimensional discrimination diagrams and probability calculations to Paleoproterozoic acid rocks from Brazilian cratons and provinces to infer tectonic settings. *J. South Am. Earth Sci.* 45, 117–146.
Verma S.K. & Oliveira E.P. 2015: Tectonic setting of basic igneous and metaigneous rocks of Borborema Province, Brazil using multi-dimensional geochemical discrimination diagrams. *J. South Am. Earth Sci.* 58, 309–317.
Verma S.P. 2010: Statistical evaluation of bivariate, ternary and discriminant function tectonomagmatic discrimination diagrams. *Turk. J. Earth Sci.* 19, 185–238.
Verma S.P. 2015a: Monte Carlo comparison of conventional ternary diagrams with new log-ratio bivariate diagrams and an example of tectonic discrimination. *Geochem. J.* 49, 393-412.
Verma S.P. 2015b: Origin, evolution, and tectonic setting of the eastern part of the Mexican Volcanic Belt and comparison with the Central American Volcanic Arc from conventional multi-element normalized and new multidimensional discrimination diagrams and discordancy and significance tests. *Turk. J. Earth Sci.* 24, 111-164.
Verma S.P. 2015c: Present state of knowledge and new geochemical constraints on the central part of the Mexican Volcanic Belt and comparison with the Central American Volcanic Arc in terms of near and far trench magmas. *Turk. J. Earth Sci.*, 24: 399-460.
Verma S.P. & Agrawal S. 2011: New tectonic discrimination diagrams for basic and ultrabasic volcanic rocks through log-transformed ratios of high field strength elements and implications for petrogenetic processes. *Rev. Mex. Cienc. Geol.* 28, 24–44.
Verma S.P. & Armstrong-Altrin J.S. 2013: New multi-dimensional diagrams for tectonic discrimination of siliciclastic sediments and their application to Precambrian basins. *Chem. Geol.* 355, 117–133.
Verma S.P. & Armstrong-Altrin J.S. 2016: Geochemical discrimination of siliciclastic sediments from active and passive margin settings. *Sediment. Geol.*, 332, 1–12.
Verma S.P. & Rivera-Gómez M.A. 2013a: Computer programs for the classification and nomenclature of igneous rocks. *Episodes* 36, 115–124.
Verma S.P. & Rivera-Gómez M.A. 2013b: New computer program TecD for tectonomagmatic discrimination from discriminant function diagrams for basic and ultrabasic magmas and its application to ancient rocks. *J. Iber. Geol.* 39, 167–179.
Verma S.P. & Verma S.K. 2013: First 15 probability-based multidimensional discrimination diagrams for intermediate magmas and their robustness against post-emplacement compositional changes and petrogenetic processes. *Turk. J. Earth Sci.* 22, 931–995.
Verma S.P., Torres-Alvarado I.S. & Sotelo-Rodríguez Z.T. 2002: SINCLAS: standard igneous norm and volcanic rock classification system. *Comput. Geosci.* 28, 711–715.
Verma S.P., Guevara M. & Agrawal S. 2006: Discriminating four tectonic settings: five new geochemical diagrams for basic and ultrabasic volcanic rocks based on log-ratio transformation of major-element data. *J. Earth Syst. Sci.* 115, 485-528.
Verma S.K., Pandarinath K. & Verma S.P. 2012: Statistical evaluation of tectonomagmatic discrimination diagrams for granitic rocks and proposal of new discriminant-function-based multidimensional diagrams for acid rocks. *Int. Geol. Rev.* 54, 325–347.
Verma S.P., Pandarinath K., Verma S.K. & Agrawal S. 2013: Fifteen new discriminant-function-based multi-dimensional robust diagrams for acid rocks and their application to Precambrian rocks. *Lithos* 168-169, 113–123.
Verma S.K., Oliveira E.P. & Verma S.P. 2015a: Plate tectonic settings for Precambrian basic rocks from Brazil by multi-dimensional tectonomagmatic discrimination diagrams and their limitations. *Int. Geol. Rev.* 57, 1566-1581.
Verma S.P., Verma S.K. & Oliveira E.P. 2015b: Application of 55 multi-dimensional tectonomagmatic discrimination diagrams to Precambrian belts. *Int. Geol. Rev.* 57, 1365-1388.
Verma S.P., Cruz-Huicochea R., Díaz-González L. & Verma S.K. 2015c: A new computer program TecDIA for multidimensional tectonic discrimination of intermediate and acid magmas and its application to the Bohemian Massif, Czech Republic. *J. Geosci.* 60, 203–218.
Verma S.P., Díaz-González L. & Armstrong-Altrin J.S. 2016: Application of a new computer program for tectonic discrimination of Cambrian to Holocene clastic sediments. *Earth Sci. Inform.*, 10.1007/s12145-015-0244-0 published on-line, in press.
Wang X.-C., Li Z.-X., Li X.-H., Li J., Liu Y., Long W.-G., Zhou J.-B. & Wang F. 2012: Temperature, pressure, and composition of the mantle source region of Late Cenozoic basalts in Hainan Island, SE Asia: a consequence of a young thermal mantle plume close to subduction zones? *J. Petrol.* 53, 177–233.
Watt S.F.L., Pyle D.M. & Mather T.A. 2011: Geology, petrology and geochemistry of the dome complex of Huequi volcano, southern Chile. *Andean Geol.* 38, 335–348.
Wood D.A. 1980: The application of a Th-Hf-Ta diagram to problems of tectonomagmatic classification and to establishing the nature of crustal contamination of basaltic lavas of the British Tertiary volcanic province. *Earth Planet. Sci. Lett.* 50, 11–30.
Yang Z., Luo Z., Zhang H., Zhang Y., Huang F., Sun C. & Dai J. 2009: Petrogenesis and Geological Implications of theTianheyong Cenozoic Basalts, Inner Mongolia China. *Earth Sci. Front.* 16, 90–106.
Yi S.-B., Oh C.-W., Pak S.J., Kim J. & Moon J.-W. 2014: Geochemistry and petrogenesis of mafic-ultramafic rocks from the Central Indian Ridge, latitude 8°–17° S: denudation of mantle harzburgites and gabbroic rocks and compositional variation of basalts. *Int. Geol. Rev.* 56, 691–1719.

Supplementary Material

The discriminant function DF1-DF2 equations were recently summarized by Verma et al. (2015b), which are reproduced here in Tables S1-S11 for an easy reference.

Table S1.
DF1-DF2 equations for the first set of five diagrams proposed by Agrawal et al. (2004) for basic and ultrabasic magmas.

Figure reference; figure type	Discrimination diagram	Discriminant function equations
Agrawal et al. (2004); adjusted major element concentrations	IAB-CRB-OIB-MORB	$DF1_{(IAB\text{-}CRB\text{-}OIB\text{-}MORB)m1} = 0.258\times(SiO_2)_{adj} + 2.395\times(TiO_2)_{adj} + 0.106\times(Al_2O_3)_{adj} + 1.019\times(Fe_2O_3)_{adj} - 6.778\times(MnO)_{adj} + 0.405\times(MgO)_{adj} + 0.119\times(CaO)_{adj} + 0.071\times(Na_2O)_{adj} - 0.198\times(K_2O)_{adj} + 0.613\times(P_2O_5)_{adj} - 24.065$ $DF2_{(IAB\text{-}CRB\text{-}OIB\text{-}MORB)m1} = 0.730\times(SiO_2)_{adj} + 1.119\times(TiO_2)_{adj} + 0.156\times(Al_2O_3)_{adj} + 1.332\times(Fe_2O_3)_{adj} + 4.376\times(MnO)_{adj} + 0.493\times(MgO)_{adj} + 0.936\times(CaO)_{adj} + 0.882\times(Na_2O)_{adj} - 0.291\times(K_2O)_{adj} - 1.572\times(P_2O_5)_{adj} - 59.472$
	IAB-CRB-OIB	$DF1_{(IAB\text{-}CRB\text{-}OIB)m1} = 0.251\times(SiO_2)_{adj} + 2.034\times(TiO_2)_{adj} - 0.100\times(Al_2O_3)_{adj} + 0.573\times(Fe_2O_3)_{adj} + 0.032\times(FeO)_{adj} - 2.877\times(MnO)_{adj} + 0.260\times(MgO)_{adj} + 0.052\times(CaO)_{adj} + 0.322\times(Na_2O)_{adj} - 0.229\times(K_2O)_{adj} - 18.974$ $DF2_{(IAB\text{-}CRB\text{-}OIB)m1} = 2.150\times(SiO_2)_{adj} + 2.711\times(TiO_2)_{adj} + 1.792\times(Al_2O_3)_{adj} + 2.295\times(Fe_2O_3)_{adj} + 1.484\times(FeO)_{adj} - 8.594\times(MnO)_{adj} + 1.896\times(MgO)_{adj} + 2.158\times(CaO)_{adj} + 1.201\times(Na_2O)_{adj} + 1.763\times(K_2O)_{adj} - 200.276$
	IAB-CRB-MORB	$DF1_{(IAB\text{-}CRB\text{-}MORB)m1} = 0.435\times(SiO_2)_{adj} - 1.392\times(TiO_2)_{adj} + 0.183\times(Al_2O_3)_{adj} + 0.148\times(FeO)_{adj} + 7.690\times(MnO)_{adj} + 0.021\times(MgO)_{adj} + 0.380\times(CaO)_{adj} + 0.036\times(Na_2O)_{adj} + 0.462\times(K_2O)_{adj} - 1.192\times(P_2O_5)_{adj} - 29.435$ $DF2_{(IAB\text{-}CRB\text{-}MORB)m1} = 0.601\times(SiO_2)_{adj} - 0.335\times(TiO_2)_{adj} + 1.332\times(Al_2O_3)_{adj} + 1.449\times(FeO)_{adj} + 0.756\times(MnO)_{adj} + 0.893\times(MgO)_{adj} + 0.448\times(CaO)_{adj} + 0.525\times(Na_2O)_{adj} + 1.734\times(K_2O)_{adj} + 2.494\times(P_2O_5)_{adj} - 78.236$
	IAB-OIB-MORB	$DF1_{(IAB\text{-}OIB\text{-}MORB)m1} = 1.232\times(SiO_2)_{adj} + 4.166\times(TiO_2)_{adj} + 1.085\times(Al_2O_3)_{adj} + 3.522\times(Fe_2O_3)_{adj} + 0.500\times(FeO)_{adj} - 3.930\times(MnO)_{adj} + 1.334\times(MgO)_{adj} + 1.085\times(CaO)_{adj} + 0.416\times(Na_2O)_{adj} + 0.827\times(K_2O)_{adj} - 119.050$ $DF2_{(IAB\text{-}OIB\text{-}MORB)m1} = 1.384\times(SiO_2)_{adj} + 1.091\times(TiO_2)_{adj} + 0.908\times(Al_2O_3)_{adj} + 2.419\times(Fe_2O_3)_{adj} + 0.886\times(FeO)_{adj} + 5.281\times(MnO)_{adj} + 1.269\times(MgO)_{adj} + 1.790\times(CaO)_{adj} + 2.572\times(Na_2O)_{adj} + 0.138\times(K_2O)_{adj} - 134.295$
	CRB-OIB-MORB	$DF1_{(CRB\text{-}OIB\text{-}MORB)m1} = 0.310\times(SiO_2)_{adj} + 1.936\times(TiO_2)_{adj} + 0.341\times(Al_2O_3)_{adj} + 0.760\times(Fe_2O_3)_{adj} + 0.351\times(FeO)_{adj} - 11.315\times(MnO)_{adj} + 0.526\times(MgO)_{adj} + 0.084\times(CaO)_{adj} + 0.312\times(K_2O)_{adj} + 1.892\times(P_2O_5)_{adj} - 32.909$ $DF2_{(CRB\text{-}OIB\text{-}MORB)m1} = 0.703\times(SiO_2)_{adj} + 2.454\times(TiO_2)_{adj} + 0.233\times(Al_2O_3)_{adj} + 1.943\times(Fe_2O_3)_{adj} - 0.182\times(FeO)_{adj} - 2.421\times(MnO)_{adj} + 0.618\times(MgO)_{adj} + 0.712\times(CaO)_{adj} - 0.866\times(K_2O)_{adj} - 1.180\times(P_2O_5)_{adj} - 56.455$

The tectonic fields are: IAB−island arc basic (or ultrabasic) rocks; CRB−continental rift basic (or ultrabasic) rocks; OIB−ocean island basic (or ultrabasic) rocks; and MORB−mid ocean ridge basic (or ultrabasic) rocks. The subscript $_{adj}$ refers to adjusted data from the SINCLAS (Verma et al. 2002) or IgRoCS computer program (Verma and Rivera-Gómez 2013a).

Table S2.
DF1-DF2 equations (approximate coefficients) for the second set of five diagrams proposed by Verma et al. (2006) for basic and ultrabasic magmas.

Figure reference; figure type	Discrimination diagram	Discriminant function equations
Verma et al. (2006); log-ratios of major elements	IAB-CRB-OIB-MORB	$DF1_{(IAB\text{-}CRB\text{-}OIB\text{-}MORB)m2} = -4.676\times\ln(TiO_2/SiO_2) + 2.533\times\ln(Al_2O_3/SiO_2) - 0.388\times\ln(Fe_2O_3/SiO_2) + 3.969\times\ln(FeO/SiO_2) + 0.898\times\ln(MnO/SiO_2) - 0.583\times\ln(MgO/SiO_2) - 0.290\times\ln(CaO/SiO_2) - 0.270\times\ln(Na_2O/SiO_2) + 1.081\times\ln(K_2O/SiO_2) + 0.184\times\ln(P_2O_5/SiO_2) + 1.544$ $DF2_{(IAB\text{-}CRB\text{-}OIB\text{-}MORB)m2} = 0.675\times\ln(TiO_2/SiO_2) + 4.590\times\ln(Al_2O_3/SiO_2) + 2.090\times\ln(Fe_2O_3/SiO_2) + 0.851\times\ln(FeO/SiO_2) - 0.433\times\ln(MnO/SiO_2) + 1.483\times\ln(MgO/SiO_2) - 2.363\times\ln(CaO/SiO_2) - 1.656\times\ln(Na_2O/SiO_2) - 0.676\times\ln(K_2O/SiO_2) + 0.413\times\ln(P_2O_5/SiO_2) + 13.164$
	IAB-CRB-OIB	$DF1_{(IAB\text{-}CRB\text{-}OIB)m2} = 4.000\times\ln(TiO_2/SiO_2) - 2.238\times\ln(Al_2O_3/SiO_2) + 0.811\times\ln(Fe_2O_3/SiO_2) - 2.586\times\ln(FeO/SiO_2) - 1.243\times\ln(MnO/SiO_2) + 0.587\times\ln(MgO/SiO_2) - 0.315\times\ln(CaO/SiO_2) + 0.432\times\ln(Na_2O/SiO_2) - 1.026\times\ln(K_2O/SiO_2) + 0.051\times\ln(P_2O_5/SiO_2) - 0.572$ $DF2_{(IAB\text{-}CRB\text{-}OIB)m2} = -1.370\times\ln(TiO_2/SiO_2) + 3.010\times\ln(Al_2O_3/SiO_2) + 0.324\times\ln(Fe_2O_3/SiO_2) + 1.900\times\ln(FeO/SiO_2) - 1.975\times\ln(MnO/SiO_2) + 1.441\times\ln(MgO/SiO_2) - 2.266\times\ln(CaO/SiO_2) + 1.866\times\ln(Na_2O/SiO_2) + 0.287\times\ln(K_2O/SiO_2) + 0.814\times\ln(P_2O_5/SiO_2) + 1.820$
	IAB-CRB-MORB	$DF1_{(IAB\text{-}CRB\text{-}MORB)m2} = -1.574\times\ln(TiO_2/SiO_2) + 6.150\times\ln(Al_2O_3/SiO_2) + 1.554\times\ln(Fe_2O_3/SiO_2) + 3.413\times\ln(FeO/SiO_2) - 0.009\times\ln(MnO/SiO_2) + 1.248\times\ln(MgO/SiO_2) - 2.110\times\ln(CaO/SiO_2) - 0.768\times\ln(Na_2O/SiO_2) + 1.143\times\ln(K_2O/SiO_2) + 0.352\times\ln(P_2O_5/SiO_2) + 16.871$ $DF2_{(IAB\text{-}CRB\text{-}MORB)m2} = 3.984\times\ln(TiO_2/SiO_2) + 0.220\times\ln(Al_2O_3/SiO_2) + 1.152\times\ln(Fe_2O_3/SiO_2) - 2.204\times\ln(FeO/SiO_2) - 1.623\times\ln(MnO/SiO_2) + 1.429\times\ln(MgO/SiO_2) - 1.252\times\ln(CaO/SiO_2) + 0.358\times\ln(Na_2O/SiO_2) - 0.641\times\ln(K_2O/SiO_2) + 0.265\times\ln(P_2O_5/SiO_2) + 5.051$
	IAB-OIB-MORB	$DF1_{(IAB\text{-}OIB\text{-}MORB)m2} = 5.340\times\ln(TiO_2/SiO_2) - 1.628\times\ln(Al_2O_3/SiO_2) + 0.834\times\ln(Fe_2O_3/SiO_2) - 4.736\times\ln(FeO/SiO_2) - 0.125\times\ln(MnO/SiO_2) + 0.645\times\ln(MgO/SiO_2) + 1.515\times\ln(CaO/SiO_2) - 0.815\times\ln(Na_2O/SiO_2) - 0.889\times\ln(K_2O/SiO_2) - 0.226\times\ln(P_2O_5/SiO_2) + 5.776$ $DF2_{(IAB\text{-}OIB\text{-}MORB)m2} = 1.180\times\ln(TiO_2/SiO_2) + 5.511\times\ln(Al_2O_3/SiO_2) + 2.774\times\ln(Fe_2O_3/SiO_2) - 0.134\times\ln(FeO/SiO_2) + 0.667\times\ln(MnO/SiO_2) + 1.104\times\ln(MgO/SiO_2) - 1.723\times\ln(CaO/SiO_2) - 3.895\times\ln(Na_2O/SiO_2) + 0.947\times\ln(K_2O/SiO_2) - 0.108\times\ln(P_2O_5/SiO_2) + 15.498$
	CRB-OIB-MORB	$DF1_{(CRB\text{-}OIB\text{-}MORB)m2} = -0.518\times\ln(TiO_2/SiO_2) + 4.989\times\ln(Al_2O_3/SiO_2) + 2.220\times\ln(Fe_2O_3/SiO_2) + 1.180\times\ln(FeO/SiO_2) - 0.301\times\ln(MnO/SiO_2) + 1.330\times\ln(MgO/SiO_2) - 2.183\times\ln(CaO/SiO_2) - 1.932\times\ln(Na_2O/SiO_2) + 0.698\times\ln(K_2O/SiO_2) + 0.900\times\ln(P_2O_5/SiO_2) + 13.262$ $DF2_{(CRB\text{-}OIB\text{-}MORB)m2} = 5.051\times\ln(TiO_2/SiO_2) - 0.497\times\ln(Al_2O_3/SiO_2) + 1.005\times\ln(Fe_2O_3/SiO_2) - 3.385\times\ln(FeO/SiO_2) + 0.553\times\ln(MnO/SiO_2) + 0.292\times\ln(MgO/SiO_2) + 0.401\times\ln(CaO/SiO_2) - 2.864\times\ln(Na_2O/SiO_2) - 0.219\times\ln(K_2O/SiO_2) - 1.056\times\ln(P_2O_5/SiO_2) + 2.888$

The tectonic fields are: IAB−island arc basic (or ultrabasic) rocks; CRB−continental rift basic (or ultrabasic) rocks; OIB−ocean island basic (or ultrabasic) rocks; and MORB−mid ocean ridge basic (or ultrabasic) rocks. The subscript $_{adj}$ refers to adjusted data from the SINCLAS (Verma et al. 2002) or IgRoCS computer program (Verma and Rivera-Gómez 2013a), but is eliminated from these equations.

Table S3.
DF1-DF2 equations for the set of five diagrams based on trace element ratios proposed by Agrawal et al. (2008) for basic and ultrabasic magmas.

Figure reference; figure type	Discrimination diagram	Discriminant function equations
Agrawal et al. (2008); log-ratios of immobile trace elements	IAB-CRB+OIB-MORB	$DF1_{(IAB\text{-}CRB+OIB\text{-}MORB)t1} = 0.3518\times\ln(La/Th) + 0.6013\times\ln(Sm/Th) - 1.3450\times\ln(Yb/Th) + 2.1056\times\ln(Nb/Th) - 5.4763$ $DF2_{(IAB\text{-}CRB+OIB\text{-}MORB)t1} = -0.3050\times\ln(La/Th) - 1.1801\times\ln(Sm/Th) + 1.6189\times\ln(Yb/Th) + 1.2260\times\ln(Nb/Th) - 0.9944$
	IAB-CRB-OIB	$DF1_{(IAB\text{-}CRB\text{-}OIB)t1} = 0.5533\times\ln(La/Th) + 0.2173\times\ln(Sm/Th) - 0.0969\times\ln(Yb/Th) + 2.0454\times\ln(Nb/Th) - 5.6305$ $DF2_{(IAB\text{-}CRB\text{-}OIB)t1} = -2.4498\times\ln(La/Th) + 4.8562\times\ln(Sm/Th) - 2.1240\times\ln(Yb/Th) - 0.1567\times\ln(Nb/Th) + 0.9400$
	IAB-CRB-MORB	$DF1_{(IAB\text{-}CRB\text{-}MORB)t1} = 0.3305\times\ln(La/Th) + 0.3484\times\ln(Sm/Th) - 0.9562\times\ln(Yb/Th) + 2.0777\times\ln(Nb/Th) - 4.5628$ $DF2_{(IAB\text{-}CRB\text{-}MORB)t1} = -0.1928\times\ln(La/Th) - 1.1989\times\ln(Sm/Th) + 1.7531\times\ln(Yb/Th) + 0.6607\times\ln(Nb/Th) - 0.4384$
	IAB-OIB-MORB	$DF1_{(IAB\text{-}OIB\text{-}MORB)t1} = 1.7517\times\ln(Sm/Th) - 1.9508\times\ln(Yb/Th) + 1.9573\times\ln(Nb/Th) - 5.0928$ $DF2_{(IAB\text{-}OIB\text{-}MORB)t1} = -2.2412\times\ln(Sm/Th) + 2.2060\times\ln(Yb/Th) + 1.2481\times\ln(Nb/Th) - 0.8243$
	CRB-OIB-MORB	$DF1_{(CRB\text{-}OIB\text{-}MORB)t1} = -0.5558\times\ln(La/Th) - 1.4260\times\ln(Sm/Th) + 2.2935\times\ln(Yb/Th) - 0.6890\times\ln(Nb/Th) + 4.1422$ $DF2_{(CAB\text{-}OIB\text{-}MORB)t1} = -0.9207\times\ln(La/Th) + 3.6520\times\ln(Sm/Th) - 1.9866\times\ln(Yb/Th) + 1.0574\times\ln(Nb/Th) - 4.4283$

The tectonic fields are: IAB−island arc basic (or ultrabasic) rocks; CRB−continental rift basic (or ultrabasic) rocks; OIB−ocean island basic (or ultrabasic) rocks; and MORB−mid ocean ridge basic (or ultrabasic) rocks.

Table S4.
DF1-DF2 equations for the set of five diagrams based on major and trace element ratios proposed by Verma and Agrawal (2011) for basic and ultrabasic magmas.

Figure reference; figure type	Discrimination diagram	Discriminant function equations
Verma and Agrawal (2011); log-ratios of immobile major and trace elements	IAB-CRB+OIB-MORB	$DF1_{(IAB\text{-}CRB+OIB\text{-}MORB)t2} = -0.6611\times\ln(Nb/(TiO_2)_{adj}) + 2.2926\times\ln(V/TiO_2)_{adj}) + 1.6774\times\ln(Y/TiO_2)_{adj}) + 1.0916\times\ln(Zr/(TiO_2)_{adj}) + 21.3603$ $DF2_{(IAB\text{-}CRB+OIB\text{-}MORB)t2} = 0.4702\times\ln(Nb/(TiO_2)_{adj}) + 3.7649\times\ln(V/TiO_2)_{adj}) - 3.911\times\ln(Y/TiO_2)_{adj}) + 2.2697\times\ln(Zr/(TiO_2)_{adj}) + 4.8487$
	IAB-CRB-OIB	$DF1_{(IAB\text{-}CRB\text{-}OIB)t2} = -0.6146\times\ln(Nb/(TiO_2)_{adj}) + 2.3510\times\ln(V/TiO_2)_{adj}) + 1.6828\times\ln(Y/TiO_2)_{adj}) + 1.1911\times\ln(Zr/(TiO_2)_{adj}) + 22.7253$ $DF2_{(IAB\text{-}CRB\text{-}OIB)t2} = 1.3765\times\ln(Nb/(TiO_2)_{adj}) - 0.9452\times\ln(V/TiO_2)_{adj}) + 4.0461\times\ln(Y/TiO_2)_{adj}) - 2.0789\times\ln(Zr/(TiO_2)_{adj}) + 22.2450$
	IAB-CRB-MORB	$DF1_{(IAB\text{-}CRB\text{-}MORB)t2} = -0.6624\times\ln(Nb/(TiO_2)_{adj}) + 2.4498\times\ln(V/TiO_2)_{adj}) + 1.2867\times\ln(Y/TiO_2)_{adj}) + 1.0920\times\ln(Zr/(TiO_2)_{adj}) + 18.7466$ $DF2_{(IAB\text{-}CRB\text{-}MORB)t2} = 0.4938 \cdot \ln(Nb/(TiO_2)_{adj}) + 3.4741 \cdot \ln(V/TiO_2)_{adj}) - 3.8053 \cdot \ln(Y/TiO_2)_{adj}) + 2.0070 \cdot \ln(Zr/(TiO_2)_{adj}) + 3.3163$
	IAB-OIB-MORB	$DF1_{(IAB\text{-}OIB\text{-}MORB)t2} = -0.2646\times\ln(Nb/(TiO_2)_{adj}) + 2.0491\times\ln(V/TiO_2)_{adj}) + 3.4565\times\ln(Y/TiO_2)_{adj}) + 0.8573\times\ln(Zr/(TiO_2)_{adj}) + 32.9472$ $DF2_{(IAB\text{-}OIB\text{-}MORB)t2} = 0.01874\times\ln(Nb/(TiO_2)_{adj}) + 4.0937\times\ln(V/TiO_2)_{adj}) - 4.8550\times\ln(Y/TiO_2)_{adj}) + 2.9900\times\ln(Zr/(TiO_2)_{adj}) + 0.1995$
	CRB-OIB-MORB	$DF1_{(CRB\text{-}OIB\text{-}MORB)t2} = -0.7829\times\ln(Nb/(TiO_2)_{adj}) + 0.3379\times\ln(V/TiO_2)_{adj}) + 3.3239\times\ln(Y/TiO_2)_{adj}) - 0.51232\times\ln(Zr/(TiO_2)_{adj}) + 16.0941$ $DF2_{(CAB\text{-}OIB\text{-}MORB)t2} = 1.7478\times\ln(Nb/(TiO_2)_{adj}) - 0.0421\times\ln(V/TiO_2)_{adj}) + 3.5301\times\ln(Y/TiO_2)_{adj}) - 1.4503\times\ln(Zr/(TiO_2)_{adj}) + 28.3592$

The tectonic fields are: IAB−island arc basic (or ultrabasic) rocks; CRB−continental rift basic (or ultrabasic) rocks; OIB−ocean island basic (or ultrabasic) rocks; and MORB−mid ocean ridge basic (or ultrabasic) rocks. The subscript $_{adj}$ refers to adjusted data from the SINCLAS (Verma et al. 2002) or IgRoCS computer program (Verma and Rivera-Gómez 2013a).

Table S5.
DF1-DF2 equations (approximate coefficients) for the set of five diagrams based on major element ratios proposed by Verma and Verma (2013) for intermediate magmas.

Figure reference; figure type	Discrimination diagram	Discriminant function equations
Verma and Verma (2013); log-ratios of major elements (mint)	IA+CA-CR+OI-Col	$DF1_{(IA+CA-CR+OI-Col)_{mint}} = (-2.456 \times \ln(TiO_2/SiO_2)_{adj}) + (1.120 \times \ln(Al_2O_3/SiO_2)_{adj}) + (-2.225 \times \ln(Fe_2O_3/SiO_2)_{adj}) + (2.489 \times \ln(FeO/SiO_2)_{adj}) + (-0.212 \times \ln(MnO/SiO_2)_{adj}) + (-0.067 \times \ln(MgO/SiO_2)_{adj}) + (1.291 \times \ln(CaO/SiO_2)_{adj}) + (-0.284 \times \ln(Na_2O/SiO_2)_{adj}) + (-0.402 \times \ln(K_2O/SiO_2)_{adj}) + (0.031 \times \ln(P_2O_5/SiO_2)_{adj}) - 11.431$ $DF2_{(IA+CA-CR+OI-Col)_{mint}} = (-0.578 \times \ln(TiO_2/SiO_2)_{adj}) + (-0.011 \times \ln(Al_2O_3/SiO_2)_{adj}) + (0.691 \times \ln(Fe_2O_3/SiO_2)_{adj}) + (-1.998 \times \ln(FeO/SiO_2)_{adj}) + (-1.720 \times \ln(MnO/SiO_2)_{adj}) + (0.305 \times \ln(MgO/SiO_2)_{adj}) + (0.816 \times \ln(CaO/SiO_2)_{adj}) + (-1.792 \times \ln(Na_2O/SiO_2)_{adj}) + (0.871 \times \ln(K_2O/SiO_2)_{adj}) + (0.335 \times \ln(P_2O_5/SiO_2)_{adj}) - 12.202$
	IA-CA-CR+OI	$DF1_{(IA-CA-CR+OI)_{mint}} = (-2.519 \times \ln(TiO_2/SiO_2)_{adj}) + (0.542 \times \ln(Al_2O_3/SiO_2)_{adj}) + (-3.790 \times \ln(Fe_2O_3/SiO_2)_{adj}) + (3.846 \times \ln(FeO/SiO_2)_{adj}) + (-0.363 \times \ln(MnO/SiO_2)_{adj}) + (-0.177 \times \ln(MgO/SiO_2)_{adj}) + (1.426 \times \ln(CaO/SiO_2)_{adj}) + (0.112 \times \ln(Na_2O/SiO_2)_{adj}) + (-0.219 \times \ln(K_2O/SiO_2)_{adj}) + (-0.072 \times \ln(P_2O_5/SiO_2)_{adj}) - 14.315$ $DF2_{(IA-CA-CR+OI)_{mint}} = (-1.049 \times \ln(TiO_2/SiO_2)_{adj}) + (3.440 \times \ln(Al_2O_3/SiO_2)_{adj}) + (-3.433 \times \ln(Fe_2O_3/SiO_2)_{adj}) + (4.807 \times \ln(FeO/SiO_2)_{adj}) + (-3.499 \times \ln(MnO/SiO_2)_{adj}) + (0.374 \times \ln(MgO/SiO_2)_{adj}) + (-2.148 \times \ln(CaO/SiO_2)_{adj}) + (3.002 \times \ln(Na_2O/SiO_2)_{adj}) + (-0.774 \times \ln(K_2O/SiO_2)_{adj}) + (1.062 \times \ln(P_2O_5/SiO_2)_{adj}) - 13.489$
	IA-CA-Col	$DF1_{(IA-CA-Col)_{mint}} = (-0.887 \times \ln(TiO_2/SiO_2)_{adj}) + (-0.782 \times \ln(Al_2O_3/SiO_2)_{adj}) + (-2.432 \times \ln(Fe_2O_3/SiO_2)_{adj}) + (4.106 \times \ln(FeO/SiO_2)_{adj}) + (2.050 \times \ln(MnO/SiO_2)_{adj}) + (-0.387 \times \ln(MgO/SiO_2)_{adj}) + (-0.740 \times \ln(CaO/SiO_2)_{adj}) + (1.360 \times \ln(Na_2O/SiO_2)_{adj}) + (-0.816 \times \ln(K_2O/SiO_2)_{adj}) + (-0.468 \times \ln(P_2O_5/SiO_2)_{adj}) + 4.312$ $DF2_{(IA-CA-Col)_{mint}} = (1.760 \times \ln(TiO_2/SiO_2)_{adj}) + (-4.329 \times \ln(Al_2O_3/SiO_2)_{adj}) + (2.601 \times \ln(Fe_2O_3/SiO_2)_{adj}) + (-4.961 \times \ln(FeO/SiO_2)_{adj}) + (2.897 \times \ln(MnO/SiO_2)_{adj}) + (-0.362 \times \ln(MgO/SiO_2)_{adj}) + (2.230 \times \ln(CaO/SiO_2)_{adj}) + (-2.967 \times \ln(Na_2O/SiO_2)_{adj}) + (0.790 \times \ln(K_2O/SiO_2)_{adj}) + (-1.326 \times \ln(P_2O_5/SiO_2)_{adj}) + 7.586$
	IA-CR+OI-Col	$DF1_{(IA-CR+OI-Col)_{mint}} = (-2.436 \times \ln(TiO_2/SiO_2)_{adj}) + (1.539 \times \ln(Al_2O_3/SiO_2)_{adj}) + (-1.517 \times \ln(Fe_2O_3/SiO_2)_{adj}) + (1.456 \times \ln(FeO/SiO_2)_{adj}) + (0.496 \times \ln(MnO/SiO_2)_{adj}) + (-0.050 \times \ln(MgO/SiO_2)_{adj}) + (1.258 \times \ln(CaO/SiO_2)_{adj}) + (-0.827 \times \ln(Na_2O/SiO_2)_{adj}) + (-0.488 \times \ln(K_2O/SiO_2)_{adj}) + (0.112 \times \ln(P_2O_5/SiO_2)_{adj}) - 7.895$ $DF2_{(IA-CR+OI-Col)_{mint}} = (-0.737 \times \ln(TiO_2/SiO_2)_{adj}) + (-0.0788 \times \ln(Al_2O_3/SiO_2)_{adj}) + (0.066 \times \ln(Fe_2O_3/SiO_2)_{adj}) + (-1.130 \times \ln(FeO/SiO_2)_{adj}) + (-2.131 \times \ln(MnO/SiO_2)_{adj}) + (0.246 \times \ln(MgO/SiO_2)_{adj}) + (0.682 \times \ln(CaO/SiO_2)_{adj}) + (-1.328 \times \ln(Na_2O/SiO_2)_{adj}) + (0.771 \times \ln(K_2O/SiO_2)_{adj}) + (0.296 \times \ln(P_2O_5/SiO_2)_{adj}) - 15.241$

CA-CR+OI-Col	$DF1_{(CA\text{-}CR+OI\text{-}Col)_{mint}} = (-2.322 \times \ln(TiO_2/SiO_2)_{adj}) + (1.971 \times \ln(Al_2O_3/SiO_2)_{adj}) + (-0.537 \times \ln(Fe_2O_3/SiO_2)_{adj}) + (0.431 \times \ln(FeO/SiO_2)_{adj}) + (-1.139 \times \ln(MnO/SiO_2)_{adj}) + (0.528 \times \ln(MgO/SiO_2)_{adj}) + (0.988 \times \ln(CaO/SiO_2)_{adj}) + (-0.894 \times \ln(Na_2O/SiO_2)_{adj}) + (0.161 \times \ln(K_2O/SiO_2)_{adj}) + (0.078 \times \ln(P_2O_5/SiO_2)_{adj}) - 12.350$
	$DF2_{(CA\text{-}CR+OI\text{-}Col)_{mint}} = (-0.407 \times \ln(TiO_2/SiO_2)_{adj}) + (2.606 \times \ln(Al_2O_3/SiO_2)_{adj}) + (0.161 \times \ln(Fe_2O_3/SiO_2)_{adj}) + (1.346 \times \ln(FeO/SiO_2)_{adj}) + (0.446 \times \ln(MnO/SiO_2)_{adj}) + (-0.260 \times \ln(MgO/SiO_2)_{adj}) + (-0.465 \times \ln(CaO/SiO_2)_{adj}) + (0.921 \times \ln(Na_2O/SiO_2)_{adj}) + (-1.277 \times \ln(K_2O/SiO_2)_{adj}) + (-0.143 \times \ln(P_2O_5/SiO_2)_{adj}) + 3.501$

The tectonic settings are: IA−island arc; CA−continental arc; CR−continental rift; OI−ocean island; and Col−collision. The subscript $_{adj}$ refers to adjusted data from the SINCLAS (Verma et al. 2002) or IgRoCS computer program (Verma and Rivera-Gómez 2013a).

Table S6.
DF1-DF2 equations (approximate coefficients) for the set of five diagrams based on immobile major and trace element ratios proposed by Verma and Verma (2013) for intermediate magmas.

Figure reference; figure type	Discrimination diagram	Discriminant function equations
Verma and Verma (2013); log-ratios of immobile major and trace elements (mtint)	IA+CA-CR+OI-Col	$DF1_{(IA+CA-CR+OI-Col)_{mtint}} = (1.023\times \ln(MgO/TiO_2)_{adj}) + (0.631\times \ln(P_2O_5/TiO_2)_{adj}) + (-0.939\times \ln(Nb/TiO_2)_{adj}) + (-0.415\times \ln(Ni/TiO_2)_{adj}) + (1.677\times \ln(V/TiO_2)_{adj}) + (0.454\times \ln(Y/TiO_2)_{adj}) + (0.583\times \ln(Zr/TiO_2)_{adj}) + 1.901$ $DF2_{(IA+CA-CR+OI-Col)_{mtint}} = (0.249\times \ln(MgO/TiO_2)_{adj}) + (-0.477 \ln(P_2O_5/TiO_2)_{adj}) + (-0.336\times \ln(Nb/TiO_2)_{adj}) + (-0.131\times \ln(Ni/TiO_2)_{adj}) + (-1.712\times \ln(V/TiO_2)_{adj}) + (0.214\times \ln(Y/TiO_2)_{adj}) + (-2.008\times \ln(Zr/TiO_2)_{adj}) - 18.638$
	IA-CA-CR+OI	$DF1_{(IA-CA-CR+OI)_{mtint}} = (0.875\times \ln(MgO/TiO_2)_{adj}) + (0.428\times \ln(P_2O_5/TiO_2)_{adj}) + (-0.686\times \ln(Nb/TiO_2)_{adj}) + (-0.372\times \ln(Ni/TiO_2)_{adj}) + (1.924\times \ln(V/TiO_2)_{adj}) + (0.835\times \ln(Y/TiO_2)_{adj}) + (0.843\times \ln(Zr/TiO_2)_{adj}) + 8.228$ $DF2_{(IA-CA-CR+OI)_{mtint}} = (-1.172\times \ln(MgO/TiO_2)_{adj}) + (-2.651\times \ln(P_2O_5/TiO_2)_{adj}) + (0.176\times \ln(Nb/TiO_2)_{adj}) + (0.118\times \ln(Ni/TiO_2)_{adj}) + (-0.185\times \ln(V/TiO_2)_{adj}) + (1.921\times \ln(Y/TiO_2)_{adj}) + (0.387\times \ln(Zr/TiO_2)_{adj}) + 12.452$
	IA-CA-Col	$DF1_{(IA-CA-Col)_{mtint}} = (-0.801\times \ln(MgO/TiO_2)_{adj}) + (0.125\times \ln(P_2O_5/TiO_2)_{adj}) + (0.908\times \ln(Nb/TiO_2)_{adj}) + (0.320\times \ln(Ni/TiO_2)_{adj}) + (-0.368\times \ln(V/TiO_2)_{adj}) + (-0.641\times \ln(Y/TiO_2)_{adj}) + (0.723\times \ln(Zr/TiO_2)_{adj}) + 8.109$ $DF2_{(IA-CA-Col)_{mtint}} = (1.317\times \ln(MgO/TiO_2)_{adj}) + (2.200\times \ln(P_2O_5/TiO_2)_{adj}) + (-0.124\times \ln(Nb/TiO_2)_{adj}) + (-0.134\times \ln(Ni/TiO_2)_{adj}) + (-0.872\times \ln(V/TiO_2)_{adj}) + (-1.783\times \ln(Y/TiO_2)_{adj}) + (-1.365\times \ln(Zr/TiO_2)_{adj}) - 20.630$
	IA-CA-CR+OI	$DF1_{(IA-CR+OI-Col)_{mtint}} = (-0.856\times \ln(MgO/TiO_2)_{adj}) + (-0.301\times \ln(P_2O_5/TiO_2)_{adj}) + (0.862\times \ln(Nb/TiO_2)_{adj}) + (0.385\times \ln(Ni/TiO_2)_{adj}) + (-1.583\times \ln(V/TiO_2)_{adj}) + (-0.757\times \ln(Y/TiO_2)_{adj}) + (-0.692\times \ln(Zr/TiO_2)_{adj}) - 4.469$ $DF2_{(IA-CR+OI-Col)_{mtint}} = (0.215\times \ln(MgO/TiO_2)_{adj}) + (-0.504\times \ln(P_2O_5/TiO_2)_{adj}) + (-0.323\times \ln(Nb/TiO_2)_{adj}) + (-0.122\times \ln(Ni/TiO_2)_{adj}) + (-1.710\times \ln(V/TiO_2)_{adj}) + (0.426\times \ln(Y/TiO_2)_{adj}) + (-1.981\times \ln(Zr/TiO_2)_{adj}) - 17.041$
	CA-CR+OI-Col	$DF1_{(CA-CR+OI-Col)_{mtint}} = (-1.256\times \ln(MgO/TiO_2)_{adj}) + (-1.082\times \ln(P_2O_5/TiO_2)_{adj}) + (1.438\times \ln(Nb/TiO_2)_{adj}) + (0.545\times \ln(Ni/TiO_2)_{adj}) + (-1.620\times \ln(V/TiO_2)_{adj}) + (0.337\times \ln(Y/TiO_2)_{adj}) + (-0.714\times \ln(Zr/TiO_2)_{adj}) + 5.752$ $DF2_{(CA-CR+OI-Col)_{mtint}} = (-0.0240\times \ln(MgO/TiO_2)_{adj}) + (-0.054\times \ln(P_2O_5/TiO_2)_{adj}) + (-0.861\times \ln(Nb/TiO_2)_{adj}) + (-0.174\times \ln(Ni/TiO_2)_{adj}) + (-1.641\times \ln(V/TiO_2)_{adj}) + (0.069\times \ln(Y/TiO_2)_{adj}) + (-1.772\times \ln(Zr/TiO_2)_{adj}) - 21.028$

The tectonic settings are: IA−island arc; CA−continental arc; CR−continental rift; OI−ocean island; and Col−collision. The subscript $_{adj}$ refers to adjusted data from the SINCLAS (Verma et al. 2002) or IgRoCS computer program (Verma and Rivera-Gómez 2013a).

Table S7.
DF1-DF2 equations (approximate coefficients) for the set of five diagrams based on immobile trace element ratios proposed by Verma and Verma (2013) for intermediate magmas.

Figure reference; figure type	Discrimination diagram	Discriminant function equations
Verma and Verma (2013); log-ratios of immobile trace elements (tint)	IA+CA-CR+OI-Col	$DF1_{(IA+CA-CR+OI-Col)\,tint} = (-0.167\times\ln(La/Yb) + (-1.254\times\ln(Ce/Yb) + (1.295\times\ln(Sm/Yb) + (1.332\times\ln(Nb/Yb) + (0.270\times\ln(Th/Yb) + (1.929\times\ln(Y/Yb) + (0.181\times\ln(Zr/Yb) - 3.816$ $DF2_{(IA+CA-CR+OI-Col)\,tint} = (-0.243\times\ln(La/Yb) + (1.727\times\ln(Ce/Yb) + (0.490\times\ln(Sm/Yb) + (-1.276\times\ln(Nb/Yb) + (0.960\times\ln(Th/Yb) + (0.851\times\ln(Y/Yb) + (-0.489\times\ln(Zr/Yb) - 3.306$
	IA-CA-CR+OI	$DF1_{(IA-CA-CR+OI)tint} = (0.018\times\ln(La/Yb) + (-1.269\times\ln(Ce/Yb) + (1.741\times\ln(Sm/Yb) + (1.324\times\ln(Nb/Yb) + (0.029\times\ln(Th/Yb) + (1.581\times\ln(Y/Yb) + (0.172\times\ln(Zr/Yb) - 3.385$ $DF2_{(IA-CA-CR+OI)tint} = (-2.100\times\ln(La/Yb) + (-2.044\times\ln(Ce/Yb) + (-0.412\times\ln(Sm/Yb) + (1.022\times\ln(Nb/Yb) + (1.244\times\ln(Th/Yb) + (1.877\times\ln(Y/Yb) + (1.070\times\ln(Zr/Yb) - 0.292$
	IA-CA-Col	$DF1_{(IA-CA-Col)\,tint} = (0.093\times\ln(La/Yb) + (0.752\times\ln(Ce/Yb) + (0.930\times\ln(Sm/Yb) + (0.124\times\ln(Nb/Yb) + (0.348\times\ln(Th/Yb) + (1.473\times\ln(Y/Yb) + (-0.034\times\ln(Zr/Yb) - 5.801$ $DF2_{(IA-CA-CR+OI)tint} = (-2.038\times\ln(La/Yb) + (-0.073\times\ln(Ce/Yb) + (-1.360\times\ln(Sm/Yb) + (-0.078\times\ln(Nb/Yb) + (1.825\times\ln(Th/Yb) + (2.774\times\ln(Y/Yb) + (0.444\times\ln(Zr/Yb) - 3.684$
	IA-CR+OI-Col	$DF1_{(IA-CR+OI-Col)\,tint} = (0.721\times\ln(La/Yb) + (-1.352\times\ln(Ce/Yb) + (1.379\times\ln(Sm/Yb) + (1.164\times\ln(Nb/Yb) + (-0.042\times\ln(Th/Yb) + (1.558\times\ln(Y/Yb) + (-0.164\times\ln(Zr/Yb) - 2.934$ $DF2_{(IA-CR+OI-Col)\,tint} = (0.238\times\ln(La/Yb) + (-2.035\times\ln(Ce/Yb) + (-0.250\times\ln(Sm/Yb) + (1.347\times\ln(Nb/Yb) + (-0.761\times\ln(Th/Yb) + (-0.787\times\ln(Y/Yb) + (0.377\times\ln(Zr/Yb) + 4.155$
	CA-CR+OI-Col	$DF1_{(CA-CR+OI-Col)\,tint} = (-0.977\times\ln(La/Yb) + (-1.389\times\ln(Ce/Yb) + (1.366\times\ln(Sm/Yb) + (1.900\times\ln(Nb/Yb) + (0.569\times\ln(Th/Yb) + (1.658\times\ln(Y/Yb) + (-0.305\times\ln(Zr/Yb) - 0.877$ $DF2_{(CA-CR+OI-Col)\,tint} = (-0.0870\times\ln(La/Yb) + (1.164\times\ln(Ce/Yb) + (0.364\times\ln(Sm/Yb) + (-0.901\times\ln(Nb/Yb) + (1.126\times\ln(Th/Yb) + (1.191\times\ln(Y/Yb) + (-0.400\times\ln(Zr/Yb) - 3.915$

The tectonic settings are: IA−island arc; CA−continental arc; CR−continental rift; OI−ocean island; and Col−collision.

Table S8.
DF1-DF2 equations (approximate coefficients) for the set of five diagrams based on major element ratios proposed by Verma et al. (2012) for acid magmas.

Figure reference; figure type	Discrimination diagram	Discriminant function equations
Verma et al. (2012); log-ratios of major elements (m3)	IA+CA-CR-Col	$DF1_{(IA+CA-CR-Col)_{m3}} = (0.361\times\ln(TiO_2/SiO_2)_{adj}) + (0.957\times\ln(Al_2O_3/SiO_2)_{adj}) + (-2.092\times\ln(Fe_2O_3/SiO_2)_{adj}) + (0.934\times\ln(FeO/SiO_2)_{adj}) + (0.427\times\ln(MnO/SiO_2)_{adj}) + (0.187\times\ln(MgO/SiO_2)_{adj}) + (0.456\times\ln(CaO/SiO_2)_{adj}) + (0.561\times\ln(Na_2O/SiO_2)_{adj}) + (-1.652\times\ln(K_2O/SiO_2)_{adj}) + (-0.156\times\ln(P_2O_5/SiO_2)_{adj}) - 1.583$ $DF2_{(IA+CA-CR-Col)_{m3}} = (0.472\times\ln(TiO_2/SiO_2)_{adj}) + (-0.955\times\ln(Al_2O_3/SiO_2)_{adj}) + (0.110\times\ln(Fe_2O_3/SiO_2)_{adj}) + (0.699\times\ln(FeO/SiO_2)_{adj}) + (0.740\times\ln(MnO/SiO_2)_{adj}) + (-0.028\times\ln(MgO/SiO_2)_{adj}) + (-0.245\times\ln(CaO/SiO_2)_{adj}) + (0.232\times\ln(Na_2O/SiO_2)_{adj}) + (0.174\times\ln(K_2O/SiO_2)_{adj}) + (-0.354\times\ln(P_2O_5/SiO_2)_{adj}) + 6.691$
	IA-CA-CR	$F1_{(IA-CA-CR)_{m3}} = (-0.479\times\ln(TiO_2/SiO_2)_{adj}) + (-0.087\times\ln(Al_2O_3/SiO_2)_{adj}) + (2.743\times\ln(Fe_2O_3/SiO_2)_{adj}) + (-1.066\times\ln(FeO/SiO_2)_{adj}) + (-0.139\times\ln(MnO/SiO_2)_{adj}) + (-0.191\times\ln(MgO/SiO_2)_{adj}) + (-0.852\times\ln(CaO/SiO_2)_{adj}) + (-0.714\times\ln(Na_2O/SiO_2)_{adj}) + (1.717\times\ln(K_2O/SiO_2)_{adj}) + (0.339\times\ln(P_2O_5/SiO_2)_{adj}) + 6.257$ $DF2_{(IA-CA-CR)_{m3}} = (-0.320\times\ln(TiO_2/SiO_2)_{adj}) + (-1.758\times\ln(Al_2O_3/SiO_2)_{adj}) + (-3.205\times\ln(Fe_2O_3/SiO_2)_{adj}) + (1.121\times\ln(FeO/SiO_2)_{adj}) + (0.217\times\ln(MnO/SiO_2)_{adj}) + (-0.074\times\ln(MgO/SiO_2)_{adj}) + (1.250\times\ln(CaO/SiO_2)_{adj}) + (1.314\times\ln(Na_2O/SiO_2)_{adj}) + (1.662\times\ln(K_2O/SiO_2)_{adj}) + (0.019\times\ln(P_2O_5/SiO_2)_{adj}) + 0.998$
	IA-CA-Col	$DF1_{(IA-CA-Col)_{m3}} = (-0.362\times\ln(TiO_2/SiO_2)_{adj}) + (-0.034\times\ln(Al_2O_3/SiO_2)_{adj}) + (0.520\times\ln(Fe_2O_3/SiO_2)_{adj}) + (-0.498\times\ln(FeO/SiO_2)_{adj}) + (-0.722\times\ln(MnO/SiO_2)_{adj}) + (-0.123\times\ln(MgO/SiO_2)_{adj}) + (-0.139\times\ln(CaO/SiO_2)_{adj}) + (-0.817\times\ln(Na_2O/SiO_2)_{adj}) + (1.507\times\ln(K_2O/SiO_2)_{adj}) + (0.268\times\ln(P_2O_5/SiO_2)_{adj}) - 3.083$ $DF2_{(IA-CA-Col)_{m3}} = (-0.142\times\ln(TiO_2/SiO_2)_{adj}) + (1.984\times\ln(Al_2O_3/SiO_2)_{adj}) + (1.747\times\ln(Fe_2O_3/SiO_2)_{adj}) + (-0.735\times\ln(FeO/SiO_2)_{adj}) + (-1.226\times\ln(MnO/SiO_2)_{adj}) + (0.062\times\ln(MgO/SiO_2)_{adj}) + (-1.152\times\ln(CaO/SiO_2)_{adj}) + (-3.189\times\ln(Na_2O/SiO_2)_{adj}) + (-2.339\times\ln(K_2O/SiO_2)_{adj}) + (0.495\times\ln(P_2O_5/SiO_2)_{adj}) - 18.190$
	IA-CR-Col	$DF1_{(IA-CR-Col)_{m3}} = (0.023\times\ln(TiO_2/SiO_2)_{adj}) + (1.288\times\ln(Al_2O_3/SiO_2)_{adj}) + (-2.641\times\ln(Fe_2O_3/SiO_2)_{adj}) + (2.949\times\ln(FeO/SiO_2)_{adj}) + (0.197\times\ln(MnO/SiO_2)_{adj}) + (0.067\times\ln(MgO/SiO_2)_{adj}) + (0.062\times\ln(CaO/SiO_2)_{adj}) + (0.622\times\ln(Na_2O/SiO_2)_{adj}) + (-2.058\times\ln(K_2O/SiO_2)_{adj}) + (-0.075\times\ln(P_2O_5/SiO_2)_{adj}) - 2.179$

	$DF2_{(IA\text{-}CR\text{-}Col)_{m3}} = (0.279\times \ln(TiO_2/SiO_2)_{adj}) + (-1.054\times \ln(Al_2O_3/SiO_2)_{adj}) + (0.827\times \ln(Fe_2O_3/SiO_2)_{adj}) + (0.303\times \ln(FeO/SiO_2)_{adj}) + (0.408\times \ln(MnO/SiO_2)_{adj}) + (-0.090\times \ln(MgO/SiO_2)_{adj}) + (-0.326\times \ln(CaO/SiO_2)_{adj}) + (0.152\times \ln(Na_2O/SiO_2)_{adj}) + (0.670 \ln(K_2O/SiO_2)_{adj}) + (-0.226\times \ln(P_2O_5/SiO_2)_{adj}) + 6.517$
CA-CR-Col	$DF1_{(CA\text{-}CR\text{-}Col)_{m3}} = (0.064\times \ln(TiO_2/SiO_2)_{adj}) + (-1.794\times \ln(Al_2O_3/SiO_2)_{adj}) + (0.526\times \ln(Fe_2O_3/SiO_2)_{adj}) + (0.638\times \ln(FeO/SiO_2)_{adj}) + (0.341\times \ln(MnO/SiO_2)_{adj}) + (-0.072\times \ln(MgO/SiO_2)_{adj}) + (-0.326\times \ln(CaO/SiO_2)_{adj}) + (0.106\times \ln(Na_2O/SiO_2)_{adj}) + (1.810\times \ln(K_2O/SiO_2)_{adj}) + (-0.034\times \ln(P_2O_5/SiO_2)_{adj}) + 8.262$
	$DF2_{(CA\text{-}CR\text{-}Col)_{m3}} = (0.876\times \ln(TiO_2/SiO_2)_{adj}) + (0.802\times \ln(Al_2O_3/SiO_2)_{adj}) + (0.247\times \ln(Fe_2O_3/SiO_2)_{adj}) + (-0.880\times \ln(FeO/SiO_2)_{adj}) + (0.754\times \ln(MnO/SiO_2)_{adj}) + (-0.001\times \ln(MgO/SiO_2)_{adj}) + (-0.062\times \ln(CaO/SiO_2)_{adj}) + (-0.205\times \ln(Na_2O/SiO_2)_{adj}) + (-3.309\times \ln(K_2O/SiO_2)_{adj}) + (-0.353\times \ln(P_2O_5/SiO_2)_{adj}) - 3.896$

The tectonic settings are: IA−island arc; CA−continental arc; CR−continental rift; and Col−collision. The subscript $_{adj}$ refers to adjusted data from the SINCLAS (Verma et al. 2002) or IgRoCS computer program (Verma and Rivera-Gómez 2013a).

Table S9.
DF1-DF2 equations (approximate coefficients) for the set of five diagrams based on major element ratios proposed by Verma et al. (2013) for acid magmas.

Figure reference; figure type	Discrimination diagram	Discriminant function equations
Verma et al. (2013); log-ratios of major elements (macid)	IA+CA-CR+OI-Col	$DF1_{(IA+CA-CR+OI-Col)_{macid}} = (0.051\times \ln(TiO_2/SiO_2)_{adj}) + (0.226\times \ln(Al_2O_3/SiO_2)_{adj}) + (-1.769\times \ln(Fe_2O_3/SiO_2)_{adj}) + (1.831\times \ln(FeO/SiO_2)_{adj}) + (-0.0652\times \ln(MnO/SiO_2)_{adj}) + (0.134\times \ln(MgO/SiO_2)_{adj}) + (0.225\times \ln(CaO/SiO_2)_{adj}) + (0.742\times \ln(Na_2O/SiO_2)_{adj}) + (-1.781\times \ln(K_2O/SiO_2)_{adj}) + (0.146\times \ln(P_2O_5/SiO_2)_{adj}) - 2.115$ $DF2_{(IA+CA-CR+OI-Col)_{macid}} = (1.091\times \ln(TiO_2/SiO_2)_{adj}) + (-1.648\times \ln(Al_2O_3/SiO_2)_{adj}) + (-1.189\times \ln(Fe_2O_3/SiO_2)_{adj}) + (1.030\times \ln(FeO/SiO_2)_{adj}) + (0.823\times \ln(MnO/SiO_2)_{adj}) + (0.026\times \ln(MgO/SiO_2)_{adj}) + (0.023\times \ln(CaO/SiO_2)_{adj}) + (0.212\times \ln(Na_2O/SiO_2)_{adj}) + (0.085\times \ln(K_2O/SiO_2)_{adj}) + (-0.854\times \ln(P_2O_5/SiO_2)_{adj}) + 2.543$
	IA-CA-CR+OI	$DF1_{(IA-CA+OI-CR+OI)_{macid}} = (0.130\times \ln(TiO_2/SiO_2)_{adj}) + (0.623\times \ln(Fe_2O_3/SiO_2)_{adj}) + (-0.761\times \ln(FeO/SiO_2)_{adj}) + (-0.083\times \ln(MnO/SiO_2)_{adj}) + (-0.147\times \ln(MgO/SiO_2)_{adj}) + (-0.239\times \ln(CaO/SiO_2)_{adj}) + (-0.520\times \ln(Na_2O/SiO_2)_{adj}) + (2.038\times \ln(K_2O/SiO_2)_{adj}) + (-0.164\times \ln(P_2O_5/SiO_2)_{adj}) + 2.650$ $DF2_{(IA-CA-CR+OI)_{macid}} = (-0.045\times \ln(TiO_2/SiO_2)_{adj}) + (5.102\times \ln(Fe_2O_3/SiO_2)_{adj}) + (-5.151\times \ln(FeO/SiO_2)_{adj}) + (1.160\times \ln(MnO/SiO_2)_{adj}) + (-0.253\times \ln(MgO/SiO_2)_{adj}) + (-0.451\times \ln(CaO/SiO_2)_{adj}) + (-2.448\times \ln(Na_2O/SiO_2)_{adj}) + (-1.405\times \ln(K_2O/SiO_2)_{adj}) + (0.002\times \ln(P_2O_5/SiO_2)_{adj}) - 2.979$
	IA-CA-Col	$DF1_{(IA-CA-Col)_{macid}} = (-0.489\times \ln(TiO_2/SiO_2)_{adj}) + (2.271\times \ln(Al_2O_3/SiO_2)_{adj}) + (0.619\times \ln(Fe_2O_3/SiO_2)_{adj}) + (-1.238\times \ln(FeO/SiO_2)_{adj}) + (-0.912\times \ln(MnO/SiO_2)_{adj}) + (0.156\times \ln(MgO/SiO_2)_{adj}) + (-1.231\times \ln(Na_2O/SiO_2)_{adj}) + (1.154\times \ln(K_2O/SiO_2)_{adj}) + (0.409\times \ln(P_2O_5/SiO_2)_{adj}) - 3.220$ $DF2_{(IA-CA-Col)_{macid}} = (0.681\times \ln(TiO_2/SiO_2)_{adj}) + (2.244\times \ln(Al_2O_3/SiO_2)_{adj}) + (-3.899\times \ln(Fe_2O_3/SiO_2)_{adj}) + (3.691\times \ln(FeO/SiO_2)_{adj}) + (-0.374\times \ln(MnO/SiO_2)_{adj}) + (0.255\times \ln(MgO/SiO_2)_{adj}) + (3.036\times \ln(Na_2O/SiO_2)_{adj}) + (1.163\times \ln(K_2O/SiO_2)_{adj}) + (-0.226\times \ln(P_2O_5/SiO_2)_{adj}) + 12.688$
	IA-CR+OI -Col	$DF1_{(IA-CR+OI-Col)_{macid}} = (-0.144\times \ln(TiO_2/SiO_2)_{adj}) + (-0.743\times \ln(Al_2O_3/SiO_2)_{adj}) + (-0.443\times \ln(MnO/SiO_2)_{adj}) + (0.075\times \ln(CaO/SiO_2)_{adj}) + (0.383\times \ln(Na_2O/SiO_2)_{adj}) + (2.577\times \ln(K_2O/SiO_2)_{adj}) + (-0.024\times \ln(P_2O_5/SiO_2)_{adj}) + 4.290$ $DF2_{(IA-CR+OI-Col)_{macid}} = (-0.873\times \ln(TiO_2/SiO_2)_{adj}) + (1.545\times \ln(Al_2O_3/SiO_2)_{adj}) + (-0.753\times \ln(MnO/SiO_2)_{adj}) + (0.023\times \ln(CaO/SiO_2)_{adj}) + (0.150\times \ln(Na_2O/SiO_2)_{adj}) + (-0.320\times \ln(K_2O/SiO_2)_{adj}) + (0.751\times \ln(P_2O_5/SiO_2)_{adj}) - 2.595$
	CA-CR+OI -Col	$DF1_{(CA-CR+OI-Col)_{macid}} = (-0.022\times \ln(TiO_2/SiO_2)_{adj}) + (1.065\times \ln(Al_2O_3/SiO_2)_{adj}) + (-1.651\times \ln(Fe_2O_3/SiO_2)_{adj}) + (1.889\times \ln(FeO/SiO_2)_{adj}) + (-0.296\times \ln(MnO/SiO_2)_{adj}) + (0.119\times \ln(MgO/SiO_2)_{adj}) + (0.650\times \ln(Na_2O/SiO_2)_{adj}) + (-2.431\times \ln(K_2O/SiO_2)_{adj}) + (0.212\times \ln(P_2O_5/SiO_2)_{adj}) - 4.332$

$$DF2_{(CA\text{-}CR+OI\text{-}Col)_{macid}} = (-1.084 \times \ln(TiO_2/SiO_2)_{adj}) + (1.626 \times \ln(Al_2O_3/SiO_2)_{adj}) + (0.992 \times \ln(Fe_2O_3/SiO_2)_{adj}) + (-0.798 \times \ln(FeO/SiO_2)_{adj}) + (-0.779 \times \ln(MnO/SiO_2)_{adj}) + (-0.018 \times \ln(MgO/SiO_2)_{adj}) + (-0.223 \times \ln(Na_2O/SiO_2)_{adj}) + (0.651 \times \ln(K_2O/SiO_2)_{adj}) + (0.726 \times \ln(P_2O_5/SiO_2)_{adj}) - 0.916$$

The tectonic settings are: IA−island arc; CA−continental arc; CR−continental rift; OI−ocean island; and Col−collision. The subscript $_{adj}$ refers to adjusted data from the SINCLAS (Verma et al. 2002) or IgRoCS computer program (Verma and Rivera-Gómez 2013a).

Table S10.
DF1-DF2 equations (approximate coefficients) for the set of five diagrams based on immobile major and trace element ratios proposed by Verma et al. (2013) for acid magmas.

Figure reference; figure type	Discrimination diagram	Discriminant function equations
Verma et al. (2013); log-ratios of immobile major and trace elements (mtacid)	IA+CA-CR+OI-Col	$DF1_{(IA+CA-CR+OI-Col)\,mtacid} = (-0.091\times \ln(MgO/TiO_2)_{adj}) + (-0.228\times \ln(P_2O_5/TiO_2)_{adj}) + (0.729\times \ln(Nb/TiO_2)_{adj}) + (-0.237\times \ln(Y/TiO_2)_{adj}) + (0.577\times \ln(Zr/TiO_2)_{adj}) + 4.704$ $DF2_{(IA+CA-CR+OI-Col)\,mtacid} = (-0.268\times \ln(MgO/TiO_2)_{adj}) + (-1.253\times \ln(P_2O_5/TiO_2)_{adj}) + (-0.476\times \ln(Nb/TiO_2)_{adj}) + (0.209\times \ln(Y/TiO_2)_{adj}) + (-0.082\times \ln(Zr/TiO_2)_{adj}) - 3.709$
	IA-CA-CR+OI	$DF1_{(IA-CA-CR+OI)\,mtacid} = (-0.018\times \ln(MgO/TiO_2)_{adj}) + (-0.025\times \ln(P_2O_5/TiO_2)_{adj}) + (1.060\times \ln(Nb/TiO_2)_{adj}) + (-0.530\times \ln(Y/TiO_2)_{adj}) + (0.301\times \ln(Zr/TiO_2)_{adj}) + 4.701$ $DF2_{(IA-CA-CR+OI)\,mtacid} = (-0.197\times \ln(MgO/TiO_2)_{adj}) + (0.118\times \ln(P_2O_5/TiO_2)_{adj}) + (-0.724\times \ln(Nb/TiO_2)_{adj}) + (1.099\times \ln(Y/TiO_2)_{adj}) + (0.742\times \ln(Zr/TiO_2)_{adj}) + 3.702$
	IA-CA-Col	$DF1_{(IA-CA-Col)\,mtacid} = (0.248\times \ln(P_2O_5/TiO_2)_{adj}) + (1.183\times \ln(Nb/TiO_2)_{adj}) + (-0.861\times \ln(Y/TiO_2)_{adj}) + (0.136\times \ln(Zr/TiO_2)_{adj}) + 3.988$ $DF2_{(IA-CA-Col)\,mtacid} = (1.129\times \ln(P_2O_5/TiO_2)_{adj}) + (-0.382\times \ln(Nb/TiO_2)_{adj}) + (1.126\times \ln(Y/TiO_2)_{adj}) + (0.682\times \ln(Zr/TiO_2)_{adj}) + 7.274$
	IA-CR+OI-Col	$DF1_{(IA-CR+OI-Col)\,mtacid} = (0.095\times \ln(MgO/TiO_2)_{adj}) + (-0.079\times \ln(P_2O_5/TiO_2)_{adj}) + (1.104\times \ln(Nb/TiO_2)_{adj}) + (-0.900\times \ln(Y/TiO_2)_{adj}) + (0.333\times \ln(Zr/TiO_2)_{adj}) + 2.771$ $DF2_{(IA-CR-Col)\,mtacid} = (-0.298\times \ln(MgO/TiO_2)_{adj}) + (-0.998\times \ln(P_2O_5/TiO_2)_{adj}) + (-0.279\times \ln(Nb/TiO_2)_{adj}) + (0.339\times \ln(Y/TiO_2)_{adj}) + (0.171\times \ln(Zr/TiO_2)_{adj}) - 0.805$
	CA-CR+OI-Col	$DF1_{(CA-CR-Col)\,mtacid} = (-0.081\times \ln(MgO/TiO_2)_{adj}) + (-0.432\times \ln(P_2O_5/TiO_2)_{adj}) + (0.444\times \ln(Nb/TiO_2)_{adj}) + (-0.131\times \ln(Y/TiO_2)_{adj}) + (0.824\times \ln(Zr/TiO_2)_{adj}) + 3.726$

$$DF2_{(CA\text{-}CR\text{-}Col)_{mtacid}} = (-0.341 \times \ln(MgO/TiO_2)_{adj}) + (-1.110 \times \ln(P_2O_5/TiO_2)_{adj}) + (-0.754 \times \ln(Nb/TiO_2)_{adj}) + (0.271 \times \ln(Y/TiO_2)_{adj}) + (-0.377 \times \ln(Zr/TiO_2)_{adj}) - 5.425$$

The tectonic settings are: IA−island arc; CA−continental arc; CR−continental rift; OI−ocean island; and Col−collision. The subscript $_{adj}$ refers to adjusted data from the SINCLAS (Verma et al. 2002) or IgRoCS computer program (Verma and Rivera-Gómez 2013a).

Table S11.
DF1-DF2 equations (approximate coefficients) for the set of five diagrams based on immobile trace element ratios proposed by Verma et al. (2013) for acid magmas.

Figure reference; figure type	Discrimination diagram	Discriminant function equations
Verma et al. (2013); log-ratios of immobile trace elements (tacid)	IA+CA-CR+OI-Col	$DF1_{(IA+CA-CR+OI-Col)_{tacid}} = (-4.994 \times \ln(La/Yb)) + (7.810 \times \ln(Ce/Yb)) + (-4.329 \times \ln(Sm/Yb)) + (0.822 \times \ln(Nb/Yb)) + (0.063 \times \ln(Th/Yb)) + (0.644 \times \ln(Y/Yb)) + (-0.567 \times \ln(Zr/Yb)) - 9.497$ $DF2_{(IA+CA-CR+OI-Col)_{tacid}} = (2.325 \times \ln(La/Yb)) + (-3.620 \times \ln(Ce/Yb)) + (2.621 \times \ln(Sm/Yb)) + (0.250 \times \ln(Nb/Yb)) + (0.843 \times \ln(Th/Yb)) + (-1.139 \times \ln(Y/Yb)) + (-1.269 \times \ln(Zr/Yb)) + 10.251$
	IA-CA-CR+OI	$DF1_{(IA-CA-CR+OI)_{tacid}} = (-5.209 \times \ln(La/Yb)) + (6.616 \times \ln(Ce/Yb)) + (-3.632 \times \ln(Sm/Yb)) + (1.692 \times \ln(Nb/Yb)) + (0.334 \times \ln(Th/Yb)) + (1.558 \times \ln(Y/Yb)) + (-0.488 \times \ln(Zr/Yb)) - 9.614$ $DF2_{(IA-CA-CR+OI)_{tacid}} = (-3.72 \times \ln(La/Yb)) + (4.792 \times \ln(Ce/Yb)) + (-2.678 \times \ln(Sm/Yb)) + (0.158 \times \ln(Nb/Yb)) + (-0.499 \times \ln(Th/Yb)) + (1.035 \times \ln(Y/Yb)) + (-0.342 \times \ln(Zr/Yb)) - 4.934$
	IA-CA-Col	$DF1_{(IA-CA-Col)_{tacid}} = (-0.047 \times \ln(La/Yb)) + (1.076 \times \ln(Ce/Yb)) + (-0.963 \times \ln(Sm/Yb)) + (0.840 \times \ln(Nb/Yb)) + (0.594 \times \ln(Th/Yb)) + (-0.878 \times \ln(Zr/Yb)) - 0.731$ $DF2_{(IA-CA-Col)_{tacid}} = (-4.067 \times \ln(La/Yb)) + (4.736 \times \ln(Ce/Yb)) + (-0.077 \times \ln(Sm/Yb)) + (-0.225 \times \ln(Nb/Yb)) + (0.774 \times \ln(Th/Yb)) + (-2.495 \times \ln(Zr/Yb)) + 5.099$
	IA-CR+OI-Col	$DF1_{(IA-CR+OI-Col)_{tacid}} = (0.259 \times \ln(La/Yb)) + (1.047 \times \ln(Ce/Yb)) + (-1.004 \times \ln(Sm/Yb)) + (0.898 \times \ln(Nb/Yb)) + (0.542 \times \ln(Th/Yb)) + (0.089 \times \ln(Y/Yb)) + (-0.620 \times \ln(Zr/Yb)) - 2.914$ $DF2_{(IA-CR+OI-Col)_{tacid}} = (-5.356 \times \ln(La/Yb)) + (8.414 \times \ln(Ce/Yb)) + (-5.369 \times \ln(Sm/Yb)) + (0.483 \times \ln(Nb/Yb)) + (-0.411 \times \ln(Th/Yb)) + (1.119 \times \ln(Y/Yb)) + (0.373 \times \ln(Zr/Yb)) - 13.950$
	CA-CR+OI-Col	$DF1_{(CA-CR+OI-Col)_{tacid}} = (-5.409 \times \ln(La/Yb)) + (8.436 \times \ln(Ce/Yb)) + (-4.783 \times \ln(Sm/Yb)) + (0.776 \times \ln(Nb/Yb)) + (-0.079 \times \ln(Th/Yb)) + (0.636 \times \ln(Y/Yb)) + (-0.263 \times \ln(Zr/Yb)) - 11.340$ $DF2_{(CA-CR+OI-Col)_{tacid}} = (1.683 \times \ln(La/Yb)) + (-1.730 \times \ln(Ce/Yb)) + (0.516 \times \ln(Sm/Yb)) + (0.838 \times \ln(Nb/Yb)) + (1.037 \times \ln(Th/Yb)) + (-0.984 \times \ln(Y/Yb)) + (-1.414 \times \ln(Zr/Yb)) + 6.088$

The tectonic settings are: IA−island arc; CA−continental arc; CR−continental rift; OI−ocean island; and Col−collision.

Table S12

Synthesis of the compilation of "fresh" rock samples used in the present study for testing of discrimination diagrams (18 test studies).

Test study		Approximate location		Number of Samples* (*Figure no; **Table no.** for results*)			Age and rock type		Inferred Tectonic setting	Reference
Region	Sub-region	Long. (°)	Lat. (°)	**B + U**	**I**	**A**	Age (Ma)	Author rock type		
				m1/m2, t1, t2	m, mt, t	m, mt, t				
Expected tectonic setting: **Ocean Island**										
1. Hawaiian Islands (Pacific Ocean)	1a. Mauna Kea	-155.5	19.8	303+3, 0, 303+3 ***(Figs. 1, S2, S3; Table 1)***	---	---	0.1-0.4	submarine basaltic lava	OIB	Rhodes and Vollinger (2004), Rhodes (2012)
	1b. Mauna Loa	-155.6	19.5	43+2, 0, 43+2 ***(Figs. S4-S6; Table S14)***	---	---	0.1-0.4	submarine basaltic lava	OIB	Rhodes and Vollinger (2004)
	1c. Maui	-156.6	20.9	10, 0, 10 ***(Figs. S7- S9; Table S15)***	---	---	1.9–2.1	basaltic lava	OIB	Sherrod et al. (2007)
	1d. Oahu	-157.9	21.5	9, 4, 9 ***(Figs. S10- S12; Table S16)***	15, 15, 3 ***(Figs. S13-S14; Table S17)***	---	2.9–3.9	basaltic lava and dike rocks	OIB; OI	Jackson et al. (1999)
2. Trindade Island (southern Atlantic Ocean)	2. Trindade	-29.3	-20.5	2+12, 2+11, 0 ***(Figs. S15- S17; Table S18)***	24, 0, 13 ***(Figs. S18-S19; Table S19)***	---	<0.27–3.6	different types of alkalic rocks	OIB; CR+OI	Marques et al.(1999)
Expected tectonic setting: **Ocean Island or Continental rift**										
3. Antarctica (Ross Sea)	3. White Island	168.0	-78.0	22, 22, 22 ***(Figs. S20- S23; Table S20)***	---	---	0.17-7.65	Alkali rocks	CRB; OIB	Cooper et al. (2007)
4. Antarctica	4. McMurdo Sound	166.9	-77.8	24, 20, 20 ***(Figs. S24- S27; Table S21)***	---	---	15.9-18.4	drill core glasses	OIB	Nyland et al. (2013)
Expected tectonic setting: **Continental rift**										
5. Spain	5. Garrotxa, NE Volcanic province	2.5	42	8+8, 8+7, 8+7 ***(Figs. S28- S31; Table S22)***	---	---	0.7-0.0115	alkaline rocks	CRB	Cebriá et al. (2000)
6. Austria	6. Styrian basin	14.4	47.5	9+30, 9+30, 9+30 ***(Figs. S32- S35; Table S18)***	---	---	Quaternary	Styrian basin lavas	CRB	Ali et al. (2013)
7. Cameroon	7. Mount Cameroon	9.2	4.2	14, 0, 14 ***(Figs. S36- S38; Table S18)***	---	---	Eruptions of years 1999 and 2000	Lava flow	CRB	Suh et al. (2003)

8. Madagascar	8. Nosy Be Archipelago	48.3	-13.3	27, 0, 27 ***(Figs. S39- S41; Table S25)***	---	---	7-10	Mafic alkaline rocks	CRB	Melluso and Morra (2000)
9. Inner Mongolia, China	9. Tianheyong	114.0	41.0	8, 8, 0 ***(Figs. S42- S44; Table S26)***	---	---	21.7±1.7	basanites	CRB; OIB	Yang et al. (2009)
10. China (north-east)	10. Halaha volcanic field, Central Great Xing'an Range	120.5	47.5	14, 14, 14 ***(Figs. S45- S48; Table S27)***	---	---	0.17-2.04	basalt	CRB	Ho et al. (2013)
Expected tectonic setting: **Continental arc**										
11. Aleutian arc, Alaska	11. Aniakchak ignimbrite	-158.1	56.9	---	---	9, 9, 9 ***(Figs. S49- S52; Table S28)***	0.0034	rhyodacitic to andesitic ignimbrite	CA	Dreher et al. (2005)
12. Guatemala	12a. Fuego volcanic complex	-90.9	14.5	---	9, 0, 0 ***(Table S29)***	---	Recent eruptions	lava	CA	Chesner and Rose Jr. (1984)
	12b. Meseta Volcano	-90.7	14.6	---	40, 0, 0 ***(Table S30)***	---	Quaternary	lava	CA	Chesner and Halsor (1997)
	12c. Santiaguito volcanic dome complex	-91.6	14.8	---	18, 5, 18 ***(Table S31)***	17, 17, 17 ***(Table S32)***	0.000112	lava	CA; IA or CA-Col	Scott et al.(2013)
13. Chile	13. Huequi volcano dome complex	-72.6	-42.5	---	9, 9, 0 ***(Table S33)***	---	0.000123	lava	CA	Watt et al. (2011)
14. Greece	14. Nisyros Island, Dodecanese	27	36.6	---	16, 0, 0 ***(Table S34)***	11, 0, 0 ***(Table S35)***	Quaternary	volcanic rocks	CA	Di Paola (1974)
Expected tectonic setting: **Island arc**										
15. Aleutian arc	15. Augustine Island	-153.4	59.36	---	21, 0, 0 ***(Table S36)***	---	6.0	volcanic rocks	IA	Johnson et al. (1996)
16. Andaman-Nicobar Islands	16a. Barren Island	93.85	12.29	25, 11, 24 ***(Table S37)***	21, 21, 9 ***(Table S38)***	---	Quaternary	volcanic rocks	Arc	Chandrasekharam et al. (2009); Streck et al. (2011)
	16b. Narcondam Island	94.28	13.43	---	10, 8, 8 ***(Table S39)***	8, 0, 0 ***(Table S40)***	Quaternary	volcanic rocks	IA	Pal et al. (2007); Streck et al. (2011)
Expected tectonic setting: **Mid-ocean ridge**										
17. Indian Ocean	17. Indian Ridge (central)	66	-14	33, 32, 33 ***(Table S41)***	[14, 14, 14] ***(---)***	---	Quaternary	basaltic rocks	MORB	Yi et al. (2014)

Expected tectonic setting: **Collision**										
18. Armenia	18. Shirak area	43.9	40.9	---	13, 9, 13 ***(Table S42)***	---	2.5-4.6	volcanic rocks	Col	Neill et al. (2013)

B−basic rock; **U**−ultrabasic rocks : m1−first set of major element based diagrams (Agrawal et al. 2004); m2−second set of major element based diagrams (Verma et al. 2006); t1−first set of trace element based diagrams (Agrawal et al. 2008); t2−second set of trace element based diagrams (Verma and Agrawal 2011); **I**−set of intermediate rocks based diagrams (Verma and Verma 2013); **A**-set of acid rocks based diagrams (Verma et al. 2012; Verma et al. 2013); m− major elements mt−(immobile) major and trace elements; t−(immobile) trace elements, for each set respectively; --- no sample; note less than five (an arbitrarily set lower number) samples are not considered for evaluation. Inferred tectonic setting: Arc−island or continental arc; CRB−continental rift for basic rocks; OIB−ocean island for basic rocks; MORB−mid-ocean ridge for basic rocks, IA−Island Arc, CA−Continental Arc, CR−continental rift; OI−ocean island; CR+OI−within-plate; Col−Collision.

Table S13

Synthesis of the compilation of hydrothermally altered rock samples used in the present study for testing of discrimination diagrams (8 application studies).

Test study		Approximate location		Number of Samples* (***Table no.* for results**)			Age and rock type		Inferred Tectonic setting	Reference
Region	Sub-region	Long. (°)	Lat. (°)	**B + U**	**I**	**A**	Age (Ma)	Author rock type		
				m1/ m2, t1, t2	m, mt, t	m, mt, t				
Expected tectonic setting: **Ocean Island**										
A1. Marquesas Islands	A1. Eaio Island	-140.67	-7.98	24+1, 0, 24+1 ***(Table S43)***	---	---	4.95-5.52	hydrothermally altered rocks	OIB	Caroff et al. (1999)
A2. Hawaiian Islands	A2. Haleakala, Koolau, and Kohala volcanoes	-156	20	4+5, 0, 0 ***(Table S44)***	---	---	0.35-4	spheroidal weathering	CRB	Patino et al. (2003)
Expected tectonic setting: **Ocean Island or continental rift**										
A3. Hainan Island, China	A3. Hainan Island	109.5	19.8	13, 4, 4 ***(Table S45)***	10, 3, 3 ***(Table S46)***	---	13-Holocene	slightly to intensely altered	CRB; WP	Wang et al. (2012)
Expected tectonic setting: **Continental arc**										
A4. Guatemala	A4. Moyuta and Tecuamburro volcanoes	-90.43	14.16	---	7, 0, 0 ***(Table S47)***	---	probably Pliocene-Pleistocene	spheroidal weathering	CA	Patino et al. (2003)
Expected tectonic setting: **Island or continental arc**										
A5. Costa Rica	A5. Sarapiqui Miocene arc	-84.23	10.77	10, 3, 10 ***(Table S48)***	14, 14, 3 ***(Table S49***	4, 4, 1	11.4-22.2	altered rocks	Arc; IA	Gazel et al. (2005)
A6. New Zealand	A6. Taupo Volcanic Zone	176.18	-38.65	---	28, 5, 0 ***(Table S50)***	---	> 0.33	drill hole hydrothermally altered rocks	IA	Browne et al. (1992)
Expected tectonic setting: **Mid-ocean ridge**										
A7. Indian and Pacific Oceans	A7a.SE Indian and SW Pacific seafloor	110 to 160	-40 to -60	9, 7, 9 ***(Table S51)***	---	---	0-4 and 15-23	altered and fresh rocks	MORB	Pyle et al. (1995)
	A7b. central Indian Ridge	66	-8 to -17	26+2, 17, 20 ***(Table S52)***	[4, 3, 3]	---	Quaternary	altered and fresh rocks	MORB	Yi et al. (2014)
Expected tectonic setting: **collision**										
A8. Italy	A8. Stromboli volcano, Aeolian Island	14.92	38.49	---	7, 3, 7 ***(Table S53)***	10, 10, 10 ***(Table S54)***	Quaternary	buchite ejecta	Col	Del Moro et al. (2011)

For more explanation, see footnote of Table S12.

Table S14.
Testing of multidimensional diagrams from Quaternary (0.1-0.4Ma) basic and ultrabasic rocks of Mauna Loa, Hawaii (Rhodes and Vollinger, 2004; Test study 1b).

Figure reference; figure type	Discrimination diagram	Total no. of samples (%)	Predicted tectonic affinity and number of discriminated samples (%)				
			IAB	CRB+OIB	CRB	OIB	MORB
Agrawal et al. (2004); adjusted major element concentrations	IAB-CRB-OIB-MORB	45 (100)	0 (0)	---	2 (4.5)	38 (84.4)	5 (11.1)
	IAB-CRB-OIB	45 (100)	0 (0)	---	1 (2.2)	44 (97.8)	---
	IAB-CRB-MORB	45 (100)	0 (0)	---	23 (51.1)	---	22 (48.9)
	IAB-OIB-MORB	45 (100)	0 (0)	---	---	45 (100)	0 (0)
	CRB-OIB-MORB	45 (100)	---	---	0 (0)	44 (97.8)	1 (2.2)
Test study 1b. Synthesis of all five diagrams of Agrawal et al. (2004)		***225 (100)***	***0 (0)***	***---***	***26 (11.6)***	***171 (76.0)***	***28 (12.4)***
Verma et al. (2006); log-ratios of major elements	IAB-CRB-OIB-MORB	45 (100)	0 (0)	---	0 (0)	37 (82.2)	8 (17.8)
	IAB-CRB-OIB	45 (100)	0 (0)	---	0 (0)	45 (100)	---
	IAB-CRB-MORB	45 (100)	0 (0)	---	1 (2.2)	---	44 (97.8)
	IAB-OIB-MORB	45 (100)	0 (0)	---	---	45 (100)	0 (0)
	CRB-OIB-MORB	45 (100)	---	---	0 (0)	45 (100)	0 (0)
Test study 1b. Synthesis of all five diagrams of Verma et al. (2006)		***225 (100)***	***0 (0)***	***---***	***1 (0.4)***	***172 (76.4)***	***52 (23.1)***
Verma and Agrawal (2011); log-ratios of immobile major and trace elements	IAB-CRB+OIB-MORB	45 (100)	0 (0)	45 (100)	---	---	0 (0)
	IAB-CRB-OIB	45 (100)	0 (0)	---	0 (0)	45 (100)	---
	IAB-CRB-MORB	45 (100)	0 (0)	---	45 (100)	---	0 (0)
	IAB-OIB-MORB	45 (100)	0 (0)	---	---	45 (100)	0 (0)
	CRB-OIB-MORB	45 (100)	---	---	0 (0)	45 (100)	0 (0)
Test study 1b. Synthesis of all five diagrams of Verma and Agrawal (2011)		***225 (100)***	***0 (0)***	***45 (---)***	***56 (24.9)***	***169 (75.1)***	***0(0)***

IAB−island (or continental) arc basic rock; CRB−continental rift basic rock; OIB−ocean island basic rock; MORB−mid-ocean ridge basic rock; CRB+OIB−combined continental rift and ocean island, i.e., within-plate (WP) basic rocks; IA, CR,, OI, and MOR will be the corresponding tectonic settings; --- means no samples; the numbers within the parentheses refer to the percent values for the corresponding number of samples; note, for the calculations of percent synthesis values, the samples plotting in the combined CR+OI field (CRB+OIB column) are proportionately distributed between the CR and OI settings.

Table S15.
Testing of multidimensional diagrams from Quaternary (1.9–2.1Ma) basic and ultrabasic rocks of the Maui Island, Hawaii (Sherrod et al. 2007; Test study 1c).

Figure reference; figure type	Discrimination diagram	Total no. of samples (%)	Predicted tectonic affinity and number of discriminated samples (%)				
			IAB	CRB+OIB	CRB	OIB	MORB
Agrawal et al. (2004); adjusted major element concentrations	IAB-CRB-OIB-MORB	10 (100)	0 (0)	---	0 (0)	10 (100)	0 (0)
	IAB-CRB-OIB	10 (100)	0 (0)	---	0 (0)	10 (100)	---
	IAB-CRB-MORB	10 (100)	0 (0)	---	9 (90)	---	1 (10)
	IAB-OIB-MORB	10 (100)	0 (0)	---	---	10 (100)	0 (0)
	CRB-OIB-MORB	10 (100)	---	---	0 (0)	10 (100)	0 (0)
Test study 1c. Synthesis of all five diagrams of Agrawal et al. (2004)		***50 (100)***	***0 (0)***	***---***	***9 (18)***	***40 (80)***	***1 (2)***
Verma *et al.* (2006); log-ratios of major elements	IAB-CRB-OIB-MORB	10 (100)	0 (0)	---	0 (0)	9 (90)	1 (10)
	IAB-CRB-OIB	10 (100)	0 (0)	---	0 (0)	10 (100)	---
	IAB-CRB-MORB	10 (100)	0 (0)	---	3 (30)	---	7 (70)
	IAB-OIB-MORB	10 (100)	0 (0)	---	---	10 (100)	0 (0)
	CRB-OIB-MORB	10 (100)	---	---	0 (0)	10 (100)	0 (0)
Test study 1c. Synthesis of all five diagrams of Verma et al. (2006)		***50 (100)***	***0 (0)***	***---***	***3 (6)***	***39 (78)***	***8 (16)***
Verma and Agrawal (2011); log-ratios of immobile major and trace elements	IAB-CRB+OIB-MORB	10 (100)	0 (0)	9 (90)	---	---	1 (10)
	IAB-CRB-OIB	10 (100)	0 (0)	---	3 (30)	7 (70)	---
	IAB-CRB-MORB	10 (100)	0 (0)	---	9 (90)	---	1 (10)
	IAB-OIB-MORB	10 (100)	0 (0)	---	---	9 (90)	1 (10)
	CRB-OIB-MORB	10 (100)	---	---	0 (0)	9 (90)	1 (10)
Test study 1c. Synthesis of all five diagrams of Verma and Agrawal (2011)		***50 (100)***	***0 (0)***	***9 (---)***	***15 (30)***	***31 (62)***	***4(8)***

For the explanation of abbreviations, see footnote of Table 1 or S14.

Table S16.
Testing of multidimensional diagrams from Quaternary (2.9–3.9 Ma) basic and ultrabasic rocks of the Oahu Island, Hawaii (Jackson et al. 1999; Test study 1d).

Figure reference; figure type	Discrimination diagram	Total no. of samples (%)	Predicted tectonic affinity and number of discriminated samples (%)				
			IAB	CRB+OIB	CRB	OIB	MORB
Agrawal et al. (2004); adjusted major element concentrations	IAB-CRB-OIB-MORB	9 (100)	0 (0)	---	0 (0)	8 (88.9)	1 (11.1)
	IAB-CRB-OIB	9 (100)	0 (0)	---	0 (0)	9 (100)	---
	IAB-CRB-MORB	9 (100)	0 (0)	---	1 (11.1)	---	8 (88.9)
	IAB-OIB-MORB	9 (100)	0 (0)	---	---	9 (100)	0 (0)
	CRB-OIB-MORB	9 (100)	---	---	0 (0)	9 (100)	0 (0)
Test study 1d. Synthesis of all five diagrams of Agrawal et al. (2004)		***45 (100)***	***0 (0)***	***---***	***1 (2)***	***35 (78)***	***9 (20)***
Verma et al. (2006); log-ratios of major elements	IAB-CRB-OIB-MORB	9 (100)	0 (0)	---	0 (0)	6 (66.7)	3 (33.3)
	IAB-CRB-OIB	9 (100)	0 (0)	---	0 (0)	9 (100)	---
	IAB-CRB-MORB	9 (100)	0 (0)	---	0 (0)	---	9 (100)
	IAB-OIB-MORB	9 (100)	0 (0)	---	---	8 (88.9)	1 (11.1)
	CRB-OIB-MORB	9 (100)	---	---	0 (0)	7 (77.8)	2 (22.2)
Test study 1d. Synthesis of all five diagrams of Verma et al. (2006)		***45 (100)***	***0 (0)***	***---***	***0 (0)***	***30 (67)***	***15 (33)***
Verma and Agrawal (2011); log-ratios of immobile major and trace elements	IAB-CRB+OIB-MORB	9 (100)	0 (0)	9 (100)	---	---	0 (0)
	IAB-CRB-OIB	9 (100)	0 (0)	---	0 (0)	9 (100)	---
	IAB-CRB-MORB	9 (100)	0 (0)	---	9 (100)	---	0 (0)
	IAB-OIB-MORB	9 (100)	0 (0)	---	---	9 (100)	0 (0)
	CRB-OIB-MORB	9 (100)	---	---	0 (0)	9 (100)	0 (0)
Test study 1d. Synthesis of all five diagrams of Verma and Agrawal (2011)		***45 (100)***	***0 (0)***	***9 (---)***	***11 (24)***	***34 (76)***	***0(0)***

For the explanation of abbreviations, see footnote of Table 1 or S14.

Table S17.
Testing of multidimensional diagrams from Quaternary (2.9–3.9 Ma) intermediate rocks of the Oahu Island, Hawaii (Jackson et al. 1999; Test study 1d).

Magma type, Figure name; Figure number	Figure type	Total number of samples	Number of discriminated samples				
			Arc			Within-plate CR+OI	Collision
			IA+CA [$\bar{x} \pm s$] (p_{IA+CA}) Θ	IA [$\bar{x} \pm s$] [p_{IA}] Θ	CA [$\bar{x} \pm s$] [p_{CA}] Θ	[$\bar{x} \pm s$] [p_{CR+OI}] Θ	Col [$\bar{x} \pm s$] [p_{Col}] Θ
Intermediate; Verma and Verma (2013); log-ratios of all major elements;	IA+CA-CR+OI-Col	15	0 (0)	---	---	15 [0.777±0.087] (0.6282-0.9942)	0 (0)
	IA-CA-CR+OI	15	---	0 (0)	0 (0)	15 [0.763±0.092] (0.6015-0.9929)	---
	IA-CA-Col	15	---	15 [0.7525±0.0444] (0.6727-0.8286)	0 (0)	---	0 (0)
	IA-CR+OI-Col	15	---	0 (0)	---	15 [0.796±0.085] (0.6617-0.9961)	0 (0)
	CA-CR+OI-Col	15	---	---	0 (0)	15 [0.780±0.084] (0.6548-0.9940)	0 (0)
Test study 1d. Diagrams based on log-ratios of major elements	***{Σn} {Σprob} [%prob]***	***75***	***{0} {0} [0%]***	***{15} {11.2869} [19%]***	***{0} {0} [0%]***	***{60} {46.7383} [81%]***	***{0} {0} [0%]***
Intermediate; Verma and Verma (2013); log-ratios of immobile major and trace elements	IA+CA-CR+OI-Col	15	0 (0)	---	---	15 [0.99334±0.00382] (0.9852-0.9985)	0 (0)
	IA-CA-CR+OI	15	---	0 (0)	0 (0)	15 [0.9925±0.0050] (0.9811-0.9993)	---
	IA-CA-Col	15	---	0 (0)	14 [0.568±0.055] (0.5048-0.6604)	---	1 (0.6189)
	IA-CR+OI-Col	15	---	0 (0)	---	15 [0.99229±0.00366] (0.9848-0.9976)	0 (0)
	CA-CR+OI-Col	15	---	---	0 (0)	15 [0.9764±0.0167] (0.9365-0.9973)	0 (0)
Test study 1d. Diagrams based on log-ratios of selected immobile major and trace elements	***{Σn} {Σprob} [%prob]***	***75***	***{0} {0} [0%]***	***{0} {0} [0%]***	***{14} {7.9546} [12%]***	***{60} {59.3177} [87%]***	***{1} {0.6189} [1%]***

IA−island arc; CA−continental arc; IA+CA–combined island and continental arcs, i.e., arc setting; CR−continental rift; OI−ocean island; CR+OI –combined continental rift and ocean island, i.e., within-plate (WP) setting; Col−collision; Θ the probability values for samples from a given locality are represented by (p_{IA+CA}) – probability for the combined island and continental arc setting in the first diagram; [p_{IA}] – probability for the island arc setting in the diagrams; [p_{CA}] – probability for the continental arc setting in the diagrams; [p_{CR+OI}] – probability for the combined continental rift and ocean island setting in all diagrams; [p_{Col}] – probability for the collision setting in the diagrams; $\bar{x} \pm s$ − mean ± 1SD (standard deviation) of the probability estimates for all samples discriminated in a given tectonic setting; these are reported in []; the final row gives a synthesis of results as **{Σn} {Σprob} [%prob]**, where {Σn} is the total number of samples or data points plotting in all five diagrams is reported in the column of total number of samples, whereas the sum of samples plotting in a given tectonic field is reported in the respective tectonic field column; {Σprob} is the sum of probability values for all samples plotting in a given tectonic field is reported in the respective tectonic field column; and [%prob] is the total probability of a given tectonic setting expressed in percent after assigning the probability of IA + CA to IA and CA (using weighing factors explained in Verma and Verma 2013).

Table S18.
Testing of multidimensional diagrams from Quaternary (<0.27-3.6 Ma) basic and ultrabasic rocks of Trindade Island, southern Atlantic Ocean (Marques et al. 1999; Test study 2).

Figure reference; figure type	Discrimination diagram	Total no. of samples (%)	Predicted tectonic affinity and number of discriminated samples (%)				
			IAB	CRB+OIB	CRB	OIB	MORB
Agrawal et al. (2004); adjusted major element concentrations	IAB-CRB-OIB-MORB	14 (100)	0 (0)	---	1 (7.1)	12 (85.8)	1 (7.1)
	IAB-CRB-OIB	14 (100)	0 (0)	---	2 (14.3)	12 (85.7)	---
	IAB-CRB-MORB	14 (100)	0 (0)	---	14 (100)	---	0 (0)
	IAB-OIB-MORB	14 (100)	0 (0)	---	---	13 (92.9)	1 (7.1)
	CRB-OIB-MORB	14 (100)	---	---	2 (14.3)	12 (85.7)	0 (0)
Test study 2. Synthesis of all five diagrams of Agrawal et al. (2004)		***70 (100)***	***0 (0)***	***---***	***19 (27)***	***49 (70)***	***2 (3)***
Verma et al. (2006); log-ratios of major elements	IAB-CRB-OIB-MORB	14 (100)	0 (0)	---	1 (7.1)	12 (85.8)	1 (7.1)
	IAB-CRB-OIB	14 (100)	0 (0)	---	2 (14.3)	12 (85.7)	---
	IAB-CRB-MORB	14 (100)	0 (0)	---	13 (92.9)	---	1 (7.1)
	IAB-OIB-MORB	14 (100)	0 (0)	---	---	13 (92.9)	1 (7.1)
	CRB-OIB-MORB	14 (100)	---	---	1 (7.1)	12 (85.8)	1 (7.1)
Test study 2. Synthesis of all five diagrams of Verma et al. (2006)		***70 (100)***	***0 (0)***	***---***	***17 (24)***	***49 (70)***	***4 (6)***
Agrawal *et al.* (2008); log-ratios of immobile trace elements	IAB-CRB+OIB-MORB	13 (100)	0 (0)	13 (100)	---	---	0 (0)
	IAB-CRB-OIB	13 (100)	0 (0)	---	6 (46.2)	7 (53.8)	---
	IAB-CRB-MORB	13 (100)	0 (0)	---	13 (100)	---	0 (0)
	IAB-OIB-MORB	13 (100)	0 (0)	---	---	13 (100)	0 (0)
	CRB-OIB-MORB	13 (100)	---	---	1 (7.7)	12 (92.3)	0 (0)
Test study 2. Synthesis of all five diagrams of Agrawal et al. (2008)		***65 (100)***	***0 (0)***	***13 (---)***	***25 (38)***	***40 (62)***	***0 (0)***

For the explanation of abbreviations, see footnote of Table 1 or S14.

Table S19.
Testing of multidimensional diagrams from Quaternary (<0.27-3.6 Ma) intermediate rocks of the Trindade Island (Marques et al. 1999; Test study 2).

Magma type, Figure name	Figure type	Total number of samples	Number of discriminated samples				
			Arc			Within-plate CR+OI [$\bar{x} \pm s$] [p_{CR+OI}] Θ	Collision Col [$\bar{x} \pm s$] [p_{Col}] Θ
			IA+CA [$\bar{x} \pm s$] (p_{IA+CA}) Θ	IA [$\bar{x} \pm s$] [p_{IA}] Θ	CA [$\bar{x} \pm s$] [p_{CA}] Θ		
Intermediate; Verma and Verma (2013); log-ratios of all major elements	IA+CA-CR+OI-Col	24	1 (0.4915)	---	---	23 [0.863±0.177] (0.4372-0.9981)	0 (0)
	IA-CA-CR+OI	24	---	1 (0.4582)	2 [0.4920±0.0240] (0.4750, 0.5089)	21 [0.887±0.151] (0.4579-0.9941)	---
	IA-CA-Col	24	---	1 (0.4845)	15 [0.718±0.095] (0.5470-0.8654)	---	8 [0.605±0.152] (0.4006-0.7849)
	IA-CR+OI-Col	24	---	1 (0.5906)	---	19 [0.920±0.063] (0.7475-0.9980)	4 [0.4938±0.0346] (0.4482-0.5291)
	CA-CR+OI-Col	24	---	---	1 (0.4758)	19 [0.807±0.121] (0.5207-0.9909)	4 [0.484±0.046] (0.4387-0.5428)
Test study 2. Diagrams based on log-ratios of major elements	***{Σn} {Σprob} [%prob]***	***120***	***{1} {0.4915} [---]***	***{3} {1.5333} [1.7%]***	***{18} {12.2347} [13.4%]***	***{82} {71.2933} [75.6%]***	***{16} {8.7540} [9.3%]***
Intermediate; Verma and Verma (2013); log-ratios of immobile trace elements	IA+CA-CR+OI-Col	13	0 (0)	---	---	13 [0.9811±0.0109] (0.9560-0.9946)	0 (0)
	IA-CA-CR+OI	13	---	0 (0)	0 (0)	13 [0.99727±0.00412] (0.9857-0.9997)	---
	IA-CA-Col	13	---	0 (0)	0 (0)	---	13 [0.9776±0.0238] (0.9199-0.9966)
	IA-CR+OI-Col	13	---	0 (0)	---	13 [0.9678±0.0147] (0.9365-0.9875)	0 (0)
	CA-CR+OI-Col	13	---	---	0 (0)	13 [0.9266±0.0329] (0.8669-0.9706)	0 (0)
Test study 2. Diagrams based on log-ratios of immobile trace elements	***{Σn} {Σprob} [%prob]***	***65***	***{0} {0} [0%]***	***{0} {0} [0%]***	***{0} {0} [0%]***	***{52} {50.3470} [80%]***	***{13} {12.7086} [20%]***

For the explanation of abbreviations, see footnote of Table S17.

Table S20.
Testing of multidimensional diagrams from Neogene-Quaternary (0.17-7.65Ma; Pliocene-Pleistocene) basic rocks from White Island, Ross Sea, Antarctica (Cooper et al. 2007; Test study 3).

Figure reference; figure type	Discrimination diagram	Total no. of samples (%)	Predicted tectonic affinity and number of discriminated samples (%)				
			IAB	CRB+OIB	CRB	OIB	MORB
Agrawal et al. (2004); adjusted major element concentrations	IAB-CRB-OIB-MORB	22 (100)	0 (0)	---	4 (18.2)	18 (81.8)	0 (0)
	IAB-CRB-OIB	22 (100)	0 (0)	---	14 (63.6)	8 (36.4)	---
	IAB-CRB-MORB	22 (100)	0 (0)	---	22 (100)	---	0 (0)
	IAB-OIB-MORB	22 (100)	0 (0)	---	---	22 (100)	0 (0)
	CRB-OIB-MORB	22 (100)	---	---	9 (40.9)	13 (59.1)	0 (0)
Test study 3. Synthesis of all five diagrams of Agrawal et al. (2004)		***110 (100)***	***0 (0)***	***---***	***49 (44.5)***	***61 (55.5)***	***0 (0)***
Verma *et al.* (2006); log-ratios of major elements	IAB-CRB-OIB-MORB	22 (100)	0 (0)	---	8 (36.4)	14 (63.6)	0 (0)
	IAB-CRB-OIB	22 (100)	0 (0)	---	12 (54.5)	10 (45.5)	---
	IAB-CRB-MORB	22 (100)	0 (0)	---	22 (100)	---	0 (0)
	IAB-OIB-MORB	22 (100)	0 (0)	---	---	22 (100)	0 (0)
	CRB-OIB-MORB	22 (100)	---	---	11 (50)	11 (50)	0 (0)
Test study 3. Synthesis of all five diagrams of Verma et al. (2006)		***110 (100)***	***0 (0)***	***---***	***53 (48.2)***	***57 (51.8)***	***0 (0)***
Agrawal et al. (2008); log-ratios of immobile trace elements	IAB-CRB+OIB-MORB	22 (100)	0 (0)	22 (100)	---	---	0 (0)
	IAB-CRB-OIB	22 (100)	0 (0)	---	*21 (95.5)*	1 (4.5)	---
	IAB-CRB-MORB	22 (100)	0 (0)	---	*22 (100)*	---	0 (0)
	IAB-OIB-MORB	22 (100)	0 (0)	---	---	22 (100)	0 (0)
	CRB-OIB-MORB	22 (100)	---	---	*14 (63.6)*	8 (36.4)	0 (0)
Test study 3. Synthesis of all five diagrams of Agrawal et al. (2008)		***110 (100)***	***0 (0)***	***22 (---)***	***71 (64.5)***	***39 (35.5)***	***0 (0)***
Verma and Agrawal (2011); log-ratios of immobile major and trace elements	IAB-CRB+OIB-MORB	22 (100)	0 (0)	22 (100)	---	---	0 (0)
	IAB-CRB-OIB	22 (100)	0 (0)	---	3 (13.6)	19 (86.4)	---
	IAB-CRB-MORB	22 (100)	0 (0)	---	22 (100)	---	0 (0)
	IAB-OIB-MORB	22 (100)	0 (0)	---	---	22 (100)	0 (0)
	CRB-OIB-MORB	22 (100)	---	---	3 (13.6)	19 (86.4)	0 (0)
Test study 3. Synthesis of all five diagrams of Verma and Agrawal (2011)		***110 (100)***	***0 (0)***	***22 (---)***	***35 (31.8)***	***75 (68.2)***	***0(0)***

For the explanation of abbreviations, see footnote of Table 1 or S14.

Table S21.
Testing of multidimensional diagrams from Miocene (15.91-18.41 Ma) drill core basic volcanic glass samples of the McMurdo Sound area, Antarctica (Nyland et al. 2013; Test study 4).

Figure reference; figure type	Discrimination diagram	Total no. of samples (%)	Predicted tectonic affinity and number of discriminated samples (%)				
			IAB	CRB+OIB	CRB	OIB	MORB
Agrawal et al. (2004); adjusted major element concentrations	IAB-CRB-OIB-MORB	24 (100)	0 (0)	---	6 (25)	18 (75)	0 (0)
	IAB-CRB-OIB	24 (100)	0 (0)	---	6 (25)	18 (75)	---
	IAB-CRB-MORB	24 (100)	0 (0)	---	24 (100)	---	0 (0)
	IAB-OIB-MORB	24 (100)	0 (0)	---	---	24 (100)	0 (0)
	CRB-OIB-MORB	24 (100)	---	---	8 (33.3)	16 (66.7)	0 (0)
Test study 4. Synthesis of all five diagrams of Agrawal et al. (2004)		***120 (100)***	***0 (0)***	***---***	***44 (36.7)***	***76 (63.3)***	***0 (0)***
Verma et al. (2006); log-ratios of major elements	IAB-CRB-OIB-MORB	24 (100)	0 (0)	---	6 (25)	18 (75)	0 (0)
	IAB-CRB-OIB	24 (100)	0 (0)	---	6 (25)	18 (75)	---
	IAB-CRB-MORB	24 (100)	0 (0)	---	24 (100)	---	0 (0)
	IAB-OIB-MORB	24 (100)	0 (0)	---	---	24 (100)	0 (0)
	CRB-OIB-MORB	24 (100)	---	---	7 (29.2)	17 (70.8)	0 (0)
Test study 4. Synthesis of all five diagrams of Verma et al. (2006)		***120 (100)***	***0 (0)***	***---***	***43 (35.8)***	***77 (64.2)***	***0 (0)***
Agrawal et al. (2008); log-ratios of immobile trace elements	IAB-CRB+OIB-MORB	20 (100)	0 (0)	20 (100)	---	---	0 (0)
	IAB-CRB-OIB	20 (100)	0 (0)	---	14 (70)	6 (30)	---
	IAB-CRB-MORB	20 (100)	0 (0)	---	20 (100)	---	0 (0)
	IAB-OIB-MORB	20 (100)	0 (0)	---	---	20 (100)	0 (0)
	CRB-OIB-MORB	20 (100)	---	---	10 (50)	10 (50)	0 (0)
Test study 4. Synthesis of all five diagrams of Agrawal et al. (2008)		***100 (100)***	***0 (0)***	***20 (---)***	***55 (55)***	***45 (45)***	***0 (0)***
Verma and Agrawal (2011); log-ratios of immobile major and trace elements	IAB-CRB+OIB-MORB	20 (100)	0 (0)	20 (100)	---	---	0 (0)
	IAB-CRB-OIB	20 (100)	0 (0)	---	1 (5)	19 (95)	---
	IAB-CRB-MORB	20 (100)	0 (0)	---	20 (100)	---	0 (0)
	IAB-OIB-MORB	20 (100)	0 (0)	---	---	20 (100)	0 (0)
	CRB-OIB-MORB	20 (100)	---	---	1 (5)	19 (95)	0 (0)
Test study 4. Synthesis of all five diagrams of Verma and Agrawal (2011)		***100 (100)***	***0 (0)***	***20 (---)***	***28 (28.0)***	***72 (72.0)***	***0(0)***

For the explanation of abbreviations, see footnote of Table 1 or S14.

Table S22.
Testing of multidimensional diagrams from Quaternary (0.70-0.0115 Ma) basic rocks of Garrotxa, NE Volcanic province, Spain (Cebriá et al. 2000; Test study 5).

Figure reference; figure type	Discrimination diagram	Total no. of samples (%)	Predicted tectonic affinity and number of discriminated samples (%)				
			IAB	CRB+OIB	CRB	OIB	MORB
Agrawal et al. (2004); adjusted major element concentrations	IAB-CRB-OIB-MORB	16 (100)	0 (0)	---	14 (88)	2 (12)	0 (0)
	IAB-CRB-OIB	16 (100)	0 (0)	---	16 (100)	0 (0)	---
	IAB-CRB-MORB	16 (100)	0 (0)	---	16 (100)	---	0 (0)
	IAB-OIB-MORB	16 (100)	1 (6)	---	---	10 (63)	5 (31)
	CRB-OIB-MORB	16 (100)	---	---	16 (100)	0 (0)	0 (0)
Test study 5. Synthesis of all five diagrams of Agrawal et al. (2004)		***80 (100)***	***1 (1)***	***---***	***62 (78)***	***12 (15)***	***5 (6)***
Verma et al. (2006); log-ratios of major elements	IAB-CRB-OIB-MORB	16 (100)	0 (0)	---	16 (100)	0 (0)	0 (0)
	IAB-CRB-OIB	16 (100)	0 (0)	---	16 (100)	0 (0)	---
	IAB-CRB-MORB	16 (100)	0 (0)	---	16 (100)	---	0 (0)
	IAB-OIB-MORB	16 (100)	0 (0)	---	---	15 (93.8)	1 (6.2)
	CRB-OIB-MORB	16 (100)	---	---	16 (100)	0 (0)	0 (0)
Test study 5. Synthesis of all five diagrams of Verma et al. (2006)		***80 (100)***	***0 (0)***	***---***	***64 (80)***	***15 (19)***	***1 (1)***
Agrawal et al. (2008); log-ratios of immobile trace elements	IAB-CRB+OIB-MORB	15 (100)	0 (0)	15 (100)	---	---	0 (0)
	IAB-CRB-OIB	15 (100)	0 (0)	---	14 (93.3)	1 (6.7)	---
	IAB-CRB-MORB	15 (100)	0 (0)	---	15 (100)	---	0 (0)
	IAB-OIB-MORB	15 (100)	0 (0)	---	---	15 (100)	0 (0)
	CRB-OIB-MORB	15 (100)	---	---	7 (46.7)	8 (53.3)	0 (0)
Test study 5. Synthesis of all five diagrams of Agrawal et al. (2008)		***75 (100)***	***0 (0)***	***15 (---)***	***45 (60)***	***30 (40)***	***0 (0)***
Verma and Agrawal (2011); log-ratios of immobile major and trace elements	IAB-CRB+OIB-MORB	15 (100)	0 (0)	15 (100)	---	---	0 (0)
	IAB-CRB-OIB	15 (100)	0 (0)	---	8 (53.3)	7 (46.7)	---
	IAB-CRB-MORB	15 (100)	0 (0)	---	15 (100)	---	0 (0)
	IAB-OIB-MORB	15 (100)	0 (0)	---	---	15 (100)	0 (0)
	CRB-OIB-MORB	15 (100)	---	---	14 (93.3)	1 (6.7)	0 (0)
Test study 5. Synthesis of all five diagrams of Verma and Agrawal (2011)		***75 (100)***	***0 (0)***	***15 (---)***	***46 (61)***	***29 (397)***	***0(0)***

For the explanation of abbreviations, see footnote of Table 1 or S14.

Table S23.
Testing of multidimensional diagrams from Quaternary (1.9-2.4 Ma) basic rocks from the Styrian basin, Austria (Ali et al. 2013; Test study 6).

Figure reference; figure type	Discrimination diagram	Total no. of samples (%)	Predicted tectonic affinity and number of discriminated samples (%)				
			IAB	CRB+OIB	CRB	OIB	MORB
Agrawal et al. (2004); adjusted major element concentrations	IAB-CRB-OIB-MORB	39 (100)	18 (46.2)	---	21 (53.8)	0 (0)	0 (0)
	IAB-CRB-OIB	39 (100)	0 (0)	---	39 (100)	0 (0)	---
	IAB-CRB-MORB	39 (100)	0 (0)	---	39 (100)	---	0 (0)
	IAB-OIB-MORB	39 (100)	0 (0)	---	---	1 (2.6)	38 (97.4)
	CRB-OIB-MORB	39 (100)	---	---	39 (100)	0 (0)	0 (0)
Test study 6. Synthesis of all five diagrams of Agrawal et al. (2004)		***195 (100)***	***18 (9.2)***	***---***	***138 (70.8)***	***1 (0.5)***	***38 (19.5)***
Verma et al. (2006); log-ratios of major elements	IAB-CRB-OIB-MORB	39 (100)	0 (0)	---	39 (100)	0 (0)	0 (0)
	IAB-CRB-OIB	39 (100)	0 (0)	---	39 (100)	0 (0)	---
	IAB-CRB-MORB	39 (100)	0 (0)	---	39 (100)	---	0 (0)
	IAB-OIB-MORB	39 (100)	0 (0)	---	---	15 (38.5)	24 (61.5)
	CRB-OIB-MORB	39 (100)	---	---	39 (100)	0 (0)	0 (0)
Test study 6. Synthesis of all five diagrams of Verma et al. (2006)		***195 (100)***	***0 (0)***	***---***	***156 (80)***	***15 (7.7)***	***24 (12.3)***
Agrawal et al. (2008); log-ratios of immobile trace elements	IAB-CRB+OIB-MORB	39 (100)	0 (0)	39 (100)	---	---	0 (0)
	IAB-CRB-OIB	39 (100)	0 (0)	---	39 (100)	0 (0)	---
	IAB-CRB-MORB	39 (100)	0 (0)	---	39 (100)	---	0 (0)
	IAB-OIB-MORB	39 (100)	0 (0)	---	---	39 (100)	0 (0)
	CRB-OIB-MORB	39 (100)	---	---	39 (100)	0 (0)	0 (0)
Test study 6. Synthesis of all five diagrams of Agrawal et al. (2008)		***195 (100)***	***0 (0)***	***39 (---)***	***146 (74.9)***	***49 (25.1)***	***0 (0)***
Verma and Agrawal (2011); log-ratios of immobile major and trace elements	IAB-CRB+OIB-MORB	39 (100)	0 (0)	39 (100)	---	---	0 (0)
	IAB-CRB-OIB	39 (100)	0 (0)	---	39 (100)	0 (0)	---
	IAB-CRB-MORB	39 (100)	0 (0)	---	39 (100)	---	0 (0)
	IAB-OIB-MORB	39 (100)	0 (0)	---	---	19 (48.7)	20 (51.3)
	CRB-OIB-MORB	39 (100)	---	---	39 (100)	0 (0)	0 (0)
Test study 6. Synthesis of all five diagrams of Verma and Agrawal (2011)		***195 (100)***	***0 (0)***	***39 (---)***	***151 (77.4)***	***24 (12.3)***	***20(10.3)***

For the explanation of abbreviations, see footnote of Table 1 or S14.

Table S24.
Testing of multidimensional diagrams from Recent (years 1999 and 2000 eruptions) basic rocks of the Mount Cameroon, Cameroon (Suh et al. 2003; Test study 7).

Figure reference; figure type	Discrimination diagram	Total no. of samples (%)	Predicted tectonic affinity and number of discriminated samples (%)				
			IAB	CRB+OIB	CRB	OIB	MORB
Agrawal et al. (2004); adjusted major element concentrations	IAB-CRB-OIB-MORB	14 (100)	0 (0)	---	7 (50)	7 (50)	0 (0)
	IAB-CRB-OIB	14 (100)	0 (0)	---	12 (86)	2 (14)	---
	IAB-CRB-MORB	14 (100)	0 (0)	---	14 (100)	---	0 (0)
	IAB-OIB-MORB	14 (100)	0 (0)	---	---	14 (100)	0 (0)
	CRB-OIB-MORB	14 (100)	---	---	8 (57)	6 (43)	0 (0)
Test study 7. Synthesis of all five diagrams of Agrawal et al. (2004)		***70 (100)***	***0 (0)***	***---***	***41 (59)***	***29 (41)***	***0 (0)***
Verma et al. (2006); log-ratios of major elements	IAB-CRB-OIB-MORB	14 (100)	0 (0)	---	5 (36)	9 (64)	0 (0)
	IAB-CRB-OIB	14 (100)	0 (0)	---	8 (57)	6 (43)	---
	IAB-CRB-MORB	14 (100)	0 (0)	---	14 (100)	---	0 (0)
	IAB-OIB-MORB	14 (100)	0 (0)	---	---	14 (100)	0 (0)
	CRB-OIB-MORB	14 (100)	---	---	12 (86)	2 (14)	0 (0)
Test study 7. Synthesis of all five diagrams of Verma et al. (2006)		***70 (100)***	***0 (0)***	***---***	***39 (56)***	***31 (44)***	***0 (0)***
Verma and Agrawal (2011); log-ratios of immobile major and trace elements	IAB-CRB+OIB-MORB	14 (100)	0 (0)	14 (100)	---	---	0 (0)
	IAB-CRB-OIB	14 (100)	0 (0)	---	14 (100)	0 (0)	---
	IAB-CRB-MORB	14 (100)	0 (0)	---	14 (100)	---	0 (0)
	IAB-OIB-MORB	14 (100)	0 (0)	---	---	14 (100)	0 (0)
	CRB-OIB-MORB	14 (100)	---	---	14 (100)	0 (0)	0 (0)
Test study 7. Synthesis of all five diagrams of Verma and Agrawal (2011)		***70 (100)***	***0 (0)***	***14 (---)***	***52 (74)***	***18 (26)***	***0 (0)***

For the explanation of abbreviations, see footnote of Table 1 or S14.

Table S25.
Testing of multidimensional diagrams from Miocene (7-10 Ma) basic rocks of the Nosy Be Archipelago, Madagascar (Melluso and Morra, 2000; Test study 8).

Figure reference; figure type	Discrimination diagram	Total no. of samples (%)	Predicted tectonic affinity and number of discriminated samples (%)				
			IAB	CRB+OIB	CRB	OIB	MORB
Agrawal et al. (2004); adjusted major element concentrations	IAB-CRB-OIB-MORB	27 (100)	0 (0)	---	3 (11)	23 (85)	1 (4)
	IAB-CRB-OIB	27 (100)	0 (0)	---	26 (96)	1 (4)	---
	IAB-CRB-MORB	27 (100)	0 (0)	---	27 (100)	---	0 (0)
	IAB-OIB-MORB	27 (100)	0 (0)	---	---	16 (59)	11 (41)
	CRB-OIB-MORB	27 (100)	---	---	20 (74)	7 (26)	0 (0)
Test study 8. Synthesis of all five diagrams of Agrawal et al. (2004)		***135 (100)***	***0 (0)***	***---***	***76 (56.3)***	***47 (34.8)***	***12 (8.9)***
Verma et al. (2006); log-ratios of major elements	IAB-CRB-OIB-MORB	27 (100)	0 (0)	---	11 (41)	15 (56)	1 (4)
	IAB-CRB-OIB	27 (100)	0 (0)	---	22 (82)	5 (18)	---
	IAB-CRB-MORB	27 (100)	0 (0)	---	26 (96)	---	1 (4)
	IAB-OIB-MORB	27 (100)	0 (0)	---	---	17 (63)	10 (37)
	CRB-OIB-MORB	27 (100)	---	---	25 (92)	1 (4)	1 (4)
Test study 8. Synthesis of all five diagrams of Verma et al. (2006)		***135 (100)***	***0 (0)***	***---***	***84 (62.2)***	***38 (28.1)***	***13 (9.6)***
Verma and Agrawal (2011); log-ratios of immobile major and trace elements	IAB-CRB+OIB-MORB	27 (100)	0 (0)	27 (100)	---	---	0 (0)
	IAB-CRB-OIB	27 (100)	0 (0)	---	26 (96)	1 (4)	---
	IAB-CRB-MORB	27 (100)	0 (0)	---	27 (100)	---	0 (0)
	IAB-OIB-MORB	27 (100)	0 (0)	---	---	27 (100)	0 (0)
	CRB-OIB-MORB	27 (100)	---	---	26 (96)	1 (4)	0 (0)
Test study 8. Synthesis of all five diagrams of Verma and Agrawal (2011)		***135 (100)***	***0 (0)***	***27 (---)***	***99 (73.3)***	***36 (26.7)***	***0(0)***

For the explanation of abbreviations, see footnote of Table 1 or S14.

Table S26.
Testing of multidimensional diagrams from Miocene (21.7 Ma) basic rocks of the Tianheyong region, Mongolia China (Yang et al. 2009; Test study 9).

Figure reference; figure type	Discrimination diagram	Total no. of samples (%)	Predicted tectonic affinity and number of discriminated samples (%)				
			IAB	CRB+OIB	CRB	OIB	MORB
Agrawal et al. (2004); adjusted major element concentrations	IAB-CRB-OIB-MORB	8 (100)	0 (0)	---	7 (88)	1 (12)	0 (0)
	IAB-CRB-OIB	8 (100)	0 (0)	---	7 (88)	1 (12)	---
	IAB-CRB-MORB	8 (100)	0 (0)	---	8 (100)	---	0 (0)
	IAB-OIB-MORB	8 (100)	0 (0)	---	---	6 (75)	2 (25)
	CRB-OIB-MORB	8 (100)	---	---	7 (88)	1 (12)	0 (0)
Test study 9 Synthesis of all five diagrams of Agrawal et al. (2004)		***40 (100)***	***0 (0)***	***---***	***29 (73)***	***9 (22)***	***2 (5)***
Verma et al. (2006); log-ratios of major elements	IAB-CRB-OIB-MORB	8 (100)	0 (0)	---	7 (87.5)	1 (12.5)	0 (0)
	IAB-CRB-OIB	8 (100)	0 (0)	---	7 (87.5)	1 (12.5)	---
	IAB-CRB-MORB	8 (100)	0 (0)	---	8 (100)	---	0 (0)
	IAB-OIB-MORB	8 (100)	2 (25)	---	---	6 (75)	0 (0)
	CRB-OIB-MORB	8 (100)	---	---	7 (87.5)	1 (12.5)	0 (0)
Test study 9. Synthesis of all five diagrams of Verma et al. (2006)		***40 (100)***	***2 (5)***	***---***	***29 (73)***	***9 (22)***	***0 (0)***
Agrawal et al. (2008); log-ratios of immobile trace elements	IAB-CRB+OIB-MORB	8 (100)	0 (0)	8 (100)	---	---	0 (0)
	IAB-CRB-OIB	8 (100)	0 (0)	---	0 (0)	8 (100)	---
	IAB-CRB-MORB	8 (100)	0 (0)	---	8 (100)	---	0 (0)
	IAB-OIB-MORB	8 (100)	0 (0)	---	---	8 (100)	0 (0)
	CRB-OIB-MORB	8 (100)	---	---	0 (0)	8 (100)	0 (0)
Test study 9. Synthesis of all five diagrams of Agrawal et al. (2008)		***40 (100)***	***0 (0)***	***8 (---)***	***10 (25)***	***30 (75)***	***0 (0)***

For the explanation of abbreviations, see footnote of Table 1 or S14.

Table S27.
Testing of multidimensional diagrams from Quaternary (0.17-2.04 Ma) basic rocks of the Halaha volcanic field, Central Great Xing 'an Range, NE China (Ho et al. 2013; Test study 10).

Figure reference; figure type	Discrimination diagram	Total no. of samples (%)	Predicted tectonic affinity and number of discriminated samples (%)				
			IAB	CRB+OIB	CRB	OIB	MORB
Agrawal et al. (2004); adjusted major element concentrations	IAB-CRB-OIB-MORB	14 (100)	0 (0)	---	11 (79)	3 (21)	0 (0)
	IAB-CRB-OIB	14 (100)	0 (0)	---	12 (86)	2 (14)	---
	IAB-CRB-MORB	14 (100)	0 (0)	---	12 (86)	---	2 (14)
	IAB-OIB-MORB	14 (100)	0 (0)	---	---	8 (57)	6 (43)
	CRB-OIB-MORB	14 (100)	---	---	12 (86)	2 (14)	0 (0)
Test study 10. Synthesis of all five diagrams of Agrawal et al. (2004)		***70 (100)***	***0 (0)***	***---***	***47 (67)***	***15 (22)***	***8 (11)***
Verma et al. (2006); log-ratios of major elements	IAB-CRB-OIB-MORB	14 (100)	0 (0)	---	11 (79)	3 (21)	0 (0)
	IAB-CRB-OIB	14 (100)	0 (0)	---	12 (86)	2 (14)	---
	IAB-CRB-MORB	14 (100)	0 (0)	---	14 (100)	---	0 (0)
	IAB-OIB-MORB	14 (100)	0 (0)	---	---	3 (21)	11 (79)
	CRB-OIB-MORB	14 (100)	---	---	13 (93)	1 (7)	0 (0)
Test study 10. Synthesis of all five diagrams of Verma et al. (2006)		***70 (100)***	***0 (0)***	***---***	***50 (71)***	***9 (13)***	***11 (16)***
Agrawal et al. (2008); log-ratios of immobile trace elements	IAB-CRB+OIB-MORB	14 (100)	5 (36)	9 (64)	---	---	0 (0)
	IAB-CRB-OIB	14 (100)	5 (36)	---	6 (43)	3 (21)	---
	IAB-CRB-MORB	14 (100)	5 (36)	---	9 (64)	---	0 (0)
	IAB-OIB-MORB	14 (100)	5 (36)	---	---	9 (64)	0 (0)
	CRB-OIB-MORB	14 (100)	---	---	10 (71)	4 (29)	0 (0)
Test study 10. Synthesis of all five diagrams of Agrawal et al. (2008)		***70 (100)***	***20 (28)***	***9 (---)***	***30 (44)***	***20 (28)***	***0 (0)***
Verma and Agrawal (2011); log-ratios of immobile major and trace elements	IAB-CRB+OIB-MORB	14 (100)	0 (0)	9 (64)	---	---	5 (36)
	IAB-CRB-OIB	14 (100)	5 (36)	---	9 (64)	0 (0)	---
	IAB-CRB-MORB	14 (100)	0 (0)	---	9 (64)	---	5 (36)
	IAB-OIB-MORB	14 (100)	0 (0)	---	---	9 (64)	5 (36)
	CRB-OIB-MORB	14 (100)	---	---	9 (64)	0 (0)	5 (36)
Test study 10. Synthesis of all five diagrams of Verma and Agrawal (2011)		***70 (100)***	***5 (7)***	***9 (---)***	***34 (49)***	***11 (16)***	***20(28)***

For the explanation of abbreviations, see footnote of Table 1 or S14.

Table S28.
Testing of multidimensional diagrams from Holocene (0.0034 Ma) acid rocks of the Aniakchak area, Aleutian arc, Alaska (Dreher et al. 2005; Test study 11).

Magma type, Figure name	Figure type	Total number of samples	Number of discriminated samples				
			Arc			Within-plate	Collision
			IA+CA [$\bar{x} \pm s$] (p_{IA+CA}) Θ	IA [$\bar{x} \pm s$] [p_{IA}] Θ	CA [$\bar{x} \pm s$] [p_{CA}] Θ	CR+OI [$\bar{x} \pm s$] [p_{CR+OI}] Θ	Col [$\bar{x} \pm s$] [p_{Col}] Θ
Acid; Verma et al. (2012); log-ratios of all major elements	**IA+CA–CR–Col**	9	9 [0.820±0.071] (0.6983-0.9389)	---	---	0 (0)	0 (0)
	IA–CA–CR	9	---	0 (0)	9 [0.707±0.078] (0.6024-0.8055)	0 (0)	---
	IA–CA–Col	9	---	0 (0)	9 [0.8195±0.0384] (0.7657-0.8627)	---	0 (0)
	IA–CR–Col	9	---	1 (0.8659)	---	8 [0.486±0.091] (0.3894-0.6456)	0 (0)
	CA–CR–Col	9	---	---	9 [0.8965±0.0422] (0.8143-0.9415)	0 (0)	0 (0)
Test study 11. Diagrams based on log-ratios of major elements	***{Σn} {Σprob} [%prob]***	***45***	***{9} {7.3795} [---]***	***{1} {0.8659} [4%]***	***{27} {21.8069} [85%]***	***{8} {3.8874} [11%]***	***{0} {0} [0%]***
Acid; Verma et al. (2013); log-ratios of all major elements	**IA+CA-CR+OI-Col**	9	4 [0.663±0.116] (0.5457-0.8222)	---	---	5 [0.5279±0.0443] (0.4685-0.5723)	0 (0)
	IA-CA-CR+OI	9	---	0 (0)	6 [0.559±0.137] (0.4338-0.8235)	3 [0.4849±0.0263] (0.4594-0.5119)	---
	IA-CA-Col	9	---	0 (0)	9 [0.727±0.061] (0.6606-0.8411)	---	0 (0)
	IA-CR+OI-Col	9	---	0 (0)	---	9 [0.688±0.086] (0.5396-0.7986)	0 (0)
	CA-CR+OI-Col	9	---	---	5 [0.646±0.134] (0.4946-0.8445)	4 [0.5220±0.0361] (0.4772-0.5573)	0 (0)
Test study 11. Diagrams based on log-ratios of major elements	***{Σn} {Σprob} [%prob]***	***45***	***{4} {2.6500} [---]***	***{0} {0} [0%]***	***{20} {13.1225} [56%]***	***{21} {12.3711} [44%]***	***{0} {0} [0%]***
Acid; Verma et al. (2013); log-ratios of immobile major and trace elements	**IA+CA-CR+OI-Col**	9	7 [0.521±0.081] (0.3854-0.6072)	---	---	2 [0.4290±0.0095] (0.4223, 0.4357)	0 (0)
	IA-CA-CR+OI	9	---	0 (0)	6 [0.600±0.060] (0.5051-0.6492)	3 [0.4812±0.0336] (0.4424-0.5019)	---
	IA-CA-Col	9	---	0 (0)	7 [0.5618±0.0443] (0.4666-0.5951)	---	2 [0.44745±0.00361] (0.4449, 0.4500)
	IA-CR+OI-Col	9	---	0 (0)	---	6 [0.497±0.066] (0.3766-0.5547)	3 [0.3694±0.0222] (0.3553-0.3950)
	CA-CR+OI-Col	9	---	---	9 [0.592±0.113] (0.4338-0.7193)	0 (0)	0 (0)
Test study 2a. Diagrams based on log-ratios of immobile major and trace elements	***{Σn} {Σprob} [%prob]***	***45***	***{7} {3.6470} [---]***	***{0} {0} [0%]***	***{22} {12.8589} [70%]***	***{11} {5.2815} [22%]***	***{5} {2.0031} [8%]***
Acid; Verma et al. (2013); log-ratios of immobile trace elements	**IA+CA-CR+OI-Col**	9	9 [0.8546±0.0157] (0.8199-0.8689)	---	---	0 (0)	0 (0)
	IA-CA-CR+OI	9	---	0 (0)	9 [0.7986±0.0247] (0.7740-0.8427)	0 (0)	---
	IA-CA-Col	9	---	0 (0)	9 [0.7761±0.0208]	---	0 (0)

					(0.7487-0.8141)		
	IA-CR+OI-Col	9	---	9 [0.764±0.071] (0.5921-0.8310)	---	0 (0)	0 (0)
	CA-CR+OI-Col	9	---	---	9 [0.9612±0.0087] (0.9412-0.9699)	0 (0)	0 (0)
Test study 11. Diagrams based on log-ratios of immobile trace elements	***{Σn} {Σprob} [%prob]***	***45***	***{9} {7.6911} [---]***	***{9} {6.8736} [23%]***	***{27} {22.8229} [77%]***	***{0} {0} [0%]***	***{0} {0} [0%]***

For the explanation of abbreviations, see footnote of Table S17.

Table S29.
Testing of multidimensional diagrams from recent intermediate rocks of the Fuego volcanic complex, Guatemala (Chesner and Rose Jr., 1984; Test study 12a).

Magma type, Figure name; Figure number	Figure type	Total number of samples	Number of discriminated samples				
			Arc			Within-plate	Collision
			IA+CA [$\bar{x} \pm s$] (p_{IA+CA}) Θ	IA [$\bar{x} \pm s$] [p_{IA}] Θ	CA [$\bar{x} \pm s$] [p_{CA}] Θ	CR+OI [$\bar{x} \pm s$] [p_{CR+OI}] Θ	Col [$\bar{x} \pm s$] [p_{Col}] Θ
Intermediate; Verma and Verma (2013); log-ratios of all major elements;	**IA+CA-CR+OI-Col**	9	8 [0.790±0.213] (0.4815-0.9661)	---	---	0 (0)	1 (0.9977)
	IA-CA-CR+OI	9	---	0 (0)	9 [0.759±0.127] (0.5884-0.9997)	0 (0)	---
	IA-CA-Col	9	---	0 (0)	8 [0.687±0.123] (0.5353-0.8289)	---	1 (0.9739)
	IA-CR+OI-Col	9	---	5 [0.891±0.075] (0.7653-0.9493)	---	0 (0)	4 [0.706±0.201] (0.5665-1.0000)
	CA-CR+OI-Col	9	---	---	6 [0.873±0.111] (0.6702-0.9621)	0 (0)	3 [0.587±0.164] (0.4865-0.7758)
Test study 12a. Diagrams based on log-ratios of major elements	***{Σn} {Σprob} [%prob]***	***45***	***{8} {6.3219} [---]***	***{5} {4.4546} [16%]***	***{23} {17.5595} [65%]***	***{0} {0} [0%]***	***{9} {6.5585} [19%]***

For the explanation of abbreviations, see footnote of Table S17.

Table S30.
Testing of multidimensional diagrams from Quaternary intermediate rocks of the Meseta volcano, Guatemala (Chesner and Halsor, 1997; Test study 12b).

Magma type, Figure name; Figure number	Figure type	Total number of samples	Number of discriminated samples				
			Arc			Within-plate	
			IA+CA [$\bar{x} \pm s$] (p_{IA+CA}) Θ	IA [$\bar{x} \pm s$] [p_{IA}] Θ	CA [$\bar{x} \pm s$] [p_{CA}] Θ	CR+OI [$\bar{x} \pm s$] [p_{CR+OI}] Θ	Collision Col [$\bar{x} \pm s$] [p_{Col}] Θ
Intermediate; Verma and Verma (2013); log-ratios of all major elements;	**IA+CA-CR+OI-Col**	40	40 [0.9617±0.0285] (0.8814-0.9815)	---	---	0 (0)	0 (0)
	IA-CA-CR+OI	40	---	0 (0)	40 [0.746±0.053] (0.6385-0.8271)	0 (0)	---
	IA-CA-Col	40	---	0 (0)	40 [0.769±0.046] (0.6789-0.8360)	---	0 (0)
	IA-CR+OI-Col	40	---	40 [0.9577±0.0287] (0.8800-0.9809)	---	0 (0)	0 (0)
	CA-CR+OI-Col	40	---	---	40 [0.9484±0.0426] (0.8093-0.9789)	0 (0)	0 (0)
Test study 12b. Diagrams based on log-ratios of major elements	***{Σn} {Σprob} [%prob]***	***200***	***{40} {38.4681} [---]***	***{40} {38.3098} [28.0%]***	***{120} {98.5657} [72.0%]***	***{0} {0} [0%]***	***{0} {0} [0%]***

For the explanation of abbreviations, see footnote of Table S17.

Table S31.
Testing of multidimensional diagrams from Holocene (0.000112) intermediate rocks of the Santiaguito complex, Guatemala (Scott et al. 2013; Test study 12c).

Magma type, Figure name	Figure type	Total number of samples	Number of discriminated samples				
			Arc			Within-plate CR+OI [$\bar{x} \pm s$] [p_{CR+OI}] Θ	Collision Col [$\bar{x} \pm s$] [p_{Col}] Θ
			IA+CA [$\bar{x} \pm s$] (p_{IA+CA}) Θ	IA [$\bar{x} \pm s$] [p_{IA}] Θ	CA [$\bar{x} \pm s$] [p_{CA}] Θ		
ntermediate; Verma and Verma (2013); log-ratios of all major elements	IA+CA-CR+OI-Col	18	18 [0.808±0.067] (0.7547-0.9500)	---	---	0 (0)	0 (0)
	IA-CA-CR+OI	18	---	0 (0)	18 [0.7359±0.0255] (0.7112-0.8137)	0 (0)	---
	IA-CA-Col	18	---	0 (0)	18 [0.687±0.048] (0.6501-0.8012)	---	0 (0)
	IA-CR+OI-Col	18	---	18 [0.7203±0.0995] (0.6322-0.9160)	---	0 (0)	0 (0)
	CA-CR+OI-Col	18	---	---	18 [0.669±0.139] (0.5705-0.9348)	0 (0)	0 (0)
Test study 12c. Diagrams based on log-ratios of major elements	***{Σn} {Σprob} [%prob]***	***90***	***{18} {14.5494} [---]***	***{18} {12.9660} [26%]***	***{54} {37.6497} [74%]***	***{0} {0} [0%]***	***{0} {0} [0%]***
Intermediate; Verma and Verma (2013); log-ratios of immobile major and trace elements	IA+CA-CR+OI-Col	5	5 [0.811±0.151] (0.5541-0.9444)	---	---	0 (0)	0 (0)
	IA-CA-CR+OI	5	---	1 (0.5617)	4 [0.594±0.068] (0.5056-0.6694)	0 (0)	---
	IA-CA-Col	5	---	1 (0.5530)	3 [0.5540±0.0275] (0.5290-0.5834)	---	1 (0.3917)
	IA-CR+OI-Col	5	---	5 [0.774±0.134] (0.5579-0.9210)	---	0 (0)	0 (0)
	CA-CR+OI-Col	5	---	---	5 [0.938±0.094] (0.7699-0.9894)	0 (0)	0 (0)
Test study 12c. Diagrams based on log-ratios of immobile major and trace elements	***{Σn} {Σprob} [%prob]***	***25***	***{5} {4.0545} [---]***	***{7} {4.9838} [36%]***	***{12} {8.7249} [62%]***	***{0} {0} [0%]***	***{1} {0.3917} [2%]***
Intermediate; Verma and Verma (2013); log-ratios of immobile trace elements	IA+CA-CR+OI-Col	18	18 [0.696±0.093] (0.5167-0.8366)	---	---	0 (0)	0 (0)
	IA-CA-CR+OI	18	---	16 [0.448±0.071] (0.3488-0.6806)	2 [0.4897±0.0062] (0.4853, 0.4941)	0 (0)	---
	IA-CA-Col	18	---	1 (0.6796)	17 [0.5055±0.0434] (0.4633-0.6348)	---	0 (0)
	IA-CR+OI-Col	18	---	18 [0.707±0.081] (0.5452-0.8419)	---	0 (0)	0 (0)
	CA-CR+OI-Col	18	---	---	18 [0.866±0.050] (0.7749-0.9509)	0 (0)	0 (0)
Test study 12c. Diagrams based on log-ratios of immobile trace elements	***{Σn} {Σprob} [%prob]***	***90***	***{18} {12.5319} [---]***	***{35} {20.5673} [45%]***	***{37} {25.1544} [55%]***	***{0} {0} [0%]***	***{0} {0} [0%]***

For the explanation of abbreviations, see footnote of Table S17.

Table S32.
Testing of multidimensional diagrams from Holocene (0.000112) acid rocks of the Santiaguito complex, Guatemala (Scott et al. 2013; Test study 12c).

Magma type, Figure name	Figure type	Total number of samples	Number of discriminated samples				
			Arc			Within-plate	Collision
			IA+CA $[\bar{x} \pm s]$ (p_{IA+CA}) Θ	IA $[\bar{x} \pm s]$ [p_{IA}] Θ	CA $[\bar{x} \pm s]$ [p_{CA}] Θ	CR+OI $[\bar{x} \pm s]$ [p_{CR+OI}] Θ	Col $[\bar{x} \pm s]$ [p_{Col}] Θ
Acid; Verma et al. (2012); All major elements	IA+CA-CR+OI-Col	17	17 [0.98126±0.00418] (0.9694-0.9859)	---	---	0 (0)	0 (0)
	IA-CA-CR+OI	17	---	15 [0.598±0.049] (0.5207-0.6870)	2 [0.590±0.088] (0.5280, 0.6528)	0 (0)	---
	IA-CA-Col	17	---	16 [0.5990±0.0392] (0.5188-0.6715)	1 (0.5823)	---	0 (0)
	IA-CR+OI-Col	17	---	17 [0.99699±0.00180] (0.9905-0.9983)	---	0 (0)	0 (0)
	CA-CR+OI-Col	17	---	---	17 [0.99280±0.00210] (0.9863-0.9954)	0 (0)	0 (0)
Test study 12c. Diagrams based on log-ratios of major elements	***{Σn} {Σprob} [%prob]***	***85***	***{17} {16.6813} [---]***	***{48} {35.4968} [66%]***	***{20} {18.6406} [34%]***	***{0} {0} [0%]***	***{0} {0} [0%]***
Acid; Verma et al. (2013); All major elements	IA+CA-CR+OI-Col	17	17 [0.9743±0.0087] (0.9476-0.9834)	---	---	0 (0)	0 (0)
	IA-CA-CR+OI	17	---	0 (0)	17 [0.7076±0.0204] (0.6708-0.7499)	0 (0)	---
	IA-CA-Col	17	---	0 (0)	17 [0.8405±0.0216] (0.7991-0.8747)	---	0 (0)
	IA-CR+OI-Col	17	---	17 [0.9331±0.0274] (0.8395-0.9611)	---	0 (0)	0 (0)
	CA-CR+OI-Col	17	---	---	17 [0.9881±0.0051] (0.9714-0.9930)	0 (0)	0 (0)
Test study 12c. Diagrams based on log-ratios of major elements	***{Σn} {Σprob} [%prob]***	***85***	***{17} {16.5629} [---]***	***{17} {15.8622} [27%]***	***{51} {43.1143} [73%]***	***{0} {0} [0%]***	***{0} {0} [0%]***
Acid; Verma et al. (2013); log-ratios of immobile major and trace elements	IA+CA-CR+OI-Col	17	6 [0.561±0.059] (0.5014-0.6376)	---	---	0 (0)	11 [0.592±0.079] (0.4825-0.7154)
	IA-CA-CR+OI	17	---	0 (0)	17 [0.6567±0.0428] (0.5394-0.7047)	0 (0)	---
	IA-CA-Col	17	---	0 (0)	10 [0.4634±0.0370] (0.4031-0.5147)	---	7 [0.484±0.065] (0.4161-0.6002)
	IA-CR+OI-Col	17	---	0 (0)	---	0 (0)	17 [0.690±0.077] (0.5354-0.7923)
	CA-CR+OI-Col	17	---	---	10 [0.581±0.072] (0.4793-0.6976)	0 (0)	7 [0.554±0.051] (0.4896-0.6350)
Test study 12c. Diagrams based on log-ratios of immobile major and trace elements	***{Σn} {Σprob} [%prob]***	***85***	***{6} {3.3668} [---]***	***{0} {0} [0%]***	***{37} {21.6074} [49%]***	***{0} {0} [0%]***	***{42} {25.5029} [51%]***
Acid; Verma et al. (2013); log-ratios of immobile trace elements	IA+CA-CR+OI-Col	17	17 [0.9236±0.0161] (0.8822-0.9449)	---	---	0 (0)	0 (0)
	IA-CA-CR+OI	17	---	0 (0)	17 [0.7405±0.0323] (0.6760-0.7861)	0 (0)	---
	IA-CA-Col	17	---	0 (0)	17 [0.7617±0.0398] (0.6809-0.8356)	---	0 (0)
	IA-CR+OI-Col	17	---	16 [0.765±0.079] (0.5939-0.8973)	---	1 (0.4833)	0 (0)
	CA-CR+OI-Col	17	---	---	17 [0.9705±0.0091] (0.9438-0.9827)	0 (0)	0 (0)
Test study 12c. Diagrams based on log-ratios of immobile trace elements	***{Σn} {Σprob} [%prob]***	***85***	***{17} {15.7007} [---]***	***{16} {12.2378} [22%]***	***{51} {42.0368} [77%]***	***{1} {0.4833} [1%]***	***{0} {0} [0%]***

For the explanation of abbreviations, see footnote of Table S17.

Table S33.
Testing of multidimensional diagrams from Holocene (0.000123) intermediate rocks of the Huequi volcano dome complex, Chile (Watt et al. 2011; Test study 13).

Magma type, Figure name	Figure type	Total number of samples	Number of discriminated samples				
			Arc			Within-plate	Collision
			IA+CA [$\bar{x} \pm s$] (p_{IA+CA}) Θ	IA [$\bar{x} \pm s$] [p_{IA}] Θ	CA [$\bar{x} \pm s$] [p_{CA}] Θ	CR+OI [$\bar{x} \pm s$] [p_{CR+OI}] Θ	Col [$\bar{x} \pm s$] [p_{Col}] Θ
Intermediate; Verma and Verma (2013); log-ratios of all major elements	IA+CA-CR+OI-Col	9	9 [0.916±0.074] (0.8015-0.9949)	---	---	0 (0)	0 (0)
	IA-CA-CR+OI	9	---	1 (0.4993)	8 [0.784±0.165] (0.5574-0.9109)	0 (0)	---
	IA-CA-Col	9	---	1 (0.5290)	8 [0.756±0.157] (0.5492-0.8786)	---	0 (0)
	IA-CR+OI-Col	9	---	9 [0.841±0.154] (0.5868-0.9970)	---	0 (0)	0 (0)
	CA-CR+OI-Col	9	---	---	9 [0.942±0.050] (0.8244-0.9877)	0 (0)	0 (0)
Test study 13. Diagrams based on log-ratios of major elements	***{Σn} {Σprob} [%prob]***	***45***	***{9} {8.2423} [---]***	***{11} {8.5945} [29%]***	***{25} {20.7899} [71%]***	***{0} {0} [0%]***	***{0} {0} [0%]***
Intermediate; Verma and Verma (2013); log-ratios of immobile major and trace elements	IA+CA-CR+OI-Col	9	8 [0.805±0.115] (0.6487-0.9461)	---	---	0 (0)	1 (0.4591)
	IA-CA-CR+OI	9	---	0 (0)	9 [0.588±0.054] (0.5038-0.7054)	0 (0)	---
	IA-CA-Col	9	---	0 (0)	8 [0.534±0.095] (0.4085-0.7079)	---	1 (0.4950)
	IA-CR+OI-Col	9	---	9 [0.737±0.150] (0.4447-0.9169)	---	0 (0)	0 (0)
	CA-CR+OI-Col	9	---	---	9 [0.859±0.150] (0.5257-0.9832)	0 (0)	0 (0)
Test study13. Diagrams based on log-ratios of immobile major and trace elements	***{Σn} {Σprob} [%prob]***	***45***	***{8} {6.4395} [---]***	***{9} {6.6365} [27%]***	***{26} {17.2963} [70%]***	***{0} {0} [0%]***	***{2} {0.9540} [3%]***

For the explanation of abbreviations, see footnote of Table S17.

Table S34.
Testing of multidimensional diagrams from Quaternary intermediate rocks of the Nisyros Island, Greece (Di Paola, 1974; Test study 14).

Magma type, Figure name; Figure number	Figure type	Total number of samples	Number of discriminated samples				
			Arc			Within-plate	Collision
			IA+CA [$\bar{x} \pm s$] (p_{IA+CA}) Θ	IA [$\bar{x} \pm s$] [p_{IA}] Θ	CA [$\bar{x} \pm s$] [p_{CA}] Θ	CR+OI [$\bar{x} \pm s$] [p_{CR+OI}] Θ	Col [$\bar{x} \pm s$] [p_{Col}] Θ
Intermediate; Verma and Verma (2013); log-ratios of all major elements;	**IA+CA-CR+OI-Col**	16	7 [0.665±0.124] (0.4966-0.8626)	---	---	1 (0.6186)	8 [0.691±0.128] (0.5344-0.9240)
	IA-CA-CR+OI	16	---	0 (0)	15 [0.761±0.134] (0.4753-0.9752)	1 (0.8251)	---
	IA-CA-Col	16	---	0 (0)	9 [0.598±0.092] (0.5049-0.7717)	---	7 [0.734±0.130] (0.5420-0.8802)
	IA-CR+OI-Col	16	---	5 [0.592±0.152] (0.3940-0.7994)	---	1 (0.6185)	10 [0.804±0.088] (0.6912-0.9615)
	CA-CR+OI-Col	16	---	---	9 [0.652±0.102] (0.5109-0.8295)	1 (0.6005)	6 [0.569±0.084] (0.4270-0.6388)
Test study 14. Diagrams based on log-ratios of major elements	***{Σn} {Σprob} [%prob]***	***80***	***{7} {4.6517} [---]***	***{5} {2.9598} [6%]***	***{33} {22.6620} [49%]***	***{4} {2.6627} [5%]***	***{31} {22.1191} [40%]***

For the explanation of abbreviations, see footnote of Table S17.

Table S35.
Testing of multidimensional diagrams from Quaternary acid rocks of the Nisyros Island, Greece (Di Paola, 1974; Test study 14).

Magma type, Figure name	Figure type	Total number of samples	Number of discriminated samples				
			Arc			Within-plate CR+OI [$\overline{x} \pm s$] [p_{CR+OI}] Θ	Collision Col [$\overline{x} \pm s$] [p_{Col}] Θ
			IA+CA [$\overline{x} \pm s$] (p_{IA+CA}) Θ	IA [$\overline{x} \pm s$] [p_{IA}] Θ	CA [$\overline{x} \pm s$] [p_{CA}] Θ		
Acid; Verma *et al.* (2012); All major elements	IA+CA-CR+OI-Col	11	10 [0.731±0.160] (0.5079-0.9313)	---	---	0 (0)	1 (0.9648)
	IA-CA-CR+OI	11	---	0 (0)	11 [0.768±0.087] (0.6230-0.8683)	0 (0)	---
	IA-CA-Col	11	---	0 (0)	10 [0.7312±0.0446] (0.6385-0.8120)	---	1 (0.9690)
	IA-CR+OI-Col	11	---	7 [0.719±0.154] (0.4796-0.8826)	---	0 (0)	4 [0.640±0.253] (0.4241-0.9568)
	CA-CR+OI-Col	11	---	---	10 [0.712±0.162] (0.4600-0.9350)	0 (0)	1 (0.9236)
Test study 14. Diagrams based on log-ratios of major elements	***{Σn} {Σprob} [%prob]***	***55***	***{10} {7.3070} [---]***	***{7} {5.0311} [16%]***	***{31} {22.8785} [71%]***	***{0} {0} [0%]***	***{7} {5.4192} [13%]***
Acid; Verma et al. (2013); All major elements	IA+CA-CR+OI-Col	11	9 [0.670±0.175] (0.3665-0.8633)	---	---	0 (0)	2 [0.552±0.262] (0.3673, 0.7376)
	IA-CA-CR+OI	11	---	0 (0)	10 [0.828±0.149] (0.4918-0.9373)	1 (0.9423)	---
	IA-CA-Col	11	---	0 (0)	10 [0.857±0.097] (0.6108-0.9346)	---	1 (0.9793)
	IA-CR+OI-Col	11	---	0 (0)	---	8 [0.5273±0.0419] (0.4764-0.6122)	3 [0.565±0.117] (0.4813-0.6979)
	CA-CR+OI-Col	11	---	---	9 [0.688±0.177] (0.3912-0.8875)	1 (0.3659)	1 (0.7049)
Test study 14. Diagrams based on log-ratios of major elements	***{Σn} {Σprob} [%prob]***	***55***	***{9} {6.0315} [---]***	***{0} {0} [0%]***	***{29} {23.0522} [75%]***	***{10} {5.5269} [14%]***	***{7} {4.4827} [11%]***

For the explanation of abbreviations, see footnote of Table S17.

Table S36.
Testing of multidimensional diagrams from Pleistocene-Holocene intermediate rocks from the Augustine volcano, Alaska (Johnson et al. 1996; Test study 15).

Magma type, Figure name; Figure number	Figure type	Total number of samples	Number of discriminated samples				
			Arc			Within-plate	Collision
			IA+CA [$\bar{x} \pm s$] (p_{IA+CA}) Θ	IA [$\bar{x} \pm s$] [p_{IA}] Θ	CA [$\bar{x} \pm s$] [p_{CA}] Θ	CR+OI [$\bar{x} \pm s$] [p_{CR+OI}] Θ	Col [$\bar{x} \pm s$] [p_{Col}] Θ
Intermediate; Verma and Verma (2013); log-ratios of all major elements;	**IA+CA-CR+OI-Col**	21	21 [0.905±0.054] (0.7810-0.9814)	---	---	0 (0)	0 (0)
	IA-CA-CR+OI	21	---	14 [0.5543±0.0344] (0.4999-0.6192)	7 [0.608±0.095] (0.4996-0.7092)	0 (0)	---
	IA-CA-Col	21	---	17 [0.585±0.059] (0.4988-0.7272)	4 [0.6371±0.0328] (0.6041-0.6730)	---	0 (0)
	IA-CR+OI-Col	21	---	21 [0.865±0.076] (0.6997-0.9733)	---	0 (0)	0 (0)
	CA-CR+OI-Col	21	---	---	21 [0.850±0.084] (0.6518-0.9607)	0 (0)	0 (0)
Test study 15. Diagrams based on log-ratios of major elements	***{Σn} {Σprob} [%prob]***	***105***	***{21} {19.0011} [---]***	***{52} {35.8767} [59.3%]***	***{32} {24.6512} [40.7%]***	***{0} {0} [0%]***	***{0} {0} [0%]***

For the explanation of abbreviations, see footnote of Table S17.

Table S37.
Testing of multidimensional diagrams from Quaternary basic rocks of the Barren Island, Andaman-Nicobar Islands (Chandrasekharam et al. 2009; Streck et al. 2011; Test study 16a).

Figure reference; figure type	Discrimination diagram	Total no. of samples (%)	Predicted tectonic affinity and number of discriminated samples (%)				
			IAB	CRB+OIB	CRB	OIB	MORB
Agrawal *et al.* (2004); adjusted major element concentrations	IAB-CRB-OIB-MORB	25 (100)	22 (88)	---	0 (0)	0 (0)	3 (12)
	IAB-CRB-OIB	25 (100)	25 (100)	---	0 (0)	0 (0)	---
	IAB-CRB-MORB	25 (100)	22 (88)	---	0 (0)	---	3 (12)
	IAB-OIB-MORB	25 (100)	22 (88)	---	---	0 (0)	3 (12)
	CRB-OIB-MORB	25 (100)	---	---	0 (0)	0 (0)	25 (100)
Test study 16a. Synthesis of all five diagrams of Agrawal et al. (2004)		***125 (100)***	***91 (72.8)***	***---***	***0 (0)***	***0 (0)***	***34 (27.2)***
Verma *et al.* (2006); log-ratios of major elements	IAB-CRB-OIB-MORB	25 (100)	25 (100)	---	0 (0)	0 (0)	0 (0)
	IAB-CRB-OIB	25 (100)	25 (100)	---	0 (0)	0 (0)	---
	IAB-CRB-MORB	25 (100)	25 (100)	---	0 (0)	---	0 (0)
	IAB-OIB-MORB	25 (100)	25 (100)	---	---	0 (0)	0 (0)
	CRB-OIB-MORB	25 (100)	---	---	0 (0)	0 (0)	25 (100)
Test study 16a. Synthesis of all five diagrams of Verma et al. (2006)		***125 (100)***	***100 (80.0)***	***---***	***0 (0)***	***0 (0)***	***25 (20.0)***
Agrawal *et al.* (2008); log-ratios of immobile trace elements	IAB-CRB+OIB-MORB	11 (100)	11 (100)	0 (0)	---	---	0 (0)
	IAB-CRB-OIB	11 (100)	11 (100)	---	0 (0)	0 (0)	---
	IAB-CRB-MORB	11 (100)	11 (100)	---	0 (0)	---	0 (0)
	IAB-OIB-MORB	11 (100)	11 (100)	---	---	0 (0)	0 (0)
	CRB-OIB-MORB	11 (100)	---	---	0 (0)	0 (0)	11 (100)
Test study 16a. Synthesis of all five diagrams of Agrawal et al. (2008)		***55 (100)***	***44 (80)***	***0 (---)***	***0 (0)***	***0 (0)***	***11 (20)***
Verma and Agrawal (2011); log-ratios of immobile major and trace elements	IAB-CRB+OIB-MORB	24 (100)	24 (100)	0 (0)	---	---	0 (0)
	IAB-CRB-OIB	24 (100)	24 (100)	---	0 (0)	0 (0)	---
	IAB-CRB-MORB	24 (100)	24 (100)	---	0 (0)	---	0 (0)
	IAB-OIB-MORB	24 (100)	24 (100)	---	---	0 (0)	0 (0)
	CRB-OIB-MORB	24 (100)	---	---	0 (0)	0 (0)	24 (100)
Test study 16a. Synthesis of all five diagrams of Verma and Agrawal (2011)		***120 (100)***	***96 (80.0)***	***0 (---)***	***0 (0)***	***0 (0)***	***24 (20.0)***

For the explanation of abbreviations, see footnote of Table 1 or S14.

Table S38.
Testing of multidimensional diagrams from Quaternary, intermediate rocks of the Barren Island, Andaman-Nicobar Islands (Chandrasekharam et al. 2009; Streck et al. 2011; Test study 16a).

Magma type, Figure name	Figure type	Total number of samples	Number of discriminated samples				
			Arc			Within-plate	Collision
			IA+CA [$\bar{x} \pm s$] (p_{IA+CA}) Θ	IA [$\bar{x} \pm s$] [p_{IA}] Θ	CA [$\bar{x} \pm s$] [p_{CA}] Θ	CR+OI [$\bar{x} \pm s$] [p_{CR+OI}] Θ	Col [$\bar{x} \pm s$] [p_{Col}] Θ
Intermediate; Verma and Verma (2013); log-ratios of all major elements	IA+CA-CR+OI-Col	21	19 [0.887±0.117] (0.6356-0.9931)	---	---	1 (0.6605)	1 (0.9189)
	IA-CA-CR+OI	21	---	9 [0.5177±0.0379] (0.4805-0.5932)	11 [0.582±0.149] (0.4730-0.9993)	1 (0.3955)	---
	IA-CA-Col	21	---	16 [0.624±0.053] (0.5341-0.7284)	4 [0.5503±0.0405] (0.5185-0.6097)	---	1 (0.9569)
	IA-CR+OI-Col	21	---	19 [0.874±0.136] (0.5863-0.9952)	---	1 (0.6915)	1 (0.9974)
	CA-CR+OI-Col	21	---	---	20 [0.830±0.168] (0.5349-0.9945)	1 (0.7049)	0 (0)
Test study 16a. Diagrams based on log-ratios of major elements	***{Σn} {Σprob} [%prob]***	***105***	***{19} {16.8541} [---]***	***{44} {31.2416} [51.6%]***	***{35} {25.2019} [41.6%]***	***{4} {2.4524} [3.1%]***	***{3} {2.8732} [3.7%]***
Intermediate; Verma and Verma (2013); log-ratios of immobile major and trace elements	IA+CA-CR+OI-Col	21	21 [0.9967±0.0051] (0.9754-0.9994)	---	---	0 (0)	0 (0)
	IA-CA-CR+OI	21	---	21 [0.890±0.047] (0.7355-0.9299)	0 (0)	0 (0)	---
	IA-CA-Col	21	---	21 [0.899±0.050] (0.7278-0.9407)	0 (0)	---	0 (0)
	IA-CR+OI-Col	21	---	21 [0.9964±0.0060] (0.9710-0.9993)	---	0 (0)	0 (0)
	CA-CR+OI-Col	21	---	---	21 [0.99959±0.00133] (0.9938-1.0000)	0 (0)	0 (0)
Test study 16a. Diagrams based on log-ratios of immobile major and trace elements	***{Σn} {Σprob} [%prob]***	***105***	***{21} {20.9317} [---]***	***{63} {58.5025} [73.6%]***	***{21} {20.9913} [26.4%]***	***{0} {0} [0%]***	***{0} {0} [0%]***
Intermediate; Verma and Verma (2013); log-ratios of immobile trace elements	IA+CA-CR+OI-Col	9	9 [0.99417±0.00303] (0.9900-0.9994)	---	---	0 (0)	0 (0)
	IA-CA-CR+OI	9	---	9 [0.9069±0.0156] (0.8855-0.9375)	0 (0)	0 (0)	---
	IA-CA-Col	9	---	9 [0.9257±0.0084] (0.9123-0.9404)	0 (0)	---	0 (0)
	IA-CR+OI-Col	9	---	9 [0.99632±0.00191] (0.9935-0.9996)	---	0 (0)	0 (0)
	CA-CR+OI-Col	9	---	---	9 [0.99555±0.00229] (0.9926-0.9996)	0 (0)	0 (0)
Test study 16a. Diagrams based on log-ratios of immobile trace elements	***{Σn} {Σprob} [%prob]***	***45***	***{9} {8.9475} [---]***	***{27} {25.4600} [74%]***	***{9} {8.9599} [26%]***	***{0} {0} [0%]***	***{0} {0} [0%]***

For the explanation of abbreviations, see footnote of Table S17.

Table S39.
Testing of multidimensional diagrams from Quaternary, intermediate rocks of the Narcondam Island, Andaman-Nicobar Islands (Pal et al. 2009; Streck et al. 2011; Test study 16b).

Magma type, Figure name	Figure type	Total number of samples	Number of discriminated samples				
			Arc			Within-plate	Collision
			IA+CA [$\bar{x} \pm s$] (p_{IA+CA}) Θ	IA [$\bar{x} \pm s$] [p_{IA}] Θ	CA [$\bar{x} \pm s$] [p_{CA}] Θ	CR+OI [$\bar{x} \pm s$] [p_{CR+OI}] Θ	Col [$\bar{x} \pm s$] [p_{Col}] Θ
Intermediate; Verma and Verma (2013); log-ratios of all major elements	IA+CA-CR+OI-Col	10	6 [0.720±0.138] (0.5329-0.8831)	---	---	0 (0)	4 [0.562±0.048] (0.5158-0.6223)
	IA-CA-CR+OI	10	---	5 [0.604±0.062] (0.5460-0.7093)	5 [0.552±0.049] (0.5031-0.6120)	0 (0)	---
	IA-CA-Col	10	---	6 [0.468±0.049] (0.4100-0.5427)	1 (0.3967)	---	3 [0.400±0.073] (0.3448-0.4822)
	IA-CR+OI-Col	10	---	6 [0.683±0.172] (0.4999-0.8629)	---	0 (0)	4 [0.645±0.066] (0.5571-0.7172)
	CA-CR+OI-Col	10	---	---	6 [0.709±0.164] (0.5194-0.8923)	0 (0)	4 [0.6253±0.0443] (0.5828-0.6696)
Test study 16b. Diagrams based on log-ratios of major elements	***{Σn} {Σprob} [%prob]***	***50***	***{6} {4.3201} [---]***	***{17} {9.9209} [41%]***	***{12} {7.4106} [31%]***	***{0} {0} [0%]***	***{15} {8.5253} [28%]***
Intermediate; Verma and Verma (2013); log-ratios of immobile major and trace elements	IA+CA-CR+OI-Col	8	8 [0.924±0.079] (0.7846-0.9952)	---	---	0 (0)	0 (0)
	IA-CA-CR+OI	8	---	8 [0.765±0.131] (0.5716-0.9087)	0 (0)	0 (0)	---
	IA-CA-Col	8	---	8 [0.743±0.144] (0.5235-0.8941)	0 (0)	---	0 (0)
	IA-CR+OI-Col	8	---	8 [0.916±0.092] (0.7515-0.9947)	---	0 (0)	0 (0)
	CA-CR+OI-Col	8	---	---	8 [0.9737±0.0279] (0.9302-0.9992)	0 (0)	0 (0)
Test study 16b. Diagrams based on log-ratios of immobile major and trace elements	***{Σn} {Σprob} [%prob]***	***40***	***{8} {7.3902} [---]***	***{24} {19.3889} [71%]***	***{8} {7.7897} [29%]***	***{0} {0} [0%]***	***{0} {0} [0%]***
Intermediate; Verma and Verma (2013); log-ratios of immobile trace elements	IA+CA-CR+OI-Col	8	4 [0.696±0.165] (0.5416-0.9013)	---	---	0 (0)	4 [0.574±0.060] (0.4999-0.6445)
	IA-CA-CR+OI	8	---	7 [0.659±0.086] (0.5372-0.8031)	1 (0.5999)	0 (0)	---
	IA-CA-Col	8	---	7 [0.607±0.123] (0.4888-0.8443)	0 (0)	---	1 (0.4605)
	IA-CR+OI-Col	8	---	6 [0.621±0.149] (0.5272-0.9209)	---	0 (0)	2 [0.565±0.049] (0.5311, 0.5998)
	CA-CR+OI-Col	8	---	---	4 [0.746±0.135] (0.6299-0.8934)	0 (0)	4 [0.6164±0.0431] (0.5543-0.6539)
Test study 16b. Diagrams based on log-ratios of immobile trace elements	***{Σn} {Σprob} [%prob]***	***40***	***{4} {2.7834} [---]***	***{20} {12.5912} [58%]***	***{5} {3.5821} [17%]***	***{0} {0} [0%]***	***{11} {6.3540} [25%]***

For the explanation of abbreviations, see footnote of Table S17.

Table S40.
Testing of multidimensional diagrams from Quaternary acid rocks of Narcondam Island, Andaman-Nicobar Islands (Pal et al. 2009; Streck et al. 2011; Test study 16b).

Magma type, Figure name	Figure type	Total number of samples	Number of discriminated samples				
			Arc			Within-plate	Collision
			IA+CA [$\bar{x} \pm s$] (p_{IA+CA}) Θ	IA [$\bar{x} \pm s$] [p_{IA}] Θ	CA [$\bar{x} \pm s$] [p_{CA}] Θ	CR+OI [$\bar{x} \pm s$] [p_{CR+OI}] Θ	Col [$\bar{x} \pm s$] [p_{Col}] Θ
Acid; Verma *et al.* (2012); All major elements	IA+CA-CR+OI-Col	8	8 [0.9733±0.0082] (0.9547-0.9820)	---	---	0 (0)	0 (0)
	IA-CA-CR+OI	8	---	8 [0.797±0.054] (0.6775-0.8414)	0 (0)	0 (0)	---
	IA-CA-Col	8	---	8 [0.807±0.054] (0.7031-0.8526)	0 (0)	---	0 (0)
	IA-CR+OI-Col	8	---	8 [0.99434±0.00397] (0.9848-0.9969)	---	0 (0)	0 (0)
	CA-CR+OI-Col	8	---	---	8 [0.9945±0.0027] (0.9881-0.9964)	0 (0)	0 (0)
Test study 16b. Diagrams based on log-ratios of major elements	***{Σn} {Σprob} [%prob]***	***40***	***{8} {7.7865} [---]***	***{24} {20.7847} [72%]***	***{8} {7.9560} [28%]***	***{0} {0} [0%]***	***{0} {0} [0%]***
Acid; Verma et al. (2013); All major elements	IA+CA-CR+OI-Col	8	8 [0.9688±0.0125] (0.9420-0.9794)	---	---	0 (0)	0 (0)
	IA-CA-CR+OI	8	---	4 [0.5586±0.0319] (0.5271-0.6014)	*4 [0.5522±0.0308] (0.5157-0.5796)*	0 (0)	---
	IA-CA-Col	8	---	1 (0.5576)	*7 [0.596±0.046] (0.5480-0.6586)*	---	0 (0)
	IA-CR+OI-Col	8	---	8 [0.9582±0.0273] (0.8975-0.9768)	---	0 (0)	0 (0)
	CA-CR+OI-Col	8	---	---	*8 [0.9858±0.0073] (0.9695-0.9913)*	0 (0)	0 (0)
Test study 16b. Diagrams based on log-ratios of major elements	***{Σn} {Σprob} [%prob]***	***40***	***{8} {7.7506} [---]***	***{13} {10.4580} [42%]***	***{19} {14.2693} [58%]***	***{0} {0} [0%]***	***{0} {0} [0%]***

For the explanation of abbreviations, see footnote of Table S17.

Table S41.
Testing of multidimensional diagrams from recent basic rocks from the Indian Ridge (Yi et al. 2014; Test study 17).

Figure reference; figure type	Discrimination diagram	Total no. of samples (%)	Predicted tectonic affinity and number of discriminated samples (%)				
			IAB	CRB+OIB	CRB	OIB	MORB
Agrawal et al. (2004); adjusted major element concentrations	IAB-CRB-OIB-MORB	33 (100)	2 (6)	---	0 (0)	0 (0)	31 (94)
	IAB-CRB-OIB	33 (100)	29 (88)	---	1 (3)	3 (9)	---
	IAB-CRB-MORB	33 (100)	2 (6)	---	0 (0)	---	31 (94)
	IAB-OIB-MORB	33 (100)	2 (6)	---	---	0 (0)	31 (94)
	CRB-OIB-MORB	33 (100)	---	---	0 (0)	0 (0)	33 (100)
Test study 17. Synthesis of all five diagrams of Agrawal et al. (2004)		***165 (100)***	***35 (21.2)***	***---***	***1 (0.6)***	***3 (1.8)***	***126 (76.4)***
Verma et al. (2006); log-ratios of major elements	IAB-CRB-OIB-MORB	33 (100)	1 (3)	---	1 (3)	0 (0)	31 (94)
	IAB-CRB-OIB	33 (100)	2 (6)	---	5 (15)	26 (79)	---
	IAB-CRB-MORB	33 (100)	1 (3)	---	1 (3)	---	31 (94)
	IAB-OIB-MORB	33 (100)	1 (3)	---	---	0 (0)	32 (97)
	CRB-OIB-MORB	33 (100)	---	---	2 (6)	0 (0)	31 (94)
Test study 17. Synthesis of all five diagrams of Verma et al. (2006)		***165 (100)***	***5 (3.0)***	***---***	***9 (5.4)***	***26 (15.8)***	***125 (75.8)***
Agrawal et al. (2008); log-ratios of immobile trace elements	IAB-CRB+OIB-MORB	32 (100)	6 (19)	1 (3)	---	---	25 (78)
	IAB-CRB-OIB	32 (100)	7 (22)	---	11 (34)	14 (44)	---
	IAB-CRB-MORB	32 (100)	7 (22)	---	2 (6)	---	23 (72)
	IAB-OIB-MORB	32 (100)	6 (19)	---	---	0 (0)	26 (81)
	CRB-OIB-MORB	32 (100)	---	---	2 (6)	0 (0)	30 (94)
Test study 17. Synthesis of all five diagrams of Agrawal et al. (2008)		***160 (100)***	***26 (16.2)***	***1 (---)***	***16 (10.0)***	***14 (8.8)***	***104 (65.0)***
Verma and Agrawal (2011); log-ratios of immobile major and trace elements	IAB-CRB+OIB-MORB	33 (100)	0 (0)	2 (6)	---	---	31 (94)
	IAB-CRB-OIB	33 (100)	31 (94)	---	2 (6)	0 (0)	---
	IAB-CRB-MORB	33 (100)	0 (0)	---	2 (6)	---	31 (94)
	IAB-OIB-MORB	33 (100)	0 (0)	---	---	2 (6)	31 (94)
	CRB-OIB-MORB	33 (100)	---	---	2 (6)	0 (0)	31 (94)
Test study 17. Synthesis of all five diagrams of Verma and Agrawal (2011)		***165 (100)***	***31 (18.8)***	***2 (---)***	***8 (4.8)***	***2 (1.2)***	***124(75.2)***

For the explanation of abbreviations, see footnote of Table 1 or S14.

Table S42.
Testing of multidimensional diagrams from late Miocene-Pleistocene (2.5-4.6 Ma) intermediate rocks of Shirak, Armenia (Neill et al. 2013; Test study 18).

Magma type, Figure name	Figure type	Total number of samples	Number of discriminated samples				
			Arc			Within-plate CR+OI [$\bar{x} \pm s$] [p_{CR+OI}] Θ	Collision Col [$\bar{x} \pm s$] [p_{Col}] Θ
			IA+CA [$\bar{x} \pm s$] (p_{IA+CA}) Θ	IA [$\bar{x} \pm s$] [p_{IA}] Θ	CA [$\bar{x} \pm s$] [p_{CA}] Θ		
Intermediate; Verma and Verma (2013); log-ratios of all major elements	IA+CA-CR+OI-Col	13	0 (0)	---	---	5 [0.591±0.188] (0.4557-0.9061)	8 [0.763±0.180] (0.4610-0.9284)
	IA-CA-CR+OI	13	---	0 (0)	7 [0.755±0.096] (0.5592-0.8473)	6 [0.649±0.156] (0.4796-0.8637)	---
	IA-CA-Col	13	---	0 (0)	5 [0.584±0.077] (0.4621-0.6596)	---	8 [0.736±0.098] (0.5234-0.8480)
	IA-CR+OI-Col	13	---	0 (0)	---	5 [0.635±0.182] (0.4899-0.9308)	8 [0.826±0.169] (0.5453-0.9688)
	CA-CR+OI-Col	13	---	---	3 [0.491±0.053] (0.4517-0.5514)	3 [0.560±0.210] (0.4118-0.7999)	7 [0.692±0.193] (0.3740-0.8926)
Test study 18. Diagrams based on log-ratios of major elements	***{Σn} {Σprob} [%prob]***	***65***	***{0} {0} [0%]***	***{0} {0} [0%]***	***{15} {9.6749} [22%]***	***{19} {11.7012} [26%]***	***{31} {23.4464} [52%]***
Intermediate; Verma and Verma (2013); log-ratios of immobile major and trace elements	IA+CA-CR+OI-Col	9	0 (0)	---	---	2 [0.794±0.112] (0.7143, 0.8728)	7 [0.807±0.167] (0.4841-0.9685)
	IA-CA-CR+OI	9	---	0 (0)	4 [0.665±0.117] (0.5211-0.7604)	5 [0.714±0.154] (0.5674-0.9279)	---
	IA-CA-Col	9	---	0 (0)	0 (0)	---	9 [0.774±0.142] (0.6140-0.9513)
	IA-CR+OI-Col	9	---	0 (0)	---	3 [0.694±0.199] (0.4774-0.8693)	6 [0.856±0.104] (0.6676-0.9684)
	CA-CR+OI-Col	9	---	---	0 (0)	2 [0.797±0.128] (0.7065, 0.8873)	7 [0.821±0.158] (0.5205-0.9807)
Test study 18. Diagrams based on log-ratios of immobile major and trace elements	***{Σn} {Σprob} [%prob]***	***45***	***{0} {0} [0%]***	***{0} {0} [0%]***	***{4} {2.6600} [8%]***	***{12} {8.8313} [25%]***	***{29} {23.5052} [67%]***
Intermediate; Verma and Verma (2013); log-ratios of immobile trace elements	IA+CA-CR+OI-Col	13	2 [0.4754±0.0419] (0.4458, 0.5050)	---	---	5 [0.573±0.077] (0.4476-0.6392)	6 [0.659±0.158] (0.3935-0.8547)
	IA-CA-CR+OI	13	---	0 (0)	6 [0.564±0.114] (0.4729-0.7587)	7 [0.634±0.134] (0.4218-0.8101)	---
	IA-CA-Col	13	---	0 (0)	6 [0.647±0.143] (0.4507-0.7845)	---	7 [0.800±0.177] (0.5330-0.9522)
	IA-CR+OI-Col	13	---	0 (0)	---	7 [0.616±0.068] (0.5380-0.7369)	6 [0.669±0.136] (0.4518-0.8473)
	CA-CR+OI-Col	13	---	---	5 [0.586±0.125] (0.3928-0.7132)	2 [0.466±0.071] (0.4158, 0.5158)	6 [0.677±0.167] (0.3677-0.8346)
Test study 18. Diagrams based on log-ratios of immobile trace elements	***{Σn} {Σprob} [%prob]***	***65***	***{2} {0.9509} [---]***	***{0} {0} [0%]***	***{17} {10.1969} [27%]***	***{21} {12.5533} [30%]***	***{25} {17.6317} [43%]***

For the explanation of abbreviations, see footnote of Table S17.

Table S43.
Testing of multidimensional diagrams from late Miocene (4.95-5.52 Ma) drill hole basic and ultrabasic rocks of the Eiao Island, French Polynesia (Caroff et al. 1999; Test study A1).

Figure reference; figure type	Discrimination diagram	Total no. of samples (%)	Predicted tectonic affinity and number of discriminated samples (%)				
			IAB	CRB+OIB	CRB	OIB	MORB
Agrawal et al. (2004); adjusted major element concentrations	IAB-CRB-OIB-MORB	25 (100)	0 (0)	---	1 (4)	24 (96)	0 (0)
	IAB-CRB-OIB	25 (100)	0 (0)	---	1 (4)	24 (96)	---
	IAB-CRB-MORB	25 (100)	0 (0)	---	24 (96)	---	1 (4)
	IAB-OIB-MORB	25 (100)	0 (0)	---	---	25 (100)	0 (0)
	CRB-OIB-MORB	25 (100)	---	---	1 (4)	24 (96)	0 (0)
Test study A1. Synthesis of all five diagrams of Agrawal et al. (2004)		***125 (100)***	***0 (0)***	***---***	***27 (21.6)***	***97 (77.6)***	***1 (0.8)***
Verma et al. (2006); log-ratios of major elements	IAB-CRB-OIB-MORB	25 (100)	0 (0)	---	2 (8)	23 (92)	0 (0)
	IAB-CRB-OIB	25 (100)	0 (0)	---	0 (0)	25 (100)	---
	IAB-CRB-MORB	25 (100)	0 (0)	---	24 (96)	---	1 (4)
	IAB-OIB-MORB	25 (100)	0 (0)	---	---	25 (100)	0 (0)
	CRB-OIB-MORB	25 (100)	---	---	0 (0)	25 (100)	0 (0)
Test study A1. Synthesis of all five diagrams of Verma et al. (2006)		***125 (100)***	***0 (0)***	***---***	***26 (20.8)***	***98 (78.4)***	***1 (0.8)***
Verma and Agrawal (2011); log-ratios of immobile major and trace elements	IAB-CRB+OIB-MORB	25 (100)	0 (0)	25 (100)	---	---	0 (0)
	IAB-CRB-OIB	25 (100)	0 (0)	---	0 (0)	25 (100)	---
	IAB-CRB-MORB	25 (100)	0 (0)	---	25 (100)	---	0 (0)
	IAB-OIB-MORB	25 (100)	0 (0)	---	---	25 (100)	0 (0)
	CRB-OIB-MORB	25 (100)	---	---	0 (0)	25 (100)	0 (0)
Test study A1. Synthesis of all five diagrams of Verma and Agrawal (2011)		***125 (100)***	***0 (0)***	***25 (---)***	***31 (24.8)***	***94 (75.2)***	***0(0)***

For the explanation of abbreviations, see footnote of Table 1 or S14.

Table S44.
Testing of multidimensional diagrams from Pliocene-Pleistocene (0.35-4 Ma) altered basic and ultrabasic rocks of Koolau, Haleakala, and Kohala volcanoes, Hawaiian Islands (Patino et al. 2003; Test study A2).

Figure reference; figure type	Discrimination diagram	Total no. of samples (%)	Predicted tectonic affinity and number of discriminated samples (%)				
			IAB	CRB+OIB	CRB	OIB	MORB
Agrawal *et al.* (2004); adjusted major element concentrations	IAB-CRB-OIB-MORB	9 (100)	0 (0)	---	9 (100)	0 (0)	0 (0)
	IAB-CRB-OIB	9 (100)	1 (11)	---	7 (78)	1 (11)	---
	IAB-CRB-MORB	9 (100)	0 (0)	---	9 (100)	---	0 (0)
	IAB-OIB-MORB	9 (100)	1 (11)	---	---	8 (89)	0 (0)
	CRB-OIB-MORB	9 (100)	---	---	7 (77.8)	2 (22)	0 (0)
Test study A2. Synthesis of all five diagrams of Agrawal et al. (2004)		***45 (100)***	***2 (4)***	***---***	***32 (71)***	***11 (25)***	***0 (0)***
Verma et al. (2006); log-ratios of major elements	IAB-CRB-OIB-MORB	9 (100)	0 (0)	---	9 (100)	0 (0)	0 (0)
	IAB-CRB-OIB	9 (100)	0 (0)	---	5 (55.6)	4 (44.4)	---
	IAB-CRB-MORB	9 (100)	0 (0)	---	9 (100)	---	0 (0)
	IAB-OIB-MORB	9 (100)	1 (11)	---	---	8 (88.9)	0 (0)
	CRB-OIB-MORB	9 (100)	---	---	5 (55.6)	4 (44.4)	0 (0)
Test study A2. Synthesis of all five diagrams of Verma et al. (2006)		***45 (100)***	***1 (2)***	***---***	***28 (62)***	***16 (36)***	***0 (0)***

For the explanation of abbreviations, see footnote of Table 1 or S14.

Table S45.
Testing of multidimensional diagrams from late Miocene to Holocene slightly to intensely altered basic rocks of the Hainan Island, China (Wang et al. 2012; Test study A3).

Figure reference; figure type	Discrimination diagram	Total no. of samples (%)	Predicted tectonic affinity and number of discriminated samples (%)				
			IAB	CRB+OIB	CRB	OIB	MORB
Agrawal et al. (2004); adjusted major element concentrations	IAB-CRB-OIB-MORB	13 (100)	0 (0)	---	11 (84.6)	1 (7.7)	1 (7.7)
	IAB-CRB-OIB	13 (100)	0 (0)	---	13 (100)	0 (0)	---
	IAB-CRB-MORB	13 (100)	0 (0)	---	10 (76.9)	---	3 (23.1)
	IAB-OIB-MORB	13 (100)	0 (0)	---	---	10 (76.9)	3 (23.1)
	CRB-OIB-MORB	13 (100)	---	---	11 (84.6)	1 (7.7)	1 (7.7)
Test study A3. Synthesis of all five diagrams of Agrawal et al. (2004)		***65 (100)***	***0 (0)***	***---***	***45 (69.2)***	***12 (18.5)***	***8 (12.3)***
Verma et al. (2006); log-ratios of major elements	IAB-CRB-OIB-MORB	13 (100)	0 (0)	---	11 (84.6)	2 (15.4)	0 (0)
	IAB-CRB-OIB	13 (100)	0 (0)	---	12 (92.3)	1 (7.7)	---
	IAB-CRB-MORB	13 (100)	0 (0)	---	13 (100)	---	0 (0)
	IAB-OIB-MORB	13 (100)	0 (0)	---	---	9 (69.2)	4 (30.8)
	CRB-OIB-MORB	13 (100)	---	---	12 (92.3)	1 (7.7)	0 (0)
Test study A3. Synthesis of all five diagrams of Verma et al. (2006)		***65 (100)***	***0 (0)***	***---***	***48 (73.8)***	***13 (20)***	***4 (6.2)***

For the explanation of abbreviations, see footnote of Table 1 or S14.

Table S46.
Testing of multidimensional diagrams from late Miocene to Holocene slightly to intensely altered intermediate rocks of the Hainan Island, China (Wang et al. 2012; Test study A3).

Magma type, Figure name	Figure type	Total number of samples	Number of discriminated samples				
			Arc			Within-plate	Collision Col [$\bar{x} \pm s$] [p_{Col}] Θ
			IA+CA [$\bar{x} \pm s$] (p_{IA+CA}) Θ	IA [$\bar{x} \pm s$] [p_{IA}] Θ	CA [$\bar{x} \pm s$] [p_{CA}] Θ	CR+OI [$\bar{x} \pm s$] [p_{CR+OI}] Θ	
Intermediate; Verma and Verma (2013); log-ratios of all major elements	IA+CA-CR+OI-Col	10	0 (0)	---	---	10 [0.760±0.114] (0.6118-0.9400)	0 (0)
	IA-CA-CR+OI	10	---	0 (0)	0 (0)	10 [0.649±0.132] (0.4636-0.8260)	---
	IA-CA-Col	10	---	4 [0.702±0.135] (0.5975-0.8870)	6 [0.584±0.077] (0.5009-0.7102)	---	0 (0)
	IA-CR+OI-Col	10	---	0 (0)	---	10 [0.843±0.083] (0.7229-0.9457)	0 (0)
	CA-CR+OI-Col	10	---	---	0 (0)	10 [0.729±0.158] (0.5172-0.9227)	0 (0)
Test study A3. Diagrams based on log-ratios of major elements	***{Σn} {Σprob} [%prob]***	***50***	***{0} {0} [0%]***	***{4} {2.8068} [8%]***	***{6} {3.5068} [9%]***	***{40} {29.8050} [83%]***	***{0} {0} [0%]***

For the explanation of abbreviations, see footnote of Table S17.

Table S47.
Testing of multidimensional diagrams from intermediate altered rocks of Moyuta and Tecuamburro volcanoes, Guatemala (Patino et al. 2003; Test study A4)

Magma type, Figure name	Figure type	Total number of samples	Number of discriminated samples				
			Arc			Within-plate	Collision Col [$\bar{x} \pm s$] [p_{Col}] Θ
			IA+CA [$\bar{x} \pm s$] (p_{IA+CA}) Θ	IA [$\bar{x} \pm s$] [p_{IA}] Θ	CA [$\bar{x} \pm s$] [p_{CA}] Θ	CR+OI [$\bar{x} \pm s$] [p_{CR+OI}] Θ	
Intermediate; Verma and Verma (2013); log-ratios of all major elements	IA+CA-CR+OI-Col	7	4 [0.773±0.166] (0.5740-0.9469)	---	---	0 (0)	3 [0.6097±0.0334] (0.5726-0.6373)
	IA-CA-CR+OI	7	---	1 (0.5005)	6 [0.645±0.129] (0.4962-0.7923)	0 (0)	---
	IA-CA-Col	7	---	2 [0.508±0.050] (0.4719, 0.5431)	5 [0.5223±0.0428] (0.4780-0.5900)	---	0 (0)
	IA-CR+OI-Col	7	---	4 [0.736±0.220] (0.5173-0.9342)	---	0 (0)	3 [0.807±0.073] (0.7236-0.8532)
	CA-CR+OI-Col	7	---	---	5 [0.707±0.161] (0.5430-0.8958)	0 (0)	2 [0.51602±0.00324] (0.5137, 0.5183)
Test study A4. Diagrams based on log-ratios of major elements	***{Σn} {Σprob} [%prob]***	***35***	***{4} {3.0921} [---]***	***{7} {4.4586} [24%]***	***{16} {10.0142} [53%]***	***{0} {0} [0%]***	***{8} {5.2829} [23%]***

For the explanation of abbreviations, see footnote of Table S17.

Table S48.
Testing of multidimensional diagrams from basic rocks from the Sarapiqui Miocene (11.4-22.2 Ma) arc, Costa Rica (Gazel et al. 2005; Test study A5).

Figure reference; figure type	Discrimination diagram	Total no. of samples (%)	Predicted tectonic affinity and number of discriminated samples (%)				
			IAB	CRB+OIB	CRB	OIB	MORB
Agrawal et al. (2004); adjusted major element concentrations	IAB-CRB-OIB-MORB	10 (100)	6 (60)	---	1 (10)	0 (0)	3 (30)
	IAB-CRB-OIB	10 (100)	6 (60)	---	1 (10)	3 (30)	---
	IAB-CRB-MORB	10 (100)	7 (70)	---	1 (10)	---	2 (20)
	IAB-OIB-MORB	10 (100)	6 (60)	---	---	1 (10)	3 (30)
	CRB-OIB-MORB	10 (100)	---	---	1 (10)	0 (0)	9 (90)
Test study A5. Synthesis of all five diagrams of Agrawal et al. (2004)		***50 (100)***	***25 (50)***	***---***	***4 (8)***	***4 (8)***	***17 (34)***
Verma et al. (2006); log-ratios of major elements	IAB-CRB-OIB-MORB	10 (100)	6 (60)	---	4 (40)	0 (0)	0 (0)
	IAB-CRB-OIB	10 (100)	7 (70)	---	1 (10)	2 (20)	---
	IAB-CRB-MORB	10 (100)	7 (70)	---	3 (30)	---	0 (0)
	IAB-OIB-MORB	10 (100)	6 (60)	---	---	4 (40)	0 (0)
	CRB-OIB-MORB	10 (100)	---	---	7 (70)	3 (30)	0 (0)
Test study A5. Synthesis of all five diagrams of Verma et al. (2006)		***50 (100)***	***26 (52)***	***---***	***15 (30)***	***9 (18)***	***0 (0)***
Verma and Agrawal (2011); log-ratios of immobile major and trace elements	IAB-CRB+OIB-MORB	10 (100)	6 (60)	1 (10)	---	---	3 (30)
	IAB-CRB-OIB	10 (100)	6 (60)	---	3 (30)	1 (10)	---
	IAB-CRB-MORB	10 (100)	6 (60)	---	2 (20)	---	2 (20)
	IAB-OIB-MORB	10 (100)	6 (60)	---	---	1 (10)	3 (30)
	CRB-OIB-MORB	10 (100)	---	---	1 (10)	1 (10)	8 (80)
Test study A5. Synthesis of all five diagrams of Verma and Agrawal (2011)		***50 (100)***	***24 (48)***	***1 (---)***	***7 (14)***	***3 (6)***	***16(32)***

For the explanation of abbreviations, see footnote of Table 1 or S14.

Table S49.
Testing of multidimensional diagrams from Miocene (11.4-22.2 Ma) basic rocks from the Sarapiqui paleoarc, Costa Rica (Gazel et al. 2005; Test study A5).

Magma type, Figure name; Figure number	Figure type	Total number of samples	Number of discriminated samples				
			Arc			Within-plate	Collision
			IA+CA [$\bar{x} \pm s$] (p_{IA+CA}) Θ	IA [$\bar{x} \pm s$] [p_{IA}] Θ	CA [$\bar{x} \pm s$] [p_{CA}] Θ	CR+OI [$\bar{x} \pm s$] [p_{CR+OI}] Θ	Col [$\bar{x} \pm s$] [p_{Col}] Θ
Intermediate; Verma and Verma (2013); log-ratios of all major elements;	IA+CA-CR+OI-Col	14	12 [0.889±0.080] (0.6909-0.9840)	---	---	0 (0)	2 [0.5734±0.0115] (0.5653, 0.5816)
	IA-CA-CR+OI	14	---	12 [0.745±0.132] (0.4222-0.9030)	2 [0.565±0.074] (0.5126, 0.6176)	0 (0)	---
	IA-CA-Col	14	---	11 [0.773±0.118] (0.5209-0.9481)	2 [0.613±0.068] (0.5652, 0.6613)	---	1 (0.3978)
	IA-CR+OI-Col	14	---	13 [0.903±0.126] (0.5191-0.9932)	---	0 (0)	1 (0.5340)
	CA-CR+OI-Col	14	---	---	12 [0.775±0.142] (0.4974-0.9492)	0 (0)	2 [0.580±0.076] (0.5267, 0.6339)
Test study A5. Diagrams based on log-ratios of major elements	***{Σn} {Σprob} [%prob]***	***70***	***{12} {10.6683} [---]***	***{36} {29.1787} [67%]***	***{16} {11.6534} [27%]***	***{0} {0} [0%]***	***{6} {3.2393} [6%]***
Intermediate; Verma and Verma (2013); log-ratios of immobile major and trace elements	IA+CA-CR+OI-Col	14	12 [0.874±0.182] (0.5066-0.9943)	---	---	0 (0)	2 [0.724±0.064] (0.6785, 0.7687)
	IA-CA-CR+OI	14	---	11 [0.670±0.057] (0.5495-0.7442)	3 [0.489±0.054] (0.4263-0.5208)	0 (0)	---
	IA-CA-Col	14	---	9 [0.641±0.060] (0.5366-0.7109)	2 [0.529±0.049] (0.4947, 0.5636)	---	3 [0.624±0.169] (0.4331-0.7548)
	IA-CR+OI-Col	14	---	12 [0.889±0.145] (0.5928-0.9917)	---	0 (0)	2 [0.669±0.065] (0.6225, 0.7150)
	CA-CR+OI-Col	14	---	---	11 [0.922±0.145] (0.5481-0.9993)	1 (0.6499)	2 [0.592±0.160] (0.4793, 0.7050)
Test study A5. Diagrams based on log-ratios of selected immobile major and trace elements	***{Σn} {Σprob} [%prob]***	***70***	***{12} {10.4894} [---]***	***{32} {23.7991} [57%]***	***{16} {12.6613} [31%]***	***{1} {0.6499} [1%]***	***{9} {5.8397} [11%]***

For the explanation of abbreviations, see footnote of Table S17.

Table S50.
Testing of multidimensional diagrams from Quaternary (> 0.33 Ma) intermediate rocks of geothermal fields of the Taupo Volcanic Zone, New Zealand (Browne et al. 1992; Test study A6).

Magma type, Figure name	Figure type	Total number of samples	Number of discriminated samples				
			Arc			Within-plate CR+OI	Collision Col
			IA+CA [$\bar{x} \pm s$] (p_{IA+CA}) Θ	IA [$\bar{x} \pm s$] [p_{IA}] Θ	CA [$\bar{x} \pm s$] [p_{CA}] Θ	[$\bar{x} \pm s$] [p_{CR+OI}] Θ	[$\bar{x} \pm s$] [p_{Col}] Θ
Intermediate; Verma and Verma (2013); log-ratios of all major elements	IA+CA-CR+OI-Col	28	22 [0.708±0.171] (0.5043-0.9941)	---	---	0 (0)	6 [0.693±0.171] (0.5458-0.9988)
	IA-CA-CR+OI	28	---	18 [0.717±0.180] (0.5042-0.9814)	10 [0.655±0.177] (0.4044-0.8706)	0 (0)	---
	IA-CA-Col	28	---	10 [0.716±0.251] (0.3534-0.9779)	9 [0.578±0.158] (0.3477-0.7784)	---	9 [0.591±0.180] (0.4102-0.9984)
	IA-CR+OI-Col	28	---	19 [0.765±0.178] (0.5048-0.9942)	---	0 (0)	9 [0.685±0.158] (0.5308-0.9926)
	CA-CR+OI-Col	28	---	---	22 [0.759±0.136] (0.5419-0.9985)	0 (0)	6 [0.671±0.215] (0.3729-0.9776)
Test study A6. Diagrams based on log-ratios of major elements	***{Σn} {Σprob} [%prob]***	***140***	***{22} {15.5813} [---]***	***{47} {34.6054} [43.9%]***	***{41} {28.4448} [36.1%]***	***{0} {0} [0%]***	***{30} {19.6639} [20.0%]***
Intermediate; Verma and Verma (2013); log-ratios of immobile major and trace elements	IA+CA-CR+OI-Col	5	5 [0.936±0.061] (0.8286-0.9766)	---	---	0 (0)	0 (0)
	IA-CA-CR+OI	5	---	4 [0.753±0.099] (0.6176-0.8295)	1 (0.6733)	0 (0)	---
	IA-CA-Col	5	---	4 [0.747±0.095] (0.6134-0.8247)	1 (0.6179)	---	0 (0)
	IA-CR+OI-Col	5	---	5 [0.919±0.073] (0.7884-0.9607)	---	0 (0)	0 (0)
	CA-CR+OI-Col	5	---	---	5 [0.9744±0.0379] (0.9072-0.9988)	0 (0)	0 (0)
Test studyA6. Diagrams based on log-ratios of immobile major and trace elements	***{Σn} {Σprob} [%prob]***	***25***	***{5} {4.6808} [---]***	***{13} {10.5968} [63%]***	***{7} {6.1633} [37%]***	***{0} {0} [0%]***	***{0} {0} [0%]***

For the explanation of abbreviations, see footnote of Table S17.

Table S51.
Testing of multidimensional diagrams from Neogene-Quaternary (0-4 and 15-23 Ma) basic rocks from SW Indian and SW Pacific seafloor, Indian and Pacific Oceans (Pyle et al. 1995; Test study A7a).

Figure reference; figure type	Discrimination diagram	Total no. of samples (%)	Predicted tectonic affinity and number of discriminated samples (%)				
			IAB	CRB+OIB	CRB	OIB	MORB
Agrawal et al. (2004); adjusted major element concentrations	IAB-CRB-OIB-MORB	9 (100)	0 (0)	---	0 (0)	0 (0)	9 (100)
	IAB-CRB-OIB	9 (100)	2 (22)	---	3 (33)	4 (45)	---
	IAB-CRB-MORB	9 (100)	0 (0)	---	0 (0)	---	9 (100)
	IAB-OIB-MORB	9 (100)	0 (0)	---	---	0 (0)	9 (100)
	CRB-OIB-MORB	9 (100)	---	---	0 (0)	0 (0)	9 (100)
Test study A7a. Synthesis of all five diagrams of Agrawal et al. (2004)		***45 (100)***	***2 (4.4)***	***---***	***3 (6.7)***	***4 (8.9)***	***36 (80)***
Verma et al. (2006); log-ratios of major elements	IAB-CRB-OIB-MORB	9 (100)	0 (0)	---	0 (0)	0 (0)	9 (100)
	IAB-CRB-OIB	9 (100)	0 (0)	---	2 (22)	7 (78)	---
	IAB-CRB-MORB	9 (100)	0 (0)	---	0 (0)	---	9 (100)
	IAB-OIB-MORB	9 (100)	0 (0)	---	---	0 (0)	9 (100)
	CRB-OIB-MORB	9 (100)	---	---	0 (0)	0 (0)	9 (100)
Test study A7a. Synthesis of all five diagrams of Verma et al. (2006)		***45 (100)***	***0 (0)***	***---***	***2 (4.4)***	***7 (15.6)***	***36 (80)***
Agrawal et al. (2008); log-ratios of immobile trace elements	IAB-CRB+OIB-MORB	7 (100)	0 (0)	0 (0)	---	---	7 (100)
	IAB-CRB-OIB	7 (100)	0 (0)	---	2 (29)	5 (71)	---
	IAB-CRB-MORB	7 (100)	0 (0)	---	0 (0)	---	7 (100)
	IAB-OIB-MORB	7 (100)	0 (0)	---	---	0 (0)	7 (100)
	CRB-OIB-MORB	7 (100)	---	---	0 (0)	0 (0)	7 (100)
Test study A7a. Synthesis of all five diagrams of Agrawal *et al.* (2008)		***35 (100)***	***0 (0)***	***0 (---)***	***2 (5.7)***	***5 (14.3)***	***28 (80)***
Verma and Agrawal (2011); log-ratios of immobile major and trace elements	IAB-CRB+OIB-MORB	7 (100)	0 (0)	1 (14)	---	---	6 (86)
	IAB-CRB-OIB	7 (100)	5 (71)	---	2 (29)	0 (0)	---
	IAB-CRB-MORB	7 (100)	0 (0)	---	1 (14)	---	6 (86)
	IAB-OIB-MORB	7 (100)	0 (0)	---	---	0 (0)	7 (100)
	CRB-OIB-MORB	7 (100)	---	---	1 (14)	0 (0)	6 (86)
Test study A7a. Synthesis of all five diagrams of Verma and Agrawal (2011)		***35 (100)***	***5 (14)***	***1 (---)***	***5 (14)***	***0 (0)***	***25(72)***

For the explanation of abbreviations, see footnote of Table 1 or S14.

Table S52.
Testing of multidimensional diagrams from Quaternary basic rocks from Central Indian Ridge, Indian Ocean (Yi et al. 2014; Test study A7b).

Figure reference; figure type	Discrimination diagram	Total no. of samples (%)	Predicted tectonic affinity and number of discriminated samples (%)				
			IAB	CRB+OIB	CRB	OIB	MORB
Agrawal et al. (2004); adjusted major element concentrations	IAB-CRB-OIB-MORB	28 (100)	2 (7)	---	2 (7)	2 (7)	22 (79)
	IAB-CRB-OIB	28 (100)	17 (61)	---	6 (21)	5 (18)	---
	IAB-CRB-MORB	28 (100)	2 (7)	---	4 (14)	---	22 (79)
	IAB-OIB-MORB	28 (100)	2 (7)	---	---	4 (14)	22 (79)
	CRB-OIB-MORB	28 (100)	---	---	0 (0)	4 (14)	24 (86)
Test study A7b. Synthesis of all five diagrams of Agrawal et al. (2004)		***140 (100)***	***23 (16.4)***	***---***	***12 (8.6)***	***15 (10.7)***	***90 (64.3)***
Verma et al. (2006); log-ratios of major elements	IAB-CRB-OIB-MORB	28 (100)	10 (36)	---	0 (0)	1 (3)	17 (61)
	IAB-CRB-OIB	28 (100)	10 (36)	---	2 (7)	16 (57)	---
	IAB-CRB-MORB	28 (100)	9 (32)	---	0 (0)	---	19 (68)
	IAB-OIB-MORB	28 (100)	10 (36)	---	---	1 (3)	17 (61)
	CRB-OIB-MORB	28 (100)	---	---	3 (11)	1 (3)	24 (86)
Test study A7b. Synthesis of all five diagrams of Verma et al. (2006)		***140 (100)***	***39 (27.9)***	***---***	***5 (3.6)***	***19 (13.6)***	***77 (55.0)***
Agrawal *et al.* (2008); log-ratios of immobile trace elements	IAB-CRB+OIB-MORB	17 (100)	3 (18)	0 (0)	---	---	14 (82)
	IAB-CRB-OIB	17 (100)	3 (18)	---	5 (29)	9 (53)	---
	IAB-CRB-MORB	17 (100)	3 (18)	---	0 (0)	---	14 (82)
	IAB-OIB-MORB	17 (100)	3 (18)	---	---	0 (0)	14 (82)
	CRB-OIB-MORB	17 (100)	---	---	0 (0)	0 (0)	17 (100)
Test study A7b. Synthesis of all five diagrams of Agrawal et al. (2008)		***85 (100)***	***12 (14.1)***	***0 (---)***	***5 (5.9)***	***9 (10.6)***	***59 (69.4)***
Verma and Agrawal (2011); log-ratios of immobile major and trace elements	IAB-CRB+OIB-MORB	20 (100)	3 (15)	0 (0)	---	---	17 (85)
	IAB-CRB-OIB	20 (100)	19 (95)	---	1 (5)	0 (0)	---
	IAB-CRB-MORB	20 (100)	3 (15)	---	0 (0)	---	17 (85)
	IAB-OIB-MORB	20 (100)	3 (15)	---	---	0 (0)	17 (85)
	CRB-OIB-MORB	20 (100)	---	---	0 (0)	1 (5)	19 (95)
Test study A7b. Synthesis of all five diagrams of Verma and Agrawal (2011)		***100 (100)***	***28 (28.0)***	***0 (---)***	***1 (1.0)***	***1 (1.0)***	***70 (70.0)***

For the explanation of abbreviations, see footnote of Table 1 or S14.

Table S53.
Testing of multidimensional diagrams from Quaternary intermediate rocks from the Aeolian Island, Italy (Del Moro et al. 2011; Test study A8).

Magma type, Figure name	Figure type	Total number of samples	Number of discriminated samples				
			Arc			Within-plate	Collision
			IA+CA [$\bar{x} \pm s$] (p_{IA+CA}) Θ	IA [$\bar{x} \pm s$] [p_{IA}] Θ	CA [$\bar{x} \pm s$] [p_{CA}] Θ	CR+OI [$\bar{x} \pm s$] [p_{CR+OI}] Θ	Col [$\bar{x} \pm s$] [p_{Col}] Θ
Intermediate; Verma and Verma (2013); log-ratios of all major elements	IA+CA-CR+OI-Col	7	0 (0)	---	---	0 (0)	7 [0.99996±0.00004] (0.9999-1.0000)
	IA-CA-CR+OI	7	---	0 (0)	6 [0.812±0.197] (0.5043-0.9999)	1 (0.4546)	---
	IA-CA-Col	7	---	0 (0)	0 (0)	---	7 [0.99868±0.00204] (0.9948-1.0000)
	IA-CR+OI-Col	7	---	0 (0)	---	0 (0)	7 [0.99993±0.00014] (0.9996-1.0000)
	CA-CR+OI-Col	7	---	---	0 (0)	0 (0)	7 [0.9722±0.0280] (0.9321-0.9994)
Test study A8. Diagrams based on log-ratios of major elements	***{Σn} {Σprob} [%prob]***	***35***	***{0} {0} [0%]***	***{0} {0} [0%]***	***{6} {4.8713} [15%]***	***{1} {0.4546} [1%]***	***{28} {27.7956} [84%]***
Intermediate; Verma and Verma (2013); log-ratios of immobile trace elements	IA+CA-CR+OI-Col	7	0 (0)	---	---	0 (0)	7 [0.939±0.071] (0.7932-0.9970)
	IA-CA-CR+OI	7	---	0 (0)	4 [0.660±0.120] (0.4889-0.7676)	3 [0.868±0.197] (0.6398-0.9823)	---
	IA-CA-Col	7	---	0 (0)	0 (0)	---	7 [0.9719±0.0256] (0.9309-0.9926)
	IA-CR+OI-Col	7	---	0 (0)	---	0 (0)	7 [0.913±0.108] (0.6929-0.9952)
	CA-CR+OI-Col	7	---	---	0 (0)	0 (0)	7 [0.922±0.109] (0.6869-0.9948)
Test study A8. Diagrams based on log-ratios of immobile trace elements	***{Σn} {Σprob} [%prob]***	***35***	***{0} {0} [0%]***	***{0} {0} [0%]***	***{4} {2.6402} [9%]***	***{3} {2.6030} [8%]***	***{28} {26.2215} [83%]***

For the explanation of abbreviations, see footnote of Table S17.

Table S54.

Testing of multidimensional diagrams from Quaternary acid rocks from the Aeolian Island, Italy (Del Moro et al. 2011; Test study A8).

Magma type, Figure name	Figure type	Total number of samples	Number of discriminated samples				
			Arc			Within-plate	Collision Col
			IA+CA [$\bar{x} \pm s$] (p_{IA+CA}) Θ	IA [$\bar{x} \pm s$] [p_{IA}] Θ	CA [$\bar{x} \pm s$] [p_{CA}] Θ	CR+OI [$\bar{x} \pm s$] [p_{CR+OI}] Θ	[$\bar{x} \pm s$] [p_{Col}] Θ
Acid; Verma et al. (2012); All major elements	IA+CA-CR+OI-Col	10	4 [0.793±0.201] (0.5185-0.9877)	---	---	1 (0.5346)	5 [0.736±0.231] (0.5020-0.9704)
	IA-CA-CR+OI	10	---	6 [0.773±0.181] (0.5775-0.9982)	1 (0.5718)	3 [0.688±0.235] (0.4576-0.9270)	---
	IA-CA-Col	10	---	3 [0.790±0.205] (0.5876-0.9983)	1 (0.8847)	---	6 [0.902±0.153] (0.5963-0.9987)
	IA-CR+OI-Col	10	---	2 [0.713±0.240] (0.5437, 0.8831)	---	1 (0.7291)	7 [0.951±0.047] (0.8596-0.9889)
	CA-CR+OI-Col	10	---	---	7 [0.9703±0.0410] (0.8924-1.0000)	1 (0.6449)	2 [0.697±0.291] (0.4917, 0.9025)
Test study A8. Diagrams based on log-ratios of major elements	***{Σn} {Σprob} [%prob]***	***50***	***{4} {3.1709} [---]***	***{11} {8.4333} [24%]***	***{9} {8.2488} [24%]***	***{6} {3.9731} [10%]***	***{20} {17.1507} [42%]***
Acid; Verma et al. (2013); All major elements	IA+CA-CR+OI-Col	10	4 [0.795±0.215] (0.5030-0.9983)	---	---	1 (0.5617)	5 [0.819±0.140] (0.6095-0.9645)
	IA-CA-CR+OI	10	---	5 [0.904±0.204] (0.5392-1.0000)	0 (0)	5 [0.802±0.096] (0.7246-0.9310)	---
	IA-CA-Col	10	---	4 [0.9991±0.0011] (0.9980-1.0000)	1 (0.8844)	---	5 [0.99939±0.00033] (0.9990-0.9997)
	IA-CR+OI-Col	10	---	5 [0.940±0.082] (0.8403-1.0000)	---	1 (0.6177)	4 [0.834±0.095] (0.7233-0.9536)
	CA-CR+OI-Col	10	---	---	4 [0.822±0.167] (0.6768-0.9997)	2 [0.5634±0.0240] (0.5465, 0.5804)	4 [0.763±0.145] (0.6131-0.9453)
Test study A8. Diagrams based on log-ratios of major elements	***{Σn} {Σprob} [%prob]***	***50***	***{4} {3.1790} [---]***	***{14} {13.2117} [37%]***	***{5} {4.1727} [12%]***	***{9} {6.3171} [14%]***	***{18} {15.4767} [37%]***
Acid; Verma et al. (2013); log-ratios of immobile major and trace elements	IA+CA-CR+OI-Col	10	0 (0)	---	---	1 (0.4611)	9 [0.766±0.119] (0.5796-0.9446)
	IA-CA-CR+OI	10	---	0 (0)	5 [0.5284±0.0195] (0.5037-0.5492)	5 [0.577±0.085] (0.5132-0.7105)	---
	IA-CA-Col	10	---	0 (0)	0 (0)	---	10 [0.748±0.122] (0.5632-0.9144)
	IA-CR+OI-Col	10	---	0 (0)	---	0 (0)	10 [0.781±0.119] (0.5388-0.9439)
	CA-CR+OI-Col	10	---	---	0 (0)	0 (0)	10 [0.685±0.163] (0.3833-0.9117)
Test study A8. Diagrams based on log-ratios of immobile major and trace elements	***{Σn} {Σprob} [%prob]***	***50***	***{0} {0} [0%]***	***{0} {0} [0%]***	***{5} {2.6418} [8%]***	***{6} {3.3471} [10%]***	***{39} {29.0341} [82%]***
Acid; Verma et al. (2013); log-ratios of immobile trace elements	IA+CA-CR+OI-Col	10	0 (0)	---	---	4 [0.773±0.195] (0.5366-0.9645)	6 [0.764±0.138] (0.5160-0.9392)
	IA-CA-CR+OI	10	---	0 (0)	6 [0.821±0.163] (0.6021-0.9999)	4 [0.907±0.105] (0.7764-0.9998)	---
	IA-CA-Col	10	---	0 (0)	1 (0.6838)	---	9 [0.812±0.084] (0.6754-0.9554)
	IA-CR+OI-Col	10	---	0 (0)	---	3 [0.755±0.213] (0.5764-0.9905)	7 [0.855±0.169] (0.5299-1.0000)
	CA-CR+OI-Col	10	---	---	0 (0)	2 [0.834±0.157] (0.7222, 0.9448)	8 [0.758±0.154] (0.4944-0.9651)
Test study A8. Diagrams based on log-ratios of immobile trace elements	***{Σn} {Σprob} [%prob]***	***50***	***{0} {0} [0%]***	***{0} {0} [0%]***	***{7} {5.6121} [14%]***	***{13} {10.6515} [26%]***	***{30} {23.9439} [60%]***

For the explanation of abbreviations, see footnote of Table S17.

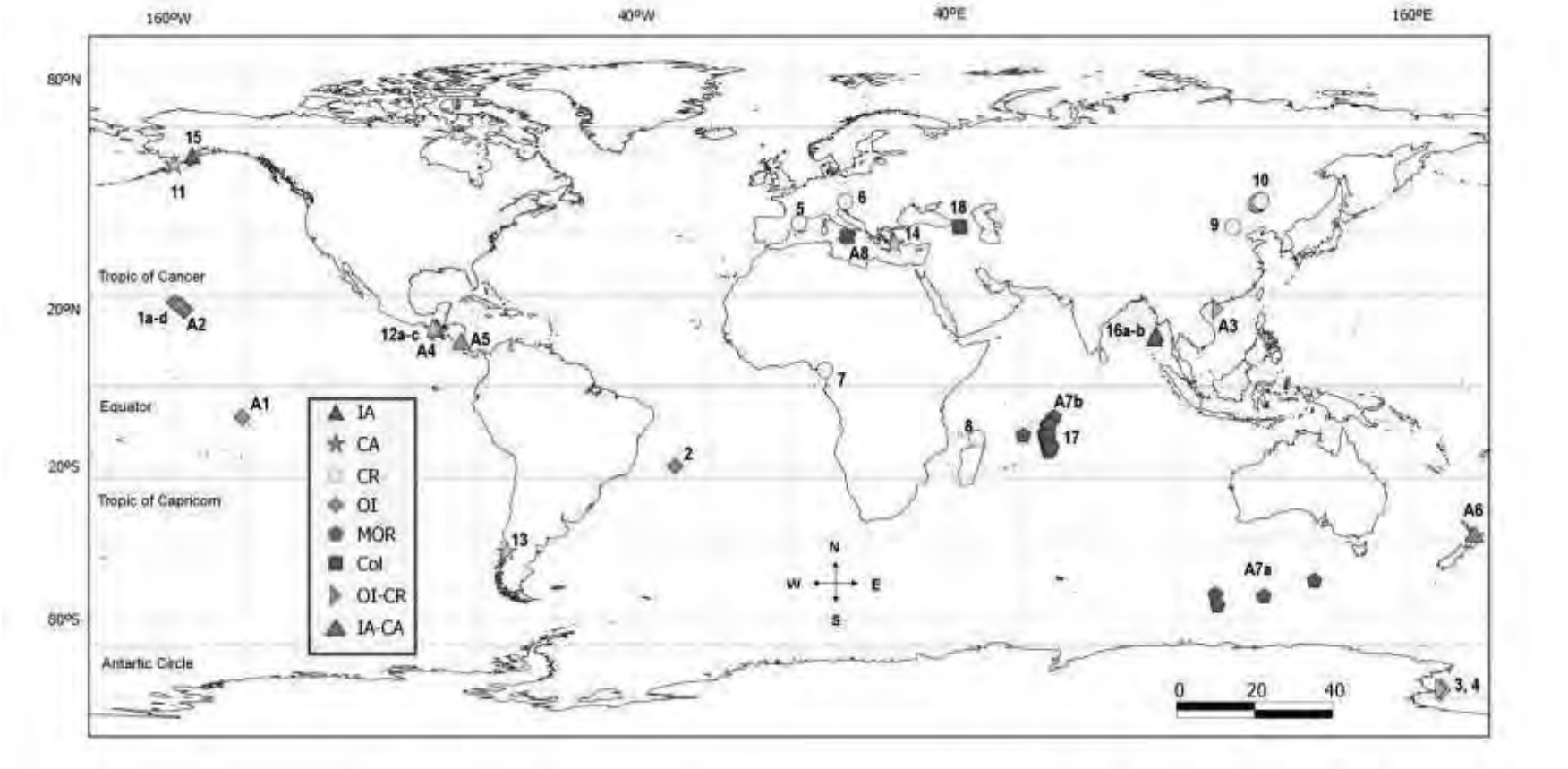

Fig. S1. Schematic locations of the 18 test (numbers 1 to 18) and 8 (numbers A1 to A8) application studies.

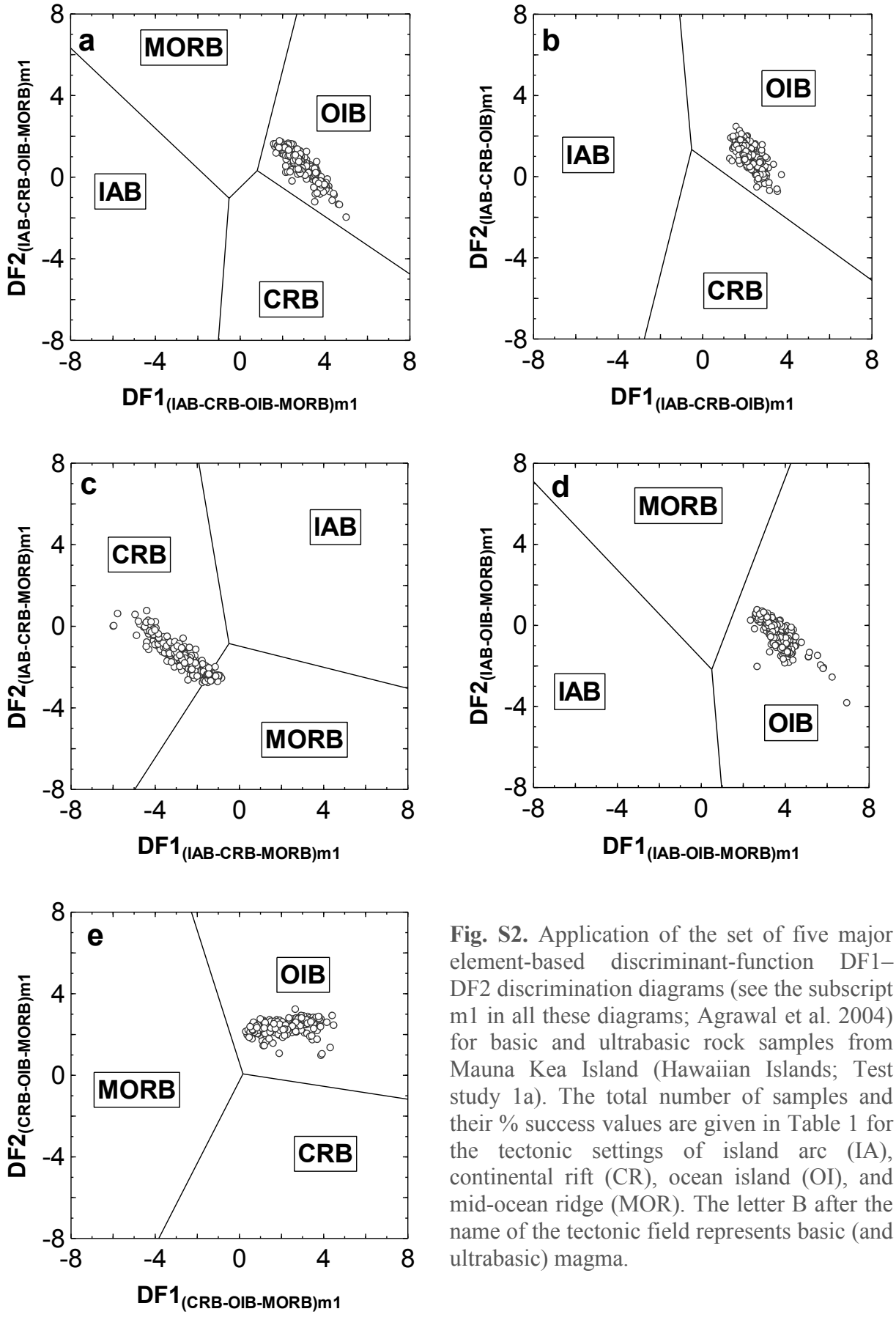

Fig. S2. Application of the set of five major element-based discriminant-function DF1–DF2 discrimination diagrams (see the subscript m1 in all these diagrams; Agrawal et al. 2004) for basic and ultrabasic rock samples from Mauna Kea Island (Hawaiian Islands; Test study 1a). The total number of samples and their % success values are given in Table 1 for the tectonic settings of island arc (IA), continental rift (CR), ocean island (OI), and mid-ocean ridge (MOR). The letter B after the name of the tectonic field represents basic (and ultrabasic) magma.

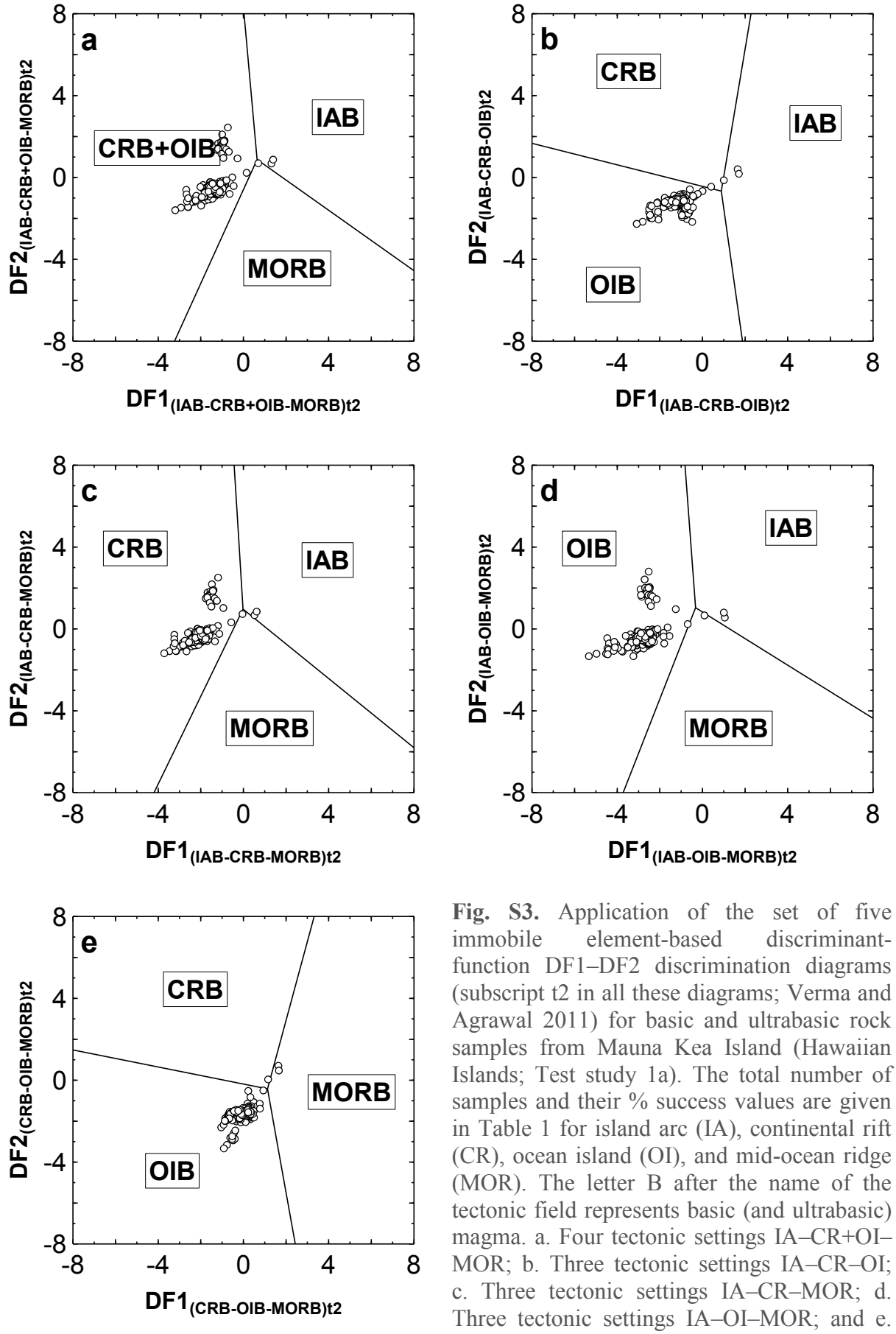

Fig. S3. Application of the set of five immobile element-based discriminant-function DF1–DF2 discrimination diagrams (subscript t2 in all these diagrams; Verma and Agrawal 2011) for basic and ultrabasic rock samples from Mauna Kea Island (Hawaiian Islands; Test study 1a). The total number of samples and their % success values are given in Table 1 for island arc (IA), continental rift (CR), ocean island (OI), and mid-ocean ridge (MOR). The letter B after the name of the tectonic field represents basic (and ultrabasic) magma. a. Four tectonic settings IA–CR+OI–MOR; b. Three tectonic settings IA–CR–OI; c. Three tectonic settings IA–CR–MOR; d. Three tectonic settings IA–OI–MOR; and e. Three tectonic settings CR–OI–MOR.

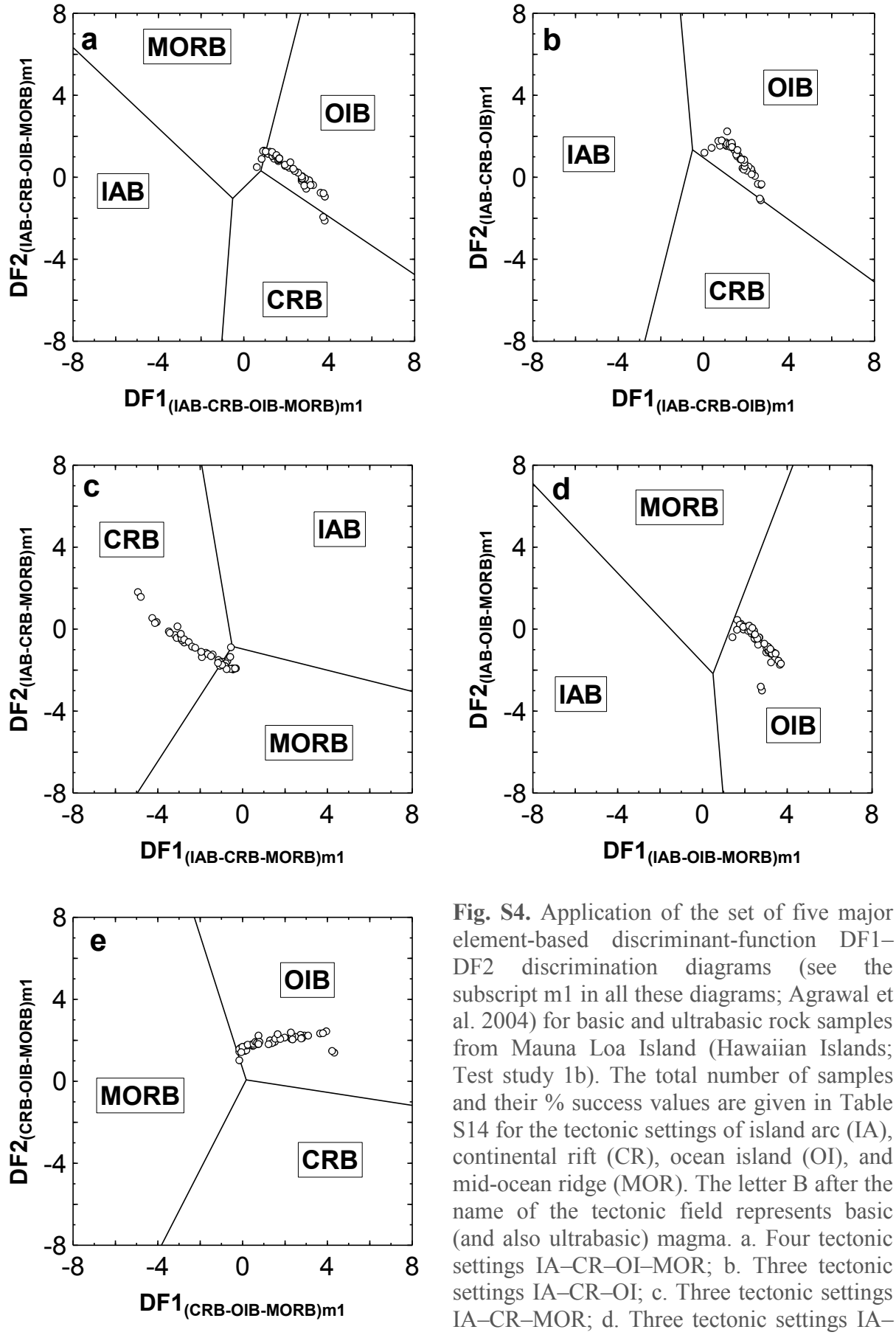

Fig. S4. Application of the set of five major element-based discriminant-function DF1–DF2 discrimination diagrams (see the subscript m1 in all these diagrams; Agrawal et al. 2004) for basic and ultrabasic rock samples from Mauna Loa Island (Hawaiian Islands; Test study 1b). The total number of samples and their % success values are given in Table S14 for the tectonic settings of island arc (IA), continental rift (CR), ocean island (OI), and mid-ocean ridge (MOR). The letter B after the name of the tectonic field represents basic (and also ultrabasic) magma. a. Four tectonic settings IA–CR–OI–MOR; b. Three tectonic settings IA–CR–OI; c. Three tectonic settings IA–CR–MOR; d. Three tectonic settings IA–OI–MOR; and e. Three tectonic settings CR–OI–MOR.

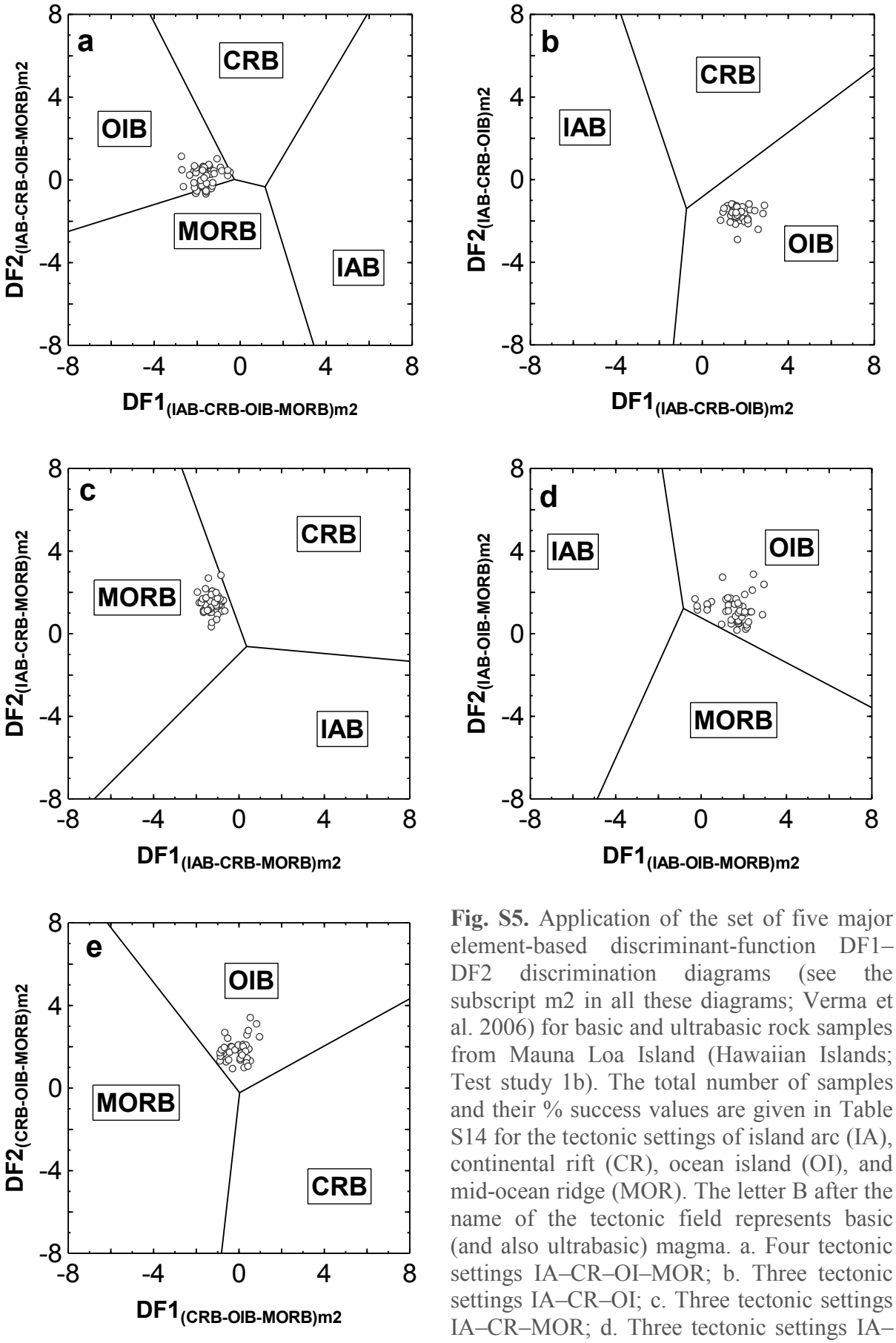

Fig. S5. Application of the set of five major element-based discriminant-function DF1–DF2 discrimination diagrams (see the subscript m2 in all these diagrams; Verma et al. 2006) for basic and ultrabasic rock samples from Mauna Loa Island (Hawaiian Islands; Test study 1b). The total number of samples and their % success values are given in Table S14 for the tectonic settings of island arc (IA), continental rift (CR), ocean island (OI), and mid-ocean ridge (MOR). The letter B after the name of the tectonic field represents basic (and also ultrabasic) magma. a. Four tectonic settings IA–CR–OI–MOR; b. Three tectonic settings IA–CR–OI; c. Three tectonic settings IA–CR–MOR; d. Three tectonic settings IA–OI–MOR; and e. Three tectonic settings CR–OI–MOR.

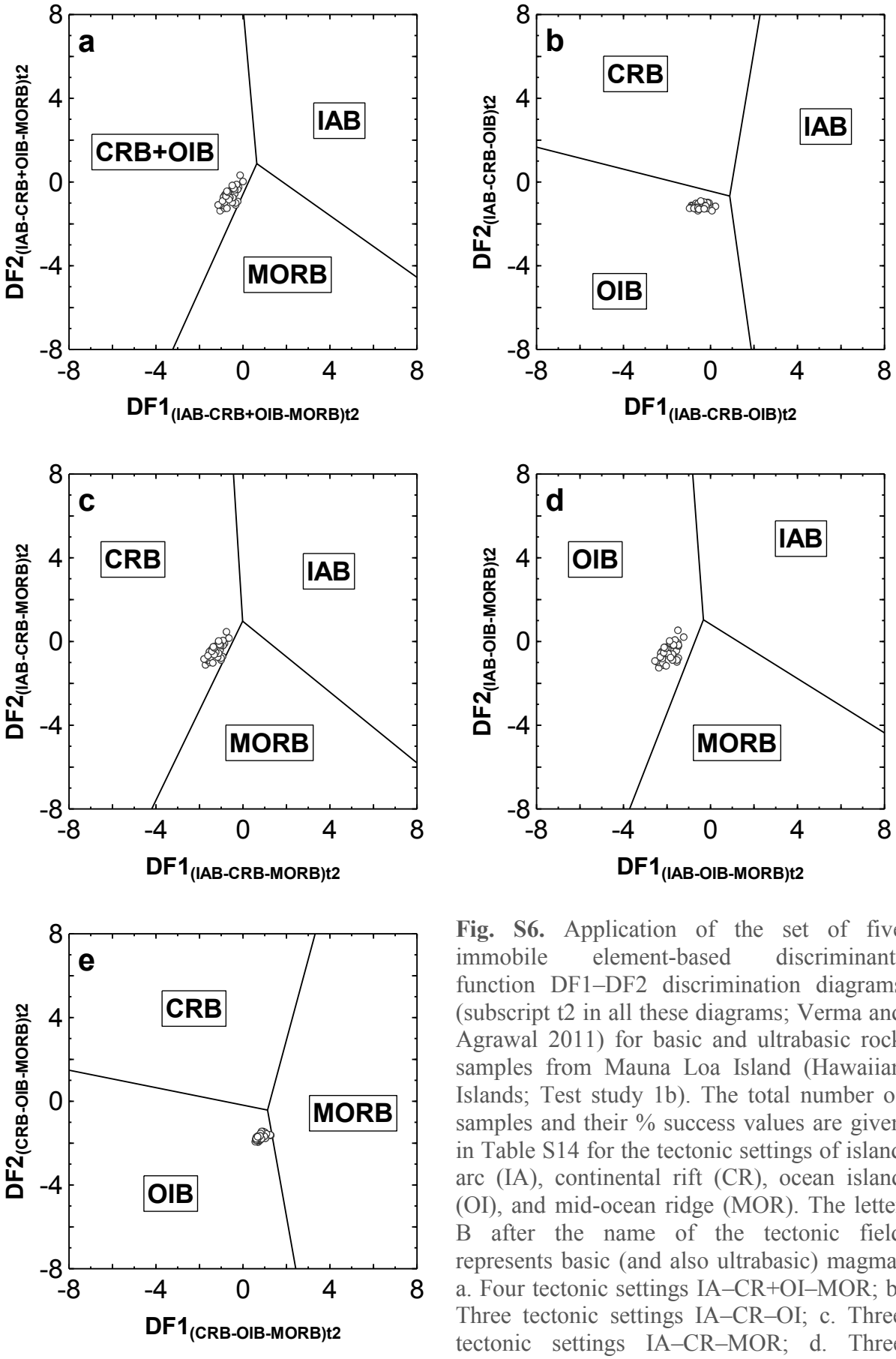

Fig. S6. Application of the set of five immobile element-based discriminant-function DF1–DF2 discrimination diagrams (subscript t2 in all these diagrams; Verma and Agrawal 2011) for basic and ultrabasic rock samples from Mauna Loa Island (Hawaiian Islands; Test study 1b). The total number of samples and their % success values are given in Table S14 for the tectonic settings of island arc (IA), continental rift (CR), ocean island (OI), and mid-ocean ridge (MOR). The letter B after the name of the tectonic field represents basic (and also ultrabasic) magma. a. Four tectonic settings IA–CR+OI–MOR; b. Three tectonic settings IA–CR–OI; c. Three tectonic settings IA–CR–MOR; d. Three tectonic settings IA–OI–MOR; and e. Three tectonic settings CR–OI–MOR.

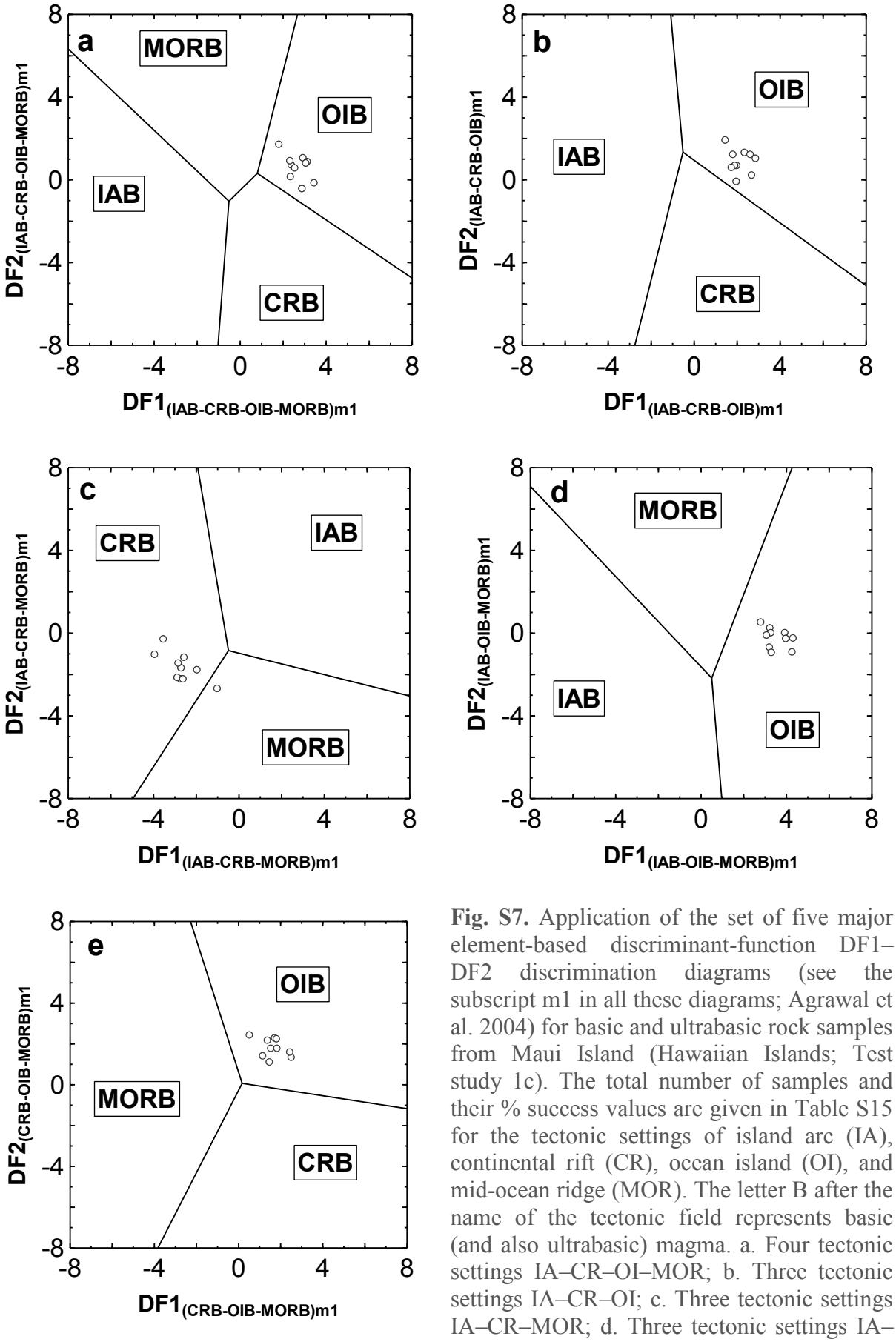

Fig. S7. Application of the set of five major element-based discriminant-function DF1–DF2 discrimination diagrams (see the subscript m1 in all these diagrams; Agrawal et al. 2004) for basic and ultrabasic rock samples from Maui Island (Hawaiian Islands; Test study 1c). The total number of samples and their % success values are given in Table S15 for the tectonic settings of island arc (IA), continental rift (CR), ocean island (OI), and mid-ocean ridge (MOR). The letter B after the name of the tectonic field represents basic (and also ultrabasic) magma. a. Four tectonic settings IA–CR–OI–MOR; b. Three tectonic settings IA–CR–OI; c. Three tectonic settings IA–CR–MOR; d. Three tectonic settings IA–OI–MOR; and e. Three tectonic settings CR–OI–MOR.

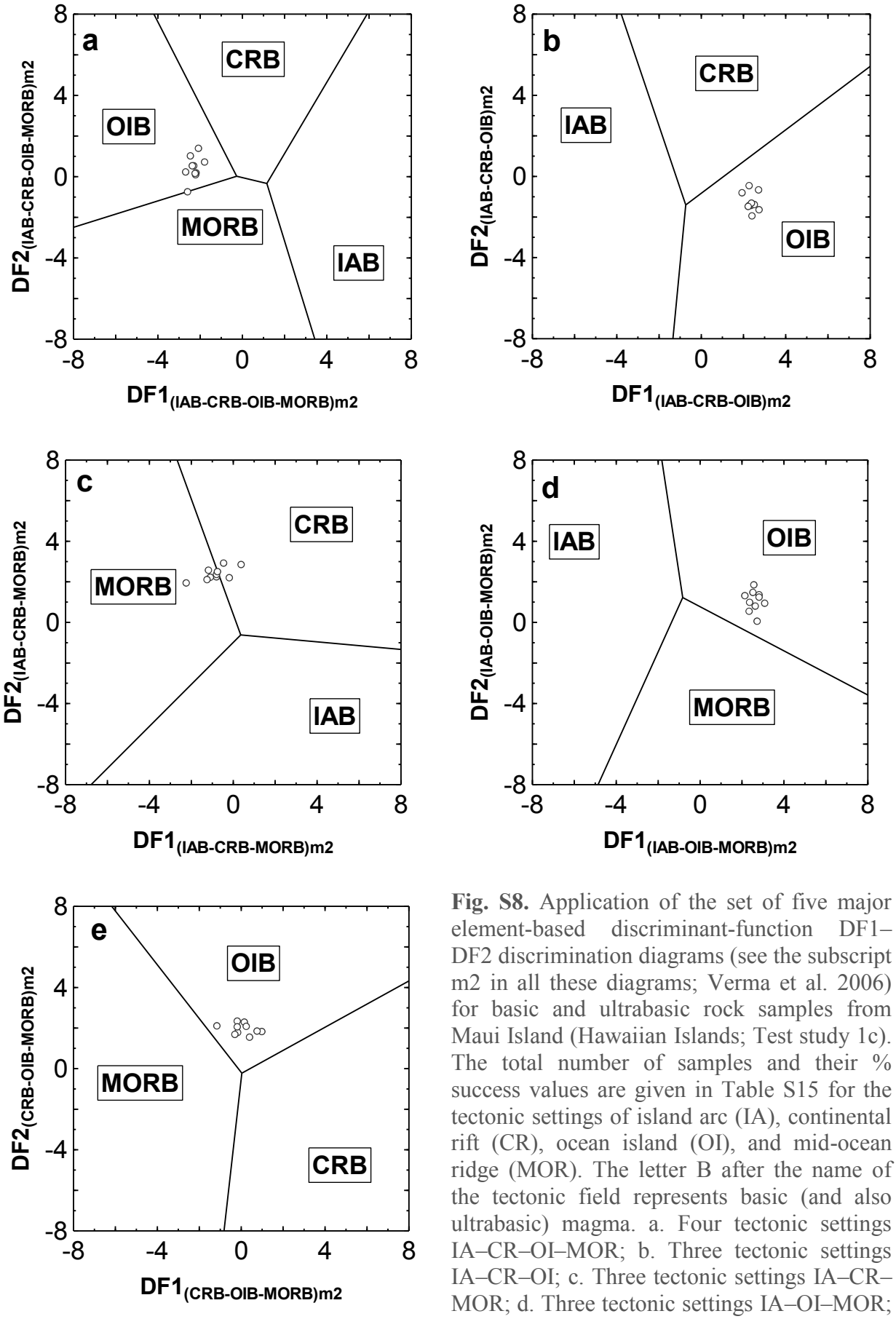

Fig. S8. Application of the set of five major element-based discriminant-function DF1–DF2 discrimination diagrams (see the subscript m2 in all these diagrams; Verma et al. 2006) for basic and ultrabasic rock samples from Maui Island (Hawaiian Islands; Test study 1c). The total number of samples and their % success values are given in Table S15 for the tectonic settings of island arc (IA), continental rift (CR), ocean island (OI), and mid-ocean ridge (MOR). The letter B after the name of the tectonic field represents basic (and also ultrabasic) magma. a. Four tectonic settings IA–CR–OI–MOR; b. Three tectonic settings IA–CR–OI; c. Three tectonic settings IA–CR–MOR; d. Three tectonic settings IA–OI–MOR; and e. Three tectonic settings CR–OI–MOR.

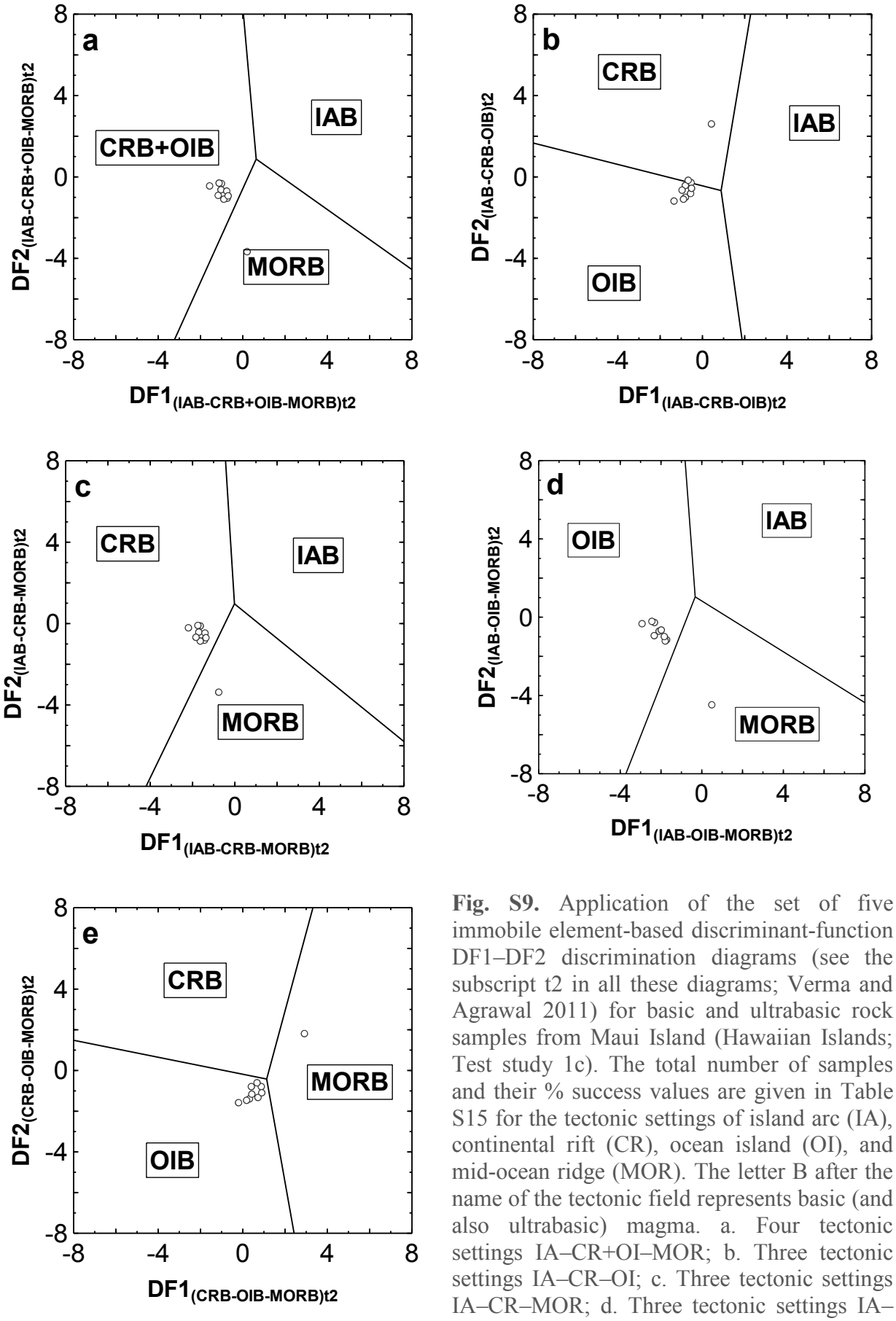

Fig. S9. Application of the set of five immobile element-based discriminant-function DF1–DF2 discrimination diagrams (see the subscript t2 in all these diagrams; Verma and Agrawal 2011) for basic and ultrabasic rock samples from Maui Island (Hawaiian Islands; Test study 1c). The total number of samples and their % success values are given in Table S15 for the tectonic settings of island arc (IA), continental rift (CR), ocean island (OI), and mid-ocean ridge (MOR). The letter B after the name of the tectonic field represents basic (and also ultrabasic) magma. a. Four tectonic settings IA–CR+OI–MOR; b. Three tectonic settings IA–CR–OI; c. Three tectonic settings IA–CR–MOR; d. Three tectonic settings IA–OI–MOR; and e. Three tectonic settings CR–OI–MOR.

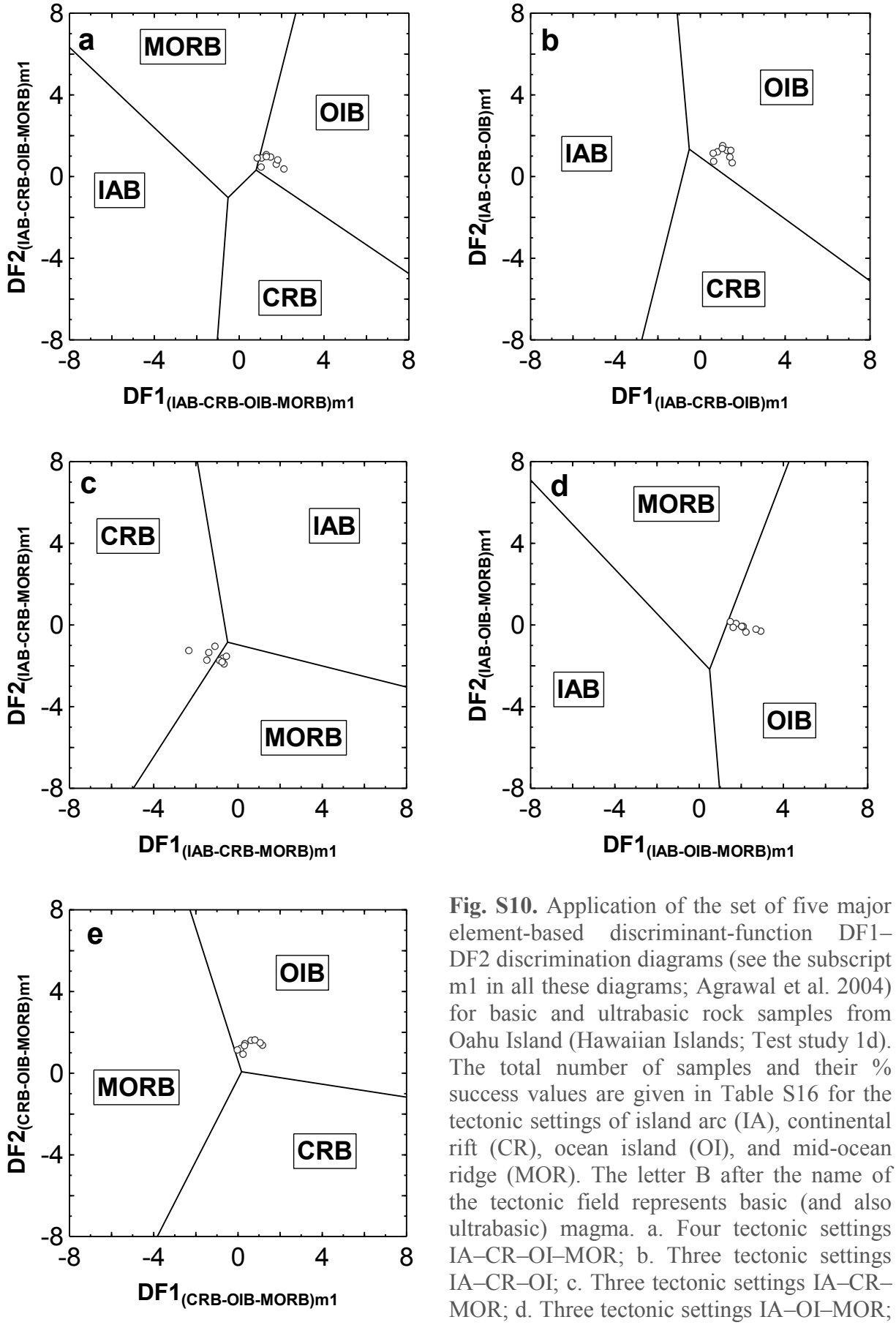

Fig. S10. Application of the set of five major element-based discriminant-function DF1–DF2 discrimination diagrams (see the subscript m1 in all these diagrams; Agrawal et al. 2004) for basic and ultrabasic rock samples from Oahu Island (Hawaiian Islands; Test study 1d). The total number of samples and their % success values are given in Table S16 for the tectonic settings of island arc (IA), continental rift (CR), ocean island (OI), and mid-ocean ridge (MOR). The letter B after the name of the tectonic field represents basic (and also ultrabasic) magma. a. Four tectonic settings IA–CR–OI–MOR; b. Three tectonic settings IA–CR–OI; c. Three tectonic settings IA–CR–MOR; d. Three tectonic settings IA–OI–MOR; and e. Three tectonic settings CR–OI–MOR.

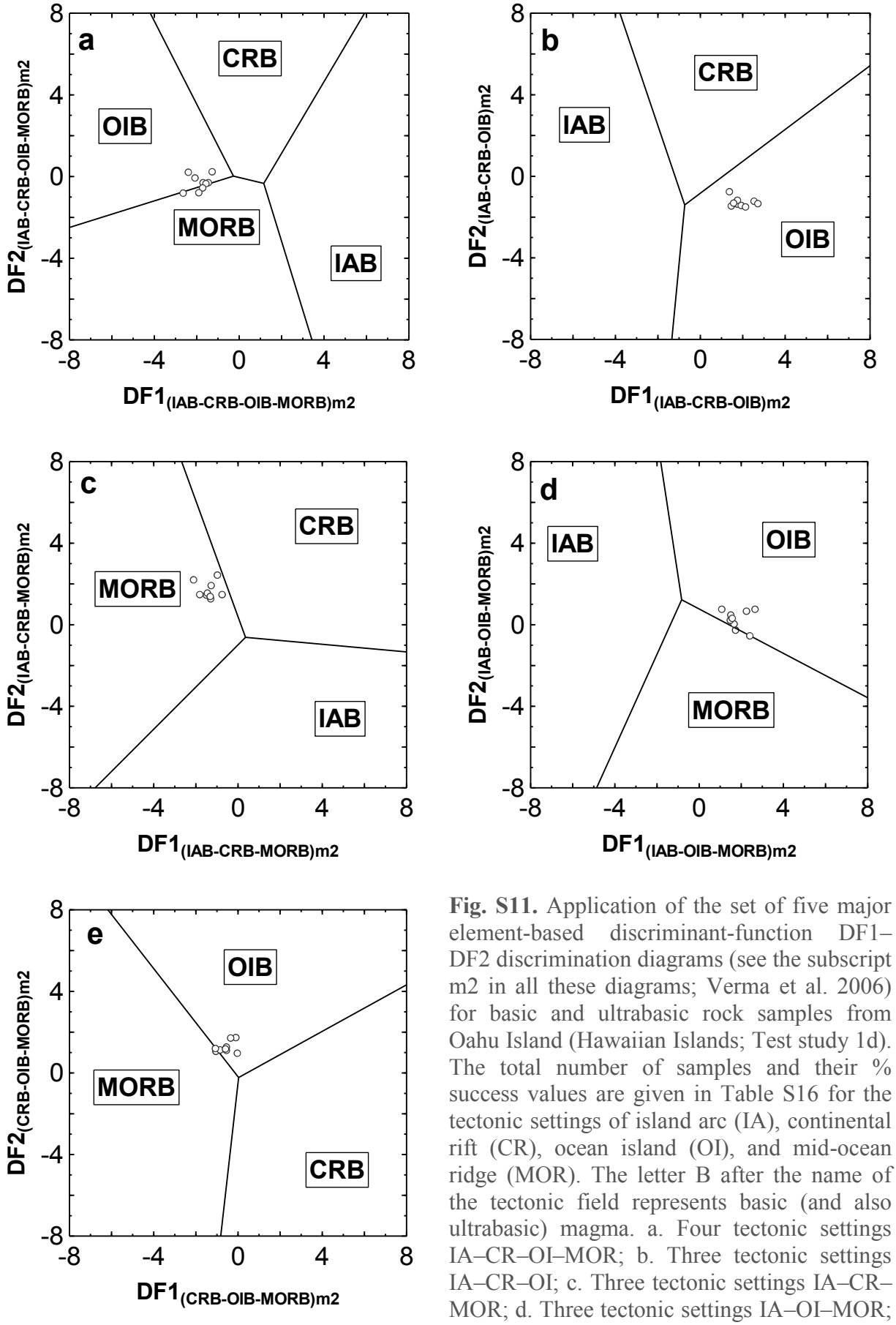

Fig. S11. Application of the set of five major element-based discriminant-function DF1–DF2 discrimination diagrams (see the subscript m2 in all these diagrams; Verma et al. 2006) for basic and ultrabasic rock samples from Oahu Island (Hawaiian Islands; Test study 1d). The total number of samples and their % success values are given in Table S16 for the tectonic settings of island arc (IA), continental rift (CR), ocean island (OI), and mid-ocean ridge (MOR). The letter B after the name of the tectonic field represents basic (and also ultrabasic) magma. a. Four tectonic settings IA–CR–OI–MOR; b. Three tectonic settings IA–CR–OI; c. Three tectonic settings IA–CR–MOR; d. Three tectonic settings IA–OI–MOR; and e. Three tectonic settings CR–OI–MOR.

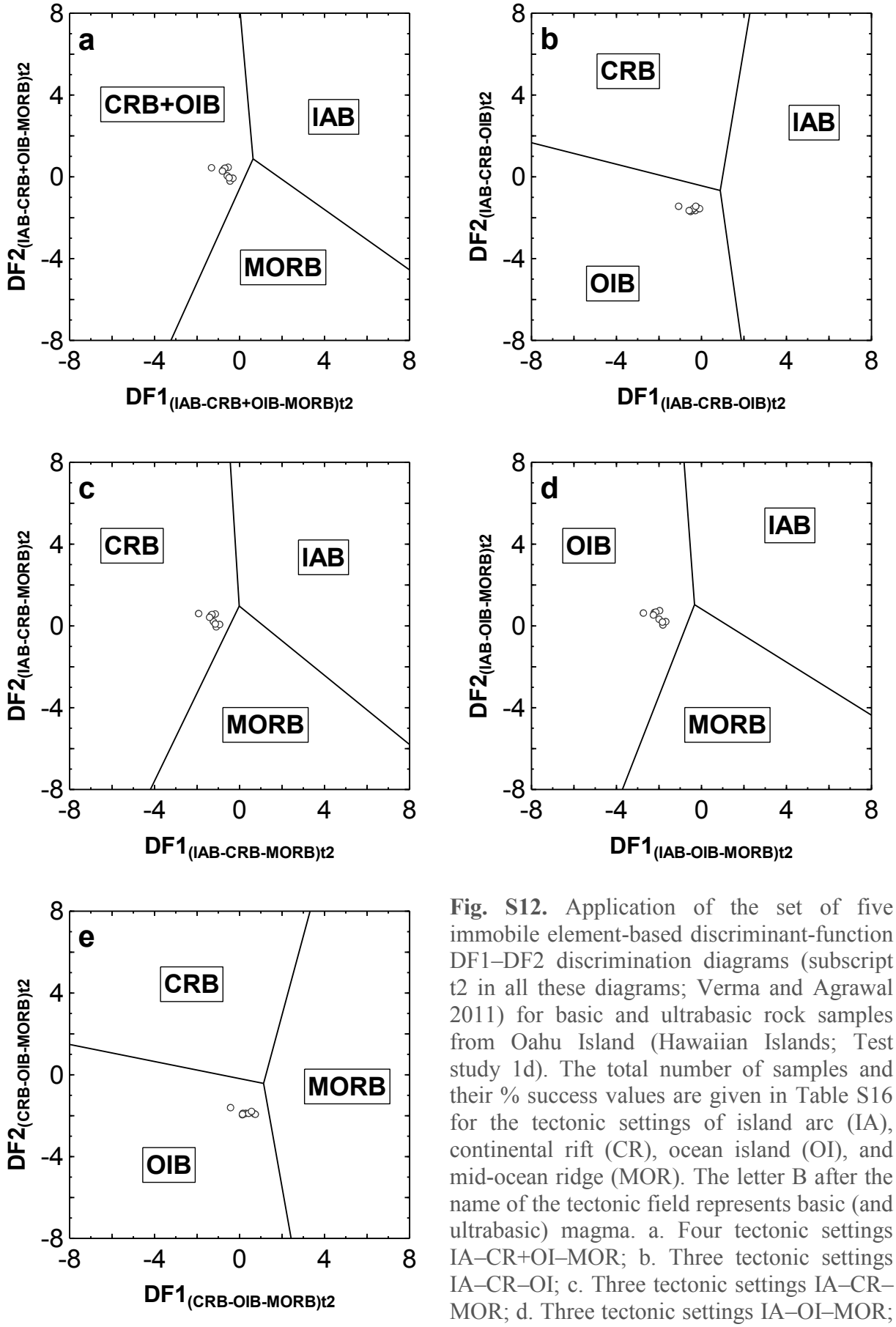

Fig. S12. Application of the set of five immobile element-based discriminant-function DF1–DF2 discrimination diagrams (subscript t2 in all these diagrams; Verma and Agrawal 2011) for basic and ultrabasic rock samples from Oahu Island (Hawaiian Islands; Test study 1d). The total number of samples and their % success values are given in Table S16 for the tectonic settings of island arc (IA), continental rift (CR), ocean island (OI), and mid-ocean ridge (MOR). The letter B after the name of the tectonic field represents basic (and ultrabasic) magma. a. Four tectonic settings IA–CR+OI–MOR; b. Three tectonic settings IA–CR–OI; c. Three tectonic settings IA–CR–MOR; d. Three tectonic settings IA–OI–MOR; and e. Three tectonic settings CR–OI–MOR.

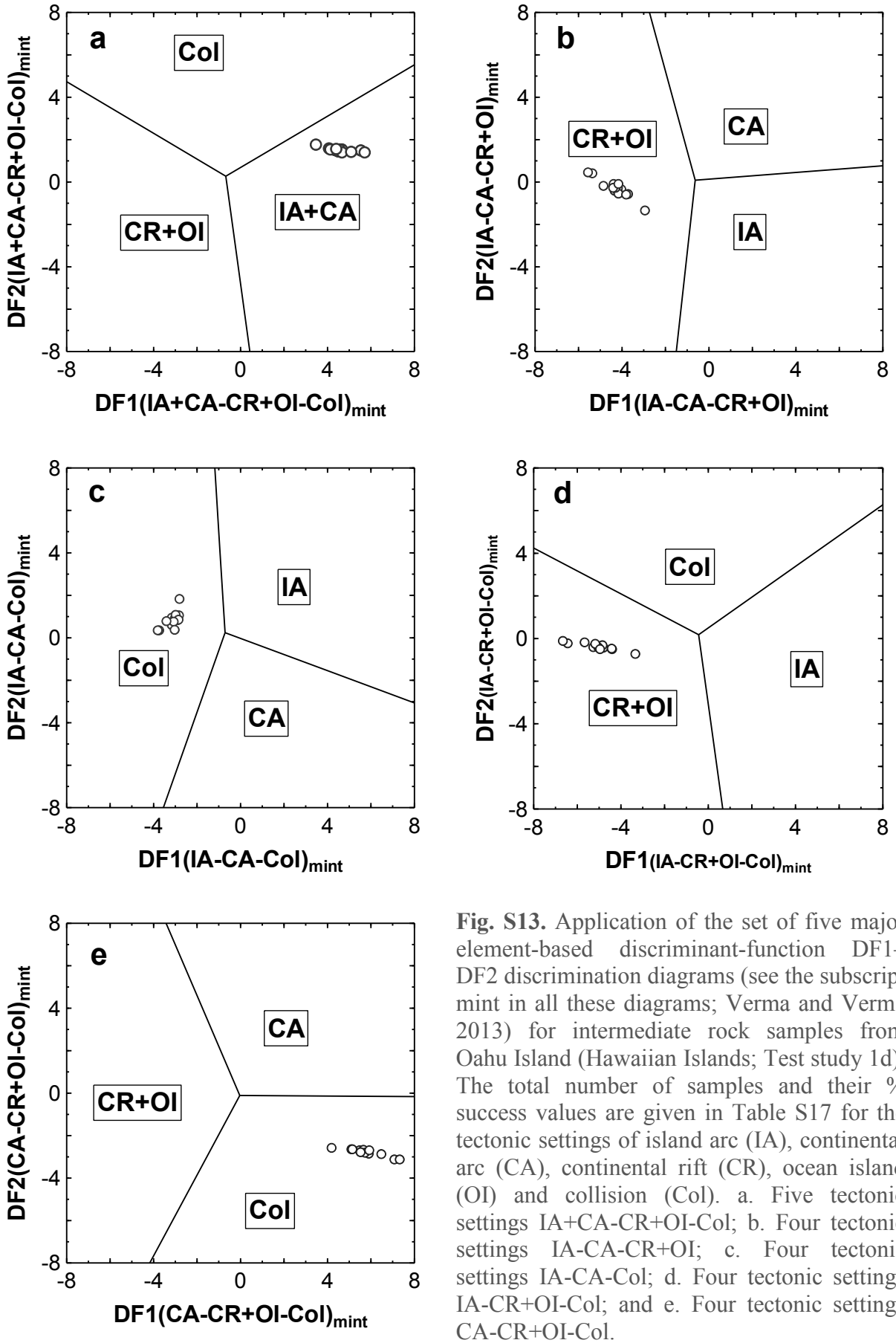

Fig. S13. Application of the set of five major element-based discriminant-function DF1–DF2 discrimination diagrams (see the subscript mint in all these diagrams; Verma and Verma 2013) for intermediate rock samples from Oahu Island (Hawaiian Islands; Test study 1d). The total number of samples and their % success values are given in Table S17 for the tectonic settings of island arc (IA), continental arc (CA), continental rift (CR), ocean island (OI) and collision (Col). a. Five tectonic settings IA+CA-CR+OI-Col; b. Four tectonic settings IA-CA-CR+OI; c. Four tectonic settings IA-CA-Col; d. Four tectonic settings IA-CR+OI-Col; and e. Four tectonic settings CA-CR+OI-Col.

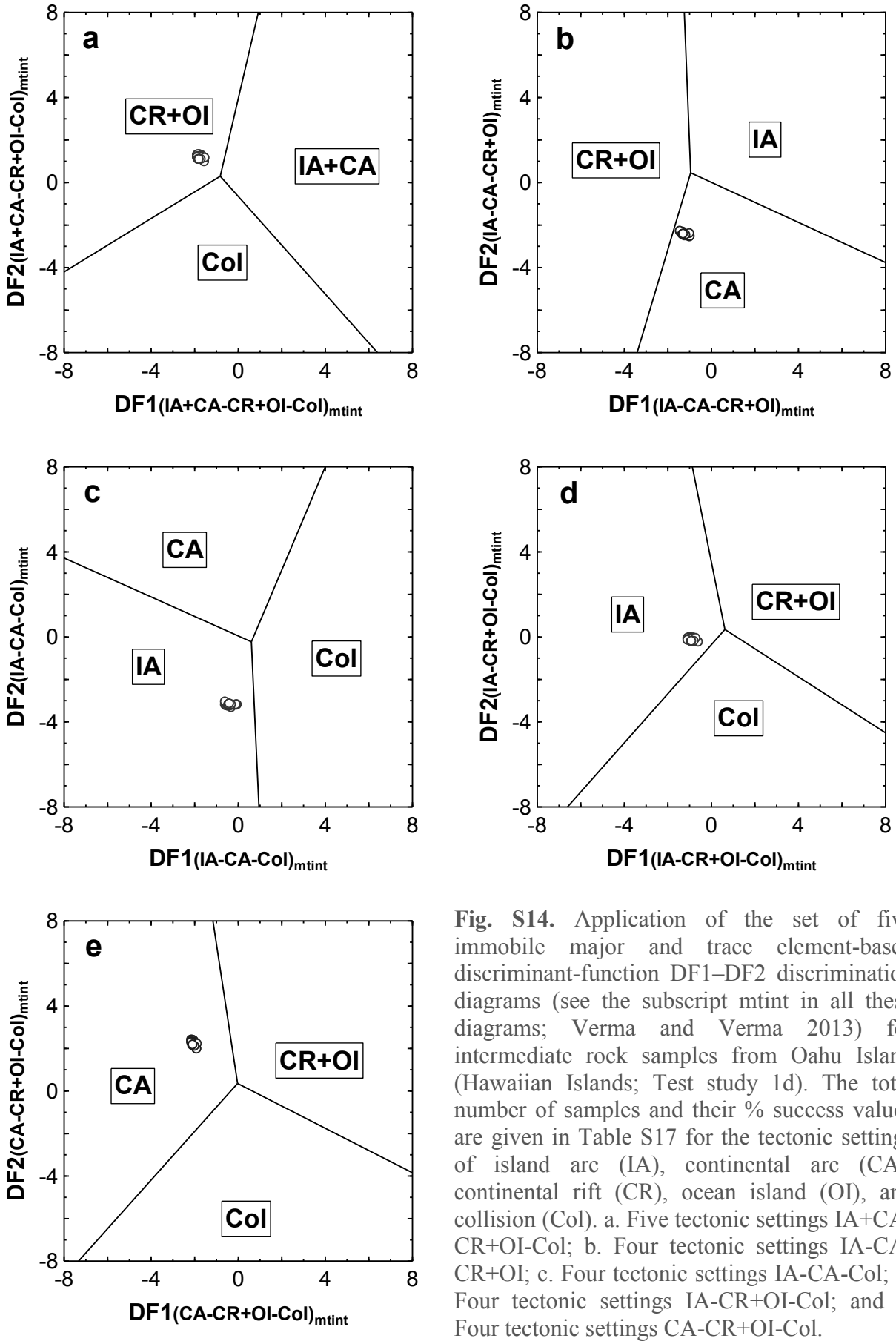

Fig. S14. Application of the set of five immobile major and trace element-based discriminant-function DF1–DF2 discrimination diagrams (see the subscript mtint in all these diagrams; Verma and Verma 2013) for intermediate rock samples from Oahu Island (Hawaiian Islands; Test study 1d). The total number of samples and their % success values are given in Table S17 for the tectonic settings of island arc (IA), continental arc (CA), continental rift (CR), ocean island (OI), and collision (Col). a. Five tectonic settings IA+CA-CR+OI-Col; b. Four tectonic settings IA-CA-CR+OI; c. Four tectonic settings IA-CA-Col; d. Four tectonic settings IA-CR+OI-Col; and e. Four tectonic settings CA-CR+OI-Col.

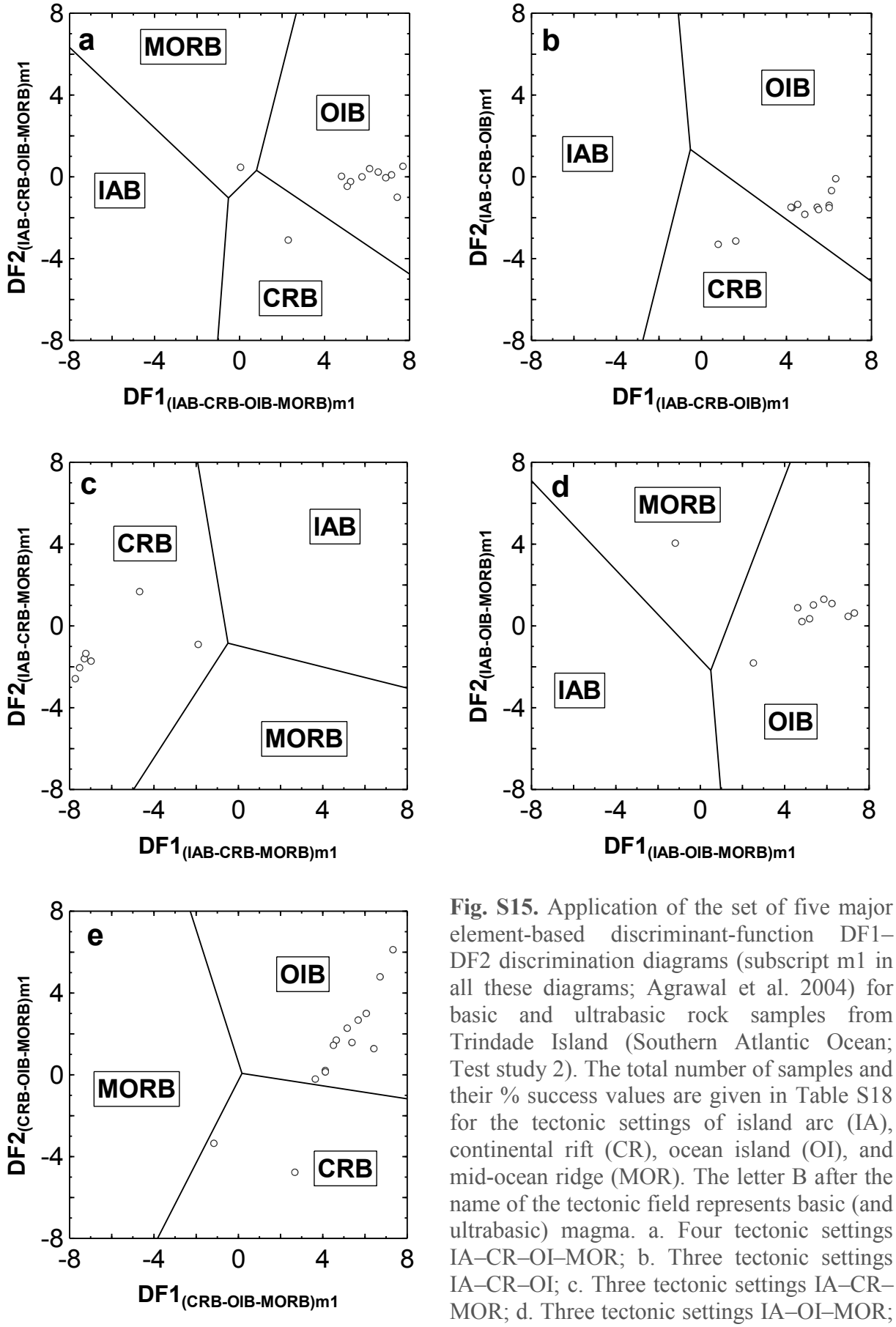

Fig. S15. Application of the set of five major element-based discriminant-function DF1–DF2 discrimination diagrams (subscript m1 in all these diagrams; Agrawal et al. 2004) for basic and ultrabasic rock samples from Trindade Island (Southern Atlantic Ocean; Test study 2). The total number of samples and their % success values are given in Table S18 for the tectonic settings of island arc (IA), continental rift (CR), ocean island (OI), and mid-ocean ridge (MOR). The letter B after the name of the tectonic field represents basic (and ultrabasic) magma. a. Four tectonic settings IA–CR–OI–MOR; b. Three tectonic settings IA–CR–OI; c. Three tectonic settings IA–CR–MOR; d. Three tectonic settings IA–OI–MOR; and e. Three tectonic settings CR–OI–MOR.

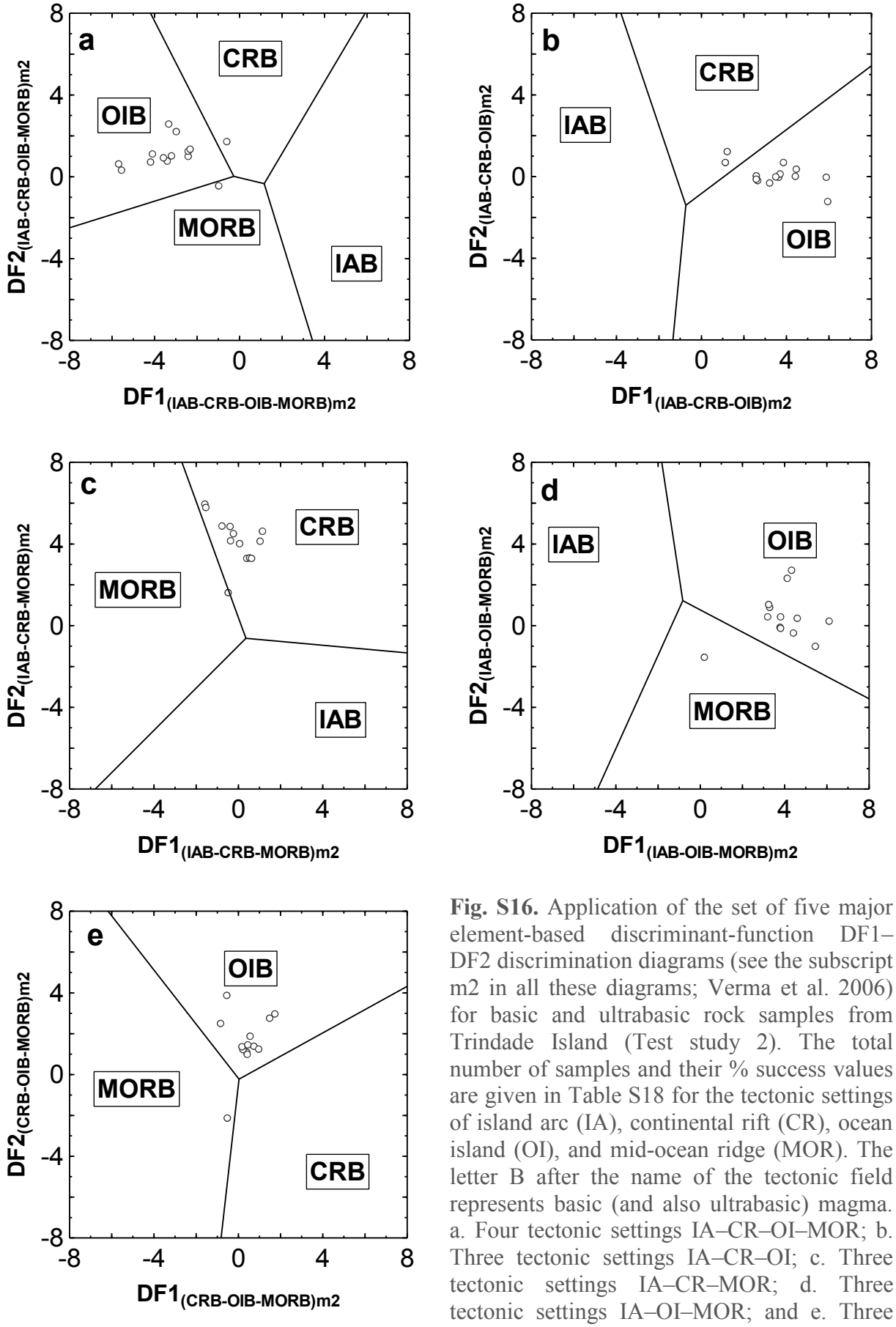

Fig. S16. Application of the set of five major element-based discriminant-function DF1–DF2 discrimination diagrams (see the subscript m2 in all these diagrams; Verma et al. 2006) for basic and ultrabasic rock samples from Trindade Island (Test study 2). The total number of samples and their % success values are given in Table S18 for the tectonic settings of island arc (IA), continental rift (CR), ocean island (OI), and mid-ocean ridge (MOR). The letter B after the name of the tectonic field represents basic (and also ultrabasic) magma. a. Four tectonic settings IA–CR–OI–MOR; b. Three tectonic settings IA–CR–OI; c. Three tectonic settings IA–CR–MOR; d. Three tectonic settings IA–OI–MOR; and e. Three tectonic settings CR–OI–MOR.

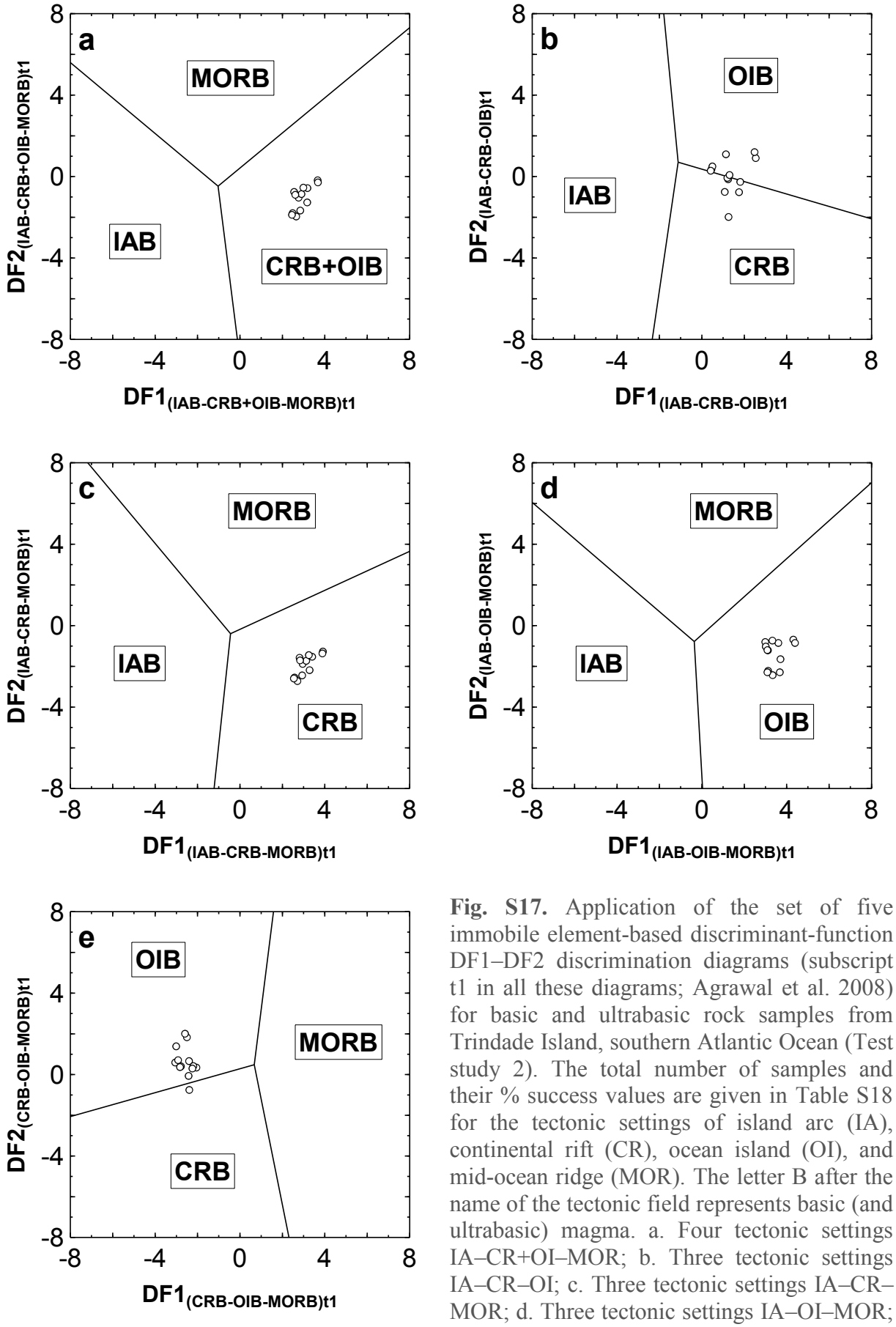

Fig. S17. Application of the set of five immobile element-based discriminant-function DF1–DF2 discrimination diagrams (subscript t1 in all these diagrams; Agrawal et al. 2008) for basic and ultrabasic rock samples from Trindade Island, southern Atlantic Ocean (Test study 2). The total number of samples and their % success values are given in Table S18 for the tectonic settings of island arc (IA), continental rift (CR), ocean island (OI), and mid-ocean ridge (MOR). The letter B after the name of the tectonic field represents basic (and ultrabasic) magma. a. Four tectonic settings IA–CR+OI–MOR; b. Three tectonic settings IA–CR–OI; c. Three tectonic settings IA–CR–MOR; d. Three tectonic settings IA–OI–MOR; and e. Three tectonic settings CR–OI–MOR.

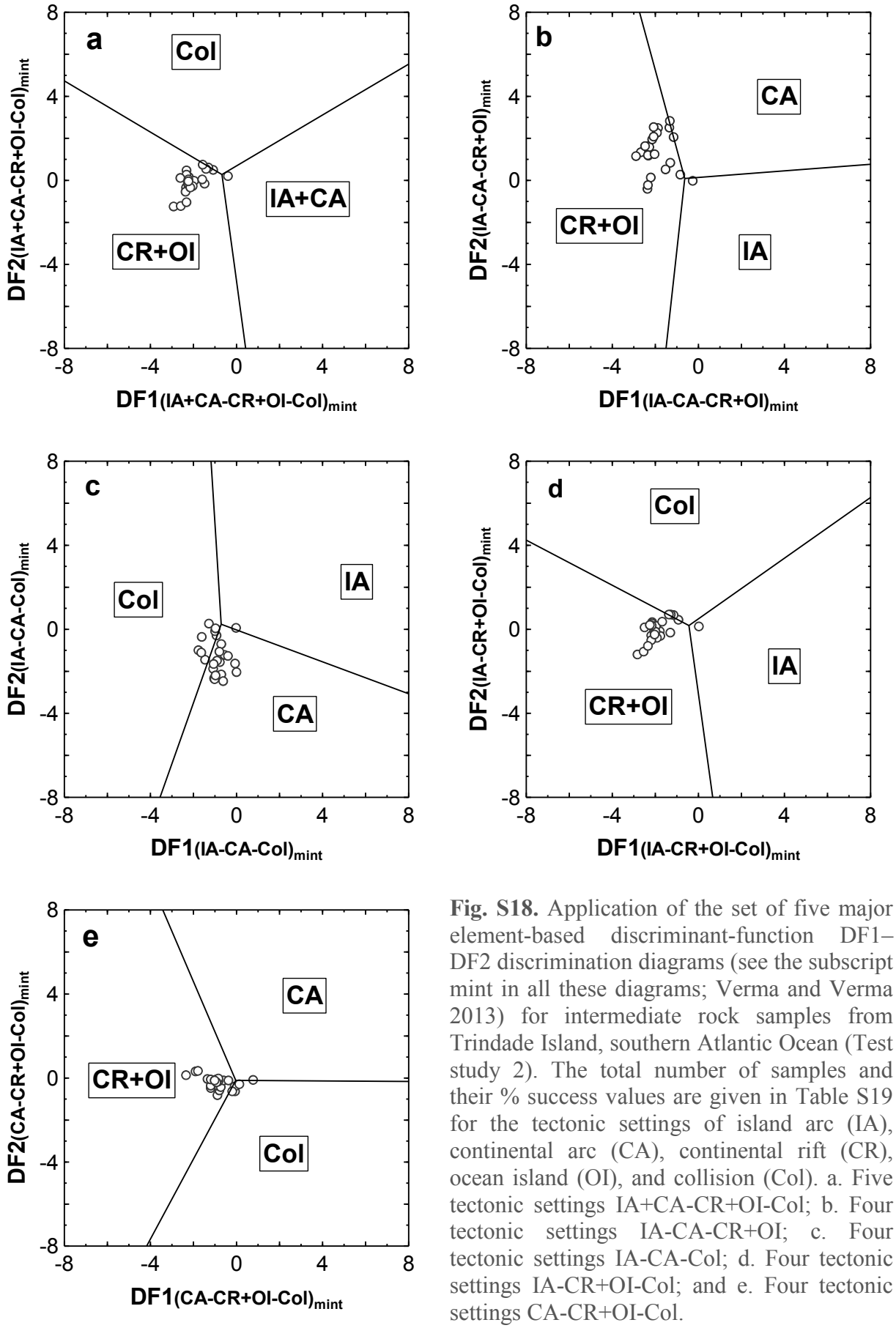

Fig. S18. Application of the set of five major element-based discriminant-function DF1–DF2 discrimination diagrams (see the subscript mint in all these diagrams; Verma and Verma 2013) for intermediate rock samples from Trindade Island, southern Atlantic Ocean (Test study 2). The total number of samples and their % success values are given in Table S19 for the tectonic settings of island arc (IA), continental arc (CA), continental rift (CR), ocean island (OI), and collision (Col). a. Five tectonic settings IA+CA-CR+OI-Col; b. Four tectonic settings IA-CA-CR+OI; c. Four tectonic settings IA-CA-Col; d. Four tectonic settings IA-CR+OI-Col; and e. Four tectonic settings CA-CR+OI-Col.

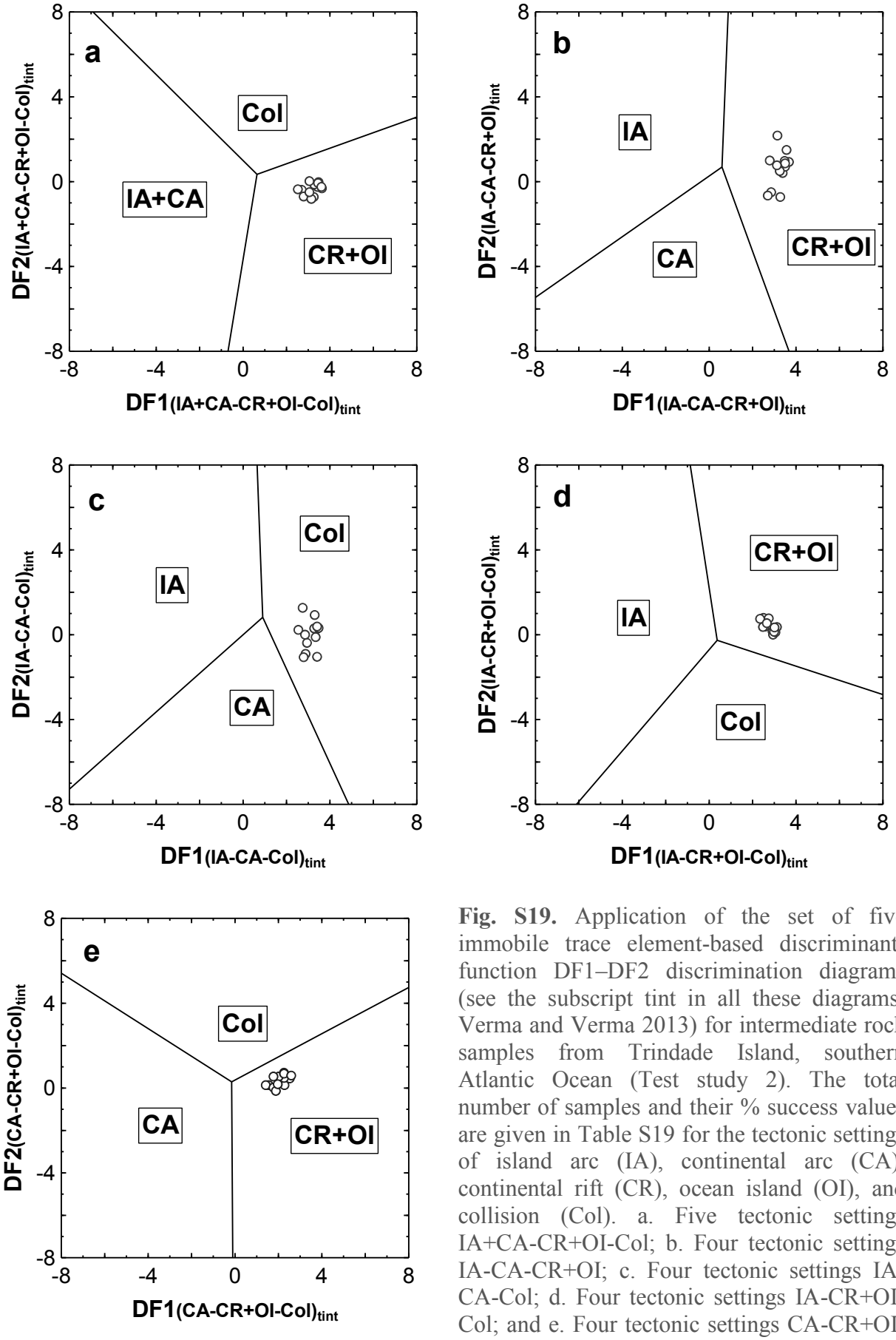

Fig. S19. Application of the set of five immobile trace element-based discriminant-function DF1–DF2 discrimination diagrams (see the subscript tint in all these diagrams; Verma and Verma 2013) for intermediate rock samples from Trindade Island, southern Atlantic Ocean (Test study 2). The total number of samples and their % success values are given in Table S19 for the tectonic settings of island arc (IA), continental arc (CA), continental rift (CR), ocean island (OI), and collision (Col). a. Five tectonic settings IA+CA-CR+OI-Col; b. Four tectonic settings IA-CA-CR+OI; c. Four tectonic settings IA-CA-Col; d. Four tectonic settings IA-CR+OI-Col; and e. Four tectonic settings CA-CR+OI-Col.

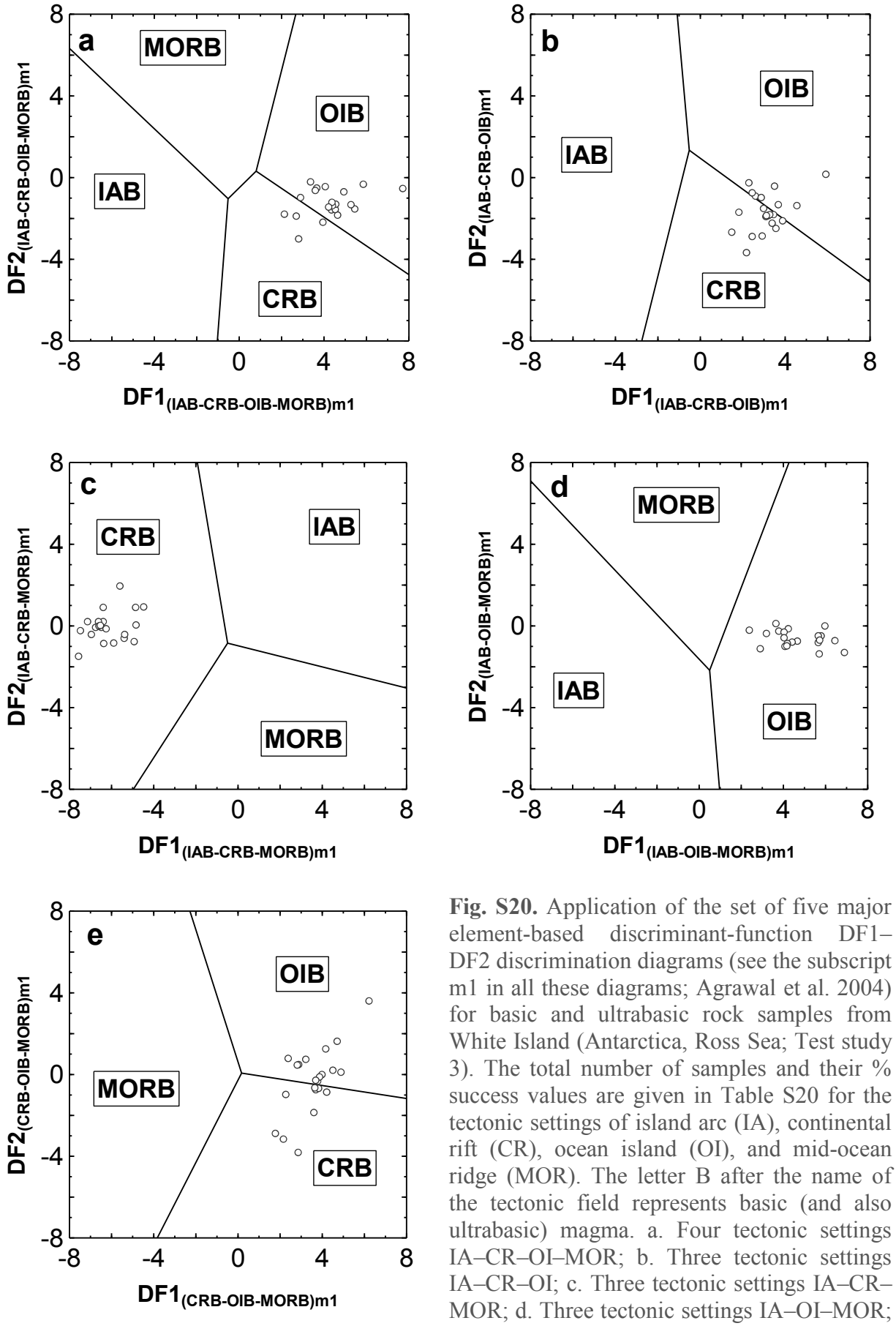

Fig. S20. Application of the set of five major element-based discriminant-function DF1–DF2 discrimination diagrams (see the subscript m1 in all these diagrams; Agrawal et al. 2004) for basic and ultrabasic rock samples from White Island (Antarctica, Ross Sea; Test study 3). The total number of samples and their % success values are given in Table S20 for the tectonic settings of island arc (IA), continental rift (CR), ocean island (OI), and mid-ocean ridge (MOR). The letter B after the name of the tectonic field represents basic (and also ultrabasic) magma. a. Four tectonic settings IA–CR–OI–MOR; b. Three tectonic settings IA–CR–OI; c. Three tectonic settings IA–CR–MOR; d. Three tectonic settings IA–OI–MOR; and e. Three tectonic settings CR–OI–MOR.

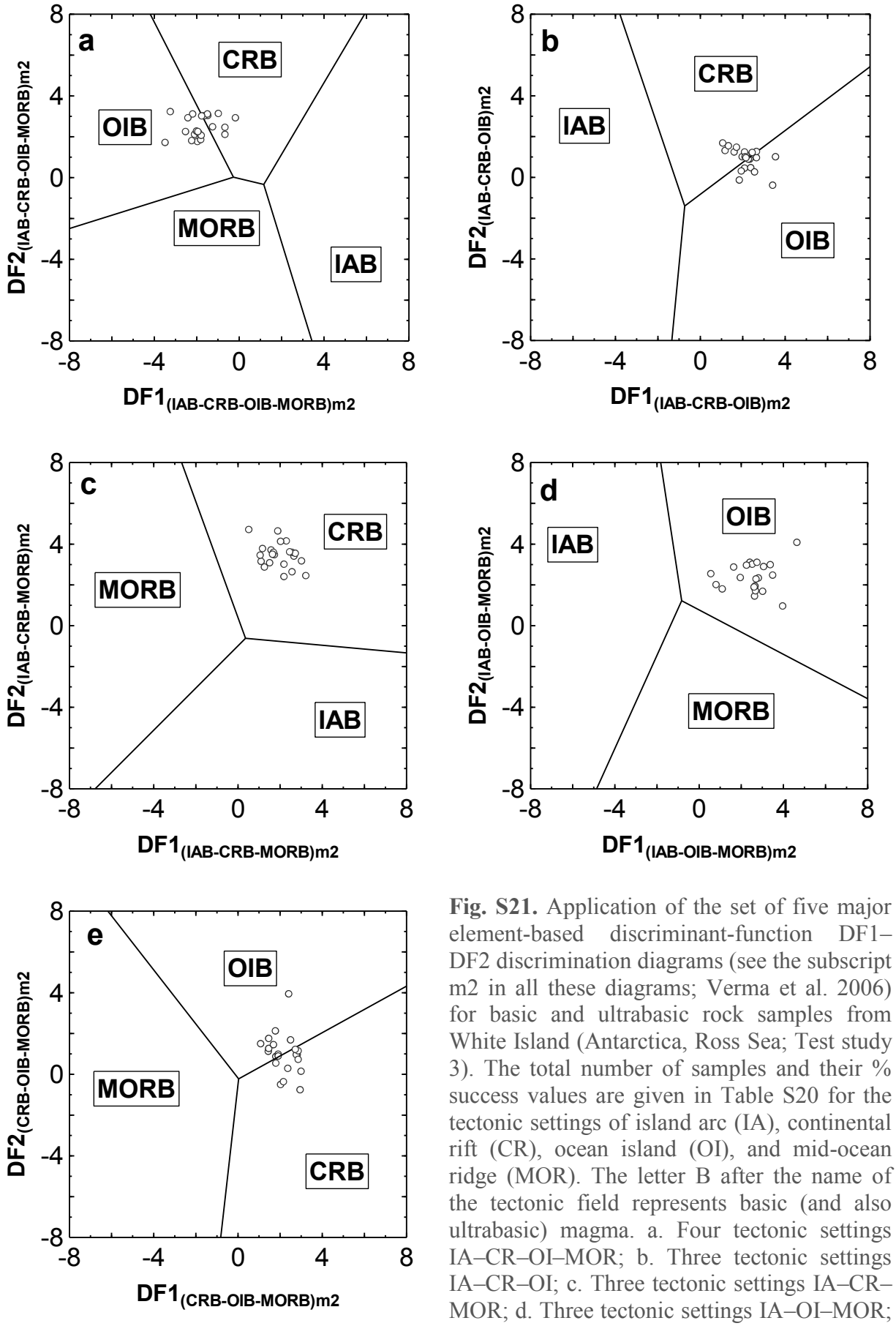

Fig. S21. Application of the set of five major element-based discriminant-function DF1–DF2 discrimination diagrams (see the subscript m2 in all these diagrams; Verma et al. 2006) for basic and ultrabasic rock samples from White Island (Antarctica, Ross Sea; Test study 3). The total number of samples and their % success values are given in Table S20 for the tectonic settings of island arc (IA), continental rift (CR), ocean island (OI), and mid-ocean ridge (MOR). The letter B after the name of the tectonic field represents basic (and also ultrabasic) magma. a. Four tectonic settings IA–CR–OI–MOR; b. Three tectonic settings IA–CR–OI; c. Three tectonic settings IA–CR–MOR; d. Three tectonic settings IA–OI–MOR; and e. Three tectonic settings CR–OI–MOR.

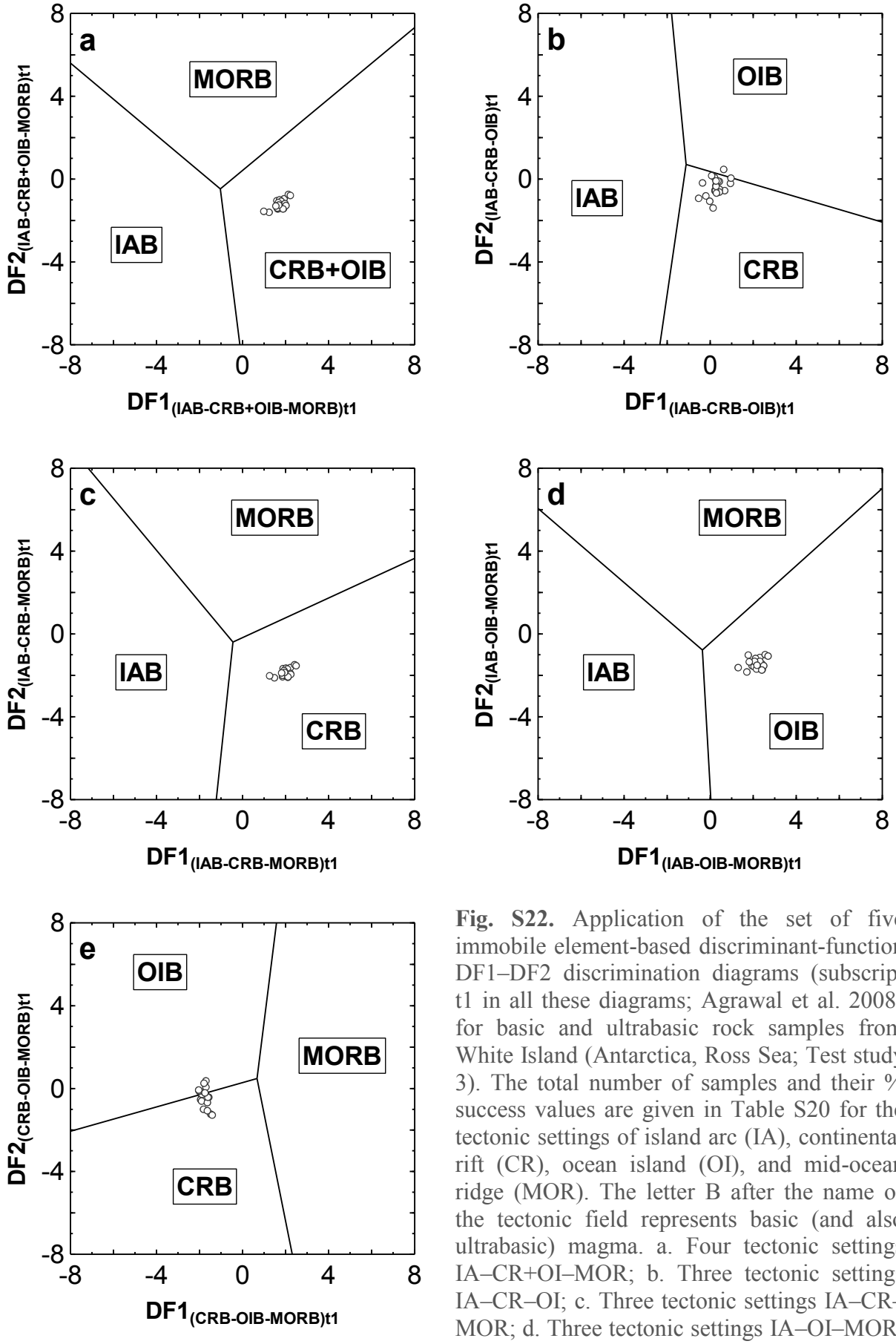

Fig. S22. Application of the set of five immobile element-based discriminant-function DF1–DF2 discrimination diagrams (subscript t1 in all these diagrams; Agrawal et al. 2008) for basic and ultrabasic rock samples from White Island (Antarctica, Ross Sea; Test study 3). The total number of samples and their % success values are given in Table S20 for the tectonic settings of island arc (IA), continental rift (CR), ocean island (OI), and mid-ocean ridge (MOR). The letter B after the name of the tectonic field represents basic (and also ultrabasic) magma. a. Four tectonic settings IA–CR+OI–MOR; b. Three tectonic settings IA–CR–OI; c. Three tectonic settings IA–CR–MOR; d. Three tectonic settings IA–OI–MOR; and e. Three tectonic settings CR–OI–MOR.

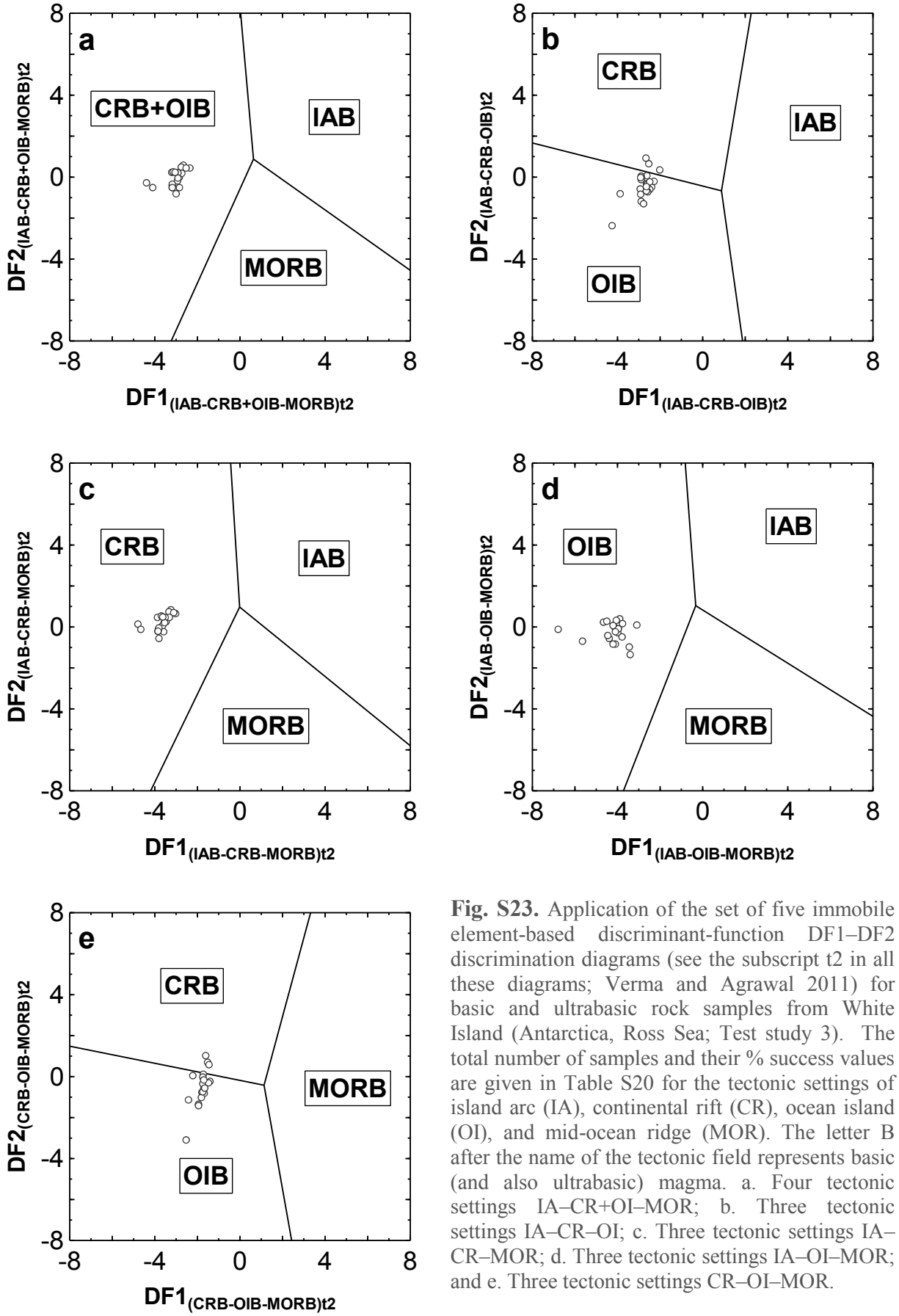

Fig. S23. Application of the set of five immobile element-based discriminant-function DF1–DF2 discrimination diagrams (see the subscript t2 in all these diagrams; Verma and Agrawal 2011) for basic and ultrabasic rock samples from White Island (Antarctica, Ross Sea; Test study 3). The total number of samples and their % success values are given in Table S20 for the tectonic settings of island arc (IA), continental rift (CR), ocean island (OI), and mid-ocean ridge (MOR). The letter B after the name of the tectonic field represents basic (and also ultrabasic) magma. a. Four tectonic settings IA–CR+OI–MOR; b. Three tectonic settings IA–CR–OI; c. Three tectonic settings IA–CR–MOR; d. Three tectonic settings IA–OI–MOR; and e. Three tectonic settings CR–OI–MOR.

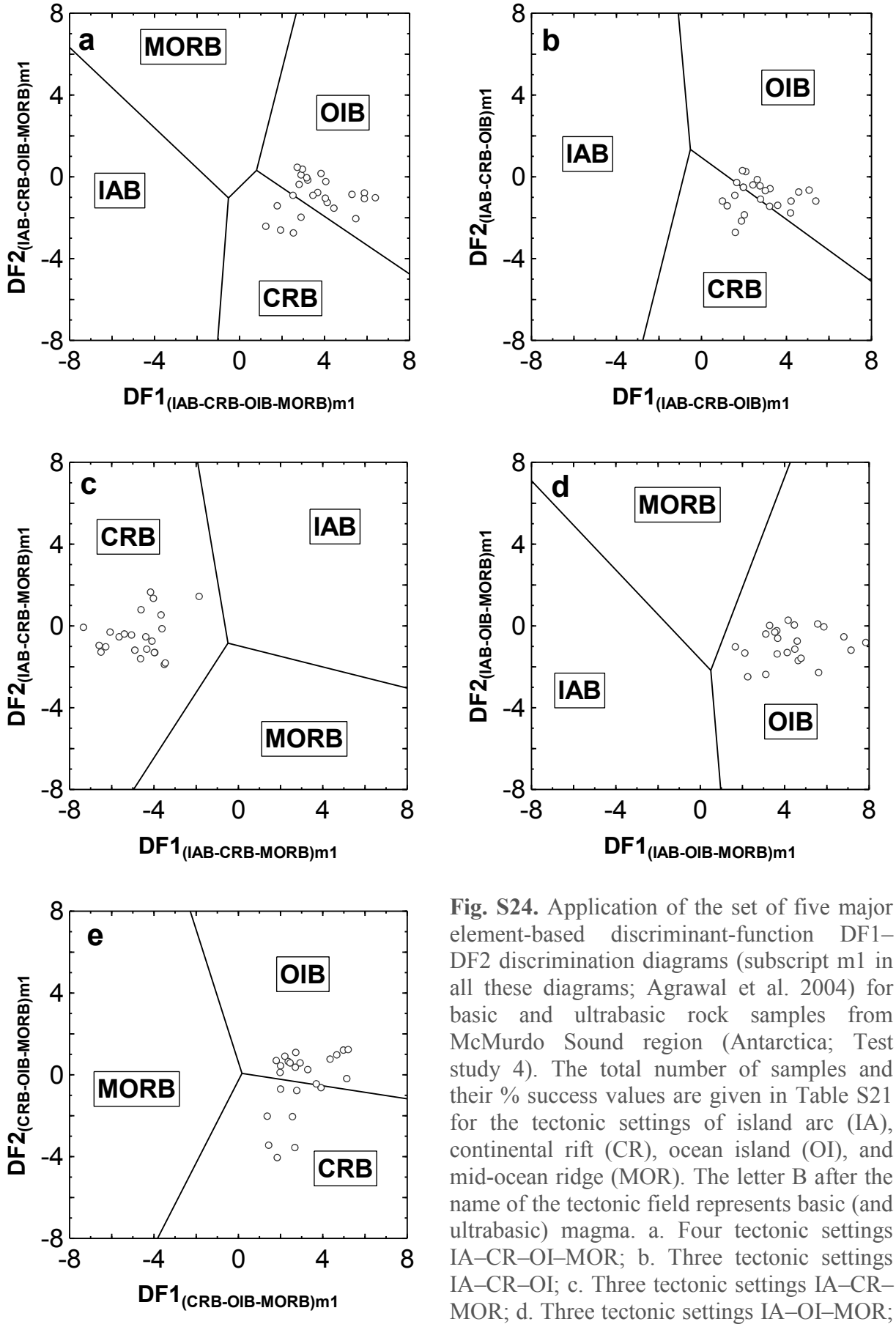

Fig. S24. Application of the set of five major element-based discriminant-function DF1–DF2 discrimination diagrams (subscript m1 in all these diagrams; Agrawal et al. 2004) for basic and ultrabasic rock samples from McMurdo Sound region (Antarctica; Test study 4). The total number of samples and their % success values are given in Table S21 for the tectonic settings of island arc (IA), continental rift (CR), ocean island (OI), and mid-ocean ridge (MOR). The letter B after the name of the tectonic field represents basic (and ultrabasic) magma. a. Four tectonic settings IA–CR–OI–MOR; b. Three tectonic settings IA–CR–OI; c. Three tectonic settings IA–CR–MOR; d. Three tectonic settings IA–OI–MOR; and e. Three tectonic settings CR–OI–MOR.

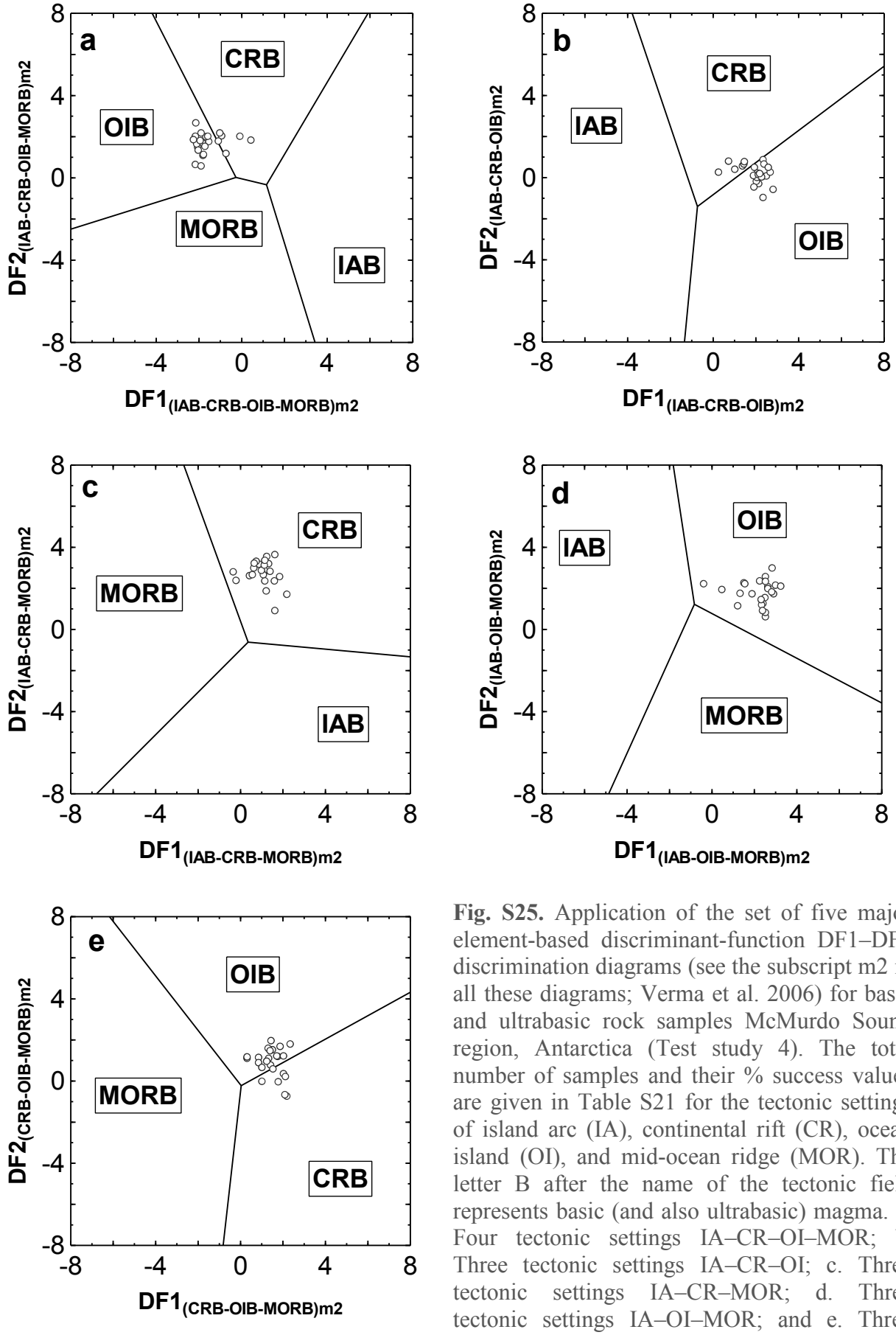

Fig. S25. Application of the set of five major element-based discriminant-function DF1–DF2 discrimination diagrams (see the subscript m2 in all these diagrams; Verma et al. 2006) for basic and ultrabasic rock samples McMurdo Sound region, Antarctica (Test study 4). The total number of samples and their % success values are given in Table S21 for the tectonic settings of island arc (IA), continental rift (CR), ocean island (OI), and mid-ocean ridge (MOR). The letter B after the name of the tectonic field represents basic (and also ultrabasic) magma. a. Four tectonic settings IA–CR–OI–MOR; b. Three tectonic settings IA–CR–OI; c. Three tectonic settings IA–CR–MOR; d. Three tectonic settings IA–OI–MOR; and e. Three tectonic settings CR–OI–MOR.

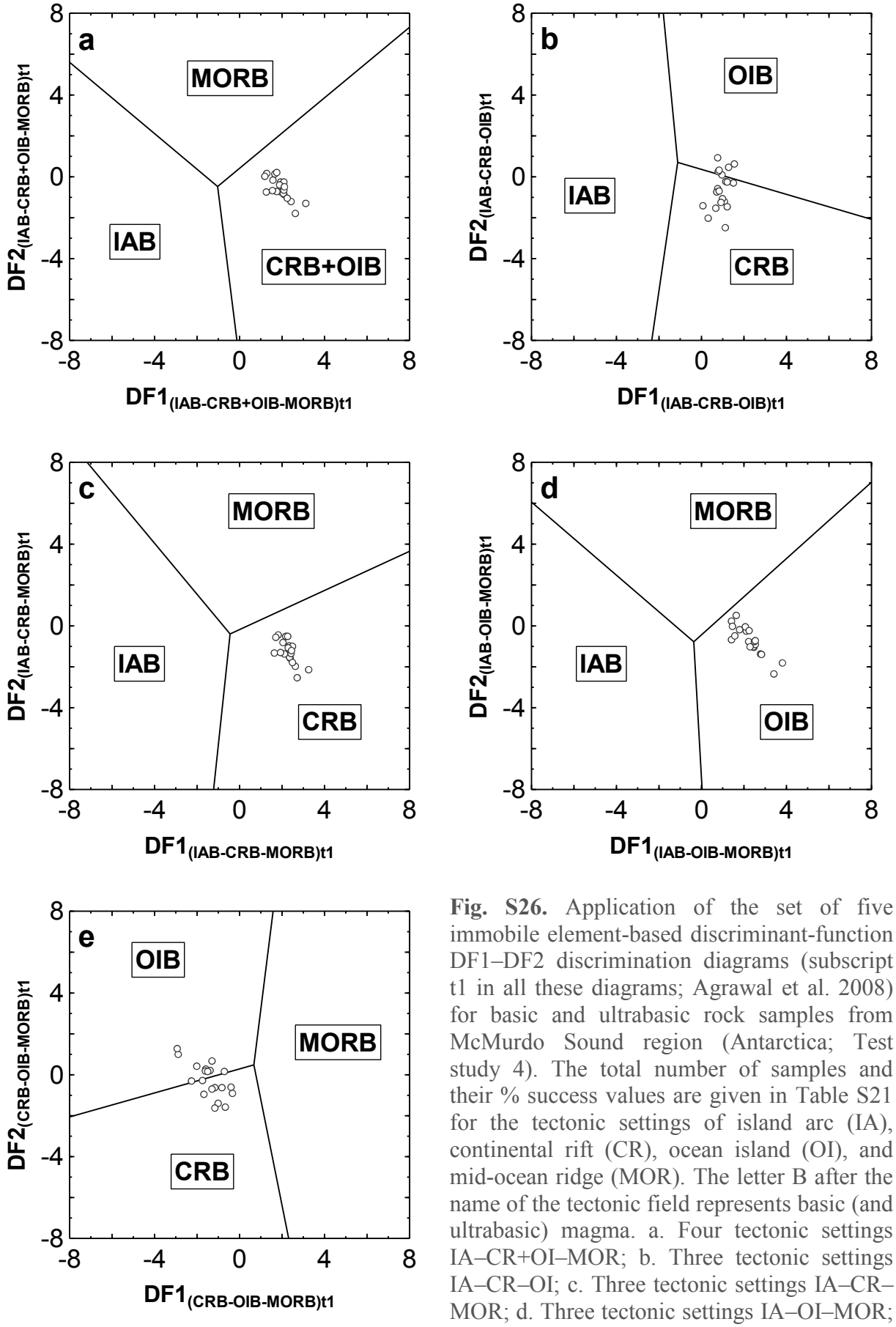

Fig. S26. Application of the set of five immobile element-based discriminant-function DF1–DF2 discrimination diagrams (subscript t1 in all these diagrams; Agrawal et al. 2008) for basic and ultrabasic rock samples from McMurdo Sound region (Antarctica; Test study 4). The total number of samples and their % success values are given in Table S21 for the tectonic settings of island arc (IA), continental rift (CR), ocean island (OI), and mid-ocean ridge (MOR). The letter B after the name of the tectonic field represents basic (and ultrabasic) magma. a. Four tectonic settings IA–CR+OI–MOR; b. Three tectonic settings IA–CR–OI; c. Three tectonic settings IA–CR–MOR; d. Three tectonic settings IA–OI–MOR; and e. Three tectonic settings CR–OI–MOR.

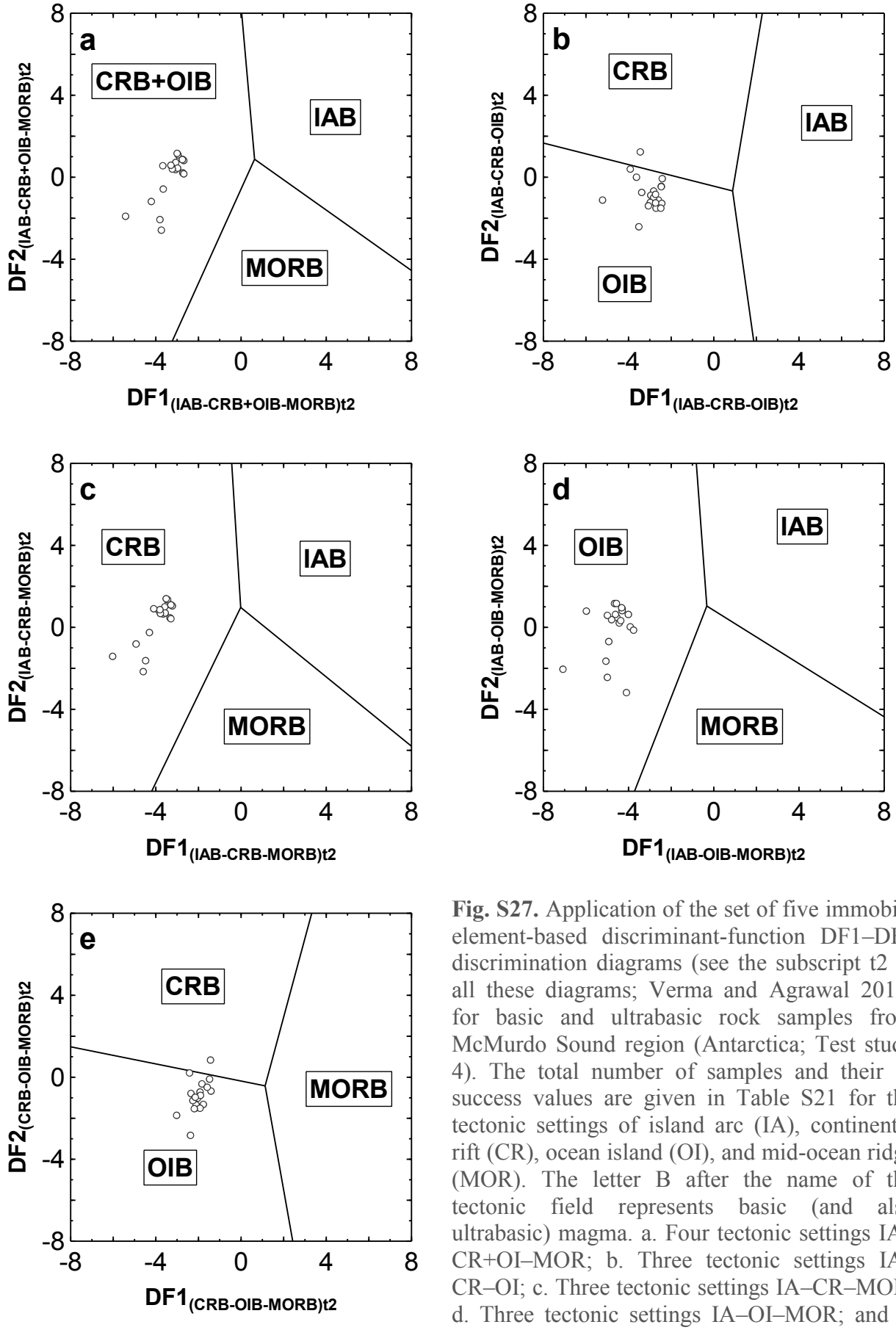

Fig. S27. Application of the set of five immobile element-based discriminant-function DF1–DF2 discrimination diagrams (see the subscript t2 in all these diagrams; Verma and Agrawal 2011) for basic and ultrabasic rock samples from McMurdo Sound region (Antarctica; Test study 4). The total number of samples and their % success values are given in Table S21 for the tectonic settings of island arc (IA), continental rift (CR), ocean island (OI), and mid-ocean ridge (MOR). The letter B after the name of the tectonic field represents basic (and also ultrabasic) magma. a. Four tectonic settings IA–CR+OI–MOR; b. Three tectonic settings IA–CR–OI; c. Three tectonic settings IA–CR–MOR; d. Three tectonic settings IA–OI–MOR; and e. Three tectonic settings CR–OI–MOR.

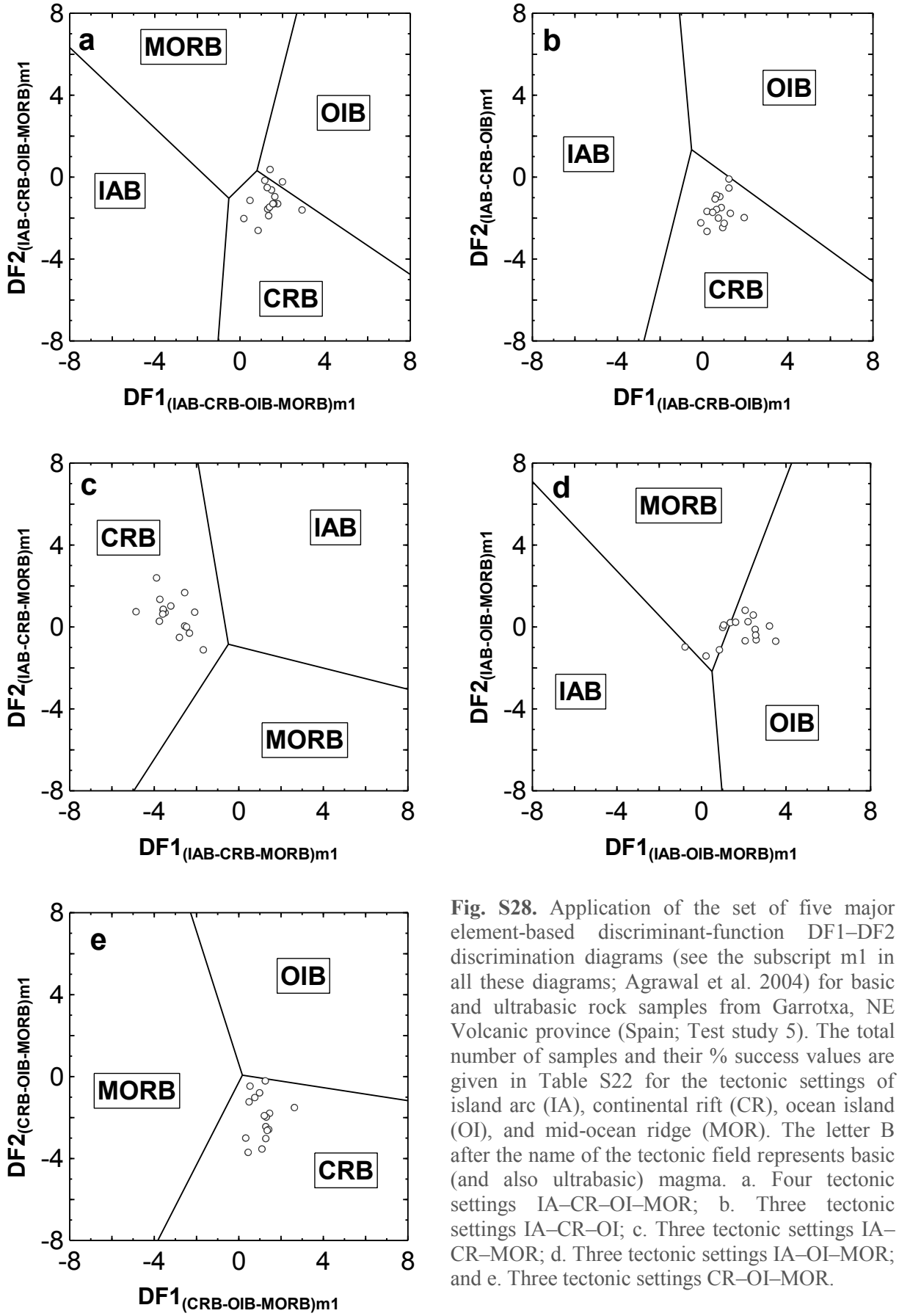

Fig. S28. Application of the set of five major element-based discriminant-function DF1–DF2 discrimination diagrams (see the subscript m1 in all these diagrams; Agrawal et al. 2004) for basic and ultrabasic rock samples from Garrotxa, NE Volcanic province (Spain; Test study 5). The total number of samples and their % success values are given in Table S22 for the tectonic settings of island arc (IA), continental rift (CR), ocean island (OI), and mid-ocean ridge (MOR). The letter B after the name of the tectonic field represents basic (and also ultrabasic) magma. a. Four tectonic settings IA–CR–OI–MOR; b. Three tectonic settings IA–CR–OI; c. Three tectonic settings IA–CR–MOR; d. Three tectonic settings IA–OI–MOR; and e. Three tectonic settings CR–OI–MOR.

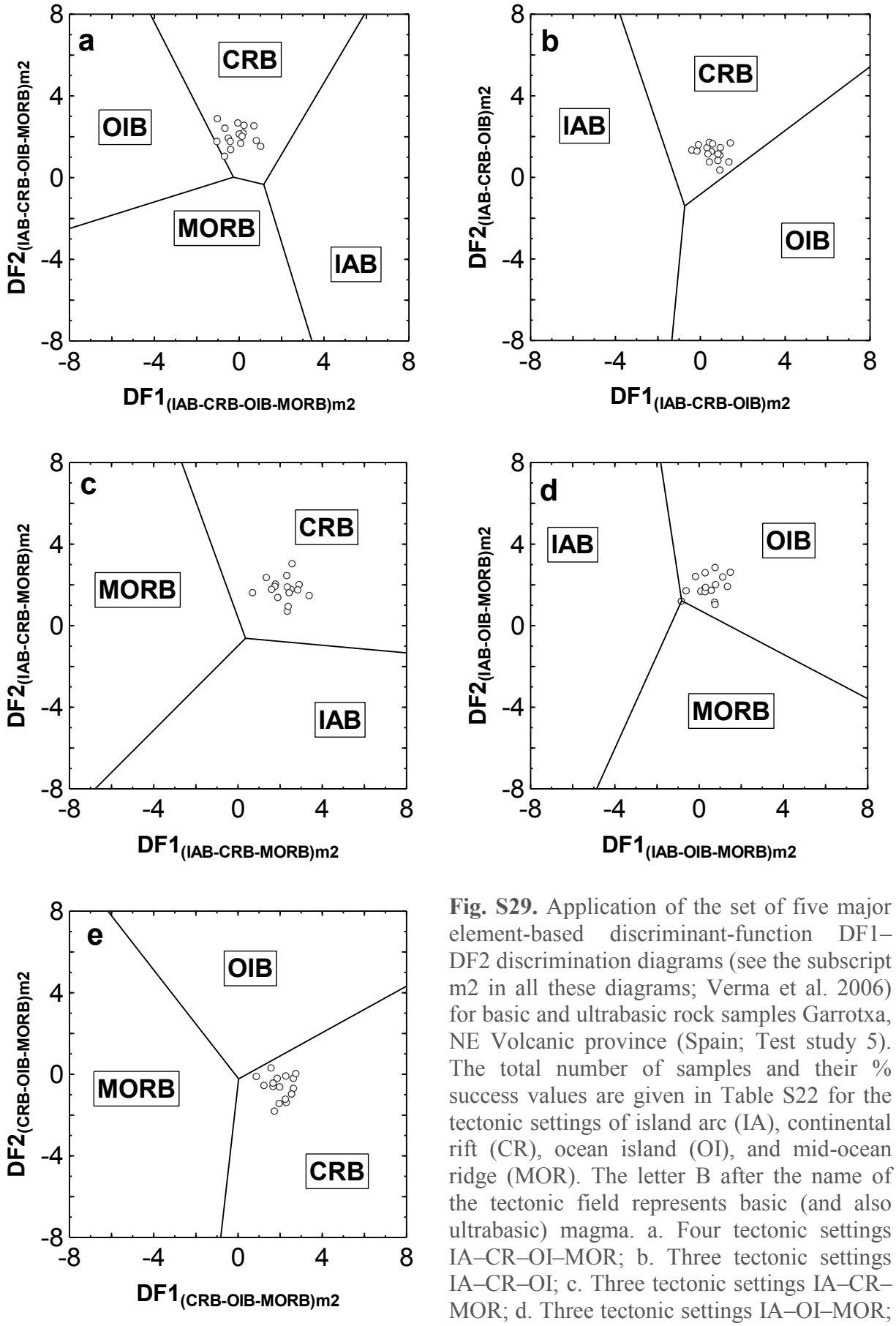

Fig. S29. Application of the set of five major element-based discriminant-function DF1–DF2 discrimination diagrams (see the subscript m2 in all these diagrams; Verma et al. 2006) for basic and ultrabasic rock samples Garrotxa, NE Volcanic province (Spain; Test study 5). The total number of samples and their % success values are given in Table S22 for the tectonic settings of island arc (IA), continental rift (CR), ocean island (OI), and mid-ocean ridge (MOR). The letter B after the name of the tectonic field represents basic (and also ultrabasic) magma. a. Four tectonic settings IA–CR–OI–MOR; b. Three tectonic settings IA–CR–OI; c. Three tectonic settings IA–CR–MOR; d. Three tectonic settings IA–OI–MOR; and e. Three tectonic settings CR–OI–MOR.

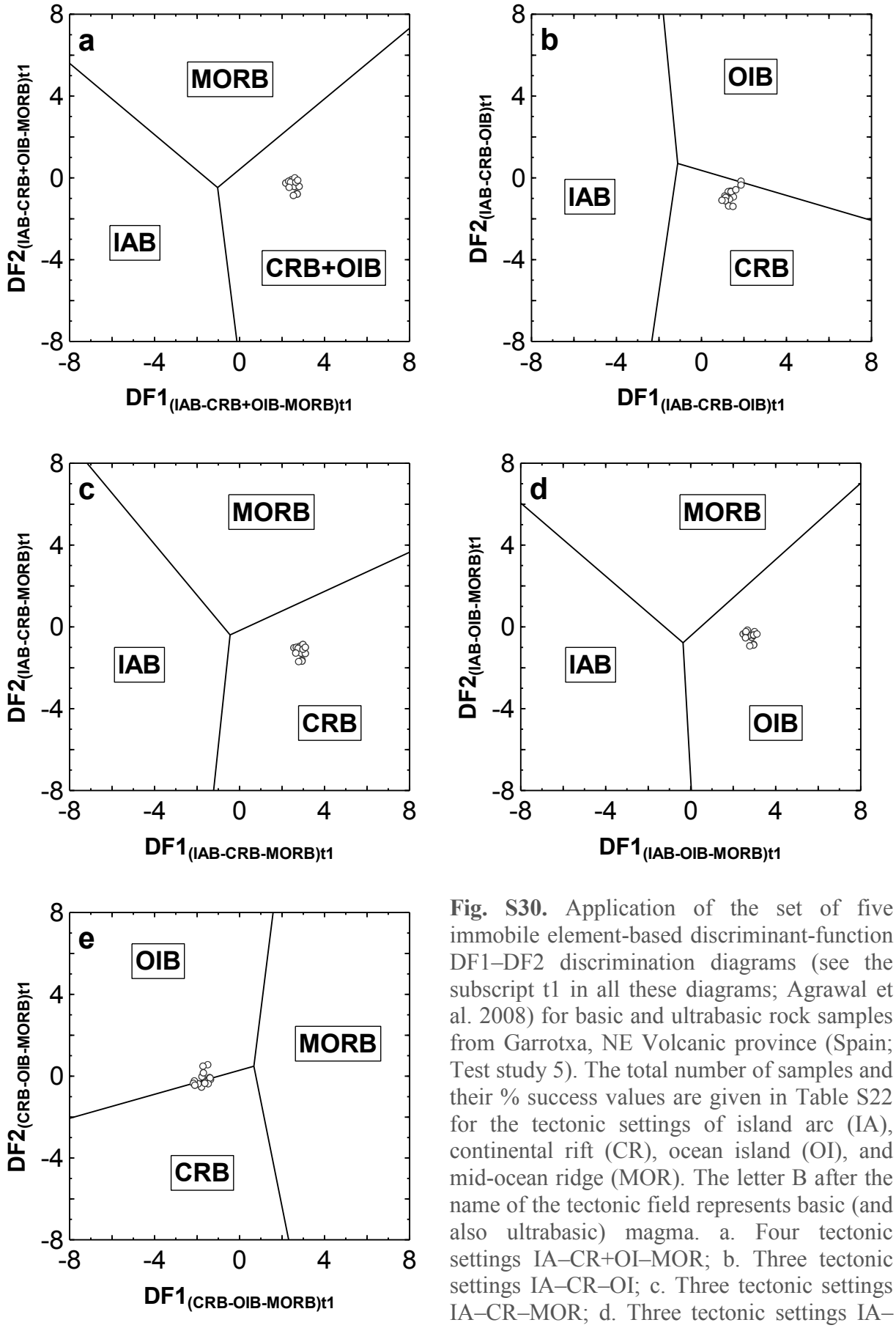

Fig. S30. Application of the set of five immobile element-based discriminant-function DF1–DF2 discrimination diagrams (see the subscript t1 in all these diagrams; Agrawal et al. 2008) for basic and ultrabasic rock samples from Garrotxa, NE Volcanic province (Spain; Test study 5). The total number of samples and their % success values are given in Table S22 for the tectonic settings of island arc (IA), continental rift (CR), ocean island (OI), and mid-ocean ridge (MOR). The letter B after the name of the tectonic field represents basic (and also ultrabasic) magma. a. Four tectonic settings IA–CR+OI–MOR; b. Three tectonic settings IA–CR–OI; c. Three tectonic settings IA–CR–MOR; d. Three tectonic settings IA–OI–MOR; and e. Three tectonic settings CR–OI–MOR.

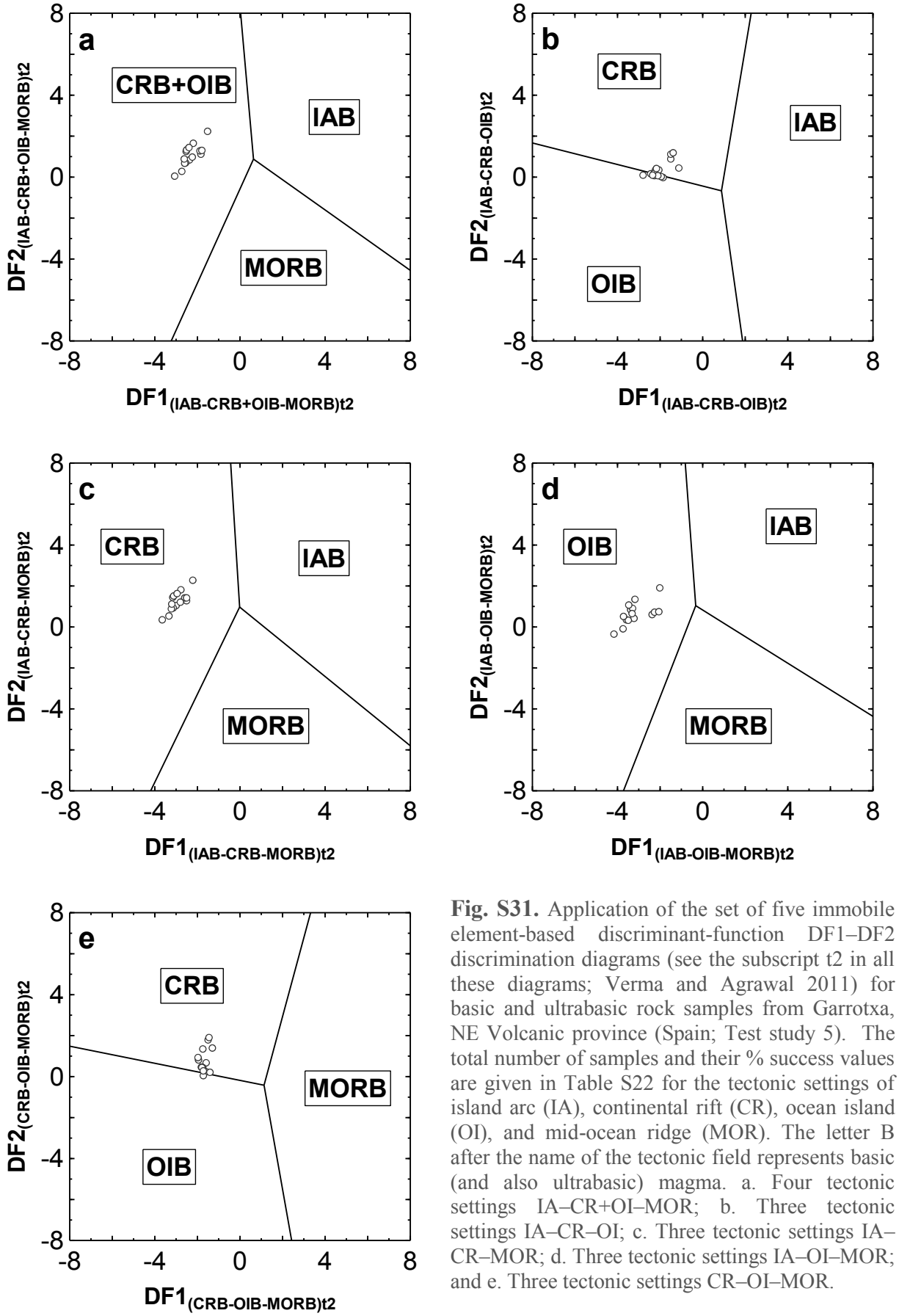

Fig. S31. Application of the set of five immobile element-based discriminant-function DF1–DF2 discrimination diagrams (see the subscript t2 in all these diagrams; Verma and Agrawal 2011) for basic and ultrabasic rock samples from Garrotxa, NE Volcanic province (Spain; Test study 5). The total number of samples and their % success values are given in Table S22 for the tectonic settings of island arc (IA), continental rift (CR), ocean island (OI), and mid-ocean ridge (MOR). The letter B after the name of the tectonic field represents basic (and also ultrabasic) magma. a. Four tectonic settings IA–CR+OI–MOR; b. Three tectonic settings IA–CR–OI; c. Three tectonic settings IA–CR–MOR; d. Three tectonic settings IA–OI–MOR; and e. Three tectonic settings CR–OI–MOR.

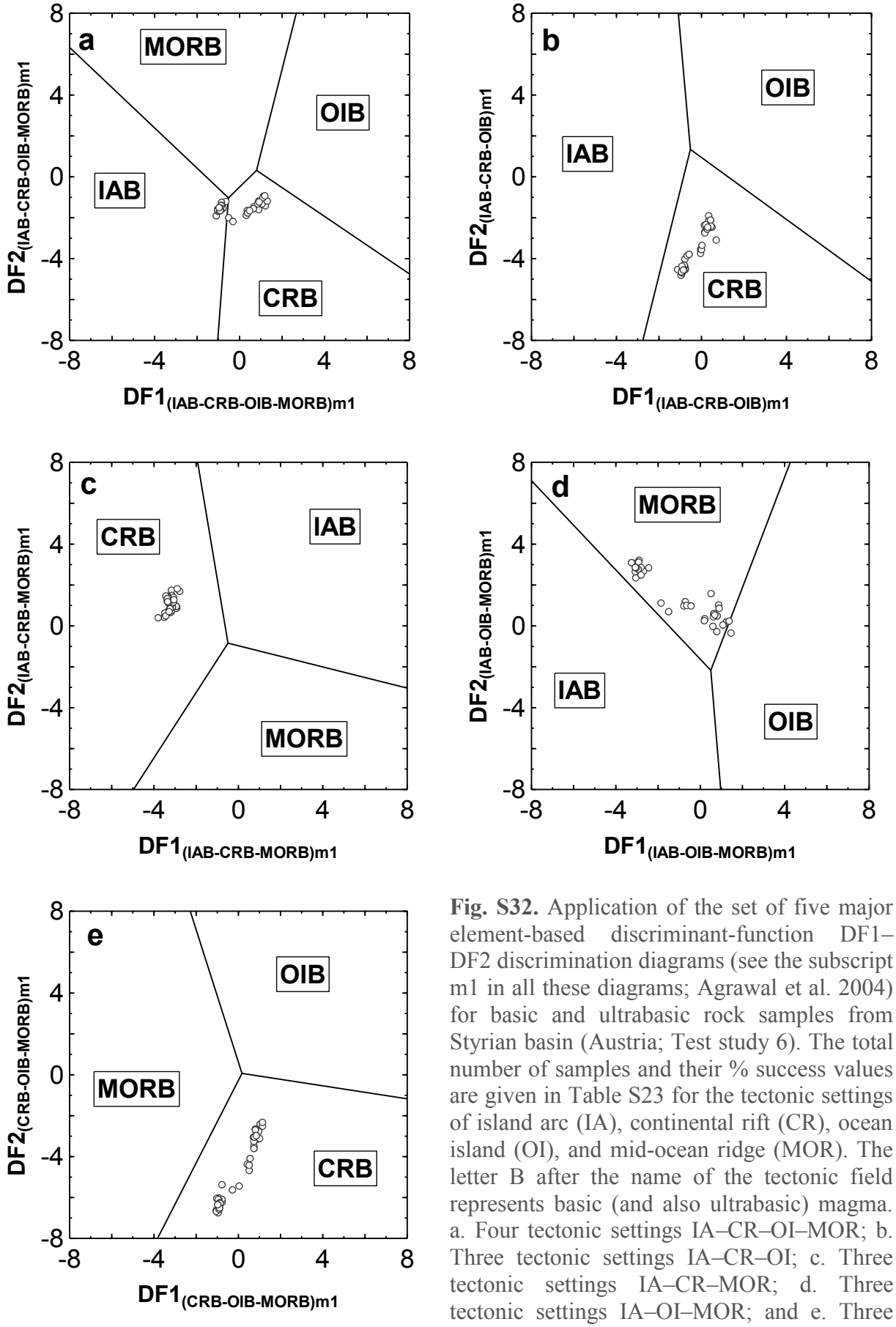

Fig. S32. Application of the set of five major element-based discriminant-function DF1–DF2 discrimination diagrams (see the subscript m1 in all these diagrams; Agrawal et al. 2004) for basic and ultrabasic rock samples from Styrian basin (Austria; Test study 6). The total number of samples and their % success values are given in Table S23 for the tectonic settings of island arc (IA), continental rift (CR), ocean island (OI), and mid-ocean ridge (MOR). The letter B after the name of the tectonic field represents basic (and also ultrabasic) magma. a. Four tectonic settings IA–CR–OI–MOR; b. Three tectonic settings IA–CR–OI; c. Three tectonic settings IA–CR–MOR; d. Three tectonic settings IA–OI–MOR; and e. Three tectonic settings CR–OI–MOR.

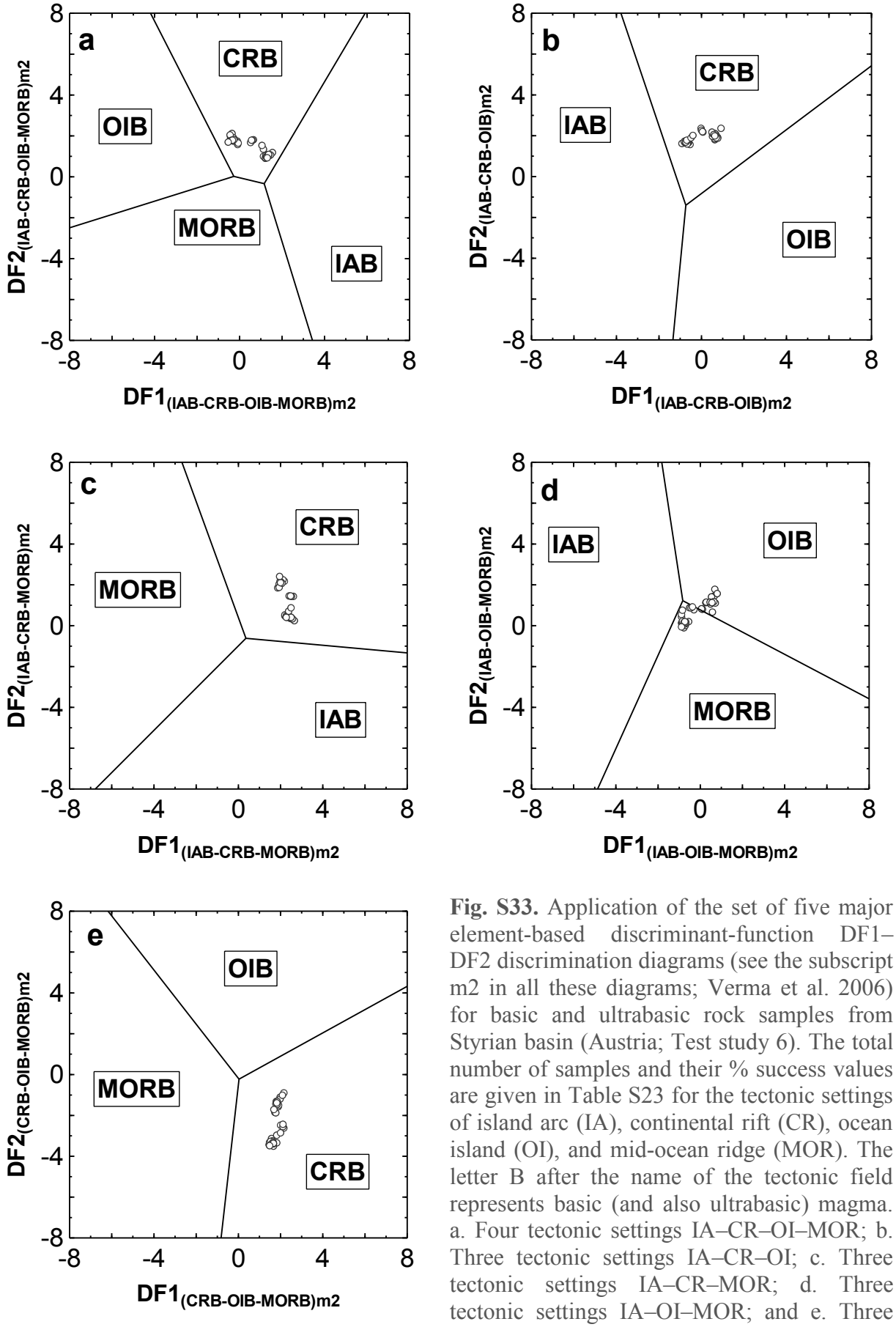

Fig. S33. Application of the set of five major element-based discriminant-function DF1–DF2 discrimination diagrams (see the subscript m2 in all these diagrams; Verma et al. 2006) for basic and ultrabasic rock samples from Styrian basin (Austria; Test study 6). The total number of samples and their % success values are given in Table S23 for the tectonic settings of island arc (IA), continental rift (CR), ocean island (OI), and mid-ocean ridge (MOR). The letter B after the name of the tectonic field represents basic (and also ultrabasic) magma. a. Four tectonic settings IA–CR–OI–MOR; b. Three tectonic settings IA–CR–OI; c. Three tectonic settings IA–CR–MOR; d. Three tectonic settings IA–OI–MOR; and e. Three tectonic settings CR–OI–MOR.

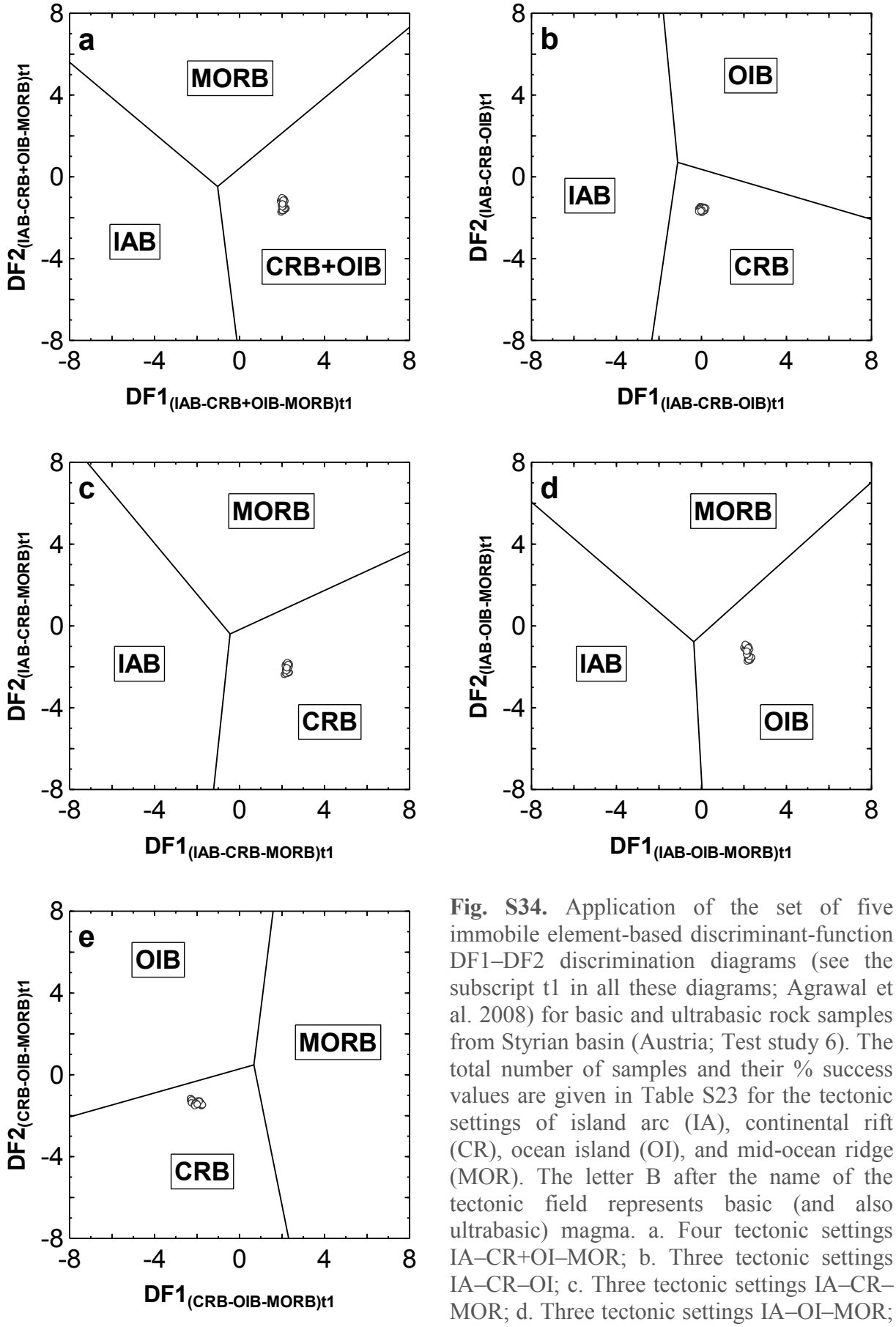

Fig. S34. Application of the set of five immobile element-based discriminant-function DF1–DF2 discrimination diagrams (see the subscript t1 in all these diagrams; Agrawal et al. 2008) for basic and ultrabasic rock samples from Styrian basin (Austria; Test study 6). The total number of samples and their % success values are given in Table S23 for the tectonic settings of island arc (IA), continental rift (CR), ocean island (OI), and mid-ocean ridge (MOR). The letter B after the name of the tectonic field represents basic (and also ultrabasic) magma. a. Four tectonic settings IA–CR+OI–MOR; b. Three tectonic settings IA–CR–OI; c. Three tectonic settings IA–CR–MOR; d. Three tectonic settings IA–OI–MOR; and e. Three tectonic settings CR–OI–MOR.

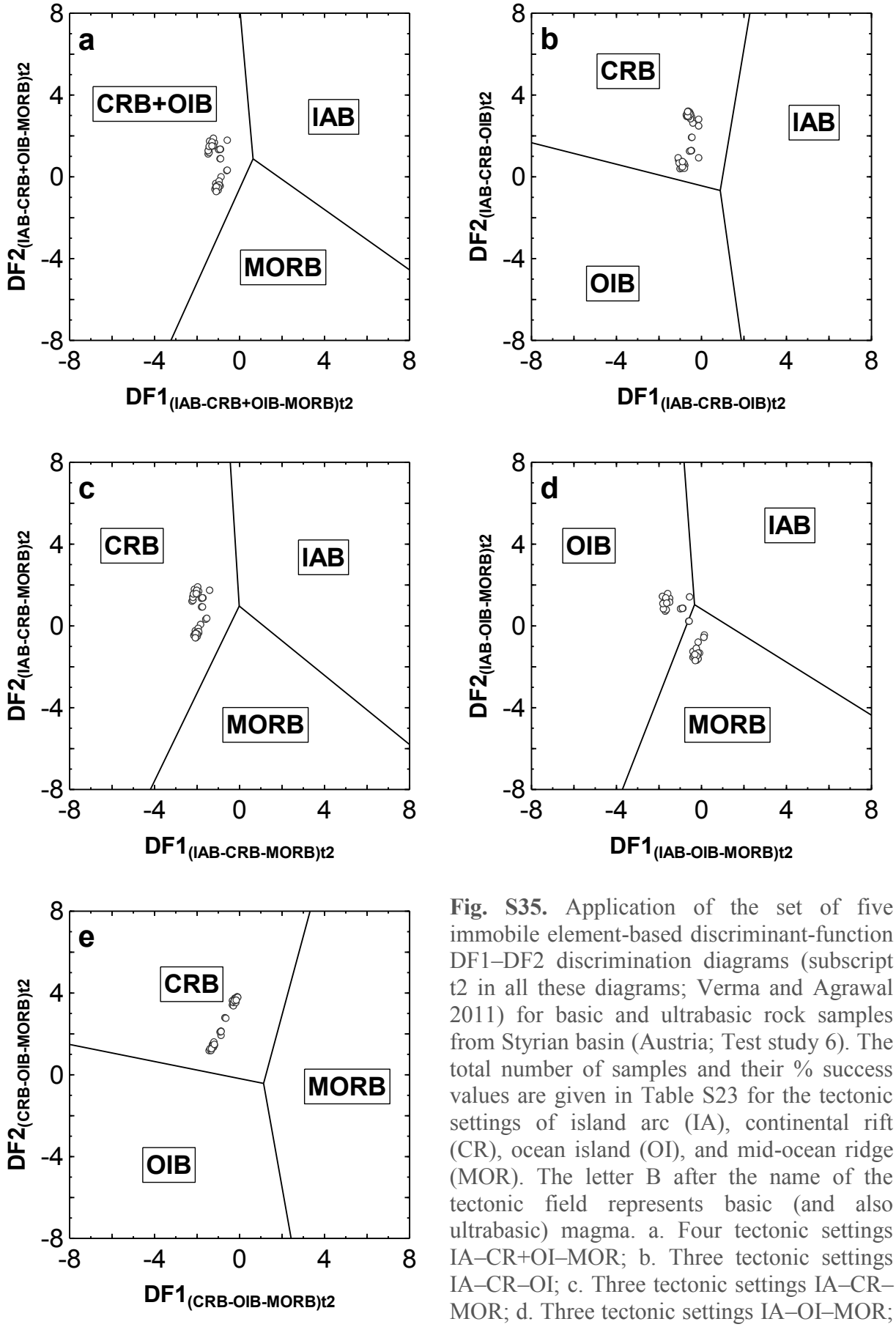

Fig. S35. Application of the set of five immobile element-based discriminant-function DF1–DF2 discrimination diagrams (subscript t2 in all these diagrams; Verma and Agrawal 2011) for basic and ultrabasic rock samples from Styrian basin (Austria; Test study 6). The total number of samples and their % success values are given in Table S23 for the tectonic settings of island arc (IA), continental rift (CR), ocean island (OI), and mid-ocean ridge (MOR). The letter B after the name of the tectonic field represents basic (and also ultrabasic) magma. a. Four tectonic settings IA–CR+OI–MOR; b. Three tectonic settings IA–CR–OI; c. Three tectonic settings IA–CR–MOR; d. Three tectonic settings IA–OI–MOR; and e. Three tectonic settings CR–OI–MOR.

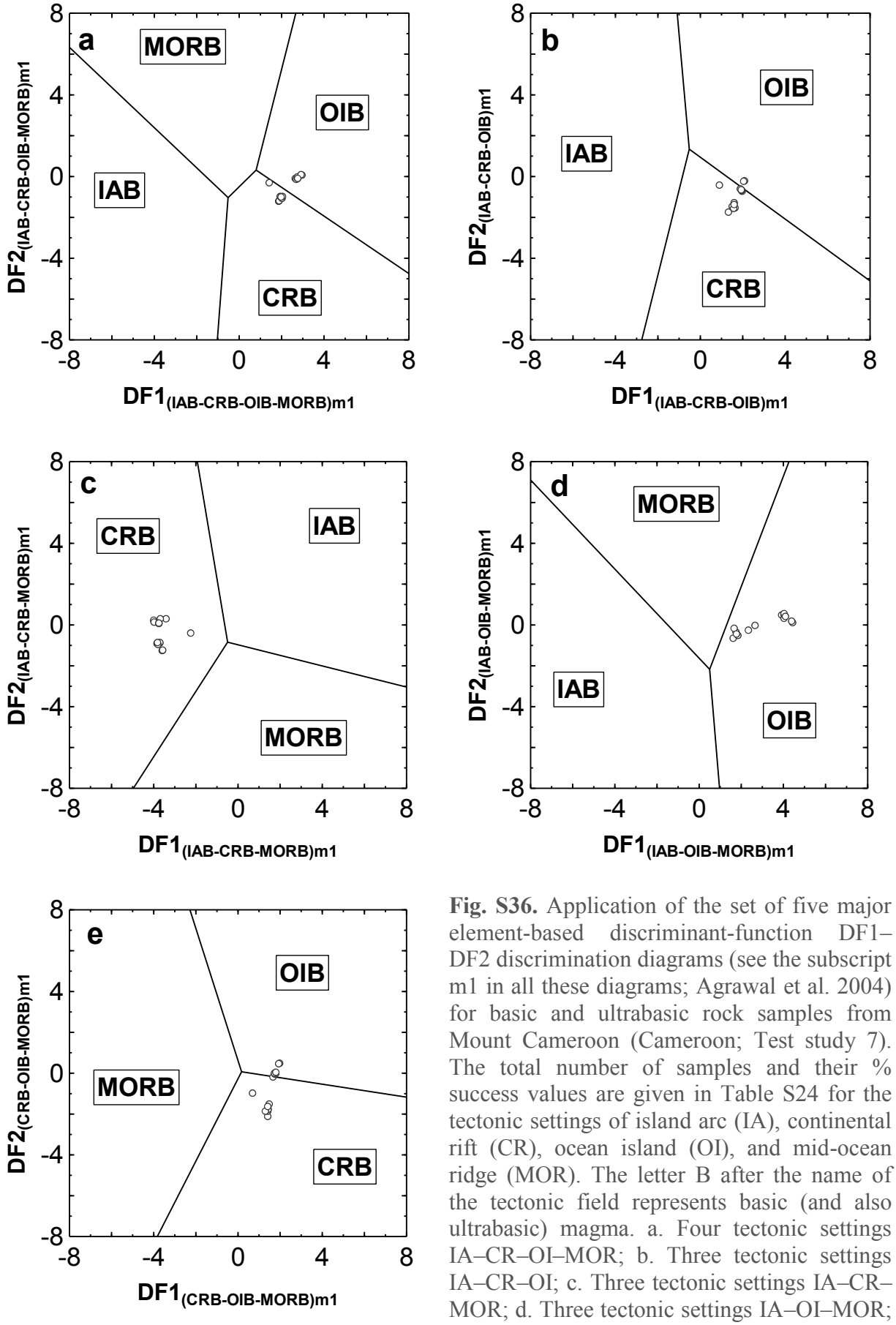

Fig. S36. Application of the set of five major element-based discriminant-function DF1–DF2 discrimination diagrams (see the subscript m1 in all these diagrams; Agrawal et al. 2004) for basic and ultrabasic rock samples from Mount Cameroon (Cameroon; Test study 7). The total number of samples and their % success values are given in Table S24 for the tectonic settings of island arc (IA), continental rift (CR), ocean island (OI), and mid-ocean ridge (MOR). The letter B after the name of the tectonic field represents basic (and also ultrabasic) magma. a. Four tectonic settings IA–CR–OI–MOR; b. Three tectonic settings IA–CR–OI; c. Three tectonic settings IA–CR–MOR; d. Three tectonic settings IA–OI–MOR; and e. Three tectonic settings CR–OI–MOR.

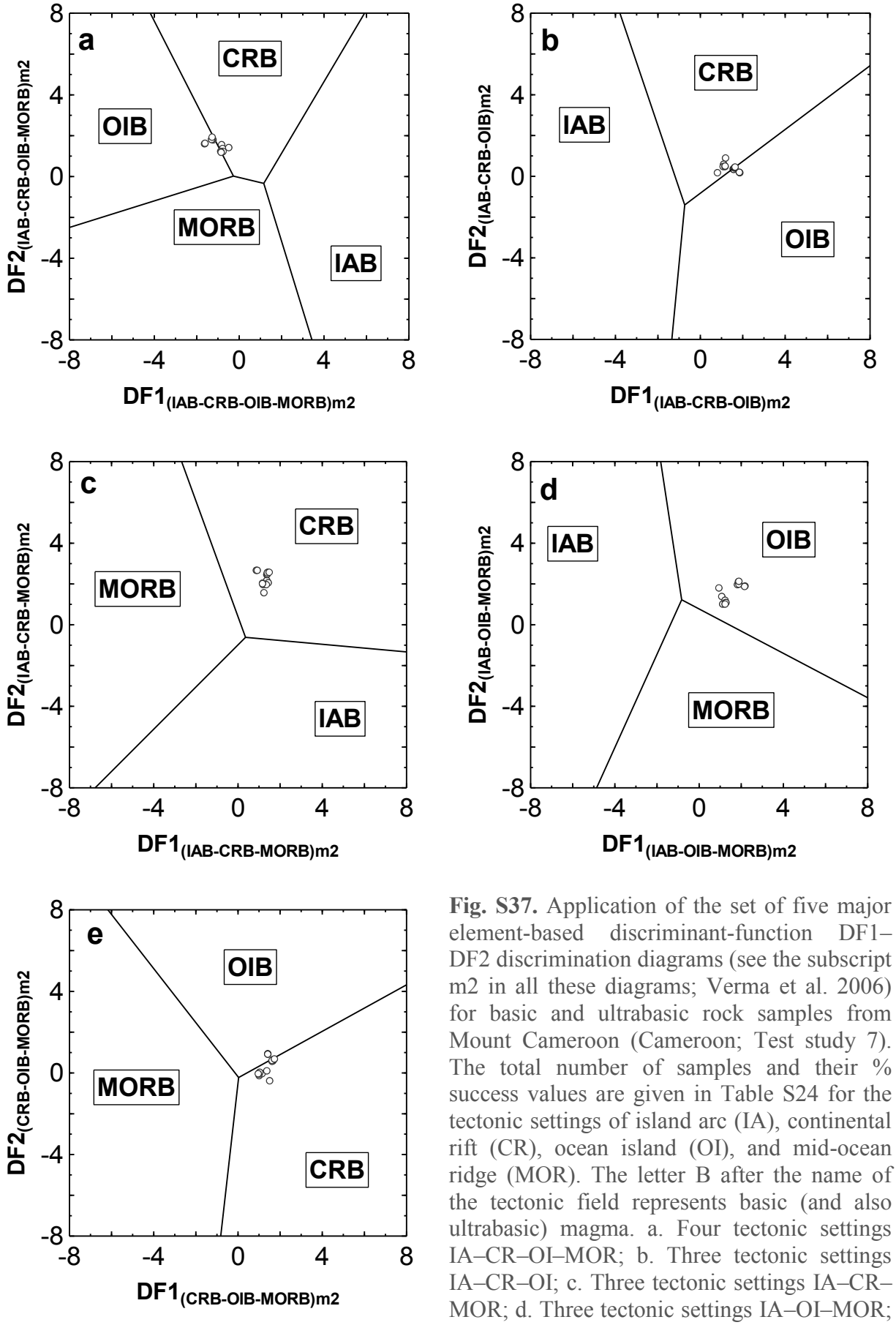

Fig. S37. Application of the set of five major element-based discriminant-function DF1–DF2 discrimination diagrams (see the subscript m2 in all these diagrams; Verma et al. 2006) for basic and ultrabasic rock samples from Mount Cameroon (Cameroon; Test study 7). The total number of samples and their % success values are given in Table S24 for the tectonic settings of island arc (IA), continental rift (CR), ocean island (OI), and mid-ocean ridge (MOR). The letter B after the name of the tectonic field represents basic (and also ultrabasic) magma. a. Four tectonic settings IA–CR–OI–MOR; b. Three tectonic settings IA–CR–OI; c. Three tectonic settings IA–CR–MOR; d. Three tectonic settings IA–OI–MOR; and e. Three tectonic settings CR–OI–MOR.

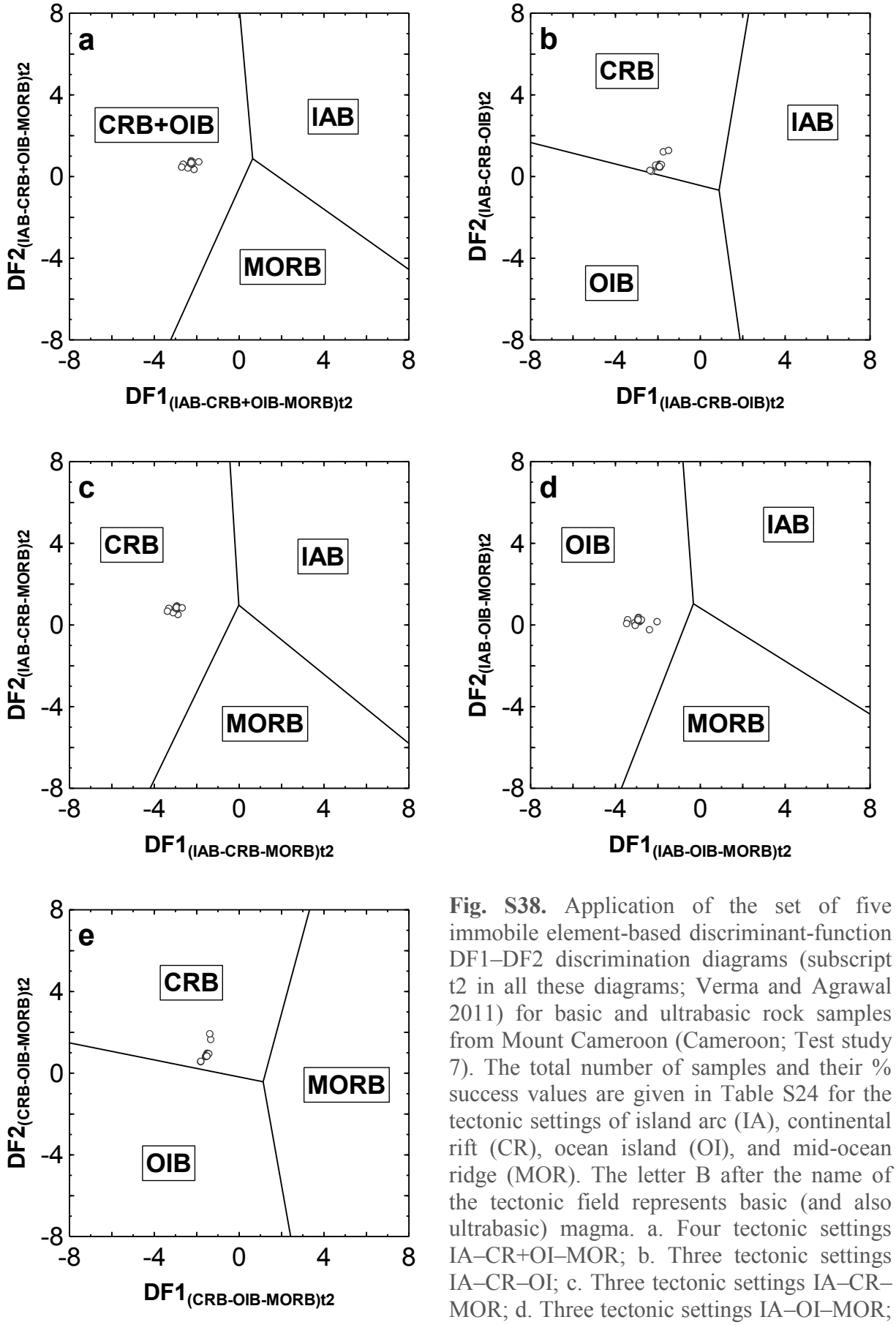

Fig. S38. Application of the set of five immobile element-based discriminant-function DF1–DF2 discrimination diagrams (subscript t2 in all these diagrams; Verma and Agrawal 2011) for basic and ultrabasic rock samples from Mount Cameroon (Cameroon; Test study 7). The total number of samples and their % success values are given in Table S24 for the tectonic settings of island arc (IA), continental rift (CR), ocean island (OI), and mid-ocean ridge (MOR). The letter B after the name of the tectonic field represents basic (and also ultrabasic) magma. a. Four tectonic settings IA–CR+OI–MOR; b. Three tectonic settings IA–CR–OI; c. Three tectonic settings IA–CR–MOR; d. Three tectonic settings IA–OI–MOR; and e. Three tectonic settings CR–OI–MOR.

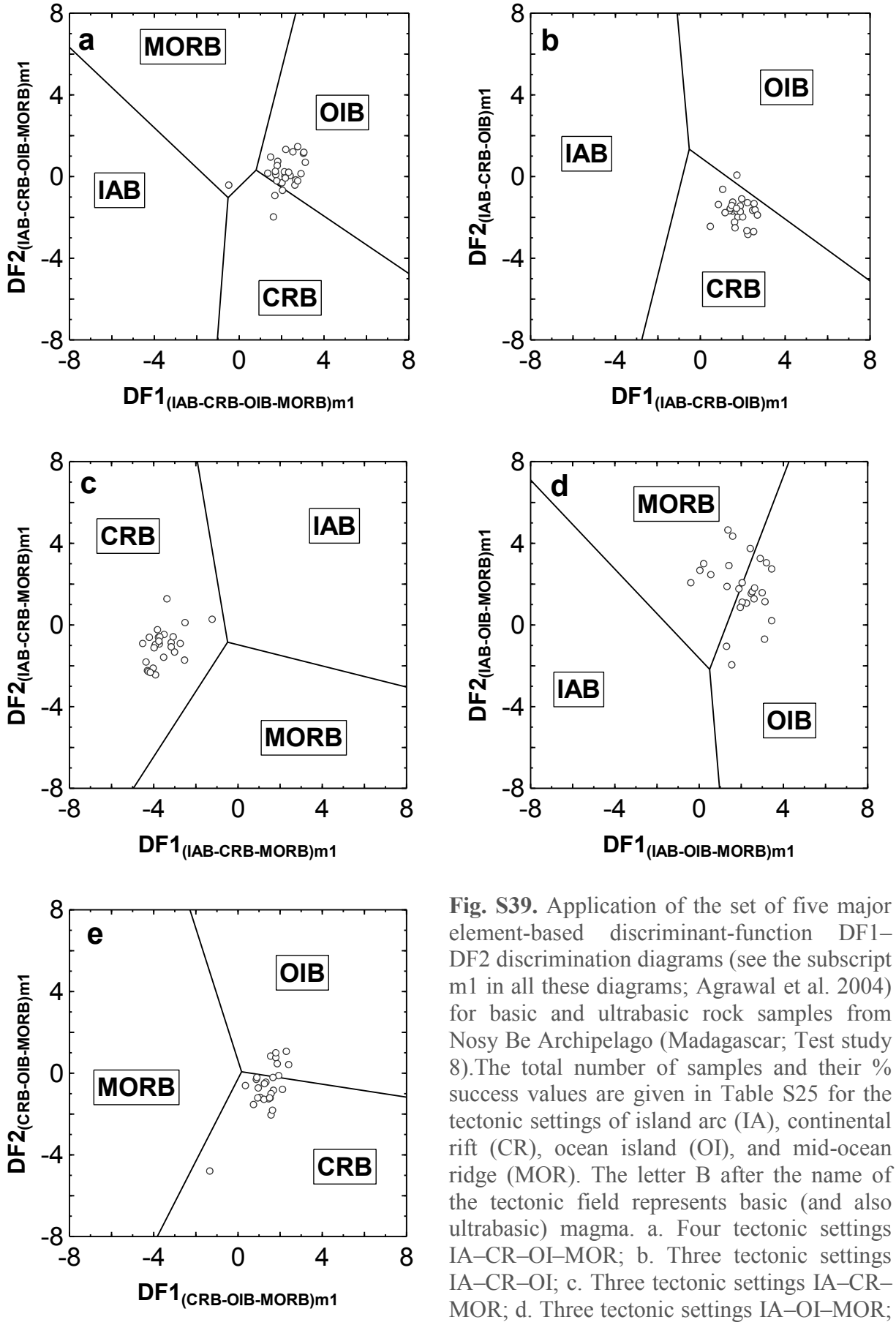

Fig. S39. Application of the set of five major element-based discriminant-function DF1–DF2 discrimination diagrams (see the subscript m1 in all these diagrams; Agrawal et al. 2004) for basic and ultrabasic rock samples from Nosy Be Archipelago (Madagascar; Test study 8).The total number of samples and their % success values are given in Table S25 for the tectonic settings of island arc (IA), continental rift (CR), ocean island (OI), and mid-ocean ridge (MOR). The letter B after the name of the tectonic field represents basic (and also ultrabasic) magma. a. Four tectonic settings IA–CR–OI–MOR; b. Three tectonic settings IA–CR–OI; c. Three tectonic settings IA–CR–MOR; d. Three tectonic settings IA–OI–MOR; and e. Three tectonic settings CR–OI–MOR.

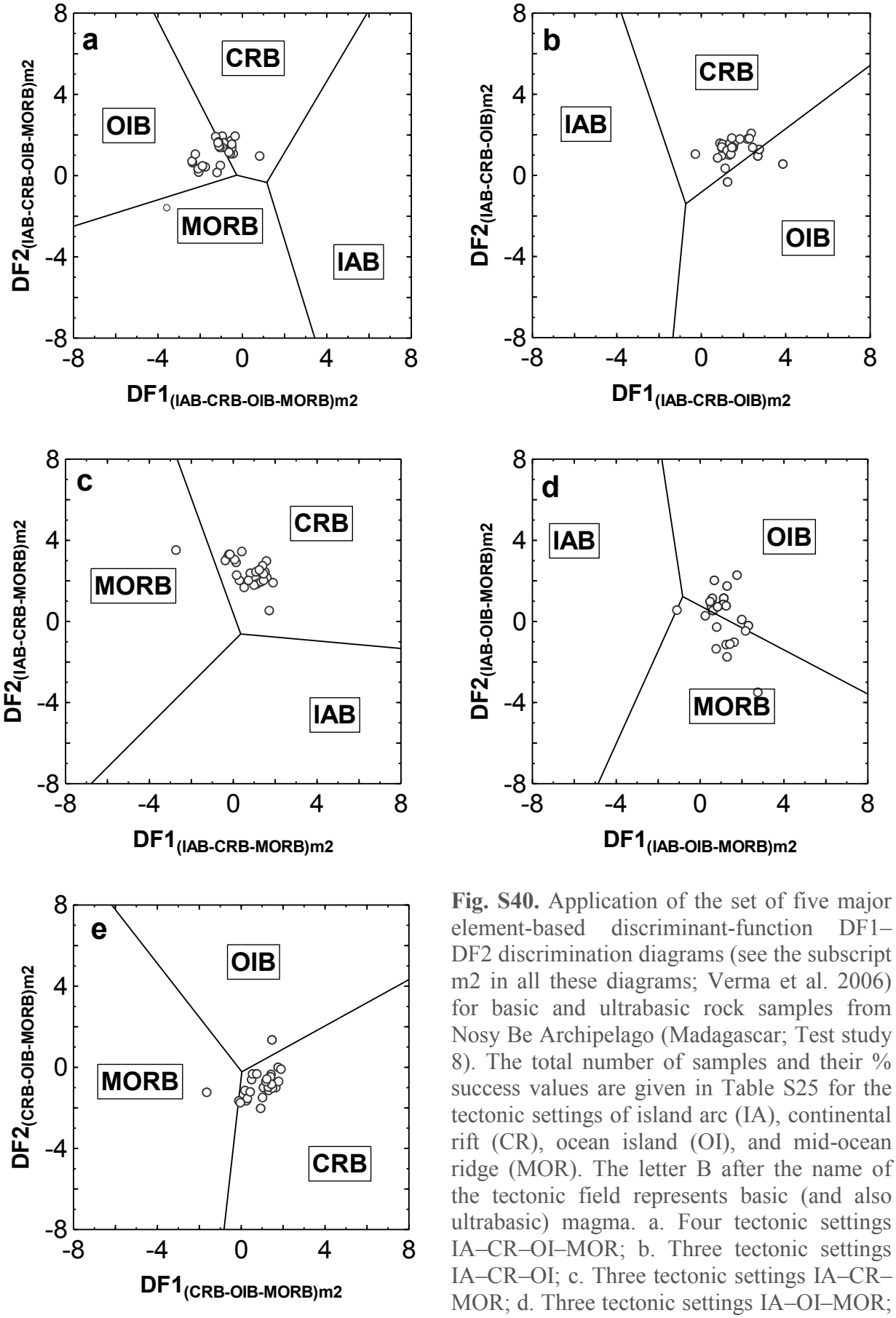

Fig. S40. Application of the set of five major element-based discriminant-function DF1–DF2 discrimination diagrams (see the subscript m2 in all these diagrams; Verma et al. 2006) for basic and ultrabasic rock samples from Nosy Be Archipelago (Madagascar; Test study 8). The total number of samples and their % success values are given in Table S25 for the tectonic settings of island arc (IA), continental rift (CR), ocean island (OI), and mid-ocean ridge (MOR). The letter B after the name of the tectonic field represents basic (and also ultrabasic) magma. a. Four tectonic settings IA–CR–OI–MOR; b. Three tectonic settings IA–CR–OI; c. Three tectonic settings IA–CR–MOR; d. Three tectonic settings IA–OI–MOR; and e. Three tectonic settings CR–OI–MOR.

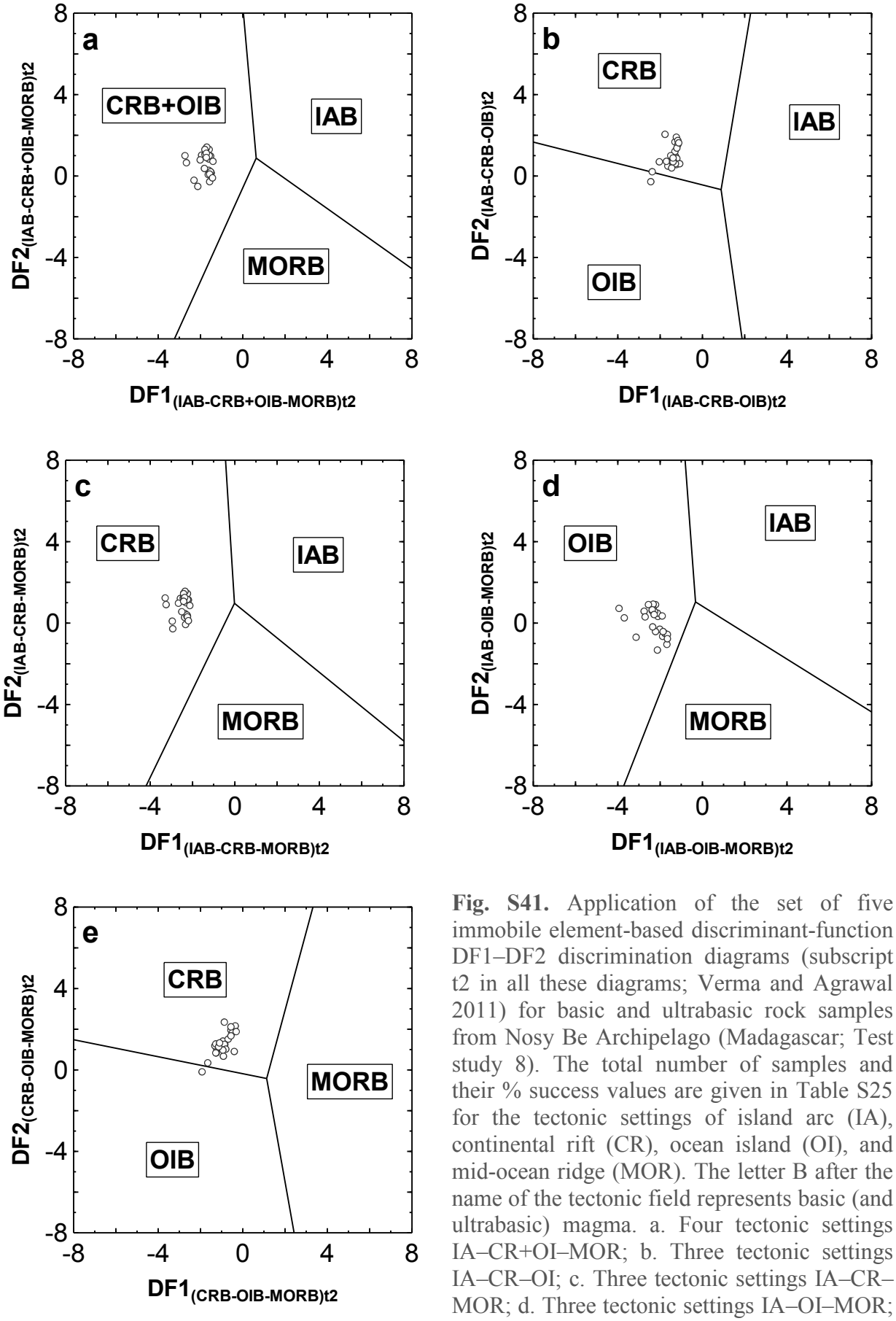

Fig. S41. Application of the set of five immobile element-based discriminant-function DF1–DF2 discrimination diagrams (subscript t2 in all these diagrams; Verma and Agrawal 2011) for basic and ultrabasic rock samples from Nosy Be Archipelago (Madagascar; Test study 8). The total number of samples and their % success values are given in Table S25 for the tectonic settings of island arc (IA), continental rift (CR), ocean island (OI), and mid-ocean ridge (MOR). The letter B after the name of the tectonic field represents basic (and ultrabasic) magma. a. Four tectonic settings IA–CR+OI–MOR; b. Three tectonic settings IA–CR–OI; c. Three tectonic settings IA–CR–MOR; d. Three tectonic settings IA–OI–MOR; and e. Three tectonic settings CR–OI–MOR.

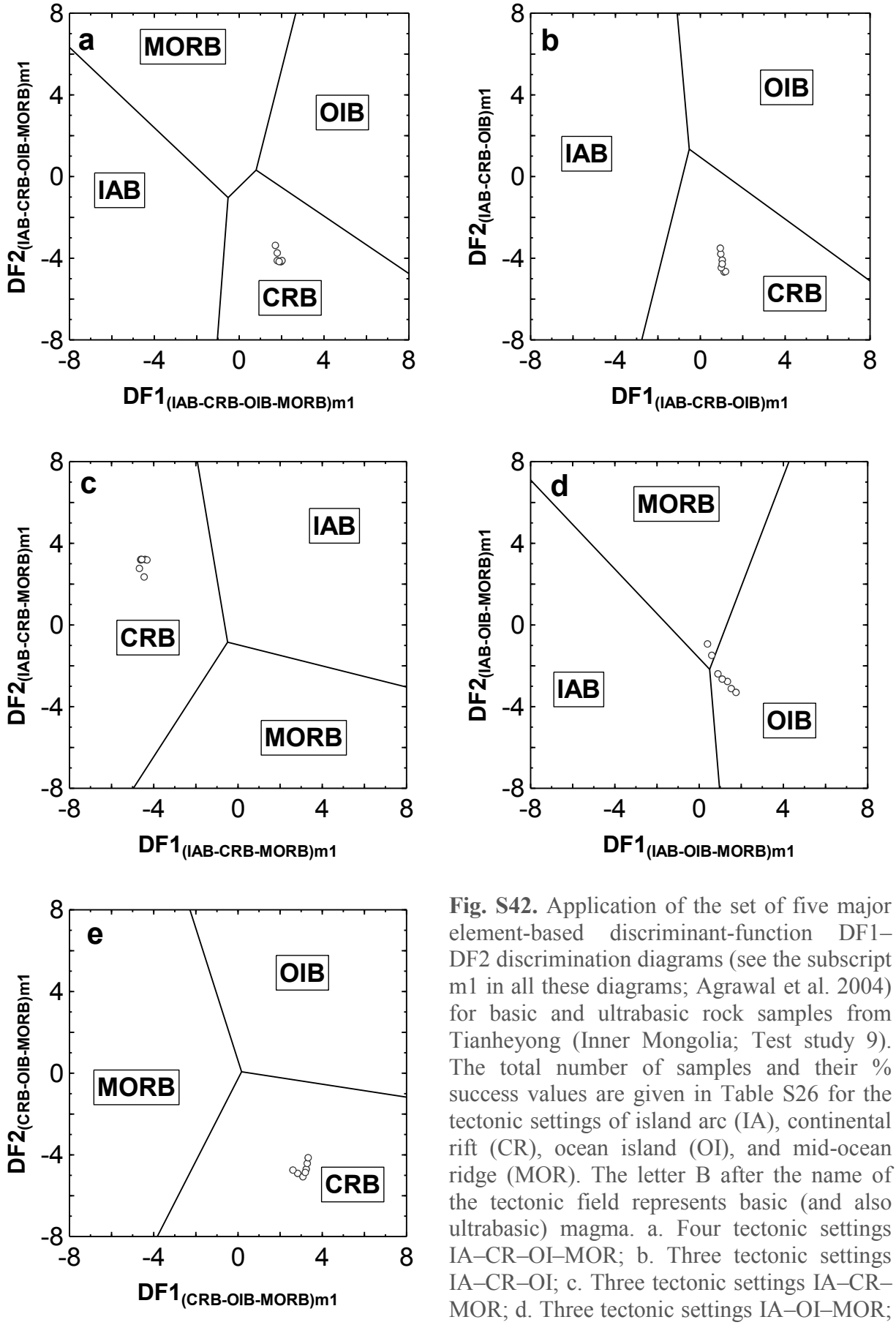

Fig. S42. Application of the set of five major element-based discriminant-function DF1–DF2 discrimination diagrams (see the subscript m1 in all these diagrams; Agrawal et al. 2004) for basic and ultrabasic rock samples from Tianheyong (Inner Mongolia; Test study 9). The total number of samples and their % success values are given in Table S26 for the tectonic settings of island arc (IA), continental rift (CR), ocean island (OI), and mid-ocean ridge (MOR). The letter B after the name of the tectonic field represents basic (and also ultrabasic) magma. a. Four tectonic settings IA–CR–OI–MOR; b. Three tectonic settings IA–CR–OI; c. Three tectonic settings IA–CR–MOR; d. Three tectonic settings IA–OI–MOR; and e. Three tectonic settings CR–OI–MOR.

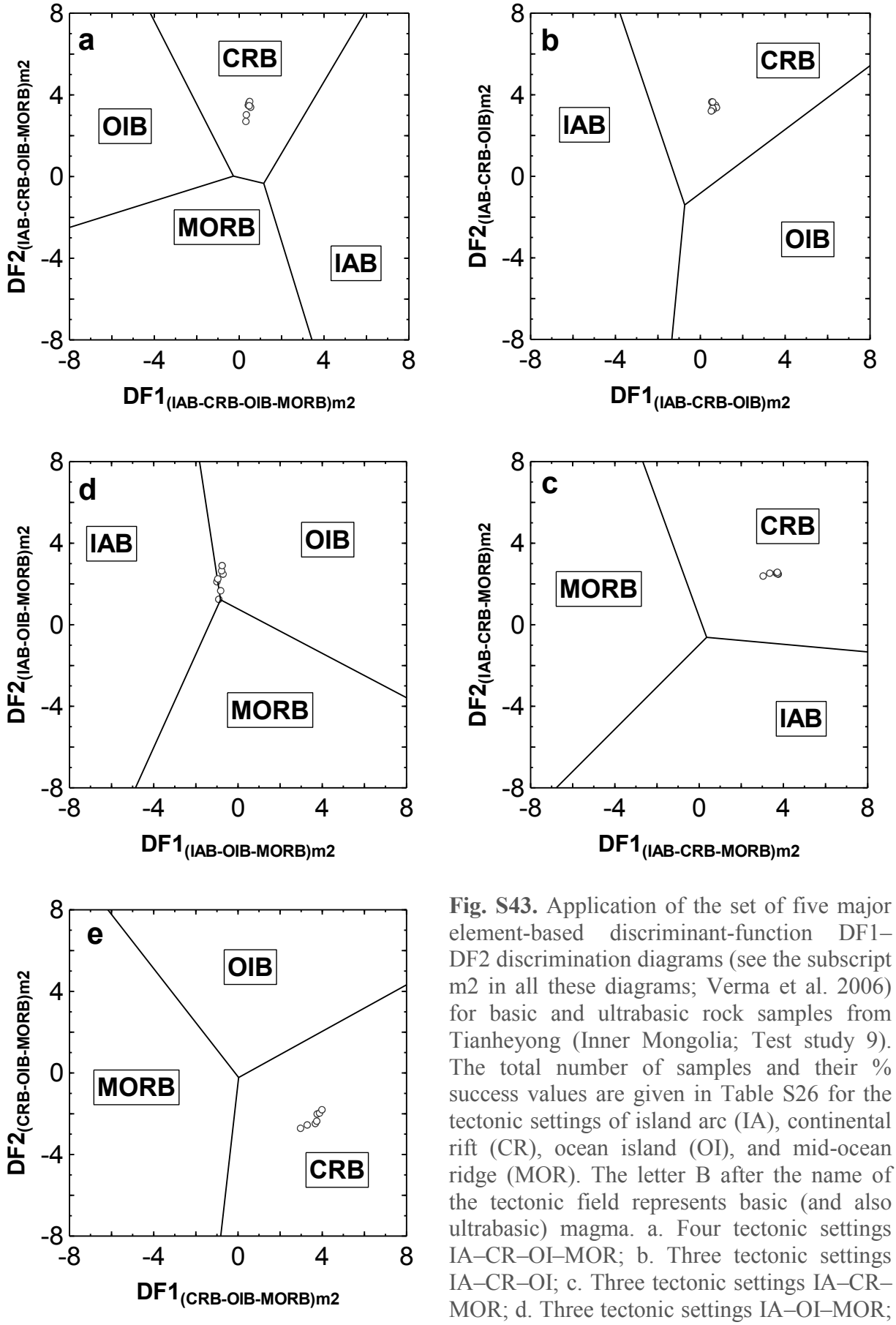

Fig. S43. Application of the set of five major element-based discriminant-function DF1–DF2 discrimination diagrams (see the subscript m2 in all these diagrams; Verma et al. 2006) for basic and ultrabasic rock samples from Tianheyong (Inner Mongolia; Test study 9). The total number of samples and their % success values are given in Table S26 for the tectonic settings of island arc (IA), continental rift (CR), ocean island (OI), and mid-ocean ridge (MOR). The letter B after the name of the tectonic field represents basic (and also ultrabasic) magma. a. Four tectonic settings IA–CR–OI–MOR; b. Three tectonic settings IA–CR–OI; c. Three tectonic settings IA–CR–MOR; d. Three tectonic settings IA–OI–MOR; and e. Three tectonic settings CR–OI–MOR.

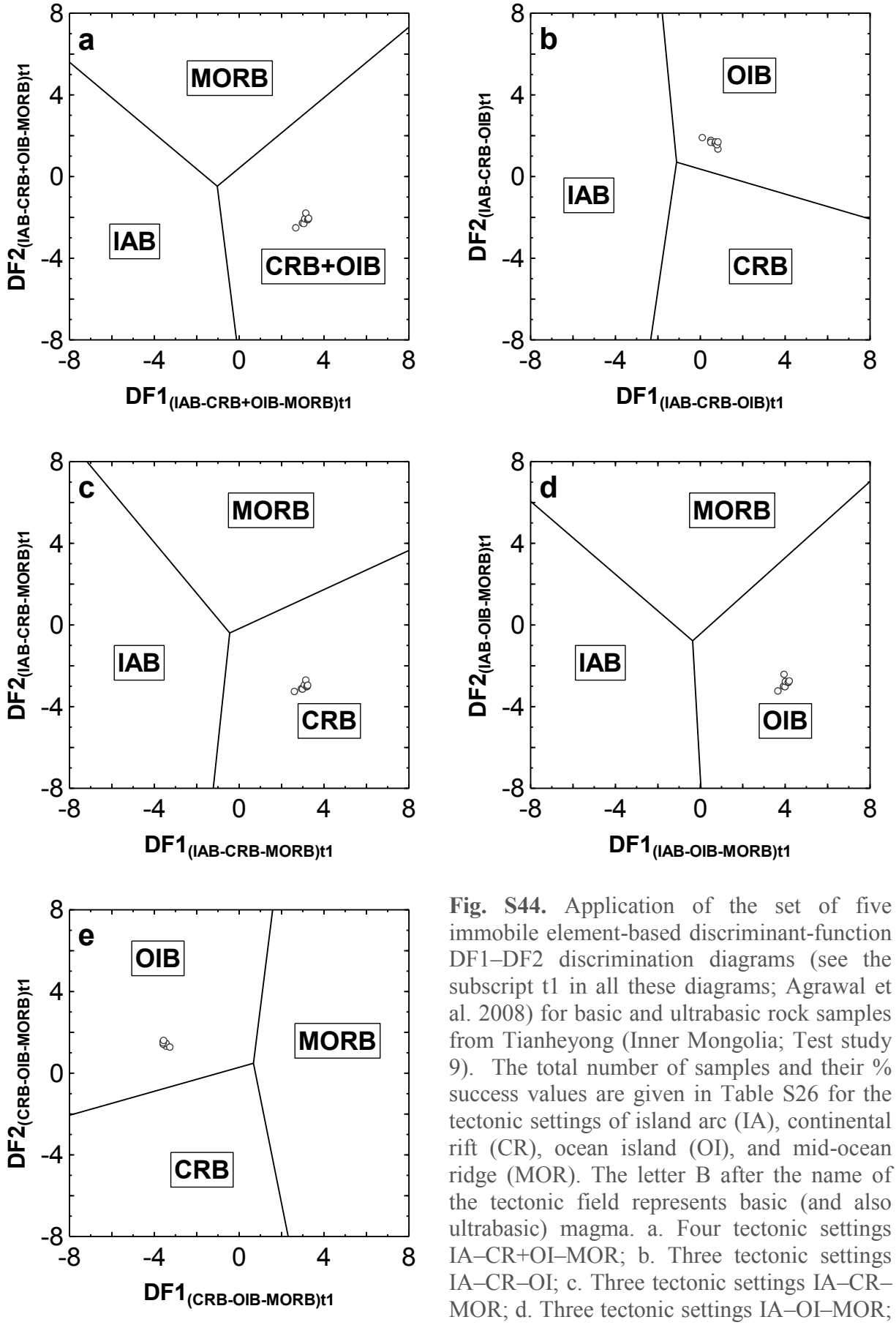

Fig. S44. Application of the set of five immobile element-based discriminant-function DF1–DF2 discrimination diagrams (see the subscript t1 in all these diagrams; Agrawal et al. 2008) for basic and ultrabasic rock samples from Tianheyong (Inner Mongolia; Test study 9). The total number of samples and their % success values are given in Table S26 for the tectonic settings of island arc (IA), continental rift (CR), ocean island (OI), and mid-ocean ridge (MOR). The letter B after the name of the tectonic field represents basic (and also ultrabasic) magma. a. Four tectonic settings IA–CR+OI–MOR; b. Three tectonic settings IA–CR–OI; c. Three tectonic settings IA–CR–MOR; d. Three tectonic settings IA–OI–MOR; and e. Three tectonic settings CR–OI–MOR

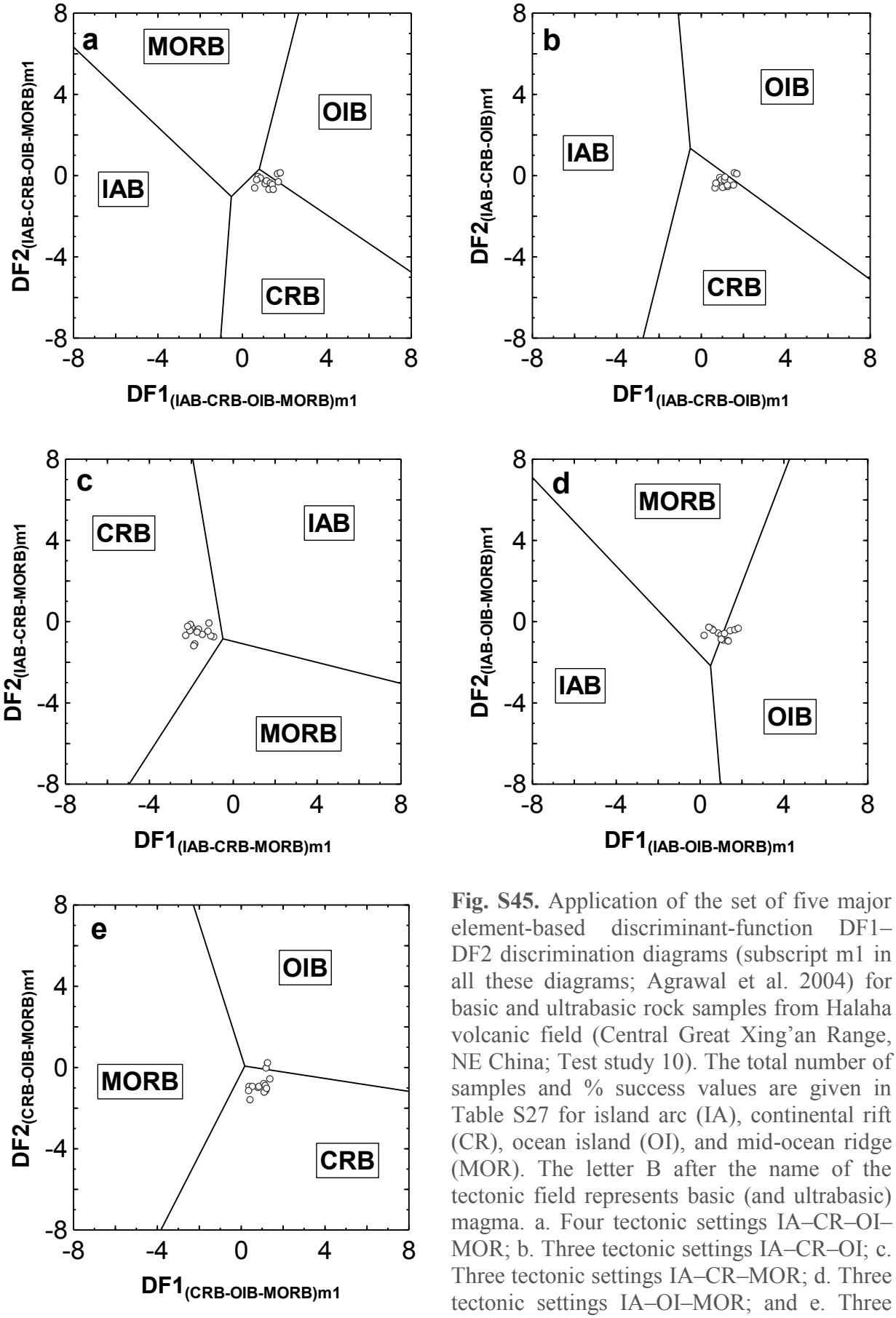

Fig. S45. Application of the set of five major element-based discriminant-function DF1–DF2 discrimination diagrams (subscript m1 in all these diagrams; Agrawal et al. 2004) for basic and ultrabasic rock samples from Halaha volcanic field (Central Great Xing'an Range, NE China; Test study 10). The total number of samples and % success values are given in Table S27 for island arc (IA), continental rift (CR), ocean island (OI), and mid-ocean ridge (MOR). The letter B after the name of the tectonic field represents basic (and ultrabasic) magma. a. Four tectonic settings IA–CR–OI–MOR; b. Three tectonic settings IA–CR–OI; c. Three tectonic settings IA–CR–MOR; d. Three tectonic settings IA–OI–MOR; and e. Three tectonic settings CR–OI–MOR.

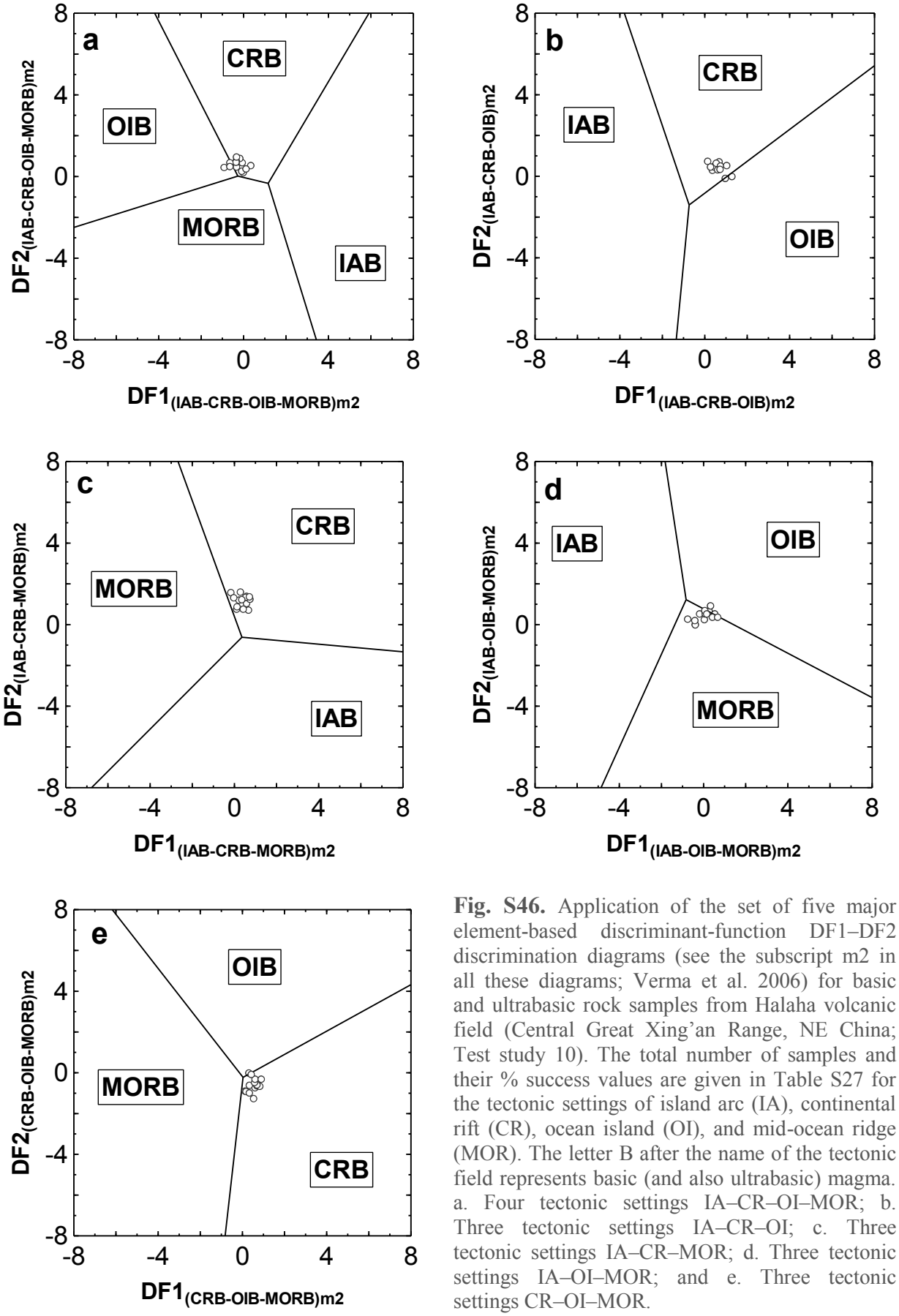

Fig. S46. Application of the set of five major element-based discriminant-function DF1–DF2 discrimination diagrams (see the subscript m2 in all these diagrams; Verma et al. 2006) for basic and ultrabasic rock samples from Halaha volcanic field (Central Great Xing'an Range, NE China; Test study 10). The total number of samples and their % success values are given in Table S27 for the tectonic settings of island arc (IA), continental rift (CR), ocean island (OI), and mid-ocean ridge (MOR). The letter B after the name of the tectonic field represents basic (and also ultrabasic) magma. a. Four tectonic settings IA–CR–OI–MOR; b. Three tectonic settings IA–CR–OI; c. Three tectonic settings IA–CR–MOR; d. Three tectonic settings IA–OI–MOR; and e. Three tectonic settings CR–OI–MOR.

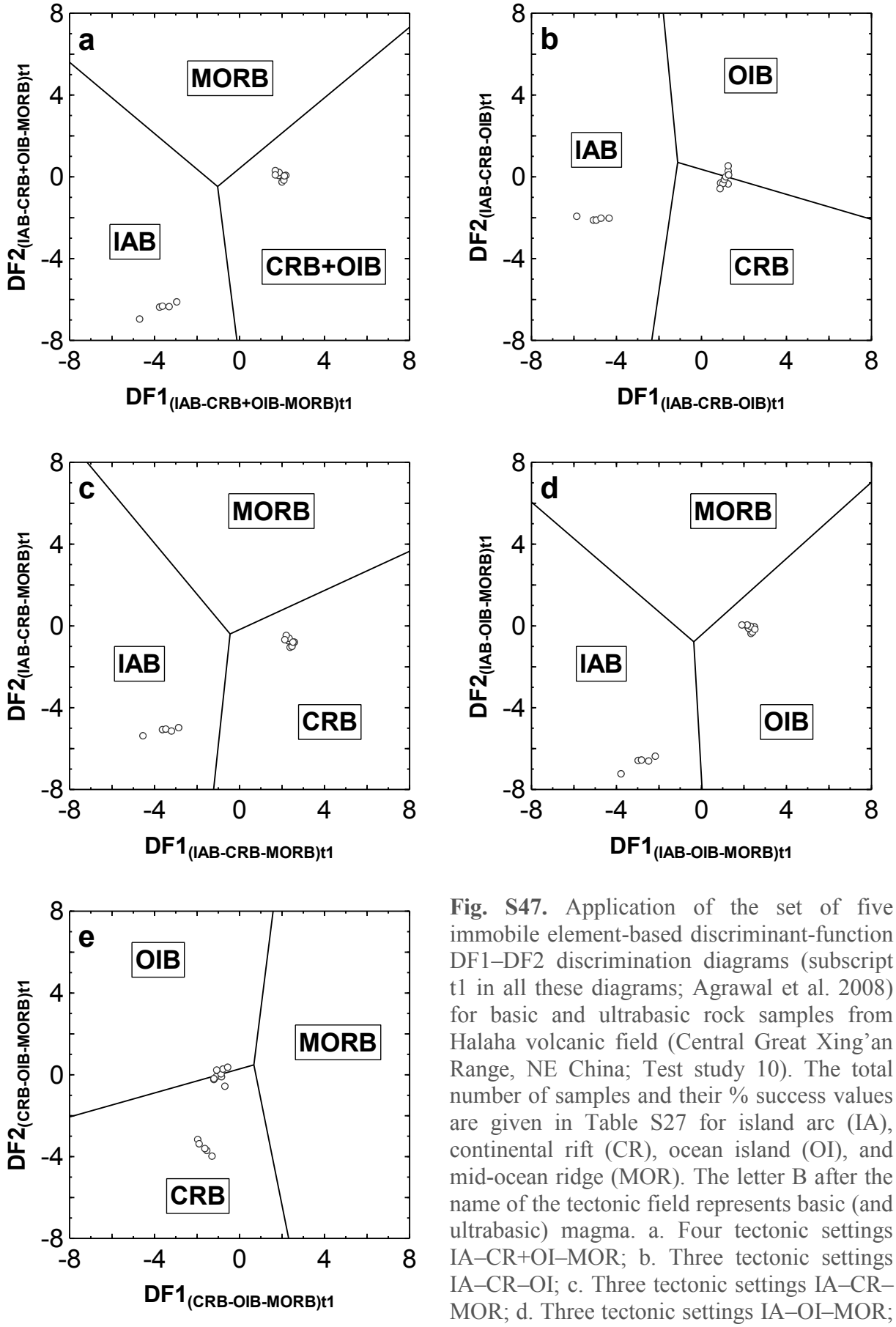

Fig. S47. Application of the set of five immobile element-based discriminant-function DF1–DF2 discrimination diagrams (subscript t1 in all these diagrams; Agrawal et al. 2008) for basic and ultrabasic rock samples from Halaha volcanic field (Central Great Xing'an Range, NE China; Test study 10). The total number of samples and their % success values are given in Table S27 for island arc (IA), continental rift (CR), ocean island (OI), and mid-ocean ridge (MOR). The letter B after the name of the tectonic field represents basic (and ultrabasic) magma. a. Four tectonic settings IA–CR+OI–MOR; b. Three tectonic settings IA–CR–OI; c. Three tectonic settings IA–CR–MOR; d. Three tectonic settings IA–OI–MOR; and e. Three tectonic settings CR–OI–MOR.

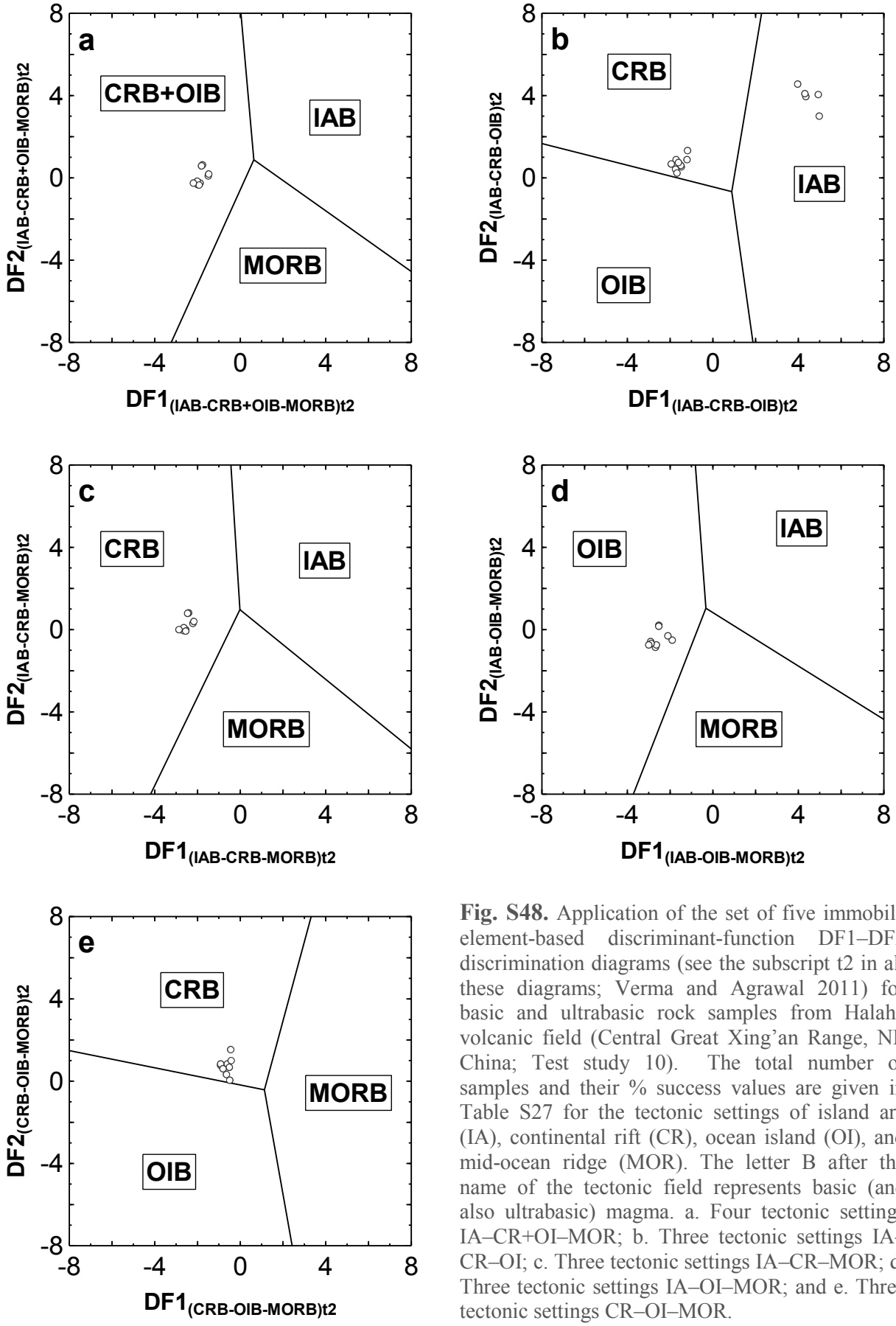

Fig. S48. Application of the set of five immobile element-based discriminant-function DF1–DF2 discrimination diagrams (see the subscript t2 in all these diagrams; Verma and Agrawal 2011) for basic and ultrabasic rock samples from Halaha volcanic field (Central Great Xing'an Range, NE China; Test study 10). The total number of samples and their % success values are given in Table S27 for the tectonic settings of island arc (IA), continental rift (CR), ocean island (OI), and mid-ocean ridge (MOR). The letter B after the name of the tectonic field represents basic (and also ultrabasic) magma. a. Four tectonic settings IA–CR+OI–MOR; b. Three tectonic settings IA–CR–OI; c. Three tectonic settings IA–CR–MOR; d. Three tectonic settings IA–OI–MOR; and e. Three tectonic settings CR–OI–MOR.

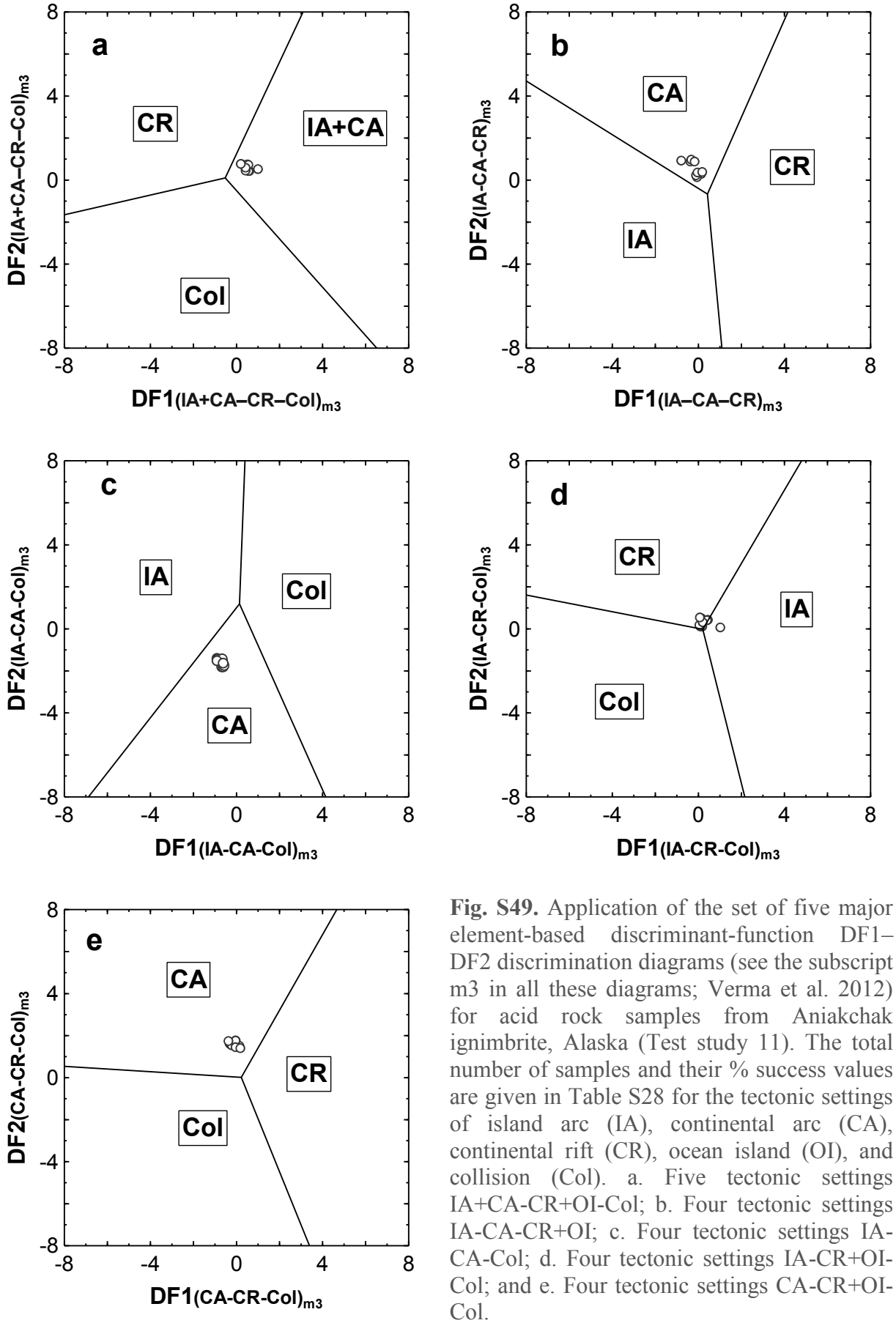

Fig. S49. Application of the set of five major element-based discriminant-function DF1–DF2 discrimination diagrams (see the subscript m3 in all these diagrams; Verma et al. 2012) for acid rock samples from Aniakchak ignimbrite, Alaska (Test study 11). The total number of samples and their % success values are given in Table S28 for the tectonic settings of island arc (IA), continental arc (CA), continental rift (CR), ocean island (OI), and collision (Col). a. Five tectonic settings IA+CA-CR+OI-Col; b. Four tectonic settings IA-CA-CR+OI; c. Four tectonic settings IA-CA-Col; d. Four tectonic settings IA-CR+OI-Col; and e. Four tectonic settings CA-CR+OI-Col.

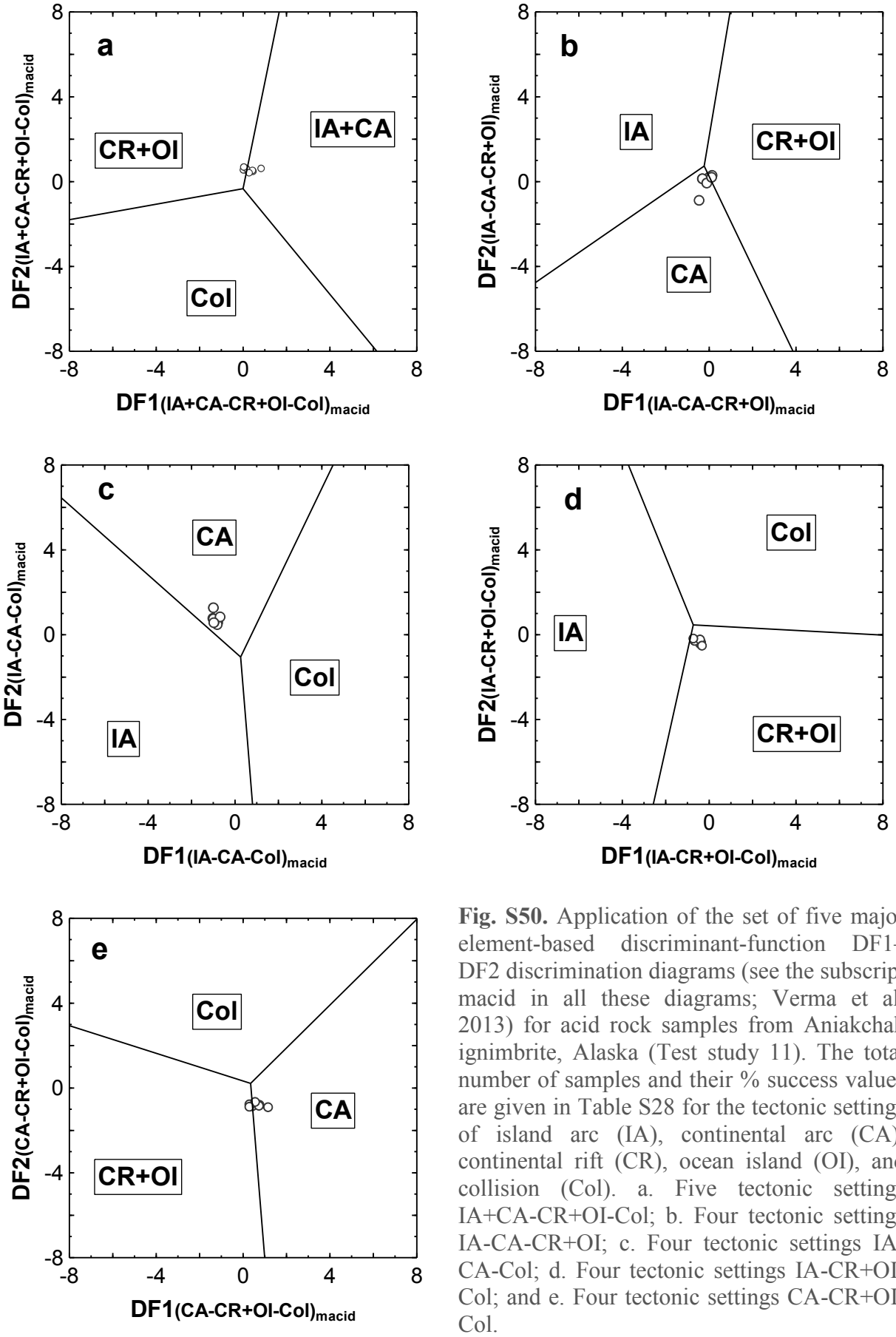

Fig. S50. Application of the set of five major element-based discriminant-function DF1–DF2 discrimination diagrams (see the subscript macid in all these diagrams; Verma et al. 2013) for acid rock samples from Aniakchak ignimbrite, Alaska (Test study 11). The total number of samples and their % success values are given in Table S28 for the tectonic settings of island arc (IA), continental arc (CA), continental rift (CR), ocean island (OI), and collision (Col). a. Five tectonic settings IA+CA-CR+OI-Col; b. Four tectonic settings IA-CA-CR+OI; c. Four tectonic settings IA-CA-Col; d. Four tectonic settings IA-CR+OI-Col; and e. Four tectonic settings CA-CR+OI-Col.

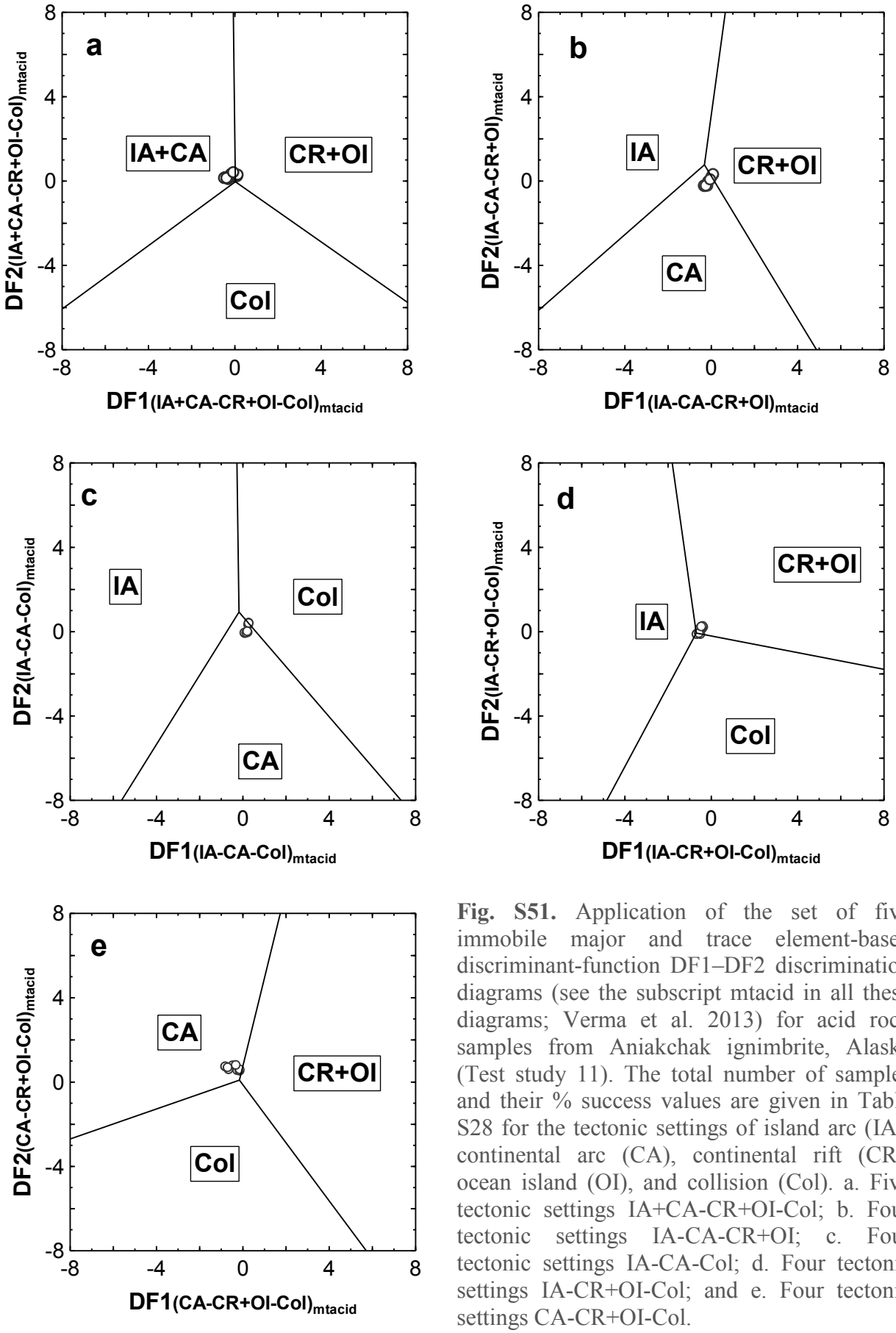

Fig. S51. Application of the set of five immobile major and trace element-based discriminant-function DF1–DF2 discrimination diagrams (see the subscript mtacid in all these diagrams; Verma et al. 2013) for acid rock samples from Aniakchak ignimbrite, Alaska (Test study 11). The total number of samples and their % success values are given in Table S28 for the tectonic settings of island arc (IA), continental arc (CA), continental rift (CR), ocean island (OI), and collision (Col). a. Five tectonic settings IA+CA-CR+OI-Col; b. Four tectonic settings IA-CA-CR+OI; c. Four tectonic settings IA-CA-Col; d. Four tectonic settings IA-CR+OI-Col; and e. Four tectonic settings CA-CR+OI-Col.

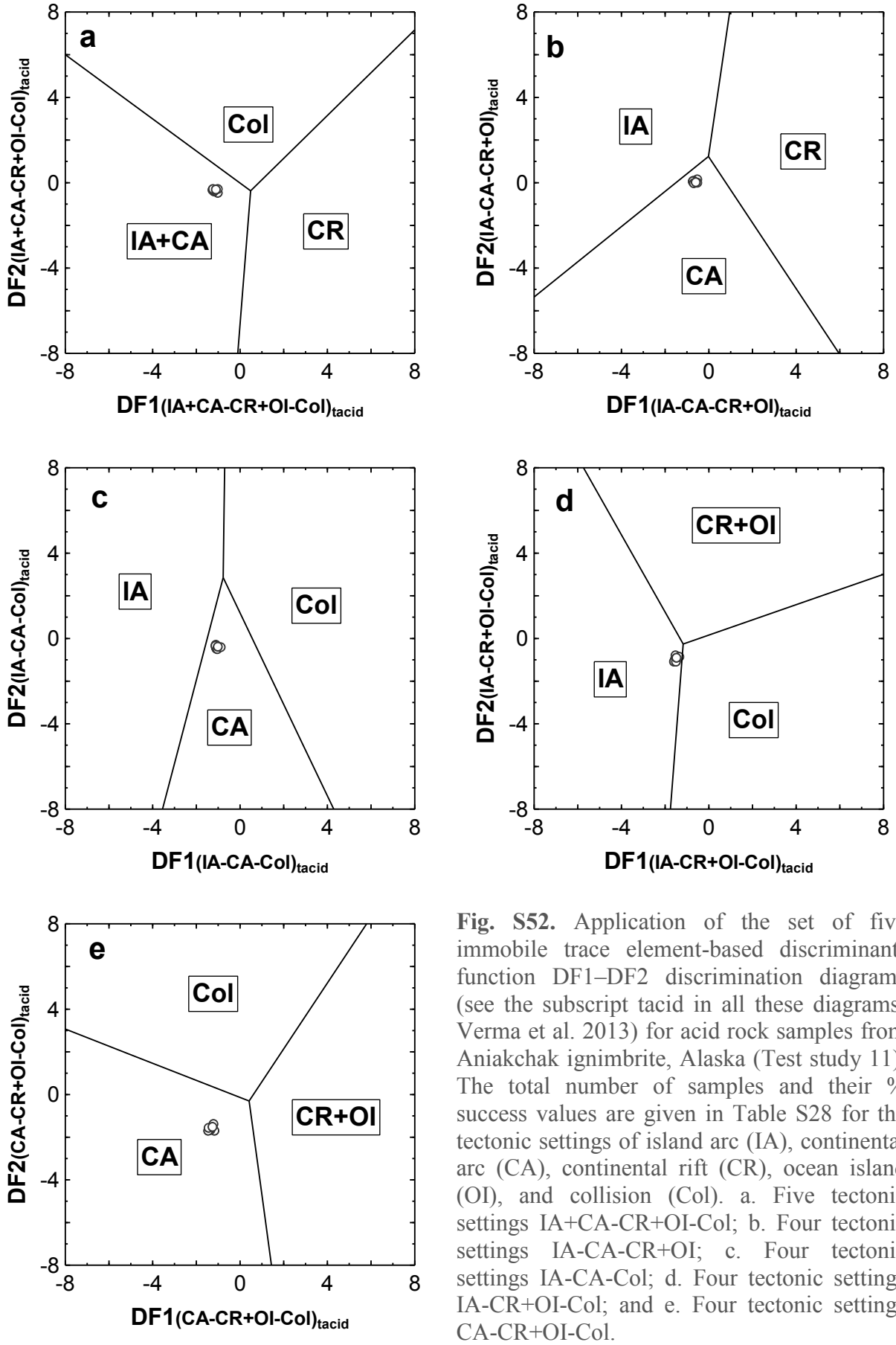

Fig. S52. Application of the set of five immobile trace element-based discriminant-function DF1–DF2 discrimination diagrams (see the subscript tacid in all these diagrams; Verma et al. 2013) for acid rock samples from Aniakchak ignimbrite, Alaska (Test study 11). The total number of samples and their % success values are given in Table S28 for the tectonic settings of island arc (IA), continental arc (CA), continental rift (CR), ocean island (OI), and collision (Col). a. Five tectonic settings IA+CA-CR+OI-Col; b. Four tectonic settings IA-CA-CR+OI; c. Four tectonic settings IA-CA-Col; d. Four tectonic settings IA-CR+OI-Col; and e. Four tectonic settings CA-CR+OI-Col.

Apéndice II

Verma, S.P., Pandarinath, K., **Rivera-Gómez, M.A.**, 2016a. Evaluation of the ongoing rifting and subduction processes in the geochemistry of magmas from the western part of the Mexican Volcanic Belt. Journal of South American Earth Sciences, 66: 125-148.

Contiene suplemento de 41 páginas.

Journal of South American Earth Sciences 66 (2016) 125–148

Contents lists available at ScienceDirect

Journal of South American Earth Sciences

journal homepage: www.elsevier.com/locate/jsames

Evaluation of the ongoing rifting and subduction processes in the geochemistry of magmas from the western part of the Mexican Volcanic Belt

Surendra P. Verma [a, *], Kailasa Pandarinath [a], M. Abdelaly Rivera-Gómez [b]

[a] Departamento de Sistemas Energéticos, Instituto de Energías Renovables, Universidad Nacional Autónoma de México, Temixco, Morelos 62580, Mexico
[b] Posgrado en Ingeniería, Instituto de Energías Renovables, Universidad Nacional Autónoma de México, Temixco, Morelos 62580, Mexico

ARTICLE INFO

Article history:
Received 7 September 2015
Received in revised form
27 November 2015
Accepted 22 December 2015
Available online 29 December 2015

Keywords:
Tectonics
Discordancy tests
Significance tests
Multidimensional diagrams
Mexico
Trans-Mexican Volcanic Belt

ABSTRACT

A compilation of new and published geochemical data for 1512 samples of volcanic rocks from the western part of the Mexican Volcanic Belt was first subdivided according to the age group (136 samples of Miocene and 1376 samples of Pliocene-Holocene). Rocks of the younger group were then subdivided as Rift (1014 samples from the triple-rift system) and No Rift (362 samples outside of the triple-rift system) or Near Trench (937 samples) and Far Trench (439 samples) magmas. These subdivisions were considered separately as basic, intermediate, and acid magmatic rocks. The application of the conventional and multidimensional techniques confirmed the great tectonic and geochemical complexity of this region. The presence of oceanic-type basalts suggested to result from a mantle plume was not confirmed from the tectonomagmatic multidimensional diagrams. The Miocene rocks, which are present at the surface far from the Middle-America Trench, showed a likely continental rift setting in most diagrams for basic rocks and a continental arc setting for intermediate rocks. These differences can be explained in terms of the petrogenetic origin of the magmas. Unlike the current thinking, the triple-rift system seems to have influenced the chemistry of Pliocene-Holocene basic rocks, which indicated a continental rift setting. The Pliocene-Holocene intermediate and acid rocks, however, did not show such an influence. The Pliocene-Holocene basic rocks indicated a continental rift setting, irrespective of the Near Trench and Far Trench subdivision because numerous Near Trench rocks also lie in the triple-rift and graben systems. However, the intermediate rocks having a crustal component in their genesis indicated a continental arc (Near Trench) or a transitional arc to within-plate setting (Far Trench). The acid rocks having a crustal component also suggested a continental arc (Near Trench) or a transitional setting (Far Trench). The application of the tectonomagmatic multidimensional diagrams to the data from the three rifts (Tepic-Zacoalco Rift, Colima Rift, and Chapala Rift) also revealed similarities and differences among them. The application of significance tests to log-transformed ratios further clarified the similarities and differences among the chemical characteristics of the Rift – No Rift and Near Trench – Far Trench subdivisions.

1. Introduction

In the western (W) part of the Mexican Volcanic Belt (MVB; also called the Trans-Mexican Volcanic Belt – TMVB), the Rivera plate and northern part of the Cocos plate are subducting beneath western Mexico along the Middle America Trench (MAT; Fig. 1; Bandy et al., 1995; Yang et al., 2009), and a triple rift system (TZR-CR-ChR) on land is simultaneously active. The Rivera and Cocos plates are kinematically different. The deformation in southwestern Mexico and the opening along the Colima rift is related to oblique subduction of the Cocos plate along the northern part of the MAT (DeMets and Stein, 1990). Based on the data on hypocenters of earthquakes recorded along western Mexico, Pardo and Suárez

* Corresponding author.
E-mail addresses: spv@ier.unam.mx (S.P. Verma), pk@ier.unam.mx (K. Pandarinath), marig@ier.unam.mx (M.A. Rivera-Gómez).

http://dx.doi.org/10.1016/j.jsames.2015.12.007
0895-9811/

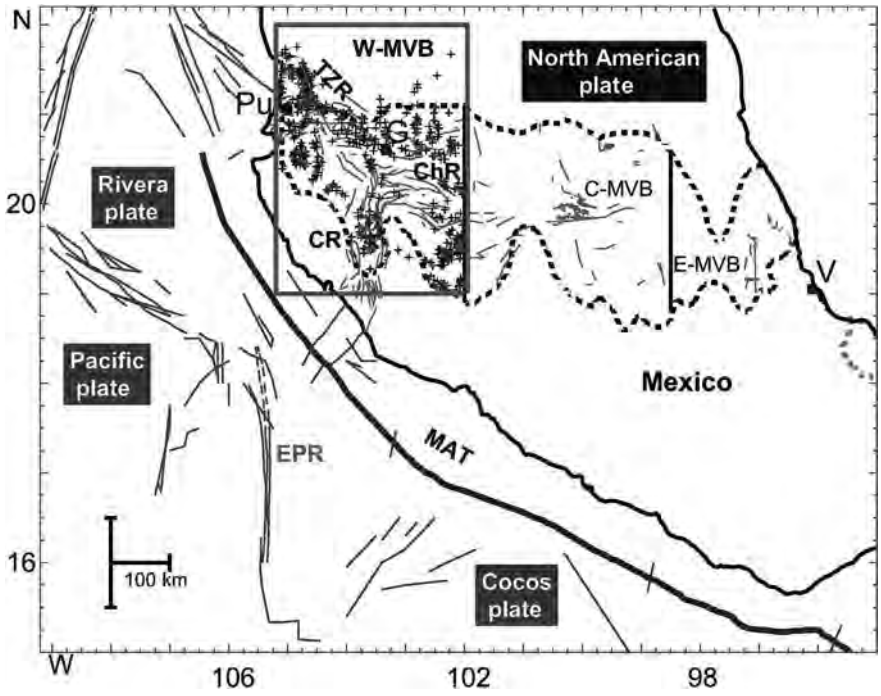

Fig. 1. Location of the study area of the western (W) part of the Mexican Volcanic Belt (MVB). The traces of the central and eastern parts of the MVB (C-MVB and E-MVB) as well as the approximate location of the Rivera, Cocos, Pacific and North American plates are also shown. An approximate scale is also included for reference. The abbreviations are as follows: Pu–Puerto Vallarta; G–Guadalajara; V–Veracruz; EPR–East Pacific Rise; MAT–Middle American Trench (thick curve); CR–Colima Rift; ChR–Chapala Rift; TZR–Tepic Zacoalco Rift. Fractures and faults are shown schematically as thin solid curves. The box shows approximate boundary of the W-MVB and represents the study area. Thick vertical line represents the approximate boundary between C-MVB and E-MVB. Similarly, the dashed line indicates the schematic limits of the Mexican Volcanic Belt. The small crosses indicate approximate sample locations from the W-MVB.

(1995) indicated a difference in the Rivera and Cocos subduction systems. According to them, the subduction of the Rivera plate is steep (similar to the geometry of the subduction of the Cocos plate beneath Central America), whereas the subduction of the Cocos plate in southern Mexico is shallower and subhorizontal. According to Pardo and Suárez (1995) the presence of Colima and other Quaternary volcanoes parallel to the MAT might have resulted from the subduction of Rivera plate below the Jalisco block in western Mexico. Based on aeromagnetic data from the western part of the MVB, Campos-Enriquez et al. (1990) have reported that the basal Miocene-Early Pliocene volcanic products become thinner, whereas the overlying Plio-Quaternary volcanism becomes thicker from west to east.

Bandy et al. (2000) interpreted marine geophysical and geological data to infer the presence of three distinct morphotectonic zones (an eastern extensional zone located adjacent to the MAT, a central zone which lacks discrete deformation, and a western zone which exhibits a complex morphology related to ridge propagation) in the vicinity of the boundary of the Rivera and Cocos plates. Another concept that may affect the interpretation of the geoscientific data from the MVB was put forth by the presence of a southern Mexico block that is uncoupled from the North American plate and has a southeast motion with respect to North America, accommodated by extension through the central part of the MVB. From offshore and inland gravimetric data, Alvarez and Yutsis (2015) proposed that the diffuse boundary between the Rivera and Cocos plates can be considered well-defined at least from the MAT to the region of the Colima Volcanic Complex. Suhardja et al. (2015) opined that southwestern Mexico is a region of complex active tectonics with subduction of the Rivera and Cocos plates and widespread magmatism and rifting in the continental interior. These authors also stated that the crustal thickness varies from about 20 km near the coast to about 42 km in the continental interior. The Rivera plate has steeper dip than the Cocos plate and is also about 10 km deeper along the coast than previously estimated by Pardo and Suárez (1995).

At the same time, a well-defined triple rift system (Tepic-Zacoalco Rift, Colima Rift, and Chapala Rift; Fig. 1; e.g. Luhr et al., 1985; Allan, 1986; Wallace et al., 1992; Garduño-Monroy et al., 1993; Campos-Enríquez and Alatorre-Zamora, 1998; Pacheco et al., 1999; Frey et al., 2007) has been causing the Jalisco block to drift westward towards the Pacific Ocean. From GPS data, Selvans et al. (2011) inferred the extension across both the Colima and Tepic-Zacoalco rifts at about 8 mm/year or less, which is less than the relative rates of motion at nearby plate boundaries.

Righter et al. (1995) noted that the junction of the W-MVB and the Gulf of California represents a superposition of subduction and continental rifting tectonic regimes in the late Cenozoic and documented that the extension at the edge of the Jalisco Block has occurred since ca. 4.2 Ma. Frey et al. (2007) suggested that the voluminous ignimbrite flare-up in the Tepic-Zacoalco rift at 5–3 Ma may reflect the initial stages of rifting of the Jalisco block away from North America, analogous to what occurred in the proto-gulf region at 12–6 Ma prior to the transfer of Baja California from North America to the Pacific plate.

The Neogene tectonic picture of southern Mexico is even more complicated from the presence of Southern Mexico block (Andreani et al., 2008), which is considered to be in motion with respect to the North American plate. According to these authors, the motion of

this block is likely to be accommodated by extension through the central MVB. Andreani et al. (2008) further hypothesized that the triple rift system of the W-MVB continues all the way through the entire MVB and define the northern boundary of the Southern Mexico block.

Moore et al. (1994) stated that oceanic-type basalts have erupted in the W-MVB since about 10 Ma and suggested the presence of a mantle plume beneath the Guadalajara region (Fig. 1) stating it to be the first manifestation of the separation of the Jalisco block from North America.

This W-MVB region has been intensely studied as shown by the sample locations in Figs. 1–4. The age of the volcanism ranges mostly from Pliocene to Holocene (Figs. 3 and 4; e.g., Luhr and Carmichael, 1980; Nelson, 1980; Mahood, 1981; Verma and Nelson, 1989; Wallace and Carmichael, 1994; Luhr, 2000; Carmichael et al., 2006; Crummy et al., 2014; this work), with some outcrops of Miocene mostly far away from the MAT (~10 Ma) age (Fig. 2a; e.g., Gastil et al., 1979; Verma et al., 1985; Ferrari et al., 1994, 2000; Moore et al., 1994; Mori et al., 2009; this work). Further, the volcanism of both subalkaline and alkaline varieties has erupted throughout the W-MVB (e.g., Nelson and Livieres, 1986; Luhr et al., 1989; Verma and Nelson, 1989; Luhr, 1997; Verma and Luhr, 2010).

Because of the complex tectonic processes operating simultaneously in the W-MVB, it may be worthwhile to evaluate their effects in the chemistry of the magmas. Therefore, the main purpose of the present work is to evaluate the chemical effects of the following processes: (1) the Miocene volcanism prior to the rifting process of Jalisco block supposedly associated to the rifting of Baja California from the W-MVB and onset of the plume activity besides, of course, the ongoing subduction of the Cocos and Rivera plates along the MAT (Righter et al., 1995; Moore et al., 1994, Fig. 2a); (2) the effect of highly heterogeneous crust documented in crustal xenoliths and older (Cretaceous to Paleogene) rocks (Fig. 2b); (3) the ongoing rifting processes along three rift zones intersecting at a triple junction by subdividing the samples as "Rift" and "No Rift" (Fig. 3) although some samples outside the triple rift system are also located in other grabens; and (4) ongoing subduction processes of the Rivera and Cocos plates beneath the W-MVB by subdividing the samples as "Near Trench" and "Far Trench" (Fig. 4). These two sample groups (Rift–No Rift and Near Trench–Far Trench) were then evaluated from tectonomagmatic multidimensional diagrams as well as discordancy and significance tests. Similarly, the three rifts were separately considered in the multidimensional diagrams to better understand their similarities and differences.

2. Previous studies on comparison of magmas in the W-MVB

Although there are several studies on the W-MVB, only some key studies are mentioned here. Luhr et al. (1985) postulated that a major, ongoing episode of continental rifting has formed a system of three intersecting grabens in the W-MVB and small volumes of unusual alkaline magmas have erupted in these grabens in close association with the more abundant, subduction-related calc-alkaline (subalkaline) magmas. We now prefer to use the term subalkaline instead of calc-alkaline (Sheth et al., 2002). Nelson and Livieres (1986) studied subalkaline and alkaline magmas from the Sanganguey volcano and its vicinity in the Tepic-Zacoalco Rift and concluded that these magma types were either derived from distinct mantle sources or the mantle-derived alkaline magmas provided heat to partially melt the lower crustal rocks which gave rise to the subalkaline magmas. Tera et al. (1986) in a worldwide study of ^{10}Be in active or historic volcanoes, reported negligible concentrations of ^{10}Be for the Colima and Ceboruco volcanoes; these results were in contrast with the Central American volcanoes, for which extremely large ^{10}Be concentrations were obtained clearly indicating significant contributions from the subducted sediments in them.

Luhr et al. (1989) compared the chemistry of primitive subalkaline and alkaline rocks from the W-MVB and concluded that both types of magmas were generated from a common source and that the eruption of lampropyric melts in an arc setting was made possible by through-crustal extensional fracture systems related to active rifting of the Jalisco block from the North American plate. Verma and Nelson (1989) also documented the geochemical and isotopic characteristics of subalkaline and alkaline magmas from the Tepic Zacoalco Rift. However, they concluded that the two types of rocks resulted from melting of two distinct sources. The subalkaline rocks originated from a mixed mantle and slab-derived fluids whereas the alkaline rocks were from an OIB-type source. Further, the evolution of both

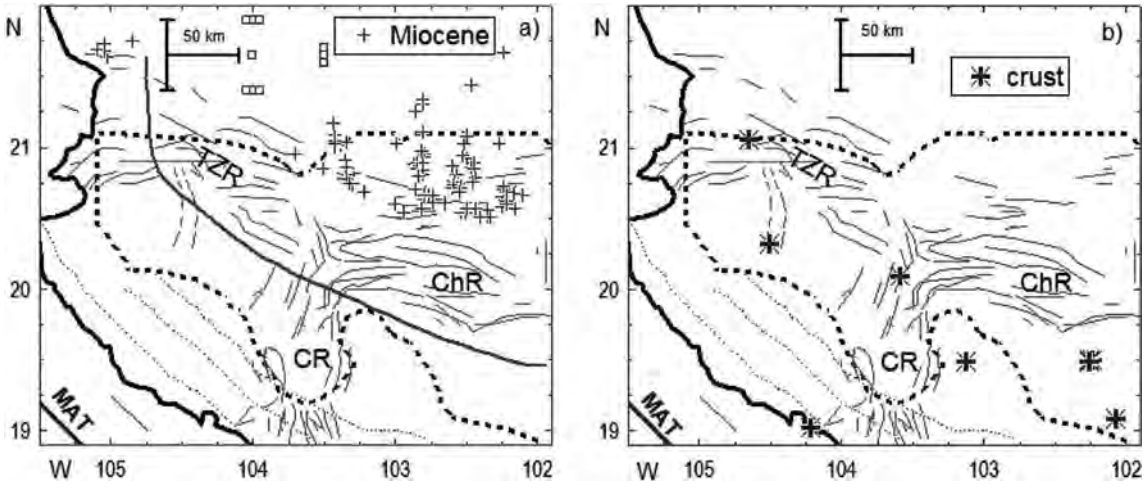

Fig. 2. Location of samples in the western part of the Mexican Volcanic Belt (W-MVB). The thick line represents schematic boundary between the Near Trench and Far Trench subdivision and dotted thin curves subparallel to the MAT indicate the subsurface trace of the subducted slab. See Fig. 1 for explanation to other lines and symbols; a) Miocene rocks; and b) crustal rocks and xenoliths.

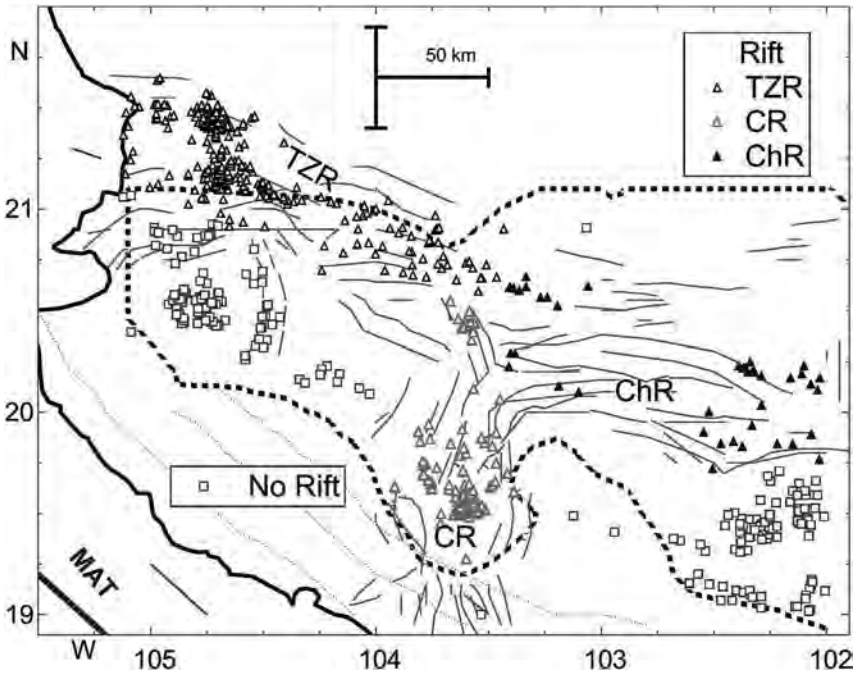

Fig. 3. Location of Pliocene-Holocene rock samples according to the subdivision of Rift and No Rift areas in the western part of the Mexican Volcanic Belt (MVB); the Rift area consists of three rifts – Tepic-Zacoalco Rift (TZR), Colima Rift (CR), and Chapala Rift (ChR); different symbols are used for each rift, whereas all samples from outside these three Rifts are designated as "No Rift" samples; see Figs. 1 and 2 for more explanation.

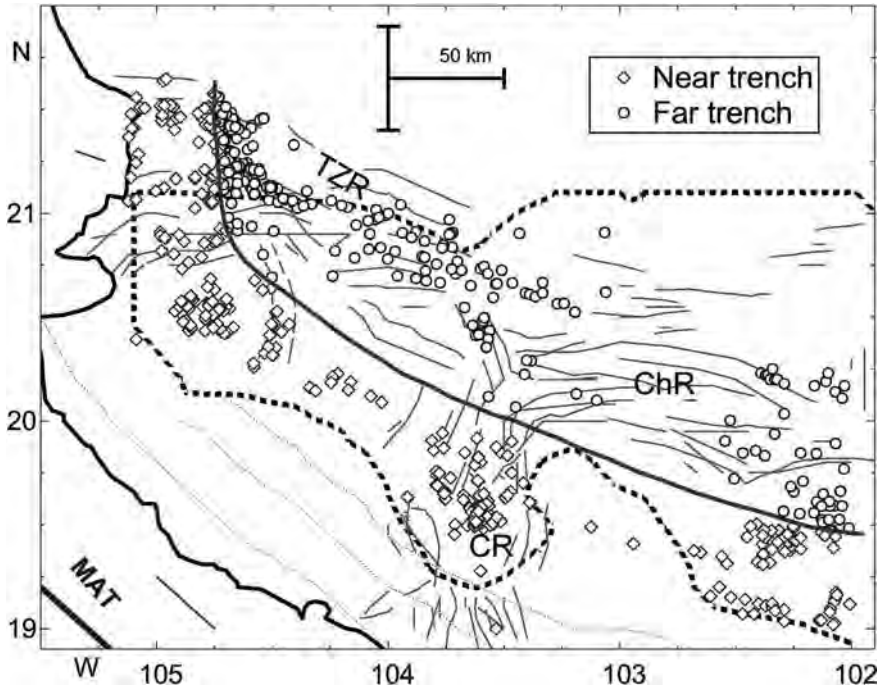

Fig. 4. Location of Pliocene-Holocene rock samples according to the subdivision of near the trench (Near Trench) and far from the trench (Far Trench) areas in the western part of the Mexican Volcanic Belt (MVB; see Figs. 1 and 2 for more explanation.

types of magmas requires the process of crystal fractionation accompanied by assimilation.

Luhr (1992) compared two historically active volcanoes–Colima and Ceboruco–in the W-MVB. Both volcanoes are located within the triple rift system–Colima in the Colima Rift and Ceboruco in the Tepic-Zacoalco Rift. Luhr (1992) concluded that the source regions for magmas from both Colima and Ceboruco are presumed to lie in the mantle wedge above the subducting slab. The differences between these two volcanoes indicate that the mantle wedge beneath Colima is more strongly affected by fluids rising from the slab and is

apparently strongly "polluted" by K, Ba, Sr, and Rb relative to other elements, and strongly hydrated, which leads to higher percentages of partial melting compared to the Ceboruco source. As a possible reason for these differences, Luhr (1992) stated that Colima lies closer to the trench than any other Mexican volcano.

From a study of Pliocene-Holocene minette lavas and associated leucitites in the W-MVB, Wallace and Carmichael (1989) concluded that the high-K magmas were derived from a source region which consists predominantly of phlogopite, clinopyroxene, and apatite formed through hydrous enrichment of the subarc mantle in response to subduction. Wallace and Carmichael (1992) further stated that the complex tectonic regime in western Mexico suggests that rifting and crustal extension play an important role in the generation and successful ascent of melts from enriched regions of the sub-arc mantle. Carmichael et al. (1996) also studied Quaternary minettes and associated volcanic rocks of the W-MVB and suggested them to be a consequence of plate extension above a subduction modified mantle wedge. Luhr (1997) stated that primitive volcanic rocks are relatively common in the W-MVB in comparison with most of the world's subduction-related areas and concluded that the intraplate-type alkaline basalts seem to reflect partial melting of convective upper mantle that was compositionally unaffected by subduction but advected into the region beneath the rifting continental lithosphere.

Petrone et al. (2003) remarked the unusual coexistence of subduction-related and continental intraplate-type magmatism in the Tepic-Zacoalco graben and from geochemical and isotopic data, concluded that the different series derived from distinct parental magmas as suggested earlier by Verma and Nelson (1989). Valdez-Moreno et al. (2006) documented Sr, Nd, Pb, and O isotopic data for the Colima volcano and plutonic xenoliths and suggested that the subalkaline magmas have a large crustal component detectable only in the combined Sr–O and O–Nd isotope diagrams. Blatter and Hammersley (2010) documented the effect of the Orozco Fracture Zone (OFZ) in the chemistry of magmas from the central part of the MVB but they also included some samples from the W-MVB. Diaz-Bravo et al. (2014) studied the intraplate ocean island type volcanism from the Tepic-Zacolaco rift and concluded that the pre-subduction mantle wedge in western Mexico must be as diverse as that below the Pacific basin and that extension-driven mantle upwelling in a continental setting melted a dry peridotitic mantle to its lowest extents.

Thus, it appears that no study has evaluated the geochemistry of Miocene rocks nor has any study so far objectively compared the Rift and No Rift or Near Trench and Far Trench magmatic rocks. To do so is the main objective of the present work. However, in this evaluation and comparison no distinction is made between the alkaline and subalkaline magmas in order to compare and contrast the overall compositions of basic, intermediate, and acid magmatic rocks.

3. General lithology and petrography of rocks and xenoliths from the western part of the Mexican Volcanic Belt (W-MVB)

The lithology of the W-MVB region is given by Nixon et al. (1987). In the Tepic-Zacoalco and Chapala rifts, Quaternary lavas and pyroclastic rocks constitute the basins within the Tertiary volcanic rocks. In the Tepic region, the Miocene sequence contains mainly rhyolites with associated andesites and basalts, whereas Late Miocene sequence consists dominantly of basalts, and Plio-Quaternary volcanic rocks comprise basalts, andesites, dacites, and rhyolites. In the Tequila region, the earliest Quaternary rocks are the basaltic lavas which contain phenocrysts of olivine and labradorite and the groundmass of andesine, olivine, clinopyroxine, magnetite and ilmenite. The Sierra La Primavera caldera–dome complex located towards the west of Guadalajara contains peralkaline rhyolites. At the Río Grande de Santiago (North of Guadalajara), the surface rocks consist of andesitic to basaltic flows and ignimbrites with phenocrysts of plagioclase, orthopyroxene, clinopyroxene, hornblende, biotite and sparsely olivine and xenoliths of rhyolite and basalts. In the Colima Rift, the Cerro El Cántaro is composed of porphyritic andesite lavas. The Colima-Cántaro volcanic complex contains basalt, dacite and K-rich basanites and lamprophyric rocks. The rocks from the Colima volcano are mainly andesites characterized by the mineral assemblage of plagioclase, pyroxenes (augite and hypersthene), hornblende, Fe–Ti oxides, and accessory apatite (Valdez-Moreno et al., 2006). These main mineral phases are present in lavas of all ages except that there is a decreasing trend of hornblende contents from older to modern eruptions.

The majority of xenoliths are from the areas of Volcán Pericutin (McBirney et al., 1987; Rowe et al., 2011) and a few from Volcán Colima (Valdez-Moreno et al., 2006). The xenoliths of Paricutin are fragments of siliceous igneous rocks, with granite, granodiorite, and quartz monzonite being most common. A few fragments were of porphyritic hypabyssal or effusive rocks of dacitic or rhyolitic composition. Most of these xenoliths contain vesicular glass with rounded grains of quartz and feldspar and lesser amounts of ferromagnesian minerals in advanced stages of alteration. Sphene, zircon, and apatite are the common accessory minerals in these xenoliths (McBirney et al., 1987). The chemical composition of these xenoliths indicates a depletion in high field strength elements (HFSE) and enrichment in large-ion lithophile elements (LILE) relative to the whole-rock lava composition (Rowe et al., 2011). The xenoliths from volcano Colima are gabbroic and granitoid xenoliths found in prehistorical lava flows and are considered to be representative of the basement beneath Colima volcano (Valdez-Moreno et al., 2006). The gabbroic xenoliths are characterized by the main mineral assemblage of plagioclase, clinopyroxene, orthopyroxene, titanomagnetite, glass, and hornblende and they exhibit the evidence of partial melting of clinopyroxene. In the case of granitoid xenoliths, they contain glass, microcline crystals and rarely quartz. The remnant mineral assembly suggests that the original rock was of granodioritic composition (Valdez-Moreno et al., 2006).

4. New analytical data from the W-MVB

Thirteen samples were collected from the W-MVB (Table 1). Major and trace element concentrations were measured from X-ray fluorescence spectrometry and rare-earth elements from high-performance liquid chromatography. The analytical details and accuracy estimates were given by Verma (1991a,b) and Verma et al. (1992). The $^{87}Sr/^{86}Sr$ and $^{143}Nd/^{144}Nd$ were determined by thermal ionization mass spectrometry; the procedures and accuracy are similar to those summarized by Verma (1992). The $^{87}Sr/^{86}Sr$ ratios are normalized to $^{86}Sr/^{88}Sr = 0.11940$ and adjusted to SRM987 $^{87}Sr/^{86}Sr$ of 0.710230. The $^{143}Nd/^{144}Nd$ are normalized to $^{146}Nd/^{144}Nd = 0.72190$ and adjusted to La Jolla $^{143}Nd/^{144}Nd$ of 0.511860. The measured $^{87}Sr/^{86}Sr$ for the SRM987 standard was 0.710216 ± 11 (1 s–one standard deviation; $n = 36$) and the measured $^{143}Nd/^{144}Nd$ for the La Jolla standard was 0.511833 ± 12 (1 s; $n = 82$). Note that the measured isotopic ratios were adjusted following the convention of Mainz, Germany (Verma, 1992).

Table 1
New geochemical and isotopic data for volcanic rock samples from the western part of the Mexican Volcanic Belt (W-MVB).

Sample:	Jal01	Jal02	Jal04	Jal05	Jal06	Jal08	RGS01
Area	Arandas-Atotonilco	Arandas-Atotonilco	Arandas-Atotonilco	Arandas-Atotonilco	Arandas-Atotonilco	Arandas-Atotonilco	Rio Grande de Santiago
Long. (°W):	−102.2167	−102.2383	−102.2167	−102.5317	−102.5450	−102.4500	−103.3348
Lat. (°N):	+20.6833	+20.71667	+20.6000	+20.7150	+20.6833	+20.7500	+20.8533
Age	Miocene	Miocene	Miocene	Miocene	Miocene	Miocene	Miocene
Magma−type:	Basic	Intermediate	Basic	Intermediate	Intermediate	Basic	Basic
Rock−type:	Subalkali basalt	Basaltic trachyandesite, shoshonite	Potassic trachybasalt	Basaltic andesite	Basaltic andesite	Subalkali basalt	Subalkali basalt
SiO_2	49.31	51.44	50.42	53.25	56.22	49.89	47.86
TiO_2	1.25	1.28	1.08	0.89	0.97	1.18	1.77
Al_2O_3	17.35	17.89	16.75	17.55	17.41	16.57	16.34
$Fe_2O_3^T$	11.31	9.24	9.55	8.64	7.77	12.09	11.54
MnO	0.152	0.155	0.145	0.134	0.111	0.166	0.156
MgO	5.58	5.08	7.11	5.05	3.93	6.33	6.49
CaO	8.65	7.77	7.85	8.05	6.72	8.22	8.77
Na_2O	3.29	3.53	3.13	3.41	3.89	3.11	3.37
K_2O	1.32	1.72	2.09	1.19	1.81	0.88	0.91
P_2O_5	0.421	0.511	0.522	0.378	0.566	0.356	0.349
LOI	0.64	0.87	0.96	1.32	0.71	0.66	2.79
Sum	99.273	99.486	99.607	99.862	100.107	99.452	100.345
$(SiO_2)_{adj}$	50.48	52.54	51.50	54.41	56.91	51.03	49.56
$(Na_2O + K_2O)_{adj}$	4.72	5.36	5.33	4.70	5.77	4.081	4.43
Q	0	0	0	3.16	5.80	0	0
Or	7.99	10.38	12.62	7.19	10.83	5.32	5.57
Ab	28.50	30.51	27.05	29.49	33.32	26.92	29.53
An	29.36	28.48	26.03	29.70	25.00	29.31	27.72
Di	9.70	6.09	8.32	7.01	4.10	8.26	12.27
Hy	7.64	16.20	9.48	18.11	15.34	19.34	3.63
Ol	10.82	1.37	10.16	0	0	4.99	14.33
Mt	2.56	3.28	3.01	2.72	2.42	2.73	2.64
Il	2.43	2.48	2.10	1.73	1.87	2.29	3.48
Ap	1.00	1.21	1.24	0.89	1.33	0.84	0.84
Mg#	53.56	58.88	65.19	59.52	55.99	55.03	56.80
FeO^T/MgO	1.82	1.64	1.21	1.54	1.78	1.72	1.60
La	30.6	24.4	19.2	25.3	23.1	16.1	8.6
Ce	54.4	59.1	43.6	47.7	50.7	27.9	22.2
Pr	8.25	7.56	5.86	7.58	7.92	4.16	3.08
Nd	38.6	31.1	26.8	32.2	32.2	19.4	14.6
Sm	9.08	5.83	6.16	6.42	6.45	4.52	3.62
Eu	2.59	1.88	1.86	1.76	1.73	1.48	1.24
Gd	9.3	5.71	6.14	6.67	6.08	5.43	3.72
Tb	1.47	0.96	1.08	1.12	1.09	0.87	0.61
Ho	1.51	0.91	1.01	1.18	0.97	1.05	0.69
Er	4.24	2.46	2.85	3.39	2.99	3.01	1.91
Tm	0.58	0.35	0.42	0.49	0.41	0.42	0.24
Yb	3.59	2.31	2.68	3.31	2.69	2.58	1.64
Lu	0.51	0.31	0.43	0.49	0.38	0.32	0.26
$(^{87}Sr/^{86}Sr)_m$[a]	0.703663	0.703458	0.703950	0.703397	0.703793	0.703652	0.703818
$(^{143}Nd/^{144}Nd)_m$[a]	0.512897	0.512935	0.512918	0.512868	0.512829	0.512867	0.512895

Sample:	RGS02	RGS03	RGS04	RGS05	LP01	CEB1
Area	Rio Grande de Santiago	Rio Grande de Santiago	Rio Grande de Santiago	Rio Grande de Santiago	Sierra La Primavera	Volcán Ceboruco
Long. (°W):	−103.3428	−103.34767	−103.3405	−103.3223	−103.5700	−104.5776
Lat. (°N):	+20.8017	+20.7815	+20.7743	+20.7383	+20.7100	+21.09353
Age	Miocene	Miocene	Miocene	Miocene	Quaternary	Holocene
Magma−type:	Intermediate	Acid	Acid	Intermediate	Acid	Intermediate
Rock−type:	Basaltic andesite	Rhyolite	Trachyte	Basaltic andesite	Peralkaline rhyolite	Trachyandesite, benmoreite
SiO_2	53.61	75.48	60.91	54.49	75.05	58.75
TiO_2	0.98	0.15	1.01	1.11	0.16	1.29
Al_2O_3	18.09	12.91	16.13	17.53	12.31	16.93
$Fe_2O_3^T$	7.41	1.15	5.22	7.68	2.33	7.14
MnO	0.116	0.052	0.108	0.118	0.066	0.124
MgO	5.12	0.12	1.79	4.35	0.02	2.84
CaO	8.84	0.58	3.75	7.26	0.41	5.62
Na_2O	3.52	4.15	4.03	3.55	4.61	4.27
K_2O	1.14	4.71	3.465	1.66	4.74	2.05
P_2O_5	0.234	0.021	0.298	0.248	0.013	0.402
LOI	1.49	0.74	2.75	1.57	0.36	−0.12
Sum	100.55	100.063	99.461	99.566	100.069	99.296
$(SiO_2)_{adj}$	54.44	76.06	63.22	55.95	75.39	59.41
$(Na_2O + K_2O)_{adj}$	4.73	8.93	7.78	5.35	9.39	6.39
Q	2.35	31.81	13.62	4.66	29.14	9.58
Or	6.84	28.05	21.25	10.07	28.14	12.25
Ab	30.25	35.38	35.39	30.84	37.09	36.54

Table 1 (*continued*)

Sample:	RGS02	RGS03	RGS04	RGS05	LP01	CEB1
An	30.66	2.71	16.28	27.72	0	21.21
Di	10.00	0.05	0.82	6.20	1.74	3.55
Hy	15.14	1.15	7.49	15.31	1.58	10.69
Ol	0	0	0	0	0	0
Mt	2.32	0.52	2.44	2.43	0.13	2.77
Il	1.89	0.29	1.99	2.16	0.31	2.48
Ap	0.55	0.049	0.72	0.59	0.03	0.94
Mg#	63.48	23.06	49.62	58.76	2.41	51.73
FeO^T/MgO	1.30	8.62	2.62	1.59	104.8	2.26
La	13.2	24.9	24.6	14.1	78	23.9
Ce	31.1	47.2	43.9	32.4	171	51.2
Pr	3.61	5.36	6.77	3.64	17.3	6.01
Nd	15.7	19.1	27.6	15.3	60	23.4
Sm	3.39	3.41	5.87	3.33	10.7	4.92
Eu	1.16	0.31	1.54	1.07	0.28	1.45
Gd	3.31	2.98	5.58	3.42	9	4.62
Tb	0.66	0.59	1.01	0.72	1.41	0.66
Ho	0.55	0.73	0.99	0.72	1.69	0.71
Er	1.44	2.12	2.86	1.85	5.2	1.93
Tm	0.16	0.31	0.44	0.24	0.71	0.31
Yb	1.31	2.49	2.88	1.69	4.9	1.79
Lu	0.21	0.39	0.42	0.34	0.7	0.46
Ba	483	271	926.5		1	786
Co	33	26	36		2	16
Cr	110	8.5	10.5		9	19
Cu	38	2	11.5		2	21
Nb	7.9	19.6	21.45		64.95	20.1
Ni	81	1.5	9.5		7	13
Rb	16.9	146.4	80		142.85	31.9
Sr	684.2	32.05	433.9		0.3	571.5
V	148	3.5	76		5	105
Y	18.4	20.35	35.95		55.45	27.1
Zn	73	39	80.5		103	85
Zr	127.5	149.1	311.75		538.45	231
$(^{87}Sr/^{86}Sr)_m$[a]	0.703819	0.705384	0.704042	0.704034	0.708240	0.703982
$(^{143}Nd/^{144}Nd)_m$[a]	0.512848	0.512852	0.512859	0.512840	0.512904	0.512765

Abbreviations: The subscript 'adj' refers to adjusted data (anhydrous 100% adjusted basis); Mg# = 100 $Mg^{2+}/(Mg^{2+} + Fe^{2+})$, atomic; FeOT = total iron expressed as FeO (the computer program for adjustments and norm calculations is SINCLAS by Verma et al., 2002, or IgRoCS by Verma and Rivera-Gómez, 2013b). Replicate analyses of major elements were performed for most samples; n1 – number of analyses for major elements; n2 – number of analyses for trace elements; n3 – number of analyses for Sr isotopes; n4 – number of analyses for Nd isotopes. Rounded concentration values were reported; the sum may, therefore, be sometimes inconsistent.

[a] Note the Sr and Nd isotopic ratios are actually measured values and are not in-situ growth corrected values.

5. Database construction and overall synthesis

Geochemical and isotopic data were compiled for a total of 1548 samples from the W-MVB, which include 13 new (Table 1) and 1535 literature analyses (1499 volcanic rocks and 36 crustal xenoliths or rocks; Table 2).

All major element data were first processed in IgRoCS computer program (Verma and Rivera-Gómez, 2013a) for assigning rock and magma types according to the nomenclature of the International Union of Geological Sciences (IUGS; Le Bas et al., 1986; Le Maitre et al., 2002). The Middlemost (1989) option for Fe-oxidation ratio was used. The subdivision of samples as basic, intermediate, and acid magmatic rocks is shown towards the end of Table 2.

Various computer programs were applied to process the data: 1) DODESSYS (Verma and Díaz-González, 2012) for the application of discordancy tests in order to identify and separate discordant outliers at a strict 99% or 99.5% confidence level ascertaining thus a normal distribution; 2) UDASYS (Verma et al., 2013a) for significance tests and other statistical calculations; 3) TecD by Verma and Rivera-Gómez (2013b) for multidimensional tectonic discrimination diagrams for basic and ultrabasic magmas (Verma et al., 2006; Agrawal et al., 2008; Verma and Agrawal, 2011); and 4) TecDIA by Verma et al. (2016a) for similar multidimensional diagrams for intermediate and acid magmas (Verma et al., 2012, 2013b; Verma and Verma, 2013). The critical values for discordancy tests were from Verma and Quiroz-Ruiz (2008, 2011) and Verma et al. (2008), whereas those for the significance tests were reported by Cruz-Huicochea and Verma (2013) and Verma and Cruz-Huicochea (2013).

To better understand the results of the multielement normalized and discrimination diagrams and the effects of the subduction and rifting processes, the appropriate version of the Student t test was applied at a strict 99% confidence level to the discordant outlier-free data for the Rift and No Rift as well as for the Near Trench and Far Trench pairs (Verma, 2005). We stress that a large number of discordancy tests for univariate data (Dixon, 1950, 1953; Grubbs, 1950, 1969; Grubbs and Beck, 1972; Barnett and Lewis, 1994; Verma, 1997, 2005, 2012; Verma and Quiroz-Ruiz, 2008; Verma et al., 2008, 2014; Verma and Díaz-González, 2012) were applied to the complete dataset to assure that the remaining discordant outlier-free data were normally distributed. This procedure has been successfully used by us in numerous other studies (e.g., Verma, 2013; Verma and Armstrong-Altrin, 2013, 2016; Verma et al., 2014, 2015, 2016a,b). Distributions other than the Gaussian are not likely for such experimental data, especially when log-ratios are involved (e.g., Aitchison, 1986; Law and Kelton, 2000; Verma, 2005, 2015a).

Table 2
Sources of geochemical data for the western part of the Mexican Volcanic Belt (W-MVB).

Reference	Number of samples					
	Geochemical data			Isotope data		
	Basic	Int.	Acid	Sr	Nd	Pb
This work (new data)	4	6	3	13	13	–
Allan and Carmichael (1984); isotope data from Luhr (1997)	–	8	–	1	1	–
Blatter and Hammersley (2010)	6	22	1	–	–	–
Carmichael et al. (1996); isotope data from Luhr (1997)	14	21	1	–	–	2
Carmichael et al. (2006)	11	1	–	–	–	–
Cavazos Tovar (2006)	–	34	1	22	7	15
Crummy et al. (2014)	–	38	–	13	13	–
Demant (1981)	18	56	19	–	–	–
Díaz-Bravo et al. (2014)	17	5	–	7	7	7
Ferrari et al. (1994)	9	15	–	–	–	–
Ferrari et al. (2000)	5	8	–	–	–	–
Frey et al. (2007)	1	1	17	–	–	–
Gastil et al. (1979)	1	3	5	–	–	–
Gilbert et al. (1985)	3	2	3	–	–	–
Gunn and Mooser (1971)	4	11	–	–	–	–
Hasenaka (1992)	9	53	3	–	–	–
Lange and Carmichael (1990); isotope data from Luhr (1997)	–	18	–	–	–	1
Lange and Carmichael (1991)	2	7	–	–	–	–
Lewis-Kenedi et al. (2005)	5	1	–	–	–	–
Luhr (1993)	–	8	2	–	–	–
Luhr (2000)	–	8	15	7	8	8
Luhr (2001)	–	4	–	–	–	–
Luhr (2002)	–	11	–	–	–	–
Luhr and Carmichael (1980); Sr and Nd isotope data from Wallace and Carmichael (1994) and Pb from Luhr (1997)	–	9	–	2	2	2
Luhr and Carmichael (1981); isotope data from Luhr (1997)	3	1	–	1	1	–
Luhr and Carmichael (1982); isotope data from Verma and Luhr (2010)	–	2	–	2	2	2
Luhr and Carmichael (1990a); isotope data from Verma and Luhr (1993)	–	45	–	1	1	–
Luhr and Carmichael (1990b)	–	26	6	–	–	–
Luhr and Lazaar (1985)	–	9	–	–	–	–
Luhr et al. (1989); isotope data from Wallace and Carmichael (1994) and Luhr (1997)	8	–	–	6	6	3
Luhr et al. (2010)	–	69	–	–	–	–
Luhr, J.F. Unpublished data given to the first author	–	25	–	–	–	1
Mahood (1977)	–	–	1	–	–	–
Mahood (1981); isotope data in Mahood and Halliday (1988)	–	–	29	9	8	–
Maldonado-Sánchez and Schaaf (2005)	–	6	7	13	13	13
Maria and Luhr (2008)	9	2	–	–	–	–
Martin del Pozzo et al. (1987)	3	2	–	–	–	–
McBirney et al. (1987)	–	1	–	1	–	–
Moore et al. (1994)	15	5	–	–	–	–
Mora et al. (2002)	–	6	–	–	–	–
Mori et al. (2009)	26	34	–	18	18	17
Nelson (1980); isotope data from Wallace and Carmichael (1994)	–	12	14	5	5	–
Nelson (1986)	1	4	–	–	–	–
Nelson and Livieres (1986)	1	25	18	–	–	–
Ownby et al. (2008)	6	28	1	–	–	–
Petrone (2010)	7	17	1	22	22	19
Petrone et al. (2001)	–	2	1	–	–	–
Petrone et al. (2003)	8	27	–	21	21	19
Petrone et al. (2006)	–	4	37	7	4	–
Righter and Carmichael (1992)	6	28	–	–	–	–
Righter and Rosas-Elguera (2001)	3	12	–	–	–	–
Righter et al. (1995)	7	33	2	–	–	–
Robin and Potrel (1993)	1	16	7	–	–	–
Robin et al. (1984)	3	27	8	–	–	–
Robin et al. (1990)	–	6	–	–	–	–
Robin et al. (1991)	–	22	–	–	–	–
Rodríguez-Elizarrarás (1995)	–	9	2	–	–	–
Rowe et al. (2011); major element and isotope data from McBirney et al. (1987)	–	11	1	10	–	–
Saucedo et al. (2010)	–	17	–	–	–	–
Savov et al. (2008)	–	11	1	–	–	–
Valdez-Moreno et al. (2006)	–	13	–	12	12	11
Varley et al. (2002)	–	6	–	–	–	–
Verma and Hasenaka (2004)	3	7	–	10	10	5
Verma and Luhr (1993)	–	2	–	2	2	1
Verma and Luhr (2010)	4	7	4	16	16	7
Verma and Nelson (1989)	10	12	8	30	30	–
Verma et al. (1985)	6	2	–	8	–	–
Vigouroux et al. (2008)	4	2	–	–	–	–
Wallace and Carmichael (1989)	13	2	–	–	–	–
Wallace and Carmichael (1992)	3	31	5	–	–	–
Wallace and Carmichael (1994)	–	12	10	4	4	–
Wilcox (1954)	–	22	4	–	–	–

Table 2 (*continued*)

Reference	Number of samples					
	Geochemical data			Isotope data		
	Basic	Int.	Acid	Sr	Nd	Pb
William (1950)	–	4	–	–	–	–
Total compilation (without crustal samples)	**259**	**1016**	**237**	**278**	**229**	**133**
Allan (1986) – upper crust	–	–	1	–	–	–
Cavazos Tovar (2006) – upper crust	–	1	–	–	–	–
McBirney et al. (1987) – crustal xenoliths		–	8	5	–	–
McBirney et al. (1987) – upper crust	–	–	3	3	–	–
Righter et al. (1995) – upper crust	1	–	–	–	–	–
Rowe et al. (2011) – crustal xenoliths	–	–	13	–	–	–
Rowe et al. (2011) and McBirney et al. (1987) – crustal xenoliths	–	–	4	4	–	–
Valdez-Moreno et al. (2006) – upper crust	–	–	1	–	–	–
Valdez-Moreno et al. (2006) – crustal xenoliths	1	1	1	3	3	–
Wallace and Carmichael (1992) – upper crust	–	–	1	–	–	–
Total crustal samples	**2**	**2**	**32**	**15**	**3**	**-**
Total compilation	**261**	**1018**	**269**	**278**	**229**	**133**

The boldface letters provide the synthesis of the relevant data.

6. Results and discussion

The average geochemical characteristics of compiled basic, intermediate, and acid W-MVB rocks of Miocene and Pliocene-Holocene ages are summarized in Table 3. The parameters include 11 adjusted major elements $(SiO_2)_{adj}$ to $(P_2O_5)_{adj}$, 14 rare-earth elements La to Lu, 24 trace elements B to Zr, 6 specially designed slab-sensitive ratios (Verma, 2009, 2015b), and 5 radiogenic Sr, Nd, and Pb isotope ratios (Table 3).

The equations used for the slab-sensitive ratios are as follows:

$$\{\text{LILE4/LREE3}\}_E = \frac{[(K_{sa}/K_E) + (Rb_{sa}/Rb_E) + (Ba_{sa}/Ba_E) + (Sr_{sa}/Sr_E)]/4}{[(La_{sa}/La_E) + (Ce_{sa}/Ce_E) + (Nd_{sa}/Nd_E)]/3} \quad (1)$$

$$\{\text{LILE4/HREE3}\}_E = \frac{[(K_{sa}/K_E) + (Rb_{sa}/Rb_E) + (Ba_{sa}/Ba_E) + (Sr_{sa}/Sr_E)]/4}{[(Er_{sa}/Er_E) + (Yb_{sa}/Yb_E) + (Lu_{sa}/Lu_E)]/3} \quad (2)$$

$$\{\text{LILE4/HFSE4}\}_E = \frac{[(K_{sa}/K_E) + (Rb_{sa}/Rb_E) + (Ba_{sa}/Ba_E) + (Sr_{sa}/Sr_E)]/4}{[(Ti_{sa}/Ti_E) + (P_{sa}/P_E) + (Hf_{sa}/Hf_E) + (Ta_{sa}/Ta_E)]/4} \quad (3)$$

$$\{\text{LILE4/HFSE3}\}_E = \frac{[(K_{sa}/K_E) + (Rb_{sa}/Rb_E) + (Ba_{sa}/Ba_E) + (Sr_{sa}/Sr_E)]/4}{[(Ti_{sa}/Ti_E) + (P_{sa}/P_E) + (Zr_{sa}/Zr_E)]/3} \quad (4)$$

$$\{\text{LREE3/HFSE5}\}_E = \frac{[(La_{sa}/La_E) + (Ce_{sa}/Ce_E) + (Nd_{sa}/Nd_E)]/3}{[(Ti_{sa}/Ti_E) + (P_{sa}/P_E) + (Zr_{sa}/Zr_E) + (Hf_{sa}/Hf_E) + (Ta_{sa}/Ta_E)]/5} \quad (5)$$

$$\{\text{LREE3/HFSE4}\}_E = \frac{[(La_{sa}/La_E) + (Ce_{sa}/Ce_E) + (Nd_{sa}/Nd_E)]/3}{[(Ti_{sa}/Ti_E) + (P_{sa}/P_E) + (Zr_{sa}/Zr_E) + (Hf_{sa}/Hf_E)]/4} \quad (6)$$

where LILE–large ion lithophile elements; LREE–light rare-earth elements; HREE–heavy rare-earth elements; HFSE–high field strength elements; the subscript "sa" represents the sample whereas the subscript "E" is for the silicate Earth values from McDonough and Sun (1995). After applying discordancy tests, these six special slab-sensitive ratios and five radiogenic isotope ratios are listed in Table 3.

6.1. Sample subdivision

Out of the total of 1512 samples of volcanic rocks, 259 samples proved to be basic, 1016 intermediate, and 237 acid rocks (Table 2). Their subdivision in terms of Miocene and Pliocene-Holocene samples was as follows (Table 3): 136 samples of Miocene (62 basic, 69 intermediate, and 5 acid); and 1376 samples of Pliocene-Holocene (197 basic, 947 intermediate, and 232 acid).

The Pliocene-Holocene (1376) samples were further subdivided either as Rift and No Rift (Fig. 3) or Near Trench and Far Trench magmatic rocks (Fig. 4). Their subdivision was as follows: 1014 samples from Rift (triple rift system–TZR, CR, and ChR; Fig. 5c; 131 basic, 666 intermediate, and 217 acid); and 362 samples from No Rift (outside the triple rift system; Fig. 5d; 66 basic, 281 intermediate, and 15 acid); 937 samples from Near Trench (Fig. 5e; 131 basic, 727 intermediate, and 79 acid); and 439 samples from Near Trench (Fig. 5f; 66 basic, 220 intermediate, and 153 acid).

The Miocene rocks are present at the surface only very far from the MAT except those (near the coast in the NW part of Fig. 2a)

Table 3
Geochemical data of volcanic rock samples from the western part of the Mexican Volcanic Belt (W-MVB).

Variable	Statistical information $\bar{x}\pm s(n)$					
	Basic		Intermediate		Acid	
	Miocene	Pliocene-Holocene	Miocene	Pliocene-Holocene	Miocene	Pliocene-Holocene
$(SiO_2)_{adj}$	50.3 ± 0.9 (62)	49.8 ± 1.3 (197)	55.3 ± 2.2 (69)	57.9 ± 2.9 (947)	69 (5)	70 ± 5 (232)
$(TiO_2)_{adj}$	1.40 ± 0.23 (62)	1.7 ± 0.6 (197)	1.18 ± 0.23 (69)	0.94 ± 0.36 (947)	0.45 (5)	0.45 ± 0.24 (232)
$(Al_2O_3)_{adj}$	17.4 ± 0.8 (62)	15.4 ± 2.5 (197)	17.6 ± 0.8 (69)	17.5 ± 1.0 (947)	15.7 (5)	15.4 ± 1.9 (232)
$(Fe_2O_3)_{adj}$	1.68 ± 0.19 (62)	1.94 ± 0.42 (197)	1.87 ± 0.23 (69)	1.62 ± 0.29 (947)	1.1 (5)	0.97 ± 0.36 (232)
$(FeO)_{adj}$	8.1 ± 0.7 (62)	7.3 ± 1.5 (197)	5.9 ± 0.8 (69)	4.7 ± 0.9 (947)	2.4 (5)	2.2 ± 0.9 (232)
$(MnO)_{adj}$	0.155 ± 0.014 (62)	0.153 ± 0.035 (197)	0.128 ± 0.019 (69)	0.112 ± 0.023 (947)	0.09 (5)	0.076 ± 0.028 (232)
$(MgO)_{adj}$	7.2 ± 1.2 (62)	8.1 ± 2.9 (197)	4.8 ± 1.0 (69)	4.3 ± 1.5 (947)	1.1 (5)	1.1 ± 1.0 (232)
$(CaO)_{adj}$	9.3 ± 0.7 (62)	8.9 ± 1.1 (197)	7.9 ± 1.0 (69)	6.8 ± 0.9 (947)	2.0 (5)	2.8 ± 1.9 (232)
$(Na_2O)_{adj}$	3.17 ± 0.34 (62)	3.4 ± 0.7 (197)	3.45 ± 0.38 (69)	4.17 ± 0.43 (947)	3.4 (5)	4.4 ± 0.6 (232)
$(K_2O)_{adj}$	1.0 ± 0.6 (62)	2.4 ± 1.7 (197)	1.6 ± 0.6 (69)	1.6 ± 0.7 (947)	4.5 (5)	3.2 ± 1.2 (232)
$(P_2O_5)_{adj}$	0.32 ± 0.14 (62)	0.8 ± 0.5 (197)	0.36 ± 0.12 (69)	0.29 ± 0.21 (947)	0.09 (5)	0.11 ± 0.09 (232)
La	15 ± 9 (56)	43 ± 34 (120)	28 ± 14 (58)	23 ± 15 (560)	24.75 (2)	32 ± 17 (135)
Ce	35 ± 13 (53)	90 ± 60 (120)	49 ± 15 (56)	45 ± 29 (575)	45.6 (2)	63 ± 34 (136)
Pr	4.8 ± 2.2 (30)	8.4 ± 3.0 (31)	7.7 ± 2.8 (39)	4.4 ± 2.3 (165)	6.1 (2)	6.5 ± 4.6 (8)
Nd	21 ± 8 (40)	46 ± 33 (93)	31 ± 11 (47)	22 ± 14 (438)	23 (2)	29 ± 15 (114)
Sm	5.3 ± 1.9 (34)	8.1 ± 3.6 (64)	6.7 ± 2.3 (41)	4.3 ± 2.1 (299)	4.6 (2)	6.6 ± 3.5 (76)
Eu	1.63 ± 0.44 (37)	2.4 ± 0.9 (60)	1.8 ± 0.53 (42)	1.3 ± 0.57 (292)	0.9 (2)	0.7 ± 0.5 (75)
Gd	5.4 ± 1.7 (33)	6.9 ± 1.5 (31)	6.5 ± 2.6 (40)	3.7 ± 1.2 (165)	4.3 (2)	7.8 ± 2.9 (31)
Tb	0.85 ± 0.26 (36)	0.93 ± 0.22 (60)	0.97 ± 0.37 (42)	0.6 ± 0.5 (322)	0.80 (2)	1.1 ± 0.7 (75)
Dy	5.1 ± 1.5 (27)	5.1 ± 1.4 (52)	5.7 ± 2.5 (35)	3.2 ± 0.9 (240)		3.7 ± 1.7 (27)
Ho	1.01 ± 0.32 (33)	1.10 ± 0.28 (31)	1.1 ± 0.56 (39)	0.63 ± 0.14 (224)	0.86 (2)	0.68 ± 0.43 (8)
Er	2.8 ± 0.9 (32)	2.9 ± 0.8 (31)	3.1 ± 1.6 (40)	0.38 ± 1.73 (213)	2.5 (2)	2.0 ± 1.4 (8)
Tm	0.36 ± 0.14 (7)	0.26 ± 0.05 (9)	0.33 ± 0.13 (5)	0.255 ± 0.035 (121)	0.38 (2)	0.75 ± 0.032 (29)
Yb	2.6 ± 1.0 (36)	2.2 ± 0.8 (60)	2.7 ± 1.3 (42)	1.65 ± 0.38 (351)	2.69 (2)	3.8 ± 2.6 (75)
Lu	0.39 ± 1.5 (37)	0.31 ± 0.13 (60)	0.43 ± 0.20 (41)	0.25 ± 0.06 (348)	0.41 (2)	0.54 ± 0.35 (75)
B		3.0 ± 1.9 (8)		10.3 ± 4.2 (32)		15 ± 7 (3)
Ba	360 ± 200 (55)	1200 ± 1100 (162)	590 ± 210 (61)	670 ± 440 (731)	600 (2)	860 ± 330 (156)
Be	1.4 ± 0.7 (26)	1.74 ± 0.43 (25)	1.57 ± 0.41 (34)	1.47 ± 0.39 (35)		1.37 ± 0.22 (3)
Co	40.8 ± 4.0 (40)	37 ± 5 (48)	28 ± 6 (53)	22 ± 9 (335)	31 (2)	8 ± 7 (80)
Cr	210 ± 90 (51)	320 ± 270 (146)	90 ± 50 (60)	100 ± 90 (670)	9.5 (2)	21 ± 32 (85)
Cs	0.6 ± 1.0 (30)	0.36 ± 0.30 (44)	0.49 ± 0.26 (36)	0.50 ± 0.21 (320)		2.2 ± 1.7 (66)
Cu	56 ± 11 (31)	54 ± 24 (126)	41 ± 16 (46)	32 ± 18 (688)	6.8 (2)	15 ± 12 (79)
Ga	18.4 ± 1.3 (26)	19.2 ± 3.6 (65)	20.0 ± 0.8 (34)	20.7 ± 2.7 (236)		20.1 ± 3.4 (22)
Hf	3.9 ± 1.8 (30)	7.9 ± 4.4 (60)	4.4 ± 0.8 (36)	3.7 ± 1.3 (342)		9 ± 5 (73)
Li	9.4 ± 2.9 (26)	7.5 ± 1.2 (22)	8.4 ± 2.7 (34)	13.2 ± 4.2 (39)		14.4 (1)
Nb	5.4 ± 2.7 (38)	21 ± 13 (132)	6.7 ± 2.5 (52)	9 ± 8 (526)	20.5 (2)	27 ± 31 (106)
Ni	120 ± 50 (51)	180 ± 140 (155)	54 ± 33 (60)	60 ± 50 (690)	6 (2)	19 ± 21 (82)
Pb	3.8 ± 1.8 (28)	11 ± 9 (78)	6.3 ± 1.7 (39)	8.3 ± 4.1 (402)		15 ± 7 (91)
Rb	21 ± 20 (55)	31 ± 38 (152)	31 ± 25 (62)	22 ± 11 (723)	110 (2)	70 ± 60 (163)
Sb	0.032 ± 0.019 (18)	0.15 ± 0.36 (19)	0.05 ± 0.05 (32)	0.11 ± 0.16 (37)		0.52 ± 0.17 (26)
Sc	29.7 ± 4.4 (26)	26.9 ± 4.3 (64)	22.8 ± 3.8 (34)	16.7 ± 4.1 (334)		4.9 ± 4.5 (76)
Sr	480 ± 140 (55)	1400 ± 1100 (158)	770 ± 220 (61)	800 ± 500 (751)	230 (2)	460 ± 330 (165)
Ta	0.37 ± 0.17 (30)	1.5 ± 1.0 (44)	0.43 ± 0.13 (36)	1 ± 6 (328)		2.3 ± 1.8 (68)
Th	1.8 ± 1.3 (32)	3.5 ± 2.3 (63)	2.8 ± 1.2 (40)	2.1 ± 1.3 (361)		10 ± 8 (73)
U	0.6 ± 0.6 (26)	1.5 ± 2.2 (51)	0.9 ± 0.6 (34)	0.70 ± 0.34 (328)		3.5 ± 2.9 (68)
V	210 ± 28 (49)	222 ± 43 (115)	189 ± 38 (54)	138 ± 39 (683)	40 (2)	63 ± 32 (105)
Y	30 ± 17 (49)	25.1 ± 9.7 (143)	33 ± 27 (54)	22 ± 29 (742)	28 (2)	29 ± 26 (186)
Zn	82 ± 10 (31)	93 ± 28 (124)	82.4 ± 7.7 (46)	75 ± 22 (644)	60 (2)	67 ± 31 (158)
Zr	150 ± 60 (49)	270 ± 150 (161)	180 ± 80 (54)	160 ± 70 (733)	230 (2)	250 ± 160 (186)
$\{LILE4/LREE3\}_E$	1.9 ± 0.6 (33)	1.8 ± 0.8 (90)	1.8 ± 0.5 (41)	2.4 ± 0.7 (405)	3.9 (2)	3.2 ± 0.7 (83)
$\{LILE4/HREE3\}_E$	8 ± 6 (28)	16 ± 19 (31)	10 ± 5 (35)	12.7 ± 4.1 (198)	18.6 (2)	21 ± 6.8 (7)
$\{LILE4/HFSE4\}_E$	3.1 ± 1.0 (38)	3.5 ± 2.0 (128)	4.6 ± 1.3 (51)	5.1 ± 1.7 (494)	7.5 (2)	10.3 ± 3.7 (76)
$\{LILE4/HFSE3\}_E$	2.8 ± 1.0 (49)	3.6 ± 1.6 (149)	4.3 ± 1.1 (53)	5.3 ± 1.6 (688)	14 (2)	10.3 ± 4.0 (134)
$\{LREE3/HFSE5\}_E$	1.58 ± 0.41 (30)	1.6 ± 0.6 (44)	2.5 ± 1.1 (35)	1.9 ± 0.5 (238)		1.9 ± 0.5 (68)
$\{LREE3/HFSE4\}_E$	1.53 ± 0.41 (30)	1.8 ± 0.5 (60)	2.4 ± 1.0 (35)	1.9 ± 0.5 (258)		2.5 ± 0.5 (73)
$^{87}Sr/^{86}Sr$[a]	0.70367 ± 0.00021 (18)	0.70356 ± 0.00029 (42)	0.70371 ± 0.00023 (15)	0.7038 ± 0.0009 (138)	0.7047 (2)	0.7043 ± 0.0009 (44)
$^{143}Nd/^{144}Nd$[a]	0.51291 ± 0.00005 (14)	0.51291 ± 0.00005 (42)	0.51287 ± 0.00006 (13)	0.51287 ± 0.00006 (112)	0.512856 (2)	0.51283 ± 0.00006 (41)
$^{206}Pb/^{204}Pb$[a]	18.670 ± 0.042 (10)	18.81 ± 0.16 (28)	18.67 ± 0.05 (7)	18.67 ± 0.06 (75)		18.71 ± 0.05 (11)
$^{207}Pb/^{204}Pb$[a]	15.579 ± 0.020 (10)	15.589 ± 0.154 (28)	15.578 ± 0.022 (7)	15.585 ± 0.019 (75)		15.606 ± 0.026 (11)
$^{208}Pb/^{204}Pb$[a]	38.36 ± 0.10 (10)	38.47 ± 0.11 (28)	38.35 ± 0.14 (7)	38.41 ± 0.10 (74)		38.52 ± 0.12 (11)

Abbreviations: The subscript 'adj' refers to adjusted data (anhydrous 100% adjusted basis, with Fe-Oxidation according to Middlemost, 1989); n–number of samples; $\bar{x}$–mean; s–standard deviation. For the ratio parameters $\{LILE4/LREE3\}_E$ to $\{LREE3/HFSE4\}_E$ (see the text for more explanation), the silicate Earth concentrations (in ppm; denoted by the subscript$_E$) were as follows (McDonough, 1995): $K_E = 240$ ppm; $Rb_E = 0.6$; $Ba_E = 6600$; $Sr_E = 19.9$; $La_E = 648$; $Ce_E = 1675$; $Nd_E = 1250$; $Er_E = 438$; $Yb_E = 441$; $Lu_E = 67.5$; $Ti_E = 1205$; $P_E = 90$; $Hf_E = 28.3$; $Ta_E = 37$; and $Zr_E = 10.5$.

[a] The isotopic ratios are actually measured ratios that have not been corrected for in-situ radiogenic isotopic growth.

probably associated to the rifting of Baja California from Mainland Mexico. The trace of the Near Trench and Far Trench subdivision is shown for reference in Figs. 2–5. Approximate locations of crustal samples are shown in Fig. 2b; they come from very few locations. The Rift and No Rift subdivision of samples was achieved as those lying in and outside of the triple rift system (TZR-CR-ChR),

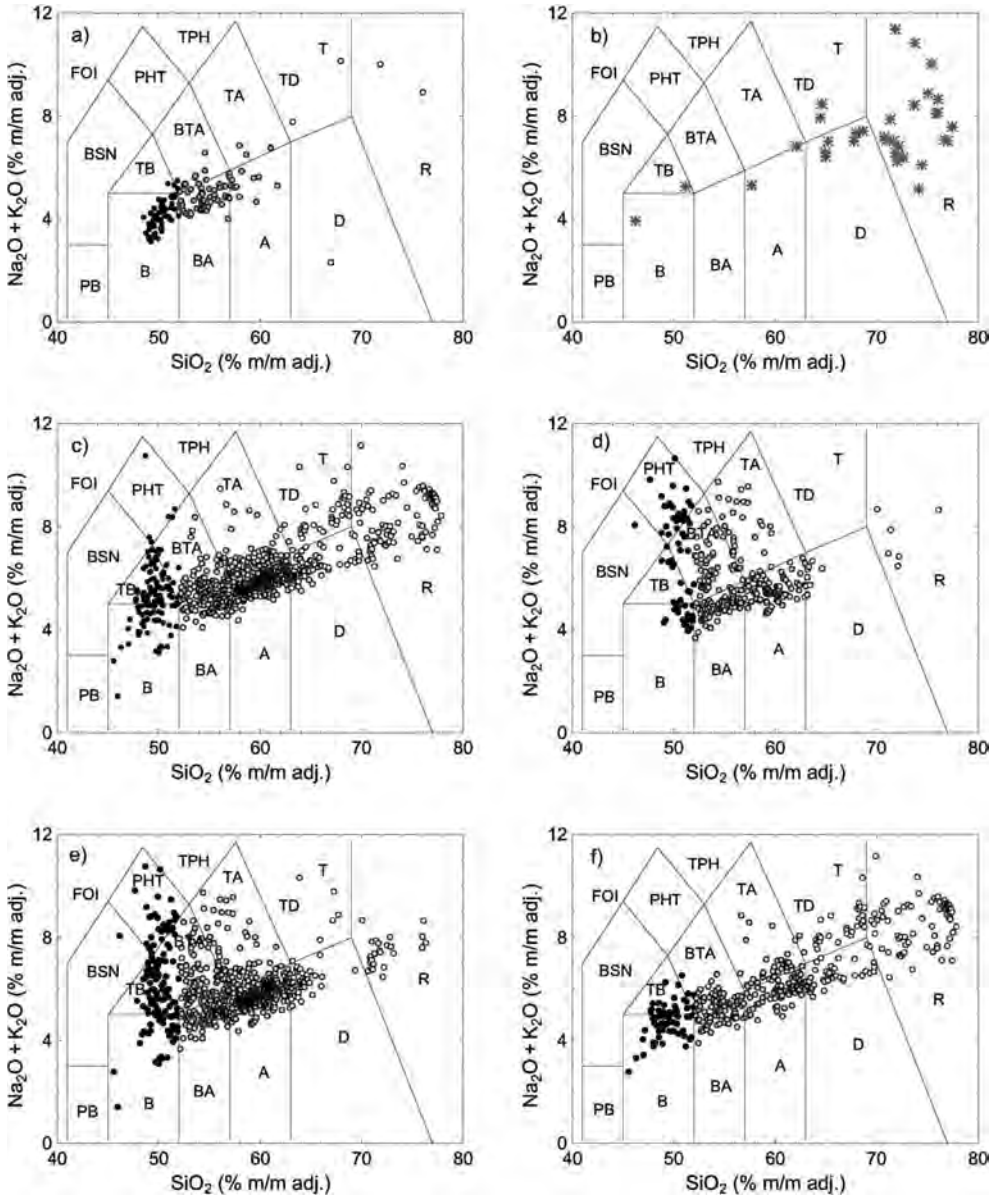

Fig. 5. Sample classification in the TAS diagram of Le Bas et al. (1986) obtained from the IgRoCS computer program (Verma and Rivera-Gómez, 2013a). The rock name abbreviations are as follows: FOI–foidite; PB–picrobasalt; BSN–basanite; B–basalt; TB–trachybasalt; PHT–phonotephrite; BA–basaltic andesite; BTA–basaltic trachyandesite; TPH–tephriphonolite; A–andesite; TA–trachyandesite; D–dacite; TD–trachydacite; T–trachyite; R–rhyolite; the filled black, filled grey and open circles represent basic, intermediate and acid rocks, respectively. a) Miocene rocks; b) crustal rocks and xenoliths; c) "Rift" samples; d) "No Rift" samples; e) "Near Trench" samples; and f) "Far Trench" samples.

respectively (Fig. 3). Finally, the subdivision of Near Trench and Far Trench samples is shown in Fig. 4, in which the trace of an arbitrarily chosen subdivision (thick) curve subdivides them. Note that some of the No Rift samples lie within other graben systems and some of the Near Trench rocks also belong to the triple-rift and other graben systems (Figs. 3 and 4).

The W-MVB compiled samples are plotted in the TAS diagram (Fig. 5). Miocene rocks are mostly subalkaline basalts and basaltic andesites, with a few more evolved rocks (Fig. 5a). Most of the crustal samples are of high-silica types, equivalent to dacitic and rhyolitic compositions (Fig. 5b). The rocks from Rift and No Rift subdivisions are plotted in Fig. 5c and d, respectively. Similarly, the rocks from Near Trench and Far Trench are shown in Fig. 5e and f, respectively. Both subalkaline and alkaline rock types were represented in all subdivisions (Rift, No Rift, Near Trench, and Far Trench), because our main aim was to better understand the similarities and differences in tectonic setting from multidimensional diagrams.

6.2. Conventional geochemical diagrams with confidence intervals of the mean

The use of the confidence intervals of the mean is a useful new concept in such diagrams (Figs. 6 and 7). Chondrite-normalized rare-earth element (REE) plots (Fig. 6) are presented for the average values and 99.5% confidence intervals in most diagrams (Fig. 6a for Miocene rocks and Fig. 6c–f for Pliocene-Holocene rocks) except Fig. 6b where individual data for the crustal samples are shown. The vertical scale is kept the same in all plots (Fig. 6a and c–f, with the exception of Fig. 6b) in order to facilitate an easy visual comparison.

The 99.5% confidence interval values of the middle to heavy REEs for Miocene intermediate rocks overlap with those for the basic rocks (Fig. 6a). Unfortunately, REE data were available for only

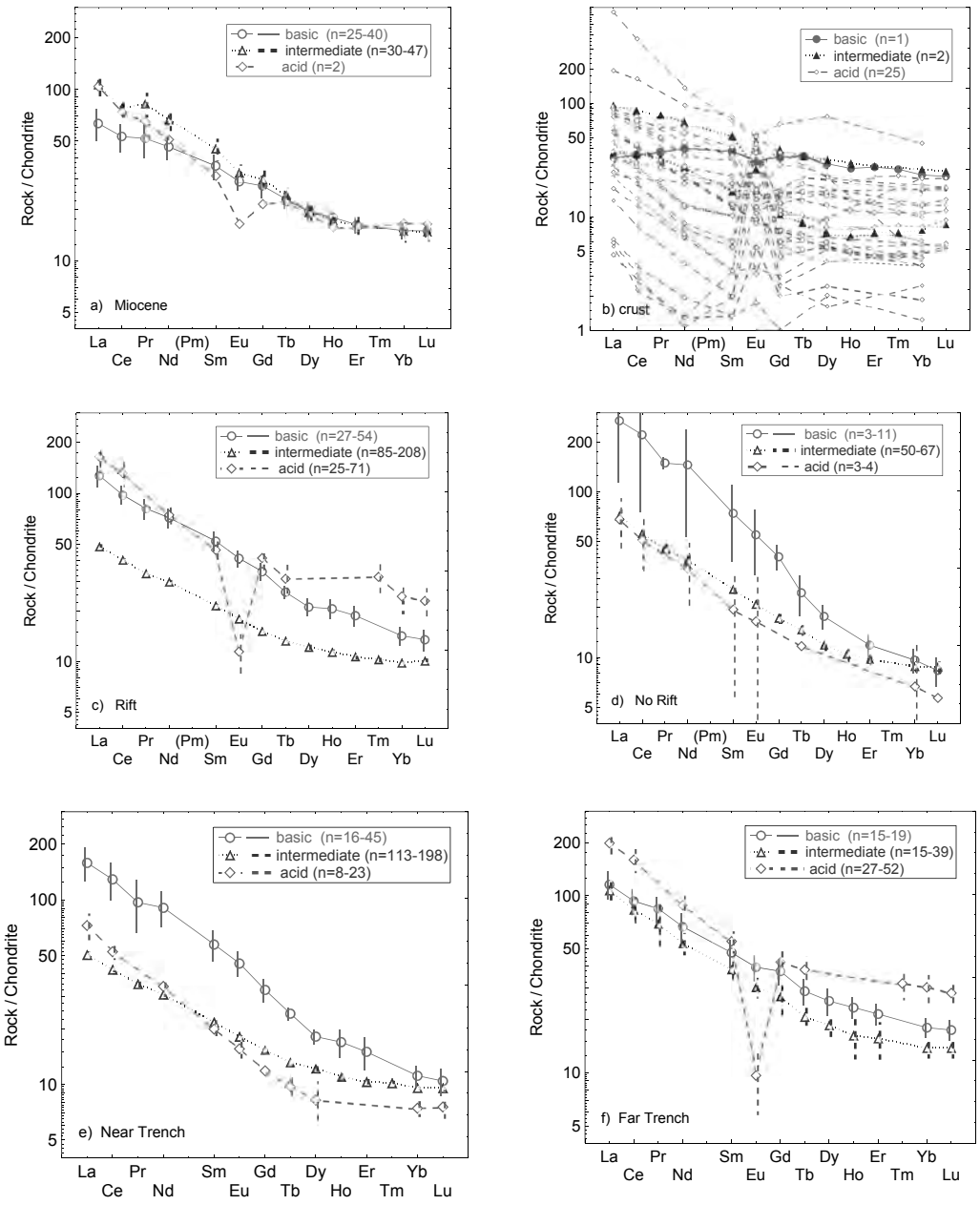

Fig. 6. Chondrite-normalized rare-earth element plots for rocks from the mean values of the western part of the Mexican Volcanic Belt; the range (n) of minimum and maximum determinations for a given subdivision are included in parentheses. The vertical error bars represent 99.5% confidence intervals of the mean. Basic, intermediate, and acid rocks are considered separately. a) Miocene rocks; b) crustal rocks and xenoliths (individual data are shown); c) rocks from the Rift subdivision; d) rocks from the No Rift subdivision; e) rocks from the Near Trench subdivision; and f) rocks from the Far Trench subdivision.

two samples of Miocene acid rocks, which also show overlapping REE concentrations; however, a distinct negative Eu anomaly is present in the acid rocks (Fig. 6a).

Only one basic crustal sample was analyzed for the REE and shows a fairly flat pattern whereas only two samples of intermediate compositions show slightly light-REE enriched patterns, one having higher concentrations and a small negative Eu anomaly and the other with lower concentrations and a small positive Eu anomaly (Fig. 6b). A large number of crustal samples of acid compositions (25 samples) depict a highly heterogeneous crust underlying the W-MVB, varying from close to the chondritic compositions to even higher REEs than the volcanic rocks; besides most samples show a positive Eu anomaly (Fig. 6b). This is an important observation because anataxis of this type of acid crust cannot match any acid rocks from the W-MVB having a negative Eu anomaly (Fig. 6a and f; see solid–liquid partition coefficients in Rollinson, 1993; Torres-Alvarado et al., 2003) unless more complex petrogenetic processes are involved.

For rocks from the triple-rift system (Rift rocks; Fig. 6c) shows that the basic rocks have significantly higher REE concentrations as compared to the intermediate rocks, which is just the opposite to what is expected from a simple fractional crystallization relationship for these rock types involving common volcanic rock forming minerals (Rollinson, 1993; Torres-Alvarado et al., 2003). However, the acid rocks with significantly higher REE concentrations than the intermediate rocks could well be related through fractional crystallization of intermediate magmas based on the involvement of common rock-forming minerals.

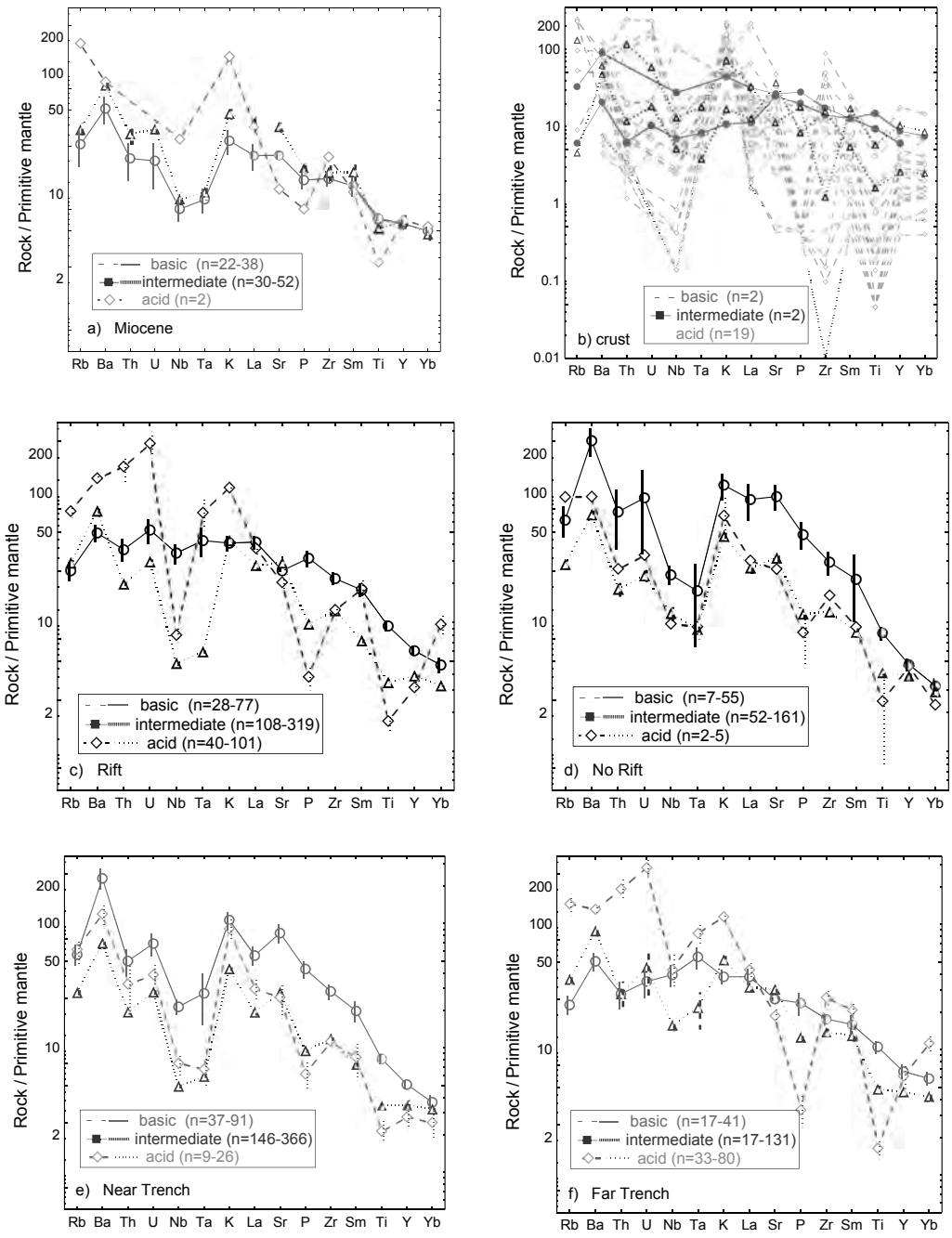

Fig. 7. Primitive mantle-normalized multi-element plots for rocks from the mean values of the western part of the Mexican Volcanic Belt; the range (n) of minimum and maximum determinations for a given subdivision are included in parentheses. The vertical error bars represent 99.5% confidence intervals of the mean. Basic, intermediate, and acid rocks are considered separately. a) Miocene rocks; b) crustal rocks and xenoliths (individual data are shown); c) rocks from the Rift subdivision; d) rocks from the No Rift subdivision; e) rocks from the Near Trench subdivision; and f) rocks from the Far Trench subdivision.

For the No Rift region, the basic rocks show a wide range in their 99.5% confidence interval values (Fig. 6d). However, both intermediate and acid rocks have lower REE concentrations for most elements than the basic rocks. None of the rock types shows a significant Eu anomaly (Fig. 6d). This implies that they cannot be related through fractional crystallization of common rock-forming minerals (Torres-Alvarado et al., 2003).

For the Near Trench locations of the W-MVB, the basic rocks show significantly higher REE concentrations for most elements than the intermediate and acid rocks (Fig. 6e). None of the rock types shows any Eu anomaly.

The relationship of the Far Trench rocks is also rather complex (Fig. 6f). The intermediate rocks cannot be related to the basic rocks through fractional crystallization; however, the acid rocks with generally higher REE concentrations and a large negative Eu anomaly could well be related to the intermediate rocks through this process (Fig. 6f).

The primitive mantle-normalized diagrams are shown in Fig. 7. Miocene basic and intermediate rocks show a negative Nb anomaly (Fig. 7a; only two acid rock samples are available in the compilation, which should not be considered representative of the W-MVB). However, the basic rocks do not depict depletion of other

high-field strength elements such as Ta, P, and Zr whereas the intermediate rock types show depletion of these elements (Fig. 7a). All intermediate and acid crustal rock types show negative Nb anomaly but the two samples of basic rocks do not (Fig. 7b).

The Rift volcanic rocks (Fig. 7c) show patterns similar to the respective Miocene rocks (Fig. 7a). On the other hand, all three types of the No Rift volcanic rocks depict negative Nb anomaly (Fig. 7d), as is the case of the Near Trench magmas (Fig. 7e). Finally, the Far Trench rocks do not show a large Nb anomaly in none of the rock types (Fig. 7f).

6.2.1. Quantification of Nb and Ta anomalies

Verma (2015b) reported statistical information on Nb and Ta anomalies (with respect to their neighbors Ba and La) for magmas from the central part of the Mexican Volcanic Belt, a large number of continental and island arcs, continental rifts or extensional areas, including post–collision extension, and continental collision zones around the world. We have estimated these values for W-MVB Miocene rocks as well as for the subdivision of Rift-No Rift and Near Trench-Far Trench magmas and compared them with the compilation of Verma (2015b) in Table S1 (Supplementary Material file). Special emphasis was given to the 99% confidence interval of the mean values.

Miocene basic rocks from the W-MVB have confidence intervals (at 99%) of 0.19–0.27 and 0.22–0.32 respectively for the Nb and Ta anomalies, which are slightly higher than the ranges for most continental and island arcs but lower than most continental rifts and extensional areas. For the W-MVB Miocene intermediate rocks, these values generally overlap with both arcs and rifts. Only two samples of W-MVB Miocene acid rocks have Nb anomaly values (Table S1), so they should not be considered statistically representative.

The Pliocene-Holocene basic rocks from the Rift (triple-rift) area show significantly higher confidence intervals for the Nb and Ta anomalies than the No Rift region. The former values are similar to most continental rifts and extensional areas whereas the latter are akin to those from arcs (Table S1). The intermediate and acid rocks from both regions show similar values as for most arcs as well as rifts. It is difficult to draw a distinction between arcs and rifts from intermediate and acid rocks without considering the basic rocks.

The Pliocene-Holocene basic rocks from the Near Trench and Far Trench areas show a similar relationship as the No Rift and Rift regions, respectively. The basic rocks from Near Trench are similar to the arcs whereas those from Far Trench region show confidence interval values generally similar to rifts. The intermediate and acid rocks from Far Trench also show somewhat higher confidence interval values than the Near Trench rocks although all of them are also similar to the both arcs and many rifts and extensional areas (see Section 5.5. Significance tests).

6.3. Conventional Sr–Nd isotope diagrams with confidence intervals

The actually measured Sr and Nd isotope ratios are reported in Tables 1 and 3. However, the in-situ ^{87}Sr growth corrected ratios of samples should be used for petrogenetic purposes. Although the $(^{143}Nd/^{144}Nd)_m$ for these Miocene to Holocene samples may not significantly vary from age correction, the $(^{87}Sr/^{86}Sr)_m$ will most likely be different, especially for samples with high Rb/Sr such as RGS03 and LP01. Unfortunately, the precise values of $^{87}Rb/^{86}Sr$ and age are not available for individual samples and only some samples have actually measured ages. Therefore, only approximate in-situ growth corrections can be achieved through measured Rb and Sr and assumed ages. The measured $(^{87}Sr/^{86}Sr)_m$ values were corrected for in-situ growth from the actually measured Rb and Sr

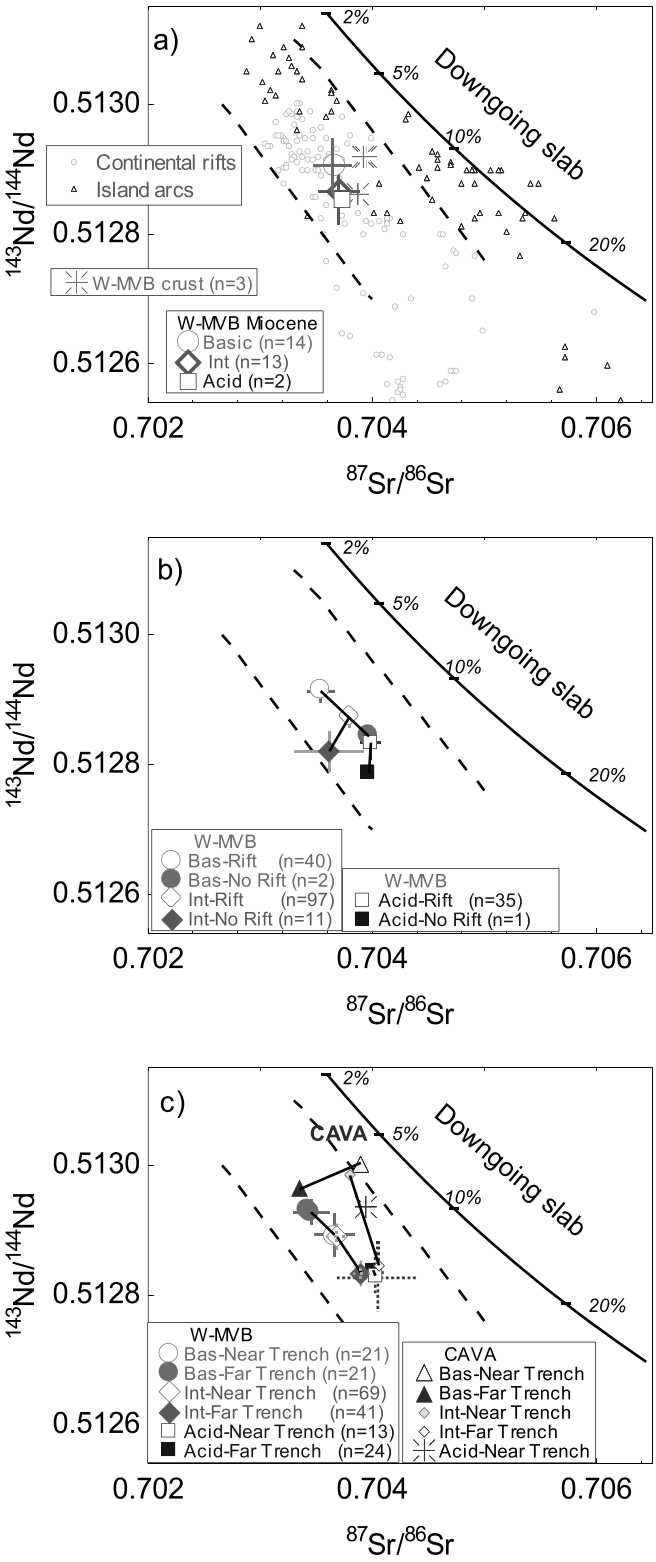

Fig. 8. Sr–Nd isotope diagram for samples from the western part of the Mexican Volcanic Belt (W-MVB) and their comparison with the Mantle Array (Faure, 1986) and Downgoing slab composition (Verma, 2000). Average values along with 99.5% confidence intervals of the mean are shown for the W-MVB data. The symbols are explained in the insets. a) Miocene rocks from the W-MVB, for comparison are included the crustal rocks or xenoliths from the W-MVB (this compilation) as well as continental rifts and island arcs from around the world (Verma, 2015c); b) Rift and No Rift subdivision; and c) Near Trench and Far Trench subdivision, also included are the data from the Central American Volcanic Arc from Verma (2015c).

concentrations and assumed ages of 10 m y. for Miocene rocks, the actually measured or assumed ages of 5-0 m y. depending on the geological period of Pliocene-Holocene. Thus, for the interpretation, age-corrected $(^{87}Sr/^{86}Sr)_i$ are plotted in Fig. 8. The 99.5% confidence intervals are shown for both the Sr and Nd isotopic ratios. Also shown for reference are the trace of the mantle array (Faure, 1986) and downgoing slab (Verma, 2000) in all plots (Fig. 8a–c).

The Sr–Nd average isotope data for the W-MVB Miocene rocks (Fig. 8a) are compared with the compiled data for worldwide continental rifts and island arcs (Verma, 2006). For comparison are also shown the crustal compositions of three samples from the W-MVB. The W-MVB Miocene rocks are isotopically similar to the continental rifts and the 99.5% confidence intervals generally overlap (Fig. 8a).

The Sr–Nd average isotope data for the W-MVB for the Rift-No Rift and Near Trench-Far Trench pairs are shown in Fig. 8b and c, respectively. All values plot well within the mantle array. Solid lines mark the basic, intermediate, and acid rocks for the Rift-No Rift and Near Trench-Far Trench pairs (Fig. 8a and b). The W-MVB basic rocks for the Rift area show slightly lower $^{87}Sr/^{86}Sr$ and higher $^{143}Nd/^{144}Nd$ than the No rift area (Fig. 8b). The intermediate rocks for the Rift area are slightly higher in both Sr and Nd ratios than the No Rift area. For the acid rocks, only one sample is available from No Rift area (Fig. 8b); therefore, the comparison is not much meaningful.

For the Near Trench-Far Trench subdivision of the W-MVB, all average compositions plot well within the mantle array and far from the downgoing slab (Fig. 8c). The basic and acid rocks from the Near Trench and Far Trench areas show overlapping $^{87}Sr/^{86}Sr$ and $^{143}Nd/^{144}Nd$ values (Fig. 8c). The intermediate rocks also have overlapping Sr isotopic values; however, the Far Trench samples have slightly lower Nd isotopic compositions. For comparison, the Central American Volcanic Arc (CAVA; Verma, 2015c) data for volcanic rocks are also shown in Fig. 8c. The isotopic compositions of the CAVA basic rocks from the Near Trench area are significantly shifted towards the downgoing slab. The compositions of intermediate rocks from these two areas are also significantly different from each other; the Near Trench rocks show significantly lower Nd isotopic values than the Far Trench rocks (Fig. 8c). This comparison for CAVA acid rocks is not possible because there are no data for the Far Trench area (Fig. 8c).

6.4. Tectonomagmatic multidimensional discrimination

The conventional bivariate and ternary diagrams for tectonic discrimination were shown to work unsatisfactorily (Verma, 2010). The most important reason for this failure is related to the violation of the basic statistical assumption of a normal distribution for compositional data (e.g., Aitchison, 1986; Egozcue et al., 2003; Buccianti and Pawlowsky-Glahn, 2005; Verma, 2012, 2015a; Buccianti, 2013; Verma and Armstrong-Altrin, 2016; Verma et al.,

Table 4
Application of multidimensional diagrams for deciphering tectonic setting of Miocene basic magmas from the western Mexican Volcanic Belt (W-MVB).

Figure reference; figure type; figure no.	Discrimination diagram[a]	Total no. of samples (%)	Predicted tectonic affinity and number of discriminated samples (%)				
			IAB	CRB + OIB	CRB	OIB	MORB
Verma et al. (2006); log-ratios of major elements (m2); Fig. 8	IAB-CRB-OIB-MORB	62 (100)	30 (48.4)	–	29 (46.8)	0 (0)	3 (4.8)
	IAB-CRB-OIB	62 (100)	22 (35.5)	–	40 (64.5)	0 (0)	–
	IAB-CRB-MORB	62 (100)	26 (41.9)	–	34 (54.9)	–	2 (3.2)
	IAB-OIB-MORB	62 (100)	49 (79.0)	–	–	0 (0)	13 (21.0)
	CRB-OIB-MORB	62 (100)	–	–	57 (91.9)	0 (0)	5 (8.1)
W-MVB Miocene rocks: Synthesis of all five diagrams of Verma et al. (2006)		**310(100)**	**127 (41.0)**	**–**	**160 (51.6)**	**0 (0)**	**23 (7.4)**
Agrawal et al. (2008); log-ratios of immobile trace elements (t1); no figure.	IAB-CRB + OIB-MORB	30 (100)	17 (56.7)	2 (6.7)	–	–	11 (36.7)
	IAB-CRB-OIB	30 (100)	15 (50.0)	–	11 (36.7)	4 (13.3)	–
	IAB-CRB-MORB	30 (100)	18 (60.0)	–	2 (6.7)	–	10 (33.3)
	IAB-OIB-MORB	30 (100)	17 (56.7)	–	–	0 (0)	13 (43.3)
	CRB-OIB-MORB	30 (100)	–	–	7 (23.3)	0 (0)	23 (76.7)
W-MVB Miocene rocks: Synthesis of all five diagrams of Agrawal et al. (2008)		150(100)	67 (44.7)	2 (–)	22 (14.7)	4 (2.7)	57 (38.0)
Verma and Agrawal (2011); log-ratios of immobile major and trace elements (t2); no figure.	IAB-CRB + OIB-MORB	62 (100)	9 (23.7)	0 (0)	–	–	29 (76.3)
	IAB-CRB-OIB	62 (100)	36 (94.7)	–	2 (5.3)	0 (0)	–
	IAB-CRB-MORB	62 (100)	9 (23.7)	–	0 (0)	–	29 (76.3)
	IAB-OIB-MORB	62 (100)	10 (26.3)	–	–	0 (0)	28 (73.7)
	CRB-OIB-MORB	62 (100)	–	–	1 (2.6)	1 (2.6)	36 (2.7)
W-MVB Miocene rocks: Synthesis of all five diagrams of Verma and Agrawal (2011)		190 (100)	64 (33.7)	0 (–)	3 (1.6)	1 (0.5)	122 (64.2)

The boldface letters provide the synthesis of the relevant data.
[a] IAB–island arc basic (or ultrabasic) rock (in fact, this is the combined island and continental arc setting); CRB–continental rift basic (or ultrabasic) rock; OIB–ocean island basic (or ultrabasic) rock; MORB–mid-ocean ridge basic (or ultrabasic) rock. The numbers in the parentheses "()" are the percentages of samples plotting in a given field.

Table 5
Application of multidimensional diagrams for deciphering tectonic setting of Miocene intermediate magmas from the western Mexican Volcanic Belt (W-MVB).

Magma type, figure name; figure number	Figure type[a]	Total number of samples	Number of discriminated samples				
			Arc			Within-plate CR + OI $[\overline{x}\pm s]$ $[p_{CR+OI}]$ Θ	Collision Col $[\overline{x}\pm s]$ $[p_{Col}]$ Θ
			IA + CA $[\overline{x}\pm s]$ (p_{IA+CA}) Θ	IA $[\overline{x}\pm s]$ $[p_{IA}]$ Θ	CA $[\overline{x}\pm s]$ $[p_{CA}]$ Θ		
Intermediate; Verma and Verma (2013); log-ratios of all major elements (mint); no figure	IA + CA-CR + OI-Col	69	34 [0.702 ± 0.119] (0.4793–0.9364)	–	–	10 [0.713 ± 0.213] (0.3946–0.9407)	25 [0.689 ± 0.158](0.4027–0.9945)
	IA-CA-CR + OI	69	–	1(0.5503)	51 [0.696 ± 0.117] (0.4077–0.9262)	17 [0.692 ± 0.171] (0.3893–0.9687)	–
	IA-CA-Col	69	–	2 [0.582 ± 0.048] (0.5478, 0.6162)	47 [0.635 ± 0.100] (0.4205–0.8242)	–	20 [0.741 ± 0.170] (0.4720–0.9983)
	IA-CR + OI-Col	69	–	27 [0.655 ± 0.122](0.4337–0.9219)	–	11 [0.724 ± 0.218](0.4382–0.9512)	31 [0.692 ± 0.163] (0.4376–0.9938)
	CA-CR + OI-Col	69	–	–	41[0.666 ± 0.135] (0.4156–0.9320)	8[0.700 ± 0.198] (0.3831–0.9201)	20 [0.620 ± 0.158] (0.4097–0.9829)
W-MVB Miocene: Diagrams based on log-ratios of major elements	***{Σn} {Σprob}[% prob]***	**345**	**{34} {23.8529}[–]**	**{30} {19.3917}[10.0%]**	**{139} {92.6562} [48.0%]**	**{46} {32.4568}[13.9%]**	**{96} {65.9249}[28.1%]**
Intermediate; Verma and Verma (2013); log-ratios of immobile major and trace elements (mtint); no figure	IA + CA-CR + OI-Col	52	28 [0.734 ± 0.154] (0.4073–0.9681)	–	–	6 [0.760 ± 0.111] (0.6165–0.9338)	18 [0.644 ± 0.136] (0.4243–0.8379)
	IA-CA-CR + OI	52	–	14 [0.663 ± 0.182] (0.4533–0.9819)	31 [0.685 ± 0.119] (0.4510–0.9102)	7 [0.667 ± 0.188] (0.4488–0.8871)	–
	IA-CA-Col	52	–	13 [0.609 ± 0.192] (0.3776–0.9640)	26 [0.593 ± 0.144] (0.4000–0.8924)	–	13 [0.576 ± 0.102] (0.4452–0.7242)
	IA-CR + OI-Col	52	–	25 [0.711 ± 0.182] (0.4692–0.9915)	–	6 [0.783 ± 0.144] (0.5494–0.9632)	21 [0.654 ± 0.168] (0.3579–0.8873)
	CA-CR + OI-Col	52	–	–	40 [0.803 ± 0.160] (0.4840–0.9714)	4 [0.711 ± 0.064] (0.6575–0.7937)	8 [0.546 ± 0.120] (0.4015–0.7119)
W-MVB Miocene: Diagrams based on log-ratios of immobile major and trace elements	***{Σn} {Σprob}[% prob]***	**260**	**{28} {20.5465}[–]**	**{52} {34.9734}[23.5%]**	**{97} {68.7958}[46.2%]**	**{23} {16.7696}[9.4%]**	**{60} {37.1714}[20.9%]**
Intermediate; Verma and Verma (2013); log-ratios of immobile trace elements (tint); no figure	IA + CA-CR + OI-Col	35	25 [0.636 ± 0.169](0.3512–0.9488)	–	–	1(0.7084)	9 [0.761 ± 0.177](0.5027–0.9926)
	IA-CA-CR + OI	35	–	1(0.5222)	28 [0.754 ± 0.111](0.5503–0.9813)	6 [0.562 ± 0.058](0.4783–0.6503)	–
	IA-CA-Col	35	–	0 (0)	28 [0.740 ± 0.109](0.4988–0.9743)	–	7 [0.798 ± 0.122](0.5788–0.9855)
	IA-CR + OI-Col	35	–	7[0.570 ± 0.209] (0.3627–0.8909)	–	11 [0.608 ± 0.192](0.3869–0.9118)	17[0.673 ± 0.203] (0.3666–0.9937)
	CA-CR + OI-Col	35	–	–	28 [0.859 ± 0.091](0.6472–0.9962)	1(0.3886)	6[0.654 ± 0.139] (0.5605–0.9295)
W-MVB Miocene: Diagrams based on log-ratios of immobile trace elements	***{Σn} {Σprob[% prob]***	**175**	**{25} {15.8913}[–]**	**{8} {4.5115}[4.4%]**	**{84} {65.8651}[64.5%]**	**{19} {11.1548}[8.8%]**	**{39} {27.7956}[22.2%]**

The boldface letters provide the synthesis of the relevant data.

[a] IA–island arc; CR–continental rift; OI–ocean island; Col–collision; $\overline{x}\pm s$ – mean ± standard deviation; **{Σn}** – total number of samples for the five diagrams; **{Σprob}** – total probability for a given tectonic setting in all five diagrams; and **[%prob]** – total percent probability value for a given tectonic setting in all five diagrams; Θ (p_{IA+CA}), [p_{IA}], [p_{CA}], [p_{CR+OI}], and [p_{Col}] – probability for the five tectonic fields.

2016b). Thus, the tectonomagmatic multidimensional diagrams proposed by Verma et al. (2006, 2012, 2013b), Agrawal et al. (2008), Verma and Agrawal (2011), and Verma and Verma (2013) through log-ratio transformation and linear discriminant analysis, were used for better understanding the tectonic regime dominant for magma genesis in the W-MVB. Verma (2015a) has explained in detail the statistical reasons for replacing the conventional ternary diagrams by multidimensional diagrams and has shown the advantages of doing so.

In the new discrimination diagrams, the basic rocks were discriminated as arc (called island arc (IAB) by Verma et al. (2006) and Agrawal et al. (2008); we clarify that the proposal of those diagrams included samples from both island and continental arcs but the continental arcs were not well represented in their database), continental rift (CRB), ocean island (OIB), and mid-ocean ridge (MORB) settings, whereas the intermediate and acid rocks were discriminated as island arc (IA), continental arc (CA), within-plate (combined continental rift and ocean island CR + OI), and collision (Col) tectonic settings. Because one tectonic setting is different in these sets (MORB in basic and Col in intermediate and acid), the results are likely to show some inconsistency (Verma et al., 2015).

Table 6
Application of multidimensional diagrams for deciphering tectonic setting of Miocene acid magmas from the western Mexican Volcanic Belt (W-MVB).

Magma type, figure name	Figure type §	Total number of samples	Number of discriminated samples				
			Arc			Within-plate CR + OI [$\bar{x}\pm s$] [p_{CR+OI}] Θ	Collision Col [$\bar{x}\pm s$] [p_{Col}] Θ
			IA + CA [$\bar{x}\pm s$] (p_{IA+CA}) Θ	IA [$\bar{x}\pm s$] [p_{IA}] Θ	CA [$\bar{x}\pm s$] [p_{CA}] Θ		
Acid; Verma et al. (2012); log-ratios of all major elements (macid)	IA + CA–CR –Col	5	2 [0.781 ± 0.292](0.5744, 0.9870)	–	–	2 [0.865 ± 0.160] (0.7515, 0.9781)	1 (0.7834)
	IA–CA–CR	5	–	1(0.9883)	2 [0.680 ± 0.341] (0.4388, 0.9205)	2 [0.9708 ± 0.0412](0.9417, 1.0000)	–
	IA–CA–Col	5	–	1(0.9960)	2 [0.645 ± 0.198] (0.5046, 0.7849)	–	2 [0.846 ± 0.216](0.6928, 0.9988)
	IA–CR–Col	5	–	1(1.0000)	–	3 [0.771 ± 0.150](0.6213 –0.9205)	1(0.8908)
	CA–CR–Col	5	–	–	2 [0.738 ± 0.370] (0.4770, 0.9999)	2 [0.803 ± 0.195] (0.6650, 0.9404)	1(0.6610)
W-MVB Miocene: Diagrams based on log-ratios of all major elements	***{Σn} {Σprob}[% prob]***	**25**	**{2} {1.5614} [–]**	**{3} {2.9842} [18%]**	**{6} {4.1258}[25%]**	**{9} {7.5902}[37%]**	**{5} {4.0268}[20%]**
Acid; Verma et al. (2013a,b); log-ratios of all major elements (macid)	IA + CA-CR + OI-Col	5	2 [0.687 ± 0.422](0.3880, 0.9853)	–	–	3 [0.895 ± 0.053] (0.8459 –0.9511)	0 (0)
	IA-CA-CR + OI	5	–	1 (0.9989)	1 (0.5908)	3 [0.9821 ± 0.0213](0.9585 –0.9999)	–
	IA-CA-Col	5	–	1 (0.9885)	2 [0.9029 ± 0.0063] (0.8985, 0.9074)	–	2 [0.868 ± 0.160] (0.7550, 0.9814)
	IA-CR + OI-Col	5	–	1 (1.0000)	–	4 [0.787 ± 0.129] (0.6213 –0.9289)	0 (0)
	CA-CR + OI-Col	5	–	–	1(0.9987)	4 [0.732 ± 0.226] (0.3974 –0.8887)	0 (0)
W-MVB Miocene: Diagrams based on log-ratios of all major elements	***{Σn} {Σprob}[% prob]***	**25**	**{2} {1.3733}[–]**	**{3} {2.9874} [17%]**	**{4} {3.3953}[19%]**	**{14} {11.7088}[55%]**	**{2} {1.7364}[9%]**
Acid; Verma et al. (2013a,b); log-ratios of immobile major and trace elements (mtacid)	IA + CA-CR + OI-Col	2	0 (0)	–	–	1 (0.9074)	1 (0.4175)
	IA-CA-CR + OI	2	–	0 (0)	1 (0.7241)	1 (0.9608)	–
	IA-CA-Col	2	–	0 (0)	1 (0.5797)	–	1 (0.8621)
	IA-CR + OI-Col	2	–	0 (0)	–	1 (0.8736)	1 (0.6313)
	CA-CR + OI-Col	2	–	–	1 (0.5268)	1 (0.8642)	0 (0)
W-MVB Miocene: Diagrams based on log-ratios of immobile major and trace elements	***{Σn} {Σprob}[% prob]***	**10**	**{0} {0} [0%]**	**{0} {0} [0%]**	**{3} {1.8306}[25%]**	**{4} {3.6059}[49%]**	**{3} {1.9109}[26%]**

The boldface letters provide the synthesis of the relevant data.
Explanation of § and Θ is given in Table 5.

6.4.1. Miocene rocks

The application of multidimensional diagrams (from TecD) to Miocene rocks from the W-MVB is summarized in Tables 4–6. We discuss in detail only the results of the application of one set of multidimensional diagrams for basic rocks (Verma et al., 2006; the first part of results in Table 4). Further, only one set of five diagrams are actually shown (Fig. 9) because it is difficult to actually count the samples plotting in different fields in diagrams. The computer program TecD does it automatically; therefore, plotting (such as in Fig. 9) can be advantageously replaced by the output of TecD (Table 4).

The results from the first set of diagrams based on log-ratio of major elements (Fig. 9) for the Miocene basic rocks (62 samples) are summarized in the first part of Table 4. In the very first diagram of this set (IAB-CRB-OIB-MORB) that discriminates four tectonic settings of island (and continental) arc, continental rift, ocean island and mid-ocean ridge, 30 samples (about 48%) plotted in the IAB field, 29 in the CRB (about 47%) and 3 (about 5%) in the MORB field (Fig. 9a; the first row of data in Table 4). Similarly, in the second diagram (IAB-CRB-OIB; Fig. 9b; the second row of data in Table 4) that discriminates three of the four tectonic setting of island (and continental) arc, continental rift, and ocean island, the (62) samples are subdivided in the IAB and CRB fields with 22 and 40 samples, about 36% and 64%, respectively. Similarly, in the third diagram (IAB-CRB-MORB; Fig. 9c; the third row of data in Table 4), the samples (62) are subdivided in the IAB and CRB fields, with 26 (42%) and 34 (55%) samples, respectively. In the fourth diagram (IAB-OIB-MORB) from with the CRB setting is absent (Fig. 9d; the fourth row of data in Table 4), 49 (out of 62) samples plotted in the IAB field and the remaining 13 samples in the MORB field. Finally, in the last diagram of this set (CRB-OIB-MORB; Fig. 9e; the fifth row of Table 4) from which the IAB setting is missing, most samples (57 out of 62; amounting to about 92%) plotted in the CRB field, with the remaining 5 samples in the MORB field. Noteworthy is the fact that not even one sample plotted in the OIB field in any of the five diagrams of this set (Fig. 9a–e; the first part of Table 4). TecD provides

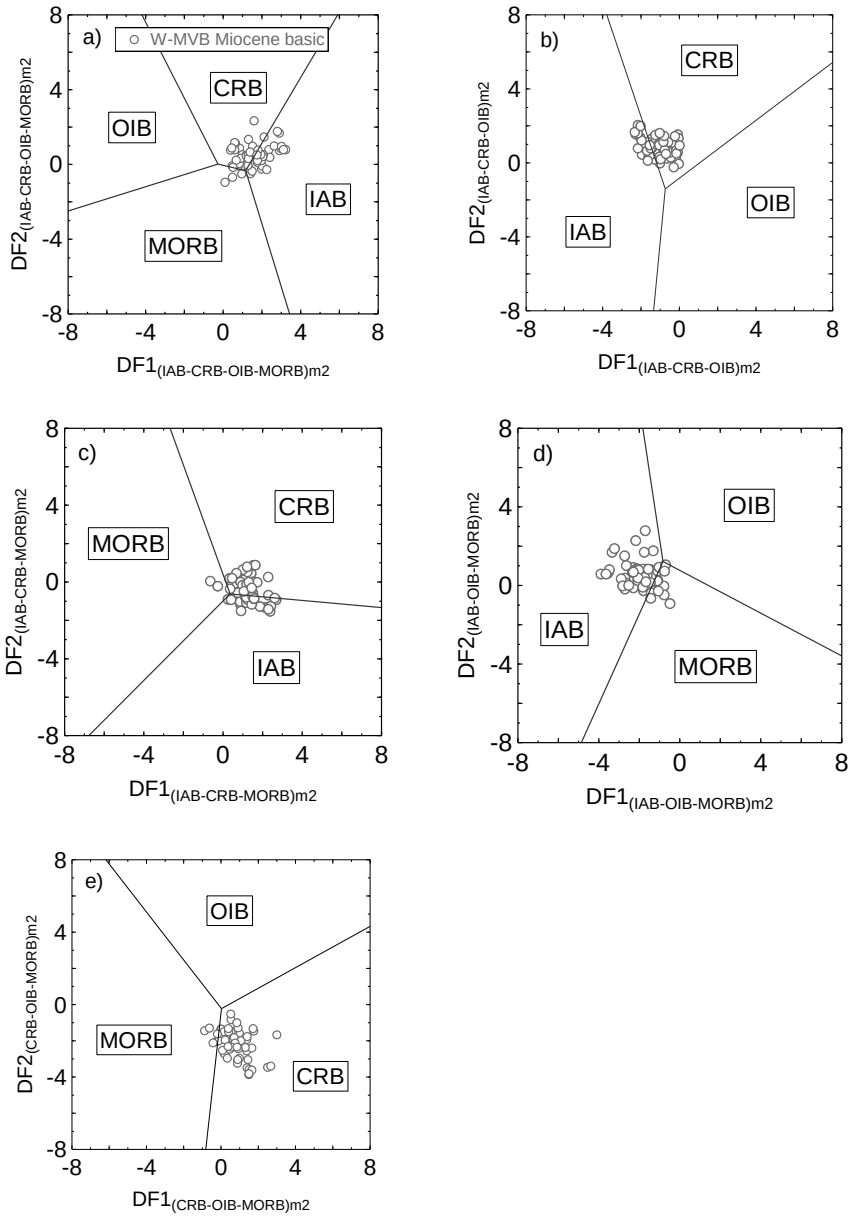

Fig. 9. Application of the set of five multidimensional tectonic discrimination diagrams based on log-ratios of major elements in basic and ultrabasic magmas (Verma et al., 2006; see subscript m2 in all diagrams indicating that this is the second set of multidimensional diagrams based on major elements) to Miocene basic rocks from the western part of the Mexican Volcanic Belt (W-MVB). The four fields that can be discriminated are: IAB–island (and continental) arc basic rocks; CRB–continental rift basic rocks; OIB–ocean island basic rocks; MORB–mid-ocean ridge basic rocks. a) IAB-CRB-OIB-MORB; c) IAB-CRB-OIB; c) IAB-CRB-MORB; d) IAB-OIB-MORB; and e) CRB-OIB-MORB.

an overall synthesis of all five diagrams from a given set (see the row of results after the five diagrams), which indicated that out of the total of 310 data points (all five diagrams Fig. 9a–e combined), 127 (about 41%) plotted in the IAB, 160 (about 56%) in the CRB, and 23 (about 7%) in the MORB field. Thus, the first set of multidimensional diagrams by Verma et al. (2006) can be taken to indicate a continental rift or a transitional arc to rift setting (Table 4).

Having described in detail the results of the first set of diagrams, the other results will only be briefly mentioned. The set of diagrams based on log-ratios of selected trace elements (La, Sm, Yb, Nb, and Th) by Agrawal et al. (2008) and that by Verma and Agrawal (2011; TiO_2, Nb, V, Y, and Zr) suggested a transitional arc to mid-ocean ridge setting.

The three sets of diagrams for intermediate rocks consistently indicated a continental arc setting, with total percent probability values of about 46%–64% (Table 5). Finally, only five samples of Miocene acid rocks with data for major elements were available in our database, with only two of them for the diagram set based on combined major and trace elements (Table 6). Their indications of a within-plate setting should be viewed with caution. Nevertheless, because most Miocene rocks compiled in this work are located very far away from the Middle America Trench (MAT; Fig. 2a). The older rocks closer to the MAT may lie under the Pliocene-Holocene cover (Figs. 3 and 4).

6.4.2. *Rift versus No rift subdivision*

This application is summarized in Tables S2 and S3 for basic, S4 to S5 for intermediate, and Tables S6–S7 for acid rocks.

Basic rocks from the Rift subdivision (the three rift areas TZR, CR, and ChR; Fig. 3) suggest a continental rift setting in the

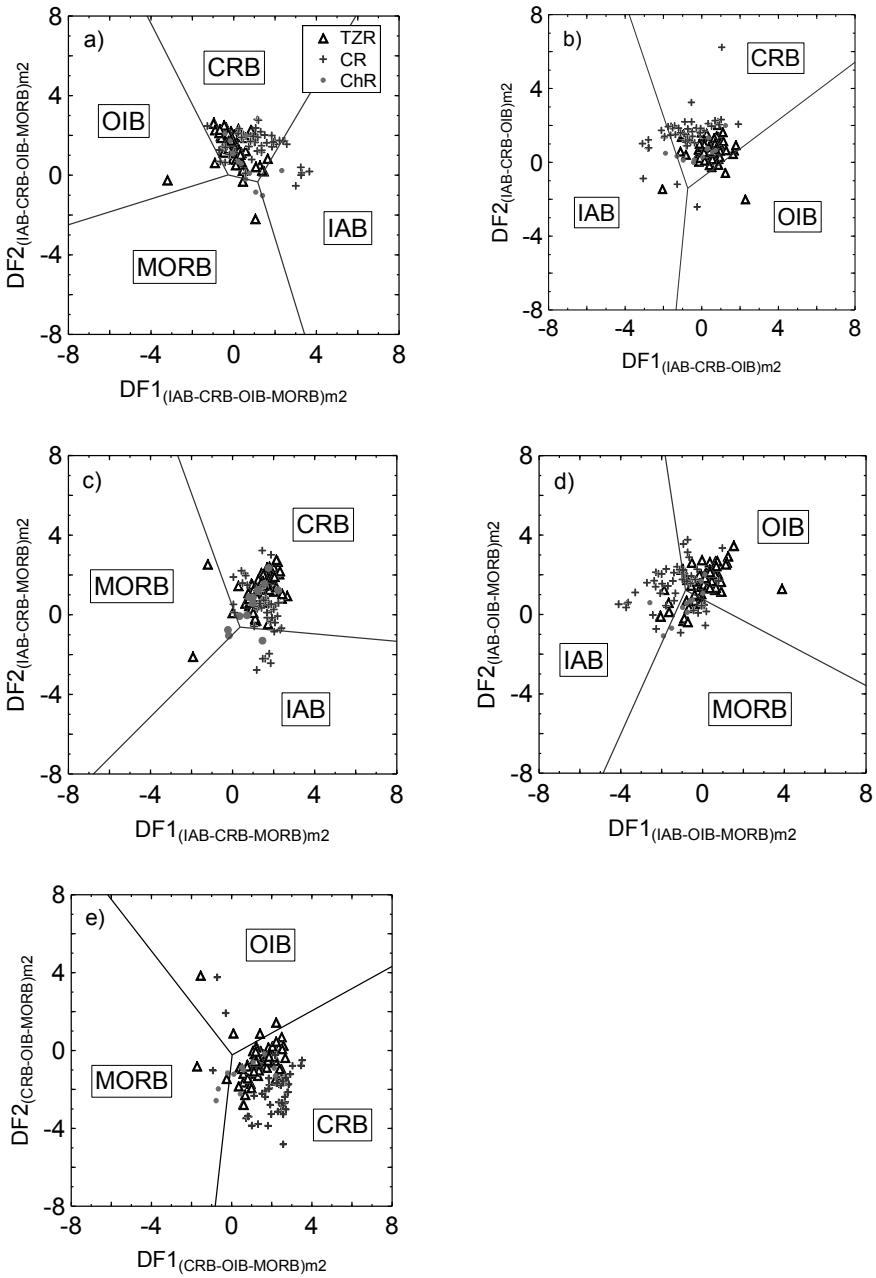

Fig. 10. Application of the set of five multidimensional tectonic discrimination diagrams based on log-ratios of major elements in basic and ultrabasic magmas to Pliocene-Holocene basic rocks from the three rifts of the western part of the Mexican Volcanic Belt (W-MVB); the rifts are as follows: Tepic-Zacoalco Rift (TZR); Colima Rift (CR); and Chapala rift (CR); more explanation is in Fig. 9 a) IAB-CRB-OIB-MORB; c) IAB-CRB-OIB; c) IAB-CRB-MORB; d) IAB-OIB-MORB; and e) CRB-OIB-MORB.

discrimination diagrams (Table S2). The overall percent (sample count) values for this setting were high at about 71% for the major-element based diagrams, relatively low at about 52% for the immobile trace element based diagrams, and still lower at about 48% for the immobile major and trace element based diagrams (Table S2). The sample percent values for the other tectonic settings were generally lower than (or similar to) the by-chance probability of 25% (Table S2).

For the No Rift area (Fig. 3), in the major element based diagrams the basic rocks also suggested a continental rift setting because the overall percent success value for this setting was about 66% (Table S3). We note that some samples from the No Rift area are also located in graben and triple-rift systems (Fig. 3). However, the other two sets of diagrams did not provide clear indications. For the second set of diagrams (Agrawal et al., 2008) only nine samples were available, which indicated a rift or ocean island setting. The last diagram set suggested an arc setting but with a low percent value of about 40% (Table S3).

The intermediate rocks from the Rift area consistently indicated a continental arc setting, with the total percent probability values of about 51%, 40%, and 54%, respectively for the three sets of diagrams (Table S4). Two sets of diagrams for the No Rift rocks showed a transitional continental arc to collision setting whereas the third set indicated a continental arc setting (Table S5).

For acid rocks from the Rift area, the first set of major element based diagrams indicated a continental arc setting with the total percent probability of about 47% (Table S6). The other sets of diagrams for acid rocks provided a consistent result of a transitional continental arc to within-plate setting (Table S6).

Much less number of acid rocks samples (15 with complete

major element data, 5 and 2 for relatively immobile element based diagrams) available from the No Rift region indicated a continental arc setting (Table S7).

6.4.3. Subdivision of rift magmas into three rifts

In order to better understand the effects of ongoing subduction and rifting processes, we further analyzed tectonic implications of rift geochemical data in terms of the subdivision into three rifts (Fig. 3): TZR (456 samples), CR (496 samples), and ChR (62 samples). The implications of multidimensional diagrams are considered separately for each rift.

For the Tepic-Zacoalco Rift (TZR), in the major element based diagrams (Verma et al., 2006) 71 samples of basic rocks indicated a continental rift setting (Fig. 10; Table S8). Twenty-seven samples (out of 71) had complete data for the combined major and trace element based diagrams (Agrawal et al., 2008), which also indicated a continental rift setting (Table S8). Thirty-seven samples with complete data for the combined major and trace element based diagrams (Verma and Agrawal, 2011) confirmed the continental rift setting (Table S8). The intermediate rocks from the TZR (211 samples) provided less consistent results in the multidimensional diagrams (Verma and Verma, 2013) with no clear indications for any tectonic setting (Table S9). The same was true for the acid rocks (174 samples; Verma et al., 2012, 2013b) although the highest percent probability values were for continental arc and within-plate settings (Table S10).

For the Colima Rift (CR), 48 basic rock samples were consistent with a continental rift setting in the major element based diagrams whereas 19 samples with complete data for the third set of diagrams were consistent with an arc setting (Fig. 10; Table S11). The trace element based diagrams, however, did not provide high percent probability values for any tectonic setting (Table S11) although the arc setting showed somewhat higher value than the continental rift. The intermediate rocks (410 samples for major element based diagrams; 157 for the combined major and trace element based diagrams; and 116 for the trace element based diagrams) clearly indicated a continental arc setting for the Colima Rift (Table S12). Similarly, the acid rocks (38 samples for major element based diagrams; 11 for the combined major and trace element based diagrams; and 10 for the trace element based diagrams) consistently indicated a continental arc setting (Table S13).

Much lesser samples were available from the Chapala Rift (ChR; Tables S14–S16). Twelve samples of basic rocks indicated a continental rift setting (Fig. 10; Table S14). Of them, only one sample with complete data for the trace element based diagrams should not be considered for any inference. Nine basic rock samples showed a within-plate setting for the Chapala Rift (Table S14). In the major element based diagrams, 45 intermediate rock samples suggested a continental arc setting (Table S15) although the combined major and trace element based diagrams did not provide a consistent answer. Only one sample for the third set of diagrams should not be considered for this inference (Table S15). Finally, only 5 acid rock samples (available in our database) did not provide a consistent answer to the probable tectonic setting of the Chapala Rift although a transitional arc to within-plate setting could be tentatively indicated (Table S16).

6.4.4. Near Trench versus Far Trench subdivision

The results for basic, intermediate, and acid rocks are summarized in Tables S17– S18, S19– S20, and S21– S22, respectively.

For the subdivision of the Near Trench-Far Trench areas (Fig. 4), basic rocks from Near Trench indicated a continental rift setting with about 68% in the major-element based diagram set (Table S17). In the immobile trace element based diagram set also, the same tectonic setting could be inferred although the percent success was low (44%; Table S17). The final set based on immobile major and trace elements, an arc setting was indicated but with only about 42% sample percent value (Table S17). We also note that most of the Near Trench rocks are situated in the triple-rift system as well as in other graben systems (Fig. 4).

For the Far Trench area (Fig. 4), the basic rocks indicated a continental rift setting in all three sets of diagrams, with high percent success value of about 72% for the major-element based diagram set, followed by about 61% and 63% for the immobile element based sets (Table S18).

The intermediate rocks For the Near Trench and Far Trench subdivision (Fig. 4), clearly indicated a continental arc setting for the Near Trench with percent probability value of about 52%, 46%, and 61%, for the three sets of diagrams (Table S19), whereas for the Far Trench the indications are not so clear (Table S20). The first set of diagrams can be interpreted as a transitional continental arc to collision setting, the second set is more consistent with a transitional within-plate to collision setting, and the third set indicates a transitional continental arc to within-plate setting.

The acid rock samples from the Near Trench area showed a continental arc setting in all diagrams, with the total percent probability values of 47%–77% (Table S21). The same type of rocks from the Far Trench area provided a less consistent result (Table S22). The first set of major element based diagrams indicated a continental arc setting with a relatively low total percent probability value of 45%. The other two sets suggested a transitional continental arc to within-plate setting whereas the final set of diagrams was more consistent with a within-plate setting (Table S22).

The differences in the tectonic inferences for basic rocks as compared to more evolved intermediate and acid rocks are commonly observed in other parts of the MVB (Verma, 2015b,c). At first sight, it may seem to be a rather puzzling inference. However, the tectonomagmatic discrimination diagrams should be used in conjunction with the analysis of petrogenetic processes (Verma et al., 2015, 2016a). If we take into account that the basic magmatic rocks from the W-MVB mainly originated in the mantle, they will indicate the actual tectonic setting of the region. The evolved intermediate and acid rocks of the W-MVB owe their origin to a combination of mantle and crustal sources. However, the crust beneath the W-MVB is highly heterogeneous. Therefore, their tectonic interference from multidimensional diagrams is likely to be influenced from the tectonic setting that gave rise to the underlying crust, or else these evolved rocks will not provide any consistent result. Thus, the tectonic inferences must be interpreted from the consideration of petrogenetic processes.

6.5. Significance tests

The appropriate version of the Student t test (Verma, 2005) was applied at a strict 99% confidence level (both One-Sided and Two-Sided versions) to all data pairs for a given elements or ratio parameters corresponding to the basic, intermediate and acid rocks form the Rift-No Rift and Near Trench-Far Trench pairs. As required, the normal distribution of the different parameters was first ascertained from the application of discordancy tests (Verma and Díaz-González, 2012). The results of the t test are summarized in Tables S23–S25 for the Rift and No Rift pairs and in Tables S26–S28 for the Near Trench and Far Trench pairs. In fact, the actual probability values in terms of confidence levels (complementary of significance levels or α values expressed in percent) are also listed in Tables S23–S28 in order to facilitate the readers to draw their own conclusions. We omitted the results from these tables when any of the two groups had less than five (an arbitrarily set lower limit) samples because less number of samples generally provided

very wide confidence intervals of the mean especially because of the larger t values required for their computations (e.g., Verma and Cruz-Huicochea, 2013). Further, the application of significance tests such as t test is not strictly valid to the conventional concentration parameters because they require the data to be normally distributed but such data from their very nature cannot represent a normal distribution (e.g., Aitchison, 1986; Egozcue et al., 2003; Verma, 2012, 2015c; Verma et al., 2016b). Therefore, although we have included them in Tables S23–S28, special consideration should be given only to the ratio or log-ratio parameters. The differences in log-ratios could explain the differences in the tectonic inferences from multidimensional diagrams.

6.5.1. Rift versus No rift

We will not describe in detail the concentration parameters but will do so for the first log-ratio parameter $\ln(TiO_2/SiO_2)$. Table S23 shows the evaluation 11 major oxides, 9 REE, and 20 trace element concentrations. Most of them (28 out of 40) show statistically significant differences at 99% confidence levels.

For $\ln(TiO_2/SiO_2)$ in basic rocks (Table S23), 130 samples from Group A (nA – Rift) and 66 from Group B (nB – No Rift) were evaluated. First, the F test was applied to evaluate the variances of the two groups; in fact, UDASYS does it internally to choose the correct version of the t test. The F test revealed no significant differences between the two variances; therefore, the combined degrees of freedom (df) was 194 being equal to (nA + nB-2). The next column in Table S23 (Sign) is + implying that group A (Rift) has "nominally" or "arithmetically" higher mean value of $\ln(TiO_2/SiO_2)$ than group B (No Rift). Then, the t statistic for these two statistical samples was calculated being 2.4617395 (t_calc). This value was compared to the critical value of t One-Sided at a confidence level of 99% (t_crit One-Sided) being 2.3457356. Because t_calc for the statistical samples of $\ln(TiO_2/SiO_2)$ in basic rocks from the Rift-No Rift pair (2.4617395) is higher than the t_crit One-Sided at the 99% confidence level (2.3457356), we infer that Group A (Rift) basic rocks have significantly higher values of $\ln(TiO_2/SiO_2)$ than those from Group B at the 99% confidence level (or 1% significance level or at α of 0.01). The inference "false" in the "H0 One–Sided" column actually means that the null hypothesis that "the particular parameter under evaluation for Group A is not significantly higher or lower (depending on the sign of + or–in the sign column) than Group B" is "false" at the 99% confidence level. In fact, the actual words in the inference column (H0 One–Sided) could be true-false, accept-reject, or even valid-invalid (see footnote of Table S23). The next column (CL_t One–Sided) gives the actual confidence level for the one-sided version of the t test. This value is 99.27% (equivalent to the significance level of 0.73% or α of 0.0073). Table S23 also lists the application of the two-sided version of the t test in the last three columns. The column "t_crit Two–Sided" gives the critical value of t for the two-sided version being 2.6014374. The comparison of the calculated t value (t_calc) of 2.4617395 is then compared with this critical value. Because t_calc < t_crit Two–Sided, we conclude that the $\ln(TiO_2/SiO_2)$ parameter does not significantly differ for basic rocks from the two groups (Group A Rift and Group B No Rift) at 99% confidence level (see "true" in the "H0 Two–Sided" column of Table S23). Had it been "false" in this column, it would have meant that a particular parameter does significantly differ for Groups A and B. The final column (CL_t Two–Sided) shows that actual confidence level that corresponds to the application of the two-sided t test, which in this case is 98.53% being somewhat less than 99% at which the t test was applied.

Out of 28 log-ratio parameters listed in Tables S23 and 18 parameters showed that Group A is significantly different from Group B (application of two-sided t test), whereas 20 parameters show that the parameter in Group A is higher (9 cases) or lower (11 cases) than Group B (Table S23; (application of one-sided t test).

The Nb and Ta anomalies ($\{Nb/Nb^*\}_{pm}$ and $\{Ta/Ta^*\}_{pm}$) were also compared for the two groups. Caution is required to fully understand the comparison of these two parameters. Higher values for these anomalies actually mean that the size of the anomaly (depletion of Nb or Ta with respect to Ba and La) is actually small. These anomaly values are significantly higher for Group A (Rift) than Group B (No Rift), implying that the No Rift rocks show higher depletion of Nb and Ta with respect to Ba and La.

Finally, five of the six slab-sensitive parameters could be evaluated from t test (Table S23). Three out of five slab-sensitive parameters show that Group A has statistically lower values than Group B; the remaining two parameters do not show statistically lower values of Group A with respect to Group B (Table S23). Sufficient numbers of analyses for the Sr, Nd, or Pb isotope parameters were not available for basic rocks from the Rift and No Rift groups, which are consequently absent from Table S23.

Having discussed the evaluation of parameters for basic rocks from the Rift and No Rift subdivision, the inference for intermediate (Table S24) and acid (Table S25) rocks will be only briefly mentioned. Intermediate rocks show 49 concentration and 41 ratio parameter pairs (Table S24). Twenty-four concentration parameters show lower values for Rift than for No Rift rocks whereas 11 samples show higher values. Similarly, 26 ratio parameters depict lower values for the Rift than the No Rift intermediate rocks, 6 higher values, and 9 no difference (Table S24). For acid rocks, lesser number of parameter pairs could be reported (28 concentration and 20 ratio parameters; Table S25). Of these, only 6 concentration parameters showed lower values and 2 higher values for Rift acid rocks than the No Rift rocks; 20 parameter values were statistically similar (Table S25). Similarly, for ratio parameters, only 6 depicted lower and 1 higher value for the Rift rocks; for 13 parameters these two groups (Rift and No Rift) had statistically similar values (Table S25).

6.5.2. Near Trench versus Far Trench

For basic rocks for the Near Trench area, 46 concentration and 41 ratio parameters are reported in Table S26. Out of them, 17 concentration parameters showed lower and 19 higher values for Near Trench than Far Trench magmas, whereas 13 ratio parameters indicated lower and 21 higher values. Noteworthy is that statistically higher values of slab-sensitive parameters were obtained for five out of six ratio variables listed in Table S26. Nb and Ta anomaly values were also consistent with a greater influence of subduction process in the Near Trench basic magmas than the Far Trench ones (Table S26).

For intermediate magmas, out of 48 concentration parameters, 34 showed lower values and only 2 higher values for the Near Trench than the Far Trench rocks. Similarly, for ratio parameters, 20 depicted lower and 11 higher values for the Near Trench rocks (Table S27).

Finally, for acid rocks, out of 40 concentration parameters, 22 showed lower and 12 higher values for the Near Trench than the Far Trench area (Table S28). Similarly, out of 37 ratio parameters listed in Tables S28 and 9 indicated lower and 22 higher values for the Near Trench acid rocks.

7. Conclusions

A compilation of new and published data for volcanic rocks from the W-MVB was subdivided as Miocene and Pliocene-Holocene rocks. A synthesis of their chemical compositions is presented as basic, intermediate, and acid rocks. The younger rock group was further subdivided as Rift-No Rift and Near Trench-Far Trench subgroups. We illustrate the use of the conventional and new multidimensional diagrams, quantification of Nb and Ta anomalies,

six slab-sensitive parameters, radiogenic isotopic ratios of Sr, Nd, and Pb, and significance tests. The crust beneath W-MVB is highly heterogeneous as can be seen from wide variation in their REE contents.

The Miocene rocks are present as surface outcrops generally very far away from the Middle America Trench. They may represent a continental rift or a transitional arc to rift setting (basic rocks) or a continental arc setting (intermediate rocks having a crustal component in their genesis). The basic rocks from the triple-rift (Rift) area depict a continental rift setting with percent probability values of 48%–71% whereas the No Rift basic rocks suggest either a rift or an arc setting. However, the intermediate rocks having a crustal component are more consistent with a continental arc setting from these subdivisions. The acid rocks from the Rift area with a crustal component indicate a continental rift or a transitional continental arc to within-plate setting whereas those from the No Rift area, although less numerous, suggest a continental arc setting. The differences among the tectonic inferences from different magma types can best be explained from the differences in their mantle or mixed mantle and crustal sources. The t test revealed similarities and differences between Rift-No Rift and Near Trench-Far Trench pairs. Most concentration and ratio parameters differed significantly for these pairs.

The subdivision of samples from the three rifts also revealed similarities and differences among them in the tectonomagmatic multidimensional diagrams. The basic rocks from the Tepic-Zacoalco and Chapala rifts consistently indicated a continental rift setting, whereas for the Colima Rift, a rift or an arc setting was suggested. The intermediate and acid rocks from the Tepic-Zacoalco Rift did not provide consistent indications, whereas those from the Colima and Chapala rifts showed an arc setting.

The differences in the tectonic inferences for basic rocks as compared to more evolved intermediate and acid rocks document their origin mainly in the mantle and mixed mantle and crustal sources, respectively. Thus, the basic rocks are likely to reflect the actual tectonic setting, whereas the evolved rocks would show the combination of the present and the past (crustal) tectonic settings.

Acknowledgments

This work was supported by DGAPA-PAPIIT project grant RN104813. M.A. Rivera-Gómez is grateful to Conacyt for a doctoral fellowship. We also thank L. Díaz-González for modifying the UDASYS computer program to facilitate us including confidence intervals of the mean in some multi-element diagrams. Alfredo Quiroz-Ruiz is thanked for efficiently maintaining our computing facility. We are much grateful to two anonymous reviewers for valuable comments and suggestions and the editor Dr. Francisco J. Vega for efficiently handling our manuscript.

Appendix A. Supplementary data

Supplementary data related to this article can be found at http://dx.doi.org/10.1016/j.jsames.2015.12.007.

References

Agrawal, S., Guevara, M., Verma, S.P., 2008. Tectonic discrimination of basic and ultrabasic rocks through log-transformed ratios of immobile trace elements. Int. Geol. Rev. 50 (12), 1057–1079.

Alvarez, R., Yutsis, V., 2015. The elusive Rivera-Cocos plate boundary: not diffuse. In: Wright, T.J., Ayele, A., Ferguson, D.J., Kidane, T., Vye-Brown, C. (Eds.), Magmatic Rifting and Active Volcanism. The Geological Society of London Geological Society. Special Publications, London, p. 420. http://dx.doi.org/10.1144/SP420.8.

Aitchison, J., 1986. The Statistical Analysis of Compositional Data. Chapman and Hall, London, UK, p. 416.

Allan, J.F., 1986. Geology of the northern Colima and Zacoalco grabens, southwest Mexico: late Cenozoic rifting in the Mexican Volcanic Belt. Geol. Soc. Am. Bull. 97 (4), 473–485.

Allan, J.F., Carmichael, I.S.E., 1984. Lamprophyric lavas in the Colima graben, SW Mexico. Contributions Mineralogy Petrology 88 (3), 203–216.

Andreani, L., Le Pichon, X., Rangin, C., Martínez-Reyes, J., 2008. The southern Mexico block: main boundaries and new estimation for its Quaternary motion. Bull. la Soc. Geéologique Fr. 179 (2), 209–223.

Bandy, W., Mortera-Gutierrez, C., Urrutia-Fucugauchi, J., Hilde, T.W.C., 1995. The subducted Rivera-Cocos plate boundary: where is it, what is it, and what is its relationship to the Colima rift? Geophycial Res. Lett. 22 (22), 3075–3078.

Bandy, W.L., Hilde, T.W.C., Yan, C.-Y., 2000. The Rivera-Cocos plate boundary: implications for Rivera-Cocos relative motion and plate fragmentation. In: Delgado-Granados, H., Aguirre-Díaz, G., Stock, J.M. (Eds.), Cenozoic Tectonics and Volcanism of Mexico. Geological Society of America Special Paper, vol. 334. Geological Society of America, Boulder, pp. 1–28.

Barnett, V., Lewis, T., 1994. Outliers in Statistical Data. John Wiley & Sons, Chichester, p. 584.

Blatter, D.L., Hammersley, L., 2010. Impact of the orozco fracture zone on the Central Mexican volcanic Belt. J. Volcanol. Geotherm. Res. 197 (1–4), 67–84.

Buccianti, A., 2013. Is compositional data analysis a way to see beyond the illusion? Comput. Geosci. 50 (1), 165–173.

Buccianti, A., Pawlowsky-Glahn, V., 2005. New perspective on water chemistry and compositional data analaysis. Math. Geol. 37 (7), 703–727.

Campos-Enríquez, J.O., Alatorre-Zamora, M.A., 1998. Shallow crustal structure of the junction of the grabens of Chapala, Tepic-Zacoalco and Colima, Mexico. Geofísica Int. 37 (4), 263–282.

Campos-Enriquez, J.O., Arroyo-Esquivel, M.A., Urrutia-Fucugauchi, J., 1990. Basement, Curie isotherm and shallow-crustal structure of the Trans-Mexican Volcanic Belt, from aeromagnetic data. Tectonophysics 172 (1–2), 77–90.

Carmichael, I.S.E., Frey, H.M., Lange, R.A., Hall, C.M., 2006. The Pleistocene cinder cones surrounding Volcán Colima, Mexico re-visited: eruption ages and volumes, oxidation states, and sulfur content. Bull. Volcanol. 68 (5), 407–419.

Carmichael, I.S.E., Lange, R.A., Luhr, J.F., 1996. Quaternary minettes and associated volcanic rocks of Mascota, western Mexico: a consequence of plate extension above a subduction modified mantle wedge. Contributions Mineral. Petrol. 124, 302–333.

Cavazos Tovar, J.G., 2006. Magmatismo adakítico en el volcán Tancítaro, Michoacán, México. Universidad Nacional Autónoma de México, México, D.F., p. 53. Master Thesis.

Crummy, J.M., Savov, I.P., Navarro-Ochoa, C., Morgan, D.J., Wilson, M., 2014. High-K mafic Plinian eruptions of Volcán de Colima, Mexico. J. Petrol. 55 (11), 2155–2192.

Cruz-Huicochea, R., Verma, S.P., 2013. New critical values for F and their use in the ANOVA and Fisher's F tests for evaluating geochemical reference material granite G-2 (U.S.A.) and igneous rocks from the Eastern Alkaline Province (Mexico). J. Iber. Geol. 39 (1), 13–30.

Demant, A., 1981. L'axe néo-volcanique transmexicain, étude volcanologique et pétrographique, signification géodynamique. Université de Droit, d'Economie et des Sciences d'Aix-Marseille. Ph.D. thesis, 259 pp and appendix Thesis.

DeMets, C., Stein, S., 1990. Present-day kinematics of the Rivera plate and implications for tectonics in southwestern Mexico. J. Geophys. Res. 95 (B13), 21931–21948.

Díaz-Bravo, B.A., Gómez-Tuena, A., Ortega-Obregón, C., Pérez-Arvizu, O., 2014. The origin of intraplate magmatism in the western Trans-Mexican Volcanic Belt. Geosphere 10 (2), 340–373.

Dixon, W.J., 1950. Analysis of extreme values. Ann. Math. Stat. 21 (4), 488–506.

Dixon, W.J., 1953. Processing data for outliers. Biometrics 9 (1), 74–89.

Egozcue, J.J., Pawlowsky-Glahn, V., Mateu-Figueras, G., Barceló-Vidal, C., 2003. Isometric logratio transformations for compositional data analysis. Math. Geol. 35 (3), 279–300.

Faure, G., 1986. Principles of Isotope Geology. Wiley, New York, p. 653.

Ferrari, L., Pasquare, G., Venegas, S., Castillo, D., Romero, F., 1994. Regional tectonics of western Mexico and its implications for the northern boundary of the Jalisco block. Geofísica Int. 33 (1), 139–151.

Ferrari, L., Stock, J.M., Urrutia, J., 2000. Cenozoic Tectonics and Volcanism of México, vol. 318. Tectonophysics (Special issue): vii–ix.

Frey, H.M., Lange, R.A., Hall, C.M., Delgado-Granados, H., Carmichael, I.S.E., 2007. A Pliocene ignimbrite flare-up along the Tepic-Zacoalco rift: evidence for the initial stages of rifting between the Jalisco block (Mexico) and North America. Geol. Soc. Am. Bull. 119 (1–2), 49–64.

Garduño-Monroy, V.H., Spinner, J., Ceragioli, E., 1993. Geological and structural study of the Chapala rift, State of Jalisco, Mexico. Geofísica Int. 32 (3), 487–499.

Gastil, G., Krummenacher, D., Minch, J., 1979. The record of Cenozoic volcanism around the Gulf of California. Geol. Soc. Am. Bull. 90 (9), 839–857.

Gilbert, C.M., Mahood, G.A., Carmichel, I.S.E., 1985. Volcanic stratigraphy of the Guadalajara area, Mexico. Geofísica Int. 24 (1), 169–191.

Grubbs, F.E., 1950. Sample criteria for testing outlying observations. Ann. Math. Stat. 21, 27–58.

Grubbs, F.E., 1969. Procedures for detecting outlying observations in samples. Technometrics 11 (1), 1–21.

Grubbs, F.E., Beck, G., 1972. Extension of sample sizes and percentage points for significance tests of outlying observations. Technometrics 14 (4), 847–854.

Gunn, B.M., Mooser, F., 1971. Geochemistry of the volcanics of central Mexico. Bull. Volcanol. 34, 577–613.

Hasenaka, T., 1992. Chemical compositions of selected samples. In: Aoki, K. (Ed.),

Subduction Volcanism and Tectonics of Western Mexican Volcanic Belt. International Scientific Research Program (No. 03041014) Japan–Mexico Cooperative Research. The Faculty of Science, Tohoku University, Sendai, Japan, pp. 238–247.
Lange, R., Carmichael, I.S.E., 1990. Hydrous basaltic andesites associated with minette and related lavas in western Mexico. J. Petrology 31 (6), 1225–1259.
Lange, R.A., Carmichael, I.S.E., 1991. A potassic volcanic front in western Mexico: the lamprophyric and related lavas of San Sabastian. Geol. Soc. Am. Bull. 103 (7), 928–940.
Law, A.M., Kelton, W.D., 2000. Simulation Modeling and Analysis. McGraw Hill, Boston, p. 760.
Le Bas, M.J., Le Maitre, R.W., Streckeisen, A., Zanettin, B., 1986. A chemical classification of volcanic rocks based on the total alkali-silica diagram. J. Petrology 27 (3), 745–750.
Le Maitre, R.W., Streckeisen, A., Zanettin, B., Le Bas, M.J., Bonin, B., Bateman, P., Bellieni, G., Dudek, A., Schmid, R., Sorensen, H., Woolley, A.R., 2002. Igneous Rocks. A Classification and Glossary of Terms: Recommendations of the International Union of Geological Sciences Subcommission of the Systematics of Igneous Rocks. Cambridge University Press, Cambridge, p. 236.
Lewis-Kenedi, C.B., Lange, R.A., Hall, C.M., Delgado Granados, H., 2005. The eruptive history of the Tequila volcanic field, western Mexico: ages, volumes, and relative proportions of lava types. Bull. Volcanol. 67 (7), 391–414.
Luhr, J.F., 1992. Slab-derived fluids and partial melting in subduction zones: insights from two contrasting Mexican volcanoes (Colima and Ceboruco). J. Volcanol. Geotherm. Res. 54, 1–18.
Luhr, J.F., 1993. Petrology and geochemistry of stage-I andesites and dacites from the caldera wall of Volcán Colima, Mexico. Geofísica Int. 32 (4), 591–603.
Luhr, J.F., 1997. Extensional tectonics and the diverse primitive volcanic rocks in the western Mexican Volcanic Belt. Can. Mineral. 35 (??), 473–500.
Luhr, J.F., 2000. The geology and petrology of Volcán San Juan (Nayarit, México) and the compositionally zoned Tepic Pumice. J. Volcanol. Geotherm. Res. 95, 109–156.
Luhr, J.F., 2001. Glass inclusions and melt volatile contents at Paricutin volcano, Mexico. Contributions Mineralogy Petrology 142 (4), 261–283.
Luhr, J.F., 2002. Petrology and geochemistry of the 1991 and 1998–1999 lava flows from Volcán de Colima, México: implications for the end of the current eruptive cycle. J. Volcanol. Geotherm. Res. 117 (1–2), 169–194.
Luhr, J.F., Allan, J.F., Carmichael, I.S.E., Nelson, S.A., Hasenaka, T., 1989. Primitive calc-alkaline and alkaline rock types from the western Mexican Volcanic Belt. J. Geophys. Res. 94 (B4), 4515–4530.
Luhr, J.F., Carmichael, I.S.E., 1980. The colima volcanic complex, Mexico. I. Post-caldera andesites from volcán colima. Contributions Mineralogy Petrology 71 (4), 343–372.
Luhr, J.F., Carmichael, I.S.E., 1981. The colima volcanic complex, Mexico: Part II. Late-Quaternary cinder cones. Contributions Mineralogy Petrology 76 (2), 127–147.
Luhr, J.F., Carmichael, I.S.E., 1982. The Colima volcanic complex, Mexico: III ash- and scoria-fall deposits from the upper slopes of Volcán Colima. Contributions Mineralogy Petrology 80, 262–275.
Luhr, J.F., Carmichael, I.S.E., 1990a. Petrological monitoring of cyclical eruptive activity at Volcán Colima, Mexico. J. Volcanol. Geotherm. Res. 42 (3), 235–260.
Luhr, J.F., Carmichael, I.S.E., 1990b. Geology of Volcán de Colima, vol. 107. Universidad Nacional Autónoma de México, Instituto de Geologia Boletín, p. 101.
Luhr, J.F., Lazaar, P., 1985. The southern guadalajara volcanic Chain, Jalisco, Mexico. Geofísica Int. 24 (4), 691–700.
Luhr, J.F., Navarro-Ochoa, C., Savov, I.P., 2010. Tephrochronology, petrology and geochemistry of Late-Holocene pyroclastic deposits from Volcán de Colima, Mexico. J. Volcanol. Geotherm. Res. 197, 1–32.
Luhr, J.F., Nelson, S.A., Allan, J.F., Carmichael, I.S.E., 1985. Active rifting in southwestern Mexico: manifestations of an incipient eastward spreading-ridge jump. Geology 13 (1), 54–57.
Mahood, G.A., 1977. A preliminary report on the comenditic dome and ash flow complex of Sierra La Primavera, Jalisco, Mexico. Rev. del Inst. Geol. UNAM 1 (2), 177–190.
Mahood, G.A., 1981. Chemical evolution of a Pleistocene rhyolitic center: Sierra La primavera, Jalisco, México. Contributions Mineralogy Petrology 77 (2), 129–149.
Mahood, G.A., Halliday, A.N., 1988. Generation of high-silica rhyolite: a Nd, Sr, and O isotopic study of Sierra La Primavera, Mexican Neovolcanic Belt. Contributions Mineralogy Petrology 100, 183–191.
Maldonado-Sánchez, G., Schaaf, P., 2005. Geochemical and isotope data from the Acatlán volcanic field, western Trans-Mexican volcanic belt: origin and evolution. Lithos 82, 455–470.
Maria, A.H., Luhr, J.F., 2008. Lamprophyres, basanites, and basalts of the western Mexican Volcanic Belt: volatile contents and a vein-wallrock melting relationship. J. Petrology 49 (12), 2123–2156.
Martin del Pozzo, A.L., Romero, V.H., Ruiz Kitcher, R.E., 1987. Los flujos piroclásticos del volcán de Colima, México. Geofísica Int. 26 (2), 291–307.
McBirney, A.R., Taylor, H.P., Armstrong, R.L., 1987. Paricutin re-examined: a classical example of crustal assimilation in calc-alkaline magma. Contributions Mineralogy Petrology 95 (1), 4–20.
McDonough, W.F., Sun, S.-s., 1995. The composition of the Earth. Chem. Geol. 120 (3–4), 223–253.
Middlemost, E.A.K., 1989. Iron oxidation ratios, norms and the classification of volcanic rocks. Chem. Geol. 77 (1), 19–26.
Moore, G., Marone, C., Carmichael, I.S.E., Renne, P., 1994. Basaltic volcanism and extension near the intersection of the Sierra Madre volcanic province and the Mexican Volcanic Belt. Geol. Soc. Am. Bull. 106, 383–394.
Mora, J.C., Macías, J.L., Saucedo, R., Orlando, A., Manetti, P., Vaselli, O., 2002. Petrology of the 1998–2000 products of Volcán de Colima, México. J. Volcanol. Geotherm. Res. 117, 195–212.
Mori, L., Gómez-Tuena, A., Schaaf, P., Goldstein, S.J., Pérez-Arvizu, O., Solís-Pichardo, G., 2009. Lithospheric removal as a trigger for flood basalt magmatism in the Trans-Mexican Volcanic Belt. J. Petrology 50, 2157–2186.
Nelson, S.A., 1980. Geology and petrology of Volcán Ceboruco, Nayarit, Mexico. Geol. Soc. Am. Bull. 91, 2290–2431.
Nelson, S.A., 1986. Geología del Volcán Ceboruco, Nayrit, con una estimación de riesgos de erupciones futuras. Rev. del Inst. Geol. UNAM 6 (2), 243–258.
Nelson, S.A., Livieres, R.A., 1986. Contemporaneous calc-alkaline and alkaline volcanism at Sanganguey volcano, Nayarit, Mexico. Geol. Soc. Am. Bull. 97 (7), 798–808.
Nixon, G.T., Demant, A., Armstrong, R.L., Harakal, J.E., 1987. K-Ar and geologic data bearing on the age and evolution of the Trans-Mexican volcanic belt. Geofísica Int. 26 (1), 109–158.
Ownby, S.E., Lange, R.A., Hall, C.M., 2008. The eruptive history of the Mascota volcanic field, western Mexico: age and volume constraints on the origin of andesite among a diverse suite of lamprophyric and calc-alkaline lavas. J. Volcanol. Geotherm. Res. 117, 1077–1091.
Pacheco, J.F., Mortera-Gutiérrez, C.A., Delgado, H., Singh, S.K., Valenzuela, R.W., Shapiro, N.M., Santoyo, M.A., Hurtado, A., Barrón, R., Gutiérrez-Moguel, E., 1999. Tectonic significance of an earthquake sequence in the Zacoalco half-graben, Jalisco, Mexico. J. S. Am. Earth Sci. 12 (6), 557–565.
Pardo, M., Suárez, G., 1995. Shape of the subducted Rivera and Cocos plates in southern Mexico: seismic and tectonic implications. J. Geophys. Res. 100 (B7), 12,357–12,373.
Petrone, C.M., 2010. Relationship between monogenetic magmatism and strato-volcanoes in western Mexico: the role of low-pressure magmatic processes. Lithos 119, 585–606.
Petrone, C.M., Tagami, T., Francalanci, L., Matsumora, A., Sudo, M., 2001. Volcanic systems in the San Pedro-Ceboruco graben (Nayarit, Mexico) in the light of new K-Ar geochronological data. Geochem. J. 35 (1), 77–88.
Petrone, C.M., Francalanci, L., Carlson, R.W., Ferrari, L., Conticelli, S., 2003. Unusual coexistence of subduction-related and intraplate-type magmatism: Sr, Nd and Pb isotope and trace element data from the magmatism of the San Pedro-Ceboruco graben (Nayarit, Mexico). Chem. Geol. 193, 1–24.
Petrone, C.M., Francalanci, L., Ferrari, L., Schaaf, P., Conticelli, S., 2006. The San Pedro-Cerro Grande volcanic complex (Nayarit, México): inferences on volcanology and magma evolution. Geol. Soc. Am. 402, 65–98. Special Paper.
Righter, K., Carmichael, I.S.E., 1992. Hawaiite and related lavas in the Atenguillo graben, western Mexican Volcanic Belt. Geol. Soc. Am. Bull. 104, 1592–1607.
Righter, K., Carmichael, I.S.E., Becker, T.A., Renne, P.R., 1995. Pliocene-Quaternary volcanism and faulting at the intersection of the Gulf of California and the Mexican Volcanic Belt. Geol. Soc. Am. Bull. 107 (6), 612–626.
Righter, K., Rosas-Elguera, J., 2001. Alkaline lavas in the volcanic front of the western Mexican Volcanic Belt: geology and petrology of the Ayutla and Tapalpa volcanic fields. J. Petrology 42 (12), 2333–2361.
Robin, C., Camus, G., Cantagrel, J.M., Gourgaud, A., Mossand, P., Vincent, P.M., Aubert, M., Dorel, J., Murray, J.M., 1984. Les volcanes de Colima (Mexique), vol. 87. Bull. P.I.R.P.S.E.V., p. 98
Robin, C., Camus, G., Gourgaud, A., 1991. Eruptive and magmatic cycles at Fuego de Colima volcano (Mexico). J. Volcanol. Geotherm. Res. 45, 209–225.
Robin, C., Komorowski, J.-C., Boudal, C., Mossand, P., 1990. Mixed-magma pyroclastic surge deposits associated with debris avalanche deposits at Colima volcanoes, Mexico. Bull. Volcanol. 52 (5), 391–403.
Robin, C., Potrel, A., 1993. Multi-stage magma mixing in the pre-caldera series of Fuego de Colima volcano. Geofísica Int. 32 (4), 605–615.
Rodríguez-Elizarrarás, S.R., 1995. Estratigrafía y estructura del Volcán de Colima, México. Rev. Mex. Ciencias Geol. 12 (1), 22–46.
Rollinson, H.R., 1993. Using Geochemical Data: Evaluation, Presentation, Interpretation. Longman Scientific Technical, Essex, p. 344.
Rowe, M.C., Peate, D.W., Peate, I.U., 2011. An investigation into the nature of the magmatic plumbing system at Paricutin volcano, Mexico. J. Petrology 52 (2), 2187–2220.
Saucedo, R., Macias, J.L., Gavilanes, J.C., Arce, J.L., Komorowski, J.C., Gardner, J.E., Valdez-Moreno, G., 2010. Eyewitness, stratigraphy, chemistry, and eruptive dynamics of the 1913 Plinian eruption of Volcán de Colima, México. J. Volcanol. Geotherm. Res. 191, 149–166.
Savov, I.P., Luhr, J.F., Navarro-Ochoa, C., 2008. Petrology and geochemistry of lava and ash erupted from volcán Colima, Mexico during 1998–2005. J. Volcanol. Geotherm. Res. 174, 241–256.
Selvans, M.M., Stock, J.M., DeMets, C., Sanchez, O., Marquez-Azua, B., 2011. Constraints on Jalisco block motion and tectonics of the Guadalajara triple junction from 1998–2001 campaign GPS data. Pure Appl. Geophys. 168, 1435–1447.
Sheth, H.C., Torres-Alvarado, I.S., Verma, S.P., 2002. What is the "calc-alkaline rock series. Int. Geol. Rev. 44, 686–701.
Suhardja, S.K., Grand, S.P., Wilson, D., Guzman-Speziale, M., Gomez-Gonzalez, J.M., Dominquez-Reyes, T., Ni, J., 2015. Crust and subduction zone structure of Southwestern Mexico. J. Geophys. Res. Solid Earth 120, 1020–1035. http://dx.doi.org/10.1002/2014JB011573.
Tera, F., Brown, L., Morris, J., Sacks, I.S., Klein, J., Middleton, R., 1986. Sediment incorporation in island-arc magmas: inferences from 10Be. Geochim. Cosmochim. Acta 50, 535–550.

Torres-Alvarado, I.S., Verma, S.P., Palacios-Berruete, H., Guevara, M., González-Castillo, O.Y., 2003. DC_Base: a database system to manage Nernst distribution coefficients and its application to partial melting modeling. Comput. Geosci. 29 (9), 1191–1198.
Valdez-Moreno, G., Schaaf, P., Macias, J.L., Kusakabe, M., 2006. New Sr-Nd-Pb-O isotope data for Colima volcano and evidence for the nature of the local basement. Geol. Soc. Am. 402, 45–63. Special Paper.
Varley, N., Gavilanes-Ruiz, J.C., Mora, J.C., Macias, J.L., Castro, R., Arias, R., 2002. Volcanic Activity Report. Colima (Western Mexico), vol. 27. Smithsonian National Museum of Natural History, Washington. Number 6.
Verma, S.K., Pandarinath, K., Verma, S.P., 2012. Statistical evaluation of tectonomagmatic discrimination diagrams for granitic rocks and proposal of new discriminant-function-based multidimensional diagrams for acid rocks. Int. Geol. Rev. 54 (3), 325–347.
Verma, S.K., Verma, S.P., 2013. Identification of Archaean plate tectonic processes from multidimensional discrimination diagrams and probability calculations. Int. Geol. Rev. 55 (2), 225–248.
Verma, S.P., 1991a. Determination of thirteen rare-earth elements by high-performance liquid chromatography in thirty and of K, Rb, Cs, Sr and Ba by isotope dilution mass spectrometry in eighteen international geochemical reference samples. Geostand. Newsl. 15 (1), 129–134.
Verma, S.P., 1991b. Usefulness of liquid chromatography for determination of thirteen rare-earth elements in rocks and minerals. Lanthan. Actinide Res. 3, 237–257.
Verma, S.P., 1992. Seawater alteration effects on REE, K, Rb, Cs, Sr, U, Th, Pb and Sr-Nd-Pb isotope systematics of mid-ocean Ridge Basalt. Geochem. J. 26, 159–177.
Verma, S.P., 1997. Sixteen statistical tests for outlier detection and rejection in evaluation of international geochemical reference materials: example of microgabbro PM-S. Geostand. Newsl. J. Geostand. Geoanal. 21 (1), 59–75.
Verma, S.P., 2000. Geochemistry of the subducting Cocos plate and the origin of subduction-unrelated mafic volcanism at the volcanic front of the central Mexican Volcanic Belt. In: Delgado-Granados, H., Aguirre-Díaz, G., Stock, J.M. (Eds.), Cenozoic Tectonics and Volcanism of Mexico, Boulder, Colorado: Geological Society of America Special Paper 334, pp. 195–222.
Verma, S.P., 2005. Estadística básica para el manejo de datos experimentales: aplicación en la Geoquímica (Geoquimiometría). Universidad Nacional Autónoma de México, México, D.F., p. 186
Verma, S.P., 2006. Extension-related origin of magmas from a garnet-bearing source in the Los Tuxtlas volcanic field, Mexico. Int. J. Earth Sci. 95 (5), 871–901.
Verma, S.P., 2009. Continental rift setting for the central part of the Mexican Volcanic Belt: a statistical approach. Open Geol. J. 3, 8–29.
Verma, S.P., 2010. Statistical evaluation of bivariate, ternary and discriminant function tectonomagmatic discrimination diagrams. Turkish J. Earth Sci. 19 (2), 185–238.
Verma, S.P., 2012. Geochemometrics. Rev. Mex. Ciencias Geol. 29 (1), 276–298.
Verma, S.P., 2013. Application of 50 multi-dimensional discrimination diagrams and significance tests to decipher compositional similarities and differences between Hawaiian and Icelandic volcanism. Int. Geol. Rev. 55 (12), 1553–1572.
Verma, S.P., 2015a. Monte Carlo comparison of conventional ternary diagrams with new log-ratio bivariate diagrams and an example of tectonic discrimination. Geochem. J. 49 (4), 393–412.
Verma, S.P., 2015b. Present state of knowledge and new geochemical constraints on the central part of the Mexican Volcanic Belt and comparison with the Central American Volcanic Arc in terms of near and far trench magmas. Turkish J. Earth Sci. 24 (5), 399–460.
Verma, S.P., 2015c. Origin, evolution, and tectonic setting of the eastern part of the Mexican Volcanic Belt and comparison with the Central American Volcanic Arc from conventional multielement normalized and new multidimensional discrimination diagrams and discordancy and significance tests. Turkish J. Earth Sci. 24 (2), 111–164.
Verma, S.P., Agrawal, S., 2011. New tectonic discrimination diagrams for basic and ultrabasic volcanic rocks through log-transformed ratios of high field strength elements and implications for petrogenetic processes. Rev. Mex. Ciencias Geol. 28 (1), 24–44.
Verma, S.P., Armstrong-Altrin, J.S., 2013. New multi-dimensional diagrams for tectonic discrimination of siliciclastic sediments and their application to Precambrian basins. Chem. Geol. 355, 117–133. September.
Verma, S.P., Armstrong-Altrin, J.S., 2016. Geochemical discrimination of siliciclastic sediments from active and passive margin settings. Sediment. Geol. 332, 1–12.
Verma, S.P., Cruz-Huicochea, R., 2013. Alternative approach for precise and accurate student's t critical values and application in geosciences. J. Iber. Geol. 39 (1), 31–56.
Verma, S.P., Díaz-González, L., 2012. Application of the discordant outlier detection and separation system in the geosciences. Int. Geol. Rev. 54 (3), 593–614.
Verma, S.P., Hasenaka, T., 2004. Sr, Nd, and Pb isotopic and trace element geochemical contraints for a veined-mantle source of magmas in the Michoacán-Guanajuato volcanic field, west-central Mexican Volcanic Belt. Geochem. J. 38 (1), 43–65.
Verma, S.P., Luhr, J.F., 1993. Sr-Nd-Pb isotope and trace element geochemistry of calc-alkaline andesites from Volcán Colima, Mexico. Geofísica Int. 32 (4), 617–633.
Verma, S.P., Luhr, J.F., 2010. Sr, Nd, and Pb isotopic evidence for the origin and evolution of the Cántaro-Colima Volcanic Chain, Western Mexican Volcanic Belt. J. Volcanol. Geotherm. Res. 197 (1–4), 33–51.
Verma, S.P., Nelson, S.A., 1989. Isotopic and trace element constraints on the origin and evolution of alkaline and calc-alkaline magmas in the northwestern Mexican Volcanic Belt. J. Geophys. Res. 94 (B4), 4531–4544.
Verma, S.P., Pandarinath, K., Verma, S.K., Agrawal, S., 2013b. Fifteen new discriminant-function-based multidimensional robust diagrams for acid rocks and their application to Precambrian rocks. Lithos 168–169, 113–123.
Verma, S.P., Quiroz-Ruiz, A., 2008. Critical values for 33 discordancy test variants for outliers in normal samples of very large sizes from 1,000 to 30,000 and evaluation of different regression models for the interpolation of critical values. Rev. Mex. Ciencias Geol. 25 (3), 369–381.
Verma, S.P., Quiroz-Ruiz, A., 2011. Corrigendum to Critical values for 22 discordancy test variants for outliers in normal samples up to sizes 100, and applications in science and engineering [Rev. Mex. Cienc. Geol., 23 (2006), 302–319]. Rev. Mex. Ciencias Geol. 28 (1), 202.
Verma, S.P., Rivera-Gómez, M.A., 2013a. Computer programs for the classification and nomenclature of igneous rocks. Episodes 36 (2), 115–124.
Verma, S.P., Rivera-Gómez, M.A., 2013b. New computer program TecD for tectonomagmatic discrimination from discriminant function diagrams for basic and ultrabasic magmas and its application to ancient rocks. J. Iber. Geol. 39 (1), 167–179.
Verma, S.P., Lopez-Martinez, M., Terrell, D.J., 1985. Geochemistry of tertiary igneous rocks from Arandas-Atotonilco area, northeast Jalisco, Mexico. Geofísica Int. 24 (1), 31–45.
Verma, S.P., Besch, T., Guevara, M., Schulz-Dobrich, B., 1992. Determination of twelve trace elements in twenty-seven and ten major elements in twenty-three geochemical reference samples by X-Ray fluorescence spectrometry. Geostand. Newsl. 16 (2), 301–309.
Verma, S.P., Torres-Alvarado, I.S., Sotelo-Rodríguez, Z.T., 2002. SINCLAS: standard igneous norm and volcanic rock classification system. Comput. Geosci. 28 (5), 711–715.
Verma, S.P., Guevara, M., Agrawal, S., 2006. Discriminating four tectonic settings: five new geochemical diagrams for basic and ultrabasic volcanic rocks based on log-ratio transformation of major-element data. J. Earth Syst. Sci. 115 (5), 485–528.
Verma, S.P., Quiroz-Ruiz, A., Díaz-González, L., 2008. Critical values for 33 discordancy test variants for outliers in normal samples up to sizes 1000, and applications in quality control in Earth Sciences. Rev. Mex. Ciencias Geol. 25 (1), 82–96.
Verma, S.P., Cruz-Huicochea, R., Díaz-González, L., 2013a. Univariate data analysis system: deciphering mean compositions of island and continental arc magmas, and influence of underlying crust. Int. Geol. Rev. 55 (15), 1922–1940.
Verma, S.P., Díaz-González, L., Rosales-Rivera, M., Quiroz-Ruiz, A., 2014. Comparative performance of four single extreme outlier discordancy tests from Monte Carlo simulations. Sci. World J. 27. http://dx.doi.org/10.1155/2014/746451. Article ID 746451.
Verma, S.P., Cruz-Huicochea, R., Díaz-González, L., Verma, S.K., 2016a. A new computer program TecDIA for multidimensional tectonic discrimination of intermediate and acid magmas and its application to the Bohemian Massif, Czech Republic. J. Geosciences (in press).
Verma, S.P., Díaz González, L., Armstrong-Altrin, J.S., 2016b. Application of a new computer program for tectonic discrimination of Cambrian to Holocene clastic sediments. Earth Sci. Inf. http://dx.doi.org/10.1007/s12145-015-0244-0 published online.
Verma, S.P., Verma, S.K., Oliveira, E.P., 2015. Application of 55 multidimensional tectonomagmatic discrimination diagrams to Precambrian belts. Int. Geol. Rev. 57 (11–12), 1365–1388.
Vigouroux, N., Wallace, P.J., Kent, A.J.R., 2008. Volatiles in high-K magmas from the western Trans-Mexican Volcanic Belt: evidence for fluid fluxing and extreme enrichment of the mantle wedge by subduction processes. J. Petrology 49 (9), 1589–1618.
Wallace, P., Carmichael, I.S.E., 1989. Minette lavas and associated leucitites from the western front of the Mexican Volcanic Belt: petrology, chemistry and origin. Contributions Mineralogy Petrology 103, 470–492.
Wallace, P., Carmichael, I.S.E., 1992. Alkaline and calc-alkaline lavas near Los Volcanes, Jalisco, Mexico: geochemical diversity and its significance in volcanic arcs. Contributions Mineralogy Petrology 111, 423–439.
Wallace, P.J., Carmichael, I.S.E., 1994. Petrology of Volcán Tequila, Jalisco, México: disequilibrium phenocryst assemblages and evolution of the subvolcanic magma system. Contributions Mineralogy Petrology 117 (4), 345–361.
Wallace, P., Carmichael, I.S.E., Righter, K., Becker, T.A., 1992. Volcanism and tectonism in western Mexico: a contrast of style and substance. Geology 20, 625–628.
Wilcox, R.E., 1954. Petrology of the Paricutin volcano. U.S. Geol. Surv. Bull. 965C, 281–353.
Williams, H., 1950. Volcanoes of the Parícutin region, Mexico. U. S. Geol. Surv. Bull. 965-B, 1–279.
Yang, T., Grand, S.P., Wilson, D.S., Guzman-Speziale, M., Gomez-Gonzalez, J.M., Dominguez-Reyes, T., Ni, J., 2009. Seismic structure beneath the Rivera subduction zone from finite-frequency seismic tomography. J. Geophys. Res. 114(B) http://dx.doi.org/10.1029/2008JB005830.

Supplementary Material

Evaluation of the ongoing rifting and subduction processes in the geochemistry of magmas from the western part of the Mexican Volcanic Belt

Surendra P. Verma [a,*], Kailasa Pandarinath [a], M. Abdelaly Rivera-Gómez [b]

[a] *Departamento de Sistemas Energéticos, Instituto de Energías Renovables, Universidad Nacional Autónoma de México, Temixco, Morelos 62580, Mexico*

[b] *Posgrado en Ingeniería, Instituto de Energías Renovables, Universidad Nacional Autónoma de México, Temixco, Morelos 62580, Mexico*

Corresponding author: Tel.: +52 55 56229745; fax: +52 55 56229791
E-mail addresses: *spv@ier.unam.mx* (S.P. Verma), *pk@ier.unam.mx* (K. Pandarinath), *marig@ier.unam.mx* (M.A. Rivera-Gómez).

Journal of South American Earth Sciences, 2016.

Table S1 Comparison of statistical information on Nb and Ta anomalies (with respect to Ba and La) for basic, intermediate, and acid rocks from the western part of the Mexican Volcanic Belt with other areas of Mexico and those representing different tectonic settings (the data for W-MVB are from this work and those for comparison are taken from Verma, 2015a).

Area	Magma type	Mean ± standard deviation (number of samples) $\bar{x} \pm s$ (n)		99% Confidence limits (CL) of the mean	
		$\{Nb/Nb^*\}_{pm}$	$\{Ta/Ta^*\}_{pm}$	$\{Nb/Nb^*\}_{pm}$	$\{Ta/Ta^*\}_{pm}$
Western Mexican Volcanic Belt (Miocene)	Basic	0.23 ± 0.09 (38)	0.28 ± 0.12 (30)	0.19 − 0.27	0.22 − 0.32
	Intermediate	0.17 ± 0.07 (51)	0.18 ± 0.07 (36)	0.14 − 0.18	0.15 − 0.22
	Acid	0.55 ± 0.27 (2)	––	––	––
Western Mexican Volcanic Belt (Pliocene-Holocene)					
Rift	Basic	0.7 ± 0.6 (69)	0.9 ± 0.7 (37)	0.52 − 0.90	0.64 – 1.24
	Intermediate	0.116 ± 0.032 (171)	0.125 ± 0.031 (144)	0.11 − 0.13	0.12 − 0.13
	Acid	0.105 ± 0.040 (58)	0.24 ± 0.14 (37)	0.09 − 0.12	0.18 − 0.30
No Rift	Basic	0.24 ± 0.16 (43)	0.065 ± 0.018 (7)	0.18 − 0.31	0.04 − 0.09
	Intermediate	0.25 ± 0.14 (144)	0.21 ± 0.09 (56)	0.22 − 0.28	0.18 − 0.24
	Acid	0.17 ± 0.07 (4)	––	––	––
Western Mexican Volcanic Belt (Pliocene-Holocene)					
Near Trench	Basic	0.12 ± 0.05 (50)	0.09 ± 0.06 (17)	0.10 − 0.13	0.05 − 0.13
	Intermediate	0.11 ± 0.05 (194)	0.134 ± 0.040 (176)	0.11 − 0.12	0.13 − 0.14
	Acid	0.116 ± 0.036 (19)	0.103 ± 0.010 (15)	0.09 − 0.13	0.09 − 0.11
Far Trench	Basic	0.9 ± 0.5 (34)	1.24 ± 0.42(17)	0.73 – 1.15	0.94 – 1.53
	Intermediate	0.28 ± 0.15 (120)	0.31 ± 0.13 (37)	0.24 − 0.31	0.26 − 0.37
	Acid	0.11 ± 0.05 (43)	0.32 ± 0.10 (20)	0.09 − 0.13	0.26 − 0.39
Central Mexican Volcanic Belt (near the trench)	Basic	0.54 ± 0.25 (38)	0.75 ± 0.16 (30)	0.43 − 0.65	0.67 − 0.84
Central Mexican Volcanic Belt (far from the trench)	Basic	0.53 ± 0.24 (28)	––	0.41 − 0.66	––
Central Mexican Volcanic Belt	Intermediate	0.21 ± 0.09 (498)	0.25 ± 0.11 (274)	0.20 − 0.22	0.23 − 0.27
Central Mexican Volcanic Belt	Acid	0.152 ± 0.033 (194)	0.22 ± 0.05 (184)	0.146 − 0.158	0.21 − 0.23
Continental and island arcs					
Central American Volcanic Arc (front arc)	Basic	0.13 ± 0.06 (59)	0.18 ± 0.11 (34)	0.11 − 0.15	0.13 − 0.23
Central American Volcanic Arc (back arc)	Basic	0.9 ± 0.7 (28)	0.304 ± 0.038 (6)	0.5 − 1.3	0.241 − 0.366
Central American Volcanic Arc	Intermediate	0.108 ± 0.030 (289)	0.13 ± 0.05 (213)	0.103 − 0.113	0.12 − 0.14
	Acid	0.105 ± 0.040 (25)	0.105 ± 0.029 (4)	0.083 − 0.127	0.020 − 0.189
Andes (Chile)	Basic	0.20 ± 0.05 (29)	0.147 ± 0.037 (9)	0.17 − 0.23	0.105 − 0.189
	Intermediate	0.186 ± 0.041 (125)	0.192 ± 0.043 (65)	0.177 − 0.196	0.177 − 0.206
	Acid	0.177 ± 0.031 (49)	0.194 ± 0.034 (41)	0.165 − 0.189	0.180 − 0.208
Andes (Peru)	Acid	0.25 ± 0.10 (37)	0.26 ± 0.11 (33)	0.21 − 0.30	0.21 − 0.31
Andes (Ecuador)	Basic	0.079 ± 0.009 (7)	––	0.065 − 0.090	––
	Intermediate	0.113 ± 0.030 (178)	0.101 ± 0.044 (44)	0.107 − 0.119	0.083 − 0.119
	Acid	0.106 ± 0.018 (210)	0.17 ± 0.07 (16)	0.103 − 0.110	0.11 − 0.22
Andes (Colombia)	Intermediate	0.23 ± 0.05 (11)	0.23 ± 0.12 (12)	0.18 − 0.28	0.12 − 0.34
Aleutians	Basic	0.18 ± 0.07 (15)	0.19 ± 0.09 (14)	0.13 − 0.24	0.12 − 0.26
	Intermediate	0.162 ± 0.010 (48)	0.212 ± 0.011 (46)	0.158 − 0.166	0.208 − 0.216
	Acid	0.23 ± 0.05 (14)	0.29 ± 0.05 (14)	0.19 − 0.28	0.24 − 0.33
Barren Island (Indian Ocean)	Basic	0.089 ± 0.010 (18)	0.121 ± 0.013 (13)	0.082 − 0.096	0.110 − 0.131
	Intermediate	0.093 ± 0.007 (16)	0.133 ± 0.017 (15)	0.088 − 0.097	0.120 − 0.146
Fiji Islands	Basic	0.064 ± 0.037 (5)	0.024 ± 0.010 (11)	––	0.015 − 0.033
	Intermediate	0.078 ± 0.041 (11)	0.053 ± 0.020 (13)	0.039 − 0.116	0.036 − 0.070
Hokkaido (Japan)	Basic	0.31 ± 0.16 (25)	0.27 ± 0.13 (25)	0.23 − 0.40	0.20 − 0.35
	Intermediate	0.16 ± 0.11 (48)	0.17 ± 0.010 (47)	0.12 − 0.20	0.13 − 0.21
	Acid	0.17 ± 0.07 (67)	0.21 ± 0.09 (67)	0.14 − 0.19	0.18 − 0.24
Izu−Bonin	Basic	0.14 ± 0.05 (20)	0.17 ± 0.07 (15)	0.11 − 0.17	0.11 − 0.22
	Intermediate	0.090 ± 0.038 (7)	––	0.037 − 0.143	––
	Acid	0.083 ± 0.016 (8)	0.21 ± 0.07 (11)	0.063 − 0.103	0.14 − 0.28
Japan	Basic	0.21 ± 0.08 (29)	0.25 ± 0.12 (22)	0.17 − 0.25	0.18 − 0.32
	Intermediate	0.20 ± 0.08 (90)	0.25 ± 0.11 (73)	0.17 − 0.22	0.21 − 0.28
	Acid	0.18 ± 0.05 (20)	––	0.15 − 0.21	––
Indonesia	Basic	0.15 ± 0.05 (27)	0.26 ± 0.13 (23)	0.13 − 0.17	0.18 − 0.33

	Intermediate	0.15 ± 0.06 (91)	0.22 ± 0.10 (71)	0.13 − 0.17	0.19 − 0.26
	Acid	0.20 ± 0.13 (7)	0.242 ± 0.014 (15)	0.01 − 0.38	0.231 − 0.252
Lesser Antilles	Basic	0.27 ± 0.12 (62)	0.29 ± 0.12 (17)	0.23 − 0.31	0.21 − 0.38
	Intermediate	0.206 ± 0.036 (148)	0.253 ± 0.028 (116)	0.198 − 0.214	0.246 − 0.260
	Acid	0.174 ± 0.035 (18)	0.167 ± 0.039 (41)	0.151 − 0.198	0.150 − 0.183
Kamchatka	Basic	0.14 ± 0.06 (54)	0.2 ± 0.10 (58)	0.12 − 0.17	0.16 − 0.23
	Intermediate	0.121 ± 0.035 (105)	0.149 ± 0.044 (102)	0.112 − 0.130	0.137 − 0.160
	Acid	0.105 ± 0.040 (68)	0.12 ± 0.06 (7)	0.092 − 0.118	0.02 − 0.21
Kermadec	Basic	0.086±0.043 (38)	0.24 ± 0.14 (13)	0.067 − 0.104	0.13 − 0.36
	Intermediate	0.11±0.05 (21)	0.5 ± 0.5 (6)	0.08 − 0.14	−−
	Acid	0.09±0.05 (44)	0.125 ± 0.007 (13)	0.07 − 0.11	0.119 − 0.131
Mariana	Basic	0.07 ±0.022 (11)	0.106 ± 0.018 (8)	0.054 − 0.097	0.084 − 0.129
	Intermediate	0.087±0.022 (58)	0.113 ± 0.018 (53)	0.079 − 0.094	0.107 − 0.120
	Acid	0.1024±0.0043 (13)	0.15 ± 0.07 (8)	0.0988 − 0.1061	0.07 − 0.24
Philippines (Bicol, Luzon)	Basic	0.18 ±0.06 (21)	0.19 ± 0.05 (15)	0.14 − 0.22	0.15 − 0.23
	Intermediate	0.20±0.09 (50)	0.21 ± 0.06 (24)	0.16 − 0.23	0.18 − 0.25
	Acid	0.156±0.013 (4)	0.191 ± 0.021 (6)	0.116 − 0.191	0.157 − 0.224
New Hebrides	Basic	0.12 ±0.06 (24)	0.053 ± 0.018 (9)	0.09 − 0.16	0.033 − 0.073
	Intermediate	0.16±0.06 (33)	0.20 ± 0.12 (5)	0.13 − 0.19	−−
	Acid	0.12±0.029 (9)	−−	0.088 − 0.153	−−
New Zealand (North Island)	Basic	0.194±0.043 (14)	0.271 ± 0.043 (11)	0.160 − 0.229	0.230 − 0.312
	Intermediate	0.19±0.06 (40)	0.42 ± 0.18 (40)	0.17 − 0.22	0.34 − 0.49
	Acid				
Ryukyu (Japan)	Basic	0.31 ±0.10 (8)	0.36 ± 0.09 (8)	0.19 − 0.44	0.25 − 0.47
	Intermediate	0.25 ± 0.08 (13)	0.31 ± 0.07 (13)	0.18 − 0.31	0.24 − 0.37
	Acid	0.188 ± 0.040 (28)	0.36 ± 0.16 (4	0.167 − 0.208	0.27 − 0.44
Taiwan	Basic	−−	−−	−−	−−
	Intermediate	0.17 ± 0.08 (5	0.23 ± 0.10 (5)	0.01 − 0.34	0.02 − 0.43
	Acid	0.143 ± 0.010 (6)	0.1873 ± 0.0044 (6)	0.127 − 0.159	0.1800−0.1945
Solomon Islands	Basic	0.088 ± 0.028 (17)	0.102 ± 0.031 (17)	0.069 − 0.108	0.080 − 0.124
	Intermediate	0.087 ± 0.042 (33)	0.16 ± 0.08 (28)	0.066 − 0.107	0.12 − 0.20
Tongan Islands	Basic	0.13 ± 0.07 (12)	0.36 ± 0.29 (10)	0.06 − 0.19	0.06 − 0.66
	Intermediate	0.20 ± 0.08 (29)	0.36 ± 0.26 (27)	0.16 − 0.25	0.22 − 0.49
	Acid	0.23 ± 0.05 (7)	0.31 ± 0.05 (6)	0.16 − 0.30	0.22 − 0.40
Vanuatu	Basic	0.064 ± 0.026 (69)	0.079 ± 0.033 (32)	0.056 − 0.073	0.063 − 0.095
	Intermediate	0.15 ± 0.07 (11)	0.15 ± 0.07 (10)	0.09 − 0.22	0.08 − 0.22
Continental rifts or extensional areas, including post−collision extension					
San Luis Potosí (Mexico)	Basic	0.78 ± 0.36 (15)	1.10 ± 0.44 (4)	0.49 − 1.06	−−
	Intermediate	0.19 ± 0.05 (4)	−−	0.04 − 0.33	−−
Baja California (Mexico) − Pliocene−Pleistocene	Basic	0.137 ± 0.012 (4)	−−	0.102 − 0.172	−−
	Intermediate	0.13 ± 0.05 (32)	−−	0.11 − 0.16	−−
Baja California (Mexico) − Miocene	Intermediate	0.126 ± 0.022 (15)	−−	0.108 − 0.143	−−
Mogollon−Datil volcanic field, New Mexico (USA)	Basic	0.75 ± 0.27 (13)	0.87 ± 0.32 (9)	0.52 − 0.98	0.51 − 1.23
	Intermediate	0.163 ± 0.030 (10)	0.19 ± 0.03 (10)	0.133 − 0.194	0.15 − 0.22
NW Cerro del Rio, New Mexico (USA)	Basic	−−	0.61 ± 0.05 (5)	−−	0.50 − 0.72
	Intermediate	−−	0.46 ± 0.10 (8)	−−	0.33 − 0.58
Basin and Range, Nevada−Arozona (USA)	Basic	0.62 ± 0.26 (20)	0.86 ± 0.27 (8)	0.45 − 0.78	0.53 − 1.19
	Intermediate	0.22 ± 0.10 (7)	−−	0.08 − 0.35	−−
Rio Grande rift, New Mexico (USA)	Basic	0.7 ± 0.5 (29)	0.8 ± 0.5 (28)	0.5 − 1.0	0.5 − 1.1
	Intermediate	0.21 ± 0.09 (14)	0.21 ± 0.07 (13)	0.13 − 0.28	0.16 − 0.27
San Juan volcanic field, Colorado (USA)	Intermediate	0.17 ± 0.08 (26)	−−	0.13 − 0.22	−−
	Acid	0.12 ± 0.05 (7)	−−	0.06 − 0.19	−−
Hurricane volcanic field, Utah (USA)	Basic	0.60 ± 0.17 (27)	0.66 ± 0.22 (27)	0.51 − 0.69	0.55 − 0.78
Santa Rosa Calico volcanic field, Nevada (USA)	Intermediate	0.22 ± 0.07 (12)	0.26 ± 0.10 (8)	0.16 − 0.28	0.14 − 0.39
Western USA	Basic	0.61 ± 0.36 (46)	0.38 ± 0.06 (14)	0.47 − 0.75	0.33 − 0.42
	Intermediate	0.17 ± 0.06 (10)	−−	0.11 − 0.24	−−
Northwest Iran	Basic	0.46 ± 0.10 (14)	0.42 ± 0.08 (8)	0.38 − 0.55	0.32 − 0.51
	Intermediate	0.422 ± 0.026 (6)	−−	0.379 − 0.465	−−
Eastern Iran	Basic	0.88 ± 0.11 (6)	0.90 ± 0.13 (6)	0.70 − 1.05	0.68 − 1.12

	Intermediate	0.70 ± 0.33 (7)	0.8 ± 0.5 (7)	0.24 − 1.16	0.1 − 1.4
Western and Northwestern Anatolia (Turkey)	Basic	0.21 ± 0.09 (30)	0.7 ± 0.7 (28)	0.17 − 0.26	0.4 − 1.1
	Basic	1.45 ± 0.25 (9)	−−	1.17 − 1.73	−−
	Intermediate	0.15 ± 0.06 (37)	0.19 ± 0.07 (37)	0.13 − 0.18	0.16 − 0.22
	Acid	0.129 ± 0.027 (17)	0.175 ± 0.038 (16)	0.110 − 0.148	0.147 − 0.202
Eastern Anatolia (Turkey)	Basic	0.782 ± 0.014 (20)	0.784 ± 0.038 (20)	0.773 − 0.791	0.760 − 0.809
	Acid	0.50 ± 0.13 (25)	0.680 ± 0.017 (24)	0.43 − 0.58	0.580 − 0.779
North and Northeast China	Basic	0.78 ± 0.17 (21)	0.49 ± 0.11 (4)	0.67 − 0.88	0.17 − 0.80
	Intermediate	0.47 ± 0.09 (8)	0.37 ± 0.09 (5)	0.36 − 0.57	0.18 − 0.56
Lhasa terrane (Tibet)	Intermediate	0.24 ± 0.06 (11)	0.263 ± 0.043 (11)	0.18 − 0.31	0.222 − 0.304
	Acid	0.232 ± 0.024 (10)	0.284 ± 0.036 (10)	0.207 − 0.256	0.247 − 0.322
Central and South Tibet	Basic	0.12 ± 0.06 (5)	0.11 ± 0.06 (5)	−−	−−
	Intermediate	0.21 ± 0.07 (42)	0.199 ± 0.041 (33)	0.19 − 0.23	0.179 − 0.218
	Acid	0.122 ± 0.029 (35)	0.15 ± 0.05 (42)	0.109 − 0.136	0.13 − 0.17
NW Africa (Morocco and Mali)	Basic	0.73 ± 0.10 (6)	0.63 ± 0.15 (5)	0.56 − 0.89	0.32 − 0.94
	Intermediate	0.72 ± 0.13 (18)	0.73 ± 0.13 (10)	0.64 − 0.81	0.60 − 0.87
Djibouti (Africa) − negative anomaly	Basic	0.78 ± 0.13 (9)	−−	0.64 − 0.92	−−
Djibouti (Africa) − positive anomaly	Basic	1.6 ± 0.5 (9)	1.7 ± 0.5 (15)	1.1 − 2.1	1.3 − 2.1
Ethiopian rift (Africa) − negative anomaly	Basic	0.6 ± 0.17 (14)	0.7 ± 0.5 (14)	0.46 − 0.74	0.4 − 1.1
Ethiopian rift (Africa) − positive anomaly	Basic	1.28 ± 0.24 (28)	1.5 ± 0.30 (28)	1.15 − 1.40	1.30 − 1.62
Massif Central (France)	Basic	1.49 ± 0.19 (17)	−−	1.36 − 1.62	−−
Saudi Arabia	Basic	1.47 ± 0.27 (11)	−−	1.21 − 1.73	−−
Continental collision (Cretaceous to Paleogene)					
Central Anatolia	Intermediate	0.224 ± 0.041 (22)	0.28 ± 0.06 (22)	0.195 − 0.253	0.23 − 0.32
	Acid	0.211 ± 0.025 (12)	0.27 ± 0.11 (13)	0.189 − 0.233	0.18 − 0.37
Western Anatolia	Acid	0.17 ± 0.08 (42)	0.35 ± 0.10 (41)	0.14 − 0.21	0.31 − 0.40
Ulubey	Intermediate	0.077 ± 0.012 (27)	0.075 ± 0.027 (27)	0.070 − 0.084	0.059 − 0.090
Western Pontides	Acid	0.114 ± 0.009 (36)	0.115 ± 0.015 (32)	0.109 − 0.118	0.108 − 0.122
Lesser Caucasus (Azerbaijan)	Basic	0.26 ± 0.06 (5)	0.28 ± 0.05 (5)	0.14 − 0.38	0.18 − 0.37
	Intermediate	0.31 ± 0.07 (7)	0.32 ± 0.08 (7)	0.213 − 0.402	0.21 − 0.42
	Acid	0.21 ± 0.07 (9)	0.27 ± 0.11 (7)	0.13 − 0.29	0.12 − 0.41
Himalayas and Tibet	Basic	0.160 ± 0.039 (4)	0.14 ± 0.05 (4)	0.045 − 0.276	−−
	Intermediate	0.169 ± 0.038 (5)	0.20 ± 0.07 (5)	0.09 − 0.25	0.05 − 0.34
	Acid	0.18 ± 0.09 (31)	0.27 ± 0.11 (28)	0.14 − 0.23	0.21 − 0.33

Table S2 Application of multidimensional diagrams for deciphering tectonic setting of Rift Pliocene-Holocene basic magmas from the western Mexican Volcanic Belt (W-MVB).

Figure reference; figure type	Discrimination diagram §	Total no. of samples (%)	Predicted tectonic affinity and number of discriminated samples (%)				
			IAB	CRB+OIB	CRB	OIB	MORB
Verma *et al.* (2006); log-ratios of major elements (m2)	IAB-CRB-OIB-MORB	131 (100)	11 (8.4)	---	113 (86.3)	3 (2.3)	4 (3.1)
	IAB-CRB-OIB	131 (100)	12 (9.2)	---	116 (88.5)	3 (2.3)	---
	IAB-CRB-MORB	131 (100)	8 (6.1)	---	117 (89.3)	---	6 (4.6)
	IAB-OIB-MORB	131 (100)	36 (27.5)	---	---	69 (52.7)	26 (19.8)
	CRB-OIB-MORB	131 (100)	---	---	118 (90.1)	7 (5.3)	6 (4.6)
W-MVB Rift Pliocene-Holocene basic rocks: Synthesis of all five diagrams of Verma *et al.* (2006)		**655 (100)**	**67 (10.2)**	**---**	**464 (70.8)**	**82 (12.5)**	**42 (6.4)**
Agrawal *et al.* (2008); log-ratios of immobile trace elements (t1)	IAB-CRB+OIB-MORB	48 (100)	12 (25.0)	36 (75.0)	---	---	0 (0)
	IAB-CRB-OIB	48 (100)	14 (29.2)	---	25 (52.1)	9 (18.8)	---
	IAB-CRB-MORB	48 (100)	8 (16.7)	---	39 (81.2)	---	1 (2.1)
	IAB-OIB-MORB	48 (100)	9 (18.8)	---	---	38 (79.2)	1 (2.1)
	CRB-OIB-MORB	48 (100)	---	---	37 (77.1)	9 (18.8)	2 (4.2)
W-MVB Rift Pliocene-Holocene basic rocks: Synthesis of all five diagrams of Agrawal *et al.* (2008)		**240 (100)**	**43 (17.9)**	**36 (---)**	**101 (51.7)**	**56 (28.8)**	**4 (1.7)**
Verma and Agrawal (2011); log-ratios of immobile major and trace elements (t2)	IAB-CRB+OIB-MORB	65 (100)	18 (27.7)	44 (67.7)	---	---	3 (4.6)
	IAB-CRB-OIB	65 (100)	19 (29.2)	---	44 (67.7)	2 (3.1)	---
	IAB-CRB-MORB	65 (100)	18 (27.7)	---	44 (67.7)	---	3 (4.6)
	IAB-OIB-MORB	65 (100)	18 (27.7)	---	---	39 (60.0)	8 (12.3)
	CRB-OIB-MORB	65 (100)	---	---	38 (58.5)	23 (35.4)	4 (6.2)
W-MVB Rift Pliocene-Holocene basic rocks: Synthesis of all five diagrams of Verma and Agrawal (2011)		**325 (100)**	**73 (22.5)**	**44 (---)**	**126 (47.7)**	**64 (24.3)**	**18 (5.5)**

Explanation of § is in Table 4.

Table S3 Application of multidimensional diagrams for deciphering tectonic setting of No Rift Pliocene-Holocene basic magmas from the western Mexican Volcanic Belt (W-MVB).

Figure reference; figure type; figure no.	Discrimination diagram §	Total no. of samples (%)	Predicted tectonic affinity and number of discriminated samples (%)				
			IAB	CRB+OIB	CRB	OIB	MORB
Verma *et al.* (2006); log-ratios of major elements (m2); no figure	IAB-CRB-OIB-MORB	66 (100)	14 (21.2)	---	45 (68.2)	7 (10.6)	0 (0)
	IAB-CRB-OIB	66 (100)	7 (10.6)	---	54 (81.8)	5 (7.6)	---
	IAB-CRB-MORB	66 (100)	8 (12.1)	---	55 (83.3)	---	3 (4.6)
	IAB-OIB-MORB	66 (100)	23 (34.8)	---	---	33 (50)	10 (15.2)
	CRB-OIB-MORB	66 (100)	---	---	62 (93.9)	3 (4.6)	1 (1.5)
W-MVB No Rift Pliocene-Holocene basic rocks: Synthesis of all five diagrams of Verma et al. (2006)		**330 (100)**	**52 (15.8)**	**---**	***216 (65.5)***	**48 (14.5)**	**14 (4.2)**
Agrawal *et al.* (2008); log-ratios of immobile trace elements (t1); no figure.	IAB-CRB+OIB-MORB	9 (100)	1 (11)	7 (78)	---	---	1 (11)
	IAB-CRB-OIB	9 (100)	6 (67)	---	2 (22)	1 (11)	---
	IAB-CRB-MORB	9 (100)	1 (11)	---	8 (89)	---	0 (0)
	IAB-OIB-MORB	9 (100)	0 (0)	---	---	8 (89)	1 (11)
	CRB-OIB-MORB	9 (100)	---	---	4 (44)	5 (56)	0 (0)
W-MVB No Rift Pliocene-Holocene basic rocks: Synthesis of all five diagrams of Agrawal et al. (2008)		**45 (100)**	**8 (18)**	**7 (---)**	**14 (39)**	**14 (39)**	**2 (4)**
Verma and Agrawal (2011); log-ratios of immobile major and trace elements (t2); no figure.	IAB-CRB+OIB-MORB	42 (100)	22 (52.4)	13 (31)	---	---	7 (16.7)
	IAB-CRB-OIB	42 (100)	21 (50)	---	12 (28.6)	9 (21.4)	---
	IAB-CRB-MORB	42 (100)	21 (50)	---	15 (35.7)	---	6 (14.3)
	IAB-OIB-MORB	42 (100)	21 (50)	---	---	11 (26.2)	10 (23.8)
	CRB-OIB-MORB	42 (100)	---	---	16 (38.1)	18 (42.9)	8 (19)
W-MVB No Rift Pliocene-Holocene basic rocks: Synthesis of all five diagrams of Verma and Agrawal (2011)		**210 (100)**	**85 (40.5)**	**13 (---)**	**50 (23.7)**	**44 (21.0)**	**31 (14.8)**

Explanation of § is in Table 4.

Table S4 Application of multidimensional diagrams for deciphering tectonic setting of Rift Pliocene-Holocene intermediate magmas from the western Mexican Volcanic Belt (W-MVB).

Magma type, Figure name; Figure number	Figure type §	Total number of samples	Number of discriminated samples				
			Arc			Within-plate	Collision
			IA+CA [$\bar{x} \pm s$] (p_{IA+CA}) Θ	IA [$\bar{x} \pm s$] [p_{IA}] Θ	CA [$\bar{x} \pm s$] [p_{CA}] Θ	CR+OI [$\bar{x} \pm s$] [p_{CR+OI}] Θ	Col [$\bar{x} \pm s$] [p_{Col}] Θ
Intermediate; Verma and Verma (2013); log-ratios of all major elements (mint); no figure	IA+CA-CR+OI-Col	666	382 [0.705±0.120] (0.3652-0.9480)	---	---	92 [0.774±0.176] (0.4182-0.9979)	192 [0.761±0.149] (0.4158-0.9987)
	IA-CA-CR+OI	666	---	56 [0.679±0.083] (0.4205-0.8774)	513 [0.810±0.111] (0.3707-1.0000)	97 [0.832±0.163] (0.3763-0.9994)	---
	IA-CA-Col	666	---	58 [0.808±0.101] (0.4811-0.9633)	425 [0.713±0.110] (0.3821-0.9711)	---	183 [0.726±0.156] (0.4000-0.9996)
	IA-CR+OI-Col	666	---	210 [0.616±0.118] (0.3710-0.9189)	---	108 [0.754±0.183] (0.3995-0.9986)	348 [0.743±0.159] (0.3638-1.0000)
	CA-CR+OI-Col	666	---	---	420 [0.711±0.116] (0.3950-0.9760)	90 [0.734±0.185] (0.3474-0.9938)	156 [0.709±0.137] (0.3842-0.9743)
W-MVB Pliocene-Holocene: Diagrams based on log-ratios of major elements	***{Σn} {Σprob} [%prob]***	**3330**	**{382} {269.1819} [---]**	**{324} {214.2072} [10.7%]**	**{1358} {1017.5515} [50.6%]**	**{387} {299.4663} [12.2%]**	**{879} {648.2484} [26.5%]**
Intermediate; Verma and Verma (2013); log-ratios of immobile major and trace elements (mtint); no figure	IA+CA-CR+OI-Col	288	142 [0.715±0.105] (0.4492-0.9508)	---	---	66 [0.832±0.142] (0.4546-0.9917)	80 [0.714±0.147] (0.4211-0.9886)
	IA-CA-CR+OI	288	---	28 [0.574±0.151] (0.3620-0.9486)	172 [0.643±0.123] (0.3516-0.9536)	88 [0.816±0.171] (0.3691-0.9943)	---
	IA-CA-Col	288	---	19 [0.534±0.178] (0.3593-0.9109)	155 [0.545±0.106] (0.3640-0.8939)	---	114 [0.717±0.157] (0.4285-0.9787)
	IA-CR+OI-Col	288	---	126 [0.662±0.113] (0.3538-0.9327)	---	66 [0.837±0.128] (0.4221-0.9914)	96 [0.702±0.144] (0.4630-0.9884)
	CA-CR+OI-Col	288	---	---	168 [0.878±0.126] (0.4080-0.9943)	63 [0.815±0.136] (0.4459-0.9875)	57 [0.755±0.144] (0.5000-0.9842)
W-MVB Pliocene-Holocene: Diagrams based on log-ratios of immobile major and trace elements	***{Σn} {Σprob} [%prob]***	**1440**	**{142} {101.4712} [---]**	**{173} {109.6690} [13.0%]**	**{495} {342.5271} [40.5%]**	**{283} {233.2912} [22.4%]**	**{347} {249.2711} [24.1%]**
Intermediate; Verma and Verma (2013); log-ratios of immobile trace elements (tint); no figure	IA+CA-CR+OI-Col	143	96 [0.824±0.112] (0.5004-0.9971)	---	---	24 [0.816±0.158] (0.4569-0.9831)	23 [0.906±0.133] (0.4783-0.9988)
	IA-CA-CR+OI	143	---	10 [0.526±0.099] (0.3857-0.6963)	105 [0.693±0.155] (0.4420-0.9695)	28 [0.820±0.117] (0.5659-0.9939)	---
	IA-CA-Col	143	---	5 [0.5257±0.0361] (0.4926-0.5867)	114 [0.689±0.135] (0.4412-0.9754)	---	24 [0.838±0.157] (0.4993-0.9998)
	IA-CR+OI-Col	143	---	88 [0.773±0.126] (0.4012-0.9854)	---	28 [0.801±0.190] (0.3514-0.9882)	27 [0.873±0.177] (0.4975-0.9994)
	CA-CR+OI-Col	143	---	---	103 [0.914±0.089] (0.4599-0.9997)	20 [0.746±0.123] (0.4541-0.9492)	20 [0.794±0.168] (0.4643-0.9940)
W-MVB Pliocene-Holocene: Diagrams based on log-ratios of immobile trace elements	***{Σn} {Σprob} [%prob]***	**715**	**{96} {79.0883} [---]**	**{103} {75.9432} [17.0%]**	**{322} {245.4828} [54.5%]**	**{100} {79.9095} [14.2%]**	**{94} {80.4195} [14.3%]**

Explanation of § and Θ is in Table 5.

Table S5 Application of multidimensional diagrams for deciphering tectonic setting of No Rift Pliocene-Holocene intermediate magmas from the western Mexican Volcanic Belt (W-MVB).

Magma type, Figure name; Figure number	Figure type §	Total number of samples	Number of discriminated samples				
			Arc			Within-plate	Collision
			IA+CA [$\bar{x} \pm s$] (p_{IA+CA}) Θ	IA [$\bar{x} \pm s$] [p_{IA}] Θ	CA [$\bar{x} \pm s$] [p_{CA}] Θ	CR+OI [$\bar{x} \pm s$] [p_{CR+OI}] Θ	Col [$\bar{x} \pm s$] [p_{Col}] Θ
Intermediate; Verma and Verma (2013); log-ratios of all major elements (mint); no figure	IA+CA-CR+OI-Col	281	109 [0.772±0.138] (0.4071-0.9557)	---	---	27 [0.816±0.187] (0.4163-0.9858)	145 [0.791±0.152] (0.4786-0.9964)
	IA-CA-CR+OI	281	---	4 [0.519±0.092] (0.4300-0.6312)	212 [0.810±0.101] (0.4707-0.9851)	65 [0.795±0.182] (0.3721-0.9958)	---
	IA-CA-Col	281	---	5 [0.518±0.099] (0.4243-0.6627)	144 [0.717±0.133] (0.3594-0.9269)	---	132 [0.776±0.199] (0.3635-0.9999)
	IA-CR+OI-Col	281	---	84 [0.716±0.130] (0.3731-0.9264)	---	29 [0.823±0.181] (0.4198-0.9895)	168 [0.818±0.141] (0.4492-0.9957)
	CA-CR+OI-Col	281	---	---	134 [0.742±0.134] (0.4315-0.9626)	26 [0.772±0.196] (0.4016-0.9729)	121 [0.760±0.159] (0.4908-0.9915)
W-MVB Pliocene-Holocene: Diagrams based on log-ratios of major elements	***{Σn} {Σprob} [%prob]***	**1405**	**{109} {84.1423} [---]**	**{93} {64.7692} [7.1%]**	**{490} {374.2241} [*41.0%*]**	**{147} {117.6268} [10.8%]**	**{566} {446.4409} [*41.1%*]**
Intermediate; Verma and Verma (2013); log-ratios of immobile major and trace elements (mtint); no figure	IA+CA-CR+OI-Col	154	34 [0.696±0.163] (0.4581-0.9897)	---	---	26 [0.672±0.159] (0.4221-0.9786)	94 [0.743±0.157] (0.3847-0.9815)
	IA-CA-CR+OI	154	---	15 [0.629±0.182] (0.3898-0.8979)	104 [0.718±0.151] (0.3655-0.9712)	35 [0.726±0.188] (0.4083-0.9874)	---
	IA-CA-Col	154	---	8 [0.599±0.111] (0.4718-0.7420)	63 [0.629±0.128] (0.3505-0.8893)	---	83 [0.710±0.144] (0.4202-0.9490)
	IA-CR+OI-Col	154	---	28 [0.702±0.166] (0.3829-0.9765)	---	27 [0.687±0.143] (0.4726-0.9741)	99 [0.760±0.157] (0.3968-0.9811)
	CA-CR+OI-Col	154	---	---	58 [0.777±0.168] (0.4391-0.9998)	21 [0.738±0.135] (0.5256-0.9674)	75 [0.763±0.153] (0.4209-0.9913)
W-MVB Pliocene-Holocene: Diagrams based on log-ratios of immobile major and trace elements	***{Σn} {Σprob} [%prob]***	**770**	**{34} {23.6781} [---]**	**{51} {33.8877} [6.9%]**	**{225} {159.3786} [32.1%]**	**{109} {76.9243} [13.9%]**	**{351} {261.1778} [*47.1%*]**
Intermediate; Verma and Verma (2013); log-ratios of immobile trace elements (tint); no figure	IA+CA-CR+OI-Col	53	33 [0.606±0.145] (0.3820-0.9147)	---	---	9 [0.636±0.104] (0.5298-0.7967)	11 [0.616±0.142] (0.4769-0.9830)
	IA-CA-CR+OI	53	---	1 (0.4234)	48 [0.771±0.122] (0.5429-0.9460)	4 [0.601±0.074] (0.5148-0.6947)	---
	IA-CA-Col	53	---	0 (0)	50 [0.758±0.090] (0.5396-0.9071)	---	3 [0.714±0.188] (0.5811-0.9290)
	IA-CR+OI-Col	53	---	10 [0.592±0.137] (0.4422-0.8174)	---	19 [0.599±0.143] (0.3981-0.8417)	24 [0.675±0.143] (0.4126-0.9878)
	CA-CR+OI-Col	53	---	---	52[0.820±0.110] (0.4940-0.9778)	0 (0)	1(0.8616)
W-MVB Pliocene-Holocene: Diagrams based on log-ratios of immobile trace elements	***{Σn} {Σprob} [%prob]***	**265**	**{33} {20.0015} [---]**	**{11} {6.3438} [3.9%]**	**{150} {117.5400} [*72.1%*]**	**{32} {19.5056} [10.3%]**	**{39} {25.9727} [13.7%]**

Explanation of § and Θ is in Table 5.

Table S6 Application of multidimensional diagrams for deciphering tectonic setting of Rift Pliocene-Holocene acid magmas from the western Mexican Volcanic Belt (W-MVB).

Magma type, Figure name	Figure type §	Total number of samples	Number of discriminated samples				
			Arc			Within-plate	Collision
			IA+CA $[\bar{x} \pm s]$ (p_{IA+CA}) Θ	IA $[\bar{x} \pm s]$ [p_{IA}] Θ	CA $[\bar{x} \pm s]$ [p_{CA}] Θ	CR+OI $[\bar{x} \pm s]$ [p_{CR+OI}] Θ	Col $[\bar{x} \pm s]$ [p_{Col}] Θ
Acid; Verma *et al.* (2012);); log-ratios of all major elements (macid)	(IA+CA–CR–Col)	217	142 [0.822±0.164] (0.3927-0.9953)	---	---	46 [0.893±0.109] (0.5152-0.9994)	29 [0.685±0.153] (0.3942-0.9991)
	(IA–CA–CR)	217	---	41[0.686±0.129] (0.4833-0.9163)	122 [0.719±0.134] (0.4683-0.9647)	54 [0.836±0.162] (0.5361-1.0000)	---
	(IA–CA–Col)	217	---	33 [0.654±0.109] (0.4997-0.8896)	138 [0.679±0.111] (0.4811-0.8808)	---	46 [0.770±0.177] (0.4692-1.0000)
	(IA–CR–Col)	217	---	97 [0.887±0.147] (0.3972-0.9996)	---	61 [0.766±0.167] (0.3973-0.9985)	59 [0.747±0.153] (0.4321-0.9929)
	(CA–CR–Col)	**1085**	**{142} {116.7770} [---]**	**{171} {135.7297} [20.3%]**	149 [0.876±0.134] (0.3648-0.9995) **{409} {312.0025} [46.6%]**	48 [0.708±0.152] (0.3725-0.9953) **{209} {166.8773} [19.8%]**	20 [0.641±0.173] (0.3774-0.9955) **{154} {112.1821} [13.3%]**
W-MVB Miocene: Diagrams based on log-ratios of all major elements	***{Σn} {Σprob} [%prob]***	217	142[0.822±0.164] (0.3927-0.9953)	---	---	46[0.893±0.109] (0.5152-0.9994)	29[0.685±0.153] (0.3942-0.9991)
Acid; Verma *et al.* (2013); log-ratios of all major elements (macid)	IA+CA-CR+OI-Col	217	107 [0.836±0.153] (0.3593-0.9950)	---	---	87 [0.771±0.212] (0.3876-0.9997)	23 [0.556±0.164] (0.4223-0.9974)
	IA-CA-CR+OI	217	---	0 (0)	126 [0.793±0.152] (0.4670-0.9697)	91 [0.878±0.183] (0.4757-0.9999)	---
	IA-CA-Col	217	---	37 [0.721±0.109] (0.4713-0.9055)	150 [0.841±0.131] (0.4459-0.9743)	---	30 [0.773±0.171] (0.4310-0.9992)
	IA-CR+OI-Col	217	---	53 [0.708±0.209] (0.3638-0.9929)	---	124 [0.712±0.200] (0.3535-0.9991)	40 [0.564±0.125] (0.3541-0.9958)
	CA-CR+OI-Col	217	---	---	119 [0.833±0.177] (0.3676-0.9989)	88 [0.752±0.213] (0.3911-0.9989)	10 [0.656±0.182] (0.4487-0.9946)
W-MVB Miocene: Diagrams based on log-ratios of all major elements	***{Σn} {Σprob} [%prob]***	**1085**	**{107} {89.4877} [---]**	**{90} {64.2103} [9.3%]**	**{395} {325.1879} [47.3%]**	**{390} {301.4220} [35.7%]**	**{103} {65.0932} [7.7%]**
Acid; Verma *et al.* (2013); log-ratios of immobile major and trace elements (mtacid)	IA+CA-CR+OI-Col	101	49 [0.699±0.133] (0.3814-0.9062)	---	---	44 [0.905±0.169] (0.5203-1.0000)	8 [0.510±0.079] (0.4135-0.6387)
	IA-CA-CR+OI	101	---	1 (0.7048)	53 [0.814±0.091] (0.5383-0.9667)	47 [0.905±0.161] (0.4869-0.9999)	---
	IA-CA-Col	101	---	1 (0.6994)	63 [0.741±0.103] (0.4904-0.9529)	---	37 [0.790±0.158] (0.4681-0.9965)
	IA-CR+OI-Col	101	---	3 [0.690±0.241] (0.4473-0.9293)	---	46 [0.894±0.174] (0.4142-0.9999)	52 [0.578±0.091] (0.4028-0.7623)
	CA-CR+OI-Col	101	---	---	54 [0.724±0.140] (0.3879-0.9223)	45 [0.876±0.202] (0.4480-0.9999)	2 [0.547±0.073] (0.4952, 0.5986)
W-MVB Miocene: Diagrams based on log-ratios of immobile major and trace elements	***{Σn} {Σprob} [%prob]***	**505**	**{49} {34.2522} [---]**	**{5} {3.4735} [1.1%]**	**{170} {128.8921} [41.2%]**	**{182} {162.9206} [41.3%]**	**{99} {64.4696} [16.4%]**
Acid; Verma *et al.* (2013); log-ratios of immobile trace elements (mtacid)	IA+CA-CR+OI-Col	45	15 [0.785±0.177] (0.3988-0.9633)	---	---	29 [0.862±0.088] (0.6667-0.9726)	1 (0.4911)
	IA-CA-CR+OI	45	---	1 (0.6697)	14 [0.873±0.115] (0.6184-0.9832)	30 [0.971±0.061] (0.6730-1.0000)	---
	IA-CA-Col	45	---	0 (0)	34 [0.725±0.131] (0.5130-0.9551)	---	11 [0.610±0.096] (0.5108-0.8612)
	IA-CR+OI-Col	45	---	5 [0.571±0.091] (0.5051-0.7268)	---	30 [0.931±0.070] (0.6795-0.9920)	10 [0.835±0.135] (0.6008-0.9556)

	CA-CR+OI-Col	45	---	---	16 [0.832±0.204] (0.4296-0.9884)	29 [0.849±0.094] (0.6112-0.9668)	0 (0)
W-MVB Miocene: Diagrams based on log-ratios of immobile trace elements	***{Σn} {Σprob} [%prob]***	**225**	**{15} {11.7741} [---]**	**{6} {3.5263} [2.3%]**	**{64} {50.1869} [32.6%]**	**{118} {106.6661} [56.8%]**	**{22} {15.5555} [8.3%]**

Explanation of § and Θ is in Table 5.

Table S7 Application of multidimensional diagrams for deciphering tectonic setting of No Rift Pliocene-Holocene acid magmas from the western Mexican Volcanic Belt (W-MVB).

Magma type, Figure name	Figure type §	Total number of samples	Number of discriminated samples				
			Arc			Within-plate	Collision
			IA+CA $[\bar{x} \pm s]$ (p_{IA+CA}) Θ	IA $[\bar{x} \pm s]$ [p_{IA}] Θ	CA $[\bar{x} \pm s]$ [p_{CA}] Θ	CR+OI $[\bar{x} \pm s]$ [p_{CR+OI}] Θ	Col $[\bar{x} \pm s]$ [p_{Col}] Θ
Acid; Verma *et al.* (2012); log-ratios of all major elements (macid)	(IA+CA–CR–Col)	15	9 [0.9616±0.0190] (0.9383-0.9881)	---	---	1 (0.8678)	5 [0.658±0.191] (0.5022-0.9883)
	(IA–CA–CR)	15	---	8 [0.660±0.094] (0.5107-0.7705)	6 [0.754±0.164] (0.5675-0.9982)	1 (0.9712)	---
	(IA–CA–Col)	15	---	7 [0.646±0.100] (0.4905-0.7386)	3 [0.532±0.058] (0.4913-0.5977)	---	5 [0.606±0.188] (0.4121-0.9137)
	(IA–CR–Col)	15	---	9 [0.9864±0.0149] (0.9577-0.9982)	---	1(0.8531)	5 [0.774±0.142] (0.6490-0.9981)
	(CA–CR–Col)	15	---	---	11 [0.9657±0.0393] (0.8748-0.9976)	1(0.8343)	3 [0.664±0.268] (0.4912-0.9726)
W-MVB Miocene: Diagrams based on log-ratios of all major elements	***{Σn} {Σprob} [%prob]***	**75**	**{9} {8.6542} [---]**	**{24} {18.6795} [*39%*]**	**{20} {16.7418} [*35%*]**	**{4} {3.5263} [6%]**	**{18} {12.1775} [20%]**
Acid; Verma *et al*. (2013); log-ratios of all major elements (macid)	IA+CA-CR+OI-Col	15	9 [0.9635±0.0221] (0.9247-0.9873)	---	---	3 [0.586±0.195] (0.4360-0.8068)	3 [0.751±0.147] (0.6433-0.9184)
	IA-CA-CR+OI	15	---	0 (0)	11 [0.842±0.139] (0.5553-0.9701)	4 [0.820±0.177] (0.6109-0.9820)	---
	IA-CA-Col	15	---	0 (0)	11 [0.858±0.159] (0.4974-0.9570)	---	4 [0.790±0.174] (0.5743-0.9979)
	IA-CR+OI-Col	15	---	8 [0.793±0.146] (0.5512-0.9467)	---	3 [0.644±0.147] (0.5222-0.8070)	4 [0.700±0.197] (0.4299-0.9019)
	CA-CR+OI-Col	15	---	---	10 [0.943±0.119] (0.6070-0.9951)	3 [0.573±0.185] (0.4222-0.7792)	2 [0.672±0.295] (0.4636, 0.8806)
W-MVB Miocene: Diagrams based on log-ratios of all major elements	***{Σn} {Σprob} [%prob]***	**75**	**{9} {8.6719} [---]**	**{8} {6.3438} [13%]**	**{32} {28.1268} [*57%*]**	**{13} {8.6926} [14%]**	**{13} {9.5578} [16%]**
Acid; Verma *et al.* (2013); log-ratios of immobile major and trace elements (mtacid)	IA+CA-CR+OI-Col	5	4 [0.602±0.197] (0.4292-0.8510)	---	---	0 (0)	1 (0.8648)
	IA-CA-CR+OI	5	---	0 (0)	4 [0.744±0.092] (0.6290-0.8257)	1(0.3895)	---
	IA-CA-Col	5	---	0 (0)	4 [0.612±0.132] (0.4192-0.7041)	---	1(0.7853)
	IA-CR+OI-Col	5	---	1 (0.5653)	---	1 (0.4601)	3 [0.751±0.141] (0.6567-0.9134)
	CA-CR+OI-Col	5	---	---	4 [0.659±0.177] (0.5012-0.8806)	0 (0)	1(0.7780)

W-MVB Miocene: Diagrams based on log-ratios of immobile major and trace elements	***{Σn} {Σprob} [%prob]***	**25**	**{4} {2.4063} [---]**	**{1} {0.5653} [5%]**	**{12} {8.0574} [*62%*]**	**{2} {0.8496} [5%]**	**{6} {4.6806} [28%]**
Acid; Verma *et al*. (2013); log-ratios of immobile trace elements (mtacid)	IA+CA-CR+OI-Col	2	2 [0.842±0.097] (0.7736, 0.9109)	---	---	0 (0)	0 (0)
	IA-CA-CR+OI	2	---	0 (0)	2 [0.912±0.062] (0.8683, 0.9559)	0 (0)	---
	IA-CA-Col	2	---	0 (0)	2 [0.9140±0.0219] (0.8985, 0.9295)	---	0 (0)
	IA-CR+OI-Col	2	---	0 (0)	---	1 (0.6451)	1 (0.6167)
	CA-CR+OI-Col	2	---	---	2 [0.903±0.093] (0.8367, 0.9689)	0 (0)	0 (0)
W-MVB Miocene: Diagrams based on log-ratios of immobile trace elements	***{Σn} {Σprob} [%prob]***	**10**	**{2} {1.6845} [---]**	**{0} {0} [0%]**	**{6} {5.4579} [*85%*]**	**{1} {0.6451} [8%]**	**{1} {0.6167} [7%]**

Explanation of § and Θ is in Table 5.

Table S8 Application of multidimensional diagrams for deciphering tectonic setting of Pliocene-Holocene basic magmas from the Tepic-Zacoalco Rift (TZR) of the western Mexican Volcanic Belt (W-MVB).

Figure reference; figure type; figure no.	Discrimination diagram §	Total no. of samples (%)	Predicted tectonic affinity and number of discriminated samples (%)				
			IAB	CRB+OIB	CRB	OIB	MORB
Verma *et al.* (2006); log-ratios of major elements (m2); no figure	IAB-CRB-OIB-MORB	71 (100)	0 (0)	---	67 (94.4)	2 (2.8)	2 (2.8)
	IAB-CRB-OIB	71 (100)	1 (1.4)	---	68 (95.8)	2 (2.8)	---
	IAB-CRB-MORB	71 (100)	0 (0)	---	68 (95.8)	---	3 (4.2)
	IAB-OIB-MORB	71 (100)	7 (9.9)	---	---	51 (71.8)	13 (18.3)
	CRB-OIB-MORB	71 (100)	---	---	64 (90.1)	5 (7.1)	2 (2.8)
TZR Pliocene-Holocene basic rocks: Synthesis of all five diagrams of Verma et al. (2006)		**355 (100)**	**8 (2.3)**	**---**	**267 (75.2)**	**60 (16.9)**	**20 (5.6)**
Agrawal *et al.* (2008); log-ratios of immobile trace elements (t1); no figure.	IAB-CRB+OIB-MORB	27 (100)	0 (0)	27 (100)	---	---	0 (0)
	IAB-CRB-OIB	27 (100)	0 (0)	27 (100)	---	---	0 (0)
	IAB-CRB-MORB	27 (100)	0 (0)	---	23 (85.2)	4 (14.8)	---
	IAB-OIB-MORB	27 (100)	0 (0)	---	27 (100)	---	0 (0)
	CRB-OIB-MORB	27 (100)	0 (0)	---	---	26 (96.3)	1 (3.7)
TZR Pliocene-Holocene basic rocks: Synthesis of all five diagrams of Agrawal et al. (2008)		**135 (100)**	**0 (0)**	**27 (---)**	**91 (67.4)**	**43 (31.9)**	**1 (0.7)**
Verma and Agrawal (2011); log-ratios of immobile major and trace elements (t2); no figure.	IAB-CRB+OIB-MORB	37 (100)	0 (0)	36 (97.3)	---	---	1 (2.7)
	IAB-CRB-OIB	37 (100)	0 (0)	---	37 (100)	0 (0)	---
	IAB-CRB-MORB	37 (100)	0 (0)	---	36 (97.3)	---	1 (2.7)
	IAB-OIB-MORB	37 (100)	0 (0)	---	---	31 (83.8)	6 (16.2)
	CRB-OIB-MORB	37 (100)	---	---	34 (91.9)	2 (5.4)	1 (2.7)
TZR Pliocene-Holocene basic rocks: Synthesis of all five diagrams of Verma and Agrawal (2011)		**185 (100)**	**0 (0)**	**36 (---)**	**135 (73.0)**	**41 (22.2)**	**9 (4.9)**

Explanation of § is in Table 4.

Table S9 Application of multidimensional diagrams for deciphering tectonic setting of Pliocene-Holocene intermediate magmas from the Tepic-Zacoalco Rift (TZR) of the western Mexican Volcanic Belt (W-MVB).

Magma type, Figure name; Figure number	Figure type §	Total number of samples	Number of discriminated samples				
			Arc			Within-plate	Collision
			IA+CA [$\bar{x} \pm s$] (p_{IA+CA}) Θ	IA [$\bar{x} \pm s$] [p_{IA}] Θ	CA [$\bar{x} \pm s$] [p_{CA}] Θ	CR+OI [$\bar{x} \pm s$] [p_{CR+OI}] Θ	Col [$\bar{x} \pm s$] [p_{Col}] Θ
Intermediate; Verma and Verma (2013); log-ratios of all major elements (mint); no figure	IA+CA-CR+OI-Col	211	36 [0.626±0.132] (0.4219-0.9141)	---	---	76 [0.805±0.168] (0.4182-0.9979)	99 [0.782±0.137] (0.4297-0.9726)
	IA-CA-CR+OI	211	---	1 (0.5401)	129 [0.743±0.125] (0.4024-0.9400)	81 [0.842±0.157] (0.4281-0.9978)	---
	IA-CA-Col	211	---	4 [0.719±0.159] (0.5456-0.9069)	90 [0.620±0.114] (0.3821-0.9239)	---	117 [0.718±0.146] (0.4052-0.9643)
	IA-CR+OI-Col	211	---	16 [0.565±0.117] (0.3869-0.8616)	---	84 [0.788±0.181] (0.3995-0.9986)	111 [0.830±0.153] (0.3638-0.9890)
	CA-CR+OI-Col	211	---	---	52 [0.643±0.156] (0.3958-0.9200)	73 [0.773±0.172] (0.3474-0.9938)	86 [0.708±0.136] (0.3842-0.9485)
TZR Pliocene-Holocene: Diagrams based on log-ratios of major elements	***{Σn} {Σprob} [%prob]***	**1055**	**{36} {22.5463} [---]**	**{21} {12.4531} [1.8%]**	**{271} {185.0879} [26.2%]**	**{314} {251.9363} [32.0%]**	**{413} {314.4987} [40.0%]**
Intermediate; Verma and Verma (2013); log-ratios of immobile major and trace elements (mtint); no figure	IA+CA-CR+OI-Col	93	16 [0.689±0.127] (0.4492-0.8619)	---	---	44 [0.868±0.123] (0.5038-0.9917)	33 [0.730±0.135] (0.4876-0.9183)
	IA-CA-CR+OI	93	---	12 [0.603±0.226] (0.3620-0.9486)	28 [0.636±0.189] (0.3516-0.9502)	53 [0.835±0.166] (0.3691-0.9943)	---
	IA-CA-Col	93	---	7 [0.690±0.211] (0.4179-0.9109)	30 [0.642±0.123] (0.4452-0.8939)	---	56 [0.732±0.158] (0.4459-0.9745)
	IA-CR+OI-Col	93	---	13 [0.652±0.204] (0.3538-0.9327)	---	45 [0.862±0.121] (0.4221-0.9914)	35 [0.729±0.125] (0.5191-0.9112)
	CA-CR+OI-Col	93	---	---	25 [0.773±0.160] (0.4670-0.9831)	44 [0.833±0.137] (0.4459-0.9875)	24 [0.771±0.130] (0.5446-0.9349)
TZR Pliocene-Holocene: Diagrams based on log-ratios of immobile major and trace elements	***{Σn} {Σprob} [%prob]***	**465**	**{16} {11.0220} [---]**	**{32} {20.5400} [6.6%]**	**{83} {56.3912} [18.2%]**	**{186} {157.9136} [44.5%]**	**{148} {109.1113} [30.7%]**
Intermediate; Verma and Verma (2013); log-ratios of immobile trace elements (tint); no figure	IA+CA-CR+OI-Col	26	11 [0.789±0.174] (0.5776-0.9971)	---	---	15 [0.839±0.146] (0.4876-0.9831)	0 (0)
	IA-CA-CR+OI	26	---	0 (0)	14 [0.822±0.117] (0.5429-0.9346)	12 [0.785±0.101] (0.5659-0.9495)	---
	IA-CA-Col	26	---	0 (0)	26 [0.863±0.060] (0.7443-0.9509)	---	0 (0)
	IA-CR+OI-Col	26	---	6 [0.707±0.292] (0.4012-0.9854)	---	18 [0.836±0.175] (0.3514-0.9882)	2 [0.5073±0.0090 (0.5009, 0.5137)
	CA-CR+OI-Col	26	---	---	13 [0.875±0.107] (0.7272-0.9994)	13 [0.744±0.114] (0.5031-0.9492)	0 (0)
TZR Pliocene-Holocene: Diagrams based on log-ratios of immobile trace elements	***{Σn} {Σprob} [%prob]***	**130**	**{11} {8.6811} [---]**	**{6} {4.2427} [4.6%]**	**{53} {45.3271} [50.3%]**	**{58} {46.7291} [44.1%]**	**{2} {1.0146} [1.0%]**

Explanation of § and Θ is in Table 5.

Table S10 Application of multidimensional diagrams for deciphering tectonic setting of Pliocene-Holocene acid magmas from the Tepic-Zacoalco Rift (TZR) of the western Mexican Volcanic Belt (W-MVB).

Magma type, Figure name	Figure type §	Total number of samples	Number of discriminated samples				
			Arc			Within-plate	Collision
			IA+CA [$\bar{x} \pm s$] (p_{IA+CA}) Θ	IA [$\bar{x} \pm s$] [p_{IA}] Θ	CA [$\bar{x} \pm s$] [p_{CA}] Θ	CR+OI [$\bar{x} \pm s$] [p_{CR+OI}] Θ	Col [$\bar{x} \pm s$] [p_{Col}] Θ
Acid; Verma *et al.* (2012); log-ratios of all major elements (macid)	IA+CA–CR–Col	174	106 [0.782±0.165] (0.3927-0.9792)	---	---	44 [0.890±0.110] (0.5152-0.9994)	24 [0.675±0.165] (0.3942-0.9991)
	IA–CA–CR	174	---	17 [0.585±0.073] (0.4833-0.7192)	106 [0.724±0.131] (0.4683-0.9647)	51 [0.835±0.160] (0.5361-1.0000)	---
	IA–CA–Col	174	---	9 [0.582±0.069] (0.4997-0.6898)	126 [0.684±0.111] (0.4811-0.8808)	---	39 [0.782±0.186] (0.4692-1.0000)
	IA–CR–Col	174	---	62 [0.842±0.158] (0.3972-0.9969)	---	58 [0.764±0.168] (0.3973-0.9985)	54 [0.736±0.155] (0.4321-0.9929)
	CA–CR–Col	174	---	---	114 [0.850±0.138] (0.3648-0.9948)	45 [0.705±0.145] (0.3725-0.9953)	15 [0.623±0.194] (0.3774-0.9955)
TZR Pliocene-Holocene: Diagrams based on log-ratios of all major elements	***{Σn} {Σprob} [%prob]***	**870**	**{106} {82.9274} [---]**	**{88} {67.4029} [12.7%]**	**{346} {259.8953} [49.1%]**	**{198} {157.7470} [23.8%]**	**{132} {95.7897} [14.4%]**
Acid; Verma *et al.* (2013); log-ratios of all major elements (macid)	IA+CA-CR+OI-Col	174	72 [0.789±0.159] (0.3593-0.9782)	---	---	79 [0.772±0.215] (0.3876-0.9997)	23 [0.556±0.164] (0.4223-0.9974)
	IA-CA-CR+OI	174	---	0 (0)	91 [0.768±0.166] (0.4670-0.9697)	83 [0.875±0.187] (0.4757-0.9999)	---
	IA-CA-Col	174	---	36 [0.726±0.106] (0.4713-0.9055)	113 [0.828±0.141] (0.4549-0.9743)	---	25 [0.751±0.178] (0.4310-0.9992)
	IA-CR+OI-Col	174	---	24 [0.579±0.179] (0.3638-0.9238)	---	116 [0.709±0.202] (0.3535-0.9991)	34 [0.574±0.132] (0.3541-0.9958)
	CA-CR+OI-Col	174	---	---	84 [0.781±0.183] (0.3676-0.9914)	80 [0.754±0.218] (0.3911-0.9989)	10 [0.656±0.182] (0.4487-0.9946)
TZR Pliocene-Holocene: Diagrams based on log-ratios of all major elements	***{Σn} {Σprob} [%prob]***	**870**	**{72} {56.7938} [---]**	**{60} {40.0486} [7.4%]**	**{288} {229.0116} [42.0%]**	**{358} {276.2038} [41.9%]**	**{92} {57.6675} [8.7%]**
Acid; Verma *et al.* (2013); log-ratios of immobile major and trace elements (mtacid)	IA+CA-CR+OI-Col	88	39 [0.693±0.141] (0.3814-0.9062)	---	---	44 [0.905±0.169] (0.5203-1.0000)	5 [0.504±0.094] (0.4135-0.6387)
	IA-CA-CR+OI	88	---	1 (0.7048)	41 [0.817±0.091] (0.5383-0.9667)	46 [0.904±0.163] (0.4869-0.9999)	---
	IA-CA-Col	88	---	1 (0.6994)	52 [0.744±0.103] (0.4904-0.9529)	---	35 [0.794±0.150] (0.5219-0.9965)
	IA-CR+OI-Col	88	---	2 [0.688±0.341] (0.4473, 0.9293)	---	45 [0.905±0.159] (0.4226-0.9999)	41 [0.564±0.083] (0.4028-0.7180)
	CA-CR+OI-Col	88	---	---	42 [0.722±0.144] (0.3879-0.9223)	44 [0.884±0.197] (0.4480-0.9999)	2 [0.547±0.073] (0.4952, 0.5986)
TZR Pliocene-Holocene:Diagrams based on log-ratios of immobile major and trace elements	***{Σn} {Σprob} [%prob]***	**440**	**{39} {27.0314} [---]**	**{4} {2.7808} [1.0%]**	**{135} {102.5468} [37.0%]**	**{179} {161.0261} [46.3%]**	**{83} {54.5294} [15.7%]**
Acid; Verma *et al.* (2013); log-ratios of immobile trace elements (tacid)	IA+CA-CR+OI-Col	35	5 [0.706±0.193] (0.4577-0.9344)	---	---	29 [0.862±0.088] (0.6667-0.9726)	1 (0.4911)
	IA-CA-CR+OI	35	---	1 (0.6697)	4 [0.839±0.150] (0.6184-0.9581)	30 [0.971±0.061] (0.6730-1.0000)	---
	IA-CA-Col	35	---	0 (0)	24 [0.671±0.108] (0.5130-0.8983)	---	11 [0.610±0.096] (0.5108-0.8612)
	IA-CR+OI-Col	35	---	2 [0.616±0.157] (0.5051, 0.7268)	---	30 [0.931±0.070] (0.6795-0.9920)	3 [0.833±0.202] (0.6008-0.9556)
	CA-CR+OI-Col	35	---	---	6 [0.738±0.240] (0.4349-0.9818)	29 [0.849±0.094] (0.6112-0.9668)	0 (0)
TZR Pliocene-Holocene:Diagrams based on log-ratios of immobile trace	***{Σn} {Σprob} [%prob]***	**175**	**{5} {3.5308} [---]**	**{3} {1.9016} [1.5%]**	**{34} {23.8847} [18.6%]**	**{118} {106.6661} [73.1%]**	**{15} {9.7032} [6.7%]**

elements
Explanation of § and Θ is given in Table 5.

Table S11 Application of multidimensional diagrams for deciphering tectonic setting of Pliocene-Holocene basic magmas from the Colima Rift (CR) of the western Mexican Volcanic Belt (W-MVB).

Figure reference; figure type; figure no.	Discrimination diagram §	Total no. of samples (%)	Predicted tectonic affinity and number of discriminated samples (%)				
			IAB	CRB+OIB	CRB	OIB	MORB
Verma *et al.* (2006); log-ratios of major elements (m2); no figure	IAB-CRB-OIB-MORB	48 (100)	9 (18.8)	---	38 (79.2)	1 (2.1)	0 (0)
	IAB-CRB-OIB	48 (100)	10 (20.8)	---	37 (77.1)	1 (2.1)	---
	IAB-CRB-MORB	48 (100)	7 (14.6)	---	40 (83.3)	---	1 (2.1)
	IAB-OIB-MORB	48 (100)	27 (56.2)	---	---	14 (29.2)	7 (14.6)
	CRB-OIB-MORB	48 (100)	---	---	45 (93.8)	2 (4.2)	1 (2.1)
CR Pliocene-Holocene basic rocks: Synthesis of all five diagrams of Verma et al. (2006)		**240 (100)**	**53 (22.1)**	**---**	**160 (66.7)**	**18 (7.5)**	**9 (3.8)**
Agrawal *et al.* (2008); log-ratios of immobile trace elements (t1); no figure.	IAB-CRB+OIB-MORB	20 (100)	11 (55)	9 (45)	---	---	0 (0)
	IAB-CRB-OIB	20 (100)	14 (70)	---	1 (5)	5 (25)	---
	IAB-CRB-MORB	20 (100)	8 (40)	---	12 (60)	---	0 (0)
	IAB-OIB-MORB	20 (100)	8 (40)	---	---	12 (60)	0 (0)
	CRB-OIB-MORB	20 (100)	---	---	14 (70)	5 (25)	1 (5)
CR Pliocene-Holocene basic rocks: Synthesis of all five diagrams of Agrawal et al. (2008)		**100 (100)**	**41 (41)**	**9 (---)**	**32 (32)**	**26 (26)**	**1 (1)**
Verma and Agrawal (2011); log-ratios of immobile major and trace elements (t2); no figure.	IAB-CRB+OIB-MORB	19 (100)	18 (94.7)	1 (5.3)	---	---	0 (0)
	IAB-CRB-OIB	19 (100)	18 (94.7)	---	0 (0)	1 (5.3)	---
	IAB-CRB-MORB	19 (100)	18 (94.7)	---	1 (5.3)	---	0 (0)
	IAB-OIB-MORB	19 (100)	18 (94.7)	---	---	1 (5.3)	0 (0)
	CRB-OIB-MORB	19 (100)	---	---	0 (0)	18 (94.7)	1 (5.3)
CR Pliocene-Holocene basic rocks: Synthesis of all five diagrams of Verma and Agrawal (2011)		**95 (100)**	**72 (75.8)**	**1 (---)**	**1 (1.1)**	**21 (22.1)**	**1 (1.1)**

Explanation of § is in Table 4.

Table S12 Application of multidimensional diagrams for deciphering tectonic setting of Pliocene-Holocene intermediate magmas from the Colima Rift (CR) of the western Mexican Volcanic Belt (W-MVB).

Magma type, Figure name; Figure number	Figure type §	Total number of samples	Number of discriminated samples				
			Arc			Within-plate	Collision
			IA+CA [$\bar{x} \pm s$] (p_{IA+CA}) Θ	IA [$\bar{x} \pm s$] [p_{IA}] Θ	CA [$\bar{x} \pm s$] [p_{CA}] Θ	CR+OI [$\bar{x} \pm s$] [p_{CR+OI}] Θ	Col [$\bar{x} \pm s$] [p_{Col}] Θ
Intermediate; Verma and Verma (2013); log-ratios of all major elements (mint); no figure	IA+CA-CR+OI-Col	410	321 [0.712±0.114] (0.4120-0.9480)	---	---	8 [0.615±0.138] (0.4537-0.8481)	81 [0.745±0.157] (0.4870-0.9987)
	IA-CA-CR+OI	410	---	53 [0.689±0.071] (0.5441-0.8774)	344 [0.846±0.084] (0.3860-1.0000)	13 [0.764±0.204] (0.3763-0.9994)	---
	IA-CA-Col	410	---	53 [0.821±0.083] (0.4811-0.9633)	304 [0.744±0.094] (0.4110-0.9711)	---	53 [0.771±0.166] (0.4500-0.9996)
	IA-CR+OI-Col	410	---	174 [0.619±0.116] (0.3710-0.9189)	---	13 [0.624±0.131] (0.4118-0.8645)	223 [0.699±0.141] (0.4236-1.0000)
	CA-CR+OI-Col	410	---	---	342 [0.720±0.103] (0.4462-0.9760)	8 [0.557±0.135] (0.4327-0.7525)	60 [0.714±0.143] (0.4837-0.9743)
CR Pliocene-Holocene: Diagrams based on log-ratios of major elements	***{Σn} {Σprob} [%prob]***	**2050**	**{321} {228.4937} [---]**	**{280} {187.6812} [15.5%]**	**{990} {763.3731} [62.8%]**	**{42} {27.4135} [1.8%]**	**{417} {299.9226} [19.9%]**
Intermediate; Verma and Verma (2013); log-ratios of immobile major and trace elements (mtint); no figure	IA+CA-CR+OI-Col	157	121 [0.720±0.098] (0.5066-0.9034)	---	---	8 [0.808±0.112] (0.6008-0.9475)	28 [0.706±0.143] (0.4996-0.9886)
	IA-CA-CR+OI	157	---	14 [0.553±0.050] (0.5040-0.6537)	130 [0.654±0.101] (0.4988-0.9536)	13 [0.872±0.141] (0.5189-0.9883)	---
	IA-CA-Col	157	---	11 [0.439±0.056] (0.3593-0.5046)	118 [0.518±0.081] (0.3640-0.7457)	---	28 [0.704±0.191] (0.4285-0.9787)
	IA-CR+OI-Col	157	---	108 [0.668±0.087] (0.5024-0.8536)	---	8 [0.816±0.110] (0.6167-0.9455)	41 [0.678±0.148] (0.5009-0.9884)
	CA-CR+OI-Col	157	---	---	135 [0.902±0.098] (0.5537-0.9940)	8 [0.775±0.115] (0.5270-0.9185)	14 [0.750±0.132] (0.5343-0.9842)
CR Pliocene-Holocene: Diagrams based on log-ratios of immobile major and trace elements	***{Σn} {Σprob} [%prob]***	**785**	**{121} {87.1011} [---]**	**{133} {84.6682} [19.2%]**	**{383} {267.9714} [61.0%]**	**{37} {30.5273} [5.6%]**	**{111} {77.7587} [14.2%]**
Intermediate; Verma and Verma (2013); log-ratios of immobile trace elements (tint); no figure	IA+CA-CR+OI-Col	116	84 [0.827±0.102] (0.5004-0.9904)	---	---	9 [0.778±0.177] (0.4569-0.9478)	23 [0.906±0.133] (0.4783-0.9988)
	IA-CA-CR+OI	116	---	10 [0.526±0.099] (0.3857-0.6963)	90 [0.671±0.150] (0.4420-0.9695)	16 [0.847±0.124] (0.6103-0.9939)	---
	IA-CA-Col	116	---	5 [0.5257±0.0361] (0.4926-0.5867)	87 [0.634±0.100] (0.4412-0.9754)	---	24 [0.838±0.157] (0.4993-0.9998)
	IA-CR+OI-Col	116	---	81 [0.779±0.107] (0.4322-0.9461)	---	10 [0.738±0.209] (0.3955-0.9362)	25 [0.903±0.148] (0.4975-0.9994)
	CA-CR+OI-Col	116	---	---	89 [0.919±0.085] (0.4599-0.9997)	7 [0.748±0.148] (0.4541-0.9055)	20 [0.794±0.168] (0.4643-0.9940)
CR Pliocene-Holocene: Diagrams based on log-ratios of immobile trace elements	***{Σn} {Σprob} [%prob]***	**580**	**{84} {69.5012} [---]**	**{96} {70.9981} [19.8%]**	**{266} {197.3752} [55.2%]**	**{42} {33.1804} [7.4%]**	**{92} {79.4049} [17.6%]**

Explanation of § and Θ is in Table 5.

Table S13 Application of multidimensional diagrams for deciphering tectonic setting of Pliocene-Holocene acid magmas from the Colima Rift (CR) of the western Mexican Volcanic Belt (W-MVB).

Magma type, Figure name	Figure type §	Total number of samples	Number of discriminated samples				
			Arc			Within-plate	Collision
			IA+CA [$\bar{x} \pm s$] (p_{IA+CA}) Θ	IA [$\bar{x} \pm s$] [p_{IA}] Θ	CA [$\bar{x} \pm s$] [p_{CA}] Θ	CR+OI [$\bar{x} \pm s$] [p_{CR+OI}] Θ	Col [$\bar{x} \pm s$] [p_{Col}] Θ
Acid; Verma *et al.* (2012); log-ratios of all major elements (macid)	IA+CA–CR–Col	38	33 [0.951±0.058] (0.7726-0.9953)	---	---	0 (0)	5 [0.731±0.077] (0.6460-0.8465)
	IA–CA–CR	38	---	23 [0.757±0.113] (0.5243-0.9163)	14 [0.685±0.162] (0.5098-0.9373)	1 (0.5745)	---
	IA–CA–Col	38	---	23 [0.680±0.113] (0.5155-0.8896)	10 [0.588±0.054] (0.5182-0.6697)	---	5 [0.686±0.103] (0.5826-0.8148)
	IA–CR–Col	38	---	33 [0.965±0.078] (0.6729-0.9996)	---	0 (0)	5 [0.866±0.047] (0.8115-0.9324)
	CA–CR–Col	38	---	---	33 [0.962±0.070] (0.7273-0.9995)	0 (0)	5 [0.695±0.077] (0.6161-0.8167)
CR Pliocene-Holocene: Diagrams based on log-ratios of all major elements	***{Σn} {Σprob} [%prob]***	**190**	**{33} {31.3825} [---]**	**{79} {64.8831} [52.2%]**	**{57} {47.2174} [37.9%]**	**{1} {0.5745} [0.4%]**	**{20} {14.8906} [9.4%]**
Acid; Verma *et al*. (2013); log-ratios of all major elements (macid)	IA+CA-CR+OI-Col	38	33 [0.934±0.077] (0.6536-0.9950)	---	---	5 [0.710±0.169] (0.5198-0.8453)	0 (0)
	IA-CA-CR+OI	38	---	0 (0)	33 [0.859±0.081] (0.6494-0.9612)	5 [0.9388±0.0378] (0.9014-0.9924)	---
	IA-CA-Col	38	---	0 (0)	33 [0.8934±0.0430] (0.7528-0.9519)	---	5 [0.882±0.075] (0.7880-0.9449)
	IA-CR+OI-Col	38	---	27 [0.823±0.158] (0.4562-0.9929)	---	5 [0.688±0.156] (0.5159-0.8159)	6 [0.503±0.047] (0.4534-0.5763)
	CA-CR+OI-Col	38	---	---	33 [0.959±0.065] (0.7564-0.9989)	5 [0.681±0.151] (0.5109-0.7991)	0 (0)
CR Pliocene-Holocene: Diagrams based on log-ratios of all major elements	***{Σn} {Σprob} [%prob]***	**190**	**{33} {30.8384} [---]**	**{27} {22.2191} [17.2%]**	**{99} {89.5020} [69.2%]**	**{20} {15.0927} [9.1%]**	**{11} {7.4257} [4.5%]**
Acid; Verma *et al.* (2013); log-ratios of immobile major and trace elements (mtacid)	IA+CA-CR+OI-Col	11	9 [0.707±0.084] (0.5880-0.8810)	---	---	0 (0)	2 [0.496±0.063] (0.4521, 0.5406)
	IA-CA-CR+OI	11	---	0 (0)	10 [0.805±0.094] (0.5826-0.8933)	1 (0.9661)	---
	IA-CA-Col	11	---	0 (0)	10 [0.704±0.085] (0.5490-0.8142)	---	1 (0.9700)
	IA-CR+OI-Col	11	---	1 (0.6927)	---	0 (0)	10 [0.619±0.102] (0.4963-0.7623)
	CA-CR+OI-Col	11	---	---	10 [0.740±0.102] (0.5316-0.8939)	1 (0.5141)	0 (0)
CR Pliocene-Holocene:Diagrams based on log-ratios of immobile major and trace elements	***{Σn} {Σprob} [%prob]***	**55**	**{9} {6.3591} [---]**	**{1} {0.6927} [2%]**	**{30} {22.4889} [73%]**	**{2} {1.4803} [4%]**	**{13} {8.1575} [21%]**

Acid; Verma *et al.* (2013); log-ratios of immobile trace elements (tacid)	IA+CA-CR+OI-Col	10	10 [0.824±0.164] (0.3988-0.9633)	---	---	0 (0)	0 (0)
	IA-CA-CR+OI	10	---	0 (0)	10 [0.887±0.104] (0.7404-0.9832)	0 (0)	---
	IA-CA-Col	10	---	0 (0)	10 [0.855±0.082] (0.6999-0.9551)	---	0 (0)
	IA-CR+OI-Col	10	---	3 [0.5416±0.0325] (0.5156-0.5779)	---	0 (0)	7 [0.836±0.118] (0.6211-0.9337)
	CA-CR+OI-Col	10	---	---	10 [0.888±0.168] (0.4296-0.9884)	0 (0)	0 (0)
CR Pliocene-Holocene:Diagrams based on log-ratios of immobile trace elements	***{Σn} {Σprob} [%prob]***	**50**	**{10} {8.2433} [---]**	**{3} {1.6247} [5%]**	**{30} {26.3023} [81%]**	**{0} {0} [0%]**	**{7} {5.8523} [14%]**

Explanation of § and Θ is given in Table 5.

Table S14 Application of multidimensional diagrams for deciphering tectonic setting of Pliocene-Holocene basic magmas from the Chapala Rift (ChR) of the western Mexican Volcanic Belt (W-MVB).

Figure reference; figure type; figure no.	Discrimination diagram §	Total no. of samples (%)	Predicted tectonic affinity and number of discriminated samples (%)				
			IAB	CRB+OIB	CRB	OIB	MORB
Verma *et al.* (2006); log-ratios of major elements (m2); no figure	IAB-CRB-OIB-MORB	12	2	---	8	0	2
	IAB-CRB-OIB	12	1	---	11	0	---
	IAB-CRB-MORB	12	1	---	9	---	2
	IAB-OIB-MORB	12	2	---	---	4	6
	CRB-OIB-MORB	12	---	---	9	0	3
ChR Pliocene-Holocene basic rocks: Synthesis of all five diagrams of Verma et al. (2006)		**60 (100)**	**6 (10)**	**---**	**37 (62)**	**4 (6)**	**13 (22)**
Agrawal *et al.* (2008); log-ratios of immobile trace elements (t1); no figure.	IAB-CRB+OIB-MORB	1	1	0	---	---	0
	IAB-CRB-OIB	1	0	---	1	0	---
	IAB-CRB-MORB	1	0	---	0	---	1
	IAB-OIB-MORB	1	1	---	---	0	0
	CRB-OIB-MORB	1	---	---	0	0	1
ChR Pliocene-Holocene basic rocks: Synthesis of all five diagrams of Agrawal et al. (2008)		**5**	**2**	**0 (---)**	**1**	**0**	**2**
Verma and Agrawal (2011); log-ratios of immobile major and trace elements (t2); no figure.	IAB-CRB+OIB-MORB	9	0	7	---	---	2
	IAB-CRB-OIB	9	1	---	7	1	---
	IAB-CRB-MORB	9	0	---	7	---	2
	IAB-OIB-MORB	9	0	---	---	7	2
	CRB-OIB-MORB	9	---	---	4	3	2
ChR Pliocene-Holocene basic rocks: Synthesis of all five diagrams of Verma and Agrawal (2011)		**45 (100)**	**1 (2)**	**7 (---)**	**22 (49)**	**14 (31)**	**8 (18)**

Explanation of § is in Table 4.

Table S15 Application of multidimensional diagrams for deciphering tectonic setting of Pliocene-Holocene intermediate magmas from the Chapala Rift (ChR) of the western Mexican Volcanic Belt (W-MVB).

Magma type, Figure name; Figure number	Figure type §	Total number of samples	Number of discriminated samples				
			Arc			Within-plate	Collision
			IA+CA [$\bar{x} \pm s$] (p_{IA+CA}) Θ	IA [$\bar{x} \pm s$] [p_{IA}] Θ	CA [$\bar{x} \pm s$] [p_{CA}] Θ	CR+OI [$\bar{x} \pm s$] [p_{CR+OI}] Θ	Col [$\bar{x} \pm s$] [p_{Col}] Θ
Intermediate; Verma and Verma (2013); log-ratios of all major elements (mint); no figure	IA+CA-CR+OI-Col	45	25 [0.726±0.147] (0.3652-0.9293)	---	---	8 [0.637±0.140] (0.5386-0.9377)	12 [0.710±0.171] (0.4158-0.8941)
	IA-CA-CR+OI	45	---	2 [0.481±0.085] (0.4205, 0.5412)	40 [0.720±0.123] (0.3707-0.9193)	3 [0.879±0.081] (0.7890-0.9469)	---
	IA-CA-Col	45	---	1 (0.4822)	31 [0.685±0.094] (0.4322-0.8364)	---	13 [0.609±0.128] (0.4000-0.7743)
	IA-CR+OI-Col	45	---	20 [0.631±0.133] (0.3883-0.9070)	---	11 [0.654±0.157] (0.4246-0.9483)	14 [0.756±0.191] (0.4490-0.9606)
	CA-CR+OI-Col	45	---	---	26 [0.732±0.142] (0.3950-0.8937)	9 [0.577±0.164] (0.3835-0.9008)	10 [0.682±0.121] (0.4814-0.8283)
ChR Pliocene-Holocene: Diagrams based on log-ratios of major elements	***{Σn} {Σprob} [%prob]***	**225**	**{25} {18.1419} [---]**	**{23} {14.0728} [11.0%]**	**{97} {69.0906} [54.2%]**	**{31} {20.1165} [13.0%]**	**{49} {33.8272} [21.8%]**
Intermediate; Verma and Verma (2013); log-ratios of immobile major and trace elements (mtint); no figure	IA+CA-CR+OI-Col	38	5 [0.670±0.185] (0.4814-0.9508)	---	---	14 [0.735±0.170] (0.4546-0.9846)	19 [0.698±0.177] (0.4211-0.9617)
	IA-CA-CR+OI	38	---	2 [0.5549±0.0455] (0.5227, 0.5871)	14 [0.557±0.115] (0.4016-0.7898)	22 [0.735±0.181] (0.4468-0.9925)	---
	IA-CA-Col	38	---	1 (0.4901)	7 [0.577±0.159] (0.3859-0.7651)	---	30 [0.699±0.118] (0.4864-0.9602)
	IA-CR+OI-Col	38	---	5 [0.572±0.238] (0.3647-0.9231)	---	13 [0.760±0.137] (0.4937-0.9798)	20 [0.705±0.165] (0.4630-0.9500)
	CA-CR+OI-Col	38	---	---	8 [0.791±0.215] (0.4080-0.9943)	11 [0.773±0.140] (0.5218-0.9874)	19 [0.740±0.173] (0.5000-0.9711)
ChR Pliocene-Holocene: Diagrams based on log-ratios of immobile major and trace elements	***{Σn} {Σprob} [%prob]***	**190**	**{5} {3.3481} [---]**	**{8} {4.4607} [3.8%]**	**{29} {18.1646} [15.7%]**	**{60} {44.8503} [33.7%]**	**{88} {62.4011} [46.8%]**
Intermediate; Verma and Verma (2013); log-ratios of immobile trace elements (tint); no figure	IA+CA-CR+OI-Col	1	1 (0.9060)	---	---	0 (0)	0 (0)
	IA-CA-CR+OI	1	---	0 (0)	1 (0.8830)	0 (0)	---
	IA-CA-Col	1	---	0 (0)	1 (0.9232)	---	0 (0)
	IA-CR+OI-Col	1	---	1 (0.7024)	---	0 (0)	0 (0)
	CA-CR+OI-Col	1	---	---	1 (0.9742)	0 (0)	0 (0)
ChR Pliocene-Holocene: Diagrams based on log-ratios of immobile trace elements	***{Σn} {Σprob} [%prob]***	**5**	**{1} {0.9060} [---]**	**{1} {0.7024} [20%]**	**{3} {2.7804} [80%]**	**{0} {0} [0%]**	**{0} {0} [0%]**

Explanation of § and Θ is in Table 5.

Table S16 Application of multidimensional diagrams for deciphering tectonic setting of Pliocene-Holocene acid magmas from the Chapala Rift (ChR) of the western Mexican Volcanic Belt (W-MVB).

Magma type, Figure name	Figure type §	Total number of samples	Number of discriminated samples				
			Arc			Within-plate	Collision
			IA+CA [$\bar{x} \pm s$] (p_{IA+CA}) Θ	IA [$\bar{x} \pm s$] [p_{IA}] Θ	CA [$\bar{x} \pm s$] [p_{CA}] Θ	CR+OI [$\bar{x} \pm s$] [p_{CR+OI}] Θ	Col [$\bar{x} \pm s$] [p_{Col}] Θ
Acid; Verma *et al.* (2012); log-ratios of all major elements (macid)	IA+CA–CR–Col	5	3 [0.822±0.253] (0.5313-0.9906)	---	---	2 [0.9575±0.0421] (0.9277, 0.9873)	0 (0)
	IA–CA–CR	5	---	1 (0.7918)	2 [0.683±0.071] (0.6329, 0.7328)	2 [0.9923±0.0053] (0.9886, 0.9961)	---
	IA–CA–Col	5	---	1 (0.7026)	2 [0.788±0.122] (0.7013, 0.8740)	---	2 [0.751±0.079] (0.6948, 0.8069)
	IA–CR–Col	5	---	2 [0.9747±0.0328] (0.9515, 0.9978)	---	3 [0.801±0.171] (0.6133-0.9478)	0 (0)
	CA–CR–Col	5	---	---	2 [0.9744±0.0333] (0.9508, 0.9979)	3 [0.751±0.272] (0.4418-0.9512)	0 (0)
ChR Pliocene-Holocene: Diagrams based on log-ratios of all major elements	***{Σn} {Σprob} [%prob]***	**25**	**{3} {2.4671} [---]**	**{4} {3.4437} [21%]**	**{6} {4.8898} [30%]**	**{10} {8.5559} [41%]**	**{2} {1.5018} [8%]**
Acid; Verma *et al.* (2013); log-ratios of all major elements (macid)	IA+CA-CR+OI-Col	5	2 [0.928±0.075] (0.8748, 0.9808)	---	---	3 [0.833±0.233] (0.5668-0.9963)	0 (0)
	IA-CA-CR+OI	5	---	0 (0)	2 [0.809±0.082] (0.7506, 0.8670)	3 [0.859±0.243] (0.5776-0.9996)	---
	IA-CA-Col	5	---	1 (0.5441)	4 [0.790±0.230] (0.4459-0.9206)	---	0 (0)
	IA-CR+OI-Col	5	---	2 [0.699±0.367] (0.4401, 0.9585)	---	3 [0.856±0.161] (0.6772-0.9896)	0 (0)
	CA-CR+OI-Col	5	---	---	2 [0.949±0.062] (0.9047, 0.9928)	3 [0.827±0.209] (0.5902-0.9871)	0 (0)
ChR Pliocene-Holocene: Diagrams based on log-ratios of all major elements	***{Σn} {Σprob} [%prob]***	**25**	**{2} {1.8556} [---]**	**{3} {1.9426} [11%]**	**{8} {6.6743} [40%]**	**{12} {10.1255} [49%]**	**{0} {0} [0%]**
Acid; Verma *et al.* (2013); log-ratios of immobile major and trace elements (mtacid)	IA+CA-CR+OI-Col	2	1 (0.8616)	---	---	0 (0)	1 (0.5711)
	IA-CA-CR+OI	2	---	0 (0)	2 [0.791±0.138] (0.6936, 0.8892)	0 (0)	---
	IA-CA-Col	2	---	0 (0)	1 (0.9126)	---	1 (0.4681)
	IA-CR+OI-Col	2	---	0 (0)	---	1 (0.4142)	1 (0.7435)
	CA-CR+OI-Col	2	---	---	2 [0.681±0.304] (0.4655, 0.8956)	0 (0)	0 (0)
ChR Pliocene-Holocene:Diagrams based on log-ratios of immobile major and trace elements	***{Σn} {Σprob} [%prob]***	**10**	**{1} {0.8616} [---]**	**{0} {0} [0%]**	**{5} {3.8564} [68%]**	**{1} {0.4142} [6%]**	**{3} {1.7827} [26%]**

Explanation of § and Θ is given in Table 5.

Table S17 Application of multidimensional diagrams for deciphering tectonic setting of Near Trench Pliocene-Holocene basic magmas from the western Mexican Volcanic Belt (W-MVB).

Figure reference; figure type; figure no.	Discrimination diagram §	Total no. of samples (%)	Predicted tectonic affinity and number of discriminated samples (%)				
			IAB	CRB+OIB	CRB	OIB	MORB
Verma *et al.* (2006); log-ratios of major elements (m2); no figure	IAB-CRB-OIB-MORB	131 (100)	21 (16.0)	---	101 (77.1)	8 (6.1)	1 (0.8)
	IAB-CRB-OIB	131 (100)	17 (13.0)	---	108 (82.4)	6 (4.6)	---
	IAB-CRB-MORB	131 (100)	14 (10.7)	---	112 (85.5)	---	5 (3.8)
	IAB-OIB-MORB	131 (100)	50 (38.2)	---	---	61 (46.6)	20 (15.3)
	CRB-OIB-MORB	131 (100)	---	---	121 (92.4)	7 (5.3)	3 (2.3)
W-MVB Near Trench Pliocene-Holocene basic rocks: Synthesis of all five diagrams of Verma et al. (2006)		**655 (100)**	**102 (15.6)**	**---**	**442 (67.5)**	**82 (12.5)**	**29 (4.4)**
Agrawal *et al.* (2008); log-ratios of immobile trace elements (t1); no figure.	IAB-CRB+OIB-MORB	38 (100)	12 (31.6)	26 (68.4)	---	---	0 (0)
	IAB-CRB-OIB	38 (100)	20 (52.6)	---	12 (31.6)	6 (15.8)	---
	IAB-CRB-MORB	38 (100)	9 (23.7)	---	29 (76.3)	---	0 (0)
	IAB-OIB-MORB	38 (100)	8 (21.1)	---	---	29 (76.3)	1 (2.6)
	CRB-OIB-MORB	38 (100)	---	---	27 (71.1)	10 (26.3)	1 (2.6)
W-MVB Near Trench Pliocene-Holocene basic rocks: Synthesis of all five diagrams of Agrawal et al. (2008)		**190 (100)**	**49 (25.8)**	**26 (---)**	**84 (44.2)**	**55 (28.9)**	**2 (1.1)**
Verma and Agrawal (2011); log-ratios of immobile major and trace elements (t2); no figure.	IAB-CRB+OIB-MORB	72 (100)	38 (52.8)	26 (36.1)	---	---	8 (11.1)
	IAB-CRB-OIB	72 (100)	38 (52.8)	---	25 (34.7)	9 (12.5)	---
	IAB-CRB-MORB	72 (100)	38 (52.8)	---	28 (38.9)	---	6 (8.3)
	IAB-OIB-MORB	72 (100)	38 (52.8)	---	---	20 (27.8)	14 (19.4)
	CRB-OIB-MORB	72 (100)	---	---	27 (37.5)	36 (50.0)	9 (12.5)
W-MVB Near Trench Pliocene-Holocene basic rocks: Synthesis of all five diagrams of Verma and Agrawal (2011)		**360 (100)**	**152 (42.2)**	**26 (---)**	**94 (26.1)**	**77 (21.4)**	**37 (10.3)**

Explanation of § is in Table 4.

Table S18 Application of multidimensional diagrams for deciphering tectonic setting of Far Trench Pliocene-Holocene basic magmas from the western Mexican Volcanic Belt (W-MVB).

Figure reference; figure type; figure no.	Discrimination diagram §	Total no. of samples (%)	Predicted tectonic affinity and number of discriminated samples (%)				
			IAB	CRB+OIB	CRB	OIB	MORB
Verma *et al.* (2006); log-ratios of major elements (m2); no figure	IAB-CRB-OIB-MORB	66 (100)	4 (6.1)	---	57 (86.4)	2 (3.0)	3 (4.5)
	IAB-CRB-OIB	66 (100)	2 (3.0)	---	62 (94.0)	2 (3.0)	---
	IAB-CRB-MORB	66 (100)	2 (3.0)	---	60 (90.9)	---	4 (6.1)
	IAB-OIB-MORB	66 (100)	9 (13.6)	---	---	41 (62.1)	16 (24.3)
	CRB-OIB-MORB	66 (100)	---	---	59 (89.4)	3 (4.5)	4 (6.1)
W-MVB Far Trench Pliocene-Holocene basic rocks: Synthesis of all five diagrams of Verma et al. (2006)		**330 (100)**	**17 (5.2)**	**---**	**238 (72.1)**	**48 (14.5)**	**27 (8.2)**
Agrawal *et al.* (2008); log-ratios of immobile trace elements (t1); no figure.	IAB-CRB+OIB-MORB	19 (100)	1 (5.3)	17 (89.5)	---	---	1 (5.3)
	IAB-CRB-OIB	19 (100)	0 (0)	---	15 (78.9)	4 (21.1)	---
	IAB-CRB-MORB	19 (100)	0 (0)	---	18 (94.7)	---	1 (5.3)
	IAB-OIB-MORB	19 (100)	1 (5.3)	---	---	17 (89.5)	1 (5.3)
	CRB-OIB-MORB	19 (100)	---	---	14 (73.7)	4 (21.1)	1 (5.3)
W-MVB Far Trench Pliocene-Holocene basic rocks: Synthesis of all five diagrams of Agrawal et al. (2008)		**95 (100)**	**2 (2.1)**	**17 (---)**	**58 (61.1)**	**31 (32.6)**	**4 (4.2)**
Verma and Agrawal (2011); log-ratios of immobile major and trace elements (t2); no figure.	IAB-CRB+OIB-MORB	35 (100)	2 (5.7)	31 (88.6)	---	---	2 (5.7)
	IAB-CRB-OIB	35 (100)	2 (5.7)	---	31 (88.6)	2 (5.7)	---
	IAB-CRB-MORB	35 (100)	1 (2.9)	---	31 (88.6)	---	3 (8.6)
	IAB-OIB-MORB *	35 (100)	1 (2.9)	---	---	30 (85.7)	4 (11.4)
	CRB-OIB-MORB	35 (100)	---	---	27 (77.1)	5 (14.3)	3 (8.6)
W-MVB Far Trench Pliocene-Holocene basic rocks: Synthesis of all five diagrams of Verma and Agrawal (2011)		**175 (100)**	**6 (3.4)**	**31 (---)**	**111 (63.4)**	**46 (26.3)**	**12 (6.9)**

Explanation of § is in Table 4.

Table S19 Application of multidimensional diagrams for deciphering tectonic setting of Near Trench Pliocene-Holocene intermediate magmas from the western Mexican Volcanic Belt (W-MVB).

Magma type, Figure name; Figure number	Figure type §	Total number of samples	Number of discriminated samples				
			Arc			Within-plate	Collision
			IA+CA [$\bar{x} \pm s$] (p_{IA+CA}) Θ	IA [$\bar{x} \pm s$] [p_{IA}] Θ	CA [$\bar{x} \pm s$] [p_{CA}] Θ	CR+OI [$\bar{x} \pm s$] [p_{CR+OI}] Θ	Col [$\bar{x} \pm s$] [p_{Col}] Θ
Intermediate; Verma and Verma (2013); log-ratios of all major elements (mint); no figure	IA+CA-CR+OI-Col	727	422 [0.722±0.122] (0.4071-0.9557)	---	---	52 [0.785±0.186] (0.4182-0.9858)	253 [0.769±0.153] (0.4303-0.9987)
	IA-CA-CR+OI	727	---	58 [0.675±0.086] (0.4300-0.8774)	579 [0.830±0.098] (0.3860-1.0000)	90 [0.808±0.173] (0.3721-0.9994)	---
	IA-CA-Col	727	---	56 [0.807±0.103] (0.4243-0.9633)	462 [0.730±0.113] (0.3594-0.9711)	---	209 [0.759±0.185] (0.3635-0.9999)
	IA-CR+OI-Col	727	---	248 [0.644±0.125] (0.3710-0.9264)	---	61 [0.775±0.184] (0.4118-0.9885)	418 [0.756±0.152] (0.4236-1.0000)
	CA-CR+OI-Col	727	---	---	477 [0.719±0.114] (0.4228-0.9760)	47 [0.754±0.186] (0.4328-0.9729)	203 [0.734±0.155] (0.3842-0.9915)
W-MVB Miocene: Diagrams based on log-ratios of major elements	***{Σn} {Σprob} [%prob]***	**3635**	**{422} {304.7410} [---]**	**{362} {244.0357} [10.9%]**	**{1518} {1160.5731} [*51.8%*]**	**{250} {196.2733} [7.2%]**	**{1083} {818.5773} [30.1%]**
Intermediate; Verma and Verma (2013); log-ratios of immobile major and trace elements (mtint); no figure	IA+CA-CR+OI-Col	328	157 [0.715±0.113] (0.4581-0.9897)	---	---	43 [0.773±0.159] (0.4528-0.9917)	128 [0.723±0.149] (0.3847-0.9886)
	IA-CA-CR+OI	328	---	26 [0.597±0.123] (0.3703-0.8979)	242 [0.685±0.133] (0.3531-0.9712)	60 [0.790±0.180] (0.3691-0.9917)	---
	IA-CA-Col	328	---	18 [0.504±0.118] (0.3593-0.7420)	186 [0.560±0.116] (0.3505-0.8939)	---	124 [0.702±0.153] (0.4202-0.9787)
	IA-CR+OI-Col	328	---	136 [0.673±0.108] (0.3829-0.9765)	---	44 [0.772±0.150] (0.4221-0.9914)	148 [0.726±0.154] (0.3968-0.9884)
	CA-CR+OI-Col	328	---	---	201 [0.863±0.135] (0.4670-0.9998)	42 [0.790±0.133] (0.4459-0.9875)	85 [0.750±0.140] (0.4209-0.9842)
W-MVB Miocene: Diagrams based on log-ratios of immobile major and trace elements	***{Σn} {Σprob} [%prob]***	**1640**	**{157} {112.1917} [---]**	**{180} {116.1365} [11.9%]**	**{629} {443.3637} [45.5%]**	**{189} {147.7653} [12.6%]**	**{485} {350.8898} [30.0%]**
Intermediate; Verma and Verma (2013); log-ratios of immobile trace elements (tint); no figure	IA+CA-CR+OI-Col	169	119 [0.762±0.155] (0.3820-0.9904)	---	---	20 [0.747±0.171] (0.4569-0.9831)	30 [0.803±0.195] (0.4769-0.9988)
	IA-CA-CR+OI	169	---	11 [0.517±0.099] (0.3857-0.6963)	139 [0.706±0.148] (0.4420-0.9695)	19 [0.801±0.137] (0.5148-0.9939)	---
	IA-CA-Col	169	---	5 [0.5257±0.0361] (0.4926-0.5867)	141 [0.690±0.117] (0.4412-0.9754)	---	23 [0.821±0.160] (0.4993-0.9998)
	IA-CR+OI-Col	169	---	90 [0.766±0.121] (0.4322-0.9507)	---	33 [0.668±0.203] (0.3514-0.9882)	46 [0.775±0.188] (0.4126-0.9994)
	CA-CR+OI-Col	169	---	---	141 [0.886±0.096] (0.4947-0.9997)	11 [0.745±0.159] (0.4541-0.9492)	17 [0.792±0.150] (0.5140-0.9940)
W-MVB Miocene: Diagrams based on log-ratios of immobile trace elements	***{Σn} {Σprob} [%prob]***	**845**	**{119} {90.7063} [---]**	**{106} {77.2814} [14.7%]**	**{421} {320.3858} [61.4%]**	**{83} {60.4156} [9.4%]**	**{116} {92.0834} [14.4%]**

Explanation of § and Θ is in Table 5.

Table S20 Application of multidimensional diagrams for deciphering tectonic setting of Far Trench Pliocene-Holocene intermediate magmas from the western Mexican Volcanic Belt (W-MVB).

Magma type, Figure name; Figure number	Figure type §	Total number of samples	Number of discriminated samples				
			Arc			Within-plate	Collision
			IA+CA [$\bar{x} \pm s$] (p_{IA+CA}) Θ	IA [$\bar{x} \pm s$] [p_{IA}] Θ	CA [$\bar{x} \pm s$] [p_{CA}] Θ	CR+OI [$\bar{x} \pm s$] [p_{CR+OI}] Θ	Col [$\bar{x} \pm s$] [p_{Col}] Θ
Intermediate; Verma and Verma (2013); log-ratios of all major elements (mint); no figure	IA+CA-CR+OI-Col	220	69 [0.704±0.155] (0.3652-0.9506)	---	---	67 [0.781±0.174] (0.4163-0.9979)	84 [0.788±0.144] (0.4158-0.9726)
	IA-CA-CR+OI	220	---	2 [0.481±0.085] (0.4205, 0.5412)	146 [0.731±0.114] (0.3707-0.9193)	72 [0.829±0.170] (0.3763-0.9978)	---
	IA-CA-Col	220	---	7 [0.612±0.175] (0.4554-0.9069)	107[0.647±0.106] (0.3821-0.8596)	---	106 [0.722±0.156] (0.3671-0.9929)
	IA-CR+OI-Col	220	---	46 [0.646±0.154] (0.3869-0.9182)	---	76 [0.764±0.185] (0.3995-0.9986)	98 [0.815±0.168] (0.3638-0.9890)
	CA-CR+OI-Col	220	---	---	77 [0.717±0.158] (0.3950-0.9380)	69 [0.735±0.190] (0.3474-0.9938)	74 [0.722±0.129] (0.4088-0.9485)
W-MVB Miocene: Diagrams based on log-ratios of major elements	***{Σn} {Σprob} [%prob]***	**1100**	**{69} {48.5831} [---]**	**{55} {34.9407} [5.1%]**	**{330} {231.2026} [33.7%]**	**{284} {220.8198} [27.2%]**	**{362} {276.1121} [34.0%]**
Intermediate; Verma and Verma (2013); log-ratios of immobile major and trace elements (mtint); no figure	IA+CA-CR+OI-Col	114	19 [0.682±0.153] (0.4492-0.9508)	---	---	49 [0.799±0.167] (0.4221-0.9846)	46 [0.747±0.163] (0.4211-0.9730)
	IA-CA-CR+OI	114	---	17 [0.588±0.213] (0.3620-0.9486)	34 [0.574±0.142] (0.3516-0.8770)	63 [0.791±0.182] (0.4468-0.9943)	---
	IA-CA-Col	114	---	9 [0.651±0.199] (0.4179-0.9109)	32 [0.621±0.127] (0.3859-0.8756)	---	73 [0.734±0.147] (0.4459-0.9745)
	IA-CR+OI-Col	114	---	18 [0.642±0.215] (0.3538-0.9327)	---	49 [0.812±0.145] (0.4726-0.9811)	47 [0.748±0.152] (0.4630-0.9728)
	CA-CR+OI-Col	114	---	---	25 [0.766±0.189] (0.4080-0.9943)	42 [0.803±0.146] (0.5218-0.9874)	47 [0.776±0.162] (0.4552-0.9913)
W-MVB Miocene: Diagrams based on log-ratios of immobile major and trace elements	***{Σn} {Σprob} [%prob]***	**570**	**{19} {12.9576} [---]**	**{44} {27.4202} [7.5%]**	**{91} {58.5421} [16.0%]**	**{203} {162.4502} [38.6%]**	**{213} {159.5590} [37.9%]**
Intermediate; Verma and Verma (2013); log-ratios of immobile trace elements (tint); no figure	IA+CA-CR+OI-Col	27	10 [0.838±0.124] (0.6558-0.9971)	---	---	13 [0.799±0.157] (0.4876-0.9743)	4 [0.885±0.173] (0.6255-0.9846)
	IA-CA-CR+OI	27	---	0 (0)	14 [0.829±0.117] (0.5703-0.9346)	13 [0.781±0.132] (0.5659-0.9756)	---
	IA-CA-Col	27	---	0 (0)	23 [0.835±0.113] (0.4908-0.9509)	---	4 [0.845±0.194] (0.5921-0.9980)
	IA-CR+OI-Col	27	---	8 [0.626±0.239] (0.4012-0.9854)	---	14 [0.839±0.124] (0.5949-0.9867)	5 [0.823±0.215] (0.5137-0.9813)
	CA-CR+OI-Col	27	---	---	14 [0.845±0.181] (0.4599-0.9994)	9 [0.746±0.066] (0.6259-0.8316)	4 [0.819±0.243] (0.4643-0.9827)
W-MVB Miocene: Diagrams based on log-ratios of immobile trace elements	***{Σn} {Σprob} [%prob]***	**135**	**{10} {8.3835} [---]**	**{8} {5.0057} [5.4%]**	**{51} {42.6369} [45.8%]**	**{49} {38.9994} [35.7%]**	**{17} {14.3088} [13.1%]**

Explanation of § and Θ is in Table 5.

Table S21 Application of multidimensional diagrams for deciphering tectonic setting of Near Trench Pliocene-Holocene acid magmas from the western Mexican Volcanic Belt (W-MVB).

Magma type, Figure name	Figure type §	Total number of samples	Number of discriminated samples				
			Arc			Within-plate	Collision
			IA+CA [$\bar{x} \pm s$] (p_{IA+CA}) Θ	IA [$\bar{x} \pm s$] [p_{IA}] Θ	CA [$\bar{x} \pm s$] [p_{CA}] Θ	CR+OI [$\bar{x} \pm s$] [p_{CR+OI}] Θ	Col [$\bar{x} \pm s$] [p_{Col}] Θ
Acid; Verma et al. (2012); All major element concentrations (macid)	(IA+CA–CR–Col)	79	67 [0.869±0.154] (0.5050-0.9953)	---	---	3 [0.955±0.075] (0.8678-0.9994)	9 [0.684±0.151] (0.5022-0.9883)
	(IA–CA–CR)	79	---	37 [0.715±0.116] (0.5014-0.9163)	39 [0.752±0.148] (0.4683-0.9982)	3 [0.9902±0.0165] (0.9712-1.0000)	---
	(IA–CA–Col)	79	---	35 [0.663±0.106] (0.4905-0.8896)	35 [0.647±0.092] (0.4913-0.8801)	---	9 [0.603±0.141] (0.4121-0.9137)
	(IA–CR–Col)	79	---	48 [0.974±0.065] (0.6729-0.9996)	---	6 [0.720±0.259] (0.4295-0.9985)	25 [0.755±0.135] (0.4999-0.9981)
	(CA–CR–Col)	79	---	---	70 [0.939±0.088] (0.4857-0.9995)	3 [0.939±0.091] (0.8343-0.9953)	6 [0.590±0.189] (0.4828-0.9726)
W-MVB Miocene: Diagrams based on all major elements	***{Σn} {Σprob} [%prob]***	**395**	**{67} {58.2003} [---]**	**{120} {96.3891} [38.4%]**	**{144} {117.7119} [*46.9%*]**	**{15} {12.9686} [4.1%]**	**{49} {34.0056} [10.6%]**
Acid; Verma et al. (2013); log-ratios of all major elements (macid)	IA+CA-CR+OI-Col	79	56 [0.884±0.162] (0.4007-0.9950)	---	---	10 [0.670±0.170] (0.4360-0.9601)	13 [0.527±0.142] (0.4223-0.9184)
	IA-CA-CR+OI	79	---	0 (0)	66 [0.788±0.151] (0.4670-0.9701)	13 [0.817±0.202] (0.4892-0.9994)	---
	IA-CA-Col	79	---	2 [0.873±0.046] (0.8405, 0.9055)	68 [0.817±0.157] (0.4898-0.9570)	---	9 [0.753±0.168] (0.4613-0.9979)
	IA-CR+OI-Col	79	---	42 [0.798±0.166] (0.4089-0.9929)	---	17 [0.614±0.148] (0.4260-0.9431)	20 [0.596±0.103] (0.4299-0.9019)
	CA-CR+OI-Col	79	---	---	67 [0.847±0.207] (0.3676-0.9989)	10 [0.671±0.159] (0.4222-0.9321)	2 [0.672±0.295] (0.4636, 0.8806)
W-MVB Miocene: Diagrams based on log-ratios of all major elements	***{Σn} {Σprob} [%prob]***	**395**	**{56} {49.5249} [---]**	**{44} {35.2542} [14.2%]**	**{201} {164.3387} [*66.1%*]**	**{50} {34.4709} [11.0%]**	**{44} {26.8824} [8.7%]**
Acid; Verma et al. (2013); log-ratios of immobile major and trace elements (mtacid)	IA+CA-CR+OI-Col	26	18 [0.644±0.145] (0.4292-0.8810)	---	---	5 [0.721±0.240] (0.5203-0.9979)	3 [0.637±0.198] (0.5041-0.8648)
	IA-CA-CR+OI	26	---	0 (0)	18 [0.798±0.086] (0.5826-0.8933)	8 [0.782±0.180] (0.3895-0.9944)	---
	IA-CA-Col	26	---	0 (0)	18 [0.702±0.098] (0.4192-0.8142)	---	8 [0.805±0.048] (0.7182-0.8879)
	IA-CR+OI-Col	26	---	2 [0.629±0.090] (0.5653, 0.6927)	---	6 [0.644±0.185] (0.4601-0.9935)	18 [0.629±0.105] (0.4963-0.9134)
	CA-CR+OI-Col	26	---	---	18 [0.704±0.132] (0.5012-0.8939)	6 [0.664±0.222] (0.4717-0.9925)	2 [0.637±0.200] (0.4952, 0.7780)
W-MVB Miocene: Diagrams based on log-ratios of immobile major and trace elements	***{Σn} {Σprob} [%prob]***	**130**	**{18} {11.5842} [---]**	**{2} {1.2580} [1.8%]**	**{54} {39.6789} [*55.8%*]**	**{25} {17.7048} [19.4%]**	**{31} {20.9441} [23.0%]**
Acid; Verma et al. (2013); log-ratios of immobile trace elements (mtacid)	IA+CA-CR+OI-Col	11	10 [0.855±0.118] (0.5611-0.9633)	---	---	1 (0.8013)	0 (0)
	IA-CA-CR+OI	11	---	0 (0)	10 [0.887±0.098] (0.7404-0.9758)	1 (0.6730)	---
	IA-CA-Col	11	---	0 (0)	11 [0.874±0.067] (0.7468-0.9551)	---	0 (0)
	IA-CR+OI-Col	11	---	3 [0.5416±0.0325]	---	2 [0.809±0.232]	6 [0.823±0.126]

				(0.5156-0.5779)		(0.6451, 0.9733)	(0.6167-0.9438)
	CA-CR+OI-Col	11	---	---	10 [0.924±0.087] (0.7108-0.9884)	1 (0.8126)	0 (0)
W-MVB Miocene: Diagrams based on log-ratios of immobile trace elements	***{Σn} {Σprob} [%prob]***	**55**	**{10} {8.5510} [---]**	**{3} {1.6247} [4%]**	**{31} {27.7154} [*77%*]**	**{5} {3.9053} [8%]**	**{6} {4.9398} [11%]**

Explanation of § and Θ is in Table 5.

Table S22 Application of multidimensional diagrams for deciphering tectonic setting of Far Trench Pliocene-Holocene acid magmas from the western Mexican Volcanic Belt (W-MVB).

Magma type, Figure name	Figure type §	Total number of samples	Number of discriminated samples				
			Arc			Within-plate CR+OI	Collision
			IA+CA [$\bar{x} \pm s$] (p_{IA+CA}) Θ	IA [$\bar{x} \pm s$] [p_{IA}] Θ	CA [$\bar{x} \pm s$] [p_{CA}] Θ	[$\bar{x} \pm s$] [p_{CR+OI}] Θ	Col [$\bar{x} \pm s$] [p_{Col}] Θ
Acid; Verma *et al.* (2012); All major element concentrations (macid)	IA+CA–CR–Col	153	84 [0.800±0.164] (0.3927-0.9906)	---	---	44 [0.888±0.109] (0.5152-0.9873)	25 [0.680±0.161] (0.3942-0.9991)
	IA–CA–CR	153	---	12 [0.580±0.086] (0.4833-0.7918)	89 [0.707±0.127] (0.4905-0.9497)	52 [0.829±0.162] (0.5361-1.0000)	---
	IA–CA–Col	153	---	5 [0.578±0.082] (0.4997-0.7026)	106 [0.685±0.117] (0.4811-0.8808)	---	42 [0.786±0.175] (0.4692-1.0000)
	IA–CR–Col	153	---	58 [0.831±0.157] (0.3972-0.9978)	---	56 [0.772±0.156] (0.3973-0.9717)	39 [0.745±0.163] (0.4321-0.9929)
	CA–CR–Col	153	---	---	90 [0.838±0.143] (0.3648-0.9979)	46 [0.696±0.142] (0.3725-0.9519)	17 [0.663±0.179] (0.3774-0.9955)
W-MVB Miocene: Diagrams based on all major elements	***{Σn} {Σprob} [%prob]***	**765**	**{84} {67.2309} [---]**	**{75} {58.0201} [12.3%]**	**{285} {211.0325} [*45.2%*]**	**{198} {157.4351} [27.0%]**	**{123} {90.3540} [15.5%]**
Acid; Verma *et al*. (2013); log-ratios of all major elements (macid)	IA+CA-CR+OI-Col	153	60 [0.811±0.131] (0.3593-0.9808)	---	---	80 [0.776±0.216] (0.3876-0.9997)	13 [0.631±0.188] (0.4229-0.9974)
	IA-CA-CR+OI	153	---	0 (0)	71 [0.804±0.152] (0.4773-0.9697)	82 [0.885±0.179] (0.4757-0.9999)	---
	IA-CA-Col	153	---	35 [0.713±0.105] (0.4713-0.8719)	93 [0.861±0.109] (0.4459-0.9743)	---	25 [0.783±0.172] (0.4310-0.9992)
	IA-CR+OI-Col	153	---	19 [0.545±0.169] (0.3638-0.9585)	---	110 [0.725±0.202] (0.3535-0.9991)	24 [0.560±0.159] (0.3541-0.9958)
	CA-CR+OI-Col	153	---	---	62 [0.836±0.136] (0.4339-0.9928)	81 [0.755±0.219] (0.3911-0.9989)	10 [0.656±0.182] (0.4487-0.9946)
W-MVB Miocene: Diagrams based on log-ratios of all major elements	***{Σn} {Σprob} [%prob]***	**765**	**{60} {48.6347} [---]**	**{54} {35.2999} [7.2%]**	**{226} {188.9761} [38.6%]**	**{353} {275.6438} [46.2%]**	**{72} {47.7687} [8.0%]**
Acid; Verma et al. (2013); log-ratios of immobile major and trace elements (mtacid)	IA+CA-CR+OI-Col	80	35 [0.716±0.130] (0.3814-0.9062)	---	---	39 [0.928±0.146] (0.5430-1.0000)	6 [0.506±0.092] (0.4135-0.6387)
	IA-CA-CR+OI	80	---	1 (0.7048)	39 [0.814±0.096] (0.5383-0.9667)	40 [0.917±0.169] (0.4869-0.9999)	---
	IA-CA-Col	80	---	1 (0.6994)	49 [0.744±0.110] (0.4904-0.9529)	---	30 [0.785±0.175] (0.4681-0.9965)
	IA-CR+OI-Col	80	---	2 [0.688±0.341] (0.4473, 0.9293)	---	41 [0.920±0.156] (0.4142-0.9999)	37 [0.568±0.094] (0.4028-0.7435)
	CA-CR+OI-Col	80	---	---	40 [0.726±0.147] (0.3879-0.9223)	39 [0.909±0.180] (0.4480-0.9999)	1(0.5986)
W-MVB Miocene: Diagrams based on log-ratios of immobile major and trace elements	***{Σn} {Σprob} [%prob]***	**400**	**{35} {25.0743} [---]**	**{4} {2.7808} [1.1%]**	**{128} {97.2706} [38.1%]**	**{159} {146.0653} [45.7%]**	**{74} {48.2061} [15.1%]**
Acid; Verma et al. (2013); log-ratios of immobile trace elements (mtacid)	IA+CA-CR+OI-Col	36	7 [0.701±0.196] (0.3988-0.9344)	---	---	28 [0.864±0.089] (0.6667-0.9726)	1 (0.4911)
	IA-CA-CR+OI	36	---	1 (0.6697)	6 [0.863±0.134] (0.6184-0.9832)	29 [0.9814±0.0236] (0.9236-1.0000)	---
	IA-CA-Col	36	---	0 (0)	25 [0.675±0.110] (0.5130-0.8983)	---	11 [0.610±0.096] (0.5108-0.8612)
	IA-CR+OI-Col	36	---	2 [0.616±0.157] (0.5051, 0.7268)	---	29 [0.930±0.071] (0.6795-0.9920)	5 [0.806±0.179] (0.6008-0.9556)
	CA-CR+OI-Col	36	---	---	8 [0.734±0.244] (0.4296-0.9818)	28 [0.850±0.095] (0.6112-0.9668)	0 (0)
W-MVB Miocene: Diagrams based on log-ratios of immobile trace elements	***{Σn} {Σprob} [%prob]***	**180**	**{7} {4.9076} [---]**	**{3} {1.9016} [1.5%]**	**{39} {27.9295} [21.8%]**	**{114} {103.4059} [69.2%]**	**{17} {11.2324} [7.5%]**

Explanation of § and Θ is in Table 5.

Table S23 Application of the appropriate version of the t test (software UDASYS: Verma et al., 2013b) to the conventional as well as log-transformed chemical data for basic volcanic rock samples from Rift and No Rift regions of the western part of the Mexican Volcanic Belt (W-MVB).

Parameter §	nA (Rift)	nB (No Rift)	df	Sign	t_calc	t_crit One−Sided	H0 One−Sided	CL_t One−Sided	t_crit Two−Sided	H0 Two−Sided	CL_t Two−Sided
$(SiO_2)_{adj}$	130	65	164.615	-	5.7900306	2.3492185	false	>99.9	2.6060401	false	>99.9
$(TiO_2)_{adj}$	130	66	194.000	+	2.2769891	2.3457356	true	98.81	2.6014374	true	97.61
$(Al_2O_3)_{adj}$	130	66	194.000	+	4.3873833	2.3457356	false	99.74	2.6014374	false	99.48
$(Fe_2O_3)_{adj}$	118	66	182.000	+	0.6558478	2.3470208	true	71.73	2.6031356	true	43.46
$(FeO)_{adj}$	130	62	188.323	+	8.6401352	2.3463230	false	>99.9	2.6022136	false	>99.9
$(MnO)_{adj}$	130	66	193.760	+	8.4298964	2.3457597	false	>99.9	2.6014693	false	>99.9
$(MgO)_{adj}$	95	64	103.146	-	7.3924617	2.3630287	false	>99.9	2.6243154	false	>99.9
$(CaO)_{adj}$	130	63	191.000	+	2.6501129	2.3460416	false	99.56	2.6018418	false	99.13
$(Na_2O)_{adj}$	130	66	194.000	-	0.2150494	2.3457356	true	<50	2.6014374	true	<50
$(K_2O)_{adj}$	93	65	69.181	-	7.7783725	2.3814477	false	>99.9	2.6487518	false	>99.9
$(P_2O_5)_{adj}$	130	66	83.711	-	4.1912873	2.3717025	false	99.92	2.6358143	false	99.83
La	65	48	50.502	-	4.7763413	2.4024769	false	99.72	2.6767319	false	99.44
Ce	63	48	50.412	-	4.5751943	2.4026168	false	99.83	2.6769184	false	99.67
Nd	52	36	38.305	-	3.7878075	2.4277287	false	99.97	2.7104371	false	99.94
Sm	50	14	14.493	-	1.0039288	2.6132265	true	83.37	2.9614045	true	66.75
Eu	50	10	10.062	-	1.8694437	2.7606040	true	95.45	3.1648523	true	90.91
Tb	50	10	58.000	+	0.6574943	2.3923637	true	70.79	2.6632656	true	41.59
Dy	43	9	29.184	+	2.7796219	2.4611384	false	99.53	2.6777969	true	90.52
Yb	50	10	45.893	+	5.5682227	2.4103882	false	>99.9	2.6872793	false	>99.9
Lu	50	10	46.461	+	5.8402965	2.4093257	false	>99.9	2.6858622	false	>99.9
Ba	64	60	60.287	-	8.9967942	2.3897929	false	>99.9	2.6598455	false	>99.9
Co	40	7	45.0	+	1.0177354	2.4121215	true	84.28	2.6895790	true	68.56
Cr	53	60	111.000	-	7.5986525	2.3603986	false	>99.9	2.6208317	false	>99.9
Cs	31	10	39.000	-	8.5897336	2.4258483	false	>99.9	2.7079232	false	>99.9
Cu	78	47	123.000	-	3.9890252	2.3570377	false	99.95	2.6163823	false	99.9
Ga	45	20	63.000	+	0.0298508	2.3869913	true	<50	2.6561197	true	<50
Hf	49	10	57.000	-	4.0647817	2.3935544	false	99.96	2.6648502	false	99.92
Nb	77	54	121.353	+	4.0208058	2.3574590	false	99.94	2.6169400	false	99.88
Ni	63	60	80.680	-	9.3675484	2.3734401	false	>99.9	2.6381197	false	>99.9
Pb	56	21	75.0	-	1.6975318	2.3770745	true	95.31	2.6429764	true	90.63
Rb	73	56	61.399	-	5.7873242	2.3886135	false	>99.9	2.6582769	false	>99.9
Sc	52	12	62.000	+	3.3882267	2.3879947	false	99.94	2.6574539	false	99.88
Sr	61	60	59.291	-	9.2434488	2.3908880	false	>99.9	2.6613023	false	>99.9
Ta	37	7	31.047	+	4.6232674	2.4526434	false	99.91	2.7438026	false	99.82
Th	51	12	12.641	-	3.1656773	2.6606934	false	99.62	3.0265497	false	99.23
U	40	10	10.256	-	2.3796805	2.7510736	true	98.1	3.1515918	true	96.19
V	66	47	111.000	+	3.9165584	2.3603986	false	99.96	2.6208317	false	99.92
Y	93	46	126.413	+	4.7522434	2.3561999	false	99.44	2.6152736	false	98.89
Zn	75	47	120.0	-	1.4382130	2.3607343	true	92.34	2.6212678	true	84.68
Zr	98	60	78.852	-	2.7197613	2.3745537	false	99.6	2.6395975	false	99.2
$\ln(TiO_2/SiO_2)$	130	66	194.000	+	2.4617395	2.3457356	false	99.27	2.6014374	true	98.53
$\ln(Al_2O_3/SiO_2)$	130	66	169.800	+	5.4326456	2.3485156	false	>99.9	2.6051110	false	>99.9
$\ln(Fe_2O_3/SiO_2)$	130	66	194.000	+	2.6774348	2.3457356	false	99.6	2.6014374	false	99.19
$\ln(FeO/SiO_2)$	130	66	172.810	+	7.6103272	2.3481269	false	>99.9	2.6045973	false	>99.9
$\ln(MnO/SiO_2)$	130	66	188.298	+	8.8366103	2.3463256	false	>99.9	2.6022170	false	>99.9
$\ln(MgO/SiO_2)$	130	66	171.263	-	2.1595725	2.3483249	true	98.39	2.6048590	true	96.78

$\ln(CaO/SiO_2)$	130	62	146.404	+	4.0434713	2.3520867	false	99.93	2.6098323	false	99.86
$\ln(Na_2O/SiO_2)$	130	66	194.000	+	0.3436395	2.3457356	true	<50	2.6014374	true	<50
$\ln(K_2O/SiO_2)$	130	66	194.000	-	4.2185660	2.3457356	false	99.85	2.6014374	false	99.7
$\ln(P_2O_5/SiO_2)$	126	66	96.370	-	2.2757586	2.3656487	true	98.75	2.6277871	true	97.49
ln(La/Th)	50	12	60.0	+	0.5103255	2.3901240	true	<50	2.6602785	true	<50
ln(Sm/Th)	50	9	34.495	+	4.6159930	2.4394400	false	99.89	2.7261072	false	99.78
ln(Yb/Th)	50	10	58.000	+	3.4478295	2.3923637	false	99.95	2.6632656	false	99.89
ln(Nb/Th)	49	11	58.000	+	3.1838333	2.3923637	false	99.88	2.6632656	false	99.77
$\ln(Nb/(TiO_2)_{adj})$	77	55	129.707	+	2.1752964	2.3554338	true	98.43	2.6142599	true	96.86
$\ln(V/(TiO_2)_{adj})$	68	47	113.000	-	2.7294828	2.3597881	false	99.63	2.6200233	false	99.26
$\ln(Y/(TiO_2)_{adj})$	93	47	72.268	+	0.5264703	2.3790421	true	<50	2.6455565	true	<50
$\ln(Zr/(TiO_2)_{adj})$	100	60	158.000	-	2.7633758	2.3501831	false	99.68	2.6073152	false	99.36
$\ln(MgO/TiO_2)_{adj}$	130	66	194.000	-	2.5902830	2.3457356	false	99.48	2.6014374	true	98.97
$\ln(P_2O_5/TiO_2)_{adj}$	127	66	191.000	-	4.4034866	2.3460416	false	99.73	2.6018418	false	99.46
$\ln(Ni/(TiO_2)_{adj})$	95	60	146.578	-	3.5304169	2.3520560	false	99.97	2.6097916	false	99.94
ln(La/Yb)	50	10	58.000	-	4.2144981	2.3923637	false	99.94	2.6632656	false	99.87
ln(Ce/Yb)	50	10	58.000	-	4.0922713	2.3923637	false	99.96	2.6632656	false	99.92
ln(Sm/Yb)	50	10	58.000	-	3.5380624	2.3923637	false	99.96	2.6632656	false	99.92
ln(Nb/Yb)	48	9	55.0	-	0.4420624	2.3960813	true	<50	2.6682150	true	<50
ln(Th/Yb)	50	10	58.000	-	3.4478295	2.3923637	false	99.95	2.6632656	false	99.89
ln(Y/Yb)	49	8	55.0	-	0.7210360	2.3960813	true	74.52	2.6682150	true	49.05
Ln(Zr/Yb)	50	10	58.000	-	3.4382060	2.3923637	false	99.95	2.6632656	false	99.89
$\{Nb/Nb^*\}_{pm}$	69	43	82.900	+	6.2653635	2.3721551	false	>99.9	2.6364148	false	>99.9
$\{Ta/Ta^*\}_{pm}$	37	7	36.282	+	7.8629005	2.4336283	false	>99.9	2.7183280	false	>99.9
$\{LILE4\_LREE3\}_E$	52	34	84.000	-	1.9420119	2.3715438	true	97.23	2.6356038	true	94.45
$\{LILE4\_HFSE4\}_E$	45	53	58.413	-	13.3595269	2.3918839	false	>99.9	2.6626272	false	>99.9
$\{LILE4\_HFSE3\}_E$	91	58	147.000	-	4.9089399	2.3519815	false	99.15	2.6096931	false	98.29
$\{LREE3\_HFSE5\}_E$	32	7	6.196	-	3.1181303	3.1096824	false	99.01	3.6597891	true	98.02
$\{LREE3\_HFSE4\}_E$	50	10	9.782	-	1.6589682	2.7751337	true	93.56	3.1850957	true	87.12

§ The subscript $_{adj}$ refers to the adjusted data from SINCLAS or IgRoCS computer program (Verma et al., 2002; Verma and Rivera-Gómez, 2013a). The outcome of the Student´s t test: One−Sided H_0 false means that this parameter for one group is either higher or lower than the other group at 99% confidence level (CL); One−Sided H_0 true means that this parameter for one group is not higher or lower than the other group at 99% confidence level; Two−Sided H_0 false means that this parameter shows a significant difference between the two areas or groups at 99% confidence level; Two−Sided H_0 true means that this parameter does not show a significant difference between the two areas or groups at 99% confidence level. Remember also that instead of "true" or "false", the outcome could have been stated, respectively, as "accept" or "reject", or even as "valid" or "invalid".

Table S24 Application of the appropriate version of the t test (software UDASYS: Verma et al., 2013b) to the conventional as well as log-transformed chemical data for intermediate volcanic rock samples from Rift and No Rift regions of the western part of the Mexican Volcanic Belt (W-MVB).

Parameter §	nA (Rift)	nB (No Rift)	df	Sign	t_calc	t_crit One−Sided	H0 One−Sided	CL_t One−Sided	t_crit Two−Sided	H0 Two−Sided	CL_t Two−Sided
$(SiO_2)_{adj}$	660	276	934.000	+	11.8258609	2.3303145	false	>99.9	2.5810544	false	>99.9
$(TiO_2)_{adj}$	501	239	327.620	-	12.7762784	2.3378080	false	>99.9	2.5909667	false	>99.9
$(Al_2O_3)_{adj}$	648	278	391.425	+	8.0834234	2.3359329	false	>99.9	2.5884896	false	>99.9
$(Fe_2O_3)_{adj}$	616	267	881.000	-	4.2915329	2.3305583	false	99.74	2.5813773	false	99.48
$(FeO)_{adj}$	571	275	382.833	-	8.8731517	2.3361491	false	>99.9	2.5887752	false	>99.9
$(MnO)_{adj}$	631	280	427.300	-	2.2691978	2.3351236	true	98.81	2.5874200	true	97.62
$(MgO)_{adj}$	617	279	360.601	-	17.7702705	2.3367561	false	>99.9	2.5895773	false	>99.9
$(CaO)_{adj}$	628	280	473.917	-	13.0311224	2.3342542	false	>99.9	2.5862705	false	>99.9
$(Na_2O)_{adj}$	660	279	937.000	+	10.6681116	2.3303016	false	>99.9	2.5810373	false	>99.9
$(K_2O)_{adj}$	489	222	279.302	-	2.1426050	2.3397969	true	98.35	2.5935936	true	96.7
$(P_2O_5)_{adj}$	593	209	422.086	-	7.3683237	2.3352328	false	>99.9	2.5875643	false	>99.9
La	170	150	167.392	-	11.6311317	2.3488365	false	>99.9	2.6055352	false	>99.9
Ce	214	136	167.454	-	11.2636481	2.3488281	false	>99.9	2.6055242	false	>99.9
Pr	85	50	55.177	-	9.2165299	2.3958388	false	>99.9	2.6678907	false	>99.9
Nd	165	118	132.736	-	8.3094673	2.3547633	false	>99.9	2.6133727	false	>99.9
Sm	157	66	74.327	-	5.7860478	2.3775512	false	>99.9	2.6435766	false	>99.9
Eu	159	59	68.786	-	5.4201446	2.3817715	false	>99.9	2.6491820	false	>99.9
Gd	87	50	62.770	-	4.7660612	2.3872188	false	99.66	2.6564222	false	99.31
Tb	195	64	73.081	-	2.6820525	2.3784434	false	99.55	2.6447614	false	99.1
Dy	155	56	66.628	+	0.9987629	2.3836100	true	83.91	2.6516249	true	67.82
Ho	160	51	55.958	+	2.5993654	2.3948414	false	99.4	2.6665630	true	98.81
Er	150	51	56.754	+	3.2178511	2.3938540	false	99.89	2.6652489	false	99.79
Tm	88	27	29.069	+	0.7912461	2.4617026	true	77.41	2.7559616	true	54.81
Yb	244	64	68.777	+	4.7205145	2.3817794	false	99.67	2.6491925	false	99.33
Lu	236	65	70.930	+	5.2060224	2.3800584	false	>99.9	2.6469063	false	>99.9
B	6	25	28.624	-	5.1605986	2.4639229	false	>99.9	2.7589436	false	>99.9
Ba	363	176	231.424	-	0.1224999	2.3425885	true	<50	2.5972803	true	<50
Be	22	12	32.000	+	4.1452739	2.4486949	false	99.97	2.7385076	false	99.94
Co	276	51	325.000	-	1.7413838	2.3379007	true	95.87	2.5910892	true	91.74
Cr	362	201	231.169	-	18.5294705	2.3426066	false	>99.9	2.5973041	false	>99.9
Cs	250	58	79.681	+	4.9268868	2.3740421	false	99.39	2.6389185	false	98.78
Cu	426	200	304.000	-	13.7826066	2.3387013	false	>99.9	2.5921466	false	>99.9
Ga	110	120	210.977	-	0.7398301	2.3441687	true	76.05	2.5993675	true	52.09
Hf	231	59	66.583	-	0.3330690	2.3836494	true	<50	2.6516773	true	<50
Li	20	19	24.399	-	2.3763765	2.4892988	true	98.72	2.7930872	true	97.43
Nb	194	160	163.166	-	13.7746014	2.3494230	false	>99.9	2.6063104	false	>99.9
Ni	403	210	219.643	-	21.8181184	2.3434629	false	>99.9	2.5984352	false	>99.9
Pb	211	130	146.723	-	10.7886901	2.3520302	false	>99.9	2.6097576	false	>99.9
Rb	447	197	306.881	+	1.8656147	2.3385850	true	96.85	2.5919930	true	93.7
Sb	13	22	33.000	+	4.3066246	2.4448100	false	99.96	2.7333006	false	99.92
Sc	270	64	96.480	+	0.8909152	2.3656031	true	81.1	2.6277267	true	62.19
Sr	386	140	151.088	-	5.5563318	2.3512822	false	>99.9	2.6087685	false	>99.9
Ta	212	55	55.086	-	5.6532236	2.3959575	false	>99.9	2.6680488	false	>99.9
Th	226	63	71.176	+	0.3980167	2.3798687	true	<50	2.6466544	true	<50
U	235	59	80.028	+	5.5575917	2.3738315	false	>99.9	2.6386391	false	>99.9
V	475	192	665.000	-	3.3963248	2.3319575	false	99.96	2.5832312	false	99.93
Y	435	187	279.201	+	1.6580749	2.3398018	true	95.08	2.5936000	true	90.16

Zn	422	205	568.264	-	6.0825926	2.3329284	false	>99.9	2.5845167	false	>99.9
Zr	444	168	244.322	+	1.9883185	2.3417285	true	97.61	2.5961445	true	95.21
$\ln(TiO_2/SiO_2)$	515	262	363.113	-	14.555156	2.3366838	false	>99.9	2.5894818	false	>99.9
$\ln(Al_2O_3/SiO_2)$	605	279	442.506	-	3.5531075	2.3348200	false	99.97	2.5870187	false	99.95
$\ln(Fe_2O_3/SiO_2)$	636	280	914.000	-	7.1002359	2.3304031	false	>99.9	2.5811718	false	>99.9
$\ln(FeO/SiO_2)$	602	280	441.341	-	9.5203211	2.3348425	false	>99.9	2.5870485	false	>99.9
$\ln(MnO/SiO_2)$	657	280	465.814	-	2.7012766	2.3343929	false	99.64	2.5864540	false	99.28
$\ln(MgO/SiO_2)$	660	280	938.000	-	16.436675	2.3302973	false	>99.9	2.5810316	false	>99.9
$\ln(CaO/SiO_2)$	660	280	938.000	-	12.106852	2.3302973	false	>99.9	2.5810316	false	>99.9
$\ln(Na_2O/SiO_2)$	658	280	436.951	+	5.3421911	2.3349285	false	>99.9	2.5871621	false	>99.9
$\ln(K_2O/SiO_2)$	485	243	292.895	-	4.7466320	2.3391711	false	99.25	2.5927670	false	98.49
$\ln(P_2O_5/SiO_2)$	603	279	447.221	-	7.7974034	2.3347300	false	>99.9	2.5868997	false	>99.9
ln(La/Th)	206	71	275.000	-	9.5772421	2.3400079	false	>99.9	2.5938722	false	>99.9
ln(Sm/Th)	216	65	83.663	-	4.0499599	2.3717291	false	99.95	2.6358496	false	99.9
ln(Yb/Th)	259	64	69.101	+	1.4505209	2.3815131	true	92.43	2.6488388	true	84.85
ln(Nb/Th)	186	62	76.296	-	9.4568748	2.3762020	false	>99.9	2.6417854	false	>99.9
$\ln(Nb/(TiO_2)_{adj})$	194	174	207.074	-	13.351518	2.3445060	false	>99.9	2.5998131	false	>99.9
$\ln(V/(TiO_2)_{adj})$	480	200	478.178	+	3.4876237	2.3341831	false	99.97	2.5861765	false	99.94
$\ln(Y/(TiO_2)_{adj})$	511	202	443.187	+	9.4626392	2.3348069	false	>99.9	2.5870014	false	>99.9
$\ln(Zr/(TiO_2)_{adj})$	500	220	718.000	+	2.9737763	2.3315360	false	99.85	2.5826729	false	99.7
$\ln(MgO/TiO_2)_{adj}$	660	280	938.000	-	7.9850896	2.3302973	false	>99.9	2.5810316	false	>99.9
$\ln(P_2O_5/TiO_2)_{adj}$	586	270	420.878	-	6.4610382	2.3352584	false	>99.9	2.5875982	false	>99.9
$\ln(Ni/(TiO_2)_{adj})$	458	210	365.683	-	19.1894459	2.3366109	false	>99.9	2.5893854	false	>99.9
ln(La/Yb)	168	62	74.669	-	8.6529507	2.3773117	false	>99.9	2.6432587	false	>99.9
ln(Ce/Yb)	146	62	65.705	-	10.2079866	2.3844337	false	>99.9	2.6527198	false	>99.9
ln(Sm/Yb)	185	59	77.889	-	9.5783299	2.3751621	false	>99.9	2.6404050	false	>99.9
ln(Nb/Yb)	170	53	62.084	-	17.3049856	2.3879089	false	>99.9	2.6573399	false	>99.9
ln(Th/Yb)	259	64	69.101	-	1.4505209	2.3815131	true	92.43	2.6488388	true	84.85
ln(Y/Yb)	276	54	102.903	-	1.6948148	2.3631168	true	95.34	2.6244321	true	90.69
ln(Zr/Yb)	250	61	68.093	-	3.2372738	2.3823486	false	99.91	2.6499488	false	99.81
$\left\{Nb/Nb^*\right\}_{pm}$	171	144	155.349	-	10.7890055	2.3505929	false	>99.9	2.6078570	false	>99.9
$\left\{Ta/Ta^*\right\}_{pm}$	144	56	60.388	-	6.7936290	2.3896834	false	>99.9	2.6596999	false	>99.9
$\{LILE4\_LREE3\}_E$	270	125	335.977	+	5.0711357	2.3375220	false	>99.9	2.5905890	false	>99.9
$\{LILE4\_HREE3\}_E$	133	50	53.639	-	3.5811565	2.3978914	false	99.96	2.6706238	false	99.92
$\{LILE4\_HFSE4\}_E$	310	170	284.550	+	1.8530686	2.3395482	true	96.75	2.5932650	true	93.51
$\{LILE4\_HFSE3\}_E$	439	220	345.658	+	0.1568639	2.3372079	true	<50	2.5901741	true	<50
$\{LREE3\_HFSE5\}_E$	144	55	63.505	-	6.9288868	2.3864972	false	>99.9	2.6554627	false	>99.9
$\{LREE3\_HFSE4\}_E$	125	63	68.576	-	9.0581953	2.3819450	false	>99.9	2.6494126	false	>99.9
$(^{87}Sr/^{86}Sr)_i$	98	38	49.145	+	0.1097709	2.4046460	true	<50	2.6796226	true	<50
$^{143}Nd/^{144}Nd$	100	11	109.000	+	2.6667734	2.3610319	false	99.56	2.6216704	false	99.12
$^{206}Pb/^{204}Pb$	58	17	73.000	+	1.2803212	2.3785023	true	89.78	2.6448396	true	79.55
$^{207}Pb/^{204}Pb$	58	17	73.000	-	0.5629180	2.3785023	true	<50	2.6448396	true	<50
$^{208}Pb/^{204}Pb$	58	17	73.000	+	0.6516589	2.3785023	true	<50	2.6448396	true	<50

For more explanation (§) see footnote of Table S23.

Table S25 Application of the appropriate version of the t test (software UDASYS: Verma et al., 2013b) to the conventional as well as log-transformed chemical data for acid volcanic rock samples from Rift and No Rift regions of the western part of the Mexican Volcanic Belt (W-MVB).

Parameter §	nA (Rift)	nB (No Rift)	df	Sign	t_calc	t_crit One−Sided	H0 One−Sided	CL_t One−Sided	t_crit Two−Sided	H0 Two−Sided	CL_t Two−Sided
$(SiO_2)_{adj}$	210	15	223.000	+	1.7405302	2.3432043	true	95.84	2.5980936	true	91.69
$(TiO_2)_{adj}$	210	15	223.000	-	1.7105829	2.3432043	true	95.57	2.5980936	true	91.15
$(Al_2O_3)_{adj}$	210	15	223.000	-	1.6514752	2.3432043	true	95.0	2.5980936	true	90.0
$(Fe_2O_3)_{adj}$	210	15	223.000	-	1.1505379	2.3432043	true	87.45	2.5980936	true	74.89
$(FeO)_{adj}$	210	15	223.000	-	1.4194322	2.3432043	true	92.14	2.5980936	true	84.28
$(MnO)_{adj}$	210	15	223.000	+	1.2966052	2.3432043	true	90.19	2.5980936	true	80.39
$(MgO)_{adj}$	134	15	14.374	-	4.7351351	2.6158585	false	99.98	2.9650071	false	99.96
$(CaO)_{adj}$	210	15	223.000	-	3.0844069	2.3432043	false	99.89	2.5980936	false	99.77
$(Na_2O)_{adj}$	210	15	223.000	+	2.1922914	2.3432043	true	98.53	2.5980936	true	97.06
$(K_2O)_{adj}$	210	15	223.000	+	2.0579677	2.3432043	true	97.96	2.5980936	true	95.92
$(P_2O_5)_{adj}$	210	15	223.000	-	2.5770254	2.3432043	false	99.47	2.5980936	true	98.94
La	107	9	114.000	+	1.9226763	2.3594910	true	97.15	2.6196300	true	94.3
Ce	89	9	96.000	+	0.2543975	2.3658027	true	<50	2.6279912	true	<50
Nd	83	6	87.000	+	2.1343695	2.3699572	true	98.22	2.6334993	true	96.44
Sm	71	5	74.000	+	1.9856869	2.3777824	true	97.46	2.6438836	true	94.92
Ba	134	9	141.000	+	5.5804748	2.3530822	false	>99.9	2.6111488	false	>99.9
Cr	74	6	5.043	-	2.5299977	3.3531124	true	97.39	4.0147183	true	94.79
Cu	66	8	72.000	-	6.7844352	2.3792428	false	>99.9	2.6458229	false	>99.9
Ga	15	7	20.0	-	2.7531251	2.5279932	false	99.39	2.8453151	true	98.77
Nb	59	5	4.162	-	0.6676722	3.6676020	true	<50	4.4838669	true	<50
Ni	72	9	8.283	-	2.2167241	2.8730334	true	97.18	3.3223308	true	94.36
Pb	81	6	85.0	+	1.4450809	2.3710263	true	92.39	2.6349266	true	84.79
Rb	119	9	126.000	+	4.0937557	2.3562988	false	99.92	2.6154045	false	99.84
Sr	155	10	9.207	-	3.3288663	2.8082699	false	99.57	3.2313838	false	99.15
V	97	8	103.000	-	1.5174405	2.3630817	true	93.39	2.6243855	true	86.78
Y	120	9	127.000	+	0.6509001	2.3560604	true	<50	2.6150890	true	<50
Zn	144	8	48.266	+	1.9437085	2.4061188	true	97.11	2.6815859	true	94.22
Zr	106	9	113.000	+	0.1300194	2.3597881	true	<50	2.6200233	true	<50
$\ln(TiO_2/SiO_2)$	210	14	222.000	-	2.0042390	2.3432805	true	97.69	2.5981943	true	95.37
$\ln(Al_2O_3/SiO_2)$	210	15	223.000	-	1.8166653	2.3432043	true	96.47	2.5980936	true	92.94
$\ln(Fe_2O_3/SiO_2)$	210	14	222.000	-	2.0495051	2.3432805	true	97.92	2.5981943	true	95.84
$\ln(FeO/SiO_2)$	210	14	222.000	-	2.1591499	2.3432805	true	98.4	2.5981943	true	96.81
$\ln(MnO/SiO_2)$	210	15	223.000	+	0.9945864	2.3432043	true	83.94	2.5980936	true	67.87
$\ln(MgO/SiO_2)$	209	14	23.939	-	5.4387056	2.4926356	false	>99.9	2.7975851	false	>99.9
$\ln(CaO/SiO_2)$	210	15	22.800	-	4.2334309	2.5015152	false	99.98	2.8095640	false	99.95
$\ln(Na_2O/SiO_2)$	210	15	223.000	+	1.0740213	2.3432043	true	85.8	2.5980936	true	71.61
$\ln(K_2O/SiO_2)$	210	15	223.000	+	2.3026270	2.3432043	true	98.89	2.5980936	true	97.78
$\ln(P_2O_5/SiO_2)$	210	14	44.251	-	6.5222054	2.4136176	false	>99.9	2.6915880	false	>99.9
$\ln(Nb/(TiO_2)_{adj})$	100	5	103.000	+	1.6566155	2.3630817	true	94.97	2.6243855	true	89.94
$\ln(V/(TiO_2)_{adj})$	95	7	32.607	-	2.2167914	2.4463066	true	98.31	2.7353062	true	96.63
$\ln(Y/(TiO_2)_{adj})$	132	9	139.000	+	2.3084878	2.3534704	true	98.88	2.6116624	true	97.76
$\ln(Zr/(TiO_2)_{adj})$	128	10	136.000	+	1.9213442	2.3540745	true	97.16	2.6124615	true	94.32
$\ln(MgO/TiO_2)_{adj}$	210	14	27.056	-	6.6486745	2.4723607	false	>99.9	2.7702845	false	>99.9
$\ln(P_2O_5/TiO_2)_{adj}$	178	15	191.000	-	2.3548244	2.3460416	false	99.02	2.6018418	true	98.05
$\ln(Ni/(TiO_2)_{adj})$	73	9	80.0	-	2.3987949	2.3738513	false	99.06	2.6386770	true	98.12
$\{LILE4\_LREE3\}_E$	77	6	81.000	-	0.6854061	2.3732503	true	72.9	2.6378679	true	45.8
$\{LILE4\_HFSE4\}_E$	71	5	74.000	+	1.6052266	2.3777824	true	94.36	2.6438836	true	88.73
$\{LILE4\_HFSE3\}_E$	111	10	119.000	+	2.4276324	2.3580816	false	99.17	2.6177640	true	98.33

For more explanation (§) see footnote of Table S23.

Table S26 Application of the appropriate version of the t test (software UDASYS: Verma et al., 2013b) to the conventional as well as log-transformed chemical data for basic volcanic rock samples from Near Trench and Far Trench regions of the western part of the Mexican Volcanic Belt (W-MVB).

Parameter §	nA (Near Trench)	nB (Far Trench)	df	Sign	t_calc	t_crit One−Sided	H0 One−Sided	CL_t One−Sided	t_crit Two−Sided	H0 Two−Sided	CL_t Two−Sided
$(SiO_2)_{adj}$	128	66	95.702	+	3.0910478	2.3659276	false	99.87	2.6281567	false	99.74
$(TiO_2)_{adj}$	130	66	194.000	-	7.8925474	2.3457356	false	>99.9	2.6014374	false	>99.9
$(Al_2O_3)_{adj}$	130	63	189.265	-	10.2249332	2.3462230	false	>99.9	2.6020815	false	>99.9
$(Fe_2O_3)_{adj}$	130	66	83.656	-	2.5251788	2.3717332	false	99.33	2.6358551	true	98.66
$(FeO)_{adj}$	129	66	103.322	-	12.1152552	2.3629656	false	>99.9	2.6242318	false	>99.9
$(MnO)_{adj}$	130	66	92.159	-	9.4150744	2.3674746	false	>99.9	2.6302074	false	>99.9
$(MgO)_{adj}$	130	65	190.984	+	11.6137795	2.3460432	false	>99.9	2.6018439	false	>99.9
$(CaO)_{adj}$	127	66	105.804	-	0.6159295	2.3620943	true	<50	2.6018418	true	45.06
$(Na_2O)_{adj}$	130	66	191.856	-	5.2303830	2.3459533	false	>99.9	2.6017251	false	>99.9
$(K_2O)_{adj}$	130	66	151.186	+	11.2329593	2.3512659	false	>99.9	2.6087469	false	>99.9
$(P_2O_5)_{adj}$	129	64	190.929	+	6.0589619	2.3460490	false	>99.9	2.6018516	false	>99.9
La	74	34	104.557	+	3.9990488	2.3625267	false	99.95	2.6236503	false	99.9
Ce	76	34	101.809	+	4.6800168	2.3635176	false	99.59	2.6249631	false	99.18
Pr	16	15	20.884	+	1.0848448	2.5188096	true	85.49	2.8329331	true	70.97
Nd	61	24	82.643	+	3.2485226	2.3722999	false	99.92	2.6366068	false	99.83
Sm	45	19	60.715	+	1.9013203	2.3893338	true	96.9	2.6592348	true	93.8
Eu	41	19	58.000	+	1.4104908	2.3923637	true	91.81	2.6632656	true	83.62
Gd	16	15	29.0	-	1.8413563	2.4620517	true	96.21	2.7563496	true	92.42
Tb	41	19	24.937	-	2.5602274	2.4855605	false	99.15	2.6632656	false	99.61
Dy	35	17	21.393	-	4.4134761	2.5138943	false	99.97	2.8262862	false	99.95
Ho	16	15	29.0	-	4.3215574	2.4620517	false	99.97	2.7563496	false	99.93
Er	16	15	29.0	-	4.4783966	2.4620517	false	99.95	2.7563496	false	99.9
Yb	39	19	56.000	-	7.8754931	2.3947889	false	>99.9	2.6664931	false	>99.9
Lu	41	19	58.000	-	6.3510983	2.3923637	false	>99.9	2.6632656	false	>99.9
Ba	110	49	116.513	+	11.0605504	2.3587672	false	>99.9	2.6186717	false	>99.9
Be	8	17	23.0	+	0.0108916	2.4998702	true	<50	2.8073604	true	<50
Co	26	21	45.0	+	0.1409466	2.4121215	true	<50	2.6895790	true	<50
Cr	98	34	129.960	+	11.1218957	2.3553764	false	>99.9	2.6141839	false	>99.9
Cs	27	16	34.966	+	5.0729246	2.4378478	false	>99.9	2.7239754	false	>99.9
Cu	87	38	114.758	+	5.3910818	2.3592693	false	>99.9	2.6193364	false	>99.9
Ga	44	20	62.000	-	4.6334073	2.3879947	false	99.76	2.6574539	false	99.51
Hf	41	19	45.017	+	6.2958594	2.4120801	false	>99.9	2.6895364	false	>99.9
Li	7	15	20.0	-	0.8182948	2.5279932	true	78.19	2.8453151	true	56.39
Nb	80	41	51.543	-	5.9336173	2.4008910	false	>99.9	2.6746190	false	>99.9
Ni	110	41	141.136	+	12.1227245	2.3530562	false	>99.9	2.6111145	false	>99.9
Pb	56	21	71.699	+	7.3660662	2.3794697	false	>99.9	2.6461243	false	>99.9
Rb	105	43	131.033	+	8.1458666	2.3551364	false	>99.9	2.6138664	false	>99.9
Sc	45	19	62.000	-	1.5098076	2.3879947	true	93.19	2.6574539	true	86.38
Sr	110	42	110.107	+	11.9179940	2.3606785	false	>99.9	2.6212023	false	>99.9
Ta	27	17	42.000	-	4.7788166	2.4184729	false	99.78	2.6980696	false	99.55
Th	43	19	59.693	+	3.8164194	2.3904413	false	99.98	2.6607080	false	99.95
U	32	17	45.514	+	4.9984702	2.4111119	false	99.59	2.6882447	false	99.18
V	80	35	45.809	-	3.7091038	2.4105470	false	99.97	2.6874912	false	99.94
Y	99	43	55.255	-	4.5017736	2.3957379	false	99.85	2.6677565	false	99.7
Zn	84	37	119.000	-	1.5033375	2.3580816	true	93.23	2.6177640	true	86.46
Zr	110	49	152.340	+	6.5749722	2.3510756	false	>99.9	2.6084953	false	>99.9

$\ln(TiO_2/SiO_2)$	130	66	194.000	-	7.2451747	2.3457356	false	>99.9	2.6014374	false	>99.9
$\ln(Al_2O_3/SiO_2)$	130	65	192.763	-	11.3055272	2.3458606	false	>99.9	2.6016026	false	>99.9
$\ln(Fe_2O_3/SiO_2)$	130	66	90.589	-	2.3408046	2.3681998	true	98.93	2.6311689	true	97.86
$\ln(FeO/SiO_2)$	130	66	194.000	-	12.5239478	2.3457356	false	>99.9	2.6014374	false	>99.9
$\ln(MnO/SiO_2)$	129	66	193.000	-	10.7080283	2.3458365	false	>99.9	2.6015708	false	>99.9
$\ln(MgO/SiO_2)$	130	66	166.777	+	10.4048262	2.3489200	false	>99.9	2.6014374	false	>99.9
$\ln(CaO/SiO_2)$	129	66	193.000	-	0.7938175	2.3458365	true	78.1	2.6015708	true	56.2
$\ln(Na_2O/SiO_2)$	130	66	193.488	-	6.1314917	2.3457871	false	>99.9	2.6015056	false	>99.9
$\ln(K_2O/SiO_2)$	130	65	192.109	+	10.0645445	2.3459274	false	>99.9	2.6016908	false	>99.9
$\ln(P_2O_5/SiO_2)$	127	65	165.976	+	4.6359326	2.3490297	false	99.52	2.6057905	false	99.04
ln(La/Th)	44	19	61.000	-	0.2753939	2.3890319	true	<50	2.6588332	true	<50
ln(Sm/Th)	34	19	23.011	-	3.5358133	2.4998008	false	99.91	2.8072502	false	99.82
ln(Yb/Th)	41	19	56.694	-	4.9227869	2.3939277	false	99.55	2.6653470	false	99.11
ln(Nb/Th)	41	16	42.201	-	9.9428844	2.4180179	false	>99.9	2.6974620	false	>99.9
$\ln(Nb/(TiO_2)_{adj})$	91	41	130.0	-	2.7532560	2.3578186	false	99.66	2.6174183	false	99.32
$\ln(V/(TiO_2)_{adj})$	80	35	80.754	+	4.4203652	2.3733962	false	99.83	2.6380615	false	99.66
$\ln(Y/(TiO_2)_{adj})$	96	38	130.295	+	6.6047132	2.3553010	false	>99.9	2.6140841	false	>99.9
$\ln(Zr/(TiO_2)_{adj})$	110	48	155.989	+	12.7121669	2.3504926	false	>99.9	2.6077245	false	>99.9
$\ln(MgO/TiO_2)_{adj}$	130	66	194.000	+	9.6688044	2.3457356	false	>99.9	2.6014374	false	>99.9
$\ln(P_2O_5/TiO_2)_{adj}$	128	65	188.989	+	10.9352501	2.3462522	false	>99.9	2.6021201	false	>99.9
$\ln(Ni/(TiO_2)_{adj})$	110	43	61.048	+	9.1288232	2.3889812	false	>99.9	2.6587659	false	>99.9
ln(La/Yb)	41	19	46.066	+	6.1086671	2.4100614	false	>99.9	2.6868434	false	>99.9
ln(Ce/Yb)	41	19	45.766	+	6.4565957	2.4106290	false	>99.9	2.6876006	false	>99.9
ln(Sm/Yb)	41	18	45.513	+	6.6017422	2.4111139	false	>99.9	2.6882473	false	>99.9
ln(Nb/Yb)	37	17	52.000	-	3.3377846	2.4002157	false	99.92	2.6737194	false	99.84
ln(Th/Yb)	41	19	56.694	+	4.9227869	2.3939277	false	99.55	2.6653470	false	99.11
ln(Y/Yb)	39	18	54.806	+	2.7312748	2.3963237	false	99.58	2.6685363	false	99.15
Ln(Zr/Yb)	41	19	47.303	+	7.0815953	2.4077975	false	>99.9	2.6838241	false	>99.9
$\left\{Nb/Nb^*\right\}_{pm}$	50	34	33.486	-	10.6898985	2.4430095	false	>99.9	2.7308882	false	>99.9
$\left\{Ta/Ta^*\right\}_{pm}$	17	17	16.697	-	11.2133323	2.5717292	false	>99.9	2.9047561	false	>99.9
$\{LILE4\_LREE3\}_E$	67	22	83.203	+	8.0373641	2.3719851	false	>99.9	2.6361892	false	>99.9
$\{LILE4\_HREE3\}_E$	16	15	15.050	+	3.4297282	2.6014688	false	99.81	2.9453249	false	99.63
$\{LILE4\_HFSE4\}_E$	89	33	102.791	+	14.2852934	2.3631575	false	>99.9	2.6244860	false	>99.9
$\{LILE4\_HFSE3\}_E$	105	38	140.028	+	13.6155469	2.3532695	false	>99.9	2.6113967	false	>99.9
$\{LREE3\_HFSE5\}_E$	27	16	27.822	+	4.8041516	2.4681133	false	99.88	2.7645742	false	99.77
$\{LREE3\_HFSE4\}_E$	41	19	57.828	+	1.5795389	2.3925654	true	94.02	2.6635340	true	88.03
$(^{87}Sr/^{86}Sr)_i$	21	21	40.0	+	2.4343974	2.4232606	false	99.03	2.7044590	true	98.05
$^{143}Nd/^{144}Nd$	21	21	32.109	-	2.5736676	2.4482596	false	99.26	2.7044590	true	98.61
$^{206}Pb/^{204}Pb$	15	13	26.0	-	2.2214617	2.4786262	true	98.24	2.7787488	true	96.48
$^{207}Pb/^{204}Pb$	15	13	26.0	-	0.4860475	2.4786262	true	<50	2.7787488	true	<50
$^{208}Pb/^{204}Pb$	15	13	26.0	-	1.0017850	2.4786262	true	83.69	2.7787488	true	67.38

For more explanation (§) see footnote of Table S23.

Table S27 Application of the appropriate version of the t test (software UDASYS: Verma et al., 2013b) to the conventional as well as log-transformed chemical data for intermediate volcanic rock samples from Near Trench and Far Trench regions of the western part of the Mexican Volcanic Belt (W-MVB).

Parameter §	nA (Near Trench)	nB (Far Trench)	df	Sign	t_calc	t_crit One−Sided	H0 One−Sided	CL_t One−Sided	t_crit Two−Sided	H0 Two−Sided	CL_t Two−Sided
$(SiO_2)_{adj}$	720	220	311.363	+	2.0064784	2.3384083	true	97.72	2.5917596	true	95.43
$(TiO_2)_{adj}$	537	178	200.001	-	15.3241212	2.3451511	false	>99.9	2.6006652	false	>99.9
$(Al_2O_3)_{adj}$	683	220	351.358	-	0.5767771	2.3370310	true	<50	2.5899405	true	<50
$(Fe_2O_3)_{adj}$	701	206	256.104	-	5.5434240	2.3410188	false	>99.9	2.5952072	false	>99.9
$(FeO)_{adj}$	662	219	256.623	-	7.8520898	2.3409890	false	>99.9	2.5951679	false	>99.9
$(MnO)_{adj}$	700	217	265.911	-	4.4160023	2.3404762	false	99.69	2.5944906	false	99.38
$(MgO)_{adj}$	558	212	292.656	+	1.1832688	2.3391815	true	88.12	2.5927809	true	76.24
$(CaO)_{adj}$	682	220	272.593	-	1.6761947	2.3401289	true	95.26	2.5940319	true	90.52
$(Na_2O)_{adj}$	719	217	934.000	+	6.7641975	2.3303145	false	>99.9	2.5810544	false	>99.9
$(K_2O)_{adj}$	570	210	249.147	-	11.8373280	2.3414297	false	>99.9	2.5957498	false	>99.9
$(P_2O_5)_{adj}$	522	202	237.887	-	5.1466226	2.3421459	false	>99.9	2.5966957	false	>99.9
La	213	144	166.648	-	15.5166077	2.3489376	false	>99.9	2.6056689	false	>99.9
Ce	237	150	166.564	-	11.9777243	2.3489491	false	>99.9	2.6056840	false	>99.9
Pr	112	14	13.217	-	5.8342837	2.6443312	false	>99.9	3.0040522	false	>99.9
Nd	220	98	105.579	-	11.2947650	2.3621714	false	>99.9	2.6231797	false	>99.9
Sm	196	38	37.811	-	8.7843542	2.4291081	false	>99.9	2.7122815	false	>99.9
Eu	194	39	38.706	-	8.1609929	2.4266360	false	>99.9	2.7089762	false	>99.9
Gd	120	15	14.114	-	5.2373534	2.6218116	false	>99.9	2.9731597	false	>99.9
Tb	235	39	39.082	-	7.5098511	2.4256315	false	>99.9	2.7076335	false	>99.9
Dy	207	28	28.310	-	6.5611874	2.4655356	false	>99.9	2.7611103	false	>99.9
Ho	200	15	14.164	-	3.5259950	2.6206431	false	99.83	2.9715590	false	99.67
Er	195	15	14.191	-	4.1947175	2.6200118	false	99.96	2.9706943	false	99.91
Tm	105	7	6.106	-	3.1664791	3.1246024	false	99.05	3.6813230	true	98.11
Yb	298	39	38.910	-	6.8035524	2.4260876	false	>99.9	2.7082431	false	>99.9
Lu	300	39	39.759	-	6.7309817	2.4238740	false	>99.9	2.7052846	false	>99.9
Ba	416	170	196.436	-	8.6978703	2.3454940	false	>99.9	2.6011183	false	>99.9
Be	28	7	6.394	-	1.3613192	3.0789983	true	89.03	3.6155964	true	78.06
Co	259	64	79.300	-	2.3262050	2.3742758	true	98.87	2.6392287	true	97.74
Cr	372	115	226.546	+	3.9985514	2.3429395	false	99.93	2.5977439	false	99.86
Cs	290	27	27.613	-	2.2410272	2.4692474	true	98.34	2.7660987	true	96.67
Cu	500	142	193.291	-	3.3605767	2.3458070	false	99.95	2.6015318	false	99.91
Ga	154	67	219.000	+	0.9817705	2.3435133	true	83.62	2.5985018	true	67.24
Hf	260	38	37.512	-	5.4930112	2.4299613	false	>99.9	2.7134224	false	>99.9
Li	34	5	37.000	+	1.1737141	2.4314572	true	87.61	2.7154234	true	75.21
Nb	225	130	131.264	-	16.0945788	2.3550851	false	>99.9	2.6137985	false	>99.9
Ni	328	131	164.727	-	6.8507188	2.3492028	false	>99.9	2.6060194	false	>99.9
Pb	213	92	108.001	-	8.5871842	2.3613571	false	>99.9	2.6221011	false	>99.9
Rb	509	169	192.836	-	6.6661473	2.3458531	false	>99.9	2.6015928	false	>99.9
Sb	30	6	34.000	-	0.6278713	2.4411640	true	<50	2.7284160	true	<50
Sc	300	30	328.000	+	0.6539383	2.3377947	true	<50	2.5909491	true	<50
Sr	347	161	186.287	-	3.5749448	2.3465425	false	99.97	2.6025036	false	99.95
Ta	238	36	35.071	-	9.3181203	2.4374983	false	>99.9	2.7235075	false	>99.9
Th	268	38	37.824	-	5.4765573	2.4290706	false	>99.9	2.7122313	false	>99.9
U	272	28	27.634	-	4.1433388	2.4691347	false	99.97	2.7659471	false	99.95
V	503	155	204.405	-	3.7468177	2.3447441	false	99.97	2.6001276	false	99.94
Y	516	161	180.735	-	9.0468923	2.3471664	false	>99.9	2.6033280	false	>99.9
Zn	463	155	199.468	-	1.2963324	2.3452016	true	90.18	2.6007320	true	80.36

Zr	460	164	191.310	-	6.5980828	2.3460095	false	>99.9	2.6017994	false	>99.9
$\ln(TiO_2/SiO_2)$	596	215	260.311	-	15.6580514	2.3407810	false	>99.9	2.5948931	false	>99.9
$\ln(Al_2O_3/SiO_2)$	716	220	299.213	-	3.0549388	2.3388995	false	99.88	2.5924084	false	99.75
$\ln(Fe_2O_3/SiO_2)$	714	220	286.901	-	5.2498449	2.3394397	false	>99.9	2.5931218	false	>99.9
$\ln(FeO/SiO_2)$	702	220	284.253	-	5.4669271	2.3395620	false	>99.9	2.5932833	false	>99.9
$\ln(MnO/SiO_2)$	717	220	284.896	-	3.3718184	2.3395321	false	99.96	2.5932438	false	99.91
$\ln(MgO/SiO_2)$	720	220	327.650	+	4.9294123	2.3378069	false	98.85	2.5909654	false	97.7
$\ln(CaO/SiO_2)$	713	220	285.042	-	0.5548102	2.3395254	true	<50	2.5932349	true	<50
$\ln(Na_2O/SiO_2)$	717	220	307.714	+	5.4852718	2.3385517	false	>99.9	2.5919491	false	>99.9
$\ln(K_2O/SiO_2)$	585	220	284.005	-	12.4033482	2.3395736	false	>99.9	2.5932986	false	>99.9
$\ln(P_2O_5/SiO_2)$	662	210	870.000	-	0.3341597	2.3306126	true	<50	2.5814494	true	<50
ln(La/Th)	245	39	50.862	-	3.7546970	2.4019199	false	99.97	2.6759897	false	99.95
ln(Sm/Th)	244	38	41.817	-	1.0039267	2.4188918	true	83.92	2.6986289	true	67.85
ln(Yb/Th)	277	38	39.190	+	1.0790416	2.4253457	true	85.65	2.7072514	true	71.29
ln(Nb/Th)	237	28	28.498	-	3.8265774	2.4645665	false	99.97	2.7598083	false	99.93
$\ln(Nb/(TiO_2)_{adj})$	390	130	518.000	-	6.4717788	2.3335750	false	>99.9	2.5853723	false	>99.9
$\ln(V/(TiO_2)_{adj})$	520	155	223.328	+	7.2486569	2.3431794	false	>99.9	2.5980607	false	>99.9
$\ln(Y/(TiO_2)_{adj})$	552	163	203.181	+	2.9619245	2.3448554	false	99.83	2.6002747	false	99.66
$\ln(Zr/(TiO_2)_{adj})$	560	170	234.179	+	6.9661496	2.3423968	false	>99.9	2.5970271	false	>99.9
$\ln(MgO/TiO_2)_{adj}$	718	220	296.841	+	13.8804415	2.3390001	false	>99.9	2.5925412	false	>99.9
$\ln(P_2O_5/TiO_2)_{adj}$	650	210	858.000	+	11.0624068	2.3306735	false	>99.9	2.5815301	false	>99.9
$\ln(Ni/(TiO_2)_{adj})$	538	147	244.730	+	3.7564557	2.3417027	false	99.97	2.5961105	false	99.94
ln(La/Yb)	174	36	208.000	-	8.9027190	2.3444248	false	>99.9	2.5997059	false	>99.9
ln(Ce/Yb)	158	33	48.429	-	15.8858976	2.4058423	false	>99.9	2.6812173	false	>99.9
ln(Sm/Yb)	198	36	232.000	-	4.6794118	2.3425481	false	99.4	2.5972269	false	98.79
ln(Nb/Yb)	162	28	27.216	-	6.9002228	2.4714570	false	>99.9	2.7690694	false	>99.9
ln(Th/Yb)	277	38	39.190	-	1.0790416	2.4253457	true	85.65	2.7072514	true	71.29
ln(Y/Yb)	299	35	38.470	-	0.7092822	2.4272756	true	73.74	2.7098313	true	47.49
Ln(Zr/Yb)	274	35	42.554	+	0.3848171	2.4172291	true	<50	2.6964088	true	<50
$\left\{Nb/Nb^*\right\}_{pm}$	194	120	127.944	-	11.9611779	2.3558388	false	>99.9	2.6147957	false	>99.9
$\left\{Ta/Ta^*\right\}_{pm}$	176	37	37.531	-	8.4608206	2.4299068	false	>99.9	2.7133496	false	>99.9
$\{LILE4\_LREE3\}_E$	300	95	203.547	+	9.1206454	2.3448220	false	>99.9	2.6002306	false	>99.9
$\{LILE4\_HREE3\}_E$	155	15	14.600	+	0.0525230	2.6108812	true	<50	2.9581953	true	<50
$\{LILE4\_HFSE4\}_E$	360	111	228.802	+	8.2165310	2.3427753	false	>99.9	2.5975270	false	>99.9
$\{LILE4\_HFSE3\}_E$	513	147	205.286	+	2.0619878	2.3446648	true	97.98	2.6000229	true	95.95
$\{LREE3\_HFSE5\}_E$	153	32	41.868	-	0.4810881	2.4187734	true	<50	2.6984708	true	<50
$\{LREE3\_HFSE4\}_E$	144	34	37.795	-	8.0785653	2.4291550	false	>99.9	2.7123442	false	>99.9
$(^{87}Sr/^{86}Sr)_i$	92	44	127.555	-	5.3276110	2.3559297	false	>99.9	2.6149160	false	>99.9
$^{143}Nd/^{144}Nd$	70	42	105.347	+	5.3222451	2.3622515	false	>99.9	2.6232858	false	>99.9
$^{206}Pb/^{204}Pb$	51	23	69.481	-	7.3774776	2.3812048	false	>99.9	2.6484291	false	>99.9
$^{207}Pb/^{204}Pb$	51	24	70.758	-	3.8682738	2.3801920	false	99.97	2.6470838	false	99.95
$^{208}Pb/^{204}Pb$	51	24	68.140	-	5.5309315	2.3823092	false	>99.9	2.6498965	false	>99.9

For more explanation (§) see footnote of Table S23.

Table S28 Application of the appropriate version of the t test (software UDASYS: Verma et al., 2013b) to the conventional as well as log-transformed chemical data for acid volcanic rock samples from Near Trench and Far Trench regions of the western part of the Mexican Volcanic Belt (W-MVB).

Parameter §	nA (Near Trench)	nB (Far Trench)	df	Sign	t_calc	t_crit One−Sided	H0 One−Sided	CL_t One−Sided	t_crit Two−Sided	H0 Two−Sided	CL_t Two−Sided
$(SiO_2)_{adj}$	75	150	195.698	-	6.8548280	2.3455665	false	>99.9	2.6012140	false	>99.9
$(TiO_2)_{adj}$	79	150	202.072	+	3.1308409	2.3449575	false	99.9	2.6004095	false	99.8
$(Al_2O_3)_{adj}$	79	150	217.784	+	7.2938324	2.3436096	false	>99.9	2.5986289	false	>99.9
$(Fe_2O_3)_{adj}$	77	150	225.000	+	3.1791637	2.3430539	false	99.92	2.5978950	false	99.83
$(FeO)_{adj}$	79	150	227.000	+	4.7078188	2.3429062	false	99.36	2.5976999	false	98.72
$(MnO)_{adj}$	75	150	222.897	+	0.9413745	2.3432121	true	82.58	2.5981039	true	65.16
$(MgO)_{adj}$	79	106	97.118	+	10.7368854	2.3653413	false	>99.9	2.6273796	false	>99.9
$(CaO)_{adj}$	79	150	227.000	+	6.8715088	2.3429062	false	>99.9	2.5976999	false	>99.9
$(Na_2O)_{adj}$	79	150	223.062	+	0.1449349	2.3431996	true	<50	2.5980874	true	<50
$(K_2O)_{adj}$	71	150	206.300	-	12.7958126	2.3445744	false	>99.9	2.5999035	false	>99.9
$(P_2O_5)_{adj}$	79	146	223.000	+	4.8200800	2.3432043	false	99.17	2.5980936	false	98.35
La	37	81	115.993	-	8.8330198	2.3589143	false	>99.9	2.6188664	false	>99.9
Ce	37	81	115.816	-	7.9098078	2.3589649	false	>99.9	2.6189333	false	>99.9
Nd	30	81	89.053	-	10.3770806	2.3689343	false	>99.9	2.6321428	false	>99.9
Sm	21	52	55.109	-	12.2545067	2.3959280	false	>99.9	2.6680095	false	>99.9
Eu	22	52	65.819	+	3.8346517	2.3843311	false	99.97	2.6525833	false	99.95
Tb	21	53	54.644	-	10.6895194	2.3965366	false	>99.9	2.6688198	false	>99.9
Dy	8	19	23.663	-	6.2362937	2.4947045	false	>99.9	2.8003749	false	>99.9
Yb	22	52	52.801	-	11.3115207	2.3990617	false	>99.9	2.6721823	false	>99.9
Lu	22	52	54.888	-	11.5911061	2.3962160	false	>99.9	2.6683929	false	>99.9
Ba	59	83	84.253	-	3.7055191	2.3714056	false	99.97	2.6354205	false	99.95
Co	27	53	36.402	+	4.2501392	2.4332595	false	99.96	2.7178345	false	99.92
Cr	30	47	75.0	+	1.5857243	2.3770745	true	94.15	2.6429764	true	88.3
Cs	19	47	52.673	-	8.6080020	2.3992437	false	>99.9	2.6724247	false	>99.9
Cu	40	36	74.000	+	2.3102313	2.3777824	true	98.82	2.6438836	true	97.63
Ga	8	14	7.987	+	2.9058608	2.8975770	false	99.01	3.3569599	true	98.03
Hf	22	50	51.196	-	11.7349062	2.4014116	false	>99.9	2.6753125	false	>99.9
Nb	20	77	76.902	-	7.0109946	2.3758011	false	>99.9	2.6412533	false	>99.9
Ni	40	39	77.000	+	1.8196631	2.3757370	true	96.37	2.6411682	true	92.73
Pb	17	72	43.407	-	3.0968802	2.4153768	false	99.83	2.6334993	true	97.05
Rb	53	76	127.000	-	6.0115539	2.3560604	false	>99.9	2.6150890	false	>99.9
Sc	29	29	28.177	+	10.3243305	2.4662262	false	>99.9	2.7620382	false	>99.9
Sr	57	105	88.718	+	5.9819734	2.3690978	false	>99.9	2.6323595	false	>99.9
Ta	17	49	48.722	-	11.4134724	2.4053486	false	>99.9	2.6805592	false	>99.9
Th	21	50	49.996	-	10.9624828	2.4032711	false	>99.9	2.6777902	false	>99.9
U	21	47	46.788	-	10.0403212	2.4087262	false	>99.9	2.6850626	false	>99.9
V	35	70	103.000	+	0.9227905	2.3630817	true	82.0	2.6243855	true	64.01
Y	55	120	141.084	-	10.0285612	2.3530661	false	>99.9	2.6111276	false	>99.9
Zn	45	105	129.253	-	6.2244010	2.3555371	false	>99.9	2.6143965	false	>99.9
Zr	54	86	118.094	-	6.8417149	2.3583280	false	>99.9	2.6180902	false	>99.9
$\ln(TiO_2/SiO_2)$	78	150	224.232	+	4.6325850	2.3431113	false	99.47	2.5979708	false	98.94
$\ln(Al_2O_3/SiO_2)$	79	150	215.771	+	7.0320467	2.3437712	false	>99.9	2.5988424	false	>99.9
$\ln(Fe_2O_3/SiO_2)$	78	150	226.000	+	3.9669717	2.3429797	false	99.94	2.5977970	false	99.87
$\ln(FeO/SiO_2)$	78	150	226.000	+	4.2630068	2.3429797	false	99.81	2.5977970	false	99.63
$\ln(MnO/SiO_2)$	78	150	224.103	+	3.8170351	2.3431210	false	99.96	2.5979837	false	99.93
$\ln(MgO/SiO_2)$	76	150	218.231	+	8.1298113	2.3435740	false	>99.9	2.5985820	false	>99.9
$\ln(CaO/SiO_2)$	78	150	213.312	+	8.4024553	2.3439729	false	>99.9	2.5991088	false	>99.9

$\ln(Na_2O/SiO_2)$	79	150	214.977	+	3.3427950	2.3438358	false	99.95	2.5989278	false	99.9
$\ln(K_2O/SiO_2)$	79	150	125.481	-	9.2508682	2.3564241	false	>99.9	2.6155703	false	>99.9
$\ln(P_2O_5/SiO_2)$	79	150	218.587	+	5.9020176	2.3435459	false	>99.9	2.5985448	false	>99.9
ln(La/Th)	23	50	68.006	+	6.8509897	2.3824221	false	>99.9	2.6500464	false	>99.9
ln(Sm/Th)	23	50	71.000	+	7.5060532	2.3800045	false	>99.9	2.6468347	false	>99.9
ln(Yb/Th)	23	50	71.000	+	4.1383926	2.3800045	false	99.94	2.6468347	false	99.88
ln(Nb/Th)	11	36	45.0	-	2.7323378	2.4121215	false	99.55	2.6895790	false	99.1
$\ln(Nb/(TiO_2)_{adj})$	26	80	93.281	-	4.4706646	2.3669720	false	99.78	2.6295411	false	99.56
$\ln(V/(TiO_2)_{adj})$	33	70	86.458	+	2.7562934	2.3702353	false	99.64	2.6338681	false	99.29
$\ln(Y/(TiO_2)_{adj})$	59	125	162.149	-	8.7105634	2.3495688	false	>99.9	2.6065032	false	>99.9
$\ln(Zr/(TiO_2)_{adj})$	59	125	180.119	-	7.9224427	2.3472379	false	>99.9	2.6034226	false	>99.9
$\ln(MgO/TiO_2)_{adj}$	77	149	223.861	+	8.9021150	2.3431392	false	>99.9	2.5980076	false	>99.9
$\ln(P_2O_5/TiO_2)_{adj}$	70	150	178.217	+	8.2824021	2.3474622	false	>99.9	2.6037189	false	>99.9
$\ln(Ni/(TiO_2)_{adj})$	42	40	66.298	+	2.5434672	2.3839015	false	99.33	2.6520124	true	98.67
ln(La/Yb)	23	52	64.781	+	3.4596239	2.3852828	false	99.95	2.6448396	false	99.51
ln(Ce/Yb)	23	52	73.000	+	3.2363680	2.3785023	false	99.91	2.6448396	false	99.82
ln(Sm/Yb)	23	52	73.000	+	6.5398426	2.3785023	false	>99.9	2.6448396	false	>99.9
ln(Nb/Yb)	11	31	10.758	-	8.6966860	2.7282238	false	>99.9	3.1198568	false	>99.9
ln(Th/Yb)	23	50	71.000	-	4.1383926	2.3800045	false	99.94	2.6468347	false	99.88
ln(Y/Yb)	23	49	29.444	+	2.0291742	2.4598850	true	97.42	2.7535209	true	94.84
Ln(Zr/Yb)	23	51	72.000	+	4.9890220	2.3792428	false	99.36	2.6458229	false	98.72
$\{Nb/Nb^*\}_{pm}$	19	43	57.465	-	0.0153254	2.3929952	true	<50	2.6641060	true	<50
$\{Ta/Ta^*\}_{pm}$	15	20	19.530	-	9.7270350	2.5332462	false	>99.9	2.8524797	false	>99.9
$\{LILE4\_LREE3\}_E$	33	50	81.000	+	4.4034828	2.3732503	false	99.84	2.6378679	false	99.68
$\{LILE4\_HFSE4\}_E$	26	50	74.000	-	1.1728847	2.3777824	true	87.77	2.6438836	true	75.55
$\{LILE4\_HFSE3\}_E$	51	72	121.000	-	0.8947468	2.3575509	true	81.24	2.6170615	true	62.48
$\{LREE3\_HFSE5\}_E$	19	49	66.000	+	2.4081471	2.3841680	false	99.06	2.6523665	true	98.12
$\{LREE3\_HFSE4\}_E$	23	50	71.000	-	4.6502793	2.3800045	false	99.71	2.6468347	false	99.42
$(^{87}Sr/^{86}Sr)_i$	13	27	13.452	+	0.2367636	2.6381019	true	<50	2.9954985	true	<50
$^{143}Nd/^{144}Nd$	13	28	39.000	-	0.2024004	2.4258483	true	<50	2.7079232	true	<50

For more explanation (§) see footnote of Table S23.

Apéndice III

Verma S.P., **Rivera-Gómez, M.A.**, Díaz-González, L., Quiroz-Ruiz, A., 2016b. Log-ratio transformed major element based multidimensional classification for altered High-Mg igneous rocks. Geochemistry, Geophysics, Geosystems, 17: doi:10.1002/2016GC006652.

Contiene un suplemento de 44 páginas así como un README of 9 páginas.

AGU PUBLICATIONS

Geochemistry, Geophysics, Geosystems

RESEARCH ARTICLE
10.1002/2016GC006652

Log-ratio transformed major element based multidimensional classification for altered High-Mg igneous rocks

Surendra P. Verma[1], M. Abdelaly Rivera-Gómez[2], Lorena Díaz-González[3], and Alfredo Quiroz-Ruiz[1]

[1]Instituto de Energías Renovables, Universidad Nacional Autónoma de México, Temixco, Mexico, [2]Posgrado en Ingeniería, Instituto de Energías Renovables, Universidad Nacional Autónoma de México, Temixco, Mexico, [3]Centro de Investigación en Ciencias, Instituto de Investigación en Ciencias Básicas y Aplicadas, Universidad Autónoma del Estado de Morelos, Cuernavaca, Mexico

Abstract A new multidimensional classification scheme consistent with the chemical classification of the International Union of Geological Sciences (IUGS) is proposed for the nomenclature of High-Mg altered rocks. Our procedure is based on an extensive database of major element (SiO_2, TiO_2, Al_2O_3, $Fe_2O_3^t$, MnO, MgO, CaO, Na_2O, K_2O, and P_2O_5) compositions of a total of 33,868 (920 High-Mg and 32,948 "Common") relatively fresh igneous rock samples. The database consisting of these multinormally distributed samples in terms of their isometric log-ratios was used to propose a set of 11 discriminant functions and 6 diagrams to facilitate High-Mg rock classification. The multinormality required by linear discriminant and canonical analysis was ascertained by a new computer program DOMuDaF. One multidimensional function can distinguish the High-Mg and Common igneous rocks with high percent success values of about 86.4% and 98.9%, respectively. Similarly, from 10 discriminant functions the High-Mg rocks can also be classified as one of the four rock types (komatiite, meimechite, picrite, and boninite), with high success values of about 88%–100%. Satisfactory functioning of this new classification scheme was confirmed by seven independent tests. Five further case studies involving application to highly altered rocks illustrate the usefulness of our proposal. A computer program HMgClaMSys was written to efficiently apply the proposed classification scheme, which will be available for online processing of igneous rock compositional data. Monte Carlo simulation modeling and mass-balance computations confirmed the robustness of our classification with respect to analytical errors and postemplacement compositional changes.

Key Points:
- The first log-ratio transformed major element discriminant function for High-Mg and Common rock subdivision
- The first 10 log-ratio transformed discriminant functions for High-Mg rock fourfold subdivision
- Highly robust performance of the new classification scheme for altered rocks

Supporting Information:
- Supporting Information S1
- Supporting Information S2

Correspondence to:
S. P. Verma,
spv@ier.unam.mx

Citation:
Verma, S. P., M. A. Rivera-Gómez, L. Díaz-González, and A. Quiroz-Ruiz (2016), Log-ratio transformed major element based multidimensional classification for altered High-Mg igneous rocks, *Geochem. Geophys. Geosyst.*, *17*, doi:10.1002/2016GC006652.

Received 15 SEP 2016
Accepted 13 NOV 2016
Accepted article online 17 NOV 2016

1. Introduction

The International Union of Geological Sciences (IUGS) has proposed a widely used classification system for High-Mg igneous rocks [*Le Bas*, 2000]. A suitable computer program IgRoCS is available for this classification of relatively fresh igneous rocks [*Verma and Rivera-Gómez*, 2013], which, besides the use of measured FeO and Fe_2O_3 concentrations, allows subdivision of total Fe as the two oxidation varieties [*Le Maitre*, 1976; *Middlemost*, 1989] and is fully consistent with the IUGS scheme. Additionally, IgRoCS provides highly precise and accurate CIPW norms [*Verma et al*., 2003].

The classification of High-Mg rocks has to be achieved prior to the use of the TAS (total alkalis versus silica) diagram [*Le Bas*, 2000]. Four different rock types are recognized in the category of High-Mg rocks [*Le Bas*, 2000]: komatiite ($MgO > 18\%$; $30\% < SiO_2 < 52\%$; $Na_2O + K_2O < 2\%$; and $TiO_2 < 1\%$); meimechite ($MgO > 18\%$; $30\% < SiO_2 < 52\%$; $Na_2O + K_2O < 2\%$; and $TiO_2 > 1\%$); picrite ($MgO > 12\%$; $30\% < SiO_2 < 52\%$; and $Na_2O + K_2O < 3\%$); and boninite ($MgO > 8\%$; $SiO_2 > 52\%$; and $TiO_2 < 0.5\%$). Although this purely chemical classification was criticized by *Kerr and Arndt* [2001], we believe in the reply of *Le Bas* [2001], a small part of which is reproduced here (in *italics*): *They (Kerr and Arndt) advocate a path of classification that emphasizes textural features, here the spinifex texture. The majority of the Subcommission took the view that for volcanic rocks, in which the mineralogical mode could not be estimated, chemical composition was the next best property to consider, with textural features a further consideration. The Subcommission also took the view that one aspect of the high-Mg rocks was the distinction of komatiite from picrite (the meimechites and picrobasalts need not concern us here)*. Furthermore, in this debate, *Le Bas* [2001] went on to conclude that *This reply is clearly not going to satisfy Kerr & Arndt. But trying to improve the definition of one particular rock without considering the adjacent rocks in a classification scheme is not a good solution*. . .

Thus, the criteria set for this High-Mg classification are based on the concentrations of MgO, SiO_2, Na_2O+K_2O, and TiO_2 [*Le Bas*, 2000]. However, all compositional data, by definition, are characterized by constant sum and closure problems [e.g., *Chayes*, 1960, 1971; *Aitchison*, 1986, 1999; *Verma*, 2015a]. Further, the compositions are susceptible to postemplacement alteration processes, which are likely to affect some or all of these elements. Therefore, the IUGS scheme is unlikely to provide the prealteration rock names when altered igneous rocks have to be classified. This is because only the postalteration compositions can be measured, with no hope of arriving at the prealteration concentrations from the classical approach. Thus, prealteration concentrations cannot be inferred. Further, due to the constant sum and closure problems [e.g., *Aitchison*, 1999], the so-called immobile elements are also affected to some extent from changes in the more mobile elements [e.g., *Aitchison*, 1986; also section 4.2 below]. Therefore, certain statistically coherent solutions for handling compositional data must be used [e.g., *Aitchison*, 1984, 1986, 1999; *Egozcue et al*., 2003; *Verma*, 2015a].

For altered rocks, the old schemes proposed by *Floyd and Winchester* [1975, 1978] and *Winchester and Floyd* [1976, 1977] cannot be used, because the High-Mg rock names were not included by these authors and the IUGS criteria for subdivision of High-Mg and Common altered igneous rocks were not available at that time. Similar reasons are valid for the newer schemes such as *Hastie et al*. [2007]. Therefore, there is still a need to provide a nomenclature to High-Mg altered igneous rocks that would be consistent with the IUGS.

We propose a statistically coherent solution to the problem of High-Mg rocks in the multidimensional space of log-ratios of all major elements (SiO_2, TiO_2, Al_2O_3, $Fe_2O_3^t$, MnO, MgO, CaO, Na_2O, K_2O, and P_2O_5). The subdivision of "High-Mg" and "Common" rocks is first achieved through the multivariate technique of linear discriminant analysis (LDA), which provides the appropriate discriminant functions for separating different groups or classes. Then, the High-Mg rocks are classified as four rock types (komatiite, meimechite, picrite, and boninite) from the LDA. Although the nomenclature of "High-Mg" rocks is the same as previously proposed [*Le Bas*, 2000], the name "Common" is used here as a collective term for all those rocks (e.g., basalt, andesite, gabbro, microgabbro, etc.) that are not classified as High-Mg rocks. When equivalent multidimensional functions are obtained from a fresh High-Mg and Common rock database, they can be used to explore the prealteration compositions of altered rocks in the multidimensional space. The only requirement is that the discriminant functions be robust in terms of log-ratios.

Thus, the new multidimensional scheme is evaluated from fresh rocks not included in the original database (section 3.3) and its application to altered rocks is suggested because the new scheme provides significant differences among the multidimensional and IUGS rock names (section 3.4). From Monte Carlo simulations and actual mass-balance log-transformed computations, the scheme is shown to be more robust when dealing analytical errors and postemplacement compositional changes as compared to the original IUGS scheme. Nevertheless, the new scheme is consistent with the IUGS nomenclature because the fresh rock names for the multidimensional procedure were based on the IUGS scheme [*Le Bas*, 2000].

2. Methods

Our method is illustrated schematically in supporting information Figure S1. The relevant steps are explained in this section.

2.1. Database

A worldwide representative database of major element compositions of igneous rocks, including some cumulate rocks, was established. The inclusion of some cumulate rocks is justified because the chemical nomenclature does not carry any genetic connotation [*Le Bas et al*., 1986]. The locations are schematically presented in Figure 1 for High-Mg igneous rocks and supporting information Figure S2 for Common igneous rocks (see supporting information data available for downloading from the journal website). The literature sources of the High-Mg rocks are summarized in supporting information Table S1 and are listed in the supporting information because these references are too many (around 140). On the other hand, although the sources of data for Common igneous rocks are too numerous to list them in this paper, a complete list of these references is available from our website http://tlaloc.ier.unam.mx/index.html. Nevertheless, the database is an updated version of the databases used by *Verma et al*. [2006, 2013], *Verma and Verma* [2013],

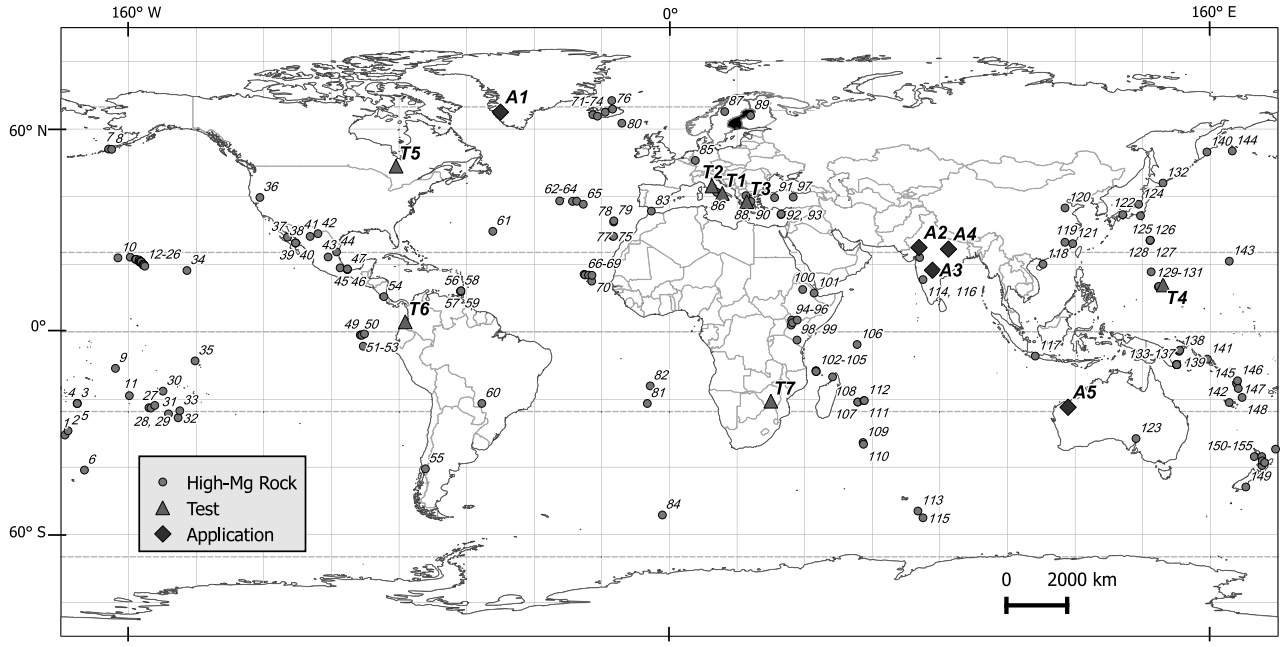

Figure 1. Schematic map for High-Mg rock sample locations. The location numbers are listed in supporting information Table S1 and the corresponding references are also in the supporting information file. The locations of Test (T1–T7) and Application (A1–A5) studies are also shown.

and *Verma* [2015b]; these authors provided the relevant literature references from which their databases were prepared.

We refrained from using the available databases such as GEOROC for the following reasons. *Agrawal and Verma* [2007] were the first to show that an indiscriminate use of GEOROC can lead to serious problems. In this critique, they pointed out that *Vermeesch* [2007] used the GEOROC database without even ascertaining if the rock names were based on the major element data [*Le Bas et al*., 1986]. More recently, *Rivera-Gómez and Verma* [2016] presented an actual case of Tongan arc data and documented the difficulties in using compiled data without critically examining the original papers from which the data were compiled. However, we have recently resorted to GEOROC database for consulting the relevant additional literature references not already compiled in our database, without actually using the geochemical data from GEOROC.

The adjustment of major elements to 100% on an anhydrous basis with total Fe as $Fe_2O_3^t$ was first carried out from equations listed in supporting information Table S2. The use of Fe as FeO^t will make no difference in the final result. The adjusted data were then used to obtain isometric log-ratio (ilr) transformed values from equations of supporting information Table S3. The ilr transformation was proposed by *Egozcue et al*. [2003] as a better alternative to the conventional additive and centered log-ratios [*Aitchison*, 1986]. The ilr transformation is based on the geometric mean as the numerator and individual compositional variables as denominators (supporting information Table S3). The log-ratio transformations would render the compositional data to comply with a normal distribution, provided no outlying observations were present [*Verma*, 2015a].

LDA [*Agrawal*, 1999; *Verma*, 2015a] was used for handling of ilr transformed data. However, multinormality is required for the LDA [e.g., *Morrison*, 1990]. The compiled samples were counted after the separation of multivariate discordant outliers in the log-ratio space represented in supporting information Table S3. Therefore, the log-ratio variables were considered as multinormally distributed [e.g., *Rencher*, 2002; *Verma*, 2015a].

In spite of the worldwide coverage (Figure 1), the number of analyses for High-Mg rocks, especially the relatively fresh ones used for this proposal, was still limited. Further, even fewer samples with complete major and trace element data were available. Therefore, combined major and trace element data could not be used in this study. This limitation would be overcome when complete (major and trace element) analyses

for more samples of relatively recent (Neogene) High-Mg fresh rocks become available in future. Nevertheless, the proposed scheme based on major elements works well as shown in this paper.

2.2. Computer Program for Multivariate Discordancy and Normality

The computer program used for achieving the required multinormality [*Morrison*, 1990] had to be developed as a part of the present study. The available technique of *Wilks* [1963] for multivariate discordant outliers was not applicable to our data, because the critical values are available for sample sizes up to 500 only [*Rencher*, 2002]. Even for these sizes, only 20 sample sizes (5, 6, 7, 8, 9, 10, 12, 14, 16, 18, 20, 25, 30, 35, 40, 45, 50, 100, 200, and 500) were actually covered, which, in terms of the statistical terminology, are 5(1)10(2)20(5)50, 100, 200, and 500.

Therefore, a transformation of the Wilks´ statistic *w* [*Wilks*, 1963] to the well-known F-test was adopted, and a suitable computer program DOMuDaF (Discordant Outlier from Multivariate Data through F-test of *w*) was written in Java (supporting information Figure S3). An example file of High-Mg komatiite ultrabasic rocks (total number of samples n = 35; supporting information Table S4) was used to illustrate the application of DOMuDaF for the detection and separation of multivariate discordant outliers in the multivariate domain of ilr. These data were compiled from several sources [*Lipman et al*., 1990; *Révillon et al*., 1999; *Upton et al*., 2000; *Snow*, 2002; *Schaaf et al*., 2005; *Bonadiman et al*., 2011; *Spice et al*., 2016]. Instead of the measured compositions, it is necessary to consider the log-transformed data [e.g., *Aitchison*, 1986; *Agrawal and Verma*, 2007; *Verma*, 2012, 2015a; *Verma and Armstrong-Altrin*, 2016]. Thus, the discordant outlier-free databases for the High-Mg and Common rocks were prepared. To apply the program DOMuDaF, the input file is validated for possible typographical errors and completeness of the data. After correctly reading the major element (M) data (supporting information Table S4), DOMuDaF adjusts them to 100% on an anhydrous basis (supporting information Table S5) from the equations listed in supporting information Table S2. These data are then converted to ilr values (supporting information Table S6) from the equations of supporting information Table S3. The Wilks statistic for each sample is then calculated as the F statistic (F_i) for the application of the F-test to the highest value max(F_i) by comparing it with the critical value $CV_{99.9}$ at the very strict 99.9% confidence level (supporting information Figure S3). Three samples were detected and separated as multivariate discordant outliers identified by an asterisk in supporting information Table S6. Their discordancy may be due to several factors, which cannot be ascertained without more knowledge of random and systematic errors of the analytical data. The complete operation of iterations 1–4 is summarized in supporting information Table S7. The last iteration number 4 did not detect the highest statistic value as discordant (see "false" in supporting information Table S7). Thus, out of a total of 35 samples (supporting information Tables S5 and S6), 32 were used for further analysis. This operation was repeated for the entire database and the multivariate discordant outlier-free database (Figure 1 and supporting information Figure S2 and Table S1) was obtained.

2.3. Linear Discriminant and Canonical Analysis

The multinormally distributed ilr data for major elements (designated M) were used for the application of the LDA and canonical analysis. The prior classification probabilities were assumed to be the same for all groups. The posterior probability values for individual samples were calculated from the method outlined by *Agrawal* [1999] and *Verma and Agrawal* [2011] and used in this work to decide the classification field in which a given sample will plot. An example of the equations for two classes is summarized as equations (S1)–(S6) in the supporting information data file from *Verma and Armstrong-Altrin* [2016]. The results are described in the following section. The probability equations corresponding to three classes or groups were presented by *Verma and Agrawal* [2011] and are not repeated here.

2.4. Computer Program for High-Mg and Common Rock Subdivision and High-Mg Classification Into Four Groups for Altered Igneous Rocks

For an efficient application of the new multidimensional scheme, a computer program HMgClaMSys (High-Mg Classification Major element based System) was written in Java (supporting information Figure S4). The first part of the program concerning data validation and transformation (supporting information Tables S2 and S3) is the same as in DOMuDaF (supporting information Figure S3). For igneous rocks, the first decision is on whether a particular rock is High-Mg or Common, for which the respective probability values ($p_{(HMg)M}$ and $p_{(Com)M}$) for major elements (M) are calculated (equations (S1)–(S6)) and compared. If the rock is decided to be a High-Mg type, the probability for the High-Mg rock should be greater than that for the Common

(igneous) rock, i.e., $p_{(HMg)M} > p_{(Com)M}$. Consequently, further calculations are carried out to determine the probability values for the four rock types, viz., komatiite (p_{kom}), meimechite (p_{mei}), picrite (p_{pic}), and boninite (p_{bon}), as a synthesis of 5 diagrams and 10 discriminant function scores.

For access to our proposed scheme, we have made HMgClaMSys available to all potential users through our website http://tlaloc.ier.unam.mx/index.html (currently under improvement *but functional*). Anyone can use our software after the registration onto this website. Nevertheless, the complete information but with rounded coefficients, is also presented in this work for those who wish to construct their own program.

3. Results

3.1. Discriminant Function Based on Major Elements for High-Mg and Common Igneous Rock Subdivision

For the subdivision of these two primary types of igneous rocks, 920 samples of High-Mg and 32,948 of Common rocks were used for obtaining the discriminant function. The Common rocks do not possess the major element characteristics of the High-Mg rocks [*Le Bas*, 2000]. However, we are interested in deciphering the appropriate function in the multidimensional space of ilr values.

In order to better understand the role of the nine transformed parameters ($ilr1_{TiM}$ to $ilr9_{PM}$), we applied both Wilks´ lambda and F statistic tests to the data set. These tests showed that all nine parameters are statistically significant at an extremely low significance level approaching 0.000000 (supporting information Table S8; i.e., the confidence level approaching 100%). In other words, all log-ratio parameters should be used for obtaining the multidimensional discriminant function.

The discriminant function for the classification of the High-Mg and Common rocks $DF_{(HMg-Com)M}$ was as follows (equation (1) assuming equal probability for each class in the LDA; for simplicity, approximate coefficients from the canonical analysis rounded arbitrarily to four decimal places are included):

$$DF_{(HMg-Com)M} = (7.3517 \times ilr1_{TiM}) + (10.3179 \times ilr2_{AlM}) + (3.8554 \times ilr3_{FeM}) + (4.5485 \times ilr4_{MnM}) + (3.5601 \times ilr5_{MgM}) + (5.9130 \times ilr6_{CaM}) + (5.8599 \times ilr7_{NaM}) + (4.7085 \times ilr8_{KM}) + (4.6514 \times ilr9_{PM}) - 6.2604 \quad (1)$$

This function was plotted in Figure 2a for all samples of our database, which were used in the LDA for obtaining the function (equation (1)). The classification field boundary at the $DF_{(HMg-Com)M}$ value of about +2.0447 is also shown for reference. Out of 920 samples of the High-Mg rocks, 795 were correctly classified as High-Mg and 125 as Common rocks, whereas out of 32948 samples of the Common rocks, 32,579 were deemed to be Common and the remainder (369) as High-Mg rocks. In terms of the correct classification, the above information gives percent success values of about 86.41% and 98.88% for the High-Mg and Common rocks, respectively. The distribution of the 125 wrongly classified High-Mg rock samples out of 920 samples was as follows: none of the 76 komatiites nor of 172 meimechites was wrongly classified; by contrast, 114 samples of picrite from 546 samples and 11 samples of boninite from 126 samples were misclassified.

Two histograms of the $DF_{(HMg-Com)M}$ variable ($DF_{(HMg)M}$ for the High-Mg rocks; Figure 2b; and $DF_{(Com)M}$ for the Common rocks; Figure 2c) graphically illustrate these misclassifications. It should also be clear at this point that because the original IUGS classification [*Le Bas*, 2000] was used for assigning categories or classes to the database, this fresh rock nomenclature by definition will always be 100% correct. On the other hand, the multidimensional function will always provide lesser or at most equal to this maximum value of 100%. The LDA and canonical analysis optimize the functions so that the total number of correctly classified samples from the different groups (and not the individual percentages) is maximized. Thus, the correct percentages of the larger groups are generally (not always) higher than the smaller groups. In this case (Figures 2a–2c), the misclassification was 125 samples of the original High-Mg rocks (amounting to about 13.6% wrong classification for the smaller group) and 369 of the Common rocks (equivalent to about 1.12% of the larger group). However, only a total of 494 out of 33,868 samples (equivalent to about 1.46%) were misclassified. In this context, we may mention that, when the initial database containing multivariate discordant outliers was used, the total number of misclassified samples was much higher (922 samples; 154 of High-Mg and 768 of Common rocks; equivalent to 2.48%). Therefore, the use of discordant outlier-free databases improves the success rates. Finally, besides the discriminant function (equation (1)), probability of individual

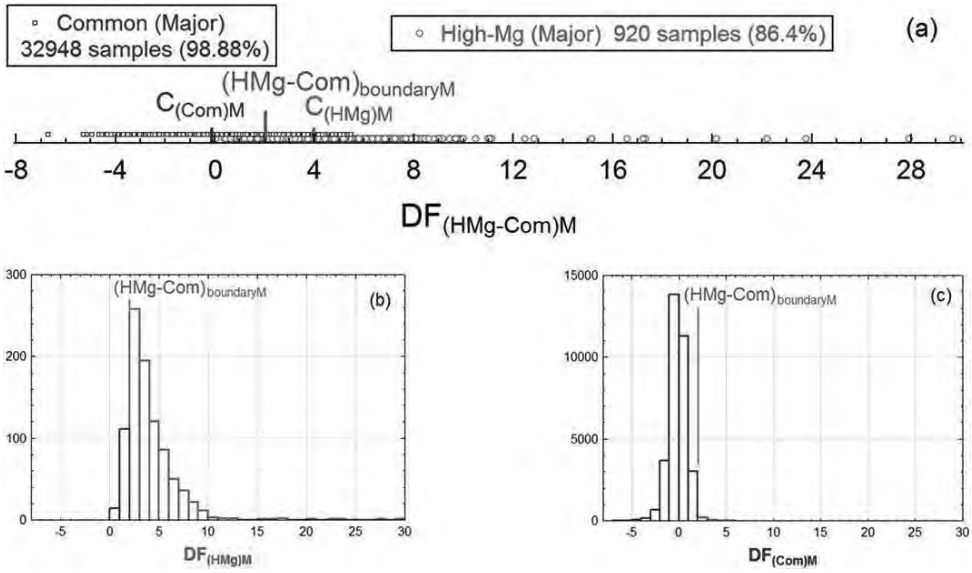

Figure 2. Discriminant function $DF_{(HMg-Com)M}$ for High-Mg (HMg) and Common (Com) rock subdivision based on ilr-transformed major element (M) compositions. The symbols are shown as insets. The percent success values for the High-Mg and Common rocks are about 88.4% and 98.88%, respectively. The respective group centroids $C_{(HMg)M}$ and $C_{(Com)M}$ are about +3.9783 and −0.1111, with the classification field boundary $(HMg-Com)_{boundaryM}$ located at about +2.0447. (a) Multidimensional diagram; (b) Histogram for the High-Mg rocks $DF_{(HMg)M}$; and (c) Histogram for the Common rocks $DF_{(Com)M}$.

samples to belong to any of the two classes—High-Mg and Common rocks—can also be calculated from equations (S1)–(S6) listed in the supporting information file.

3.2 Classification (Subdivision) of High-Mg Rocks Into Four Varieties

The High-Mg rocks (920 samples) were divided into four types [*Le Bas*, 2000] as follows: komatiite (76), meimechite (172), picrite (546), and boninite (126). The discriminant functions were calculated from equations (2)–(11) listed in Table 1. They were used for obtaining the discriminant functions in five diagrams (Figures 3a–3e) in order to separate them as different High-Mg rock classes. Probability-based field boundaries (Figures 3a–3e) were also calculated (supporting information Table S9). The correct as well as incorrect classification of High-Mg samples from the database for constructing the diagrams (Figures 3a–3e) is presented in supporting information Table S10. The correct classification or percent success values were generally high ranging from about 91% to 100% (supporting information Table S10).

A summary of classification (correct and incorrect) from all five diagrams (Figures 3a–3e) can now be prepared for each High-Mg rock sample in terms of probability values for each classification field, depending on the distances from the three centroids. To illustrate the probability concept, we will first concentrate on a single sample UPSJ0004 (CB2-10 of *Upton et al.* [2000]) shown as a filled rhombus in Figures 3a–3e. The probability values for this sample corresponding to the three fields in Figure 3a are listed in the first row of supporting information Table S11; the highest value of about 0.9971 is for the combined komatiite + meimechite field whereas the smaller value of about 0.0029 is for the field of picrite and the third field of boninite shows close to 0.000000. Similarly, the highest probability values correspond to the komatiite field in the other three diagrams (Figures 3b–3d). In the final diagram (Figure 3e), the komatiite field is absent and the meimechite field shows the highest probability value of about 0.9974 for this sample, with the picrite field indicating a very small value of about 0.0026 (supporting information Table S11). The final probability synthesis of the five diagrams (Figures 3a–3e) presented in the next three rows of supporting information Table S11 clearly shows that the sample CB2-10 with the highest probability of about 74% for the komatiite field can be assigned to this field, which is consistent with its IUGS classification.

This procedure was repeated for all samples of a given rock group. The results for the High-Mg rocks of our database are summarized in supporting information Table S12. The incorrect classification was as follows: 9 samples of komatiite out of 76 samples; 4 samples of meimechite out of 160; 35 samples of picrite out of

546; and no sample of boninite out of 126. The correct classification percentages were, therefore, as follows: about 88% for komatiite, 98% for meimechite, 94% for picrite, and 100% for boninite (supporting information Table S12). Thus, the new classification scheme for the High-Mg subdivision is well documented and can therefore be used for further testing and applications.

For the evaluation from relatively fresh rocks, the data for High-Mg rocks (for approximate locations see T1–T7 in Figure 1) were compiled from the following sources: T1–*Beccaluva et al*. [2002] from Mount Vulture, southern Italy; T2–*Bianchini et al*. [2008] from the rifted Apennines/Adriatic domain, Italy; T3–*Tsikouras et al*. [2008] from Pelagonian continental margin, Greece; T4–*Bloomer and Hawkins* [1987] from the Mariana Trench; T5–*Arndt* [1986] from the Abitibi Greenstone Belt, Canada; T6–*Révillon et al*. [2000] from the Gorgona Island, Colombia; and T7–*Shimizu et al*. [2005] from the Belingwe Greenstone Belt, Zimbabwe. The results are shown graphically in supporting information Figures S4 and S6a–S6e and summarized in Tables 2–5 and supporting information Tables S13–S36.

For the application to altered rocks, the data for the IUGS-classified High-Mg rocks (for locations see A1–A5 in Figure 1) were from the following sources: A1–*Polat et al*. [2002] from Isua Greenstone Belt, West Greenland; A2–*Ahmad and Tarney* [1994] from Aravalli volcanics, Rajasthan, India; A3–*Manikyamba et al*. [2005] from Gadwal Greenstone Belt, India; A4–*Srivastava* [2013] from Mahakoshal Supracrustal Belt, India; and A5–*Smithies* [2002] from Mallina Basin, Pilbara Craton, Northwest Australia. The results are summarized in Table 6 and supporting information Figures S7, S8a–S8e, and Tables S37–S40.

Finally, for demonstrating the robustness of the diagrams, two new computer subroutines for simulating the analytical errors and chemical processes, respectively, were written and applied in conjunction with HMgClaMSys and IgRoCS programs. The results are summarized in Tables 4–6 and supporting information Table S41.

3.3. Independent Evaluation of the New Multidimensional Classification Scheme from Relatively Fresh High-Mg Rocks (Test Studies T1–T7)

For the evaluation of the new classification diagrams and discriminant functions, measured compositional data for samples not included in the original database were newly compiled. Such an action would provide an independent evidence for the performance of the multidimensional scheme. We note that the number of samples outside our database used in testing our classification scheme was generally small because the

Table 1. Discriminant Function (DF1–DF2) Equations for Five Diagrams Based on Isometric Log-Ratio (ilr) Transformation of Major Elements (M) for the Classification of High-Mg Rocks as Komatiite, Meimechite, Picrite, and Boninite (Coefficients Reported as Arbitrarily Rounded to Four Decimal Places)[a]

$$DF1_{(Kom+Mei-Pic-Bon)M} = (-11.4707\times ilr1_{TiM}) + (-10.0761\times ilr2_{AlM}) + (-7.2390\times ilr3_{FeM}) + (-7.1873\times ilr4_{MnM}) + (-14.3149\times ilr5_{MgM}) + (-8.4732\times ilr6_{CaM}) + (-7.4913\times ilr7_{NaM}) + (-6.9885\times ilr8_{KM}) + (-7.8016\times ilr9_{PM}) + 7.2553 \quad (2)$$

$$DF2_{(Kom+Mei-Pic-Bon)M} = (-1.9538\times ilr1_{TiM}) + (-0.9237\times ilr2_{AlM}) + (-3.3566\times ilr3_{FeM}) + (-2.3803\times ilr4_{MnM}) + (1.8499\times ilr5_{MgM}) + (-3.4133\times ilr6_{CaM}) + (-1.1176\times ilr7_{NaM}) + (-1.3388\times ilr8_{KM}) + (-1.8301\times ilr9_{PM}) + 8.6530 \quad (3)$$

$$DF1_{(Kom-Mei-Pic)M} = (7.3431\times ilr1_{TiM}) + (7.4554\times ilr2_{AlM}) + (3.4976\times ilr3_{FeM}) + (5.7740\times ilr4_{MnM}) + (12.2602\times ilr5_{MgM}) + (4.7760\times ilr6_{CaM}) + (4.5508\times ilr7_{NaM}) + (4.8036\times ilr8_{KM}) + (4.8198\times ilr9_{PM}) - 3.0032 \quad (4)$$

$$DF2_{(Kom-Mei-Pic)M} = (-5.9801\times ilr1_{TiM}) + (-3.6842\times ilr2_{AlM}) + (1.0570\times ilr3_{FeM}) + (-4.9084\times ilr4_{MnM}) + (5.3759\times ilr5_{MgM}) + (0.6302\times ilr6_{CaM}) + (-4.2403\times ilr7_{NaM}) + (-2.4705\times ilr8_{KM}) + (-2.3292\times ilr9_{PM}) + 17.0855 \quad (5)$$

$$DF1_{(Kom-Mei-Bon)M} = (-11.1286\times ilr1_{TiM}) + (-6.1153\times ilr2_{AlM}) + (-8.0086\times ilr3_{FeM}) + (-4.8132\times ilr4_{MnM}) + (-10.8082\times ilr5_{MgM}) + (-6.7296\times ilr6_{CaM}) + (-6.6979\times ilr7_{NaM}) + (-5.8308\times ilr8_{KM}) + (-6.5703\times ilr9_{PM}) + 7.8428 \quad (6)$$

$$DF2_{(Kom-Mei-Bon)M} = (-1.2854\times ilr1_{TiM}) + (-3.6882\times ilr2_{AlM}) + (0.2607\times ilr3_{FeM}) + (0.2174\times ilr4_{MnM}) + (-8.0746\times ilr5_{MgM}) + (-5.6156\times ilr6_{CaM}) + (-1.5237\times ilr7_{NaM}) + (-2.0659\times ilr8_{KM}) + (-2.2625\times ilr9_{PM}) - 14.0915 \quad (7)$$

$$DF1_{(Kom-Pic-Bon)M} = (-10.9790\times ilr1_{TiM}) + (-9.6385\times ilr2_{AlM}) + (-8.0619\times ilr3_{FeM}) + (-7.1423\times ilr4_{MnM}) + (-13.1814\times ilr5_{MgM}) + (-8.8858\times ilr6_{CaM}) + (-7.3456\times ilr7_{NaM}) + (-6.8806\times ilr8_{KM}) + (-7.8419\times ilr9_{PM}) + 7.9447 \quad (8)$$

$$DF2_{(Kom-Pic-Bon)M} = (-0.3969\times ilr1_{TiM}) + (1.0727\times ilr2_{AlM}) + (-0.0470\times ilr3_{FeM}) + (-1.5790\times ilr4_{MnM}) + (4.4157\times ilr5_{MgM}) + (0.6633\times ilr6_{CaM}) + (-0.1964\times ilr7_{NaM}) + (0.1713\times ilr8_{KM}) + (0.3064\times ilr9_{PM}) + 12.2737 \quad (9)$$

$$DF1_{(Mei-Pic-Bon)M} = (-20.5630\times ilr1_{TiM}) + (-22.4274\times ilr2_{AlM}) + (-14.7761\times ilr3_{FeM}) + (-15.2005\times ilr4_{MnM}) + (-21.2090\times ilr5_{MgM}) + (-13.9677\times ilr6_{CaM}) + (-13.8880\times ilr7_{NaM}) + (-13.6341\times ilr8_{KM}) + (-13.6398\times ilr9_{PM}) + 21.6918 \quad (10)$$

$$DF2_{(Mei-Pic-Bon)M} = (4.7260\times ilr1_{TiM}) + (6.3615\times ilr2_{AlM}) + (5.0364\times ilr3_{FeM}) + (6.2937\times ilr4_{MnM}) + (0.0317\times ilr5_{MgM}) + (5.2722\times ilr6_{CaM}) + (3.5443\times ilr7_{NaM}) + (3.9064\times ilr8_{KM}) + (3.6234\times ilr9_{PM}) - 16.6946 \quad (11)$$

[a]The subscripts used are as follows: komatiite—Kom; meimechite—Mei; picrite—Pic; and boninite—Bon. The subscript M is for major element-based diagrams.

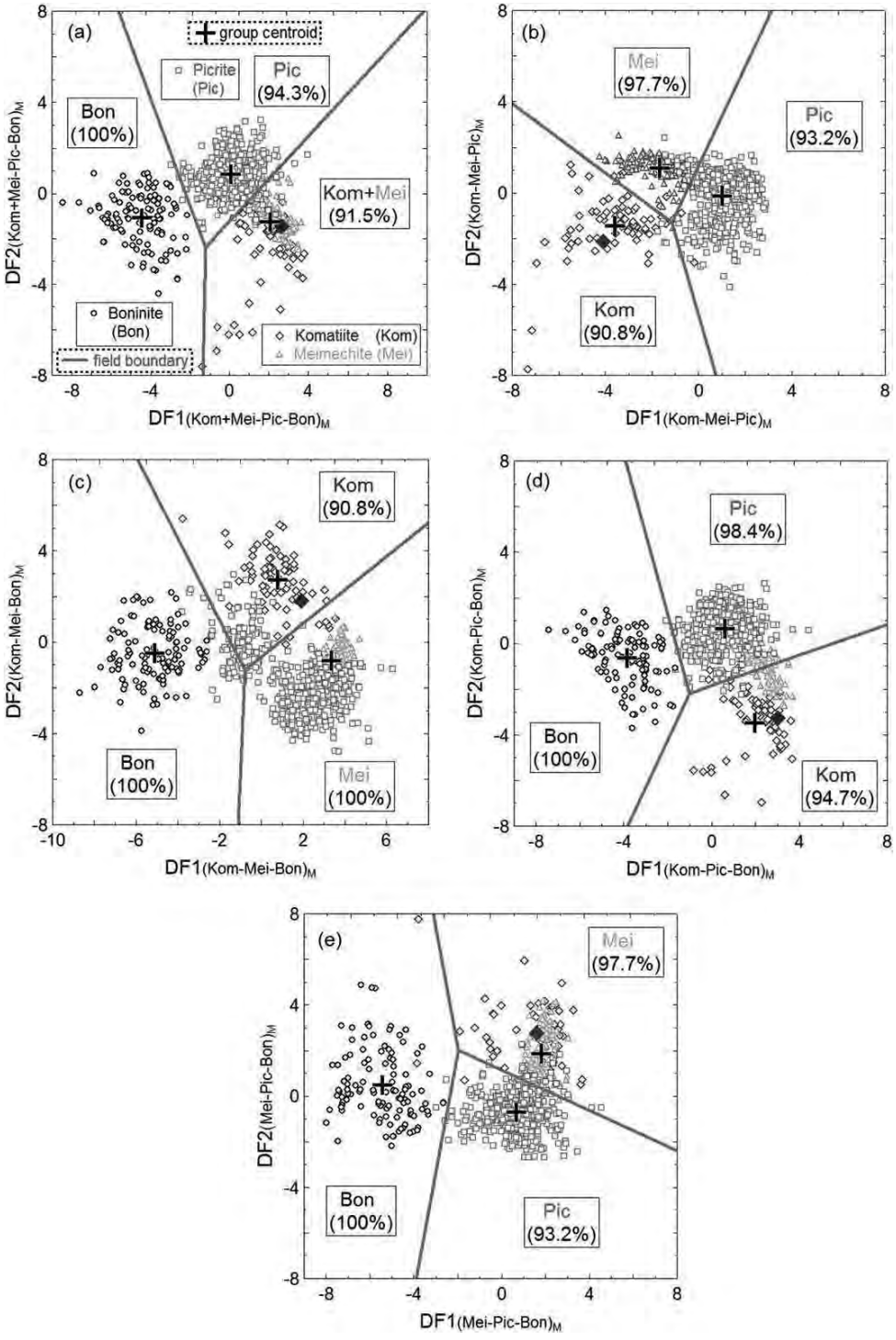

Figure 3. Five diagrams based on ilr-transformed major elements (M) for achieving the subdivision of High-Mg rocks (1—komatiite; 2—meimechite; 3—picrite; 4—boninite); the symbols are explained as insets in (a); the sample CB2-10 of *Upton et al*. [2000] (supporting information Table S4) is shown by a filled rhombus; the discriminant function equations are in Table 1; the probability-based boundary coordinates are given in supporting information Table S9; the overall percent success values (supporting information Table S13) are included in each diagram; group centroids are also shown by large crosses (+). (a) 1 + 2-3-4 $(Kom+Mei\text{-}Pic\text{-}Bon)_M$; (b) 1-2-3 $(Kom\text{-}Mei\text{-}Pic)_M$; (c) 1-2-4 $(Kom\text{-}Mei\text{-}Bon)_M$; (d) 1-3-4 $(Kom\text{-}Pic\text{-}Bon)_M$; and (e) 2-3-4 $(Mei\text{-}Pic\text{-}Bon)_M$.

Table 2. Major Element Composition and Other Calculations of Compiled Quaternary High-Mg Igneous Rock Samples From Mount Volture, Southern Italy (Test Study T1; *Beccaluva et al*. [2002]; Rock Type From the IUGS Classification Scheme)

	Sample Name												IUGS Scheme
Consec	Original Authors'	This Work	SiO_2	TiO_2	Al_2O_3	FeO^t	MnO	MgO	CaO	Na_2O	K_2O	P_2O_5	High-Mg Rock Type
1	VU18	BCGM0004	36.61	1.36	6.01	6.19	0.10	12.97	22.29	0.73	1.20	2.68	Picrite
2	VU21	BCGM0007	42.44	1.34	8.19	6.14	0.12	11.98	21.57	0.72	1.95	4.54	Picrite
3	EL6	BCGM0008	43.33	1.08	7.04	6.46	0.09	13.54	22.07	0.67	0.97	3.23	Picrite
Adjusted data			SiO_2A	TiO_2A	Al_2O_3A	$Fe_2O_3^tA$	MnOA	MgOA	CaOA	Na_2OA	K_2OA	P_2O_5A	
1	VU18	BCGM0004	40.306403	1.497315	6.616812	7.573818	0.1100967	14.279542	24.540555	0.803706	1.321160	2.950592	Picrite
2	VU21	BCGM0007	42.578946	1.344387	8.216814	6.846014	0.1203929	12.019222	21.640619	0.722357	1.956384	4.554864	Picrite
3	EL6	BCGM0008	43.679741	1.088717	7.096824	7.237254	0.0907264	13.649289	22.248140	0.675408	0.977829	3.256071	Picrite
ilr transformed data			$ilr1_{TiM}$	$ilr2_{AlM}$	$ilr3_{FeM}$	ilr4MnM	ilr5MgM	ilr6CaM	$ilr7Na_M$	$ilr8_{KM}$	ilr9PM		
1	VU18	BCGM0004	0.62031027	−0.49699237	−0.64412589	3.11915471	−1.25784769	−1.77702119	1.4026039	0.9450853	0.18871123		
2	VU21	BCGM0007	0.73708157	−0.62694978	−0.5069173	3.09053566	−1.04813852	−1.60744875	1.55612204	0.62907142	−0.16873911		
3	EL6	BCGM0008	0.78011371	−0.62984525	−0.68502107	3.20934254	−1.30124259	−1.77202966	1.47859636	1.1414284	0.00732981		

				High-Mg−Common Subdivision			High-Mg Rock (kom-mei-pic-bon) Subdivision				
Probability values			Discriminant Function $DF_{(HMg\text{-}Com)M}$	$p_{(HMg)M}$	$p_{(Com)M}$	High-Mg or Common	p_{kom}	p_{mei}	p_{pic}	p_{bon}	Inference From New Classification Scheme
1	VU18	BCGM0004	3.43732565	0.99786954	0.00213046	High-Mg	0.207506	0.004818	0.787556	0.000120	Picrite
2	VU21	BCGM0007	2.85200633	0.97715004	0.02284996	High-Mg	0.197907	0.002249	0.792401	0.007443	Picrite
3	EL6	BCGM0008	3.89509477	0.99967171	0.00032829	High-Mg	0.236230	0.000092	0.580079	0.183598	Picrite

relatively fresh High-Mg rocks that could be used for testing are scarce. Most such rocks were already included in constructing the initial database.

The data for the major elements were adjusted to 100% (supporting information Table S2) and transformed to ilr values (supporting information Table S3). Then, the discriminant function $DF_{(HMg-Com)M}$ for the High-Mg and Common igneous rock subdivision was estimated from equation (1). The probability values were calculated for the High-Mg-Common rock subdivision from equations (S1) to (S6) (supporting information file) and for the High-Mg subdivision in terms of komatiite, meimechite, picrite, and boninite from equations (2) to (11) (Table 1). The computer program HMgClaMSys was used for all calculations. Statistica® software and spreadsheets were used to confirm the correct functioning of HMgClaMSys.

Although probability-based calculations would suffice for the application of the new multidimensional classification scheme, the data for these seven evaluation cases (T1 to T7) are also plotted to illustrate

Table 3. Application Study (A1) of Compiled Archean High-Mg Igneous Rock Samples From the Isua Greenstone Belt, West Greenland [*Polat et al*., 2002]

Consec	Sample Id (Original Authors)	SiO_2A	TiO_2A	Al_2O_3A	$Fe_2O_3^tA$	MnOA	MgOA	CaOA	Na_2OA	K_2OA	P_2O_5A	IUGS Scheme (High-Mg)	$p_{(HMg)M}$	$p_{(Com)M}$	High-Mg or Common	p_{kom}	p_{mei}	p_{pic}	p_{bon}	New Scheme (High-Mg)
1	462901	49.09	0.23	16.94	10.12	0.170	15.57	6.82	0.95	0.09	0.010	Picrite	0.9996	0.0004	High-Mg	0.1296	0.0451	0.2741	0.5512	Boninite
2	462904	48.62	0.20	14.09	10.68	0.240	12.46	12.82	0.76	0.11	0.010	Picrite	0.9999	0.0001	High-Mg	0.0023	0.0000	0.3941	0.6036	Boninite
3	462905	49.40	0.24	16.90	10.40	0.160	15.96	5.23	1.62	0.07	0.010	Picrite	0.9990	0.0010	High-Mg	0.0166	0.2300	0.1834	0.5700	Boninite
4	462946	51.58	0.36	18.34	10.62	0.170	8.46	7.11	3.24	0.10	0.020	Boninite	0.0946	0.9054	Common					
5	462946b	51.65	0.35	18.46	10.41	0.130	8.49	6.98	3.40	0.11	0.020	Boninite	0.0555	0.9445	Common					
6	462965	47.92	0.23	16.00	10.80	0.210	13.56	9.82	1.33	0.13	0.010	Picrite	0.9944	0.0056	High-Mg	0.0017	0.0008	0.4118	0.5857	Boninite
7	242718	49.56	0.23	16.88	10.46	0.170	13.91	7.48	0.01	1.07	0.220	Picrite	1.0000	0.0000	High-Mg	0.3545	0.0001	0.3444	0.3010	Meimechite
8	242729	48.15	0.20	13.86	11.38	0.240	14.75	10.50	0.07	0.64	0.210	Picrite	1.0000	0.0000	High-Mg	0.2516	0.0000	0.4673	0.2811	Picrite
9	242717A	48.60	0.17	15.87	10.38	0.200	13.49	10.23	0.05	0.82	0.190	Picrite	1.0000	0.0000	High-Mg	0.2126	0.0000	0.3177	0.4697	Boninite
10	462906	52.34	0.22	19.01	8.18	0.130	11.40	7.49	1.18	0.04	0.010	Boninite	0.9622	0.0378	High-Mg	0.0003	0.0016	0.3604	0.6377	Boninite
11	462944	50.93	0.30	16.64	11.50	0.180	12.61	5.86	1.91	0.06	0.010	Picrite	0.9948	0.0052	High-Mg	0.0000	0.0035	0.3967	0.5997	Boninite
12	462966	46.78	0.22	16.58	11.94	0.230	16.06	7.07	0.95	0.16	0.010	Picrite	0.9998	0.0002	High-Mg	0.1151	0.0232	0.3267	0.5351	Boninite
13	810381	49.22	0.27	17.95	10.54	0.130	12.92	7.66	0.15	0.97	0.180	Picrite	1.0000	0.0000	High-Mg	0.0418	0.0002	0.4083	0.5497	Boninite
14	242725	46.72	0.22	15.12	11.85	0.240	15.41	9.07	0.16	0.99	0.230	Picrite	1.0000	0.0000	High-Mg	0.1912	0.0000	0.5565	0.2522	Picrite

Table 4. Sensitivity Analysis of Analytical Errors in the Classification of High-Mg Igneous Rock Samples Used in the Database Construction

Sample Id (Original Authors)	SiO_2A	TiO_2A	Al_2O_3A	$Fe_2O_3^t$A	MnOA	MgOA	CaOA	Na_2OA	K_2OA	P_2O_5A	Reference	Initial Name of the High-Mg Rock	Total Simulated Analyses[a]	Classification From the HMgClaMSys Scheme (This Work)		Classification From the IUGS Scheme [*Le Bas*, 2000]	
														Correct	Incorrect	Correct	Incorrect
9381	46.557	0.497	11.968	9.839	0.159	18.573	11.172	1.194	0.012	0.030	*Stracke et al*. [2003]	Komatiite	2200	2200	0	2179	21 picrite
SSI	46.689	0.369	7.851	10.782	0.190	24.043	8.011	1.197	0.718	0.150	*Schuth et al*. [2004]	Komatiite	2200	2199	1 picrite	1956	224 picrite
B9	45.623	0.569	16.059	7.755	0.200	18.245	10.849	0.659	0.010	0.030	*Gysi et al*. [2011]	komatiite	2200	2200	0	1975	225 picrite
762-4.60	46.816	1.825	10.007	12.714	0.180	17.979	8.423	1.634	0.251	0.170	*Ireland et al*. [2009]	Meimechite	2200	1793	407 picrite	1502	698 picrite
68622	46.806	0.539	9.331	11.587	0.200	19.311	9.950	1.267	0.838	0.170	*Eggins* [1993]	Picrite	2200	2200	0	2142	58 komatiite
689-1.2	46.01	1.82	9.39	12.95	0.19	18.26	9.17	1.56	0.47	0.18	*Rhodes et al*. [2012]	Picrite	2200	1878	322 meimechite	1748	452 meimechite
FGMc0003	52.384	0.148	7.835	10.665	0.208	20.667	7.103	0.841	0.139	0.010	*Falloon et al*. [1989]	Boninite	2200	2200	0	2168	32 komatiite
TVZ-11	52.380	0.471	12.729	9.301	0.160	13.200	9.632	1.644	0.431	0.050	*Gamble et al*. [1990]	Boninite	2200	2200	0	2164	36 (10 basaltic andesite; 26 picrite)
VUW17439	52.114	0.469	12.664	9.763	0.160	13.133	9.583	1.635	0.429	0.050	*Gamble et al*. [1993]	Boninite	2200	2200	0	2095	105 (4 basaltic andesite; 101 picrite)

[a]The analytical errors (relative standard deviation, RSD %) assumed in the simulation runs were as follows: 1% for SiO_2 and Al_2O_3; 2% for TiO_2, $Fe_2O_3^t$, MgO, and CaO; 4% for Na_2O and K_2O; and 5% for MnO and P_2O_5.

the functioning of the diagrams. The subdivision of the High-Mg and Common rocks is presented in supporting information Figure S5, whereas the subdivision of the High-Mg rocks in terms of the four rock types (komatiite, meimechite, picrite, and boninite) is included in supporting information Figure S6a–S6e.

3.3.1. Test Study T1: Mount Vulture, Italy

This test study will be described in detail in order to better illustrate the new classification scheme; others will be briefly presented. The major element geochemical data for 60 Quaternary igneous rock samples from Mount Vulture (location T1 in Figure 1) were compiled from *Beccaluva et al*. [2002]. Only three samples proved to be of the High-Mg type (picrite; Table 2) from the IUGS scheme [*Le Bas*, 2000; *Verma and Rivera-Gómez*, 2013]. The major element data (from equations of supporting information Table S2) and ilr transformed values (from equations of supporting information Table S3) are also shown in Tables 2.

The discriminant function ($DF_{(HMg\text{-}Com)M}$; T1 in supporting information Figure S5) and probability ($p_{(HMg)M}$ and $p_{(Com)M}$ for High-Mg and Common rocks, respectively) values for individual samples are listed in Table 2. Note the sum of the two probabilities ($p_{(HMg)M}$ and $p_{(Com)M}$) is 1 for each sample. Similarly, the respective probability values (p_{kom}, p_{mei}, p_{pic}, and p_{bon}, to belong to the four subdivision classes of kom, mei, pic, and bon, respectively; T1 in supporting information Figures S6a–S6e) are also included in Table 2. Again, the sum of the four probability values (p_{kom}, p_{mei}, p_{pic}, and p_{bon}) is 1 for each sample.

The $p_{(HMg)M}$ values for all three samples are higher than the respective $p_{(Com)M}$ values, implying that all of them are of High-Mg type (Table 2). Similarly, the probability of picrite (p_{pic}) for any sample is higher than the respective probability values for any other rock type (p_{kom}, p_{mei}, or p_{bon}), implying that all of them should be classified as picrite (Table 2). Therefore, all three picrite samples (IUGS; Table 2) were classified as High-Mg rock and picrite from our proposed classification scheme (Table 2), in agreement with the IUGS.

3.3.2. Test Study T2: Rifted Apennines/Adriatic Domain, Italy

Data for Cenozoic High-Mg igneous rock samples from Italy reported by *Bianchini et al*. [2008] were compiled (location T2 in Figure 1). Only three samples proved to be of the High-Mg type (two meimechite and one picrite; supporting information Table S13) according to the IUGS classification [*Le Bas*, 2000] used as a reference. Supporting information Tables S14 and S15 present the adjusted and ilr-transformed data for these three samples, respectively. Two samples of meimechite were correctly classified by HMgClaMSys, whereas the third sample (picrite) was classified as a Common rock (supporting information Table S16; T2 in supporting information Figures S5 and S6a–S6e). Such a misclassification is possible because the new

Table 5. Sensitivity Analysis of all High-Mg Rock Centroids (Adjusted Compositions) With Respect to Postemplacement Compositional Changes (One Element at a Time) in the High-Mg-Common Rock Subdivision Based on Major Elements (M)

		HMgClaMSys (This Work)				IUGS [*Le Bas*, 2000]			
Original High-Mg Centroid Composition		Maximum "Tolerable" Change[a]		Maximum Compositional Range of 100% Adjusted Data[b]		Maximum "Tolerable" Change[a]		Maximum Compositional Range of 100% Adjusted Data[b]	
Chemical Parameter	Major Element Concentration (% m/m)	Loss (% m/m)	Gain (% m/m)	Minimum Concentration (% m/m)	Maximum Concentration (% m/m)	Loss (% m/m)	Gain (% m/m)	Minimum Concentration (% m/m)	Maximum Concentration (% m/m)
Centroid of all 920 High-Mg rocks									
SiO_2A	47.49	−30	+110	38.77	65.51	−52	+19	30.27	51.84
TiO_2A	1.45	−99	+636	0.01	9.80	−99	+2793	0.01	29.92
MgOA	16.88	−74	+492	5.01	54.59	−32	+345	12.13	47.46
Na_2OA	1.53	−99	+334	0.02	6.30	−99	+72	0.02	2.60
K_2OA	0.40	−97	+24784	0.01	50.10	−97	+275	0.01	1.49
Centroid of 76 High-Mg komatiite rocks									
SiO_2A	45.07	−66	+68	21.81	57.95	−47	+32	30.31	51.99
TiO_2A	0.45	−96	+167	0.02	1.20	−97	+122	0.01	1.00
MgOA	26.62	−33	+275	19.55	57.63	−39	+188	18.12	51.10
Na_2OA	0.75	−98	+347	0.02	3.25	−98	+153	0.02	1.86
K_2OA	0.14	−92	+72938	0.01	50.03	−92	+833	0.01	1.26
Centroid of 172 High-Mg meimechite rocks									
SiO_2A	45.80	−52	+37	28.86	53.65	−49	+28	30.12	51.96
TiO_2A	1.56	−65	+5944	0.55	48.98	−36	+1478	1.01	20.04
MgOA	22.16	−19	+191	18.74	45.31	−22	+237	18.17	48.97
Na_2OA	1.27	−80	+1948	0.26	20.91	−99	+39	0.01	1.76
K_2OA	0.23	−95	+6484	0.01	13.22	−95	+218	0.01	0.73
Centroid of 542 High-Mg picrite rocks									
SiO_2A	46.45	−12	+45	43.29	55.71	−50	+24	30.25	51.82
TiO_2A	1.84	−91	+104	0.17	3.67	−99	+1212	0.02	19.70
MgOA	14.67	−38	+26	9.63	17.81	−20	+71	12.09	22.72
Na_2OA	1.72	−97	+69	0.05	2.87	−99	+47	0.02	2.50
K_2OA	0.49	−97	+20139	0.01	50.12	−97	+164	0.01	1.29
126 High-Mg boninite rocks									
SiO_2A	55.77	−22	+79	49.59	69.30	−14	+79	52.03	69.30
TiO_2A	0.26	−96	+528	0.01	1.60	−96	+94	0.01	0.50
MgOA	13.34	−92	+60	1.22	19.76	−43	+54	8.07	19.16
Na_2OA	1.51	−99	+1668	0.02	21.36	−99	+479	0.02	8.17
K_2OA	0.40	−97	+25194	0.01	50.10	−97	+1835	0.01	7.13

[a]This refers to the minimum and maximum % change in any given element before the rock name changes from the original name to some other rock name.
[b]These are independent estimates for any given element and are not directly related to the other ranges (changes simulated for one element at a time).

classification scheme (High-Mg and Common subdivision; Figure 1) did not show 100% success; the correct classification was about 86% for High-Mg and 99% for Common rocks. Other possible reasons for misclassification may be related to varying data quality (random or systematic analytical errors) for different samples.

3.3.3. Test Study T3: Rift-Related Pelagonian Continental Margin, Greece

Out of 34 Triassic igneous rock samples (location T3 in Figure 1) reported by *Tsikouras et al*. [2008], 6 proved to be of High-Mg type from the IUGS scheme (1 komatiite and 5 picrite; supporting information Table S17). The data (supporting information Table S18) transformed to ilr (supporting information Table S19) were processed in HMyClaMSys and all of them were correctly classified (supporting information Table S20; T3 in supporting information Figures S5 and S6a–S6e) as predicted by the IUGS scheme (supporting information Table S17).

3.3.4. Test Study T4: Mariana Trench

Out of 23 samples of Paleogene igneous rocks dredged from the Mariana Trench (location T4 in Figure 1) reported by *Bloomer and Hawkins* [1987], 16 proved to be of High-Mg type (boninite; supporting information Table S21). Their data and ilr values are reported in supporting information Tables S22 and S23, respectively. The classification results from HMgClaMSys (supporting information Table S24; T4 in supporting information Figures S5 and S6a–S6e) are fully consistent with the IUGS scheme (supporting information Table S21).

Table 6. Sensitivity Analysis of All High-Mg Rock Centroids (Adjusted Compositions) With Respect to Postemplacement Compositional Changes of Three Elements at a Time (Simultaneous Loss of Na_2O and K_2O and Gain of SiO_2) in the High-Mg-Common Rock Subdivision Based on Major Elements (M)

		HMgClaMSys (This Work)			IUGS [*Le Bas*, 2000]		
Original High-Mg Centroid Composition		Maximum "Tolerable" Change[a]		Maximum Compositional Change of 100% Adjusted Data[b]	Maximum "Tolerable" Change[a]		Maximum Compositional Range of 100% Adjusted Data[b]
Chemical Parameter	Major Element Concentration (% m/m)	Loss (% m/m)	Gain (% m/m)	Final Concentration (% m/m)	Loss (% m/m)	Gain (% m/m)	Final Concentration (% m/m)
Centroid of all 920 High-Mg rocks							
SiO_2A	47.49	—	+97	64.88	—	+19	52.01
TiO_2A	1.45	—	—	1.01	—	—	1.34
MgOA	16.88	—	—	11.70	—	—	15.53
Na_2OA	1.53	−97	—	0.032	−19	—	1.38
K_2OA	0.40	−97	—	0.008	−19	—	0.30
Centroid of 76 High-Mg komatiite rocks							
SiO_2A	47.07	—	+92	61.52	—	+32	52.12
TiO_2A	0.45	—	—	0.32	—	—	0.40
MgOA	26.62	—	—	18.93	—	—	23.32
Na_2OA	0.75	−92	—	0.042	−32	—	0.44
K_2OA	0.14	−92	—	0.008	−32	—	0.082
Centroid of 172 High-Mg meimechite rocks							
SiO_2A	45.80	—	+40	54.29	—	+28	52.16
TiO_2A	1.56	—	—	1.33	—	—	1.39
MgOA	22.16	—	—	18.90	—	—	19.72
Na_2OA	1.27	−40	—	0.66	−28	—	0.82
K_2OA	0.23	−40	—	0.12	−28	—	0.15
Centroid of 542 High-Mg picrite rocks							
SiO_2A	46.45	—	+54	57.57	—	+24	52.07
TiO_2A	1.84	—	—	1.49	—	—	1.66
MgOA	14.67	—	—	11.88	—	—	13.26
Na_2OA	1.72	−54	—	0.65	−24	—	1.18
K_2OA	0.49	−54	—	0.19	−24	—	0.34
centroid of 126 High-Mg boninite rocks							
SiO_2A	55.77	—	+79	70.03	—	+?	—
TiO_2A	0.26	—	—	0.18	—	—	—
MgOA	13.34	—	—	9.36	—	—	—
Na_2OA	1.51	−79	—	0.22	−?	—	—
K_2OA	0.40	−79	—	0.06	−?	—	—

[a,b]See footnote Table 5.

3.3.5. Test Study T5: Abitibi Greenstone Belt, Canada

From textural considerations, *Arndt* [1986] documented the presence of komatiite rocks in the Archaean Abitibi Greenstone Belt (location T5 in Figure 1). All 17 samples of igneous rocks from this belt [*Arndt*, 1986] proved to be of High-Mg type from the IUGS scheme (komatiite; supporting information Table S25). These major element data and ilr values are reported in supporting information Tables S26 and S27, respectively. The classification results from HMgClaMSys (supporting information Table S28; T5 in supporting information Figures S5 and S6a–S6e) are fully consistent with the IUGS scheme (supporting information Table S25) because all resulted as High-Mg and komatiite.

3.3.6. Test Study T6: Gorgona Island, Colombia

Révillon et al. [2000] analyzed Cretaceous-Paleogene igneous rocks from the Gorgona Island (location T6 in Figure 1) and identified the presence of High-Mg rocks. Thus, a total of 20 samples compiled from *Révillon et al*. [2000] proved to be of High-Mg type from the IUGS scheme (16 komatiite and 4 picrite; supporting information Table S29). These major element data and ilr values are reported in supporting information Tables S30 and S31, respectively. The classification results from HMgClaMSys (supporting information Table S32; T5 in supporting information Figures S5 and S6a–S6e) are consistent with the IUGS scheme (compare supporting information Table S32 with Table S29).

3.3.7. Test Study T7: Belingwe Greenstone Belt, Zimbabwe

Nisbet et al. [1987] and *Renner et al*. [1994] documented the occurrence of fresh komatiite rocks in the Neoarchaean Belingwe Greenstone Belt. More recently, *Shimizu et al*. [2005] reported extensive geochemical

data from this belt. Data for 10 High-Mg rock samples (according to the IUGS criteria) were compiled (location T7 in Figure 1; 7 komatiite and 3 picrite; supporting information Table S33; adjusted data in supporting information Table S34) from *Shimizu et al*. [2005]. The ilr-transformed data (supporting information Table S35) were processed in HMgClaMSys. The results of rock classification (supporting information Table S36) were exactly the same as indicated by the IUGS scheme (compare supporting information Tables S36 with S33).

3.4. Application of the New Multidimensional Classification Scheme to High-Mg Altered Rocks (Application Studies A1–A5)

Plotting the High-Mg rock compositions in the multidimensional diagrams is unnecessary because all inferences can be made directly from the probability calculations. Nevertheless, we provided the relevant diagrams (supporting information Figures S7 and S8). However, to keep the paper short, we will present neither the original major element compositions of the High-Mg rocks, nor the ilr-transformed data. Nevertheless, the sample identification from the original authors, the adjusted compositions, the IUGS [*Le Bas*, 2000] rock name (obtained from the IgRoCS computer program), and the output from HMgClaMSys will be shown.

Importantly, if the new multidimensional classification scheme is useful, we should observe significantly lesser consistency for A1–A5 between the IUGS nomenclature and the multidimensional scheme, as compared to the seven test studies (T1–T7). Thus, lesser consistency between the new classification scheme (proposed for altered rocks) for the application studies (A1–A5) and the IUGS scheme (recommended to be used for fresh rocks), as compared to the test studies (T1–T7) would suggest that the new scheme should be used for the classification of altered rocks. It is clear that, because of postemplacement compositional changes, the IUGS scheme may provide rock names for altered rocks different from when they were fresh; the multidimensional scheme, on the other hand, will try to recover the original names because it is more robust that the IUGS scheme (see also Section 4).

3.4.1. Application Study A1: Isua Greenstone Belt, West Greenland

Polat et al. [2002] reported geochemical data for least-altered Archean (3700–3800 Ma) igneous (metavolcanic) rock samples, 14 of which proved to be of High-Mg type (11 picrite and 3 boninite; Table 3; supporting information Figure S7) from the IUGS scheme [*Le Bas*, 2000]. The new classification scheme suggested 12 (11 picrite and 1 boninite) to be High-Mg but 2 boninites to be Common rocks. Out of 11 picrite samples from the IUGS scheme, only 2 proved to be picrite; all others were classified as boninite with the exception of one picrite identified as meimechite (Table 3; supporting information Figure S8). The remaining boninite rock from the IUGS scheme was boninite from the new scheme. Thus, the IUGS scheme wrongly classified 11 samples of High-Mg Archean rocks but 3 were correctly classified. This application study shows a lesser consistency between the two schemes than any test study (T1–T7) presented above. Had we compiled the variably altered metavolcanic rocks reported by *Polat et al*. [2002], the consistencies would have been similar or less than those reported for this application.

3.4.2. Application Study A2: Aravalli Volcanics, Rajasthan, India

The geochemical data presented by *Ahmad and Tarney* [1994] for Archean rocks were compiled. From the IUGS scheme, five samples proved to be of High-Mg type (2 komatiite, 1 meimechite, and 2 boninite; supporting information Table S37 and Figure S7). The new scheme (HMyClaMSys) provided different results, namely, 4 komatiite and 1 boninite (supporting information Table S37 and Figure S8).

3.4.3. Application Study A3: Gadwal Greenstone Belt, India

Manikyamba et al. [2005] reported geochemical data for Neoarchean rocks from the Gadwal Greenstone Belt of Eastern Dharwar Craton. According to the IUGS scheme, eight samples of High-Mg rocks (seven picrite and one boninite; supporting information Table S38, Figures S7 and S8) were classified very differently by HMgClaMSys (one picrite and seven boninite).

3.4.4. Application Study A4: Mahakoshal Supracrustal Belt, India

Srivastava [2013] reported geochemical data for Proterozoic rocks from the Chitrangi area. Three of the four samples of High-Mg type (IUGS: two picrite and two meimechite) were classified differently as komatiite (three samples; supporting information Table S39, Figures S7, and S8). Only one picrite was classified as such.

3.4.5. Application Study A5: Mallina Basin, Pilbara Craton, Northwest Australia

From the data reported by *Smithies* [2002] for Archean (3010–2935 Ma) rocks, five samples were identified as of High-Mg type (IUGS: three boninite, one picrite, and one komatiite; supporting information Table S40

and Figure S7). In contrast, HMgClaMSys identified three samples (two boninite and one komatiite) consistent with the IUGS scheme. However, one boninite sample was classified differently as Common rock and one picrite as boninite (supporting information Table S40 and Figure S8).

4. Discussion

The sensitivity of petrogenetic processes of partial melting and fractional crystallization in such multidimensional diagrams for basic and ultrabasic magmas was covered by *Verma and Agrawal* [2011]. Such considerations were also documented by *Verma and Verma* [2013] and *Verma et al*. [2013] in multidimensional tectonomagmatic diagrams for intermediate and acid magmas, respectively. Therefore, the discussion is limited to two other processes: (1) higher robustness of the new classification scheme with respect to analytical errors as compared to the IUGS scheme; and (2) higher robustness of the new scheme for postemplacement chemical changes as compared to the original IUGS scheme.

4.1. Robustness of the New Multidimensional Classification Scheme Based on Major Elements With Respect to Analytical Errors

The role of analytical errors or uncertainties in such multidimensional diagrams has been recently documented by *Verma* [2015a]. To illustrate the robustness of HMgClaMSys, we used major element compositions of nine selected samples (three komatiite; one meimechite; two picrite; and three boninite; Table 4) from our compiled database. Although we should be dealing with the analytical errors or total uncertainties [*Verma*, 2012] for "individual" samples, these errors are seldom reported in geochemical literature by the original authors. Therefore, we assumed small errors from 1% to 5% in individual major element determinations and applied the methodology of Monte Carlo simulation [*Verma*, 2012, 2015a] to generate 2200 independent simulated analyses for each sample (Table 4). These 2200 simulated analyses were evaluated in the two systems to infer the rock name as follows: the new scheme (computer program HMgClaMSys) and the conventional IUGS scheme (computer program IgRoCS). These simulated data are shown graphically in supporting information Figure S9a–S9e for the multidimensional scheme and supporting information Figures S10 and S11 for the IUGS procedure.

For example, for the komatiite analysis (sample 9381; Table 4) reported by *Stracke et al*. [2003], the HMgClaMSys reproduced the same name (komatiite) for all 2200 simulated analyses (supporting information Figure S9a–S9e), whereas IgRoCS provided the correct name in 2179 cases and incorrect name (picrite) in 21 cases (Table 4; supporting information Figure S10). Thus, for this particular sample, the new scheme is more robust than the conventional IUGS scheme. This means that if this sample (sample 9381) were analyzed repeatedly under the assumed error model, 21 out of 2200 times (amounting to about 1% of events) the IUGS will classify it incorrectly as picrite, whereas the new scheme is always likely to classify it correctly as komatiite.

Higher robustness of the new scheme is true for all other samples compiled in Table 4. For five other samples, HMgClaMSys provided the correct name for all simulated analyses and for only three remaining samples, the incorrect classification varied from 1 to 407 simulated analyses (Table 4; supporting information Figure S9). The IUGS scheme, on the other hand, provided incorrect names for significantly more simulated analyses (32–698 times out of 2200 simulations; Table 4; supporting information Figures S10 and S11). Thus, the incorrect classification of the IUGS scheme amounted to about 1.5%–32%. Therefore, it is clear that the new scheme is more robust as compared to the IUGS scheme with respect to the effects of analytical errors.

4.2. Robustness of the New Multidimensional Classification Scheme Based on Major Elements With Respect to Postemplacement Compositional Changes

In order to determine the robustness of the multidimensional scheme, we used the mean (centroid) concentration values for calculating the effects of concentration changes that might be caused by postemplacement chemical effects.

We carried out systematic simulation work to estimate the maximum postemplacement compositional changes (loss or gain) of an element of interest that will still keep the centroid of each rock type within its own field (HMgClaMSys). In other words, the maximum loss or gain (% m/m) of an element in the centroid composition is estimated as the value that will still give the same magma or rock type as determined from our multidimensional diagrams. However, the minimum and maximum changes possible for any given

element are also automatically set for that particular element to show final concentrations between 0% (no concentration can become negative) and 100% (no concentration can be >100% m/m). Therefore, our sensitivity analysis was carried out within these two limits for the final composition, although more stringent conditions could be used in future. Similarly, the IUGS scheme was also evaluated to better understand the robustness of HMgClaMSys as compared to the original scheme [*Le Bas*, 2000].

Our method is illustrated from the High-Mg centroid of 920 major element analyses used in proposing the first discriminant function (Figure 2). The maximum loss or gain of an element at a time was simulated. For this work, we restricted our discussion to the elements of interest in the IUGS classification of High-Mg rocks (SiO_2, TiO_2, MgO, Na_2O, and K_2O) [*Le Bas*, 2000].

The initial mean composition of the High-Mg rock from our database is reported in the second column of Table 5. Let this rock be initially emplaced in the crust with this composition. However, we assume that the rock in the field (before sampling) was subject to postemplacement changes. Assuming the sample had a pre-alteration SiO_2 content of 47.49% and lost about 30% (the loss of a single element is not a likely process, but it serves the purpose of illustrating the mass-balance computations and robustness of the new diagrams; Figures 2 and 3), the total mass of SiO_2 that was lost during alteration from a 100 g portion of the rock will be about 14.247 g [$=30 \times 47.49/100$], but the new total mass will only be 85.753 g [$=100 - 14.247$]. Similarly, the new SiO_2 content (mass) of the 85.75 g portion of the altered rock will be 33.243 g [$=47.49 - 14.247$]. All major element concentrations will, therefore, have to be readjusted to sum up to 100 g. As a result, the SiO_2 concentration of the altered rock will be about 38.77% m/m [$=(33.243/85.747) \times 100$; Table 5]. It is important to note that, although we have modeled only a change in SiO_2, concentrations of all other elements will change (in this case, increase) as a result of the constant sum constraint. Similarly, let us assume a gain of +110% of SiO_2 (Table 5). In this case, the total mass will increase from 100 to 152.239 g [$=100+(110 \times 47.49/100)$] and of SiO_2 to 99.729 g [$=47.49+(110 \times 47.49/100)$], and the new SiO_2 concentration will therefore be 65.51% m/m [$=99.729/152.239) \times 100$].

Our probability calculations suggest that these compositions ("SiO_2 loss (−30%)" and "SiO_2 gain (+110%)" columns) will still plot in the High-Mg field of Figure 2. Any further loss or gain of SiO_2 will change the new composition to plot in the Common rock field.

The minimum and maximum SiO_2 values (%) of the altered rock (38.77 and 65.51) are given in the first row of the "minimum concentration (% m/m)" and "maximum concentration (% m/m)," respectively. Thus, the centroid of the High-Mg rock is fairly robust with respect to compositional changes in SiO_2. The conventional nomenclature (IUGS), on the other hand, showed the loss or gain of about −52% and +19%, with the corresponding minimum and maximum concentrations of altered rocks as 30.27% and 51.84%, respectively. Any additional change (loss or gain) will change the nomenclature of the High-Mg rock to a Common rock name.

Similar behavior seems to be valid for all other major elements, although such extreme changes (−99% to +24784%; Table 5) in individual element concentrations are not likely. Nevertheless, more complex postemplacement chemical changes along with more stringent evaluation conditions can be similarly modeled.

Now, we document the sensitivity of chemical changes for the four High-Mg rock types in the ilr-based diagrams (Figures 2 and 3a–3e). We modeled the minimum and maximum percent changes of individual element concentrations in the set of five diagrams (Figures 3a–3e) that will still leave the modified composition as the initial High-Mg rock type: komatiite, meimechite, picrite, or boninite. In other words, we modeled the overall synthesis of the five diagrams and watched for the change in the rock type from one of the above four to any other, including the Common rock. The sensitivity of komatiite (mean composition of selected elements from our database) is reported in Table 5. The komatiite rock used for mass-balance simulations can decrease SiO_2 up to about −66% (loss of SiO_2) or gain +68% (gain of SiO_2) and the resulting rock will still be classified as of High-Mg type (Figure 2) and komatiite (Figures 3a–3e). Any further change will cause the komatiite having the composition of the komatiite centroid to change to another rock type. The sensitivity of changes in other major elements (TiO_2 to K_2O) is summarized in the remaining part of Table 5. In most cases (6 out of 10; Table 5), the maximum loss or gain permissible by HMgClaMSys is more than the IUGS scheme, whereas in the remaining 4 cases, the maximum losses are generally similar.

Having pointed out the sensitivity (or robustness) of the komatiite classification, the other three rock types (meimechite, picrite, and boninite) are also presented in Table 5. The percent loss values for the

HMgClaMSys and IUGS are generally similar, but the percent gain values for the new scheme are higher (in four out of five cases for meimechite; three out of five for picrite; and four out of five for boninite; Table 5). Thus, generally greater robustness for the new scheme is documented as compared to the conventional IUGS procedure (Table 5). Furthermore, the IUGS scheme was not recommended for the nomenclature of altered rocks.

Now, instead of the loss or gain of a single element, we can also model simultaneous loss and gain for two or more elements from our computer program HMgClaMSys. For example, a likely hydrothermal alteration process can involve simultaneous loss of Na_2O and K_2O and gain of SiO_2. If we run this process in HMgClaMSys for the different centroids, we can estimate the simultaneous maximum loss and gain percent values. Table 6 shows that the new scheme will identify the High-Mg centroid as a High-Mg rock for up to +97% (gain) of SiO_2 and −97% (loss) of both Na_2O and K_2O (simultaneous process), whereas the conventional IUGS scheme will provide such a classification for only +19% (gain) of SiO_2 and −19% (loss) of both Na_2O and K_2O. Thus, the new scheme is more robust than the conventional scheme. Similarly, the sensitivity analysis of the other four centroids (komatiite, meimechite, picrite, and boninite) is also presented in Table 6. For three centroids (komatiite, meimechite, and picrite), the MagClaMSys is more robust than the IUGS scheme (Table 6). Although the HMgClaMSys is fairly robust for boninite, this rock will remain as such for an extreme gain of SiO_2 combined with extreme losses of Na_2O and K_2O. This is because the IUGS definition of boninite does not specify the highest concentration of SiO_2 and the alkalis do not enter in its nomenclature [*Le Bas*, 2000].

Other combinations of postemplacement (low-temperature or hydrothermal) processes are valid. For example, it is quite possible that all three elements (SiO_2, Na_2O, and K_2O) are lost. This process is simulated for the boninite centroid for estimating its robustness. The HMgClaMSys will maintain the classification as boninite up to −22% loss, whereas the IUGS scheme will identify it as boninite only up to −15% (supporting information Table S41). Any other postemplacement chemical change in our new classification scheme can be modeled through the computer program HMgClaMSys available at http://tlaloc.ier.unam.mx/index.html. Thus, the availability of this program solves the major problem that the multidimensional procedures is rather complex.

5. Conclusions

The multidimensional classification scheme proposed in this work provides a robust technique for the nomenclature of the four types of High-Mg rocks (komatiite, meimechite, picrite, and boninite). For fresh rocks, the conventional IUGS classification scheme should be used. For altered igneous rocks, a new geochemical method based on coherent statistical methodology is now available first to detect if they are of High-Mg type and then as one of the four varieties. The computer program HMgClaSys should facilitate the use of this rather cumbersome method. From Monte Carlo simulation modeling and mass-balance computations, the proposed scheme is shown to be more robust when dealing with analytical errors and postemplacement compositional changes as compared to the conventional IUGS classification recommended for fresh rocks only.

Acknowledgments
This work constitutes a part of the second author's (MARG) doctoral thesis in preparation under the guidance of the first author (SPV). We are thankful to Sanjeet K. Verma and Kailasa Pandarinath, both of whom participated in the construction of earlier databases used for the multidimensional tectonomagmatic discrimination diagrams. An updated version of this database achieved by the authors of this paper was used for this new classification scheme. This work was funded by the DGAPA-PAPIIT grant IN100816 and IER-UNAM internal grant to the first author. An earlier version of this paper was reviewed by Robin Offler and Nick Arndt who made several important suggestions for improvement. We are also much grateful to the editor Janne Blichert-Toft for efficient handling of our manuscript and giving us the opportunity to revise and resubmit. We also sincerely thank four reviewers (Robin Offler, Vinod K. Singh, and two anonymous) who provided useful comments to still improve our presentation. Supporting information file includes additional information. We have no conflicts of interest.

References

Agrawal, S. (1999), Geochemical discrimination diagrams: A simple way of replacing eye-fitted boundaries with probability based classifier surfaces, *J. Geol. Soc. India*, *54*, 335–346.

Agrawal, S., and S. P. Verma (2007), Comment on ''Tectonic classification of basalts with classification trees'' by Pieter Vermeesch (2006), *Geochim. Cosmochim. Acta*, *71*, 3388–3390.

Ahmad, T., and J. Tarney (1994), Geochemistry and petrogenesis of late Archaean Aravalli volcanics, basement enclaves and granitoids, Rajasthan, *Precambrian Res.*, *65*, 1–23.

Aitchison, J. (1984), Statistical analysis of geochemical compositions, *J. Int. Assoc. Math. Geol.*, *16*, 531–564.

Aitchison, J. (1986), *The Statistical Analysis of Compositional Data*, p. 416, Chapman and Hall, London, U. K.

Aitchison, J. (1999), Logratios and natural laws in compositional data analysis, *Math. Geol.*, *31*, 563–580.

Arndt, N. T. (1986), Differentiation of komatiite flows, *J. Petrol.*, *27*, 279–301.

Beccaluva, L., M. Coltorti, P. Di Girolamo, L. Melluso, L. Milani, V. Morra, and F. Siena (2002), Petrogenesis and evolution of Mt. Vulture alkaline volcanism (Southern Italy), *Mineral. Petrol.*, *74*, 277–297.

Bianchini, G., L. Beccaluva, and F. Siena (2008), Post-collisional and intraplate Cenozoic volcanism in the rifted Apennines/Adriatic domain, *Lithos*, *101*, 125–140.

Bloomer, S. H., and J. W. Hawkins (1987), Petrology and geochemistry of boninite series volcanic rocks from the Mariana trench, *Contrib. Mineral. Petrol.*, *97*, 361–377.

Bonadiman, C., M. Coltori, L. Beccaluva, W. L. Griffin, S. Y. O'Reilly, and F. Siena, (2011), Metasomatism versus host magma infiltration: A case study of Sal mantle xenoliths, Cape Verde Archipelago, in: *Volcanism and Evolution of the African Lithosphere*, edited by L. Beccaluva, pp. 283–306, Geol. Soc. of Am., Boulder, Colo.
Chayes, F. (1960), On correlation between variables of constant sum, *J. Geophys. Res.*, *65*, 4185–4193.
Chayes, F. (1971), *Ratio Correlation. A Manual for Students of Petrology and Geochemistry*, p. 108, Univ. of Chicago Press, Chicago.
Eggins, S. M. (1993), Origin and differentation of picritic arc magmas, Ambae (Aoba), Vanuatu, *Contrib. Mineral. Petrol.*, *114*, 79–100.
Egozcue, J. J., V. Pawlowsky-Glahn, G. Mateu-Figueras, and C. Barceló-Vidal (2003), Isometric logratio transformations for compositional data analysis, *Math. Geol.*, *35*, 279–300.
Falloon, T. J., D. H. Green, and M. T. McCulloch (1989), Petrogenesis of high-Mg and associated lavas from the north Tonga trench, chap. 14, in *Boninites*, edited by A. J. Crawford, pp. 357–395, Unwin Hyman, London.
Floyd, P. A., and J. A. Winchester (1975), Magma type and tectonic setting discrimination using immobile elements, *Earth Planet. Sci. Lett.*, *27*, 211–218.
Floyd, P. A., and J. A. Winchester (1978), Identification and discrimination of altered and metamorphosed volcanic rocks using immobile elements, *Chem. Geol.*, *21*, 291–306.
Gamble, J. A., I. E. M. Smith, B. P. Kokelaar, J. W. Cole, B. F. Houghton, and J. N. Wilson (1990), The petrology, phase relations and tectonic setting of basalts from Taupo volcanic zone, New Zealand and the Kermadec island arc: Havre trough, SW Pacific, *J. Volcanol. Geotherm. Res.*, *43*, 235–270.
Gamble, J. A., I. E. M. Smith, M. T. McCulloch, I. J. Graham, and B. P. Kokelaar (1993), The geochemistry and petrogenesis of basalts from the Taupo volcanic zone and Kermadec Island arc, S.W. Pacific, *J. Volcanol. Geotherm. Res.*, *54*, 265–290.
Gysi, A. P., O. Jagoutz, M. W. Schmidt, and K. Targuisti (2011), Petrogenesis of proxenites and melt infiltrations in the ultramafic complex of Beni Bousera, Northern Morocco, *J. Petrol.*, *52*, 1679–1735.
Hastie, A. R., A. C. Kerr, J. A. Pearce, and S. F. Mitchell (2007), Classification of altered volcanic island arc rocks using immobile trace elements: Development of the Th-Co discrimination diagram, *J. Petrol.*, *48*, 2341–2357.
Ireland, T. J., R. J. Walker, and M. O. Garcia (2009), Highly siderophile elements and ^{187}Os isotope systematics of Hawaiian picrites: Implications for parental melt composition and source heterogeneity, *Chem. Geol.*, *260*, 112–128.
Kerr, A. C., and N. T. Arndt (2001), A note on the IUGS reclassification of the high-Mg and picritic volcanic rocks, *J. Petrol.*, *42*, 2169–2171.
Le Bas, M. J. (2000), IUGS reclassification of the high-Mg and picritic volcanic rocks, *J. Petrol.*, *41*, 1467–1470.
Le Bas, M. J. (2001), Reply to comment by Kerr and Arndt, *J. Petrol.*, *42*, 2173–2174.
Le Bas, M. J., R. W. Le Maitre, A. Streckeisen, and B. Zanettin (1986), A chemical classification of volcanic rocks based on the total alkali-silica diagram, *J. Petrol.*, *27*, 745–750.
Le Maitre, R. W. (1976), Some problems of the projection of chemical data into mineralogical classifications, *Contrib. Mineral. Petrol.*, *56*, 181–189.
Lipman, P. W., R. M. Rhodes, and G. B. Dalrymple (1990), The Ninole Basalt: Implications for the structural evolution of Mauna Loa volcano, Hawaii, *Bull. Volcanol.*, *53*, 1–19.
Manikyamba, C., S. M. Naqvi, D. V. S. Rao, M. R. Mohan, T. C. Khanna, T. G. Rao, and G.L.N. Reddy (2005), Boninites from the Neoarchaean Gadwal greenstone belt, eastern Dharwar craton, India: Implications for Archaean subduction processes, *Earth Planet. Sci. Lett.*, *230*, 65–83.
Middlemost, E. A. K. (1989), Iron oxidation ratios, norms and the classification of volcanic rocks, *Chem. Geol.*, *77*, 19–26.
Morrison, D. F. (1990), *Multivariate Statistical Methods*, 3rd ed., 495 pp., McGraw-Hill, New York.
Nisbet, E. G., et al. (1987), Uniquely fresh 2.7 Ga komatiites from the Belingwe Greenstone Belt, Zimbabwe, *Geology*, *15*, 1147–1150.
Polat, A., A. W. Hofmann, and M. T. Rosing (2002), Boninite-like volcanic rocks in the 3.7-3.8 Ga Isua greenstone belt, West Greenland: Geochemical evidence for intra-oceanic subduction zone processes in the early Earth, *Chem. Geol.*, *184*, 231–254.
Rencher, A. C. (2002), *Methods of Multivariate Analysis*, 2nd ed., 708 pp., Wiley-Interscience, New York.
Renner, R., E. G. Nisbet, M. J. Cheadle, N. T. Arndt, M. J. Bickle, and W. E. Cameron (1994), Komatiite flows from the Reliance Formation, Belingwe Belt, Zimbabwe: I. Petrography and mineralogy, *J. Petrol.*, *35*, 361–400.
Révillon, S., N. T. Arndt, E. Hallot, A. C. Kerr, and J. Tarney (1999), Petrogenesis of picrites from the Caribbean Plateau and the North Atlantic magmatic province, *Lithos*, *49*, 1–21.
Révillon, S., N. T. Arndt, C. Chauvel, and E. Hallot (2000), Geochemical study of ultramafic volcanic and plutonic rocks from Gorgona Island, Colombia: The plumbing system of an oceanic plateau, *J. Petrol.*, *41*, 1127–1153.
Rhodes, J. M., S. W. Huang, F. A. Frey, M. Pringle, and G. Xu (2012), Compositional diversity of Mauna Kea shield lavas recovered by the Hawaii Scientific Drilling Project: Inferences on source lithology, magma supply, and the role of multiple volcanoes, *Geochem. Geophys. Geosyst.*, *13*, Q03014, doi:10.1029/2011GC003812.
Rivera-Gómez, M. A., and S. P. Verma (2016), Testing of multidimensional tectonomagmatic discrimination diagrams on fresh and hydrothermally altered rocks, *Geol. Carpath.*, *67*, 195–208.
Schaaf, P., J. Stimac, C. Siebe, and J. L. Macías (2005), Geochemical evidence for mantle origin and crustal processes in volcanic rocks from Popocatépetl and surrounding monogenetic volcanoes, central Mexico, *J. Petrol.*, *46*, 1243–1282.
Schuth, S., A. Rohrbach, C. Münker, C. Ballhaus, D. Garbe-Schönberg, and C. Qopoto (2004), Geochemical constraints on the petrogenesis of arc picrites and basalts, New Georgia group, Solomon Islands, *Contrib. Mineral. Petrol.*, *148*, 288–304.
Shimizu, K., E. Nakamura, and S. Maruyama (2005), The geochemistry of ultramafic to mafic volcanics from the Belingwe greenstone belt, Zimbabwe: Magmatism in an Archean continental large igneous province, *J. Petrol.*, *46*, 2367–2394.
Smithies, R. H. (2002), Archaean boninite-like rocks in an intracratonic setting, *Earth Planet. Sci. Lett.*, *197*, 19–34.
Snow, J. E. (2002), Major and trace element evolution of Hole 735B gabbros, *Proc. Ocean Drill. Program Sci. Res.*, *176*, 1–18.
Spice, H. E., J. G. Fitton, and L. A. Kirstein (2016), Temperature fluctuation of the Iceland mantle plume through time, *Geochem. Geophys. Geosyst.*, *17*, 243–254, doi:10.1002/2015GC006059.
Srivastava, R. K. (2013), Petrological and geochemical characteristics of Paleoproterozoic ultramafic lamprophyres and carbonatites from the Chitrangi region, Mahakoshal Supracrustal Belt, central India, *J. Earth Syst. Sci.*, *122*, 759–776.
Stracke, A., A. Zindler, V. J. M. Salters, D. McKenzie, J. Blichert-Toft, F. Albarede, and K. Grönvold (2003), Theistareykir revisited. *Geochem. Geophys. Geosyst.*, *4*(2), 8507, doi:10.1029/2001GC000201.
Tsikouras, B., S. Karipi, I. Rigopoulos, and M. Perraki (2008), Geochemical processes and petrogenetic evolution of rondingite dykes in the ophiolite complex of Othrys (Central Greece), *Lithos*, *113*, 540–554.
Upton, B. G. J., M. P. Semet, and J.-L. Joron (2000), Cumulate clasts in the Bellecombe ash member, Piton de la Fournaise, Réunion island, and their bearing on cumulative processes in the petrogenesis of the Réunion lavas, *J. Volcanol. Geotherm. Res.*, *104*, 297–318.

Verma, S. P. (2012), Geochemometrics, *Rev. Mex. Cienc. Geol.*, *29*, 276–298.
Verma, S.P. (2015a), Monte Carlo comparison of conventional ternary diagrams with new log-ratio bivariate diagrams and an example of tectonic discrimination, *Geochem. J.*, *49*, 393–412.
Verma, S. P. (2015b), Present state of knowledge and new geochemical constraints on the central part of the Mexican Volcanic Belt and comparison with the Central American Volcanic Arc in terms of near and far trench magmas, *Turkish J. Earth Sci.*, *24*, 399–460.
Verma, S. P., and S. Agrawal (2011), New tectonic discrimination diagrams for basic and ultrabasic volcanic rocks through log-transformed ratios of high field strength elements and implications for petrogenetic processes, *Rev. Mex. Cienc. Geol.*, *28*, 24–44.
Verma, S. P., and J. S. Armstrong-Altrin (2016), Geochemical discrimination of siliciclastic sediments from active and passive margin settings, *Sediment. Geol.*, *332*, 1–12.
Verma, S. P., and M. A. Rivera-Gómez (2013), Computer programs for the classification and nomenclature of igneous rocks, *Episodes*, *36*, 115–124.
Verma, S. P., and S. K. Verma (2013), First 15 probability-based multi-dimensional discrimination diagrams for intermediate magmas and their robustness against post-emplacement compositional changes and petrogenetic processes, *Turkish J. Earth Sci.*, *22*, 931–995.
Verma, S. P., I. S. Torres-Alvarado, and F. Velasco-Tapia (2003), A revised CIPW norm, *Schweiz. Mineral. Petrogr. Mitteil.*, *83*, 197–216.
Verma, S. P., M. Guevara, and S. Agrawal (2006), Discriminating four tectonic settings: Five new geochemical diagrams for basic and ultrabasic volcanic rocks based on log-ratio transformation of major-element data. *J. Earth Syst. Sci.*, *115*, 485–528.
Verma, S. P., K. Pandarinath, S. K. Verma, and S. Agrawal (2013), Fifteen new discriminant-function-based multi-dimensional robust diagrams for acid rocks and their application to Precambrian rocks, *Lithos*, *168-169*, 113–123.
Vermeesch, P. (2007), Tectonic discrimination diagrams revisited, *Geochem. Geophys. Geosyst.*, *7*, Q06017, doi:10.1029/2005GC001092.
Wilks, S. S. (1963), Multivariate statistical outliers, *Sankhya*, *25*, 407–426.
Winchester, J. A., and P. A. Floyd (1976), Geochemical magma type discrimination: Application to altered and metamorphosed basic igneous rocks, *Earth Planet. Sci. Lett.*, *28*, 459–469.
Winchester, J. A., and P. A. Floyd (1977), Geochemical discrimination of different magma series and their differentiation products using immobile elements, *Chem. Geol.*, *20*, 325–343.

SUPPLEMENT

Log-ratio transformed major element based multidimensional classification for altered High-Mg igneous rocks

Surendra P. Verma[a,*], M. Abdelaly Rivera-Gómez[b], Lorena Díaz-González[c], Alfredo Quiroz-Ruiz[a]

[a] *Instituto de Energías Renovables, Universidad Nacional Autónoma de México, Temixco, Mor. 62580, Mexico*

[b] *Posgrado en Ingeniería, Instituto de Energías Renovables, Universidad Nacional Autónoma de México, Temixco, Mor. 62580, Mexico*

[c] *Centro de Investigación en Ciencias, Instituto de Investigación en Ciencias Básicas y Aplicadas, Universidad Autónoma del Estado de Morelos, Cuernavaca, Mor. 62209, Mexico*

Corresponding author E-mail: spv@ier.unam.mx

This file contains Figures S1-S11, Tables S1-S40, the references for the High-Mg databases, and additional equations S1 to S6.

Throughout the paper we erroneously called the log-ratio transformation as isometric log-ratio (ilr), they could be correctly called modified centered log-ratio (mclr). The use of one or the other type would make no difference in the final result as shown by Verma (2015a, Geochemical Journal, 49, 393–412). We will compare the success rates for ilr and mclr in a forthcoming paper.

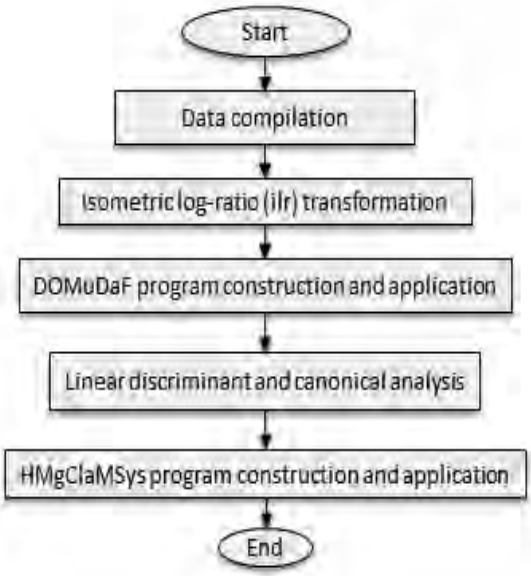

Figure S1. Schematic flow diagram for the methods used in this work

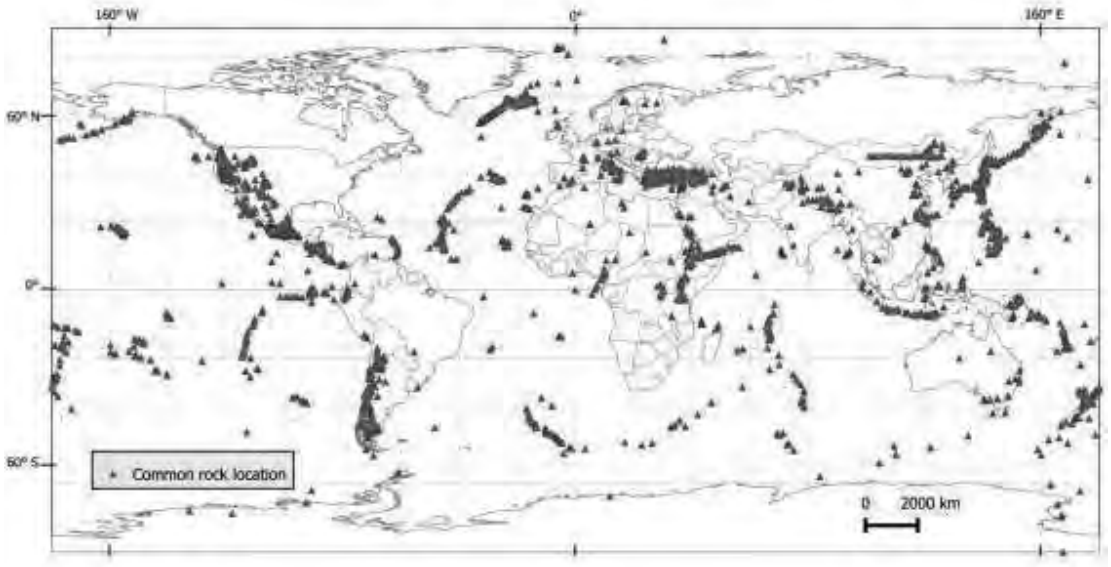

Figure S2. Schematic location of Common igneous rock samples used in this work

Table S1. Sample locations for the database construction (all multivariate discordant outlier-free High-Mg rock samples); Site # refers to the location no. in Figure 1.

Site #	Longitude (°)	Latitude (°)	Country / Region	Number of High-Mg igneous rock samples (IUGS)				Reference
				Major (M)				
				Kom	Mei	Pic	Bon	
1	-178.833	-30.523	KermadecArc	0	0	1	0	Haase et al. (2002) Geochem. Geophys. Geosys.
2	-177.920	-29.270	KermadecArc	0	0	1	0	Gamble et al. (1993) J. Volcanol. Geotherm. Res.
3	-175.198	-21.179	TongaArc	0	0	0	1	Coish (1989) Crawford_Ed Boninite Chap 10
4	-175.198	-21.179	TongaArc	0	0	0	15	Falloon et al. (1989) Crawford_Ed Boninite Chap 14
5	-175.198	-21.179	Tonga	0	0	0	1	Crawford et al. (1989) Crawford_Ed Boninite Chap 1
6	-173.067	-40.890	TongaArc	0	0	0	11	Fallon and Crawford (1991) Earth Planet. Sci. Lett.
7	-165.920	54.080	AleutianArc	0	0	2	0	Romick et al. (1990) Contrib. Min. Petrol.
8	-165.000	54.000	AleutianArc	0	0	1	0	Nye and Reid (1986) J. Geophys. Res.
9	-163.900	-10.800	Suvorov Trough	0	0	1	0	Timm et al. (2011) Earth Planet. Sci. Lett.
10	-163.157	21.892	HawaiianIslands	0	0	1	0	Dixon et al. (2008) Geochem. Geophys. Geosys.
11	-159.782	-18.872	FrenchPolynesia	0	0	1	0	Palacz and Saunders (1986) Earth Planet. Sci. Lett.
12	-159.526	22.096	HawaiianIslands	0	0	4	0	Maalooe et al. (1992) J. Petrol.

Table S1. Sample locations for the database construction (all multivariate discordant outlier-free High-Mg rock samples); Site # refers to the location no. in Figure 1.

Site #	Longitude (°)	Latitude (°)	Country / Region	Number of High-Mg igneous rock samples (IUGS)				Reference
				Major (M)				
				Kom	Mei	Pic	Bon	
13	-157.983	21.467	HawaiianIslands	0	0	1	0	Jackson et al. (1999) Bull. Volcanol.
14	-157.826	21.444	HawaiianIslands	0	0	3	0	Frey et al. (1994) Geochim. Cosmochim. Acta
15	-156.927	20.808	HawaiianIslands	0	0	4	0	West et al. (1992) Contrib. Min. Petrol.
16	-156.881	21.259	HawaiianIslands	0	1	17	0	Xu et al. (2005) Geochem. Geophys. Geosys.
17	-156.606	20.558	HawaiianIslands	0	0	1	0	Rudek et al. (1992) Bull. Volcanol.
18	-156.583	20.917	Hawaiian islands	0	0	1	0	Sherrod et al. (2007) Bull. Volcanol.
19	-156.260	20.682	HawaiianIslands	0	0	1	0	Bergmanis et al. (2000) Bull. Volcanol.
20	-156.250	20.708	HawaiianIslands	0	2	2	0	Chen et al. (1991) Contrib. Min. Petrol.
21	-156.250	20.720	HawaiianIslands	0	12	27	0	Ren et al. (2004) J. Petrol.
22	-155.717	20.083	HawaiianIslands	0	0	1	0	Spengler and Gracia (1988) Contrib. Min. Petrol.
23	-155.672	19.715	HawaiianIslands	0	31	14	0	Ireland et al. (2009) Chem. Geol.
24	-155.490	19.770	HawaiianIslands	2	84	85	0	Rhodes and Vollinger (2004) Geochem. Geophys. Geosys.
25	-155.470	19.820	HawaiianIslands	0	13	17	0	Rhodes et al. (2012) Geochem. Geophys. Geosys.
26	-155.222	19.429	HawaiianIslands	1	0	0	0	Lipman et al. (1990) Bull. Volcanol.
27	-153.992	-22.429	FrenchPolynesia	0	3	8	0	Takamasa et al. (2009) Chem. Geol.
28	-153.413	-22.537	FrenchPolynesia	0	3	7	0	Hanyu et al. (2011) Geochem. Geophys. Geosys.
29	-152.265	-21.755	FrenchPolynesia	0	0	6	0	Dupuy et al. (1989) Chem. Geol.
30	-149.833	-17.533	FrenchPolynesia	0	1	4	0	Cheng et al. (1993) J. Volcanol. Geotherm. Res.
31	-148.204	-24.257	FrenchPolynesia	0	1	7	0	Dupuy et al. (1988) Contrib. Min. Petrol.
32	-145.366	-25.412	FrenchPolynesia	0	0	13	0	Lassiter et al. (2003) Chem. Geol.
33	-144.855	-23.334	FrenchPolynesia	0	0	4	0	Hémond et al. (1994) Chem. Geol.
34	-142.751	18.151	HawaiianIslands	0	5	7	0	Ren et al. (2009) J. Petrol.
35	-140.346	-8.587	FrenchPolynesia	0	0	5	0	Liotard et al. (1986) Contrib. Min. Petrol.
36	-121.167	39.767	U.S.A	0	0	1	0	USGS439_DB_USGS, National Geochemical Database
37	-113.000	28.000	Mexico	0	0	0	1	Pallares et al. (2007) J. Volcanol. Geotherm. Res.
38	-110.620	26.310	Mexico	0	0	1	0	Grechin et al. (1981) DSDP Leg 63
39	-110.620	26.310	Mexico	0	0	1	0	Perfit et al. (1982) DSDP Leg 64
40	-110.620	26.310	Mexico	0	0	1	0	Saunders et al. (1982) DSDP Leg 64
41	-106.300	28.233	EastAlkalineP	0	0	1	0	Morton-Bermea (1990) Thesis
42	-104.000	29.050	EastAlkalineP	0	0	6	0	Nick (1988) Doctoral Thesis
43	-100.986	22.156	Mexico	1	0	0	0	Heinrich and Besch (1992) Contrib. Min. Petrol.
44	-98.483	23.650	EastAlkalineP	0	0	1	0	Elías-Herrera et al. (1991) Can Min
45	-97.431	18.939	Mexico	6	0	0	0	Dávalos-Elizando (2009) Masters Thesis
46	-95.296	18.459	Mexico	0	0	1	0	Verma et al. (1993) Geofís. Int.
47	-95.296	18.459	Mexico	0	0	1	0	Verma (2006) Int. J. Earth Sci.
48	-95.258	18.603	Mexico	0	0	5	0	Espíndola et al. (2010) J. Volcanol. Geotherm. Res.
49	-91.408	-0.920	Galapagos	0	0	2	0	Naumann et al. (2002) Journal of Petrology
50	-91.408	-0.920	Galapagos Islands	0	0	7	0	Teasdale et al. (2005) Bull Volcanol
51	-91.000	-1.000	Galapagos	0	0	1	0	Kurt and Geist (1999) Geochim. Cosmochim. Acta
52	-90.230	-0.600	Pacific Ocean	0	0	1	0	White et al. (1993) J. Geophys. Res.
53	-84.471	10.422	CAVA_CostaRica	0	0	1	0	Chan et al. (1999) Chem. Geol.
54	-72.200	-40.500	CA_Andes_Chile	0	0	1	0	Gerlach et al. (1988) J. Petrol.
55	-61.777	12.023	lesserAntillesArc	0	0	3	0	Shimizu and Arculus (1975) Contrib. Min. Petrol.
56	-61.777	12.023	LesserAntillesArc	0	0	18	0	Thirlwall et al. (1996) Geochim. Cosmochim. Acta
57	-61.738	12.085	LesserAntillesArc	0	0	2	0	Arculus (1976) Geol. Soc. Am. Bull.
58	-61.694	12.107	LesserAntillesArc	0	0	5	0	Devine (1995) J. Volcanol. Geotherm. Res.
59	-55.500	-21.167	Reunion	0	8	10	0	Albarède et al. (1997) J. Petrol.
60	-52.262	29.736	CaribbeanPlateau	5	0	1	0	Révillon et al. (1999) Lithos
61	-32.490	38.730	MAR52-28N	0	0	2	0	Schilling et al. (1983) J. Geophys. Res.
62	-28.696	38.591	AzoresIslands	0	0	1	0	de Lima et al. (2011) Int. Geol. Rev.
63	-27.436	38.648	AzoresIslands	0	0	2	0	Beier et al. (2008) Geochem. Geophys. Geosys.
64	-25.500	37.750	AzoresIslands	0	0	1	0	Storey et al. (1989) Geol. Soc. Am. Spec. Pap Saunders Norry

Table S1. Sample locations for the database construction (all multivariate discordant outlier-free High-Mg rock samples); Site # refers to the location no. in Figure 1.

Site #	Longitude (°)	Latitude (°)	Country / Region	Number of High-Mg igneous rock samples (IUGS)				Reference
				Major (M)				
				Kom	Mei	Pic	Bon	
65	-25.242	17.016	CapeVerdeIslands	0	0	10	0	Holm et al. (2006) J. Petrol.
66	-24.975	16.828	CapeVerdeIslands	0	0	3	0	Jorgensen and Holm(2002) Chem. Geol.
67	-23.953	16.777	CapeVerdeIslands	0	1	1	0	Doucelance et al. (2003) Geochim. Cosmochim. Acta
68	-23.000	15.000	CapeVerdeIslands	0	0	6	0	Barker et al. (2009) J. Petrol.
69	-22.930	16.727	Cape Verde Archi.	9	0	0	0	Bonadiman et al. (2011) Geol. Soc. Am. Spec. Paper
70	-22.654	64.230	Iceland	2	0	4	0	Kokfelt et al. (2006) J. Petrol.
71	-21.317	63.800	Iceland	0	0	1	0	Peate et al. (2009) Contrib. Min. Petrol.
72	-19.021	64.963	Iceland	8	0	30	0	Maclennan et al. (2001) Earth Planet. Sci. Lett.
73	-17.080	68.420	Kolbeinsey_R	0	0	1	0	Schilling et al. (1983) J. Geophys. Res.
74	-16.850	28.310	CanaryIslands	0	0	6	0	Longpré et al. (2009) Geochem. Geophys. Geosys.
75	-16.841	65.894	Iceland	4	0	7	0	Stracke et al. (2003) Geochem. Geophys. Geosys.
76	-16.550	28.250	CanaryIslands	0	0	4	0	Thirlwall et al. (2000) J. Volcanol. Geotherm. Res.
77	-16.500	32.500	Madeira	0	0	6	0	Schwarz et al. (2005) J. Volcanol. Geotherm. Res.
78	-16.455	32.846	Medeira	0	1	15	0	Geldmacher and Hoernle (2000) Earth Planet. Sci. Lett.
79	-14.081	61.722	Iceland	18	1	4	0	Spice et al. (2016) G3
80	-6.554	-21.188	St. Helena, Ttristan	0	0	4	0	Willbold and Stracke (2006) Geochem. Geophys. Geosys.
81	-5.699	-15.980	StHelenaIsland	0	0	3	0	Kawabata et al. (2011) J. Petrol.
82	-5.370	35.730	Morocco	5	0	2	0	Gysi et al. (2011) J. Petrol.
83	-4.250	-90.600	Galapagos	0	0	2	0	Saal et al. (2007) EPSL
84	-2.100	-54.170	AtlanticOcean	0	0	1	0	Le Roex et al. (1987) Geochim. Cosmochim. Acta
85	7.646	50.710	Germany	0	0	2	0	Haase et al. (2004) J. Petrol.
86	13.967	41.283	Italy	0	0	1	0	Nikogosian and Van Bergen (2010) J. Volcanol. Geotherm. Res.
87	16.350	65.167	Iceland	0	0	1	0	Macpherson et al. (2005) Earth Planet. Sci. Lett.
88	22.592	40.280	Greece_cyprus	0	0	0	2	Cameron et al. (1983) Earth Planet. Sci. Lett.
89	24.000	64.000	Iceland	2	0	7	0	Slater et al. (2001) J. Petrol.
90	24.100	38.567	Japan	0	0	0	2	Pe-Piper and Piper (1994) Lithos
91	31.098	39.705	Azores	0	0	1	0	Genske et al. (2012) J. Petrol.
92	33.013	34.712	Greece	0	0	0	4	Rogers and Saunders (1989) Crawford_Ed BoniniteChap 11
93	33.036	34.838	Cyprus	0	0	0	2	Crawford et al. (1989) Crawford_Ed Boninite Chap 1
94	36.000	2.000	KeniaRift	0	0	1	0	Macdonald et al. (2001) J. Petrol.
95	36.140	3.480	Africa	0	2	2	0	Furman et al. (2006) Journal of Petrology
96	36.400	2.700	KeniaRift	0	0	4	0	Furman et al. (2004) J. Petrol.
97	36.600	39.867	Turkey	0	0	2	0	Boztug et al. (1998) Turk. J. Earth Sci.
98	37.725	-2.417	KeniaRift	0	0	1	0	Späth et al. (2001) J. Petrol.
99	37.783	3.500	KeniaRift	0	0	1	0	Class et al. (1994) Chem. Geol.
100	39.409	12.531	EthiopiaRift	0	0	4	0	Beccaluva et al. (2009) J. Petrol.
101	42.796	11.471	EthiopiaRift	0	0	2	0	Deniel et al. (1994) J. Geophys. Res.
102	43.340	-11.461	GrandeComore	0	0	2	0	Class and Goldstein (1997) Earth Planet. Sci. Lett.
103	43.360	-11.750	Indian Ocean	0	0	1	0	Deniel (1998) Chem. Geol.
104	43.368	-11.717	GrandeComore	0	0	2	0	Class et al. (1998) J. Petrol.
105	48.258	-13.317	Madagascar	0	0	1	0	Melluso and Morra (2000) J. Volcanol. Geotherm. Res.
106	55.512	-3.750	SW Pacific	0	0	3	0	Schuth et al. (2009) J. Petrol.
107	55.712	-20.756	Reunion	0	2	2	0	Albarède and Tamagnan (1988) J. Petrol.
108	55.712	-20.756	Reunion	5	1	1	0	Upton et al. (2000) J. Volcanol. Geotherm. Res.
109	57.266	-32.723	Indian ocean	1	0	3	2	Snow (2002) Proc. ODP v176
110	57.400	-33.250	Indian Ocean	0	0	0	7	Coogan et al. (2001) Chem. Geol.
111	57.500	-20.333	FrenchPolynesia	0	0	2	0	Paul et al. (2005) Geochem. Geophys. Geosys.
112	57.650	-20.317	Indian Ocean	0	0	3	0	Paul et al. (2007) J. Volcanol. Geotherm. Res.
113	73.500	-53.000	KerguelenArchi	0	0	1	0	Barling et al. (1994) J. Petrol.
114	74.000	22.000	Pavagadh	0	0	2	0	Sheth and Melluso (2008) J. Asian Earth Sci.
115	75.000	-55.000	KerguelenArchi	0	0	4	0	Borisova et al. (2002) Chem. Geol.
116	75.003	15.465	India	0	0	2	0	Dessai et al. (2004) Lithos

Table S1. Sample locations for the database construction (all multivariate discordant outlier-free High-Mg rock samples); Site # refers to the location no. in Figure 1.

Site #	Longitude (°)	Latitude (°)	Country / Region	Number of High-Mg igneous rock samples (IUGS)				Reference
				Major (M)				
				Kom	Mei	Pic	Bon	
117	108.200	-7.160	IndianO_SundaArc	0	0	1	0	Turner and Foden (2001) Contrib. Min. Petrol.
118	110.500	20.000	China E	0	0	1	0	Fan and Hooper (1991) J. Petrol.
119	117.000	26.500	China SE	0	0	3	0	Zou et al. (2000) Chem. Geol.
120	117.020	36.660	China	0	0	1	0	Dostal et al. (1991) Geochemical Journal
121	119.297	26.100	Taiwan	0	0	1	0	Chung et al. (1994) Chem. Geol.
122	134.093	34.665	Setouchi	0	0	0	1	Crawford et al. (1989) Crawford_Ed Boninite Chap 1
123	138.016	-31.571	Australia	0	0	4	0	Foden et al. (2002) Chem. Geol.
124	138.801	37.745	Japan back arc basin	1	0	0	0	Shuto et al. (2006) Lithos
125	139.350	34.350	BoninIslands	0	0	0	25	Taylor et al. (1994) J. Petrol.
126	142.167	27.000	BoninIslands	0	0	0	1	Cameron et al. (1983) Earth Planet. Sci. Lett.
127	142.210	27.112	BoninIslands	0	0	0	1	Crawford et al. (1989) Crawford_Ed Boninite Chap 1
128	142.210	27.112	BoninIslands	0	0	0	4	Umino and Kushiro (1989) Crawford_Ed Boninite Chap 4
129	142.500	17.750	MarianaTrench	0	0	0	3	Crawford et al. (1989) Crawford_Ed Boninite Chap 1
130	144.635	13.342	MarianaArc	0	0	0	1	Reagan et al. (2008) J. Petrol.
131	144.794	13.444	MarianaArc	0	0	0	5	Reagan and Meijer (1984) Geol. Soc. Am. Bull.
132	145.983	44.017	KurileArc	0	0	1	0	Martynov et al. (2010) Island Arc
133	150.050	-9.700	PapuaNewGuinea	0	0	0	3	Cameron et al. (1983) Earth Planet. Sci. Lett.
134	150.050	-9.700	Nosy Be archi	0	0	0	2	Crawford et al. (1989) Crawford_Ed Boninite Chap 1
135	150.050	-9.700	PapuaNewGuinea	0	0	0	4	Hickey and Frey (1982) Geochim. Cosmochim. Acta
136	150.050	-9.700	Nosy Be archi	0	0	0	16	Jenner (1981) Chem. Geol.
137	150.050	-9.700	RyukyuArc	0	0	0	2	Walker and Cameron (1983) Contrib. Min. Petrol.
138	150.768	-5.747	NewBritainArc	0	0	0	3	Woodhhead et al. (1998) J. Petrol.
139	150.961	-5.448	NewBritainArc	0	0	0	1	Woodhead and Johnson (1993) Contrib. Min. Petrol.
140	159.000	53.200	KamchatkaArc	1	0	0	0	Kepezhinskas et al. (1997) Geochim. Cosmochim. Acta
141	159.145	-8.059	SolomonIslands	5	0	20	0	Schuth et al. (2004) Contrib. Min. Petrol.
142	165.618	-20.904	NewCaledonia	0	0	0	1	Crawford et al. (1989) Crawford_Ed Boninite Chap 1
143	165.618	20.904	New Caledonia	0	0	0	1	Cameron et al. (1983) Earth Planet. Sci. Lett.
144	166.500	53.500	AleutianArc	0	0	1	0	Kay and Kay (1994) Geol. Soc. Am. Book Sec
145	167.814	-15.375	VanuatuArc	0	0	11	0	Eggins (1993) Contrib. Min. Petrol.
146	168.048	-14.463	VanuatuArc	0	0	1	0	Barsdell (1988) J. Petrol.
147	168.271	-16.742	VanuatuArc	0	0	1	0	Barsdell and Berry (1990) J. Petrol.
148	169.400	-19.400	NewHebridesArc	0	0	1	0	Dupuy et al. (1982) Earth Planet. Sci. Lett.
149	170.503	-45.879	New Zealand	0	0	1	0	Price et al. (2003) J. Petrol.
150	174.869	-36.900	New Zealand	0	0	2	0	Needham et al. (2011) J. Volcanol. Geotherm. Res.
151	175.217	-36.900	New Zealand	0	0	2	0	Booden et al. (2012) J. Volcanol. Geotherm. Res.
152	175.292	-39.552	New Zealand	0	0	0	1	Gamble et al. (1993) J. Volcanol. Geotherm. Res.
153	175.360	-38.151	New zeland	0	0	0	2	Cameron et al. (1983) Earth Planet. Sci. Lett.
154	176.065	-38.680	KermadecArc	0	0	1	1	Gamble et al. (1990) J. Volcanol. Geotherm. Res.
155	179.303	-34.687	KermadecArc	0	0	1	0	Wright et al. (2006) J. Volcanol. Geotherm. Res.
	Total number of samples (920)			**76**	**172**	**546**	**126**	

References (cited in Table S1)

Albarède, F., Luais, B., Fitton, G., Semet, M., Kaminski, E., Upton, B. G. J., et al. (1997). The geochemical regimes of Piton de la Fournaise Volcano (Réunion) during the last 530 000 years. *Journal of Petrology, 38*(2), 171-201.

Albarède, F., & Tamagnan, V. (1988). Modelling the Recent geochemical evolution of the Piton de la Fournaise volcano, Réunion Island, 1931-1986. *Journal of Petrology, 29*, 997-1030.

Arculus, R. J. (1976). Geology and geochemistry of the alkali basalt-andesite association of Grenada, Lesser Antilles island arc. *Geological Society of America Bulletin, 87*, 612-624.

Barker, A. K., Holm, P. M., Peate, D. W., & Barker, J. A. (2009). Geochemical stratigraphy of submarine lavas (3-5 Ma) from the Flamengos valley, Santiago, southern Cape Verde Islands. *Journal of Petrology, 50*(1), 169-193.

Barling, J., Goldstein, S. L., & Nicholls, I. A. (1994). Geochemistry of Heard Island (Southern Indian Ocean): characterization of an enriched mantle component and implication for enrichment of the Sub-Indian ocean mantle. *Journal of Petrology, 35*(4), 1017-1053.

Barsdell, M. (1988). Petrology and petrogenesis of clinopyroxene-rich tholeiitic lavas, Merelava volcano, Vanuatu. *Journal of Petrology, 29*, 927-964.

Barsdell, M., & Berry, R. F. (1990). Origin and evolution of primitive island arc ankaramites from western Epi, Vanuatu. *Journal of Petrology, 31*, 747-777.

Beccaluva, L., Bianchini, G., Natali, C., & Siena, F. (2009). Continental flood basalts and mantle plumes: a case study of the northern Ethiopian Plateau. *Journal of Petrology, 50*(7), 1377-1403.

Beier, C., Haase, K., Abouchami, W., Krienitz, M.-S., & Hauff, F. (2008). Magma genesis by rifting of oceanic lithosphere above anomalous mantle: Terceira Rift, Azores. *Geochemistry Geophysics Geosystems, 9*(12), 1-26.

Bergmanis, E. C., Sinton, J. M., & Trusdell, F. A. (2000). Rejuvenated volcanism along the southwest rift zone, East Maui, Hawaii. *Bulletin Volcanologique, 62*, 239-255.

Bonadiman, C., Coltori, M., Beccaluva, L., Griffin, W. L., O'Reilly, S. Y., & Siena, F. (2011). Metasomatism versus host magma infiltration: A case study of Sal mantle xenoliths, Cape Verde Archipelago. In L. Beccaluva (Ed.), *Volcanism and Evolution of the African Lithosphere* (pp. 283-306). Boulder, Colorado: The Geological Society of America.

Booden, M. A., Smith, I. E. M., Black, P. M., & Mauk, J. L. (2011). Geochemistry of the Early Miocene volcanic succession of Northland, New Zealand, and implications for the evolution of subduction in the Southwest Pacific. *Journal of Volcanology and Geothermal Research, 199*, 25-37.

Borisova, A. Y., Nikogosian, I. K., Scoates, J. S., Weis, D., Damasceno, D., Shimizu, N., et al. (2002). Melt, fluid and crystal inclusions in olivine phenocrysts from Kerguelen plume-derived picritic basalts: evidence for interaction with the Kerguelen plateau lithosphere. *Chemical Geology, 183*, 195-220.

Boztug, D., Yagmur, M., Otlu, N., Tatar, S., & Yesiltas, A. (1998). Petrology of the post-collisional, within-plate yildizdag gabbroic pluton, Yildizeli-Sivas region, central Anatolia, Turkey. *Turkish Journal of Earth Sciences, 7*, 37-51.

Cameron, W. E., McCulloch, M. T., & Walker, D. A. (1983). Boninite petrogenesis: chemical and Nd-Sr isotopic constraints. *Earth and Planetary Science Letters, 65*, 75-89.

Chan, L. H., Leeman, W. P., & You, C.-F. (1999). Lithium isotopic composition of Central American Volcanic Arc lavas: implications for modification of subarc mantle by slab-derived fluids. *Chemical Geology, 160*, 255-280.

Chen, C. Y., Frey, F. A., Garcia, M. O., Dalrymple, G. B., & Hart, S. R. (1991). The tholeiite to alkalic basalt transition at Haleakala volcano, Maui, Hawaii. *Contributions to Mineralogy and Petrology, 106*, 183-200.

Cheng, Q. C., Macdougall, J. D., & Lugmair, G. W. (1993). Geochemical studies of Tahiti, Teahitia and Mahetia, Society Island Chain. *Journal of Volcanology and Geothermal Research, 55*, 155-184.

Chung, S.-L., Sun, S. S., Tu, K., Chen-Hong, C., & Lee, C. L. (1994). Late Cenozoic basaltic volcanism around the Taiwan Strait, SE China: product of lithosphere-asthenosphere interaction during continental extension. *Chemical Geology, 112*, 1-20.

Class, C., Altherr, R., Volker, F., Eberz, G., & McCulloch, M. T. (1994). Geochemistry of Pliocene to Quaternary alkali basalts from the Huri Hills, northern Kenya. *Chemical Geology, 113*, 1-22.

Class, C., & Goldstein, S. L. (1997). Plume-lithosphere interactions in the ocean basins: constraints from the source mineralogy. *Earth and Planetary Science Letters, 150*, 245-260.

Class, C., Goldstein, S. L., Altherr, R., & Bachèlery, P. (1998). The process of plume-lithosphere interactions in the ocean basins - the case of Grande Comore. *Journal of Petrology, 39*(5), 881-903.

Coish, R. A. (1989). Boninite lavas in Appalachian ophiolites: a review. In A. J. Crawford (Ed.), *Boninites* (pp. 264-288). London: Unwin Hyman.

Coogan, L. A., MacLeod, C. J., Dick, H. J. B., Edwards, S. J., Kvassnes, A., Natland, J. H., et al. (2001). Whole-rock geochemistry of gabbros from the Southwest Indian Ridge: constraints on geochemical fractionations between the upper and lower oceanic crust and magma chamber processes at (very) slow-spreading ridges. *Chemical Geology, 178*, 1-22.

Crawford et al. (1989) In A. J. Crawford (Ed.), Boninites. London: Unwin Hyman, Chapter 1.

Dávalos-Elizando, M. G. (2009). *Petrología y geoquímica de xenolitos ultramáficos en Cd. Serdán, porción oriental de la Faja Volcánica Trans-Mexicana*. Unpublished MS thesis, Universidad Nacional Autónoma de México, Mexico City.

De Lima, E. F., Machado, A., Nardi, L. V. S., Saldanha, D. L., Azevedo, J. M. M., Sommer, C. A., et al. (2011). Geochemical evidence concerning sources and petrologic evolution of Faial Island, Central Azores. *International Geology Review, 53*(14), 1684-1708.

Deniel, C. (1998). Geochemical and isotopic (Sr, Nd, Pb) evidence for plume-lithosphere interactions in the genesis of Grande Comore magmas (Indian ocean). *Chemical Geology, 144*, 281-303.

Deniel, C., Vidal, P., Coulon, C., Vellutini, P., & Piguet, P. (1994). Temporal evolution of mantle sources during continental rifting: The volcanism of Djibouti (Afar). *Journal of Geophysical Research, 99*(B2), 2853-2869.

Dessai, A. G., Markwick, A., Vaselli, O., & Downes, H. (2004). Granulite and pyroxenite xenoliths from the Deccan Trap: insight into the nature and composition of the lower lithosphere beneath cratonic India. *Lithos, 78*, 263-290.

Devine, J. D. (1995). Petrogenesis of the basalt-andesite-dacite association of Grenada, Lesser Antilles island arc, revisited. *Journal of Volcanology and Geothermal Research, 69*(1), 1-33.

Dixon, J., Clague, D. A., Cousens, B., Monsalve, M. L., & Uhl, J. (2008). Carbonatite and silicate melt metasomatism of the mantle surrounding the Hawaiian plume: Evidence from volatiles, trace elements, and radiogenic isotopes in rejuvenated-stage lavas from Niihau, Hawaii. *Geochemistry Geophysics Geosystems, 9*(9), doi:1029/2008GC002076.

Dostal, J. (1991). Geochemistry of Cenozoic alkali basaltic lavas from Shandong Province, eastern China. *Geochemical Journal, 25*(1), 1-16.

Doucelance, R., Escrig, S., Moreira, M., Gariépy, C., & Kurz, M. D. (2003). Pb-Sr-He isotope and trace element geochemistry of the Cape Verde archipelago. *Geochimica et Cosmochimica Acta, 67*(19), 3717-3733.

Dupuy, C., Barsczus, H. G., Dostal, J., Vidal, P., & Liotard, J.-M. (1989). Subducted and recycled lithosphere as the mantle source of Ocean Island basalts from southern Polynesia, central Pacific. *Chemical Geology, 77*(1), 1-18.

Dupuy, C., Barsczus, H. G., Liotard, J. M., & Dostal, J. (1988). Trace element evidence for the origin of ocean island basalts: an example from the Austral Islands (French Polynesia). *Contributions to Mineralogy and Petrology, 98*, 293-302.

Dupuy, C., Dostal, J., Marcelot, G., Bougault, H., Joron, J. L., & Treuil, M. (1982). Geochemistry of basalts from central and southern New Hebrides arc: implication for their source rock composition. *Earth and Planetary Science Letters, 60*, 207-225.

Eggins, S. M. (1993). Origin and differentation of picritic arc magmas, Ambae (Aoba), Vanuatu. *Contributions to Mineralogy and Petrology, 114*, 79-100.

Elías-Herrera, M., Rubinovich-Kogan, R., Lozano-Santa Cruz, R., & Sánchez-Zavla, J. L. (1991). Nepheline-rich foidolites and rare-earth mineralization in the El Picacho Tertiary intrusive complex, Sierra de Tamaulipas, northeastern Mexico. *Canadian Mineralogist, 29*, 319-336.

Espíndola, J. M., Zamora-Camacho, A., Godinez, M. L., Schaaf, P., & Rodríguez, S. R. (2010). The 1793 eruption of San Martín Tuxtla volcano, Veracruz, Mexico. *Journal of Volcanology and Geothermal Research, 197*(1-4), 188-208.

Fallon, T. J., & Crawford, A. J. (1991). The petrogenesis of high-calcium boninite lavas dredged from the northern Tonga ridge. *Earth and Planetary Science Letters, 102*, 375-394.

Falloon, T. J., Green, D. H., and M. T. McCulloch (1989), Petrogenesis of high-Mg and associated lavas from the north Tonga trench, in: A. J. Crawford (Ed.), Boninites. London: Unwin Hyman, Chapter 14, pp 357-395.

Fan, Q., & Hooper, P. R. (1991). The Cenozoic basaltic rocks of eastern China: petrology and chemical composition. *Journal of Petrology, 32*(4), 765-810.

Foden, J., Song, S. H., Turner, S., Elburg, M., Smith, P. B., Van der Steldt, B., et al. (2002). Geochemical evolution of lithospheric mantle beneath S.E. South Australia. *Chemical Geology, 182*, 663–695.

Frey, F. A., Garcia, M. O., & Roden, M. F. (1994). Geochemical characteristics of Koolau volcano: implications of intershield geochemical differences among Hawaiian volcanoes. *Geochimica et Cosmochimica Acta, 58*(5), 1441-1462.

Furman, T., Bryce, J. G., Karson, J., & Iotti, A. (2004). East African rift system (EARS) plume structure: insights from Quaternary mafic lavas of Turkana, Kenya. *Journal of Petrology, 45*(5), 1069-1088.

Furman, T., Kaleta, K., Bryce, J. G., & Hanan, B. B. (2006). Tertiary mafic lavas of Turkana, Kenya: constraints on East African plume structure and the occurrence of high-□ volcanism in Africa. *Journal of Petrology, 47*(6), 1221-1244.

Gamble, J. A., Smith, I. E. M., Kokelaar, B. P., Cole, J. W., Houghton, B. F., & Wilson, J. N. (1990). The petrology, phase relations and tectonic setting of basalts from Taupo volcanic zone, New Zealand and the Kermadec island arc - Havre trough, SW Pacific. *Journal of Volcanology and Geothermal Research, 43*, 235-270.

Gamble, J. A., Smith, I. E. M., McCulloch, M. T., Graham, I. J., & Kokelaar, B. P. (1993). The geochemistry and petrogenesis of basalts from the Taupo volcanic zone and Kermadec Island arc, S.W. Pacific. *Journal of Volcanology and Geothermal Research, 54*(3-4), 265-290.

Geldmacher, J., & Hoernle, K. (2000). The 72 Ma geochemical evolution of the Medeira hotspot (eastern North Atlantic): recycling of Paleozoic (□ 500 Ma) oceanic lithosphere. *Earth and Planetary Science Letters, 183*, 73-92.

Genske, F. S., Turner, S. P., Beier, C., & Schaefer, B. F. (2012). The petrology and geochemistry of lavas from the western Azores Islands of Flores and Corvo. *Journal of Petrology, 53*(8), 1673-1708.

Gerlach, D. C., Frey, F. A., Moreno-Roa, H., & Lopez-Escobar, L. (1988). Recent volcanism in the Puyehue-Cordon Caulle region, southern Andes, Chile (40.5°S): petrogenesis of evolved lavas. *Journal of Petrology, 29*(2), 333-382.

Grechin, V. I., Eroshchev-Shak, V. A., & Zolotarev, B. P. (1981). Petrochemistry of abyssal oceanic basalts and dolerites, and their secondary alterations, Sites 469, 470, 471, 472, 473. In R. S. Yeats, B. U. Haq & e. al. (Eds.), *Initial Reports of the Deep Sea Drilling Project* (Vol. 63, pp. 711-732). Washington, D. C.: U.S. Government Printing Office.

Gysi, A. P., Jagoutz, O., Schmidt, M. W., & Targuisti, K. (2011). Petrogenesis of proxenites and melt infiltrations in the ultramafic complex of Beni Bousera, Northern Morocco. *Journal of Petrology, 52*(9), 1679-1735.

Haase, K. M., Goldschmidt, B., & Garbe-Schönberg, C.-D. (2004). Petrogenesis of Tertiary continental intra-plate lavas from the Westerwald region, Germany. *Journal of Petrology, 45*(5), 883-905.

Haase, K. M., Worthington, T. J., Stoffers, P., Garbe-Schönberg, D., & Wright, I. (2002). Mantle dynamics, element recycling, and magma genesis beneath the Kermadec arc-Havre Trough. *Geochemistry Geophysics Geosystems, 3*(11), 1071, doi:1010.1029/2002GC00035.

Hanyu, T., Tatsumi, Y., Senda, R., Miyazaki, T., Chang, Q., Hirahara, Y., et al. (2011). Geochemical characteristics and origin of the HIMU reservoir: A possible mantle plume source in the lower mantle. *Geochemistry Geophysics Geosystems, 12*(2), 1-30.

Heinrich, W., & Besch, T. (1992). Thermal history of the upper mantle beneath a young back-arc extensional zone: ultramafic xenoliths from San Luis Potosí, central Mexico. *Contributions to Mineralogy and Petrology, 111*, 126-142.

Hémond, C., Devey, C. W., & Chauvel, C. (1994). Source compositions and melting processes in the Society and Austral plumes (South Pacific Ocean): element and isotope (Sr, Nd, Pb, Th) geochemistry. *Chemical Geology, 115*, 7-45.

Hickey, R. L., & Frey, F. A. (1982). Geochemical characteristics of boninite series volcanics: implications for their source. *Geochimica et Cosmochimica Acta, 46*, 2099-2115.

Holm, P. M., Wilson, J. R., Christensen, B. P., Hansen, L., Hansen, S. L., Hein, K. M., et al. (2006). Sampling the Cape Verde mantle plume: evolution of melt compositions on Santo Antão, Cape Verde Islands. *Journal of Petrology, 47*(1), 145-189.

Ireland, T. J., Walker, R. J., & Garcia, M. O. (2009). Highly siderophile elements and 187Os isotope systematics of Hawaiian picrites: Implications for parental melt composition and source heterogeneity. *Chemical Geology, 260*(1-2), 112-128.

Jackson, M. C., Frey, F. A., Garcia, M. O., & Wilmoth, R. A. (1999). Geology and geochemistry of basaltic lava flows and dikes from the Trans-Koolau tunnel, Oahu, Hawaii. *Bulletin of Volcanology, 60*, 381-401.

Jenner, G. A. (1981). Geochemistry of high-Mg andesites from Cape Vogel, Papua New Guinea. *Chemical Geology, 33*, 307-332.

Jørgensen, J. O., & Holm, P. M. (2002). Temporal variation and carbonatite contamination in primitive ocen island volcanics from São Vicente, Cape Verde islands. *Chemical Geology, 192*, 249-267.

Kawabata, H., Hanyu, T., Chang, Q., Kimura, J.-I., Nichols, A. R. L., & Tatsumi, Y. (2011). The petrology and geochemistry of St. Helena alkali basalts: evaluation of the oceanic crust-recycling model for HIMU OIB. *Journal of Petrology, 52*(4), 791-838.

Kay, S. M., & Kay, R. W. (1994). Aleutian magmas in space and time. In G. Plafker & H. C. Berg (Eds.), *The Geology of North America* (Vol. G-1, pp. 687-722). USA: Geological Society of America.

Kepezhinskas, P., McDermott, F., Defant, M. J., Hochstaedter, A., Drummond, M. S., Hawkesworth, C. J., et al. (1997). Trace element and Sr-Nd-Pb isotopic constraints on a three-component model of Kamchatka arc petrogenesis. *Geochimica et Cosmochimica Acta, 61*(3), 577-600.

Kokfelt, T. F., Hoernle, K., Hauff, F., Fiebig, J., Werner, R., & Garbe-Schönberg, D. (2006). Combined trace element and Pb–Nd–Sr–O isotope evidence for recycled oceanic crust (upper and lower) in the Iceland mantle plume. *Journal of Petrology, 47*(9), 1705-1749.

Kurt, M. D., & Geist, D. (1999). Dynamics of the Galapagos hotspot from helium isotope geochemistry. *Geochimica et Cosmochimica Acta,, 63*(23/24), 4139-4156.

Lassiter, J. C., Blichert-Toft, J., Hauri, E. H., & Barsczus, H. G. (2003). Isotope and trace element variations in lavas from Raivavae and Rapa, Cook-Austral islands: constraints on the nature of HIMU- and EM-mantle and the origin of mid-plate volcanism in French Polynesia. *Chemical Geology, 202*, 115-138.

Le Roex, A. P., Dick, H. J. B., Gulen, L., Reid, A. M., & Erlank, A. J. (1987). Local and regional heterogeneity in MORB from the Mid-Atlantic Ridge between 54.5°S and 51°S: evidence for geochemical enrichment. *Geochimica et Cosmochimica Acta, 51*, 541-555.

Liotard, J. M., Barsczus, H. G., Dupuy, C., & Dostal, J. (1986). Geochemistry and origin of basaltic lavas from Marquesas Archipelago, French Polynesia. *Contributions to Mineralogy and Petrology, 92*, 260-268.

Lipman, P. W., Rhodes, R. M., & Dalrymple, G. B. (1990). The Ninole Basalt - Implications for the structural evolution of Mauna Loa volcano, Hawaii. *Bulletin of Volcanology, 53*(1), 1-19.

Longpre´, M.-A., Troll, V. R., Walter, T. R., & Hansteen, T. H. (2009). Volcanic and geochemical evolution of the Teno massif, Tenerife, Canary Islands: Some repercussions of giant landslides on ocean island magmatism. *Geochemistry Geophysics Geosystems, 10*(12), Q12017.

Maaløe, S., James, D., Smedley, P., Petersen, S., & Germann, L. B. (1992). The Koloa volcanic suite of Kauai, Hawaii. *Journal of Petrology, 33*(4), 761-784.

Macdonald, R., Rogers, N. W., Fitton, J. G., Black, S., & Smith, M. (2001). Plume-lithosphere interactions in the generation of the basalts of the Kenya rift, East Africa. *Journal of Petrology, 42*(3), 877-900.

Maclennan, J., McKenzie, D., Gronvold, K., & Slater, L. (2001). Crustal accretion under northern Iceland. *Earth and Planetary Science Letters, 191*, 295-310.

Macpherson, C. G., Hilton, D. R., Day, J. M. D., Lowry, D., & Grfnvold, K. (2005). High-3He/4He, depleted mantle and low-d18O, recycled oceanic lithosphere in the source of central Iceland magmatism. *Earth and Planetary Science Letters, 233*, 411– 427.

Martynov, A. Y., Kimura, J.-I., Martynov, Y. A., & Rybin, A. V. (2010). Geochemistry of late Cenozoic lavas on Kunashir Island, Kurile Arc. *Island Arc, 19*, 86-104.

Melluso, L., & Morra, V. (2000). Petrogenesis of Late Cenozoic mafic alkaline rocks of the Nosy Be archipelago (northern Madagascar): relationships with Comorean magmatism. *Journal of Volcanology and Geothermal Research, 96*(1-2), 129-142.

Morton-Bermea, O. (1990). *Zur petrologie des alkaligesteins-intrusivkomplexes der Sierra de Picachos (Nuevo León, Mexiko)*. Unpublished MS thesis, Universität Karlsruhe.

Naumann, T., Geist, D., & Kurz, M. (2002). Petrology and geochemistry of Volcán Cerro Azul: petrologic diversity among the western Galápagos volcanoes. *Journal of Petrology, 48*(5), 859-883.

Needham, A. J., Lindsay, J. M., Smith, I. E. M., Augustinus, P., & Shane, P. A. (2011). Sequential eruption of alkaline and sub-alkaline magmas from a small monogenetic volcano in the Auckland Volcanic Field, New Zealand. *Journal of Volcanology and Geothermal Research, 201*(1-4), 126-142.

Nick, K. (1988). *Mineralogische, Geochemische und Petrographische Untersuchungen in der Sierra de San Carlos (Mexiko)*. Unpublished Doctoral thesis, Universitaet (TH) Fridericiana Karlsruhe, Karlsruhe, Germany.

Nikogosian, I., & van Bergen, M. J. (2010). Heterogeneous mantle sources of potassium-rich magmas in central-southern Italy: Melt inclusion evidence from Roccamonfina and Ernici (Mid Latina Valley). *Journal of Volcanology and Geothermal Research, 197*, 279-302.

Nye, C. J., & Reid, M. R. (1986). Geochemistry of primary and least fractionated lavas from Okmok volcano, central Aleutians: implications for arc magma genesis. *Journal of Geophysical Research, 91*, 10271-10287.

Palacz, Z. A., & Saunders, A. D. (1986). Coupled trace element and isotope enrichment in the Cook-Austral-Samoa islands, southwest pacific. *Earth and Planetary Science Letters, 79*, 270-280.

Pallares, C., Maury, R. C., Bellon, H., Royer, J.-Y., Calmus, T., Aguillón-Robles, A., et al. (2007). Slab-tearing following ridge-trench collision: evidence from Miocene volcanism in Baja California, Mexico. *Journal of Volcanology and Geothermal Research, 161*, 95-117.

Paul, D., Kamenetsky, V. S., Hofmann, A. W., & Stracke, A. (2007). Compositional diversity among primitive lavas of Mauritius, Indian Ocean: Implications for mantle sources. *Journal of Volcanology and Geothermal Research, 164*, 76–94.

Paul, D., & White, W. M. (2005). Geochemistry of Mauritius and the origin of rejuvenescent volcanism on oceanic island volcanoes. *Geochemistry Geophysics Geosystems, 6*(5), 1-22.

Peate, D. W., Baker, J. A., Jakobsson, S. P., Waight, T. E., Kent, A. J. R., Grassineau, N. V., et al. (2009). Historic magmatism on the Reykjanes Peninsula, Iceland: a snap-shot of melt generation at a ridge segment. *Contributions to Mineralogy and Petrology, 157*, 359-382.

Pe-Piper, G., & Piper, D. J. W. (1994). Miocene magnesian andesites and dacites, Evia, Greece: adakites associated with subducting slab detachment and extension. *Lithos, 31*, 125-140.

Perfit, M. R., Saunders, A. D., & Fornari, D. J. (1982). Phase chemistry, fractional crystallization, and magma mixing in basalts from the Gulf of California, Deep Sea Drilling Project Leg 64. In J. R. Curray, D. G. Moore & e. al. (Eds.), *Initial Reports of the Deep Sea Drilling Project, 64* (Vol. 64, pp. 649-666). Washington: U.S. Govt. Printing Office.

Price, R. C., Cooper, A. F., Woodhead, J. D., & Cartwright, I. (2003). Phonolitic diatremes within the Dunedin volcano, South Island, New Zealand. *Journal of Petrology, 44*(11), 2053-2080.

Reagan, M. K., Hanan, B. B., Heizler, M. T., Hartman, B. S., & Hickey-Vargas, R. (2008). Petrogenesis of volcanic rocks from Saipan and Rota, Mariana Islands, and implications for evolution of Nascent Island Arcs. *Journal of Petrology, 49*(3), 441-464.

Reagan, M. K., & Meijer, A. (1984). Geology and geochemistry of early arc-volcanic rocks from Guam. *Geological Society of America Bulletin, 95*, 701-713.

Ren, Z.-Y., Hanyu, T., Miyazaki, T., Chang, Q., Kawabata, H., Takahashi, T., et al. (2009). Geochemical Differences of the Hawaiian Shield Lavas: Implications for Melting Process in the Heterogeneous Hawaiian Plume. *Journal of Petrology, 8*, 1553-1573.

Ren, Z.-Y., Takahashi, E., Orihashi, Y., & Johnson, K. T. M. (2004). Petrogenesis of tholeiitic lavas from the submarine Hana ridge, Haleakala volcano, Hawaii. *Journal of Petrology, 45*(10), 2067-2099.

Révillon, S., Arndt, N. T., Hallot, E., Kerr, A. C., & Tarney, J. (1999). Petrogenesis of picrites from the Caribbean Plateau and the North Atlantic magmatic province. *Lithos, 49*(1), 1-21.

Rhodes, J. M., Huang, S. W., Frey, F. A., Pringle, M., & Xu, G. (2012). Compositional diversity of Mauna Kea shield lavas recovered by the Hawaii Scientific Drilling Project: Inferences on source lithology, magma supply, and the role of multiple volcanoes. *Geochemistry Geophysics Geosystems, 13*(3), 2-28.

Rhodes, J. M., & Vollinger, M. J. (2004). Composition of basaltic lavas sampled by phase-2 of the Hawaii Scientific Drilling Project: Geochemical stratigraphy and magma types. *Geochemistry Geophysics Geosystems, 5*(3), 1-38.

Rogers, G., & Saunders, A. D. (1989). Magnesian and andesites from Mexico, Chile and the Aleutian Islands: implications for magmatism associated with ridge-trench collision. In A. J. Crawford (Ed.), *Boninites ad realted rocks* (pp. 416-445).

Romick, J. D., Perfit, M. R., Swanson, S. E., & Shuster, R. D. (1990). Magmatism in the eastern Aleutian arc: temporal characteristic of igneous activity on Akutan Island. *Contributions to Mineralogy and Petrology, 104*, 700-721.

Rudek, E. A., Fodor, R. V., & Bauer, G. R. (1992). Petrology of ultramafic and mafic xenoliths in picrite of Kahoolawe Island, Hawaii. *Bulletin of Volcanology, 55*, 74-84.

Saal, A. E., Kurz, M. D., Hart, S. R., Blusztajn, J. S., Blichert-Toft, J., Liang, Y., et al. (2007). The role of lithospheric gabbros on the composition of Galapagos lavas. *Earth and Planetary Science Letters, 257*, 391-406.

Saunders, A. D., Fornari, D. J., Tarney, J., & Treuil, M. (1982). Geochemistry of basic igneous rocks, Gulf of California, Deep Sea Drilling Project Leg 64. In J. R. Curray, D. G. Moore & e. al. (Eds.), *Initial Reports of the Deep Sea Drilling Project, 64* (Vol. 64, pp. 595-642). Washington: U.S. Govt. Printing Office.

Schilling, J.-G., Zajac, M., Evans, R., Johnston, T., White, W., Devine, J. D., et al. (1983). Petrologic and geochemical variations along the Mid-Atlantic Ridge from 29°N to 73°N. *American Journal of Science, 283*, 510-586.

Schuth, S., Münker, C., Konig, S., Qopoto, C., Basi, S., Garbe-Schönberg, D., et al. (2009). Petrogenesis of lavas along the Solomon island arc, SW Pacific: coupling of compositional variations and subduction zone geometry. *Journal of Petrology, 50*(5), 781-811.

Schuth, S., Rohrbach, A., Münker, C., Ballhaus, C., Garbe-Schönberg, D., & Qopoto, C. (2004). Geochemical constraints on the petrogenesis of arc picrites and basalts, New Georgia group, Solomon Islands. *Contributions to Mineralogy and Petrology, 148*, 288-304.

Schwarz, S., Klügel, A., van den Bogaard, P., & Geldmacher, J. (2005). Internal structure and evolution of a volcanic rift system in the eastern North Atlantic: the Desertas rift zone, Madeira archipelago. *Journal of Volcanology and Geothermal Research, 141*, 123-155.

Sherrod, D. R., Murai, T., & Tagami, T. (2007). New K–Ar ages for calculating end-of-shield extrusion rates at West Maui volcano, Hawaiian island chain. *Bulletin of Volcanology, 69*(6), 627–642.

Sheth, H. C., & Melluso, L. (2008). The Mount Pavagadh volcanic suite, Deccan Traps: geochemical stratigraphy and magmatic evolution. *Journal of Asian Earth Sciences, 32*(1), 5-21.

Shimizu, N., & Arculus, R. J. (1975). Rare earth element concentrations in a suite of basanitoids and alkali olivine basalts from Grenada, Lesser Antilles. *Contributions to Mineralogy and Petrology, 50*, 231-240.

Shuto, K., Ishimoto, H., Hirahara, Y., Sato, M., Matsui, K., Fujibayashi, N., et al. (2006). Geochemical secular variation of magma source during Early to Middle Miocene time in the Niigata area, NE Japan: asthenospheric mantle upwelling during back-arc basin opening. *Lithos, 86*, 1-33.

Slater, L., McKenzie, D., Gronvold, K., & Shimizu, N. (2001). Melt Generation and Movement beneath Theistareyir, NE Iceland. *Journal of Petrology, 42*, 321-354.

Snow, J. E. (2002). Major and trace element evolution of Hole 735B gabbros. *Proceedings of the Ocean Drilling Program, Scientific Results, 176*, 1-18.

Späth, A., Le Roex, A. P., & Opiyo-Akech, N. (2001). plume-lithosphere interaction and the origin of continental rift-related alkaline volcanism - the Chyulu hills volcanic province, southern Kenya. *Journal of Petrology, 42*(4), 765-787.

Spengler, S. R., & Garcia, M. O. (1988). Geochemistry of the Hawi lavas, Kohala Volcano, Hawaii. *Contributions to Mineralogy and Petrology, 99*, 90-104.

Spice, H. E., Fitton, J. G., & Kirstein, L. A. (2016). Temperature fluctuation of the Iceland mantle plume through time. *Geochemistry Geophysics Geosystems, 17*, 243–254, doi:210.1002/2015GC006059.

Storey, M., Wolff, J. A., Norry, M. J., & Marriner, G. F. (1989). Origin of hybrid lavas from Agua de Pau volcano, Sao Miguel, Azores. In A. D. Saunders & M. J. Norry (Eds.), *Magmatism in the ocean basins* (pp. 161-180). Oxford: Geological Society Special Publication No. 42.

Stracke, A., Zindler, A., Salters, V. J. M., McKenzie, D., Blichert-Toft, J., Albarede, F., et al. (2003). Theistareykir revisited. *Geochemistry Geophysics Geosystems, 4*(2), 1-49.

Takamasa, A., Nakai, S., Sahoo, Y., Hanyum, T., & Tatsumi, Y. (2009). W isotope compositions of oceanic islands basalts from French Polynesia and their meaning for core-mantle interaction. *Chemical Geology, 260*(1-2), 37-46.

Taylor, R. N., Nesbitt, R. W., Vidal, P., Harmon, R. S., Auvray, B., & Croudace, I. W. (1994). Mineralogy, chemistry, and genesis of the boninite series volcanics, Chichijima, Bonin Islands, Japan. *Journal of Petrology, 35*(3), 577-617.

Teasdale, R., Geist, D., Kurz, M., & Harpp, K. (2005). 1998 eruption at Volcán Cerro Azul, Galápagos Islands: I. Syn-eruptive petrogenesis. *Bulletin of Volcanology, 67*, 170-185.

Thirlwall, M. F., Graham, A. M., Arculus, R. J., Harmon, R. S., & Macpherson, C. G. (1996). Resolution of the effects of crustal assimilation, sediment subduction, and fluid transport in island arc magmas: Pb-Sr-Nd-O isotope geochemistry of Grenada, Lesser Antilles. *Geochimica et Cosmochimica Acta, 60*(23), 4785-4810.

Thirlwall, M. F., Singer, B. S., & Marriner, G. F. (2000). ^{39}Ar-^{40}Ar ages and geochemistry of the basaltic shield stage of Tenerife, Canary Islands, Spain. *Journal of Volcanology and Geothermal Research, 103*, 247-297.

Timm, C., Hoernle, K., Werner, R., Hauff, F., van den Bogaard, P., Michael, P., et al. (2011). Age and geochemistry of the oceanic Manihiki Plateau, SW Pacific: New evidence for a plume origin. *Earth and Planetary Science Letters, 304*, 135-146.

Turner, S., & Foden, J. (2001). U, Th and Ra disequilibria, Sr, Nd and Pb isotope and trace element variations in Sunda arc lavas: predominance of a subducted sediment component. *Contributions to Mineralogy and Petrology, 142*, 43-57.

Umino, S. (1986). Magma mixing in boninite sequence of Chichijima Bonin islands. *Journal of Volcanology and Geothermal Research, 29*, 125-157.

Upton, B. G. J., Semet, M. P., & Joron, J.-L. (2000). Cumulate clasts in the Bellecombe ash member, Piton de la Fournaise, Réunion island, and their bearing on cumulative processes in the petrogenesis of the Réunion lavas. *Journal of Volcanology and Geothermal Research, 104*, 297-318.

USGS439_DB_U.S. Geological Survey, National Geochemical Database, internet address.

Verma, S. P. (2006). Extension-related origin of magmas from a garnet-bearing source in the Los Tuxtlas volcanic field, Mexico. *International Journal of Earth Sciences, 95*(5), 871-901.

Verma, S. P., Salazar-V., A., Negendank, J. F. W., Milán, M., Navarro-L., I., & Besch, T. (1993). Características petrográficas y geoquímicas de elementos mayores del campo volcánico de Los Tuxtlas, Veracruz, México. *Geofísica Internacional, 32*(2), 237-248.

Walker, D. A., & Cameron, W. E. (1983). Boninite primary magmas: evidence from Cape Vogel Peninsula, PNG. *Contributions to Mineralogy and Petrology, 83*, 150-158.

West, H. B., Garcia, M. O., Gerlach, D. C., & Romero, J. (1992). Geochemistry of tholeiites from Lanai, Hawaii. *Contributions to Mineralogy and Petrology, 112*(4), 520-542.

White, W. M., McBirney, A. R., & Duncan, R. A. (1993). Petrology and geochemistry of the Galápagos Islands: portrait of a pathological mantle plume. *Journal of Geophysical Research, 98*(B11), 19533-19563.

Willbold, M., & Stracke, A. (2006). Trace element composition of mantle end-members: implications for recycling and upper and lower continental crust. *Geochemistry Geophysics Geosystems, 7*(4), doi:10.1029/2005GC001005.

Woodhead, J. D., Eggins, S. M., & Johnson, R. W. (1998). Magma genesis in the New Britain island arc: further insights into melting and mass transfer processes. *Journal of Petrology, 39*(9), 1641-1668.

Woodhead, J. D., & Johnson, R. W. (1993). Isotopic and trace-element profiles across the New Britain island arc, Papua New Guinea. *Contributions to Mineralogy and Petrology, 113*, 479-491.

Wright, I. C., Worthington, T. J., & Gamble, J. A. (2006). New multibeam and geochemistry of the 30°-35°S sector, and overview, of southern Kermadec arc volcanism. *Journal of Volcanology and Geothermal Research, 149*(3/4), 263-296.

Xu, G., Frey, F. A., Clague, D. A., Weis, D., & Beeson, M. H. (2005). East Molokai and other Kea-trend volcanoes: magmatic processes and sources as they migrate away from the Hawaiian hot spot. *Geochemistry Geophysics Geosystems, 6*(5), Q05008, doi: 05010.01029/02004GC000830.

Zou, H., Zindler, A., Xisheng, X., & Qi, Q. (2000). Major, trace element, and Nd, Sr and Pb isotope studies of Cenozoic basalts in SE China: mantle sources, regional variations and tectonic significance. *Chemical Geology, 171*, 33-47.

Table S2. Adjustment of major elements used for computing the isometric log-ratio (ilr) transformations (in fact, we used modified centered log-ratio (mclr) transformations).

Function	Equation for adjustment
SiO_2A	$= \frac{100 \times SiO_2}{[SiO_2 + TiO_2 + Al_2O_3 + Fe_2O_3{}^t + MnO + MgO + CaO + Na_2O + K_2O + P_2O_5)]}$
TiO_2A	$= \frac{100 \times TiO_2}{[SiO_2 + TiO_2 + Al_2O_3 + Fe_2O_3{}^t + MnO + MgO + CaO + Na_2O + K_2O + P_2O_5)]}$
Al_2O_3A	$= \frac{100 \times Al_2O_3}{[SiO_2 + TiO_2 + Al_2O_3 + Fe_2O_3{}^t + MnO + MgO + CaO + Na_2O + K_2O + P_2O_5)]}$
$Fe_2O_3{}^tA$	$= \frac{100 \times Fe_2O_3{}^t}{[SiO_2 + TiO_2 + Al_2O_3 + Fe_2O_3{}^t + MnO + MgO + CaO + Na_2O + K_2O + P_2O_5)]}$
$MnOA$	$= \frac{100 \times MnO}{[SiO_2 + TiO_2 + Al_2O_3 + Fe_2O_3{}^t + MnO + MgO + CaO + Na_2O + K_2O + P_2O_5)]}$
$MgOA$	$= \frac{100 \times MgO}{[SiO_2 + TiO_2 + Al_2O_3 + Fe_2O_3{}^t + MnO + MgO + CaO + Na_2O + K_2O + P_2O_5)]}$
$CaOA$	$= \frac{100 \times CaO}{[SiO_2 + TiO_2 + Al_2O_3 + Fe_2O_3t + MnO + MgO + CaO + Na_2O + K_2O + P_2O_5)]}$
Na_2OA	$= \frac{100 \times Na_2O}{[SiO_2 + TiO_2 + Al_2O_3 + Fe_2O_3{}^t + MnO + MgO + CaO + Na_2O + K_2O + P_2O_5)]}$
K_2OA	$= \frac{100 \times K_2O}{[SiO_2 + TiO_2 + Al_2O_3 + Fe_2O_3{}^t + MnO + MgO + CaO + Na_2O + K_2O + P_2O_5)]}$
P_2O_5A	$= \frac{100 \times P_2O_5}{[SiO_2 + TiO_2 + Al_2O_3 + Fe_2O_3{}^t + MnO + MgO + CaO + Na_2O + K_2O + P_2O_5)]}$

Table S3. Isometric log-ratio (ilr) transformation equations for major elements (the function ln represents natural logarithm; the final letter A after chemical symbols refer to the adjusted concentrations on an anhydrous basis to 100% with total Fe as $Fe_2O_3{}^t$): (in fact, we used modified centered log-ratio (mclr) transformations).

Isometric log-ratio	Equation for transformation
$ilr1_{TiM}$	$= \sqrt{\frac{1}{2}} \times \ln\{[\sqrt[10]{(SiO_2A \times TiO_2A \times Al_2O_3A \times Fe_2O_3{}^tA \times MnOA \times MgOA \times CaOA \times Na_2OA \times K_2OA \times P_2O_5A)}]/TiO_2A\}$
$ilr2_{AlM}$	$= \sqrt{\frac{2}{3}} \times \ln\{[\sqrt[10]{(SiO_2A \times TiO_2A \times Al_2O_3A \times Fe_2O_3{}^tA \times MnOA \times MgOA \times CaOA \times Na_2OA \times K_2OA \times P_2O_5A)}]/Al_2O_3A\}$
$ilr3_{FeM}$	$= \sqrt{\frac{3}{4}} \times \ln\{[\sqrt[10]{(SiO_2A \times TiO_2A \times Al_2O_3A \times Fe_2O_3{}^tA \times MnOA \times MgOA \times CaOA \times Na_2OA \times K_2OA \times P_2O_5A)}]/Fe_2O_3{}^tA\}$
$ilr4_{MnM}$	$= \sqrt{\frac{4}{5}} \times \ln\{[\sqrt[10]{(SiO_2A \times TiO_2A \times Al_2O_3A \times Fe_2O_3{}^tA \times MnOA \times MgOA \times CaOA \times Na_2OA \times K_2OA \times P_2O_5A)}]/MnOA\}$
$ilr5_{MgM}$	$= \sqrt{\frac{5}{6}} \times \ln\{[\sqrt[10]{(SiO_2A \times TiO_2A \times Al_2O_3A \times Fe_2O_3{}^tA \times MnOA \times MgOA \times CaOA \times Na_2OA \times K_2OA \times P_2O_5A)}]/MgOA\}$
$ilr6_{CaM}$	$= \sqrt{\frac{6}{7}} \times \ln\{[\sqrt[10]{(SiO_2A \times TiO_2A \times Al_2O_3A \times Fe_2O_3{}^tA \times MnOA \times MgOA \times CaOA \times Na_2OA \times K_2OA \times P_2O_5A)}]/CaOA\}$
$ilr7_{NaM}$	$= \sqrt{\frac{7}{8}} \times \ln\{[\sqrt[10]{(SiO_2A \times TiO_2A \times Al_2O_3A \times Fe_2O_3{}^tA \times MnOA \times MgOA \times CaOA \times Na_2OA \times K_2OA \times P_2O_5A)}]/Na_2OA\}$
$ilr8_{KM}$	$= \sqrt{\frac{8}{9}} \times \ln\{[\sqrt[10]{(SiO_2A \times TiO_2A \times Al_2O_3A \times Fe_2O_3{}^tA \times MnOA \times MgOA \times CaOA \times Na_2OA \times K_2OA \times P_2O_5A)}]/K_2OA\}$
$ilr9_{PM}$	$= \sqrt{\frac{9}{10}} \times \ln\{[\sqrt[10]{(SiO_2A \times TiO_2A \times Al_2O_3A \times Fe_2O_3{}^tA \times MnOA \times MgOA \times CaOA \times Na_2OA \times K_2OA \times P_2O_5A)}]/P_2O_5A\}$

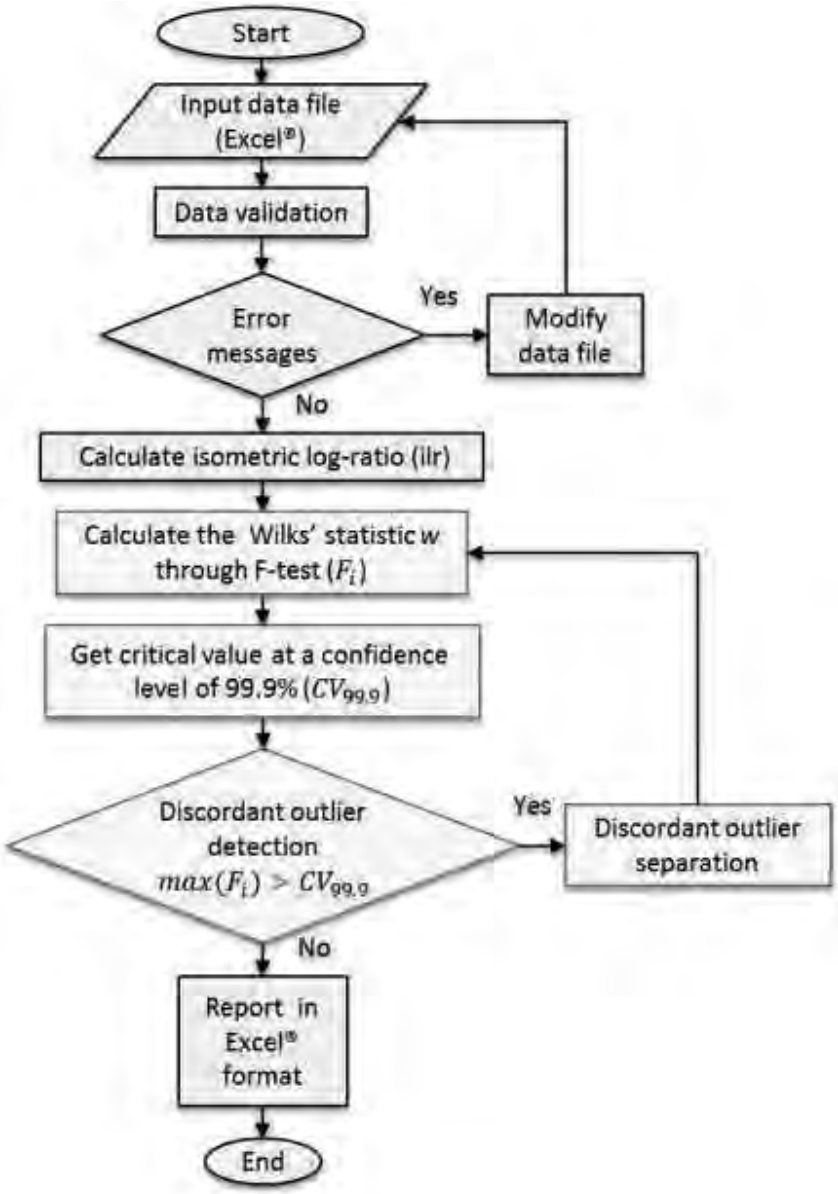

Figure S3. Schematic flow diagram for the computer program DOMuDaF

Table S4. Measured major element composition of the High-Mg komatiite rock samples in the original database before multivariate discordant outlier detection and separation (total Fe is input as $Fe_2O_3^t$*).

Consec	Name	SiO_2	TiO_2	Al_2O_3	$Fe_2O_3^t$*	FeO^t*	MnO	MgO	CaO	Na_2O	K_2O	P_2O_5
1	UPSJ0004	41.63	0.42	5.99	0	15.48	0.22	27.87	7.08	0.53	0.03	0.02
2	UPSJ0005	43.09	0.51	5.41	0	13.40	0.21	26.27	9.53	0.55	0.01	0.01
3	UPSJ0006	43.06	0.55	7.50	0	13.10	0.20	24.67	9.47	0.75	0.03	0.01
4	LRDa0013	42.70	0.65	4.07	12.94	0	0.17	34.90	3.26	0.37	0.08	0.06
5	RAHK0001	43.38	0.43	5.90	11.94	0	0.18	31.91	5.96	0.18	0.07	0.04
6	RAHK0002	43.92	0.47	6.29	11.98	0	0.18	31.31	5.56	0.20	0.05	0.03
7	SFKi020	44.45	0.25	9.10	0	9.85	0.15	27.52	7.81	0.70	0.00	0.02
8	SFKi017	44.92	0.96	8.01	0	12.49	0.18	24.69	7.49	0.90	0.05	0.08
9	SFKi001	44.37	0.46	9.69	0	10.50	0.17	25.98	7.65	0.76	0.04	0.04
10	SFKi002	43.87	0.33	7.63	0	10.32	0.17	31.94	5.28	0.24	0.08	0.03
11	SFKi003	44.75	0.50	10.57	0	10.56	0.17	23.34	8.52	1.26	0.12	0.05
12	SFKi004	44.38	0.42	9.10	0	10.67	0.16	27.52	6.90	0.64	0.07	0.04
13	SFKi005	43.45	0.36	7.56	0	10.87	0.18	31.11	5.73	0.32	0.05	0.03
14	SFKi006	44.71	0.65	9.53	0	11.04	0.17	24.80	7.63	0.84	0.11	0.05
15	SFKi010	42.38	0.59	7.31	0	12.12	0.18	30.69	5.44	0.95	0.05	0.05
16	SFKi011	41.87	0.53	5.86	0	10.70	0.16	34.14	4.50	0.79	0.08	0.03
17	SFKi012	44.97	0.53	9.73	0	10.74	0.17	24.85	8.08	0.87	0.08	0.04
18	SFKi013	44.08	0.39	8.93	0	10.27	0.16	28.62	6.85	0.75	0.09	0.03
19	SFKi014	44.30	0.44	9.38	0	10.24	0.16	27.22	7.46	0.81	0.13	0.04
20	SFKi015	44.25	0.46	8.23	0	10.82	0.17	28.91	6.52	0.84	0.14	0.04
21	SSSM0034	37.59	0.18	20.37	3.19	0	0.05	22.27	17.13	0.02	0.01	0.01
22	SSSM0035	41.21	0.93	10.21	3.15	0	0.07	31.89	13.03	0.01	0.01	0.01
23	UPSJ0007	41.87	0.83	7.04	0	15.18	0.22	24.07	8.58	0.57	0.05	0.05
24	BCBG0012	42.75	0.01	0.37	0	7.89	0.12	47.60	0.58	0.01	0.01	0.02
25	BCBG0011	43.33	0.04	0.40	0	7.72	0.12	46.82	0.79	0.01	0.05	0.02
26	BCBG0008	42.76	0.05	0.71	0	8.18	0.12	44.92	2.40	0.01	0.01	0.03
27	BCBG0001	44.68	0.12	1.81	0	8.34	0.13	41.81	1.52	0.33	0.45	0.05
28	BCBG0003	43.89	0.21	2.21	0	10.08	0.14	39.19	2.79	0.23	0.49	0.02
29	BCBG0009	43.91	0.15	1.84	0	8.36	0.13	41.79	2.52	0.08	0.03	0.03
30	BCBG0005	41.91	0.12	0.81	0	10.71	0.13	43.60	1.45	0.26	0.21	0.01
31	UPSJ0002	41.83	0.46	3.92	0	14.77	0.21	30.71	6.62	0.33	0.04	0.02
32	Snow0011	42.82	0.10	9.38	11.05	0	0.16	29.08	5.84	1.01	0.05	0.01
33	BCBG0004	43.38	0.09	0.34	0	7.68	0.12	45.52	1.35	0.26	0.29	0.06
34	BCBG0002	43.75	0.12	1.82	0	8.28	0.13	42.39	2.13	0.12	0.15	0.01
35	BCBG0007	43.42	0.11	0.47	0	7.56	0.12	45.07	1.46	0.26	0.18	0.07

* Either $Fe_2O_3^t$ or FeO^t should be input; the progam will use the conversion to $Fe_2O_3^t$ (see Table S5).

Table S5. Adjusted major element composition of the High-Mg komatiite rock samples in the original database before multivariate discordant outlier detection and separation (equations in Table S1 and data from Table S4).

Consec	Name	SiO_2A	TiO_2A	Al_2O_3A	$Fe_2O_3^tA$	MnOA	MgOA	CaOA	Na_2OA	K_2OA	P_2O_5A
1	UPSJ0004	41.22	0.42	5.93	17.03	0.220	27.59	7.01	0.52	0.03	0.022
2	UPSJ0005	42.88	0.51	5.38	14.82	0.207	26.14	9.48	0.55	0.01	0.013
3	UPSJ0006	42.72	0.55	7.44	14.44	0.196	24.47	9.39	0.74	0.03	0.014
4	LRDa0013	43.05	0.65	4.10	13.04	0.171	35.18	3.29	0.37	0.08	0.060
5	RAHK0001	43.38	0.43	5.90	11.94	0.180	31.91	5.96	0.18	0.07	0.040
6	RAHK0002	43.92	0.47	6.29	11.98	0.180	31.31	5.56	0.20	0.05	0.030
7	SFKi020	44.03	0.25	9.02	10.84	0.146	27.26	7.74	0.69	0.00	0.018
8	SFKi017	44.41	0.94	7.92	13.72	0.178	24.41	7.40	0.89	0.05	0.079
9	SFKi001	44.00	0.46	9.61	11.57	0.166	25.77	7.59	0.76	0.04	0.035
10	SFKi002	43.42	0.32	7.55	11.35	0.165	31.61	5.22	0.23	0.08	0.029
11	SFKi003	44.30	0.50	10.46	11.61	0.167	23.11	8.43	1.25	0.12	0.046
12	SFKi004	43.91	0.42	9.00	11.73	0.163	27.22	6.82	0.63	0.07	0.036
13	SFKi005	43.07	0.36	7.50	11.98	0.178	30.84	5.68	0.32	0.05	0.031
14	SFKi006	44.37	0.64	9.46	12.18	0.166	24.61	7.58	0.84	0.11	0.050
15	SFKi010	41.91	0.58	7.23	13.32	0.173	30.35	5.39	0.94	0.05	0.052
16	SFKi011	41.93	0.53	5.87	11.91	0.160	34.19	4.51	0.79	0.08	0.030
17	SFKi012	44.42	0.52	9.61	11.79	0.164	24.54	7.98	0.86	0.07	0.043
18	SFKi013	43.50	0.39	8.81	11.26	0.156	28.25	6.76	0.74	0.09	0.032
19	SFKi014	43.73	0.44	9.26	11.23	0.157	26.87	7.37	0.80	0.13	0.035
20	SFKi015	43.57	0.45	8.10	11.84	0.163	28.46	6.42	0.83	0.13	0.036
21	SSSM0034	37.28	0.18	20.20	3.16	0.050	22.09	16.99	0.02	0.01	0.010
22	SSSM0035	41.00	0.93	10.16	3.13	0.070	31.73	12.96	0.01	0.01	0.010
23	UPSJ0007	41.81	0.83	7.03	16.84	0.220	24.03	8.57	0.57	0.05	0.050
24	BCBG0012	42.65	0.01	0.37	8.75	0.120	47.49	0.58	0.01	0.01	0.020
25	BCBG0011	43.26	0.04	0.40	8.57	0.120	46.75	0.79	0.01	0.05	0.020
26	BCBG0008	42.72	0.05	0.71	9.08	0.120	44.87	2.40	0.01	0.01	0.030
27	BCBG0001	44.60	0.12	1.81	9.25	0.130	41.74	1.52	0.33	0.45	0.050
28	BCBG0003	43.73	0.21	2.20	11.16	0.139	39.04	2.78	0.23	0.49	0.020
29	BCBG0009	44.01	0.15	1.84	9.31	0.130	41.89	2.53	0.08	0.03	0.030
30	BCBG0005	41.74	0.12	0.81	11.85	0.129	43.43	1.44	0.26	0.21	0.010
31	UPSJ0002	41.60	0.46	3.90	16.32	0.209	30.54	6.58	0.33	0.04	0.020
32	Snow0011	43.04	0.10	9.43	11.11	0.161	29.23	5.87	1.02	0.05	0.010
33	BCBG0004	43.40	0.09	0.34	8.54	0.120	45.54	1.35	0.26	0.29	0.060
34	BCBG0002	43.83	0.12	1.82	9.22	0.130	42.47	2.13	0.12	0.15	0.010
35	BCBG0007	43.61	0.11	0.47	8.44	0.121	45.27	1.47	0.26	0.18	0.070

Table S6. Isometric log-ratio transformed data of the High-Mg komatiite rock samples before multivariate discordant outlier detection and separation (equations in Table S3; adjusted data from Table S5); * Discordant multivariate outlier.

Consec	Name	$ilr1_{TiM}$	$ilr2_{AlM}$	$ilr3_{FeM}$	$ilr4_{MnM}$	$ilr5_{MgM}$	$ilr6_{CaM}$	$ilr7_{NaM}$	$ilr8_{KM}$	$ilr9_{PM}$
1	UPSJ0004	0.833395	-1.20178	-2.18837	1.630803	-2.74714	-1.51747	0.891537	3.740947	3.922737
2	UPSJ0005	0.634519	-1.19716	-2.1467	1.603041	-2.78096	-1.88164	0.766922	4.233906	4.330591
3	UPSJ0006	0.669863	-1.35389	-2.01043	1.767591	-2.60063	-1.75109	0.602801	3.707398	4.388075
4	LRDa0013	0.579807	-0.82956	-1.88159	1.93161	-2.88909	-0.73517	1.29265	2.782794	3.036792
5	RAHK0001	0.817474	-1.1944	-1.87735	1.812925	-2.87628	-1.36369	1.896002	2.801438	3.34979
6	RAHK0002	0.723567	-1.28248	-1.91823	1.773697	-2.89899	-1.33998	1.756421	3.077317	3.581103
7	SFKi020	1.015717	-1.75489	-2.02106	1.764772	-2.97198	-1.84817	0.394006	5.252962	3.858798
8	SFKi017	0.477081	-1.18559	-1.73365	2.096044	-2.35315	-1.28219	0.686604	3.475437	2.992507
9	SFKi001	0.862178	-1.49364	-1.74478	1.99486	-2.56998	-1.47503	0.664797	3.457478	3.581681
10	SFKi002	0.999316	-1.41452	-1.85359	1.871822	-2.88871	-1.26303	1.630618	2.63329	3.643888
11	SFKi003	0.946861	-1.39338	-1.56848	2.176826	-2.28139	-1.38075	0.389746	2.587006	3.533621
12	SFKi004	0.940805	-1.42608	-1.74137	2.027575	-2.6044	-1.36027	0.849569	2.955178	3.576942
13	SFKi005	0.939567	-1.40139	-1.89222	1.810739	-2.85781	-1.33225	1.348939	3.169412	3.58466
14	SFKi006	0.747939	-1.33394	-1.63363	2.156402	-2.36411	-1.30671	0.741383	2.667252	3.4248
15	SFKi010	0.738882	-1.20764	-1.80965	2.014445	-2.65933	-1.09612	0.520932	3.390452	3.274414
16	SFKi011	0.7514	-1.09442	-1.77367	2.021712	-2.83237	-0.99647	0.620632	2.784577	3.732423
17	SFKi012	0.845312	-1.40379	-1.66566	2.102136	-2.42521	-1.41923	0.646708	2.966206	3.50911
18	SFKi013	1.000201	-1.39267	-1.6898	2.079904	-2.62074	-1.33428	0.715826	2.692536	3.70984
19	SFKi014	0.966654	-1.37639	-1.62722	2.136768	-2.51169	-1.34922	0.717097	2.441518	3.69943
20	SFKi015	0.948055	-1.26586	-1.67127	2.108037	-2.56197	-1.21949	0.684049	2.404384	3.659133
21*	SSSM0034	0.92348	-2.79476	-1.35864	2.313823	-3.20604	-3.00857	3.276965	3.956376	3.981026
22*	SSSM0035	-0.18403	-2.16878	-1.28192	2.080818	-3.46446	-2.68496	3.996404	4.027997	4.053094
23	UPSJ0007	0.526892	-1.13722	-1.96306	1.854091	-2.39369	-1.47263	1.048532	3.351254	3.372134
24	BCBG0012	2.436287	-0.13512	-2.88465	0.859118	-4.58496	-0.56939	3.222904	3.248382	2.611044
25	BCBG0011	1.693466	0.075393	-2.57499	1.159455	-4.26335	-0.5446	3.537004	2.047573	2.9296
26*	BCBG0008	1.585698	-0.33536	-2.56385	1.222724	-4.16096	-1.50787	3.603173	3.631657	2.612049
27	BCBG0001	1.620023	-0.345	-1.78041	1.977593	-3.25196	-0.22953	1.196823	0.913867	3.004031
28	BCBG0003	1.249453	-0.47899	-1.91373	1.943106	-3.16043	-0.75889	1.567775	0.867098	3.907028
29	BCBG0009	1.186021	-0.67736	-2.12078	1.628204	-3.60811	-1.05922	2.156968	3.098754	3.118061
30	BCBG0005	1.391405	0.047521	-2.27702	1.688411	-3.58537	-0.48521	1.117403	1.327596	4.224155
31	UPSJ0002	0.73547	-0.9002	-2.19502	1.631641	-2.88559	-1.50586	1.283618	3.283293	3.961327
32	Snow0011	1.755925	-1.68028	-1.9241	1.800705	-2.91149	-1.46656	0.159692	2.994739	4.540245
33	BCBG0004	1.633878	0.801405	-1.94118	1.8094	-3.5743	-0.36792	1.169063	1.07535	2.576736
34	BCBG0002	1.380228	-0.62639	-2.06785	1.674274	-3.57411	-0.85587	1.82587	1.629923	4.20916
35	BCBG0007	1.510032	0.557875	-1.90544	1.832231	-3.54192	-0.41681	1.19294	1.549064	2.454711

Table S7. Application of **Wilks' Statistic** through F-test (F_i) for the identification and separation of multivariate discordant outliers in isometric log-ratio transformed data of the High-Mg komatiite rock samples (data from Table S6).

Iteration	Consec	Name	Statistic test ($\max(F_i)$)	Critical value ($CV_{99.9}$)	Test result
1	**22***	SSSM0034	8.73727	5.21654	True
2	**21***	SSSM0035	12.71558	5.31437	True
3	**26***	BCBG0008	6.63585	5.42801	True
4	24	BCBG0012	4.82405	5.55151	False

Probability calculations for the major element based discriminant function

Let us refer to Figure 2 in the main paper, which classifies an igneous rock as a High-Mg or Common rock. First, the distances $\mathrm{d1_{sM}}$ and $\mathrm{d2_{sM}}$ of a given sample in the DF space ($\mathrm{DF_{sM}}$) from the two centroids ($\mathrm{C_{(HMg)M}}$ and $\mathrm{C_{(Com)M}}$) are estimated from equations S1 and S2 as follows:

$$\mathrm{d1_{sM}} = \mathrm{DF_{sM}} - \mathrm{C_{(HMg)M}} \qquad \text{(S1)}$$

$$\mathrm{d2_{sM}} = \mathrm{DF_{sM}} - \mathrm{C_{(Com)M}} \qquad \text{(S2)}$$

Inverse exponential functions ($\mathrm{ied1_{sM}}$ and $\mathrm{ied2_{sM}}$) of these distances are then estimated as equations S3 and S4:

$$\mathrm{ied1_{sM}} = e{-}(\mathrm{d1_{sM}^2}/2) \qquad \text{(S3)}$$

$$\mathrm{ied2_{sM}} = e{-}(\mathrm{d2_{sM}^2}/2) \qquad \text{(S4)}$$

The probabilities for the High-Mg and Common rock, $\mathrm{p_{(HMg)M}}$ and $\mathrm{p_{(Com)M}}$ are calculated as equations S5 and S6:

$$\mathrm{p_{(HMg)M}} = \frac{\mathrm{ied1_{sM}}}{(\mathrm{ied1_{sM}} + \mathrm{ied2_{sM}})} \qquad \text{(S5)}$$

$$\mathrm{p_{(Com)M}} = \frac{\mathrm{ied2_{sM}}}{(\mathrm{ied1_{sM}} + \mathrm{ied2_{sM}})} \qquad \text{(S6)}$$

These probability values would sum up to 1. The highest value of the probability indicates the field in which the sample will plot, either the High-Mg or the Common rock field.

Similar considerations apply for probability-based boundaries for the three-field diagrams and samples therein.

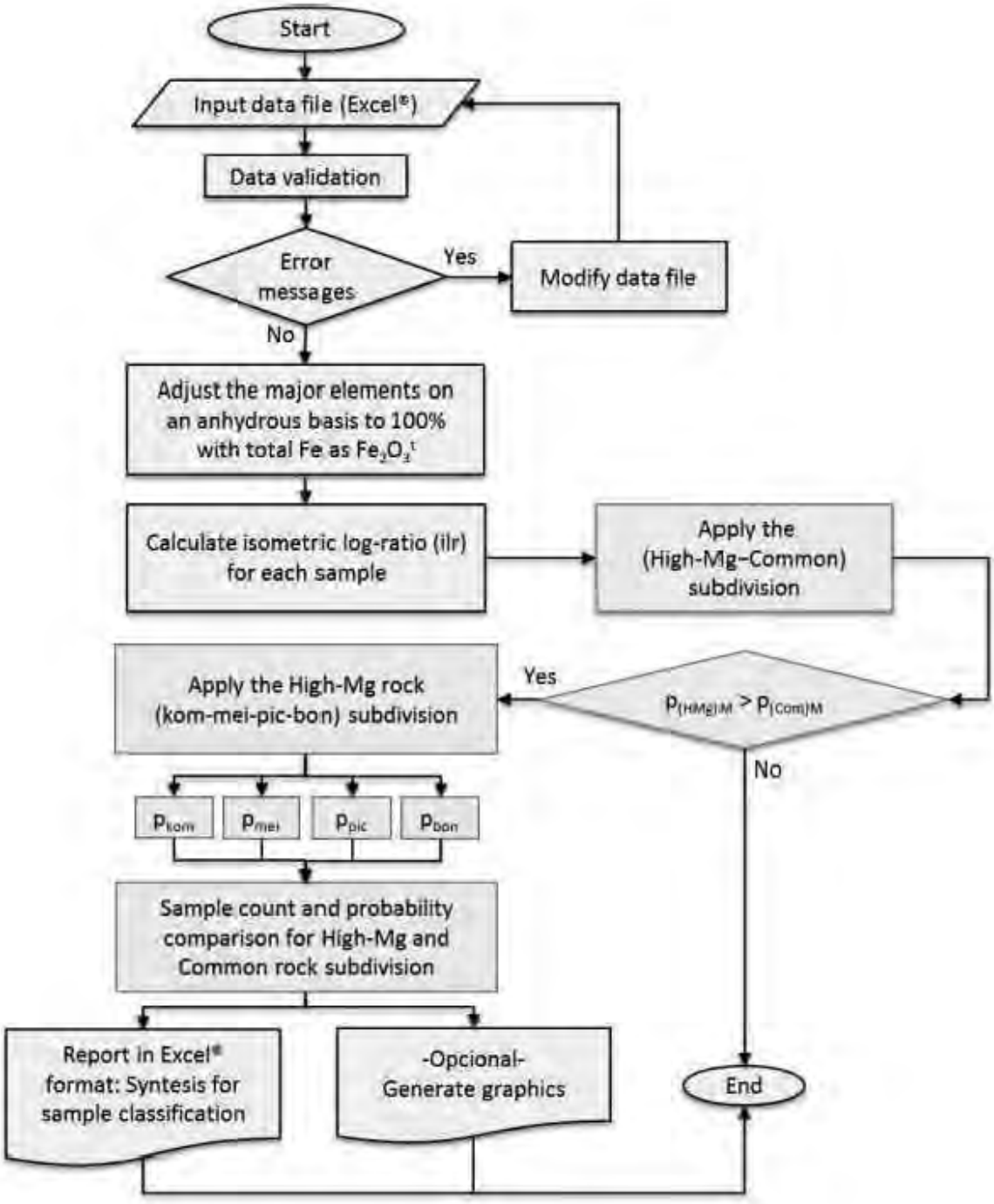

Figure S4. Schematic flow diagram for the computer program HMgClaMSys subdivision

Table S8. Tests for equality of group means for High-Mg and Common rock subdivision based on major elements (M).

Log-ratio transformed variable	Wilks' Lambda	F-ratio	Significance
$ilr1_{TiM}$	0.802709	5331.667	0.000000
$ilr2_{AlM}$	0.772456	3854.624	0.000000
$ilr3_{FeM}$	0.725029	1539.180	0.000000
$ilr4_{MnM}$	0.763234	3404.383	0.000000
$ilr5_{MgM}$	0.737868	2165.980	0.000000
$ilr6_{CaM}$	0.820809	6215.310	0.000000
$ilr7_{NaM}$	0.785921	4512.026	0.000000
$ilr8_{KM}$	0.779101	4179.061	0.000000
$ilr9_{PM}$	0.809712	5673.541	0.000000

Table S9. Probability-based boundary coordinates estimated for the High-Mg subdivision diagrams (1—komatiite (Kom or K); 2—meimechite (Mei or M); 3—picrite (Pic or P); 4—boninite (Bon or B); each diagram is considered as of three fields 1 to 3; the triple point common to all field boundaries is repeated in each set of coordinates). The final subscript M refers to major element based classification.

Field Boundary	12_3_4		1_2_3		1_2_4		1_3_4		2_3_4	
	$DF1_{(K+M-P-B)M}$	$DF2_{(K+M-P-B)M}$	$DF1_{(K-M-P)M}$	$DF2_{(K-M-P)M}$	$DF1_{(K-M-B)M}$	$DF2_{(K-M-B)M}$	$DF1_{(K-P-B)M}$	$DF2_{(K-P-B)M}$	$DF1_{(M-P-B)M}$	$DF2_{(M-P-B)M}$
B(1_2)	-1.4901	-12	1.8692	-12	-8.12595	12	-5.75642	-12	-3.89109	12
	-1.3797	-8	0.7441	-8	-5.92986	8	-3.8168235	-8	-3.12253	8
	-1.22465924	-2.38389782	-1.13907143	-1.30493236	-0.79774007	-1.24128818	-0.99985837	-2.19061488	-1.97064144	2.00497249
B(1_3)	-7.341	12	4.9825	12	-1.3027	-12	-5.0464035	12	-4.636485	-12
	-5.6401	8	3.1421	8	-1.1	-8	-3.905778	8	-3.8750845	-8
	-1.22465924	-2.38389782	-1.13907143	-1.30493236	-0.79774007	-1.24128818	-0.99985837	-2.19061488	-1.97064144	2.00497249
B(2_3)	12	10.0313	-12	6.9469	12	8.1418605	12	2.1481115	12	-4.168978
	9.836	8	-8	3.9078	8	5.2384375	8	0.8131045	8	-2.401282
	-1.22465924	-2.38389782	-1.13907143	-1.30493236	-0.79774007	-1.24128818	-0.99985837	-2.19061488	-1.97064144	2.00497249

Table S10. Classification of High-Mg rock samples used for constructing the five diagrams based on log-ratio transformed major elements (M; Figure 3a-e).

Figure type	Sample type	Total number of samples	Number of classified High-Mg rock samples in major element based diagrams					
			komatiite + meimechite (Kom+Mei)	komatiite (Kom)	meimechite (Mei)	picrite (Pic)	boninite (Bon)	percent success (correct classification)
Kom+Mei-Pic-Bon	komatiite+meimechite	248	227	---	---	20	1	91.5%
	picrite	546	29	---	---	515	2	94.3%
	boninite	126	0	---	---	0	126	100.0%
Kom-Mei-Pic	komatiite	76	---	69	5	2	---	90.8%
	meimechite	172	---	2	168	2	---	97.7%
	picrite	546	---	5	32	509	---	93.2%
Kom-Mei-Bon	komatiite	76	---	69	7	---	0	90.8%
	meimechite	172	---	0	172	---	0	100.0%
	boninite	126	---	0	0	---	126	100.0%
Kom-Pic-Bon	komatiite	76	---	72	---	4	0	94.7%
	picrite	546	---	6	---	537	3	98.4%
	boninite	126	---	0	---	0	126	100.0%
Mei-Pic-Bon	meimechite	172	---	---	168	4	0	97.7%
	picrite	546	---	---	35	509	2	93.2%
	boninite	126	---	---	0	0	126	100.0%

Kom−komatiite; Mei−meimechite; Kom+Mei–combined komatiite and meimechite field; Pic−picrite; Bon−boninite.

Table S11. Synthesis of four field classification of one sample of komatiite (CB2-10−internal name given by the original authors [*Upton et al.,* 2000]; assigned name UPSJ0004) in five diagrams for High-Mg rock subdivision (original data plotted in Figure 3a-e).

Figure name	Figure type	Total probability of the sample	Probability distribution for the sample				
			Kom+Mei ($p_{kom+mei}$) Θ	Kom (p_{kom}) Θ	Mei (p_{mei}) Θ	Pic (p_{pic}) Θ	Bon (p_{bon}) Θ
High-Mg rock subdivision	Kom+Mei-Pic-Bon	1	0.997124	---	---	0.002876	0.000000
	Kom-Mei-Pic	1	---	0.999573	0.000426	0.000000	---
	Kom-Mei-Bon	1	---	0.967809	0.032191	---	0.000000
	Kom-Pic-Bon	1	---	0.999956	---	0.000044	0.000000
	Mei-Pic-Bon	1	---	---	0.997366	0.002634	0.000000
Synthesis for the komatiite sample classification	***{Σprob_5}***	***{5}***	***{0.997124}***	***{2.967337}***	***{1.029984}***	***{0.005554}***	***{0.000000}***
	{Σprob_4}	***{5}***	***{---}***	***{3.707534}***	***{1.286911}***	***{0.005554}***	***{0.000000}***
	[%prob]	***[100%]***	***[---]***	***[74.2%]***	***[25.7%]***	***[0.1%]***	***[0.0%]***

Θ Kom−komatiite; Mei−meimechite; Kom+Mei–combined komatiite and meimechite field; Pic−picrite; Bon−boninite; the probability values for a sample from a given locality are represented by ($p_{Kom+Mei}$) – probability for the combined komatiite and meimechite field in the first diagram; [p_{Kom}] – probability for komatiite in the diagrams; [p_{Mei}] – probability for the meimechite filed in the diagrams; [p_{Pic}] – probability for the picrite field in the diagrams; [p_{Bon}] – probability for the boninite field in the diagrams; the final rows give a synthesis of results as ***{Σprob_5}***, ***{Σprob_4}***, and ***[%prob]***, where **{Σprob_5}** is the total probability of a sample plotting in all five diagrams to be subdivided in five classification fields (Kom + Mei, Kom, Mei, Pic, and Bon); ***{Σprob_4}*** is the sum of probability values of a sample for the four classification fields (Kom, Mei, Pic, and Bon) after assigning the probability of Kom + Mei to Kom and Mei (using weighing factors explained in Verma and Verma [2013]); and the final row identified by ***[%prob]*** is the subdivision of the total percent probability value of 100% that corresponds to the four classification fields.

Table S12. Synthesis of four field classification of original High-Mg rock samples in five diagrams based on major elements (M; original data plotted in Figure 3a-e).

High-Mg rock name (IUGS)	Total number of samples	Number of classified High-Mg rock samples **(percent success)**			
		komatiite (Kom)	meimechite (Mei)	picrite (Pic)	boninite (Bon)
komatiite	76	**67 (88%)**	6 (8%)	3 (4%)	0 (0%)
meimechite	172	0 (0%)	**168 (97.7%)**	4 (2.3%)	0 (0%)
picrite	546	5 (0.9%)	27 (5.0%)	**511 (93.6%)**	3 (0.5%)
boninite	126	0 (0%)	0 (0%)	0 (0%)	**126 (100%)**

The correct classification is shown in **bold** face.

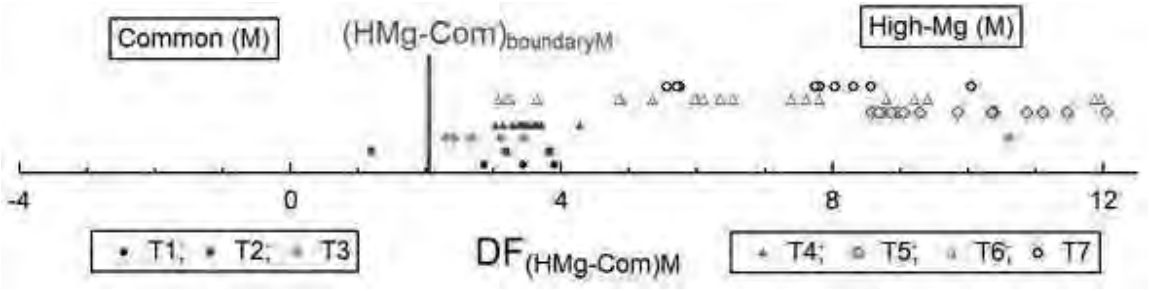

Figure S5. Testing of the discriminant function $DF_{(HMg-Com)M}$ for High-Mg (HMg) and Common (Com) rock subdivision based on major element compositions (M); the classification field boundary $(HMg-Com)_{boundaryM}$ is shown for reference. The symbols for evaluations (T1−T7) are shown as insets; see text for explanation on T1−T7.

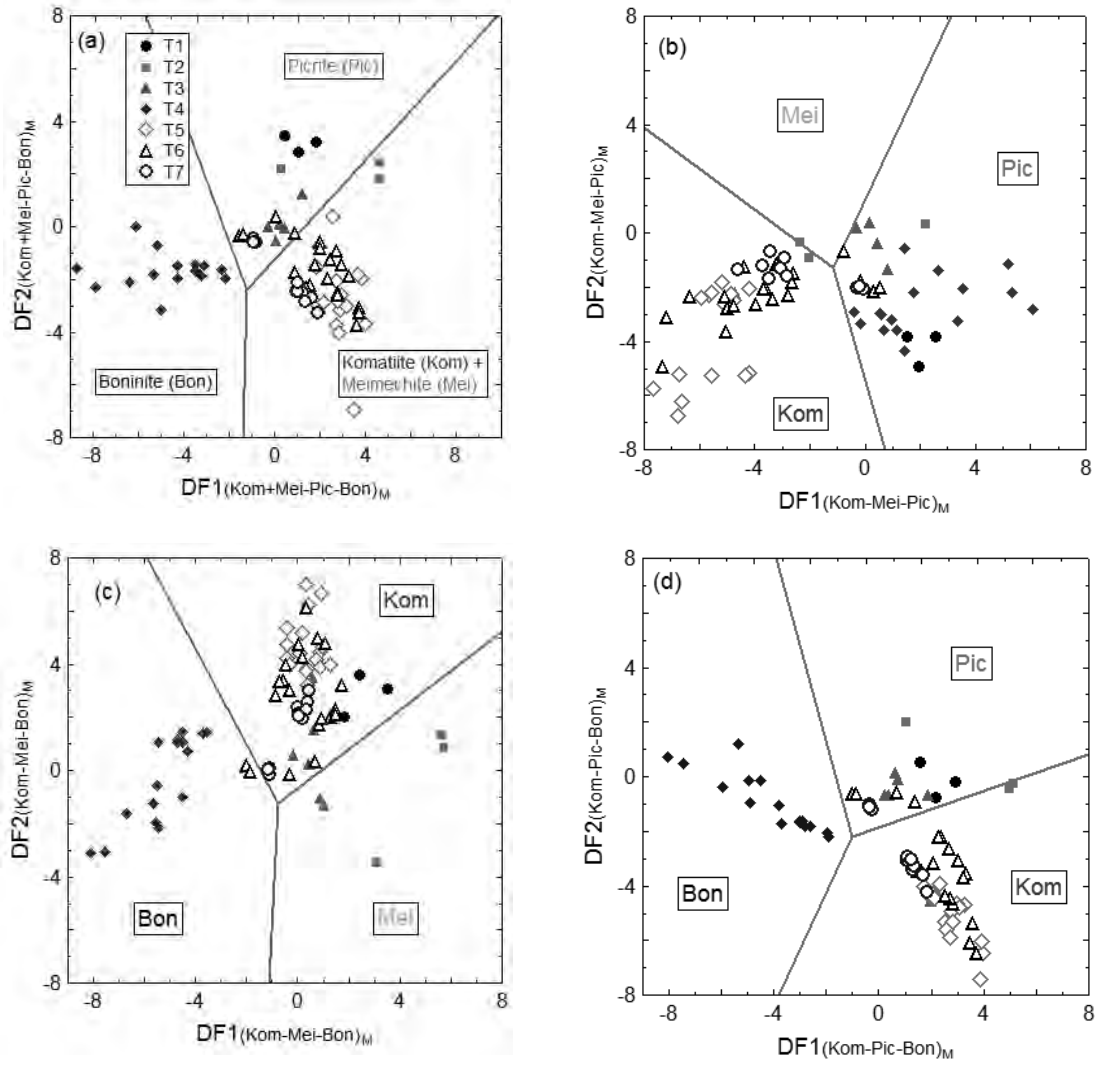

Figure S6. Testing of five diagrams based on transformed major elements (M) for the subdivision of High-Mg rocks (1—komatiite; 2—meimechite; 3—picrite; 4—boninite) from seven test studies (T1−T7); the symbols are explained as inset in (a); the discriminant function equations are in Table 1; the probability-based boundary coordinates are given in Table S9. (**a**) 1+2-3-4 $(Kom+Mei-Pic-Bon)_M$; (**b**) 1-2-3 $(Kom-Mei-Pic)_M$; (**c**) 1-2-4 $(Kom-Mei-Bon)_M$; (**d**) 1-3-4 $(Kom-Pic-Bon)_M$; and (**e**) 2-3-4 $(Mei-Pic-Bon)_M$.

Table S13. Major element composition of compiled Cenozoic high-Mg igneous rock samples from the rifted Apennines/Adriatic domain, Italy (Test study T2; *Bianchini et al.* [2008]; rock type from the IUGS classification scheme).

Consec	Sample name		SiO_2	TiO_2	Al_2O_3	$Fe_2O_3^t$	MnO	MgO	CaO	Na_2O	K_2O	P_2O_5	IUGS scheme
	Original authors'	This work											High-Mg rock type
1	Queglia1	BBSi0001	34.60	3.38	8.38	9.98	0.18	17.66	15.92	0.38	0.53	0.98	meimechite
2	Queglia2	BBSi0002	36.37	3.63	8.28	10.26	0.18	19.04	12.87	0.35	0.50	0.95	meimechite
3	IB374	BBSi0006	42.19	3.00	12.14	13.51	0.17	12.42	11.17	1.89	0.99	0.58	picrite

Table S14. Adjusted major element composition of compiled Cenozoic high-Mg igneous rock samples from the rifted Apennines/Adriatic domain, Italy (equations in Table S2 and data from Table S13).

Consec	Name	SiO_2A	TiO_2A	Al_2O_3A	$Fe_2O_3^tA$	MnOA	MgOA	CaOA	Na_2OA	K_2OA	P_2O_5A
1	BBSi0001	37.61278	3.674312	9.109686	10.849005	0.195673	19.197739	17.306229	0.413088	0.576150	1.065333
2	BBSi0002	39.34870	3.927296	8.958130	11.100292	0.194742	20.599372	13.924051	0.378665	0.540950	1.027805
3	BBSi0006	43.02468	3.059351	12.380175	13.777279	0.173363	12.665715	11.390985	1.927391	1.009586	0.591475

Table S15. Isometric log-ratio transformed data of compiled Cenozoic high-Mg igneous rock samples from the rifted Apennines/Adriatic domain, Italy (equations in Table S3; adjusted data from Table S14).

Consec	Name	$ilr1_{TiM}$	$ilr2_{AlM}$	$ilr3_{FeM}$	ilr4MnM	ilr5MgM	ilr6CaM	$ilr7Na_M$	$ilr8_{KM}$	ilr9PM
1	BBSi0001	-0.04873251	-0.79762766	-0.99733699	2.5614212	-1.57227837	-1.49854968	1.97984334	1.68181653	1.10916279
2	BBSi0002	-0.11136039	-0.80187941	-1.03620595	2.54602609	-1.6566752	-1.31758434	2.04066944	1.72052511	1.12232893
3	BBSi0006	0.1553507	-0.96199172	-1.11294552	2.76401991	-1.09635499	-1.01369918	0.63770426	1.25239142	1.76743354

Table S16. Probability values related to the new classification scheme for samples from the rifted Apennines/Adriatic domain, Italy (data from Table S15 were processed; the results are plotted in Figures S5 and S6a-e).

Consec	Name	Discriminant function	High-Mg–Common subdivision		High-Mg or Common	High-Mg rock (kom-mei-pic-bon) subdivision				Inference from new classification scheme
		$DF_{(HMg\text{-}Com)M}$	$p_{(HMg)M}$	$p_{(Com)M}$		p_{kom}	p_{mei}	p_{pic}	p_{bon}	
1	BBSi0001	3.17817799	0.99387682	0.00612318	High-Mg	0.324247	0.440242	0.235511	0.000000	meimechite
2	BBSi0002	3.82351674	0.99956012	0.00043988	High-Mg	0.308832	0.591449	0.099719	0.000000	meimechite
3	BBSi0006	1.19487259	0.04648784	0.95351216	Common	---	---	---	---	---

Table S17. Major element composition of Triassic high-Mg igneous rock samples from rift-related Pelagonian continental margin, Greece (Test study T3; *Tsikouras et al.* [2008]; rock type from the IUGS classification scheme).

Consec	Sample name		SiO_2	TiO_2	Al_2O_3	FeO^t	MnO	MgO	CaO	Na_2O	K_2O	P_2O_5	IUGS scheme
	Original authors`	This work											High-Mg rock type
1	E177	TPPH0003	44.64	1.06	11.57	10.04	0.19	16.42	8.18	1.23	0.40	0.17	picrite
2	E42	TPPH0010	44.45	1.10	11.20	9.89	0.18	15.80	8.52	1.61	0.45	0.19	picrite
3	LA28	TPPH0016	47.64	0.74	12.02	7.92	0.13	13.34	10.64	1.68	0.08	0.13	picrite
4	LA33	TPPH0017	46.31	0.85	12.92	8.24	0.12	14.69	8.95	1.87	0.28	0.16	picrite
5	LA8	TPPH0020	42.56	0.29	5.17	8.56	0.14	28.83	4.15	0.19	0.17	0.08	komatiite
6	LA23	TPPH0025	44.67	0.93	12.08	7.75	0.17	13.43	15.35	1.04	0.03	0.17	picrite

Table S18. Adjusted major element composition of Triassic high-Mg igneous rock samples from rift-related Pelagonian continental margin, Greece (equations in Table S2 and data from Table S17).

Consec	Name	SiO_2A	TiO_2A	Al_2O_3A	$Fe_2O_3^tA$	MnOA	MgOA	CaOA	Na_2OA	K_2OA	P_2O_5A
1	TPPH0003	46.9806069	1.11557893	12.1766492	11.7429729	0.19996226	17.280949	8.60890153	1.29449253	0.42097318	0.1789136
2	TPPH0010	47.0414039	1.16412923	11.8529522	11.6320084	0.19049387	16.7211289	9.01671004	1.70386187	0.47623469	0.20107687
3	TPPH0016	50.0410324	0.77729563	12.625802	9.24548285	0.13655194	14.0123294	11.1762507	1.76467117	0.08403196	0.13655194
4	TPPH0017	48.5900879	0.89185003	13.5561204	9.60837674	0.12590824	15.4132669	9.39065616	1.96207006	0.29378589	0.16787765
5	TPPH0020	46.7214131	0.31835549	5.67551	10.4433065	0.15368886	31.6489271	4.55577688	0.20857774	0.18662219	0.0878222
6	TPPH0025	46.2983386	0.96390094	12.5203477	8.92690812	0.17619695	13.9195587	15.9095477	1.07791073	0.03109358	0.17619695

Table S19. Isometric log-ratio transformed data of compiled Triassic high-Mg igneous rock samples from rift-related Pelagonian continental margin, Greece (equations in Table S3; adjusted data from Table S18).

Consec	Name	$ilr1_{TiM}$	$ilr2_{AlM}$	$ilr3_{FeM}$	ilr4MnM	ilr5MgM	ilr6CaM	$ilr7Na_M$	$ilr8_{KM}$	ilr9PM
1	TPPH0003	0.62883033	-1.22543584	-1.26836448	2.33293488	-1.68966094	-1.06851015	0.69272588	1.75726408	2.57996901
2	TPPH0010	0.6331581	-1.16365691	-1.21794912	2.41989904	-1.61512335	-1.06625348	0.48126766	1.68691037	2.51539786
3	TPPH0016	0.71440172	-1.4512087	-1.26937934	2.45916704	-1.71761734	-1.5326109	0.17811947	3.04993083	2.60834054
4	TPPH0017	0.73187862	-1.37682777	-1.16225798	2.67682137	-1.6565442	-1.22128613	0.23065008	2.02277739	2.56627864
5	TPPH0020	1.106433	-1.07452133	-1.66780498	2.05089566	-2.77016007	-1.01493041	1.85921964	1.9787818	2.70620149
6	TPPH0025	0.5242922	-1.48819627	-1.28550708	2.18316018	-1.76056339	-1.90924939	0.5890021	3.93665045	2.31559105

Table S20. Probability values related to the new classification scheme for samples from rift-related Pelagonian continental margin, Greece (data from Table S19 were processed; the results are plotted in Figures S5 and S6a-e).

Consec	Name	Discriminant function	High-Mg–Common subdivision		High-Mg or Common	High-Mg rock (kom-mei-pic-bon) subdivision				Inference from new classification scheme
		$DF_{(HMg\text{-}Com)M}$	$p_{(HMg)M}$	$p_{(Com)M}$		p_{kom}	p_{mei}	p_{pic}	p_{bon}	
1	TPPH0003	3.44029173	0.99789517	0.00210483	High-Mg	0.0044727	0.3346094	0.6609116	6.248E-06	picrite
2	TPPH0010	3.10744507	0.99183967	0.00816033	High-Mg	0.0012482	0.2719413	0.7268021	8.383E-06	picrite
3	TPPH0016	2.66940162	0.95297685	0.04702315	High-Mg	0.2082907	0.014809	0.7767336	0.0001667	picrite
4	TPPH0017	2.30241488	0.81879455	0.18120545	High-Mg	0.1974256	0.105668	0.6968333	7.322E-05	picrite
5	TPPH0020	10.6215285	1.00000000	3.7178E-16	High-Mg	0.7499350	0.2499914	7.359E-05	1.684E-08	komatiite
6	TPPH0025	2.41376498	0.87691714	0.12308286	High-Mg	0.2353264	0.0100036	0.7546700	6.726E-08	picrite

Table S21. Major element composition of compiled Paleogene high-Mg igneous rock samples dredged from the Mariana Trench (Test study T4; *Bloomer and Hawkins* [1987]; rock type from the IUGS classification scheme).

Consec	Sample name		SiO_2	TiO_2	Al_2O_3	Fe_2O_3	FeO	MnO	MgO	CaO	Na_2O	K_2O	P_2O_5	IUGS scheme
	Original authors`	This work												High-Mg rock type
1	28-1	BlHaw0001	59.46	0.16	11.16	1.37	5.90	0.13	11.26	4.97	2.19	0.64	0.04	boninite
2	28-2	BlHaw0002	60.66	0.17	12.53	1.9	4.85	0.10	7.81	4.81	2.56	1.32	0.04	boninite
3	28-9	BlHaw0006	61.90	0.17	11.66	1.32	4.78	0.11	8.92	4.13	3.48	0.70	0.05	boninite
4	28-14	BlHaw0008	57.34	0.22	10.88	0	8.26	0.17	13.01	5.35	1.97	0.84	0.04	boninite
5	28-15	BlHaw0009	57.12	0.18	10.18	0	7.70	0.16	15.25	4.36	1.96	0.98	0.02	boninite
6	28-18	BlHaw0010	55.09	0.20	10.26	2.16	7.80	0.15	15.21	5.10	1.51	0.77	0.05	boninite
7	50-14	BlHaw0013	53.60	0.18	10.77	2.09	6.19	0.15	15.53	6.98	1.00	0.66	0.05	boninite
8	50-17	BlHaw0014	55.65	0.18	10.47	2.04	5.93	0.14	14.18	6.9	0.60	0.72	0.05	boninite
9	50-22i	BlHaw0015	53.00	0.19	11.27	1.63	6.49	0.14	14.82	7.15	0.87	0.78	0.06	boninite
10	50-22r	BlHaw0016	51.70	0.22	10.65	3.07	5.72	0.15	16.00	6.41	0.80	1.06	0.04	boninite
11	50-23	BlHaw0017	54.75	0.26	13.28	2.40	5.33	0.13	10.72	8.11	1.50	0.91	0.05	boninite
12	50-28i	BlHaw0018	52.95	0.19	10.68	2.48	5.82	0.15	16.06	6.45	0.87	0.68	0.05	boninite
13	50-28-r	BlHaw0019	50.42	0.22	10.48	2.87	5.90	0.15	18.06	6.13	0.63	0.92	0.06	boninite
14	50-29i	BlHaw0020	52.98	0.19	11.01	1.83	6.47	0.15	15.61	7.49	0.84	0.52	0.05	boninite
15	50-29r	BlHaw0021	51.66	0.22	10.59	2.87	6.29	0.16	17.82	6.65	0.60	0.84	0.07	boninite
16	51-8	BlHaw0022	55.22	0.40	14.45	1.84	4.45	0.11	7.76	8.44	2.60	0.76	0.09	boninite

Table S22. Adjusted major element composition of compiled Paleogene high-Mg igneous rock samples dredged from the Mariana Trench (equations in Table S2 and data from Table S21).

Consec	Name	SiO_2A	TiO_2A	Al_2O_3A	$Fe_2O_3^tA$	MnOA	MgOA	CaOA	Na_2OA	K_2OA	P_2O_5A
1	BlHaw0001	60.71253	0.16337	11.39509	8.09393	0.13274	11.49719	5.07469	2.23613	0.65348	0.04084
2	BlHaw0002	62.34965	0.17474	12.87902	7.49310	0.10279	8.02754	4.94398	2.63131	1.35677	0.04111
3	BlHaw0006	63.32336	0.17391	11.92812	6.78475	0.11253	9.12511	4.22497	3.56002	0.71610	0.05115
4	BlHaw0008	57.91935	0.22222	10.98993	9.27248	0.17172	13.14145	5.40406	1.98990	0.84849	0.04040
5	BlHaw0009	57.83286	0.18225	10.30705	8.66417	0.16200	15.44032	4.41441	1.98446	0.99223	0.02025
6	BlHaw0010	55.55191	0.20168	10.34603	10.91930	0.15126	15.33753	5.14276	1.52266	0.77646	0.05042
7	BlHaw0013	54.75576	0.18388	11.00223	9.16264	0.15323	15.86487	7.13051	1.02156	0.67423	0.05108
8	BlHaw0014	57.06505	0.18458	10.73623	8.84974	0.14356	14.54056	7.07545	0.61526	0.73831	0.05127
9	BlHaw0015	54.57018	0.19563	11.60388	9.10462	0.14415	15.25906	7.36183	0.89577	0.80311	0.06178
10	BlHaw0016	53.59906	0.22808	11.04120	9.77318	0.15551	16.58772	6.64545	0.82939	1.09894	0.04147
11	BlHaw0017	55.84827	0.26522	13.54639	8.49045	0.13261	10.93504	8.27268	1.53009	0.92825	0.05100
12	BlHaw0018	54.57185	0.19582	11.00713	9.22212	0.15459	16.55192	6.64756	0.89665	0.70083	0.05153
13	BlHaw0019	52.25036	0.22799	10.86045	9.76917	0.15545	18.71562	6.35253	0.65287	0.95340	0.06218
14	BlHaw0020	54.13833	0.19415	11.25072	9.21764	0.15328	15.95129	7.65376	0.85837	0.53137	0.05109
15	BlHaw0021	52.46248	0.22342	10.75450	10.01355	0.16249	18.09681	6.75330	0.60932	0.85305	0.07109
16	BlHaw0022	57.15439	0.41401	14.95619	7.02320	0.11385	8.03184	8.73566	2.69108	0.78662	0.09315

Table S23. Isometric log-ratio transformed data of compiled Paleogene high-Mg igneous rock samples dredged from the Mariana Trench (equations in Table S3; adjusted data from Table S22).

Consec	Name	$ilr1_{TiM}$	$ilr2_{AlM}$	$ilr3_{FeM}$	ilr4MnM	ilr5MgM	ilr6CaM	$ilr7Na_M$	$ilr8_{KM}$	ilr9PM
1	BlHaw0001	1.70867656	-1.49295082	-1.28727431	2.34704218	-1.67731317	-0.94393631	-0.18712912	0.97122455	3.60758447
2	BlHaw0002	1.6892647	-1.5604079	-1.18600815	2.61137794	-1.31305598	-0.88292952	-0.30212299	0.31998228	3.63905429
3	BlHaw0006	1.67691521	-1.51591147	-1.11923689	2.51050892	-1.45031142	-0.7579856	-0.60565545	0.90154637	3.41079315
4	BlHaw0008	1.55816173	-1.38598704	-1.32289899	2.20154538	-1.71279469	-0.914387	0.01067512	0.81439761	3.70775937
5	BlHaw0009	1.629934	-1.41266047	-1.34798353	2.1670699	-1.94834331	-0.81675453	-0.07732896	0.57556517	4.27125619
6	BlHaw0010	1.61315318	-1.35240219	-1.48114365	2.29780598	-1.87142914	-0.8863203	0.24301648	0.87989536	3.47942641
7	BlHaw0013	1.65199628	-1.43318615	-1.36167253	2.25270172	-1.93646993	-1.22353774	0.5813386	0.97768596	3.43158613
8	BlHaw0014	1.60783632	-1.46111126	-1.38239542	2.25855241	-1.91046269	-1.2706843	1.00075409	0.8367709	3.37233933
9	BlHaw0015	1.6273671	-1.45453225	-1.33270286	2.3316163	-1.87619095	-1.2280068	0.72960026	0.83832202	3.27686987
10	BlHaw0016	1.52249374	-1.40972734	-1.38959371	2.26837786	-1.94768786	-1.12844111	0.80646478	0.54752189	3.65990574
11	BlHaw0017	1.45467354	-1.53184046	-1.22017381	2.46000234	-1.51716023	-1.2803652	0.28500231	0.75844846	3.51570425
12	BlHaw0018	1.60501725	-1.43643539	-1.37033701	2.24163663	-1.97839739	-1.16188031	0.70003419	0.93787668	3.41984982
13	BlHaw0019	1.5267514	-1.39167259	-1.38438307	2.27376343	-2.0527498	-1.08151521	1.03556006	0.68674816	3.28096002
14	BlHaw0020	1.59488914	-1.47297723	-1.389718	2.22882547	-1.96552896	-1.31354074	0.71946088	1.17729424	3.40626153
15	BlHaw0021	1.5427787	-1.3816913	-1.40368298	2.23631153	-2.01984614	-1.13591277	1.1024012	0.7938869	3.15622272
16	BlHaw0022	1.20853334	-1.53326701	-0.97164066	2.68337855	-1.14670174	-1.24073669	-0.15217127	1.00623214	3.03652569

Table S24. Probability values related to the new classification scheme for samples dredged from the Mariana Trench (data from Table S23 were processed; the results are plotted in Figures S5 and S6a-e).

Consec	Name	Discriminant function	High-Mg–Common subdivision		High-Mg or Common	High-Mg rock (kom-mei-pic-bon) subdivision				Inference from new classification scheme
		$DF_{(HMg\text{-}Com)M}$	$p_{(HMg)M}$	$p_{(Com)M}$		p_{kom}	p_{mei}	p_{pic}	p_{bon}	
1	BlHaw0001	5.31358934	0.99999901	9.9349E-07	High-Mg	0.000000	0.000000	0.200000	0.800000	boninite
2	BlHaw0002	4.13129044	0.99987501	0.00012499	High-Mg	0.000000	0.000000	0.200000	0.800000	boninite
3	BlHaw0006	4.44629689	0.99996553	3.4471E-05	High-Mg	0.000000	0.000000	0.200000	0.800000	boninite
4	BlHaw0008	5.44658254	0.99999942	5.7672E-07	High-Mg	0.000000	0.000007	0.199993	0.800000	boninite
5	BlHaw0009	6.16500522	0.99999997	3.0553E-08	High-Mg	0.000001	0.000461	0.199539	0.800000	boninite
6	BlHaw0010	6.23415737	0.99999998	2.3027E-08	High-Mg	0.000001	0.000025	0.199977	0.799996	boninite
7	BlHaw0013	5.9365933	0.99999992	7.7752E-08	High-Mg	0.000139	0.000060	0.199882	0.799919	boninite
8	BlHaw0014	6.60298059	0.99999999	5.0958E-09	High-Mg	0.000070	0.000004	0.199929	0.799997	boninite
9	BlHaw0015	5.68703893	0.99999978	2.1573E-07	High-Mg	0.000093	0.000022	0.199978	0.799906	boninite
10	BlHaw0016	6.06836211	0.99999995	4.5362E-08	High-Mg	0.000633	0.000256	0.199336	0.799776	boninite
11	BlHaw0017	3.7357331	0.99937027	0.00062973	High-Mg	0.000000	0.000000	0.200000	0.799999	boninite
12	BlHaw0018	6.1427741	0.99999997	3.3461E-08	High-Mg	0.000627	0.000228	0.199323	0.799823	boninite
13	BlHaw0019	6.4693705	0.99999999	8.8004E-09	High-Mg	0.041723	0.005558	0.184323	0.768396	boninite
14	BlHaw0020	5.88527555	0.9999999	9.5907E-08	High-Mg	0.000767	0.000082	0.199642	0.799509	boninite
15	BlHaw0021	6.55686273	0.99999999	6.1534E-09	High-Mg	0.023612	0.001094	0.189270	0.786024	boninite
16	BlHaw0022	1.81495276	0.38102099	0.61897901	High-Mg	0.000000	0.000000	0.200000	0.800000	boninite

Table S25. Major element composition of compiled Archaean high-Mg igneous rock samples from the Abitibi Greenstone Belt, Canada (Test study T5; *Arndt* [1986]; rock type from the IUGS classification scheme).

Consec	Sample name		SiO_2	TiO_2	Al_2O_3	Fe_2O_3	FeO	MnO	MgO	CaO	Na_2O	K_2O	P_2O_5	IUGS scheme
	Original authors`	This work												High-Mg rock type
1	M651	Arnd0001	45.50	0.34	6.50	11.30	0	0.2	29.20	6.20	0.28	0.08	0.02	komatiite
2	M652	Arnd0002	44.60	0.30	5.60	10.80	0	0.1	32.70	5.00	0.23	0.06	0.02	komatiite
3	M626	Arnd0003	45.20	0.31	6.10	11.00	0	0.2	30.70	5.70	0.26	0.02	0.02	komatiite
4	M653	Arnd0004	44.60	0.29	5.30	10.60	0	0.1	33.70	4.60	0.20	0.06	0.02	komatiite
5	M654	Arnd0005	43.80	0.26	5.00	11.20	0	0.1	34.70	4.40	0.03	0.01	0.02	komatiite
6	M655	Arnd0006	44.40	0.35	6.70	10.70	0	0.2	28.90	8.20	0.03	0.01	0.02	komatiite
7	M656	Arnd0007	44.70	0.41	7.90	12.30	0	0.2	23.60	10.60	0.12	0.04	0.02	komatiite
8	M657	Arnd0008	43.20	0.50	9.40	13.40	0	0.2	19.90	12.80	0.03	0.01	0.02	komatiite
9	M658	Arnd0009	43.40	0.32	6.00	11.80	0	0.2	29.80	7.90	0.04	0.01	0.02	komatiite
10	M661	Arnd0010	43.70	0.19	3.20	9.10	0	0.1	42.10	0.99	0.01	0.01	0.02	komatiite
11	M667	Arnd0011	45.10	0.33	6.64	12.00	0	0.2	30.40	4.80	0.03	0.03	0.02	komatiite
12	M666	Arnd0012	45.40	0.35	7.00	12.00	0	0.2	27.90	6.50	0.29	0.01	0.02	komatiite
13	M662	Arnd0013	45.00	0.32	6.30	11.50	0	0.2	29.60	6.10	0.44	0.01	0.02	komatiite
14	M663	Arnd0014	45.30	0.34	6.80	11.90	0	0.2	28.40	6.20	0.42	0.11	0.02	komatiite
15	M664	Arnd0015	45.00	0.34	6.70	11.20	0	0.2	29.40	6.30	0.30	0.09	0.02	komatiite
16	M665	Arnd0016	44.70	0.37	6.70	11.80	0	0.2	28.20	7.40	0.07	0.04	0.02	komatiite
17	M668	Arnd0017	45.80	0.44	8.60	12.70	0	0.2	23.50	7.80	0.09	0.04	0.02	komatiite

Table S26. Adjusted major element composition of compiled Archaean high-Mg igneous rock samples from the Abitibi Greenstone Belt (equations in Table S2 and data from Table S25).

Consec	Name	SiO_2A	TiO_2A	Al_2O_3A	$Fe_2O_3^tA$	MnOA	MgOA	CaOA	Na_2OA	K_2OA	P_2O_5A
1	Arnd0001	45.69	0.34	6.53	11.35	0.161	29.32	6.23	0.28	0.08	0.020
2	Arnd0002	44.85	0.30	5.63	10.86	0.141	32.88	5.03	0.23	0.06	0.020
3	Arnd0003	45.44	0.31	6.13	11.06	0.171	30.86	5.73	0.26	0.02	0.020
4	Arnd0004	44.82	0.29	5.33	10.65	0.131	33.87	4.62	0.20	0.06	0.020
5	Arnd0005	44.00	0.26	5.02	11.25	0.121	34.86	4.42	0.03	0.01	0.020
6	Arnd0006	44.64	0.35	6.74	10.76	0.151	29.06	8.24	0.03	0.01	0.020
7	Arnd0007	44.74	0.41	7.91	12.31	0.210	23.62	10.61	0.12	0.04	0.020
8	Arnd0008	43.44	0.50	9.45	13.48	0.181	20.01	12.87	0.03	0.01	0.020
9	Arnd0009	43.63	0.32	6.03	11.86	0.181	29.96	7.94	0.04	0.01	0.020
10	Arnd0010	43.95	0.19	3.22	9.15	0.121	42.34	1.00	0.01	0.01	0.020
11	Arnd0011	45.31	0.33	6.67	12.06	0.181	30.54	4.82	0.03	0.03	0.020
12	Arnd0012	45.56	0.35	7.03	12.04	0.171	28.00	6.52	0.29	0.01	0.020
13	Arnd0013	45.25	0.32	6.33	11.56	0.161	29.76	6.13	0.44	0.01	0.020
14	Arnd0014	45.46	0.34	6.82	11.94	0.161	28.50	6.22	0.42	0.11	0.020
15	Arnd0015	45.22	0.34	6.73	11.25	0.171	29.54	6.33	0.30	0.09	0.020
16	Arnd0016	44.94	0.37	6.74	11.86	0.161	28.35	7.44	0.07	0.04	0.020
17	Arnd0017	46.19	0.44	8.67	12.81	0.161	23.70	7.87	0.09	0.04	0.020

Table S27. Isometric log-ratio transformed data of compiled Archaean high-Mg igneous rock samples from the Abitibi Greenstone Belt (equations in Table S3; adjusted data from Table S26).

Consec	Name	$ilr1_{TiM}$	$ilr2_{AlM}$	$ilr3_{FeM}$	ilr4MnM	ilr5MgM	ilr6CaM	$ilr7Na_M$	$ilr8_{KM}$	ilr9PM
1	Arnd0001	0.9531	-1.3086	-1.8669	1.8798	-2.8345	-1.4401	1.4425	2.6350	3.9666
2	Arnd0002	0.9667	-1.2734	-1.9194	1.9045	-3.0346	-1.3390	1.5274	2.8063	3.8661
3	Arnd0003	0.9037	-1.3893	-1.9842	1.6804	-3.0284	-1.5125	1.3600	3.7890	3.8126
4	Arnd0004	0.9642	-1.2591	-1.9357	1.9372	-3.0963	-1.2965	1.6231	2.7710	3.8305
5	Arnd0005	0.7646	-1.5311	-2.3224	1.6587	-3.4803	-1.6178	3.0315	4.0912	3.4591
6	Arnd0006	0.6407	-1.6704	-2.1772	1.5683	-3.2019	-2.0811	3.1457	4.2063	3.5749
7	Arnd0007	0.7857	-1.5084	-1.9833	1.5922	-2.6854	-1.9825	2.1887	3.2417	3.9195
8	Arnd0008	0.4696	-1.8532	-2.2726	1.5078	-2.7566	-2.3872	3.2530	4.3145	3.6838
9	Arnd0009	0.7280	-1.5527	-2.2326	1.4355	-3.1990	-2.0153	2.9082	4.2382	3.6070
10	Arnd0010	0.7483	-1.4416	-2.4342	1.3576	-3.9641	-0.5485	3.7442	3.7738	3.1397
11	Arnd0011	0.7430	-1.5930	-2.2021	1.4820	-3.1698	-1.5058	3.2260	3.2515	3.6564
12	Arnd0012	0.8038	-1.5178	-2.0767	1.6627	-2.9592	-1.6524	1.2393	4.4238	3.7938
13	Arnd0013	0.8747	-1.4232	-2.0307	1.7264	-3.0036	-1.5838	0.8592	4.4338	3.8038
14	Arnd0014	1.0089	-1.2811	-1.8434	1.9503	-2.7372	-1.3671	1.1370	2.4091	4.0414
15	Arnd0015	0.9730	-1.3104	-1.8349	1.8507	-2.8152	-1.4289	1.4042	2.5504	3.9932
16	Arnd0016	0.7663	-1.4801	-2.0600	1.7191	-2.9668	-1.7702	2.5711	3.1191	3.7961
17	Arnd0017	0.6892	-1.6315	-2.0680	1.7765	-2.7417	-1.7595	2.3961	3.1796	3.8570

Table S28. Probability values related to the new classification scheme for samples from the Abitibi Greenstone Belt (data from Table S27 were processed; the results are plotted in Figures S5 and S6a-e).

Consec	Name	Discriminant function	High-Mg–Common subdivision		High-Mg or Common	High-Mg rock (kom-mei-pic-bon) subdivision				Inference from new classification scheme
		$DF_{(HMg\text{-}Com)M}$	$p_{(HMg)M}$	$p_{(Com)M}$		p_{kom}	p_{mei}	p_{pic}	p_{bon}	
1	Arnd0001	9.3001883	1	9.36E-16	High-Mg	0.7499	0.2499	0.0001	0.0000	komatiite
2	Arnd0002	10.3957127	1	8.36E-15	High-Mg	0.7500	0.2500	0.0000	0.0000	komatiite
3	Arnd0003	9.86024604	1	1.33E-16	High-Mg	0.7500	0.2500	0.0000	0.0000	komatiite
4	Arnd0004	10.8720266	1	6.12E-21	High-Mg	0.7500	0.2500	0.0000	0.0000	komatiite
5	Arnd0005	13.3148547	1	4.91E-17	High-Mg	0.7500	0.2500	0.0000	0.0000	komatiite
6	Arnd0006	11.1166379	1	1.53E-12	High-Mg	0.7500	0.2500	0.0000	0.0000	komatiite
7	Arnd0007	8.58588939	1	7.82E-13	High-Mg	0.7460	0.2246	0.0294	0.0000	komatiite
8	Arnd0008	8.75037141	1	1.19E-17	High-Mg	0.7341	0.1922	0.0737	0.0000	komatiite
9	Arnd0009	11.4635508	1	1.83E-29	High-Mg	0.7500	0.2499	0.0001	0.0000	komatiite
10	Arnd0010	18.1143587	1	1.09E-18	High-Mg	0.7500	0.2500	0.0000	0.0000	komatiite
11	Arnd0011	12.048751	1	3.09E-13	High-Mg	0.7500	0.2500	0.0000	0.0000	komatiite
12	Arnd0012	8.97753148	1	2.25E-13	High-Mg	0.7500	0.2500	0.0001	0.0000	komatiite
13	Arnd0013	9.05525113	1	1.05E-12	High-Mg	0.7500	0.2500	0.0000	0.0000	komatiite
14	Arnd0014	8.67812088	1	2.26E-13	High-Mg	0.7498	0.2499	0.0003	0.0000	komatiite
15	Arnd0015	9.0541741	1	1.09E-15	High-Mg	0.7499	0.2499	0.0002	0.0000	komatiite
16	Arnd0016	10.3590163	1	4.83E-13	High-Mg	0.7499	0.2498	0.0003	0.0000	komatiite
17	Arnd0017	8.86851998	1	9.36E-16	High-Mg	0.7484	0.2473	0.0043	0.0000	komatiite

Table S29. Major element composition of compiled Cretaceous-Paleogene high-Mg igneous rock samples from the Gorgona Island, Colombia (Test study T6; *Révillon et al.* [2000]; rock type from the IUGS classification scheme).

Consec	Sample name		SiO_2	TiO_2	Al_2O_3	Fe_2O_3	FeO	MnO	MgO	CaO	Na_2O	K_2O	P_2O_5	IUGS scheme
	Original authors`	This work												High-Mg rock type
1	GOR501	RACH001	44.65	0.61	10.10	0	11.30	0.19	22.08	8.91	0.81	0.02	0.03	komatiite
2	GOR502	RACH002	46.07	0.74	13.08	0	11.37	0.20	14.53	11.38	1.26	0.04	0.04	picrite
3	GOR519	RACH003	46.90	0.48	12.60	0	10.57	0.19	15.58	10.62	1.25	0.59	0.03	picrite
4	GOR521	RACH004	47.89	0.49	13.22	0	10.54	0.18	14.44	10.34	1.53	0.16	0.03	picrite
5	GOR525	RACH005	44.56	0.64	11.17	0	11.42	0.20	20.11	9.88	0.68	0.03	0.04	komatiite
6	GOR537	RACH006	44.70	0.66	11.62	0	11.37	0.19	17.31	10.68	2.08	0.06	0.05	picrite
7	GOR538	RACH007	43.65	0.51	8.72	0	10.60	0.18	26.48	8.01	0.59	0.03	0.04	komatiite
8	GOR539	RACH008	44.50	0.62	10.55	0	10.94	0.19	20.98	10.05	0.85	0.05	0.04	komatiite
9	GOR512	RACH010	45.27	0.30	9.76	0	10.00	0.18	24.44	8.21	0.66	0.07	0.02	komatiite
10	GOR512	RACH011	45.36	0.33	9.98	0	10.08	0.18	23.54	8.68	0.66	0.05	0.01	komatiite
11	GOR512	RACH012	45.93	0.34	10.30	0	10.05	0.18	22.74	8.50	0.63	0.17	0.03	komatiite
12	GOR512	RACH013	44.46	0.27	8.71	0	9.84	0.17	27.29	7.73	0.37	0.02	0.02	komatiite
13	GOR517	RACH014	44.58	0.32	8.50	0	9.84	0.18	27.87	7.24	0.33	0.03	0.02	komatiite
14	GOR503	RACH015	41.88	0.22	5.03	0	11.2	0.18	35.41	4.67	0.13	0.01	0.01	komatiite
15	GOR505	RACH017	41.70	0.21	5.37	0	11.06	0.18	34.20	5.94	0.07	0.01	0.01	komatiite
16	GOR542	RACH018	42.85	0.31	6.81	0	10.6	0.17	31.50	6.28	0.26	0.01	0.01	komatiite
17	GOR506	RACH019	43.25	0.47	6.52	0	13.36	0.23	27.60	6.50	0.22	0.02	0.04	komatiite
18	GOR509	RACH022	44.04	0.28	8.15	0	11.23	0.22	27.20	7.40	0.19	0.03	0.02	komatiite
19	GOR518	RACH023	44.96	0.34	10.12	0	10.86	0.20	22.21	9.38	0.66	0.02	0.02	komatiite
20	GOR535	RACH025	43.57	0.64	8.56	0	13.07	0.21	24.13	8.03	0.28	0.03	0.04	komatiite

Table S30. Adjusted major element composition of compiled Cretaceous-Paleogene high-Mg igneous rock samples from the Gorgona Island, Colombia (equations in Table S2 and data from Table S29).

Consec	Name	SiO_2A	TiO_2A	Al_2O_3A	$Fe_2O_3^tA$	MnOA	MgOA	CaOA	Na_2OA	K_2OA	P_2O_5A
1	RACH001	44.669	0.610	10.104	12.563	0.190	22.089	8.914	0.810	0.020	0.030
2	RACH002	46.081	0.740	13.083	12.639	0.200	14.533	11.383	1.260	0.040	0.040
3	RACH003	46.906	0.480	12.602	11.748	0.190	15.582	10.621	1.250	0.590	0.030
4	RACH004	47.893	0.490	13.221	11.714	0.180	14.441	10.341	1.530	0.160	0.030
5	RACH005	44.559	0.640	11.170	12.691	0.200	20.110	9.880	0.680	0.030	0.040
6	RACH006	44.706	0.660	11.622	12.638	0.190	17.312	10.681	2.080	0.060	0.050
7	RACH007	43.654	0.510	8.721	11.781	0.180	26.483	8.011	0.590	0.030	0.040
8	RACH008	44.505	0.620	10.551	12.160	0.190	20.982	10.051	0.850	0.050	0.040
9	RACH010	45.259	0.300	9.758	11.111	0.180	24.434	8.208	0.660	0.070	0.020
10	RACH011	45.363	0.330	9.981	11.203	0.180	23.542	8.681	0.660	0.050	0.010
11	RACH012	45.935	0.340	10.301	11.170	0.180	22.742	8.501	0.630	0.170	0.030
12	RACH013	44.471	0.270	8.712	10.938	0.170	27.297	7.732	0.370	0.020	0.020
13	RACH014	44.577	0.320	8.500	10.935	0.180	27.868	7.240	0.330	0.030	0.020
14	RACH015	41.885	0.220	5.031	12.449	0.180	35.415	4.671	0.130	0.010	0.010
15	RACH017	41.708	0.210	5.371	12.294	0.180	34.206	5.941	0.070	0.010	0.010
16	RACH018	42.858	0.310	6.811	11.783	0.170	31.506	6.281	0.260	0.010	0.010
17	RACH019	43.381	0.471	6.540	14.893	0.231	27.684	6.520	0.221	0.020	0.040
18	RACH022	44.035	0.280	8.149	12.479	0.220	27.197	7.399	0.190	0.030	0.020
19	RACH023	44.969	0.340	10.122	12.072	0.200	22.215	9.382	0.660	0.020	0.020
20	RACH025	43.563	0.640	8.559	14.523	0.210	24.126	8.029	0.280	0.030	0.040

Table S31. Isometric log-ratio transformed data of compiled Cretaceous-Paleogene high-Mg igneous rock samples from the Gorgona Island, Colombia (equations in Table S3; adjusted data from Table S30).

Consec	Name	$ilr1_{TiM}$	$ilr2_{AlM}$	$ilr3_{FeM}$	ilr4MnM	ilr5MgM	ilr6CaM	$ilr7Na_{M}$	$ilr8_{KM}$	ilr9PM
1	RACH001	0.6422	-1.5502	-1.8329	1.8556	-2.4472	-1.6417	0.5843	4.0785	3.7193
2	RACH002	0.6321	-1.6152	-1.6833	1.9698	-1.9018	-1.7026	0.3384	3.5937	3.6161
3	RACH003	1.0669	-1.4361	-1.4625	2.1784	-1.7994	-1.4701	0.5161	1.2280	4.0617
4	RACH004	0.9694	-1.5711	-1.5616	2.1219	-1.8371	-1.5540	0.2173	2.3477	3.9504
5	RACH005	0.6604	-1.5723	-1.7783	1.8756	-2.2946	-1.6692	0.8169	3.7657	3.5163
6	RACH006	0.7786	-1.4429	-1.6030	2.0986	-1.9770	-1.5580	-0.0438	3.2989	3.4924
7	RACH007	0.7677	-1.4315	-1.7788	1.9026	-2.6144	-1.5445	0.8793	3.6948	3.4449
8	RACH008	0.7259	-1.4759	-1.6883	1.9760	-2.2777	-1.6286	0.6651	3.3415	3.5740
9	RACH010	1.1268	-1.5422	-1.7482	1.8822	-2.5622	-1.5886	0.7530	2.8744	4.0808
10	RACH011	0.9969	-1.6326	-1.8317	1.8031	-2.6086	-1.7219	0.6703	3.1083	4.6545
11	RACH012	1.1378	-1.4712	-1.6306	2.0080	-2.3679	-1.4904	0.9282	2.1705	3.8296
12	RACH013	1.0533	-1.6201	-1.9154	1.7462	-2.8538	-1.7265	1.0987	3.8583	3.8823
13	RACH014	0.9652	-1.5632	-1.8763	1.7355	-2.8318	-1.6240	1.2480	3.5186	3.9252
14	RACH015	0.9646	-1.4414	-2.3135	1.3996	-3.3931	-1.5657	1.7682	4.2004	4.2266
15	RACH017	0.9684	-1.5284	-2.3383	1.3628	-3.3989	-1.8265	2.3088	4.1616	4.1876
16	RACH018	0.8232	-1.5721	-2.1421	1.5786	-3.1558	-1.7076	1.2535	4.3351	4.3621
17	RACH019	0.7219	-1.3137	-2.1061	1.5524	-2.7860	-1.4867	1.6651	3.9390	3.3060
18	RACH022	1.0306	-1.5623	-2.0262	1.5193	-2.8469	-1.6821	1.7261	3.4800	3.8864
19	RACH023	0.9765	-1.6430	-1.8952	1.7098	-2.5545	-1.7927	0.6714	3.9732	3.9980
20	RACH025	0.5884	-1.4380	-1.9832	1.7410	-2.5538	-1.5714	1.5517	3.6698	3.4198

Table S32. Probability values related to the new classification scheme for samples from the Gorgona Island, Colombia (data from Table S31 were processed; the results are plotted in Figures S5 and S6a-e).

Consec	Name	Discriminant function	High-Mg–Common subdivision		High-Mg or Common	High-Mg rock (kom-mei-pic-bon) subdivision				Inference from new classification scheme
		$DF_{(HMg\text{-}Com)M}$	$p_{(HMg)M}$	$p_{(Com)M}$		p_{kom}	p_{mei}	p_{pic}	p_{bon}	
1	RACH001	5.3480	1.0000	0.0000	High-Mg	0.7424	0.2532	0.0044	0.0000	komatiite
2	RACH002	3.0775	0.9908	0.0092	High-Mg	0.1928	0.0331	0.7738	0.0002	picrite
3	RACH003	3.6348	0.9990	0.0010	High-Mg	0.0268	0.0023	0.7581	0.2127	picrite
4	RACH004	3.2597	0.9956	0.0044	High-Mg	0.0290	0.0025	0.7766	0.1919	picrite
5	RACH005	4.8814	1.0000	0.0000	High-Mg	0.7398	0.2179	0.0423	0.0000	komatiite
6	RACH006	3.2122	0.9947	0.0053	High-Mg	0.2403	0.2114	0.5482	0.0000	picrite
7	RACH007	6.5432	1.0000	0.0000	High-Mg	0.7493	0.2504	0.0002	0.0000	komatiite
8	RACH008	4.8424	1.0000	0.0000	High-Mg	0.7355	0.2344	0.0301	0.0000	komatiite
9	RACH010	6.3455	1.0000	0.0000	High-Mg	0.7494	0.2465	0.0041	0.0000	komatiite
10	RACH011	6.1082	1.0000	0.0000	High-Mg	0.7494	0.2459	0.0047	0.0000	komatiite
11	RACH012	6.0003	1.0000	0.0000	High-Mg	0.7448	0.2241	0.0310	0.0000	komatiite
12	RACH013	7.6205	1.0000	0.0000	High-Mg	0.7500	0.2498	0.0002	0.0000	komatiite
13	RACH014	7.8202	1.0000	0.0000	High-Mg	0.7500	0.2499	0.0002	0.0000	komatiite
14	RACH015	11.8660	1.0000	0.0000	High-Mg	0.7500	0.2500	0.0000	0.0000	komatiite
15	RACH017	11.9750	1.0000	0.0000	High-Mg	0.7500	0.2500	0.0000	0.0000	komatiite
16	RACH018	9.2064	1.0000	0.0000	High-Mg	0.7500	0.2500	0.0000	0.0000	komatiite
17	RACH019	9.4068	1.0000	0.0000	High-Mg	0.7493	0.2500	0.0007	0.0000	komatiite
18	RACH022	8.7911	1.0000	0.0000	High-Mg	0.7499	0.2488	0.0013	0.0000	komatiite
19	RACH023	5.9804	1.0000	0.0000	High-Mg	0.7490	0.2371	0.0139	0.0000	komatiite
20	RACH025	7.3959	1.0000	0.0000	High-Mg	0.7482	0.2481	0.0038	0.0000	komatiite

Table S33. Major element composition of compiled Neoarchaean high-Mg igneous rock samples from the Belingwe Greenstone Belt, Zimbabwe (Test study T7; *Shimizu et al.* [2005]; rock type from the IUGS classification scheme).

Consec	Sample name		SiO_2	TiO_2	Al_2O_3	Fe_2O_3	FeO	MnO	MgO	CaO	Na_2O	K_2O	P_2O_5	IUGS scheme
	Original authors`	This work												High-Mg rock type
1	BW116	ShiNM001	48.10	0.45	8.98	0	11.44	0.200	16.46	9.02	1.25	0.07	0.033	picrite
2	BW130	ShiNM002	45.35	0.30	6.08	0	10.38	0.180	27.02	6.20	0.76	0.04	0.022	komatiite
3	BW135	ShiNM003	44.86	0.31	6.22	0	10.42	0.180	25.42	6.32	0.60	0.06	0.019	komatiite
4	BW272	ShiNM004	45.51	0.32	6.48	0	10.48	0.180	25.42	6.60	0.83	0.10	0.022	komatiite
5	BW460	ShiNM005	44.11	0.25	5.06	0	10.25	0.180	30.16	5.15	0.52	0.05	0.019	komatiite
6	BW478	ShiNM006	44.60	0.29	5.90	0	10.19	0.180	26.99	6.11	1.01	0.08	0.021	komatiite
7	BW483	ShiNM007	45.06	0.32	6.37	0	10.38	0.180	25.29	6.57	1.04	0.10	0.023	komatiite
8	BX001	ShiNM011	46.00	0.34	6.88	0	10.7	0.180	24.02	6.94	0.80	0.06	0.025	komatiite
9	BX003	ShiNM012	47.80	0.43	8.72	0	11.31	0.200	17.07	8.94	1.22	0.08	0.03	picrite
10	BX004	ShiNM013	47.70	0.43	8.73	0	11.25	0.200	16.90	8.89	1.24	0.09	0.03	picrite

Table S34. Adjusted major element composition of compiled Neoarchaean high-Mg igneous rock samples from the Belingwe Greenstone Belt, Zimbabwe (equations in Table S2 and data from Table S33).

Consec	Name	SiO_2A	TiO_2A	Al_2O_3A	$Fe_2O_3{}^tA$	MnOA	MgOA	CaOA	Na_2OA	K_2OA	P_2O_5A
1	ShiNM001	49.446	0.463	9.231	13.069	0.206	16.920	9.272	1.285	0.074	0.034
2	ShiNM002	46.518	0.308	6.237	11.833	0.185	27.716	6.360	0.780	0.043	0.023
3	ShiNM003	46.939	0.324	6.508	12.117	0.188	26.598	6.613	0.628	0.064	0.020
4	ShiNM004	46.865	0.330	6.673	11.994	0.185	26.177	6.796	0.855	0.103	0.023
5	ShiNM005	45.527	0.258	5.223	11.757	0.186	31.129	5.315	0.537	0.049	0.020
6	ShiNM006	46.216	0.301	6.114	11.735	0.187	27.968	6.331	1.047	0.081	0.022
7	ShiNM007	46.700	0.332	6.602	11.956	0.187	26.210	6.809	1.078	0.104	0.024
8	ShiNM011	47.357	0.350	7.083	12.242	0.185	24.729	7.145	0.824	0.060	0.026
9	ShiNM012	49.249	0.443	8.984	12.950	0.206	17.588	9.211	1.257	0.080	0.031
10	ShiNM013	49.324	0.445	9.027	12.928	0.207	17.475	9.193	1.282	0.088	0.031

Table S35. Isometric log-ratio transformed data of compiled Neoarchaean high-Mg igneous rock samples from the Belingwe Greenstone Belt, Zimbabwe (equations in Table S3; adjusted data from Table S34).

Consec	Name	$ilr1_{TiM}$	$ilr2_{AlM}$	$ilr3_{FeM}$	ilr4MnM	ilr5MgM	ilr6CaM	$ilr7Na_M$	$ilr8_{KM}$	ilr9PM
1	ShiNM001	0.9454	-1.3526	-1.7357	1.9211	-2.0654	-1.5378	0.2949	2.9882	3.7470
2	ShiNM002	1.0639	-1.2283	-1.8575	1.8026	-2.7349	-1.4109	0.5379	3.2722	3.9060
3	ShiNM003	1.0405	-1.2472	-1.8611	1.8023	-2.6795	-1.4289	0.7587	2.9200	4.0448
4	ShiNM004	1.0959	-1.1907	-1.7707	1.9009	-2.5789	-1.3671	0.5582	2.5579	4.0102
5	ShiNM005	1.1295	-1.1515	-1.9241	1.7225	-2.9171	-1.3220	0.8091	3.0817	3.9601
6	ShiNM006	1.1403	-1.1432	-1.7772	1.8690	-2.6662	-1.3287	0.3413	2.7585	4.0206
7	ShiNM007	1.1117	-1.1584	-1.7430	1.9209	-2.5538	-1.3422	0.3682	2.5790	3.9893
8	ShiNM011	1.0313	-1.2647	-1.8153	1.8733	-2.5554	-1.4421	0.5638	3.0424	3.8597
9	ShiNM012	0.9701	-1.3371	-1.7349	1.9117	-2.1081	-1.5392	0.3079	2.9029	3.8275
10	ShiNM013	0.9758	-1.3315	-1.7233	1.9189	-2.0917	-1.5266	0.3002	2.8295	3.8351

Table S36. Probability values related to the new classification scheme for samples from the Belingwe Greenstone Belt, Zimbabwe (data from Table S35 were processed; the results are plotted in Figures S5 and S6a-e).

Consec	Name	Discriminant function	High-Mg–Common subdivision		High-Mg or Common	High-Mg rock (kom-mei-pic-bon) subdivision				Inference from new classification scheme
		$DF_{(HMg\text{-}Com)M}$	$p_{(HMg)M}$	$p_{(Com)M}$		p_{kom}	p_{mei}	p_{pic}	p_{bon}	
1	ShiNM001	5.5608	1.0000	0.0000	High-Mg	0.1896	0.0149	0.7662	0.0293	picrite
2	ShiNM002	8.5732	1.0000	0.0000	High-Mg	0.7476	0.2518	0.0006	0.0000	komatiite
3	ShiNM003	8.5637	1.0000	0.0000	High-Mg	0.7482	0.2496	0.0022	0.0000	komatiite
4	ShiNM004	8.0339	1.0000	0.0000	High-Mg	0.7422	0.2536	0.0041	0.0000	komatiite
5	ShiNM005	10.0482	1.0000	0.0000	High-Mg	0.7497	0.2502	0.0001	0.0000	komatiite
6	ShiNM006	8.3179	1.0000	0.0000	High-Mg	0.7364	0.2626	0.0010	0.0000	komatiite
7	ShiNM007	7.8054	1.0000	0.0000	High-Mg	0.7275	0.2683	0.0042	0.0000	komatiite
8	ShiNM011	7.7513	1.0000	0.0000	High-Mg	0.7429	0.2501	0.0070	0.0000	komatiite
9	ShiNM012	5.7505	1.0000	0.0000	High-Mg	0.2170	0.0231	0.7445	0.0154	picrite
10	ShiNM013	5.7053	1.0000	0.0000	High-Mg	0.2027	0.0198	0.7531	0.0244	picrite

Table S37. Application study (A2) of compiled late Archean high-Mg igneous rock samples from Aravalli, Rajasthan, India [*Ahmad and Tarney*, 1994].

Consec	Sample Id (Original Author)	SiO_2A	TiO_2A	Al_2O_3A	$Fe_2O_3^tA$	MnOA	MgOA	CaOA	Na_2OA	K_2OA	P_2O_5A	IUGS scheme (High-Mg)	$p_{(HMg)M}$	$p_{(Com)M}$	High-Mg or Common	p_{kom}	p_{mei}	p_{pic}	p_{bon}	New scheme (High-Mg)
1	KM2	50.787	0.518	6.473	10.436	0.199	22.008	9.201	0.259	0.110	0.010	komatiite	1.0000	0.0000	High-Mg	0.7125	0.1475	0.1045	0.0354	komatiite
2	KM3	53.408	0.246	3.836	9.600	0.236	20.753	11.567	0.256	0.059	0.039	boninite	1.0000	0.0000	High-Mg	0.5860	0.0000	0.2063	0.2077	komatiite
3	KM4	50.835	0.142	5.266	11.180	0.233	20.962	10.957	0.365	0.041	0.020	komatiite	1.0000	0.0000	High-Mg	0.5685	0.0000	0.1869	0.2446	komatiite
4	KM5	51.860	0.219	6.482	9.335	0.349	20.545	10.462	0.598	0.100	0.050	boninite	1.0000	0.0000	High-Mg	0.2173	0.0031	0.3631	0.4165	boninite
5	KM6	50.119	1.070	5.547	13.788	0.218	19.414	9.459	0.248	0.040	0.099	meimechite	1.0000	0.0000	High-Mg	0.4057	0.1674	0.2726	0.1543	komatiite

Table S38. Application study (A3) of compiled Neoarchean high-Mg igneous rock samples from Gadwal Greenstone Belt, Eastern Dharwar Craton, India [*Manikyamba et al.*, 2005].

Consec	Sample Id (Original Author)	SiO_2A	TiO_2A	Al_2O_3A	$Fe_2O_3^tA$	MnOA	MgOA	CaOA	Na_2OA	K_2OA	P_2O_5A	IUGS scheme (High-Mg)	$p_{(HMg)M}$	$p_{(Com)M}$	High-Mg or Common	p_{kom}	p_{mei}	p_{pic}	p_{bon}	New scheme (High-Mg)
1	G22	51.085	0.240	11.991	9.961	0.130	12.941	12.021	1.150	0.450	0.030	picrite	0.9999	0.0001	High-Mg	0.0000	0.0000	0.2013	0.7987	boninite
2	G23	50.260	0.350	10.330	11.930	0.150	17.210	8.640	0.760	0.330	0.040	picrite	1.0000	0.0000	High-Mg	0.1737	0.0107	0.5862	0.2294	picrite
3	G24	52.300	0.280	10.640	11.040	0.160	13.270	10.600	1.320	0.350	0.040	boninite	1.0000	0.0000	High-Mg	0.0000	0.0000	0.2015	0.7985	boninite
4	G26	50.535	0.300	11.321	11.221	0.140	15.462	9.421	0.950	0.610	0.040	picrite	1.0000	0.0000	High-Mg	0.0024	0.0002	0.2505	0.7469	boninite
5	G41	50.768	0.361	12.805	11.781	0.151	12.303	10.426	0.933	0.421	0.050	picrite	0.9999	0.0001	High-Mg	0.0000	0.0000	0.2113	0.7887	boninite
6	G42	49.900	0.300	14.100	10.170	0.130	12.510	11.370	0.960	0.510	0.050	picrite	0.9984	0.0016	High-Mg	0.0001	0.0000	0.2667	0.7332	boninite
7	G44	50.840	0.270	11.530	10.750	0.140	14.120	10.760	0.950	0.600	0.040	picrite	1.0000	0.0000	High-Mg	0.0002	0.0000	0.2068	0.7930	boninite
8	G45	50.890	0.310	12.000	11.300	0.140	12.820	11.420	0.980	0.100	0.040	picrite	1.0000	0.0000	High-Mg	0.0014	0.0000	0.3044	0.6942	boninite

Table S39. Application study (A4) of compiled Proterozoic high-Mg igneous rock samples from Mahakoshal Supracrustal Belt, India [*Srivastava*, 2005].

Consec	Sample Id (Original Author)	SiO_2A	TiO_2A	Al_2O_3A	$Fe_2O_3^t$A	MnOA	MgOA	CaOA	Na_2OA	K_2OA	P_2O_5A	IUGS scheme (High-Mg)	$p_{(HMg)M}$	$p_{(Com)M}$	High-Mg or Common	p_{kom}	p_{mei}	p_{pic}	p_{bon}	New scheme (High-Mg)
1	CH18	45.664	3.906	12.072	18.205	0.194	14.482	5.057	0.032	0.011	0.377	picrite	1.0000	0.0000	High-Mg	0.4124	0.4002	0.1875	0.0000	komatiite
2	CH22	48.380	0.996	6.007	14.509	0.115	20.086	9.613	0.115	0.042	0.136	meimechite	1.0000	0.0000	High-Mg	0.6858	0.2140	0.0956	0.0046	komatiite
3	CH23	46.213	1.174	5.934	14.375	0.159	22.022	9.858	0.085	0.053	0.127	meimechite	1.0000	0.0000	High-Mg	0.7179	0.2335	0.0487	0.0000	komatiite
4	CH27	42.150	2.271	9.797	15.206	0.187	12.606	16.215	0.757	0.527	0.285	picrite	0.9898	0.0102	High-Mg	0.0000	0.2001	0.7999	0.0000	picrite

Table S40. Application study (A5) of compiled Archean high-Mg igneous rock samples from Mallina Basin, Australia [*Smithies*, 2002].

Consec	Sample Id (Original Author)	SiO_2A	TiO_2A	Al_2O_3A	$Fe_2O_3^t$A	MnOA	MgOA	CaOA	Na_2OA	K_2OA	P_2O_5A	IUGS scheme (High-Mg)	$p_{(HMg)M}$	$p_{(Com)M}$	High-Mg or Common	p_{kom}	p_{mei}	p_{pic}	p_{bon}	New scheme (High-Mg)
1	142194	54.336	0.264	17.384	9.149	0.162	8.347	8.235	1.675	0.396	0.051	boninite	0.8642	0.1358	High-Mg	0.0000	0.0000	0.2000	0.8000	boninite
2	142 359	53.705	0.245	18.010	8.643	0.173	8.806	7.553	2.732	0.092	0.041	boninite	0.4548	0.5452	Common	---	---	---	---	---
3	142368	54.067	0.267	17.098	9.889	0.175	8.184	8.318	1.777	0.185	0.041	boninite	0.8950	0.1050	High-Mg	0.0000	0.0000	0.2000	0.8000	boninite
4	142360	51.053	0.176	13.943	9.773	0.176	16.661	6.328	0.654	1.203	0.031	picrite	1.0000	0.0000	High-Mg	0.0187	0.0036	0.3659	0.6118	boninite
5	142363	44.820	0.169	12.499	12.139	0.243	23.918	5.831	0.212	0.148	0.021	komatiite	1.0000	0.0000	High-Mg	0.6310	0.2235	0.0354	0.1101	Komatiite

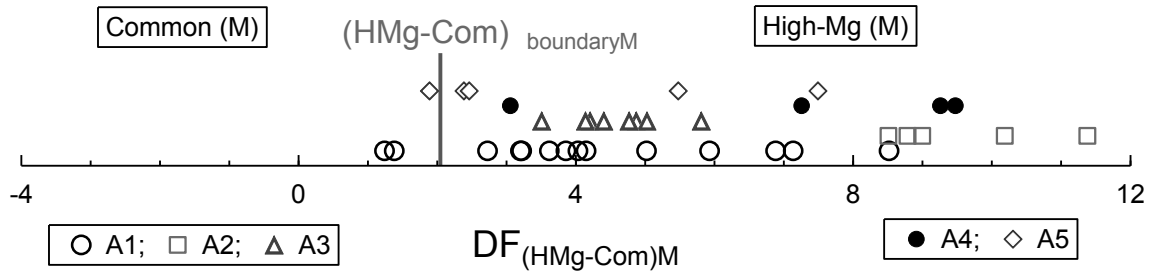

Figure S7. Application of the discriminant function $DF_{(HMg-Com)M}$ for High-Mg (HMg) and Common (Com) rock subdivision based on major element compositions (M); the classification field boundary $(HMg-Com)_{boundaryM}$ is shown for reference. The symbols for applications (A1−A5) are shown as insets; see text for explanation on A1−A5.

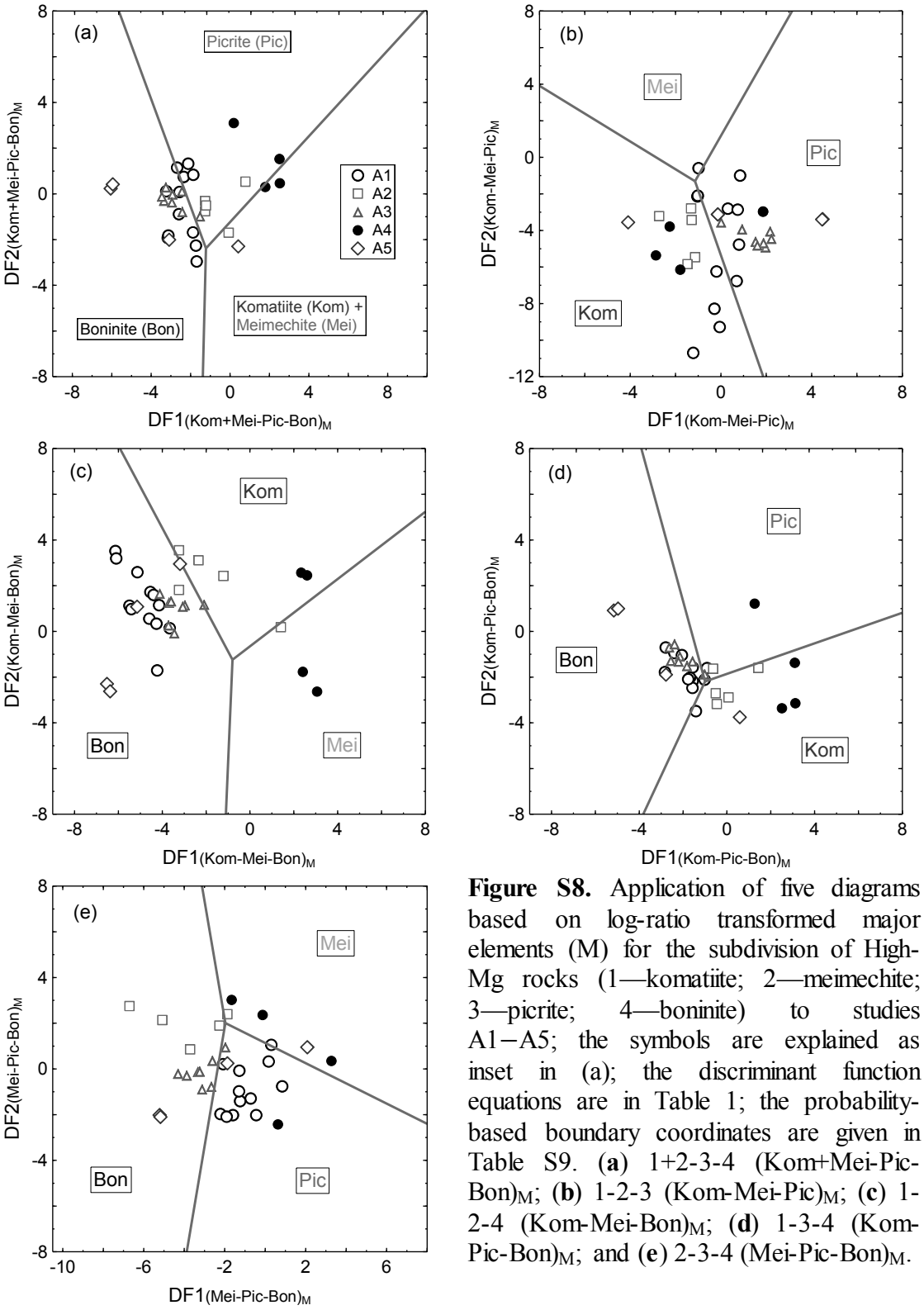

Figure S8. Application of five diagrams based on log-ratio transformed major elements (M) for the subdivision of High-Mg rocks (1—komatiite; 2—meimechite; 3—picrite; 4—boninite) to studies A1−A5; the symbols are explained as inset in (a); the discriminant function equations are in Table 1; the probability-based boundary coordinates are given in Table S9. (**a**) 1+2-3-4 (Kom+Mei-Pic-Bon)$_M$; (**b**) 1-2-3 (Kom-Mei-Pic)$_M$; (**c**) 1-2-4 (Kom-Mei-Bon)$_M$; (**d**) 1-3-4 (Kom-Pic-Bon)$_M$; and (**e**) 2-3-4 (Mei-Pic-Bon)$_M$.

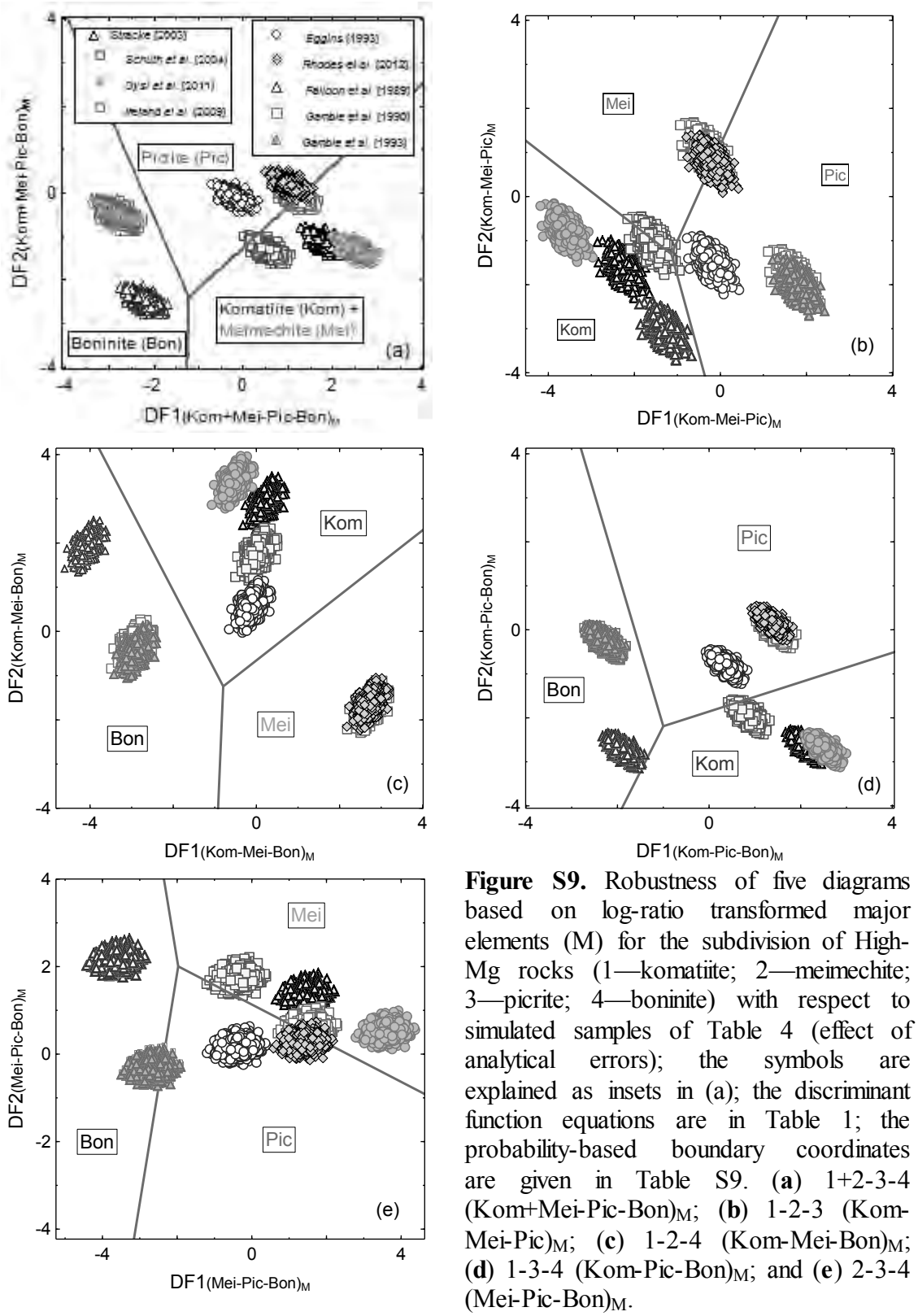

Figure S9. Robustness of five diagrams based on log-ratio transformed major elements (M) for the subdivision of High-Mg rocks (1—komatiite; 2—meimechite; 3—picrite; 4—boninite) with respect to simulated samples of Table 4 (effect of analytical errors); the symbols are explained as insets in (a); the discriminant function equations are in Table 1; the probability-based boundary coordinates are given in Table S9. (**a**) 1+2-3-4 $(Kom+Mei-Pic-Bon)_M$; (**b**) 1-2-3 $(Kom-Mei-Pic)_M$; (**c**) 1-2-4 $(Kom-Mei-Bon)_M$; (**d**) 1-3-4 $(Kom-Pic-Bon)_M$; and (**e**) 2-3-4 $(Mei-Pic-Bon)_M$.

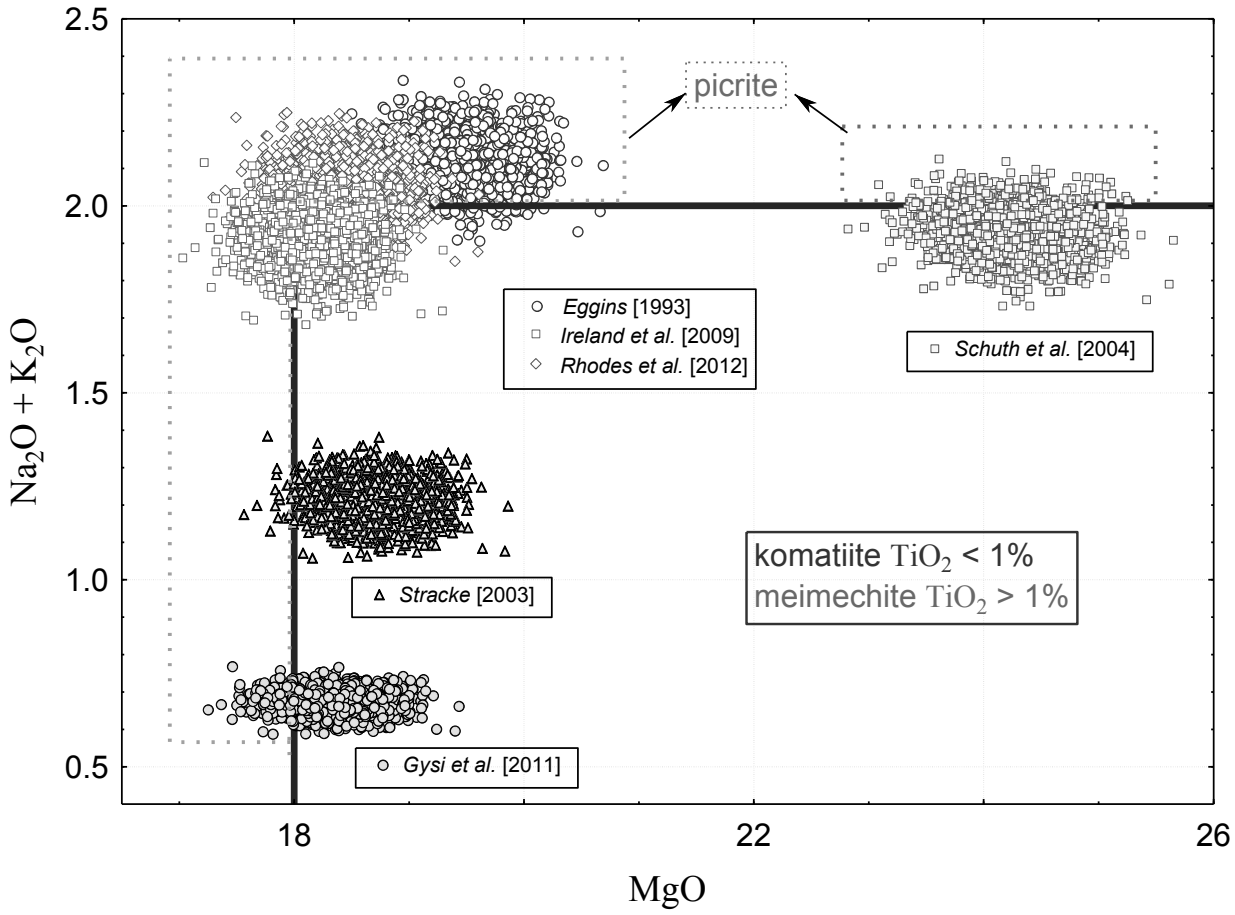

Figure S10. Less robustness of the IUGS classification scheme for the subdivision of High-Mg rocks with respect to some simulated samples of Table 4 (effect of analytical errors or uncertainties). The incorrect classification of komatiite and meimechite is shown as picrite and of picrte as komatiite or meimechite (for more details see Table 4).

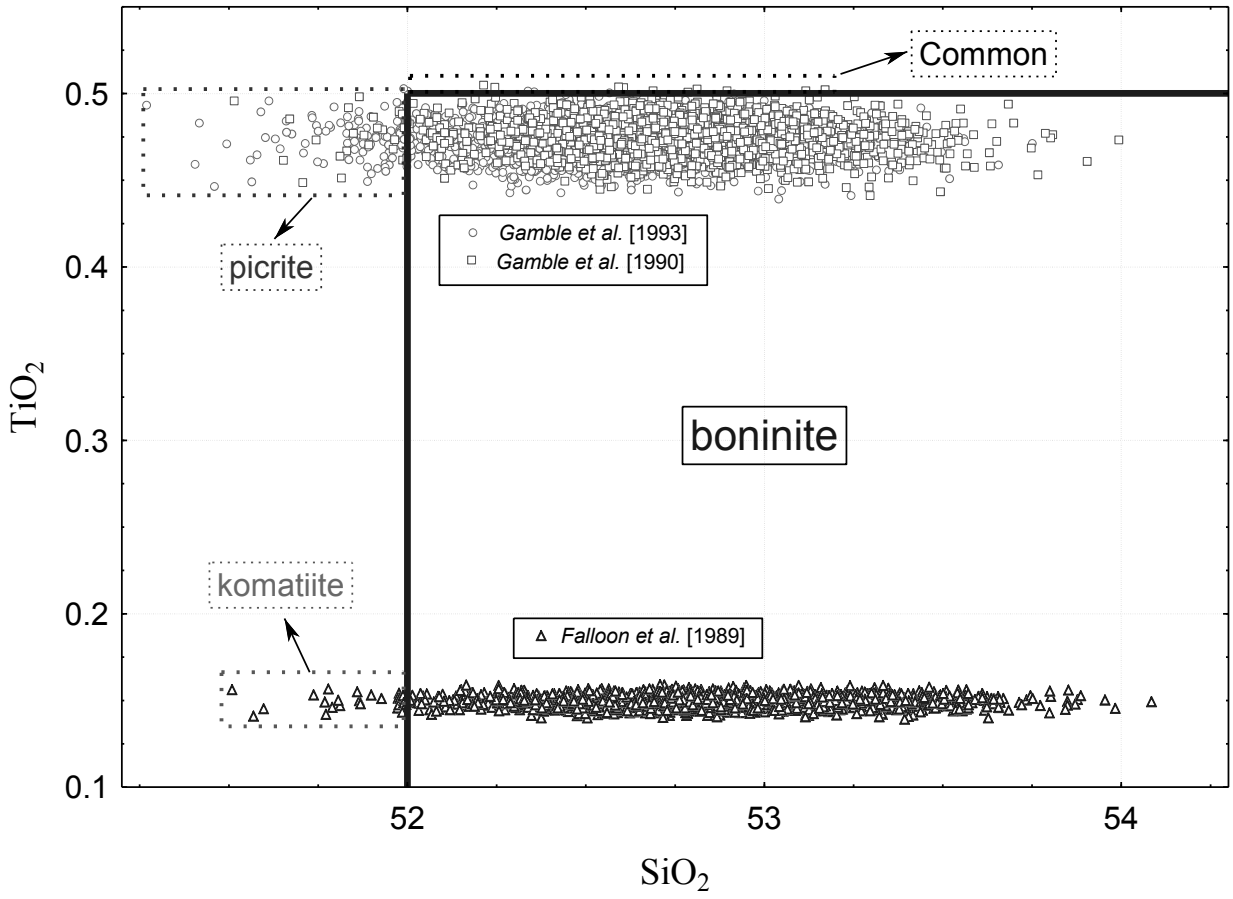

Figure S11. Less robustness of the IUGS classification scheme for the subdivision of High-Mg rocks with respect to the remaining simulated samples of Table 4 (effect of analytical errors or uncertainties). The incorrect classification of boninite is shown as either a Common rock or picrite or as komatiite (for more details see Table 4).

Table S41. Sensitivity analysis of the centroid of 126 High-Mg boninite rocks (adjusted compositions) from post-emplacement compositional changes of three elements at a time (simultaneous loss of SiO_2, Na_2O, and K_2O) in the High-Mg–Common rock subdivision based on major elements (M).

Original High-Mg centroid composition		HMgClaMSys [*this work*]			IUGS [*Le Bas*, 2000]		
Chemical parameter	Major element concentration (% m/m)	Maximum "tolerable" change *		Maximum compositional change of 100% adjusted data **	Maximum "tolerable" change *		Maximum compositional range of 100% adjusted data **
		loss (% m/m)	gain (% m/m)	final concentration (% m/m)	loss (% m/m)	gain (% m/m)	final concentration (% m/m)
SiO_2A	55.77	---	-22	50.13	---	-15	51.90
TiO_2A	0.26	---	---	0.29	---	---	0.28
MgOA	13.34	---	---	15.18	---	---	14.60
Na_2OA	1.51	-22	---	1.36	-15	---	1.41
K_2OA	0.40	-22	---	0.36	-15	---	0.37

*; ** See footnote Table 5.

HMgClaMSys (**H**igh-**Mg** **Cla**ssification **M**ajor element based **Sys**tem)

README

A computer program HMgClaMSys is available for online processing of High-Mg igneous rock compositional data from http://tlaloc.ier.unam.mx. The relevant paper and the supplementary file can also be downloaded from this website.

Simulation modelling confirmed the robustness of our classification with respect to analytical errors and post-emplacement compositional changes. From robustness considerations, our proposal for the nomenclature of High-Mg altered igneous rocks is shown superior to the IUGS scheme which was recommended for the classification of relatively fresh rocks only.

The interested person is invited to enter the web server http://tlaloc.ier.unam.mx (see Fig. 1a). If you are a new user, you must register and provide the information requested: first Name, last name, institutional email address and affiliation as shown in Fig. 1b. If you do not have an institutional email account, you must provide all institutional details.

Afterwords, the user will then receive an e-mail message with a temporary password, which can be changed. If you are a registered user, you must sign in using your email address and password (see Fig. 1c).

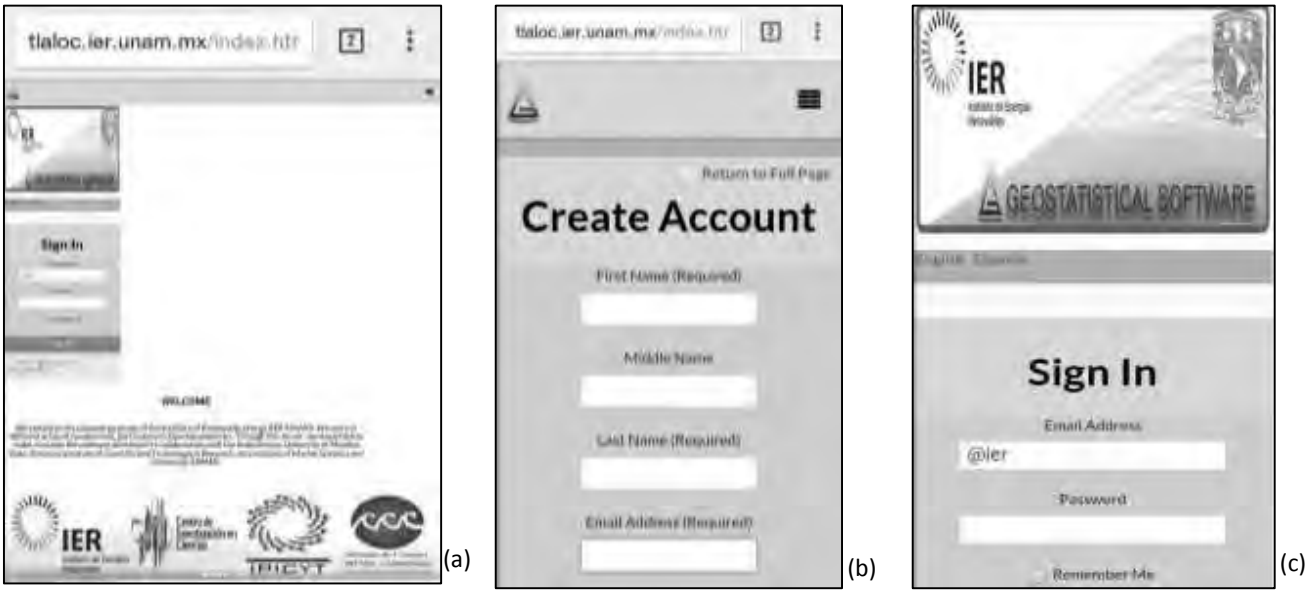

(a) (b) (c)

Fig. 1 Welcome screen of web server and user authentication. (a) Welcome screen of web server; (b) The screen to create a new account; and (c) The screen to user authentication.

As a registered user, you may use the "HMgClaMSys" option of "Online program" menu as shown in Fig. 3.

Fig. 2 "HMgClaMSys" option of "Online program" menu.

Once you access the online program HMgClaMSys, you can open an input file, for which there are three options as shown in Fig. 3a: (i) HMgClaMSys; (ii) Sensitivity analysis; and (iii) Analytical errrors_Uncertainty Propagation. You can download each of several input file folders available from web server (see Fig. 3b). These templates are required for testing the different processing options. The literature sources of the Common igneous rocks are summarized in pdf file available (link identified by a blue rectangle).

Fig. 3 Menu options and input files available. (a) Three options of "File Open" menu; and (b) Input files available for download.

1. New multidimensional classification scheme based on major elements

HMgClaMSys offers a set of 11 discriminant functions and 6 diagrams to facilitate High-Mg rock classification. The user must download the input file "*File_input_uptonetal2000_tableS11.xl*s" as shown in Fig. 4a. Optionally you can download the input file "Applications study" (Fig. 4b) and "Test study" (Fig. 4c) folders.

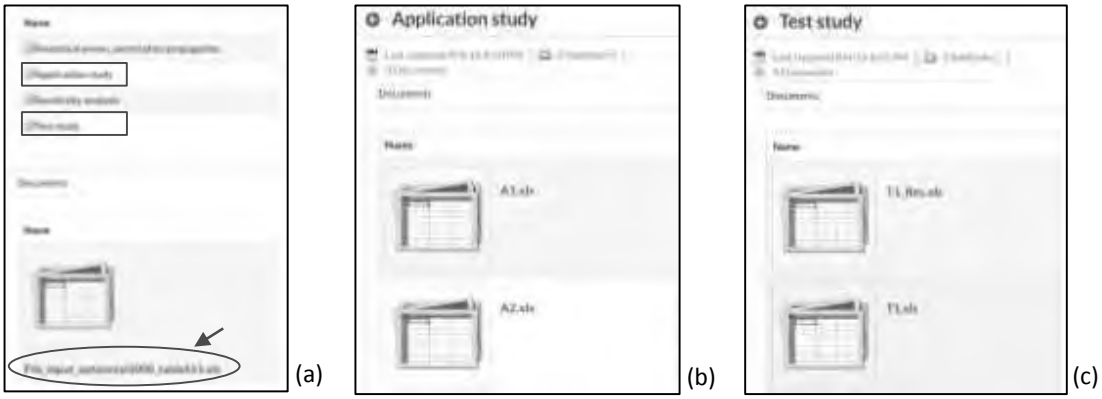

Fig. 4 Input file available for download from web server. (a) Input file "*File_input_uptonetal2000_tableS11.xls*"; (b) "Applications study" folder; and (c) "Test study" folder.

If you downloaded the file "*File_input_uptonetal2000_tableS11.xls*", click on the "Download (31k)" hyperlink to download the input file as shown in Fig. 5a (identified by a red circle). Once the download is successfully completed, click on the downloaded file (identified by a blue circle in Fig. 5a) to open it as shown in Fig 5b. HMgClaMSys requires 10 oxides from SiO_2 to P_2O_5 (see Fig 5b). It is important to note that **the measured data are input with total Fe as Fe2O3T**. If you do not have Fe2O3T values, please calculate it as follows (it is immaterial if you have either FeOT or separately FeO and Fe2O3, the equation will give you the Fe2O3T value; * means multiplication):

$$Fe2O3T = Fe2O3 + (FeO * 159.6882 / (2 * 71.8444))$$

From the measured major element compositions, HMgClaMSys efficiently calculates the adjusted values on an anhydrous 100% basis.

Fig. 5 Download of input file "*File_input_uptonetal2000_tableS11.xls*". (a) Hyperlink to download the file; and (b) View the contents of the file in Excel.

The user must open the "*File_input_uptonetal2000_tableS11.xls*" file as shown in Fig. 6.

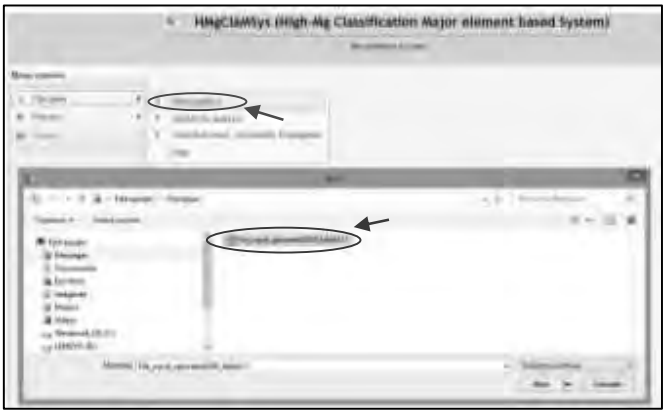

Fig. 6 Open file option of HMgClaMSys.

If everything is fine, the file will open as shown in Fig. 7.

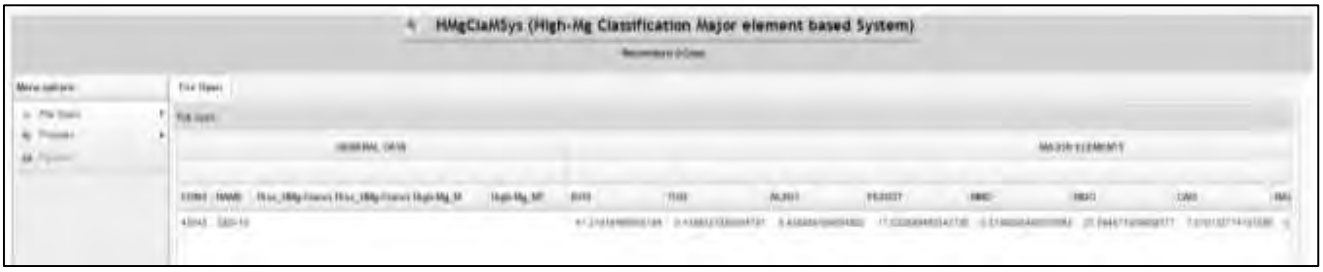

Fig. 7 Input data file already open and validated in HMgClaMSys.

Once the Excel input data file is correctly loaded without errors, the user can process the data using "Process" as shown in Fig. 8a. After the job is done (Fig. 8b), the user can download the general report (see Fig. 9a-c).

(a)

(b)

Fig. 8 Process option to be chosen.

The Excel output file contains:

- Classification summary, adjusted major element concentrations and Log-transformed ratios of individual samples (see Fig 9a).
- The detailed results of discriminant function $DF_{(HMg-Com)M}$ (see Fig 9b).

- The detailed results of five diagrams for the subdivision of High-Mg rocks (1—komatiite; 2—meimechite; 3—picrite; 4—boninite); see Fig 9c.

Fig. S9 The Excel output file contains: (a) Classification summary, adjusted major element concentrations and log-transformed ratios of individual samples; (b) The detailed results of discriminant function $DF_{(HMg-Com)M}$ and probability ($p_{(HMg)M}$ and $p_{(Com)M}$) for High-Mg and Common rocks; and (c) The detailed results of five diagrams for the subdivision and probabilities of High-Mg rocks (1—komatiite; 2—meimechite; 3—picrite; 4—boninite).

2. Robustness of the new multidimensional classification scheme based on major elements with respect to post-emplacement compositional changes

The maximum loss or gain (% m/m) of an element in the centroid composition is estimated as the value that will still give the same magma or rock type as determined from our multidimensional diagrams. However, the minimum and maximum changes possible for any given element are also automatically set for that particular element to show final concentrations between 0% (no concentration can become negative) and 100% (no concentration can be >100% m/m). Therefore, our sensitivity analysis was carried out within these two limits for the final composition, although more stringent conditions could be used in future.

To try this option, the user must download the "*Sensitivity_Format.xls*" template which is in the folder "Sensitivity analysis" (Fig. 10a). This template contains the composition (Fig. 10b) of the centroid of all 920 High-Mg rocks to estimate the post-emplacement compositional changes of three elements at a time (simultaneous gain of SiO_2, Na_2O and K_2O) in the High-Mg–Common rock subdivision based on major elements (M).

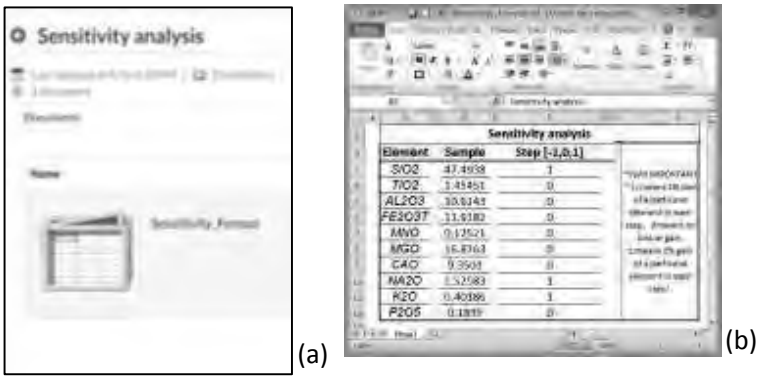

Fig. 10 Template available for sensitivity analysis.

If you downloaded successfully the template "*Sensitivity_Format.xls*", you can click on "Sensitivity analysis" option of "File Open" menu (see Fig. 11).

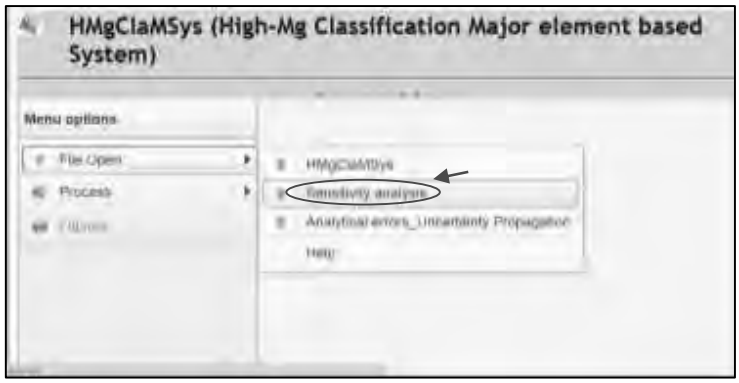

Fig. 11 "Sensitivity analysis" option of "File Open" menu.

Once the Excel input data file is correctly loaded without errors, the user can proceed to run the sensitivity analysis. HMgClaMSys provides two options in the "Process" menu as in Fig. 12. "Sensitivity Hmg-Comm" option performs sensitivity analysis of discriminant function $DF_{(HMg-Com)M}$. "Sensitivity Hmg-Comm" option performs sensitivity analysis of High-Mg rocks (1—komatiite; 2—meimechite; 3—picrite; 4—boninite).

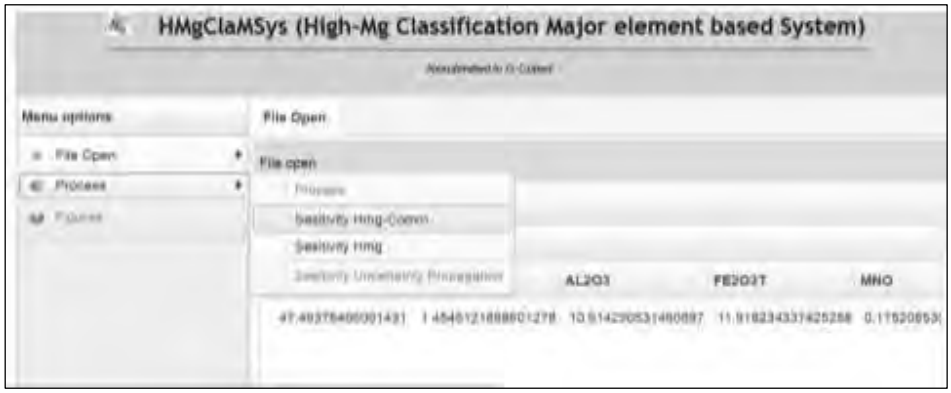

Fig. 12 "Sensitivity Hmg-Comm" option of "Process" menu.

For this example will use the "Sensitivity Hmg-Comm". After the job is done, the user can download (click on link identified with red circle in Fig. 13a) and open the sensibility report (see Fig. 13b).

(a)

(b)

Fig. 13 Sensibility report. (a) The sensibility process is done; (b) Sensibility report opened.

Thus, you are free to input your own sample replacing the concentration values in the example file (Fig. 10). You can similarly choose any element(s) for loss, gain or no change by simply inputting -1, 1 or 0 for that element(s).

3. Robustness of the new multidimensional classification scheme based on major elements with respect to analytical errors

To illustrate the robustness of HMgClaMSys, we used major element compositions of 9 selected samples (3 komatiite; 1 meimechite; 2 picrite; and 3 boninite; Fig. 14a-c) from our compiled database. You can download these input files to use this simulation module.

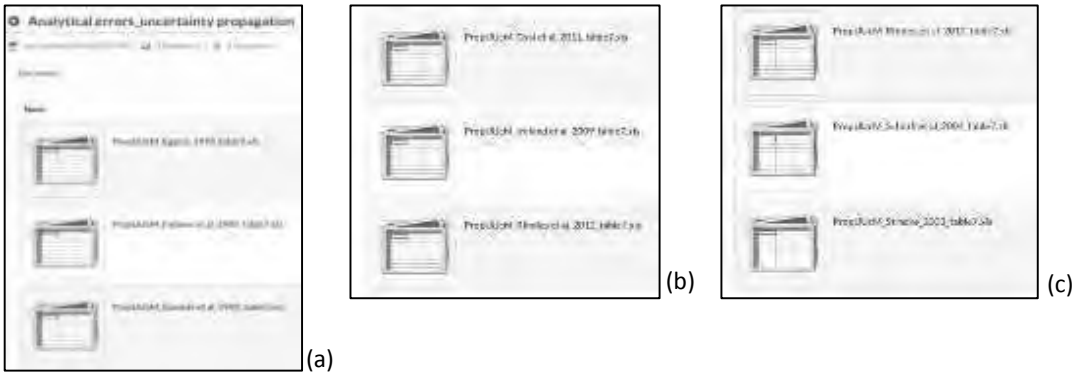

Fig. 14 Selected samples for sensitivity analysis with respect to analytical errors. (a-c) Templates of 9 selected samples.

For example, the picrite analysis reported by *Eggins* [1993] is shown in Fig. 15. We assumed small errors from 1% to 5% in individual major element determinations and applied the methodology of Monte Carlo simulation to generate 2200 independent simulated analyses for each sample. The analytical errors (relative standard deviation, RSD % column of Fig. 15) assumed in the simulation runs were as follows: 1% for SiO_2 and Al_2O_3; 2% for TiO_2, $Fe_2O_3^t$, MgO, and CaO; 4% for Na_2O and K_2O; and 5% for MnO and P_2O_5. You can download the input files to testing this module.

	A	B	C	D
1		Error propagation		
2	**Element**	**Sample**	***u***	***RSD%***
3	*SIO2*	46.8064	0.468	1
4	*TIO2*	0.53892	0.011	2
5	*AL2O3*	9.33134	0.093	1
6	*FE2O3T*	11.5868	0.232	2
7	*MNO*	0.1996	0.010	5
8	*MGO*	19.3114	0.386	2
9	*CAO*	9.9501	0.199	2
10	*NA2O*	1.26747	0.051	4
11	*K2O*	0.83832	0.034	4
12	*P2O5*	0.16966	0.008	5

Fig. 15 The picrite analysis (Sample Id = 68622) reported by *Eggins* [1993].

In order to simulate this sample (Fig. 15), you must download the "*PropUUcM_Eggins_1993_table7.xls*" file. After, you must open this file as shown in Fig. 16.

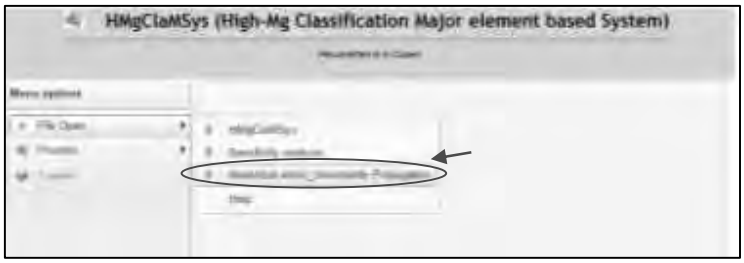

Fig. 16 "Analytical errors_Uncertainty Propagation" option of "File Open" menu.

Once the Excel input data file is correctly loaded without errors, the user can proceed to simulate the sample as a shown in

Fig. 17a (click on the option identified with red circle). After the process is done, the user can download the general report as a shown in Fig. 17b (click on the output file identified with blue circle).

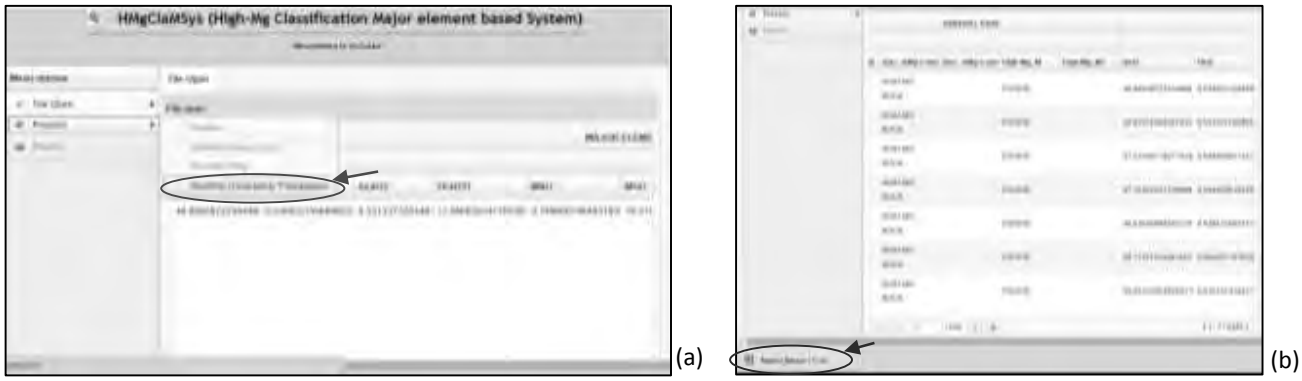

Fig. 17 "Sensitivity Uncertainty Propagation" option of "Process" menu.

The Excel output file contains: classification summary, initial concentration and adjusted concentrations (see Fig 18a), log-transformed ratios of individual samples, detailed results of discriminant function $DF_{(HMg-Com)M}$ (see Fig 18b), and detailed results of five diagrams for the subdivision of High-Mg rocks (1—komatiite; 2—meimechite; 3—picrite; 4—boninite) (see Fig 18c). For the picrite analysis reported by *Eggins* [1993] the HMgClaMSys reproduced the same name (picrite) for all 2200 simulated analyses.

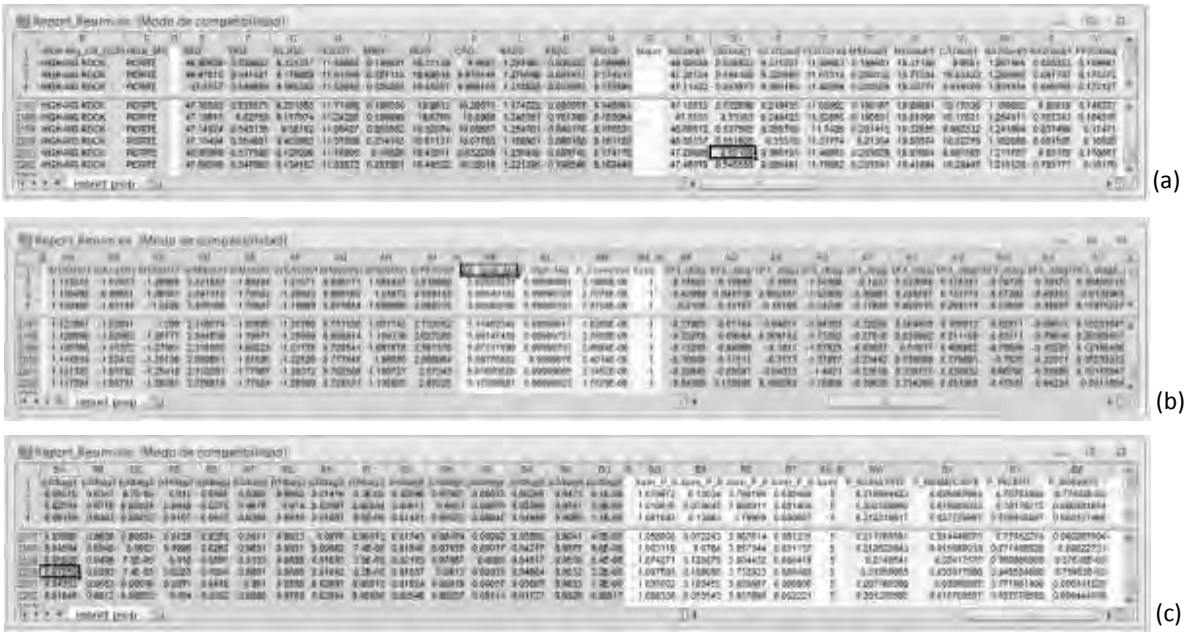

Fig. 18 The Excel output file contains: (a) first section; (b) second section; and (c) third section.

You are free to input your own sample replacing the concentration values in the example file and changing the uncertainty or %RSD values (see Fig. 15).

Apéndice IV

Verma S.P., **Rivera-Gómez, M.A.**, Díaz-González, L., Pandarinath, K., Amezcua-Valdez, A., Rosales-Rivera, M., Verma, S.K., Quiroz-Ruiz, A., Armstrong-Altrin, J.S., 2017. Multidimensional classification of magma types for altered igneous rocks and application to their tectonomagmatic discrimination and igneous provenance of siliciclastic sediments. Lithos, 278-281: 321-330, doi: 10.1016/j.lithos.2017.02.005.

Contiene un suplemento de 28 páginas así como un README of 10 páginas.

Lithos 278–281 (2017) 321–330

Contents lists available at ScienceDirect

Lithos

journal homepage: www.elsevier.com/locate/lithos

Multidimensional classification of magma types for altered igneous rocks and application to their tectonomagmatic discrimination and igneous provenance of siliciclastic sediments

Surendra P. Verma [a,*], M. Abdelaly Rivera-Gómez [b], Lorena Díaz-González [c], Kailasa Pandarinath [a], Alejandra Amezcua-Valdez [d], Mauricio Rosales-Rivera [e], Sanjeet K. Verma [f], Alfredo Quiroz-Ruiz [a], John S. Armstrong-Altrin [g]

[a] Instituto de Energías Renovables, Universidad Nacional Autónoma de México, Temixco, Mor 62580, Mexico
[b] Posgrado en Ingeniería, Instituto de Energías Renovables, Universidad Nacional Autónoma de México, Temixco, Mor 62580, Mexico
[c] Centro de Investigación en Ciencias, Instituto de Investigación en Ciencias Básicas y Aplicadas, Universidad Autónoma del Estado de Morelos, Cuernavaca, Mor 62209, Mexico
[d] Prácticas Profesionales, Instituto de Energías Renovables, Universidad Nacional Autónoma de México, Temixco, Mor 62580, Mexico
[e] Doctorado en Ciencias, Instituto de Investigación en Ciencias Básicas Y Aplicadas, Cuernavaca, Morelos 62209, Mexico
[f] División de Geociencias, Instituto Potosino de Investigación en Ciencia y Tecnología, Camino a la Presa San José # 2055, Col. Lomas 4ª Sec., San Luis Potosí SLP 78216, Mexico
[g] Instituto de Ciencias del Mar y Limnología, Unidad de Procesos Oceánicos y Costeros, Universidad Nacional Autónoma de México, Circuito Exterior s/n, 04510 México D.F., Mexico

ARTICLE INFO

Article history:
Received 19 October 2016
Accepted 7 February 2017
Available online 20 February 2017

Keywords:
Rock classification
Multivariate discordant outliers
Multidimensional diagrams
Isometric log-ratio transformation

ABSTRACT

A new multidimensional scheme consistent with the International Union of Geological Sciences (IUGS) is proposed for the classification of igneous rocks in terms of four magma types: ultrabasic, basic, intermediate, and acid. Our procedure is based on an extensive database of major element composition of a total of 33,868 relatively fresh rock samples having a multinormal distribution (initial database with 37,215 samples). Multinormally distributed database in terms of log-ratios of samples was ascertained by a new computer program DOMuDaF, in which the discordancy test was applied at the 99.9% confidence level. Isometric log-ratio (ilr) transformation was used to provide overall percent correct classification of 88.7%, 75.8%, 88.0%, and 80.9% for ultrabasic, basic, intermediate, and acid rocks, respectively. Given the known mathematical and uncertainty propagation properties, this transformation could be adopted for routine applications. The incorrect classification was mainly for the "neighbour" magma types, e.g., basic for ultrabasic and vice versa. Some of these misclassifications do not have any effect on multidimensional tectonic discrimination. For an efficient application of this multidimensional scheme, a new computer program MagClaMSys_ilr (MagClaMSys—**Mag**ma **Cla**ssification **M**ajor-element based **Sys**tem) was written, which is available for on-line processing on http://tlaloc.ier.unam.mx/index.html. This classification scheme was tested from newly compiled data for relatively fresh Neogene igneous rocks and was found to be consistent with the conventional IUGS procedure. The new scheme was successfully applied to inter-laboratory data for three geochemical reference materials (basalts JB-1 and JB-1a, and andesite JA-3) from Japan and showed that the inferred magma types are consistent with the rock name (basic for basalts JB-1 and JB-1a and intermediate for andesite JA-3). The scheme was also successfully applied to five case studies of older Archaean to Mesozoic igneous rocks. Similar or more reliable results were obtained from existing tectonomagmatic discrimination diagrams when used in conjunction with the new computer program as compared to the IUGS scheme. The application to three case studies of igneous provenance of sedimentary rocks was demonstrated as a novel approach. Finally, we show that the new scheme is more robust for post-emplacement compositional changes than the conventional IUGS procedure.

1. Introduction

According to the International Union of Geological Sciences (IUGS), the magma type of "fresh" igneous rocks is achieved solely from the consideration of anhydrous-basis adjusted SiO_2 content as follows (Le Bas et al., 1986): ultrabasic <45%; basic 45–52%; intermediate 52–63%; and acid >63%. For altered rocks, the IUGS did not recommend any classification procedure (Le Bas et al., 1986; Le Maitre et al., 2002).

* Corresponding author.
E-mail addresses: spv@ier.unam.mx (S.P. Verma), marig@ier.unam.mx (M.A. Rivera-Gómez), ldg@uaem.mx (L. Díaz-González), pk@ier.unam.mx (K. Pandarinath), a.amezcuavaldez@hotmail.com (A. Amezcua-Valdez), rorm@uaem.mx (M. Rosales-Rivera), sanjeet.verma@ipicyt.edu.mx (S.K. Verma), aqr@ier.unam.mx (A. Quiroz-Ruiz), armstrong@cmarl.unam.mx (J.S. Armstrong-Altrin).

http://dx.doi.org/10.1016/j.lithos.2017.02.005
0024-4937/

This has made it difficult to infer "correct" pre-alteration magma types for older (Paleogene to Archaean) or even Neogene altered igneous rocks.

The chemical compositions of altered rocks can be considerably modified from their initial concentrations (e.g., Humphris and Thompson, 1978; Nakamura et al., 2007; Pandarinath et al., 2008; Patten et al., 2016; Thompson et al., 1985; Torres-Alvarado et al., 2007). This includes SiO_2 as well. Besides, the compositional data per se are characterized by a constant sum and closure problem (e.g., Butler, 1979; Chayes, 1960, 1978) and certain statistically coherent solutions must be called for (e.g. Aitchison, 1984, 1986, 1999; Egozcue et al., 2003; Pawlowsky-Glahn et al., 2015; Verma, 2012, 2015), especially to deal with the altered rock geochemistry.

Deciphering the correct pre-alteration magma types is also required for several other purposes: (1) this information is essential for obtaining an unbiased estimate of thermal energy budget of a geothermal area (e.g., Verma and Gómez-Arias, 2013a, 2013b); (2) the likely pre-alteration magma types are also required for the choice of the correct set of multidimensional diagrams (basic and ultrabasic, intermediate, or acid magma) for tectonomagmatic discrimination (Agrawal et al., 2008; Verma and Agrawal, 2011; Verma and Verma, 2013; Verma et al., 2006, 2013); and (3) the provenance of sediments and sedimentary rocks is an important academic and applied problem (e.g., Alarcón and Pinto, 2015; Ishiga et al., 2000; Lee et al., 2004; Odoma et al., 2015; Pinto et al., 2004), which can be indirectly handled from this work.

We propose a statistically coherent solution to the classification of magma types (ultrabasic, basic, intermediate, and acid) in the multidimensional space of all major element log-ratios. For three chemical variables (Zr, Y, and TiO_2), Verma (2015) has shown that all log-ratio transformations (additive log-ratio—alr and centred log-ratio—clr of Aitchison, 1986; and isometric log-ratio—ilr of Egozcue et al., 2003; see also Pawlowsky-Glahn et al., 2015) provided essentially the same result when discrimination analysis was applied to the transformation of these compositional variables in an extensive worldwide dataset. Kovács et al. (2006) had reached a similar conclusion for major element data of Cenozoic volcanic rocks from Hungary. We use the ilr transformation (Egozcue et al., 2003) of the complete set of 10 major elements (SiO_2 to P_2O_5) to propose a new multidimensional scheme along with a suitable computer program for the classification of four magma types. The new scheme is evaluated from fresh rocks and its application to altered rocks is suggested as an essential step towards an adequate classification of magma types of altered igneous rocks. As stated by Le Bas et al. (1986), the magma type classification does not imply any genetic significance; it is simply a nomenclature procedure. We also apply the new multidimensional procedure to decipher tectonomagmatic discrimination as well as igneous provenance of sedimentary rocks.

2. Methodology

2.1. Database

A worldwide representative database of major element compositions (SiO_2, TiO_2, Al_2O_3, Fe as either FeO^t, $Fe_2O_3^t$, or both FeO and Fe_2O_3, MnO, MgO, CaO, Na_2O, K_2O, and P_2O_5) of relatively fresh Neogene igneous rocks from all continents was updated (Fig. 1) by us. The current database is a modified version of our earlier databases (Rivera-Gómez and Verma, 2016; Verma and Agrawal, 2011; Verma and Verma, 2013; Verma et al., 2006, 2013, 2016a).

The data were first processed in IgRoCS computer program (Verma and Rivera-Gómez, 2013a) to assign rock nomenclature according to the IUGS (Le Bas, 2000; Le Bas et al., 1986; Le Maitre et al., 2002). This program carries out the subdivision of Fe into two oxidation varieties (FeO and Fe_2O_3) exactly, adjusts the sum to 100% on an anhydrous basis, and uses the revised CIPW norm proposed by Verma et al. (2003) as the standard igneous norm. All four magma types and related rock types were well represented in our database (1872 ultrabasic, 14,031 basic, 12,901 intermediate, and 8415 acid rock samples). However, for proposing the new multidimensional procedure it is not necessary to use the subdivision of Fe as its two varieties. Thus, the complete list of major elements used in this work is as follows: SiO_2, TiO_2, Al_2O_3, $Fe_2O_3^t$, MnO, MgO, CaO, Na_2O, K_2O, and P_2O_5. A new adjustment of

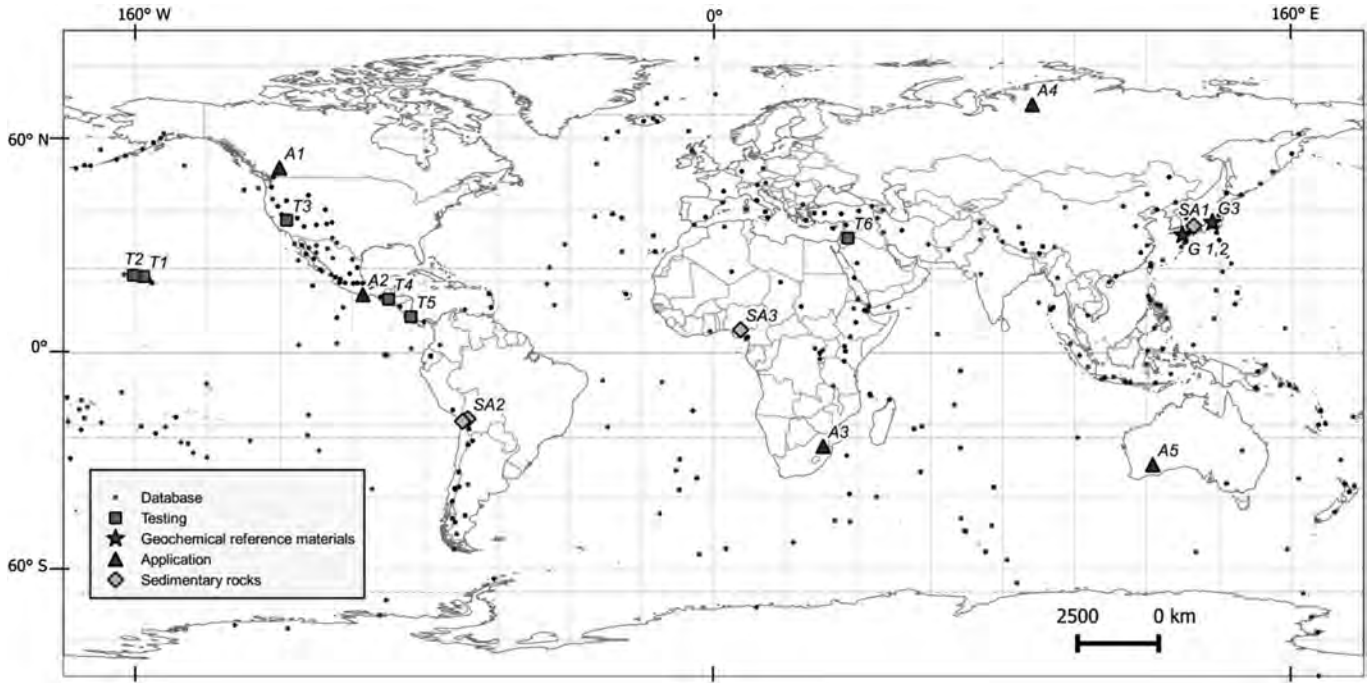

Fig. 1. Map for sample locations used in constructing the database (for more details, see the website http://tlaloc.ier.unam.mx/index.html) as well as for testing, geochemical reference materials, and igneous and sedimentary rock application studies.

major elements to 100% on an anhydrous basis with total Fe as $Fe_2O_3^t$ was therefore carried out from equations listed in Table S1 (see Supplementary data available for downloading from the journal website). The conversion of Fe as $Fe_2O_3^t$ was achieved from the first equation in Table S1. Although the adjustment to 100% on an anhydrous basis is not required for log-ratio transformations (the correction factor will cancel out), it is useful for geoscientists to better understand the importance of closed field and constant sum effect (e.g., Aitchison, 1986, 1999; Chayes, 1978; Egozcue et al., 2003; Verma, 2015), irrespective of the element mobility. Besides, not all major element data are reported with Fe as $Fe_2O_3^t$ (sometimes as FeO^t, or as both FeO and Fe_2O_3) and the analytical sum (without volatiles) is seldom 100%. In other words, the complete analysis may have different compositional variables and their number may also vary between 10 and 11 (or more) parameters. Therefore, it was necessary to make the chemical analyses uniform with respect to the same 10 compositional variables from SiO_2 to P_2O_5, before proceeding to obtain log-ratio transformations. The adjusted data were then used to transform to ilr from equations of Table S2.

The sources of data are too numerous to list them in the main paper. Even the supplementary file will unnecessarily grow if included here. Therefore, these references are listed in a pdf file available from our website http://tlaloc.ier.unam.mx/index.html.

A new computer program DOMuDaF has been recently published by Verma et al. (2016a) for the detection of multivariate discordant outliers in very large statistical samples (sample sizes up to 30,000), which was used for the ilr transformed variables of our initial database. The multivariate discordancy test (Rencher, 2002; Verma et al., 2016a) was applied at a very strict confidence level of 99.9%. The samples were counted after the separation of multivariate discordant outliers in the log-ratio space of nine dimensions represented in Table S2. The reasons for discordancy may be related to data quality (systematic and random errors in different laboratories and analytical techniques; Verma, 2012, 2016). The log-ratio variables were considered as multinormally distributed (e.g., Rencher, 2002; Verma, 2015; Verma et al., 2016a), being the basic assumption for the multivariate technique of linear discriminant analysis (e.g., Morrison, 1990). The discordant outlier free samples were 33,868 (1671 ultrabasic, 12,832 basic, 11,876 intermediate, and 7489 acid rock samples) in our database used for later statistical analysis. Because of the availability of an adequate modern computer program DOMuDaF (Verma et al., 2016a) for achieving multinormality in large datasets, we decided to use the multivariate technique of linear discriminant and canonical analysis that requires multinormality. Therefore, any nonparametric multivariate procedures (not requiring multinormally distributed data) were not considered.

2.2. Linear discriminant and canonical analysis

The multinormally distributed ilr data were used for the application of the multivariate technique of linear discriminant analysis (LDA) and canonical analysis. Filzmoser et al. (2012) have provided the relevant mathematics and the need to work in the domain of log-ratio transformations. We followed our earlier work on the use of log-ratio transformations for proposing multidimensional discriminant function based diagrams (Agrawal et al., 2008; Verma, 2015, 2016; Verma and Agrawal, 2011; Verma and Verma, 2013; Verma et al., 2006, 2013, 2015), in which the LDA was used to obtain acceptably high percent success (or correct classification) values.

Commercial software *Statistica*® was used for the LDA and canonical analysis. The prior classification probabilities were assumed to be the same for all four groups (ultrabasic, basic, intermediate, and acid). *Statistica*® ("Discriminant Analysis" submodule of "Exploratory Multivariate Techniques") provided the so called "Raw coefficients" for all 10 log-ratio variables used in the analysis and also a constant term, which were used to formulate the discriminant function (DF1 and DF2) equations. In terms of the discriminant functions, the centroid values in the DF1-DF2 space were estimated by the sample means as suggested recently from Monte Carlo simulations (Verma et al., 2016b, 2017). These centroid values were used for calculating posterior probability values for individual samples to belong to the classification fields, from the method outlined by Agrawal (1999) and Verma and Agrawal (2011). Thus, the probability values were used to decide the classification field in which a given sample will plot.

We did not resort to other techniques, such as classification trees or artificial neural network, because our earlier work on these techniques had not provided any special advantage (Agrawal and Verma, 2007; Verma and Quiroz-Ruiz, 2008; Verma et al., 2008). More importantly, the LDA provides acceptable results in terms of percent success values (Agrawal and Verma, 2007; Agrawal et al., 2008; Verma, 2015, 2016; Verma and Agrawal, 2011; Verma and Verma, 2013; Verma et al., 2006, 2013, 2015). Nevertheless, we do acknowledge that quadratic discriminant analysis (QDA; Filzmoser et al., 2012) may provide still higher success values, but its application should constitute a separate paper in future.

The complete databases of multinormally distributed log-ratios of a total of 33,868 samples were used for the proposal of 5 new diagrams and 10 discriminant functions for the ilr transformation. After carrying out the LDA, probabilities for individual samples were calculated from the method outlined by Agrawal (1999) and Verma and Agrawal (2011) and used in this work to decide the classification field in which a given sample will plot. This multidimensional classification scheme can be used for igneous rocks of all ages.

3. New multidimensional classification of magma types

The complete database of 33,868 igneous rock samples was used to classify them as one of the four magma types (ultrabasic, basic, intermediate, and acid) through five multidimensional diagrams and related probability calculations. The respective discriminant functions (DF1 and DF2) are presented in Table S3 (Eqs. S1–S10).

All samples are plotted in Fig. S1a–e. The centroids in the discriminant function coordinates are reported in Table S4. The boundary coordinates for the diagrams are listed in Table S5. These values were used to construct the field boundaries in Fig. S1a–e. The percent success or correct classification values from probability calculations for each diagram are listed in Table S6, which varied from 79.5% to 99.2%.

We used the example of one ultrabasic rock sample ME90-11 (Binard et al., 1993) identified by a filled diamond symbol in Fig. S1. The measured and adjusted major element concentrations as well as ilr-transformed values are listed in Table S7. The respective probability values for all five diagrams (Fig. S1a–e) and the final synthesis are presented in Table S8. The percent probability values (the final row in Table S8) clearly show that the multidimensional diagrams also suggest that this sample is ultrabasic (percent value of 71.6% for ultrabasic but much less for others; Table S8). This result is consistent with its IUGS classification (Table S7).

For the complete dataset, the overall synthesis of percent success (correct classification) values obtained for this subdivision of ultrabasic, basic, intermediate and acid magmas are presented in Table S9. Out of 1671 samples of ultrabasic rocks, 1483 were classified as ultrabasic (representing correct classification or percent success of about 88.7%) and 169 as basic (incorrect classification of about 10.1%) and only 13 and 6, respectively, as intermediate (0.8%) and acid (0.4%). The percent success value for intermediate rocks was similarly high (88.0%; Table S9); for them, the incorrect classification for basic rocks amounted to about 10.7% but much less for acid (0.9%) and ultrabasic rocks (0.4%). However, the classification for basic and acid rocks represented lesser percent success values of about 75.8% and 80.9%, respectively. Basic rocks were incorrectly classified as ultrabasic (14.6%) and intermediate (9.6%). Finally, the incorrect classification of acid rocks was only as intermediate rocks (19.1%).

4. Computer program for magma type classification for altered igneous rocks

For an efficient application of the new multidimensional scheme, a computer program MagClaMSys_ilr (**Mag**ma **Cla**ssification **M**ajor-element based **Sys**tem) was written in Java Framework ZK (Fig. S2). The first part of the program concerns data validation and transformations (Tables S1 and S2). The information on whether the user is dealing with igneous or sedimentary rocks is to be provided. Consequently, the appropriate way to process the data is decided in MagClaMSys_ilr. Calculations involve the probability values for the four magma types, viz., ultrabasic (p_U), basic (p_B), intermediate (p_I), and acid (p_A), as a synthesis of five diagrams. The rock is given the name for which the probability is highest (Fig. S2). Modules in MagClaMSys_ilr include conventional application to older or altered igneous rocks, specially designed application to siliciclastic sediments or sedimentary rocks for igneous provenance, robustness with respect to analytical errors or uncertainties, and robustness of the new classification for post-emplacement alteration changes. This program is available to interested users for on-line processing of their major element data and to check the robustness of any given sample, on our website http://tlaloc.ier.unam.mx/index.html, after a previous registration onto the server. A Readme file to facilitate the use of our program is included as a Supplementary file to this paper.

5. Testing and applications of the new magma classification scheme

This classification scheme (MagClaMSys_ilr program) is applied for the following purposes: (i) testing from relatively fresh rock data not included in the database (Fig. 1); (ii) application to inter-laboratory data on geochemical reference materials; (iii) application to older igneous rocks to decide the appropriate set of tectonomagmatic discrimination diagrams that should be used for inferring tectonic setting; and (iv) application to siliciclastic sediments for type of igneous provenance. In addition, robustness of the scheme can also be tested for any individual analysis or an average composition.

5.1. Testing from fresh igneous rocks

For 6 test studies (for locations, see Fig. 1), geochemical data for relatively fresh rocks were newly compiled from several sources (Blondes et al., 2008; Clague et al., 2016; Di Piazza et al., 2015; Garcia et al., 2016; Mora et al., 2013; Shaw et al., 2003). The similarity of magma types of the compiled samples from both the conventional IUGS and the new multidimensional scheme (Table 1) is briefly pointed out below.

5.1.1. Honolulu volcanics, Hawaii (test study T1)

Eighteen Quaternary rock samples compiled from Clague et al. (2016) proved to be ultrabasic from both the conventional IUGS procedure and the new multidimensional scheme (Tables 1 and 2), confirming thus good functioning of the new procedure.

5.1.2. Hawaiian Islands (test study T2)

Geochemical data for 62 Quaternary rock samples from the Hawaiian Islands reported by Garcia et al. (2016) were classified as ultrabasic (10 samples) and basic (52 samples) from the IUGS scheme (Tables 1 and S10). From the multidimensional scheme, these ultrabasic rock samples (from the IUGS scheme) also proved to be ultrabasic from the new scheme, but out of 52 basic rock samples, 5 were identified as ultrabasic, with the remaining 47 basic rocks correctly classified as such (Table S10). Thus, out of 62 samples, 5 were incorrectly classified. This result of correct and incorrect classification is consistent with the percent success values of the new classification procedure (Table S9), according to which a small percentage of basic rocks may be classified as ultrabasic but less likely as intermediate magma and probably not as acid magma.

5.1.3. Big Pine Volcanic Field, California, U.S.A. (test study T3)

From the conventional IUGS procedure, 25 Quaternary rock samples (Blondes et al., 2008) proved to be mostly basic (24 samples) with one sample as ultrabasic (Tables 1 and S11). The MagClaMSys scheme confirmed all 24 basic rocks as basic but the only ultrabasic sample was incorrectly classified as basic.

5.1.4. Tacaná volcanic complex, Mexico–Guatemala (test study T4)

Out of 14 Holocene rock samples (IUGS: 11 intermediate and 3 acid) compiled from Mora et al. (2013), 13 (11 intermediate and 2 acid) were correctly classified from MagClaMSys (Tables 1 and S12). Only 1 acid rock sample according to the IUGS scheme was incorrectly classified as intermediate from MagClaMSys (Table S12).

5.1.5. Turrialba volcano, Costa Rica (test study T5)

Seven Quaternary rock samples (IUGS: 6 intermediate and 1 acid) reported by Di Piazza et al. (2015) were classified as intermediate from MagClaMSys (Tables 1 and S13); thus, only 1 acid rock sample was incorrectly classified as intermediate.

5.1.6. Harrat Ash Shaam, Jordan (Test study T6)

Out of 32 samples (Shaw et al., 2003), the IUGS scheme classified 6 samples as ultrabasic and 26 as basic, whereas the MagClaMSys indicated 10 ultrabasic and 22 basic (Tables 1 and S14).

5.2. Evaluation from geochemical reference materials

Data for three reference materials (basalt JB-1, basalt JB-1a, and andesite JA-3; locations in Fig. 1) were compiled from Cantagrel and Pin (1994), Gazel et al. (2009), Guevara et al. (2005), Han et al. (1999), Hoang and Uto (2003), Hunt et al. (2013), Kusano et al. (2014), Mashima (2016), Minifie et al. (2013), Ryan and Williams (2007), Tani et al. (2005), Terashima et al. (1998), and Tsuchiya et al. (1989). The statistical parameters (sample mean $\bar{x}$, number of individual analyses n, sample standard deviation s, and total uncertainty at 99% confidence level U_{99}) were then calculated from the inter-laboratory data. Instead of evaluating small number of analyses from individual laboratories, the mean and total uncertainty values for each geological

Table 1
Comparison of magma types from the conventional IUGS and new multidimensional approach from 6 test studies (T1 to T6).

Application	Epoch	Total number of samples	Number of samples from IUGS (IgRoCS) classification*				Number of samples from MagClaMSys_ilr*			
			Ultrabasic	Basic	Intermediate	Acid	Ultrabasic	Basic	Intermediate	Acid
T1: Honolulu, Hawaii	Quaternary	18	18	0	0	0	18	0	0	0
T2: Hawaiian Islands	Quaternary	62	10	52	0	0	15	47	0	0
T3: California, U.S.A	Quaternary	25	1	24	0	0	0	25	0	0
T4: Mexico–Guatemala	Holocene	14	0	0	11	3	0	0	12	2
T5: Costa Rica	Quaternary	7	0	0	6	1	0	0	7	0
T6: Jordan	Late Neogene	32	6	26	0	0	10	22	0	0

* Magma types from the IUGS system was achieved from IgRoCS (Verma and Rivera-Gómez, 2013a) and for the new classification from MagClaMSys_ilr (this work).

Table 2
Comparison of magma types of compiled Quaternary volcanic rock samples from the Honolulu, Hawaii (test study T1; Clague et al., 2016).

Consec	Sample name		Magma type (IUGS scheme; Le Bas et al., 1986; IgRoCS)	Probability from MagClaMSys (this work)*				Magma type (MagClaMSys_ilr)
	Original authors`	This work		p_U	p_B	p_I	p_A	
1	GMQ1	CFGH0001	Ultrabasic	0.7487	0.2512	0.0001	0.0000	Ultrabasic
2	GMQ2	CFGH0002	Ultrabasic	0.7489	0.2510	0.0001	0.0000	Ultrabasic
3	GMQ3	CFGH0003	Ultrabasic	0.7489	0.2510	0.0001	0.0000	Ultrabasic
4	GMQ4	CFGH0004	Ultrabasic	0.7489	0.2510	0.0001	0.0000	Ultrabasic
5	GMQ5	CFGH0005	Ultrabasic	0.7484	0.2515	0.0001	0.0000	Ultrabasic
6	GMQ6	CFGH0006	Ultrabasic	0.7482	0.2518	0.0001	0.0000	Ultrabasic
7	GMQ7	CFGH0007	Ultrabasic	0.7489	0.2510	0.0001	0.0000	Ultrabasic
8	GMQ7.5	CFGH0008	Ultrabasic	0.7481	0.2519	0.0001	0.0000	Ultrabasic
9	GMQ8	CFGH0009	Ultrabasic	0.7468	0.2531	0.0000	0.0000	Ultrabasic
10	GMQ9	CFGH0010	Ultrabasic	0.7492	0.2507	0.0001	0.0000	Ultrabasic
11	GMQ11	CFGH0011	Ultrabasic	0.7487	0.2512	0.0001	0.0000	Ultrabasic
12	65MOIL2	CFGH0012	Ultrabasic	0.7477	0.2523	0.0001	0.0000	Ultrabasic
13	GMQ12	CFGH0013	Ultrabasic	0.7393	0.1868	0.0738	0.0000	Ultrabasic
14	MQ1	CFGH0015	Ultrabasic	0.7349	0.1827	0.0824	0.0000	Ultrabasic
15	GMQ10L	CFGH0017	Ultrabasic	0.7392	0.2015	0.0593	0.0000	Ultrabasic
16	MQ2L	CFGH0018	Ultrabasic	0.7373	0.1963	0.0664	0.0000	Ultrabasic
17	GMQ10D	CFGH0020	Ultrabasic	0.7348	0.2194	0.0458	0.0000	Ultrabasic
18	MQ2D	CFGH0021	Ultrabasic	0.7330	0.2268	0.0401	0.0000	Ultrabasic

* p_U — probability for ultrabasic magma; p_B — probability for basic magma; p_I — probability for intermediate magma; and p_A — probability for acid magma; also see footnote of Table 1.

material were used to simulate a large number of analyses (2200 + 1 initial analysis) from the Monte Carlo simulation procedure (Verma and Quiroz-Ruiz, 2006). The 2201 analyses from the initial inter-laboratory data were processed from our new multidimensional procedure (MagClaMSys_ilr) and compared with the conventional IUGS approach. The comparison of magma types resulting from our new scheme (Table S15) clearly showed that the multidimensional approach gave more consistent results: basic magma for both basalt materials JB-1 (2098 times out of 2201) and JB-1a (1842 times out of 2201) and intermediate for andesite JA-3 (2201 times out of 2201). On the other hand, the IUGS scheme indicated that basalts JB-1 and JB-1a were both intermediate magma (2201 times out of 2201) and andesite JA-3 was also intermediate magma in most cases (2162 out of 2201) but acid in 39 out of 2201 cases (Table S15).

5.3. Application to older igneous rocks

We illustrate the implications of our classification scheme from five application studies from Archaean to Mesozoic igneous rocks (Fig. 1). The magma types of the compiled samples were established from the conventional IUGS and the new multidimensional schemes (Table 3). We decided to report the inference of tectonic setting for only those magma types for which the total number of samples was ≥5 (an arbitrarily chosen small number).

5.3.1. Star Lake Pluton, Canada (application study A1)

The geochemical data for 78 Proterozoic igneous rock samples were compiled from Janser (1992, 1994). The IUGS classification scheme (applied through IgRoCS software by Verma and Rivera-Gómez, 2013a) indicated 9 samples to be basic, 33 intermediate and 36 acid rocks (Tables 3 and 4). We applied the new probability-based multidimensional approach proposed here, which indicated that 55 samples are intermediate and 23 acid, with no samples classified as basic (Table 4).

Nine samples of basic rocks (IUGS–IgRoCS and TecD by Verma and Rivera-Gómez, 2013b) suggested a likely arc setting (table not shown), whereas the combined MagClaMSys_ilr (this work) and TecD system could not be applied because no rock proved to be basic (Table 4). To further explore the implications of these differences, we used the tectonic discrimination for intermediate and acid rocks proposed by Verma and Verma (2013) and Verma et al. (2013), respectively. The results are summarized in Table 5. Although both procedures (IgRoCS + TecDIA) and (MagClaMSys_ilr and Statistica®) provided similarly consistent inference for intermediate and acid rocks for a likely collision setting, the newer option is based on a greater number of samples (78 versus 69 samples; Table 5). Thus, if we use the proposed multidimensional scheme for magma classification, the apparent controversy between the basic and evolved intermediate and acid magmas disappears because all the samples reported by Janser (1992, 1994) proved to be devoid of basic magmas. Janser (1994) suggested an island arc setting for these samples.

5.3.2. Paleozoic Juchatengo complex; Mexico (application study A2)

Thirteen samples from the Juchatengo complex (Grajales-Nishimura et al., 1999) from the IUGS scheme were divided as basic (9 samples) and intermediate (4 samples), whereas all 13 proved to be basic from MagClaMSys_ilr (Table S16). Both sets of basic rock samples indicated a mid-ocean ridge setting; however, the higher number (13) of samples identified as basic from the new scheme additionally provided a higher percent value for this setting (60% versus 51% from 9 samples;

Table 3
Comparison of magma types from the conventional IUGS and new multidimensional approach from 5 application studies (A1 to A5).

Application	Epoch	Total number of samples	Number of samples from IUGS classification*				Number of samples from MagClaMSys_ilr*			
			Ultrabasic	Basic	Intermediate	Acid	Ultrabasic	Basic	Intermediate	Acid
A1: Canada	Proterozoic	78	0	9	33	36	0	0	55	23
A2: Mexico	Paleozoic	13	0	9	4	0	0	13	0	0
A3: South Africa	Archaean	16	0	7	9	0	5	7	3	1
A4: Russia	Paleozoic–Mesozoic	14	0	8	6	0	0	14	0	0
A5: Australia	Archaean	35	0	17	17	1	0	27	7	1

* Magma types from the IUGS system was achieved from IgRoCS (Verma and Rivera-Gómez, 2013a) and for the new classification from MagClaMSys_ilr.

Table 4
Comparison of magma type of compiled Proterozoic igneous rock samples from Star Lake Pluton, Canada (Application study A1; Janser, 1992, 1994).

Consec	Sample name		Magma type (IUGS scheme; Le Bas et al., 1986; IgRoCS)*	Probability from MagClaMSys (this work)*				Magma type (MagClaMSys_ilr)
	Original authors	This work		p_U	p_B	p_I	p_A	
1	LS0075	Jans0132	Intermediate	0.0035	0.2110	0.7824	0.0032	Intermediate
2	LS0076	Jans0133	Basic	0.1737	0.2382	0.5879	0.0002	Intermediate
3	LS0078	Jans0134	Intermediate	0.0047	0.2295	0.7655	0.0003	Intermediate
4	LS0080	Jans0135	Intermediate	0.0032	0.2162	0.7795	0.0011	Intermediate
5	LS0081	Jans0136	Intermediate	0.0142	0.1848	0.7911	0.0099	Intermediate
6	LS0082	Jans0137	Intermediate	0.1047	0.2459	0.6486	0.0009	Intermediate
7	LS0087	Jans0138	Intermediate	0.0043	0.1947	0.7902	0.0108	Intermediate
8	LS0093	Jans0139	Intermediate	0.0034	0.1994	0.7903	0.0070	Intermediate
9	LS0123	Jans0140	Intermediate	0.0016	0.1236	0.7965	0.0783	Intermediate
10	LS0148	Jans0141	Intermediate	0.0151	0.2242	0.7569	0.0038	Intermediate
11	LS0155	Jans0142	Basic	0.0009	0.3341	0.6649	0.0001	Intermediate
12	LS0156	Jans0143	Basic	0.0415	0.3711	0.5873	0.0001	Intermediate
13	LS0157	Jans0144	Intermediate	0.0106	0.2154	0.7733	0.0007	Intermediate
14	LS0164	Jans0145	Basic	0.0096	0.3685	0.6218	0.0001	Intermediate
15	LS0165	Jans0146	Intermediate	0.0005	0.2065	0.7880	0.0049	Intermediate
16	LS0168	Jans0147	Intermediate	0.0159	0.1869	0.7902	0.0070	Intermediate
17	LS0170	Jans0148	Basic	0.0094	0.3200	0.6705	0.0001	Intermediate
18	LS0197	Jans0149	Intermediate	0.0000	0.0008	0.7524	0.2468	Intermediate
19	LS0210	Jans0150	Intermediate	0.0000	0.0010	0.7756	0.2234	Intermediate
20	LS0220	Jans0151	Basic	0.0202	0.4217	0.5581	0.0000	Intermediate
21	LS0222	Jans0152	Intermediate	0.0034	0.2086	0.7870	0.0010	Intermediate
22	LS0224	Jans0153	Basic	0.0093	0.2693	0.7212	0.0002	Intermediate
23	LS0229	Jans0154	Intermediate	0.0019	0.2038	0.7892	0.0051	Intermediate
24	LS0230	Jans0155	Intermediate	0.0082	0.2509	0.7407	0.0002	Intermediate
25	LS0231	Jans0156	Basic	0.0105	0.2759	0.7133	0.0002	Intermediate
26	LS0233	Jans0157	Basic	0.0035	0.3145	0.6820	0.0001	Intermediate
27	LS0234	Jans0158	Intermediate	0.0044	0.2134	0.7806	0.0016	Intermediate
28	LS0235	Jans0159	Intermediate	0.0026	0.1509	0.7963	0.0502	Intermediate
29	LS0240	Jans0160	Intermediate	0.0048	0.2127	0.7813	0.0013	Intermediate
30	LS0056	Jans0161	Acid	0.0000	0.0001	0.3902	0.6097	Acid
31	LS0057	Jans0162	Acid	0.0000	0.0005	0.6175	0.3821	Intermediate
32	LS0059	Jans0163	Acid	0.0000	0.0000	0.4419	0.5580	Acid
33	LS0063	Jans0164	Intermediate	0.0002	0.0098	0.7904	0.1996	Intermediate
34	LS0064	Jans0165	Intermediate	0.0019	0.0516	0.7915	0.1550	Intermediate
35	LS0070	Jans0166	Intermediate	0.0019	0.0885	0.7850	0.1247	Intermediate
36	LS0072	Jans0167	Intermediate	0.0077	0.0548	0.7939	0.1435	Intermediate
37	LS0094	Jans0168	Acid	0.0000	0.0002	0.4640	0.5358	Acid
38	LS0096	Jans0169	Acid	0.0000	0.0000	0.3246	0.6754	Acid
39	LS0097	Jans0170	Acid	0.0000	0.0004	0.6296	0.3700	Intermediate
40	LS0099	Jans0171	Acid	0.0000	0.0001	0.4551	0.5448	Acid
41	LS0100	Jans0172	Acid	0.0000	0.0004	0.6280	0.3716	Intermediate
42	LS0101	Jans0173	Acid	0.0000	0.0002	0.6063	0.3935	Intermediate
43	LS0103	Jans0174	Acid	0.0000	0.0001	0.4001	0.5999	Acid
44	LS0104	Jans0175	Acid	0.0000	0.0000	0.2147	0.7853	Acid
45	LS0105	Jans0176	Intermediate	0.0004	0.0180	0.7899	0.1917	Intermediate
46	LS0106	Jans0177	Intermediate	0.0011	0.1357	0.7898	0.0734	Intermediate
47	LS0147	Jans0178	Intermediate	0.0000	0.0066	0.7702	0.2232	Intermediate
48	LS0151	Jans0179	Intermediate	0.0067	0.1975	0.7893	0.0065	Intermediate
49	LS0152	Jans0180	Intermediate	0.0002	0.0120	0.7840	0.2038	Intermediate
50	LS0207	Jans0181	Acid	0.0000	0.0005	0.6452	0.3543	Intermediate
51	LS0215	Jans0182	Intermediate	0.0000	0.0007	0.7754	0.2238	Intermediate
52	LS0236	Jans0183	Intermediate	0.0001	0.0089	0.7829	0.2081	Intermediate
53	LS0276	Jans0184	Acid	0.0000	0.0006	0.6419	0.3575	Intermediate
54	LS0277	Jans0185	Acid	0.0000	0.0002	0.4860	0.5138	Acid
55	LS0058	Jans0186	Acid	0.0000	0.0004	0.5999	0.3997	Intermediate
56	LS0061	Jans0187	Acid	0.0000	0.0003	0.6232	0.3765	Intermediate
57	LS0200	Jans0188	Acid	0.0000	0.0000	0.2021	0.7979	Acid
58	LS0241	Jans0189	Intermediate	0.0000	0.0013	0.7594	0.2392	Intermediate
59	LS0242	Jans0190	Acid	0.0000	0.0001	0.5185	0.4814	Intermediate
60	LS0244	Jans0191	Acid	0.0000	0.0004	0.6247	0.3749	Intermediate
61	LS0245	Jans0192	Acid	0.0000	0.0000	0.2992	0.7007	Acid
62	LS0246	Jans0193	Acid	0.0000	0.0004	0.5742	0.4254	Intermediate
63	LS0247	Jans0194	Acid	0.0000	0.0000	0.3429	0.6570	Acid
64	LS0250	Jans0195	Acid	0.0000	0.0001	0.4008	0.5991	Acid
65	LS0251	Jans0196	Acid	0.0000	0.0000	0.2814	0.7186	Acid
66	LS0254	Jans0197	Acid	0.0000	0.0001	0.3653	0.6346	Acid
67	LS0257	Jans0198	Acid	0.0000	0.0000	0.2226	0.7774	Acid
68	LS0259	Jans0199	Acid	0.0000	0.0000	0.2068	0.7932	Acid
69	LS0262	Jans0200	Acid	0.0000	0.0000	0.3184	0.6816	Acid
70	LS0264	Jans0201	Acid	0.0000	0.0000	0.2378	0.7622	Acid
71	LS0266	Jans0202	Acid	0.0000	0.0000	0.2056	0.7944	Acid
72	LS0267	Jans0203	Acid	0.0000	0.0000	0.2130	0.7870	Acid
73	LS0270	Jans0204	Acid	0.0000	0.0000	0.2443	0.7557	Acid
74	LS0274	Jans0205	Acid	0.0000	0.0004	0.6267	0.3729	Intermediate

Table 4 (*continued*)

Consec	Sample name		Magma type (IUGS scheme; Le Bas et al., 1986; IgRoCS)*	Probability from MagClaMSys (this work)*				Magma type (MagClaMSys_ilr)
	Original authors	This work		p_U	p_B	p_I	p_A	
75	LS0203	Jans0206	Intermediate	0.0000	0.0042	0.7783	0.2175	Intermediate
76	LS0205	Jans0207	Acid	0.0000	0.0035	0.7545	0.2419	Intermediate
77	LS0206	Jans0208	Acid	0.0000	0.0001	0.3479	0.6520	Acid
78	LS0271	Jans0209	Acid	0.0000	0.0000	0.3655	0.6345	Acid

* See footnotes of Tables 1 and 2.

Table S17). Grajales-Nishimura et al. (1999) suggested a continental rift or a back-arc setting.

5.3.3. Archaean Barberton Belt, South Africa (application study A3)

Sixteen samples (Lahaye et al., 1995) were subdivided as 7 basic and 9 intermediate from the IUGS scheme but as 5 ultrabasic, 7 basic, 3 intermediate and 1 acid from the new scheme (Table S18). The classification provided by the IUGS scheme showed conflicting indications of tectonic setting: an ocean island for 7 basic rock samples (Table S19) but an arc for 9 intermediate rock samples (Table S20). From the new scheme, the magma classification was mainly basic and ultrabasic, which indicated a mid-ocean ridge or a combined ocean island with mid-ocean ridge setting (Table S19). In this context, from multidimensional discrimination diagrams, Verma (2013) showed that although Hawaiian volcanism pertains to an ocean island setting, Icelandic volcanism is akin to a mid-ocean ridge setting.

5.3.4. Paleozoic–Mesozoic Siberia Trap, Russia (application study A4)

Out of 14 drill core samples (Lightfoot et al., 1993), the IUGS scheme identified 8 as basic and 6 as intermediate, whereas the new scheme suggested all 14 as basic (Table S21). The 8 basic rock samples indicated an arc setting (Table S22) but the 6 intermediate samples did not provide a consistent result (Table S23). From the new scheme, all samples were classified as basic and indicated an arc setting (Table S22). However, the multidimensional diagrams do not include a continental flood basalt setting from which these samples likely erupted (Lightfoot et al., 1993).

5.3.5. Archaean Kambalda craton, Australia (application study A5)

Geochemical data for 35 samples compiled from Arndt and Jenner (1986) were subdivided as 17 basic, 17 intermediate and 1 acid from the IUGS but as 27 basic, 7 intermediate and 1 acid from the new scheme (Table S24). Although the rock classification was different, the same tectonic inference of an arc setting was obtained (Tables S25 and S26).

5.4. Application for igneous provenance of sedimentary rocks

For this application, the user must ascertain that the likely provenance is, in fact, igneous. If not, the program should not be applied to those samples. The U-B-I-A subdivision is available for deciphering the type of igneous provenance (ultrabasic, basic, intermediate, and acid) for each individual sediment sample or a group of samples. Therefore, we present a different application of the new classification scheme for inferring the type of magmatic provenance (ultrabasic, basic, intermediate, and acid) if there is independent evidence of igneous provenance for the sediments or sedimentary rocks under study. We highlight this application from mostly Neogene sediments whose igneous provenance is expected from surface geology (for locations, see Fig. 1).

Table 5
Synthesis of the application of multidimensional diagrams (Verma and Verma, 2013; Verma et al., 2013) to compiled Proterozoic intermediate and acid rock samples from Star Lake Pluton, Canada (Application study A1; Janser, 1992, 1994).

Inferred magma type	IUGS (IgRoCS) + TecDIA					MagClaMSys_ilr + Statistica®				
	No. of samples	p_{IA} (%)	p_{CA} (%)	p_{WP} (%)	p_{Col} (%)	No. of samples	p_{IA} (%)	p_{CA} (%)	p_{WP} (%)	p_{Col} (%)
Intermediate	33	12%	39%	3%	46%	55	13%	37%	3%	47%
Acid	36	1%	27%	16%	56%	23	1%	26%	16%	57%

Magma types from the IUGS system was achieved from IgRoCS (Verma and Rivera-Gómez, 2013a) and tectonic setting from TecDIA for intermediate and acid rocks (Verma et al., 2015) and TecD for basic rocks (Verma and Rivera-Gómez, 2013b); p_{IA} (%) — total probability for island arc in percent; p_{CA} (%) — total probability for continental arc in percent; p_{WP} (%) — total probability for within-plate (combined continental rift and ocean island) in percent; p_{Col} (%) — total probability for collision in percent.

5.4.1. Miocene-Holocene sediments from southwest Japan (sediment application SA1)

Our first application of the new classification scheme is Miocene to Holocene lake sediments from southwest Japan. Geochemical data for a total of 49 coastal lagoon mud samples from the Lake Shinji located in the back-arc side of southwest Japan (near the Sea of Japan) were compiled from Ishiga et al. (2000). This lake is surrounded mostly by igneous rocks but it is not clear which type of magma from ultrabasic to acid would have dominated in the genesis of these sediments. Ishiga et al. (2000) did not comment on the provenance of their samples. We used probability concept related to the five diagrams (Fig. S1a–e), for inferring the dominant magma type(s). Thus, it was not necessary to plot the data in diagrams but simply calculate the final probability synthesis for all five diagrams.

The measured major element data (Table S27) from Ishiga et al. (2000) adjusted from equations of Table S1, are presented in Table S28. From equations of Table S2, these data were converted to ilr (Table S29) in MagClaMSys_ilr. This computer program was used to further process the data in order to decipher the type of igneous provenance of these sediments. The respective probability estimates for individual samples are summarized in Table S30.

If we consider all Miocene to Holocene sediment samples together, 44 out of 49 samples indicate an intermediate magmatic provenance with the remaining 5 samples showing an acid provenance (Table S30). However, if we separate the sediment samples into two groups (Table S30)—the younger group of Holocene Nakaumi Formation (44 samples) and the older group of Miocene to Pleistocene sediments (5 samples), we can also infer an intermediate magmatic provenance for the younger group (43 out of 44 indicating an intermediate provenance) and a probable acid provenance for the older group (4 out of 5 indicating an acid provenance) although the total number of these older samples is very small.

5.4.2. Neogene sedimentary rocks from Central Andes, Bolivia and Chile (sediment application SA2)

Pinto et al. (2004) reported geochemical data for 38 samples of Neogene sedimentary rocks from basins in the Altiplano of Bolivia and the Central Depression in Chile. These authors used the Zr/TiO_2–Nb/Y of Winchester and Floyd (1977) to infer the igneous provenance of their samples. This diagram did not provide any conclusive evidence. The Bolivian samples plotted in the alkaline fields from basic to acid rocks, whereas the Chilean samples indicated sub-alkaline fields also from basic to acid rocks.

We used their sediment data in our multidimensional classification scheme to infer igneous provenance. The probability values for individual samples and the inferred igneous provenance are summarized in Table S31. The Bolivian samples clearly indicated an acid or felsic

Table 6
Sensitivity analysis of the four rock centroids (adjusted compositions) of the database used for proposing the diagrams, with respect to post-emplacement compositional changes of the loss or gain of SiO_2 in MagClaMSys_ilr as compared to the conventional IUGS approach.

Original centroid composition		MagClaMSys_ilr [this work]			IUGS [Le Bas, 2000]		
Loss or gain	Concentration f SiO_2A (% m/m)	Maximum "tolerable" change[a]		Maximum compositional change of 100% adjusted data[b]	Maximum "tolerable" change[a]		Maximum compositional range of 100% adjusted data[b]
		Loss (% m/m)	Gain (% m/m)	Final concentration (% m/m)	Loss (% m/m)	Gain (% m/m)	Final concentration (% m/m)
Centroid of 1671 ultrabasic magma							
Loss	42.71	−72	–	17.78	−29	–	–
Gain	42.71	–	+134	63.57	–	+7	44.83
Centroid of 12,832 basic magma							
Loss	48.73	−99	–	0.94	−15	–	44.98
Gain	48.73	–	+46	57.95	–	+11	51.79
Centroid of 11,876 intermediate magma							
Loss	56.85	−54	–	38.25	−18	–	51.94
Gain	56.85	–	+43	65.17	–	+27	62.96
Centroid of 7489 acid magma							
Loss	69.68	−22	–	64.49	−26	–	62.98
Gain	69.68	–	+43	76.67	–	+?[c]	–

[a] This refers to the minimum and maximum % change in SiO_2A before the rock name changes from the original name to some other rock name.
[b] These are independent estimates for SiO_2A and are not directly related to the other ranges (changes simulated for one element at a time).
[c] The? sign is shown here because there is no consensus what could be the highest SiO_2 concentration for an acid magma.

provenance (12 out of 12 samples) whereas the Chilean data were more consistent with an intermediate provenance (21 out of 26 samples; Table S31).

5.4.3. Cretaceous claystone sediments from Enugu, southeastern Nigeria (sediment application SA3)

Geochemical data for 9 Cretaceous clay-rich sediment samples (out of 10 reported by Odoma et al., 2015; except one with very low SiO_2 content) from southeastern Nigeria were compiled. We will not present these measured concentration data in a table. They were processed for the multidimensional classification scheme to obtain the probability values summarized in Table S32. Eight samples (out of 9) showed highest probability values for basic magma provenance (Table S32).

Odoma et al. (2015) used the TAS classification diagram (Le Bas et al., 1986), calling it a discrimination diagram, for inferring acid magmatic provenance for their sedimentary rocks. It was not really necessary to plot the samples in the TAS diagram, because the magmatic provenance as ultrabasic to acid or felsic was judged by Odoma et al. (2015) by the adjusted SiO_2 contents of their sedimentary rock samples. It is important to remember that the IUGS had discouraged the use of their classification scheme for the nomenclature of altered rocks. The compiled samples have extremely high LOI values (11.6%–19.0%; Odoma et al., 2015). Therefore, the IUGS classification for magmatic rocks should not be used for inferring igneous provenance of sedimentary rocks. Instead, our new multidimensional scheme is shown to be useful for this purpose.

5.5. Robustness analysis

MagClaMSys_ilr allows the evaluation of the effects of analytical uncertainties or post-emplacement changes for individual samples or average compositions. As an example, the robustness of the nomenclature is evaluated for the centroids of each magma type from our initial database for changes (loss or gain) of SiO_2 concentrations. The results are compared with the IUGS approach in Table 6 and the complete major element compositions of the four centroids are reported in Table S33. For example, the ultrabasic centroid will maintain the same ultrabasic magma type for up to 72% loss or 134% gain of SiO_2 in the new scheme, whereas the highest loss of up to 29% or gain of 7% only for the IUGS classification (Table 6). The final simulated compositions of the centroids after the chemical changes can be observed in Table S33. Similar conclusions can be reached for other magma types although the results for acid magmas are not clearly comparable (Table 6). More such cases of post-emplacement changes were also discussed recently by Verma et al. (2016a). Thus, the new scheme can be considered more robust with respect to post-emplacement compositional changes than the traditional IUGS approach.

6. Conclusions

A new multidimensional classification scheme based on isometric log-ratio (ilr) transformation (MagClaMSys_ilr program) involving 5 diagrams and probability estimates, showed high percent success (correct classification) values. For fresh Neogene rocks (6 test studies), this scheme is shown consistent with the IUGS classification. MagClaMSys_ilr showed magma types consistent with the names of three geochemical reference materials from Japan. For older igneous rocks (5 case studies of Archaean to Mesozoic), this new proposal is useful for the identification of magma types prior to the alteration. This also affects the application of tectonomagmatic discrimination diagrams. Finally, from 3 case studies, igneous provenance of sedimentary rocks was also successfully inferred. The new scheme is more robust than the traditional IUGS scheme for the nomenclature of magma types.

Acknowledgements

This work funded by the DGAPA-PAPIIT grant IN100816 constitutes a part of the second author's (MARG) doctoral thesis in preparation under the guidance of the first author (SPV). AAV thanks SNI-CONACYT for scholarship as "Ayudante de Investigador Nivel 3". MARG and MRR acknowledge doctoral fellowships from CONACYT. Participation of JSA was facilitated from the Instituto de Ciencias del Mar y Limnología Institutional Project (no. 161). We are much grateful to the journal reviewers (V.K. Singh and anonymous) and the editor Nelson Eby; their comments helped us to significantly improve our presentation.

Appendix A. Supplementary data

Supplementary data to this article can be found online at http://dx.doi.org/10.1016/j.lithos.2017.02.005.

References

Agrawal, S., 1999. Geochemical discrimination diagrams: a simple way of replacing eye-fitted boundaries with probability based classifier surfaces. Journal of the Geological Society of India 54, 335–346.

Agrawal, S., Verma, S.P., 2007. Comment on "tectonic classification of basalts with classification trees" by Pieter Vermeesch (2006). Geochimica et Cosmochimica Acta 71, 3388–3390.

Agrawal, S., Guevara, M., Verma, S.P., 2008. Tectonic discrimination of basic and ultrabasic rocks through log-transformed ratios of immobile trace elements. International Geology Review 50, 1057–1079.

Aitchison, J., 1984. Statistical analysis of geochemical compositions. Mathematical Geology 16, 531–564.

Aitchison, J., 1986. The Statistical Analysis of Compositional Data. Chapman and Hall, London, UK (416 pp.).

Aitchison, J., 1999. Logratios and natural laws in compositional data analysis. Mathematical Geology 31, 563–580.

Alarcón, P., Pinto, L., 2015. Neogene erosion of the Andean Cordillera in the flat-slab segment as indicated by petrography and whole-rock geochemistry from the Manantiales Foreland Basin (32°–32°30′ S). Tectonophysics 639, 1–22.

Arndt, N.T., Jenner, G.A., 1986. Crustally contaminated komatiites and basalts from Kambalda, western Australia. Chemical Geology 56, 229–255.

Binard, N., Maury, R.C., Guille, G., Talandier, J., Gillot, P.Y., Cotten, J., 1993. Mehetia island, South Pacific: geology and petrology of the emerged part of the society hot spot. Journal of Volcanology and Geothermal Research 55, 239–260.

Blondes, M.S., Reiners, P.W., Ducea, M.N., Singer, B.S., Chesley, J., 2008. Temporal-compositional trends over short and long time-scales in basalts of the Big Pine Volcanic Field, California. Earth and Planetary Science Letters 269, 140–154.

Butler, J.C., 1979. Trends in ternary petrologic variation diagrams — fact or fantasy? American Mineralogist 64, 1115–1121.

Cantagrel, F., Pin, C., 1994. Major, minor and rare-earth element determinations in 25 rock standards by ICP-atomic emission spectrometry. Geostandards Newsletter 18, 123–138.

Chayes, F., 1960. On correlation between variables of constant sum. Journal of Geophysical Research 65, 4185–4193.

Chayes, F., 1978. Ratio Correlation. A Manual for Students of Petrology and Geochemistry. The University of Chicago Press, Chicago and London (99 pp.).

Clague, D.A., Frey, F.A., Garcia, M.O., Huang, S., McWilliams, M., Beeson, M.H., 2016. Compositional heterogeneity of the Sugarloaf melilite nephelinite flow, Honolulu Volcanics, Hawaii. Geochimica et Cosmochimica Acta 185, 251–277.

Di Piazza, A., Rizzo, A.L., Barberi, F., Carapezza, M.L., De Astis, G., Romano, C., Sortino, F., 2015. Geochemistry of the mantle source and magma feeding system beneath Turrialba volcano, Costa Rica. Lithos 232, 319–335.

Egozcue, J.J., Pawlowsky-Glahn, V., Mateu-Figueras, G., Barceló-Vidal, C., 2003. Isometric logratio transformations for compositional data analysis. Mathematical Geology 35, 279–300.

Filzmoser, P., Hron, K., Templ, M., 2012. Discriminant analysis for compositional data and robust parameter estimation. Computational Statistics 27, 585–604.

Garcia, M.O., Weis, D., Jicha, B.R., Ito, G., Hanano, D., 2016. Petrology and geochronology of lavas from Ka'ula Volcano: implications for rejuvenated volcanism of the Hawaiian mantle plume. Geochimica et Cosmochimica Acta 185, 278–301.

Gazel, E., Carr, M.J., Hoernle, K., Feigenson, M.D., Szymanski, D., Hauff, F., van den Bogaard, P., 2009. Galapagos-OIB in southern Central America: mantle refertilization by arc-hot spot interaction. Geochemistry, Geophysics, Geosystems 10. http://dx.doi.org/10.1029/2008GC002246.

Grajales-Nishimura, J.M., Centeno-García, E., Keppie, J.D., Dostal, J., 1999. Geochemistry of Paleozoic basalts from the Juchatengo complex of southern México: tectonic implications. Journal of South American Earth Sciences 12, 537–544.

Guevara, M., Verma, S.P., Velasco-Tapia, F., Lozano-Santa Cruz, R., Girón, P., 2005. Comparison of linear regression models for quantitative geochemical analysis: an example using x-ray fluorescence spectrometry. Geostandards and Geoanalytical Research 29, 271–284.

Han, B.-f., Wang, S.-g., Kagami, H., 1999. Trace element and Nd–Sr isotope constraints on origin of the Chifeng flood basalts, North China. Chemical Geology 155, 187–199.

Hoang, N., Uto, K., 2003. Geochemistry of Cenozoic basalts in the Fukuoka district (northern Kyushu, Japan): implications for asthenosphere and lithospheric mantle interaction. Chemical Geology 198, 249–268.

Humphris, S.E., Thompson, G., 1978. Trace element mobility during hydrothermal alteration of oceanic basalts. Geochimica et Cosmochimica Acta 42, 127–136.

Hunt, J.E., Wynn, R.B., Talling, P.J., Masson, D.G., 2013. Multistage collapse of eight western Canary Island landslides in the last 1.5 Ma: sedimentological and geochemical evidence from subunits in submarine flow deposits. Geochemistry, Geophysics, Geosystems 14, 2159–2181.

Ishiga, H., Nakamura, T., Sampei, Y., Tokuoka, T., Takayasu, K., 2000. Geochemical record of the Holocene Jomon transgression and human activity in coastal lagoon sediments of the San'in district SW Japan. Global and Planetary Change 25, 223–237.

Janser, B.W., 1992. The Geology, Geochemistry, and Metallogeny of the Star Lake Area, Northern Saskatchewan. (Master's Thesis). University of Sasketchawan, Sasketchawan, Canada (503 pp.).

Janser, B.W., 1994. The Star lake pluton, La Ronge domain, northern Saskatchewan: petrogenesis of a Proterozoic island-arc pluton. Precambrian Research 70, 145–164.

Kovács, Ó.L., Kovácz, G.P., Martín-Fernández, J.A., Barceló-Vidal, C., 2006. Major-oxide compositional discrimination in Cenozoic volcanites of Hungary. In: Buccianti, A., Mateu-Figueras, G., Pawlowsky-Glahn, V. (Eds.), Compositional Data Analysis in the Geosciences: From Theory to Practice, Special Publication. The Geological Society of London Special Publications Vol. 264, pp. 11–23.

Kusano, Y., Umino, S., Kobayashi, J., Nizukami, T., Okuno, M., Arai, S., 2014. Quantitative analysis of major elements in igneous rocks with X-ray fluorescence spectrometer "ZSX primus II" using a 1:10 dilution glass bead. The Science Reports of the Kanazawa University 58, 31–44.

Lahaye, Y., Arndt, N., Byerly, G., Chauvel, C., Fourcade, S., Gruau, G., 1995. The influence of alteration on the trace-element and Nd isotopic compositions of komatiites. Chemical Geology 126, 43–64.

Le Bas, M.J., 2000. IUGS reclassification of the high-Mg and picritic volcanic rocks. Journal of Petrology 41, 1467–1470.

Le Bas, M.J., Le Maitre, R.W., Streckeisen, A., Zanettin, B., 1986. A chemical classification of volcanic rocks based on the total alkali–silica diagram. Journal of Petrology 27, 745–750.

Le Maitre, R.W., Streckeisen, A., Zanettin, B., Le Bas, M.J., Bonin, B., Bateman, P., Bellieni, G., Dudek, A., Schmid, R., Sorensen, H., Woolley, A.R., 2002. Igneous Rocks. A Classification and Glossary of Terms: Recommendations of the International Union of Geological Sciences Subcommission of the Systematics of Igneous Rocks. Cambridge University Press, Cambridge (236 pp.).

Lee, Y.I., Lim, H.S., Yoon, H.I., 2004. Geochemistry of soils of King George Island, South Shetland Islands, West Antarctica: implications for pedogenesis in cold polar regions. Geochimica et Cosmochimica Acta 21, 4319–4333.

Lightfoot, P.C., Hawkesworth, C.J., Hergt, J., Naldrett, A.J., Gorbachev, N.S., Fedorenko, V.A., Doherty, W., 1993. Remobilisation of the continental lithosphere by a mantle plume: major-, trace element, and Sr-, Nd-, and Pb-isotope evidence from picritic and tholeiitic lavas of the Noril'sk District, Siberian Trap, Russia. Contributions to Mineralogy and Petrology 114, 171–188.

Mashima, H., 2016. XRF analyses of major and trace elements in silicate rocks calibrated with synthetic standard samples. Natural Resource Environment and Humans, pp. 39–50.

Minifie, M.J., Kerr, A.C., Ernst, R.E., Hastie, A.R., Ciborowski, T.J.R., Desharnais, G., Millar, I.L., 2013. The northern and southern sections of the western ca. 1880 Ma Circum-Superior Large Igneous Province, North America: the Pickle Crow dyke connection? Lithos 174, 217–235.

Mora, J.C., Gardner, J.E., Macías, J.L., Meriggi, L., Santo, A.P., 2013. Magmatic controls on eruption dynamics of the 1950 yr B.P. eruption of San Antonio Volcano, Tacaná Volcanic Complex, Mexico–Guatemala. Journal of Volcanology and Geothermal Research 262, 134–152.

Morrison, D.F., 1990. Multivariate Statistical Methods. McGraw-Hill Publishing Co., New York (495 pp.).

Nakamura, K., Kato, Y., Tamaki, K., Ishii, T., 2007. Geochemistry of hydrothermally altered basaltic rocks from the Southwest Indian Ridge near the Rodriguez Triple Junction. Marine Geology 239, 125–141.

Odoma, A.N., Obaje, N.G., Omada, J.I., Idakwo, S.O., Erbacher, J., 2015. Mineralogical, chemical composition and distribution of rare earth elements in clay-rich sediments from southeastern Nigeria. Journal of African Earth Sciences 102, 50–60.

Pandarinath, K., Dulski, P., Torres-Alvarado, I.S., Verma, S.P., 2008. Element mobility during the hydrothermal alteration of rhyolitic rocks of the Los Azufres geothermal field, Mexico. Geothermics 37, 53–72.

Patten, C.G.C., Pitcairn, I.K., Teagle, D.A., Harris, M., 2016. Sulphide mineral evolution and metal mobility during alteration of the oceanic crust: insights from IODP Site 1256D. Geochimica et Cosmochimica Acta 193, 132–159.

Pawlowsky-Glahn, V., Egozcue, J.J., Tolosana-Delgado, R., 2015. Modeling and Analysis of Compositional Data. Wiley, Chichester (247 pp.).

Pinto, L., Hérail, G., Moine, B., Fontan, F., Charrier, R., Dupré, B., 2004. Using geochemistry to establish the igneous provenances of the Neogene continental sedimentary rocks in the Central Depression and Atliplano, Central Andes. Sedimentary Geology 166, 157–183.

Rencher, A.C., 2002. Methods of Multivariate Analysis. Wiley-Interscience, New York (708 pp.).

Rivera-Gómez, M.A., Verma, S.P., 2016. Testing of multidimensional tectonomagmatic discrimination diagrams on fresh and hydrothermally altered rocks. Geologica Carpathica 67, 195–208.

Ryan, K.M., Williams, D.M., 2007. Testing the reliability of discrimination diagrams for determining the tectonic depositional environment of ancient sedimentary basins. Chemical Geology 242, 103–125.

Shaw, J.E., Baker, J.A., Menzies, M.A., Thirlwall, M.F., Ibrahim, K.M., 2003. Petrogenesis of the largest intraplate volcanic field on the Arabian Plate (Jordan): a mixed lithosphere-asthenosphere source activated by lithospheric extension. Journal of Petrology 44, 1657–1679.

Tani, K., Kawabata, H., Chang, Q., Sato, K., Tatsumi, Y., 2005. Quantitative analyses of silicate rock major and trace elements by X-ray fluorescence spectrometer: evaluation of analytical precision and sample preparation. Frontier Research on Earth Evolution 2, 1–8.

Terashima, S., Taniguchi, M., Mikoshiba, M., Imai, N., 1998. Preparation of two new GSJ geochemical reference materials: basalt JB-1b and coal fly ash JCFA-1. Geostandards Newsletter 22, 113–117.

Thompson, G., Mottl, M.J., Rona, P.A., 1985. Morphology, mineralogy and chemistry of hydrothermal deposits from the TAG area, 26°N Mid-Atlantic Ridge. Chemical Geology 49, 243–257.

Torres-Alvarado, I.S., Pandarinath, K., Verma, S.P., Dulski, P., 2007. Mineralogical and geochemical effects due to hydrothermal alteration in the Los Azufres geothermal field, Mexico. Revista Mexicana de Ciencias Geológicas 24, 15–24.

Tsuchiya, N., Shibata, T., Koide, Y., Owada, M., Takazawa, E., Goto, Y., Choi, J.H., Terada, S., Hariya, Y., 1989. Major element analysis of rock samples by X-ray fluorescence spectrometry, using scandium anode tube. Journal of Faculty of Science Hokkaido University 22, 489–502.

Verma, S.P., 2012. Geochemometrics. Revista Mexicana de Ciencias Geológicas 29, 276–298.

Verma, S.P., 2013. Application of 50 multi-dimensional discrimination diagrams and significance tests to decipher compositional similarities and differences between Hawaiian and Icelandic volcanism. International Geology Review 55, 1553–1572.
Verma, S.P., 2015. Monte Carlo comparison of conventional ternary diagrams with new log-ratio bivariate diagrams and an example of tectonic discrimination. Geochemical Journal 49, 393–412.
Verma, S.P., 2016. Análisis estadístico de datos composicionales. Universidad Nacional Autónoma de México, Ciudad de México (746 pp.).
Verma, S.P., Agrawal, S., 2011. New tectonic discrimination diagrams for basic and ultrabasic volcanic rocks through log-transformed ratios of high field strength elements and implications for petrogenetic processes. Revista Mexicana de Ciencias Geológicas 28, 24–44.
Verma, S.P., Gómez-Arias, E., 2013a. Three-dimensional temperature field simulation of magma chamber in the Los Humeros geothermal field, Puebla, Mexico. Applied Thermal Engineering 52, 512–515.
Verma, S.P., Gómez-Arias, E., 2013b. Three-dimensional thermal sensitivity analysis of cooling of a magma chamber in the Los Azufres geothermal field, Michoacán, Mexico. Geothermal Energy 1, 1–14.
Verma, S.P., Quiroz-Ruiz, A., 2006. Critical values for six Dixon tests for outliers in normal samples up to sizes 100, and applications in science and engineering. Revista Mexicana de Ciencias Geológicas 23, 133–161.
Verma, S.P., Quiroz-Ruiz, A., 2008. Critical values for 33 discordancy test variants for outliers in normal samples of very large sizes from 1,000 to 30,000 and evaluation of different regression models for the interpolation of critical values. Revista Mexicana de Ciencias Geológicas 25, 369–381.
Verma, S.P., Rivera-Gómez, M.A., 2013a. Computer programs for the classification and nomenclature of igneous rocks. Episodes 36, 115–124.
Verma, S.P., Rivera-Gómez, M.A., 2013b. New computer program TecD for tectonomagmatic discrimination from discriminant function diagrams for basic and ultrabasic magmas and its application to ancient rocks. Journal of Iberian Geology 39, 167–179.
Verma, S.P., Verma, S.K., 2013. First 15 probability-based multi-dimensional discrimination diagrams for intermediate magmas and their robustness against post-emplacement compositional changes and petrogenetic processes. Turkish Journal of Earth Sciences 22, 931–995.
Verma, S.P., Torres-Alvarado, I.S., Velasco-Tapia, F., 2003. A revised CIPW norm. Schweizerische Mineralogische und Petrographische Mitteilungen 83, 197–216.
Verma, S.P., Guevara, M., Agrawal, S., 2006. Discriminating four tectonic settings: five new geochemical diagrams for basic and ultrabasic volcanic rocks based on log-ratio transformation of major-element data. Journal of Earth System Science 115, 485–528.
Verma, S.P., Quiroz-Ruiz, A., Díaz-González, L., 2008. Critical values for 33 discordancy test variants for outliers in normal samples up to sizes 1000, and applications in quality control in earth sciences. Revista Mexicana de Ciencias Geológicas 25, 82–96.
Verma, S.P., Pandarinath, K., Verma, S.K., Agrawal, S., 2013. Fifteen new discriminant-function-based multi-dimensional robust diagrams for acid rocks and their application to Precambrian rocks. Lithos 168-169, 113–123.
Verma, S.P., Cruz-Huicochea, R., Díaz-González, L., Verma, S.K., 2015. A new computer program TecDIA for multidimensional tectonic discrimination of intermediate and acid magmas and its application to the Bohemian Massif, Czech Republic. Journal of Geosciences 60, 203–218.
Verma, S.P., Rivera-Gómez, M.A., Díaz-González, L., Quiroz-Ruiz, A., 2016a. Log-ratio transformed major-element based multidimensional classification for altered high-Mg igneous rocks. Geochemistry, Geophysics, Geosystems 17:1–18. http://dx.doi.org/10.1002/2016GC006652.
Verma, S.P., Díaz-González, L., Pérez-Garza, J.A., Rosales-Rivera, M., 2016b. Quality control in geochemistry from a comparison of four central tendency and five dispersion estimators and example of a geochemical reference material. Arabian Journal of Geosciences 9 (Art 740):1–14. http://dx.doi.org/10.1007/s1251701627644.
Verma, S.P., Díaz-González, L., Pérez-Garza, J.A., Rosales-Rivera, M., 2017. Erratum to: quality control in geochemistry from a comparison of four central tendency and five dispersion estimators and example of a geochemical reference material. Arabian Journal of Geosciences 10 (Art. 24):1–3. http://dx.doi.org/10.1007/s12517-016-2764-4.
Winchester, J.A., Floyd, P.A., 1977. Geochemical discrimination of different magma series and their differentiation products using immobile elements. Chemical Geology 20, 325–343.

SUPPLEMENT

Multidimensional Classification of Magma Types for Altered Igneous Rocks and Application to their Tectonomagmatic Discrimination and Igneous Provenance of Siliciclastic Sediments

Surendra P. Verma[1,*], M. Abdelaly Rivera-Gómez[2], Lorena Díaz-González[3], Kailasa Pandarinath[1], Alejandra Amezcua-Valdez[4], Mauricio Rosales-Rivera[5], Sanjeet K. Verma[6], Alfredo Quiroz-Ruiz[1], John S. Armstrong-Altrin[7]

Corresponding author E-mail: spv@ier.unam.mx

This file contains Tables S1-S33, Figures S1 and S2, and references cited in the supplement.

Table S1.
Adjustment of major elements used for computing the isometric log-ratio transformations.

Function	Equation for adjustment
Fe conversion equation	$Fe_2O_3{}^t = Fe_2O_3 + [FeO \times \frac{159.6882}{(2 \times 71.8444)}]$
SiO_2A	$= \frac{100 \times SiO2}{[SiO2 + TiO2 + Al2O3 + Fe2O3t + MnO + MgO + CaO + Na2O + K2O + P2O5]}$
TiO_2A	$= \frac{100 \times TiO2}{[SiO2 + TiO2 + Al2O3 + Fe2O3t + MnO + MgO + CaO + Na2O + K2O + P2O5]}$
Al_2O_3A	$= \frac{100 \times Al2O3}{[SiO2 + TiO2 + Al2O3 + Fe2O3t + MnO + MgO + CaO + Na2O + K2O + P2O5]}$
$Fe_2O_3{}^tA$	$= \frac{100 \times Fe2O3t}{[SiO2 + TiO2 + Al2O3 + Fe2O3t + MnO + MgO + CaO + Na2O + K2O + P2O5]}$
MnOA	$= \frac{100 \times MnO}{[SiO2 + TiO2 + Al2O3 + Fe2O3t + MnO + MgO + CaO + Na2O + K2O + P2O5]}$
MgOA	$= \frac{100 \times MgO}{[SiO2 + TiO2 + Al2O3 + Fe2O3t + MnO + MgO + CaO + Na2O + K2O + P2O5]}$
CaOA	$= \frac{100 \times CaO}{[SiO2 + TiO2 + Al2O3 + Fe2O3t + MnO + MgO + CaO + Na2O + K2O + P2O5]}$
Na_2OA	$= \frac{100 \times Na2O}{[SiO2 + TiO2 + Al2O3 + Fe2O3t + MnO + MgO + CaO + Na2O + K2O + P2O5]}$
K_2OA	$= \frac{100 \times K2O}{[SiO2 + TiO2 + Al2O3 + Fe2O3t + MnO + MgO + CaO + Na2O + K2O + P2O5]}$
P_2O_5A	$= \frac{100 \times P2O5}{[SiO2 + TiO2 + Al2O3 + Fe2O3t + MnO + MgO + CaO + Na2O + K2O + P2O5]}$

Table S2.
Isometric log-ratio (ilr) transformation equations for major elements (the function ln represents natural logarithm; the final letter A after chemical symbols refer to the adjusted concentrations on an anhydrous basis to 100% with total Fe as $Fe_2O_3^t$).

Isometric log-ratio	Equation for transformation
$ilr1_M$	$= \sqrt{\frac{1}{2}} \times \ln\{SiO2A/TiO2A\}$
$ilr2_M$	$= \sqrt{\frac{2}{3}} \times \ln\{[\sqrt[2]{(SiO2A \times TiO2A)}]/Al2O3A\}$
$ilr3_M$	$= \sqrt{\frac{3}{4}} \times \ln\{[\sqrt[3]{(SiO2A \times TiO2A \times Al2O3A)}]/Fe2O3tA\}$
$ilr4_M$	$= \sqrt{\frac{4}{5}} \times \ln\{[\sqrt[4]{(SiO2A \times TiO2A \times Al2O3A \times Fe2O3tA)}]/MnOA\}$
$ilr5_M$	$= \sqrt{\frac{5}{6}} \times \ln\{[\sqrt[5]{(SiO2A \times TiO2A \times Al2O3A \times Fe2O3tA \times MnOA)}]/MgOA\}$
$ilr6_M$	$= \sqrt{\frac{6}{7}} \times \ln\{[\sqrt[6]{(SiO2A \times TiO2A \times Al2O3A \times Fe2O3tA \times MnOA \times MgOA)}]/CaOA\}$
$ilr7_M$	$= \sqrt{\frac{7}{8}} \times \ln\{[\sqrt[7]{(SiO2A \times TiO2A \times Al2O3A \times Fe2O3tA \times MnOA \times MgOA \times CaOA)}]/Na2OA\}$
$ilr8_M$	$= \sqrt{\frac{8}{9}} \times \ln\{[\sqrt[8]{(SiO2A \times TiO2A \times Al2O3A \times Fe2O3tA \times MnOA \times MgOA \times CaOA \times Na2OA)}]/K2OA\}$
$ilr9_M$	$= \sqrt{\frac{9}{10}} \times \ln\{[\sqrt[9]{(SiO2A \times TiO2A \times Al2O3A \times Fe2O3tA \times MnOA \times MgOA \times CaOA \times Na2OA \times K2OA)}]/P2O5A\}$

Table S3.
Discriminant function (DF1-DF2) equations for five diagrams based on isometric log-ratio (ilr) transformation of major-elements (M) for the classification of igneous rocks as ultrabasic, basic, intermediate, and acid (coefficients reported as arbitrarily rounded to four decimal places).

$$\mathrm{DF1}_{i(\mathrm{U+B-I-A})\mathrm{M}} = (3.1920 \times \mathrm{ilr1_M}) + (3.1505 \times \mathrm{ilr2_M}) + (1.4768 \times \mathrm{ilr3_M}) + (0.2753 \times \mathrm{ilr4_M}) + (0.2201 \times \mathrm{ilr5_M}) + (-0.1721 \times \mathrm{ilr6_M}) + (-0.5571 \times \mathrm{ilr7_M}) + (-0.0887 \times \mathrm{ilr8_M}) + (-0.2205 \times \mathrm{ilr9_M}) - 7.8440 \quad (S1)$$

$$\mathrm{DF2}_{i(\mathrm{U+B-I-A})\mathrm{M}} = (1.4029 \times \mathrm{ilr1_M}) + (5.3998 \times \mathrm{ilr2_M}) + (2.4743 \times \mathrm{ilr3_M}) + (0.1126 \times \mathrm{ilr4_M}) + (1.0230 \times \mathrm{ilr5_M}) + (0.0599 \times \mathrm{ilr6_M}) + (1.3237 \times \mathrm{ilr7_M}) + (0.5943 \times \mathrm{ilr8_M}) + (0.2240 \times \mathrm{ilr9_M}) - 3.3077 \quad (S2)$$

$$\mathrm{DF1}_{i(\mathrm{U-B-I})\mathrm{M}} = (-4.2259 \times \mathrm{ilr1_M}) + (-1.9064 \times \mathrm{ilr2_M}) + (-1.4579 \times \mathrm{ilr3_M}) + (-1.7889 \times \mathrm{ilr4_M}) + (-0.9671 \times \mathrm{ilr5_M}) + (-0.7498 \times \mathrm{ilr6_M}) + (-0.1510 \times \mathrm{ilr7_M}) + (-0.0047 \times \mathrm{ilr8_M}) + (0.2479 \times \mathrm{ilr9_M}) + 15.5530 \quad (S3)$$

$$\mathrm{DF2}_{i(\mathrm{U-B-I})\mathrm{M}} = (-1.3637 \times \mathrm{ilr1_M}) + (-5.8168 \times \mathrm{ilr2_M}) + (0.5134 \times \mathrm{ilr3_M}) + (2.7915 \times \mathrm{ilr4_M}) + (0.8546 \times \mathrm{ilr5_M}) + (2.8261 \times \mathrm{ilr6_M}) + (2.4547 \times \mathrm{ilr7_M}) + (0.9311 \times \mathrm{ilr8_M}) + (-0.1231 \times \mathrm{ilr9_M}) - 10.3178 \quad (S4)$$

$$\mathrm{DF1}_{i(\mathrm{U-B-A})\mathrm{M}} = (2.6998 \times \mathrm{ilr1_M}) + (2.5152 \times \mathrm{ilr2_M}) + (1.5243 \times \mathrm{ilr3_M}) + (0.1449 \times \mathrm{ilr4_M}) + (0.0245 \times \mathrm{ilr5_M}) + (0.0233 \times \mathrm{ilr6_M}) + (-0.8195 \times \mathrm{ilr7_M}) + (-0.0785 \times \mathrm{ilr8_M}) + (-0.2399 \times \mathrm{ilr9_M}) - 6.1056 \quad (S5)$$

$$\mathrm{DF2i}_{i(\mathrm{U-B-A})\mathrm{M}} = (-1.2574 \times \mathrm{ilr1_M}) + (-6.0060 \times \mathrm{ilr2_M}) + (0.0376 \times \mathrm{ilr3_M}) + (1.4361 \times \mathrm{ilr4_M}) + (0.5251 \times \mathrm{ilr5_M}) + (1.3959 \times \mathrm{ilr6_M}) + (1.3984 \times \mathrm{ilr7_M}) + (0.6415 \times \mathrm{ilr8_M}) + (-0.0229 \times \mathrm{ilr9_M}) - 5.6830 \quad (S6)$$

$$\mathrm{DF1}_{i(\mathrm{U-I-A})\mathrm{M}} = (-2.7734 \times \mathrm{ilr1_M}) + (-2.4119 \times \mathrm{ilr2_M}) + (-1.7030 \times \mathrm{ilr3_M}) + (-0.4884 \times \mathrm{ilr4_M}) + (-0.3979 \times \mathrm{ilr5_M}) + (-0.1366 \times \mathrm{ilr6_M}) + (0.0557 \times \mathrm{ilr7_M}) + (-0.3078 \times \mathrm{ilr8_M}) + (0.2037 \times \mathrm{ilr9_M}) + 9.1719 \quad (S7)$$

$$\mathrm{DF2}_{i(\mathrm{U-I-A})\mathrm{M}} = (-1.7397 \times \mathrm{ilr1_M}) + (-8.4119 \times \mathrm{ilr2_M}) + (-1.5099 \times \mathrm{ilr3_M}) + (0.7283 \times \mathrm{ilr4_M}) + (-0.2239 \times \mathrm{ilr5_M}) + (0.7731 \times \mathrm{ilr6_M}) + (0.1961 \times \mathrm{ilr7_M}) + (0.0299 \times \mathrm{ilr8_M}) + (-0.1904 \times \mathrm{ilr9_M}) - 1.9097 \quad (S8)$$

$$\mathrm{DF1}_{i(\mathrm{B-I-A})\mathrm{M}} = (3.4339 \times \mathrm{ilr1_M}) + (3.5676 \times \mathrm{ilr2_M}) + (1.3212 \times \mathrm{ilr3_M}) + (0.2556 \times \mathrm{ilr4_M}) + (0.1679 \times \mathrm{ilr5_M}) + (-0.2186 \times \mathrm{ilr6_M}) + (-0.6437 \times \mathrm{ilr7_M}) + (-0.0789 \times \mathrm{ilr8_M}) + (-0.2440 \times \mathrm{ilr9_M}) - 8.2314 \quad (S9)$$

$$\mathrm{DF2}_{i(\mathrm{B-I-A})\mathrm{M}} = (1.4078 \times \mathrm{ilr1_M}) + (4.9311 \times \mathrm{ilr2_M}) + (2.5521 \times \mathrm{ilr3_M}) + (0.2645 \times \mathrm{ilr4_M}) + (1.0923 \times \mathrm{ilr5_M}) + (0.3481 \times \mathrm{ilr6_M}) + (1.7256 \times \mathrm{ilr7_M}) + (0.6614 \times \mathrm{ilr8_M}) + (0.1935 \times \mathrm{ilr9_M}) - 4.1001 \quad (S10)$$

The subscripts used are as follows: *i*—isometric log-ratio transformation (ilr); ultrabasic—U; basic—B; intermediate—I; acid—A; the subscript M is for major-element based diagrams.

Table S4.
Centroids (reported as arbitrarily rounded to four decimal places) of the four magma types (1—ultrabasic (ultrab or U); 2—basic (bas or B); 3—intermediate (int or I); 4—acid (acid or A)) in the five diagrams based on isometric log-ratio (ilr) transformation. The initial and final subscripts *i* and M refer to ilr transformation and major element based classification, respectively.

Magma type	1+2_3_4		1_2_3		1_2_4		1_3_4		2_3_4	
	$C1_{i(U+B-I-A)M}$	$C2_{i(U+B-I-A)M}$	$C1_{i(U-B-I)M}$	$C2_{i(U-B-I)M}$	$C1_{i(U-B-A)M}$	$C2_{i(U-B-A)M}$	$C1_{i(U-I-A)M}$	$C2_{i(U-I-A)M}$	$C1_{i(B-I-A)M}$	$C2_{i(B-I-A)M}$
U+B	-1.7774	0.4067	---	---	---	---	---	---	---	---
U	---	---	2.7213	-1.3381	-2.1119	-1.4446	2.8267	-2.1942	---	---
B	---	---	1.1413	0.2741	-1.6146	0.2074	---	---	-1.8131	0.4483
I	0.0220	-0.7606	-1.6161	-0.1079	---	---	0.8450	0.5260	-0.1023	-0.7302
A	3.4072	0.4186	---	---	3.2378	-0.0330	-1.9707	-0.3446	3.2690	0.3898

Table S5.
Probability-based boundary coordinates estimated for magma type subdivision diagrams (1—ultrabasic (ultrab or U); 2—basic (bas or B); 3—intermediate (int or I); 4—acid (acid or A); each diagram is considered as of three fields 1 to 3; the triple point common to all field boundaries is repeated in each set of coordinates). The initial and final subscripts i and M refer to isometric log-ratio (ilr) transformation and major element based classification, respectively.

Field Boundary	1+2_3_4		1_2_3		1_2_4		1_3_4		2_3_4	
	$DF1_{i(U+B-I-A)M}$	$DF2_{i(U+B-I-A)M}$	$DF1_{i(U-B-I)M}$	$DF2_{i(U-B-I)M}$	$DF1_{i(U-B-A)M}$	$DF2_{i(U-B-A)M}$	$DF1_{i(U-I-A)M}$	$DF2_{i(U-I-A)M}$	$DF1_{i(B-I-A)M}$	$DF2_{i(B-I-A)M}$
B(1_2)	-8.546915	-12	12	9.335593	-12	2.43285	12	6.5703	-9.127238	-12
	-5.9522445	-8	8	5.41547	-8	1.2287	8	3.6564	-6.3717025	-8
	0.8096429	2.42558464	0.09733498	-2.33013311	0.73778473	-1.40082509	0.11148764	-2.09030558	0.74968964	2.3382997
B(1_3)	0.78814	12	-2.64585	-12	3.53425	-12	-3.70925	-12	0.86126	12
	0.797	8	-1.511	-8	2.479	-8	-2.167	-8	0.815	8
	0.8096429	2.42558464	0.09733499	-2.33013311	0.73778473	-1.40082509	0.11148764	-2.09030558	0.74968964	2.3382997
B(2_3)	5.8351615	-12	-1.888154	12	1.402	12	-4.245	12	5.513374	-12
	4.4417855	-8	-1.334062	8	1.20365	8	-3.0083	8	4.1845045	-8
	0.8096429	2.42558464	0.09733499	-2.33013311	0.73778473	-1.40082509	0.11148764	-2.09030558	0.74968964	2.3382997

Table S6.
Classification of magma types used for constructing the five diagrams (Fig. S1a-e) based on transformed major elements (M).

Figure type	Sample type	Total number of samples	Number of classified magma types in major element based diagrams					
			ultrabasic + basic (ultrab+bas)	ultrabasic (ultrab)	basic (bas)	intermediate (int)	acid (acid)	percent success (correct classification)
ultrab+bas-int-acid	ultrabasic + basic	14503	12501	---	---	1993	9	86.2%
	intermediate	11876	1194	---	---	10541	141	88.8%
	acid	7489	0	---	---	1429	6060	80.9%
ultrab-bas-int	ultrabasic	1671	---	1504	157	10	---	90.0%
	basic	12832	---	1642	10837	353	---	84.5%
	intermediate	11876	---	7	1700	10169	---	85.6%
ultrab-bas-acid	ultrabasic	1671	---	1462	206	---	3	87.5%
	basic	12832	---	2634	10196	---	2	79.5%
	acid	7489	---	0	58	---	7431	99.2%
ultrab-int-acid	ultrabasic	1671	---	1599	---	71	1	95.7%
	intermediate	11876	---	570	---	11240	66	94.6%
	acid	7489	---	7	---	1397	6085	81.3%
bas-int-acid	basic	12832	---	---	11005	1827	0	85.8%
	intermediate	11876	---	---	1369	10404	103	87.6%
	acid	7489	---	---	0	1412	6077	81.1%

ultrab−ultrabasic; bas−basic; ultrab+bas–combined ultrabasic and basic field; int−intermediate; acid−acid.

Table S7.
Major element composition of compiled ultrabasic (magma type from the IUGS classification scheme) rock (ME90-11−internal name given by the original authors (Binard et al., 1993; assigned name BMGT0007) from French Polynesia used for illustration of probability estimates (Table S8).

Original authors` (Binard et al., 1993) Sample name	Chemical Parameter type	SiO_2	TiO_2	Al_2O_3	$Fe_2O_3^t$	MnO	MgO	CaO	Na_2O	K_2O	P_2O_5	IUGS scheme Magma type
ME90-11	measured	43.9	3.74	11.21	14.44	0.16	11.9	10.03	2.83	1.53	0.52	ultrabasic
	adjusted	44.33	3.78	11.32	2.22	11.12	0.162	12.02	10.13	2.86	1.54	
	ilr-transformed	---	1.7415	0.1092	-0.1421	3.9172	-0.7353	-0.4632	0.7825	1.2699	2.1596	

Table S8.
Synthesis of four field classification of one sample of ultrabasic rock (ME90-11−internal name given by the original authors (Binard et al., 1993; assigned name BMGT0007) in five diagrams (Fig. S1a-e) for igneous rock subdivision (original data plotted in Fig. S1a-e).

Figure name	Figure type	Total probability of the sample	Probability distribution for the sample (MagClaMSys_ilr)				
			U+B (p_{U+B}) Θ	U (p_U) Θ	B (p_B) Θ	I (p_I) Θ	A (p_A) Θ
Subdivision as magma type	U+B-I-A	1	0.983328	---	---	0.016671	0.000000
	U-B-I	1	---	0.943219	0.056744	0.000037	---
	U-B-A	1	---	0.925358	0.074642	---	0.000000
	U-I-A	1	---	0.976239	---	0.000210	0.000000
	B-I-A	1	---	---	0.997366	0.002634	0.000000
Synthesis for the ultrabasic sample classification	***{Σprob_5}***	***{5}***	***{0.983328}***	***{2.868367}***	***{1.107625}***	***{0.040679}***	***{0.000001}***
	{Σprob_4}	***{5}***	***{---}***	***{3.577761}***	***{1.381559}***	***{0.040679}***	***{0.000001}***
	[%prob]	***[100%]***	***[---]***	***[71.6%]***	***[27.6%]***	***[0.8%]***	***[0.0%]***

Θ U−ultrabasic; B−basic; U+B−combined ultrabasic and basic field; I−intermediate; A−acid; the probability values for a sample from a given locality are represented by (p_{U+B}) – probability for the combined ultrabasic and basic field in the first diagram; [p_U] – probability for the ultrabasic magma field in the diagrams; [p_B] – probability for the basic magma field in the diagrams; [p_I] – probability for the intermediate magma field in the diagrams; [p_A] – probability for the acid magma field in the diagrams; the final rows give a synthesis of results as ***{Σprob_5}***, ***{Σprob_4}***, and ***[%prob]***, where ***{Σprob_5}*** is the total probability of a sample plotting in all five diagrams to be subdivided in five classification fields (U + B, U, B, I, and A); ***{Σprob_4}*** is the sum of probability values of a sample for the four classification fields (U, B, I, and A) after assigning the probability of U + B to U and B (using weighing factors explained in Verma and Verma 2013); and the final row identified by ***[%prob]*** is the subdivision of the total percent probability value of 100% that corresponds to the four classification fields.

Table S9.
Synthesis of four field classification of magma types in five diagrams (Fig. S1a-e) based on major elements (M; original data plotted in Fig. S1a-e).

Magma type name (IUGS)	Total number of samples	Number of classified magma types **(percent success)**			
		ultrabasic (ultrab)	basic (bas)	intermediate (int)	acid (acid)
ultrabasic	1671	**1483 (88.7%)**	*169 (10.1%)*	13 (0.8%)	6 (0.4%)
basic	12832	*1875 (14.6%)*	**9731 (75.8%)**	1226 (9.6%)	0 (0.0%)
intermediate	11876	53 (0.4%)	1271 (10.7%)	**10446 (88.0%)**	106 (0.9%)
acid	7489	0 (0.0%)	0 (0.0%)	1429 (19.1%)	**6060 (80.9%)**

The correct classification is shown in **bold** face; for tectonomagmatic discrimination, because the multidimensional diagrams treat the basic and ultrabasic magmas together, the success for such applications are the combination of bold face and italic values, i.e., 98.8% for ultrabasic and 90.4% for basic rocks.

Table S10.
Comparison of magma types of compiled Quaternary samples from the Hawaiian Islands (Test study T2; Garcia et al., 2016).

Consec	Sample name		Magma type (IUGS scheme; Le Bas et al., 1986; IgRoCS)	Probability from MagClaMSys (this work) *				Magma type (MagClaMSys_ilr)
	Original authors` (García et al., 2016)	This work		p_U	p_B	p_I	p_A	
1	KA-14	GWJI0001	basic	0.0352	0.7096	0.2550	0.0002	basic
2	KA-29	GWJI0002	basic	0.3518	0.4939	0.1542	0.0001	basic
3	KA-15	GWJI0003	ultrabasic	0.7160	0.2580	0.0260	0.0000	ultrabasic
4	KA-17	GWJI0004	ultrabasic	0.7131	0.2515	0.0354	0.0000	ultrabasic
5	KA-19	GWJI0005	ultrabasic	0.6209	0.3717	0.0074	0.0000	ultrabasic
6	KA-28	GWJI0006	ultrabasic	0.7073	0.2583	0.0344	0.0000	ultrabasic
7	KA-31	GWJI0007	ultrabasic	0.7157	0.2529	0.0314	0.0000	ultrabasic
8	KA-34	GWJI0008	ultrabasic	0.7260	0.2649	0.0090	0.0000	ultrabasic
9	300-02	GWJI0009	basic	0.1480	0.6632	0.1887	0.0001	basic
10	300-04	GWJI0010	basic	0.1887	0.6111	0.2001	0.0001	basic
11	300-05	GWJI0011	basic	0.1000	0.6662	0.2338	0.0000	basic
12	300-06	GWJI0012	basic	0.1277	0.6454	0.2269	0.0000	basic
13	300-07	GWJI0013	basic	0.1296	0.6677	0.2026	0.0000	basic
14	300-08	GWJI0014	basic	0.1553	0.6494	0.1952	0.0000	basic
15	300-10	GWJI0015	basic	0.5204	0.4131	0.0666	0.0000	ultrabasic
16	300-15	GWJI0016	basic	0.0163	0.7014	0.2822	0.0001	basic
17	300-18	GWJI0017	basic	0.1179	0.6506	0.2315	0.0000	basic
18	300-20	GWJI0018	basic	0.0780	0.6799	0.2420	0.0000	basic
19	300-23	GWJI0019	basic	0.1813	0.5842	0.2344	0.0000	basic
20	300-26	GWJI0020	basic	0.0692	0.6728	0.2580	0.0000	basic
21	300-27	GWJI0021	basic	0.0727	0.6523	0.2750	0.0000	basic
22	300-29	GWJI0022	basic	0.0883	0.6471	0.2646	0.0000	basic
23	300-30	GWJI0023	basic	0.1298	0.6300	0.2402	0.0000	basic
24	300-32	GWJI0024	basic	0.1026	0.6497	0.2476	0.0001	basic
25	300-34	GWJI0025	basic	0.0995	0.6598	0.2406	0.0001	basic
26	300-36	GWJI0026	basic	0.1299	0.6412	0.2289	0.0000	basic
27	300-38	GWJI0027	ultrabasic	0.7219	0.2450	0.0332	0.0000	ultrabasic
28	300-41	GWJI0028	basic	0.2775	0.5531	0.1694	0.0000	basic
29	300-42	GWJI0029	basic	0.2431	0.5914	0.1654	0.0000	basic
30	300-44	GWJI0030	basic	0.4382	0.4625	0.0993	0.0000	basic
31	300-46	GWJI0031	basic	0.4739	0.4254	0.1007	0.0000	ultrabasic
32	300-47	GWJI0032	basic	0.6162	0.3123	0.0715	0.0000	ultrabasic
33	300-48	GWJI0033	basic	0.5661	0.3532	0.0807	0.0000	ultrabasic
34	304-01	GWJI0034	basic	0.4357	0.4907	0.0736	0.0000	basic
35	304-04	GWJI0035	basic	0.6066	0.3309	0.0625	0.0000	ultrabasic
36	304-05	GWJI0036	basic	0.2054	0.5492	0.2454	0.0000	basic
37	304-06	GWJI0037	basic	0.1581	0.5754	0.2665	0.0000	basic
38	304-07	GWJI0038	basic	0.1796	0.5754	0.2450	0.0000	basic
39	304-08	GWJI0039	basic	0.1769	0.5729	0.2502	0.0000	basic
40	304-09	GWJI0040	basic	0.2042	0.5211	0.2747	0.0000	basic
41	304-10	GWJI0041	basic	0.1602	0.5616	0.2781	0.0000	basic
42	304-11	GWJI0042	basic	0.1492	0.5679	0.2829	0.0000	basic
43	304-13	GWJI0043	basic	0.1671	0.5705	0.2624	0.0000	basic
44	304-15	GWJI0044	basic	0.2569	0.5173	0.2258	0.0000	basic
45	304-16	GWJI0045	basic	0.1951	0.5613	0.2436	0.0000	basic
46	304-17	GWJI0046	basic	0.1018	0.6045	0.2936	0.0000	basic
47	304-18	GWJI0047	basic	0.1363	0.5729	0.2908	0.0000	basic
48	304-19	GWJI0048	basic	0.2749	0.4726	0.2525	0.0000	basic
49	304-21	GWJI0049	ultrabasic	0.7023	0.2461	0.0517	0.0000	ultrabasic
50	304-22	GWJI0050	ultrabasic	0.7143	0.2429	0.0428	0.0000	ultrabasic
51	304-23	GWJI0051	ultrabasic	0.7031	0.2464	0.0505	0.0000	ultrabasic
52	304-24	GWJI0052	basic	0.3135	0.4541	0.2324	0.0000	basic
53	304-25	GWJI0053	basic	0.2727	0.5202	0.2070	0.0000	basic
54	304-26	GWJI0054	basic	0.3047	0.4892	0.2061	0.0000	basic
55	304-30	GWJI0055	basic	0.2908	0.5049	0.2043	0.0000	basic
56	304-32	GWJI0056	basic	0.2152	0.5313	0.2535	0.0000	basic
57	304-33	GWJI0057	basic	0.1486	0.5892	0.2622	0.0000	basic
58	304-34	GWJI0058	basic	0.1827	0.5641	0.2532	0.0000	basic
59	304-35	GWJI0059	basic	0.2467	0.5251	0.2282	0.0000	basic
60	304-36	GWJI0060	basic	0.2528	0.5074	0.2398	0.0000	basic
61	304-37	GWJI0061	basic	0.1856	0.5665	0.2479	0.0000	basic
62	304-38	GWJI0062	basic	0.3731	0.4444	0.1825	0.0000	basic

* See footnotes of Tables 1 and 2.

Table S11.
Comparison of magma types of compiled Quaternary volcanic rock samples from the Big Pine Volcanic Field, California, U.S.A. (Test study T3; Blondes et al., 2008).

Consec	Sample name		Magma type (IUGS scheme; Le Bas et al., 1986; IgRoCS)	Probability from MagClaMSys (this work) *				Magma type (MagClaMSys_ilr)
	Original authors` (Blondes et al., 2008)	This work		p_U	p_B	p_I	p_A	
1	29	BRDS001	basic	0.2582	0.4831	0.2586	0.0001	basic
2	30	BRDS002	ultrabasic	0.1503	0.6595	0.1902	0.0000	basic
3	34	BRDS003	basic	0.2823	0.4452	0.2725	0.0000	basic
4	35	BRDS004	basic	0.2719	0.4539	0.2742	0.0000	basic
5	36	BRDS005	basic	0.2985	0.4094	0.2921	0.0000	basic
6	37	BRDS006	basic	0.2527	0.4568	0.2905	0.0001	basic
7	38B	BRDS007	basic	0.2126	0.4916	0.2958	0.0000	basic
8	39	BRDS008	basic	0.2596	0.4227	0.3177	0.0001	basic
9	40	BRDS009	basic	0.2594	0.4290	0.3116	0.0001	basic
10	41	BRDS010	basic	0.2633	0.4245	0.3121	0.0001	basic
11	42	BRDS011	basic	0.2342	0.4510	0.3148	0.0001	basic
12	43	BRDS012	basic	0.2066	0.5069	0.2864	0.0001	basic
13	44	BRDS013	basic	0.2086	0.4703	0.3211	0.0001	basic
14	7	BRDS014	basic	0.2132	0.4640	0.3227	0.0001	basic
15	8	BRDS015	basic	0.1767	0.4971	0.3261	0.0001	basic
16	9	BRDS016	basic	0.1648	0.5215	0.3136	0.0001	basic
17	10	BRDS017	basic	0.1751	0.5381	0.2867	0.0001	basic
18	11	BRDS018	basic	0.1913	0.4973	0.3113	0.0001	basic
19	12	BRDS019	basic	0.1883	0.4957	0.3160	0.0001	basic
20	13	BRDS020	basic	0.1496	0.5511	0.2993	0.0001	basic
21	14	BRDS021	basic	0.1672	0.5196	0.3131	0.0001	basic
22	15	BRDS022	basic	0.1997	0.4959	0.3044	0.0001	basic
23	17	BRDS023	basic	0.1526	0.5455	0.3018	0.0001	basic
24	18	BRDS024	basic	0.1691	0.5174	0.3134	0.0001	basic
25	19	BRDS025	basic	0.1589	0.5217	0.3193	0.0001	basic

* See footnotes of Tables 1 and 2.

Table S12.
Comparison of magma types of compiled Holocene volcanic rock samples from Tacaná volcanic complex (Test study T4; Mora et al., 2013).

Consec	Sample name		Magma type (IUGS scheme; Le Bas et al., 1986; IgRoCS)	Probability from MagClaMSys (this work) *				Magma type (MagClaMSys_ilr)
	Original authors` (Mora et al., 2013)	This work		p_U	p_B	p_I	p_A	
1	9721 (2)a	MGMM0001	intermediate	0.0023	0.0387	0.7527	0.2062	intermediate
2	9721 (2)b	MGMM0002	intermediate	0.0020	0.0327	0.7551	0.2102	intermediate
3	9721 (2)c	MGMM0003	intermediate	0.0040	0.0550	0.7635	0.1775	intermediate
4	9721 (2)d	MGMM0004	intermediate	0.0027	0.0475	0.7584	0.1915	intermediate
5	9821	MGMM0005	intermediate	0.0022	0.0345	0.7492	0.2141	intermediate
6	9320	MGMM0006	intermediate	0.0097	0.2839	0.7059	0.0005	intermediate
7	9721	MGMM0007	intermediate	0.0082	0.3790	0.6126	0.0002	intermediate
8	360	MGMM0008	intermediate	0.0082	0.3790	0.6126	0.0002	intermediate
9	9735 (2)a	MGMM0009	intermediate	0.0050	0.1515	0.7789	0.0646	intermediate
10	TAC9735b	MGMM0010	intermediate	0.0035	0.1325	0.7765	0.0875	intermediate
11	358	MGMM0011	intermediate	0.0058	0.1554	0.7793	0.0595	intermediate
12	9866	MGMM0012	acid	0.0001	0.0019	0.5500	0.4480	intermediate
13	9864d	MGMM0013	acid	0.0000	0.0000	0.2002	0.7998	acid
14	9719	MGMM0014	acid	0.0000	0.0000	0.2022	0.7978	acid

* See footnotes of Tables 1 and 2.

Table S13.
Comparison of magma types of compiled Quaternary volcanic rock samples from Tirrialba volcano, Costa Rica (Test study T5; Di Piazza et al., 2015).

Consec	Sample name		Magma type (IUGS scheme; Le Bas et al., 1986; IgRoCS)	Probability from MagClaMSys (this work) *				Magma type (MagClaMSys_ilr)
	Original authors` (Di Piazza et al., 2015)	This work		p_U	p_B	p_I	p_A	
1	9721 (2)a	MGMM0001	intermediate	0.0206	0.3004	0.6782	0.0009	intermediate
2	9721 (2)b	MGMM0002	intermediate	0.0241	0.3345	0.6407	0.0006	intermediate
3	9721 (2)c	MGMM0003	intermediate	0.0235	0.3250	0.6507	0.0007	intermediate
4	9721 (2)d	MGMM0004	intermediate	0.0252	0.1591	0.7691	0.0466	intermediate
5	9821	MGMM0005	acid	0.0005	0.0031	0.5191	0.4773	intermediate
6	9320	MGMM0006	intermediate	0.0088	0.1949	0.7735	0.0228	intermediate
7	9721	MGMM0007	intermediate	0.0081	0.1884	0.7745	0.0290	intermediate

* See footnotes of Tables 1 and 2.

Table S14.
Comparison of magma types of compiled late Neogene volcanic rock samples from Harrat Ash Shaam, Jordan (Test study T6; Shaw et al., 2003).

Consec	Sample name		Magma type (IUGS scheme; Le Bas et al., 1986; IgRoCS)	Probability from MagClaMSys (this work) *				Magma type (MagClaMSys_ilr)
	Original authors` (Shaw et al., 2003)	This work		p_U	p_B	p_I	p_A	
1	JS001	SBMT0001	basic	0.5269	0.4024	0.0707	0.0000	ultrabasic
2	JS004	SBMT0002	ultrabasic	0.5230	0.4445	0.0325	0.0000	ultrabasic
3	JS007	SBMT0003	basic	0.3366	0.5694	0.0940	0.0000	basic
4	JS009	SBMT0004	basic	0.1636	0.6913	0.1450	0.0001	basic
5	JS011	SBMT0005	basic	0.2504	0.6167	0.1329	0.0001	basic
6	JS013	SBMT0006	basic	0.2251	0.6224	0.1524	0.0001	basic
7	JS015	SBMT0007	basic	0.2407	0.6522	0.1071	0.0000	basic
8	JS022	SBMT0008	basic	0.4854	0.4563	0.0583	0.0000	ultrabasic
9	JS026	SBMT0009	basic	0.0906	0.6998	0.2096	0.0001	basic
10	JS028	SBMT0010	basic	0.5510	0.3710	0.0779	0.0000	ultrabasic
11	JS029	SBMT0011	basic	0.0993	0.6886	0.2120	0.0001	basic
12	JS030	SBMT0012	basic	0.5435	0.3838	0.0727	0.0000	ultrabasic
13	JS031	SBMT0013	ultrabasic	0.6739	0.2685	0.0576	0.0000	ultrabasic
14	JS034	SBMT0014	basic	0.3992	0.4914	0.1094	0.0000	basic
15	JS041	SBMT0015	basic	0.3688	0.5678	0.0634	0.0000	basic
16	JS042	SBMT0016	basic	0.2806	0.5848	0.1346	0.0000	basic
17	JS044	SBMT0017	basic	0.2599	0.5935	0.1466	0.0000	basic
18	JS049	SBMT0018	basic	0.2580	0.5974	0.1446	0.0000	basic
19	JS050	SBMT0019	basic	0.2726	0.6096	0.1178	0.0000	basic
20	JS058	SBMT0020	basic	0.4444	0.4847	0.0708	0.0000	basic
21	JS059	SBMT0021	basic	0.2002	0.6373	0.1625	0.0001	basic
22	JS068	SBMT0022	ultrabasic	0.6303	0.2999	0.0697	0.0000	ultrabasic
23	JS069	SBMT0023	basic	0.4698	0.5065	0.0237	0.0000	basic
24	JS073	SBMT0024	basic	0.3607	0.5815	0.0577	0.0000	basic
25	JS076	SBMT0025	basic	0.3342	0.5411	0.1246	0.0000	basic
26	JS078	SBMT0026	ultrabasic	0.7024	0.1548	0.1428	0.0000	ultrabasic
27	JS080	SBMT0027	ultrabasic	0.6487	0.2989	0.0525	0.0000	ultrabasic
28	JS082	SBMT0028	basic	0.2737	0.5555	0.1708	0.0001	basic
29	JS083	SBMT0029	basic	0.2441	0.6270	0.1289	0.0000	basic
30	JS090	SBMT0030	ultrabasic	0.6348	0.3238	0.0414	0.0000	ultrabasic
31	JS096	SBMT0031	basic	0.3971	0.4998	0.1031	0.0000	basic
32	JS119	SBMT0032	basic	0.2035	0.6383	0.1581	0.0001	basic

* See footnotes of Tables 1 and 2.

Table S15.
Sensitivity analysis of analytical errors in the classification of geochemical reference materials.

Name of reference material*	Parameter **	SiO_2	TiO_2	Al_2O_3	$Fe_2O_3^t$	MnO	MgO	CaO	Na_2O	K_2O	P_2O_5	Total simulated analyses **	Magma classification					
													MagClaMSys scheme (this work)			IUGS scheme (Le Bas et al., 1986)		
													basic	intermediate	acid	basic	intermediate	acid
Basalt JB-1	$\bar{x}$	52.222	1.295	14.462	8.895	0.147	7.674	9.206	2.737	1.402	0.249	2201	2098	103	0	0	2201	0
	n	37	37	37	37	37	37	37	37	37	37							
	s	0.350	0.047	0.201	0.195	0.011	0.199	0.137	0.130	0.076	0.019							
	U_{99}	0.150	0.020	0.086	0.083	0.005	0.085	0.059	0.056	0.033	0.008							
Basalt JB-1a	$\bar{x}$	52.412	1.301	14.811	9.178	0.175	7.707	8.983	2.738	1.398	0.281	2201	1842	359	0	0	2201	0
	n	65	65	65	65	65	65	65	65	65	65							
	s	1.019	0.278	1.005	1.082	0.084	0.866	0.574	0.246	0.105	0.118							
	U_{99}	0.329	0.090	0.324	0.349	0.027	0.279	0.185	0.079	0.034	0.038							
Andesite JA-3	$\bar{x}$	62.202	0.685	15.573	6.587	0.105	3.712	6.268	3.191	1.403	0.120	2201	0	2201	0	0	2162	39
	n	31	31	31	31	31	31	31	31	31	31							
	s	0.520	0.028	0.381	0.135	0.007	0.113	0.085	0.089	0.028	0.044							
	U_{99}	0.243	0.013	0.178	0.063	0.003	0.053	0.040	0.041	0.013	0.020							

* For data sources, see the complete list of references below. ** $\bar{x}$—sample mean; *n*—number of individual analyses; s—sample standard deviation; U_{99}—total uncertainty at 99% confidence level.

Table S16.
Comparison of magma type of compiled Paleozoic igneous rock samples from Juchatengo complex, Mexico (Application study A2; Grajales-Nishimura et al., 1999).

Consec	Sample name		Magma type (IUGS scheme; Le Bas et al., 1986; IgRoCS)	Probability from MagClaMSys (this work) *				Magma type (MagClaMSys_ilr)
	Original authors` (Grajales-Nishimura et al., 1999)	This work		p_U	p_B	p_I	p_A	
1	I-73	Gngkd001	Intermediate	0.1780	0.6367	0.1799	0.0053	Basic
2	I-74	Gngkd002	Intermediate	0.2450	0.5774	0.1738	0.0037	Basic
3	I-75	Gngkd003	Basic	0.1916	0.7237	0.0831	0.0016	Basic
4	I-76	Gngkd004	Basic	0.1525	0.7332	0.1139	0.0004	Basic
5	I-77	Gngkd005	Intermediate	0.2092	0.6615	0.1247	0.0046	Basic
6	I-78	Gngkd006	Basic	0.3027	0.6151	0.0820	0.0002	Basic
7	I-79	Gngkd007	Basic	0.2912	0.6928	0.0160	0.0000	Basic
8	I-80	Gngkd008	Basic	0.0419	0.6387	0.3193	0.0001	Basic
9	I-81	Gngkd009	Basic	0.0452	0.6072	0.3474	0.0002	Basic
10	I-82	Gngkd010	Basic	0.1071	0.5449	0.3479	0.0001	Basic
11	Qui-6a	Gngkd011	Basic	0.0054	0.6687	0.3259	0.0000	Basic
12	Qui-15	Gngkd012	Basic	0.1818	0.6796	0.1364	0.0022	Basic
13	Qui-17a	Gngkd013	Intermediate	0.0002	0.6831	0.2866	0.0301	Basic

* See footnotes of Tables 1 and 2.

Table S17.
Synthesis of the application of multidimensional diagrams (Verma et al., 2006) to compiled Paleozoic igneous rock samples from Juchatengo complex, Mexico (Application study A2; Grajales-Nishimura et al., 1999)

Inferred magma type	IUGS (IgRoCS) + TecD					MagClaMSys_ilr + TecD				
	No. of samples	n_{IA} (%)	n_{CR} (%)	n_{OI} (%)	n_{MOR} (%)	No. of samples	n_{IA} (%)	n_{CR} (%)	n_{OI} (%)	n_{MOR} (%)
basic + ultrabasic	9	11%	18%	20%	51%	13	8%	12%	20%	60%

* Magma types from the IUGS system was achieved from IgRoCS (Verma and Rivera-Gómez, 2013a) and tectonic setting from TecD (Verma and Rivera-Gómez, 2013b); n_{IA} (%) – total number of samples for island arc expressed in percent value of the four tectonic fields; n_{CA} (%) – total number of samples for continental arc in percent; n_{WP} (%) – total number of samples for within-plate (combined continental rift and ocean island) in percent; n_{Col} (%) – total number of samples for collision in percent.

Table S18.
Comparison of magma type of compiled Archaean igneous rock samples from the Barberton Belt, South Africa (Application study A3; Lahaye et al., 1995).

Consec	Sample name		Magma type (IUGS scheme; Le Bas et al., 1986; IgRoCS)	Probability from MagClaMSys (this work) *				Magma type (MagClaMSys_ilr)
	Original authors` (Lahaye et al., 1995)	This work		p_U	p_B	p_I	p_A	
1	SA355-1	LABC0024	Intermediate	0.0707	0.2777	0.6377	0.0139	Intermediate
2	SA412-8	LABC0025	Intermediate	0.0280	0.3196	0.6337	0.0187	Intermediate
3	SA412-9	LABC0026	Intermediate	0.0699	0.2955	0.6235	0.0111	Intermediate
4	SA107-1	LABC0027	Intermediate	0.4847	0.4615	0.0525	0.0013	Ultrabasic
5	SA107-3	LABC0028	Intermediate	0.3297	0.0078	0.1698	0.4927	Acid
6	SA107-6B	LABC0029	Basic	0.5792	0.4019	0.0186	0.0003	Ultrabasic
7	SA107-8	LABC0030	Intermediate	0.6677	0.1526	0.1731	0.0066	Ultrabasic
8	SA107-8	LABC0031	Basic	0.4497	0.5364	0.0135	0.0004	Basic
9	SA107-10	LABC0032	Intermediate	0.6976	0.1431	0.1568	0.0025	Ultrabasic
10	SA107-11	LABC0033	Intermediate	0.6234	0.0678	0.2186	0.0902	Ultrabasic
11	B12	LABC0038	Basic	0.2446	0.7421	0.0100	0.0033	Basic
12	B14	LABC0039	Basic	0.2537	0.7250	0.0201	0.0012	Basic
13	B20B13	LABC0041	Basic	0.2517	0.7274	0.0191	0.0018	Basic
14	B8B21	LABC0042	Basic	0.2432	0.7236	0.0267	0.0065	Basic
15	OtherFlow	LABC0043	Intermediate	0.2379	0.6465	0.1002	0.0155	Basic
16	OtherFlow	LABC0044	Basic	0.2448	0.7286	0.0215	0.0050	Basic

* See footnotes of Tables 1 and 2.

Table S19.
Synthesis of the application of multidimensional diagrams (Verma et al., 2006) to compiled Archaean igneous rock samples from the Barberton Belt, South Africa (Application study A3; Lahaye et al., 1995).

Inferred magma type	IUGS (IgRoCS) + TecD					MagClaMSys_ilr + TecD				
	No. of samples	n_{IA} (%)	n_{CR} (%)	n_{OI} (%)	n_{MOR} (%)	No. of samples	n_{IA} (%)	n_{CR} (%)	n_{OI} (%)	n_{MOR} (%)
basic + ultrabasic	7	0%	14%	49%	37%	12	2%	8%	40%	50%

See footnote of Table 5.

Table S20.
Synthesis of the application of multidimensional diagrams to compiled Archaean igneous rock samples from the Barberton Belt, South Africa (Application study A3; Lahaye et al., 1995).

Inferred magma type	IUGS (IgRoCS) + TecDIA					MagClaMSys_ilr+ Statistica®				
	No. of samples	p_{IA} (%)	p_{CA} (%)	p_{WP} (%)	p_{Col} (%)	No. of samples	p_{IA} (%)	p_{CA} (%)	p_{WP} (%)	p_{Col} (%)
Intermediate	9	68%	24%	3%	5%	3	---	---	---	---
Acid	0	---	---	---	---	1	---	---	---	---

* See footnote of Table 5.

Table S21.
Comparison of magma type of compiled Paleozoic-Mesozoic igneous rock samples from the Siberia Trap, Russia (Application study A4; Lightfoot et al., 1993).

Consec	Sample name		Magma type (IUGS scheme; Le Bas et al., 1986; IgRoCS)	Probability from MagClaMSys (this work) *				Magma type (MagClaMSys_ilr)
	Original authors` (Lightfoot et al., 1993)	This work		p_U	p_B	p_I	p_A	
1	IF 2	LHHN0001	Intermediate	0.3481	0.4434	0.2084	0.0002	Basic
2	IF 7	LHHN0002	Intermediate	0.2183	0.4085	0.3728	0.0004	Basic
3	IF 11	LHHN0003	Intermediate	0.1393	0.5598	0.3006	0.0003	Basic
4	IF 16	LHHN0004	Basic	0.1214	0.5487	0.3296	0.0003	Basic
5	IF18	LHHN0005	Basic	0.2861	0.7115	0.0024	0.0001	Basic
6	IF 22	LHHN0006	Basic	0.0275	0.6029	0.3695	0.0001	Basic
7	IF 25	LHHN0007	Basic	0.0038	0.7545	0.2415	0.0002	Basic
8	IF 28	LHHN0008	Basic	0.0127	0.7312	0.2561	0.0000	Basic
9	IF30	LHHN0009	Basic	0.0196	0.7690	0.2113	0.0001	Basic
10	IF33	LHHN0010	Basic	0.0045	0.7117	0.2838	0.0000	Basic
11	IF 34	LHHN0011	Intermediate	0.0336	0.5169	0.4492	0.0002	Basic
12	IF 38	LHHN0012	Intermediate	0.0839	0.5341	0.3820	0.0000	Basic
13	IF 41	LHHN0013	Intermediate	0.0518	0.5348	0.4131	0.0003	Basic
14	IF44	LHHN0014	Basic	0.0612	0.7028	0.2359	0.0001	Basic

* See footnotes of Tables 1 and 2.

Table S22.
Synthesis of the application of multidimensional diagrams (Verma et al., 2006) to compiled Paleozoic-Mesozoic igneous rock samples from the Siberia Trap, Russia (Application study A4; Lightfoot et al., 1993).

Inferred magma type	IUGS (IgRoCS) + TecD					MagClaMSys_ilr + TecD				
	No. of samples	n_{IA} (%)	n_{CR} (%)	n_{OI} (%)	n_{MOR} (%)	No. of samples	n_{IA} (%)	n_{CR} (%)	n_{OI} (%)	n_{MOR} (%)
basic + ultrabasic	8	53%	15%	10%	22%	14	51%	30%	6%	13%

See footnote of Table 5.

Table S23.
Synthesis of the application of multidimensional diagrams to compiled Paleozoic-Mesozoic igneous rock samples from the Siberia Trap, Russia (Application study A4; Lightfoot et al., 1993).

Inferred magma type	IUGS (IgRoCS) + TecDIA					MagClaMSys + Statistica®				
	No. of samples	p_{IA} (%)	p_{CA} (%)	p_{WP} (%)	p_{Col} (%)	No. of samples	p_{IA} (%)	p_{CA} (%)	p_{WP} (%)	p_{Col} (%)
Intermediate	6	38%	13%	35%	14%	0	---	---	---	---
Acid	0	---	---	---	---	0	---	---	---	---

See footnote of Table 5.

Table S24.
Comparison of Magma type of compiled Archaean igneous rock samples from Australia (Application study A5; Arndt and Jenner, 1986).

Consec	Sample name		Magma type (IUGS scheme; Le Bas et al., 1986; IgRoCS)	Probability from MagClaMSys (this work) *				Magma type (MagClaMSys_ilr)
	Original authors` (Arndt and Jenner, 1986)	This work		p_U	p_B	p_I	p_A	
1	CD339	ArJe0001	Intermediate	0.0022	0.7394	0.2490	0.0095	Basic
2	CD339	ArJe0002	Intermediate	0.0429	0.6474	0.3095	0.0001	Basic
3	CD339	ArJe0003	Basic	0.0543	0.6110	0.3342	0.0004	Basic
4	CD339	ArJe0004	Basic	0.0770	0.5277	0.3952	0.0001	Basic
5	CD339	ArJe0005	Intermediate	0.0906	0.3447	0.5646	0.0002	Intermediate
6	CD339	ArJe0006	Intermediate	0.0057	0.6989	0.2942	0.0012	Basic
7	CD339	ArJe0007	Intermediate	0.0390	0.5002	0.4602	0.0006	Basic
8	CD339	ArJe0008	Basic	0.0022	0.7856	0.2068	0.0054	Basic
9	CD339	ArJe0009	Basic	0.0221	0.7831	0.1807	0.0141	Basic
10	CD339	ArJe0010	Intermediate	0.0041	0.6727	0.3226	0.0006	Basic
11	CD339	ArJe0011	Intermediate	0.0902	0.4903	0.4192	0.0003	Basic
12	CD339	ArJe0012	Intermediate	0.0201	0.3909	0.5889	0.0002	Intermediate
13	CD339	ArJe0013	Intermediate	0.0101	0.5952	0.3944	0.0003	Basic
14	CD339	ArJe0014	Intermediate	0.0173	0.5618	0.4196	0.0013	Basic
15	CD339W	ArJe0015	Intermediate	0.0010	0.5984	0.3943	0.0064	Basic
16	CD339W	ArJe0016	Intermediate	0.0007	0.6293	0.3554	0.0145	Basic
17	KD330	ArJe0017	Intermediate	0.0333	0.2457	0.7136	0.0074	Intermediate
18	KD330	ArJe0018	Intermediate	0.0012	0.6235	0.3705	0.0048	Basic
19	KD4088	ArJe0019	Intermediate	0.0087	0.4619	0.4993	0.0301	Intermediate
20	CD339	ArJe0020	Basic	0.0122	0.7024	0.2853	0.0002	Basic
21	CD339	ArJe0021	Basic	0.0022	0.7408	0.2568	0.0002	Basic
22	CD339	ArJe0022	Basic	0.0055	0.6511	0.3432	0.0002	Basic
23	KD330	ArJe0023	Basic	0.0047	0.5592	0.4359	0.0002	Basic
24	KD4088	ArJe0024	Basic	0.0013	0.7763	0.2223	0.0000	Basic
25	KD4088	ArJe0025	Basic	0.0007	0.7745	0.2248	0.0000	Basic
26	F	ArJe0026	Acid	0.0048	0.1097	0.2733	0.6122	Acid
27	I	ArJe0027	Intermediate	0.0012	0.6609	0.3365	0.0015	Basic
28	M	ArJe0028	Basic	0.0010	0.7878	0.2112	0.0000	Basic
29	KD330-1	ArJe0029	Basic	0.0278	0.7330	0.2365	0.0026	Basic
30	KD330-2	ArJe0030	Intermediate	0.0202	0.3513	0.5046	0.1239	Intermediate
31	KD330-3	ArJe0031	Basic	0.0064	0.7700	0.2210	0.0026	Basic
32	KD330-4	ArJe0032	Basic	0.2486	0.1023	0.6347	0.0143	Intermediate
33	KD330-5	ArJe0033	Basic	0.0222	0.7658	0.2085	0.0034	Basic
34	KD330-7	ArJe0035	Basic	0.0454	0.1863	0.7675	0.0008	Intermediate
35	KD330-10	ArJe0038	Basic	0.0539	0.5090	0.4307	0.0064	Basic

* See footnotes of Tables 1 and 2.

Table S25.
Synthesis of the application of multidimensional diagrams (Verma et al., 2006) to compiled Archaean igneous rock samples from Australia (Application study A5; Arndt and Jenner, 1986).

Inferred magma type	IUGS (IgRoCS) + TecD					MagClaMSys + TecD				
	No. of samples	n_{IA} (%)	n_{CR} (%)	n_{OI} (%)	n_{MOR} (%)	No. of samples	n_{IA} (%)	n_{CR} (%)	n_{OI} (%)	n_{MOR} (%)
basic + ultrabasic	17	68%	7%	7%	18%	27	59%	5%	8%	27%

See footnote of Table 5.

Table S26.
Synthesis of the application of multidimensional diagrams to compiled Archaean igneous rock samples from Australia (Application study A5; Arndt and Jenner, 1986).

Inferred magma type	IUGS (IgRoCS) + TecDIA					MagClaMSys + Statistica®				
	No. of samples	p_{IA} (%)	p_{CA} (%)	p_{WP} (%)	p_{Col} (%)	No. of samples	p_{IA} (%)	p_{CA} (%)	p_{WP} (%)	p_{Col} (%)
Intermediate	17	63%	32%	1%	4%	7	61%	34%	1%	4%
Acid	1	---	---	---	---	1	---	---	---	---

See footnote of Table 5.

Table S27.
Major element composition of Holocene to Miocene coastal lagoon sediments from back-arc side of south-west Japan (Sediment provenance application study SA1; Ishiga et al., 2000).

Consec	Sample name		SiO_2	TiO_2	Al_2O_3	$Fe_2O_3^t$	MnO	MgO	CaO	Na_2O	K_2O	P_2O_5
	Original authors` (Ishiga et al., 2000)	This work										
1	SB-1-1	INST0001	62.82	0.82	21.57	7.12	0.12	2.16	0.71	2.34	2.23	0.17
2	SB-1-5	INST0002	59.60	0.80	26.96	6.61	0.11	1.91	0.57	1.86	2.26	0.16
3	SB-1-10	INST0003	63.78	0.86	21.79	7.12	0.10	1.89	0.52	1.70	2.20	0.16
4	SB-1-15	INST0004	62.83	0.87	22.64	6.99	0.09	1.98	0.55	1.61	2.37	0.15
5	SB-1-20	INST0005	63.35	0.88	19.48	8.10	0.12	2.44	0.50	1.64	2.57	0.12
6	SB-1-25	INST0006	63.38	0.87	19.38	8.14	0.11	2.50	0.52	1.72	2.62	0.12
7	SB-1-30	INST0007	63.35	0.85	19.35	7.90	0.05	2.53	0.63	1.93	2.62	0.12
8	SB-1-35	INST0008	63.66	0.84	19.38	7.42	0.12	2.56	0.54	2.05	2.63	0.13
9	SB-1-40	INST0009	62.56	0.84	19.65	6.96	0.17	2.61	0.64	2.09	2.56	0.13
10	SB-1-45	INST0010	62.08	0.82	19.07	7.60	0.21	2.64	0.63	2.12	2.62	0.14
11	SB-1-50	INST0011	63.00	0.83	19.09	7.48	0.19	2.65	0.86	2.20	2.66	0.14
12	SB-1-55	INST0012	63.06	0.85	19.01	7.71	0.19	2.68	0.76	2.13	2.73	0.13
13	SB-1-60	INST0013	63.22	0.84	18.94	7.41	0.17	2.60	0.89	2.27	2.70	0.13
14	SB-1-65	INST0014	63.94	0.86	19.32	6.85	0.16	2.69	0.55	2.14	2.74	0.12
15	SB-1-70	INST0015	63.51	0.76	18.59	6.72	0.23	2.47	1.68	2.56	2.58	0.13
16	SB-1-75	INST0016	63.20	0.84	18.65	6.85	0.14	2.53	1.88	2.14	2.72	0.12
17	SB-1-80	INST0017	63.53	0.88	20.11	7.15	0.11	2.58	0.44	2.06	2.79	0.12
18	SB-1-85	INST0018	63.80	0.88	19.66	6.47	0.12	2.48	1.05	2.02	2.76	0.12
19	SB-1-90	INST0019	65.24	0.87	19.79	5.81	0.06	2.34	0.44	2.14	2.81	0.11
20	SB-1-95	INST0020	64.85	0.86	19.61	6.37	0.05	2.32	0.48	2.19	2.75	0.11
21	SB-1-100	INST0021	64.68	0.86	19.37	6.68	0.05	2.26	0.51	2.26	2.67	0.11
22	SB-1-105	INST0022	65.76	0.85	18.94	6.11	0.05	2.20	0.59	2.20	2.68	0.11
23	SB-1-110	INST0023	65.31	0.84	19.59	6.19	0.04	2.24	0.57	2.08	2.72	0.11
24	SB-1-115	INST0024	64.31	0.82	18.83	5.85	0.06	2.28	1.58	1.96	2.63	0.12
25	SB-1-120	INST0025	64.89	0.83	18.80	5.96	0.06	2.23	2.23	1.79	2.71	0.11
26	SB-1-125	INST0026	65.50	0.85	18.90	6.31	0.06	2.15	0.93	1.84	2.70	0.12
27	SB-1-130	INST0027	65.74	0.87	19.40	5.92	0.03	2.09	0.41	1.90	2.72	0.11
28	SB-1-135	INST0028	66.09	0.88	19.26	6.18	0.03	2.05	0.36	1.85	2.68	0.10
29	SB-1-140	INST0029	65.23	0.87	19.32	6.14	0.06	2.21	0.89	1.97	2.39	0.11
30	SB-1-145	INST0030	66.11	0.87	18.96	6.27	0.04	2.00	0.64	1.88	2.63	0.10
31	SB-1-150	INST0031	65.76	0.88	19.45	6.17	0.04	2.10	0.44	1.85	2.72	0.11
32	SB-1-155	INST0032	65.31	0.88	19.44	6.31	0.04	2.10	0.55	1.85	2.71	0.11
33	SB-1-160	INST0033	65.16	0.87	19.32	6.14	0.05	2.13	0.49	1.79	2.74	0.11
34	SB-1-165	INST0034	65.84	0.88	19.41	6.08	0.04	2.10	0.47	1.38	2.78	0.11
35	SB-1-169	INST0035	65.19	0.87	19.13	6.78	0.04	2.16	0.55	1.80	2.75	0.11
36	SB-1-173	INST0036	66.00	0.89	19.63	5.81	0.04	2.10	0.46	1.72	2.78	0.11
37	SB-1-177	INST0037	65.35	0.88	19.16	6.24	0.04	2.04	0.62	1.86	2.67	0.11
38	SB-1-181	INST0038	66.04	0.88	19.10	5.90	0.04	2.01	0.46	1.91	2.69	0.10
39	SB-1-185	INST0039	64.36	0.87	18.76	7.45	0.11	2.02	0.66	1.80	2.59	0.14
40	SB-1-189	INST0040	66.58	0.88	18.44	6.30	0.04	1.91	0.46	1.85	2.60	0.10
41	SB-1-194	INST0041	64.97	0.87	19.05	7.04	0.05	2.17	0.85	1.67	2.66	0.12
42	SB-1-199	INST0042	66.72	0.90	18.86	5.88	0.04	1.93	0.66	1.81	2.54	0.10
43	SB-1-203	INST0043	69.78	0.85	16.00	5.50	0.03	1.80	0.67	2.17	2.24	0.08
44	SB-1-209	INST0044	69.05	0.90	17.47	5.33	0.06	1.86	0.56	1.70	2.37	0.12
45	SB-1-214	INST0045	70.40	0.87	18.18	4.88	0.03	1.88	0.49	1.70	2.26	0.10
46	SB-1-219	INST0046	71.81	0.75	15.54	4.56	0.10	1.28	0.96	2.26	2.40	0.08
47	SB-1-224	INST0047	73.56	0.67	15.39	2.25	0.02	1.01	1.11	2.50	2.56	0.06
48	SB-1-229	INST0048	76.13	0.51	13.81	1.81	0.03	0.84	0.14	2.74	2.74	0.04
49	SB-1-233	INST0049	70.99	0.83	15.20	5.44	0.04	1.54	0.54	1.76	2.65	0.09

Table S28.
Adjusted major element composition (arbitrarily rounded to three decimal places for presentation) of Holocene to Miocene coastal lagoon sediments from back-arc side of south-west Japan (Sediment provenance application study SA1; data from Table S27 adjusted from equations of Table S2).

Consec	Name	SiO_2A	TiO_2A	Al_2O_3A	$Fe_2O_3^t$A	MnOA	MgOA	CaOA	Na_2OA	K_2OA	P_2O_5A
1	INST0001	62.782	0.820	21.557	7.116	0.120	2.159	0.710	2.339	2.229	0.170
2	INST0002	59.104	0.793	26.735	6.555	0.109	1.894	0.565	1.845	2.241	0.159
3	INST0003	63.704	0.859	21.764	7.111	0.100	1.888	0.519	1.698	2.197	0.160
4	INST0004	62.780	0.869	22.622	6.984	0.090	1.978	0.550	1.609	2.368	0.150
5	INST0005	63.861	0.887	19.637	8.165	0.121	2.460	0.504	1.653	2.591	0.121
6	INST0006	63.788	0.876	19.505	8.192	0.111	2.516	0.523	1.731	2.637	0.121
7	INST0007	63.777	0.856	19.481	7.953	0.050	2.547	0.634	1.943	2.638	0.121
8	INST0008	64.089	0.846	19.511	7.470	0.121	2.577	0.544	2.064	2.648	0.131
9	INST0009	63.700	0.855	20.008	7.087	0.173	2.658	0.652	2.128	2.607	0.132
10	INST0010	63.392	0.837	19.473	7.761	0.214	2.696	0.643	2.165	2.675	0.143
11	INST0011	63.572	0.838	19.263	7.548	0.192	2.674	0.868	2.220	2.684	0.141
12	INST0012	63.537	0.856	19.154	7.768	0.191	2.700	0.766	2.146	2.751	0.131
13	INST0013	63.749	0.847	19.099	7.472	0.171	2.622	0.897	2.289	2.723	0.131
14	INST0014	64.345	0.865	19.442	6.893	0.161	2.707	0.553	2.154	2.757	0.121
15	INST0015	64.003	0.766	18.734	6.772	0.232	2.489	1.693	2.580	2.600	0.131
16	INST0016	63.793	0.848	18.825	6.914	0.141	2.554	1.898	2.160	2.746	0.121
17	INST0017	63.676	0.882	20.156	7.166	0.110	2.586	0.441	2.065	2.796	0.120
18	INST0018	64.211	0.886	19.787	6.512	0.121	2.496	1.057	2.033	2.778	0.121
19	INST0019	65.495	0.873	19.867	5.833	0.060	2.349	0.442	2.148	2.821	0.110
20	INST0020	65.117	0.864	19.691	6.396	0.050	2.330	0.482	2.199	2.761	0.110
21	INST0021	65.038	0.865	19.477	6.717	0.050	2.272	0.513	2.272	2.685	0.111
22	INST0022	66.097	0.854	19.037	6.141	0.050	2.211	0.593	2.211	2.694	0.111
23	INST0023	65.513	0.843	19.651	6.209	0.040	2.247	0.572	2.086	2.728	0.110
24	INST0024	65.329	0.833	19.128	5.943	0.061	2.316	1.605	1.991	2.672	0.122
25	INST0025	65.144	0.833	18.874	5.983	0.060	2.239	2.239	1.797	2.721	0.110
26	INST0026	65.922	0.855	19.022	6.351	0.060	2.164	0.936	1.852	2.717	0.121
27	INST0027	66.277	0.877	19.558	5.968	0.030	2.107	0.413	1.916	2.742	0.111
28	INST0028	66.435	0.885	19.361	6.212	0.030	2.061	0.362	1.860	2.694	0.101
29	INST0029	65.763	0.877	19.478	6.190	0.060	2.228	0.897	1.986	2.410	0.111
30	INST0030	66.442	0.874	19.055	6.302	0.040	2.010	0.643	1.889	2.643	0.101
31	INST0031	66.077	0.884	19.544	6.200	0.040	2.110	0.442	1.859	2.733	0.111
32	INST0032	65.770	0.886	19.577	6.354	0.040	2.115	0.554	1.863	2.729	0.111
33	INST0033	65.951	0.881	19.555	6.215	0.051	2.156	0.496	1.812	2.773	0.111
34	INST0034	66.445	0.888	19.588	6.136	0.040	2.119	0.474	1.393	2.806	0.111
35	INST0035	65.597	0.875	19.249	6.822	0.040	2.173	0.553	1.811	2.767	0.111
36	INST0036	66.305	0.894	19.721	5.837	0.040	2.110	0.462	1.728	2.793	0.111
37	INST0037	66.030	0.889	19.359	6.305	0.040	2.061	0.626	1.879	2.698	0.111
38	INST0038	66.620	0.888	19.268	5.952	0.040	2.028	0.464	1.927	2.714	0.101
39	INST0039	65.168	0.881	18.996	7.544	0.111	2.045	0.668	1.823	2.623	0.142
40	INST0040	67.144	0.887	18.596	6.353	0.040	1.926	0.464	1.866	2.622	0.101
41	INST0041	65.329	0.875	19.155	7.079	0.050	2.182	0.855	1.679	2.675	0.121
42	INST0042	67.096	0.905	18.966	5.913	0.040	1.941	0.664	1.820	2.554	0.101
43	INST0043	70.400	0.858	16.142	5.549	0.030	1.816	0.676	2.189	2.260	0.081
44	INST0044	69.453	0.905	17.572	5.361	0.060	1.871	0.563	1.710	2.384	0.121
45	INST0045	69.848	0.863	18.038	4.842	0.030	1.865	0.486	1.687	2.242	0.099
46	INST0046	71.997	0.752	15.581	4.572	0.100	1.283	0.963	2.266	2.406	0.080
47	INST0047	74.206	0.676	15.525	2.270	0.020	1.019	1.120	2.522	2.582	0.061
48	INST0048	77.065	0.516	13.980	1.832	0.030	0.850	0.139	2.774	2.774	0.040
49	INST0049	71.649	0.838	15.341	5.491	0.040	1.554	0.545	1.776	2.675	0.091

Table S29.
Isometric log-ratio (ilr) transformed data (arbitrarily rounded to four decimal places for presentation) of Holocene to Miocene coastal lagoon sediments from back-arc side of south-west Japan (Sediment provenance application study SA1; adjusted data from Table S28 calculated from equations of Table S2).

Consec	Name	$ilr1_M$	$ilr2_M$	$ilr3_M$	$ilr4_M$	$ilr5_M$	$ilr6_M$	$ilr7_M$	$ilr8_M$	$ilr9_M$
1	INST0001	3.0675	-0.8982	0.3247	3.9031	0.5488	1.4934	0.1781	0.2025	2.6226
2	INST0002	3.0485	-1.1123	0.4309	3.9979	0.6579	1.6760	0.3444	0.1204	2.6177
3	INST0003	3.0450	-0.8811	0.3457	4.0818	0.6507	1.7455	0.4029	0.1124	2.5858
4	INST0004	3.0265	-0.9139	0.3716	4.1800	0.5922	1.6854	0.4555	0.0374	2.6510
5	INST0005	3.0240	-0.7830	0.2063	3.9270	0.4567	1.8537	0.4943	0.0122	2.9177
6	INST0006	3.0320	-0.7831	0.1976	4.0003	0.4173	1.8070	0.4453	-0.0041	2.9198
7	INST0007	3.0483	-0.7916	0.2161	4.7015	0.2506	1.4993	0.2508	-0.0671	2.8638
8	INST0008	3.0600	-0.7956	0.2689	3.8958	0.3888	1.7687	0.2844	0.0159	2.8663
9	INST0009	3.0482	-0.8143	0.3230	3.5710	0.4217	1.6574	0.3289	0.0986	2.9183
10	INST0010	3.0598	-0.8029	0.2289	3.3891	0.4544	1.7111	0.3462	0.1059	2.8733
11	INST0011	3.0610	-0.7924	0.2511	3.4784	0.4358	1.4100	0.3426	0.1232	2.9053
12	INST0012	3.0456	-0.7793	0.2305	3.4929	0.4340	1.5331	0.3641	0.0869	2.9661
13	INST0013	3.0554	-0.7799	0.2613	3.5809	0.4316	1.3578	0.2996	0.1005	2.9685
14	INST0014	3.0471	-0.7821	0.3450	3.6275	0.3855	1.7963	0.2837	0.0175	2.9813
15	INST0015	3.1293	-0.8036	0.3130	3.2601	0.4957	0.7757	0.2777	0.2377	3.0473
16	INST0016	3.0551	-0.7673	0.3248	3.7332	0.4039	0.6162	0.4127	0.1376	3.0850
17	INST0017	3.0260	-0.8078	0.3244	3.9870	0.3730	1.9529	0.2471	-0.0678	2.9263
18	INST0018	3.0287	-0.7875	0.4057	3.8791	0.4043	1.1372	0.3730	0.0346	3.0038
19	INST0019	3.0531	-0.7887	0.5036	4.4839	0.3132	1.8112	0.0897	-0.1779	2.9188
20	INST0020	3.0564	-0.7880	0.4166	4.6619	0.2996	1.7120	0.0628	-0.1592	2.9151
21	INST0021	3.0547	-0.7792	0.3710	4.6704	0.3295	1.6562	0.0423	-0.1202	2.9149
22	INST0022	3.0752	-0.7591	0.4430	4.6460	0.3344	1.5010	0.0689	-0.1255	2.9133
23	INST0023	3.0781	-0.7940	0.4364	4.8503	0.2828	1.5057	0.0937	-0.1704	2.8937
24	INST0024	3.0845	-0.7780	0.4622	4.4537	0.3166	0.6071	0.3241	0.0085	2.9358
25	INST0025	3.0825	-0.7682	0.4517	4.4664	0.3427	0.2896	0.4565	0.0115	3.0539
26	INST0026	3.0725	-0.7591	0.4133	4.4900	0.3931	1.1081	0.3213	-0.0780	2.8821
27	INST0027	3.0583	-0.7692	0.4840	5.1091	0.2902	1.7540	0.0835	-0.2643	2.8060
28	INST0028	3.0536	-0.7563	0.4497	5.1184	0.3179	1.8790	0.0963	-0.2644	2.8787
29	INST0029	3.0528	-0.7690	0.4490	4.4946	0.3703	1.1553	0.2570	0.0442	2.9594
30	INST0030	3.0625	-0.7483	0.4291	4.8579	0.3908	1.3855	0.1918	-0.1475	2.9651
31	INST0031	3.0505	-0.7666	0.4522	4.8613	0.3492	1.7423	0.1651	-0.2177	2.8445
32	INST0032	3.0457	-0.7690	0.4308	4.8666	0.3513	1.5372	0.1968	-0.1863	2.8712
33	INST0033	3.0516	-0.7692	0.4488	4.6434	0.3734	1.6760	0.2395	-0.1899	2.8831
34	INST0034	3.0513	-0.7643	0.4648	4.8617	0.3456	1.6785	0.4453	-0.2676	2.8249
35	INST0035	3.0526	-0.7614	0.3600	4.8753	0.3338	1.5491	0.2319	-0.1951	2.8764
36	INST0036	3.0450	-0.7680	0.5113	4.8531	0.3425	1.6957	0.2345	-0.2459	2.8399
37	INST0037	3.0461	-0.7568	0.4364	4.8640	0.3728	1.4183	0.2001	-0.1646	2.8798
38	INST0038	3.0531	-0.7498	0.4871	4.8518	0.3776	1.6847	0.1271	-0.2108	2.9336
39	INST0039	3.0432	-0.7504	0.2691	3.9820	0.5915	1.5358	0.3909	0.0018	2.7682
40	INST0040	3.0595	-0.7181	0.4224	4.8599	0.4314	1.6823	0.1551	-0.1839	2.9250
41	INST0041	3.0497	-0.7590	0.3254	4.6820	0.3759	1.1851	0.3950	-0.0907	2.8559
42	INST0042	3.0448	-0.7263	0.4958	4.8526	0.4183	1.3466	0.2230	-0.1227	2.9547
43	INST0043	3.1165	-0.5968	0.5028	5.0585	0.3846	1.2399	-0.0253	-0.0524	3.1110
44	INST0044	3.0692	-0.6498	0.5686	4.4587	0.5003	1.5347	0.2899	-0.0576	2.7763
45	INST0045	3.1068	-0.6883	0.6523	5.0524	0.3553	1.5453	0.1742	-0.1146	2.8574
46	INST0046	3.2256	-0.6126	0.6287	3.9060	0.8597	0.9922	0.0589	-0.0046	3.2249
47	INST0047	3.3223	-0.6408	1.2120	5.1710	0.6338	0.4481	-0.3712	-0.3495	3.2406
48	INST0048	3.5400	-0.6500	1.3003	4.6851	0.7727	2.3295	-0.7829	-0.6904	3.4041
49	INST0049	3.1456	-0.5577	0.4954	4.7861	0.5670	1.4493	0.1501	-0.2538	2.9803

Table S30.
Probability values related to the igneous provenance of Holocene to Miocene coastal lagoon sediments from back-arc side of south-west Japan (Sediment application study SA1; data from Tables S27 used for MagClaMSys_ilr; see Table S29 for transformed values).

Consec	Name	Age / Period (Ishiga et al., 2000)	Igneous provenance (U-B-I-A) subdivision				Type of igneous provenance
			p_U	p_B	p_I	p_A	
1	INST0001	Holocene	0.0000	0.2686	0.7259	0.0055	intermediate
2	INST0002	Holocene	0.0000	0.3240	0.6758	0.0003	intermediate
3	INST0003	Holocene	0.0000	0.3319	0.6648	0.0033	intermediate
4	INST0004	Holocene	0.0000	0.3416	0.6567	0.0017	intermediate
5	INST0005	Holocene	0.0000	0.3605	0.6376	0.0018	intermediate
6	INST0006	Holocene	0.0000	0.3369	0.6609	0.0022	intermediate
7	INST0007	Holocene	0.0000	0.2528	0.7397	0.0074	intermediate
8	INST0008	Holocene	0.0000	0.2884	0.7046	0.0070	intermediate
9	INST0009	Holocene	0.0001	0.3153	0.6797	0.0049	intermediate
10	INST0010	Holocene	0.0001	0.3195	0.6772	0.0031	intermediate
11	INST0011	Holocene	0.0002	0.3029	0.6922	0.0047	intermediate
12	INST0012	Holocene	0.0002	0.3197	0.6767	0.0034	intermediate
13	INST0013	Holocene	0.0003	0.2923	0.7011	0.0063	intermediate
14	INST0014	Holocene	0.0001	0.3039	0.6865	0.0095	intermediate
15	INST0015	Holocene	0.0015	0.2574	0.7251	0.0160	intermediate
16	INST0016	Holocene	0.0009	0.2868	0.7025	0.0098	intermediate
17	INST0017	Holocene	0.0000	0.2970	0.6968	0.0062	intermediate
18	INST0018	Holocene	0.0002	0.2995	0.6896	0.0107	intermediate
19	INST0019	Holocene	0.0000	0.1910	0.7353	0.0737	intermediate
20	INST0020	Holocene	0.0000	0.1965	0.7483	0.0551	intermediate
21	INST0021	Holocene	0.0000	0.2003	0.7508	0.0488	intermediate
22	INST0022	Holocene	0.0000	0.1560	0.7411	0.1029	intermediate
23	INST0023	Holocene	0.0000	0.1746	0.7509	0.0745	intermediate
24	INST0024	Holocene	0.0001	0.2098	0.7297	0.0604	intermediate
25	INST0025	Holocene	0.0003	0.2390	0.7140	0.0467	intermediate
26	INST0026	Holocene	0.0001	0.2321	0.7193	0.0486	intermediate
27	INST0027	Holocene	0.0000	0.1465	0.7383	0.1152	intermediate
28	INST0028	Holocene	0.0000	0.1683	0.7339	0.0978	intermediate
29	INST0029	Holocene	0.0000	0.2372	0.7165	0.0463	intermediate
30	INST0030	Holocene	0.0000	0.1968	0.7240	0.0791	intermediate
31	INST0031	Holocene	0.0000	0.2005	0.7292	0.0703	intermediate
32	INST0032	Holocene	0.0000	0.2153	0.7308	0.0539	intermediate
33	INST0033	Holocene	0.0000	0.2304	0.7188	0.0508	intermediate
34	INST0034	Holocene	0.0000	0.2724	0.6885	0.0391	intermediate
35	INST0035	Holocene	0.0000	0.2298	0.7333	0.0369	intermediate
36	INST0036	Holocene	0.0000	0.2068	0.7154	0.0777	intermediate
37	INST0037	Holocene	0.0000	0.2070	0.7275	0.0655	intermediate
38	INST0038	Holocene	0.0000	0.1712	0.7214	0.1074	intermediate
39	INST0039	Holocene	0.0001	0.3115	0.6783	0.0101	intermediate
40	INST0040	Holocene	0.0000	0.1786	0.7120	0.1094	intermediate
41	INST0041	Holocene	0.0000	0.2665	0.7145	0.0190	intermediate
42	INST0042	Holocene	0.0000	0.1869	0.6958	0.1173	intermediate
43	INST0043	Holocene	0.0000	0.0166	0.3968	0.5866	acid
44	INST0044	Holocene	0.0000	0.1132	0.5556	0.3312	intermediate
45	INST0045	Pleistocene	0.0000	0.0425	0.4823	0.4752	intermediate
46	INST0046	Pleistocene	0.0001	0.0057	0.2545	0.7397	acid
47	INST0047	Pleistocene	0.0000	0.0000	0.2003	0.7997	acid
48	INST0048	Pleistocene	0.0000	0.0000	0.2001	0.7999	acid
49	INST0049	Miocene	0.0000	0.0135	0.3119	0.6746	acid

Table S31.
Probability values related to the igneous provenance of Neogene sediments from Bolivia and Chile (Sediment application study SA2; Pinto et al., 2004).

Consec	Sample name		Region	Igneous provenance (U-B-I-A) subdivision				Type of igneous provenance
	Original authors` (Pinto et al., 2000)	This work		p_U	p_B	p_I	p_A	
1	B32	PHMF0001	Bolivia	0.0000	0.0000	0.2001	0.7999	acid
2	B33	PHMF0002	Bolivia	0.0004	0.0414	0.2006	0.7576	acid
3	B34	PHMF0003	Bolivia	0.0000	0.0006	0.3138	0.6856	acid
4	B63	PHMF0004	Bolivia	0.0058	0.0142	0.4520	0.5280	acid
5	B49	PHMF0005	Bolivia	0.0000	0.0000	0.2000	0.8000	acid
6	B50	PHMF0006	Bolivia	0.0000	0.0000	0.2000	0.8000	acid
7	B56	PHMF0007	Bolivia	0.0000	0.0000	0.2000	0.8000	acid
8	B57	PHMF0008	Bolivia	0.0000	0.0000	0.2000	0.8000	acid
9	B58	PHMF0009	Bolivia	0.0000	0.0000	0.2005	0.7995	acid
10	B60	PHMF0010	Bolivia	0.0000	0.0000	0.2003	0.7997	acid
11	B61	PHMF0011	Bolivia	0.0000	0.0000	0.2030	0.7970	acid
12	B62	PHMF0012	Bolivia	0.0000	0.0000	0.2131	0.7869	acid
13	A26	PHMF0013	Chile	0.0001	0.0000	0.2087	0.7912	acid
14	A1	PHMF0014	Chile	0.0403	0.1938	0.7273	0.0386	intermediate
15	A2	PHMF0015	Chile	0.0237	0.0806	0.6224	0.2733	intermediate
16	A7	PHMF0016	Chile	0.0035	0.0290	0.6371	0.3305	intermediate
17	A8	PHMF0017	Chile	0.0064	0.1962	0.7728	0.0246	intermediate
18	A18	PHMF0018	Chile	0.0000	0.0000	0.2037	0.7962	acid
19	A20	PHMF0019	Chile	0.0000	0.0002	0.2140	0.7858	acid
20	C1	PHMF0020	Chile	0.0003	0.0040	0.3655	0.6302	acid
21	L2	PHMF0021	Chile	0.0139	0.1755	0.7751	0.0355	intermediate
22	S1	PHMF0022	Chile	0.0121	0.0938	0.7747	0.1195	intermediate
23	S8	PHMF0023	Chile	0.0069	0.0986	0.7591	0.1354	intermediate
24	A10	PHMF0024	Chile	0.0051	0.0333	0.6603	0.3013	intermediate
25	M12	PHMF0025	Chile	0.0063	0.0624	0.7411	0.1902	intermediate
26	A9	PHMF0026	Chile	0.0038	0.1062	0.7780	0.1121	intermediate
27	S2	PHMF0027	Chile	0.0232	0.1904	0.7614	0.0250	intermediate
28	S3	PHMF0028	Chile	0.0092	0.1490	0.7755	0.0664	intermediate
29	N2	PHMF0029	Chile	0.0034	0.3326	0.6635	0.0006	intermediate
30	N3	PHMF0030	Chile	0.0006	0.1981	0.7824	0.0189	intermediate
31	N5	PHMF0031	Chile	0.0106	0.0954	0.7487	0.1452	intermediate
32	P10	PHMF0032	Chile	0.0005	0.0247	0.7496	0.2252	intermediate
33	N8	PHMF0033	Chile	0.0054	0.1264	0.7765	0.0917	intermediate
34	M8	PHMF0034	Chile	0.0174	0.1900	0.7750	0.0176	intermediate
35	A4	PHMF0035	Chile	0.0001	0.0009	0.3769	0.6220	acid
36	A5	PHMF0036	Chile	0.0492	0.1235	0.7807	0.0465	intermediate
37	A17	PHMF0037	Chile	0.0472	0.2192	0.7159	0.0177	intermediate
38	A24	PHMF0038	Chile	0.0016	0.1789	0.7709	0.0485	intermediate

Table S32.
Probability values related to the igneous provenance of Cretaceous clay-rich sediments from Southeastern Nigeria (Sediment application study SA3; Odoma et al., 2015).

Consec	Sample name		Igneous provenance (U-B-I-A) subdivision				Type of igneous provenance
	Original authors` (Odoma et al., 2015)	This work	p_U	p_B	p_I	p_A	
1	Enu 1.1	OOOI0001	0.0000	0.5983	0.4000	0.0017	basic
2	Enu 1.2	OOOI0002	0.0000	0.5781	0.2514	0.1705	basic
3	Enu 1.3	OOOI0003	0.0000	0.2390	0.2054	0.5555	acid
4	Enu 1.4	OOOI0004	0.0000	0.5961	0.3536	0.0503	basic
5	Enu 1.5	OOOI0005	0.0000	0.5974	0.3718	0.0308	basic
6	Enu 2.2	OOOI0007	0.0000	0.5972	0.4027	0.0000	basic
7	Enu 2.3	OOOI0008	0.0000	0.5973	0.4017	0.0010	basic
8	Enu 2.4	OOOI0009	0.0000	0.5871	0.3966	0.0163	basic
9	Enu 2.5	OOOI0010	0.0000	0.5980	0.3887	0.0133	basic

Table S33. Sensitivity analysis of all rock centroids (adjusted compositions) with respect to post-emplacement compositional changes (one element at a time; in this case SiO_2).

Original High-Mg centroid composition		MagClaMSys_ilr [*this work*]				IUGS [TAS]			
Chemical parameter	Major element concentration (% m/m)	Maximum "tolerable" change *		Maximum compositional range of 100% adjusted data **		Maximum "tolerable" change *		Maximum compositional range of 100% adjusted data **	
		loss (% m/m)	gain (% m/m)	minimum concentration (% m/m)	maximum concentration (% m/m)	loss (% m/m)	gain (% m/m)	minimum concentration (% m/m)	maximum concentration (% m/m)
centroid of Ultrabasic magma									
SiO_2A	42.71201087	-71	+134	17.77764904	63.56516	-29	+7	30.32553	44.88
TiO_2A	3.272333743			4.696603556	2.081186			3.272334	3.21
Al_2O_3A	12.67996013			18.19886067	8.064383			12.67996	12.45
Fe_2O_3TA	13.60829196			19.53124511	8.654797			13.60829	2.04
MnOA	0.283929873			0.407509183	0.180578			0.28393	10.19
MgOA	10.76344261			15.44818677	6.845489			10.76344	0.279
CaOA	11.28854978			16.20184468	7.179454			11.28855	10.57
Na_2OA	3.161701568			4.537819182	2.010824			3.161702	11.09
K_2OA	1.44680434			2.076519983	0.920159			1.446804	3.10
P_2O_5A	0.782975129			1.123761836	0.497968			0.782975	1.42
centroid of Basic magma									
SiO_2A	48.73091	-99	+45	0.941544	57.95165	-15	+11	45.16	51.82
TiO_2A	1.928348			3.725815	1.581534			2.10	1.85
Al_2O_3A	15.24691			29.45898	12.50475			16.62	14.61
Fe_2O_3TA	11.50233			22.22397	9.433633			1.91	1.68
MnOA	0.18254			0.35269	0.14971			9.56	8.40
MgOA	7.789191			15.04972	6.388305			0.199	0.175
CaOA	10.27391			19.85052	8.426151			8.49	7.46
Na_2OA	2.906579			5.615883	2.383831			11.20	9.84
K_2OA	1.054883			2.03817	0.865163			3.17	2.78
P_2O_5A	0.384404			0.742717	0.315269			1.15	1.01
centroid of Intermediate magma									
SiO_2A	56.8547	-53	+42	38.24653	65.17141	-18	+27	52.28	62.91
TiO_2A	0.983331			1.407433	0.793784			1.10	0.86
Al_2O_3A	17.13452			24.52448	13.83166			19.21	14.93
Fe_2O_3TA	7.664969			10.9708	6.187465			2.06	1.60
MnOA	0.136389			0.195213	0.110099			5.88	4.57
MgOA	4.140495			5.926252	3.342371			0.153	0.119
CaOA	6.984841			9.997337	5.638439			4.64	3.61
Na_2OA	3.770955			5.397333	3.044064			7.83	6.09
K_2OA	2.033791			2.910946	1.641756			4.23	3.29
P_2O_5A	0.29601			0.423677	0.238951			2.28	1.77
centroid of Acid magma									
SiO_2A	69.68341	-22	+43	64.48654	76.67306	-26	---	63.16	---
TiO_2A	0.443792			0.519867	0.341474			0.54	
Al_2O_3A	14.95936			17.52369	11.5104			18.32	
Fe_2O_3TA	3.529595			4.134638	2.715828			1.34	
MnOA	0.084459			0.098937	0.064987			2.68	
MgOA	1.021815			1.196974	0.78623			0.103	
CaOA	2.677426			3.13639	2.060131			1.25	
Na_2OA	4.05785			4.753446	3.122291			3.28	
K_2OA	3.422033			4.008637	2.633065			4.97	
P_2O_5A	0.120257			0.140872	0.092531			4.19	

* This refers to the minimum and maximum % change in any given element before the rock name changes from the original name to some other rock name; ** These are independent estimates for any given element and are not directly related to the other ranges (changes simulated for one element at a time).

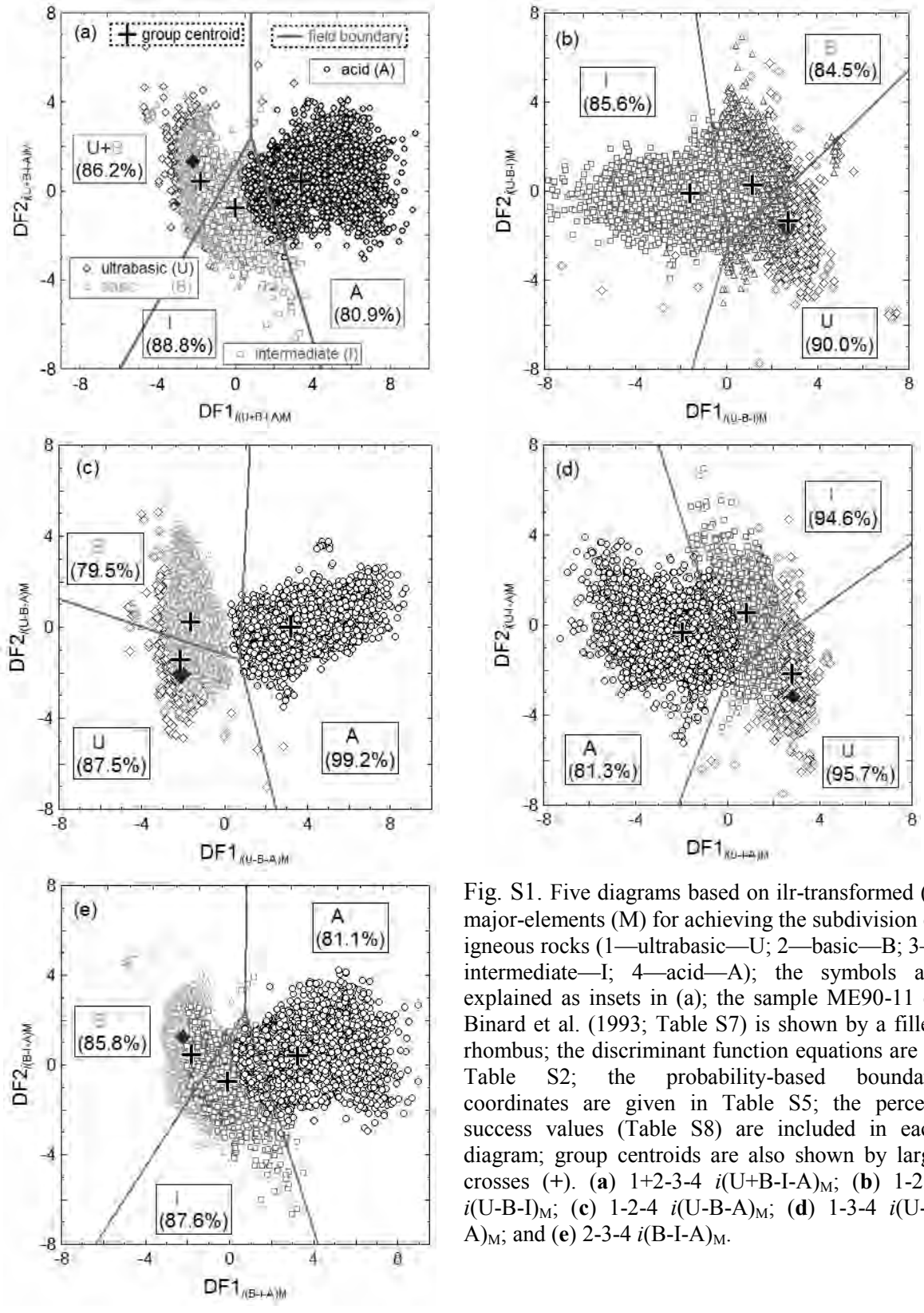

Fig. S1. Five diagrams based on ilr-transformed (*i*) major-elements (M) for achieving the subdivision of igneous rocks (1—ultrabasic—U; 2—basic—B; 3—intermediate—I; 4—acid—A); the symbols are explained as insets in (a); the sample ME90-11 of Binard et al. (1993; Table S7) is shown by a filled rhombus; the discriminant function equations are in Table S2; the probability-based boundary coordinates are given in Table S5; the percent success values (Table S8) are included in each diagram; group centroids are also shown by large crosses (+). (**a**) 1+2-3-4 $i(\text{U+B-I-A})_\text{M}$; (**b**) 1-2-3 $i(\text{U-B-I})_\text{M}$; (**c**) 1-2-4 $i(\text{U-B-A})_\text{M}$; (**d**) 1-3-4 $i(\text{U-I-A})_\text{M}$; and (**e**) 2-3-4 $i(\text{B-I-A})_\text{M}$.

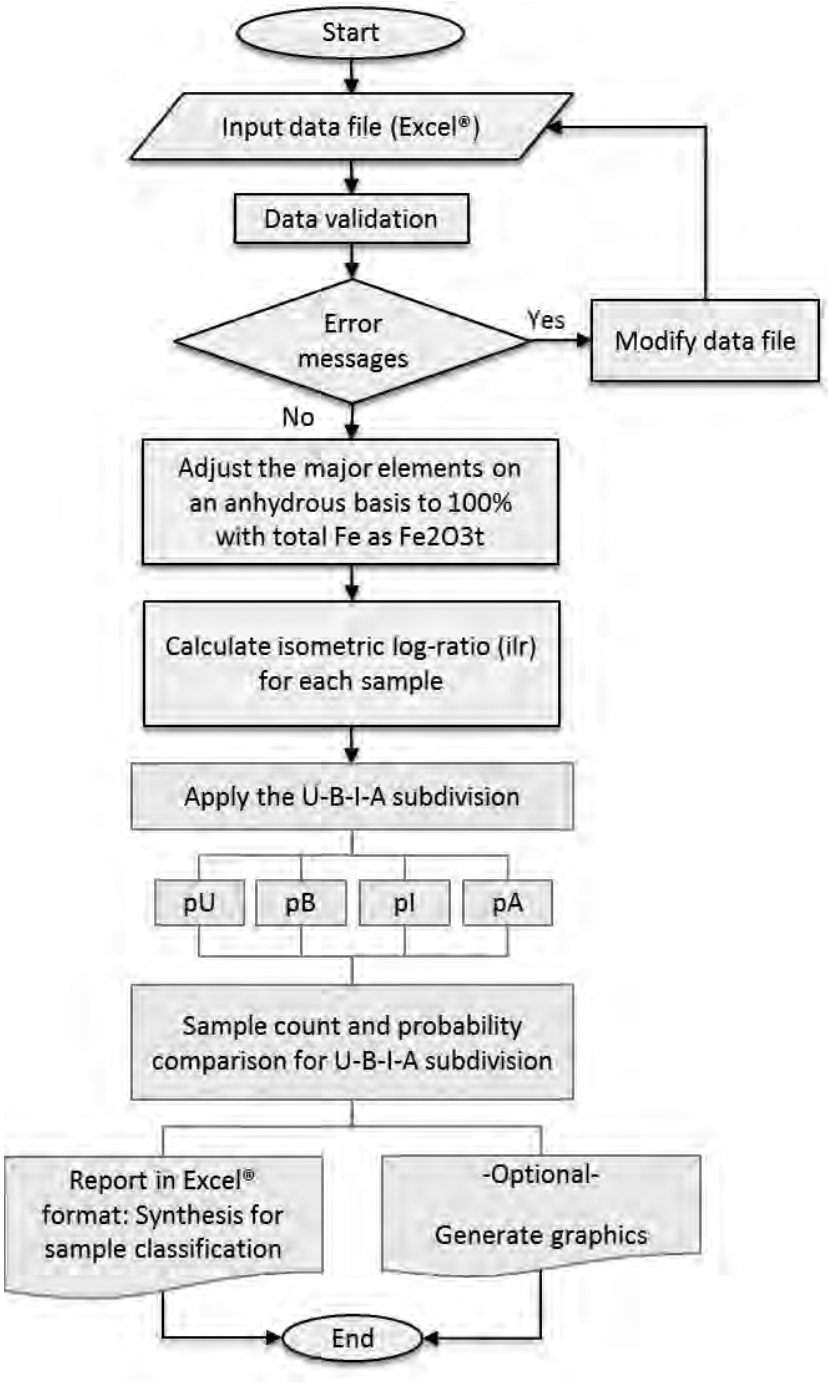

Figure S2. Schematic flow diagram for the computer program MagClaMSys_ilr

REFERENCES

Arndt, N.T., Jenner, G.A., 1986. Crustally contaminated komatiites and basalts from Kambalda, western Australia. Chemical Geology 56, 229-255.

Binard, N., Maury, R.C., Guille, G., Talandier, J., Gillot, P.Y., Cotten, J., 1993. Mehetia Island, South Pacific: geology and petrology of the emerged part of the Society hot spot. Journal of Volcanology and Geothermal Research 55, 239-260.

Blondes, M.S., Reiners, P.W., Ducea, M.N., Singer, B.S., Chesley, J., 2008. Temporal-compositional trends over short and long time-scales in basalts of the Big Pine Volcanic Field, California. Earth and Planetary Science Letters 269, 140-154.

Di Piazza, A., Rizzo, A.L., Barberi, F., Carapezza, M.L., De Astis, G., Romano, C., Sortino, F., 2015. Geochemistry of the mantle source and magma feeding system beneath Turrialba volcano, Costa Rica. Lithos 232, 319-335.

Garcia, M.O., Weis, D., Jicha, B.R., Ito, G., Hanano, D., 2016. Petrology and geochronology of lavas from Ka'ula Volcano: Implications for rejuvenated volcanism of the Hawaiian mantle plume. Geochimica et Cosmochimica Acta 185, 278-301.

Grajales-Nishimura, J.M., Centeno-García, E., Keppie, J.D., Dostal, J., 1999. Geochemistry of Paleozoic basalts from the Juchatengo complex of southern México: tectonic implications. Journal of South American Earth Sciences 12, 537-544.

Ishiga, H., Nakamura, T., Sampei, Y., Tokuoka, T., Takayasu, K., 2000. Geochemical record of the Holocene Jomon transgression and human activity in coastal lagoon sediments of the San'in district SW Japan. Global and Planetary Change 25, 223-237.

Lahaye, Y., Arndt, N., Byerly, G., Chauvel, C., Fourcade, S., Gruau, G., 1995. The influence of alteration on the trace-element and Nd isotopic compositions of komatiites. Chemical Geology 126, 43-64.

Le Bas, M.J., Le Maitre, R.W., Streckeisen, A., Zanettin, B., 1986. A chemical classification of volcanic rocks based on the total alkali-silica diagram. Journal of Petrology 27, 745-750.

Lightfoot, P.C., Hawkesworth, C.J., Hergt, J., Naldrett, A.J., Gorbachev, N.S., Fedorenko, V.A., Doherty, W., 1993. Remobilisation of the continental lithosphere by a mantle plume: major-, trace element, and Sr-, Nd-, and Pb-isotope evidence from picritic and tholeiitic lavas of the Noril'sk District, Siberian Trap, Russia. Contributions to Mineralogy and Petrology 114, 171-188.

Mora, J.C., Gardner, J.E., Macías, J.L., Meriggi, L., Santo, A.P., 2013. Magmatic controls on eruption dynamics of the 1950 yr B.P. eruption of San Antonio Volcano, Tacaná Volcanic Complex, Mexico-Guatemala. Journal of Volcanology and Geothermal Research 262, 134-152.

Odoma, A.N., Obaje, N.G., Omada, J.I., Idakwo, S.O., Erbacher, J., 2015. Mineralogical, chemical composition and distribution of rare earth elements in clay-rich sediments from southeastern Nigeria. Journal of African Earth Sciences 102, 50-60.

Pinto, L., Hérail, G., Moine, B., Fontan, F., Charrier, R., Dupré, B., 2004. Using geochemistry to establish the igneous provenances of the Neogene continental sedimentary rocks in the Central Depression and Atliplano, Central Andes. Sedimentary Geology 166, 157-183.

Shaw, J.E., Baker, J.A., Menzies, M.A., Thirlwall, M.F., Ibrahim, K.M., 2003. Petrogenesis of the largest intraplate volcanic field on the Arabian Plate (Jordan): a mixed lithosphere-asthenosphere source activated by lithospheric extension. Journal of Petrology 44, 1657-1679.

Verma, S.P., Guevara, M., Agrawal, S., 2006. Discriminating four tectonic settings: five new geochemical diagrams for basic and ultrabasic volcanic rocks based on log-ratio transformation of major-element data. Journal of Earth System Science 115, 485-528.

Verma, S.P., Rivera-Gómez, M.A., 2013a. Computer programs for the classification and nomenclature of igneous rocks. Episodes 36, 115-124.

Verma, S.P., Rivera-Gómez, M.A., 2013b. New computer program TecD for tectonomagmatic discrimination from discriminant function diagrams for basic and ultrabasic magmas and its application to ancient rocks. Journal of Iberian Geology 39, 167-179.

Verma, S.P., Verma, S.K., 2013. First 15 probability-based multi-dimensional discrimination diagrams for intermediate magmas and their robustness against post-emplacement compositional changes and petrogenetic processes. Turkish Journal of Earth Sciences 22, 931-995.

(**Mag**ma **Cla**ssification **M**ajor-element based **Sys**tem)

README

A computer program MagClaMSys available from http://tlaloc.ier.unam.mx/hmgclamsys for the classification of igneous rocks in terms of four magma types: ultrabasic, basic, intermediate, and acid. Simulation modelling confirmed the robustness of our classification with respect to analytical errors and post-emplacement compositional changes. From robustness considerations, our proposal for the nomenclature of altered igneous rocks is shown superior to the IUGS scheme which was recommended for the classification of relatively fresh rocks only.

The interested person is invited to enter the web server http://tlaloc.ier.unam.mx (see Fig. 1a). If you are a new user, you must register and provide the information requested: first name, last name, institutional email address and affiliation as shown in Fig. 1b. If you do not have an institutional email account, you must provide all institutional details.

Afterwords, the user will then receive an e-mail message with a temporary password, which can be changed. If you are a registered user, you must sign in using your email address and password (see Fig. 1c).

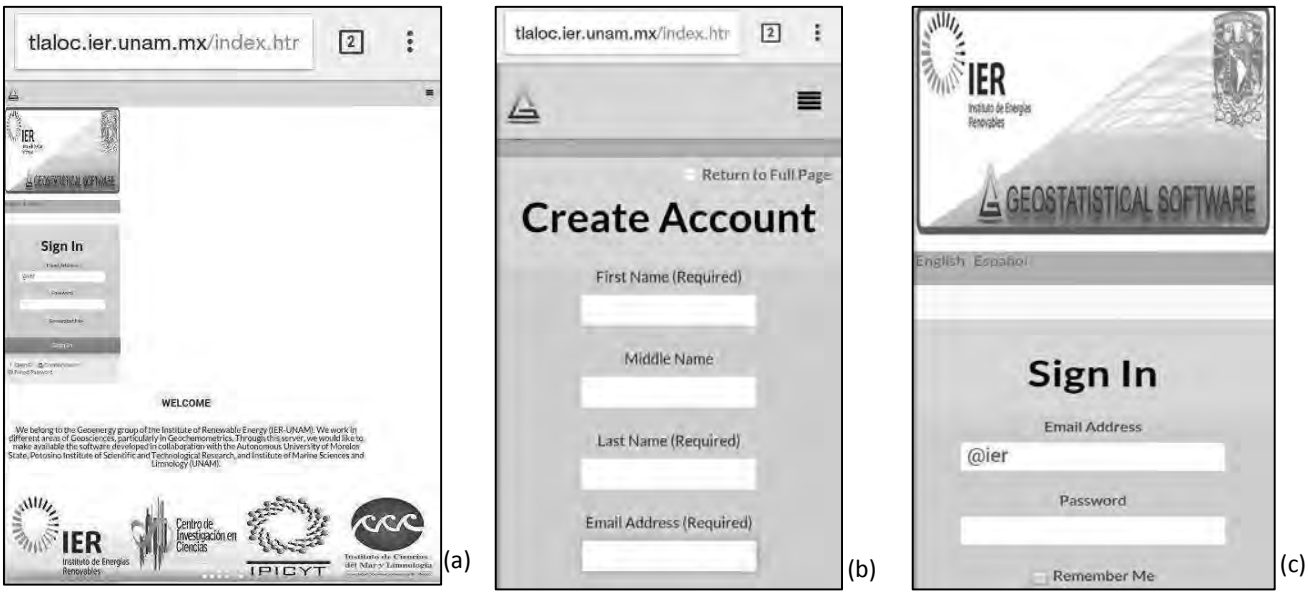

Fig. 1 Welcome screen of web server and user authentication. (a) Welcome screen of web server; (b) The screen to create a new account; and (c) The screen to user authentication.

As a registered user, you may use the "MagClaMSys_ilr" option of "Online program" menu as shown in Fig. S2.

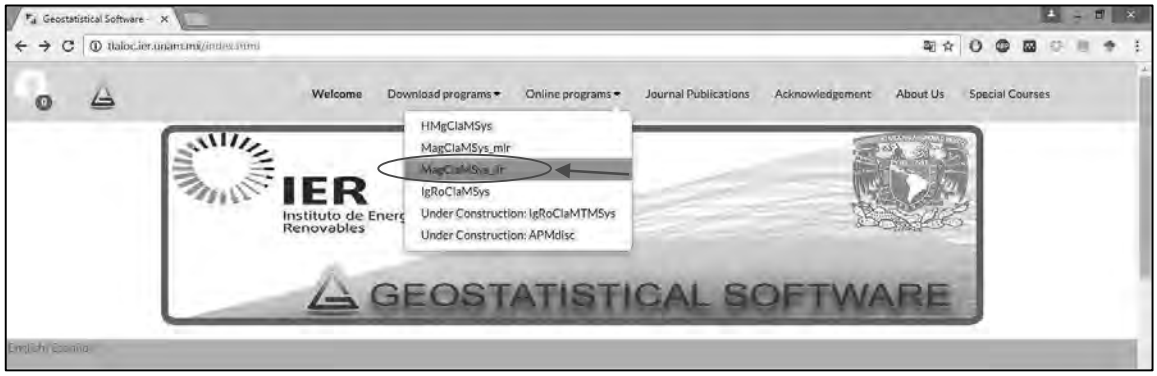

Fig. 2 "HMgClaMSys_ilr" options of "Online program" menu.

Once you access the online program MagClaMSys_ilr, you can open an input file, for which there are three options as shown in Fig. 3a: (i) Magma Type; (ii) Sensitivity analysis; and (iii) Analytical errrors_Uncertainty Propagation. The literature sources of the igneous rocks are summarized in pdf file available (link identified by a blue rectangle: "Download MagClaMSys DatabaseInfo"; see Fig. 3a). You can download each of several input file folders available from web server (see Fig. 3b): "*InputFile_MagClaMSys.xls", "PropUcM_Format", "Sensitivity_Ultrabasic"*. These templates are required for testing the different processing options. At least the user must download the input file "*InputFile_MagClaMSys.xl*s" as shown in Fig. 3b (link identified by a blue circle and an arrow).

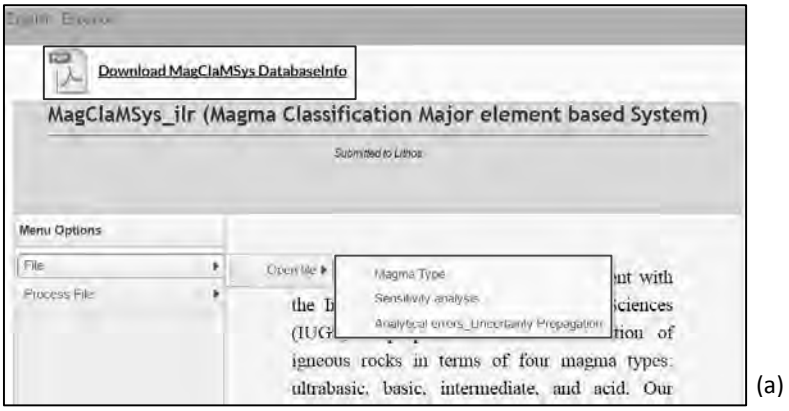

(a)

(b)

Fig. 3 Menu options and input files available. (a) Three options of "Open file" menu; and (b) Input files available for download.

Optionally you can download the file "Applications" (Fig. 4a; ten files) and "Sediments" (Fig. 4b; five files) and "Test" (Fig. 4c; five files) folders. Altogether, twenty documents are available in these folders (Fig. 4a-c).

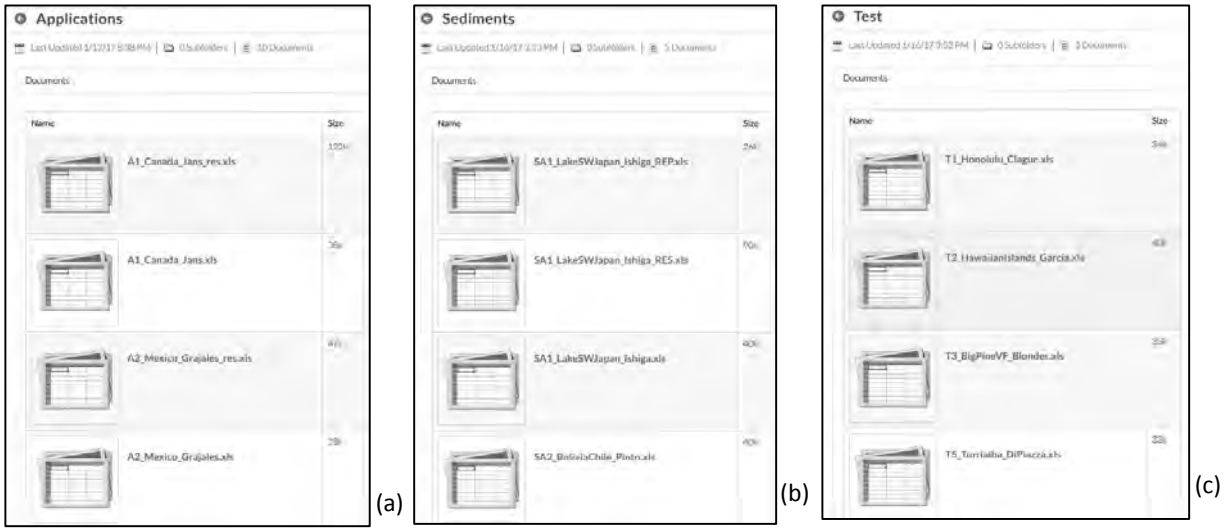

Fig. 4 Input files available for download from web server. (a) "Applications" folder; (b) "Sediments" folder; and (c) "Test" folder.

1. New multidimensional magma type classification scheme based on major elements

MagClaMSys offers a set of 10 discriminant functions and 5 diagrams to facilitate magma type classification. The user must download the input file "*InputFile_MagClaMSys.xls*" as shown in Fig. 3b (link identified by a blue circle and an arrow). If you downloaded this file click on the "Download (30k)" hyperlink to download the input file as shown in Fig. 5a (identified by a red circle). Once the download is successfully completed, click on the downloaded file (identified by a blue circle in Fig. 5a) to open it as shown in Fig 5b. MagClaMSys requires 10 oxides from SiO_2 to P_2O_5 (see Fig 5b). It is important to note that **the measured data are input with total Fe as Fe2O3T**. If you do not have Fe2O3T values, please calculate it as follows (it is immaterial if you have either FeOT or separately FeO and Fe2O3, the equation will give you the Fe2O3T value; * means multiplication):

$$Fe2O3T = Fe2O3 + (FeO * 159.6882 / (2 * 71.8444))$$

From the measured major element compositions, MagClaMSys efficiently calculates the adjusted values on an anhydrous 100% basis.

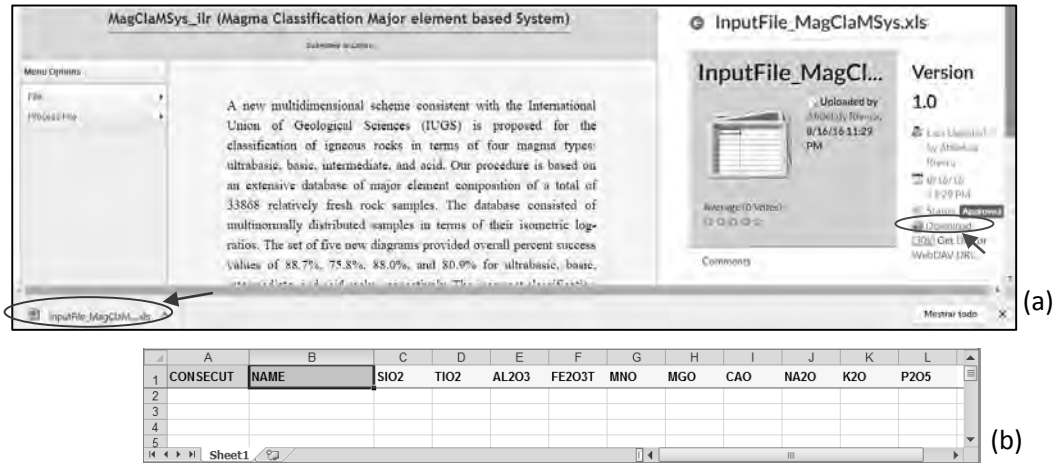

Fig. 5 Download of input file "*InputFile_MagClaMSys.xls*". (a) Hyperlink to download the file; and (b) View the contents of the file in Excel.

In this case, we will use "T1_Honolulu_Clague.xls" test file (see Fig. 6a-b) to explain how the program works. This file is available in "Test" folder. The user can download this file from web server (see Fig. 6a).

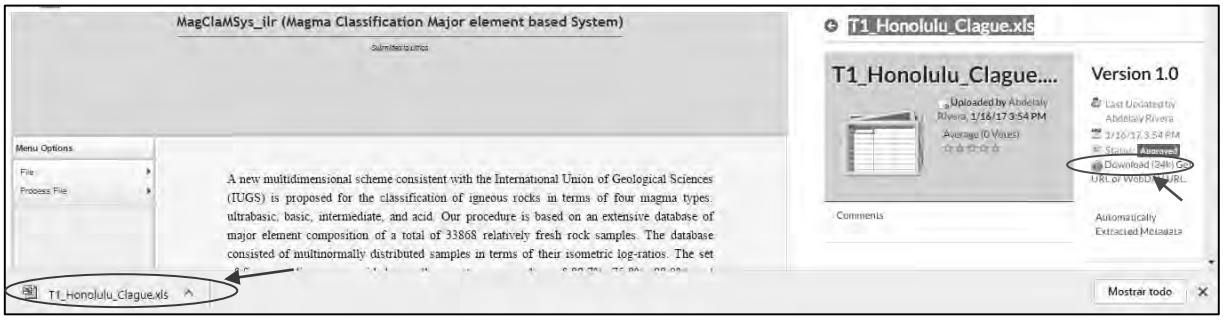

	A	B	C	D	E	F	G	H	I	J	K	L
1	CONSECUT	NAME	SIO2	TIO2	AL2O3	FE2O3T	MNO	MGO	CAO	NA2O	K2O	P2O5
2	1	GMQ1	37.72	2.81	10.57	16.427	12.78	12.15	4.8	1.66	1.11	1.05
3	2	GMQ2	38.32	2.91	11.04	16.948	11.77	10.52	5.35	1.94	1.25	1.2
4	3	GMQ3	37.17	2.77	10.64	16.247	11.98	13.01	5.19	1.86	1.17	1.13
5	4	GMQ4	37.23	2.84	10.58	16.608	12.03	12.86	4.86	1.84	1.18	1.14
6	5	GMQ5	37.9	2.87	10.6	16.308	11.65	13.65	4.03	1.77	1.23	1.17
7	6	GMQ6	37.46	2.8	10.73	16.087	11.57	14.1	4.48	1.6	1.2	1.14
8	7	GMQ7	36.99	2.83	10.72	16.408	11.85	12.88	5.31	1.84	1.2	1.16
9	8	GMQ7.5	38.46	2.75	10.63	15.859	11.46	13.76	4.48	1.46	1.17	1.12
10	9	GMQ8	37.4	2.8	10.7	16.287	11.97	14.41	4.02	1.24	1.2	1.13
11	10	GMQ9	37.67	2.84	10.26	16.247	11.77	13.31	4.95	1.79	1.2	1.16
12	11	GMQ11	37.54	2.82	10.64	16.318	11.99	13.03	4.75	1.74	1.2	1.15
13	12	65MOIL2	36.71	2.87	11.38	16.789	11.84	12.58	5	1.78	1.09	1.05
14	13	GMQ12	36.59	2.96	10.17	16.51	0.24	11.54	13.71	5.25	1.89	1.14
15	14	MQ1	37.09	2.91	10.86	16.38	0.23	10.76	13.31	5.35	1.95	1.14
16	15	GMQ10L	37.72	2.81	10.13	16.37	0.25	12.78	12.68	4.49	1.63	1.14
17	16	MQ2L	36.52	2.88	10.82	17.05	0.26	11.38	12.98	5.05	1.94	1.13
18	17	GMQ10D	38.5	2.88	10.43	16.65	0.26	15.29	9.06	4.07	1.67	1.2
19	18	MQ2D	37.98	2.93	10.74	16.9	0.27	15.58	8.6	4.01	1.81	1.17
20												

Sheet1

(b)

Fig. 6 Download of test file "T1_Honolulu_Clague.xls". (a) Hyperlink to download the file; and (b View the contents of the file in Excel.

After saving the download file to a location on your computer, you must open the "T1_Honolulu_Clague.xls" file as shown in Fig. 7.

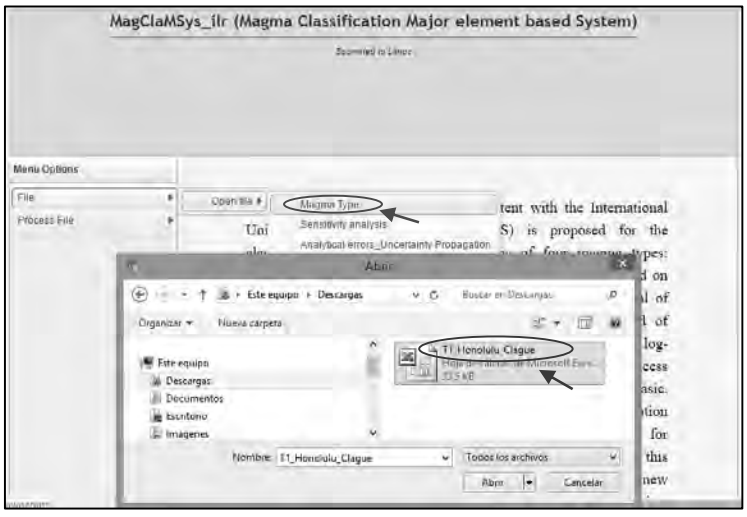

Fig. 7 Open file option of MagClaMSys.

If everything is fine, the file will open as shown in Fig. 8.

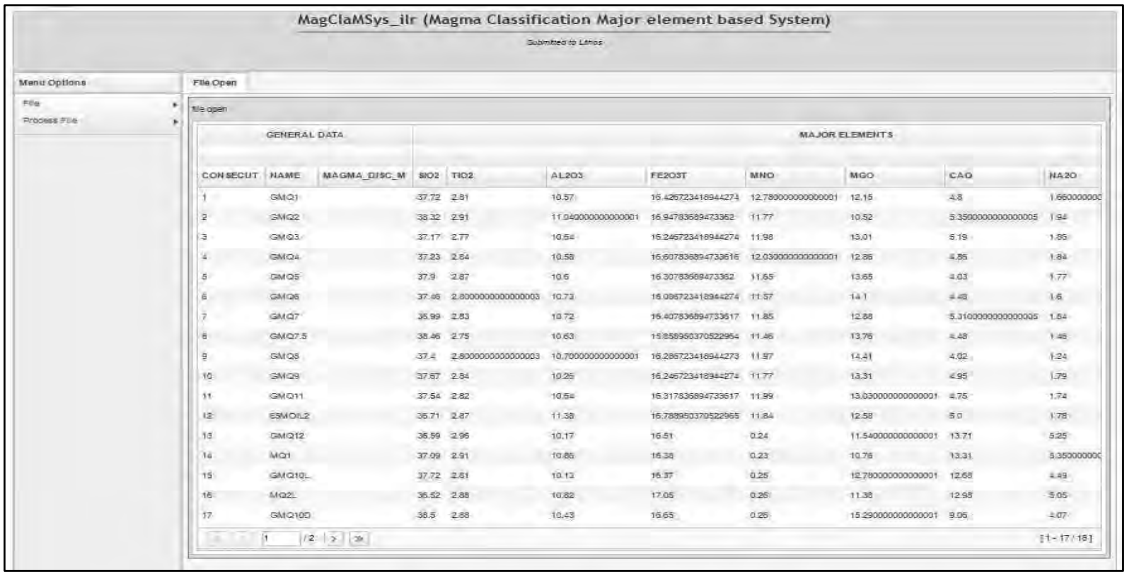

Fig. 8 Input data file already open and validated in MagClaMSys.

Once the Excel input data file is correctly loaded without errors, the user can process the data using "Process Magma-Type" as shown in Fig. 9a. After the job is done, the user can download the general report (Fig. 9b).

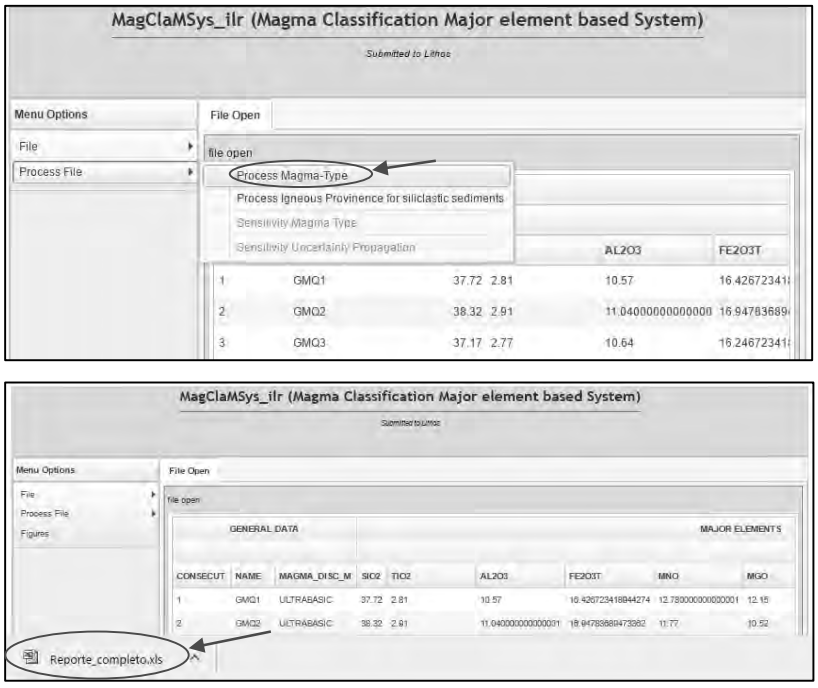

Fig. 9 Process Magma-Type option to be chosen.

The general report contains:

- Classification summary, adjusted major element concentrations and Log-transformed ratios of individual samples (see Fig 10a).
- The discriminant function (DF1-DF2) values for five diagrams for the classification of magma type as ultrabasic, basic, intermediate, and acid; see Fig 10b.
- The probability values for the four magma types (1—ultrabasic; 2—basic; 3—intermediate; 4—acid); see Fig 10c.

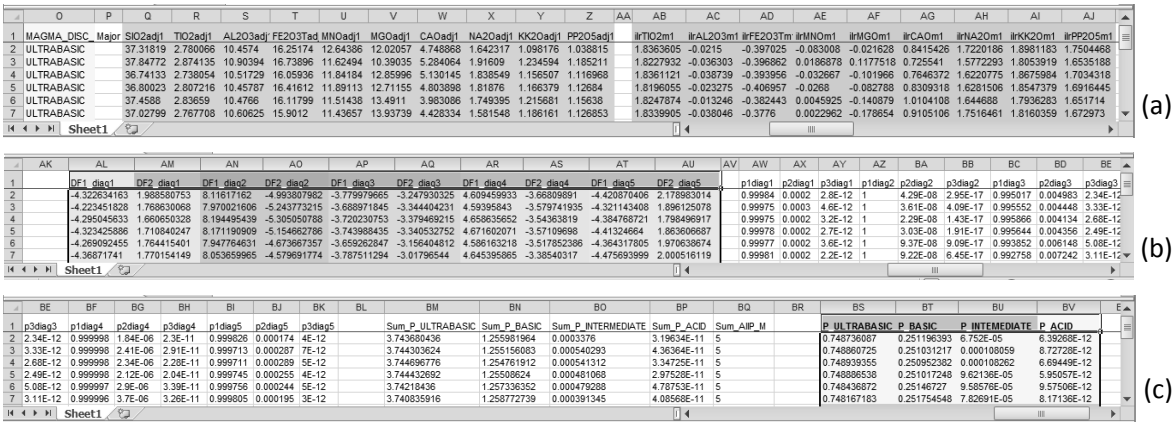

Fig. 10 The Excel output file contains: (a) Classification summary, adjusted major element concentrations and log-transformed ratios of individual samples; (b) The detailed results of discriminant function (DF1-DF2) for five diagrams; and (c) The probability values for the four magma types (1—ultrabasic; 2—basic; 3—intermediate; 4—acid).

2. Robustness of the new multidimensional classification scheme based on major elements with respect to post-emplacement compositional changes

The maximum loss or gain (% m/m) of an element in the centroid composition is estimated as the value that will still give the same magma or rock type as determined from our multidimensional diagrams. However, the minimum and maximum changes possible for any given element are also automatically set for that particular element to show final concentrations between 0% (no concentration can become negative) and 100% (no concentration can be >100% m/m). Therefore, our sensitivity analysis was carried out within these two limits for the final composition, although more stringent conditions could be used in future.

To try this option, the user must download the "*Sensitivity_Ultrabasic.xls*" file (Fig. 11a). This template contains the composition (Fig. 11b) of the centroid of all 1671 ultrabasic rocks to estimate the post-emplacement compositional changes of SiO_2 at a time in the classification of magma type as ultrabasic, basic, intermediate, and acid

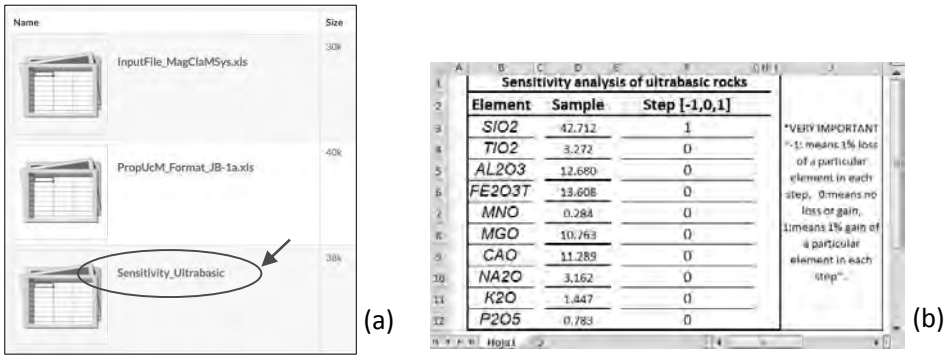

Fig. 11 Template available for sensitivity analysis.

If you downloaded successfully the template "*Sensitivity_Format.xls*", you can click on "Sensitivity analysis" option of "File Open" menu (see Fig. 12).

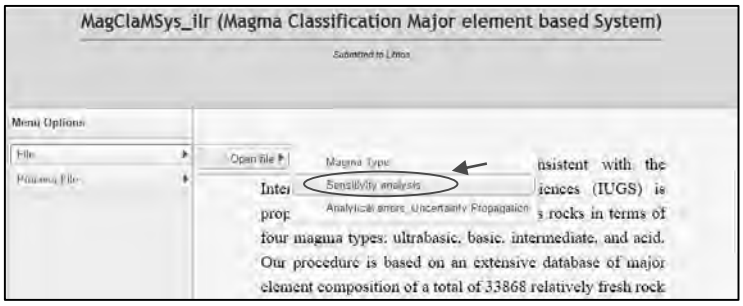

Fig. 12 "Sensitivity analysis" option of "File Open" menu.

Once the Excel input data file is correctly loaded without errors, the user can proceed to run the sensitivity analysis. MagClaMSys provides two options in the "Process File" menu as in Fig. 13. "Sensitivity Magma Type" option performs sensitivity analysis of MagClaMSys.

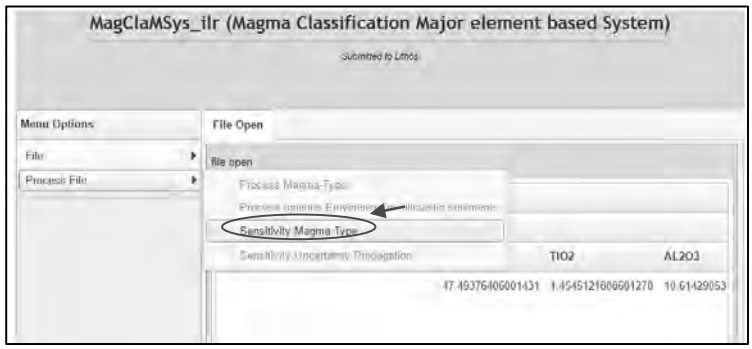

Fig. 13 "Sensitivity Magma Type" option of "Process File" menu.

After the job is done, the user can download (click on link identified with blue circle in Fig. 14a) and open the sensibility report (see Fig. 14b).

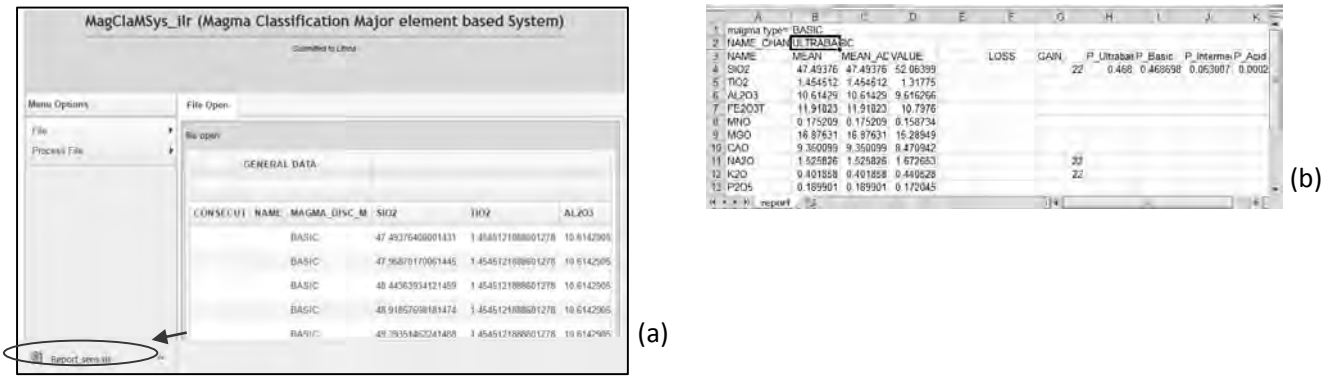

Fig. 14 Sensibility report. (a) The sensibility process is done; (b) Sensibility report opened.

Thus, you are free to input your own sample replacing the concentration values in the example file (Fig. 10b). You can similarly choose any element(s) for loss, gain or no change by simply inputting -1, 1 or 0 for that element(s).

3. Robustness of the new multidimensional classification scheme based on major elements with respect to analytical errors

To illustrate the robustness of MagClaMSys, we used major element compositions of three reference materials (basalt JB-1, basalt JB-1a, and andesite JA-3). These files are available in "Reference Material PropuC" folder (see Fig. 15a). You can download these three files ("Andesite JA-3.xls", "Basalt JB-1a.xls" and "Basalt JB-1.xls"; see Fig. 15b) to use this simulation module.

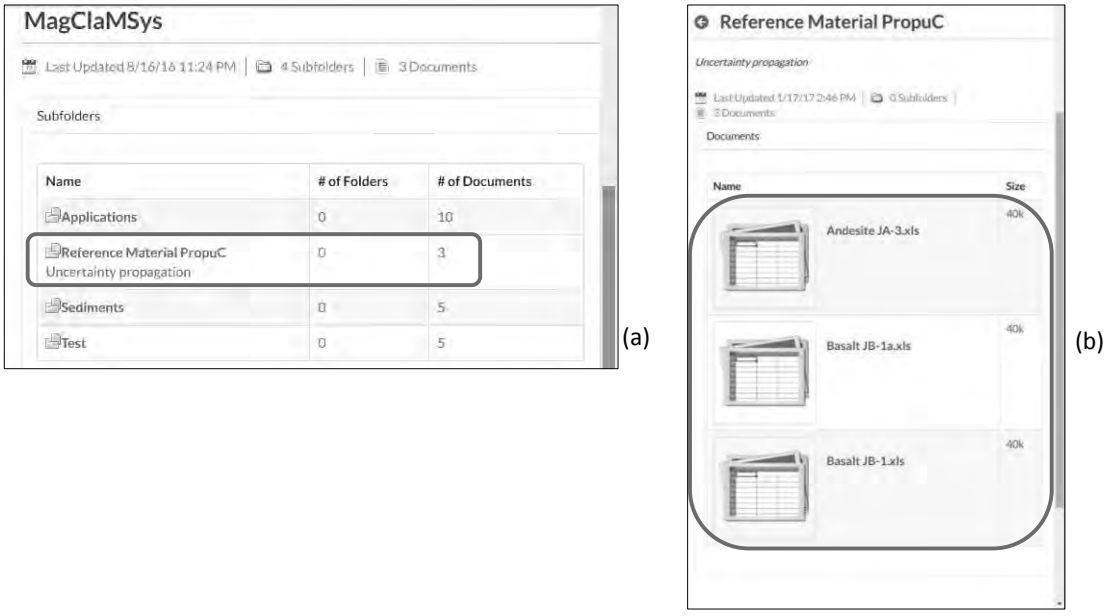

Fig. 15 Selected samples for sensitivity analysis with respect to analytical errors. (a-b) Templates of 3 selected samples.

In this case, we will use "Andesite JA-3.xls" file (see Fig. 16) to explain how this module program works. The mean and total uncertainty values for this geological material were used to simulate a large number of analyses (2200 + 1 initial analysis) from the Monte Carlo simulation procedure. The 2201 analyses from the initial inter-laboratory data were processed from our new multidimensional procedure (MagClaMSys_ilr) and compared with the conventional IUGS approach. "Andesite JA-3.xls" file contains the mean and total uncertainty values for JA-3 geological material (see Fig. 16).

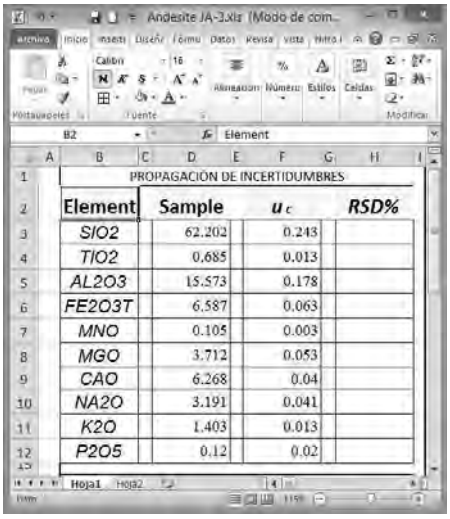

PROPAGACIÓN DE INCERTIDUMBRES

Element	Sample	u_c	RSD%
SIO2	62.202	0.243	
TIO2	0.685	0.013	
AL2O3	15.573	0.178	
FE2O3T	6.587	0.063	
MNO	0.105	0.003	
MGO	3.712	0.053	
CAO	6.268	0.04	
NA2O	3.191	0.041	
K2O	1.403	0.013	
P2O5	0.12	0.02	

Fig. 16 View the contents of the "Andesite JA-3.xls" file in Excel.

In order to simulate this sample (Fig. 16), you must download the ""Andesite JA-3.xls".*xls*" file. After, you must open this file as shown in Fig. 17a (click on the option identified with red circle). Once the Excel input data file is correctly loaded without errors, the user can proceed to simulate the sample as a shown in Fig. 17b (click on the option identified with red circle). After the process is done, the user can download the general report as a shown in Fig. 17c (click on the output file identified with blue circle).

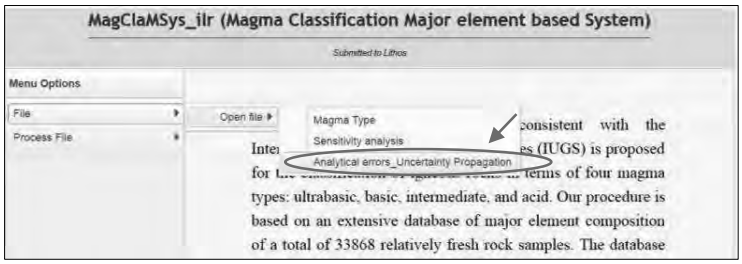

(a)

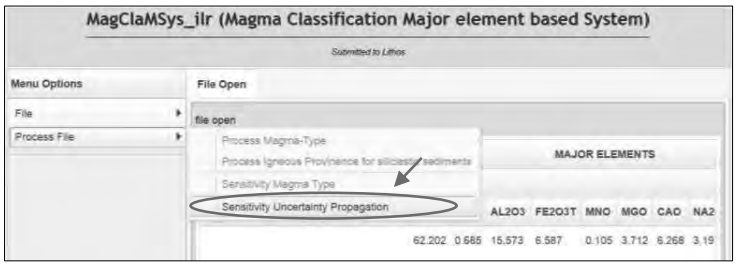

(b)

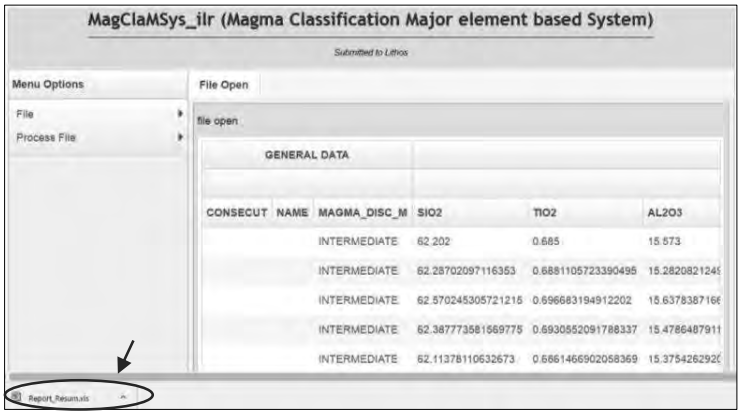

(c)

Fig. 17 Process "Sensitivity Uncertainty Propagation" option to be chosen.

The Excel output file contains: classification summary, initial concentration and adjusted concentrations (see Fig 18a), log-transformed ratios of individual samples, detailed results of discriminant function DF1-DF2 (see Fig 18b), and probability values for the four magma types (1—ultrabasic; 2—basic; 3—intermediate; 4—acid) (see Fig 18c). MagClaMSys showed that the inferred magma type is consistent with the rock name (intermediate for andesite JA-3; see 18a) for all 2200 simulated analyses.

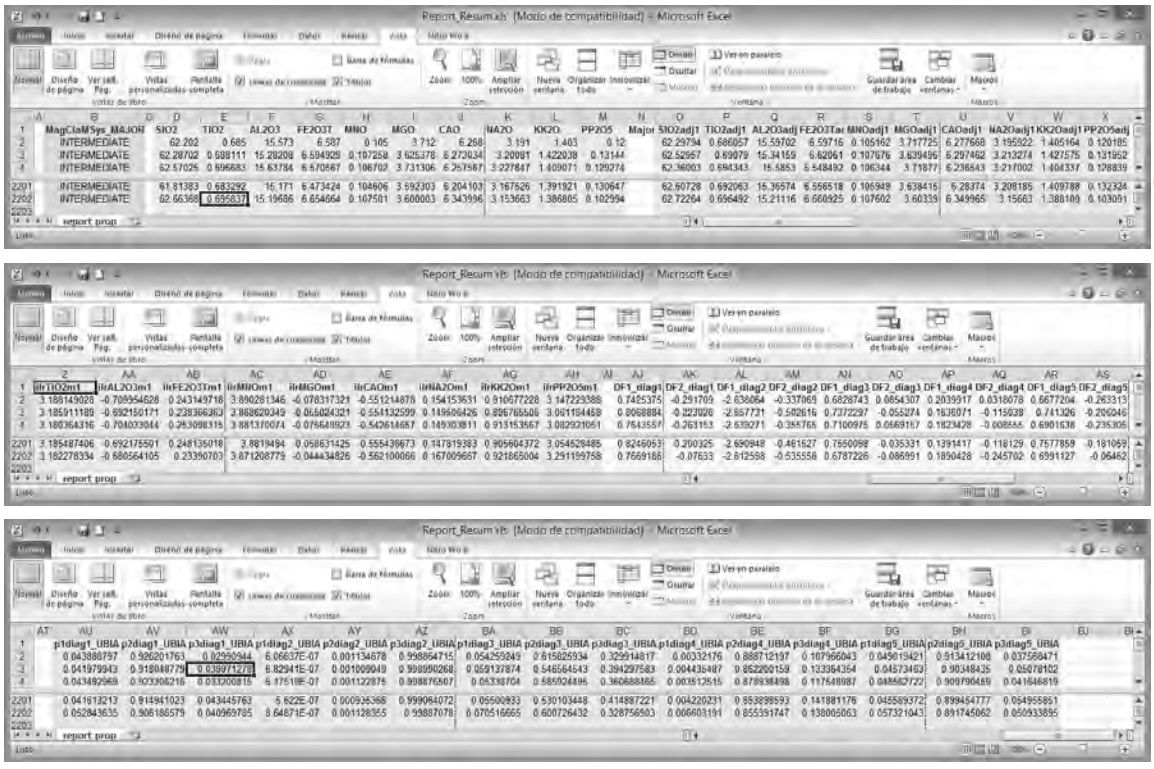

Fig. 18 The Excel output file contains: (a) first section; (b) second section; and (c) third section.

You are free to input your own sample replacing the concentration values in the example file and changing the uncertainty or %RSD values (see Fig. 16).

Apéndice V

Verma, S.P., **Rivera-Gómez, M.A.**, 2017. Transformed major element based multidimensional classification of altered volcanic rocks. Episodes (aceptado).

Contiene un suplemento de 62 páginas.

Episodes Journal of International Geoscience

The Geological Society of Korea
c/o The Korean Federation of Science and Technology Societies, Room #813, 22, Teheran-ro 7-gil, Gangnam-gu, Seoul 06130, Republic of Korea, Tel: +82-2-887-6526, Fax: +82-2-3453-1824
E-mail: episodes.me@gmail.com; URL: http://www.episodes.org

Prof. Surendra P. Verma
Instituto de Energías Renovables
Universidad Nacional Autónoma de México
Temixco, Mor. 62580,
Mexico

May 26, 2017

Dear Prof. Surendra P. Verma,

I am pleased to announce that your revised manuscript entitled "Transformed major element based multidimensional classification of altered volcanic rocks" by Surendra P. Verma and M. Abdelaly Rivera-Gómez, is accepted for publication in the journal. I would appreciate your endeavors to have put in the manuscript.

Sincerely yours,

Daekyo Cheong
Editor, *Episodes*
Professor of Geology
Kangwon National University, Korea

Transformed Major Element based Multidimensional Classification of Altered Volcanic Rocks

Surendra P. Verma [1,*] and M. Abdelaly Rivera-Gómez [2]

[1]Instituto de Energías Renovables, Universidad Nacional Autónoma de México, Temixco, Mor. 62580, Mexico. spv@ier.unam.mx,

[2]Posgrado en Ingeniería, Instituto de Energías Renovables, Universidad Nacional Autónoma de México, Temixco, Mor. 62580, Mexico. marig@ier.unam.mx

[*] Corresponding author.

Submitted to **Episodes**, October 10, 2016; Revised March 10, 2017

Abstract

To fill the gap of the nomenclature of altered igneous rocks, a new exhaustive multidimensional classification scheme consistent with the International Union of Geological Sciences (IUGS) is proposed. Our procedure is based on an extensive database of major element compositions of a total of 32948 relatively fresh rock samples. The database consisted of multinormally distributed samples in terms of their 9 isometric log-ratios. The set of 48 new diagrams along with 76 discriminant functions provided acceptable success rates for most of the 17 root-names and 10 additional sub-root names. A new computer program IgRoClaMSys_ilr was written to facilitate an efficient use of our proposal. Good functioning of our multidimensional procedure was ascertained from 4 test studies of relatively fresh rocks, whereas 5 application studies of altered igneous rocks showed, as expected, greater discrepancy between the new and the IUGS schemes. Another important and novel application of this scheme for inferring the rock type of igneous provenance of siliciclastic sediments was demonstrated through 3 further application studies. IgRoClaMSys_ilr is also equipped with modules for ascertaining robustness of the new scheme with respect to analytical errors and post-emplacement compositional changes.

Key words: rock classification; TAS scheme; multivariate discordant outliers; multidimensional diagrams; isometric log-ratio transformation

Introduction

According to the International Union of Geological Sciences (IUGS), the volcanic rocks can be classified from the well-known TAS (total alkalis versus silica) diagram after the separation of high-Mg rocks (Le Bas *et al.*, 1986; Middlemost, 1994; Le Bas, 2000; Le Maitre *et al.*, 2002). It is also clear that the TAS scheme proposed for 17 root names and 10 more sub-root names (Le Bas *et al.*, 1986) should not be used for the classification of altered rocks. Le Bas *et al.* (1986) made the following points clear in their IUGS proposal (only some salient features are reproduced): (i) "*The classification is purely descriptive*" and "*no genetic relationships are implied*"; (ii) "*It was designed for unaltered volcanic rocks*", however, Middlemost (1994) has proposed a similar scheme for plutonic rocks; and (iii) "*Analyses with $H_2O^+ > 2$ weight per cent or with $CO_2 > 0.5$ per cent should be regarded with suspicion. All analyses must be recalculated to 100 per cent and free of H_2O and CO_2*".

The IUGS classification will not be suitable for metamorphic rocks involving post-emplacement chemical changes. For altered rocks, the IUGS did not recommend any classification procedure (Le Bas *et al.*, 1986; Le Maitre *et al.*, 2002). The available schemes, such as Floyd and Winchester (1975, 1978) Winchester and Floyd (1976, 1977), have been shown unsuitable for this purpose (Verma *et al.*, 2010).

The chemical compositions of altered rocks can be considerably modified from their initial concentrations. This includes SiO_2 and total alkalis (Na_2O and K_2O) as well. Besides, the compositional data *per se* are characterized by a constant sum and closure problem (e.g.

Chayes, 1960; 1978; Butler, 1979, 1982) and certain statistically coherent solutions are required (e.g. Aitchison, 1984, 1986; 1999; Egozcue *et al.*, 2003; Verma, 2015). The constant sum also renders that concentrations of *all* elements, whether mobile or immobile, will change if the rock is altered after its emplacement (Verma, 2015; Verma et al., 2016a, 1017a).

The IUGS has recommended that the classification of plutonic rocks be achieved through mineralogical considerations (e.g., Streckeisen, 1966, 1967; Le Bas *et al.*, 1986; Le Maitre *et al.*, 2002). However, there are certain well documented problems with the use of ternary diagrams (Butler, 1979; Verma, 2012, 2015). Nevertheless, the use of chemical classification for plutonic rocks consistent with the TAS scheme was suggested by Middlemost (1994). Such a classification will be especially useful when precise modal compositions are not available, being the case of most modern geochemical studies. However, this classification scheme meant for fresh rocks will not be applicable to altered rocks.

We propose a statistically coherent solution to the problem of altered rock nomenclature in terms of all 17 root-names and 10 additional sub-root names for volcanic and plutonic rocks in the multidimensional space of all major element log-ratios. The new multidimensional scheme is evaluated from fresh igneous rocks not included in the original database and its application to altered volcanic or plutonic rocks is suggested as an essential step towards an adequate classification. A novel application is also documented for deciphering the rock type of igneous provenance of siliciclastic sediments.

Methods

Database

A worldwide representative database of major element compositions of relatively fresh Neogene igneous rocks was established. A total of 32948 samples with their schematic locations in Figure 1 are summarized in Table S1 (see Supplementary data file available for downloading from the journal website, as well as from our website tlaloc.ier.unam.mx). The samples compiled from over 1000 papers were first classified from the IUGS scheme applied through the IgRoCS computer program (Verma and Rivera-Gómez, 2013). A synthesis of the complete database is available from http://tlaloc.ier.unam.mx/index.html.

For the proposal of the new scheme, major elements were adjusted to 100% on an anhydrous basis with total Fe as $Fe_2O_3^t$ from equations listed in Table S2. The conversion to $Fe_2O_3^t$ was achieved from the first equation in Table S2. This equation will be useful, irrespective of whether Fe was reported as FeO^t or as its two oxidation varieties FeO and Fe_2O_3. The use of FeO^t instead of $Fe_2O_3^t$ for the proposal of our multivariate classification technique will not change the conclusions; only the coefficients of the discriminant function equations will change. The major element adjusted data were then transformed to isometric log-ratios from equations of Table S3. The conversion of Fe and later adjustment to 100% anhydrous, render the database more uniform and suitable for their log-ratio transformation.

Log-ratio transformation and multinormality tests

Isometric log-ratio (ilr) transformation of Egozcue *et al.* (2003) was used. The other transformations (additive and centred log-ratios of Aitchison, 1986) would provide the same final results for any given database (Verma, 2015). The multinormality test (Wilks, 1963; Barnett and Lewis, 1994; Rencher, 2002) was applied through a new computer program DOMuDaF by Verma *et al.* (2016a), which has also been successfully used by Verma *et al*. (2017a) for inferring discordancy of multivariate outliers and proposing new a magma type classification scheme. Thus, only the multinormally distributed samples in terms of their 9 log-ratios were considered.

Linear discriminant and canonical analysis

The multinormally distributed ilr data of 32948 samples were used for the application of the multivariate technique of linear discriminant analysis (LDA) and canonical analysis (Table S1; the individual transformed data are not shown here but will be available as Excel files from http://tlaloc.ier.unam.mx/index.html). The tests for equality of group means show that all 9 log-ratios (ilr1TiM to ilr9PM) have statistically significant differences among the four main classes or groups of magma types at a low significance level approaching 0.000000 (Table S4). All ratios can therefore be used for further analysis. Similarly significant differences were also observed for different rock types but are not reported here to keep the paper short.

The complete database of multinormally distributed isometric log-ratios of 32948 (1505 ultrabasic, 12204 basic, 11750 intermediate and 7489 acid; Table S1) rock samples

was used for proposing a set of 48 new diagrams (only a few diagrams are shown in the Supplementary file) and 76 discriminant functions (all equations are listed in the Supplementary file). After carrying out LDA, probabilities for individual samples were calculated from the method outlined by Agrawal (1999), Verma and Agrawal (2011) or Verma and Verma (2013). They were used in this work to decide the classification field in which a given sample will plot. For probability calculations, group centroids represented by the mean values were used, because this statistical parameter would provide the best estimate of the central tendency when appropriate discordancy tests are used for identifying and separating discordant outliers from the datasets (Verma *et al*., 2016b, 2017b).

Computer program for classification for altered igneous rocks

For an efficient application of the new multidimensional scheme, a computer program IgRoClaMSys_ilr (**Ig**neous **Ro**ck **Cla**ssification **M**ajor-element based **Sys**tem from **i**sometric **l**og-**r**atios) was written in Java Framework ZK (Figure 2). Before using the program, the user must make sure that the rocks to be processed in IgRoClaMSys_ilr are not of high-Mg type (Le Bas, 2000). For such fresh rocks, the original criteria (Le Bas, 2000) can be used but, for altered rocks, it may be necessary to first use an unpublished computer program HMgClaMSys_mlr (Verma *et al*., 2016a; downloadable from http://tlaloc.ier.unam.mx/index.html) in order to ascertain the high-Mg nature of altered rocks. If the rocks are classified as of high-Mg type, HMgClaMSys_mlr will provide their nomenclature (komatiite, meimechite, picrite, and boninite), consistent with the IUGS (Le Bas, 2000).

The first part of IgRoClaMSys_ilr concerns data validation and transformation (Tables S2 and S3). The information on whether one is dealing with volcanic or plutonic rocks is to be provided. Consequently, IgRoClaMSys_ilr decides the appropriate way to process the data. Calculations involve the probability values for all competing rock types corresponding to different diagram sets. Plotting of samples in diagrams is not at all needed. The rock is given the name for which the probability is highest (Figure 2). IgRoClaMSys_ilr reports the results as two different Excel output files (a brief or an extensive report at user´s choice; as the default option, only brief report is generated). This program will be available on http://tlaloc.ier.unam.mx/index.html to interested users for online processing of their major element data.

The modules in IgRoClaMSys_ilr include the following: (a) Conventional application to older or altered igneous rocks as well as the inference for igneous rock type provenance of siliciclastic sediments; (b) Robustness against analytical errors or uncertainties; and (c) Robustness of the new classification for post-emplacement alteration changes.

Results

New multidimensional scheme

The complete database was subdivided into four magma types, for which 10 multidimensional discriminant functions (equations S1 to S10 in Table S5) in 5 DF1-DF2 type diagrams (Figure S1a-e) were proposed. The probability-based boundary coordinates in these five diagrams are listed in Table S6. The percent success in these diagrams (Figure S1a-e) varied from 79.3% to 99.3% (Table S7). One sample (ME90-11; Binard *et al.*, 1993)

was used to illustrate the procedure. According to the IUGS scheme, this is an ultrabasic rock; the data are plotted in Figure 1a-e (filled diamond) and the respective probability values are summarized in Table S8. The final synthesis of percent probability (%prob of 70.8%; Table S8) from the new scheme clearly confirmed that this is an ultrabasic rock. Because a given field is always absent in any set of such diagrams (Figure S1a-e), the final percent probability for any given field can never reach 100%. The overall percent success (correct classification as a synthesis of all five diagrams; Figure 1a-e) for the entire database varied from about 76.8% for basic to 92.3% for ultrabasic rocks (Table S9). This division was followed by 17 root and 10 sub-root names.

The ultrabasic rocks were subdivided by 10 discriminant functions (equations S11 to S20 in Table S10) and 5 diagrams (Figure S2a-e; probability-based boundaries in Table S11) as basanite, tephrite, picrobasalt and foidite. The percent success varied from about 76% to 92.1% (Table S12). The same sample ME90-11 (Binard *et al.*, 1993; filled diamond symbol in Figure 2a-e) was used to illustrate the probability concept in these diagrams, where the IUGS name basanite was confirmed from the new classification scheme (total probability value for this field 77%; Table S13). The overall percent success (correct classification) varied from 78% for picrobasalt to about 89% for ultrabasic tephrite (Table S14).

These ultrabasic rocks were further subdivided for their sub-root names. Basanite as basanite, melanephelinite and nephelinite varieties (2 discriminant function equations S21 and S22 in Table S15; Figure S3a); picrite as basanite, melanephelinite and nephelinite varieties (2 discriminant function equations S23 and S24 in Table S16; Figure S3b); and foidite also as basanite, melanephelinite and nephelinite varieties (2 discriminant function

equations S25 and S26 in Table S17; Figure S3c). Probability-based boundaries in Figure S3a-c, are provided in Table S18. The percent success varied from about 84% to 98%, with the exception of foidite, basanite represented by only 7 samples (Table S19). The ultrabasic basanite, basanite sample ME90-11 (IUGS classification) used for illustration (Figure S3a) proved to have the same name from the present scheme (percent probability of about 0.8123 for the basanite subfield (Table S20).

The basic rocks were first subdivided as basalt (B), trachybasalt (TB), group of basanite, tephrite and foidite (BsnTepFoi), and group of basaltic trachyandesite, phonotephrite, tephriphonolite and phonolite (BtaPhtTphPh). The discriminant function equations S27 to S36 are listed in Table S21. It is really not necessary to construct diagrams and plot samples therein. Nevertheless, we provide the boundary coordinates (Table S22) in case someone wants to actually plot the samples and construct diagrams. Table S23 gives the percent success values for each of the five diagrams and Table S24 lists the overall success for this four-fold division of basic rocks.

Basalt can be subdivided into its two varieties (alkali and subalkali basalts) from the discriminant function (equation S37 in Table S25). The percent success for this rock type was high (95.7% for alkali basalt and 91.4% for subalkali basalt; Table S26). Similarly, trachybasalt was subdivided as hawaiite and potassic varieties (discriminant function equation S38; Table S27). The success values for this subdivision were also high (94.2% for hawaiite and 86.9% for potassic variety or sub-root name; Table S28).

The group BsnTepFoi was separated into three rock types (basanite, tephrite, and foidite) from the discriminant function equations S39 and S40 (Table S29). The

probability-based boundary coordinates are listed in Table S30. The percent success values for this three-fold division varied from 84.3% to 95.1% (Table S31). Using equations S41 and S42 (Table S32), the basanite was further subdivided three subvarieties (basanite, melanephelinite, and nephelinite). Similarly, tephrite was subdivided into the same three subvarieties from equations S43 and S44 (Table S33) and foidite into two subvarieties (melanephelinite and nephelinite) from equation S45 (Table S34). The boundary coordinates for the basanite and tephrite subdivision are listed in Table S35. The percent success values ranged from 87.3%-93% for basanite, 84%-91% for tephrite, and 100% for foidite (Table S36).

The group BtaPhtTphPh was also divided into three rock types (basaltic trachyandesite, phonotephrite, and combined tephriphonolite and phonolite) from equations S46 and S47 (Table S37). The field boundaries are listed in Table S38. The percent success values varied from about 83% to 93.6% (Table S39). Basaltic trachyandesite was subdivided as two subvarieties (mugearite and shoshonite) from equation S48 (Table S40) with percent success of 96.4% and 88.9%, respectively (Table S41). The two rock types (tephriphonolite and phonolite) were divided into these two varieties from equation S49 (Table S42) with success values of 100% (Table S43).

The intermediate rocks were first divided as basaltic andesite (BA), andesite (A), group of basaltic trachyandesite, trachyandesite and trachyte (BtaTAT), and group of phonotephrite, tephriphonolite and phonolite (PhtTphPh). The relevant discriminant function equations S50 to S59 and field boundaries are given in Tables S44 and S45, respectively. Table S46 provides the percent success values that vary from 83.5% to 95.6%, whereas Table S47 reports the overall success rates for the classification of the intermediate

rocks as four rock groups which varied from 80.8% for the group of BtaTAT to 91.5% for basaltic andesite.

The intermediate rock group BtaTAT was further divided into the three rock types (basaltic trachyandesite, trachyandesite, and trachyte) from discriminant function equations S60 and S61 (Table S48; boundary coordinates in Table S49) with percent success values of 85.5% to 94.8% (Table S50). The basaltic trachyandesite rocks were further subdivided for sub-root rock names of mugearite and shoshonite from equation S62 (Table S51), with percent success values of 98.5% and 82.9%, respectively (Table S52). Trachyandesite rocks were similarly subdivided as its two sub-root rock names of benmorite and latite (equation S63; Table S53) with percent success values of 97.3% and 78.9%, respectively (Table S54). The intermediate trachyte rocks were subdivided as trachyte and peralkaline trachyte from discriminant function equation S64 (Table S55) and percent success values of 96.2% and 90% were obtained for this subdivision (Table S56).

The intermediate rock group PhtTphPh was divided into three rock types phonotephrite (Pht), tephriphonolite (Tph), and phonolite (Ph) from equations S65 and S66 (Table S57; boundary coordinates in Table S58) with percent success values listed in Table S59.

Finally, the acid rocks were first divided in five diagram set as dacite, trachydacite, trachyte, and rhyolite (equations S67 to S76; Table S60; boundary coordinates in Table S61). The percent success values for individual diagrams varied from 72.9% to 98.5% (Table S62), whereas the overall success values ranged from 77.6% for trachyte to 86.9% for dacite (Table S63).

The acid trachyte rocks were subdivided as two sub-root names (trachyte and peralkaline trachyte) from equation S77 (Table S64) and percent success values of 95.9% and 88.9% were obtained (Table S65). Finally, rhyolites were subdivided as rhyolite and peralkaline rhyolite from equation S78 (Table S66) obtaining success values of 99.4% and 95.9%, respectively (Table S67).

DISCUSSION

This section is subdivided into four subsections: (1) Overall success of the alternative IgRoClaMSys_ilr scheme for assigning root and sub-root names for the complete database evaluated in the light of the IUGS scheme as a reference; (2) Success of the new scheme for individual test studies of fresh rocks also evaluated against the IUGS scheme; (3) Application of IgRoClaMSys_ilr to altered igneous rocks evaluated against the original IUGS scheme proposed for fresh rocks only; (4) Additional application studies for igneous provenance of siliciclastic sediments; and (5) Mention of the additional modules of IgRoClaMSys_ilr for ascertaining the robustness of the new scheme with respect to analytical errors and post-emplacement compositional changes.

Overall success for the alternative IgRoClaMSys_ilr scheme

The complete database (32948 analyses) was first processed to evaluate the correctness or percent success of the classification of 17 root names (Table 1) and all 29 root and sub-root names (Table S68). The IUGS scheme (Le Bas *et al.*, 1986) was used as reference. For

12 root names, the percent success was relatively high 62.4% for tephriphonolite to 86.7% for rhyolite (Table 1). For the remaining 5 root names, it was lower, although for only two cases (picrobasalt and phonotephrite), it could be considered unacceptably low (Table 1). Similarly, for 29 root and sub-root names of Le Bas *et al*. (1986) percent success values of > 50% were obtained for 22 rock types, with the remaining rock types showing lower values (Table S68). Nevertheless, these percent success values are significantly higher than those obtained for the available alternative diagrams of Floyd and Winchester (1975, 1978) Winchester and Floyd (1976, 1977) as demonstrated by Verma *et al.* (2010).

Testing of the new rock classification scheme from fresh rocks

This IgRoClaMSys_ilr scheme was then applied for testing from relatively fresh rock data not included in the initial database (Tests T1 to T4 in Figure 1).

For the first test (T1; Figure 1; Table S69), the data for 62 Quaternary volcanic rock samples of Kaula volcanics, Hawaiian Islands (Garcia *et al*., 2016) indicated from the IUGS classification that 14 rocks were ultrabasic (3 basanite, basanite; 4 basanite, melanephelinite; 4 foidite, melanephelinite; 1 foidite, nephelinite; and 2 picrobasalt) and 48 basic (40 basalt, alkali; 1 basalt, subalkali; 6 basanite, basanite; and 1 trachybasalt, hawaiite). In terms of magma types, the IgRoClaMSys_ilr scheme provided 10 ultrabasic and 52 basic rocks, thus misclassifying only 4 ultrabasic as basic rocks. Thus, 58 out of 62 magma types as correctly classified amounted to about 94% correct classification. Now, in terms of rock types, the IgRoClaMSys_ilr correctly classified 40 samples of alkali basalt; 1 subalkali basalt; 1 basanite, basanite; and 4 basanite, melanephelinite (Table S69)

amounting to about 74% correct classification. The incorrect classification was mainly the "neighbour" rock types, not drastically different from the original IUGS rock types (Table S69) because 8 basanite, basanite were classified as alkali basalt; 1 foidite, nephelinite as basanite, basanite; 4 foidite, melanephelinite as basanite, melanephelinite; 2 picrobasalt as alkali basalt; and 1 trachybasalt, hawaiite as alkali basalt.

The next test (T2; Figure 1; Table S70) was from Holocene volcanic rocks of San Antonio volcano, Tacaná volcanic complex, Mexico-Guatemala (Mora *et al*., 2004). Out of 14 rock samples (IUGS: 12 intermediate and 2 acid rocks), 13 were correctly classified in terms of magma types (IgRoClaMSys_ilr: 11 intermediate and 3 acid rocks). In terms of rock types, 3 basaltic andesite, 8 andesite, and 1 rhyolite were correctly classified, with only 2 rocks (1 andesite and 1 rhyolite) incorrect as dacitic rocks.

Test T3 (Figure 1; Table S71; Di Piazza *et al*., 2015) included 7 Quaternary volcanic rock samples of Turrialba volcano, Costa Rica. Out of 7 intermediate rocks, 6 proved to be as such, with the remaining classified as an acid rock, whereas, in terms of rock types, 5 (3 basaltic andesite and 2 andesite) were correctly classified (Table S71). One trachyandesite, benmorite was wrongly classified as andesite and 1 andesite as trachyte.

For Test T4 (Figure 1; Table S72; Shaw *et al*., 2003), 32 Miocene-Pleistocene volcanic rock samples of Harrat Ash Shaam, Jordan were compiled. From the IUGS scheme, they were classified as 9 ultrabasic (8 basanite, basanite; and 1 basanite, nephelinite) and 23 basic (17 basalt, alkali; and 6 basalt, subalkali) rocks. The IgRoClaMSys_ilr identified 6 samples as ultrabasic and 26 as basic, thus correctly classifying 29 samples for their magma types (Table S72), amounting to about 90% success. In terms of rock types, 29 samples (16

alkali basalt; 6 subalkali basalt; 6 basanite, basanite; and 1 basanite, nephelinite) were correctly classified by IgRoClaMSys_ilr. Only 2 basanite, basanite were misclassified as 2 alkali basalt and 1 alkali basalt as subalkali basalt (Table S72).

Thus, all four tests clearly show that the new scheme works well for the classification of fresh rocks.

Application to older igneous rocks

For the new IgRoClaMSys_ilr scheme to be useful for the classification of older rocks, there should be more differences or inconsistencies with the IUGS scheme put forth for fresh rocks only. We present 4 application case studies (A1 to A4; Figure 1) to illustrate the usefulness of IgRoClaMSys_ilr.

The first application is for the Paleoproterozoic Star Lake pluton, Canada (Application study A1; Figure 1; Janser, 1992, 1994). Out of 78 analyses, 33 intermediate and 23 acid rocks from the IUGS scheme also proved to be as such from the IgRoClaMSys_ilr (Table S73). Nine basic and 13 acid rocks were classified as intermediate rocks by the new scheme, amounting to about 28% incorrect classification of magma types. The classification of rock types was even worse because only 38 samples (out of 78; Table S73) were correctly classified, amounting to only 49% correct classification. Because the studied rocks are plutonic, the equivalent plutonic rock names are provided in the last column (Table S73).

Our next application is for Paleozoic volcanic rocks of Juchatengo Complex, Mexico (Application study A2; Figure 2; Table S74; Grajales-Nishimura *et al*., 1999). Out of 13 samples classified as basic rocks from the IUGS scheme, 4 were classified as intermediate rocks from the IgRoClaMSys_ilr. Similarly, for their rock types, 5 out of 13 were differently classified by the IgRoClaMSys_ilr (Table S74).

Another application is concerned with Paleoproterozoic lava and sheeted dyke samples from Jormua ophiolite, Finland (Application study A3; Figure 2; Table S75; Peltonen *et al*., 1996). Twenty-four out of 33 basic rock samples (according to the IUGS scheme) were classified as basic rocks, with the remaining 9 samples differently classified as ultrabasic (3 samples) and intermediate (6 samples). Similarly, only 21 out of 33 samples (amounting to about 64%) were classified as the same rock types by both schemes (Table S75).

The next application is to Mesoproterozoic rocks of Delhi area, India (Application study A4; Figure 2; Table S76; Abu-Hamatteh, 2000). From the IUGS scheme, 24 rock samples were classified as 1 ultrabasic, 13 basic, and 10 intermediate rocks, whereas from the IgRoClaMSys_ilr, the same rocks were subdivided as 2 ultrabasic, 20 basic, and 2 intermediate rocks. Similarly, The IUGS scheme determined these rocks as 1 picrobasalt, 2 alkali basalt, 11 subalkali basalt, 6 basaltic andesite, 2 basaltic trachyandesite (1 mugearite and 1 shoshonite), and 2 andesite. From the IgRoClaMSys_ilr scheme, 10 subalkali basalt and 1 basaltic andesite samples were classified as such, which represented only about 46% agreement between the two schemes. However, the two schemes provided different names for more (13) samples (Table S76), which once again suggests that the new scheme should be used for the nomenclature of altered rocks.

The final application to Archaean mafic magmatism in the Kalgoorlie area of the Yilgarn craton, Western Australia (Application study A5; Figure 2; Table S77; Bateman *et al*., 2001). The IUGS scheme indicated that the magma types of 70 samples were distributed as follows: 2 ultrabasic, 31 basic, and 37 intermediate. The IgRoClaMSys_ilr scheme, on the other hand, classified them as 1 ultrabasic, 63 basic, and 6 intermediate rocks (Table S77). Only 30 basic and 5 intermediate rocks were consistently classified by both schemes (IUGS and IgRoClaMSys_ilr). The remaining 35 samples (amounting to 50%) were classified differently (Table S77) for magma types. The two classification schemes differed even more for rock types because 41 samples out of 70 (amounting to 59%) were classified differently (Table S77).

Because the good functioning of the new classification scheme was documented from the initial database as well as 4 independent tests, these significantly higher differences between the new and IUGS schemes for older rocks make it clear that the new scheme (IgRoClaMSys_ilr) should be used for the nomenclature of altered rocks.

Application to igneous provenance of siliciclastic sediments

As an innovation, the new IgRoClaMSys_ilr scheme can be used for deciphering igneous provenance of sediments and sedimentary rocks. We illustrate this application from 3 studies (sediment application SA1 to SA3; data from Pinto *et al*., 2004; Odoma *et al*., 2015; and Ishiga *et al*., 2000, respectively). These applications contrast the provenance suggested by the original authors (Pinto *et al*., 2004; Odoma *et al*., 2015).

Pinto *et al*. (2004) presented sediment data from Bolivia and Chile (Figure 2; adjusted major element chemical data in Table S78). Twelve samples from Bolivia indicated an acid and mainly rhyolitic provenance (12 acid rocks; 8 rhyolites, 3 trachydacite, and 1 dacite; Table S78). On the other hand, 26 Chilean samples were more consistent with an intermediate and andesitic provenance (21 intermediate and 5 acid rocks; 19 andesite, 3 dacite, 1 each basaltic andesite, trachyandesite, trachydacite and rhyolite; Table S78).

The second sediment application study (SA2; Figure 2; Table S79) concerns sediments from Enugu, southeastern Nigeria (Sediment application study SA2; Odoma *et al*., 2015). The provenance is likely of basic rocks (6 out of 7 samples; Table S79). More specifically, it appears to be basaltic trachyandesite, mugearite (4 samples; 2 phonolite, and 1 rhyolite; Table S79), i.e., basic alkaline provenance.

The final application is for coastal lagoon sediments from south-west Japan (SA3; Figure 2; Table S80; Ishiga *et al*., 2000). The sediment provenance can be inferred as from intermediate rocks (43 out of 49 rocks; about 88%) and more specifically, basaltic andesite rocks (37 out of 49 rocks; about 76%).

Thus, igneous provenance of sediments can be successfully inferred from the IgRoClaMSys_ilr.

Robustness of the new multidimensional classification scheme

The additional modules programmed in IgRoClaMSys_ilr enable the user to determine the robustness of their own samples (one at a time) with respect to analytical errors or

uncertainties as well as post-emplacement compositional changes. The appropriate templates are included for an efficient use of these capabilities. The user is free to input data of an actual sample in the appropriate Excel file and watch the robustness of the multidimensional procedure.

Conclusions

The new multidimensional classification scheme proposed from linear discriminant and canonical analysis of 9 isometric log-transformed ratios of all major elements showed high percent success values (generally > 50%) for most of the 17 root names and 10 sub-root names. New computer program IgRoClaMSys_ilr for online processing of data would facilitate its use by all those interested in correctly classifying old or altered igneous rocks as compared to the IUGS and other alternative procedures.

The available IUGS scheme is certainly suitable for the classification of fresh rocks and was used as a reference for the evaluation of the new scheme. Independent evaluation of the IgRoClaMSys_ilr scheme from data not used for proposing it fully confirmed its good functioning. The application studies documented in this work clearly suggest that the new scheme should be used for the nomenclature of altered igneous rocks. An innovative application was also suggested for inferring igneous provenance of siliciclastic sediments and sedimentary rocks.

Acknowledgements

This work constitutes a part of the second author´s (MARG) doctoral thesis in preparation under the guidance of the first author (SPV). This work was funded by DGAPA-PAPIIT grant IN100816 and IER-UNAM internal grant to the first author. We are grateful to two reviewers (Vinod K. Singh and Rajesh K. Srivastava) and the editors (Fareeduddin and Bokyun Ko) for appreciation of our work and comments to help us improve our presentation. Alfredo Quiroz-Ruiz is thanked for the computing facility and server maintenance.

References

Abu-Hamatteh, J.H.S., 2002. Geochemistry and tectonic framework of Proterozoic mafic metavolcanics of Aravalli-Delhi Orogen, NW India. Chemie der Erde, v. 62, pp. 123-144.

Agrawal, S., 1999. Geochemical discrimination diagrams: a simple way of replacing eye-fitted boundaries with probability based classifier surfaces. Journal of the Geological Society of India, v. 54, no. 4, pp. 335-346.

Aitchison, J., 1984. Statistical analysis of geochemical compositions. Mathematical Geology, v. 16, no. 6, pp. 531-564.

Aitchison, J., 1986. The statistical analysis of compositional data. London, UK: Chapman and Hall.

Aitchison, J., 1999. Logratios and natural laws in compositional data analysis. Mathematical Geology, v. 31, no. 5, pp. 563-580.

Barnett, V., and Lewis, T. 1994. Outliers in statistical data. Third edition, Chichester: John Wiley & Sons.

Bateman, R., Costa, S., Swe, T., and Lambert, D., 2001. Archaean mafic magmatism in the Kalgoorlie area of the Yilgarn Craton, western Australia: a geochemical and Nd isotopic study of the petrogenetic and tectonic evolution of a greenstone belt. Precambrian Research, v. 108, pp. 75-112.

Binard, N., Maury, R.C., Guille, G., Talandier, J., Gillot, P.Y., and Cotten, J., 1993. Mehetia island, South Pacific: geology and petrology of the emerged part of the Society hot spot. Journal of Volcanology and Geothermal Research, v. 55, pp. 239-260.

Butler, J.C., 1979. Trends in ternary petrologic variation diagrams - fact or fantasy? American Mineralogist, v. 64, no. 9-10, pp. 1115-1121.

Butler, J.C., 1982. The closure problem as reflected in discriminant function analysis. Chemical Geology, v. 37, pp. 367-375.

Chayes, F., 1960. On correlation between variables of constant sum. Journal of Geophysical Research, v. 65, no. 12, pp. 4185-4193.

Chayes, F., 1978. Ratio correlation. A manual for students of petrology and geochemistry. Chicago and London: The University of Chicago Press.

Di Piazza, A., Rizzo, A.L., Barberi, F., Carapezza, M.L., De Astis, G., Romano, C., and Sortino, F., 2015. Geochemistry of the mantle source and magma feeding system beneath Turrialba volcano, Costa Rica. Lithos, v. 232, pp. 319-335.

Egozcue, J.J., Pawlowsky-Glahn, V., Mateu-Figueras, G., and Barceló-Vidal, C., 2003. Isometric logratio transformations for compositional data analysis. Mathematical Geology, v. 35, no. 3, pp. 279-300.

Floyd, P.A., and Winchester, J.A., 1975. Magma type and tectonic setting discrimination using immobile elements. Earth and Planetary Science Letters, v. 27, no. 2, pp. 211-218.

Floyd, P.A., and Winchester, J.A., 1978. Identification and discrimination of altered and meta-morphosed volcanic rocks using immobile elements. Chemical Geology, v. 21, no. 3-4, pp. 291-306.

Garcia, M.O., Weis, D., Jicha, B.R., Ito, G., and Hanano, D., 2016. Petrology and geochronology of lavas from Ka'ula Volcano: Implications for rejuvenated volcanism of the Hawaiian mantle plume. Geochimica et Cosmochimica Acta, v. 185, pp. 278-301.

Grajales-Nishimura, J.M., Centeno-García, E., Keppie, J.D., and Dostal, J., 1999. Geochemistry of Paleozoic basalts from the Juchatengo complex of southern México: tectonic implications. Journal of South American Earth Sciences, v. 12, pp. 537-544.

Ishiga, H., Nakamura, T., Sampei, Y., Tokuoka, T., Takayasu, K., 2000. Geochemical record of the Holocene Jomon transgression and human activity in coastal lagoon

sediments of the San'in district SW Japan. Global and Planetary Change, v. 25, pp. 223-237.

Janser, B.W., 1992.The geology, geochemistry, and metallogeny of the Star lake area, northern Saskatchewan [Master´s]. University of Sasketchawan.

Janser, B.W., 1994. The Star lake pluton, La Ronge domain, northern Saskatchewan: petrogenesis of a Proterozoic island-arc pluton. Precambrian Research, v. 70, pp. 145-164.

Le Bas, M.J., 2000. IUGS reclassification of the high-Mg and picritic volcanic rocks. Journal of Petrology, v. 41, no. 10, pp. 1467-1470.

Le Bas, M.J., Le Maitre, R.W., Streckeisen, A., and Zanettin, B., 1986. A chemical classification of volcanic rocks based on the total alkali-silica diagram. Journal of Petrology, v. 27, no. 3, pp. 745-750.

Le Maitre, R.W., Streckeisen, A., Zanettin, B., Le Bas, M.J., Bonin, B., Bateman, P., Bellieni, G., Dudek, A., Schmid, R., Sorensen, H., and Woolley, A.R., 2002. Igneous rocks. A classification and glossary of terms: recommendations of the International Union of Geological Sciences Subcommission of the Systematics of Igneous Rocks. 2nd ed. Cambridge: Cambridge University Press.

Middlemost, E.A.K., 1994. Naming materials in the magma/igneous rock system. Earth Science Reviews, v. 37, no. 3-4, pp. 215-224.

Mora, J.C., Macías, J.L., García-Palomo, A., Arce, J.L., Espíndola, J.M., Manetti, P., Vaselli, O., and Sánchez, J.M., 2004. Petrology and geochemistry of the Tacaná

Volcanic complex, Mexico-Guatemala: evidence for the last 40 000 yr of activity. Geofísica Internacional, v. 43, no. 3, pp. 331-359.

Odoma, A.N., Obaje, N.G., Omada, J.I., Idakwo, S.O., Erbacher, J., 2015. Mineralogical, chemical composition and distribution of rare earth elements in clay-rich sediments from southeastern Nigeria. Journal of African Earth Sciences, v. 102, pp. 50-60.

Peltonen, P., Kontinen, A., and Huhma, H., 1996. Petrology and geochemistry of metabasalts from the 1.95 Ga Jormua ophiolite, northeastern Finland. Journal of Petrology, v. 37, no. 6, pp. 1359-1383.

Pinto, L., Hérail, G., Moine, B., Fontan, F., Charrier, R., and Dupré, B., 2004. Using geochemistry to establish the igneous provenances of the Neogene continental sedimentary rocks in the Central Depression and Atliplano, Central Andes. Sedimentary Geology, v. 166, pp. 157-183.

Rencher, A.C., 2002. Methods of multivariate analysis. Second edition, New York: Wiley-Interscience, 708 pp.

Shaw, J.E., Baker, J.A., Menzies, M.A., Thirlwall, M.F., and Ibrahim, K.M., 2003. Petrogenesis of the largest intraplate volcanic field on the Arabian Plate (Jordan): a mixed lithosphere-asthenosphere source activated by lithospheric extension. Journal of Petrology, v. 44, no. 9, pp. 1657-1679.

Streckeisen, A., 1976. To each plutonic rock its proper name. Earth Science Reviews, v. 12, pp. 1-33.

Streckeisen, A.L., 1967. Classification and nomenclature of igneous rocks. Neues Jahrbuch für Mineralogie-Abhandlungen, v. 107, no. 2-3, pp. 144-240.

Verma, S.P., 2012. Geochemometrics. Revista Mexicana de Ciencias Geológicas, v. 29, no. 1, pp. 276-298.

Verma, S.P., 2015. Monte Carlo comparison of conventional ternary diagrams with new log-ratio bivariate diagrams and an example of tectonic discrimination. Geochemical Journal, v. 49, no. 4, pp. 393-412.

Verma, S.P., and Agrawal, S., 2011. New tectonic discrimination diagrams for basic and ultrabasic volcanic rocks through log-transformed ratios of high field strength elements and implications for petrogenetic processes. Revista Mexicana de Ciencias Geológicas, v. 28, no. 1, pp. 24-44.

Verma, S.P., and Rivera-Gómez, M.A., 2013. Computer programs for the classification and nomenclature of igneous rocks. Episodes, v. 36, no. 2, pp. 115-124.

Verma, S.P., and Verma, S.K., 2013. First 15 probability-based multi-dimensional discrimination diagrams for intermediate magmas and their robustness against post-emplacement compositional changes and petrogenetic processes. Turkish Journal of Earth Sciences, v. 22, no. 6, pp. 931-995.

Verma, S.P., Rodríguez-Rios, R., and González-Ramírez, R., 2010. Statistical evaluation of classification diagrams for altered igneous rocks. Turkish Journal of Earth Sciences, v. 19, pp. 239-265.

Verma, S. P., Rivera-Gómez, M.A., Díaz-González, L., and Quiroz-Ruiz, A., 2016a. Log-ratio transformed major-element based multidimensional classification for altered High-Mg igneous rocks. Geochemistry Geophysics Geosystems, v. 17, pp. 1-14, doi:10.1002/2016GC006652.

Verma, S.P., Díaz-González, L., Pérez-Garza, J.A., Rosales-Rivera, M., 2016b. Quality control in geochemistry from a comparison of four central tendency and five dispersion estimators and example of a geochemical reference material. Arabian Journal of Geosciences v. 9, Art. 740, pp. 1-14, doi: 10.1007/s1251701627644.

Verma, S.P., Rivera-Gómez, M.A., Díaz-González, L., Pandarinath, K., Amezcua-Valdez, A., Rosales-Rivera, M.A., Verma, S.K., Quiroz-Ruiz, A., Armstrong-Altrin, J.A., 2017a. Multidimensional classification of magma types for altered igneous rocks and application to their tectonomagmatic discrimination and igneous provenance of siliciclastic sediments. Lithos, v. 278-281, pp. 321-330.

Verma, S.P., Díaz-González, L., Pérez-Garza, J.A., Rosales-Rivera, M., 2017b. Erratum to: Quality control in geochemistry from a comparison of four central tendency and five dispersion estimators and example of a geochemical reference material. Arabian Journal of Geosciences v. 10, Art. 24, pp. 1-3, doi: 10.1007/s12517-016-2764-4.

Wilks, S.S., 1963. Multivariate statistical outliers. Sankhya, v. 25, pp. 407-426.

Winchester, J.A., and Floyd, P.A., 1976. Geochemical magma type discrimination: application to altered and metamorphosed basic igneous rocks. Earth and Planetary Science Letters, v. 28, no. 3, pp. 459-469.

Winchester, J.A., and Floyd, P.A., 1977. Geochemical discrimination of different magma series and their differentiation products using immobile elements. Chemical Geology, v. 20, pp. 325-343.

Figure legends

Figure 1: Map for schematic locations of samples used for constructing the database, including locations of tests and application studies.

Figure 2: Schematic flow diagram of the new computer program IgRoClaMSys_ilr. The abbreviations used are as follows: U−ultrabasic; B−basic; I−intermediate; A−acid; BSN−basanite; TEP−tephrite; PB−picrobasalt; FOI−foidite; BSN, bsn−basanite, basanite; BSN, mnp−basanite, melanephelinite; BSN, np−basanite, nephelinite; TEP, bsn−tephrite, basanite; TEP, mnp−tephrite, melanephelinite; TEP, np−tephrite, nephelinite; FOI, bsn−foidite, basanite; FOI, mnp−foidite, melanephelinite; FOI, np−foidite, nephelinite; B−basalt; TB−trachybasalt; BsnTepFoi−group of basic basanite, tephrite, and foidite; BtaPhtTphPh−group of basaltic trachyandesite, phonotephrite, tephriphonolite, and phonolite; B, alk−basalt, alkali; B, subalk−basalt, subalkali; TB, haw−trachybasalt, hawaiite; TB, pot−trachybasalt, potassic; BA−basaltic andesite; A−andesite; BtaTAT−group of basaltic trachyandesite, trachyandesite, and trachyte; BtaPhtTphPh−group of basaltic trachyandesite, phonotephrite, tephriphonolite, and phonolite; Bta, mug−basaltic trachyandesite, mugearite; Bta, sho−basaltic trachyandesite, shoshonite; TA, ben−trachyandesite, benmorite; TA, lat−trachyandesite, latite; T, palk−trachyte, peralkaline; D−dacite; TD−trachydacite; T−trachyte; R−rhyolite; T, palk−trachyte, peralkaline; R palk−rhyolite, peralkaline.

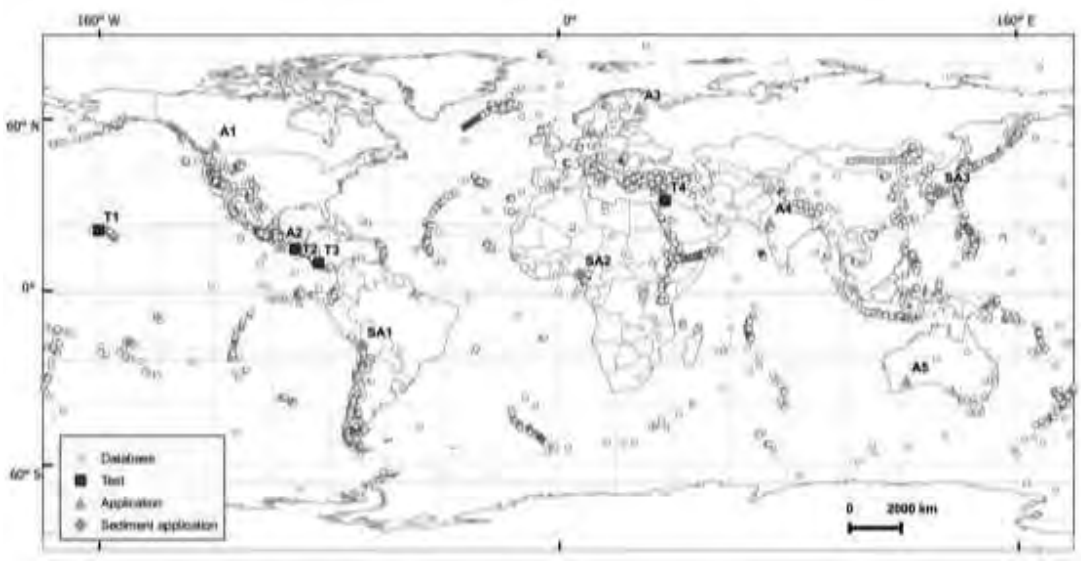
160° W
0°
160° E
60° N
0°
60° S
A1
A2
A3
A4
A5
T1
T2, T3
T4
SA1
SA2
SA3
Database
Test
Application
Sediment application
0
2000 km

Figure 1.

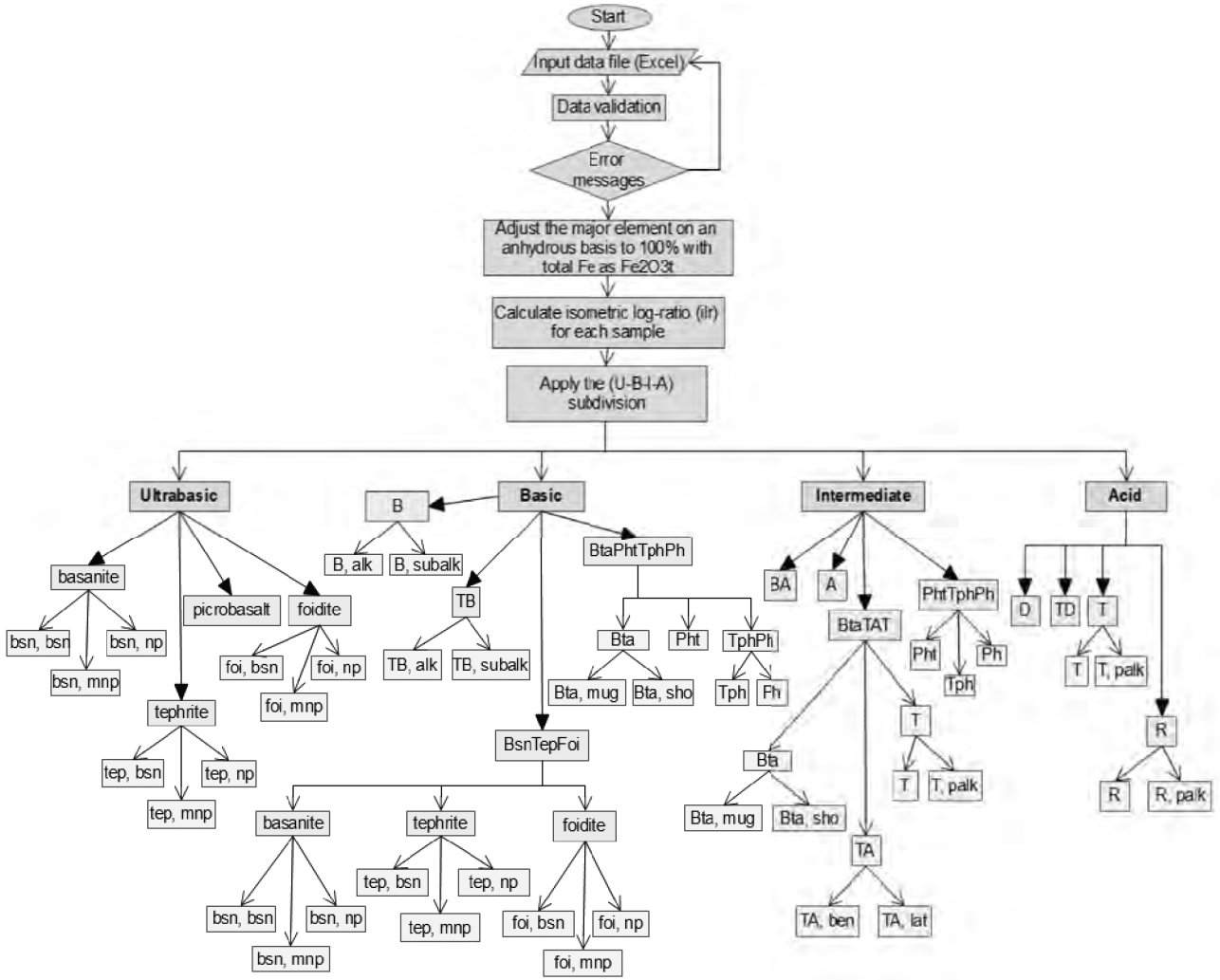
Start
Input data file (Excel)
Data validation
Error messages
Adjust the major element on an anhydrous basis to 100% with total Fe as Fe2O3t
Calculate isometric log-ratio (ilr) for each sample
Apply the (U-B-I-A) subdivision
Ultrabasic
Basic
Intermediate
Acid
B
BtaPhtTphPh
basanite
picrobasalt
foidite
B, alk
B, subalk
TB
bsn, bsn
bsn, np
bsn, mnp
foi, bsn
foi, np
foi, mnp
TB, alk
TB, subalk
Bta
Pht
TphPh
Bta, mug
Bta, sho
Tph
Ph
tephrite
BsnTepFoi
tep, bsn
tep, np
tep, mnp
basanite
tephrite
foidite
bsn, bsn
bsn, np
bsn, mnp
tep, bsn
tep, np
tep, mnp
foi, bsn
foi, np
foi, mnp
BA
A
BtaTAT
PhtTphPh
Pht
Ph
Tph
T
Bta
T
T, palk
Bta, mug
Bta, sho
TA
TA, ben
TA, lat
D
TD
T
T
T, palk
R
R
R, palk

Figure 2.

1

Table 1: Classification of rock types (root names) from the initial database from the new multidimensional classification scheme and comparison with the IUGS classification scheme.

Rock no.	Rock name (IUGS)	no. of samples (IUGS)	Number of samples classified from IgRoClaMSys_ilr in any given field																	Percent success (IgRoClaMSys_ilr)
			1	2	3	4	5	6	7	8	9	10	11	12	13	14	15	16	17	
1	basanite	**1484**	**1073**	189	3	71		65	20	63										72.3
2	tephrite	**312**	1	**245**	1	13		6	1	44		1								78.5
3	picrobasalt	**72**	7	5	**21**	39														29
4	foidite	**268**	12	25	2	**186**				21		22								69.4
5	phonolite	**267**		1			**236**					24				6				88.4
6	basalt	**9349**	616	271	26			**6705**	1317	49			365							71.7
7	trachybasalt	**1486**	259	288				6	**667**	245	3		18							44.9
8	basaltic trachyandesite	**1678**	3	76				1	34	**1359**	13	4	113	8	67					81.0
9	phonotephrite	**341**	7	94					3	140	**49**	41			7					14.4
10	tephriphonolite	**133**		13						13	6	**83**			18					62.4
11	basaltic andesite	**3884**	2	3				540	254	502			**2486**	97						64.0
12	andesite	**4136**								75			258	**3653**	150					88.3
13	trachyandesite	**1538**		4						152	25	30	1	173	**1142**	5		6		74.3
14	trachyte	**1301**					224				18	38		106	65	**725**	23	102		55.7
15	dacite	**2750**												1134	8	8	**1289**	311		46.9
16	trachydacite	**224**												8	1	42	3	**170**		75.9
17	rhyolite	**3725**														93	117	286	**3229**	86.7

2

1

SUPPLEMENT

Transformed Major Element based Multidimensional Classification of Altered Igneous Rocks

Surendra P. Verma[1,*] and M. Abdelaly Rivera-Gómez[2]

Corresponding author E-mail: spv@ier.unam.mx

This file contains Tables S1-S80 and Figures S1-S3.

Table S1: Distribution of rock types in the relatively fresh igneous rock database used for proposing new multidimensional classification scheme.

ultrabasic		basic		intermediate		acid	
Rock type	No. of samples	Rock type	No. of samples	Rock type	No. of samples	Rock type	No. of samples
basanite, basanite	658	basalt, alkali	2005	basaltic andesite	3884	dacite	2750
basanite, melanephelinite	369	basalt, subalkali	7344	andesite	4136	trachydacite	224
basanite, nephelinite	44	trachybasalt, hawaiite	829	basaltic trachyandesite, mugearite	657	trachyte	664
tephrite, basanite	87	trachybasalt, potassic	657	basaltic trachyandesite, shoshonite	648	trachyte, peralkaline	126
tephrite, melanephelinite	45	basanite, basanite	346	trachyandesite, benmorite	474	rhyolite	3337
tephrite, nephelinite	18	basanite, melanephelinite	52	trachyandesite, latite	1064	rhyolite, peralkaline	388
picrobasalt	72	basanite, nephelinite	15	trachyte	451		
foidite, basanite	7	tephrite, basanite	102	trachyte, peralkaline	60		
foidite, melanephelinite	142	tephrite, melanephelinite	49	phonotephrite	13		
foidite, nephelinite	62	tephrite, nephelinite	11	tephriphonolite	101		
phonolite	1	foidite, melanephelinite	40	phonolite	262		
		foidite, nephelinite	17				
		basaltic trachyandesite, mugearite	193				
		basaltic trachyandesite, shoshonite	180				
		phonotephrite	328				
		tephriphonolite	32				
		phonolite	4				
Total no. of samples	**1505**	Total no. of samples	**12204**	Total no. of samples	**11750**	Total no. of samples	**7489**

Table S2: Adjustment of major elements used for computing the isometric log-ratio transformations.

Function	Equation for adjustment
Fe conversion equation	When $Fe_2O_3^t$ concentration is not reported; i.e., when either FeO^t or both Fe_2O_3 and FeO are available, the following simple equation is used for calculating $Fe_2O_3^t$ from the reported data:
$Fe_2O_3^t$	$= Fe2O3 + [FeO \times \frac{159.6882}{(2 \times 71.8444)}]$
SiO_2A	$= \frac{100 \times SiO2}{[SiO2 + TiO2 + Al2O3 + Fe2O3t + MnO + MgO + CaO + Na2O + K2O + P2O5)]}$
TiO_2A	$= \frac{100 \times TiO2}{[SiO2 + TiO2 + Al2O3 + Fe2O3t + MnO + MgO + CaO + Na2O + K2O + P2O5)]}$
Al_2O_3A	$= \frac{100 \times Al2O3}{[SiO2 + TiO2 + Al2O3 + Fe2O3t + MnO + MgO + CaO + Na2O + K2O + P2O5)]}$
$Fe_2O_3^tA$	$= \frac{100 \times Fe2O3t}{[SiO2 + TiO2 + Al2O3 + Fe2O3t + MnO + MgO + CaO + Na2O + K2O + P2O5)]}$
MnOA	$= \frac{100 \times MnO}{[SiO2 + TiO2 + Al2O3 + Fe2O3t + MnO + MgO + CaO + Na2O + K2O + P2O5)]}$
MgOA	$= \frac{100 \times MgO}{[SiO2 + TiO2 + Al2O3 + Fe2O3t + MnO + MgO + CaO + Na2O + K2O + P2O5)]}$
CaOA	$= \frac{100 \times CaO}{[SiO2 + TiO2 + Al2O3 + Fe2O3t + MnO + MgO + CaO + Na2O + K2O + P2O5)]}$
Na_2OA	$= \frac{100 \times Na2O}{[SiO2 + TiO2 + Al2O3 + Fe2O3t + MnO + MgO + CaO + Na2O + K2O + P2O5)]}$
K_2OA	$= \frac{100 \times K2O}{[SiO2 + TiO2 + Al2O3 + Fe2O3t + MnO + MgO + CaO + Na2O + K2O + P2O5)]}$
P_2O_5A	$= \frac{100 \times P2O5}{[SiO2 + TiO2 + Al2O3 + Fe2O3t + MnO + MgO + CaO + Na2O + K2O + P2O5)]}$

Table S3: Isometric log-ratio transformation equations for major elements (the function ln represents natural logarithm; the final letter A after chemical symbols refer to the adjusted concentrations on an anhydrous basis to 100% with total Fe as $Fe_2O_3^t$).

Isometric log-ratio	Equation for transformation
$ilr1_{TiM}$	$= \sqrt{\frac{1}{2}} \times \ln\{SiO2A/TiO2A\}$
$ilr2_{AlM}$	$= \sqrt{\frac{2}{3}} \times \ln\{[\sqrt[2]{(SiO2A \times TiO2A)}]/Al2O3A\}$
$ilr3_{FeM}$	$= \sqrt{\frac{3}{4}} \times \ln\{[\sqrt[3]{(SiO2A \times TiO2A \times Al2O3A)}]/Fe2O3tA\}$
$ilr4_{MnM}$	$= \sqrt{\frac{4}{5}} \times \ln\{[\sqrt[4]{(SiO2A \times TiO2A \times Al2O3A \times Fe2O3tA)}]/MnOA\}$
$ilr5_{MgM}$	$= \sqrt{\frac{5}{6}} \times \ln\{[\sqrt[5]{(SiO2A \times TiO2A \times Al2O3A \times Fe2O3tA \times MnOA)}]/MgOA\}$
$ilr6_{CaM}$	$= \sqrt{\frac{6}{7}} \times \ln\{[\sqrt[6]{(SiO2A \times TiO2A \times Al2O3A \times Fe2O3tA \times MnOA \times MgOA)}]/CaOA\}$
$ilr7_{NaM}$	$= \sqrt{\frac{7}{8}} \times \ln\{[\sqrt[7]{(SiO2A \times TiO2A \times Al2O3A \times Fe2O3tA \times MnOA \times MgOA \times CaOA)}]/Na2OA\}$
$ilr8_{KM}$	$= \sqrt{\frac{8}{9}} \times \ln\{[\sqrt[8]{(SiO2A \times TiO2A \times Al2O3A \times Fe2O3tA \times MnOA \times MgOA \times CaOA \times Na2OA)}]/K2OA\}$
$ilr9_{PM}$	$= \sqrt{\frac{9}{10}} \times \ln\{[\sqrt[9]{(SiO2A \times TiO2A \times Al2O3A \times Fe2O3tA \times MnOA \times MgOA \times CaOA \times Na2OA \times K2OA)}]/P2O5A\}$

Table S4: Test for equality of group means for the four groups of main rock types considered as three groups (1+2-3-4: ultrabasic+basic-intermediate-acid rock subdivision) based on major elements (M).

Log_e-transformed ratio variable	Wilks' Lambda	F-ratio	Significance
$ilr1_{TiM}$	0.203809	5115.9	0.000000
$ilr2_{AlM}$	0.192634	3932.4	0.000000
$ilr3_{FeM}$	0.221985	7040.8	0.000000
$ilr4_{MnM}$	0.213198	6110.2	0.000000
$ilr5_{MgM}$	0.220561	6890.0	0.000000
$ilr6_{CaM}$	0.203302	5062.1	0.000000
$ilr7_{NaM}$	0.193826	4058.6	0.000000
$ilr8_{KM}$	0.211461	5926.2	0.000000
$ilr9_{PM}$	0.221848	7026.3	0.000000

Table S5: Discriminant function (DF1-DF2) equations for five diagrams (Figure S1a-e) based on isometric log-ratio transformation of major-elements (M) for the classification of igneous rocks as ultrabasic, basic, intermediate, and acid rocks (coefficients reported as arbitrarily rounded to four decimal places).

$$DF1_{(U+B-I-A)M} = (3.6537 \times ilr1_{TiM}) + (3.8014 \times ilr2_{AlM}) + (1.3099 \times ilr3_{FeM}) + (0.2312 \times ilr4_{MnM}) + (0.1408 \times ilr5_{MgM}) + (-0.0905 \times ilr6_{CaM}) + (-0.4853 \times ilr7_{NaM}) + (-0.0920 \times ilr8_{KM}) + (-0.2506 \times ilr9_{PM}) - 8.4701 \quad (S1)$$

$$DF2_{(U+B-I-A)M} = (1.6960 \times ilr1_{TiM}) + (5.8630 \times ilr2_{AlM}) + (2.3342 \times ilr3_{FeM}) + (0.0845 \times ilr4_{MnM}) + (0.9735 \times ilr5_{MgM}) + (0.1199 \times ilr6_{CaM}) + (1.3890 \times ilr7_{NaM}) + (0.5980 \times ilr8_{KM}) + (0.2013 \times ilr9_{PM}) - 3.6030 \quad (S2)$$

$$DF1_{(U-B-I)M} = (-4.9845 \times ilr1_{TiM}) + (-2.7012 \times ilr2_{AlM}) + (-1.1503 \times ilr3_{FeM}) + (-1.8526 \times ilr4_{MnM}) + (-0.9191 \times ilr5_{MgM}) + (-1.1351 \times ilr6_{CaM}) + (-0.3359 \times ilr7_{NaM}) + (-0.0343 \times ilr8_{KM}) + (0.3287 \times ilr9_{PM}) + 17.0472 \quad (S3)$$

$$DF2_{(U-B-I)M} = (0.7464 \times ilr1_{TiM}) + (5.2395 \times ilr2_{AlM}) + (-0.2103 \times ilr3_{FeM}) + (-2.9438 \times ilr4_{MnM}) + (-0.8379 \times ilr5_{MgM}) + (-3.2957 \times ilr6_{CaM}) + (-2.7704 \times ilr7_{NaM}) + (-0.9519 \times ilr8_{KM}) + (0.1848 \times ilr9_{PM}) + 11.8836 \quad (S4)$$

$$DF1_{(U-B-A)M} = (-3.1079 \times ilr1_{TiM}) + (-3.0889 \times ilr2_{AlM}) + (-1.3219 \times ilr3_{FeM}) + (-0.1216 \times ilr4_{MnM}) + (0.0490 \times ilr5_{MgM}) + (-0.0437 \times ilr6_{CaM}) + (0.7679 \times ilr7_{NaM}) + (0.0956 \times ilr8_{KM}) + (0.2653 \times ilr9_{PM}) + 6.7543 \quad (S5)$$

$$DF2_{(U-B-A)M} = (0.7511 \times ilr1_{TiM}) + (5.5444 \times ilr2_{AlM}) + (0.1431 \times ilr3_{FeM}) + (-1.5192 \times ilr4_{MnM}) + (-0.5010 \times ilr5_{MgM}) + (-1.5309 \times ilr6_{CaM}) + (-1.6622 \times ilr7_{NaM}) + (-0.6417 \times ilr8_{KM}) + (0.0500 \times ilr9_{PM}) + 7.0355 \quad (S6)$$

$$DF1_{(U-I-A)M} = (3.6618 \times ilr1_{TiM}) + (3.6107 \times ilr2_{AlM}) + (1.5118 \times ilr3_{FeM}) + (0.4570 \times ilr4_{MnM}) + (0.3103 \times ilr5_{MgM}) + (0.3106 \times ilr6_{CaM}) + (0.1790 \times ilr7_{NaM}) + (0.3609 \times ilr8_{KM}) + (-0.2511 \times ilr9_{PM}) - 10.6614 \quad (S7)$$

$$DF2_{(U-I-A)M} = (1.4559 \times ilr1_{TiM}) + (8.3695 \times ilr2_{AlM}) + (1.4222 \times ilr3_{FeM}) + (-0.8494 \times ilr4_{MnM}) + (0.1996 \times ilr5_{MgM}) + (-1.0189 \times ilr6_{CaM}) + (-0.4598 \times ilr7_{NaM}) + (-0.1459 \times ilr8_{KM}) + (0.1977 \times ilr9_{PM}) + 3.2032 \quad (S8)$$

$$DF1_{(B-I-A)M} = (3.7211 \times ilr1_{TiM}) + (3.9723 \times ilr2_{AlM}) + (1.2140 \times ilr3_{FeM}) + (0.2199 \times ilr4_{MnM}) + (0.1024 \times ilr5_{MgM}) + (-0.1454 \times ilr6_{CaM}) + (-0.5831 \times ilr7_{NaM}) + (-0.0833 \times ilr8_{KM}) + (-0.2535 \times ilr9_{PM}) - 8.6059 \quad (S9)$$

$$DF2_{(B-I-A)M} = (1.5746 \times ilr1_{TiM}) + (5.1846 \times ilr2_{AlM}) + (2.4761 \times ilr3_{FeM}) + (0.2545 \times ilr4_{MnM}) + (1.0592 \times ilr5_{MgM}) + (0.4260 \times ilr6_{CaM}) + (1.7888 \times ilr7_{NaM}) + (0.6745 \times ilr8_{KM}) + (0.1834 \times ilr9_{PM}) - 4.2880 \quad (S10)$$

The subscripts used are as follows: U—ultrabasic; B—basic; I—intermediate; and A—acid. The subscript M is for major-element based diagrams.

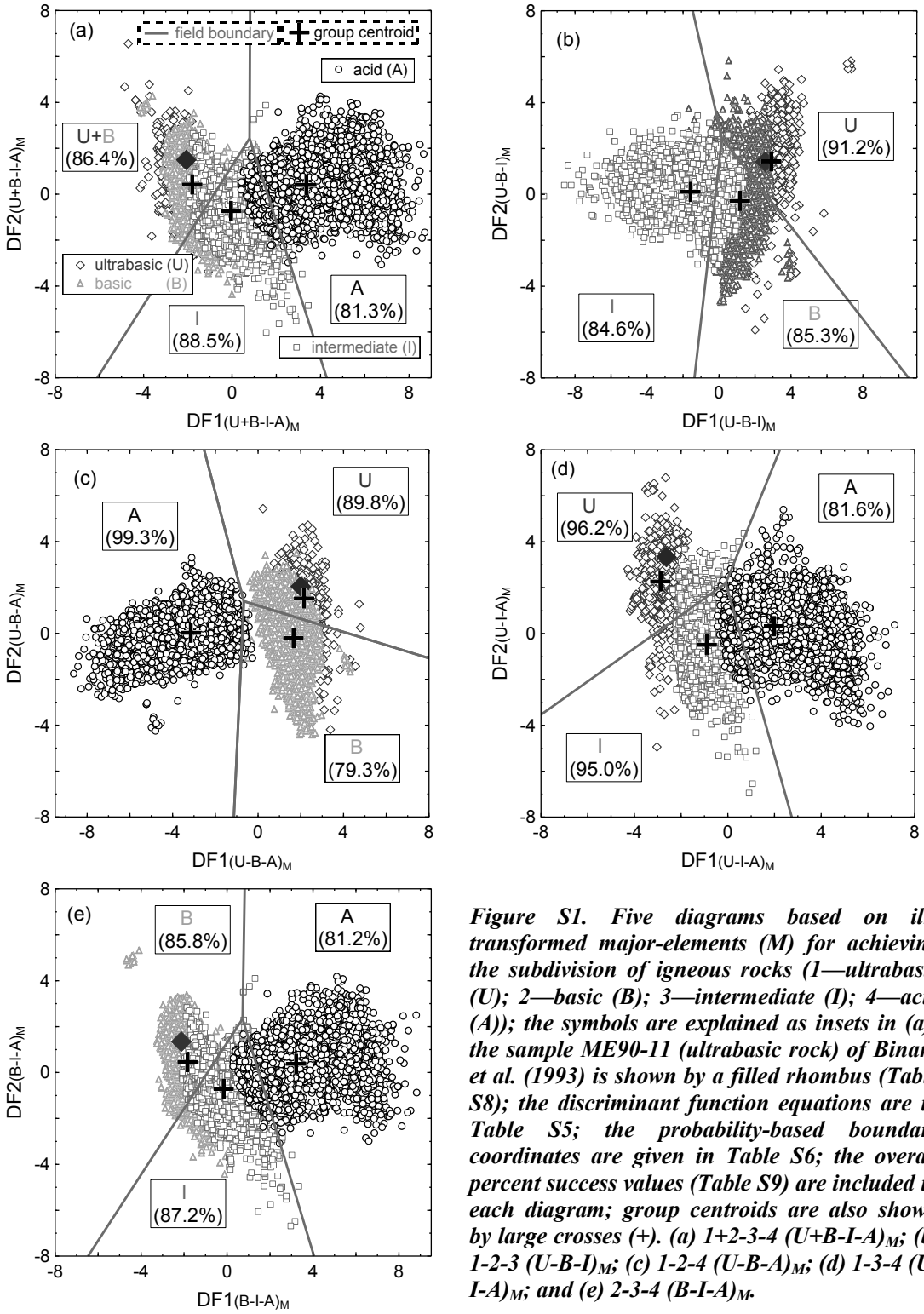

Figure S1. Five diagrams based on ilr-transformed major-elements (M) for achieving the subdivision of igneous rocks (1—ultrabasic (U); 2—basic (B); 3—intermediate (I); 4—acid (A)); the symbols are explained as insets in (a); the sample ME90-11 (ultrabasic rock) of Binard et al. (1993) is shown by a filled rhombus (Table S8); the discriminant function equations are in Table S5; the probability-based boundary coordinates are given in Table S6; the overall percent success values (Table S9) are included in each diagram; group centroids are also shown by large crosses (+). (a) 1+2-3-4 $(U+B-I-A)_M$; (b) 1-2-3 $(U-B-I)_M$; (c) 1-2-4 $(U-B-A)_M$; (d) 1-3-4 $(U-I-A)_M$; and (e) 2-3-4 $(B-I-A)_M$.

Table S6: Probability-based boundary coordinates estimated for rock subdivision into main rock types (Figure S1a-e; 1—ultrabasic (ultrab or U); 2—basic (bas or B); 3—intermediate (int or I); 4—acid (acid or A); each diagram is considered as of three fields 1 to 3; the triple point common to all field boundaries is repeated in each set of coordinates). The final subscript M refers to major element based classification.

Field Boundary	12_3_4		1_2_3		1_2_4		1_3_4		2_3_4	
	$DF1_{(U+B-I-A)M}$	$DF2_{(U+B-I-A)M}$	$DF1_{(U-B-I)M}$	$DF2_{(U-B-I)M}$	$DF1_{(U-B-A)M}$	$DF2_{(U-B-A)M}$	$DF1_{(U-I-A)M}$	$DF2_{(U-I-A)M}$	$DF1_{(B-I-A)M}$	$DF2_{(B-I-A)M}$
B(1_2)	-8.728678	-12	12	-9.4712525	12	-2.2307715	-12	-6.433744	-9.252367	-12
	-6.0909205	-8	10.540097	-8	8	-1.084543	-8	-3.537513	-6.468838	-8
	0.79022577	2.43345545	0.16420594	2.45725878	-0.66610579	1.39879698	-0.08572174	2.19288389	0.72649818	2.34108944
B(1_3)	0.83086	12	-2.63577	12	-3.65832	12	3.8256	12	0.89141	12
	0.814	8	-1.462	8	-2.52931	8	2.2303	8	0.823	8
	0.79022577	2.43345545	0.16420594	2.45725878	-0.66610579	1.39879698	-0.08572174	2.19288389	0.72649818	2.34108944
B(2_3)	5.618504	-12	-1.951291	-12	-1.3348535	-12	3.843733	-12	5.3344315	-12
	4.2802935	-8	-1.366102	-8	-1.13521	-8	2.73629	-8	4.049309	-8
	0.79022577	2.43345545	0.16420594	2.45725878	-0.66610579	1.39879698	-0.08572174	2.19288389	0.72649818	2.34108944

Table S7: Succees of classification of igneous rocks as main rock types in five diagrams (Figure S1a-e) based on transformed major elements (M).

Figure type	Sample type	Total number of samples	Number of classified main rock types in major element based diagrams					
			ultrabasic + basic (ultrab+bas)	ultrabasic (ultrab)	basic (bas)	intermediate (int)	acid (acid)	percent success (correct classification)
ultrab+bas-int-acid (U+B-I-A)	ultrabasic + basic	13709	11850			1859	0	86.4%
	intermediate	11750	1261			10400	89	88.5%
	acid	7489	0			1429	6060	81.3%
ultrab-bas-int (U-B-I)	ultrabasic	1505		1372	133	0		91.2%
	basic	12204		1446	10411	347		85.3%
	intermediate	11750		2	1802	9946		84.6%
ultrab-bas-acid (U-B-A)	ultrabasic	1505		1352	153		0	89.8%
	basic	12204		2523	9681		0	79.3%
	acid	7489		1	49		7439	99.3%
ultrab-int-acid (U-I-A)	ultrabasic	1505		1448		57	0	96.2%
	intermediate	11750		563		11158	29	95.0%
	acid	7489		3		1377	6109	81.6%
bas-int-acid (B-I-A)	basic	12204			10467	1737	0	85.8%
	intermediate	11750			1420	10250	103	87.2%
	acid	7489			0	6080	6077	81.2%

U−ultrab−ultrabasic; B−bas−basic; ultrab+bas–combined ultrabasic and basic field; I−int−intermediate; A−acid−acid.

Table S8: Synthesis of four-field multidimensional classification of one sample of ultrabasic (IUGS classification) rock (ME90-11−internal name given by the original authors (Binard et al., 1993); assigned name BMGT0007) in five diagrams for igneous rock subdivision (original data plotted in Figure S1a-e).

Figure name	Figure type	Total probability of the sample	Probability distribution for the sample				
			U+B (p_{U+B}) Θ	U (p_U) Θ	B (p_B) Θ	I (p_I) Θ	A (p_A) Θ
Subdivision as main rock type	U+B-I-A	1	0.981213			0.018786	0.000000
	U-B-I	1		0.917337	0.082593	0.000069	
	U-B-A	1		0.920624	0.079376		0.000000
	U-I-A	1		0.999719		0.000280	0.000000
	B-I-A	1			0.973756	0.026244	0.000000
Synthesis for the ultrabasic sample classification	***{Σprob_5}***	***{5}***	***{0.981213}***	***{2.837681}***	***{1.135724}***	***{1.416186}***	***{0.045380}***
	{Σprob_4}	***{5}***	***{}***	***{3.53843214}***	***{1.4161861}***	***{1.416186}***	***{0.045380}***
	[%prob]	***[100%]***	***[]***	***[70.8%]***	***[28.3%]***	***[0.9%]***	***[0.0%]***

Θ U−ultrabasic; B−basic; U+B−combined ultrabasic and basic field; I−intermediate; A−acid; the probability values for a sample from a given locality are represented by (p_{U+B}) – probability for the combined ultrabasic and basic field in the first diagram; [p_U] – probability for the ultrabasic rock field in the diagrams; [p_B] – probability for the basic rock field in the diagrams; [p_I] – probability for the intermediate rock field in the diagrams; [p_A] – probability for the acid rock field in the diagrams; the final rows give a synthesis of results as ***{Σprob_5}***, ***{Σprob_4}***, and ***[%prob]***, where **{Σprob_5}** is the total probability of a sample plotting in all five diagrams to be subdivided in five classification fields (U + B, U, B, I, and A); ***{Σprob_4}*** is the sum of probability values of a sample for the four classification fields (U, B, I, and A) after assigning the probability of U + B to U and B (using weighing factors explained in Verma and Verma, 2013); and the final row identified by ***[%prob]*** is the subdivision of the total percent probability value of 100% that corresponds to the four classification fields.

Table S9: Synthesis of four field multidimensional classification of igneous rocks as main rock types in five diagrams based on major elements (M; original data plotted in Figure 1a-e).

Main rock type name (IUGS)	Total number of samples	Number of classified main rock types **(percent success)**			
		ultrabasic (ultrab−U)	basic (bas−B)	intermediate (int−I)	acid (acid−A)
ultrabasic	1505	**1358 (90.23%)**	138(9.17%)	9(0.6%)	0 (0%)
basic	12204	1724 (14.13%)	**9378 (76.84%)**	1102 (9.03%)	0 (0%)
intermediate	11750	0 (0%)	1353 (11.51%)	**10345 (88.04%)**	52 (0.44%)
acid	7489	0 (0%)	0 (0%)	1417 (18.92%)	**6072 (81.08%)**

The correct classification is shown in **bold** face.

Table S10: Discriminant function (DF1-DF2) equations for five multidimensional diagrams (Figure S2a-e) based on isometric log-ratio transformation of major-elements (M) for the classification of ultrabasic (U) igneous rocks as four varieties: 1—basanite (BSN or Bsn); 2—tephrite (TEP or Tep); 3—picrobasalt (PB); 4—foidite (FOI or Foi); coefficients reported as arbitrarily rounded to four decimal places.

$$\mathrm{DF1}_{U(\mathrm{Bsn+Tep-PB-Foi})\mathrm{M}} = (6.9297 \times \mathrm{ilr1}_{\mathrm{TiM}}) + (4.6310 \times \mathrm{ilr2}_{\mathrm{AlM}}) + (2.8706 \times \mathrm{ilr3}_{\mathrm{FeM}}) + (1.0021 \times \mathrm{ilr4}_{\mathrm{MnM}}) + (2.6277 \times \mathrm{ilr5}_{\mathrm{MgM}}) + (-0.3524 \times \mathrm{ilr6}_{\mathrm{CaM}}) + (1.1376 \times \mathrm{ilr7}_{\mathrm{NaM}}) + (1.6294 \times \mathrm{ilr8}_{\mathrm{KM}}) + (0.8139 \times \mathrm{ilr9}_{\mathrm{PM}}) - 19.2233 \quad \text{(S11)}$$

$$\mathrm{DF2}_{U(\mathrm{Bsn+Tep-PB-Foi})\mathrm{M}} = (10.3688 \times \mathrm{ilr1}_{\mathrm{TiM}}) + (8.8311 \times \mathrm{ilr2}_{\mathrm{AlM}}) + (7.3878 \times \mathrm{ilr3}_{\mathrm{FeM}}) + (3.9266 \times \mathrm{ilr4}_{\mathrm{MnM}}) + (1.3689 \times \mathrm{ilr5}_{\mathrm{MgM}}) + (5.6080 \times \mathrm{ilr6}_{\mathrm{CaM}}) + (-0.8053 \times \mathrm{ilr7}_{\mathrm{NaM}}) + (0.7340 \times \mathrm{ilr8}_{\mathrm{KM}}) + (-0.6365 \times \mathrm{ilr9}_{\mathrm{PM}}) - 27.3343 \quad \text{(S12)}$$

$$\mathrm{DF1}_{U(\mathrm{Bsn-Tep-PB})\mathrm{M}} = (-3.1834 \times \mathrm{ilr1}_{\mathrm{TiM}}) + (-1.6791 \times \mathrm{ilr2}_{\mathrm{AlM}}) + (-0.0123 \times \mathrm{ilr3}_{\mathrm{FeM}}) + (0.9596 \times \mathrm{ilr4}_{\mathrm{MnM}}) + (-2.9011 \times \mathrm{ilr5}_{\mathrm{MgM}}) + (1.9395 \times \mathrm{ilr6}_{\mathrm{CaM}}) + (-1.9944 \times \mathrm{ilr7}_{\mathrm{NaM}}) + (-0.9505 \times \mathrm{ilr8}_{\mathrm{KM}}) + (-0.9361 \times \mathrm{ilr9}_{\mathrm{PM}}) + 6.3743 \quad \text{(S13)}$$

$$\mathrm{DF2}_{U(\mathrm{Bsn-Tep-PB})\mathrm{M}} = (2.7818 \times \mathrm{ilr1}_{\mathrm{TiM}}) + (4.9135 \times \mathrm{ilr2}_{\mathrm{AlM}}) + (5.5450 \times \mathrm{ilr3}_{\mathrm{FeM}}) + (-0.3915 \times \mathrm{ilr4}_{\mathrm{MnM}}) + (3.0696 \times \mathrm{ilr5}_{\mathrm{MgM}}) + (-4.8393 \times \mathrm{ilr6}_{\mathrm{CaM}}) + (-1.8452 \times \mathrm{ilr7}_{\mathrm{NaM}}) + (-0.2838 \times \mathrm{ilr8}_{\mathrm{KM}}) + (0.5044 \times \mathrm{ilr9}_{\mathrm{PM}}) - 3.2762 \quad \text{(S14)}$$

$$\mathrm{DF1}_{U(\mathrm{Bsn-Tep-Foi})\mathrm{M}} = (11.0299 \times \mathrm{ilr1}_{\mathrm{TiM}}) + (6.7218 \times \mathrm{ilr2}_{\mathrm{AlM}}) + (2.8494 \times \mathrm{ilr3}_{\mathrm{FeM}}) + (5.8567 \times \mathrm{ilr4}_{\mathrm{MnM}}) + (1.9009 \times \mathrm{ilr5}_{\mathrm{MgM}}) + (5.8551 \times \mathrm{ilr6}_{\mathrm{CaM}}) + (0.8871 \times \mathrm{ilr7}_{\mathrm{NaM}}) + (1.2353 \times \mathrm{ilr8}_{\mathrm{KM}}) + (-0.4867 \times \mathrm{ilr9}_{\mathrm{PM}}) - 37.9841 \quad \text{(S15)}$$

$$\mathrm{DF2}_{U(\mathrm{Bsn-Tep-Foi})\mathrm{M}} = (-8.5767 \times \mathrm{ilr1}_{\mathrm{TiM}}) + (-9.0295 \times \mathrm{ilr2}_{\mathrm{AlM}}) + (-9.5081 \times \mathrm{ilr3}_{\mathrm{FeM}}) + (-1.5864 \times \mathrm{ilr4}_{\mathrm{MnM}}) + (-4.2665 \times \mathrm{ilr5}_{\mathrm{MgM}}) + (0.8854 \times \mathrm{ilr6}_{\mathrm{CaM}}) + (-0.1331 \times \mathrm{ilr7}_{\mathrm{NaM}}) + (-0.7451 \times \mathrm{ilr8}_{\mathrm{KM}}) + (-0.1356 \times \mathrm{ilr9}_{\mathrm{PM}}) + 19.7072 \quad \text{(S16)}$$

$$\mathrm{DF1}_{U(\mathrm{Bsn-PB-Foi})\mathrm{M}} = (7.5434 \times \mathrm{ilr1}_{\mathrm{TiM}}) + (5.1395 \times \mathrm{ilr2}_{\mathrm{AlM}}) + (3.2503 \times \mathrm{ilr3}_{\mathrm{FeM}}) + (1.1979 \times \mathrm{ilr4}_{\mathrm{MnM}}) + (2.6044 \times \mathrm{ilr5}_{\mathrm{MgM}}) + (-0.1294 \times \mathrm{ilr6}_{\mathrm{CaM}}) + (1.1140 \times \mathrm{ilr7}_{\mathrm{NaM}}) + (1.6255 \times \mathrm{ilr8}_{\mathrm{KM}}) + (0.7297 \times \mathrm{ilr9}_{\mathrm{PM}}) - 20.6955 \quad \text{(S17)}$$

$$\mathrm{DF2}_{U(\mathrm{Bsn-PB-Foi})\mathrm{M}} = (9.0090 \times \mathrm{ilr1}_{\mathrm{TiM}}) + (7.3324 \times \mathrm{ilr2}_{\mathrm{AlM}}) + (5.7385 \times \mathrm{ilr3}_{\mathrm{FeM}}) + (3.6805 \times \mathrm{ilr4}_{\mathrm{MnM}}) + (0.6034 \times \mathrm{ilr5}_{\mathrm{MgM}}) + (5.9706 \times \mathrm{ilr6}_{\mathrm{CaM}}) + (-0.8836 \times \mathrm{ilr7}_{\mathrm{NaM}}) + (0.6327 \times \mathrm{ilr8}_{\mathrm{KM}}) + (-0.7016 \times \mathrm{ilr9}_{\mathrm{PM}}) - 24.0991 \quad \text{(S18)}$$

$$\mathrm{DF1}_{U(\mathrm{Tep-PB-Foi)M}} = (5.0464 \times \mathrm{ilr1}_{\mathrm{TiM}}) + (3.9219 \times \mathrm{ilr2}_{\mathrm{AlM}}) + (1.7324 \times \mathrm{ilr3}_{\mathrm{FeM}}) + (0.5096 \times \mathrm{ilr4}_{\mathrm{MnM}}) + \left(1.9313 \times \mathrm{ilr5}_{\mathrm{MgM}}\right) + (-1.0722 \times \mathrm{ilr6}_{\mathrm{CaM}}) + (1.2100 \times \mathrm{ilr7}_{\mathrm{NaM}}) + (1.2185 \times \mathrm{ilr8}_{\mathrm{KM}}) + (0.5519 \times \mathrm{ilr9}_{\mathrm{PM}}) - 13.8742 \quad \text{(S19)}$$

$$\mathrm{DF2}_{U(\mathrm{Tep-PB-Foi)M}} = (-6.4752 \times \mathrm{ilr1}_{\mathrm{TiM}}) + (-6.2510 \times \mathrm{ilr2}_{\mathrm{AlM}}) + (-8.3932 \times \mathrm{ilr3}_{\mathrm{FeM}}) + (-1.9524 \times \mathrm{ilr4}_{\mathrm{MnM}}) + \left(-2.7511 \times \mathrm{ilr5}_{\mathrm{MgM}}\right) + (-1.6159 \times \mathrm{ilr6}_{\mathrm{CaM}}) + (0.3767 \times \mathrm{ilr7}_{\mathrm{NaM}}) + (-0.6539 \times \mathrm{ilr8}_{\mathrm{KM}}) + (0.2411 \times \mathrm{ilr9}_{\mathrm{PM}}) + 15.7290 \quad \text{(S20)}$$

The subscripts used are as follows: Bsn—basanite; Tep—tephrite; PB—picrobasalt; and Foi—foidite. The subscript M is for major-element based diagrams.

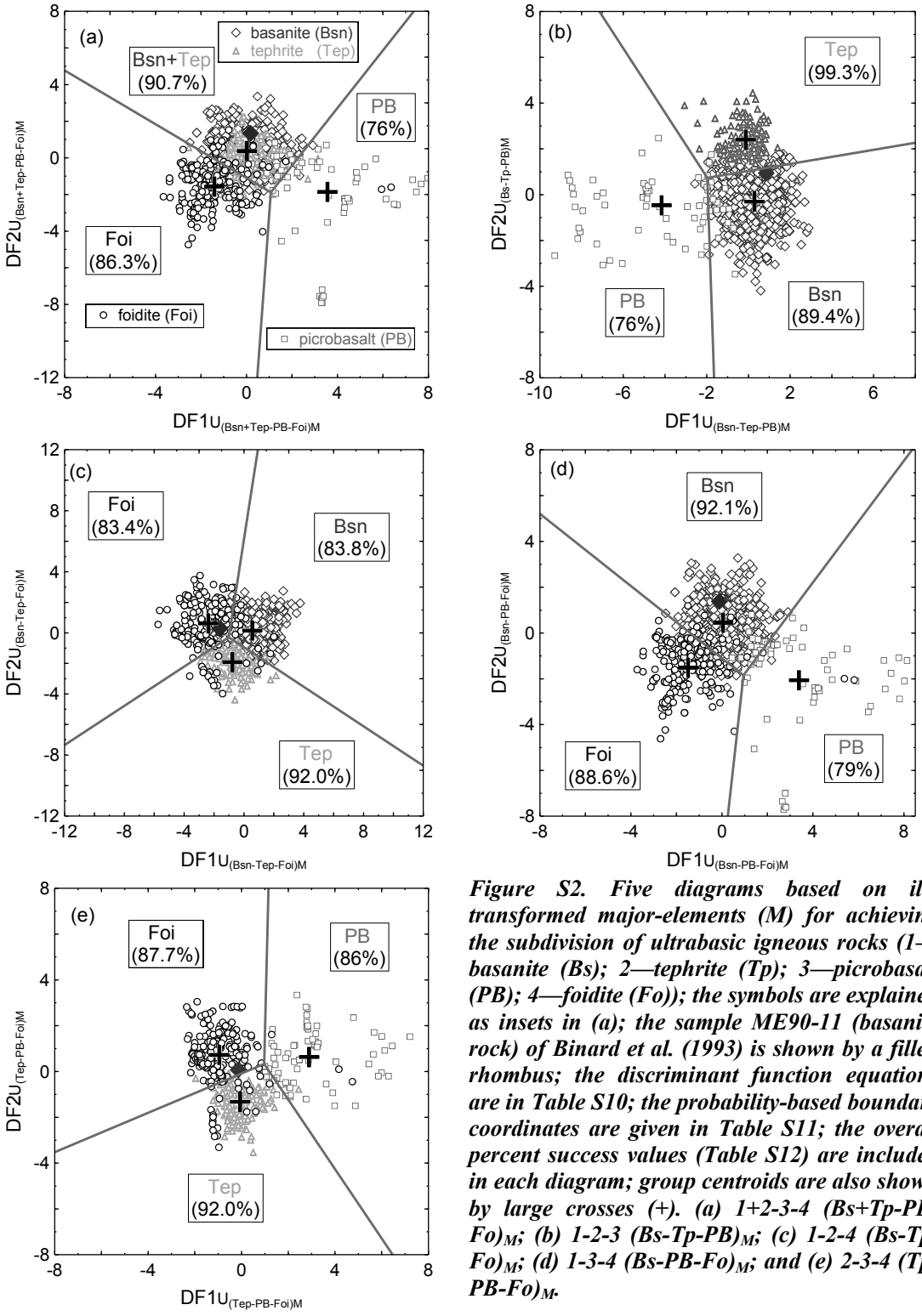

Figure S2. Five diagrams based on ilr-transformed major-elements (M) for achieving the subdivision of ultrabasic igneous rocks (1—basanite (Bs); 2—tephrite (Tp); 3—picrobasalt (PB); 4—foidite (Fo)); the symbols are explained as insets in (a); the sample ME90-11 (basanite rock) of Binard et al. (1993) is shown by a filled rhombus; the discriminant function equations are in Table S10; the probability-based boundary coordinates are given in Table S11; the overall percent success values (Table S12) are included in each diagram; group centroids are also shown by large crosses (+). (a) 1+2-3-4 (Bs+Tp-PB-Fo)$_M$; (b) 1-2-3 (Bs-Tp-PB)$_M$; (c) 1-2-4 (Bs-Tp-Fo)$_M$; (d) 1-3-4 (Bs-PB-Fo)$_M$; and (e) 2-3-4 (Tp-PB-Fo)$_M$.

Table S11: Probability-based boundary coordinates estimated for ultrabasic (U) rock subdivision diagrams (Figure 2a-e; 1—basanite (Bsn); 2—tephrite (Tep); 3—picrobasalt (PB); 4—foidite (Foi); each diagram is considered as of three fields 1 to 3; the triple point common to all field boundaries is repeated in each set of coordinates). The final subscript M refers to major element based classification.

Field Boundary	12_3_4		1_2_3		1_2_4		1_3_4		2_3_4	
	$DF1_{(Bsn+Tep-PB-Foi)M}$	$DF2_{(Bsn+Tep-PB-Foi)M}$	$DF1_{(Bsn-Tep-PB)M}$	$DF2_{(Bsn-Tep-PB)M}$	$DF1_{(Bsn-Tep-Foi)M}$	$DF2_{(Bsn-Tep-Foi)M}$	$DF1_{(Bsn-PB-Foi)M}$	$DF2_{(Bsn-PB-Foi)M}$	$DF1_{(Tep-PB-Foi)M}$	$DF2_{(Tep-PB-Foi)M}$
B(1_2)	9.9028	12	12	2.883	12	-8.6988035	11.3718915	12	9.110606	-12
	7.35925	8	8	2.266983	10.9188705	-8	8.361862	8	6.470247	-8
	1.07345336	-1.88478178	-1.96933623	0.73166317	-1.00829711	-0.29069826	0.95037795	-1.84904967	0.96920466	0.33377994
B(1_3)	-12	7.70165	-1.49992	-12	0.932002	12	-11.544445	8	-12	-5.238942
	-8	4.76865	-1.6474	-8	0.300533	8	-8	5.2060905	-8	-3.5201865
	1.07345336	-1.88478178	-1.96933623	0.73166317	-1.00829711	-0.29069826	0.95037795	-1.84904967	0.96920466	0.33377994
B(2_3)	0.474	-12	-9.9929795	12	-12	-7.344821	-0.1874545	-12	1.2533185	12
	0.711	-8	-7.144771	8	-8	-4.777749	0.26091	-8	1.1559045	8
	1.07345336	-1.88478178	-1.96933623	0.73166317	-1.00829711	-0.29069826	0.95037795	-1.84904967	0.96920466	0.33377994

Table S12: Classification of ultrabasic rocks as four rock types (1—basanite (Bsn); 2—tephrite (Tep); 3—picrobasalt (PB); 4—foidite (Foi) used for constructing the five diagrams (Figure 2a-e) based on transformed major elements (M).

Figure type	Sample type	Total number of samples	Number of classified rock types in major element based diagrams					
			basanite + tephrite (Bsn+Tep)	basanite (Bsn)	tephrite (Tep)	picrobasalt (PB)	foidite (Foi)	percent success (correct classification)
basanite+tephrite -picrobasalt-foidite	basanite + tephrite	1221	1107			7	107	90.7%
	picrobasalt	72	17			55	0	76%
	foidite	211	27			2	182	86.3%
Basanite-tephrite-picrobasalt	basanite	1071		958	110	3		89.4%
	tephrite	150		1	149	0		99.3%
	picrobasalt	72		13	4	55		76%
basanite-tephrite--foidite	basanite	1071		898	106		67	83.8%
	tephrite	150		3	138		9	92.0%
	foidite	211		17	18		176	83.4%
Basanite-picrobasalt-foidite	basanite	1071		986		4	81	92.1%
	picrobasalt	72		15		57	0	79%
	foidite	211		21		3	187	88.6%
tephrite-picrobasalt-foidite	tephrite	150			138	3	9	92.0%
	picrobasalt	72			9	62	1	86%
	foidite	211			23	3	185	87.7%

Table S13: Synthesis of four field multidimensional classification of rock name for one sample of ultrabasic basanite (IUGS classification) rock (ME90-11−internal name given by the original authors (Binard et al., 1993); assigned name BMGT0007) in five diagrams for U igneous rock subdivision (original data plotted in Figure S2a-e).

Figure name	Figure type	Total probability of the sample	Probability distribution for the sample				
			Bsn+Tep ($p_{Bsn+Tep}$) Θ	Bsn (p_{Bsn}) Θ	Tep (p_{Tep}) Θ	PB (p_{PB}) Θ	Fo (p_{Foi}) Θ
Subdivision as U rock type	Bsn+Tep-PB-Foi	1	0.989028			0.000008	0.010964
	Bsn-Tep-PB	1		0.996732	0.009000	0.000004	
	Bsn-Tep-Foi	1		0.990406	0.074642		0.000594
	Bsn-PB-Foi	1		0.990887		0.000009	0.009104
	Tep-PB-Foi	1			0.387744	0.008539	0.603717
Synthesis for the U rock classification	***{Σprob_5}*** ***{Σprob_4}*** ***[%prob]***	***{5}*** ***{5}*** ***[100%]***	***{0.989028}*** ***{}*** ***[]***	***{2.978025}*** ***{3.849938}*** ***[77.0%]***	***{0.400007}*** ***{0.517122}*** ***[10.3%]***	***{0.008561}*** ***{0.008561}*** ***[0.2%]***	***{0.624379}*** ***{0.624379}*** ***[12.5%]***

Θ Bsn−basanite; Tep−tephrite; Bsn+Tep–combined basanite and tephrite field; PB−picrobasalt; Foi−foidite; the probability values for a sample from a given locality are represented by ($p_{Bsn+Tep}$) – probability for the combined basanite and tephrite field in the first diagram; [p_{Bsn}] – probability for the basanite rock field in the diagrams; [p_{Tep}] – probability for the tephirte rock field in the diagrams; [p_{PB}] – probability for the picrobasalt rock field in the diagrams; [p_{Foi}] – probability for the foidite rock field in the diagrams; the final rows give a synthesis of results as ***{Σprob_5}***, ***{Σprob_4}***, and ***[%prob]***, where **{Σprob_5}** is the total probability of a sample plotting in all five diagrams to be subdivided in five classification fields (Bs + Tp, Bs, Tp, PB, and Fo); ***{Σprob_4}*** is the sum of probability values of a sample for the four classification fields (Bsn, Tep, PB, and Foi) after assigning the probability of Bsn + Tep to Bsn and Tep (using weighing factors explained in Verma and Verma, 2013); and the final row identified by ***[%prob]*** is the subdivision of the total percent probability value of 100% that corresponds to the four classification fields.

Table S14: Synthesis of four field classification of ultrabasic rocks in five diagrams based on major elements (M; original data plotted in Figure 2a-e).

U rock name (IUGS)	Total number of samples	Number of classified rock types **(percent success)**			
		basanite (Bsn)	tephrite (Tep)	picrobasalt (PB)	foidite (Foi)
basanite	1071	**900(84.03%)**	95 (9.87%)	5 (0.47%)	71 (6.63%)
tephrite	150	1 (0.6%)	**133 (88.7%)**	3(2.0%)	13 (8.7%)
picrobasalt	72	11 (15%)	5 (7%)	**56 (78%)**	0 (0%)
foidite	211	14 (6.6%)	19 (9.0%)	2 (1.0%)	**176 (83.4%)**

The correct classification is shown in **bold** face.

Table S15: Discriminant function (DF1-DF2) equations for the diagram (Figure 3a) based on isometric log-ratio transformation of major-elements (M) for the classification of ultrabasic basanite (UBsn) igneous rocks as three sub-varieties: 1—basanite (bsn); 2—melanephelinite (mnp); 3—nephelinite (np); coefficients reported as arbitrarily rounded to four decimal places.

$$\mathrm{DF1}_{UBsn(\mathrm{bsn-mnp-np})\mathrm{M}} = (-15.3633 \times \mathrm{ilr1}_{\mathrm{TiM}}) + (-10.4476 \times \mathrm{ilr2}_{\mathrm{AlM}}) + (-7.7088 \times \mathrm{ilr3}_{\mathrm{FeM}}) + (-4.5098 \times \mathrm{ilr4}_{\mathrm{MnM}}) + \left(-7.1144 \times \mathrm{ilr5}_{\mathrm{MgM}}\right) + (-10.8099 \times \mathrm{ilr6}_{\mathrm{CaM}}) + (-3.3662 \times \mathrm{ilr7}_{\mathrm{NaM}}) + (-2.5963 \times \mathrm{ilr8}_{\mathrm{KM}}) + (0.8466 \times \mathrm{ilr9}_{\mathrm{PM}}) + 37.9343 \quad (S21)$$

$$\mathrm{DF2}_{UBsn(\mathrm{bsn-mnp-np})\mathrm{M}} = (-3.8510 \times \mathrm{ilr1}_{\mathrm{TiM}}) + (-2.4887 \times \mathrm{ilr2}_{\mathrm{AlM}}) + (-0.2253 \times \mathrm{ilr3}_{\mathrm{FeM}}) + (-0.1289 \times \mathrm{ilr4}_{\mathrm{MnM}}) + \left(-1.6278 \times \mathrm{ilr5}_{\mathrm{MgM}}\right) + (-1.7013 \times \mathrm{ilr6}_{\mathrm{CaM}}) + (4.2070 \times \mathrm{ilr7}_{\mathrm{NaM}}) + (0.2630 \times \mathrm{ilr8}_{\mathrm{KM}}) + (-0.4303 \times \mathrm{ilr9}_{\mathrm{PM}}) + 3.0896 \quad (S22)$$

Table S16: Discriminant function (DF1-DF2) equations for the diagram (Figure 3b) based on isometric log-ratio transformation of major-elements (M) for the classification of ultrabasic tephrite igneous rocks as three sub-varieties: 1—basanite (bsn); 2—melanephelinite (mnp); 3—nephelinite (np); coefficients reported as arbitrarily rounded to four decimal places.

$$\mathrm{DF1}_{UTep(\mathrm{bsn-mnp-np})\mathrm{M}} = (10.9749 \times \mathrm{ilr1}_{\mathrm{TiM}}) + (5.9416 \times \mathrm{ilr2}_{\mathrm{AlM}}) + (6.2385 \times \mathrm{ilr3}_{\mathrm{FeM}}) + (6.0762 \times \mathrm{ilr4}_{\mathrm{MnM}}) + \left(4.7555 \times \mathrm{ilr5}_{\mathrm{MgM}}\right) + (11.1551 \times \mathrm{ilr6}_{\mathrm{CaM}}) + (3.0858 \times \mathrm{ilr7}_{\mathrm{NaM}}) + (3.1315 \times \mathrm{ilr8}_{\mathrm{KM}}) + (-1.2114 \times \mathrm{ilr9}_{\mathrm{PM}}) - 36.6969 \quad (S23)$$

$$\mathrm{DF2}_{UTep(\mathrm{bsn-mnp-np})\mathrm{M}} = (-4.1516 \times \mathrm{ilr1}_{\mathrm{TiM}}) + (-5.3378 \times \mathrm{ilr2}_{\mathrm{AlM}}) + (-1.9139 \times \mathrm{ilr3}_{\mathrm{FeM}}) + (2.6195 \times \mathrm{ilr4}_{\mathrm{MnM}}) + \left(-0.5539 \times \mathrm{ilr5}_{\mathrm{MgM}}\right) + (-2.3920 \times \mathrm{ilr6}_{\mathrm{CaM}}) + (4.5526 \times \mathrm{ilr7}_{\mathrm{NaM}}) + (0.1220 \times \mathrm{ilr8}_{\mathrm{KM}}) + (-1.4099 \times \mathrm{ilr9}_{\mathrm{PM}}) - 5.0142 \quad (S24)$$

Table S17. Discriminant function (DF1-DF2) equations for the diagram (Figure 3c) based on isometric log-ratio transformation of major-elements (M) for the classification of foidite igneous rocks as three sub-varieties: 1—basanite (bs); 2—melanephelinite (mne); 3—nephelinite (ne); coefficients reported as arbitrarily rounded to four decimal places.

$$\mathrm{DF1}_{UFoi(\mathrm{bsn-mnp-np})\mathrm{M}} = (1.6204 \times \mathrm{ilr1}_{\mathrm{TiM}}) + (3.5774 \times \mathrm{ilr2}_{\mathrm{AlM}}) + (1.2073 \times \mathrm{ilr3}_{\mathrm{FeM}}) + (2.0330 \times \mathrm{ilr4}_{\mathrm{MnM}}) + \left(-1.0882 \times \mathrm{ilr5}_{\mathrm{MgM}}\right) + (-1.2227 \times \mathrm{ilr6}_{\mathrm{CaM}}) + (4.4825 \times \mathrm{ilr7}_{\mathrm{NaM}}) + (-0.2244 \times \mathrm{ilr8}_{\mathrm{KM}}) + (-0.3192 \times \mathrm{ilr9}_{\mathrm{PM}}) - 12.9908 \quad (S25)$$

$$\mathrm{DF2}_{UFoi(\mathrm{bsn-mnp-np})\mathrm{M}} = (2.9267 \times \mathrm{ilr1}_{\mathrm{TiM}}) + (0.5815 \times \mathrm{ilr2}_{\mathrm{AlM}}) + (-4.1265 \times \mathrm{ilr3}_{\mathrm{FeM}}) + (2.5678 \times \mathrm{ilr4}_{\mathrm{MnM}}) + \left(3.0980 \times \mathrm{ilr5}_{\mathrm{MgM}}\right) + (2.4095 \times \mathrm{ilr6}_{\mathrm{CaM}}) + (0.3563 \times \mathrm{ilr7}_{\mathrm{NaM}}) + (1.6069 \times \mathrm{ilr8}_{\mathrm{KM}}) + (0.2384 \times \mathrm{ilr9}_{\mathrm{PM}}) - 14.1044 \quad (S26)$$

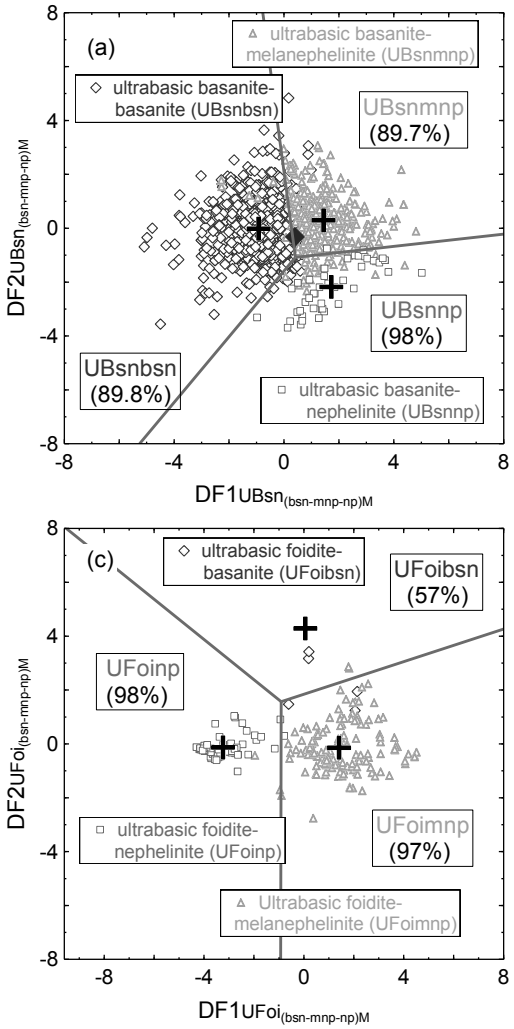

Figure S3. Diagrams based on ilr-transformed major-elements (M) for achieving further subdivision (3 subvarieties each) of ultrabasic (U) igneous rocks (all diagrams are of 1-2-3 type, where 1—basanite (bs); 2—melanephelinite (mne); 3— nephelinite (ne)); probability-based boundary coordinates in Table S16, the overall percent success values (Table S17) included in each diagram, group centroids shown by crosses (+). (a) for basanite (UBs); the sample ME90-11 (basanite, basanite rock) of Binard et al. (1993) is shown by a filled rhombus, discriminant function equations in Table S13; (b) for tephrite (UTp), discriminant function equations in Table S14; and (c) for foidite (UFo), discriminant function equations in Table S15.

Table S18: Probability-based boundary coordinates estimated for ultrabasic (U) basanite, tephrite, and foidite subdivision diagrams in three subvarieties (1—basanite (bsn); 2—melanephelinite (nmp); 3—nephelinite (np); each diagram is of three fields 1 to 3; probability-based boundaries shown in each diagram (Figure 3a-c) are listed below). The final subscript M refers to major element based classification.

Field Boundary	basanite 1_2_3		tephrite 1_2_3		foidite 1_2_3	
	$DF1_{UBsn(bsn-mnp-np)M}$	$DF2_{UBsn(bsn-mnp-np)M}$	$DF1_{UTep(bsn-mnp-np)M}$	$DF2_{UTep(bsn-mnp-np)M}$	$DF1_{UFoi(bsn-mnp-np)M}$	$DF2_{UFoi(bsn-mnp-np)M}$
B(1_2)	-1.2935775	12	1.667296	12	12	5.474186
	-0.7702	8	0.995436	8	8	4.2640865
	0.41773434	-1.07899684	-0.39871089	-0.30022605	-0.90946016	1.56875385
B(1_3)	-8.540539	-12	6.725209	-12	-12	9.8510255
	-5.259421	-8	4.289634	-8	-9.5213475	8
	0.41773434	-1.07899684	-0.39871089	-0.30022605	-0.90946016	1.56875385
B(2_3)	12	0.236048	-12	-2.382448	-0.9401635	-12
	8	-0.2181105	-8	-1.6645205	-0.9311125	-8
	0.41773434	-1.07899684	-0.39871089	-0.30022605	-0.90946016	1.56875385

Table S19: Classification of ultrabasic (U) basanite (Bsn), tephrite (Tep), and foidite (Foi); Figure 3a-c, respectively, each as three sub-varieties (1—basanite (bsn); 2—melanephelinite (mnp); 3—nephelinite (np)) in a diagram based on transformed major elements (M).

Figure type	Subvariety type	Total number of samples	Number of classified rock types in major-element based diagrams			
			basanite (bsn)	melanephelinite (mnp)	nephelinite (np)	percent success (correct classification)
basanite (Bsn) subdivision	Basanite	658	591	51	16	89.8%
	melanephelinite	369	7	331	31	89.7%
	nephelinite	44	0	1	43	98%
tephrite (Tep) subdivision	basanite	87	84	2	1	97%
	melanephelinite	45	2	38	5	84%
	nephelinite	18	1	1	16	89%
foidite (Foi) subdivision	basanite	7	4	3	0	57%
	melanephelinite	142	2	138	2	97%
	nephelinite	62	0	1	61	98%

Table S20: Synthesis of three field multidimensional subclassification of rock name for one sample of ultrabasic basanite, basanite (IUGS classification) rock (ME90-11−internal name given by the original authors (Binard et al., 1993); assigned name BMGT0007) in the diagram for Ubasanite igneous rock subdivision (original data plotted in Figure S3a).

Figure name	Figure type	Total probability of the sample	Probability distribution for the sample		
			basanite bsn (p_{bsn}) Θ	melanephelinite mnp (p_{mnp}) Θ	nephelinite np (p_{np}) Θ
Subdivision as Ubasanite rock type	bsn-mnp-np	1	**0.812323**	0.183128	0.004549

Θ bsn−basanite; mnp−melanephelinite; nephelinite−np; the probability values for a sample from a given locality are represented by (p_{bsn}) – probability for the subvariety basanite field in the diagram; [p_{mnp}] – probability for the subvariety melanephelinite field in the diagram; [p_{Tep}] – probability for the subvariety nephelinite field in the diagram.

Table S21: Discriminant function (DF1-DF2) equations for five diagrams (not shown for here onwards; see text for explanation) based on isometric log-ratio transformation of major-elements (M) for the classification of basic (B) igneous rocks as 1—basalt (B), 2—trachybasalt (TB), 3—subgroup of basanite, tephrite and foidite (BsnTepFoi), and 4—subgroup of basaltic trachyandesite, phonotephrite, tephriphonolite and phonolite (BtaPhtTphPh).

$$\mathrm{DF1}_{B(\mathrm{B+TB-BsnTepFoi-BtaPhtTphPh})\mathrm{M}} = (-5.6959 \times \mathrm{ilr1}_{\mathrm{TiM}}) + (-5.5610 \times \mathrm{ilr2}_{\mathrm{AlM}}) + (-4.7442 \times \mathrm{ilr3}_{\mathrm{FeM}}) + (1.1748 \times \mathrm{ilr4}_{\mathrm{MnM}}) + (-1.1817 \times \mathrm{ilr5}_{\mathrm{MgM}}) + (-0.4471 \times \mathrm{ilr6}_{\mathrm{CaM}}) + (1.1727 \times \mathrm{ilr7}_{\mathrm{NaM}}) + (0.2972 \times \mathrm{ilr8}_{\mathrm{KM}}) + (0.9788 \times \mathrm{ilr9}_{\mathrm{PM}}) + 2.1192 \quad \text{(S27)}$$

$$\mathrm{DF2}_{B(\mathrm{B+TB-BsnTepFoi-BtaPhtTphPh})\mathrm{M}} = (9.0901 \times \mathrm{ilr1}_{\mathrm{TiM}}) + (7.3098 \times \mathrm{ilr2}_{\mathrm{AlM}}) + (4.2840 \times \mathrm{ilr3}_{\mathrm{FeM}}) + (5.0446 \times \mathrm{ilr4}_{\mathrm{MnM}}) + (2.6362 \times \mathrm{ilr5}_{\mathrm{MgM}}) + (4.2233 \times \mathrm{ilr6}_{\mathrm{CaM}}) + (1.8790 \times \mathrm{ilr7}_{\mathrm{NaM}}) + (0.3710 \times \mathrm{ilr8}_{\mathrm{KM}}) + (0.4232 \times \mathrm{ilr9}_{\mathrm{PM}}) - 36.3718 \quad \text{(S28)}$$

$$\mathrm{DF1}_{B(\mathrm{B-TB-BsnTepFoi})\mathrm{M}} = (0.0326 \times \mathrm{ilr1}_{\mathrm{TiM}}) + (-0.2585 \times \mathrm{ilr2}_{\mathrm{AlM}}) + (-1.5101 \times \mathrm{ilr3}_{\mathrm{FeM}}) + (2.6619 \times \mathrm{ilr4}_{\mathrm{MnM}}) + (0.1257 \times \mathrm{ilr5}_{\mathrm{MgM}}) + (0.5064 \times \mathrm{ilr6}_{\mathrm{CaM}}) + (2.4389 \times \mathrm{ilr7}_{\mathrm{NaM}}) + (0.3751 \times \mathrm{ilr8}_{\mathrm{KM}}) + (1.2219 \times \mathrm{ilr9}_{\mathrm{PM}}) - 15.2596 \quad \text{(S29)}$$

$$\mathrm{DF2}_{B(\mathrm{B-TB-BsnTepFoi})\mathrm{M}} = (7.3355 \times \mathrm{ilr1}_{\mathrm{TiM}}) + (4.3438 \times \mathrm{ilr2}_{\mathrm{AlM}}) + (2.5131 \times \mathrm{ilr3}_{\mathrm{FeM}}) + (6.8214 \times \mathrm{ilr4}_{\mathrm{MnM}}) + (2.5854 \times \mathrm{ilr5}_{\mathrm{MgM}}) + (6.5598 \times \mathrm{ilr6}_{\mathrm{CaM}}) + (1.4027 \times \mathrm{ilr7}_{\mathrm{NaM}}) + (0.3533 \times \mathrm{ilr8}_{\mathrm{KM}}) + (-0.0506 \times \mathrm{ilr9}_{\mathrm{PM}}) - 37.0634 \quad \text{(S30)}$$

$$\mathrm{DF1}_{B(\mathrm{B-TB-BtaPhtTphPh})\mathrm{M}} = (-5.3686 \times \mathrm{ilr1}_{\mathrm{TiM}}) + (-4.6313 \times \mathrm{ilr2}_{\mathrm{AlM}}) + (-5.1012 \times \mathrm{ilr3}_{\mathrm{FeM}}) + (1.2685 \times \mathrm{ilr4}_{\mathrm{MnM}}) + (-1.3204 \times \mathrm{ilr5}_{\mathrm{MgM}}) + (-1.8654 \times \mathrm{ilr6}_{\mathrm{CaM}}) + (1.1018 \times \mathrm{ilr7}_{\mathrm{NaM}}) + (0.2990 \times \mathrm{ilr8}_{\mathrm{KM}}) + (1.1894 \times \mathrm{ilr9}_{\mathrm{PM}}) - 0.1423 \quad \text{(S31)}$$

$$\mathrm{DF2}_{B(\mathrm{B-TB-BtaPhtTphPh})\mathrm{M}} = (-8.8071 \times \mathrm{ilr1}_{\mathrm{TiM}}) + (-8.6210 \times \mathrm{ilr2}_{\mathrm{AlM}}) + (-7.0448 \times \mathrm{ilr3}_{\mathrm{FeM}}) + (0.5359 \times \mathrm{ilr4}_{\mathrm{MnM}}) + (-2.0836 \times \mathrm{ilr5}_{\mathrm{MgM}}) + (-1.5764 \times \mathrm{ilr6}_{\mathrm{CaM}}) + (-2.1142 \times \mathrm{ilr7}_{\mathrm{NaM}}) + (-0.0364 \times \mathrm{ilr8}_{\mathrm{KM}}) + (-0.4602 \times \mathrm{ilr9}_{\mathrm{PM}}) + 15.8404 \quad \text{(S32)}$$

$$\mathrm{DF1}_{B(\mathrm{B-BsnTepFoi-BtaPhtTphPh})\mathrm{M}} = (-5.3575 \times \mathrm{ilr1}_{\mathrm{TiM}}) + (-4.9707 \times \mathrm{ilr2}_{\mathrm{AlM}}) + (-4.4228 \times \mathrm{ilr3}_{\mathrm{FeM}}) + (1.2998 \times \mathrm{ilr4}_{\mathrm{MnM}}) + (-1.0877 \times \mathrm{ilr5}_{\mathrm{MgM}}) + (-0.5967 \times \mathrm{ilr6}_{\mathrm{CaM}}) + (1.4542 \times \mathrm{ilr7}_{\mathrm{NaM}}) + (0.2651 \times \mathrm{ilr8}_{\mathrm{KM}}) + (1.4103 \times \mathrm{ilr9}_{\mathrm{PM}}) - 0.3192 \quad \text{(S33)}$$

$$\mathrm{DF2}_{B(\mathrm{B-BsnTepFoi-BtaPhtTphPh})\mathrm{M}} = (-9.5949 \times \mathrm{ilr1}_{\mathrm{TiM}}) + (-7.7752 \times \mathrm{ilr2}_{\mathrm{AlM}}) + (-4.6890 \times \mathrm{ilr3}_{\mathrm{FeM}}) + (-4.9780 \times \mathrm{ilr4}_{\mathrm{MnM}}) + (-2.6437 \times \mathrm{ilr5}_{\mathrm{MgM}}) + (-4.2891 \times \mathrm{ilr6}_{\mathrm{CaM}}) + (-1.9111 \times \mathrm{ilr7}_{\mathrm{NaM}}) + (-0.3263 \times \mathrm{ilr8}_{\mathrm{KM}}) + (-0.3624 \times \mathrm{ilr9}_{\mathrm{PM}}) + 36.8929 \quad \text{(S34)}$$

$$\mathrm{DF1}_{B(\mathrm{TB-BsnTepFoi-BtaPhtTphPh})\mathrm{M}} = (5.8660 \times \mathrm{ilr1}_{\mathrm{TiM}}) + (5.7034 \times \mathrm{ilr2}_{\mathrm{AlM}}) + (4.5937 \times \mathrm{ilr3}_{\mathrm{FeM}}) + (0.7376 \times \mathrm{ilr4}_{\mathrm{MnM}}) + (1.2588 \times \mathrm{ilr5}_{\mathrm{MgM}}) + (1.9712 \times \mathrm{ilr6}_{\mathrm{CaM}}) + (-1.4797 \times \mathrm{ilr7}_{\mathrm{NaM}}) + (-1.1922 \times \mathrm{ilr8}_{\mathrm{KM}}) + (-0.4435 \times \mathrm{ilr9}_{\mathrm{PM}}) - 10.5397 \quad \text{(S35)}$$

$$\mathrm{DF2}_{B(\mathrm{TB-BsnTepFoi-BtaPhtTphPh})\mathrm{M}} = (-9.5288 \times \mathrm{ilr1}_{\mathrm{TiM}}) + (-7.5312 \times \mathrm{ilr2}_{\mathrm{AlM}}) + (-4.6904 \times \mathrm{ilr3}_{\mathrm{FeM}}) + (-3.4043 \times \mathrm{ilr4}_{\mathrm{MnM}}) + (-2.6458 \times \mathrm{ilr5}_{\mathrm{MgM}}) + (-2.1155 \times \mathrm{ilr6}_{\mathrm{CaM}}) + (-2.8044 \times \mathrm{ilr7}_{\mathrm{NaM}}) + (-2.7220 \times \mathrm{ilr8}_{\mathrm{KM}}) + (-0.4587 \times \mathrm{ilr9}_{\mathrm{PM}}) + 34.0503 \quad \text{(S36)}$$

Table S22: Probability-based boundary coordinates estimated for basic (B) rock subdivision (1—basalt (B), 2—trachybasalt (TB), 3—subgroup of basanite, tephrite and foidite (BsnTepFoi), and 4—subgroup of basaltic trachyandesite, phonotephrite, tephriphonolite and phonolite (BtaPhtTphPh)); each diagram is considered as of three fields 1 to 3; the triple point common to all field boundaries is repeated in each set of coordinates).

Field Boundary	12_3_4		1_2_3		1_2_4		1_3_4		2_3_4	
	$\mathrm{DF1}_{B(\mathrm{B+TB-BsnTepFoi-BtaPht(TphPh)})\mathrm{M}}$	$\mathrm{DF2}_{B(\mathrm{B+TB-BsnTepFoi-BtaPht(TphPh)})\mathrm{M}}$	$\mathrm{DF1}_{B(\mathrm{B-TB-BsnTepFoi})\mathrm{M}}$	$\mathrm{DF2}_{B(\mathrm{B-TB-BsnTepFoi})\mathrm{M}}$	$\mathrm{DF1}_{B(\mathrm{B-TB-BtaPht(TphPh)})\mathrm{M}}$	$\mathrm{DF2}_{B(\mathrm{B-TB-BtaPht(TphPh)})\mathrm{M}}$	$\mathrm{DF1}_{B(\mathrm{B-BsnTepFoi-BtaPht(TphPh)})\mathrm{M}}$	$\mathrm{DF2}_{B(\mathrm{B-BsnTepFoi-BtaPht(TphPh)})\mathrm{M}}$	$\mathrm{DF1}_{B(\mathrm{TB-BsnTepFoi-BtaPht(TphPh)})\mathrm{M}}$	$\mathrm{DF2}_{B(\mathrm{TB-BsnTepFoi-BtaPht(TphPh)})\mathrm{M}}$
B(1_2)	12	-12	2.0855	12	4.1115	12	7.9519565	12	-12	1.438877
	7.707629	-8	1.1695	8	2.5375	8	4.8680295	8	-8	1.0820885
	-1.36483992	-0.00827106	-0.84075319	-0.77742455	-1.23690497	-1.59204808	-1.51380878	-0.27754777	0.39325132	0.3334344
B(1_3)	1.0103705	12	2.401	-12	0.5585	-12	0.8514685	-12	2.8211355	-12
	0.219179	8	1.2455	-8	-0.1315	-8	0.0443755	-8	2.03372	-8
	-1.36483992	-0.00827106	-0.84075319	-0.77742455	-1.23690497	-1.59204808	-1.51380878	-0.27754777	0.39325132	0.3334344
B(2_3)	-12	-7.563679	-12	5.1485	-11.4105	12	-12	6.577417	8	11.44252
	-8	-4.7220075	-8	3.0245	-8.4165	8	-8	3.962563	5.642796	8
	-1.36483992	-0.00827106	-0.84075319	-0.77742455	-1.23690497	-1.59204808	-1.51380878	-0.27754777	0.39325132	0.3334344

Table S23: Classification (percent success) of basic (B) rocks as four types (1—basalt (B), 2—trachybasalt (TB), 3—subgroup of basanite tephrite and foidite (BsnTepFoi), and 4—subgroup of basaltic trachyandesite, phonotephrite, tephriphonolite and phonolite (BtaPhtTphPh)).

Figure type	Sample type	Total number of samples	Number of classified rock types in major element based diagrams					
			basalt + trachybasalt (B+TB)	basalt (B)	trachybasalt (TB)	Subgroup of basanite, tephrite and foidite (BsnTepFoi)	subgroup of basaltic trachyandesite, phonotephrite, tephriphonolite and phonolite (BtaPhtTphPh)	percent success (correct classification)
basalt+trachybasalt-BsnTepFoi-BtaPhtTphPh	basalt + trachybasalt	10835	8855			1348	632	81.7%
	BsnTepFoi	632	44			531	57	84.0%
	BtaPhtTphPh	737	6			74	657	82.3%
basalt-trachybasalt-BsnTepFoi	Basalt	9349		7482	1350	517		80.0%
	Trachybasalt	1486		39	1052	395		70.8%
	BsnTepFoi	632		20	179	433		68.5%
basalt-trachybasalt-BtaPhtTphPh	Basalt	9349		7683	1580		86	82.2%
	Trachybasalt	1486		49	1215		222	81.8%
	BtaPhtTphPh	737		1	85		651	88.3%
basalt-BsnTepFoi-BtaPhtTphPh	Basalt	9349		8353		735	261	82.2%
	BsnTepFoi	632		27		540	65	79%
	BtaPhtTphPh	737		4		73	660	88.6%
trachybasalt-BsnTepFoi-BtaPhtTphPh	Trachybasalt	1486			1216	170	100	81.8%
	BsnTepFoi	632			47	532	53	84.2%
	BtaPhtTphPh	737			95	78	564	76.5%

Table S24: Synthesis of four field classification of basic rocks in five diagrams based on major elements (M).

B rock name (IUGS)	Total number of samples	Number of classified rock types **(percent success)**			
		basalt (B)	trachybasalt (TB)	BsnTepFoi	BtaPhtTphPh
basalt	9349	**7295(78.03%)**	1693(18.11%)	311(3.33%)	50(0.53%)
trachybasalt	1486	39(2.62%)	**859(57.81%)**	377(25.37%)	211(14.2%)
BsnTepFoi	632	13(2.1%)	50(7.9%)	**516(81.6%)**	53(8.4%)
BtaPhtTphPh	737	1(0.1%)	27(3.7%)	72(9.8%)	**637(86.4%)**

The correct classification is shown in **bold** face.

Table S25: Discriminant function (DF1) equation for single axis diagram (probability-based one-axis boundary = 0.851643) based on isometric log-ratio transformation of major-elements (M) for the classification of basalt (B) as 1—alkali basalt (Balk) and 2—subalkali basalt (Bsubalk).

$$\begin{aligned}\mathrm{DF1}_{B(\mathrm{Balk-Bsubalk})\mathrm{M}} &= (-13.1571 \times \mathrm{ilr1}_{\mathrm{TiM}}) + (-9.4610 \times \mathrm{ilr2}_{\mathrm{AlM}}) + (-7.2854 \times \mathrm{ilr3}_{\mathrm{FeM}}) + (-3.4176 \times \mathrm{ilr4}_{\mathrm{MnM}}) \\ &+ (-5.1692 \times \mathrm{ilr5}_{\mathrm{MgM}}) + (-8.8971 \times \mathrm{ilr6}_{\mathrm{CaM}}) + (-4.4608 \times \mathrm{ilr7}_{\mathrm{NaM}}) + (-0.8270 \times \mathrm{ilr8}_{\mathrm{KM}}) \\ &+ (-0.5160 \times \mathrm{ilr9}_{\mathrm{PM}}) + 38.0880 \end{aligned} \quad (S37)$$

Table S26: Percent success for the subdivision of basalt (B) in two varieties (1—alkali basalt (Balk); 2—subalkali basalt (Bsubalk) in the one-axis diagram.

Figure type	Subvariety type	Total number of samples	Number of classified rock types in major-element based diagram		
			alkali basalt (Balk)	subalkali basalt (Bsubalk)	percent success (correct classification)
basalt (B) subdivision	alkali basalt	2005	1919	86	95.7%
	subalkali basalt	7344	630	6714	91.4%

Table S27: Discriminant function (DF1) equation for single axis diagram (probability-based one-axis boundary = -0.122177) based on isometric log-ratio transformation of major-elements (M) for the classification of trachybasalt (TB) as variety of 1—hawaiite (TBhaw) and 2—potassic (TBpot).

$$\begin{aligned}\mathrm{DF1}_{B(\mathrm{TBhaw-TBpot})\mathrm{M}} &= (3.9990 \times \mathrm{ilr1}_{\mathrm{TiM}}) + (4.0185 \times \mathrm{ilr2}_{\mathrm{AlM}}) + (1.5796 \times \mathrm{ilr3}_{\mathrm{FeM}}) + (0.1531 \times \mathrm{ilr4}_{\mathrm{MnM}}) \\ &+ (1.2878 \times \mathrm{ilr5}_{\mathrm{MgM}}) + (-0.0937 \times \mathrm{ilr6}_{\mathrm{CaM}}) + (-0.8933 \times \mathrm{ilr7}_{\mathrm{NaM}}) + (4.2458 \times \mathrm{ilr8}_{\mathrm{KM}}) \\ &+ (-0.4506 \times \mathrm{ilr9}_{\mathrm{PM}}) - 10.9972 \end{aligned} \quad (S38)$$

Table S28: Percent success for the subdivision of trachybasalt (TB) in two varieties (1—hawaiite (TBhaw); 2—potassic (TBpot).

Figure type	Subvariety type	Total number of samples	Number of classified rock types in major-element based diagram		
			trachybasalt hawaiite (TBhaw)	trachybasalt potassic (TBpot)	percent success (correct classification)
trachybasalt (TB) subdivision	hawaiite	829	781	48	94.2%
	potassic	657	86	571	86.9%

Table S29: Discriminant function (DF1-DF2) equations for the diagram based on isometric log-ratio transformation of major-elements (M) for the classification of basic (B) igneous rocks (BsnTepFoi) as three rock types: 1—basanite (Bsn); 2—tephrite (Tep); 3—foidite (Foi); coefficients reported as arbitrarily rounded to four decimal places.

$$\mathrm{DF1}_{BBsnTepFoi(\mathrm{Bsn-Tep-Foi})\mathrm{M}} = (-1.1738 \times \mathrm{ilr1}_{\mathrm{TiM}}) + (-1.9078 \times \mathrm{ilr2}_{\mathrm{AlM}}) + (-2.1709 \times \mathrm{ilr3}_{\mathrm{FeM}}) + (1.4166 \times \mathrm{ilr4}_{\mathrm{MnM}}) + (-2.4020 \times \mathrm{ilr5}_{\mathrm{MgM}}) + (0.9310 \times \mathrm{ilr6}_{\mathrm{CaM}}) + (0.7837 \times \mathrm{ilr7}_{\mathrm{NaM}}) + (2.1033 \times \mathrm{ilr8}_{\mathrm{KM}}) + (-0.4937 \times \mathrm{ilr9}_{\mathrm{PM}}) - 4.1820 \quad \text{(S39)}$$

$$\mathrm{DF2}_{BBsnTepFoi(\mathrm{Bsn-Tep-Foi})\mathrm{M}} = (4.3933 \times \mathrm{ilr1}_{\mathrm{TiM}}) + (2.4965 \times \mathrm{ilr2}_{\mathrm{AlM}}) + (-1.8738 \times \mathrm{ilr3}_{\mathrm{FeM}}) + (1.5867 \times \mathrm{ilr4}_{\mathrm{MnM}}) + (-0.6246 \times \mathrm{ilr5}_{\mathrm{MgM}}) + (5.4719 \times \mathrm{ilr6}_{\mathrm{CaM}}) + (-0.9717 \times \mathrm{ilr7}_{\mathrm{NaM}}) + (-0.3855 \times \mathrm{ilr8}_{\mathrm{KM}}) + (0.8607 \times \mathrm{ilr9}_{\mathrm{PM}}) - 12.4736 \quad \text{(S40)}$$

Table S30: Probability-based boundary coordinates estimated for the basic (B) basanite, tephrite, and foidite subdivision diagram in three rock types (1—basanite (Bsn); 2—tephrite (Tep); 3—foidite (Foi); probability-based boundaries shown in each diagram are listed below). The final subscript M refers to major element based classification.

Field Boundary	basanite-tephrite-foidite 1_2_3	
	$\mathrm{DF1}_{\mathrm{BBsnTepFoi(Bsn-Tep-Foi)M}}$	$\mathrm{DF2}_{\mathrm{BBsnTepFoi(Bsn-Tep-Foi)M}}$
B(1_2)	-1.146	12
	-1.4605	8
	-1.92875363	2.04151056
B(1_3)	-7.6995	-12
	-6.0555	-8
	-1.92875363	2.04151056
B(2_3)	10.23	-12
	6.7665	-8
	-1.92875363	2.04151056

Table S31: Classification of basic (B) combined basanite (Bsn), tephrite (Tep), and foidite (Foi) rocks as the three rock types (1—basanite (Bsn); 2—tephrite (Tep); 3—foidite (Foi)) in a diagram based on transformed major elements (M).

Figure type	Rock type	Total number of samples	Number of classified rock types in major-element based diagrams			
			basanite (Bsn)	tephrite (Tep)	foidite (Foi)	percent success (correct classification)
Basanite-tephrite-foidite (Bsn-Tep-Foi) subdivision	basanite	413	0	348	65	84.3%
	tephrite	162	0	8	154	95.1%
	foidite	57	50	1	6	88%

Table S32: Discriminant function (DF1-DF2) equations for the diagram based on isometric log-ratio transformation of major-elements (M) for the classification of basic (B) basanite igneous rocks (Bsn) as three sub-varieties: 1—basanite (bsn); 2—melanephelinite (mnp); 3—nephelinite (np); coefficients reported as arbitrarily rounded to four decimal places.

$$\mathrm{DF1}_{BBsn(\mathrm{bsn-mnp-np})\mathrm{M}} = (-5.1802 \times \mathrm{ilr1}_{\mathrm{TiM}}) + (-2.7415 \times \mathrm{ilr2}_{\mathrm{AlM}}) + (-0.3820 \times \mathrm{ilr3}_{\mathrm{FeM}}) + (-1.8180 \times \mathrm{ilr4}_{\mathrm{MnM}}) + (-1.1903 \times \mathrm{ilr5}_{\mathrm{MgM}}) + (3.7125 \times \mathrm{ilr6}_{\mathrm{CaM}}) + (-3.6147 \times \mathrm{ilr7}_{\mathrm{NaM}}) + (0.7613 \times \mathrm{ilr8}_{\mathrm{KM}}) + (0.6114 \times \mathrm{ilr9}_{\mathrm{PM}}) + 17.9582 \quad \text{(S41)}$$

$$\mathrm{DF2}_{BBsn(\mathrm{bsn-mnp-np})\mathrm{M}} = (10.2479 \times \mathrm{ilr1}_{\mathrm{TiM}}) + (7.6202 \times \mathrm{ilr2}_{\mathrm{AlM}}) + (6.0319 \times \mathrm{ilr3}_{\mathrm{FeM}}) + (3.7770 \times \mathrm{ilr4}_{\mathrm{MnM}}) + (3.8249 \times \mathrm{ilr5}_{\mathrm{MgM}}) + (6.3120 \times \mathrm{ilr6}_{\mathrm{CaM}}) + (6.6493 \times \mathrm{ilr7}_{\mathrm{NaM}}) + (2.7004 \times \mathrm{ilr8}_{\mathrm{KM}}) + (-0.0029 \times \mathrm{ilr9}_{\mathrm{PM}}) - 33.6662 \quad \text{(S42)}$$

Table S33: Discriminant function (DF1-DF2) equations for the diagram based on isometric log-ratio transformation of major-elements (M) for the classification of basic (B) tephrite igneous rocks (Tep) as three sub-varieties: 1—basanite (bsn); 2—melanephelinite (mnp); 3—nephelinite (np); coefficients reported as arbitrarily rounded to four decimal places.

$$\mathrm{DF1}_{BTep(\mathrm{bsn-mnp-np})\mathrm{M}} = (0.4339 \times \mathrm{ilr1}_{\mathrm{TiM}}) + (0.9161 \times \mathrm{ilr2}_{\mathrm{AlM}}) + (-0.9292 \times \mathrm{ilr3}_{\mathrm{FeM}}) + (-3.0416 \times \mathrm{ilr4}_{\mathrm{MnM}}) + (-0.7075 \times \mathrm{ilr5}_{\mathrm{MgM}}) + (-6.5347 \times \mathrm{ilr6}_{\mathrm{CaM}}) + (-0.0676 \times \mathrm{ilr7}_{\mathrm{NaM}}) + (-1.4120 \times \mathrm{ilr8}_{\mathrm{KM}}) + (-0.0029 \times \mathrm{ilr9}_{\mathrm{PM}}) + 7.4123 \quad \text{(S43)}$$

$$\mathrm{DF2}_{BTep(\mathrm{bsn-mnp-np})\mathrm{M}} = (-12.5079 \times \mathrm{ilr1}_{\mathrm{TiM}}) + (-13.0349 \times \mathrm{ilr2}_{\mathrm{AlM}}) + (-1.8174 \times \mathrm{ilr3}_{\mathrm{FeM}}) + (-3.2786 \times \mathrm{ilr4}_{\mathrm{MnM}}) + (-3.9746 \times \mathrm{ilr5}_{\mathrm{MgM}}) + (-3.1698 \times \mathrm{ilr6}_{\mathrm{CaM}}) + (-4.0304 \times \mathrm{ilr7}_{\mathrm{NaM}}) + (-2.9369 \times \mathrm{ilr8}_{\mathrm{KM}}) + (-0.0908 \times \mathrm{ilr9}_{\mathrm{PM}}) + 35.4505 \quad \text{(S44)}$$

Table S34: Discriminant function (DF1-DF2) equations for the diagram based on isometric log-ratio transformation of major-elements (M) for the classification of basic (B) foidite igneous rocks (Bsn) as two sub-varieties: 1—melanephelinite (mnp); 2—nephelinite (np); probability-based one-axis boundary = -2.817012; coefficients reported as arbitrarily rounded to four decimal places.

$$\mathrm{DF1}_{BFoi(\mathrm{mnp-np})\mathrm{M}} = (-0.8838 \times \mathrm{ilr1}_{\mathrm{TiM}}) + (-1.1514 \times \mathrm{ilr2}_{\mathrm{AlM}}) + (0.2935 \times \mathrm{ilr3}_{\mathrm{FeM}}) + (-1.5238 \times \mathrm{ilr4}_{\mathrm{MnM}}) + (-2.7781 \times \mathrm{ilr5}_{\mathrm{MgM}}) + (-4.3521 \times \mathrm{ilr6}_{\mathrm{CaM}}) + (3.2636 \times \mathrm{ilr7}_{\mathrm{NaM}}) + (-6.6599 \times \mathrm{ilr8}_{\mathrm{KM}}) + (0.0483 \times \mathrm{ilr9}_{\mathrm{PM}}) - 0.6743 \quad \text{(S45)}$$

Table S35: Probability-based boundary coordinates estimated for ultrabasic (U) basanite and tephrite subdivision diagrams, each in three subvarieties (1—basanite (bsn); 2—melanephelinite (nmp); 3—nephelinite (np); each diagram is of three fields 1 to 3; probability-based boundaries shown in each diagram are listed below). The final subscript M refers to major element based classification.

Field Boundary	basanite 1_2_3		tephrite 1_2_3	
	$DF1_{BBsn(bsn-mnp-np)M}$	$DF2_{BBsn(bsn-mnp-np)M}$	$DF1_{BTep(bsn-mnp-np)M}$	$DF2_{BTep(bsn-mnp-np)M}$
B(1_2)	-2.2937975	-12	-1.2686835	-12
	-2.18523	-8	-1.162	-8
	-1.9288375	1.44633899	-0.941719329	0.259260556
B(1_3)	12	-0.5636645	12	3.7816755
	8	0.0135555	8	2.6929755
	-1.9288375	1.44633899	-0.941719329	0.259260556
B(2_3)	-6.03115	12	-6.1015935	12
	-4.47631	8	-4.3436555	8
	-1.9288375	1.44633899	-0.941719329	0.259260556

Table S36: Classification of ultrabasic (U) basanite (Bsn), tephrite (Tep), and foidite (Foi), the first two as three sub-varieties (1—basanite (bsn); 2—melanephelinite (mnp); 3—nephelinite (np)) and the last as two sub-varieties (1—melanephelinite (mnp); and 2—nephelinite (np)) in multidimensional diagrams based on transformed major elements (M).

Figure type	Subvariety type	Total number of samples	Number of classified rock types in major-element based diagrams			
			basanite (bsn)	melanephelinite (mnp)	nephelinite (np)	percent success (correct classification)
basanite (Bsn) subdivision	Basanite	346	302	3	41	87.3%
	melanephelinite	52	4	46	2	88%
	nephelinite	15	1	0	14	93%
tephrite (Tep) subdivision	basanite	102	86	0	16	84%
	melanephelinite	49	3	42	4	86%
	nephelinite	11	1	0	10	91%
foidite (Foi) subdivision	melanephelinite	40		40	0	100%
	nephelinite	17		0	17	100%

Table S37: Discriminant function (DF1-DF2) equations for the diagram based on isometric log-ratio transformation of major-elements (M) for the classification of basic (B) basaltic trachyandesite, phonotephrite, tephriphonolite and phonolite igneous rocks (BtaPhtTphPh) as three rock types: 1—basaltic trachyandesite (Bta); 2—phonotephrite (Pht); 3—tephriphonolite and phonolite (TphPh); coefficients reported as arbitrarily rounded to four decimal places.

$$\mathrm{DF1}_{BBtaPhtTphPh(\mathrm{Bta-Pht\_TphPh})\mathrm{M}} = (5.8105 \times \mathrm{ilr1}_{\mathrm{TiM}}) + (4.2536 \times \mathrm{ilr2}_{\mathrm{AlM}}) + (1.3053 \times \mathrm{ilr3}_{\mathrm{FeM}}) + (1.9423 \times \mathrm{ilr4}_{\mathrm{MnM}}) + (1.1722 \times \mathrm{ilr5}_{\mathrm{MgM}}) + (1.9002 \times \mathrm{ilr6}_{\mathrm{CaM}}) + (3.2755 \times \mathrm{ilr7}_{\mathrm{NaM}}) + (4.0003 \times \mathrm{ilr8}_{\mathrm{KM}}) + (-0.6641 \times \mathrm{ilr9}_{\mathrm{PM}}) - 19.5581 \quad \text{(S46)}$$

$$\mathrm{DF2}_{BBtaPhtTphPh(\mathrm{Bta-Pht-TphPh})\mathrm{M}} = (10.7845 \times \mathrm{ilr1}_{\mathrm{TiM}}) + (10.2783 \times \mathrm{ilr2}_{\mathrm{AlM}}) + (4.9023 \times \mathrm{ilr3}_{\mathrm{FeM}}) + (0.8320 \times \mathrm{ilr4}_{\mathrm{MnM}}) + (3.1224 \times \mathrm{ilr5}_{\mathrm{MgM}}) + (3.4326 \times \mathrm{ilr6}_{\mathrm{CaM}}) + (0.0159 \times \mathrm{ilr7}_{\mathrm{NaM}}) + (0.3162 \times \mathrm{ilr8}_{\mathrm{KM}}) + (1.2007 \times \mathrm{ilr9}_{\mathrm{PM}}) - 25.1446 \quad \text{(S47)}$$

Table S38: Probability-based boundary coordinates estimated for the basic (B) basaltic trachyandesite, phonotephrite, tephriphonolite and phonolite igneous rocks (BtaPhtTphPh) as three rock types: 1—basaltic trachyandesite (Bta); 2—phonotephrite (Pht); 3—tephriphonolite and phonolite (TphPh); probability-based boundaries shown in each diagram are listed below). The final subscript M refers to major element based classification.

Field Boundary	Basaltic trachyandesite-phonotephrite-tephriphonolite+phonolite 1_2_3	
	$DF1_{BBtaPhtTphPh(Bta\text{-}Pht\text{-}TphPh)M}$	$DF2_{BBtaPhtTphPh(Bta\text{-}Pht\text{-}TphPh)M}$
B(1_2)	-3.846516	-12
	-2.567588	-8
	0.671991972	2.13217299
B(1_3)	-6.2302915	12
	-3.4323975	8
	0.671991972	2.13217299
B(2_3)	12	-3.0774165
	8	-1.2378735
	0.671991972	2.13217299

Table S39: Classification of basic (B) basaltic trachyandesite, phonotephrite, tephriphonolite and phonolite igneous rocks (BtaPhtTphPh) as three rock types: 1—basaltic trachyandesite (Bta); 2—phonotephrite (Pht); 3—tephriphonolite and phonolite (TphPh)) in a diagram based on transformed major elements (M).

Figure type	Rock type	Total number of samples	Number of classified rock types in major-element based diagrams			
			basaltic trachyandesite (Bta)	phonotephrite (Pht)	tephriphonolite and phonolite (Tph+Ph)	percent success (correct classification)
basaltic trachyandesite, phonotephrite, tephriphonolite and phonolite (Bta-Pht-TphPh) subdivision	basaltic trachyandesite	373	333	40	0	89.3%
	phonotephrite	328	15	307	6	93.6%
	tephriphonolite and phonolite	36	0	6	30	83%

The third group of basic rocks (phonolite) is not numerous (only total of 36 samples); consequently, a five diagram set was not proposed to separate the third group (tephriphonolite 32 samples and phonolite 4 samples) in competition with the other rocks (basaltic trachyandesite 373 samples). Instead of this, it was later separated easily as tephriphonolite and phonolite; see Tables S42 amd S43 below.

Table S40: Discriminant function (DF1) equation for single axis diagram (probability-based one-axis boundary = -0.043473) based on isometric log-ratio transformation of major-elements (M) for the classification of basic (B) basaltic trachyandesite (Bta) as 1—mugearite (Btamug) and 2—shoshonite (Btasho).

$$\begin{aligned}\mathrm{DF1}_{BBta(\mathrm{Btamug-Btasho})\mathrm{M}} &= (7.2247 \times \mathrm{ilr1}_{\mathrm{TiM}}) + (6.5434 \times \mathrm{ilr2}_{\mathrm{AlM}}) + (4.8225 \times \mathrm{ilr3}_{\mathrm{FeM}}) + (-0.3136 \times \mathrm{ilr4}_{\mathrm{MnM}}) \\ &+ \left(1.6961 \times \mathrm{ilr5}_{\mathrm{MgM}}\right) + (2.5488 \times \mathrm{ilr6}_{\mathrm{CaM}}) + (-1.3826 \times \mathrm{ilr7}_{\mathrm{NaM}}) + (3.7089 \times \mathrm{ilr8}_{\mathrm{KM}}) \\ &+ (-0.3825 \times \mathrm{ilr9}_{\mathrm{PM}}) - 14.0839 \end{aligned} \quad (S48)$$

Table S41: Percent success for the subdivision for the classification of basic (B) basaltic trachyandesite (Bta) as 1—mugearite (Btamug) and 2—shoshonite (Btasho), in one-axis diagram.

Figure type	rock type	Total number of samples	Number of classified rock types in major-element based diagram		
			mugearite (Btamug)	shoshonite (Btasho)	percent success (correct classification)
basaltic trachyandesite subdivision	mugearite	193	186	7	96.4%
	shoshonite	180	20	160	88.9%

Table S42: Discriminant function (DF1) equation for single axis diagram (probability-based one-axis boundary = -3.351816) based on isometric log-ratio transformation of major-elements (M) for the classification of basic (B) group of tephriphonolite and phonolite as separate rock types; 1— tephriphonolite (Tph) and 2—phonolite (Ph).

$$\begin{aligned}\mathrm{DF1}_{BTphPh(\mathrm{Tph-Ph})\mathrm{M}} &= (-9.4808 \times \mathrm{ilr1}_{\mathrm{TiM}}) + (-9.6500 \times \mathrm{ilr2}_{\mathrm{AlM}}) + (-7.1436 \times \mathrm{ilr3}_{\mathrm{FeM}}) + (-4.5238 \times \mathrm{ilr4}_{\mathrm{MnM}}) \\ &+ \left(-2.6766 \times \mathrm{ilr5}_{\mathrm{MgM}}\right) + (-0.0180 \times \mathrm{ilr6}_{\mathrm{CaM}}) + (2.6044 \times \mathrm{ilr7}_{\mathrm{NaM}}) + (2.4203 \times \mathrm{ilr8}_{\mathrm{KM}}) \\ &+ (1.1477 \times \mathrm{ilr9}_{\mathrm{PM}}) + 36.5795 \end{aligned} \quad (S49)$$

Table S43: Percent success for the subdivision of basic (B) group of phonotephrite and tephriphonolite as separate rock types; 1— tephriphonolite (Tph) and 2—phonolite (Ph), in one-axis diagram.

Figure type	rock type	Total number of samples	Number of classified rock types in major-element based diagram		
			tephriphonolite (Tph)	phonolite (Ph)	percent success (correct classification)
tephriphonolite and phonolite subdivision	tephriphonolite	32	32	0	100%
	phonolite	4	0	4	100%

Table S44: Discriminant function (DF1-DF2) equations for five diagrams based on isometric log-ratio transformation of major-elements (M) for the classification of intermediate (I) igneous rocks as 1—basaltic andesite (BA), 2—andesite (A), 3—subgroup of basaltic trachyandesite, trachyandesite and trachyte (BtaTAT), and 4—subgroup of phonotephrite, tephriphonolite and phonolite (PhtTphPh).

$$\mathrm{DF1}_{I(\mathrm{BA+A-BtaTAT-PhtTphPh})\mathrm{M}} = (5.4014 \times \mathrm{ilr1}_{\mathrm{TiM}}) + (4.9576 \times \mathrm{ilr2}_{\mathrm{AlM}}) + (1.2720 \times \mathrm{ilr3}_{\mathrm{FeM}}) + (1.4882 \times \mathrm{ilr4}_{\mathrm{MnM}}) + (0.4269 \times \mathrm{ilr5}_{\mathrm{MgM}}) + (-0.1296 \times \mathrm{ilr6}_{\mathrm{CaM}}) + (1.6744 \times \mathrm{ilr7}_{\mathrm{NaM}}) + (2.1042 \times \mathrm{ilr8}_{\mathrm{KM}}) + (0.1989 \times \mathrm{ilr9}_{\mathrm{PM}}) - 20.8072 \quad \text{(S50)}$$

$$\mathrm{DF2}_{I(\mathrm{BA+A-BtaTAT-PhtTphPh})\mathrm{M}} = (3.4610 \times \mathrm{ilr1}_{\mathrm{TiM}}) + (6.8212 \times \mathrm{ilr2}_{\mathrm{AlM}}) + (-1.7903 \times \mathrm{ilr3}_{\mathrm{FeM}}) + (0.7534 \times \mathrm{ilr4}_{\mathrm{MnM}}) + (0.2533 \times \mathrm{ilr5}_{\mathrm{MgM}}) + (-1.3852 \times \mathrm{ilr6}_{\mathrm{CaM}}) + (0.0767 \times \mathrm{ilr7}_{\mathrm{NaM}}) + (-0.0918 \times \mathrm{ilr8}_{\mathrm{KM}}) + (-1.3679 \times \mathrm{ilr9}_{\mathrm{PM}}) - 4.8853 \quad \text{(S51)}$$

$$\mathrm{DF1}_{I(\mathrm{BA-A-BtaTAT})\mathrm{M}} = (-0.5220 \times \mathrm{ilr1}_{\mathrm{TiM}}) + (-2.9607 \times \mathrm{ilr2}_{\mathrm{AlM}}) + (0.2003 \times \mathrm{ilr3}_{\mathrm{FeM}}) + (0.7400 \times \mathrm{ilr4}_{\mathrm{MnM}}) + (-0.1108 \times \mathrm{ilr5}_{\mathrm{MgM}}) + (1.0590 \times \mathrm{ilr6}_{\mathrm{CaM}}) + (1.8754 \times \mathrm{ilr7}_{\mathrm{NaM}}) + (1.6122 \times \mathrm{ilr8}_{\mathrm{KM}}) + (0.6654 \times \mathrm{ilr9}_{\mathrm{PM}}) - 6.2789 \quad \text{(S52)}$$

$$\mathrm{DF2}_{I(\mathrm{BA-A-BtaTAT})\mathrm{M}} = (9.1712 \times \mathrm{ilr1}_{\mathrm{TiM}}) + (10.5562 \times \mathrm{ilr2}_{\mathrm{AlM}}) + (3.0229 \times \mathrm{ilr3}_{\mathrm{FeM}}) + (1.1968 \times \mathrm{ilr4}_{\mathrm{MnM}}) + (0.9290 \times \mathrm{ilr5}_{\mathrm{MgM}}) + (-1.3435 \times \mathrm{ilr6}_{\mathrm{CaM}}) + (0.0875 \times \mathrm{ilr7}_{\mathrm{NaM}}) + (1.2216 \times \mathrm{ilr8}_{\mathrm{KM}}) + (0.0664 \times \mathrm{ilr9}_{\mathrm{PM}}) - 26.5728 \quad \text{(S53)}$$

$$\mathrm{DF1}_{I(\mathrm{BA-A-PhtTphPh})\mathrm{M}} = (2.1756 \times \mathrm{ilr1}_{\mathrm{TiM}}) + (1.9332 \times \mathrm{ilr2}_{\mathrm{AlM}}) + (2.4150 \times \mathrm{ilr3}_{\mathrm{FeM}}) + (-0.6872 \times \mathrm{ilr4}_{\mathrm{MnM}}) + (1.0534 \times \mathrm{ilr5}_{\mathrm{MgM}}) + (1.9843 \times \mathrm{ilr6}_{\mathrm{CaM}}) + (-0.1212 \times \mathrm{ilr7}_{\mathrm{NaM}}) + (-1.1734 \times \mathrm{ilr8}_{\mathrm{KM}}) + (0.3988 \times \mathrm{ilr9}_{\mathrm{PM}}) - 1.5505 \quad \text{(S54)}$$

$$\mathrm{DF2}_{I(\mathrm{BA-A-PhtTphPh})\mathrm{M}} = (-12.2498 \times \mathrm{ilr1}_{\mathrm{TiM}}) + (-14.9610 \times \mathrm{ilr2}_{\mathrm{AlM}}) + (-2.0900 \times \mathrm{ilr3}_{\mathrm{FeM}}) + (-2.4752 \times \mathrm{ilr4}_{\mathrm{MnM}}) + (-1.2130 \times \mathrm{ilr5}_{\mathrm{MgM}}) + (2.6402 \times \mathrm{ilr6}_{\mathrm{CaM}}) + (-0.6826 \times \mathrm{ilr7}_{\mathrm{NaM}}) + (-1.2446 \times \mathrm{ilr8}_{\mathrm{KM}}) + (0.9435 \times \mathrm{ilr9}_{\mathrm{PM}}) + 35.3888 \quad \text{(S55)}$$

$$\mathrm{DF1}_{I(\mathrm{BA-BtaTAT-PhtTphPh})\mathrm{M}} = (0.7996 \times \mathrm{ilr1}_{\mathrm{TiM}}) + (-0.7804 \times \mathrm{ilr2}_{\mathrm{AlM}}) + (-0.1874 \times \mathrm{ilr3}_{\mathrm{FeM}}) + (0.6284 \times \mathrm{ilr4}_{\mathrm{MnM}}) + (-0.0918 \times \mathrm{ilr5}_{\mathrm{MgM}}) + (0.7943 \times \mathrm{ilr6}_{\mathrm{CaM}}) + (1.6342 \times \mathrm{ilr7}_{\mathrm{NaM}}) + (1.5741 \times \mathrm{ilr8}_{\mathrm{KM}}) + (0.5254 \times \mathrm{ilr9}_{\mathrm{PM}}) - 7.6267 \quad \text{(S56)}$$

$$\mathrm{DF2}_{I(\mathrm{BA-BtaTAT-PhtTphPh})\mathrm{M}} = (6.2508 \times \mathrm{ilr1}_{\mathrm{TiM}}) + (9.3257 \times \mathrm{ilr2}_{\mathrm{AlM}}) + (-0.3445 \times \mathrm{ilr3}_{\mathrm{FeM}}) + (1.1835 \times \mathrm{ilr4}_{\mathrm{MnM}}) + (0.5819 \times \mathrm{ilr5}_{\mathrm{MgM}}) + (-1.4042 \times \mathrm{ilr6}_{\mathrm{CaM}}) + (0.1818 \times \mathrm{ilr7}_{\mathrm{NaM}}) + (0.5112 \times \mathrm{ilr8}_{\mathrm{KM}}) + (-1.2234 \times \mathrm{ilr9}_{\mathrm{PM}}) - 13.9244 \quad \text{(S57)}$$

$$DF1_{I(\mathrm{A-BtaTAT-PhtTphPh)M}} = (-7.7269 \times \mathrm{ilr1_{TiM}}) + (-7.2435 \times \mathrm{ilr2_{AlM}}) + (-2.6515 \times \mathrm{ilr3_{FeM}}) + (-1.7922 \times \mathrm{ilr4_{MnM}}) + \left(-1.1543 \times \mathrm{ilr5_{MgM}}\right) + (-0.5629 \times \mathrm{ilr6_{CaM}}) + (-2.8180 \times \mathrm{ilr7_{NaM}}) + (-2.8252 \times \mathrm{ilr8_{KM}}) + (-0.1617 \times \mathrm{ilr9_{PM}}) + 27.2840 \quad \text{(S58)}$$

$$DF2_{I(\mathrm{A-BtaTAT-PhtTphPh)M}} = (-2.2471 \times \mathrm{ilr1_{TiM}}) + (-6.0041 \times \mathrm{ilr2_{AlM}}) + (2.1419 \times \mathrm{ilr3_{FeM}}) + (-0.5164 \times \mathrm{ilr4_{MnM}}) + \left(-0.1243 \times \mathrm{ilr5_{MgM}}\right) + (0.7730 \times \mathrm{ilr6_{CaM}}) + (0.0438 \times \mathrm{ilr7_{NaM}}) + (0.0714 \times \mathrm{ilr8_{KM}}) + (1.0469 \times \mathrm{ilr9_{PM}}) + 1.4745 \quad \text{(S59)}$$

Table S45: Probability-based boundary coordinates estimated for the classification of intermediate (I) igneous rocks as 1—basaltic andesite (BA), 2—andesite (A), 3—subgroup of basaltic trachyandesite, trachyandesite and trachyte (BtaTAT), and 4—subgroup of phonotephrite, tephriphonolite and phonolite (PhtTphPh); each diagram is considered as of three fields 1 to 3; the triple point common to all field boundaries is repeated in each set of coordinates).

Field Boundary	12_3_4		1_2_3		1_2_4		1_3_4		2_3_4	
	$DF1_{I(BA+A-BtaTAT-PhtTphPh)M}$	$DF2_{I(BA+A-BtaTAT-PhtTphPh)M}$	$DF1_{I(BA-A-BtaTAT)M}$	$DF2_{I(BA-A-BtaTAT)M}$	$DF1_{I(BA-A-PhtTphPh)M}$	$DF2_{I(BA-A-PhtTphPh)M}$	$DF1_{I(BA-BtaTAT-PhtTphPh)M}$	$DF2_{I(BA-BtaTAT-PhtTphPh)M}$	$DF1_{I(A-BtaTAT-PhtTphPh)M}$	$DF2_{I(A-BtaTAT-PhtTphPh)M}$
B(1_2)	3.0041105	12	12	9.417208	-11.9681265	-12	2.467592	12	-3.011746	-12
	1.8665	8	10.2496795	8	-8.0322765	-8	1.6556955	8	-2.018093	-8
	-1.1270551	-2.52741915	-0.0938215	-0.37497553	2.2246306	2.42407782	-0.40904798	-2.17241857	0.72469604	3.04116422
B(1_3)	2.964	-12	0.1216275	-12	-1.74205	12	4.238628	-12	-2.324733	12
	1.2365	-8	0.0474945	-8	-0.08511	8	2.34694	-8	-0.9632	8
	-1.1270551	-2.52741915	-0.0938215	-0.37497553	2.2246306	2.42407782	-0.40904798	-2.17241857	0.72469604	3.04116422
B(2_3)	-12	7.693	-12	9.5827145	12	-7.35298	-12	5.4014645	12	-9.409761
	-8	3.933	-10.107585	8	8	-3.35229	-8	2.787744	10.723347	-8
	-1.1270551	-2.52741915	-0.0938215	-0.37497553	2.2246306	2.42407782	-0.40904798	-2.17241857	0.72469604	3.04116422

Table S46: Classification (percent success) of intermediate (I) igneous rocks as four rock types as (1—basaltic andesite (BA), 2—andesite (A), 3—subgroup of basaltic trachyandesite, trachyandesite and trachyte (BtaTAT), and 4—subgroup of phonotephrite, tephriphonolite and phonolite (PhtTphPh)).

Figure type	Sample type	Total number of samples	Number of classified rock types in major element based diagrams					
			basaltic andesite + andesite (BA+A)	basaltic andesite (BA)	andesite (A)	Subgroup of basaltic trachyandesite, trachyandesite and trachyte (BtaTAT)	subgroup of of phonotephrite, tephriphonolite and phonolite (PhtTphPh)	percent success (correct classification)
basaltic andesite + andesite-BtaTAT-PhtTphPh	basaltic andesite + andesite	8020	7315			705	0	91.2%
	BtaTAT	3354	223			2828	303	84.3%
	PhtTphPh	376	0			47	329	87.5%
basaltic andesite - andesite - BtaTAT	basaltic andesite	3884		3520	138	226		90.6%
	andesite	4136		320	3573	243		86.4%
	BtaTAT	3354		176	376	2802		83.5%
basaltic andesite - andesite - PhtTphPh	basaltic andesite	3384		3802	82		0	97.9%
	andesite	4136		300	3836		0	92.7%
	PhtTphPh	376		26	13		337	89.6%
basaltic andesite - BtaTAT - PhtTphPh	basaltic andesite	3884		3619		265	0	93.2%
	BtaTAT	3354		190		2858	306	85.2%
	PhtTphPh	376		0		43	333	88.6%
andesite - BsnTepFoi-PhtTphPh	andesite	4136			3953	183	0	95.6%
	BtaTAT	3354			242	2792	320	83.2%
	PhtTphPh	376			0	34	342	91.0%

Table S47: Synthesis of four field classification of intermediate rocks in five diagrams based on major elements (M).

I rock name (IUGS)	Total number of samples	Number of classified rock types **(percent success)**			
		basaltic andesite (BA)	andesite (A)	BtaTAT	PhtTphPh
Basaltic andesite	3884	**3554(91.5%)**	97(2.50%)	233(6.00%)	0(0.0%)
andesite	4136	259(6.26%)	**3653(88.32%)**	224(5.42%)	0(0.0%)
BtaTAT	3354	138(4.11%)	206(6.14%)	**2710(80.8%)**	300(8.94%)
PhtTphPh	376	0(0.0%)	0(0.0%)	44(11.7%)	**332(88.3%)**

The correct classification is shown in **bold** face.

Table S48: Discriminant function (DF1-DF2) equations for the diagram based on isometric log-ratio transformation of major-elements (M) for the classification of intermediate (I) basaltic trachyandesite, trachyandesite and trachyte (BtaTAT) as three rock types: 1—basaltic trachyandesite (Bta); 2—trachyandesite (TA); 3—trachyte (T); coefficients reported as arbitrarily rounded to four decimal places.

$$\mathrm{DF1}_{IBtaTAT(\mathrm{Bta-TA\_T})\mathrm{M}} = (6.5032 \times \mathrm{ilr1}_{\mathrm{TiM}}) + (7.4279 \times \mathrm{ilr2}_{\mathrm{AlM}}) + (2.9722 \times \mathrm{ilr3}_{\mathrm{FeM}}) + (0.7138 \times \mathrm{ilr4}_{\mathrm{MnM}}) + \left(1.1395 \times \mathrm{ilr5}_{\mathrm{MgM}}\right) + (1.2058 \times \mathrm{ilr6}_{\mathrm{CaM}}) + (-0.7137 \times \mathrm{ilr7}_{\mathrm{NaM}}) + (-0.7694 \times \mathrm{ilr8}_{\mathrm{KM}}) + (-0.1393 \times \mathrm{ilr9}_{\mathrm{PM}}) - 16.5901 \quad (S60)$$

$$\mathrm{DF2}_{IBtaTAT(\mathrm{Bta-TA\_T})\mathrm{M}} = (-6.1471 \times \mathrm{ilr1}_{\mathrm{TiM}}) + (-7.7919 \times \mathrm{ilr2}_{\mathrm{AlM}}) + (-1.6248 \times \mathrm{ilr3}_{\mathrm{FeM}}) + (-0.7555 \times \mathrm{ilr4}_{\mathrm{MnM}}) + \left(-0.8489 \times \mathrm{ilr5}_{\mathrm{MgM}}\right) + (2.2574 \times \mathrm{ilr6}_{\mathrm{CaM}}) + (-0.6667 \times \mathrm{ilr7}_{\mathrm{NaM}}) + (-0.5657 \times \mathrm{ilr8}_{\mathrm{KM}}) + (0.9739 \times \mathrm{ilr9}_{\mathrm{PM}}) + 14.9094 \quad (S61)$$

Table S49: Probability-based boundary coordinates estimated for the intermediate (I) basaltic trachyandesite, trachyandesite and trachyte (BtaTAT) as three rock types: 1—basaltic trachyandesite (Bta); 2— trachyandesite (TA); 3— trachyte (T); probability-based boundaries shown in each diagram are listed below). The final subscript M refers to major element based classification.

Field Boundary	Basaltic trachyandesite-trachyandesite-trachyte 1_2_3	
	$\mathrm{DF1}_{\mathrm{IBtaTAT(Bta\text{-}TA\text{-}T)M}}$	$\mathrm{DF2}_{\mathrm{IBtaTAT(Bta\text{-}TA\text{-}T)M}}$
B(1_2)	-4.504555	-12
	-3.2788655	-8
	0.788763283	5.47300714
B(1_3)	0.6	12
	0.7	8
	0.788763283	5.47300714
B(2_3)	5.4778435	-12
	4.4145125	-8
	0.788763283	5.47300714

Table S50: Classification of intermediate (I) igneous rock group of basaltic trachyandesite, trachyandesite and trachyte (BtaTAT) as three rock types: 1—basaltic trachyandesite (Bta); 2—trachyandesite (TA); 3—trachyte (T)) in a diagram based on transformed major elements (M).

Figure type	Rock type	Total number of samples	Number of classified rock types in major-element based diagrams			
			basaltic trachyandesite (Bta)	Trachyandesite (TA)	Trachyte (T)	percent success (correct classification)
basaltic trachyandesite, trachyandesite, trachyte (Bta-TA-T) subdivision	basaltic trachyandesite	1305	1237	68	0	94.8%
	trachyandesite	1538	165	1364	9	88.7%
	trachyte	511	9	74	437	85.5%

Table S51: Discriminant function (DF1) equation for single axis diagram (probability-based one-axis boundary = -0.008017) based on isometric log-ratio transformation of major-elements (M) for the classification of intermediate (I) basaltic trachyandesite as two sub-varieties; 1—mugearite (Btamug) and 2—shoshonite (Btasho).

$$\begin{aligned}\mathrm{DF1}_{IBta(\mathrm{mug-sho})\mathrm{M}} &= (0.7117 \times \mathrm{ilr1}_{\mathrm{TiM}}) + (2.8674 \times \mathrm{ilr2}_{\mathrm{AlM}}) + (0.9104 \times \mathrm{ilr3}_{\mathrm{FeM}}) + (-0.4382 \times \mathrm{ilr4}_{\mathrm{MnM}}) \\ &+ (-0.2529 \times \mathrm{ilr5}_{\mathrm{MgM}}) + (0.4349 \times \mathrm{ilr6}_{\mathrm{CaM}}) + (-4.1477 \times \mathrm{ilr7}_{\mathrm{NaM}}) + (2.8989 \times \mathrm{ilr8}_{\mathrm{KM}}) \\ &+ (-0.1518 \times \mathrm{ilr9}_{\mathrm{PM}}) + 0.3819 \end{aligned} \quad \text{(S62)}$$

Table S52: Percent success for the subdivision of intermediate (I) basaltic trachyandesite as two sub-varieties; 1—mugearite (Btamug) and 2—shoshonite (Btasho), in one-axis diagram.

Figure type	rock type	Total number of samples	Number of classified sub-rock types in major-element based diagram		
			mugearite (Btamug)	shoshonite (Btasho)	percent success (correct classification)
basaltic trachyandesite—mugearite and shoshonite subdivision	mugearite	657	647	10	98.5%
	shoshonite	648	111	537	82.9%

Table S53: Discriminant function (DF1) equation for single axis diagram (probability-based one-axis boundary = -0.368409) based on isometric log-ratio transformation of major-elements (M) for the classification of intermediate (I) trachyandesite as two sub-varieties; 1—benmorite (TAben) and 2—latite (TAlat).

$$\begin{aligned}\mathrm{DF1}_{ITA(\mathrm{ben-lat})\mathrm{M}} &= (-0.6268 \times \mathrm{ilr1}_{\mathrm{TiM}}) + (-0.9071 \times \mathrm{ilr2}_{\mathrm{AlM}}) + (-1.5968 \times \mathrm{ilr3}_{\mathrm{FeM}}) + (0.1951 \times \mathrm{ilr4}_{\mathrm{MnM}}) \\ &+ (0.1526 \times \mathrm{ilr5}_{\mathrm{MgM}}) + (-1.3250 \times \mathrm{ilr6}_{\mathrm{CaM}}) + (1.0755 \times \mathrm{ilr7}_{\mathrm{NaM}}) + (-3.1605 \times \mathrm{ilr8}_{\mathrm{KM}}) \\ &+ (0.2291 \times \mathrm{ilr9}_{\mathrm{PM}}) + 0.5717 \end{aligned} \quad \text{(S63)}$$

Table S54: Percent success for the subdivision of intermediate (I) basaltic trachyandesite as two sub-varieties; 1—mugearite (Btamug) and 2—shoshonite (Btasho), in one-axis diagram.

Figure type	rock type	Total number of samples	Number of classified sub-rock types in major-element based diagram		
			benmorite (TAben)	latite (TAlat)	percent success (correct classification)
trachyandesite— benmorite and latite subdivision	benmorite	474	461	13	97.3%
	latite	1064	225	839	78.9%

Table S55: Discriminant function (DF1) equation for single axis diagram (probability-based one-axis boundary = 1.243592) based on isometric log-ratio transformation of major-elements (M) for the classification of intermediate (I) trachyte as two sub-varieties; 1—trachyte (T) and 2—peralkaline (Tpalk).

$$\begin{aligned}\mathrm{DF1}_{IT(\mathrm{T-Tpalk})\mathrm{M}} &= (7.8641 \times \mathrm{ilr1}_{\mathrm{TiM}}) + (12.8931 \times \mathrm{ilr2}_{\mathrm{AlM}}) + (-0.6730 \times \mathrm{ilr3}_{\mathrm{FeM}}) + (-0.6863 \times \mathrm{ilr4}_{\mathrm{MnM}}) \\ &+ \left(0.4272 \times \mathrm{ilr5}_{\mathrm{MgM}}\right) + (0.4277 \times \mathrm{ilr6}_{\mathrm{CaM}}) + (-0.6424 \times \mathrm{ilr7}_{\mathrm{NaM}}) + (-0.7544 \times \mathrm{ilr8}_{\mathrm{KM}}) \\ &+ (0.0641 \times \mathrm{ilr9}_{\mathrm{PM}}) - 13.2979 \end{aligned} \quad (S64)$$

Table S56: Percent success for the subdivision of intermediate (I) trachyte as two sub-varieties; 1—trachyte (T) and 2—peralkaline (Tpalk), in one-axis diagram.

Figure type	rock type	Total number of samples	Number of classified sub-rock types in major-element based diagram		
			trachyte (T)	trachyte, peralkaline (Tpalk)	percent success (correct classification)
trachyte and trachyte, peralkaline subdivision	trachyte	451	434	17	96.2%
	peralkaline	60	6	54	90%

Table S57: Discriminant function (DF1-DF2) equations for the diagram based on isometric log-ratio transformation of major-elements (M) for the classification of intermediate (I) phonotephrite, tephriphonolite and phonolite (Pht-Tph-Ph) as three rock types: 1—phonotephrite (Pht); 2—tephriphonolite (Tph); 3—phonolite (Ph)); coefficients reported as arbitrarily rounded to four decimal places.

$$\mathrm{DF1}_{IPhtTphPh(\mathrm{Pht-Tph\_Ph})\mathrm{M}} = (2.0471 \times \mathrm{ilr1}_{\mathrm{TiM}}) + (0.5830 \times \mathrm{ilr2}_{\mathrm{AlM}}) + (-0.3799 \times \mathrm{ilr3}_{\mathrm{FeM}}) + (1.1241 \times \mathrm{ilr4}_{\mathrm{MnM}}) + (0.4277 \times \mathrm{ilr5}_{\mathrm{MgM}}) + (-0.2637 \times \mathrm{ilr6}_{\mathrm{CaM}}) + (2.5064 \times \mathrm{ilr7}_{\mathrm{NaM}}) + (3.9124 \times \mathrm{ilr8}_{\mathrm{KM}}) + (0.1346 \times \mathrm{ilr9}_{\mathrm{PM}}) - 6.0305 \quad (S65)$$

$$\mathrm{DF2}_{IPhtTphPh(\mathrm{Pht-Tph\_Ph})\mathrm{M}} = (6.5160 \times \mathrm{ilr1}_{\mathrm{TiM}}) + (9.2354 \times \mathrm{ilr2}_{\mathrm{AlM}}) + (1.0094 \times \mathrm{ilr3}_{\mathrm{FeM}}) + (3.5016 \times \mathrm{ilr4}_{\mathrm{MnM}}) + (1.5057 \times \mathrm{ilr5}_{\mathrm{MgM}}) + (1.1138 \times \mathrm{ilr6}_{\mathrm{CaM}}) + (1.2355 \times \mathrm{ilr7}_{\mathrm{NaM}}) + (2.3318 \times \mathrm{ilr8}_{\mathrm{KM}}) + (0.0672 \times \mathrm{ilr9}_{\mathrm{PM}}) - 24.1922 \quad (S66)$$

Table S58: Probability-based boundary coordinates estimated for the intermediate (I) phonotephrite, tephriphonolite and phonolite (PhtTphPh) as three rock types: 1—phonotephrite (Pht); 2—tephriphonolite (Tph); 3—phonolite (Ph); probability-based boundaries shown in each diagram are listed below). The final subscript M refers to major element based classification.

Field Boundary	phonotephrite, tephriphonolite and phonolite 1_2_3	
	$\mathbf{DF1}_{\mathbf{IPhtTphPh(Pht-Tph-Ph)M}}$	$\mathbf{DF2}_{\mathbf{IPhtTphPh(Pht-Tph-Ph\ M}}$
B(1_2)	-2.4035	12
	-1.122	8
	0.752815879	2.14897676
B(1_3)	-0.743	-12
	-0.32	-8
	0.752815879	2.14897676
B(2_3)	12	-7.2965
	8	-3.937
	0.752815879	2.14897676

Table S59: Classification of intermediate (I) igneous rock group of phonotephrite, tephriphonolite and phonolite (Pht-Tph-Ph) as three rock types: 1—phonotephrite (Pht); 2—tephriphonolite (Tph); 3—phonolite (Ph)) in a diagram based on transformed major elements (M).

Figure type	Rock type	Total number of samples	Number of classified rock types in major-element based diagrams			
			phonotephrite (Pht)	tephriphonolite (Tph)	phonolite (Ph)	percent success (correct classification)
phonotephrite, tephriphonolite and phonolite (Pht-Tph-Ph) subdivision	phonotephrite	262	238	1	23	90.8%
	tephriphonolite	13	0	11	2	85%
	trachyte	101	0	18	83	82%

Table S60: Discriminant function (DF1-DF2) equations for five diagrams based on isometric log-ratio transformation of major-elements (M) for the classification of acid (A) igneous rocks as 1—dacite (D), 2—trachydacite (TD), 3—trachyte (T), and 4—rhyolite (R).

$$\mathrm{DF1}_{A(\mathrm{D+TD-T-R})\mathrm{M}} = (5.4888 \times \mathrm{ilr1}_{\mathrm{TiM}}) + (7.8739 \times \mathrm{ilr2}_{\mathrm{AlM}}) + (2.3461 \times \mathrm{ilr3}_{\mathrm{FeM}}) + (0.2950 \times \mathrm{ilr4}_{\mathrm{MnM}}) + (0.3712 \times \mathrm{ilr5}_{\mathrm{MgM}}) + (0.2999 \times \mathrm{ilr6}_{\mathrm{CaM}}) + (0.7710 \times \mathrm{ilr7}_{\mathrm{NaM}}) + (0.1996 \times \mathrm{ilr8}_{\mathrm{KM}}) + (0.1758 \times \mathrm{ilr9}_{\mathrm{PM}}) - 16.7689 \quad \text{(S67)}$$

$$\mathrm{DF2}_{A(\mathrm{D+TD-T-R})\mathrm{M}} = (5.1984 \times \mathrm{ilr1}_{\mathrm{TiM}}) + (3.8569 \times \mathrm{ilr2}_{\mathrm{AlM}}) + (0.2568 \times \mathrm{ilr3}_{\mathrm{FeM}}) + (2.0507 \times \mathrm{ilr4}_{\mathrm{MnM}}) + (0.7469 \times \mathrm{ilr5}_{\mathrm{MgM}}) + (0.8066 \times \mathrm{ilr6}_{\mathrm{CaM}}) + (3.4281 \times \mathrm{ilr7}_{\mathrm{NaM}}) + (2.4764 \times \mathrm{ilr8}_{\mathrm{KM}}) + (0.0334 \times \mathrm{ilr9}_{\mathrm{PM}}) - 21.9303 \quad \text{(S68)}$$

$$\mathrm{DF1}_{A(\mathrm{D-TD-T})\mathrm{M}} = (-4.1218 \times \mathrm{ilr1}_{\mathrm{TiM}}) + (-3.4981 \times \mathrm{ilr2}_{\mathrm{AlM}}) + (-1.7287 \times \mathrm{ilr3}_{\mathrm{FeM}}) + (-1.5217 \times \mathrm{ilr4}_{\mathrm{MnM}}) + (-0.5699 \times \mathrm{ilr5}_{\mathrm{MgM}}) + (-0.1079 \times \mathrm{ilr6}_{\mathrm{CaM}}) + (-3.4121 \times \mathrm{ilr7}_{\mathrm{NaM}}) + (-2.2435 \times \mathrm{ilr8}_{\mathrm{KM}}) + (-0.5735 \times \mathrm{ilr9}_{\mathrm{PM}}) + 18.8947 \quad \text{(S69)}$$

$$\mathrm{DF2}_{A(\mathrm{D-TD-T})\mathrm{M}} = (-6.2811 \times \mathrm{ilr1}_{\mathrm{TiM}}) + (-6.8253 \times \mathrm{ilr2}_{\mathrm{AlM}}) + (-1.0924 \times \mathrm{ilr3}_{\mathrm{FeM}}) + (-1.7339 \times \mathrm{ilr4}_{\mathrm{MnM}}) + (-1.2804 \times \mathrm{ilr5}_{\mathrm{MgM}}) + (-1.4673 \times \mathrm{ilr6}_{\mathrm{CaM}}) + (-3.8200 \times \mathrm{ilr7}_{\mathrm{NaM}}) + (0.0835 \times \mathrm{ilr8}_{\mathrm{KM}}) + (0.9160 \times \mathrm{ilr9}_{\mathrm{PM}}) + 19.6139 \quad \text{(S70)}$$

$$\mathrm{DF1}_{A(\mathrm{D-TD-R})\mathrm{M}} = (3.7583 \times \mathrm{ilr1}_{\mathrm{TiM}}) + (6.3760 \times \mathrm{ilr2}_{\mathrm{AlM}}) + (2.2444 \times \mathrm{ilr3}_{\mathrm{FeM}}) + (-0.2353 \times \mathrm{ilr4}_{\mathrm{MnM}}) + (0.2283 \times \mathrm{ilr5}_{\mathrm{MgM}}) + (0.1617 \times \mathrm{ilr6}_{\mathrm{CaM}}) + (-0.0118 \times \mathrm{ilr7}_{\mathrm{NaM}}) + (-0.4494 \times \mathrm{ilr8}_{\mathrm{KM}}) + (0.1578 \times \mathrm{ilr9}_{\mathrm{PM}}) - 10.1866 \quad \text{(S71)}$$

$$\mathrm{DF2}_{A(\mathrm{D-TD-R})\mathrm{M}} = (3.2786 \times \mathrm{ilr1}_{\mathrm{TiM}}) + (1.0006 \times \mathrm{ilr2}_{\mathrm{AlM}}) + (1.0677 \times \mathrm{ilr3}_{\mathrm{FeM}}) + (1.3483 \times \mathrm{ilr4}_{\mathrm{MnM}}) + (0.1738 \times \mathrm{ilr5}_{\mathrm{MgM}}) + (0.8636 \times \mathrm{ilr6}_{\mathrm{CaM}}) + (0.8799 \times \mathrm{ilr7}_{\mathrm{NaM}}) + (2.8008 \times \mathrm{ilr8}_{\mathrm{KM}}) + (0.5260 \times \mathrm{ilr9}_{\mathrm{PM}}) - 17.7981 \quad \text{(S72)}$$

$$\mathrm{DF1}_{A(\mathrm{D-T-R})\mathrm{M}} = (5.2512 \times \mathrm{ilr1}_{\mathrm{TiM}}) + (7.9199 \times \mathrm{ilr2}_{\mathrm{AlM}}) + (2.2249 \times \mathrm{ilr3}_{\mathrm{FeM}}) + (0.1491 \times \mathrm{ilr4}_{\mathrm{MnM}}) + (0.3515 \times \mathrm{ilr5}_{\mathrm{MgM}}) + (0.1766 \times \mathrm{ilr6}_{\mathrm{CaM}}) + (0.6257 \times \mathrm{ilr7}_{\mathrm{NaM}}) + (-0.0618 \times \mathrm{ilr8}_{\mathrm{KM}}) + (0.1353 \times \mathrm{ilr9}_{\mathrm{PM}}) - 15.2661 \quad \text{(S73)}$$

$$\mathrm{DF2}_{A(\mathrm{D-T-R})\mathrm{M}} = (5.2857 \times \mathrm{ilr1}_{\mathrm{TiM}}) + (3.6638 \times \mathrm{ilr2}_{\mathrm{AlM}}) + (0.4375 \times \mathrm{ilr3}_{\mathrm{FeM}}) + (2.1154 \times \mathrm{ilr4}_{\mathrm{MnM}}) + (0.7148 \times \mathrm{ilr5}_{\mathrm{MgM}}) + (0.9144 \times \mathrm{ilr6}_{\mathrm{CaM}}) + (3.3558 \times \mathrm{ilr7}_{\mathrm{NaM}}) + (2.6608 \times \mathrm{ilr8}_{\mathrm{KM}}) + (0.1118 \times \mathrm{ilr9}_{\mathrm{PM}}) - 23.0220 \quad \text{(S74)}$$

$$\mathrm{DF1}_{A(\mathrm{TD-T-R})\mathrm{M}} = (-6.9111 \times \mathrm{ilr1}_{\mathrm{TiM}}) + (-7.7539 \times \mathrm{ilr2}_{\mathrm{AlM}}) + (-2.1890 \times \mathrm{ilr3}_{\mathrm{FeM}}) + (-1.2550 \times \mathrm{ilr4}_{\mathrm{MnM}}) + (-0.8405 \times \mathrm{ilr5}_{\mathrm{MgM}}) + (-0.9231 \times \mathrm{ilr6}_{\mathrm{CaM}}) + (-2.4475 \times \mathrm{ilr7}_{\mathrm{NaM}}) + (-2.0163 \times \mathrm{ilr8}_{\mathrm{KM}}) + (-0.1177 \times \mathrm{ilr9}_{\mathrm{PM}}) + 24.9011 \quad \text{(S75)}$$

$$\mathrm{DF2}_{A(\mathrm{TD-T-R})\mathrm{M}} = (-2.7967 \times \mathrm{ilr1}_{\mathrm{TiM}}) + (-3.4645 \times \mathrm{ilr2}_{\mathrm{AlM}}) + (1.0119 \times \mathrm{ilr3}_{\mathrm{FeM}}) + (-0.9534 \times \mathrm{ilr4}_{\mathrm{MnM}}) + \left(-0.6383 \times \mathrm{ilr5}_{\mathrm{MgM}}\right) + (-0.0826 \times \mathrm{ilr6}_{\mathrm{CaM}}) + (-3.3088 \times \mathrm{ilr7}_{\mathrm{NaM}}) + (0.1212 \times \mathrm{ilr8}_{\mathrm{KM}}) + (0.5061 \times \mathrm{ilr9}_{\mathrm{PM}}) + 7.0497 \quad \text{(S76)}$$

Table S61: Probability-based boundary coordinates estimated for of acid (A) igneous rocks as 1—dacite (D), 2—trachydacite (TD), 3—trachyte (T), and 4—rhyolite (R)); each diagram is considered as of three fields 1 to 3; the triple point common to all field boundaries is repeated in each set of coordinates).

Field Boundary	12_3_4		1_2_3		1_2_4		1_3_4		2_3_4	
	$DF1_{A(D+TD-T-R)M}$	$DF2_{A(D+TD-T-R)M}$	$DF1_{A(D-TD-T)M}$	$DF2_{A(D-TD-T)M}$	$DF1_{A(D-TD-R)M}$	$DF2_{A(D-TD-R)M}$	$DF1_{A(D-T-R)M}$	$DF2_{A(D-T-R)M}$	$DF1_{A(TD-T-R)M}$	$DF2_{A(-TD-T-R)M}$
B(1_2)	-12	-0.371292	-9.5152525	-12	-12	-6.2191075	-12	-1.3372185	11.674	-8
	-8	-0.533765	-6.09426	-8	-8	-4.1766495	-8	-1.14098	8	-4.9605
	-0.17345286	-0.85166549	0.75613108	0.00982864	-0.24332293	-0.21597515	-0.24682517	-0.76061193	1.13932719	0.71509942
B(1_3)	2.0181335	12	-0.041434	12	0.02115	12	1.9150855	12	-4.207	-12
	1.336016	8	0.224639	8	-0.0654495	8	1.237403	8	-2.525	-8
	-0.17345286	-0.85166549	0.75613108	0.00982864	-0.24332293	-0.21597515	-0.24682517	-0.76061193	1.13932719	0.71509942
B(2_3)	6.3501025	-12	12	-7.9402995	8.327986	-12	7.228544	-12	0.5325	12
	4.009464	-8	8	-5.112046	5.418517	-8	4.5681255	-8	0.7475	8
	-0.17345286	-0.85166549	0.75613108	0.00982864	-0.24332293	-0.21597515	-0.24682517	-0.76061193	1.13932719	0.71509942

Table S62: Classification (percent success) of acid (A) igneous rocks as 1—dacite (D), 2—trachydacite (TD), 3—trachyte (T), and 4—rhyolite (R).

Figure type	Sample type	Total number of samples	Number of classified rock types in major element based diagrams					
			dacite + trachydacite (D+TD)	basalt (B)	trachybasalt (TB)	trachyte (T)	rhyolite (R)	percent success (correct classification)
dacite + trachydacite - trachyte - rhyolite	dacite + trachydacite	2974	2858			198	8	96.1%
	trachyte	790	125			664	1	84.1%
	rhyolite	3725	232			148	3345	89.8%
dacite - trachydacite - trachyte	dacite	2750		2411	323	16		87.8%
	trachydacite	224		6	193	25		86.2%
	trachyte	790		65	145	580		73.4%
dacite - trachydacite - rhyolite	dacite	2750		2331	419		0	84.8%
	trachydacite	224		6	218		0	97.3%
	rhyolite	3725		135	412		3178	85.3%
dacite - trachyte - rhyolite	dacite	2750		2709		35	6	98.5%
	trachyte	790		92		697	1	88.2%
	rhyolite	3725		191		165	3369	90.4%
trachydacite - trachyte - rhyolite	trachydacite	224			205	19	0	91.5%
	trachyte	790			214	576	0	72.9%
	rhyolite	3725			355	87	3283	88.1%

Table S63: Synthesis of four field classification of acid rocks in five diagrams based on major elements (M).

U rock name (IUGS)	Total number of samples	Number of classified rock types **(percent success)**			
		dacite (D)	trachydacite (TD)	trachyte (T)	rhyolite (R)
dacite	2750	**2390(86.91%)**	347(12.62%)	13(0.47%)	0(0.0%)
trachydacite	224	3(1.3%)	**184(82.1%)**	37(16.5%)	0(0.0%)
trachyte	790	50(6.3%)	127(16.1%)	**613(77.6%)**	0(0.0%)
rhyolite	3725	117(3.14%)	286(7.68%)	93(2.50%)	**3229(86.68%)**

The correct classification is shown in **bold** face.

Table S64: Discriminant function (DF1) equation for single axis diagram (probability-based one-axis boundary =1.353807) based on isometric log-ratio transformation of major-elements (M) for the classification of acid (A) trachyte as two sub-varieties; 1—trachyte (T) and 2—trachyte, peralkaline (Tpalk).

$$\begin{aligned}\mathrm{DF1}_{AT(\mathrm{T-Tpalk})\mathrm{M}} &= (1.7809 \times \mathrm{ilr1}_{\mathrm{TiM}}) + (6.2784 \times \mathrm{ilr2}_{\mathrm{AlM}}) + (-3.6827 \times \mathrm{ilr3}_{\mathrm{FeM}}) + (-0.5972 \times \mathrm{ilr4}_{\mathrm{MnM}}) \\ &+ (-0.3802 \times \mathrm{ilr5}_{\mathrm{MgM}}) + (-0.2100 \times \mathrm{ilr6}_{\mathrm{CaM}}) + (-2.9421 \times \mathrm{ilr7}_{\mathrm{NaM}}) + (-1.5828 \times \mathrm{ilr8}_{\mathrm{KM}}) \\ &+ (0.1549 \times \mathrm{ilr9}_{\mathrm{PM}}) + 0.7687 \end{aligned} \quad (S77)$$

Table S65: Percent success for the subdivision of acid (A) trachyte as two sub-varieties; 1—trachyte (T) and 2—trachyte, peralkaline (Tpalk), in one-axis diagram.

Figure type	rock type	Total number of samples	Number of classified rock types in major-element based diagram		
			trachyte (T)	trachyte, peralkaline (Tpalk)	percent success (correct classification)
trachyte and trachyte, perakaline subdivision	trachyte	664	637	27	95.9%
	trachyte, perakaline	126	14	112	88.9%

Table S66: Discriminant function (DF1) equation for single axis diagram (probability-based one-axis boundary = -2.072273) based on isometric log-ratio transformation of major-elements (M) for the classification of acid (A) trachyte as two sub-varieties; 1—rhyolite (R) and 2— rhyolite, peralkaline (Rpalk).

$$\begin{aligned}\mathrm{DF1}_{AR(\mathrm{R-Rpalk})\mathrm{M}} &= (-0.1550 \times \mathrm{ilr1}_{\mathrm{TiM}}) + (-2.3449 \times \mathrm{ilr2}_{\mathrm{AlM}}) + (2.7244 \times \mathrm{ilr3}_{\mathrm{FeM}}) + (0.2027 \times \mathrm{ilr4}_{\mathrm{MnM}}) \\ &+ (0.1944 \times \mathrm{ilr5}_{\mathrm{MgM}}) + (-0.9018 \times \mathrm{ilr6}_{\mathrm{CaM}}) + (2.0316 \times \mathrm{ilr7}_{\mathrm{NaM}}) + (0.6418 \times \mathrm{ilr8}_{\mathrm{KM}}) \\ &+ (-0.2656 \times \mathrm{ilr9}_{\mathrm{PM}}) - 1.6981 \end{aligned} \quad (S78)$$

Table S67: Percent success for the subdivision of acid (A) rhyolite as two sub-varieties; 1—rhyolite (T) and 2—rhyolite, peralkaline (Tpalk), in one-axis diagram.

Figure type	rock type	Total number of samples	Number of classified rock types in major-element based diagram		
			rhyolite (R)	rhyolite, perakaline (Rpalk)	percent success (correct classification)
rhyolite and rhyolite, perakaline subdivision	rhyolite	3387	3316	21	99.4%
	rhyolite, perakaline	388	16	372	95.9%

Table S68: Classification of rock types (root and sub-root names) from the initial database from the new multidimensional classification scheme and comparison with the IUGS classification scheme.

Rock no.	Rock name	no. of samples	Number of samples classified from IgRoClaMSys for any field																												Percent success
			1	2	3	4	5	6	7	8	9	10	11	12	13	14	15	16	17	18	19	20	21	22	23	24	25	26	27	28	29	
1	basanite, basanite	**1004**	**666**	48	27	135	1	17		1	1	1		62		11	8	21	5													66.3
2	basanite, melanephelinite	**421**	6	**265**	27	4	15	6	3		52	4		3			1		35													62.9
3	basanite, nephelinite	**59**	1	1	**32**	1		10		1	1	10						2													54
4	tephrite, basanite	**189**	1			**174**	2	9								1		2													92.1
5	tephrite, melanephelinite	**94**				2	**23**	9	1		11	1		4	2				40		1											24
6	tephrite, nephelinite	**29**				6	1	**19**				1						2													66
7	picrobasalt	**72**	6	1		5			**21**					31	8																29
8	foidite, basanite	7	2	1					2	**1**	1																				14
9	foidite, melanephelinite	**182**		7		3	1			2	**134**	1							21		13										73.6
10	foidite, nephelinite	**79**			2	2		19			1	**46**									9										58
11	phonolite	**267**						1					**236**								24					6					88.4
12	basalt, alkali	**2005**	527	33		175	2	2	18					**724**	23	388	24	1	15			73									36.1
13	basalt, subalkali	**7344**	40	16		92			8					434	**5524**	878	27	11	22			292									75.2
14	trachybasalt, hawaiite	**829**	108			186		1						1	1	**425**	25	68	4			10									51.3
15	trachybasalt, potassic	**657**	149	2		98	2	1						2	2	37	**180**	10	163	3		8									27.4
16	basaltic trachyandesite, mugearite	**850**				47										24	3	**636**	15	2	1	102	7	13							74.8
17	basaltic trachyandesite, shoshonite	**828**	3			29									1		7	135	**573**	11	3	11	1	8	46						69.2
18	phonotephrite	**341**	6		1	77		17								1	2	16	124	**49**	41				7						14.4
19	tephriphonolite	**133**				12		1										2	11	6	**83**				18						62.4
20	basaltic andesite	**3884**	2			3									540	253	1	418	84			**2486**	97								64.0
21	andesite	**4136**																45	30			258	**3653**	101	49						88.3
22	trachyandesite, benmorite	**474**				3												72		12	1		105	**275**	5	1					58.0
23	trachyandesite, latite	**1064**				1												13	67	13	29	1	68	173	**689**	4			6		64.8
24	trachyte	**1115**											194							13	36		106	27	38	**550**	36	23	92			49.3
25	trachyte, peralkaline	**186**											30							5	2					13	**126**		10			67.7
26	dacite	**2750**																					1134	5	3	7	1	**1289**	311			46.9
27	trachydacite	**224**																					8	1		39	3	3	**170**			75.9
28	rhyolite	**3337**																								54	8	117	278	**2861**	19	85.7
29	rhyolite, peralkaline	**388**																									31		8	16	**333**	85.8

Table S69: Testing of the new classification scheme IgRoClaMSys from Quaternary volcanic rocks of Kaula volcanics, Hawaiian Islands (Test study T1; Garcia et al., 2016).

Consec	Sample name		SiO_2	TiO_2	Al_2O_3	$Fe_2O_3^t$	MnO	MgO	CaO	Na_2O	K_2O	P_2O_5	IUGS (Le Bas *et al.*, 1986) IgRoCS (Verma & Rivera-Gómez, 2013)		New scheme IgRoClaMSys (this work)	
	Original authors`	This work											Magma type	Rock type	Magma type	Rock type
1	KA-14	GWJI0001	48.41	1.62	15.36	13.67	0.120	5.49	11.69	2.43	0.46	0.45	Basic	Basalt, subalkali	Basic	Basalt, subalkali
2	KA-29	GWJI0002	47.05	2.15	14.84	11.50	0.160	8.68	10.05	3.73	1.04	0.63	Basic	Trachybasalt, hawaiite	Basic	Basalt, alkali
3	KA-15	GWJI0003	42.18	2.73	11.53	14.32	0.220	13.38	10.44	3.31	1.16	0.70	Ultrabasic	Basanite, melanephelinite	Ultrabasic	Basanite, melanephelinite
4	KA-17	GWJI0004	41.49	2.62	11.94	14.23	0.250	12.41	11.41	3.35	1.22	1.13	Ultrabasic	Foidite,melanephelinite	Ultrabasic	Basanite, melanephelinite
5	KA-19	GWJI0005	42.79	2.73	12.12	13.97	0.200	12.71	11.53	1.75	1.27	0.69	Ultrabasic	Basanite, basanite	Ultrabasic	Basanite, basanite
6	KA-28	GWJI0006	42.42	2.83	12.55	14.60	0.220	10.44	10.67	3.75	1.49	0.74	Ultrabasic	Basanite, melanephelinite	Ultrabasic	Basanite, melanephelinite
7	KA-31	GWJI0007	40.97	2.83	12.03	14.20	0.230	12.83	10.85	3.74	1.23	0.86	Ultrabasic	Foidite,melanephelinite	Ultrabasic	Basanite, melanephelinite
8	KA-34	GWJI0008	40.89	2.83	11.91	14.74	0.330	11.87	12.62	2.52	1.35	0.87	Ultrabasic	Foidite,melanephelinite	Ultrabasic	Basanite, melanephelinite
9	300-02	GWJI0009	47.30	1.78	16.02	12.12	0.180	6.70	11.81	3.04	0.62	0.29	Basic	Basalt, alkali	Basic	Basalt, alkali
10	300-04	GWJI0010	46.80	1.46	14.41	12.29	0.200	10.33	10.59	2.91	0.45	0.23	Basic	Basalt, alkali	Basic	Basalt, alkali
11	300-05	GWJI0011	45.80	1.27	14.42	12.78	0.200	11.45	10.57	2.74	0.33	0.18	Basic	Basalt, alkali	Basic	Basalt, alkali
12	300-06	GWJI0012	45.90	1.33	14.58	12.76	0.210	10.99	10.79	2.76	0.38	0.21	Basic	Basalt, alkali	Basic	Basalt, alkali
13	300-07	GWJI0013	46.60	1.44	14.51	13.07	0.190	10.05	10.76	2.61	0.44	0.21	Basic	Basalt, alkali	Basic	Basalt, alkali
14	300-08	GWJI0014	46.70	1.46	14.56	13.19	0.200	9.83	10.86	2.71	0.44	0.21	Basic	Basalt, alkali	Basic	Basalt, alkali
15	300-10	GWJI0015	46.90	1.68	15.76	13.27	0.530	6.19	11.86	2.83	0.56	0.27	Ultrabasic	Picrobasalt	Basic	Basalt, alkali
16	300-15	GWJI0016	47.13	1.15	17.57	10.36	0.160	6.55	14.02	2.77	0.35	0.16	Basic	Basalt, alkali	Basic	Basalt, alkali
17	300-18	GWJI0017	46.10	1.27	14.89	12.95	0.220	10.42	11.02	2.39	0.54	0.20	Basic	Basalt, alkali	Basic	Basalt, alkali
18	300-20	GWJI0018	46.00	1.29	15.16	12.74	0.200	10.37	11.13	2.66	0.40	0.20	Basic	Basalt, alkali	Basic	Basalt, alkali
19	300-23	GWJI0019	46.00	1.25	14.34	13.07	0.220	11.45	10.60	2.51	0.61	0.19	Basic	Basalt, alkali	Basic	Basalt, alkali
20	300-26	GWJI0020	45.40	1.21	14.94	12.62	0.200	11.01	10.87	2.67	0.37	0.21	Basic	Basalt, alkali	Basic	Basalt, alkali
21	300-27	GWJI0021	45.50	1.19	14.99	12.64	0.200	11.00	10.91	2.78	0.39	0.23	Basic	Basalt, alkali	Basic	Basalt, alkali
22	300-29	GWJI0022	45.90	1.34	15.68	12.62	0.200	9.10	11.62	2.91	0.50	0.27	Basic	Basalt, alkali	Basic	Basalt, alkali
23	300-30	GWJI0023	46.50	1.31	14.70	12.60	0.200	10.54	10.74	2.82	0.46	0.19	Basic	Basalt, alkali	Basic	Basalt, alkali
24	300-32	GWJI0024	46.30	1.24	14.09	12.43	0.190	11.75	10.24	2.79	0.34	0.19	Basic	Basalt, alkali	Basic	Basalt, alkali
25	300-34	GWJI0025	46.50	1.28	14.26	12.52	0.190	11.25	10.39	2.76	0.35	0.20	Basic	Basalt, alkali	Basic	Basalt, alkali
26	300-36	GWJI0026	46.80	1.29	14.43	12.55	0.210	10.75	10.46	2.51	0.49	0.21	Basic	Basalt, alkali	Basic	Basalt, alkali
27	300-38	GWJI0027	44.10	2.17	13.27	14.08	0.730	10.33	8.75	3.89	1.40	0.80	Ultrabasic	Foidite, nephelinite	Ultrabasic	Basanite, basanite
28	300-41	GWJI0028	45.20	1.57	14.17	13.16	0.210	11.47	10.53	2.67	0.66	0.30	Basic	Basalt, alkali	Basic	Basalt, alkali
29	300-42	GWJI0029	45.30	1.61	14.39	13.07	0.210	11.04	10.70	2.72	0.54	0.29	Basic	Basalt, alkali	Basic	Basalt, alkali
30	300-44	GWJI0030	46.30	1.84	13.40	12.03	0.180	11.39	10.40	2.74	0.91	0.46	Basic	Basalt, alkali	Basic	Basalt, alkali
31	300-46	GWJI0031	46.30	1.86	13.28	12.20	0.180	11.58	10.38	2.94	0.89	0.47	Basic	Basalt, alkali	Basic	Basalt, alkali
32	300-47	GWJI0032	46.30	1.81	12.76	12.18	0.240	12.62	10.16	2.89	0.96	0.46	Ultrabasic	Basanite, basanite	Basic	Basalt, alkali
33	300-48	GWJI0033	46.30	1.84	13.14	12.31	0.220	11.45	10.29	2.91	0.97	0.47	Ultrabasic	Basanite, basanite	Basic	Basalt, alkali
34	304-01	GWJI0034	44.56	1.77	13.97	13.86	0.270	12.26	10.15	2.48	0.61	0.26	Basic	Basalt, alkali	Basic	Basalt, alkali
35	304-04	GWJI0035	45.08	1.49	14.56	13.06	0.690	10.91	10.55	3.03	0.66	0.30	Ultrabasic	Picrobasalt	Basic	Basalt, alkali
36	304-05	GWJI0036	45.61	1.42	14.60	12.55	0.200	11.46	10.60	2.94	0.67	0.28	Basic	Basalt, alkali	Basic	Basalt, alkali
37	304-06	GWJI0037	45.91	1.42	14.77	12.16	0.170	10.81	11.02	2.73	0.87	0.29	Basic	Basalt, alkali	Basic	Basalt, alkali
38	304-07	GWJI0038	46.01	1.45	14.95	12.32	0.190	10.32	10.90	2.70	0.88	0.29	Basic	Basalt, alkali	Basic	Basalt, alkali
39	304-08	GWJI0039	46.24	1.48	15.22	12.52	0.190	9.41	11.15	2.84	0.89	0.30	Basic	Basalt, alkali	Basic	Basalt, alkali
40	304-09	GWJI0040	47.47	1.56	15.68	11.93	0.190	7.91	10.95	3.35	1.03	0.34	Basic	Basanite, basanite	Basic	Basalt, alkali
41	304-10	GWJI0041	47.77	1.57	16.38	11.93	0.200	6.15	11.32	3.40	1.00	0.35	Basic	Basanite, basanite	Basic	Basalt, alkali
42	304-11	GWJI0042	45.30	1.29	14.76	12.38	0.200	11.77	10.96	2.79	0.64	0.30	Basic	Basalt, alkali	Basic	Basalt, alkali

43	304-13	GWJI0043	45.04	1.32	14.39	12.45	0.200	12.45	10.89	2.71	0.59	0.31	Basic	Basalt, alkali	Basic	Basalt, alkali
44	304-15	GWJI0044	45.63	1.64	16.35	12.28	0.250	6.78	12.63	3.38	0.73	0.42	Basic	Basanite, basanite	Basic	Basalt, alkali
45	304-16	GWJI0045	45.62	1.64	16.23	12.36	0.210	6.75	12.60	3.32	0.77	0.42	Basic	Basanite, basanite	Basic	Basalt, alkali
46	304-17	GWJI0046	47.28	1.47	15.82	12.21	0.180	8.26	10.69	3.13	0.82	0.34	Basic	Basalt, alkali	Basic	Basalt, alkali
47	304-18	GWJI0047	47.16	1.47	15.77	12.09	0.190	7.76	10.95	3.20	0.87	0.34	Basic	Basalt, alkali	Basic	Basalt, alkali
48	304-19	GWJI0048	47.16	1.51	15.90	12.26	0.260	7.49	10.75	3.39	0.95	0.35	Basic	Basanite, basanite	Basic	Basalt, alkali
49	304-21	GWJI0049	41.63	2.59	12.69	13.82	0.220	11.56	11.29	3.89	1.46	0.77	Ultrabasic	Basanite, melanephelinite	Ultrabasic	Basanite, melanephelinite
50	304-22	GWJI0050	41.77	2.55	12.30	13.94	0.250	12.14	11.18	3.72	1.41	0.74	Ultrabasic	Foidite,melanephelinite	Ultrabasic	Basanite, melanephelinite
51	304-23	GWJI0051	41.76	2.59	12.67	13.65	0.220	11.63	11.41	3.86	1.43	0.77	Ultrabasic	Basanite, melanephelinite	Ultrabasic	Basanite, melanephelinite
52	304-24	GWJI0052	45.57	1.39	13.94	12.89	0.220	12.26	9.82	2.89	0.85	0.29	Basic	Basalt, alkali	Basic	Basalt, alkali
53	304-25	GWJI0053	46.75	1.75	15.28	12.18	0.180	8.70	10.62	3.22	1.14	0.35	Basic	Basalt, alkali	Basic	Basalt, alkali
54	304-26	GWJI0054	46.65	1.73	15.19	12.33	0.190	8.74	10.54	3.31	1.13	0.35	Basic	Basalt, alkali	Basic	Basalt, alkali
55	304-30	GWJI0055	46.62	1.71	15.12	12.75	0.190	8.72	10.44	3.16	1.18	0.34	Basic	Basalt, alkali	Basic	Basalt, alkali
56	304-32	GWJI0056	46.06	1.46	14.81	12.84	0.200	10.18	10.62	3.04	0.80	0.31	Basic	Basalt, alkali	Basic	Basalt, alkali
57	304-33	GWJI0057	46.68	1.54	15.64	11.89	0.180	8.85	11.16	3.08	0.84	0.32	Basic	Basalt, alkali	Basic	Basalt, alkali
58	304-34	GWJI0058	46.00	1.42	14.60	12.25	0.190	11.22	10.57	2.85	0.72	0.30	Basic	Basalt, alkali	Basic	Basalt, alkali
59	304-35	GWJI0059	45.73	1.44	14.38	12.63	0.210	11.10	10.29	2.83	0.77	0.30	Basic	Basalt, alkali	Basic	Basalt, alkali
60	304-36	GWJI0060	45.91	1.42	14.35	12.61	0.210	11.40	10.20	2.91	0.78	0.30	Basic	Basalt, alkali	Basic	Basalt, alkali
61	304-37	GWJI0061	45.82	1.43	14.77	12.58	0.200	10.48	10.65	2.87	0.72	0.30	Basic	Basalt, alkali	Basic	Basalt, alkali
62	304-38	GWJI0062	45.53	1.40	14.11	13.11	0.290	11.96	10.20	2.78	0.66	0.30	Basic	Basanite, basanite	Basic	Basalt, alkali

Table S70: Testing of the new classification scheme IgRoClaMSys from Holocene volcanic rocks of San Antonio volcano, Tacaná volcanic complex, Mexico-Guatemala (Test study T2; Mora et al., 2004).

Consec	Sample name		SiO_2	TiO_2	Al_2O_3	$Fe_2O_3^t$	MnO	MgO	CaO	Na_2O	K_2O	P_2O_5	IUGS (Le Bas *et al.*, 1986) IgRoCS (Verma & Rivera-Gómez, 2013)		New scheme IgRoClaMSys (this work)	
	Original authors`	This work											Magma type	Rock type	Magma type	Rock type
1	9721 (2)a	MGMM0001	61.88	0.57	16.77	5.78	0.100	2.33	5.66	3.80	2.27	0.15	Intermediate	Andesite	Intermediate	Andesite
2	9721 (2)b	MGMM0002	61.69	0.53	16.51	5.84	0.100	2.36	5.67	3.79	2.28	0.15	Intermediate	Andesite	Intermediate	Andesite
3	9721 (2)c	MGMM0003	61.01	0.59	16.60	6.01	0.110	2.40	5.73	3.83	2.21	0.17	Intermediate	Andesite	Intermediate	Andesite
4	9721 (2)d	MGMM0004	61.06	0.57	16.65	5.83	0.100	2.30	5.60	3.74	2.19	0.15	Intermediate	Andesite	Intermediate	Andesite
5	9821	MGMM0005	61.98	0.56	16.70	5.71	0.100	2.30	5.64	3.80	2.34	0.14	Intermediate	Andesite	Intermediate	Andesite
6	9320	MGMM0006	53.86	0.88	18.23	8.65	0.130	4.07	8.40	3.52	1.31	0.15	Intermediate	Basaltic andesite	Intermediate	Basaltic andesite
7	9721	MGMM0007	52.30	0.98	18.52	8.80	0.130	4.75	8.93	3.42	1.02	0.16	Intermediate	Basaltic andesite	Intermediate	Basaltic andesite
8	360	MGMM0008	52.30	0.98	18.52	8.80	0.130	4.75	8.93	3.42	1.02	0.16	Intermediate	Basaltic andesite	Intermediate	Basaltic andesite
9	9735 (2)a	MGMM0009	59.67	0.67	17.86	6.18	0.110	2.73	5.77	3.60	1.88	0.17	Intermediate	Andesite	Intermediate	Andesite
10	9735 (2)b	MGMM0010	59.81	0.65	18.14	5.84	0.110	2.46	5.61	3.59	1.83	0.17	Intermediate	Andesite	Intermediate	Andesite
11	TAC9735b	MGMM0011	59.56	0.65	17.46	6.50	0.110	2.60	6.04	3.57	1.79	0.17	Intermediate	Andesite	Intermediate	Andesite
12	358	MGMM0012	63.74	0.51	17.48	4.39	0.080	1.75	4.73	4.54	2.01	0.16	Intermediate	Andesite	Acid	Dacite
13	9866	MGMM0013	64.41	0.45	17.30	0.90	0.090	2.31	5.04	3.82	2.17	0.15	Acid	Rhyolite	Acid	Dacite
14	9864d	MGMM0014	70.66	0.29	15.28	2.73	0.070	0.67	2.83	4.37	2.75	0.10	Acid	Rhyolite	Acid	Rhyolite

Table S71: Testing of the new classification scheme IgRoClaMSys from Quaternary volcanic rocks of Turrialba volcano, Costa Rica (Test study T3; Di Piazza et al., 2015).

Consec	Sample name		SiO_2	TiO_2	Al_2O_3	$Fe_2O_3^t$	MnO	MgO	CaO	Na_2O	K_2O	P_2O_5	IUGS (Le Bas *et al.*, 1986) IgRoCS (Verma & Rivera-Gómez, 2013)		New scheme IgRoClaMSys (this work)	
	Original authors`	This work											Magma type	Rock type	Magma type	Rock type
1	TU 5	DRBC0001	53.20	1.04	17.31	8.26	0.130	5.83	9.39	3.27	1.47	0.39	Intermediate	Basaltic andesite	Intermediate	Basaltic andesite
2	TU 6	DRBC0002	52.97	1.05	17.21	8.34	0.140	6.17	9.43	3.21	1.44	0.35	Intermediate	Basaltic andesite	Intermediate	Basaltic andesite
3	TU 16	DRBC0003	53.07	1.04	17.24	8.26	0.140	6.09	9.35	3.26	1.43	0.35	Intermediate	Basaltic andesite	Intermediate	Basaltic andesite
4	TU 37/1	DRBC0004	58.15	0.91	16.59	6.64	0.120	3.74	6.83	3.74	2.35	0.35	Intermediate	Trachyandesite, benmorite	Intermediate	Andesite
5	TU 4	DRBC0005	64.22	0.65	16.04	4.73	0.090	2.18	4.51	4.00	3.35	0.22	Intermediate	Andesite	Acid	Trachyte
6	TU 7	DRBC0006	57.95	0.85	17.81	6.73	0.100	4.23	7.27	3.92	1.40	0.26	Intermediate	Andesite	Intermediate	Andesite
7	TU 8	DRBC0007	57.86	0.83	17.76	6.52	0.100	4.13	6.99	3.93	1.40	0.25	Intermediate	Andesite	Intermediate	Andesite

Table S72: Testing of the new classification scheme IgRoClaMSys from Miocene-Pleistocene volcanic rocks of Harrat Ash Shaam, Jordan (Test study T4; Shaw et al., 2003).

Consec	Sample name		SiO_2	TiO_2	Al_2O_3	$Fe_2O_3^t$	MnO	MgO	CaO	Na_2O	K_2O	P_2O_5	IUGS (Le Bas *et al.*, 1986) IgRoCS (Verma & Rivera-Gómez, 2013)		New scheme IgRoClaMSys (this work)	
	Original authors`	This work											Magma type	Rock type	Magma type	Rock type
1	JS001	SBMT0001	44.66	2.53	14.79	12.99	0.18	9.27	9.84	3.65	1.53	0.54	Ultrabasic	Basanite, basanite	Basic	Basanite, basanite
2	JS004	SBMT0002	43.82	3.10	14.64	13.26	0.17	10.37	9.05	3.92	1.10	0.57	Ultrabasic	Basanite, basanite	Ultrabasic	Basanite, basanite
3	JS007	SBMT0003	46.96	2.22	14.90	12.30	0.16	9.43	9.38	3.33	0.97	0.34	Basic	Basalt, alkali	Basic	Basalt, alkali
4	JS009	SBMT0004	49.52	2.25	16.79	12.03	0.15	4.31	10.64	3.12	0.83	0.35	Basic	Basalt, subalkali	Basic	Basalt, subalkali
5	JS011	SBMT0005	48.86	2.13	16.13	11.32	0.16	6.00	10.71	3.39	1.00	0.31	Basic	Basalt, alkali	Basic	Basalt, alkali
6	JS013	SBMT0006	49.23	2.12	16.22	11.11	0.16	6.16	10.22	3.45	1.03	0.32	Basic	Basalt, alkali	Basic	Basalt, alkali
7	JS015	SBMT0007	46.76	2.20	15.66	12.46	0.17	8.43	10.28	2.95	0.80	0.31	Basic	Basalt, alkali	Basic	Basalt, alkali
8	JS022	SBMT0008	47.22	2.13	13.63	12.46	0.16	9.11	10.93	3.12	0.91	0.33	Basic	Basalt, alkali	Basic	Basalt, alkali
9	JS026	SBMT0009	48.13	1.73	15.26	11.78	0.15	10.47	8.80	2.85	0.60	0.23	Basic	Basalt, subalkali	Basic	Basalt, subalkali
10	JS028	SBMT0010	45.51	2.08	13.76	12.21	0.17	9.87	11.64	3.33	1.07	0.36	Ultrabasic	Basanite, basanite	Basic	Basalt, alkali
11	JS029	SBMT0011	48.12	1.64	15.15	12.10	0.16	9.84	9.31	2.90	0.56	0.22	Basic	Basalt, subalkali	Basic	Basalt, subalkali
12	JS030	SBMT0012	45.92	2.13	13.86	12.06	0.16	9.55	11.54	3.39	1.03	0.36	Ultrabasic	Basanite, basanite	Basic	Basalt, alkali
13	JS031	SBMT0013	42.87	2.84	12.65	14.15	0.18	10.97	9.86	4.20	1.19	1.10	Ultrabasic	Basanite, basanite	Ultrabasic	Basanite, basanite
14	JS034	SBMT0014	47.63	2.02	14.04	12.63	0.16	9.52	9.19	3.49	0.99	0.34	Basic	Basalt, alkali	Basic	Basalt, alkali
15	JS041	SBMT0015	46.27	2.40	15.00	12.52	0.17	8.73	10.48	3.09	0.95	0.40	Basic	Basalt, alkali	Basic	Basalt, alkali
16	JS042	SBMT0016	47.72	1.93	14.59	12.29	0.16	9.76	9.16	3.23	0.88	0.27	Basic	Basalt, alkali	Basic	Basalt, alkali
17	JS044	SBMT0017	45.80	1.94	15.13	12.08	0.17	10.11	10.57	3.08	0.81	0.31	Basic	Basalt, alkali	Basic	Basalt, alkali
18	JS049	SBMT0018	46.70	2.01	15.48	11.75	0.16	8.53	10.97	3.18	0.88	0.34	Basic	Basalt, alkali	Basic	Basalt, alkali
19	JS050	SBMT0019	46.29	2.15	15.81	12.00	0.17	7.91	11.32	3.17	0.86	0.31	Basic	Basalt, alkali	Basic	Basalt, alkali
20	JS058	SBMT0020	45.67	2.31	14.46	13.28	0.17	9.21	10.03	3.42	1.08	0.38	Basic	Basalt, alkali	Basic	Basalt, alkali
21	JS059	SBMT0021	48.58	1.80	14.69	12.03	0.16	9.84	8.79	3.23	0.65	0.22	Basic	Basalt, subalkali	Basic	Basalt, subalkali
22	JS068	SBMT0022	43.61	2.57	13.66	14.20	0.19	9.55	10.00	4.29	1.21	0.72	Ultrabasic	Basanite, basanite	Ultrabasic	Basanite, basanite
23	JS069	SBMT0023	45.31	2.96	14.45	13.35	0.17	8.95	9.98	2.76	1.44	0.63	Basic	Basalt, alkali	Basic	Basalt, alkali
24	JS073	SBMT0024	49.58	2.40	14.93	11.61	0.15	7.10	9.60	3.47	0.90	0.26	Basic	Basalt, subalkali	Basic	Basalt, subalkali
25	JS076	SBMT0025	46.81	1.87	14.46	11.96	0.16	9.51	11.02	3.19	0.75	0.27	Basic	Basalt, alkali	Basic	Basalt, alkali
26	JS078	SBMT0026	42.02	2.61	11.63	14.51	0.20	12.34	8.40	5.21	2.02	1.07	Ultrabasic	Basanite, nephelinite	Ultrabasic	Basanite, nephelinite
27	JS080	SBMT0027	44.04	3.09	14.03	14.19	0.17	7.86	9.59	4.60	1.77	0.65	Ultrabasic	Basanite, basanite	Ultrabasic	Basanite, basanite
28	JS082	SBMT0028	47.39	1.82	14.49	12.39	0.17	9.53	9.71	3.36	0.79	0.35	Basic	Basalt, alkali	Basic	Basalt, alkali
29	JS083	SBMT0029	47.50	1.93	14.80	12.15	0.16	9.32	10.21	2.67	0.90	0.35	Basic	Basalt, alkali	Basic	Basalt, subalkali
30	JS090	SBMT0030	44.40	3.44	14.65	13.12	0.17	7.73	9.15	4.53	2.12	0.69	Ultrabasic	Basanite, basanite	Ultrabasic	Basanite, basanite
31	JS096	SBMT0031	47.54	2.04	13.97	12.65	0.16	9.87	9.03	3.38	1.02	0.34	Basic	Basalt, alkali	Basic	Basalt, alkali
32	JS119	SBMT0032	48.55	1.79	14.70	12.03	0.16	9.66	9.09	3.17	0.64	0.21	Basic	Basalt, subalkali	Basic	Basalt, subalkali

Table S73: Application of the new classification scheme IgRoClaMSys to Paleoproterozoic Star Lake pluton, Canada (Application study A1; Janser, 1992, 1994).

Consec	Sample name		SiO_2	TiO_2	Al_2O_3	$Fe_2O_3^t$	MnO	MgO	CaO	Na_2O	K_2O	P_2O_5	IUGS (Le Bas *et al.*, 1986) IgRoCS (Verma & Rivera-Gómez, 2013)		New scheme IgRoClaMSys (this work)		
	Original authors`	This work											Magma type	Rock type	Magma type	Rock type	Intrusive equivalent
1	LS0075	Jans0132	56.51	0.78	18.97	7.99	0.112	3.39	5.83	2.84	3.04	0.539	Intermediate	Basaltic trachyandesite, shoshonite	Intermediate	Basaltic trachyandesite, shoshonite	Monzodiorite
2	LS0076	Jans0133	50.68	0.82	18.35	9.64	0.484	4.29	7.76	4.62	2.30	1.070	Basic	Basaltic trachyandesite, mugearite	Intermediate	Basaltic trachyandesite, mugearite	Monzodiorite
3	LS0078	Jans0134	52.68	0.80	19.57	9.49	0.153	3.31	7.46	3.20	2.54	0.794	Intermediate	Basaltic trachyandesite, shoshonite	Intermediate	Basaltic trachyandesite, shoshonite	Monzodiorite
4	LS0080	Jans0135	52.81	0.88	20.69	8.44	0.132	2.78	6.82	3.73	2.65	1.057	Intermediate	Basaltic trachyandesite, shoshonite	Intermediate	Basaltic trachyandesite, shoshonite	Monzodiorite
5	LS0081	Jans0136	54.59	0.76	18.14	7.81	0.135	3.85	6.05	4.21	3.92	0.530	Intermediate	Trachyandesite, latite	Intermediate	Basaltic trachyandesite, shoshonite	Monzodiorite
6	LS0082	Jans0137	53.24	0.85	17.93	8.84	0.424	3.73	6.65	4.09	3.40	0.848	Intermediate	Basaltic trachyandesite, shoshonite	Intermediate	Basaltic trachyandesite, shoshonite	Monzodiorite
7	LS0087	Jans0138	56.66	0.82	18.94	7.82	0.112	3.11	4.33	3.68	4.00	0.530	Intermediate	Trachyandesite, latite	Intermediate	Trachyandesite, latite	Monzonite
8	LS0093	Jans0139	54.52	0.74	19.67	7.45	0.111	4.09	6.70	4.11	1.98	0.638	Intermediate	Basaltic trachyandesite, mugearite	Intermediate	Basaltic trachyandesite, shoshonite	Monzodiorite
9	LS0123	Jans0140	54.01	0.71	21.55	5.82	0.083	1.94	7.10	5.51	2.67	0.619	Intermediate	Basaltic trachyandesite, mugearite	Intermediate	Trachyandesite, latite	Monzonite
10	LS0148	Jans0141	56.08	0.67	19.40	7.54	0.412	3.14	5.76	3.56	2.64	0.793	Intermediate	Basaltic trachyandesite, shoshonite	Intermediate	Basaltic trachyandesite, shoshonite	Monzodiorite
11	LS0155	Jans0142	50.92	0.90	21.66	8.50	0.132	3.88	9.62	2.35	1.16	0.887	Basic	Subalkali basalt	Intermediate	Basaltic andesite	Gabbroic diorite
12	LS0156	Jans0143	49.30	0.83	18.82	9.41	0.370	4.58	9.82	3.26	1.51	2.108	Basic	Subalkali basalt	Intermediate	Basaltic trachyandesite, shoshonite	Monzodiorite
13	LS0157	Jans0144	52.83	0.75	17.63	8.95	0.132	5.48	7.20	2.92	3.49	0.609	Intermediate	Basaltic trachyandesite, shoshonite	Intermediate	Basaltic trachyandesite, shoshonite	Monzodiorite
14	LS0164	Jans0145	50.48	1.05	17.69	11.43	0.151	4.49	9.46	2.79	1.41	1.039	Basic	Subalkali basalt	Intermediate	Basaltic trachyandesite, shoshonite	Monzodiorite
15	LS0165	Jans0146	51.97	0.77	23.17	6.07	0.081	2.27	9.77	3.95	1.08	0.876	Intermediate	Basaltic trachyandesite, mugearite	Intermediate	Basaltic trachyandesite, mugearite	Monzodiorite
16	LS0168	Jans0147	54.48	0.76	17.86	8.40	0.143	3.53	6.51	4.08	3.59	0.644	Intermediate	Basaltic trachyandesite, shoshonite	Intermediate	Basaltic trachyandesite, shoshonite	Monzodiorite
17	LS0170	Jans0148	49.73	1.01	18.00	11.75	0.161	4.05	8.80	2.88	2.06	1.572	Basic	Subalkali basalt	Intermediate	Basaltic trachyandesite, shoshonite	Monzodiorite
18	LS0197	Jans0149	59.74	0.38	18.54	4.88	0.081	1.97	4.82	8.32	1.06	0.203	Intermediate	Trachyandesite, benmoreite	Intermediate	Andesite	Diorite
19	LS0210	Jans0150	60.68	0.35	19.86	4.40	0.051	2.33	3.87	5.52	2.74	0.193	Intermediate	Trachyandesite, benmoreite	Intermediate	Andesite	Diorite
20	LS0220	Jans0151	49.45	1.26	17.77	12.11	0.182	4.00	8.56	2.98	2.28	1.403	Basic	Potassic trachybasalt	Intermediate	Basaltic trachyandesite, shoshonite	Monzodiorite
21	LS0222	Jans0152	52.46	0.69	20.21	8.73	0.121	3.61	7.00	4.43	2.33	0.414	Intermediate	Basaltic trachyandesite, mugearite	Intermediate	Basaltic trachyandesite, shoshonite	Monzodiorite

22	LS0224	Jans0153	50.23	1.04	19.27	10.41	0.151	3.37	8.13	3.95	2.34	1.116	Basic	Basaltic trachyandesite, shoshonite	Intermediate	Basaltic trachyandesite, shoshonite	Monzodiorite
23	LS0229	Jans0154	55.77	0.67	19.75	7.64	0.112	3.25	7.19	3.14	1.74	0.733	Intermediate	Basaltic andesite	Intermediate	Basaltic trachyandesite, shoshonite	Monzodiorite
24	LS0230	Jans0155	51.76	0.92	18.62	10.17	0.152	3.84	7.65	3.02	2.81	1.056	Intermediate	Basaltic trachyandesite, shoshonite	Intermediate	Basaltic trachyandesite, shoshonite	Monzodiorite
25	LS0231	Jans0156	51.57	0.96	17.91	10.18	0.151	4.81	8.21	3.10	2.04	1.079	Basic	Basaltic trachyandesite, shoshonite	Intermediate	Basaltic trachyandesite, shoshonite	Monzodiorite
26	LS0233	Jans0157	50.00	0.77	18.44	10.32	0.152	5.37	10.18	2.32	1.33	1.133	Basic	Subalkali basalt	Intermediate	Basaltic andesite	Gabbroic diorite
27	LS0234	Jans0158	54.55	0.83	19.33	8.47	0.122	3.18	6.79	3.17	2.85	0.723	Intermediate	Basaltic trachyandesite, shoshonite	Intermediate	Basaltic trachyandesite, shoshonite	Monzodiorite
28	LS0235	Jans0159	57.71	0.51	19.24	6.75	0.121	2.97	5.96	4.02	2.39	0.332	Intermediate	Trachyandesite, latite	Intermediate	Trachyandesite, latite	Monzonite
29	LS0240	Jans0160	53.17	0.72	19.17	8.64	0.130	3.62	8.52	3.72	1.69	0.619	Intermediate	Basaltic trachyandesite, mugearite	Intermediate	Basaltic trachyandesite, shoshonite	Monzodiorite
30	LS0056	Jans0161	66.06	0.33	16.72	3.82	0.079	1.64	3.15	4.02	3.99	0.198	Acid	Trachyte	Acid	Trachydacite	Quartz monzonite
31	LS0057	Jans0162	64.22	0.35	17.59	4.20	0.071	2.01	3.97	3.79	3.58	0.214	Acid	Trachyte	Intermediate	Andesite	Diorite
32	LS0059	Jans0163	63.92	0.32	17.17	3.79	0.063	1.43	3.41	5.61	4.10	0.178	Acid	Trachyte	Acid	Trachyte	Syenite
33	LS0063	Jans0164	60.07	0.40	18.60	5.65	0.103	2.27	4.57	4.32	3.57	0.433	Intermediate	Trachyandesite, latite	Intermediate	Trachyandesite, latite	Monzonite
34	LS0064	Jans0165	59.75	0.56	17.84	6.42	0.111	2.41	4.56	4.00	3.94	0.392	Intermediate	Trachyandesite, latite	Intermediate	Trachyandesite, latite	Monzonite
35	LS0070	Jans0166	60.99	0.59	18.00	6.47	0.102	1.93	4.51	3.05	3.99	0.357	Intermediate	Trachyandesite, latite	Intermediate	Trachyandesite, latite	Monzonite
36	LS0072	Jans0167	58.55	0.57	17.71	6.37	0.224	2.61	4.60	5.04	3.90	0.427	Intermediate	Trachyandesite, latite	Intermediate	Trachyandesite, latite	Monzonite
37	LS0094	Jans0168	65.53	0.34	17.55	3.85	0.070	1.64	3.41	3.69	3.72	0.199	Acid	Dacite	Acid	Dacite	Granodiorite
38	LS0096	Jans0169	65.17	0.36	17.19	4.12	0.010	1.66	3.41	3.89	3.91	0.283	Acid	Trachyte	Acid	Dacite	Granodiorite
39	LS0097	Jans0170	63.84	0.39	17.16	4.37	0.082	1.98	3.51	4.50	3.96	0.204	Acid	Trachyte	Intermediate	Andesite	Diorite
40	LS0099	Jans0171	65.32	0.36	16.63	4.07	0.072	1.70	2.88	4.10	4.65	0.215	Acid	Trachyte	Acid	Trachyte	Syenite
41	LS0100	Jans0172	63.62	0.38	17.25	4.35	0.082	1.86	3.56	4.59	4.08	0.216	Acid	Trachyte	Intermediate	Andesite	Diorite
42	LS0101	Jans0173	63.83	0.36	17.16	4.21	0.082	1.83	3.27	4.91	4.17	0.184	Acid	Trachyte	Intermediate	Andesite	Diorite
43	LS0103	Jans0174	65.80	0.30	17.03	3.77	0.070	1.56	3.33	4.17	3.78	0.190	Acid	Trachyte	Acid	Dacite	Granodiorite
44	LS0104	Jans0175	66.25	0.35	17.14	3.99	0.072	0.17	3.41	4.49	3.89	0.225	Acid	Trachyte	Acid	Trachyte	Syenite
45	LS0105	Jans0176	60.49	0.42	18.52	5.74	0.111	2.32	4.82	4.44	2.86	0.282	Intermediate	Trachyandesite, latite	Intermediate	Trachyandesite, latite	Monzonite
46	LS0106	Jans0177	60.97	0.55	19.04	6.20	0.105	2.29	4.21	2.63	3.68	0.315	Intermediate	Andesite	Intermediate	Trachyandesite, latite	Monzonite
47	LS0147	Jans0178	62.27	0.35	19.38	4.67	0.092	1.89	4.67	3.42	3.03	0.214	Intermediate	Andesite	Intermediate	Andesite	Diorite
48	LS0151	Jans0179	54.84	0.79	19.24	7.57	0.121	3.14	6.61	3.72	3.36	0.605	Intermediate	Basaltic trachyandesite, shoshonite	Intermediate	Basaltic trachyandesite, shoshonite	Monzodiorite
49	LS0152	Jans0180	61.29	0.39	18.71	5.32	0.101	2.25	4.81	4.01	2.87	0.253	Intermediate	Trachyandesite, latite	Intermediate	Andesite	Diorite
50	LS0207	Jans0181	64.55	0.33	18.08	4.28	0.070	1.70	3.37	3.97	3.47	0.160	Acid	Trachyte	Intermediate	Andesite	Diorite
51	LS0215	Jans0182	58.95	0.37	19.01	4.79	0.080	1.91	4.89	7.16	2.52	0.329	Intermediate	Trachyandesite, benmoreite	Intermediate	Trachyandesite, benmorite	Monzonite
52	LS0236	Jans0183	61.17	0.35	19.80	4.76	0.092	2.15	5.17	3.74	2.51	0.255	Intermediate	Andesite	Intermediate	Andesite	Diorite
53	LS0276	Jans0184	64.31	0.33	17.87	4.13	0.080	1.95	3.87	3.72	3.57	0.181	Acid	Trachyte	Intermediate	Andesite	Diorite
54	LS0277	Jans0185	66.12	0.31	17.54	4.07	0.069	1.68	3.38	3.94	2.73	0.157	Acid	Dacite	Acid	Dacite	Granodiorite
55	LS0058	Jans0186	64.33	0.37	17.32	4.29	0.081	1.92	3.57	4.05	3.83	0.242	Acid	Trachyte	Intermediate	Andesite	Diorite
56	LS0061	Jans0187	63.89	0.36	17.39	4.29	0.074	1.83	3.42	4.25	4.27	0.212	Acid	Trachyte	Intermediate	Andesite	Diorite
57	LS0200	Jans0188	71.14	0.22	16.20	2.66	0.051	0.32	2.02	3.13	4.12	0.132	Acid	Rhyolite	Acid	Trachydacite	Quartz monzonite
58	LS0241	Jans0189	61.96	0.35	18.62	4.58	0.089	2.10	4.22	4.74	3.14	0.208	Intermediate	Trachyte	Intermediate	Andesite	Diorite
59	LS0242	Jans0190	64.66	0.31	17.57	3.94	0.081	1.52	3.62	4.30	3.81	0.191	Acid	Trachyte	Intermediate	Andesite	Diorite
60	LS0244	Jans0191	63.67	0.37	17.35	4.24	0.080	1.94	3.69	4.49	3.94	0.210	Acid	Trachyte	Intermediate	Andesite	Diorite
61	LS0245	Jans0192	66.83	0.30	16.64	3.50	0.071	1.31	2.98	4.05	4.16	0.151	Acid	Trachydacite	Acid	Trachydacite	Quartz monzonite
62	LS0246	Jans0193	64.70	0.36	17.67	4.16	0.079	1.73	3.65	3.94	3.50	0.197	Acid	Trachyte	Intermediate	Andesite	Diorite
63	LS0247	Jans0194	65.81	0.30	17.57	3.46	0.070	1.16	3.15	4.47	3.85	0.150	Acid	Trachyte	Acid	Trachyte	Syenite

64	LS0250	Jans0195	65.93	0.33	17.10	3.84	0.070	1.42	3.00	3.94	4.18	0.181	Acid	Trachyte	Acid	Trachyte	Syenite
65	LS0251	Jans0196	64.27	0.30	17.23	3.59	0.010	1.46	2.91	6.00	3.96	0.270	Acid	Trachyte	Acid	Dacite	Granodiorite
66	LS0254	Jans0197	66.44	0.29	17.56	3.41	0.070	1.50	3.18	3.45	3.93	0.170	Acid	Dacite	Acid	Dacite	Granodiorite
67	LS0257	Jans0198	69.06	0.24	16.46	2.83	0.059	1.09	2.61	3.40	4.12	0.129	Acid	Dacite	Acid	Trachydacite	Quartz monzonite
68	LS0259	Jans0199	67.43	0.23	16.15	2.79	0.010	1.00	2.54	5.54	4.10	0.211	Acid	Trachyte	Acid	Dacite	Granodiorite
69	LS0262	Jans0200	66.92	0.28	17.13	3.33	0.070	1.52	2.95	3.73	3.90	0.171	Acid	Dacite	Acid	Dacite	Granodiorite
70	LS0264	Jans0201	68.53	0.24	16.52	3.00	0.071	1.17	2.71	3.77	3.87	0.122	Acid	Dacite	Acid	Trachydacite	Quartz monzonite
71	LS0266	Jans0202	70.13	0.21	16.10	2.43	0.051	0.78	2.36	3.64	4.22	0.091	Acid	Rhyolite	Acid	Trachydacite	Quartz monzonite
72	LS0267	Jans0203	69.76	0.25	16.68	2.92	0.061	0.93	2.50	4.55	2.26	0.102	Acid	Dacite	Acid	Dacite	Granodiorite
73	LS0270	Jans0204	68.22	0.27	16.61	3.15	0.060	1.25	2.92	3.70	3.69	0.131	Acid	Dacite	Acid	Dacite	Granodiorite
74	LS0274	Jans0205	64.10	0.34	17.73	4.18	0.080	1.90	3.97	4.04	3.46	0.201	Acid	Trachyte	Intermediate	Andesite	Diorite
75	LS0203	Jans0206	62.30	0.36	18.95	4.75	0.081	2.35	3.43	3.84	3.76	0.182	Intermediate	Trachyte	Intermediate	Andesite	Diorite
76	LS0205	Jans0207	63.14	0.36	18.61	4.74	0.081	1.96	3.85	3.69	3.39	0.172	Acid	Trachyte	Intermediate	Andesite	Diorite
77	LS0206	Jans0208	66.74	0.28	17.17	3.53	0.041	1.38	2.99	2.20	5.50	0.163	Acid	Trachydacite	Acid	Trachydacite	Quartz monzonite
78	LS0271	Jans0209	66.64	0.32	17.03	3.48	0.061	1.70	1.63	3.86	5.07	0.202	Acid	Trachydacite	Acid	Trachydacite	Quartz monzonite

Table S74: Application of the new classification scheme IgRoClaMSys to Paleozoic volcanic rocks of Juchatengo Complex, Mexico (Application study A2; Grajales-Nishimura et al., 1999).

Consec	Sample name		SiO_2	TiO_2	Al_2O_3	$Fe_2O_3^t$	MnO	MgO	CaO	Na_2O	K_2O	P_2O_5	IUGS (Le Bas *et al.*, 1986) IgRoCS (Verma & Rivera-Gómez, 2013)		New scheme IgRoClaMSys (this work)	
	Original authors`	This work											Magma type	Rock type	Magma type	Rock type
1	I-73	GnGKD001	53.97	2.00	14.82	11.10	0.151	4.30	7.77	5.54	0.14	0.212	Intermediate	Basaltic trachyandesite, mugearite	Basic	Basaltic trachyandesite, mugearite
2	I-74	GnGKD002	53.98	1.93	14.36	11.31	0.142	3.64	9.22	5.04	0.19	0.192	Intermediate	Basaltic andesite	Basic	Basaltic trachyandesite, mugearite
3	I-75	GnGKD003	50.82	2.19	14.86	12.83	0.152	3.52	11.79	3.54	0.09	0.202	Basic	Basalt, subalkali	Basic	Basalt, subalkali
4	I-76	GnGKD004	49.89	2.48	15.55	14.47	0.164	4.49	7.60	5.00	0.13	0.226	Basic	Trachybasalt, hawaiite	Basic	Basalt, subalkali
5	I-77	GnGKD005	53.46	2.03	14.41	12.12	0.146	3.31	9.67	4.56	0.10	0.188	Intermediate	Basaltic andesite	Basic	Trachybasalt, hawaiite
6	I-78	GnGKD006	50.29	2.24	15.33	11.82	0.239	5.88	9.46	3.74	0.42	0.582	Basic	Basalt, subalkali	Basic	Trachybasalt, hawaiite
7	I-79	GnGKD007	47.71	3.22	15.25	14.96	0.240	5.77	8.93	3.33	0.20	0.397	Basic	Basalt, subalkali	Basic	Basalt, subalkali
8	I-80	GnGKD008	49.30	1.31	16.20	10.70	0.147	8.90	9.27	3.45	0.58	0.126	Basic	Basalt, subalkali	Basic	Basalt, subalkali
9	I-81	GnGKD009	50.22	1.43	16.13	10.11	0.125	8.64	8.79	3.77	0.63	0.146	Basic	Basalt, subalkali	Basic	Basalt, subalkali
10	I-82	GnGKD010	48.48	1.23	15.81	10.91	0.173	7.75	10.91	4.08	0.50	0.141	Basic	Basalt, alkali	Basic	Basalt, alkali
11	QUI-6A	GnGKD011	50.34	1.04	18.85	10.05	0.166	6.10	10.34	2.21	0.75	0.145	Basic	Basalt, subalkali	Basic	Basalt, subalkali
12	QUI-15	GnGKD012	51.29	1.38	13.50	11.15	0.206	6.93	12.37	2.85	0.11	0.206	Basic	Basalt, subalkali	Basic	Basalt, subalkali
13	QUI-17A	GnGKD013	56.02	0.70	15.52	8.99	0.164	4.62	12.92	0.94	0.01	0.113	Intermediate	Basaltic andesite	Basic	Basalt, subalkali

Table S75: Application of the new classification scheme IgRoClaMSys to Paleoproterozoic lavas and sheeted dyke rocks of JormuaOphiolite, Finland (Application study A3; Peltonen et al., 1996).

Consec	Sample name		SiO_2	TiO_2	Al_2O_3	$Fe_2O_3^t$	MnO	MgO	CaO	Na_2O	K_2O	P_2O_5	IUGS (Le Bas *et al.*, 1986) IgRoCS (Verma & Rivera-Gómez, 2013)		New scheme IgRoClaMSys (this work)	
	Original authors`	This work											Magma type	Rock type	Magma type	Rock type
1	1JD	PKHu0001	48.94	1.09	16.85	9.44	0.140	8.96	11.28	3.06	0.17	0.080	Basic	Basalt, subalkali	Basic	Basalt, subalkali
2	2JD	PKHu0002	48.63	1.14	16.74	10.30	0.208	9.06	11.04	2.63	0.18	0.079	Basic	Basalt, subalkali	Basic	Basalt, subalkali
3	3JD	PKHu0003	49.70	1.28	16.21	10.13	0.180	8.13	10.72	3.46	0.10	0.090	Basic	Basalt, subalkali	Basic	Basalt, subalkali
4	5JD	PKHu0005	49.73	1.33	17.55	9.74	0.197	10.35	7.48	3.43	0.09	0.083	Basic	Basalt, subalkali	Basic	Basalt, subalkali
5	6JD	PKHu0006	49.46	1.18	16.44	9.27	0.122	9.73	10.98	2.59	0.15	0.071	Basic	Basalt, subalkali	Basic	Basalt, subalkali
6	7JD	PKHu0007	48.39	1.16	16.22	9.84	0.163	7.73	13.97	2.32	0.11	0.092	Basic	Basalt, subalkali	Basic	Basalt, subalkali
7	JD-5	PKHu0008	50.09	1.01	15.68	9.22	0.162	9.69	11.63	2.30	0.14	0.071	Basic	Basalt, subalkali	Basic	Basalt, subalkali
8	JD-7	PKHu0009	50.38	0.91	16.68	8.86	0.161	8.56	11.46	2.73	0.19	0.060	Basic	Basalt, subalkali	Basic	Basalt, subalkali
9	525-1B	PKHu0010	49.29	0.90	16.58	10.08	0.132	10.00	10.30	2.49	0.14	0.081	Basic	Basalt, subalkali	Basic	Basalt, subalkali
10	596-1	PKHu0011	50.54	1.46	15.34	10.59	0.181	7.59	11.03	3.01	0.16	0.090	Basic	Basalt, subalkali	Basic	Basalt, subalkali
11	606	PKHu0012	49.63	1.16	16.71	9.02	0.130	8.51	11.30	3.29	0.16	0.080	Basic	Basalt, subalkali	Basic	Basalt, subalkali
12	500-3	PKHu0013	49.25	1.17	16.84	10.02	0.180	8.36	10.90	3.04	0.15	0.080	Basic	Basalt, subalkali	Basic	Basalt, subalkali
13	8JD	PKHu0014	49.34	1.34	16.15	10.78	0.191	8.76	10.19	2.95	0.22	0.080	Basic	Basalt, subalkali	Basic	Basalt, subalkali
14	1PL	PKHu0015	48.81	1.03	17.71	6.75	0.154	6.03	17.96	1.44	0.03	0.082	Basic	Basalt, subalkali	Basic	Basalt, subalkali
15	2PL	PKHu0016	52.52	1.16	16.47	7.10	0.111	8.25	10.98	3.24	0.08	0.081	Basic	Basalt, subalkali	Intermediate	Basaltic andesite
16	3PL	PKHu0017	50.94	1.07	16.55	8.69	0.121	8.69	10.98	2.78	0.11	0.070	Basic	Basalt, subalkali	Basic	Basalt, subalkali
17	4PL	PKHu0018	51.93	1.51	18.71	6.87	0.101	6.13	10.59	3.90	0.15	0.101	Basic	Basalt, subalkali	Intermediate	Basaltic andesite
18	5PL	PKHu0019	52.45	1.28	17.11	7.47	0.110	6.51	11.40	3.49	0.09	0.090	Basic	Basalt, subalkali	Intermediate	Basaltic andesite
19	502	PKHu0020	51.87	1.35	18.27	6.74	0.120	6.30	11.65	3.49	0.11	0.090	Basic	Basalt, subalkali	Intermediate	Basaltic andesite
20	526	PKHu0021	51.04	0.96	16.50	8.73	0.142	8.97	10.47	3.03	0.08	0.081	Basic	Basalt, subalkali	Basic	Basalt, subalkali
21	501-1C	PKHu0022	49.76	1.24	17.90	6.98	0.124	5.61	14.94	3.19	0.12	0.114	Basic	Basalt, subalkali	Basic	Basalt, alkali
22	568	PKHu0023	52.92	1.08	15.64	7.04	0.126	7.26	13.21	2.53	0.09	0.095	Basic	Basalt, subalkali	Intermediate	Basaltic andesite
23	1ML	PKHu0024	52.90	1.68	18.32	4.80	0.082	4.11	15.94	1.85	0.18	0.133	Basic	Basaltic trachyandesite, mugearite	Intermediate	Basaltic andesite
24	2ML	PKHu0025	49.75	1.18	17.43	8.43	0.121	7.09	13.52	2.28	0.12	0.081	Basic	Basalt, subalkali	Basic	Basalt, subalkali
25	3ML	PKHu0026	49.65	1.03	15.11	9.84	0.152	8.62	13.35	2.00	0.16	0.071	Basic	Basalt, subalkali	Basic	Basalt, subalkali
26	556	PKHu0027	49.36	0.98	16.15	9.09	0.164	7.71	15.06	1.32	0.09	0.072	Basic	Basalt, subalkali	Basic	Basalt, subalkali
27	528	PKHu0028	47.46	1.21	17.22	9.77	0.165	9.51	12.41	2.00	0.16	0.093	Basic	Basalt, subalkali	Basic	Basalt, subalkali
28	MD52	PKHu0029	39.74	1.25	19.95	11.15	0.187	11.11	14.64	1.54	0.36	0.073	Basic	Basalt, alkali	Ultrabasic	Foidite, melanephelinite
29	MD54	PKHu0030	47.85	1.28	17.18	10.20	0.174	8.14	9.96	4.77	0.36	0.092	Basic	Basalt, alkali	Basic	Trachybasalt, hawaiite
30	MD57a	PKHu0031	40.99	1.52	15.92	13.24	0.287	10.89	14.51	2.17	0.37	0.113	Basic	Basalt, alkali	Ultrabasic	Picrobasalt
31	MD58	PKHu0033	41.21	1.54	17.37	12.42	0.265	9.72	15.40	1.78	0.21	0.081	Basic	Basalt, alkali	Ultrabasic	Picrobasalt
32	MD72	PKHu0034	44.71	1.32	17.30	11.15	0.183	9.05	13.48	2.35	0.39	0.081	Basic	Basalt, alkali	Basic	Basalt, alkali
33	MD78	PKHu0035	49.03	1.12	15.88	10.14	0.173	9.92	9.05	4.34	0.25	0.081	Basic	Basalt, subalkali	Basic	Basalt, alkali

Table S76: Application of the new classification scheme IgRoClaMSys to Mesoproterozoic rocks of Delhi area, India (Application study A4; Abu-Hamatteh, 2000).

Consec	Sample name		SiO_2	TiO_2	Al_2O_3	$Fe_2O_3^t$	MnO	MgO	CaO	Na_2O	K_2O	P_2O_5	IUGS (Le Bas *et al.*, 1986) IgRoCS (Verma & Rivera-Gómez, 2013)		New scheme IgRoClaMSys (this work)	
	Original authors`	This work											Magma type	Rock type	Magma type	Rock type
1	BL1	Abuh0001	48.60	0.76	13.70	12.90	0.210	7.00	10.30	2.90	0.45	0.09	Basic	Basalt, subalkali	Basic	Basalt, subalkali
2	BL6	Abuh0002	50.20	1.78	14.10	14.10	0.250	6.20	11.00	1.10	0.51	0.22	Basic	Basalt, subalkali	Basic	Basalt, subalkali
3	BL7	Abuh0003	48.40	1.82	14.20	15.80	0.290	6.80	10.00	0.60	0.54	0.18	Basic	Basalt, subalkali	Basic	Basalt, subalkali
4	BL11	Abuh0004	48.30	1.50	14.40	14.60	0.180	7.70	8.80	1.90	1.10	0.10	Basic	Basalt, subalkali	Basic	Basalt, subalkali
5	TH1	Abuh0005	59.10	0.96	9.10	12.60	0.230	8.10	8.00	1.20	0.11	0.07	Intermediate	Andesite	Basic	Basaltic trachyandesite, mugearite
6	TH9	Abuh0006	52.80	1.08	11.80	12.70	0.260	6.60	8.80	4.40	1.12	0.16	Intermediate	Basaltic trachyandesite, mugearite	Ultrabasic	Picrobasalt
7	TH18	Abuh0007	55.30	1.77	13.40	14.50	0.230	5.00	6.20	2.40	2.20	0.20	Intermediate	Basaltic andesite	Basic	Basaltic trachyandesite, shoshonite
8	TH23	Abuh0008	56.20	1.67	13.60	11.70	0.160	4.20	7.20	4.90	0.35	0.22	Intermediate	Basaltic andesite	Basic	Basaltic trachyandesite, mugearite
9	SG12	Abuh0009	50.10	1.52	13.30	12.00	0.180	5.90	11.30	1.00	0.80	0.16	Intermediate	Basaltic andesite	Basic	Basalt, subalkali
10	DB14	Abuh0010	54.10	1.40	12.80	13.50	0.350	4.80	5.10	3.50	3.20	0.15	Intermediate	Basaltic trachyandesite, shoshonite	Ultrabasic	Basanite, basanite
11	SN15	Abuh0011	49.80	0.65	13.80	10.80	0.200	6.40	7.10	2.50	1.31	0.14	Intermediate	Basaltic andesite	Intermediate	Basaltic andesite
12	BR16	Abuh0012	48.70	1.53	13.80	13.60	0.230	7.40	9.20	3.80	0.65	0.14	Basic	Basalt, alkali	Basic	Basalt, subalkali
13	BV10	Abuh0013	48.30	1.23	12.80	11.90	0.180	9.70	11.70	2.12	0.31	0.13	Basic	Basalt, subalkali	Basic	Basalt, subalkali
14	BV27	Abuh0014	52.20	1.00	11.50	12.13	0.130	9.70	11.93	1.43	0.21	0.11	Intermediate	Basaltic andesite	Basic	Basalt, subalkali
15	GV21	Abuh0016	47.30	1.50	11.60	14.62	0.190	9.40	11.75	1.63	0.48	0.15	Basic	Basalt, subalkali	Basic	Basalt, subalkali
16	GD26	Abuh0017	43.10	1.16	12.30	15.31	0.200	11.00	14.12	1.03	0.52	0.13	Ultrabasic	Picrobasalt	Basic	Basalt, alkali
17	BG50	Abuh0018	58.70	0.73	11.50	3.80	0.350	8.80	10.80	0.50	3.36	0.14	Intermediate	Andesite	Basic	Basaltic trachyandesite, mugearite
18	BG51	Abuh0019	55.10	0.73	13.20	8.20	0.340	8.00	10.40	0.80	2.39	0.10	Intermediate	Basaltic andesite	Basic	Basaltic trachyandesite, shoshonite
19	AG53	Abuh0020	49.00	0.77	14.30	13.10	0.290	8.80	9.50	3.10	0.88	0.05	Basic	Basalt, alkali	Intermediate	Basaltic andesite
20	DR19	Abuh0021	47.30	1.99	13.80	16.00	0.240	6.40	10.80	2.00	0.34	0.21	Basic	Basalt, subalkali	Basic	Basalt, subalkali
21	DR24	Abuh0022	48.70	1.90	14.20	15.20	0.230	6.90	10.10	1.90	0.20	0.19	Basic	Basalt, subalkali	Basic	Basalt, subalkali
22	DR26	Abuh0023	48.60	2.85	13.60	14.60	0.260	6.30	10.30	1.40	0.65	0.45	Basic	Basalt, subalkali	Basic	Basalt, subalkali
23	AM39	Abuh0024	49.60	1.31	13.60	14.50	0.240	6.90	10.80	1.30	0.53	0.10	Basic	Basalt, subalkali	Basic	Basalt, subalkali
24	AM40	Abuh0025	44.10	4.26	13.90	16.70	0.240	5.60	8.70	2.30	1.73	1.21	Basic	Basalt, subalkali	Basic	Basanite, basanite

Table S77: Application of the new classification scheme IgRoClaMSys to Archaean mafic magmatism in the Kalgoorlie area of the Yilgarn craton, western Australia (Application study A5; Bateman et al., 2001).

Consec	Sample name		SiO_2	TiO_2	Al_2O_3	$Fe_2O_3^t$	MnO	MgO	CaO	Na_2O	K_2O	P_2O_5	IUGS (Le Bas *et al.*, 1986) IgRoCS (Verma & Rivera-Gómez, 2013)		New scheme IgRoClaMSys (this work)	
	Original authors`	This work											Magma type	Rock type	Magma type	Rock type
1	K 634	BCSL0001	49.83	1.76	15.04	15.20	0.199	5.48	9.48	2.07	0.70	0.234	Basic	Basalt, subalkali	Basic	Basalt, subalkali
2	K 635	BCSL0002	49.26	1.51	15.57	14.24	0.189	6.74	9.84	1.96	0.49	0.200	Basic	Basalt, subalkali	Basic	Basalt, subalkali
3	K 636	BCSL0003	50.92	1.60	18.07	11.31	0.184	4.04	10.69	2.12	0.86	0.195	Basic	Basalt, subalkali	Basic	Basalt, subalkali
4	K 637	BCSL0004	49.87	1.49	17.98	13.68	0.230	4.75	9.22	1.76	0.83	0.195	Basic	Basalt, subalkali	Basic	Basalt, subalkali
5	K 638	BCSL0005	49.84	1.79	15.32	14.39	0.224	4.61	10.76	1.66	1.16	0.247	Basic	Basalt, subalkali	Basic	Basalt, subalkali
6	K 639	BCSL0006	51.58	1.88	16.59	13.52	0.197	4.21	8.96	1.74	1.08	0.255	Intermediate	Basaltic andesite	Basic	Basalt, subalkali
7	K 640	BCSL0007	51.91	1.97	17.11	13.12	0.173	4.21	8.53	1.81	0.89	0.266	Intermediate	Basaltic andesite	Basic	Basalt, subalkali
8	K 641	BCSL0008	51.07	2.38	14.20	15.85	0.267	4.14	9.31	1.51	0.98	0.302	Basic	Basalt, subalkali	Basic	Basalt, subalkali
9	K 642	BCSL0009	49.88	1.81	14.36	15.28	0.224	4.74	10.79	1.57	1.12	0.224	Basic	Basalt, subalkali	Basic	Basalt, subalkali
10	K 643	BCSL0010	52.87	1.96	16.50	15.01	0.169	3.83	7.14	1.74	0.53	0.259	Intermediate	Basaltic andesite	Basic	Basalt, subalkali
11	K 644	BCSL0011	53.08	2.10	15.69	12.98	0.205	3.83	9.20	1.87	0.75	0.284	Intermediate	Basaltic andesite	Basic	Basalt, subalkali
12	K 645	BCSL0012	49.94	2.85	14.58	16.62	0.241	4.41	8.77	1.71	0.53	0.332	Basic	Basalt, subalkali	Basic	Basalt, subalkali
13	K 646	BCSL0013	46.50	2.34	15.35	17.44	0.244	5.42	9.62	1.47	1.30	0.326	Basic	Basalt, subalkali	Basic	Basalt, subalkali
14	K 280	BCSL0014	50.78	1.43	18.82	11.65	0.411	3.25	10.33	2.49	0.73	0.106	Basic	Basalt, subalkali	Basic	Basalt, subalkali
15	K 286	BCSL0015	48.76	1.29	16.04	16.71	0.481	3.66	11.02	1.46	0.48	0.094	Basic	Basalt, subalkali	Basic	Basalt, subalkali
16	K 287	BCSL0016	56.40	1.52	18.03	11.84	0.235	2.78	6.75	2.05	0.37	0.022	Intermediate	Basaltic andesite	Basic	Basalt, subalkali
17	K 288	BCSL0017	54.73	1.46	16.13	13.21	0.274	3.43	8.52	1.74	0.39	0.114	Intermediate	Basaltic andesite	Basic	Basalt, subalkali
18	K 289	BCSL0018	56.49	1.51	16.45	13.04	0.191	3.52	6.66	1.67	0.34	0.123	Intermediate	Andesite	Basic	Basalt, subalkali
19	K 290	BCSL0019	58.52	1.55	13.89	13.67	0.202	3.41	7.13	1.23	0.25	0.146	Intermediate	Andesite	Basic	Basaltic trachyandesite, mugearite
20	K 291	BCSL0020	54.68	1.48	17.64	12.24	0.284	3.13	7.84	2.15	0.44	0.125	Intermediate	Basaltic andesite	Basic	Basalt, subalkali
21	K 292	BCSL0021	59.77	1.50	17.05	10.80	0.143	2.75	5.49	1.95	0.42	0.121	Intermediate	Andesite	Basic	Basaltic trachyandesite, mugearite
22	K 293	BCSL0022	46.90	1.50	17.17	17.22	0.352	3.78	10.68	1.89	0.39	0.117	Basic	Basalt, subalkali	Basic	Basalt, subalkali
23	K 294	BCSL0023	50.45	1.44	15.65	14.91	0.284	3.00	11.46	1.90	0.79	0.106	Basic	Basalt, subalkali	Basic	Basalt, subalkali
24	K 295	BCSL0024	54.85	1.79	17.51	12.91	0.246	2.54	6.74	2.72	0.55	0.134	Intermediate	Basaltic andesite	Basic	Basaltic trachyandesite, mugearite
25	K 296	BCSL0025	54.88	1.76	17.52	12.27	0.270	2.38	7.42	2.87	0.51	0.135	Intermediate	Basaltic andesite	Basic	Basaltic trachyandesite, mugearite
26	K 297	BCSL0026	54.32	1.57	15.17	14.73	0.318	2.76	8.36	2.23	0.41	0.136	Intermediate	Basaltic andesite	Basic	Basalt, subalkali
27	K 298	BCSL0027	51.42	1.74	17.49	15.35	0.287	2.83	7.84	2.50	0.41	0.138	Intermediate	Basaltic andesite	Basic	Basalt, subalkali
28	K 299	BCSL0028	51.29	1.55	16.46	14.75	0.325	3.24	9.74	2.15	0.37	0.116	Basic	Basalt, subalkali	Basic	Basalt, subalkali
29	K 300	BCSL0029	51.77	1.56	17.87	13.25	0.300	2.72	9.53	2.37	0.52	0.115	Intermediate	Basaltic andesite	Basic	Basalt, subalkali
30	K 301	BCSL0030	49.31	1.48	17.70	15.64	0.266	3.52	9.46	2.15	0.36	0.104	Basic	Basalt, subalkali	Basic	Basalt, subalkali
31	K 302	BCSL0031	51.86	1.40	17.34	12.62	0.264	3.70	9.12	3.07	0.53	0.103	Intermediate	Basaltic andesite	Basic	Basalt, subalkali
32	K 303	BCSL0032	52.16	1.35	16.35	12.55	0.252	3.93	10.29	2.64	0.38	0.103	Intermediate	Basaltic andesite	Basic	Basalt, subalkali
33	K 304	BCSL0033	51.34	1.29	15.28	12.94	0.294	3.73	11.47	3.39	0.18	0.102	Basic	Basalt, subalkali	Basic	Basalt, subalkali
34	K 305	BCSL0034	50.68	1.35	15.10	14.90	0.235	4.91	10.58	1.75	0.40	0.094	Basic	Basalt, subalkali	Basic	Basalt, subalkali
35	K 306	BCSL0035	56.05	1.31	17.20	12.14	0.314	2.26	7.72	2.44	0.46	0.101	Intermediate	Basaltic andesite	Basic	Basaltic trachyandesite,

															mugearite
36	K 307	BCSL0036	52.84	1.21	17.48	11.01	0.185	2.70	11.42	2.44	0.62	0.093	Intermediate	Basaltic andesite	Basic	Basalt, subalkali
37	K 308	BCSL0037	48.13	1.25	19.29	12.49	0.236	3.02	12.43	2.49	0.55	0.094	Basic	Basalt, subalkali	Basic	Basalt, subalkali
38	K 395	BCSL0038	52.89	3.35	12.02	19.20	0.249	2.43	5.71	3.07	0.81	0.260	Intermediate	Basaltic andesite	Basic	Trachybasalt, hawaiite
39	K 396	BCSL0039	59.80	1.54	11.58	16.85	0.214	1.26	4.99	2.88	0.53	0.364	Intermediate	Andesite	Basic	Basaltic trachyandesite, mugearite
40	K 403	BCSL0041	47.79	2.83	11.58	21.10	0.295	4.77	9.27	2.27	0.01	0.088	Basic	Basalt, subalkali	Basic	Basalt, subalkali
41	K 405	BCSL0043	47.11	2.99	10.91	21.15	0.301	5.26	9.08	3.08	0.02	0.089	Basic	Basalt, subalkali	Basic	Basalt, subalkali
42	K 406	BCSL0044	46.21	2.49	12.39	20.50	0.270	5.43	8.67	3.90	0.06	0.079	Basic	Basalt, alkali	Basic	Basalt, subalkali
43	K 407	BCSL0045	49.51	2.66	11.24	20.00	0.262	4.64	9.78	1.62	0.16	0.125	Basic	Basalt, subalkali	Basic	Basalt, subalkali
44	K 397	BCSL0046	50.71	3.56	11.66	21.71	0.227	3.62	7.33	1.02	0.01	0.162	Basic	Basalt, subalkali	Basic	Basalt, subalkali
45	K 398	BCSL0047	46.77	0.92	19.30	12.58	0.173	5.97	8.00	5.90	0.30	0.076	Basic	Basanite, basanite	Basic	Basalt, alkali
46	K 399	BCSL0048	44.49	0.83	22.06	10.10	0.177	5.32	10.57	4.85	1.53	0.077	Ultrabasic	Basanite, basanite	Intermediate	Phonotephrite
47	K632	BCSL0051	49.70	1.28	15.36	14.80	0.251	5.69	10.58	1.94	0.30	0.108	Basic	Basalt, subalkali	Basic	Basalt, subalkali
48	K633	BCSL0052	51.09	1.23	14.59	13.77	0.191	6.09	10.87	1.94	0.12	0.108	Basic	Basalt, subalkali	Basic	Basalt, subalkali
49	K281	BCSL0053	43.77	1.83	22.63	17.50	0.365	3.33	7.31	2.18	0.95	0.137	Ultrabasic	Tephrite, basanite	Basic	Basalt, subalkali
50	K 350	BCSL0054	57.12	0.75	14.88	9.89	0.170	7.28	5.14	4.54	0.11	0.127	Intermediate	Andesite	Intermediate	Basaltic andesite
51	K 351	BCSL0055	53.03	0.67	12.99	10.89	0.201	9.45	8.63	3.56	0.47	0.117	Intermediate	Basaltic andesite	Intermediate	Basaltic andesite
52	K 352	BCSL0056	54.86	0.65	12.34	10.37	0.187	11.05	6.99	3.37	0.07	0.114	Intermediate	Basaltic andesite	Intermediate	Andesite
53	K 353	BCSL0057	54.63	0.62	11.56	12.04	0.231	12.77	6.06	1.47	0.50	0.105	Intermediate	Basaltic andesite	Intermediate	Basaltic andesite
54	K 354	BCSL0058	51.75	0.60	11.43	11.82	0.219	14.18	7.52	2.31	0.07	0.094	Intermediate	Basaltic andesite	Basic	Basalt, subalkali
55	K 355	BCSL0059	52.00	0.66	12.69	12.44	0.200	12.03	6.87	2.99	0.03	0.084	Intermediate	Basaltic andesite	Basic	Basalt, subalkali
56	K 357	BCSL0061	56.63	0.60	11.99	9.50	0.176	9.78	7.77	3.46	0.02	0.077	Intermediate	Andesite	Intermediate	Andesite
57	K 360	BCSL0064	51.64	1.35	16.01	13.53	0.270	4.73	8.88	2.41	1.05	0.124	Intermediate	Basaltic andesite	Basic	Basalt, subalkali
58	K 361	BCSL0065	53.96	1.32	15.78	14.04	0.277	3.60	7.00	2.87	1.04	0.122	Intermediate	Basaltic andesite	Basic	Basalt, subalkali
59	K 362	BCSL0066	52.04	1.29	15.71	14.27	0.235	4.43	8.07	1.48	2.38	0.112	Intermediate	Basaltic andesite	Basic	Basalt, subalkali
60	K 363	BCSL0067	51.69	1.63	16.75	12.32	0.424	2.89	10.48	1.52	2.10	0.195	Intermediate	Basaltic andesite	Basic	Basalt, subalkali
61	K 364	BCSL0068	49.48	1.80	15.04	13.82	0.245	4.74	11.77	2.07	0.81	0.234	Basic	Basalt, subalkali	Basic	Basalt, subalkali
62	K 365	BCSL0069	53.92	2.03	16.99	11.61	0.382	2.65	8.25	2.38	1.52	0.269	Intermediate	Basaltic andesite	Basic	Basaltic trachyandesite, mugearite
63	K 366	BCSL0070	52.44	1.93	15.93	12.45	0.384	3.20	9.51	2.91	0.98	0.260	Intermediate	Basaltic andesite	Basic	Tephrite, basanite
64	K 367	BCSL0071	50.73	1.85	15.45	13.03	0.378	3.07	10.06	2.82	2.36	0.252	Basic	Trachybasalt, potassic	Ultrabasic	Picrobasalt
65	K 369	BCSL0073	52.11	0.68	13.99	10.53	0.178	8.16	12.95	1.29	0.01	0.084	Intermediate	Basaltic andesite	Basic	Basalt, subalkali
66	K 370	BCSL0074	53.17	0.69	14.69	10.82	0.194	8.77	8.97	2.59	0.01	0.097	Intermediate	Basaltic andesite	Basic	Basalt, subalkali
67	K/371?	BCSL0075	51.86	0.69	14.55	11.46	0.196	7.87	10.65	2.62	0.02	0.098	Intermediate	Basaltic andesite	Basic	Basalt, subalkali
68	K 372	BCSL0076	51.53	0.69	14.64	10.94	0.233	7.75	10.81	3.30	0.02	0.089	Basic	Basalt, subalkali	Basic	Basalt, subalkali
69	K 374	BCSL0078	50.88	0.66	14.43	10.58	0.202	7.63	13.08	2.45	0.01	0.085	Basic	Basalt, subalkali	Basic	Basalt, subalkali
70	K 375	BCSL0079	50.42	0.68	14.21	11.27	0.198	11.39	10.05	1.66	0.04	0.094	Basic	Basalt, subalkali	Basic	Basalt, subalkali

Table S78: Application of the new classification scheme IgRoClaMSys to siliciclastic sediments from Bolivia and Chile (Sediment application study SA1; Pinto et al., 2004).

Consec	Sample name		SiO_2	TiO_2	Al_2O_3	$Fe_2O_3^t$	MnO	MgO	CaO	Na_2O	K_2O	P_2O_5	IUGS (Le Bas *et al.*, 1986) IgRoCS (Verma & Rivera-Gómez, 2013)	
	Original authors`	This work											Magma type	Rock type
1	B32_Bolivia	PHMF0001	65.40507	0.920622	14.61743	6.321604	0.102291	1.667349	3.856383	3.385843	3.375614	0.347791	Acid	Rhyolite
2	B33_Bolivia	PHMF0002	92.56332	0.202634	3.465046	1.712259	0.002	0.324215	0.364742	0.445795	0.840932	0.081054	Acid	Rhyolite
3	B34_Bolivia	PHMF0003	85.8635	0.382627	6.204757	2.409514	0.031024	0.579111	2.057911	0.889349	1.4788	0.103413	Acid	Dacite
4	B63_Bolivia	PHMF0004	87.55624	0.276074	6.308793	1.973415	0.002	0.460123	0.858896	1.104294	1.400818	0.06135	Acid	Trachydacite
5	B49_Bolivia	PHMF0005	89.52547	0.21523	5.216767	1.711592	0.002	0.481705	0.809675	0.768679	1.18889	0.081992	Acid	Rhyolite
6	B50_Bolivia	PHMF0006	72.46346	0.243592	14.38255	1.969922	0.095319	0.804914	2.658335	3.209066	4.098708	0.074137	Acid	Rhyolite
7	B56_Bolivia	PHMF0007	75.22358	0.497967	13.04878	3.231707	0.030488	0.619919	1.392276	2.825203	3.079268	0.050813	Acid	Rhyolite
8	B57_Bolivia	PHMF0008	71.00906	0.499844	14.18307	3.071957	0.052067	1.228783	1.916068	2.780381	5.071332	0.187441	Acid	Rhyolite
9	B58_Bolivia	PHMF0009	68.91344	0.577742	15.20373	3.618488	0.050679	1.206163	2.584634	3.912427	3.780661	0.152037	Acid	Rhyolite
10	B60_Bolivia	PHMF0010	67.81394	0.472839	13.45942	3.79371	0.065978	1.374533	6.586761	3.067957	3.232901	0.131955	Acid	Rhyolite
11	B61_Bolivia	PHMF0011	60.12743	0.771294	15.12408	7.109323	0.111782	2.805723	9.244355	2.280349	2.246814	0.178851	Acid	Trachydacite
12	B62_Bolivia	PHMF0012	62.89874	0.733578	14.24919	6.257641	0.088919	2.789819	7.780371	2.345226	2.656441	0.200067	Acid	Trachydacite
13	A26_Chile	PHMF0013	64.82956	0.70086	15.57821	5.606881	0.106191	2.421153	4.343209	2.973346	3.270681	0.169905	Acid	Dacite
14	A1_Chile	PHMF0014	60.09476	0.839884	16.81921	7.537418	0.064606	3.036503	5.868418	2.831916	2.71347	0.193819	Intermediate	Andesite
15	A2_Chile	PHMF0015	72.89485	0.502723	13.51068	3.85421	0.052367	1.288228	1.895685	2.618349	3.257227	0.125681	Intermediate	Andesite
16	A7_Chile	PHMF0016	71.60108	0.64543	13.36665	5.080158	0.062461	1.207579	1.686446	2.977306	3.23756	0.135332	Intermediate	Andesite
17	A8_Chile	PHMF0017	66.60269	0.586479	15.51504	5.203668	0.074643	1.354233	4.691832	2.921732	2.889742	0.159949	Intermediate	Andesite
18	A18_Chile	PHMF0018	60.02491	0.674554	15.8572	6.693649	0.103778	5.261519	6.330428	2.895392	2.013284	0.145289	Acid	Rhyolite
19	A20_Chile	PHMF0019	59.57518	0.733986	15.70285	6.639235	0.066726	3.56984	6.983986	3.647687	2.891459	0.189057	Acid	Trachydacite
20	C1_Chile	PHMF0020	62.21762	0.746114	16.1658	6.238342	0.082902	3.481865	4.963731	3.34715	2.621762	0.134715	Acid	Dacite
21	L2_Chile	PHMF0021	64.14185	0.739233	15.26677	6.181701	0.085708	2.260553	4.681808	3.428327	3.07478	0.139276	Intermediate	Andesite
22	S1_Chile	PHMF0022	63.11467	0.728878	15.26537	6.292988	0.082127	3.64439	4.383534	3.100298	3.233754	0.153988	Intermediate	Andesite
23	S8_Chile	PHMF0023	60.64905	0.704153	17.5222	6.25574	0.081641	3.010511	5.612818	3.939177	2.05123	0.173487	Intermediate	Andesite
24	A10_Chile	PHMF0024	60.33184	0.936482	15.80822	8.29601	0.111971	3.287866	5.099756	3.440554	2.442997	0.2443	Intermediate	Andesite
25	M12_Chile	PHMF0025	60.65153	0.729627	16.24705	6.484431	0.082211	4.305827	5.662316	3.000719	2.671873	0.164423	Intermediate	Andesite
26	A9_Chile	PHMF0026	58.39982	0.728408	19.53983	6.914094	0.265927	5.283848	4.451382	2.092727	2.150538	0.17343	Intermediate	Andesite
27	S2_Chile	PHMF0027	58.34207	0.817439	20.22637	7.440788	0.0524	1.771117	5.98407	3.877594	1.215678	0.27248	Intermediate	Andesite
28	S3_Chile	PHMF0028	62.5179	0.777255	15.7701	6.350992	0.10227	3.344242	4.796482	3.10902	3.037431	0.194314	Intermediate	Andesite
29	N2_Chile	PHMF0029	61.63904	0.586842	18.37743	5.055081	0.072068	2.162051	5.683105	3.665191	2.563575	0.195614	Intermediate	Basaltic andesite
30	N3_Chile	PHMF0030	60.85694	0.715842	17.23208	6.120967	0.082996	3.319846	5.519245	3.361345	2.635128	0.155618	Intermediate	Andesite
31	N5_Chile	PHMF0031	58.98646	0.800164	16.08535	7.45794	0.102585	4.821502	5.919163	3.149364	2.482561	0.194912	Intermediate	Andesite
32	P10_Chile	PHMF0032	67.10771	0.537523	14.86459	5.209841	0.072359	1.829646	3.380194	4.145131	2.739301	0.113707	Intermediate	Andesite
33	N8_Chile	PHMF0033	57.86641	0.812493	15.23689	7.565685	0.105519	4.178538	6.858711	4.727234	2.479688	0.16883	Intermediate	Andesite
34	M8_Chile	PHMF0034	63.05812	0.808039	15.47705	8.764115	0.290065	2.216927	3.750129	3.118202	2.372319	0.145033	Intermediate	Andesite
35	A4_Chile	PHMF0035	60.83479	0.712095	18.1858	5.828221	0.054777	3.757669	6.058282	2.651183	1.785714	0.131464	Acid	Dacite
36	A5_Chile	PHMF0036	65.40507	0.920622	14.61743	6.321604	0.102291	1.667349	3.856383	3.385843	3.375614	0.347791	Intermediate	Trachyandesite, benmorite
37	A17_Chile	PHMF0037	92.56332	0.202634	3.465046	1.712259	0.002	0.324215	0.364742	0.445795	0.840932	0.081054	Intermediate	Andesite
38	A24_Chile	PHMF0038	85.8635	0.382627	6.204757	2.409514	0.031024	0.579111	2.057911	0.889349	1.4788	0.103413	Intermediate	Andesite

Table S79: Application of the new classification scheme IgRoClaMSys to siliciclastic sediments from Enugu, southeastern Nigeria (Sediment application study SA2; Odoma et al., 2015).

Consec	Sample name		SiO_2	TiO_2	Al_2O_3	$Fe_2O_3^t$	MnO	MgO	CaO	Na_2O	K_2O	P_2O_5	IUGS (Le Bas *et al.*, 1986) IgRoCS (Verma & Rivera-Gómez, 2013)	
	Original authors`	This work											Magma type	Rock type
1	Enu 1.1	OOOI0001	63.98122	1.779947	24.03488	7.39057	0.06459	0.745268	0.069558	0.260844	1.422219	0.250907	Basic	Basaltic trachyandesite, mugearite
2	Enu 1.2	OOOI0002	71.37464	1.970383	18.47387	5.406985	0.034098	0.560183	0.053583	0.401871	1.626967	0.097423	Basic	phonolite
3	Enu 1.3	OOOI0003	72.95741	1.994596	18.93859	3.223589	0.018962	0.592572	0.053331	0.426651	1.69594	0.098367	Acid	Rhyolite
4	Enu 1.4	OOOI0004	68.68379	1.890905	20.4919	6.404481	0.041398	0.450505	0.045051	0.37745	1.528065	0.086448	Basic	phonolite
5	Enu 2.1	OOOI0006	57.62342	1.705941	24.35518	14.12433	0.015574	0.503157	0.025158	0.203659	1.219556	0.224025	Basic	Basaltic trachyandesite, mugearite
6	Enu 2.2	OOOI0007	62.03986	2.037219	23.93343	9.784407	0.010792	0.491619	0.047963	0.227823	1.26262	0.164273	Basic	Basaltic trachyandesite, mugearite
7	Enu 2.3	OOOI0008	64.77857	1.808157	25.8644	4.338165	0.009405	0.717149	0.041148	0.258644	2.064449	0.119917	Basic	Basaltic trachyandesite, mugearite

Table S80: Application of the new classification scheme IgRoClaMSys to lagoon sediments from south-west Japan (Sediment application study SA3; Ishiga et al., 2000).

Consec	Sample name		SiO_2	TiO_2	Al_2O_3	$Fe_2O_3^t$	MnO	MgO	CaO	Na_2O	K_2O	P_2O_5	IUGS (Le Bas *et al.*, 1986) IgRoCS (Verma & Rivera-Gómez, 2013)	
	Original authors`	This work											Magma type	Rock type
1	SB-1-1	INST0001	62.82	0.82	21.57	7.12	0.120	2.16	0.71	2.34	2.23	0.17	Intermediate	Basaltic andesite
2	SB-1-5	INST0002	59.60	0.80	26.96	6.61	0.110	1.91	0.57	1.86	2.26	0.16	Intermediate	Phonotephrite
3	SB-1-10	INST0003	63.78	0.86	21.79	7.12	0.100	1.89	0.52	1.70	2.20	0.16	Intermediate	Basaltic andesite
4	SB-1-15	INST0004	62.83	0.87	22.64	6.99	0.090	1.98	0.55	1.61	2.37	0.15	Intermediate	Basaltic andesite
5	SB-1-20	INST0005	63.35	0.88	19.48	8.10	0.120	2.44	0.50	1.64	2.57	0.12	Intermediate	Basaltic andesite
6	SB-1-25	INST0006	63.38	0.87	19.38	8.14	0.110	2.50	0.52	1.72	2.62	0.12	Intermediate	Basaltic andesite
7	SB-1-30	INST0007	63.35	0.85	19.35	7.90	0.050	2.53	0.63	1.93	2.62	0.12	Intermediate	Basaltic andesite
8	SB-1-35	INST0008	63.66	0.84	19.38	7.42	0.120	2.56	0.54	2.05	2.63	0.13	Intermediate	Basaltic andesite
9	SB-1-40	INST0009	62.56	0.84	19.65	6.96	0.170	2.61	0.64	2.09	2.56	0.13	Intermediate	Phonotephrite
10	SB-1-45	INST0010	62.08	0.82	19.07	7.60	0.210	2.64	0.63	2.12	2.62	0.14	Intermediate	Phonotephrite
11	SB-1-50	INST0011	63.00	0.83	19.09	7.48	0.190	2.65	0.86	2.20	2.66	0.14	Intermediate	Basaltic andesite
12	SB-1-55	INST0012	63.06	0.85	19.01	7.71	0.190	2.68	0.76	2.13	2.73	0.13	Intermediate	Basaltic andesite
13	SB-1-60	INST0013	63.22	0.84	18.94	7.41	0.170	2.60	0.89	2.27	2.70	0.13	Intermediate	Basaltic andesite
14	SB-1-65	INST0014	63.94	0.86	19.32	6.85	0.160	2.69	0.55	2.14	2.74	0.12	Intermediate	Phonotephrite
15	SB-1-70	INST0015	63.51	0.76	18.59	6.72	0.230	2.47	1.68	2.56	2.58	0.13	Intermediate	Basaltic andesite
16	SB-1-75	INST0016	63.20	0.84	18.65	6.85	0.140	2.53	1.88	2.14	2.72	0.12	Intermediate	Basaltic andesite

17	SB-1-80	INST0017	63.53	0.88	20.11	7.15	0.110	2.58	0.44	2.06	2.79	0.12	Intermediate	Phonotephrite
18	SB-1-85	INST0018	63.80	0.88	19.66	6.47	0.120	2.48	1.05	2.02	2.76	0.12	Intermediate	Basaltic andesite
19	SB-1-90	INST0019	65.24	0.87	19.79	5.81	0.060	2.34	0.44	2.14	2.81	0.11	Intermediate	Basaltic andesite
20	SB-1-95	INST0020	64.85	0.86	19.61	6.37	0.050	2.32	0.48	2.19	2.75	0.11	Intermediate	Basaltic andesite
21	SB-1-100	INST0021	64.68	0.86	19.37	6.68	0.050	2.26	0.51	2.26	2.67	0.11	Intermediate	Basaltic andesite
22	SB-1-105	INST0022	65.76	0.85	18.94	6.11	0.050	2.20	0.59	2.20	2.68	0.11	Intermediate	Basaltic andesite
23	SB-1-110	INST0023	65.31	0.84	19.59	6.19	0.040	2.24	0.57	2.08	2.72	0.11	Intermediate	Basaltic andesite
24	SB-1-115	INST0024	64.31	0.82	18.83	5.85	0.060	2.28	1.58	1.96	2.63	0.12	Intermediate	Basaltic andesite
25	SB-1-120	INST0025	64.89	0.83	18.80	5.96	0.060	2.23	2.23	1.79	2.71	0.11	Intermediate	Andesite
26	SB-1-125	INST0026	65.50	0.85	18.90	6.31	0.060	2.15	0.93	1.84	2.70	0.12	Intermediate	Basaltic andesite
27	SB-1-130	INST0027	65.74	0.87	19.40	5.92	0.030	2.09	0.41	1.90	2.72	0.11	Intermediate	Basaltic andesite
28	SB-1-135	INST0028	66.09	0.88	19.26	6.18	0.030	2.05	0.36	1.85	2.68	0.1	Intermediate	Basaltic andesite
29	SB-1-140	INST0029	65.23	0.87	19.32	6.14	0.060	2.21	0.89	1.97	2.39	0.11	Intermediate	Basaltic andesite
30	SB-1-145	INST0030	66.11	0.87	18.96	6.27	0.040	2.00	0.64	1.88	2.63	0.1	Intermediate	Basaltic andesite
31	SB-1-150	INST0031	65.76	0.88	19.45	6.17	0.040	2.10	0.44	1.85	2.72	0.11	Intermediate	Basaltic andesite
32	SB-1-155	INST0032	65.31	0.88	19.44	6.31	0.040	2.10	0.55	1.85	2.71	0.11	Intermediate	Basaltic andesite
33	SB-1-160	INST0033	65.16	0.87	19.32	6.14	0.050	2.13	0.49	1.79	2.74	0.11	Intermediate	Basaltic andesite
34	SB-1-165	INST0034	65.84	0.88	19.41	6.08	0.040	2.10	0.47	1.38	2.78	0.11	Intermediate	Basaltic andesite
35	SB-1-169	INST0035	65.19	0.87	19.13	6.78	0.040	2.16	0.55	1.80	2.75	0.11	Intermediate	Basaltic andesite
36	SB-1-173	INST0036	66.00	0.89	19.63	5.81	0.040	2.10	0.46	1.72	2.78	0.11	Intermediate	Basaltic andesite
37	SB-1-177	INST0037	65.35	0.88	19.16	6.24	0.040	2.04	0.62	1.86	2.67	0.11	Intermediate	Basaltic andesite
38	SB-1-181	INST0038	66.04	0.88	19.10	5.90	0.040	2.01	0.46	1.91	2.69	0.1	Intermediate	Basaltic andesite
39	SB-1-185	INST0039	64.36	0.87	18.76	7.45	0.110	2.02	0.66	1.80	2.59	0.14	Intermediate	Basaltic andesite
40	SB-1-189	INST0040	66.58	0.88	18.44	6.30	0.040	1.91	0.46	1.85	2.60	0.1	Intermediate	Basaltic andesite
41	SB-1-194	INST0041	64.97	0.87	19.05	7.04	0.050	2.17	0.85	1.67	2.66	0.12	Intermediate	Basaltic andesite
42	SB-1-199	INST0042	66.72	0.90	18.86	5.88	0.040	1.93	0.66	1.81	2.54	0.1	Intermediate	Basaltic andesite
43	SB-1-203	INST0043	69.78	0.85	16.00	5.50	0.030	1.80	0.67	2.17	2.24	0.08	Acid	Dacite
44	SB-1-209	INST0044	69.05	0.90	17.47	5.33	0.060	1.86	0.56	1.70	2.37	0.12	Intermediate	Basaltic andesite
45	SB-1-214	INST0045	70.40	0.87	18.18	4.88	0.030	1.88	0.49	1.70	2.26	0.1	Acid	Dacite
46	SB-1-219	INST0046	71.81	0.75	15.54	4.56	0.100	1.28	0.96	2.26	2.40	0.08	Acid	Dacite
47	SB-1-224	INST0047	73.56	0.67	15.39	2.25	0.020	1.01	1.11	2.50	2.56	0.06	Acid	Rhyolite
48	SB-1-229	INST0048	76.13	0.51	13.81	1.81	0.030	0.84	0.14	2.74	2.74	0.04	Acid	Rhyolite
49	SB-1-233	INST0049	70.99	0.83	15.20	5.44	0.040	1.54	0.54	1.76	2.65	0.09	Acid	Dacite